20442
Bloch

Number 7 Volume 20 1956

P11

BULLETIN
of the
Academy of Sciences of the USSR
- Physical Series -

(Izvestiia Akademii Nauk SSSR)
(Seriia fizicheskaia)

Reproduction rights reserved
by

Columbia Technical Translations
5 Vermont Avenue
White Plains, New York

Single Issues Annual Subscription
$20 $215

Transactions of the Fifth All-Union Conference on the Application of X-rays to the Investigation of Materials
(Leningrad 23-29 June 1955)

Continued from Vol. 20, No. 6

INFLUENCE OF HEAT AND MECHANICAL TREATMENT ON THE THERMAL FACTOR IN SCATTERING OF X-RAYS BY SOLID SOLUTIONS

- V.A. Il'ina, V.K. Kritskaia, G.V. Kurdiumov & T.I. Stelletskaia

Investigations of the interaction between the atoms in crystals of iron alloyed with different elements have shown that the alloying may have an appreciable influence on the strength of the interatomic bonds of α-iron.[1,2] The character and magnitude of the changes in the strength of the bonds depend on the nature of the alloying element and its concentration in the solid solution.[1-3]

It has been found, however, that the strength of the interatomic bonds in some solid solutions can be altered substantially only as a result of thermal or mechanical treatment not leading to a change in the chemical composition of the α-phase.[1,2,5] Investigation of these changes is of great interest from the point of view of clarifying the physical nature of the strength of metals and alloys.

As we showed earlier,[6] the bond strengths are the same in plastically deformed iron and iron annealed at different temperatures. This means that different types of treatment of a material whose crystals consist of atoms of only one kind does not lead to changes in the bond strength. This also indicates that the changes in the crystal lattice produced by plastic deformation are not in themselves the cause of changes in the strength of the interatomic bonds.

The fact that the change in bond strength with the type of treatment has beenobserved only in solid solutions, i.e., in materials whose crystal lattice is formed by atoms of different elements, gives reason to assume that the reason for these changes lies in alterations of the atomic distribution in the crystal lattice. In the case of pure metals redistribution of the atoms can have no effect, for if certain atoms exchange places in the crystal lattice, there is no resultant change in the lattice energy (inasmuch as all the atoms are identical).

The purpose of the present work was to study the influence of heat treatment and deformation on the strength of the interatomic bonds in crystals of iron alloyed with chromium, nickel, manganese and tungsten. The chemical composition of the investigated alloys is given in Table 1.

Table 1

Chemical composition of the investigated iron alloys (in %)

Alloy	C	Mn	Si	Ni	W	S	P	Cr	Cu	Al
Fe-Cr	0,014	Сл.	0,011	—	—	0,019	Сл.	8,05	—	
Fe-Mn	0,02	2,90	0,02	—	—	0,017	0,003	—	—	—
Fe-W	0,02	0,02	Сл.	—	1,8	0,017	0,001	—	—	—
Fe-W	0,03	0,20	0,047	0,14	5,24	0,025	0,002	0,11	0,04	0,02
Fe-Ni	0,02	Сл.	0,05	4,0	—	0,016	0,001	—	—	—

All the investigated alloys were single-phase solid solutions. The treatments employed (deformation, heating, quenching and drawing) did not change the composition of the α-phase. Changes in the magnitude of the atomic interaction in the crystals of the investigated alloys were determined from the changes in the thermal factor of scattering intensity [change in the relative intensity of lines with a change in temperature], knowledge of which made it feasible to determine the amplitude of the atomic thermal vibrations and the characteristic temperature. The x-ray patterns were registered using molybdenum radiation at two temperatures: room temperature and that of liquid nitrogen. The samples were prepared of powder obtained by filing and had the form of cylinders 0.9 mm in diameter.

The procedure for determining the thermal factor in the intensity of x-ray scattering and the method of computing the characteristic temperature are described in Refs. 3 and 7.

Experimental Results

Fe-Cr alloy. The alloy of iron with 8% chromium was investigated after great plastic deformation, after annealing at 680°, in the quenched state and after tempering at 680°.

The experimental data for this alloy are listed in Table 2.

Table 2

Values of the characteristic temperature θ and the root mean square displacement $\sqrt{\overline{U^2}}$ of the atoms of the Fe + 8% Cr alloy after different treatments

Treatment	$\frac{\alpha_1}{\alpha_2}=\frac{(I_{(211)}/I_{(510)})_{23^\circ}}{(I_{(211)}/I_{(510)})_{-185^\circ}}$	$\overline{\Delta U^2}=\overline{U^2_{23}}-\overline{U^2_{-185}}$, Å	$\sqrt{\overline{U^2_{23^\circ}}}$, Å	θ°
Deformation by filing...	1,27	0,0074	0,115	430
Annealing at 680° after deformation.....	1,14	0,0041	0,090	560
Quenching...	1,27	0,0074	0,115	430
Tempering at 680° after quenching.	1,14	0,0041	0,090	560
Heating at 680° then deformation by filing...	1,27	0,0074	0,115	430

The changes in the thermal factor of scattering intensity, the corresponding changes in the mean square of the displacement of the atoms in the thermal vibrations and the values of the characteristic temperature calculated on the basis of this data show in which direction the binding forces change in this alloy depending on that character of the treatment. Thus after strong plastic deformation the change in the ratio of the intensity of the (211) and (510) interference lines when the temperature of the specimen is increased from -180° to +23° amounts to 27%. From this change one can directly determine the change in the mean square displacement $\overline{\Delta U^2}$ of the atoms in the thermal vibrations and calculate the characteristic temperature θ.

Heating of the previously deformed alloy for two hours at 680° led to an appreciably smaller (14% instead of 27%)change in the thermal factor over the same temperature interval; this must be regarded as a consequence of a reduction of the amplitude of the atomic thermal vibrations, i.e., a consequence of an increase in the strength of the interatomic bonds. As may be seen from Table 2, the value of $\overline{\Delta U^2}$ in this case is appreciably smaller than for the deformed sample, while the characteristic temperature is correspondingly higher (θ = 430° for the deformed alloy and 560° for the sample annealed after deformation at 680°).

Quenching yielded the same effect as strong plastic deformation, i.e., led to a reduction of the binding forces ($\overline{\Delta U^2}$ and θ in both cases were identical).

Finally, after drawing of the quenched specimen at 680° the ratio $\frac{[I_{(211)}/I_{(510)}]_{23^\circ}}{[I_{(211)}/I_{(510)}]_{-185^\circ}}$ decreased to 1.14 just as in the case of annealing of the deformed samples. Hence tempering after quenching, just as annealing after deformation, leads to an increase in the strength of the interatomic bonds in the crystals of the Fe-Cr solid solution.

At the bottom of Table 2 we give the data obtained for a deformed specimen, the deformation of which was preceded by heating to 680°. These data clearly show the complete reproducibility of the processes occurring in the solid solution as a result of the various treatments leading to strengthening or weakening of the atomic bonds.

Fe-Mn alloy. The most appreciable effect as regards changes in the characteristics of the binding forces as a function of the treatment were observed in the alloy of iron with 3% manganese.

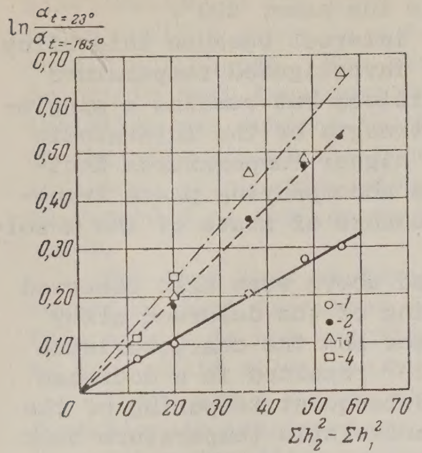

Fig. 1. Logarithmic dependence of the ratio of intensities at 23° and -180° on the difference between the sums of the squares of the indices of the reflecting faces for a deformed sample of Fe + 3% Mn alloy after annealing at different temperatures: 1) 610°, 2) 750°, 3) 800°, 4) deformed state prior to annealing.

It was established in the experiments that the values of θ and $\overline{U^2}$ characterizing the strength of the interatomic bonds change very appreciably with the treatment to which the alloy is subjected. We found that after heating of a deformed specimen for 2 hours at 610° the characteristic temperature of the solid solution increased to 630° (from 430° for the deformed specimen). Annealing of the deformed alloy for the same period at 750° increases θ only to 470°. After heating to 800° the thermal vibrations of the atoms in the lattice of the solid solution have the same amplitude as after strong plastic deformation: in both cases $\theta = 430°$ and $\sqrt{\overline{U^2}} = 0.115$ A. The same value of θ was obtained for the quenched alloy. The experimental data for the Fe-Mn alloy are shown in Fig. 1, in the form of the logarithmic dependence of the ratio of the intensities $\frac{[I_{h_1k_1l_1}/I_{h_2k_2l_2}]_{23°}}{[I_{h_1k_1l_1}/I_{h_2k_2l_2}]_{-185°}}$ on the difference between the sum of the squares of the indices of the reflecting faces after different treatments of the solid solution.

The values of $\overline{\Delta U^2}$ and θ were determined from the slope (tangent) of the curves in Fig. 1 by means of the following expression[3,7]

$$\ln\frac{\alpha_1}{\alpha_2} = A\overline{\Delta U^2}(\Sigma h_2^2 - \Sigma h_1^2) = B\varphi(\Theta)(\Sigma h_2^2 - \Sigma h_1^2).$$

The minimal slope is exhibited by the straight line representing the specimen tempered at 610°; this corresponds to a minimum value of the root mean square amplitude of the thermal vibrations ($\sqrt{\overline{U^2}}$) and, consequently, to the highest value of the characteristic temperature θ.

Fe-W alloy. We investigated two iron-tungsten alloys: Fe + 0.6% W and Fe + 1.7% W.

The 0.6% W alloy was investigated in the deformed state after annealing at 650 and 820°, while the 1.7% W alloy was investigated after heating at 850°.

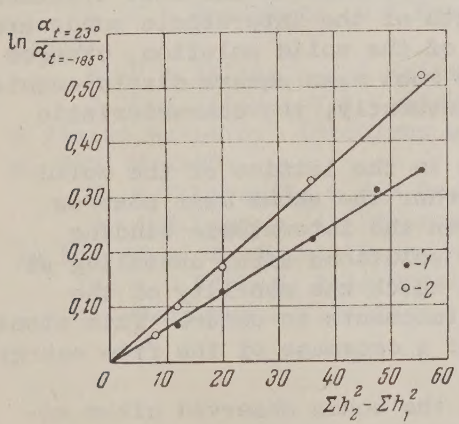

Fig. 2. Same as Fig. 1 but for a deformed sample of Fe + 0.6% W alloy annealed at: 1) 650°, 2) 820°.

Comparison of the determined values of θ and $\overline{U^2}$ for the two alloys subjected to approximately the same heat treatment (annealing at 820 and 850°) showed that the interatomic binding forces are stronger in the solid solution with the higher tungsten concentration. For the 1.7% W alloy the characteristic temperature is 540°, while for the 0.6% W alloy it is 490°. The experimental data for the latter alloy are shown in Fig. 2. The difference in the slopes of the two lines corresponding to different annealing temperatures indicates that the values of $\overline{\Delta U^2}$ and θ for this alloy change markedly with the heat treatment.

Just as in the case of the Fe-Mn alloy, annealing of the deformed Fe + 0.6% W alloy at 650° results in an increase in the strength of the interatomic bonds, while annealing at a higher temperature (820°) does not result in any appreciable increase. The characteristic temperature of the Fe + 0.6% W alloy after deformation and after annealing at 820° is the same: 490°.

Investigation of the Fe-W alloy is of particular interest because this alloy in the given range of tungsten concentrations and the investigated temperature intervals (650-850°) does not undergo any phase transitions but remains a single-phase α-solid solution. The observed fact that the strength of the interatomic bonds does not increase when the alloy is annealed at higher temperatures indicates that this effect is not connected with processes accompanying phase transitions but is a consequence of a temperature-induced change of state of the α-solution.

Fe-Ni alloy. Effects analogous to those described above were also observed for the Fe + 4% Ni alloy.[5] In this case after annealing of the deformed alloy at 600°, the strength of the interatomic bonds increased and the characteristic temperature rose from 460 to 540°. Quenching from 1020° resulted in a decrease of the characteristic temperature from 540 to 430°. Subsequent tempering of the hardened sample at 600° brought the value of the characteristic temperature back to its initial value, i.e., 540°. Thus for this alloy, also, we established the possibility of strengthening or weakening of the interatomic bonds by successive appropriate heat treatments (for example, quenching — θ = 430°; tempering — θ = 540°; quenching — θ = 430°, etc.). The data obtained for the Fe + 4% Ni alloy are listed in Table 3.

Table 3

Values of θ and $\sqrt{\overline{U^2}}$ of the Fe + 4% Ni alloy after different heat treatments

Treatment	$\frac{\alpha_1}{\alpha_2}=\frac{(I(211)/I(510))_{23^\circ}}{(I(211)/I(510))_{-185}}$	$\overline{\Delta U^2}=\overline{U^2}_{23}-\overline{U^2}_{-185^\circ}$, Å	$\sqrt{\overline{U^2}_{23^\circ}}$, Å	θ°
Deformation by filing	1,22	0,0062	0,108	460
Annealing at 600° after deformation	1,15	0,0046	0,095	540
Quenching from 1020°	1,27	0,0074	0,115	430
Tempering at 600° after quenching	1,15	0,0046	0,095	540

Discussion of results

Our investigation of the binary alloys of iron with chromium, nickel, manganese and tungsten showed that the strengths of the interatomic bonds in the crystals of these solid solutions can change appreciably as a result of plastic deformation and heat treatment. It appears probable that the changes in the strength of the interatomic bonds are due to redistribution of the atoms in the lattice of the solid solution, changes in the short-range order, as a result of which the root mean square displacements of the atoms in their thermal vibrations and, consequently, the characteristic temperature as well can change.

For there to occur a regroupment of the atoms in the lattice of the solid solution leading to establishment of short-range order the atoms must possess sufficient mobility. As indicated above increase in the interatomic binding forces was observed for all the investigated solid solutions after annealing at temperatures of 600-700°, i.e., at temperatures at which the mobility of the atoms is already sufficiently high for atomic displacements to occur. This atomic regrouping process must proceed in the direction of a decrease of the free energy of the solid solution.

The diminution of the effect of strengthening the bonds observed after annealing at 800° (Fe-Mn and Fe-W alloys) may be connected with the fact that heating to elevated temperatures, at which the thermal vibrations of the atoms have greater amplitude, leads to a reduction of the degree of short-range ordering. The absence of the effect of strengthening the interatomic bonds in hardened alloys (Fe-Cr, Fe-Mn and Fe-Ni) is apparently due to the fact that the disordered distribution of the atoms, corresponding to the high temperature, is fixed by the rapid cooling since in a martensite γ-α-transition the distribution of the atoms should not change. The strengthening of the interatomic bonds observed after appropriate heat treatment in all the investigated alloys disappeared as soon as the alloy was subject to plastic deformation. If the assumption that the increase in the strength of the bonds is due to enhancement of the short-range order, the influence of plastic deformation and the weakening of the interatomic bonds must be regarded as the consequence of the reduction of the degree of short-range order.

The fact that we have detected changes in the strength of the bonds as a result of heat treatment in a number of different solid solutions indicates that this effect is not peculiar to one or even a few alloys, but is presumably common to many solid solutions.

There are a number of studies[8-11] devoted to an investigation of the possible formation in single-phase solid solutions under certain conditions of concentration inhomogeneities (short-range order, atomic "complexes", etc.) localized in very small volumes. The formation or destruction of such inhomogeneities presumably results in changes in certain properties (the conductivity, hardness, etc.) of the solid solutions.

Our investigations have shown that there is also a change in the magnitude of the interatomic binding forces. Further investigation of this problem would be of interest and should be directed both towards clarifying the nature of the distribution of the atoms in the solid solution after different heat treatments and towards studying the changes in the different properties of the alloys that are influenced by processes occurring in submicroscopic volumes of the solution.

Institute of Metallurgy and Metal Physics
of the Central Scientific Research Institute of Ferrous Metallurgy

References

1. V.K.Kritskaia, G.V.Kurdiumov & T.I.Steletskaia, Doklady AN SSSR, 98, 63 (1954).
2. V.A.Il'ina, V.K.Kritskaia, Doklady AN SSSR, 100, 69 (1955).
3. G.V.Kurdiumov, V.K.Kristkaia & N.M.Nodia, in "Problemy metallurgii" (Problems of metallurgy), M.-L. 1953; Zhur. tekh. fiz., 25, 177 (1955).
4. G.V.Kurdiumov & N.T.Travina, Zhur. tekh. fiz., 25, 77 (1955).
5. V.K.Kritskaia, G.V.Kurdiumov & L.V.Tikhonov, Doklady AN SSSR, 102, 271 (1955).
6. V.A.Il'ina & V.K.Kritskaia, Doklady AN SSSR, 87, 107 (1952).
7. V.A.Il'ina, V.K.Kritskaia, & G.V.Kurdiumov, in "Problemy metallovedeniia i fiziki metallov" (Problems of metallurgy and the physics of metals) No. 2, p. 222, M. 1951.
8. B.F.Livshits & M.P.Ravdel', Doklady AN SSSR, 93, 1033 (1953).
9. A.G.Lesnik, in "Voprosy fiziki metallov i metallovedeniia" (Questions in the physics of metals and metallurgy), No. 5, Kiev, 1954.
10. I.C.Fisher, Acta Metallurg., 2, 9 (1954).
11. T.Assmus & T.Pfeifer, ZS. f. Metallkunde, 10, 342 (1951).

ON THE INTENSITY OF X-RAY SCATTERING BY SOLID SOLUTIONS

- V.I.Iveronova & A.P.Zviagina

Investigations of the structure and properties of solid solutions are constantly gaining in importance. Whereas even a few years ago a solid solution could justifiably be regarded as a homogeneous (in a volume extending over several unit cells) mixture of the atoms of both components distributed at random over the lattice points (except in the presence of superstructure), at the present we must admit that the structure of solid solutions is highly complex. The presence of superstructure is no longer the exception, but the rule for alloys of stoichiometric proportions.

A solid solution close to saturation can hardly be considered homogeneous; it can be expected to comprise significant fluctuations in concentration. Finally, even in alloys, which are far from having a rational stoichiometric composition and are far from being saturated, we can expect to find a short-range order, the establishment of which must depend on the temperature of heat treatment.

The great importance of solid solutions, which often represent one phase of alloys used in technology, calls for their wide and detailed study. In investigating their structure, x-ray methods are of importance in determining the mean square static displacements of the atoms from their equilibrium positions, which characterize the magnitude of the distortions of the crystal lattice; also of importance are methods based on determining the characteristic temperature of alloys, a quantity which characterizes the strength of the interatomic bonds.

Several experimental works[1,2] have shown that the intensity of the x-ray interferences on the patterns for solid solutions differs from that calculated using Laue's rule by a factor

$$\exp(-2\alpha\sin^2\theta/\lambda^2)$$

The coefficient α consists of two parts:

$$\alpha = \alpha_{st} + \alpha_d$$

One part, α_d, depends on the temperature at which the x-ray patterns are registered; i.e., the coefficient α is related to the amplitude of thermal vibrations of the lattice. It is therefore natural to take it into account in the form of a change of the exponent in the thermal factor of the solvent. This procedure is used in determining the characteristic temperature of alloys by x-ray analysis. In the temperature range in which the Debye-Waller theory is applicable, x-ray determination of the characteristic temperature of alloys is feasible. Several authors have indicated good agreement of this theory with experiment for pure metals in a wide temperature range.[3,4]

The other part of the coefficient α, i.e., α_{st}, is temperature independent. The factor $\exp(-\alpha_{st}\sin^2\theta/\lambda^2)$ is interpreted as the result of the influence of static displacements of the atoms from the lattice sites, due to differences in the atomic radii of the alloy components and differences in the binding forces between different kinds of atoms. The same argument is used by several authors to justify the introduction of a similar factor for metals that have undergone plastic deformation (for the case of so-called stresses of the third kind). For metals that have undergone plastic deformation the term "frozen thermal motion" has been widely used. However, whether there even exists weakening of the back lines in the x-ray patterns of plastically deformed metals is questioned by some investigators.[5,6]

Conclusions made on the basis of x-ray studies are arrived at by comparing intensities in x-ray patterns for solid solutions with those in the patterns of the pure components or with the intensities calculated for the solid solution by Laue's rule. But in both cases such a comparison can be made only if the theory of scattering from the material (i.e., the solid solution) is known. In these cases it is common to use simply the results of calculation for scattering of x-rays by the lattice, taking into account its thermal vibrations.

The validity of transferring the results of calculations for thermal vibrations to static displacements is, however, not a priori obvious, since in the first case in calculating the scattered wave amplitude an average over time is taken, whereas in the second case the averaging is over space.

In the present work we present a calculation of the influence of static displacements of the atoms from the solid solution lattice sites on the intensity of the selective x-ray scattering maxima. The effect due to the difference between the atomic structure factors of the two constituents is known and is accounted for by Laue's rule:

$$f = (1 - c) f_1 + c f_2,$$

where f_1 and f_2 are the amplitudes of atomic scattering from the solvent and solute, respectively, taking into account the temperture correction α_d.

An extraneous atom, replacing an atom of the solvent, acts as a perturbation center in the lattice; its neighboring atoms undergo radial displacements decreasing with distance. The presence of many randomly distributed extraneous atoms in the lattice leads, on the one hand, to an overall increase (or decrease) of the lattice period and, on the other hand, to a displacement of the atoms from the lattice points. In the first approximation as well as shown below, we can neglect the correlation between the displacements of separate atoms in the calculation and consider these displacements to be entirely random. Taking this correlation into account leads to a change in the background structure.

The intensity of scattering by a lattice in which the atoms are displaced a distance U from the lattice points can be written in the form

$$I = Af^2 \sum_n \sum_m \exp\{i(\mathbf{k}, \mathbf{R}_n - \mathbf{R}_m + \mathbf{U}_n - \mathbf{U}_m)\}, \qquad (1)$$

where $\mathbf{k}$ is the wave vector $\mathbf{R}_n$ and $\mathbf{R}_m$ are vectors which give the positions of the nth and mth lattice points of the solid solution, and $\mathbf{U}_n$ and $\mathbf{U}_m$ are the displacement vectors of the atoms from these points. To determine the law governing the displacement from the equilibrium position, we shall make use of the theory of elasticity, as was done by Pines.[7] Let us assume that there is an extraneous atom at the ith lattice point. Then all the atoms surrounding it are displaced an amount depending on the distance r from this atom[8]

$$\mathbf{U}' = a\mathbf{r} + \frac{b\mathbf{r}}{r^3},$$

where $\mathrm{r} = \mathrm{R}'_n - \mathrm{R}'_l$

Taking the sum of the displacements U' of the atom due to influence of the extraneous atoms, we obtain

$$\mathrm{U}'_n = \sum_i a\,(\mathrm{R}_n - \mathrm{R}'_i) + \sum_i \frac{b\,(\mathrm{R}'_n - \mathrm{R}'_l)}{|\,\mathrm{R}_n - \mathrm{R}_i\,|^3}\,,$$

or, for the difference between displacements

$$\mathrm{U}'_n - \mathrm{U}'_m = na\,(\mathrm{R}'_n - \mathrm{R}'_m) + \mathrm{U}_n - \mathrm{U}_m.$$

Here n is the number of dissolved atoms (proportional to the concentration c). The first term does not depend on the positions of the dissolved atoms and describes the overall change in the lattice period. The second term depends on the value of R_i and gives the displacements of the atoms from the lattice points. Therefore

$$I = Af^2 \sum_n \sum_m \exp\{i\,(\mathbf{k}, \mathrm{R}'_n - \mathrm{R}'_m)\,(1 + \beta c)\} \exp\{i\,(\mathbf{k}, \dot{\mathrm{U}}_n - \mathrm{U}_m)\}.$$

Setting $\mathrm{R}_m = \mathrm{R}'_m\,(1 + \beta c)$, we obtain equation (1).

The summation is carried over all the atoms of the crystal. Let us separate out all the terms having the same value of the difference

$$\mathrm{R}_n - \mathrm{R}_m = \mathrm{R}_l. \tag{2}$$

Then equation (1) can be written

$$I = Af^2 \sum_l e^{i(\mathbf{k}\mathrm{R}_l)} \sum_{n'} \sum_{m'} e^{i(\mathbf{k}, \mathrm{U}_{n'} - \mathrm{U}_{m'})}\,. \tag{1a}$$

Here the summation is carried out over all n' and m', which satisfy condition (2). For $U_{n'} = U_{m'} = 0$, the first summation gives simply the number P_l of terms with a given distance between the lattice points R_l, and the intensity can be written in the form

$$I = Af^2 \sum_l P_l e^{i(\mathbf{k}\mathrm{R}_l)}\,.$$

In (1a) we can take a space average in the first summation. Obviously

$$\sum_{n'} \sum_{m'} e^{i(\mathbf{k}, \mathrm{U}_{n'} - \mathrm{U}_{m'})} = P_l e^{-\frac{p_l^2}{2}},$$

where $p_l^2 = \overline{(\mathbf{k}, \mathrm{U}_{n'} - \mathrm{U}_{m'})^2}$.

The last expression can be obtained if we denote $(\mathbf{k}, \mathrm{U}_{n'} - \mathrm{U}_{m'})$ by $p_{n'm'}$, expand $e^{ip_{n'm'}}$ into a series and sum over all n' and m', taking account of the fact that

$$\sum_{n'} \sum_{m'} p_{n'm'} = 0 \quad \text{and} \quad \sum_{n'} \sum_{m'} p^2_{n'm'} = P_l p_l^2.$$

Then the intensity I can be written in the form

$$I = Af^2 \sum_l e^{i(\mathbf{k}\mathrm{R}_l)}\, P_l e^{-\frac{p_l^2}{2}}, \tag{3}$$

where

$$p^2 = \left(\frac{4\pi \sin\theta}{\lambda}\right)^2 \cdot \overline{(U_{n'k} - U_{m'k})^2} = k^2\,(\overline{U^2_{n'k}} + \overline{U^2_{m'k}} - \overline{2U_{n'k}U_{m'k}}).$$

If we assume $U_{n'k}$ and $U_{m'k}$ to be independent, then $\overline{U_{n'k}U_{m'k}} = 0$ and $\frac{p^2}{2} = k^2 U_k^2$, whenever $n' \neq m'$ and when $p^2 = 0$ with $n' = m'$.

With this assumption p^2 no longer depends on the index of the second summation l, and therefore the expression for the intensities of the selective maxima can be written

$$I = Af^2 e^{-\frac{p^2}{2}} L = Af^2 \exp\left\{-\left(\frac{4\pi \sin\theta}{\lambda}\right)^2 U_k^2\right\} L, \tag{4}$$

(where L is Laue's function). The validity, however, of the assumptions we have made concerning the absence of correlation between the displacements of the separate atoms, requires special analysis.

For scattering in dilute solid solutions, we can assume that the statistical displacements caused by different randomly distributed extraneous atoms do not depend on each other. In this case, if $R_l > R_0$ (where R_0 is the average distance between the extraneous atoms), we may consider the displacements U_n and U_m to be independent of each other, since each of them is determined basically by displacements due to different extraneous atoms. With $R_l < R_0$, this assumption is clearly incorrect. However, the number of terms in (3) in which p_l depends on R_l is small compared with the total number of terms in the sum.

To verify this, let us divide a coherently scattering block of the crystal into volumes containing one extraneous atom each. The number of such volumes will be equal to the number $n = cN$ of extraneous atoms in the block, where c is the concentration of the solid solution, and N is the number of atoms in the block. The total number of terms in equation (3) will be N^2, while the number of terms with $R_l < R_0$, in which p^2 depends on R_l will obviously equal $Nc(1/c^2 - 1/c) \approx N/c$ (the number of atoms in a volume with linear dimensions R_0 equals $1/c$). From this we see that the number of terms for which we cannot make the assumption that $\overline{U_n U_m} = 0$ is given by the fraction $1/Nc$ of the total number of terms. Even for $c = 0.01$, the fraction $1/Nc$ is of the order of 10^{-4} (since $N \approx 10^6$). Thus equation (3) can be written in the form

$$I = Af^2 e^{-\frac{p^2}{2}} \sum_{R_l > R_0} P_l e^{i(\mathbf{k}\mathbf{R}_l)} + Af^2 \sum_{R_l < R_0} P_l e^{i(\mathbf{k}\mathbf{R}_l)} e^{-\frac{p^2}{2}} e^{(k^2, \overline{U_{n'k}U_{m'k}})} + Af^2 N.$$

Whence, expanding the last factor in the second term in a series, we obtain

$$I = Af^2 \left\{ e^{-\frac{p^2}{2}} L + Nc e^{-\frac{p^2}{2}} \sum_l q_l e^{i(\mathbf{k}\mathbf{R}_l)} (k^2, \overline{U_{nk}U_{mk}})_l + N\left[1 - e^{-\frac{p^2}{2}}\left(1 + \frac{k^2\overline{U^2}}{3}\right)\right]\right\}. \tag{5}$$

The coefficient $q_l = \frac{P_l}{Nc}$ is the number of pairs with equal values of R_l in each volume $(v < R_0^3)$. The first term in expression (5) corresponds to equation (4) and describes the weakening of the coherent maxima. The second term gives the monotonic increase of the background with angle and, finally, the middle term gives the background, determined by correlation of the displacements*. This sum is multiplied by the factor Nc, which is equal to the number of the small volumes (or the number of extraneous atoms in the block), i.e., the second term in expression (5) is the sum of the intensities of scattering from these volumes; it can, therefore, be interpreted as the scattering of the mutually independent small volumes with changes in the electron density distribution associated with the factor $(k^2, \overline{U_{nk}U_{mk}})_l$ The linear dimensions of these regions should be of the order of $R \approx a\sqrt[3]{\frac{1}{c}}$, i.e., several angstroms. These regions should yield diffuse maxima (diffusion due to the smallness of the regions) close to the selective maxima, the intensities of which are Nc times weaker than those of the principal maxima; in addition, these regions should produce appreciable scattering at small angles.

---

*In this expression, of course, no account is taken of the background due to the difference between atomic structure factors of the components.

For the case of plastically deformed metal, if we assume the presence of dislocation chains in the lattice, the correlation of the displacements of the various atoms will be appreciably more rigorous. If we take into account the crystallographic character of slip and, consequently, also the location of the dislocation lines, then $(k^2, \overline{U_{nk}U_{mk}})_l$ will depend on the direction of the wave vector k. In this case we may expect the appearance of diffuse maxima differing significantly in magnitude near different points of the reciprocal lattice; these diffuse maxima can also disrupt the general variation of the selective line intensities with the scattering angle. This question requires additional, more rigorous investigation.

We can now attempt to evaluate the concentration dependence of $\overline{U_k^2}$ for a solid solution (U_k is the projection of the displacement vector U on the wave vector k).

The following calculation of the mean square displacements was carried out utlizing the model of elastic deformation of the lattice in formation of the solid solution. It must be borne in mind that in using the elastic model, one should not attribute a purely geometric meaning to it. An extraneous atom introduced into the solid solution lattice causes displacements of the other atoms which result in changes in the strength of the interatomic bonds; therefore, the coefficients, entering into the expressions for the mean square displacements cannot always be deduced from the elastic constants of the lattice and the differences in atomic radii. A preliminary calculation based on the pure elastic model may nevertheless be of value. Comparison with experiment makes it possible to judge to what extent the strength of the interatomic bonds changes and short-range order is established.

Let us consider the projection of the displacement of an arbitrary atom onto the wave vector k due to the solute atoms located on the first coordination sphere. If only one extraneous atom is located on the first coordination sphere and this displaces the original atom a distance $\overline{U}$, then,

$$\overline{U}_{k_1}^2 = \int_0^{\pi} U^2 \cos^2\alpha \frac{2\pi r^2 \sin\alpha \overline{d}\alpha}{4\pi r^2} = \frac{U^2}{3}.$$

Here α is the angle between U and k. If there are n atoms on the coordination sphere, then

$$\overline{U}_{k_1}^2 = \int_0^{\pi}\int_0^{\pi} \cdots \int_0^{\pi} \left(\frac{1}{2}\right)^n (U\cos\alpha_2 + U\cos\alpha_2 + \ldots + U\cos\alpha_n)^2 \sin\alpha_1 \sin\alpha_2 \ldots \sin\alpha_n d\alpha_1 d\alpha_2 \ldots d\alpha_n = \frac{n}{3}U^2.$$

Extraneous atoms on other coordination spheres will displace the atom smaller distances. Assuming $U = b/r^2$, let us find the displacement of the atom due to the extraneous atoms on all the coordination spheres.

If the i^{th} coordination sphere contains N_i atoms, then obviously the number of extraneous atoms on this sphere is

$$n_l = cN_i,$$

where c is the concentration. The displacement due to the atoms on this coordination sphere will be

$$\frac{\overline{U}_l^2}{3}\, cN_i,$$

and the total resultant displacement will be

$$\overline{U}_k^2 = \sum_i \frac{\overline{U}_l^2}{3}\, cN_i = \frac{cb^2}{3} \int_{2R}^{\infty} \frac{n4\pi r^2 dr}{r^4} = 4\pi nc\, \frac{b^2}{6R},$$

where n is the number of atoms per unit volume and R is the atomic radius.

From Ref.7,

$$U_1 = \frac{2}{3}\Delta R = \frac{b}{(2R)^2},$$

whence

$$b = \frac{8}{3} R^2 \Delta R.$$

Replacing n by N_0/a^3, where N_0 is the number of atoms in the unit cell, and a^3 is its volume, we obtain for a face-centered cell

$$U_{st} = \sqrt{\overline{U^2}} = 2{,}8 \sqrt{c}\, \Delta R,$$

and for a body-centered cell,

$$U_{st} = \sqrt{\overline{U^2}} = 2{,}7 \sqrt{c}\, \Delta R.$$

Similar results have been obtained by Huang[9], although with a slightly different numerical coefficient.

Calculation shows that the coefficient α_{st} for static distortions of the crystal lattice increases in direct proportion with the solid solution concentration (i.e., $U_{st} \approx \sqrt{c}$). As the concentration increases, the actual variation should deviate from the above rule, since at high concentrations, positions of the extraneous (solute) atoms on the coordination spheres can no longer be regarded as independent.

Kurdiumov and Travina[10] showed that α and c are proportional for Ni-Cr alloys. Deviation from proportionality at high concentrations is observed in the alloy Fe-Co[12]. In addition, calculation based on the elastic model requires a proportionality between the difference in atomic radii ΔR and the quantity U_{st}.

The values of U_{st} calculated by means of the deduced equation and those obtained experimentally are listed in the accompanying table. (The listed experimental data from Refs. 10 and 11 are limited to the values obtained with Mo radiation, as the most accurate.)

The table shows that although the calculated and experimental values of U agree as to order of magnitude, as has been noted earlier[1], there is no consistent proportionality between the quantities U and ΔR. In the case of the Ni-Cr alloys, the experimentally determined value of U is greater than the value calculated on the basis of the elastic model.

For Ni-Al and Ni-Ti alloys, on the other hand, the experimentally determined average static displacements are smaller

Computed and experimental (from Refs.10 and 11) values of the statistic displacements U_{st} of the atoms from their equilibrium positions

Element	R	Alloy	ΔR	C, %	U_{st} theo	U_{st} exp [Ref]
Ni	1,24	Ni-Cr	0,04	20	0,051	0,07 [10]
Cr	1,28	Ni-Cr		32	0,063	0,088 [10]
Al	1,43	Ni-Al	0,19	3,5	0,10	0,053 [10]
Ti	1,45	Ni-Ti	0,21	4	0,12	0,058 [10]
Au	1,44	Cu-Au	0,16	15	0,17	0, 11 [11].
Cu	1,27					

than the calculated ones, which indicates a relaxation of the static distortions, possibly connected with the formation of regions supersaturated with the second constituent and the establishment of long-range order in these regions. The presence of short-range order, it seems to us, should also significantly alter the magnitude of the observed mean square static displacements.

Physics Department of
Moscow State University

References

1. V.I.Iveronova, Trudy Instituta kristallografii AN SSSR (Transactions of the Institute of Crystallography of the USSR Ac. of Sci.) No.10, 149 (1954).
2. G.V.Kurdiumov, in "Problemy metallovedeniia i fiziki metallov" (Problems of metallurgy and the physics of metals) M.-L. 1952.
3. Ia.S.Umanskii & V.G.Veksler, Sow. Phys., 7, 336 (1935).
4. E.A.Owen & R.W.Williams, Proc. Roy. Soc., A188, No.1015, 509 (1946).
5. W.H.Hall & G.K.Williamson, Proc. Phys. Soc.,64,946(1951).
6. B.L.Averbach & B.E.Warren, J.App.Phys., 20,1066 (1949).
7. B.Ia.Pines, J. of Phys.USSR, 3, 309 (1940).
8. L.D.Landau & E.M.Lifshits, Mekhanika sploshnykh sred (Mechanics of continuous media). M.-L. 1944.
9. F.Huang, Proc.Roy.Soc., A190, 102 (1947).
10. G.V.Kurdiumov & &.T.Travina, Doklady AN SSSR, 99, 77 (1954).
11. R.A.Coyle & B.Gale, Acta crystallogr., 8, 105 (1955).
12. V.I.Iveronova & A.A.Katsnel'son, Doklady AN SSSR, 99, 391 (1954).

X-RAY INVESTIGATION OF STRUCTURAL CHANGES IN THE SURFACE LAYER OF STEEL MACHINED BY TURNING

- O.N.Shivrin

Introduction

The present investigation was concerned with the structural distortions occurring in the surface layers of metal machined on a lathe at turning regimes approximating those indicated by the "power method". We studied the processes of development of stresses of the first kind as well as of the second and third kinds with different cutting parameters and the processes of relief of these stresses during annealing. We felt that observation of both the direct and reverse processes is desirable for a better understanding of the physical nature of the effects taking place in the surface layers of the metal.

Specimens and experimental procedure

We investigated specimens of St.2 and St.40 steel in the tempered state. The tempering was carried out in cast iron filings at a temperature of 800-850°C, the specimens being held for 2 hours at this temperature; the samples were cooled with the furnace over a period of 36 hours. Most of the specimens were cylindrical, 25 and 50 mm in diameter. For investigating the dependence of structural changes on the depth of cut we prepared tapered specimens similar to those described in Ref. 1.

The specimens were all turned on a 161 AM lathe; for each series of specimens one of the cutting parameters (for example, the feed) was varied, while the other two (speed and depth of cut) were kept constant.

For purposes of checking, the conditions for each series of samples were duplicated on a control specimen which was divided into 25-30 mm long sections, each section of the control specimen being subjected to the machining of one of the specimens of the given series.

The shape of the tool bit conformed to the designed specification developed by Kolesov (described in Ref. 2). For turning the St.2 steel we used tools tipped with plates of R9 steel; for cutting the St.40 steel, with plates of the hard T15-K6 alloy. Each series of samples was turned with the same setting of the tool. No cooling was employed.

The x-ray patterns of the turned samples were registered by the method of back-reflection on a KROS camera using the radiation from a cobalt anode. The reference standard employed for evaluating the stresses was aluminum foil 40 μ thick (the (331) line of aluminum served simultaneously as the standard for evaluating the intensity of the (310) iron line). A parallel series of x-ray patterns recording the two (310) and (220) lines of iron were obtained for all specimens. Thus we could evaluate the stresses of the third kind both by the method of an independent standard and by the method of comparing the intensity of two lines. In addition the intensity of the (310) iron line was evaluated directly with reference to the intensity of the background in its vicinity.

The x-ray patterns were photometered on an MF-2 microphotometer, using a wide slit and defocused optics in order to minimize scattering of the photometric curve points.

In order to minimize the errors arising in determining stresses of the first and second kinds due to an appreciable width of the interference line, as well as the errors involved in measuring the areas under the photometric curve, in determining the stresses of the third kind the microphotometric curves were processed by the method of approximating the α-doublet by an isosceles triangle obtained by graphic addition of the α_1 and α_2 lines.

Simple calculations show that the area of such a triangle equals the sum of the areas of both lines of the doublet; the half-width of the line equals a quarter of the triangle's base, while the apex of the triangle lies at a distance equal to 1/3 δ from the α_1 peak (δ is the distance between the α_1 and α_2 peaks).

It can readily be shown that the isosceles triangle approximation leads to fully as accurate results as approximation by curves described by $e^{-k^2x^2}$ or $1/(1 + \gamma^2x^2)$; hence by means of this construction we can determine all the necessary quantities with the requisite accuracy.

Experimental results and discussion

In the range of cutting speeds from 3 to 59 meters/min with a depth of cut of 1 mm and a feed of 0.5 mm/rev, tensile stresses of the first kind equal to 30-60 kg/mm^2 develop in the surface layer. No consistent regularity in regard to their dependence on the speed of cut is observed. The residual stresses of the second and third kinds also are independent of the cutting speed under these conditions.

It must be noted that the stresses vary from point to point on the same specimen, the variation frequently being greater than the maximum possible error. As the feed is increased the stresses of the first kind increase at first rapidly and then more slowly tending to a very high stable value. It was established that, in addition to the speed, the depth of cut also has an appreciable influence on the magnitude and sign of the stresses of the first kind.

With a small depth of cut and a slow feed, compressive stresses develop in the surface layer; as the feed (or depth of cut) is increased the compressive stresses decrease, then change sign and become tensile stresses.

With increasing cutting speed the critical values of the feed and depth of cut at which the change of sign occurs also increase.

It should be noted that compressive stresses which have a positive influence on the further behavior of the work develop not only at high cutting speeds and with tools have a large negative rake angle but also at comparatively low cutting speeds and with tools having a positive rake (3-5°).

The development of compressive stresses of the first kind with a small depth of cut and low feed is apparently due primarily to the mechanical action of the tool analogous to that obtaining in rolling or upsetting. With large depths of cut and at high speeds, an appreciable amount of heat is generated and its influence exceeds the effect of mechanical deformation. The inner layers of the metal, cooling more slowly than the outer, stretch the latter and further the formation of tensile stresses in the surface layer. The process of formation of stresses of the second kind proceeds parallel with the process of development of stresses of the first kind but in contrast to the latter exhibits little dependence on the depth of cut.

The decrease in the magnitude of the stresses of the second kind at fast feeds can readily be explained by their partial relief under the influence of the heat generated during the cutting.

In like manner the competing influence of the thermal and mechanical factors determines the at first rapid and then slower development of stresses of the third kind.

Experiments analogous to those described for the samples of St.2 steel above were carried out with samples of St.40 steel but at higher cutting speeds (up to 118 m/min). The results obtained are in qualitative agreement with those described above. The principal difference is that at high cutting speeds stresses of the second and third kinds do not attain such high values as in St.2 steel, but level off earlier.

From the point of view of better understanding of the processes of hardening and softening of the surface layer, investigation of the process of relief of stresses at relatively moderate temperatures was of interest. To this end the turned samples of St.2 steel were subjected to step annealing (drawing) at temperatures ranging from 100-400° with intermediate x-raying at the different stages.

Heating to temperatures below 200° even for a prolonged period (36 hours) does not result in any noticeable changes in the character of the structural distortions. At an annealing temperature of 200° there is a partial relief of stresses of the first kind only. Noticeable relief of stresses of the second and third kinds is observed only after annealing at 300° (about 30% of the stresses are relieved after holding for 10 hours at 300°). Thus stresses of the first kind possess appreciable thermal stability.

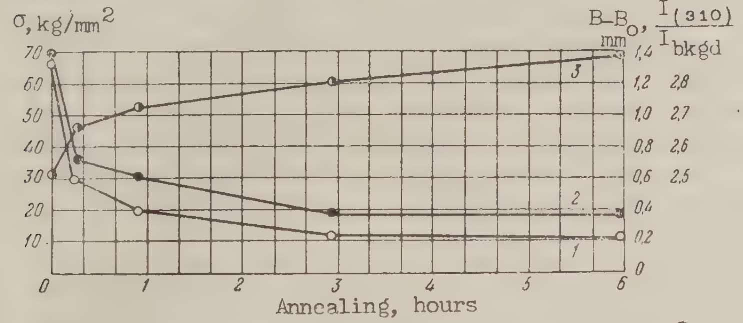

Relief of strains in St.2 grade steel at 400°: 1) stresses of the second kind, 2) difference in the half-widths of the lines of the deformed (B) and undeformed (B_0) metal, 3) relative intensity of the (310) line.

An analogous picture is observed at higher temperatures. Thus, for example, at 400° (see figure) the stresses are relieved to the extent of about 50% during the first 15 minutes; with further annealing time the relief process slows down. After a period of 3 hours there is no further reduction of stresses of the first and second kinds although the relief of stresses of the third kind continues, but slowly. Noteworthy is the parallel relief of stresses of the first and second kinds and their nearly equal thermal stability.

The above facts do not fit in with the commonly accepted concept of the development and relief of stresses in metals, but can be explained by the unique character of the stress state in the thin surface layer.

We feel that the commonly accepted definition of stresses of the first kind as stresses balancing out in rather large volumes is hardly applicable to thin surface layers having a depth of only a few crystal grains. In thin surface layers the character of stresses of the first kind is apparently such that it would be more correct to treat them as oriented stresses of the second kind inasmuch as both the former and the latter are determined by the value of $\Delta d/d$.

It may be assumed that in addition to random changes in the parameter $\Delta d/d$, responsible for the appearance of actual stresses of the second kind, there appear as the result of some oriented influence (for example, the influence of nonuniformly cooling layers) preferred changes in this parameter resulting, in the final analysis, in displacement of the lines in the x-ray pattern, displacements which we attribute to stresses of the first kind in the classical sense.

Karilo-Finnish State University

References

1. "Svoistva metallicheskikh poverkhnostei" (Properties of metallic surfaces), Collection of translations edited by D'iachenko, M. 1954.

2. V.S.Gus'kov, Rezhimy rezaniia pri tochenii silovym metodom (Cutting regimes in turning by the power method), Kiev 1954.

REFINEMENT OF THE STRUCTURAL PARAMETERS OF NICKEL TRIAMINODITHIOCYANOGEN (II) AND CESIUM TETRACHLOROCOBALTATE BY THE METHOD OF DIFFERENTIAL FOURIER SYNTHESIS ON AN ELECTRONIC COMPUTER

- M.A.Porai-Koshits

1. Determination of the interatomic spacing and valence angles is a no less important physical-chemical problem than establishing the "motif" of the arrangement of the atoms. From the distances between atoms one can judge of the character and multiplicity of the chemical bonds, their equivalence or difference, the possible influences of the atoms on each other, the existence of steric hinderances, etc. Obviously such judgement and evaluations are feasible only if sufficiently accurate data are available. Unfortunately the situation in this regard is far from satisfactory. Aside from the practical difficulties where accurate determination of the integral intensities is concerned, the application of the equations of the kinematic theory of intensity is not entirely legitimate and leads to errors, the magnitude of which is difficult to evaluate (but which should not be exaggerated).

Nevertheless experience shows that an accuracy of 0.01-0.02 Å in determining atomic distances is realizable and that one can make legitimate deductions regarding the chemical characteristics of the atomic interaction associated with changes in the interatomic spacing exceeding 0.03-0.05 Å.

2. In modern structural analysis there are two approaches to the problem of refining the coordinates of atoms on the basis of x-ray data. The first of these is based on analysis of the electron density distribution or of different functions deriving therefrom, obtained by summing up appropriate Fourier series. Among the principal variants of this approach are the following:

a) the usual electronic density method (the F-series method - Bragg[1]),

b) the differential synthesis method (the D-series method - Booth[2]) and

c) the method of "null synthesis" or "difference synthesis" (R-series method - Booth and Cochran[3]).

The second approach is based on the idea of the closest approximation of the value of the structure amplitude $F(hkl)$, calculated from the atomic coordinates and the atomic amplitudes, to the value of the structure amplitudes $F_э(hkl)$ found from the intensity of the reflections.

The basic method employed here is the method of least squares.[4] The unique "steepest descent" procedure proposed by Booth[5] and subsequently refined by Vand[6] and perfected by Quaraschi[7] proved to be only a particular case of application of the general formulas of the method of least squares.

One requirement of this method is minimalization of a function of the type

$$\Phi = \sum_{hkl} w_{hkl} [F_э(hkl) - F_p(hkl)]^2$$

where w_{hkl} are weighed coefficients of the individual reflections, dependent on the degree of reliability of the measurement of their intensity.

The structure amplitudes $F_p(hkl)$ are determined through the atomic amplitudes $f_j(hkl)$. Inasmuch as the latter are taken from theoretical calculations for isolated (spherically symmetric) atoms one can assert a priori that this entire approach is less objective than the first, i.e., that based on the electron density distribution over the cell.

Comparing the method of electron densities (and its different variants), on the one hand, with the method of approaching the values of $F_э(hkl)$ and $F_p(hkl)$, on the other hand, a number of investigators[8-10] have noted that the two procedures should give equal results, provided that the weighted coefficients w_{hkl} used in the individual amplitudes in the method of least squares are inversely proportional to $f_j(hkl)$. This condition has been taken as the criterion of the closeness of the results yielded by the different methods. Actually, however, the requirement that $w_{hkl} \cdot f_j(hkl) = \text{const}$ is evidence of the difference in principle between the methods. There is no reason to assume that our evaluations of the structure amplitudes have a high degree of reliability and, consequently, that the weighted coefficients w_{hkl} are inverseley proportional to $f_j(hkl)$. On the contrary, the two methods must be compared under identical conditions, i.e., assuming in the method of least squares that $w_{hkl} = \text{const}$, as is assumed in calculating the electron density. Inasmuch as actually $f_j(hkl) \neq \text{const}$, the methods must lead to different results. Only in the case of point atoms when $f_j(hkl) = Z_j = \text{const}$ should the results of refinement by both methods be identical in principle.

Thus the true meaning of $w_{hkl} \cdot f_j(hkl) = \text{const}$ is that only in going over to normalized or individual structure amplitudes (and, consequently, to point atoms) do both approaches to the solution of the problem become equivalent. We note further that their results should in general agree with the results of density distribution analysis based on the direct method of statistical equalities,[11] employed for establishing the signs of all the reflections.

3. The usual F-series method reduces to a successive solution of two computational problems: 1) calculation of the distribution of electron density in the vicinity of the maxima and 2) finding the positions of the maxima either from the usual conditions defining the extremum values of the function or by subdivision of each maximum into appreciably smaller sections and identifying the points having the maximum density values. In the first case the result depends in principle on the assumed interpolation formula.

The most suitable procedure, based on the method of least squares, is that described in Ref. 12. The calculations require a number of successive approximations in view of the change in sign of the structure amplitudes of part of the reflections (changes in the initial phases in the general case) in refining the atomic coordinates. Virtually no distortions are introduced into the final results by the circumstance that in determining the signs of the structure amplitudes in the case of a centrosymmetric structure use is made of the formula

$$F(hkl) = 2\sum_{j=1}^{N/2} f_j \cos 2\pi\left(h\frac{x_j}{a} + k\frac{y_j}{b} + l\frac{z_j}{c}\right)$$

which comprises values of the atomic structure factors obtained not from the given experiment and implies the assumption of spherical symmetry of the atoms. Experience shows that in going from approximate values of $f_j = \hat{f} Z_j$ ($\hat{f}$ is the individual atomic amplitude and Z_j is the atomic number of the j-th atom) based on the assumption of similarity of the atomic curves, to more precise individual values of the factor f_j, the signs of the structure amplitudes change comparatively rarely. Even less likely is the change in sign in consequence of inaccuracy of our knowledge regarding the individual factors f_j and, in particular, in consequence of neglecting the anisotropy of the atomic amplitudes and the thermal vibrations of the atoms.

In the case of non-centrosymmetric structures the result of refinement is appreciably less objective since the assumption regarding isotropism of the atomic factors affects the initial phases of all the reflections and, consequently, enters into the final result.

At the concluding stage of refinement of the coordinates one must make a correction for the cutoff of the Fourier series. Booth's method[13], which is based on evaluation of displacement of the maximum in the "theoretical" Fourier series, assumes only equality of the slopes of the termination waves at the point of the maximum in the "theoretical" and "experimental" series but not complete coincidence of the termination waves. Consequently here, too, our inadequate knowledge of the atomic factors has little effect. Booth's method should undoubtedly be used in investigation structures with heavy atoms, where the termination waves in the region of light atoms depend on the location of the heavy atoms, which can be situated with great accuracy. This method in all probability is also applicable to structures with light atoms, although the corrections obtained in determining the coordinates.

4. The method of differential synthesis is a more direct approach to the problem of finding the coordinates of the maxima. It derives directly from the extremum requirements:

$$\frac{\partial\rho}{\partial x}=0, \qquad \frac{\partial\rho}{\partial y}=0, \qquad \frac{\partial\rho}{\partial z}=0,$$

and transforms the initial computational formulas accordingly.

Bearing in mind that the electron density is given by the familiar Fourier series, after differentiation we obtain three conditions of the following type

$$\frac{\partial\rho}{\partial x}=-\frac{2\pi}{Va}\sum_{hkl} h\,|F(hkl)|\sin\left[2\pi\left(h\frac{x_m}{a}+k\frac{y_m}{b}+l\frac{z_m}{c}\right)-\alpha(hkl)\right]=0,$$

where x_m, y_m and z_m are the coordinates of the maximum and V is the volume of the unit cell.

At this point, however, we encounter difficulties: first, it is necessary to make sure that in all three equations we are dealing with the coordinates of one and the same atom, and second, the variables appear in a trigonometric function.

The problem is readily solved if we utilize the expansion of the derivative into a Taylor series about the point corresponding to the initial coordinates of some atom. Then

$$\frac{\partial\rho}{\partial x}=\left(\frac{\partial\rho}{\partial x}\right)_0+\frac{\partial^2\rho}{\partial x^2}(x-x_0)+\frac{\partial^2\rho}{\partial x\partial y}(y-y_0)+\frac{\partial^2\rho}{\partial x\partial z}(z-z_0)+\ldots$$

Assuming $\frac{\partial\rho}{\partial x}=0$ and neglecting the powers of $x-x_0$, $y-y_0$ and $z-z_0$ above the first we obtain a system of linear equations for the corrections δx, δy, δz:

$$\begin{aligned}
A_{hh}\delta x+A_{hk}\delta y+A_{hl}\delta z+A_h&=0,\\
A_{hk}\delta x+A_{hk}\delta y+A_{hl}\delta z+A_k&=0,\\
A_{hl}\delta x+A_{kl}\delta y+A_{ll}\delta z+A_l&=0,
\end{aligned}$$

where

$$A_h=\left(\frac{\partial\rho}{\partial x}\right)_0=-\frac{2\pi}{Va}\sum_{hkl} h\,|F_{\text{э}}(hkl)|\sin\left[2\pi\left(h\frac{x_0}{a}+k\frac{y_0}{b}+l\frac{z_0}{c}\right)-\alpha(hkl)\right],$$

$$A_{hh}=\left(\frac{\partial^2\rho}{\partial x^2}\right)_0=-\frac{4\pi^2}{Va^2}\sum_{hkl} h^2\,|F_{\text{э}}(hkl)|\cos\left[2\pi\left(h\frac{x_0}{a}+k\frac{y_0}{b}+l\frac{z_0}{c}\right)-\alpha(hkl)\right],$$

$$A_{hk}=\left(\frac{\partial^2\rho}{\partial x\partial y}\right)_0=-\frac{4\pi^2}{Vab}\sum_{hkl} hk\,|F_{\text{э}}(hkl)|\cos\left[2\pi\left(h\frac{x_0}{a}+k\frac{y_0}{b}+l\frac{z_0}{c}\right)-\alpha(hkl)\right]$$

The presence of mixed derivatives in these equations means that no assumptions regarding spherical symmetry of the atoms were made in the process of refinement. Successive refinements are necessary not only to take into account the changes in sign of the individual amplitudes but also to eliminate the errors arising due to neglect of higher power terms in the Taylor expansion.

In general the D-series method differs from the F-series method only as regards the order of carrying out the mathematical operations: in the D-series method, instead of carrying out the calculations in two stages, all the practical computations are made after first transforming the equations.

Application of differential synthesis is allowable at the same stage of the analysis as in the ordinary electron density method used for refining the coordinates, while the results of the refinement cannot in principle be different.

5. At the concluding stage of the refinement an appropriate correction is made for the termination of the series. If this correction is introduced not at the concluding stage but at each stage of the refinement this will be equivalent to modification of the system of equations given above:

$$\begin{aligned}
A_{hh}\delta x+A_{hk}\delta y+A_{hl}\Delta z+(A_h-C_h)&=0,\\
A_{hk}\delta x+A_{kk}\delta y+A_{kl}\Delta z+(A_k-C_h)&=0,\\
A_{hl}\delta x+A_{kl}\delta y+A_{ll}\Delta z+(A_l-C_l)&=0,
\end{aligned}$$

where

$$A_h - C_h = -\frac{2\pi}{Va}\sum_{hkl} h\left[\,|F_{\text{э}}(hkl)| - |F_{\text{р}}(hkl)|\,\right] \times \sin\left[2\pi\left(h\,\frac{x_0}{a} + k\,\frac{y_0}{b} + l\,\frac{z_0}{c}\right) - \alpha(hkl)\right]$$

On the other hand, the same system of equations for corrections to the coordinates can be obtained on the basis of the method of difference synthesis, which is evidence of the equivalence of the D-series and R-series methods.

Thus the F-, D- and R-series methods are equivalent to each other but differ in principle from the method of least squares and its variants.

6. The method of differential synthesis is the most convenient one from the practical standpoint. It is best adopted for automatization of the entire computational process of successive approximations. Yielding the coordinates of the maxima directly (without the necessity of interpolational computations), it permits automatic feeding of the results to the computing program for the signs of the structure amplitudes; the latter in turn can be represented in the form of moduli $|F_{\text{э}}(hkl)|$ and, consequently, included in the next cycle of refinement of the coordinates. For this reason the differential synthesis method is the most economical as regards programming on high-speed computers, whether electronic or other, special or universal.

In the case of special machines, one must realize the appropriate communications joining into a whole the units intended for the solution of particular problems; in the case of universal computers, one need only set up appropriate programs. The differential synthesis method appreciably shortens the computer time as compared with that required for other methods of calculation, for example, as compared with the method of finding the maxima by subdividing each peak into smaller parts and identifying the highest point therein.

Complete automatization of the process of successive refinements of coordinates was realized on a universal high-speed electronic BESM [initials for Rapid Electronic Computing Machine. Trans.] by N.P.Trifonov (Moscow State University) at the request of the Laboratory of Crystal Chemistry of the Institute of General and Inorganic Chemistry of the USSR Academy of Sciences (see Ref. 14).

Use of an electronic computer in conjunction with the differental synthesis method sharply reduces the calculating time. The time is reduced not only by virtue of the rapidity with which the individual mathematical operations are performed by a computer but also thanks to the elimination of a number of intermediate operations: printing out the computed structure amplitudes and complete electron density distribution, interpolational calculations for determining the coordinates of the maxima, etc.

Trifonov set up programs for both the two-dimensional and three-dimensional cases. The two-dimensional calculation program was applied for refining the structure parameters of nickel triaminodithiocyanogen - $Ni(NH_3)_3(NCS)_2$; the three-dimensional calculation program was used for refining the coordinates of the atoms in the structure of cesium tetrachlorocobaltate - Cs_2CoCl_4. The computer time per refinement cycle in the two-dimensional case was 5 min; in the three-dimensional calculations, 30 min.

7. The crystals of nickel triaminodithiocyanogen belong to the space group $D_{2h}^{16} = Pbnm$. The unit cell with edges $\underline{a} = 10.7 \pm 0.05$ $b = 10.2 \pm 0.05$ and $c = 7.6 \pm 0.05$ kX comprises four formular units. Most of the atoms, including the Ni and S_I and S_{II} atoms, occupy particular quadruple positions in the m symmetry planes.

In the initial variant of the crystal structure obtained by us as a result of analysis of the (001) projection of the interatomic function, the existence of complex $[Ni(NH_3)_3NCS]^+$ cations and NCS^- anions was assumed. The interpretation of the projection of the electron density maxima is shown in Fig. 1 which represents the projection of the first approximation.

In this projection the strongest maximum, due undoubtedly to Ni atoms, is surrounded by four other maxima (located approximately at the corners of a square) of which one, the strongest, corresponds to a sulfur atom, while the other three were ascribed to NH_3 groups. The second strong maximum, located to the side of the Ni maximum was assumed to be associated with the sulfur atom of the NCS^- anion.

Further investigations showed, however, that this interpretation is not correct. Actually, of the four maxima surrounding the Ni one, one belongs to an S atom, two to nitrogen atoms of the thiocyanogen groups N_I and N_{II} and only one is associated with the NH_3 group (Fig. 2).

Thus the second thiocyanogen group $(NCS)_{II}$ is joined to the Ni by its nitrogen "ring", while the first thiocyanogen group serves as a bridge linking two neighboring Ni atoms. The two unaccounted for NH_3 groups are apparently situated above and below the plane of symmetry, supplementing the coordination of the nickel atoms to the octahedral. At this stage of the analysis the structure could be described as a chain one, consisting of octahedral trans-trans-cis $[Ni(NH_3)_3(NCS)_2]^-$ complexes linked by common $(NCS)_I$ groups. This interpretation was substantiated by the evident "clearing up" of the projection picture in the process of subsequent refinements (Fig. 2), the distribution of the density of the projections of the interatomic functions to other coordinate planes and the results of calculation of "weighted" *hk*1 and *hk*2 projections (Figs. 3 and 4).

In the refinement of the atomic coordinates, carried out with respect to the (001) projection by the method of differential synthesis on the electronic computer, it was necessary to carry out eight cycles of

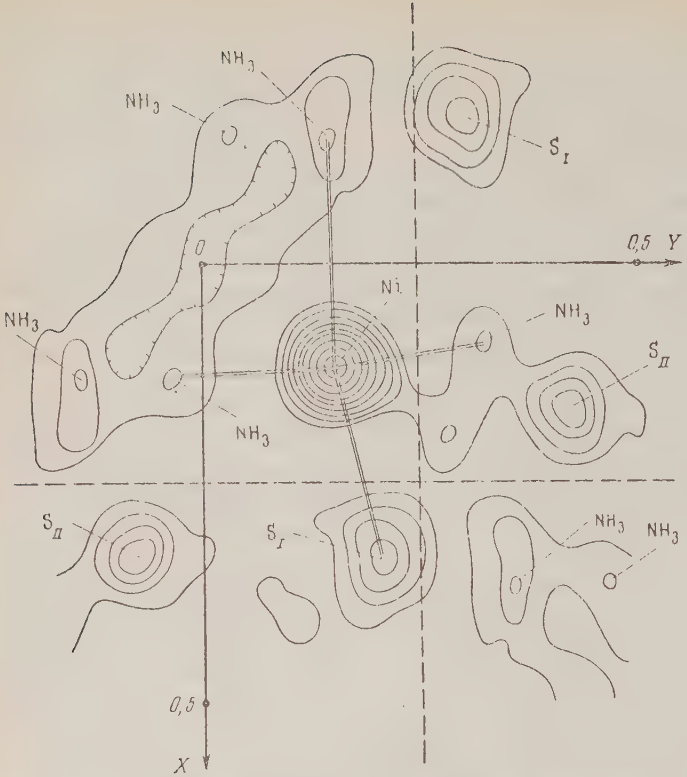

Fig. 1 Projection of the first approximation electron density on the (001) plane for nickel triaminodithiocyanogen - $Ni(NH_3)_3(NCS)_2$.

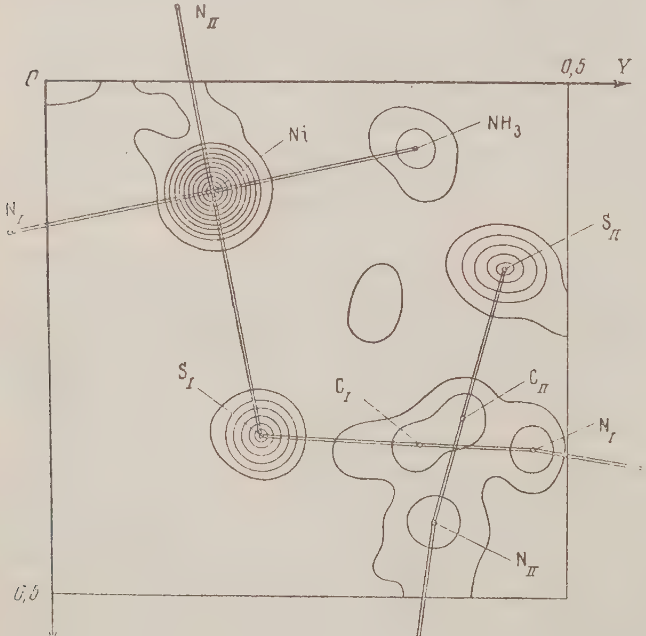

Fig. 2. Projection of 4th approximation electron density on the (001) plane.

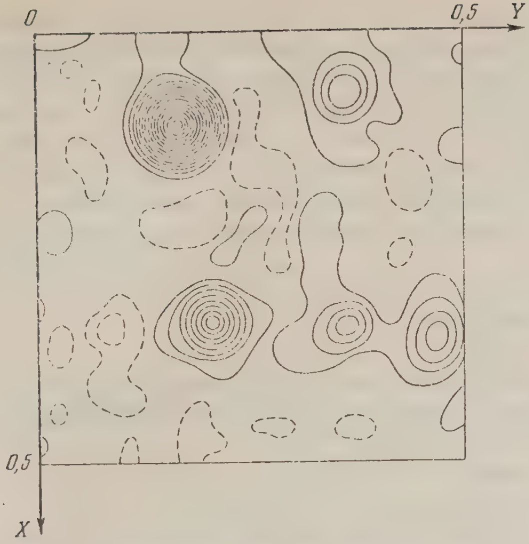

Fig. 3. Weighted projection $\sigma(hk1)$ for nickel triaminodithiocyanogen.

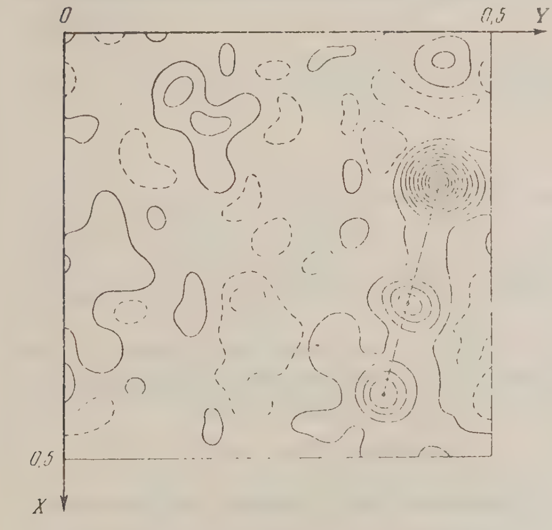

Fig. 4. Weighted $\sigma(hk2)$ projection for the same compound.

approximation which required a total of 40 min of computer time (the number of independent $hk0$ reflections equals 250; the plane symmetry group is pgg).

In the first four cycles the coordinates of the C_I and C_{II} atoms, yielding partially overlapping maxima, were not refined (were kept constant); the general process of refinement was introduced in the succeeding cycles. The following distances were obtained as a result of the refinement:

Ni-S_I = 2.52 kX (2.5_0),
Ni-N_I = 2.02 kX (2.1_5),
Ni-N_{II} = 1.98 kX (2.0_0),
Ni-NH_{3I} = 2.02 kX (2.0_0).

The figures in parentheses are the spacings obtained prior to refinement on the basis of the electron density projection shown in Fig. 2.

The Ni-NH_3 distance according to the data of the projections on the (100) and (010) planes is 2.05 kX (within ± 0.05 kX).

Hence all the Ni-N and Ni-NH_3 distances correspond to predominantly covalent bonds, while the Ni-S spacings correspond to purely ionic bonds.

Consequently the "chain structure" can be regarded only as a formal description of the general "motif" of the atomic structure. Actually the crystal is built up of isolated five-neighbor complex molecules - $Ni(NH_3)_3(NCS)_2$.

The nickel coordination polyhedron has the form of a tetragonal pyramid; the complexes are polar: the positive pole of the dipole is at the nickel atom, at the center of the pyramid base. A sulfur atom of one of the thiocyanogen groups of the neighboring molecule is linked to the base of each complex, thereby bringing the coordination number of nickel to six.

It should be noted that such a pyramidal form of complexes is met with comparatively rarely in crystallochemistry of complex compounds. Some chemical consequences ensuing from this structure of the compound in the solid state have been examined by the writer elsewhere (Ref. 15).

8. The crystals of cesium tetrachlorocobaltate (Cs_2CoCl_4) belong to the space group $D_{2h}^{16} = Pnam$. The parameters of the unit cell are $\underline{a}$ = 9.737 ± 0.0005 A, b = 12.472 ± 0.001 A and c = 7.392 ± 0.003 A (based on x-ray patterns obtained with Co $K\alpha_1$ = 1.78892 and Fe $K\alpha_1$ = 1.93547 A radiation). There are three formular units per cell; the structural type is K_2SO_4. The Cs_I, Cs_{II}, Co, Cl_I and Cl_{II} atoms occupy quadruple positions in the m planes of symmetry; the Cl_{III} atoms occupy the octuple position. A detailed description of the structural investigation has been given in Ref. 16.

Initially the atomic coordinates were determined from the (001) and (100) projections of the electronic density and combinations of the weighted projec-

$hk1$ and $hk2$.

The averaged values of the coordinates based on the above data were taken as the initial values in the process of refinement by the method of differential synthesis applied to the three-dimensional electron distribution density. Naturally, in this case the refinement could not yield appreciable changes in the coordinates, while the refinement process proved to be brief. Altogether it was necessary to carry out three refinement cycles which required a total of 1.5 hours of computer time; the last of these cycles was essentially superfluous. The Co-Cl distances increased somewhat as a result of the refinement and turned out to be equal to each other:

$\text{Co-Cl}_{I} = 2.26_1$ A (instead of 2.22 A),
$\text{Co-Cl}_{II} = 2.26_0$ A (instead of 2.25 A),
$\text{Co-Cl}_{III} = 2.26_0$ A (instead of 2.23 A).

Judging from the interatomic spacing, the Co-Cl bonds are predominantly covalent. The shape of the $[\text{CoCl}_4]^{--}$ tetrahedron proved to be somewhat distorted:

$\text{Cl}_{I}\text{-Co-Cl}_{II} = 116^{\circ}20'$ (instead of 117°),
$\text{Cl}_{I}\text{-Co-Cl}_{III} = 109^{\circ}20'$ (instead of 109°),
$\text{Cl}_{II}\text{-Co-Cl}_{III} = 107^{\circ}20'$ (instead of $107^{\circ}30'$),
$\text{Cl}_{III}\text{-Co-Cl}_{III} = 108^{\circ}50'$ (instead of 107°).

There was only an insignificant modification of the Cl^{-}-Cs^{+} distance.

9. The probable error in determining the coordinates of the atoms in the octagonal structure with spherical symmetry of the atoms is characterized by the relationship

$$\varepsilon(x_j) = \frac{\varepsilon\left(\frac{\partial\rho}{\partial x}\right)_j}{\left(\frac{\partial^2\rho}{\partial x^2}\right)_j},$$

where $\varepsilon\left(\frac{\partial\rho}{\partial x}\right)_j$ is the value of the probable error in the derivative $\frac{\partial\rho}{\partial x}$ and $\left(\frac{\partial^2\rho}{\partial x^2}\right)_j$ is the value of the second derivative.

Both quantities are taken at the point corresponding to the maximum density of the j-th atom.

The difference in the value of the error $\varepsilon(x)$ for the individual atoms is determined both by the difference in the denominator (in the shape of the maxima) and by the difference in the value of the numerator (i.e., the error $\varepsilon\left(\frac{\partial\rho}{\partial x}\right)$ at different points of the cell).

In practical computations of the error this second difference is commonly neglected, the "error wave" $\varepsilon\left(\frac{\partial\rho}{\partial x}\right)$ being replaced by the mean value of the error equal to

$$\overline{\varepsilon\left(\frac{\partial\rho}{\partial x}\right)} = \frac{2\pi}{Va}\left\{\sum_{hkl}^{HKL} h^2\varepsilon[\varepsilon(F)]^2 + \sum_{HKL}^{\infty} h^2\,|F_{p}(hkl)|^2\right\}^{1/2},$$

where through H, K and L we have indicated the maximum values of the reflection indices h, k and l appearing in the x-ray patterns.

Next we have the matter of evaluating the magnitude of the probable error in the values of the structure amplitudes

Substitution of the differences $|F_{э}(hkl)| - |F_{p}(hkl)|$ for $\varepsilon(F)$ leads to a somewhat modified form of Cruickshank's expression[17]:

$$\overline{\varepsilon\left(\frac{\partial\rho}{\partial x}\right)} = \frac{2\pi}{Va}\left\{\sum_{hkl}^{HKL} h^2\,[\,|F_{э}(hkl)| - |F_{p}(hkl)|\,]^2 + \sum_{HKL}^{\infty} h^2\,|F_{p}(hkl)|^2\right\}^{1/2}.$$

Computations by means of this formula are tedious. However, if it is included in the program of the universal computer (which presents no particular difficulties), the additional computer time involved is a matter of a few seconds.

A rougher evaluation of the probable errors is obtained by replacing $\varepsilon(F)$ by $\Phi\,|F_{\text{э}}(hkl)|$, where Φ is the mean value of relative error, for which it is common to take the standard "convergence factor" of the structure:

$$\Phi = \frac{\sum\limits_{hkl} [\,|F_{\text{э}}(hkl)| - |F_{\text{p}}(hkl)|\,]}{\sum\limits_{hkl}' |F_{\text{э}}(hkl)|}.$$

In this case the expression for the average probable error in the derivative assumes the form

$$\overline{\varepsilon\left(\frac{\partial\rho}{\partial x}\right)} = \frac{2\pi}{Va}\left\{\Phi^2 \sum_{hkl}^{HKL} h^2\,|F_{\text{э}}(hkl)|^2 + \sum_{HKL}^{\infty} h^2\,|F_{\text{p}}(hkl)|^2\right\}^{1/2}.$$

This last expression is a step toward the simplified formulas involving the introduction of different types of approximation functions (Booth[18], Kitaigorodski[19] and Vainshtein[20]), wherein the summation over hkl is replaced by integration over reciprocal space.

For practical calculations the most convenient are the formulas of Vainshtein in which the empirical dependence is introduced after integration. The advantage of Vainshtein's formulas are that they take into account the difference in the character of the atomic scattering functions of the different atoms (do not involve assumptions regarding the "similarity" of the atomic scattering curves).

The general expression for the error in the x coordinate on the basis of Vainshtein's formulas can be written in the following form

$$\varepsilon(x) = \varkappa\frac{1}{\sqrt{V}}\cdot\frac{\left\{\sum\limits_{j=1}^{N} Z_j^{\alpha_1}\right\}}{Z_0^{\alpha_2}}\left\{\Phi^2 q_1 + q_2\right\}^{1/2},$$

where V is the volume of the unit cell (projection area in the two-dimensional case), Z_0 is the atomic number of the atom, the error in whose coordinates is being evaluated; $\varkappa$, α_1, α_2, q_1 and q_2 are numerical coefficients: $\varkappa = \frac{\sqrt{k_1}}{k_2}$, $q_1 = p_1/p_2^2$, $q_2 = \frac{1-p_1}{p_2^2}$ (the values of $\alpha_1, \alpha_2, k_1, k_2, p_1$ and p_2 are tabulated in Ref.20).

In applying this expression one must distinguish between three cases:

1) the series cutoff is appreciable and no previous correction made therefor;

2) the series is terminated but in refining the coordinates correction has been made for displacement of the maxima connected with the termination of the series; in this case $p_1 = 1$ and, consequently

$$q_1 = \frac{1}{p_2^2} \text{ and } q_2 = 0,$$

while the general formula for the error assumes the form

$$\varepsilon(x) = \varkappa\frac{1}{\sqrt{V}}\cdot\frac{\left\{\sum\limits_{j=1}^{N} Z_j^{\alpha_1}\right\}^{1/2}}{Z_0^{\alpha_2}}\cdot\frac{\Phi}{p_2};$$

3) the series converges to such an extent that there is practically no cutoff:

$$\varepsilon(x) = \varkappa\frac{1}{\sqrt{V}}\cdot\frac{\left\{\sum\limits_{j=1}^{N} Z_j^{\alpha_1}\right\}^{1/2}}{Z_0^{\alpha_2}}\,\Phi.$$

10. To evaluate the probable error in the atomic coordinates in the case of the two examined structures we used both Cruickshank's equation and that of Vain-

shtein. The calculations according to Cruickshank's formula were carried out on the computer. In the calculations according to Vainshtein's expression, we set $(\sin\vartheta/\lambda)_{\max} = 1$ and $B = 2$, in accordance with the available experimental material. The correction for termination was not taken into account.

For the structure of $Ni(NH_3)_3(NCS)_2$ (projection) we obtained:

according to Cruickshank	according to Vainshtein
$\varepsilon(x)_{Ni} = 0{,}005$ kX	$\varepsilon(x)_{Ni} = 0{,}003$ kX
$\varepsilon(x)_{S} = 0{,}010$	$\varepsilon(x)_{S} = 0{,}006$
$\varepsilon(x)_{NH_3} = 0{,}020$	$\varepsilon(x)_{NH_3} = 0{,}015$
$\varepsilon(x)_{N} = 0{,}035$	$\varepsilon(x)_{N} = 0{,}020$
$\varepsilon(Ni-S) = 0{,}011$	$\varepsilon(Ni-S) = 0{,}007$
$\varepsilon(Ni-NH_3) = 0{,}020$	$\varepsilon(Ni-NH_3) = 0{,}016$
$\varepsilon(Ni-N) = 0{,}035$	$\varepsilon(Ni-N) = 0{,}020$

For the structure of Cs_2CoCl_4 (three-dimensional distribution):

according to Cruickshank	according to Vainshtein
$\varepsilon(x)_{Cs} = 0{,}002$ kX	$\varepsilon(x)_{Cs} = 0{,}0008$ kX
$\varepsilon(x)_{Co} = 0{,}005$	$\varepsilon(x)_{Co} = 0{,}002$
$\varepsilon(x)_{Cl} = 0{,}09$	$\varepsilon(x)_{Cl} = 0{,}0036$
$\varepsilon(Co-Cl) = 0{,}01$	$\varepsilon(Co-Cl) = 0{,}004$

The divergence between the two evaluations of the error is quite considerable, particularly in the three-dimensional case. The reasons for this divergence are not clear. In the light of previous experience, however, there is reason to think that the values of the error evaluated according to Vainshtein's equation are underestimates.

Institute of General and Inorganic Chemistry of the
Academy of Sciences of the USSR

References

1. W.L.Bragg, Phil. Trans., 215, 253 (1915); Proc. Roy. Soc., A 123, 538 (1929
2. A.D.Booth, Trans. Faraday Soc., 42, 444 (1946).
3. A.D.Booth, Nature, 161, 765 (1948); W.Cochran, Acta crystallogr., 4,81(1951
4. E.W.Hughes, J.Am. Chem. Soc., 63, 1737 (1941).
5. A.D.Booth, Nature, 160, 196(1947); Proc.Roy.Soc.L., A 197, 336(1949).
6. V.Vand, Nature, 161, 600 (1948).
7. H.Quaraschi, Acta crystallogr., 2, 404 (1949).
8. W.Cochran, Acta crystallogr., 1, 138 (1948).
9. A.D.Booth, Nature, 161, 765 (1948).
10. D.W.Cruickshank, Acta Crystallogr., 3, 10(1950).
11. W.H.Zachariasen, Acta crystallogr., 5, 68 (1952).
12. A.I.Kitaigorodskii, Iu.T.Struchkov & T.L.Khotsianova, Zhur. tekh. fiz., 27, 1490 (1953).
13. A.D.Booth, Nature, 156, 51 (1945).
14. M.A.Porai-Koshits, Kristallografiia (Crystallography), 1, 248 (1956).
15. M.A.Porai-Koshits, Trudy (Transactions) of the Institute of Crystallography of the USSR Ac. of Sci., No. 10, 117 (1954).
16. M.A.Porai-Koshits, Kristallografiia (Crystallography), 1, 291 (1956).
17. D.W.Cruickshank, Acta crystallogr., 2, 65, 154 (1949).
18. A.D.Booth, Proc. Roy. Soc., A 188, 77 (1946).
19. A.I.Kitaigorodskii, Zhur. tekh. fiz., 17, 1003, 1947; Rengenostrukturnyi analiz (X-ray structural analysis), M.-L. 1950.
20. B.K.Vainshtein, Zhur. eksp. i teor. fiz., 27, 44 (1954).

X-RAY ANALYSIS OF THE MOLECULAR STRUCTURE OF THE SUBSTANCE OF COAL AND COKE

- V.I.Kasatochkin & L.L.Razumova

Separated from the mineral admixtures, the principal organic components of coal (vitrain, fusain and the formative elements) as well as the hard residue left by thermal decomposition of coal (coke) yield x-ray diffraction patterns characteristic of the general class of carbonized substances. This class also includes different forms of carbon, lamp black, the humic components of peat and soils, as well as graphite which, in a sense, represents the limiting case of carbonization.

The superficial similarity of the x-ray patterns of powdered graphite and coals led Debye and Scherrer to an erroneous conclusion regarding the polycrystallene, highly dispersed graphitic structure of coals. Warren[2] provided a theoretical basis for the assumption made by a number of investigators regarding the two-dimensional character of the interference bands in the x-ray patterns of coal. For carbon black, Biscoe and Warren[3] proposed a turbostratic structural model, based on the concept of primary carbon particles in the form of stacks of parallel graphitic carbon-networks, arbitrarily arranged about a common normal. Subsequently the turbostratic theory was extended to coals and cokes.

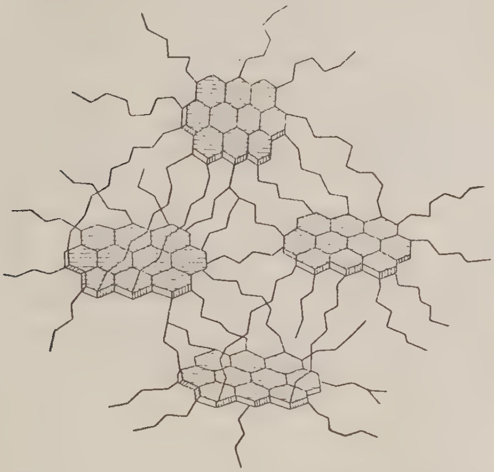

Fig. 1. Schematic sketch of the macromolecular structure of the organic mass of coal.

The interference bands in the x-ray patterns of coals and cokes, which are usually indexed by analogy with graphite, are divided into two interference groups: volumetric with indices (hkl) and two-dimensional with the indices (h00) and (hk0). The linear dimensions of the atomic carbon network can be determined from the broadening of the two-dimensional bands or from their angular displacement. Calculations of the thickness L_c of the stacks have been made on the basis of the broadening of the (002) band on the unproved assumption that the angular widening of this band depends on the number of parallel carbon networks in the stack. However, there are no adequate experimental data for assuming the existence of individual particles of elementary carbon in coals or for postulating a parallel arrangement of the carbon networks in them.

On the basis of a general examination of scattering of x-rays in carbonized materials from the point of view of the theory of scattering in liquids[4] the appearance of the inter-network interference (002) can be explained by the formation of coherent diffraction regions in homogeneous carbonized material with a certain statistical ordering in the packing of the carbon networks[5]. From this viewpoint the scattering intensity I is given by the sum of the intensities of the three scattering components: I_1 the intensity of scattering from the particles of carbon and other atoms not entering into the composition of the carbon networks, I_2 the intensity of scattering from the carbon particles entering into the composition of the networks and I_{incoh} the intensity of incoherent atomic scattering:

$$I = I_1 + I_2 + I_{incoh} = I_1 + PN\overline{F^2}G(s) + I_{incoh} \tag{1}$$

where $\overline{F^2}$ is the average value of the square of the structure factor of the carbon network, N is the number of networks, P is the polarization factor, and G(s) is an interference function.

If we assume that the scattering units are the carbon networks, the interference function G(s) can be written in the following form:

$$G(s) = 1 + 4\pi\rho_0 \int_0^\infty (W - 1) \frac{\sin sl_{pq}}{sl_{pq}} . \tag{2}$$

Here $W = \rho(R)/\rho_0$ is a quantity characterizing the degree of inter-network ordering which is determined by the packing of the carbon networks, $\rho(R)$ is the radial density of the network packing, ρ_0 is the mean value of this density, l_{pq} is the distance between scattering units identified by the numbers p and q and $s = \frac{4\pi \sin\theta}{\lambda}$.

The angular widening of the (002) interference band is determined by the magnitude of W, characterizing the degree of inter-network ordering, and depends on the size of the coherent volumes. The broadening of these (002) bands may therefore be taken as a roentgenographic index of the inter-network ordering.

The organic mass of coal when heated to above 300° gives off a large amount of volatile products comprising carbon, hydrogen, oxygen, sulfur, nitrogen and other elements. The percentage of carbon in the solid residue increases with the temperature and heating time. At high coking temperatures the carbon crystallizes with the formation of graphite. Numerous chemical studies indicate that the volatile products driven off by heating originally form strong chemical bonds in the substance of the coal. As a working hypothesis in our investigation we assumed that the carbon skeleton of the substance of coal is represented by a macromolecular structure in the form of a steric polymer in which the plane hexagonal carbon networks are linked to each other by side chains of organic radicals (Fig. 1)[5]. Experimental verification of the assumed structure of the carbon skeleton in the substance of coal and coke was obtained from the results of integral analysis of the curves for the intensity of scattering of monochromatic x-rays[6]. In view of the fact that until now there have been no satisfactory methods for determining the true density ρ_0 of coals and cokes, i.e., methods taking into account the ultrafine porosity of these substances, we constructed atomic distribution curves in the form of analytic curves described by the following equation

$$4\pi r^2 \Delta\rho = \frac{2}{\pi} \int_0^\infty s\, i(s) \sin srdr, \tag{3}$$

where

$$\Delta\rho = \rho_0 - \rho(r), \quad i(s) = \frac{I(s)}{nf^2P} - 1,$$

I(s) is the experimental intensity curve, n is the number of scattering atoms, f^2 is the atomic factor and P is the polarization factor.

Fig. 2 shows the curves for the radial atomic distribution $4\pi r^2 \Delta\rho$ for cokes obtained from the vitrainized mass of coking coal by heating at 500° (curve 1) and at 1100° (curve 2). The $4\pi r^2 \Delta\rho$ curve computed from the experimental intensity distribution can be approximately represented as the result of surposition of two types of carbon structure in coke: 1) carbon in graphitic type networks, and 2) carbon in the form of the side radicals of the chain structure.

The height of the maxima in the $4\pi r^2 \Delta\rho$ curve is determined by the average number Z of neighbors possessed by a carbon atom (the coordination number) on a sphere of radius r, corresponding to the position of the given maximum on the curve. Let us examine the difference in the heights of the second peak ($r \approx 2.5$Å) in the atomic distribution curves for different cokes. It is obvious that the cokes differ as regards the average number of carbon-atom neighbors; this number in any given coke depends on the ratio of the number of carbon atoms located in the networks (Z = 9) and the number of carbon atoms in the side chain (Z = 2). Thus from a comparison of the heights of the second peak in curves 1 and 2 we

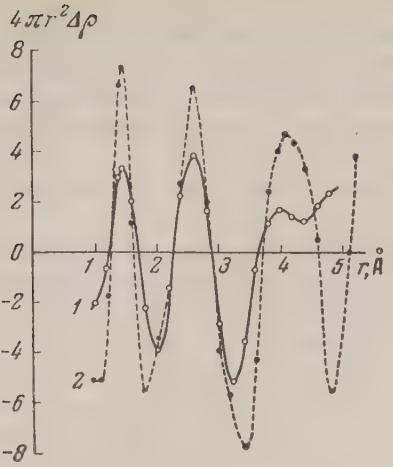

Fig. 2. Curves characterizing the radial atomic distribution in the products obtained from the vitrainized part of grade K coal obtained by 4-hour heating: 1) at 500° and 2) at 1100°.

find that the coke obtained from coking coal at 1100° has a relatively lower amount of carbon in the side chains as compared with the coke prepared from the same coal but at 500°. This is consistent with the concepts regarding the transition of the carbon in the side chains to the networks in the process of carbonization.

The results of integral analysis of the intensity of scattering obtained by Razumova[6] may be regarded as experimental confirmation of our assumed scheme for the structure of the carbon skeleton of the substance of coal. Moreover, the results show that analysis of the second maximum on the radial atomic distribution curves can be utilized for quantitative evaluation of the ratio between the carbon in the carbon networks and the carbon in the side chains.

It should be noted that for coke obtained from polyvinylidene chloride at 1000° Franklin[7] drew a quantitative conclusion regarding the fraction of carbon not organized into networks from the height of the first peak in the atomic distribution curve. Franklin based his deductions on the assumption of independent scattering of the carbon atoms not entering into the composition of the carbon networks. Actually the carbon atoms in the side chains are characterized by a regular arrangement and it is natural to assume that they participate in the interference recorded in the scattering intensity curve.

X-ray investigations of the molecular mechanism of the thermodecomposition of coal and the formation of coke[8] yield a picture characterized by the growth of the networks and changes in their degree of ordering.

Curves characterizing the temperature dependence of the dimensions L_a of the carbon networks and their degree of ordering for the case of the vitrainized mass of Donets coking coal are reproduced in Fig. 3. These curves were constructed from the x-ray patterns of powdered samples of cokes obtained by 4-hour heating of the vitrainized mass at the indicated temperatures. The values of L_a were computed from the broadening of the (100) band. The degree of ordering of the networks was characterized by the half-width of the (002) band. It will be seen that the curve characterizing the growth of the carbon networks has an S-shape with a steep rise in the 400-800° interval and an inflection point at about 700°. It will be seen that the curve for the variation of the half-width of the (002) band has a minimum at about 500° and a maximum at about 700°. It indicates that the ordering increases to 500° then sharply decreases going to 700° and then again increases at higher temperatures. The shape of the ordering curve may be explained on the assumption that we are dealing here with two opposed processes. The first of these is thermal destruction in the side chains with freeing of structural units which then

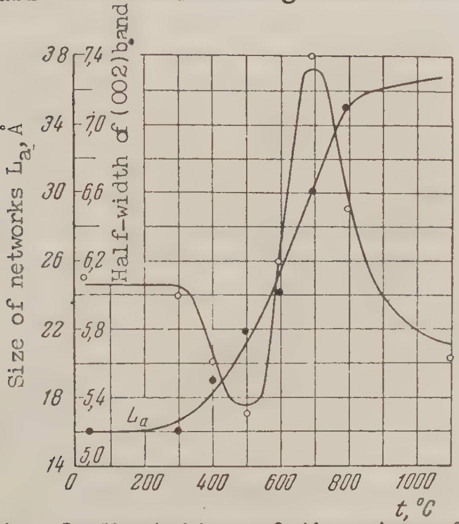

Fig. 3. Variation of the size of the carbon networks (solid points) and the degree of inter-network ordering (circles) for the vitrainized mass of grade K coal with the coking temperature.

become kinetic units; by virtue of this the coal substance goes over into a fluid or so-called plastic state. Under the influence of the molecular force field the carbon networks freed of the side bonds tend to orient themselves in a parallel packing. The other, reverse process is the successive joining or recombination of the side radicals, leading to the formation of bonds between the structural units and solidification of the organic mass of the coal.

Thus the shape of the ordering curve can be explained in terms of different rates of destruction and recombination.

We have also utilized x-ray methods for investigating the texture of the organic mass of coals, developing under natural conditions, when the coal layers are subject to the pressure of overlying mineral formations[9] and under the influence of high pressures when the coal is in powdered form.[10]

Institute of Mineral Fuels of the
Academy of Sciences of the USSR

References

1. P.Debye & P.Scherrer, Phys. ZS., 17, 277 (1916); 18, 291 (1917).
2. B.E.Warren, Phys. Rev., 9, 693 (1941).
3. J.Biscoe & B.E.Warren, J. Appl. Phys., 13, 364 (1942).
4. H.Menke, Phys. ZS., 33, 593 (1932).
5. V.I.Kasatochkin, Izv. AN SSSR Otd. tekh. nauk., No. 9, 1321 (1953).
6. L.L.Razumova, Thesis, Institute of Mineral Fuels, M. 1954.
7. R.E.Franklin, Acta crystallogr., 3, 107 (1950).
8. V.I.Kasatochkin & L.L.Razumova, Doklady AN SSSR, 78, 172 (1953).
9. L.B.Nepomniashchii, Thesis, Institute of Mineral Fuels, M. 1954.
10. L.L.Razumova, V.I.Kasatochkin & M.P.Volarovich, Doklady AN SSSR, 103, 1033 (1955).

APPLICATION OF X-RAY STRUCTURAL ANALYSIS TO INVESTIGATIONS OF OXIDE-COATED CATHODES

- E.P.Ostapchenko

Introduction

The exceptionally wide use of oxide-coated cathodes in the vacuum tubes employed in most modern electronic instruments and devices serves to explain the great scientific and practical interest in the physical processes occurring in such cathodes. Despite the great number of studies of the properties of oxide-coated cathodes and the physical and chemical processes occurring therein, there is still much to be learned about the behavior and characteristics of such cathodes and the number of diverse investigations devoted to such cathodes may be expected to increase. The use of x-ray structural analysis should make it possible to delve more deeply into the processes occurring in such cathodes during their operation and allow of establishing some of the reasons for their premature failure.

In the present report we give the results of x-ray investigations of the carbonates and oxides of alkaline earth metals used as coatings for oxide-coated cathodes and of the interlayers developing between the base and the coating of the cathode during its operation.

Procedure

The investigated alkaline earth metal carbonates were obtained by precipitation from solutions of barium, strontium and calcium nitrate by means of sodium carbonate; a series of samples for establishing the identity of the structures was also precipitated by means of ammonium carbonate. The precipitation temperature was 80-90°C.

The x-ray patterns were registered by copper or cobalt radiation in 57.4 mm diameter cameras. In a few cases, for the purpose of obtaining a more accurate value of the parameters, we used a VRS camera having a diameter of 143.25 mm. In a number of cases selective radiation filters were employed.

In investigating the structure of alkaline earth metal oxides obtained in a tube with a heater cathode 1.4 mm in diameter (after decomposition of the carbonate), it was necessary to employ a special procedure for obtaining the x-ray patterns due to the instability of the oxides of barium, strontium and calcium in the presence of carbon dioxide and water vapor. Part of the work in investigating the process of decomposition of the different carbonates into oxides was carried out in a specially designed vacuum temperature chamber, which made it possible to obtain five patterns from one cathode at different stages of its processing without disturbing the vacuum. The most of the x-ray patterns, however, were recorded using the following procedure: at the appropriate stage of processing or after a certain period of service the tube was broken open in a special hermetically sealed chamber through which was passed a stream of carefully purified and dried nitrogen; the filament was carefully detached and dipped briefly into molten wax after which it was mounted in the camera for x-raying. The wax lines on the x-ray patterns were taken into account in the subsequent calculations.

For investigating the interlayers forming between the base and the coating the latter was removed mechanically and the base with the remaining layer was x-rayed in the usual manner.

Structure of barium, strontium and calcium carbonates

When precipitated by sodium carbonate, the carbonates of barium and strontium are crystallized in a rhombic lattice of the aragonite type, while calcium carbonate has a rhombohedral lattice of the calcite type. Precipitation with ammonium carbonate does not result in a change in the lattice of barium and strontium carbonate, but calcium carbonate in this case also crystallizes in a rhombic lattice (aragonite type).

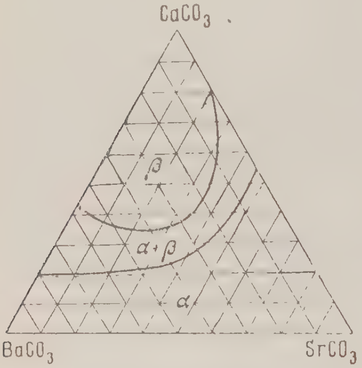

Fig. 1. Crystal state of ternary, jointly precipitated carbonates of barium, strontium and calcium: α) aragonite type solid solution, β) calcite type solid solution.

When precipitated together by soda the carbonates of barium and strontium in all proportions form solid solutions having the same structure with lattice constants varying from those for pure $BaCo_3$ to $SrCO_3$.

In the case of precipitation of barium and calcium carbonate solid solutions are also formed: in the case of 80 to 100% $BaCO_3$, there is formed a solid solution with an aragonite structure; with a $BaCO_3$ content under 55% the solid solution has a calcite structure, while in the intermediate range (80-55% $BaCO_3$) two solid solutions are present - one with an aragonite type structure, the other with a calcite structure. An analogous situation is observed when the carbonates of strontium and calcium are precipitated with soda: with an $SrCO_3$ content above 45%, an aragonite type structure is formed; with an $SrCO_3$ content under 20% - a calcite type solution forms, while in the intermediate range, two solutions are formed. The results of our investigation of joint precipitation of the three carbonates are shown in Fig. 1.

Precipitation with ammonium carbonate does not alter the results substantially (only the regions of formation of the different phases are modified somewhat).

Decomposition of the carbonates into oxides

We investigated the process of decomposition of jointly precipitated carbonates and of mechanical mixtures of the following composition: the equimolar binary carbonate of barium and strontium, the ternary carbonate having the proportion of components $BaCO_3:SrCO_3:CaCO_3 = 40:20:40$ and the ternary carbonate having the component proportions 50:45:5.

In the case of the equimolar solid solution the process of decomposition begins at 600°; the time required for decomposition to start decreases with increasing temperature (10 min at 600°, 2 min at 700°, 1 min at 745°, etc.). With further increase in temperature (or prolongation of the heating time at 700-745°) two phases of the solid solution of the oxides are formed (face-centered cubic lattice), characterized by the constants $a_1 = 5.358$ and $a_2 = 5.091$ A, which values correspond approximately to the following compositions: 95% SrO + 5% BaO and 73% BaO + 27% SrO. Further increase in the temperature or heating time leads to the formation of a single phase solid solution of the oxides with a lattice constant $a = 5.268$ A (equimolar solid solution).

In the case of decomposition of an equimolar mixture of barium and strontium carbonate approximately the same sequence is observed, but in this case the carbonates decompose with the formation initially of a mechanical mixture of the oxides of barium and strontium which is then followed by the formation of two phases and finally by the formation of the single phase. Moreoever, in the case of decomposition of the mechanical mixture of the carbonates into the oxides a higher temperature is required to obtain the two phases, as compared with the temperature needed for attaining the same stage of decomposition in the case of the carbonate solid solution. Thus, for decomposition of the mechanical mixture of the carbonates and formation of the oxide solid solution higher heating temperatures are required than in the case of joint precipitation of the carbonates.

An analogous behavior is observed in the case of decomposition of the ternary carbonates; however, in this case the temperatures of decomposition and formation of the oxide solid solutions are higher than in the case of the binary carbonates; different compositions of the ternary carbonates require different temperature conditions for complete decomposition. For example, the formation of the single phase oxide solid solutions in the case of the 50:45:5 ternary carbonate occurs only at temperatures above 1050°C.

Crystal structure of barium, strontium and calcium oxides

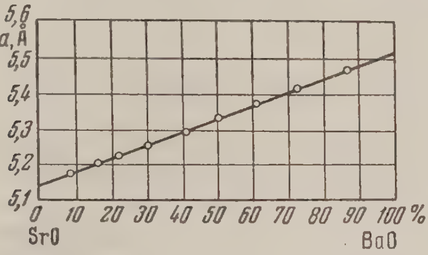

Fig. 2. Variation of the lattice parameter of the (Ba, Sr)O solid solutions with the composition.

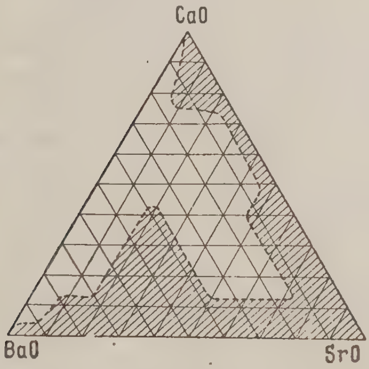

Fig. 3. Formation of the single phase solid solution of the oxides (hatched area) in the BaO-SrO-CaO system.

The oxides of barium and strontium when heated together form a continuous series of solid solutions characterized by linear variation of the lattice parameter (Fig. 2). Formation of a solid oxide solution is also observed in the case of joint heating of the oxides of strontium and calcium, whereas the oxides of barium and calcium do not form mixed crystals even at a temperature of 1200°. At all proportions of the components the cathode coating in our experiments consisted of a mechanical mixture of barium and calcium oxides.

Investigation of the ternary oxides obtained by the decomposition of the jointly precipitated carbonates of Ba, Sr and Ca presented the greatest difficulties. As noted above, the ternary carbonates of different composition require different heat treatments for complete transformation into solid solutions. Obviously, the single phase solid solution could not be expected to form with all compositions. On the other hand, appreciable overheating of the cathode would undoubtedly lead to evaporation of the more volatile component (BaO), which would, of course, affect the results of measurements of the lattice parameters. However, the conditions of the experiment required bringing the heating temperature up to 1200° at least for a short time.

The results of our study of ternary oxides are shown in Fig. 3. The formation of two phases of solid solution is observed in a large range of concentration, while the single phase solid solution forms only at low concentrations of calcium oxide (up to ~12%) and in a narrow interval of concentrations with a BaO and CaO content up to 40%. In the last case, to judge from the results of careful measurements of the lattice parameters, a second phase is also present, but in such minute amounts that it cannot be detected on the x-ray patterns.

The variations of the lattice parameter are not regular in all directions over the diagram which indicates the possibility of formation of different mixed crystals, for example, (Ba,Sr)O, (Sr,Ca)O and (Ba,Sr,Ca)O.

Changes in the composition of the oxide coating during service and growth of the oxide crystals

The fact that we obtained a linear dependence of the lattice constant of the (Ba,Sr)O solid solutions on their composition made it possible to carry out an investigation of the change in the initial equimolar oxide coating with the service time of the cathode at different temperatures. The results show that appreciable evaporation of barium oxide, as evinced the increase in the SrO content of the coating, occurs even at a temperature of 820°. As the temperature is increased, the rate of vaporization of BaO rapidly rises and at 1100° half the initial content of BaO evaporates within 15 hours, after which the rate of evaporation falls off.

Investigation of the growth of the oxide crystals during the period of service of the coating showed that the rate of growth is highest for the BaO crystals and lowest for the crystals of the (Ba,Sr,Ca)O solid solution. It has been found in other studies that growth of the oxide crystals results in impared emission, hence in this respect a coating consisting of ternary oxides is best where longevity of the cathode is concerned.

Qualitative relation between the emission and the crystal structure

The question of whether there is a connection between the crystal structure of the initial carbonate and the emission characteristic of the cathode is not yet definitively resolved. It has been established that the structure of the carbonates has a substantial influence on the rate of their decomposition and probably on the final homogeneity of the resultant oxides. The emission characteristics of cathodes, however, also depend on a number of other factors and at present there is no reliable procedure for measuring the emission of oxide coatings while eliminating the influence of all the diverse technological factors.

We can, however, note the following regarding the relationship between the crystallographic properties of the oxides and their emission characteristics.

The character of the dependence of the saturation current of oxide-coated cathodes, their work function and their crystal structure on the composition of the coating indicates that in the case of mixed (Ba,Sr)O crystals the work function is smaller, and, consequently, the emissivity is higher than in the case of barium oxide or strontium oxide alone. A similar decrease in the work function results from the formation of mixed (Sr,Ca)O crystals, while in the case of a mixture of BaO and CaO which does not form a solid solution, there is observed only a small decrease in the work function, amounting to 0.07 ev, due probably to the fact that where both the "outside" and "inside" parts of the work function are concerned the interaction of barium atoms with calcium oxide is more advantageous than their interaction with barium oxide. Apparently, the formation of mixed crystals appreciably lowers the rate of diffusion of barium. This naturally involves a change in the equilibrium concentration of free barium which in turn leads to a change in the work function for mixed crystals.

In addition, some part in determining the emissivity of mixed crystals may be played by imperfections of the lattice at sufficiently high temperatures in connection with the disappearance (evaporation) of the barium oxide, since it is known that in solid solutions disordering is more appreciable than in the case of simple components. In the case of ternary oxide coatings the greatest pulse emission is also observed in the region where the oxides of barium, strontium and calcium form their single phase solid solution. In fact the pulse emission from ternary oxides may exceed the maximum emission from (Ba,Sr)O; this is probably due to the greater change in the rate of diffusion of the barium. Experiments showed, for example, that a coating having the composition BaO:SrO:CaO = 50:45:5 after calcination at 1050° yields a sharp increase in emission; according to the x-ray data the single phase solid solution forms at this calcination temperature.

Investigation of oxide-coated cathode interlayers

During the period of operation of an oxide-coated cathode there may form between its base and coating an interlayer consisting of some product of the reaction between the oxide coating and the metal of the base or admixtures therein. We investigated cathodes having bases of nickel with additions of silicon and magnesium as well as cathodes with tungsten and nickel-tungsten bases.

In the case of nickel bases with ~0.3% silicon, an interlayer of barium orthosilicate (Ba_2SiO_4) was found to be present even immediately after decomposition of the carbonate. It must be emphasized that even when the coating consists of a solid solution of the oxides of barium and strontium only barium orthosilicate is observed; this is presumably due to replacement of the strontium by barium atoms in Sr_2SiO_4. Careful measurements of the lattice parameters of synthetically prepared Ba_2SiO_4 and of the compound formed in the interlayer of an oxide-coated cathode indicates that the composition of the interlayer includes a certain number of strontium atoms. Presumably the strontium enters into the composition of the interlayer only at the time of its formation; the amount of it in the interlayer does not increase with time due to the anti-diffusional characteristics of Ba_2SiO_4 with respect to strontium atoms. The difference in the concentrations of barium and strontium entering into the composition of the intermediate layer, in addition to the probable replacement of Sr atoms by Ba in Sr_2SiO_4, may be attributed to the difference in the heats of formation of the oxides of barium and strontium (133 and 141 cal per mole, respectively). We were unable to detect any interlayer in cathodes on bases of nickel plus ~0.2% magnesium after decomposition of the carbonates and periods of service up to 400-500 hours.

Investigation of the interlayers on a tungsten base and on bases of nickel-tungsten alloys containing from 4 to 20% tungsten showed that an interlayer is present even immediately after decomposition of the carbonates by the usual treatment. Attempts to identify the interlayer substance with reference to tables of interplanar spacing on the assumption that in this case $BaWO_4$ is formed failed to yield positive results. Investigation of the solid phase reaction of barium oxide with tungsten trioxide showed that whereas barium tungstate can be obtained synthetically by heating in air a mixture of $BaCo_3$ with WO_3 in the ratio 1:1, when the proportion of barium carbonate in the initial mixture is increased to 3:1 there is formed, after 2 hours heating at 1200°, a compound having a different structure, the probable formula of which is Ba_3WO_6(3 BaO·WO). The substance found in the interlayers of oxide-coated cathodes on tungsten and nickel-tungsten bases is identical in structure with synthetically prepared Ba_3WO_6. Just as in the case of interlayers on silicon-containing nickel bases, where the coating of the cathode consists of a solid solution of Ba and Sr oxides, in this case we have the formation primarily of barium tungstate.

Our investigation of the tungstates of barium and strontium showed first that they formed solid solutions and second that the barium atoms tend to displace the strontium in Sr_2WO_6, whereas there is no replacement of barium by strontium in Ba_3WO_6. The crystal structure of tungstate of the type R_3WO_6 (where R is one of the alkaline earth elements) is close to the face-centered cubic structure, however, splitting of a number of the lines and the appearance of a number of additional lines indicate that the true structure of such tungstates differs from the ideal cubic and is probably either triclinic or monoclinic. It must be noted that the extent to which the different tungstates differ from the ideal cubic structure varies with the composition: thus, whereas the "monotungstates" (R_3WO_6) differ markedly from the ideal cubic structure, the tungstate whose composition includes two alkaline earth metals (Ba_2SRWO_6, $BaCa_2WO_6$, etc.) exhibit only minor differences, while the ternary tungstate ($BaSrCaWO_6$) shows no difference at all.

Conclusion

The results of our x-ray structural investigation made it possible to explain a number of the experimentally observed regularities in the operation of oxide-coated cathodes and the dependence of their emission on the composition and crystal state of the oxides.

The results of our investigation of the decomposition of the carbonates should be of help in correctly selecting the conditions of treatment of electron tube cathodes, particularly for those prepared with coatings of ternary carbonates.

Investigation of the system of ternary oxides established the region of concentrations which it is desirable to obtain in preparing oxide coatings. We have obtained valuable information on the formation of interlayers in oxide-coated cathodes; the results show why it is preferrable to use bases of nickel with the addition of magnesium instead of nickel with silicon.

In conclusion the writers desire to express their deep gratitude to B.M. Tsarev for his constant interest in the work and his valuable advice and suggestions.

X-RAY INVESTIGATION OF THE DEPENDENCE OF THE STRUCTURE OF A PALADIUM CATALYST ON THE CONDITIONS OF ITS ELECTROLYTIC PREPARATION AND HEAT TREATMENT

- V.D.Ruchkina

The role of catalysts in the chemical industry and hence in the national economy cannot be overrated. Upon them depend such important branches of industry as ammonia synthesis, cracking of petroleum and the production of many synthetics. Hence it is highly important to determine the optimal conditions of preparation of the most active and stable catalysts with the requisite characteristics and to establish the causes that lower their activity in order to develop effective means for assuring a long and effective service life.

We used x-ray analysis to determine the dependence of the structural characteristics (dispersion, parameters and degree of perfection of the crystal lattice) of paladium catalysts on the current density in their electrolytic preparation and on the temperature of heating in hydrogen.

The samples were prepared by electrolysis from an aqueous solution of $PdCl_2$ with deposition on a platinum wire 15 mm long and 0.5 mm in diameter. The specimens were x-rayed in standard powder cameras; the resultant patterns were photometered on an MF-2 photometer.

Utilizing the different regularities characterizing the change in line breadth with θ due to dispersion of the catalyst substance and residual stresses of the second kind[1], we established that the influence of stresses of the second kind can be neglected as compared with the influence of dispersion.

The crystal size (dispersion) was calculated according to the Selikov-Sherrer equation[2] with an accuracy of within 2% for the finely dispersed samples and to within 12% for the coarse-grained ones.

In determining the true line breadth we utilized the procedure described by Jones[3]. A coarse crystal sample of paladium heated in air to 500° served as a standard. The degree of perfection of the crystal lattice was determined from the ratio of integral intensities of the (420) and (311) lines. The period of the lattice was determined with an accuracy of 0.1%.

As a result of our studies of paladium specimens obtained with different current densities (the current density was varied from 0.001 to 0.009 amp/cm^2) we established that all the structural characteristics exhibit a regular dependence on the current density. The computed crystal particle size shows a consistent decrease with increasing current density.

At a current density of 0.005-0.006 amp/cm^2 there is a pronounced bend in the curve characterizing the variation in crystal size (Fig. 1). The character of this variation can be explained by the fact that at a low current density, when relatively few new centers of crystallization are born, the already formed crystals tend to grow, since this requires less expenditure of energy than the creation of new nuclei. As the current density is increased the number of centers of crystallization increases and the mean size of the crystal particles goes down. With further increase in current density we arrive at the point where there are so many crystal nuclei that the concentration of the solution about the developing and growing crystals decreases and the creation of new centers of crystallization becomes difficult or impossible.

A change in the period of the crystal lattice of paladium is observed in specimens ob-

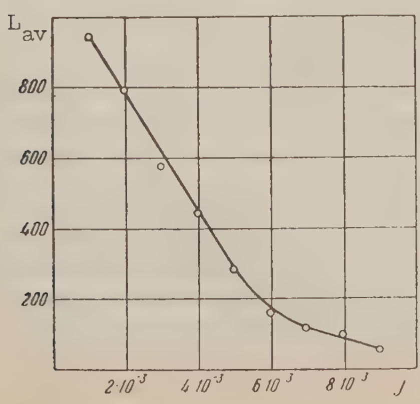

Fig. 1. Dependence of mean crystal size on the current density (j, amp/cm^2).

tained at high current densities (0.008 amp/cm^2 and higher). This change is apparently connected with the penetration of hydrogen, evolved during the electrolysis, into the paladium lattice.

Determinations of the integral intensity of the (420) and (311) lines indicate that the crystal lattice of paladium obtained with a low current density (0.001 amp/cm^2 and under) is characterized by a high degree of perfection (the equilibrium lattice is assumed to be that of paladium obtained with a very low current density and then heated in air at a temperature above 500°).

With increasing current density the degree of perfection of the crystal lattice monotonously deteriorates; this is presumably due to the increased rate of crystal formation. A high rate of crystallization results in the appearance of different types of imperfections in the structure of the crystals. Moreover, as the current density is increased the amount of hydrogen evolved also increases and this, penetrating into the crystals in the process of their formation, favors the development of structural defects.

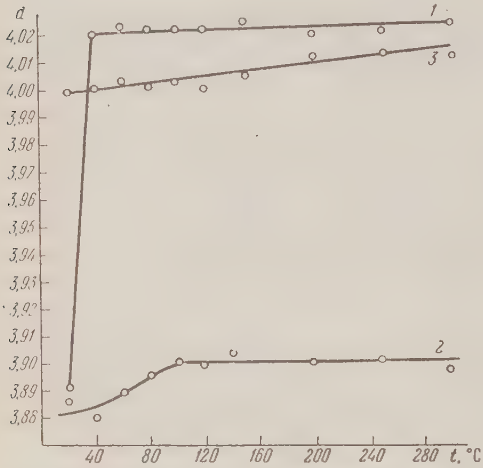

Fig. 2. Dependence of the lattice periods of paladium and paladium hydride on the temperature of heating in hydrogen: 1) coarse crystal Pd, 2) fine crystal α-phase of PdH, 3) finely dispersed β-phase of PdH.

It was found that the variation of the lattice constant of paladium with the temperature of heating in hydrogen differs for specimens with different degrees of initial dispersion. The lattice period of coarse crystal paladium even at 20° increases from 3.88 to 3.90 A and further to 4.02 A at 40°. However, further increase in temperature brings little additional increase in the lattice period (Fig. 2, curve 1). This is probably due to the fact that the α-phase of the PdH system forms at about 40°.

It must be noted that the paladium hydride which readily forms in coarse crystal specimens of paladium does not remain unchanged with time. Part of it is spontaneously transformed into the α-phase, as is evinced by the appearance of additional lines in the x-ray patterns of samples stored for 24 hours after heating. In the course of determining the ratio between the α- and β-phases, we found that the amount of α-phase separating out decreases with increasing temperature of heating in hydrogen.

As a result of investigation of the influence of heat treatment on the period of the crystal lattice of a finely dispersed specimen of paladium it was established that the lattice constant of the main mass of paladium remains unchanged in heating to 20° and 40°. However, in the x-ray patterns of finely dispersed specimens heated in hydrogen to these temperatures, in addition to the lines associated with the main lattice, there appear weak lines pertaining to the β-phase and exhibiting the periods characteristic of this phase. The intensity ratios of the lines associated with the α- and β-phases for a fine crystal specimen indicate the predominance of the α-phase in paladium hydride (after heating at 60°). As the temperature is increased the amount of the β-phase increases, while the amount of the α-phase goes down accordingly so that in the region of high temperatures the β-phase predominates.

The lattice period of the α-phase of a fine crystal specimen decreases somewhat as the heating temperature in hydrogen rises to 100-120°; above this temperature the lattice period remains virtually constant (Fig. 2, curve 2). The lattice constant of the β-phase in a finely dispersed specimen (in contrast to the case of coarse crystal paladium) gradually increases with rising temperature up to 250-300° (Fig. 2, curve 3).

Absorption of hydrogen by paladium leads to some smearing out of the lines, due to inhomogeneity of composition of the forming phases. Hence the accuracy in measuring the breadth and integral intensity of the lines is appreciably reduced. However, judging from the changes in the breadth of the interference lines we established that beginning with 100° the mean size of the crystals increases as the temperature of heating in hydrogen is increased.

Conclusions

1. The effects produced by the different factors studied on the structural characteristics of electrolytically prepared paladium catalyzors are not identical.
2. The current density has a pronounced influence on the degree of dispersion (size) of the crystals, the parameters and the degree of perfection of the paladium lattice.
3. The dependence of the lattice periods on the temperature of heating in hydrogen is complex. This dependence differs for coarse crystal as against fine crystal specimens.

Frunze Polytechnical Institute

References

1. L.Moroz, Zhur. tekh. fiz., 22, 498 (1952).
2. A.I.Kitaigorodskii, Rengenovskii analiz melkokristallicheskikh i amorfnykh tel (X-ray analysis of fine-crystal and amorphous materials), M.-L. 1952.
3. F.W.Jones, Proc. Roy. Soc., A 166, 16 (1938).

POSSIBLE USE OF X-RAY ANALYSIS OF POLYCRYSTALS IN GEOLOGICAL STUDIES

- B.G.Erenburg

X-Ray analysis of polycrystals is rather widely used in the laboratories of geological agencies as one of the methods of mineralogical phase analysis. Commonly the patterns are recorded from powdered specimens compressed into small cylinders. The well-known registration procedure "from a flat specimen" at large and small glancing angles has not until now been applied to any extent in studying of mineral and ore deposits.

We used photography from a flat specimen at small glancing angles for mass investigation of the composition of manganese ores from one extensive deposit. These ores consist mainly (70-80%) of carbonates of the calcite type, containing variable amounts of manganese and calcium and appreciably smaller amounts of iron and magnesium. The non-carbonate remainder consists primarily of quartz, opal and complex silicates (chloritic). For detailed reconnaissance of the deposit it was necessary to find a procedure which would clearly characterize the mineralogical composition of the carbonate part of the ore. This proved to be a difficult task in view of the high degree of the dispersion of the material and the difficulty of separating out the carbonates in more or less pure form. In this case the powder x-ray method proved to be the only suitable one and use of the registration from a flat specimen procedure made it possible to carry out mass analyses.

The criterion for identifying carbonates from the x-ray patterns was the distance Δl from the $(10\bar{1}4)$ carbonate line to the (1011) quartz line (d = 3.336 kX). In most cases quartz was present in the ore; when absent an appropriate amount was added to the sample. The photography was carried out on ordinary Debye cameras, 57.3 mm in diameter, by the radiation from iron and chromium anodes. The ore specimens were coated on a flat metal plate mounted on a special stand. The angle between the plane of the specimen and the primary beam was selected so as to obtain the sharpest α- and β-reflections from the indicated sets of planes; for the Fe rays this angle was 28°; for the rays from Cr, 34°. The exposure for flat specimens was approximately one tenth that required for equivalent cylindrical specimens: of the order of 30 min at a voltage of 30 kv and a current of 10 ma. This made it possible to obtain up to 20 x-ray patterns with one camera and tube per working day. On these patterns, in addition to sharp $(10\bar{1}4)$ reflections, there also usually appear a number of reasonably sharp lines characteristic of calcite type carbonates: $(11\bar{2}0)$, $(11\bar{2}3)$, $(202\bar{2})$ and $(11\bar{2}6)$. Not infrequently other lines associated with impurities are discernible on the patterns, however, in most cases, there are weak.

The error in determining $d_{(10\bar{1}4)}$ usually does not exceed 0.02 kX, inasmuch as the error in determining Δl amounts to 0.1-0.2 mm. The average divergence between the results (mean value for 20 specimens) of carbonate determinations by the two methods - from a cylindrical and from a flat specimen - amounted to 0.01 kX. The reproducibility in determining d was approximately of the same magnitude. In cases when it was necessary to determine the value of d with greater accuracy, we utilized an RKE type camera by means of which we registered x-ray patterns of the ore samples with small amounts of sodium chloride added. In this case we utilized the $(10\bar{1}4)$ reflection of carbonate and the (002) reflection of NaCl.

Samples for analysis were taken from the cores at intervals of about 1 meter. In this manner we analyzed about 1800 samples of ore characterizing fully or partly 12 bore holes from three geological profiles. On the basis of the results obtained it was possible to draw a number of conclusions regarding both the mineralogy of the carbonate ores and the geological structure of the ore body. Some of these conclusions were unexpected by the geologists and chemists concerned and apparently could not have been arrived at by any other method.

The mass x-ray studies showed that the values of $d_{(10\bar{1}4)}$ for the carbonates of this deposit in almost all cases fall between 3.03 and 2.91 kX or 2.86 and 2.81 kX. Obviously the values of $d_{(10\overline{1}4)}$ falling in the 3.03-2.91 kX interval correspond to manganocalcites with a rising manganese content (and possibly also iron and magnesium), while the values between 2.86 and 2.81 kX correspond to rhodochrosite, which may also contain admixtures of calcium, iron and magnesium; values of $d < 2.84$ kX correspond to highly ferruginous (or possibly magnesium-containing) rhodochrosites. The presence of the latter type of carbonate in the given deposits was established for the first time by the x-ray studies. In addition there are encountered in this deposit, although more rarely, carbonates of the dolomite-ankerite type with a value of $d_{(10\overline{1}4)} \approx 2.88$-$2.90$ kX, the x-ray patterns for which differ from those described above by a greater sharpness and larger number of lines. Given the great diversity of carbonates present in the formation, the complete absence of members of the isomorphic series $CaCO_3$-$MnCO_3$ with values of $d \approx 2.87$-2.90 kX showed that very special conditions are necessary for the formation of these carbonates (if they exist at all). Thus the isomorphic series $CaCO_3$-$MnCO_3$ under ordinary conditions apparently is not continuous, contrary to the assertions of Dana[1]. Vegard[2] indicates that artificially prepared isomorphic mixtures of $CaCO_3$ and $MnCO_3$ do not yield a continuous series.*

Thus the x-ray data obtained provided a solid mineralogical basis for classifying the carbonate ores of this deposit and made it possible to establish the presence of hitherto unreported minerals; furthermore the accumulated data led to new conclusions regarding the conditions of equilibrium in the carbonate systems in question.

The roentgenometric procedure made it possible to detect a highly unusual type of carbonate minerals, representing a heterogeneous system in which there are simultaneously present two or three complex carbonates of the calcite type forming separate phases. The carbonate lines are double or triple in the patterns of such specimens. Thus we frequently encountered pairs of lines corresponding to carbonates with $d = 2.91$ and 2.86 kX or with $d \approx 2.91$ and 2.98 kX as well as triple lines corresponding to carbonates with $d = 2.91$, 2.86 and 2.81 kX. As far as we know such carbonate systems are nowhere described in the literature. At present we can advance only the following speculations regarding the conditions of their formation. Probably the carbonate deposits with $d = 2.91$ and 2.86 kX were formed from solutions as equilibrium binary systems in consequence of the impossibility of formation of one carbonate of intermediate composition owing to the presence of the above-mentioned break in the $CaCO_3$-$MnCO_3$ isomorphic series. This hypothesis is supported by the fact that these two carbonates almost always accompany each other in varying proportions.

The systems with $d = 2.91$ and 2.96 kX, while not common over the entire area of the deposit, do form isolated heavy layers in some sections. Here the different carbonates cannot apparently be in equilibrium with each other. It is not impossible that these systems are aggregations of fine fragments of different carbonates formed at different times.

The geological profiles for the northern and southern parts of the deposit, shown in Figs. 1 and 2, were plotted on the basis of the x-ray data (the southern and northern sites are an appreciable distance apart). Even a cursory glance at these profiles reveals appreciable differences in the composition of the carbonates in the two sections: the southern site is characterized by an abundance of rhodochrosites and manganocalcites rich in manganese as well as by the presence of ferruginous rhodochrosites, while the northern site is characterized

---

*Note added in proof. The results of chemical analyses obtained after presentation of the present report appear to cast doubt on our assertion regarding the absence of continuity in the $CaCO_3$-$MnCO_3$ isomorphic series inasmuch as the content of $FeCO_3$ and $MgCO_3$ in mixed carbonates proved to be somewhat greater than we first assumed. Possibly the break in the continuous series of the observed values of $d_{(10\overline{1}4)}$ is due to the presence of these carbonates.

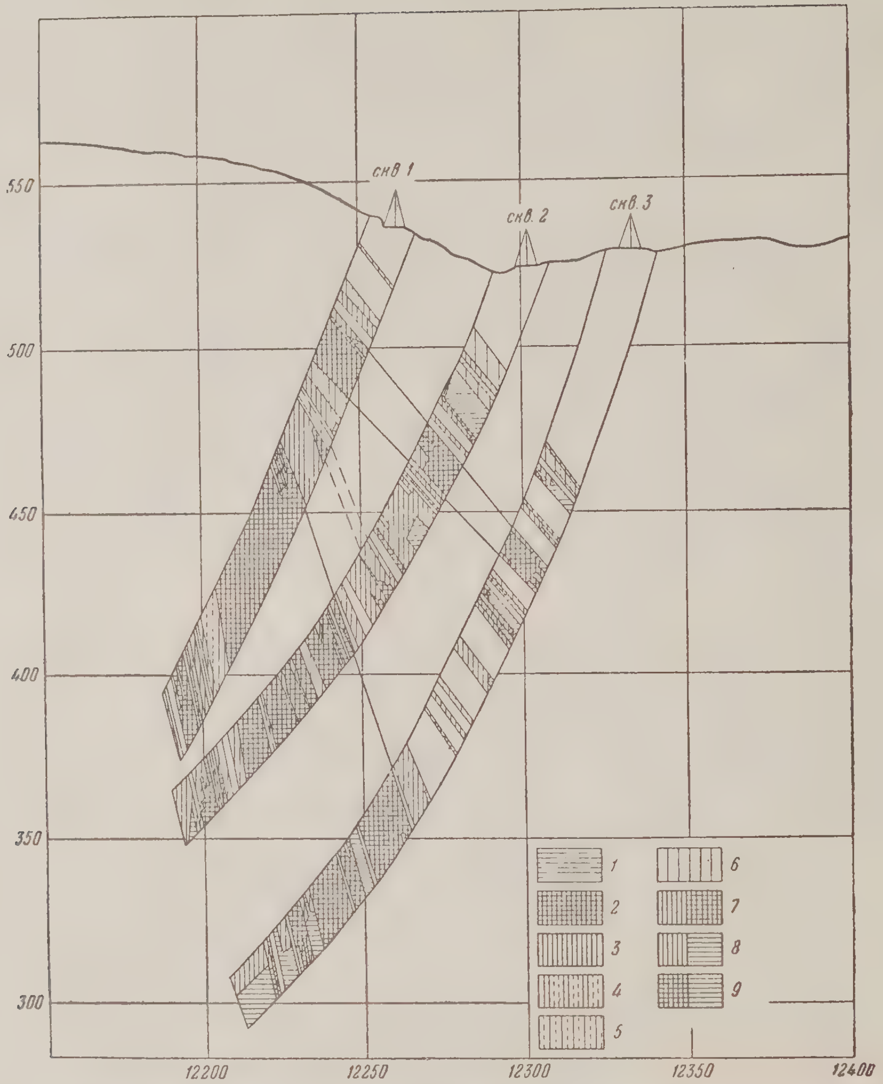

Fig. 1. Geological section of deposits (southern part) along the first line of exploration: 1) ferrorhodochrosite with $d_{(10\bar{1}4)} < 2.84$ A, 2) rhodochrosite with $d_{(10\bar{1}4)} \approx 2.84-2.86$ A, 3) manganocalcite-1 with $d_{(10\bar{1}4)} \approx 2.91-2.93$ A, 4) manganocalcite-2 with $d_{(10\bar{1}4)} \approx 2.93-2.96$ A, 5) manganocalcite-3 with $d_{(10\bar{1}4)} \approx 2.96-2.98$ A, 6) calcite and manganocalcite-4 with $d_{(10\bar{1}4)} > 2.98$ A, 7) manganocalcite-1 + rhodochrosite, 8) manganocalcite-1 + ferrorhodochrosite, 9) rhodochrosite + ferrorhodochrosite.

by the absence of ferruginous rhodochrosites and a relative abundance of poorer manganocalcites. Apparently the conditions of chemical formation obtaining in the two sections were not the same: going from south to north the concentrations of iron and then of manganese went down, while the concentrations of calcium in the solutions from which the layers were deposited increased. Ordinary chemical analyses for manganese could not bring out this regular variation since due to the increase in the content of iron and non-carbonate minerals in the ores of the southern part of the deposit, the mean content of manganese is approximately the same in the ores of the southern and northern sections.

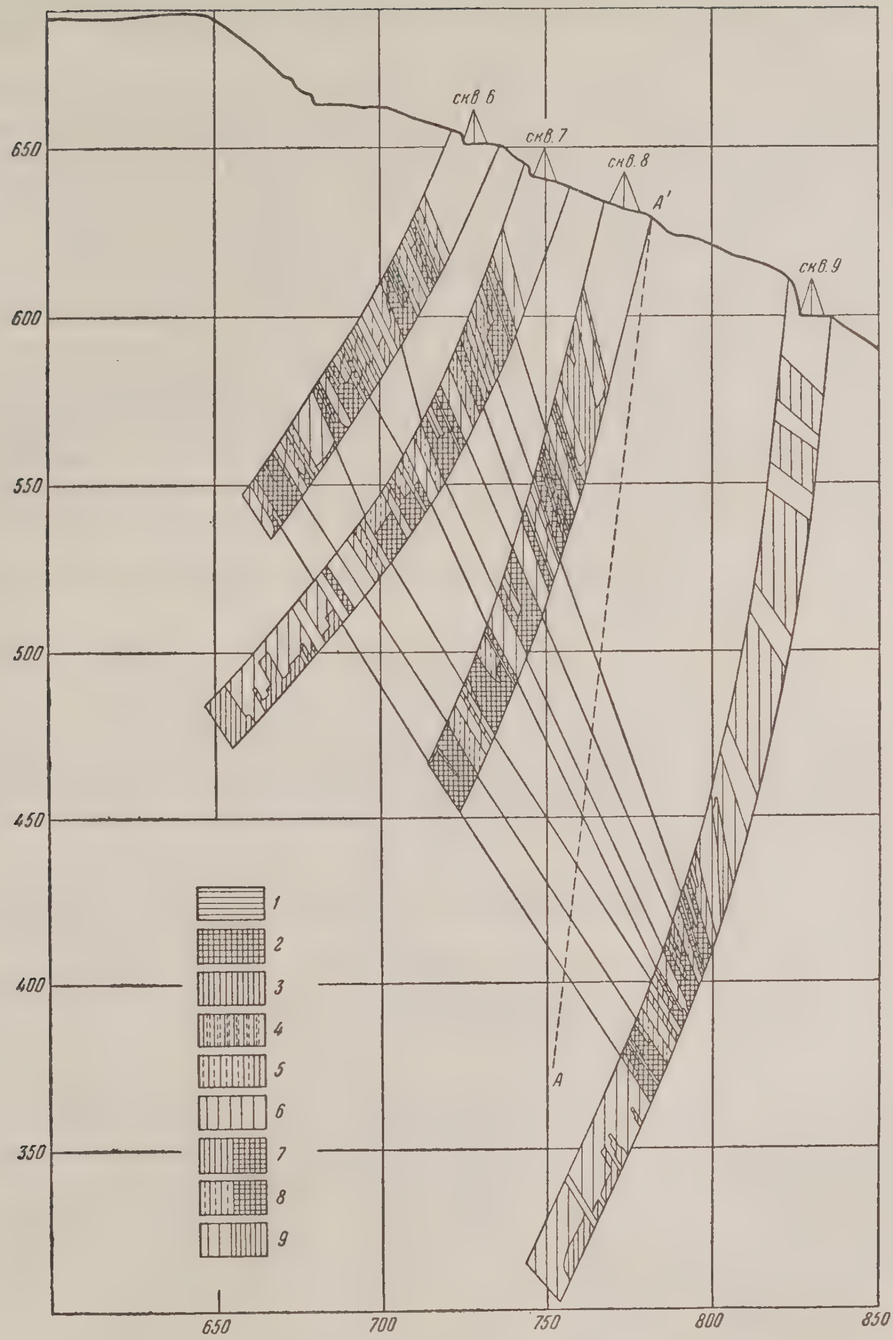
скв 6
скв.7
скв.8
скв.9
A'
A
650
600
550
500
450
400
350
650
700
750
800
850
1
2
3
4
5
6
7
8
9

Fig. 2. Geological section of deposits (northern part) along the fourth line of exploration (AA' - suspected tectonic fault line): 1) ferro-rhodochrosite with $d_{(10\bar{1}4)} < 2.84$ A, 2) rhodochrosite with $d_{(10\bar{1}4)} \approx 2.84-2.86$ A, 3) manganocalcite-1 with $d_{(10\bar{1}4)} \approx 2.91-2.93$ A, 4) manganocalcite-2 with $d_{(10\bar{1}4)} \approx 2.93-2.96$ A, 5) manganocalcite-3 with $d_{(10\bar{1}4)} \approx 2.96-2.98$ A, 6) calcite and manganocalcite-4 with $d_{(10\bar{1}4)} > 2.98$ A, 7) manganocalcite-1 + rhodochrosite, 8) manganocalcite-2 + rhodochrosite, 9) manganocalcite-4 + manganocalcite-1.

Thus mass x-ray analysis made it possible to bring out the variations in the mineralogical and chemical composition of the ores over the extent of the ore body, i.e., the so-called environmental or phase variations. This result is of both theoretical and practical value.

The usefullness of roentgenological analysis for constructing geological sections is illustrated by Figs. 1 & 2. From them one can readily see the stratified structure of the ore body which could be expected in view of the geological data on the sedimentary origin of the deposits. On the basis of the x-ray data one can readily connect the different strata in geological profiles. Previously this was done on the basis of chemical analysis taking into account various geological considerations; however, the results obtained in this way are never certain since they involved a certain amount of guesswork, which is largely eliminated by using the x-ray data.

Mass roentgenometric analysis of core samples can also help solve purely geological problems. Thus on the basis of certain geological data it was assumed that the eastern part of the ore body (Fig. 2) is not a direct continuation of the western part but is separated from it by a tectonic fault (shown by the dash line AA'). However, the correspondence of the ore formations and strata in exploratory holes Nos. 8 & 9 established by x-ray analyses shows that this assumption is ill-founded.

As far as we know there have been no previous attempts to plot geological profiles on the basis of x-ray data.

Conclusions

1. Mass x-ray analyses from flat samples at small glancing angles can serve as an important means for studying the composition of ores and the structure of ore bodies. This has been demonstrated on the example of one large deposit of carbonate ores, the mineralogy of which has been studied in detail by means of the roentgenometric method.

2. The results of our x-ray investigations of the carbonate ore bodies lead us to the assumption that the isomorphic $CaCO_3$-$MnCO_3$ series is not continuous under ordinary conditions.

3. Use of the x-ray method led to the detection of an unusual type of carbonate minerals: heterogeneous carbonate systems in which two or three complex carbonates of the calcite type, forming separate phases, are present simultaneously.

4. Mass x-ray analysis provided the means of bringing out the variations in the mineralogical and chemical compositions of the carbonate ores over the extent of the ore body - the environmental variations - which in the given case could hardly be established by any other analytic procedure.

5. Mass x-ray analysis can be utilized for studying the geological structure of deposits by comparing the composition of strata encountered in boring and correlating the different layers in the plotted geological profiles.

West-Siberian Geological Administration

References

1. J.D.Dana, System of Mineralogy, revised by Palache et al, Vol.II. (in Russian trans.).

2. L.Vegard, Skrifter Norske Videnskaps - Akad. Oslo, I Math.-Naturv. Klasse, 2 (1947).

RECENT ADVANCES OF X-RAY SPECTROSCOPY IN THE FIELD OF INVESTIGATION OF MATTER

- M.A.Blokhin

Since the Fourth Conference on the Application of X-Rays to Investigation of Materials, the x-ray techniques for the study of chemical bonds have been developed further. As was shown by the Conference on X-Ray Spectroscopy held in Moscow at the end of January 1955, the number of institutions in which x-ray investigations are conducted has grown significantly.

Since the Fourth Conference there have been carried out a number of important experimental and theoretical studies on the fine structure of the atomic and molecular absorption spectra of ionic crystals, the temperature dependence of the fine structure, emission and absorption spectra of ions in solutions, the characteristics and behavior of metals and alloys, magnetic transformations in metals, etc. Much has been accomplished, also, in the area of equipment design: there were developed several new types of efficient spectrographs with ionization and photographic recording of primary and secondary x-ray spectra, ultra-long wave spectrographs with concave diffraction gratings, a powerful wide-focus x-ray tube operating at 200 ma and 50 kv for excitation of fluorescence spectra and for studies of absorption spectra. During this period significant advances were also made in methods of x-ray analysis of the elementary composition of matter.

Heightened interest in the theoretical aspects of x-ray spectroscopy was brought about by the pressing need of understanding and systematizing the large amount of experimental information on the fine structure of x-ray spectra accumulated over the last few years. These theoretical investigations have been particularly extensive in the Soviet Union. The approach in these studies has been that of clarification of the fundamental problems in the fine structure of x-ray spectra of simple substances (gases, solutions) and the gradual transition to more complex substances in step with growth in theoretical understanding. Research along these lines, initiated by Vainshtein and Narbutt back in 1945, was especially effectively pushed forward during the last few years in the contributions of Vainshtein, Barinski and Narbutt.

These authors[1] proposed a theory and developed a procedure for calculating the fine structure of x-ray spectra. In this theory the electron ejected during the process of x-ray absorption is assumed to move in the Coulomb field of the polarized molecular remnant. The latter is regarded as a system consisting of the nuclear charge of the absorbing atom, a single positive charge (a hole in the K-shell) and of filled electronic shells of this atom (or molecule) created incident to the formation of the chemical bond. The said potential leads to the formation of a system of stationary energy levels with a limit determined by the ionization potential.

The problem is fully analogous to the problem of the motion of an electron in the field of a hydrogen-like atom and is completely solved in quantum mechanical terms. Vainshtein, Barinskii and Narbutt deduced equations allowing of calculating 1) the energy (position) and intensity of the selective absorption lines associated with the transition of an electron ejected from the K-level to any of the stationary energy levels of the molecule, 2) the true absorption edge of the spectrum produced in the transition of the K-electron to the region of continuous energies and 3) the shape and width of the absorption lines as well as the shape and intensity of the true absorption edge. In these calculations, to determine the actual absorption limit of a molecule it is necessary to know only a single parameter from the experimental absorption curve: the distance between the first two absorption lines or the ratio of the intensities of the first absorption line and the true absorption edge.

The above-mentioned calculating method was employed for interpreting the K absorption edges in the spectra of the following atoms and molecules: argon, chlorine in HCl, sulphur in H_2S and CS_2, germanium in GeH_6 and Ge_2H_6. In addition, it was possible to explain the specific character of the K-edges in the absorption spectra of Kr, Xe, Br in HBr and Br_2 and Cl in Cl_2. At present the above method is being successfully applied abroad in investigations of the fine structure of x-ray spectra. For example, the Czech physicist, Barchkovskii[2], has used this method for interpreting the fine structure of the experimental x-ray absorption spectrum of Ne. Fig. 1 illustrates the results obtained by him.

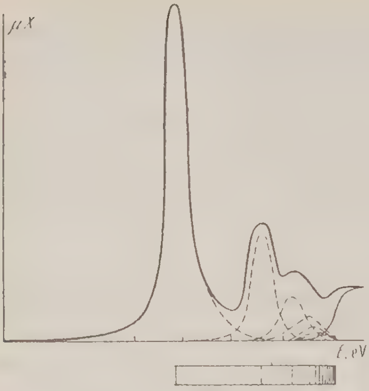

Fig. 1. The K absorption spectrum of neon. The dash curves indicate the lines of selective absorption by the np-levels; the light solid curve defines the true absorption edge. Each division on horizontal scale equals 1 ev.

Experience shows that the above theory is equally useful in analyzing and interpreting the principal absorption edge of heavy atoms bound in complex molecules which do not contain any other heavy atoms, aside from the absorbing one. The validity of this statement is substantiated by the example of Fig. 2.

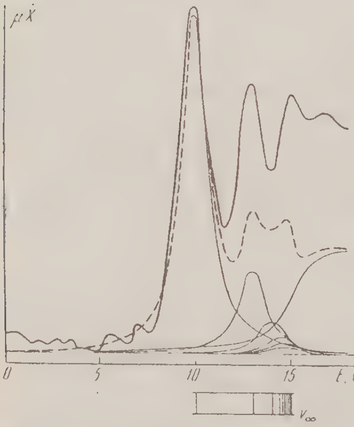

Fig. 2. The K absorption spectrum of sulphur in CS_2. The heavy solid line represents the microphotometric curve; the light solid curves represent the selective absorption lines and the true absorption edge. The dash curve indicates the total theoretical absorption curve.

Matters are somewhat more complicated in the case of molecules comprising several heavy atoms. In this case the fine structure of the principal absorption edge must consist of several series of absorption lines connected with the transitions of the ejected K-electron to the excited levels of the molecule, comprising wave functions of each of the components. That this is so was shown for the first time by Vainshtein, Barinskii and Narbutt[3] for the case of the K absorption spectra of K and Cl in a KCl crystal and later by Narbutt[4] who investigated experimentally the K absorption spectrum of Zn and Br bound in $ZnBr_2$. The above explains the appearance of several additional peaks, not predicted by the original, simplest variant of the theory, in the fine structure range of the principal absorption edge of Ge in $GeCl_4$ and $GeBr_4$ and of S in CS_2.

The transitions of the electron, ejected during the x-ray absorption process, to the excited molecular levels, i.e., the transitions which, according to Vainshtein, Barinskii and Narbutt, determine the strucure of the absorption edges of the atoms bound in a molecule, are also reflected in the emission spectrum. This was proved by the above-mentioned authors in the case of the emission spectrum of gaseous Zn, the spectrum of which includes several weak lines that could not hitherto be explained. An analogous explanation was recently shown by Backovsky[5] to be valid in the case of the fine structure of the emission bands of carbon atoms bound in a number of different carbon compounds.

Borovskii and Barinskii[6] investigated the $M_{IV,V}$, M_{III} and L_{III} absorption edges of U in UO_2 and UO_3 crystals and studied the structure of the electron shell of uranium in these compounds. Their results proved to be in good agreement with magnetic and optical data. The specific structure of the $M_{IV,V}$-spectra, characterized by an exceptionally bright absorption line on the low energy side and deriving from the capture of the electrons by the 5f-levels of U, constitutes an additional argument for including U in the actinide group. The method developed by Borovskii and Barinskii for recording the spectra in the different line series, taking into account selection rules, made it possible to investigate the influence of chemical bonds on the fine structure of the absorption spectra and show that the chemical bond between U and O in compounds with the hexavalent U (including the uranyl group) - the so-called "uranyl bond" - is determined by the 6d-levels of U. In addition, on the basis of their studies of the distribution of the filled and excited electronic levels in UO_3 and UO_2 crystals the authors were able to construct the energy level scheme of these crystals.

Barinskii[7] studied the $M_{IV,V}$-spectra of Th bound in compounds and showed that a filling of the 5f-shell occurs in Th. In view of the fact that assignment of Th to the actinide group has been questioned, this observation can be taken as evidence in favor of this assignment.

Barinskii's investigations of the L_{III} and K absorption spectra of Mo in ammonium molybdate, potassium molybdenum cyanide and molybdenite enabled him to show that the marked difference between the spectra of ammonium molybdate, on the one hand, and of potassium molybdenum cyanide and molybdenite, on the other, can be explained by the participation of the 4d-levels of Mo in the chemical bonds of the last two compounds. This deduction is in complete agreement with magnetic and x-ray data.

Application of the above-mentioned method of Vainshtein, Narbutt and Barinskii to the analysis of the structure of the principal K absorption edge of Zn, Cu, Ni and Mn ions in solutions[1] enabled these authors to reduce this problem to that of resolution of the absorption edge of an ion having the structure of a noble gas. The basic distinction here from the case of a free molecule lies in the fact that the charge of the atomic remnant after K-ionization is equal to three units rather than unity, while the multiplet structure of the np-terms of these ions, determined by the Stark effect in the molecular field of the solvent, distorts the classic dispersion shape of the absorption lines. It should also be noted that the method of Vainshtein, Barinskii and Narbutt, in addition to facilitating the interpretation of molecular absorption spectra, makes it possible to calculate[1] the ionization potential and the polarizability of normal and excited molecules and of ions in solution, the energy of the K-level of the absorbing atom and the changes which accompany the entry of the atom into chemical combination with its neighbor in the compound.

Later Vainshtein and Kavetskii[8] investigated experimentally the K absorption spectra of Zn, Cu and Ni ions in aqueous and non-aqueous solutions and found that the nature of the solvent affects the structure of the absorption spectrum. Calculation of spectra was carried out using the method mentioned above, as refined by Vainshtein[9] with respect to the absorption spectra of ions in solution, where the multiplet splitting of the terms is related by the author with the linear Stark effect due to the solvent molecules. In this study Vainshtein and Kavetskii discovered the linear dependence of the extent of the spectrum of Zn and Cu ions on the magnitude of the dipole moment of the solvent molecule. Narbutt[10] studied experimentally the dependence of the K absorption spectrum of Zn ions in solution on the chemical composition of the salt, the concentration of the solution, the nature of the solvent and type of ion formed in solution. Calculations of the absorption spectra were carried out by the same method, and, in the case of zinc chloride made it feasible to establish a correlation between changes in the absorption line width, due to the linear Stark effect, and the magnitude of the dipole moment of the solvent molecules. The absorption spectrum of the Zn^{2+} ion in aqueous solution and its calculation are shown in Fig. 3. For more complex ions (such as radicals, etc.) there is observed additional splitting of the spectral lines associated with fields of the attached NH_3, OH or CN groups. Narbutt also investigated the effect of freezing solutions of zinc chloride in glycerin; he discovered that freezing of

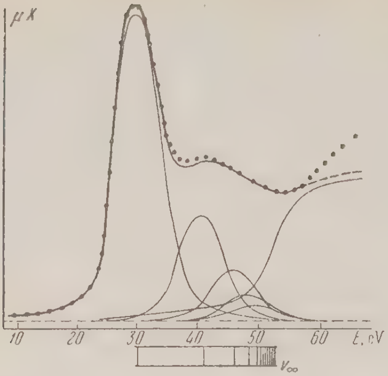

Fig. 3. K absorption spectrum of Zn^{2+} in a normal aqueous solution. Points - experimental data; light curves - the lines of selective absorption; heavy line - theoretical total curve.

the solution is accompanied by strong splitting of Zn ion levels and that the transition from the liquid to the solid state does not occur directly, but passes through an intermediate state, characterized by an intermediate temperature.

Later Vainshtein, Barinskii and Narbutt[3] applied their method to the interpretation of the K absorption spectra of K and Cl in crystal KCl. The authors succeeded in detecting, in the spectrum of each of the components, two series of narrow absorption lines with a common limit coinciding with the continuous absorption edge. For computation of the positions and relative intensities of the lines of each of the series the equations previously deduced for gas molecules were found to be applicable. The analysis of absorption spectra and the emission lines of K and Cl allowed of plotting the energy level scheme of the KCl crystal and predicting the structure of its ultraviolet spectrum. The predicted structure was found to be in good agreement with optical data. The quantitative deductions following from their theory allowed Vainshtein, Barinskii and Narbutt[11] to explain a number of facts concerning absorption spectra of transition elements having defects in the d- and f-shells in different series and to predict the structure of the optical absorption spectrum of Sm. Their predictions turned out to be in good agreement with experimental data.

Another theory of x-ray absorption and emission spectra of ionic crystals, in particular those of KCl, was developed by Kostarev[12]. According to this theory the initial region of the K absorption of K^+ and Cl^- ions is determined by transitions of the K-electrons of these ions to the common levels and zones of the entire lattice; which explains the similarity of both spectra and allows of interpreting the individual peaks. In the process, account is also taken of the possibility of K-electron transitions to the highest filled 3p zone of Cl^- since, under the influence of x-rays, when these are incoherently scattered, this zone is partly free. Account is also taken of transitions to local levels, due to structure defects, for example, dislocated Cl^- ions and the F-center levels. One of the peaks is assigned to K-electron transitions to the conduction zone of the crystal and into local "adhesion" levels. The beginning of continuous absorption corresponds to the threshold of the external photoeffect.

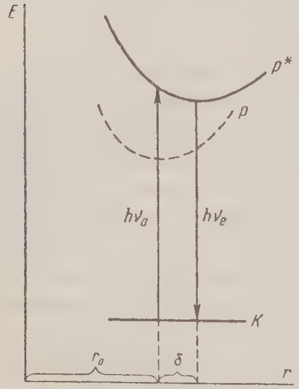

Fig. 4. Dependence of the energy E of the electronic levels of the ions in a crystal lattice on the interionic distance r.

Juxtaposing the emission lines of K and Cl in KCl with the peaks in the fine structure of their absorption spectra, Kostarev concludes that there is a unique correspondence between them. However, it appears that the emission lines and, in particular, the short-wave satellites are displaced to the side of lower energies relative to the corresponding peaks of the absorption spectrum. Kostarev explains this shift in the following manner. In Fig. 4 is given the dependence of the energy E of the internal K-level and of the external free p-state on the interionic distance r. The dash curve p pertains to a normal ion, while the solid-line curve p* pertains to the same ion but with a vacancy in the K-shell. The left arrow indicates the electron transition in the process of K-absorption. The absorbed energy equals $h\nu_a$. After the transition, the absorbing ion is in a metastable state and there occurs a local change δ in the distance r_0 between the absorbing ion and its neighbors, part of the energy of the excited state being transformed into heat. After transition of the given lattice section to a new, equilibrium state, an emission transition, shown in Fig. 4 by the right hand arrow, takes place. The corresponding energy $h\nu_e < h\nu_a$ accounts for the displacement of the emission lines relative to the absorption peaks in the ionic crystal spectrum.

On a number of problems involved in the theory of the fine structure of absorption spectra of complex molecules and solids, there arose a discussion in print between Kostarev and Borovskii[13] on the one hand, and Vainshtein, Narbutt and Barinskii[14] on the other hand. The exchange of views contributed greatly to the development of the theory of absorption spectra of molecules and ionic crystals.

Blokhin[15] obtained interesting results in his studies of the x-ray K absorption and emission spectra of titanium and the L_{II} and L_{III} absorption limits of barium bound in barium titanate, which is a dielectric with a perovskite type lattice. It turned out that the 3d-band of titanium splits into at least three bands, i.e., the degeneracy of the 3d-state is partly removed. One of these bands is filled with electrons, while the other two are unoccupied. The components of these free 3f-bands of titanium, together with the 5d-band of barium, form one common d-band of the barium titanate lattice.

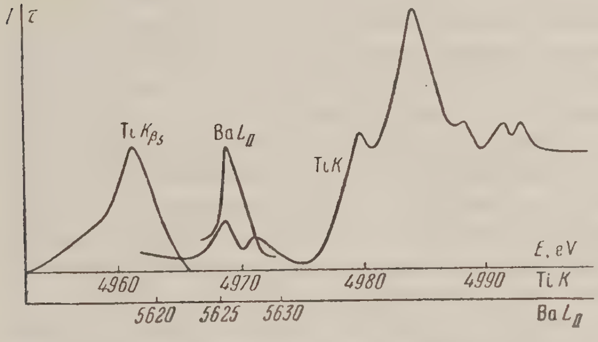

Fig. 5. The K absorption spectrum of titanium, the Ti $K\beta_5$ emission line and the L_{II} absorption spectrum of Ba in $BaTiO_3$.

Fig. 5 shows the K absorption spectrum and the $K\beta_5$ emission line of Ti in $BaTiO_3$. The splitting of the 3d-band is clearly discernible. The L_{II} absorption spectrum of Ba, which consists of a single narrow line is also given in this figure. The last has been purposely displaced to the side of lower energies by the magnitude of the energy difference between the internal levels, i.e., between the Ba L_{II} and Ti K levels. The main rise in the K absorption curve of titanium corresponds to dipole transitions to the 4p-band and exhibits two peaks, associated, evidently, with differently ionized titanium ions. It may be assumed that the first of these peaks is associated with singly-charged Ti^+ ions; the second, with doubly-charged T^{2+} ions.

Many valuable researches have been effected by Soviet x-ray spectroscopists and theoreticians in the field of metals and alloys. Sokolov[16] calculated the density of conduction electrons in ferromagnetic crystals on the basis of Vonsovskii's model of interacting internal d- and external p-electrons for transition metals. The calculations showed that this density is a function of the spontaneous magnetization and, consequently, is temperature dependent. Hence theory predicts an anomalous (temperature) variation of the density of electronic states in ferromagnetic compared with non-ferromagnetic crystals.

A theoretical examination of the absorption and emission of x-rays by ferromagnetic metals was carried out with reference to the same model.[17] It follows from this theory that the absorption and emission of x-rays must depend on the spontaneous magnetization of the ferromagnetic metal. In the vicinity of the Curie point this dependence is quadratic (i.e., is described by the simple square law). Calculation also shows that the intensity curve of K-emission of a metal

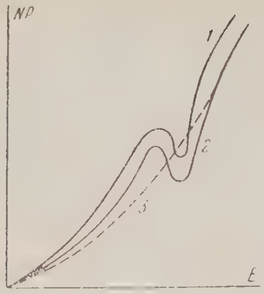

Fig. 6. Dependence of the product NP on the energy E for ferromagnetic metals: 1) ferromagnetic state, 2) paramagnetic state, 3) according to the free electron model.

in the ferromagnetic state must lie somewhat above the intensity curve in the absence of magnetization. Hence the character of the x-ray spectrum of a metal must undergo a noticeable change incident to going through the ferromagnetic transition point. Two typical curves are shown in Fig. 6. The vertical axis is scaled in terms of the product of the density of states N(E) times the transition probability P(E).

The anomalous temperature effect predicted by Sokolov has not yet been investigated experimentally. The curves shown in Fig. 6 differ as regards shape from the experimental curves obtained for transition elements and, in particular, for the ferromagnetic elements. However, the dependence of the intensity of the emission spectra (or of the absorption coefficient) on the photon energy derived directly from experimental data does not yield the form of the function N(E)P(E), in view of the fact that the experimental curves are distorted, first due to the finite resolution of the apparatus and, second, due to the finite width of the internal atomic level to (or from) which the transitions of the external electrons of the atom proceed.

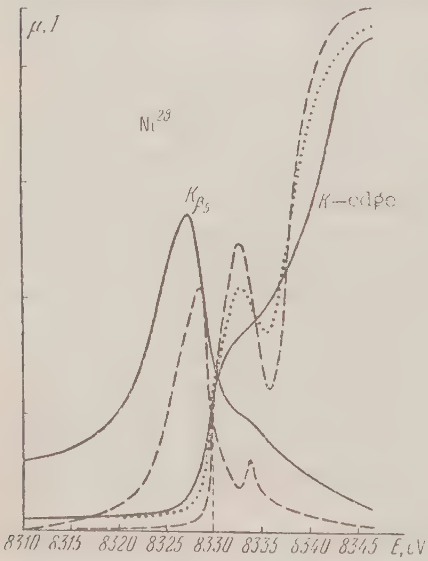

Fig. 7. The solid lines give the shape of the $K\beta_5$ emission spectrum of metallic nickel and its K absorption edge. The point curve shows the same K absorption edge curve but after correction for instrument distortions. Dash line: N(E)P(E).

In order to determine the true dependence N(E)P(E) from experimental data, one must first find the distortion function, which can be done for any instrument by using data obtained on a two-crystal spectrometer. Knowing the distortions, it is possible to establish the actual form of the N(E)P(E) curve. This problem was solved in practice by Blokhin[18], who used harmonic analysis to solve the integral equation relating the shape of the experimental curve with the shape of the actual N(E)P(E) curve. Application of this method to the K absorption and emission spectra of metallic nickel led to determination of N(E)P(E) curves for filled and free states (Fig. 7). These curves turned out to be in sharp contradiction with the theoretical curve for the density of states in metallic nickel computed on the basis of the one-electron model. The width of the 3d-band, both in its filled and in its free parts, turned out to be several times greater than the theoretical width; instead of the two peaks predicted by theory, only one peak was detected in the filled part. At the same time it became clear that the width of the free part of the 3d-band was far too small to permit approximation of the initial part of the absorption curve by an arc tangent function. It follows that determination of the K-level width for the transition group elements by the usual methods cannot yield exact results and that the data obtained in a number of earlier investigations are erroneous. Moreover, determination of the N(E)P(E) curve from experimental data requires knowing the width of the internal atomic level. For this reason determination of this width constitutes an extremely important problem. Ways of solving this problem, at this time, can be only roughly indicated. Investigations of the spectra of metallic vapors can yield valuable information in this connection.

In comparing the free states curve for nickel (Fig. 7) with the theoretical curves (Fig. 6) obtained by Sokolov, an amazing similarity becomes apparent. This is evidence of a great step forward in the theory of metals and the validity of the model of interacting internal d- and external p-electrons in transition metals.

Let us now turn to x-ray spectroscopic studies of alloys. Of great interest is the investigation of alloys of iron with chromium carried out by Kazantsev[19,20]. He investigated the wavelength, width and shape of the $K\beta_5$ emission band of iron and chromium in alloys of various compositions, at temperatures above and below the Curie point and incident to the $\alpha \rightarrow \delta$ phase transition. Identical changes were observed in going through the Curie point and in passing the magnetic transformation line in the phase diagram as the proportion of components is varied: in both cases the ferromagnetic state is characterized by a longer wavelength of the short-wave branch of the $K\beta_5$ band of iron and a shorter wavelength of the corresponding branch of the chromium; the width of this band in iron is greater in the ferromagnetic than in the paramagnetic state; the intensity of the band for iron is appreciably higher in the ferromagnetic state than it is in the paramagnetic state; the intensity of the band for chromium changes little. Kazantsev concludes from this that in the transformation from the ferromagnetic to the paramagnetic state, some of the electrons from the 3d-shell of chromium make transitions to the 3d-shell of iron and that these transitions are responsible for the change in the magnetic state of the alloy.

The transformation of an alloy with 52.38% Fe from the α-phase to the δ-phase was effected by prolonged isothermal annealing. It was found that in the δ-phase the $K\beta_5$ band of iron is displaced to the short-wave side. The width of the $K\beta_5$ band of iron is greater in the δ-phase, while that of chromium is smaller than in the α-phase. The integral intensity of the band for iron in the δ-phase increases by a factor of 1.5, but decreases by a factor of nearly 2 for chromium. All this leads Kazantsev to the conclusion that with prolonged isothermal annealing a significant fraction of the chromium 3d-electrons make transitions into the 3d-shell of iron. This change significantly modifies the interaction of the iron and chromium atoms and thus results in a radical change in the structure of the alloy: ferromagnetism disappears, brittleness appears, the hardness increases and the electrical conductivity decreases by a factor of 35-40.

A series of researches devoted to clarification of the role of small admixtures in alloys of the iron transition group is of great interest.

The K absorption spectra of all the components of binary and ternary alloys were studied by Karal'nik and Dekhtiar[21,22]. A significant displacement of the K absorption edge of the base component was observed upon the addition of only 1% of various impurities. It was noted that the shifts of the K absorption edges of all the alloy components, with respect to the positions of the edges in the spectra of the pure metals, all take place in the same direction: the wavelength of the edge in the alloy always decreases. As Dekhtiar and Karal'nik point out, these facts cannot be explained by the zone theory of metals. The authors introduce the hypothesis that local distortions produced by the impurity atoms are involved: the electrons of these atoms are not uniformly distributed throughout the volume of the alloy but are concentrated in the immediate vicinity of the impurity atoms. Such microvolumes can be regarded as quasi-chemical formations. Thus, in diluted solid solutions, one may expect to encounter the existence of two energetically non-equivalent atomic states of the base component of the alloy: some of these atoms are linked with the impurity atoms, while the others are outside the local distortion regions. The superposition of the two absorption edges corresponding to these two states leads to the observed overall displacement of the edge. Karal'nik also comes to a conclusion about the probable existence in these alloys of some interaction, close to ionic in nature, superposed on the ordinary metallic bonds. He also calls attention to the importance of the redistribution of electrons between the interacting atoms of the alloy components, which leads to change in the number of holes in the 3d-bands of the atoms.

An investigation of the K absorption spectra of iron in Fe-Al (3 and 7% Al) and Fe-Si (2% Si) alloys was carried out by Nemnonov and Trapeznikov[23]. It was established that the addition of 3% Al and 2% Si (separately) to iron leads to a 1-1.5 ev displacement of the K absorption edge of iron to the short-wave side. A significant decrease in contrastiness of the fine structure of the iron absorption edge was observed as a result of the addition of 3% Al or 2% Si.

From an analysis of the results obtained by Dekhtiar and Karal'nik, and in view of the distinctive characteristics of the phase diagrams of the alloys investigated, Nemnonov and Trapeznikov also come to the conclusion that in primary unsaturated solid solutions, close in composition to obvious intermetallic compounds, there may be formed in individual microregions of the crystal lattice quasi-chemical formations with a concentration of the dissolved element well above the average concentration for the entire alloy.

Thus, in place of statistically homogeneous distribution of the atoms of the dissolved element one may expect to find in some unsaturated solid solutions, under certain heat treatment conditions, appreciable concentrational inhomogeneities which can result in changes in the electronic structure of the alloy and, therefore, pronounced modifications in its physico-mechanical properties.

Such quasi-complexes are "variants" of the intermetallic compounds nearest to them in composition and are coherently linked with the lattice of the solid solution.

In this connection, mention should be made of the interesting work of Lesnik[24] in which proof is given of the existence of such concentration inhomogeneities in the particular case of the Fe-Cr system. However, much work still remains to be done in this field, before we can fully understand the nature of these effects.

Summarizing this review of x-ray work in the field of matter investigations carried out during the last three years, we can note with satisfaction that during this period our scientists accomplished much in a number of directions. However, it is also necessary to mention a number of areas in x-ray research (that have seen marked development abroad in recent years) in which intense efforts are indicated. First, we must mention the isochromatic method,[25] the third direction in x-ray spectroscopy, which allows investigating solid states free of electrons. This method consists of studying the dependence of the intensity of a given spectrum line on the voltage applied to the x-ray tube in the vicinity of the excitation potential of an internal atomic level. Use of a very stable, well smoothed out voltage made it possible to attain double the resolving power obtainable in absorption spectra work with a two-crystal spectrometer. Application of the isochromatic method to investigation of the structure of the free levels in elements of the iron transition group led to discovery of a number of new details, not previously detected from absorption spectra.

It is also necessary to develop methods of x-ray spectrum investigation not employing crystals. By combining the isochromatic method in the soft x-ray region with a differentiating electronic circuit[26] it proved feasible to obtain on an oscillograph screen the intensity distribution over the width of an emission band and to record this curve in an interval of 1/25 sec with a very high resolution. With this procedure the rays from the x-ray tube are recorded directly by a special photoelectric device. A constant stable voltage, a little lower than the excitation potential of the internal atomic level, is applied to the tube. A variable sawtooth wave voltage is superposed on this constant voltage.

In a number of papers, it is shown that the use of a single-channel pulse analyzer coupled to a proportional counter[27], or to a scintillation counter, allows of studying the intensity distribution over the spectrum of the x-ray beam incident on the counter. While this method is characterized by a low resolution, it can be used to advantage in certain cases: in elementary x-ray spectroscopic analysis, in studying the fluorescence efficiencies, etc.

It is also necessary to note the development of investigations using two-crystal spectrometers, the design of new instruments of this type and the increasing application of diffraction grating spectrographs.

For the further development of such research and the creation of the new, advanced instruments needed therefor, it is essential, first, that x-ray spectroscopists cooperate actively with workers in the field of electronic equipment design and, second, that production of the appropriate instruments and components be initiated. For this purpose we have all the requisite means and it is only necessary to solve the organizational issues involved.

In conclusion I wish to express my sincere appreciation to E.E.Vainshtein, K.I.Narbutt, R.L.Barinskii, S.A.Nemnonov and A.V.Sokolov for the data they put at my disposal; their kindness has greatly facilitated the preparation of this review.

"V.M.Molotov" Rostov State University

References

1. E.E.Vainshtein, R.L.Barinskii & K.I.Narbutt, Zhur.eksp.i teor.fiz., 23, 593 (1952).
2. J.Bačkovsky, Českosl.časop. fys., 4, 118 (1954).
3. E.E.Vainshtein, K.I.Narbutt & R.L.Barinskii, Doklady AN SSSR, 82,701(1952).
4. K.I.Narbutt, Doklady AN SSSR, 93, 21 (1953).
5. J.Bačkovsky, Českosl. časop. fys., 4, 300 (1954).
6. I.B.Borovskii & R.L.Barinskii, Izv. AN SSSR, Ser. fiz., 15, 225 (1951).
7. R.L.Barinskii, Dissertation, Inst. of Geological Sciences of the USSR Ac. of Sci., M. 1951.
8. E.E.Vainshtein & V.S.Kavetskii, Doklady AN SSSR, 91, 775 (1953).
9. E.E.Vainshtein, Doklady AN SSSR, 91, 1059 (1953).
10. K.I.Narbutt, Zhur. eksp. i teor. fiz., 26, 208 (1954).
11. R.L.Barinskii, E.E.Vainshtein & K.I.Narbutt, Doklady AN SSSR, 83, 199(1952).
12. A.I.Kostarev, Zhur. eksp. i teor. fiz., 22, 628 (1952).
13. A.I.Kostarev, I.B.Borovskii, Zhur. eksp. i teor. fiz., 26, 377 (1954).
14. E.E.Vainshtein, R.L.Barinskii & K.I.Narbutt, Zhur.eksp.i teor.fiz.,27, 521 (1954).
15. M.A.Blokhin, Doklady AN SSSR, 95, 965 (1954).
16. A.V.Sokolov & S.M.Tsipis, Zhur.eksp.i teor.fiz., 28, 321 (1955).
17. A.V.Sokolov, Zhur.eksp.i teor.fiz., 28, 326 (1955).
18. M.A.Blokhin, Izv. AN SSSR, Ser. fiz., 20, 142 (1956) (Trans. in Bulletin, Vol. 20, No. 1, p. 127).
19. M.A.Blokhin, Fizika rentgenovskikh luchei (Physics of x-rays)M. 1953.
20. V.A.Kazantsev, Doklady AN SSSR, 101, 477 (1955).
21. S.M.Karal'nik, Dissertation, Kiev State University, 1952.
22. I.Ia.Dekhtiar & S.M.Karal'nik, Doklady AN SSSR, 88, 277 (1953).
23. S.A.Nemnonov & V.A.Trapeznikov, Trudy Instituta fiziki metallov (Transactions of the Institute of the Physics of Metals) of the Ural Branch of the Ac. of Sci., issue 16, 123 (1955).
24. A.G.Lesnik, in "Voprosy fiziki metallov i metallovedeniia" (Problems of the physics of metals and metallurgy) pp. 118 & 123, Kiev 1954.
25. A.Nilsson, Ark. fys., 6, 513 (1953).
26. G.Shinoda, T.Suzuki & S.Kato, Phys. Rev., 95, 840 (1954).
27. A.A.Jaffe, Bull. Res. Council Israel, 3, 316 (1954).

ON THE NATURE OF THE FINE STRUCTURE IN THE K-EDGE OF THE ABSORPTION SPECTRUM OF GERMANIUM HALIDE MOLECULES

- K. I. Narbutt

The fine structure in the K absorption edge of molecules of germanium tetrachloride has been the subject of a number of experimental and theoretical investigations.[1-4] Two points concerning these investigations must be noted:

1) In the experimental investigations only the structure of the K absorption edge of germanium itself was studied; the structure of the K-edge of the halide was not investigated.

2) The theoretical investigations were devoted to calculation of the structure of the K-edge of germanium on the basis of the Kronig-Petersen theory. In the calculations, all the fluctuations of the absorption coefficients without exception were treated as elements of the fine structure of the spectrum in the sense of the Kronig-Petersen theory. Despite further developments of the Kronig-Petersen theory (Kostarev[5] and Corson[6]) agreement with experiment remained unsatisfactory.

In 1955 the writer together with Vainshtein and Barinski[7] proposed a new, different interpretation of the K absorption of germanium bound in $GeCl_4$ molecules; in this interpretation the more intense fluctuations of the absorption coefficient were related to transitions of the K-electron to excited levels of the molecule. However, the initial variant of this interpretation of the absorption spectrum of germanium bound in $GeCl_4$ yielded no satisfactory explanation of the third absorption maximum since no account was taken of the important, but then unknown fact, that the K absorption spectrum of each of the components forming the molecule in the general case represents the surposition of two series of absorption lines. The results of the author's investigation[8] of the K absorption spectrum of $ZnBr_2$, which showed that determination of the absorption spectra of both components often permits of interpreting the structure of complex spectra, demonstrated the necessity of investigating the structure in the K-edge of the halogen in the germanium halide molecules.

It must be noted that, as was shown in the investigation of Ref. 3, the K absorption spectra of Ge in $GeCl_4$ and in $GeBr_4$ are identical. In view of this and desiring to avoid certain experimental difficulties arising in investigating the K-spectrum of Cl bound in the $GeCl_4$ molecules, we decided to investigate the K-spectrum of bromine bound in $GeBr_4$.

The experimental procedure used was that developed earlier by the writer[9] for recording the x-ray absorption spectra of gaseous substances. The quartz absorption cell with thin windows contained 1.55 mg germanium tetrabromide. The experiments were carried out at a temperature of 300°. The effective absorption path was 26 cm; the volume of the absorption cell was 220 cm^3. We used a focusing x-ray spectrograph with a bent (1000 mm radius) quartz crystal. The reflections were obtained from the $(13\overline{4}0)$ system of planes. The dispersion was 2.46 XE mm^{-1}. The width of the slit located on the focal circle of the spectrograph in front of the GM counter was 0.05 mm (~1.8 ev). The experimental points were recorded at intervals of 0.1 mm. At least 10,000 pulses were counted for each point. The x-ray continuum source was a BFV-70 x-ray tube with a tungsten anode.[10]

A number of experimental curves of the K absorption spectrum of bromine in $GeBr_4$ were obtained. The curve shown in the accompanying figure is the average for several experimental determinations.

The interpretation of the spectrum was based on the premise[8] that the observed spectrum is a superposition of two series of selective absorption lines: a principal and a secondary series. The calculations of the principal series in the K spectrum of Ge bound in $GeBr_4$ was carried out on the basis of the experimentally measured distance (5.5 ev) between the first two absorption peaks on the assumption that they are associated with 1s → 5p and 1s → 6p transitions, respectively.

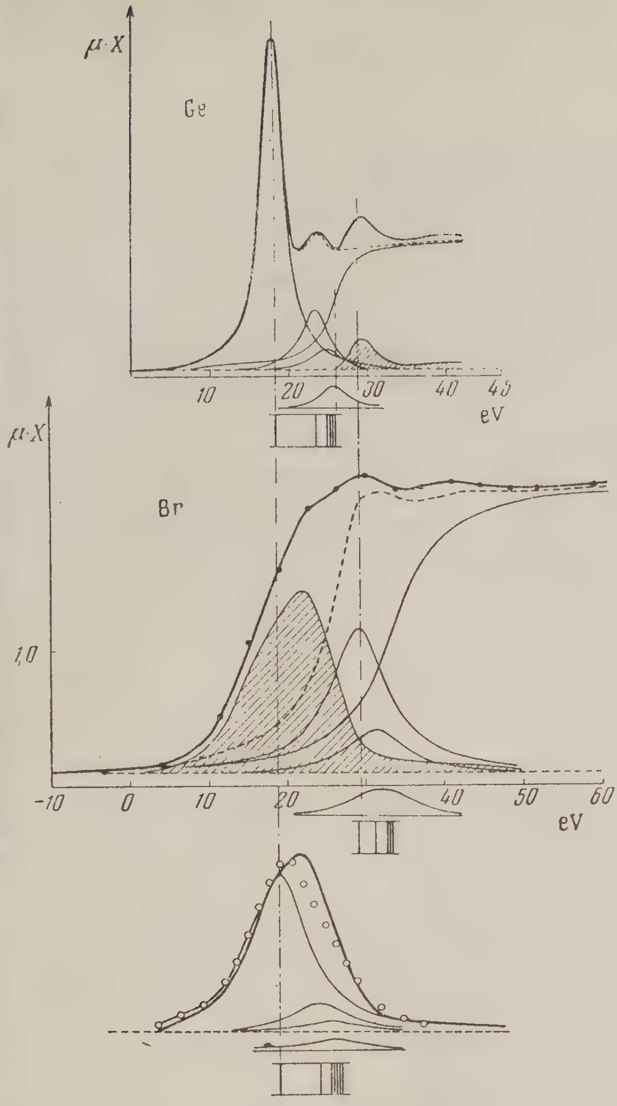

K absorption spectra of $GeBr_4$ molecules and analysis of their structure. Heavy solid lines - experimental absorption curves; fine solid lines - selective absorption lines and true edges; dash lines - total theoretical curves for the principal series of the given component. Hatching - sums of the secondary series equal to the difference between the experimental curve and the theoretical. Circles - theoretical total curve for the secondary series in the spectrum of bromine.

Calculations by the method described in Ref. 1 lead to a value of 1.34 for the principal quantum number (n^*_{Ge}) for germanium. Utilizing this value we constructed the series of selective absorption lines shown in the accompanying figure by fine solid lines. The total absorption curve for the principal series is shown in the figure by dashes. After subtracting this curve from the experimental one there is obtained the hatched remainder which represents the total absorption curve of the secondary series. Thus analysis of the spectrum of germanium itself yields two reference points (beginning of the principal series and centroid of the secondary series) for subsequent matching of the germanium spectrum with that of bromine. The K spectrum of the bromine in $GeBr_4$ obtained in this investigation is shown in the middle part of the figure. In plotting we shifted the bromine absorption curve relative to the germanium absorption curve so that the peak of the secondary series (hatched) in the germanium spectrum would coincide with the principal maximum in the bromine spectrum. The axial line through the peaks was assumed to be the beginning of the principal series in the bromine spectrum. The calculation of this series was carried out by the method described in Ref. 12; the computed value of the principal quantum number n^*_{Br} was 1.90. The series of the selective absorption lines (solid fine lines) and the total curve (dash lines) of the principal series in the spectrum of bromine plotted on the basis of this value are shown in the middle part of the figure. Subtracting the total curve for the principal series from the experimental curve gives the hatched remainder which represents the total curve for the secondary series in the bromine spectrum. In the lower part of the figure we show the theoretical construction of the secondary series for the bromine spectrum on the basis of the value $n^*_{Ge} = 1.34$. The total curve for this series is shown by the small circles in the figure. It may be seen that this curve virtually coincides with the total curve (solid line) of the secondary series separated from the bromine spectrum.

In making the constructions described above, the width of the selective absorption line was assumed to be equal to 4.5 ev for the germanium spectrum and 9.1 ev for the bromine spectrum, the difference being due to the greater width of the K-level in bromine.

In the light of the analytic results we can formulate the following conclusions:

1. The K absorption spectrum of germanium in $GeBr_4$ comprises two series of selective absorption lines: a principal series characterized by a value of $n^*_{Ge} = 1.34$ and a secondary, much weaker series characterized by a value of $n^*_{Br} = 1.90$.

2. The K absorption spectrum of bromine in $GeBr_4$ comprises two series of selective absorption lines: a principal series characterized by a value of $n^*_{Br} = 1.90$ and a secondary series characterized by a value of $n^*_{Ge} = 1.34$. The primary and secondary series in the bromine spectrum are nearly equal in intensity.

3. The third absorption peak, for which no satisfactory explanation could be found earlier[7], represents the secondary series, i.e., is associated with electron transition from the K-level of the germanium atom to levels of the $GeBr_4$ molecule, formed primarily by the bromine atom wave functions.

4. The results of the present investigation may be assumed to resolve the question of the origin of the third absorption peak in the K-absorption spectrum of germanium in $GeBr_4$, i.e., the controversial point discussed in Refs. 13 & 14 is settled in favor of the hypothesis then advanced by the writer[14].

Institute of Geological Sciences of the
Academy of Sciences of the USSR

References

1. D.Coster & G.Klamer, Physica, 1, 1889 (1934).
2. D.R.Hartree, R.L.Kronig & H.Petersen, Physica, 1, 895 (1934).
3. C.H.Shaw, Phys. Rev., 70, 643 (1946).
4. H.Glaser, Phys. Rev., 82, 616 (1951).
5. A.I.Kostarev, Zhur. fiz. khim., 20, 1 (1946).
6. E.Corson, Phys. Rev., 70, 645 (1946).
7. R.L.Barinskii, K.I.Narbutt & E.E.Vainshtein, Doklady AN SSSR, 79, 49 (1951).
8. K.I.Narbutt, Doklady AN SSSR, 93, 21 (1953).
9. K.I.Narbutt, Doklady AN SSSR, 92, 273 (1953).
10. K.I.Narbutt & E.M.Fridman, Izv. AN SSSR, Ser. fiz., 20, 136 (1956). (Trans. in Bulletin, Vol. 20, No. 1, p. 123.)
11. E.E.Vainshtein, R.L.Barinskii & K.I.Narbutt, Zhur. eksp. i teor. fiz., 23, 593 (1952).
12. R.L.Barinskii, E.E.Vainshtein & K.I.Narbutt, Doklady AN SSSR, 82, 355 (195
13. A.I.Kostarev & I.B.Borovskii, Zhur. eksp. i teor.fiz., 26, 377 (1954).
14. E.E.Vainshtein, R.L.Barinskii & K.I.Narbutt, Zhur. eksp. i teor. fiz., 27, 521 (1954).

K SERIES EMISSION LINES IN THE X-RAY SPECTRUM OF TITANIUM IN THE METALLIC STATE AND IN CERTAIN DIELECTRIC MATERIALS

- E.E.Vainshtein, I.B.Staryi & M.N.Bril'

In our preceding investigation[1] we studied the fine structure of the x-ray absorption spectra of titanium in the metal state and in certain of its compounds: three oxide modifications, perovskite and ilmenite. The present report is devoted to the description of the experimental data obtained for the emission spectra of this element in the same compounds. Specifically we studied the three diagram lines of titanium: $K\alpha_1$, $K\beta_1$ and $K\beta_5$ and the two satellites: $K\beta'$ and $K\beta''$. The work was carried out on the high-resolution vacuum x-ray tube-spectrograph described in Ref. 2. The analyzer was a quartz crystal plate cut parallel to a rhombohedron plane, having a lattice constant of 3.33 A. The crystal was bent in the holder of the instrument by the method of pure flexure on four supports as described in Ref. 3; the bending radius was 2.5 m; the length of the reflecting surface of the crystal, 15 mm. The linear dispersion of the spectrograph in the region of the investigated spectra was 2.5 X/mm. In order to obviate irreversible changes in the investigated substances in the process of excitation, the x-ray spectra were excited by the fluorescence method. The design of the x-ray tube used in these investigations is described in Ref. 2.

The investigated specimens were mounted in the immediate vicinity of the bent crystal outside the tube, at a distance of 28 mm from the anode. The anode was chromium plated copper. The tube was operated at 35 kv and 50 ma. Under these conditions an exposure of 20-25 hours was required to obtain the desired blackening of the $K\beta_5$ line ($D = 0.4$-0.5). We used the $K\alpha_1$ and $K\alpha_2$ lines of vanadium as references in determining the absolute wavelength of the x-ray lines of titanium. The spectra were recorded photographically. The accuracy in establishing the positions of the line maxima and individual points on the line contours was ±0.2 ev.

The experimental results obtained for the $K\alpha_1$, $K\beta_5$, $K\beta'$ and $K\beta''$ lines of titanium in the metallic state and in compounds are given in Tables 1 and 2 and in Figs. 1 and 2. The data characterizing the shape and relative location of the $K\beta_1$ line of titanium in the metal and in compounds are summarized in Table 1. The energy of the line was computed by means of the equation

$$\log E = 1.09237 - \log \lambda$$

where λ is the wavelength in kX and E is in kev. The cited values were obtained as the averages for three to five parallel experiments.

The following deductions can be drawn from the experimental data.

1. The $K\alpha_1$ line of titanium in the x-ray spectra of the metal and the investigated compounds has an asymmetric shape with an asymmetry index of 1.42 in the metal and an average value of 1.19 in the compounds. The width of the $K\alpha_1$ line remains unchanged within the limits of the experimental error in going from the metal to the compounds.

2. The $K\beta_1$ line of titanium in the x-ray spectra of the metal and the titanium compound is asymmetric with a steeper short-wave side. Its asymmetry index, equal to 1.70 in the metal, in going to the compounds decreases to 1.24 and is virtually the same for all the investigated compounds. The width of the $K\beta_1$ line varies in a more complex manner: It is minimal in the metal and perovskite, increases in brookite and anatase and reaches a maximum value in rutile and ilmenite. In the latter the line width is approximately 30% greater than in the metal. The experimental data also show that in going from the metal to the compounds there is a small shift of the $K\beta_1$ peak to the side of longer waves. For anatase and brookite the observed shift is within the limits of the experimental error. It is approximately the same for the three other substances (rutile, perovskite and ilmenite) and definitely exceeds the experimental error.

Table 1

Position, width and asymmetry index of the $K\alpha_1$ and $K\beta_1$ lines in the x-ray emission spectrum of titanium metal state and in compounds

Substance	$K\beta_1$ line				$K\alpha_1$ line	
	Position E, ev	ΔE	Relative width	Asymmetry index	Relative width	Asymmetry index
Ti(metal)	4931.5	0	1.00	1.70	1.00	1.42
Perovskite	4930.9	-0.6	1.02	1.25	0.98	1.21
Anatase	4931.3	-0.2	1.18	1.23	0.99	1.19
Brookite	4931.2	-0.3	1.10	1.25	0.98	1.18
Rutile	4930.8	-0.7	1.29	1.25	1.01	1.20
Ilmenite	4930.8	-0.7	1.29	1.24	1.00	1.18

Table 2

Positions of the $K\beta_5$ and $K\beta''$ lines in the x-ray spectrum of titanium metal and in compounds

Substance	$K\beta_5$		$K\beta''$	Remarks
	Position E,ev	ΔE		
Ti(metal)	4962.4	0	--	
Perovskite	4961.6	-0.8	4947.0	
Anatase	4961.8	-0.6	4947.2	
Brookite	4962.0	-0.4	4947.0	
Rutile	4961.8	-0.6	4946.6	$K\beta''$ line apparently a doublet; second peak at 4951.4 ev
Ilmenite	4960.5	-1.9	4945.0	

3. In going from the metal to the compounds the $K\beta_5$ line of titanium undergoes a number of remarkable changes that qualitatively repeat the changes that have been observed earlier for this line in other elements.[4-7] Exhibiting pronounced asymmetry in the metal (asymmetry index ~1.70) the $K\beta_5$ line becomes virtually symmetric in the compounds. The width of this line remains constant (within ± 3-4%) in all the investigated substances. The position of the $K\beta_5$ peak in going from the metal to the compounds is displaced to the side of longer wavelengths. It is noteworthy that despite the fact that the valence of the titanium in all the investigated compounds is the same, the magnitude of the observed displacement of the $K\beta_5$ peak differs in the oxides, perovskite and ilmenite: in the oxides and perovskite the shift equals 0.6±0.2 ev, while in ilmenite it amounts to almost 2 ev.

4. The changes in the $K\beta''$ line in going from the metal to the compounds are particularly pronounced. In fact this satellite is undetectable in the x-ray spectrum of titanium in the metallic state and appears only in the spectra of the compounds wherein it is located on the longwave side of the $K\beta_5$ line. The position of the $K\beta''$ peak of titanium in perovskite and the three oxides is the same within the limits of the accuracy of measurement. In going to ilmenite, however, there is an appreciable shift (close to 2 ev) of the peak to the side of longer wavelengths. The integral intensity of the $K\beta''$ line of titanium in all the investigated compounds amounts to about 42% relative to the intensity of the $K\beta_5$ line. Except in rutile, the shape and half-width are identical with those of the $K\beta_5$ line. In rutile the shape of the $K\beta''$ line is more complicated. However, the above observation remains valid for each of the two components ($K\beta_1$ and $K\beta''_2$ in Fig. 1) into which the experimental $K\beta''$ line

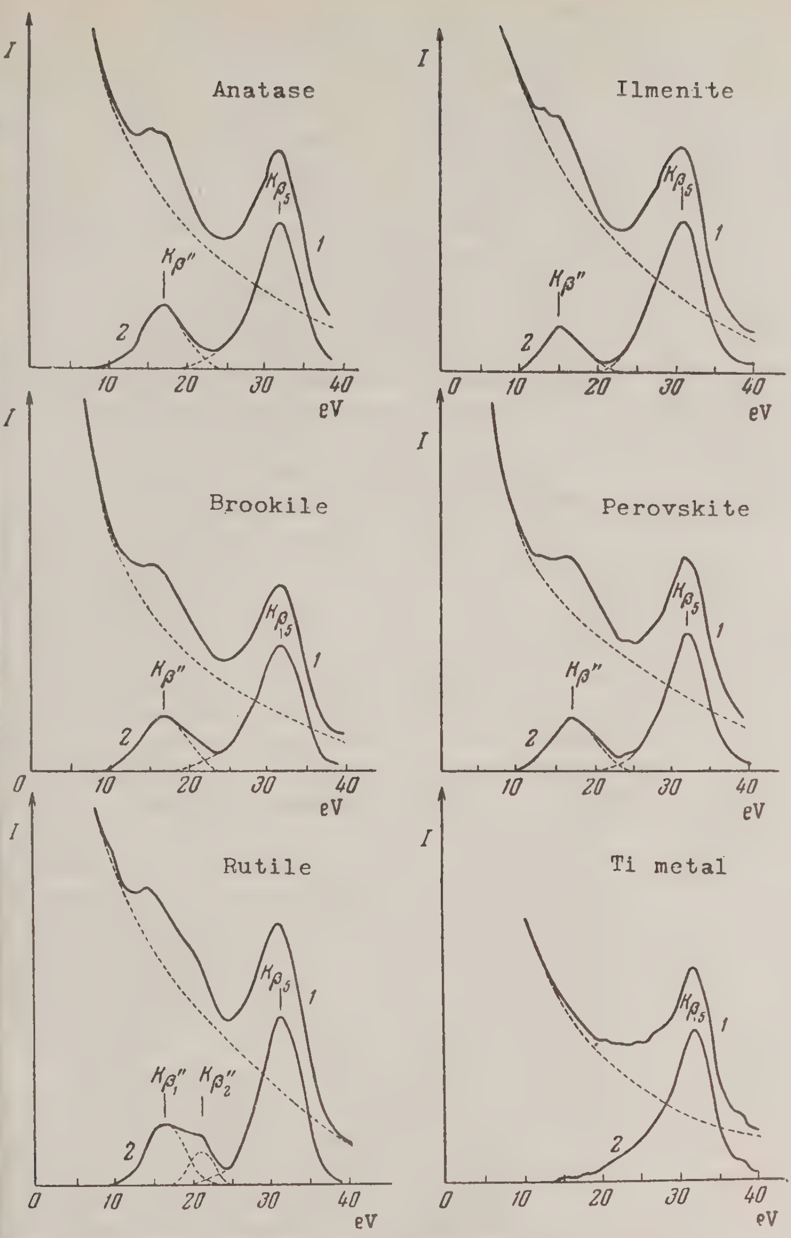

Fig. 1. Intensities of the $K\beta_5$ and $K\beta''$ lines in the x-ray spectrum of titanium in the metallic state and in compounds: 1) integral experimental curve, 2) $K\beta_5$ and $K\beta''$ lines after allowing for the intensity of the $K\beta_1$ line.

of rutile can be resolved. The ratio of intensities of these two components (in rutile) is about 1:2.

Despite numerous attempts to clarify the mechanism of formation of this nondiagram line,[8,6] its origin is still unclear. As has been noted by Blokhin[6] the appearance of this line cannot be satisfactorily explained by any of the extant theories of the formation of satellites. In this connection it might be noted that many of the characteristics of the behavior of this line of titanium, detected in the present investigation, as well as some of the observations of Blokhin[6] regarding the $K\beta''$ line of chromium of different valences bound in compounds, would find a simple and consistent explanation if we assume that the $K\beta''$ line (in contrast to the $K\beta_5$ line) appears in compounds as a result of a relatively low probability electron transition (i.e., less probable than transitions within the same atom) from certain peripheral energy levels of oxygen to free K-levels of the titanium atom.*

In the light of this assumption the following would become perfectly understandable: a) the pronounced dependence of the relative intensity of the $K\beta''$ line on the character of the atomic bonds of the absorbing atom in the compound and the absence of this line in the spectrum of the pure metal; b) the fact that the ratio of the intensities of the $K\beta_5$ and $K\beta''$ lines remains constant in different compounds in which the valence and character of the bonds of the absorbing atom are the same and that this ratio increases in proportion to the increase in valence, as observed for chromium by Blokhin**; c) the similarity of the shapes and widths of the $K\beta''$ and $K\beta_5$ lines in most compounds and even such relatively fine changes in the shape of the $K\beta''$ line in certain compounds as those we observed in the case of rutile. The splitting of this line in rutile into two components of different intensity could be explained by the presence in the structure of rutile within the titano-oxygen octahedron of two oxygen atoms with a Ti-O distance differing from that of the other oxygen atoms. If the above assumption is substantiated by further experiments, investigation of the $K\beta''$ line of atoms in compounds could be utilized as a very sensitive method for investigating chemical bonds.

---

*This mechanism of the formation of some emission and absorption lines in the x-ray spectrum of atoms and compounds have already been examined in another connection by a number of investigators.[9-11]

**According to Blokhin[6], in going from trivalent to hexavalent chromium the ratio of intensities of $K\beta''$ to $K\beta_5$ changes from 0.143 to 0.309.

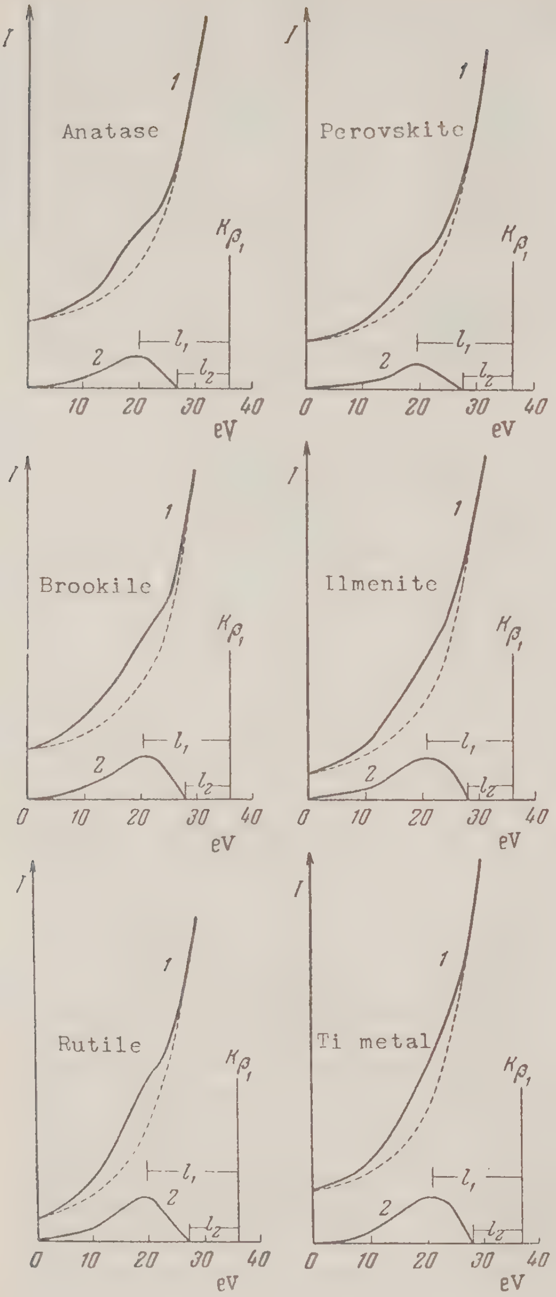

Fig. 2. Intensity of the $K\beta'$ band in the x-ray spectrum of titanium in the metallic state and compounds: 1) integral experimental curve, 2) $K\beta'$ band after allowing for the intensity of the $K\beta_1$ line; l_1 and l_2 distance from the $K\beta_1$ peak to the peak of the $K\beta'$ band and to its short-wave edge, respectively.

5. The $K\beta'$ satellite appears on the longwave side of the $K\beta_1$ line of titanium. It is present in the spectrum of the element both in the metallic state and in compounds (Fig. 2). In all cases the $K\beta'$ band is a relatively low intensity broad band, the short-wave edge of which, within the limits of the experimental error (±0.4 ev), is located at the same distance from the peak of the $K\beta_1$ line. This distance (l_2 in Fig. 2) equals about 8.3 ev or 0.6 Ry. The location of the maximum of this band relative to the $K\beta_1$ peak of titanium in the metal and compounds (l_1 in Fig. 2) varies from 16.3 ± 0.3 ev in anatase and perovskite to 15.1 ± 0.3 ev in the metal and ilmenite. The peak separation has an intermediate value in rutile and brookite. Clearly discernible changes are also observed in the shape of the $K\beta'$ band in the metal and compounds. These changes are clearly evident despite the relatively lower accuracy (as compared with that for the other lines) with which one can separate this line from the background formed by the neighboring intense $K\beta_1$ line.* As may be seen from the curves shown in Fig. 2 the $K\beta'$ band in the metal and in ilmenite is markedly asymmetric. Its asymmetry index in both cases is close to 1.5, while the half-width of the band is maximal. In contrast to this in anatase and

---

*The separation of the $K\beta'$ line was affected, as shown in Fig. 2, by subtracting the dash line, representing the extrapolation into this energy region of the $K\beta_1$ band, from the integral curve 1.

perovskite the Kβ' band becomes virtually symmetrical, while its half-width decreases by 10-15% relative to the half-width in the pure metal. The asymmetry index and half-width have intermediate values in rutile and brookite. The extent of the Kβ' band in the x-ray spectra of titanium in the metallic state and in compounds as measured at the base of the line, remains constant within the accuracy of measurement.

It must be noted that the half-width of the Kβ' band in all cases is much (approximately two times) greater than the half-width of the $K\beta_5$ line of titanium in compounds and in the metallic state. It is difficult to reconcile this as well as the appreciable divergence between the quantities characterizing the distance from the short-wave edge of the Kβ' band to the $K\beta_1$ peak (0.6 Ry) and the energy of the $M_{IV,V}$ level of the titanium atom (0.26 Ry) with the currently accepted concepts regarding the mechanism of formation and structure of this line.[6] These concepts are apparently in need of further development and revision.

"V.I.Vernadski" Institute of Geochemistry and Analytic Chemistry.
"K.D.Ushinski" Odessa Pedagogical Institute.

References

1. E.E.Vainshtein, I.B.Staryi & M.N.Bril', Doklady AN SSSR, 105, 943 (1955).
2. I.B.Staryi, Present issue of the Bulletin.
3. A.B.Gil'varg, Doklady AN SSSR, 72, 489 (1950).
4. H.Karlsson & M.Siegbahn, ZS. f. Phys., 88, 76 (1934).
5. S.Tanaka & G.Okuno, Proc. Phys. Math. Soc. Jap., 17, 540 (1935).
6. M.A.Blokhin, Zhur. eksp. i teor. fiz., 8, 1515 (1939).
7. E.E.Vainshtein, Rengenovskie spektry atomov v molekylakh khimicheskikh soedinenii i v splavakh (X-ray spectra of atoms in the molecules of chemical compounds and in alloys), M.-L. 1950.
8. M.Druvesteyn, ZS. f. Phys., 43, 707 (1927).
9. H.O'Bryan & H.Skinner, Proc. Roy. Soc., A176, 229 (1940).
10. J.Valasek, Phys. Rev., 53, 274 (1938).
11. E.E.Vainshtein, R.L.Barinskii & K.I.Narbutt, Doklady AN SSSR, 82, 701 (1952).

INVESTIGATION OF THE ASYMMETRY AND WIDTH OF THE Kα_1 LINES OF COPPER AND MANGANESE ATOMS IN HEUSLER ALLOYS BY THE FLUORESCENCE ANALYSIS METHOD

- B.I.Kotliar

As we know, alloys of the Cu-Mn system exhibit an anomalously high paramagnetic susceptibility in the 15-25 atomic % Mn concentration range. The addition of a small amount of aluminum brings these alloys from the paramagnetic to the ferromagnetic state (Heusler alloys). The alloy having the composition Cu_2MnAl, after appropriate heat treatment, has superstructure[1-2] and the most highly pronounced ferromagnetic characteristics.

The present report is concerned with an investigation of the shape of the Kα_1 lines of manganese and copper in alloys of the Cu-Mn system in the above indicated concentration range and in some ternary alloys of the Cu-Mn-Al system.

The spectra were obtained in the first order of reflection from the $(13\bar{4}0)$ planes of a quartz crystal in a vacuum x-ray spectrograph with focusing by the Johann method. The dispersion was 2 X/mm for the Mn Kα_1 line and 3.5 X/mm for the Cu Kα_1 line.

All the spectra were obtained by the fluorescence method. In order to utilize the spectrograph built in the instrument shop of the Petroleum Institute of the USSR Academy of Sciences, we developed and constructed a fluorescence tube, differing from those described earlier[5] in that controlled temperature conditions in the range from 50 to 700° can be provided for the specimen. Other advantages of the new design are that the tube is easy to mount and that one can convert from primary to secondary excitation of the spectra in the matter of a few minutes. A cross-section of the tube is shown in Fig. 1.

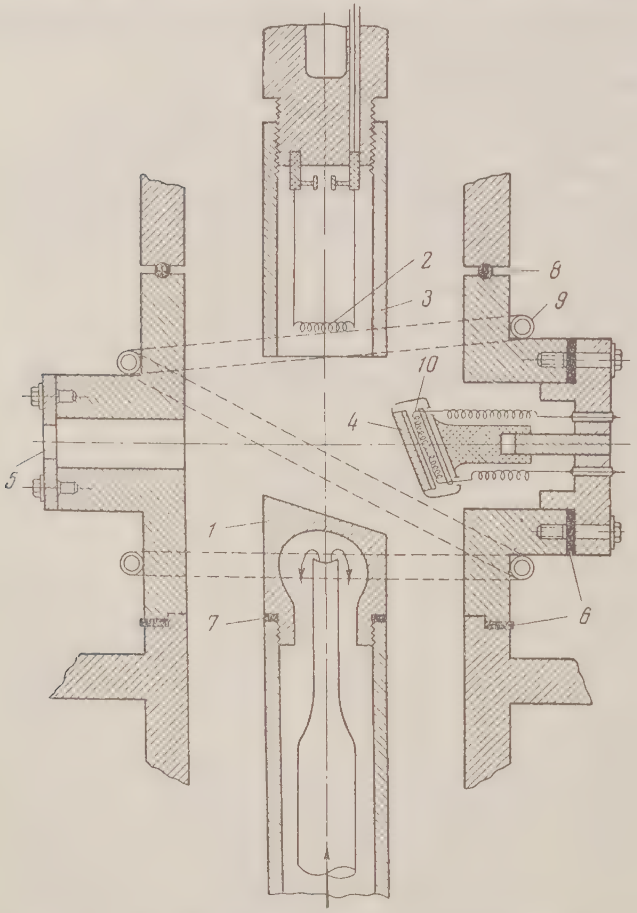

Fig. 1. Section through fluorescence tube: 1) anode, 2) cathode heater, 3) focusing cylinder, 4) radiator, 5) window for emission of radiation, 6,7,8) rubber gaskets, 9) tubing for cooling water, 10) heating element for investigated substance.

The asymmetry and width of the Kα_1 lines were measured directly from the microphotograms at the level of the peak of the Kα_2 line. The results of measurement are listed in Tables 1 & 2.

The following deductions may be drawn from the experimental results:

1. There is a change in the magnitude of the index of asymmetry of the Kα_1 lines of Mn and Cu atoms in the investigated alloys of the Cu-Mn system. Symmetrization of the line in the spectra of both components is observed at certain compositions of the alloy.

2. The magnitude of the index of asymmetry of the Kα_1

Table 1

Asymmetry and relative width of the $K\alpha_1$ lines of manganese and copper atoms in alloys of the Mn-Cu system

Alloy No.	Chem.comp., %		Asymmetry index		Relative width	
	Mn	Cu	Mn K_{α_1}	Cu K_{α_1}	Mn K_{α_1}	Cu K_{α_1}
1	9,6	90,4	1,56	1,19	1,08	0,93
2	14,2	85,8	1,56	1,18	1,04	0,96
3	19,1	80,9	1,55	1,10	1,00	1,03
4	23,9	76,1	1,43	1,17	1,04	0,97
5	33,5	66,5	1,67	1,09	1,05	0,95
	100	—	1,42	—	1,00	—
		100	—	1,05	—	1,00

Table 2

Asymmetry of the $K\alpha_1$ lines of manganese and copper in alloys of the Mn-Cu-Al system

Alloy No.	Chem. comp., %			Asymmetry index		Temperature of alloy, °C
	Cu	Mn	Al	Mn K_{α_1}	Cu K_{α_1}	
6	69,1	22,7	8,2	1,48	1,17	60
7	50,9	24,5	24,6	1,37	0,92	60

lines of Mn and Cu also varies in the ternary alloys of the Cu-Mn-Al system. The minimal value of the index of asymmetry is observed in the spectra of the Mn and Cu atoms in the alloy having the composition Cu_2MnAl with the ordered distribution of the atoms.

3. The width of the $K\alpha_1$ lines of the Mn and Cu atoms in the investigated alloys varies very little. There is no pronounced regularity in the changes of this characteristic as a function of the composition of the alloy.

The results of the investigation of the asymmetry of the $K\alpha_1$ line can be explained with the aid of Vainshtein's theory[6,7] connecting the asymmetry of these lines with the presence of atoms in a number of different energy states in the crystal lattice. Under the circumstances, one might expect ordering to lead to symmetrization of the $K\alpha_1$ line and in fact the alloy closest to Cu_2MnAl in composition (alloy No. 7 in Table 2) after appropriate heat treatment is distinguished by an ordered arrangement of the atoms and a minimal value of the index of asymmetry of the $K\alpha_1$ lines of Mn and Cu. The exceptionally low value of the index of asymmetry in the No. 4 alloy in the Cu-Mn system (Table 1) can also be explained by the fact that at this concentration of the components, as Valentiner and Becker[8] suggest, the alloy may be in the ordered state.

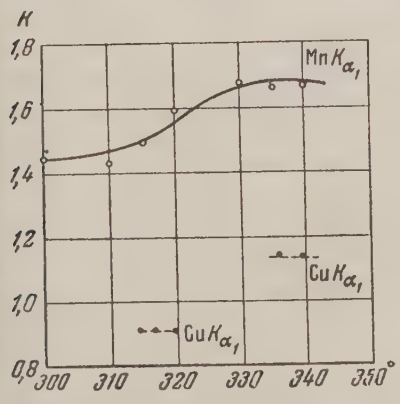

Fig. 2. Temperature dependence of the index of asymmetry of the $K\alpha_1$ lines of Mn and Cu atoms in the alloy having a composition close to Cu_2MnAl.

In view of the change in the magnetic state of Heusler alloys incident to going through the Curie point, in studying the shape of the $K\alpha_1$ lines of Cu and Mn in this alloy we obtained the spectra at a number of different temperatures of the radiator (specimen) close to the Curie point. For these experiments we chose the No. 7 alloy which is close to Cu_2MNAl in composition. This alloy has a stable superstructure which can be destroyed only by prolonged artificial aging of the alloy at temperatures appreciably above the Curie point (T_C = 330°).

The exposures in recording the spectra varied from 30 min to 2 hours. The agreement of the results obtained in several series of experiments indicates that even after a total of 6-12 hours of exposure in the temperature interval characterized by the change in magnetic state of the alloy, there is no noticeable decomposition of the ferromagnetic β-phase or oxidation of the radiator (specimen) surface. The absence of decomposition of the β-phase was substantiated by the x-ray diffraction patterns obtained of the specimens. Inasmuch as partial decomposition of the β-phase leads to lowering of the ferro-magnetic characteristics of the alloy, relative magnetic measurements of the investigated specimens were carried out each time after obtaining the spectrum, as an additional control of the state of the alloy during the series of experiments.

The temperature dependence of the asymmetry index of the $K\alpha_1$ lines of Mn and Cu atoms in the alloy having a composition close to Cu_2MnAl is shown in Fig. 2.

Analysis of the experimental data leads to the following deductions.

1. The index of asymmetry of $K\alpha_1$ line of copper and the $K\alpha_1$ line of manganese atoms in the alloy differs according to whether the alloy is in the ferromagnetic or the paramagnetic state.

2. In the temperature interval of the magnetic transformation of this alloy there is observed a gradual increase in the index of asymmetry of the $K\alpha_1$ line of manganese atoms: from 1.4 at 310° to 1.69 at 330-335°.

3. The width of the $K\alpha_1$ lines of Cu and Mn atoms remains virtually unchanged during the magnetic state transformation.

In conclusion I wish to thank E.E.Vainshtein for suggesting the subject and for his guidance in the investigation.

Roentgenospectral Laboratory of the
"K.D.Ushinski" Odessa Pedagogical Institute

References

1. E.Person, ZS. f. Phys., 54, 115 (1929).
2. S.Valentiner & G.Becker, ZS. f. Phys., 83, 371 (1933).
3. O.Heusler, Ann. d. Phys., 19, 155 (1934).
4. A.Kliucharev, Zhur. eksp. i teor. fiz., 9, 1501 (1939).
5. M.A.Blokhin, Zavod. labor., 6, 681; 8, 741 (1950).
6. E.E.Vainshtein, Rentgenovskie spektry atomov v molekylakh khimicheskikh soedinenii i v splavakh (X-ray spectra of atoms in the molecules of chemical compounds and in alloys), M.-L., 1950.
7. E.E.Vainshtein, Zhur. eksp. i teor. fiz., 20, 442 (1950).
8. S.Valentiner & G.Becker, ZS. f. Phys., 80, 735 (1933).

A RECORDING VACUUM X-RAY SPECTROGRAPH (FOR THE 20-300 A REGION)

- A.I.Efremov & A.M.Tiutikov

Among the advantages of x-ray spectrum analysis in the long-wave vacuum region of the x-ray spectrum is the feasibility of obtaining extremely high dispersion and resolution. For example, in the vicinity of 100 A the theoretically possible resolution is 0.006-0.007 ev. These potentialities make the method valuable in investigating the energy structure of solids, in particular that of semiconductors (investigation of the filling of electronic levels and bands, their energy structure, possible admixtures of levels, etc.). Naturally where actual realization of the theoretically possible resolution is concerned the width of the initial and final levels of the transitions are important factors.

Experimental work in the long-wave x-ray region encounters a number of serious difficulties in view of the low efficiency of x-ray sources in this region (and, consequently, the low intensities of radiation available) and to the strong absorption of this radiation by air and other substances. Hence in working in this region one must use a high-vacuum spectrograph and extremely sensitive radiation detectors. In order to obtain a high resolution one must use slits no more than 1-2 μ wide. This requires exceptionally fine adjustments of the instrument and further reduces the radiation flux incident on the detecting or recording component.

In view of the extremely low values of the recorded radiation flux, quantum fluctuations are a serious obstacle to realizing the theoretically possible resolution. It becomes necessary to employ averaging electronic circuits with a large time constant. This in turn makes it necessary to use very low rates of radiation detector travel along the focal surface of the spectograph in order not to impair the resolution and imposes extremely rigid requirements as regards stabilization of the operating regime of the x-ray tube.

The photoelectric recording spectrograph described below was designed by us for operation in the 20-300 A wavelength region. The spectrum is recorded automatically by a galvanometer on photographic paper wound on a drum. This spectrograph is intended primarily for absorption x-ray analysis. However, the instrument has the necessary provisions for emission and fluorescent analyses. The analyzer is a concave spherical diffraction grating with a radius of curvature R = 2 meters. The grating constant $\sigma = 1/1200$ mm. The use of a grating with R = 2 m and $\sigma = 1/600$ makes it possible to extend the recordable spectrum to 600 A.

The optical part of the spectrograph is diagramed in Fig. 1. The x-ray source is a demountable x-ray tube 1 with an interchangeable anode. For fluorescent analysis it can be replaced by a tube with two anodes. These tubes have appropriate provision for adjustment of their cathodes and anodes. The focusing cap on the cathode has an insulated lead for bringing in the focusing voltage. The mounts of both these tubes form airtight seals with the spectrograph. The tubes are evacuated together with the instrument. The width of the entrance slit 2 can be regulated by means of a suitable adjustment device graduated in microns. The maximum opening is 200 μ. Behind the entrance slit is the limiting slit 3; its purpose is to limit the angular width of the x-ray beam. Next we have the vaporization chamber which is a device for evaporating the investigated material onto a thin collodion film and bringing this specimen 4 into the x-ray beam without disturbing the vacuum. The vacuum chamber has provision for evaporating two or three different materials successively on six collodion films. After passing through the specimen, the x-ray beam falls on the diffraction grating 5, which is ruled on aluminum evaporated on glass. The grating is mounted in a special adjusting head by means of which it can be displaced as necessary. The glancing angle of the entering beam is 5°. The arm 6 mounted on the shaft 7 at the center of the Rowland circle carries the receiving slit

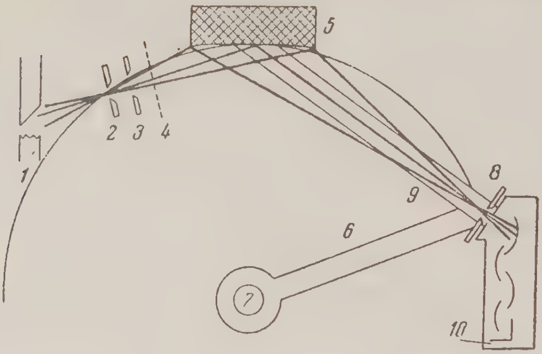

Fig. 1. Diagram of the recording vacuum x-ray spectrograph for the 20-300 A region: 1) demountable x-ray tube, 2) entrance slit, 3) limiting slit, 4) specimen, 5) diffraction grating, 6) arm, 7) shaft, 8) receiving slit assembly, 9) guide rail, 10) radiation receiver.

assembly 8. This consists of a table riding on the guide rail 9. The table is moved by rotating the shaft 7. The end of guide rail 9 is pivoted at the center of the grating and thus the plane of the receiving slit is always kept normal to the diffracted beam. The receiving slit itself is similar to the entrance slit 2 but has a "flag" type shutter for regulating the slit height. Finally, behind the receiving slit and mounted on the same table we have the radiation detector (counter) 10.

The kinematic equipment of the spectrograph includes a reversible motor with a 5-speed gear box. The rotation is transmitted through an appropriate gear train to the drum carrying the photographic paper and to a worm gear, which through a gear sector having a radius of 0.5 m and a special vacuum-seal link transmits the rotation to the shaft 7. The worm pair mesh without play. Each division of worm gear indicator equals 0.05 mm (or about $0^\circ 0'5.16''$) on the Rowland circle along which the receiving slit and detector move. By way of example, we note that in the vicinity of 100 A the linear dispersion equals 0.737 A/mm.

The gear box makes it possible to vary the rate of displacement of the receiving slit along the Rowland circle in steps from 0.1 μ/sec to 1 mm/sec. The speed increases by a factor of 10 with each step. The highest speed is used mainly for bringing the counter from one part of the spectrum to another and is not intended for recording. The 100 and 10 μ/sec speeds are intended for rapid recording of spectra in working with wide slits (200-20 μ). At these speeds the shape of the recorded spectral lines is greatly distorted; hence the primary purpose of recording in such cases is to search for spectral lines. The 1 μ/sec speed is the one normally used in working with moderately narrow slits (5-20 μ). Finally the 0.1 μ/sec speed is intended for recording the fine structure in working at the highest possible resolution (2-5 μ wide slits).

The vacuum equipment of the spectrograph consists of an RVN-20 (PBH-20) fore pump, an N-5 (H-5) diffusion pump, a vacuum distributor, a liquid nitrogen trap, a water-cooled spiral injector between the trap and diffusion pump and a high-vacuum valve. Ionization and thermocouple gages are provided for measuring the vacuum. The vacuum distributor makes it possible to let air into the spectrograph without stopping the diffusion and fore pumps and thus provides for rapid re-evacuation of the spectrograph. A vacuum of better than 10^{-5} mm Hg is attained in the instrument. The housing of the spectrograph is a flat trapezoidal box, having a volume of approximately 170 liters, welded of 15 mm steel and lined on the inside. There are appropriate access hatches in the top and bottom walls. The hatches are sealed with rubber gaskets.

The x-ray tube is mounted on one of the side walls of the instrument. The tube is fed from a half-wave rectifier with a ripple filter. The rectifier can supply up to 2.5 kw at a voltage of 10 kv. The heater and anode supplies are stabilized by a common ferroresonance regulator.

The x-ray radiation detector (Fig. 2) is a 13-15 stage secondary-electron multiplier 1. The electrodes of the multiplier (the dynodes) are trough-shaped, made of a Cu-Mg-Al alloy and subjected to special heat treatment to obtain the desired coefficient of secondary-electron emission. The multiplier is mounted inside the spectrograph housing; it has no evacuated envelope inasmuch as most envelope materials are almost wholly opaque to x-rays in the given spectral region. A positive attribute of the Cu-Mg-Al alloy (shared by Al-Mg, Ag-Mg, Cu-Be and certain other alloys) is that its coefficient of secondary emission decreases very little as a result of short-term exposure to the atmosphere and is rapidly re-established by appropriate heat treatment.

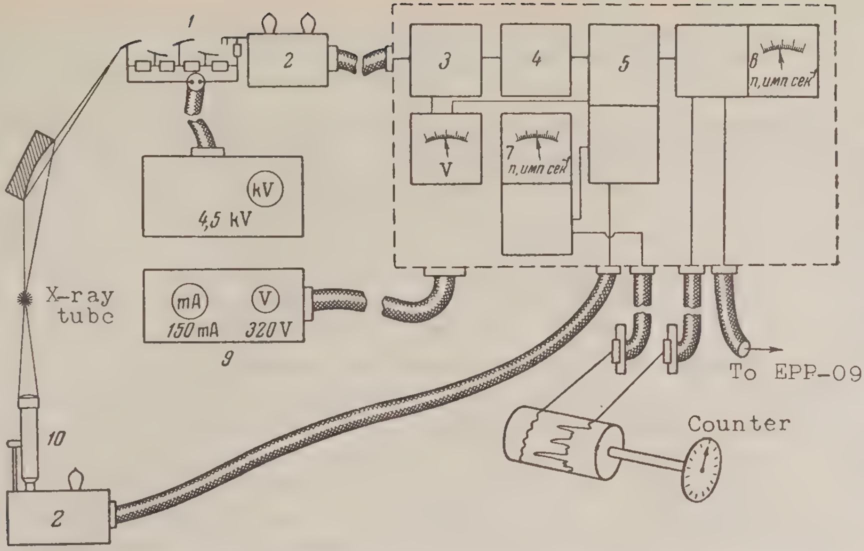

Fig. 2. Diagram of x-ray radiation detector: 1) secondary--electron multiplier, 2) preamplifier, 3) pulse limiter unit, 4) multivibrator, 5) corrector tube, 6) integrator, 7) unit recording intensity of x-ray tube emission, 9) rectifier for recording circuit supply, 10) ionization chamber; rectifier for 4.5 kv voltage divider. On units 6 & 7, η = pulses per sec.

The detector together with the two tube preamplifier and the voltage divider for sypplying the detector are mounted in a special metal box which is fastened to the receiving slit carriage. The pulses from the multiplier are carried to the input of the electronic circuit unit by a coaxial cable. The electronic unit (Fig. 2) comprises the pulse limiter 3, a multivibrator 4 for shaping standard square pulses, an integrator 6 with a wide selection of time constants τ and a unit 7 for recording the emission intensity of the x-ray tube, as well as a high voltage stabilized rectifier for supplying the multiplier voltage divider and a stabilized rectifier for supplying the recording electronic circuit 9.

To prevent fluctuations in the operation of the x-ray tube from affecting the accuracy of recording the instrument incorporates a special automatic correction circuit. Whereas in conventional instruments the accuracy of recording is enhanced mainly by rigorous stabilization of the x-ray tube supply, in our instrument as the intensity of emission of the x-ray tube increases or decreases the height of the square pulses from the multivibrator is reduced or increased accordingly to compensate for the intensity change. The height of the square pulses is regulated by a special vacuum tube corrector 5 which is located between the multivibrator and the integrator and is controlled by signals from the ionization chamber 10 mounted in the immediate proximity of the x-ray tube and receiving part of its radiation. Variations in the intensity of the x-ray tube emission can also be recorded by a separate galvanometer.

I take this occasion to express my gratitude to A.A.Lebedev for his guidance in developing the spectrograph.

A UNIVERSAL X-RAY VACUUM TUBULAR SPECTROGRAPH

- I.B.Staryi

In view of current progress in x-ray spectroscopic investigations there is urgent need for the development of improved equipment: instruments with enhanced resolution and transmission which can be used not only for absorption spectroscopy but also for fluorescence analysis, a branch of spectroscopy that holds great promise. In recent years, efforts towards the development of such instruments have been made here in the USSR and abroad. The introduction of bent crystals having a large reflecting surface has greatly increased the transmission factor of spectrographs.

The geometric theory of these instruments shows that the resolving power does not depend on the radius of curvature of the reflecting crystal. However, the theory does not take into account the influence of the mosaic structure of the crystals and certain other factors. Yet it is obvious that with a short radius of curvatures and, consequently, small deformations of the crystal, the adverse effect of its mosaic structure on the quality of the spectral lines will be weaker. In other words, the less the crystal is bent the more closely will its x-ray optical properties approach those of plane crystals, the resolution of which is generally superior to that of bent crystals.

On the other hand, the appreciable linear dispersion obtained with a large radius of curvature of bent crystals reduces the negative influence of graininess of the film and various errors involved in processing the spectrograms.

Increasing the radius of the curvature of the crystal makes it necessary to go over to the tubular design. The first x-ray tube-spectrograph with focusing by the Johann method was patented in the Soviet Union by N.D.Borisov. This spectrograph was equipped with a unique kinematic system which provided for appropriate displacement of the film cassette with changes in the Bragg angle. The design of our instrument, shown in Fig. 1, differs in principle from that of Borisov. The solid lines in Fig. 1 show the actual physical contours of the spectrograph.

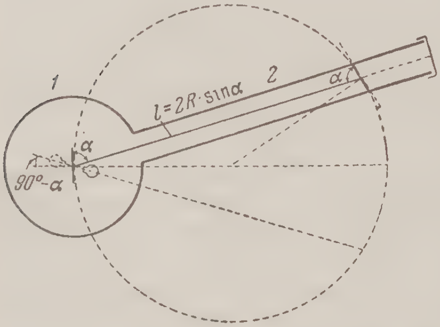

Fig. 1. Diagram of x-ray tubular spectrograph: 1) cylindrical housing, 2) tube.

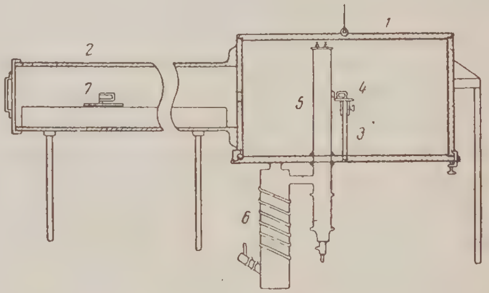

Fig. 2. Section through spectrograph: 1) cylindrical housing, 2) tube, 3) pivot pin, 4) crystal holder, 5) x-ray tube, 6) diffusion vacuum pump, 7) cassette.

The spectrograph (Fig. 1 & 2) consists of a cylindrical housing 1 having a diameter of 500 mm and a height of 250 mm and the tube 2 measuring 150 mm in diameter and 1800 mm in length. The replaceable stand 4 with the crystal holder pivots on the vertical rod 3 set in the bottom of the housing 1. The demountable vacuum tube 5 with its diffusion pump 6 is also set in the bottom of the housing at a distance of 50 mm from the crystal. The end of the spectrograph tube is attached by special screw clamps to the walls of the housing so that it can be pulled up to the latter to form a tight seal. The two units rotate about a common vertical axis. On the inside of the bottom there is a graduated circle along which the pointer of the crystal holder angle indicator moves. When installed the crystal must first be turned to the requisite Bragg angle relative to the incident beam; then when the housing together with the crystal and x-ray tube are rotated the reflected beam is always directed into the tube.

As may be seen from the diagram of Fig. 1 the angle between the tangent to the cassette (i.e., the plane of the film holder) at the point of incidence of the beam and the beam axis equals the Bragg angle α, while the distance between the crystal and the cassette $l = 2R \sin \alpha$.

Thus the requirements for focusing are satisfied by linking the cassette with a graduated circle for measuring its rotation and locating it in the path of the reflected beam at a distance l from the crystal. The cassette 7 (Fig. 2) is a rigid metal frame measuring 15 x 140 mm and may be either flat or curved along the arc of the Rowland circle; it is mounted on a slide moving along a rack with a millimeter scale. Before loading the cassette, the rack is pulled out of the tube and the slide is locked at the requisite distance l from the crystal, while the cassette is positioned at the requisite Bragg angle to the incident beam. When narrow spectral intervals are being studied the cassette can be mounted normal to the beam.

The crystal is bent by the "four point support" method proposed by Gil'varg[1]; to provide for this the crystal is loosely held between two metallic plates with 12 x 6 mm openings. This method of bending makes it easy to vary the radius of curvature as required by the experiment. The exact radius of bending of a given crystal is determined in adjusting the instrument, usually first optically and then by the method of photographing on a plate or film positioned at the appropriate angle. It is known that temperature fluctuations and other factors produce variations in the radius of curvature of the crystal with time and thereby defocus the instrument. The design of this spectrograph, providing for fine adjustment, makes it possible to always photograph at the point of optimum focusing.

The spectrograph cover has a counter-weighted suspension. The cover and other joints are fitted with rubber gaskets which insure the necessary seal for maintaining a vacuum of 10^{-2} mm Hg. The window between the spectrograph housing and the tube is equipped with a shutter controlled from the outside; this permits opening the housing for necessary operations therein (for example, changing the emitter, recoating the filament of the x-ray tube, etc.) without exposing the film.

The demountable x-ray tube of the spectrograph is equipped with an anode of new design giving it a power rating of over 2 kw (Ref. 2).

In working by the Johann method the interval of obtainable reflection angles is 20-88°. However, the design of the instrument makes it easy to go over from the Johann to the Cauchois method. To do this one need merely turn the housing around so that the x-ray tube will be on the other side of the crystal. The necessary seals are provided so that the Cauchois spectrograph is also a vacuum instrument. In Fig. 1 the dotted line shows the position of the tube for working by the Cauchois method with a reflection angle $90^\circ - \alpha$.

For working by the fluorescence method the upper part of the demountable x-ray tube is replaced by the attachment shown in Fig. 3. As may be seen from the figure the cathode in this case is oriented horizontally. The x-ray emission from the cathode falls on the emitter E mounted at an angle of 45° relative to the exit window. The crystal holder K is mounted immediately next to the emitter right on the tube and can be rotated about the vertical axis thus allowing variation of the reflection angle. The distance between the anode and emitter is 28 mm, that between the emitter and the crystal is 15 mm. A significant gain in transmission is attained by mounting the anode, emitter and reflecting crystal close to each other. Bringing the emitter out of the tube has a number of advantages and facilitates various studies such as investigations of the effect of

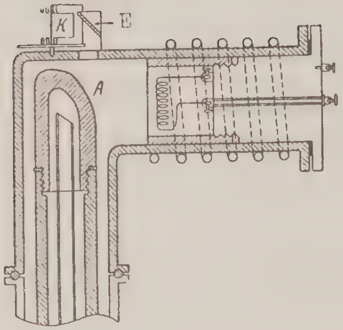

Fig. 3. Fluorescence analysis attachment for the x-ray tube: A) anode of x-ray tube, K) crystal holder, E) emitter.

temperature, magnetic fields and other factors on the emitter. Furthermore, freeing the tube of the emitter makes it possible to increase its power, thereby appreciably shortening the exposure. For example, by means of this tube operated at 50 ma and 35 kv we recorded the $K\alpha_1\alpha_2$ spectral lines of Ti with a blackening of 0.5-0.6 in 8 min; an equal blackening for the $K\beta_5$ line of Ti was obtained with an exposure of 16 hours.

So far we have used only the photographic method of recording spectra; however, ionization methods can readily be used with the instrument by locating a moving counter behind the cassette. Obviously, the Johansson method of focusing can also be used in this spectrograph.

In conclusion it should be noted that the simplicity of design of this spectrograph makes it very inexpensive to construct.

"K.D.Ushinski" Odessa Pedagogical Institute

References

1. A.B.Gil'varg, Doklady AN SSSR, 72, 489 (1950).
2. I.B.Staryi, Zavod. labor., 20, 626 (1954).

EXPERIMENTAL USE OF A SCINTILLATION COUNTER FOR RECORDING X-RAY SPECTRA

- L.M.Beliaev, K.I.Narbutt, E.L.Stoliarova,
I.E.Konstantinov, V.A.Alekseev, A.B.Gil'varg & I.S.Smirnova

Introduction

The photographic method, which is the one generally employed for recording x-ray spectra, has a number of serious shortcomings. With this method it is impossible to observe the peak intensities and shapes of the characteristic lines directly; the film must first be developed, the spectrogram photometered and the photographic densities converted to intensity values. In some cases, as when working with chemically unstable compounds, it is impossible to utilize the photographic method since the exposure time may be longer than the stable life of the material. Thus, study of the structure of albumin compounds[1] became feasible only with the introduction of electric methods of measuring the intensity.

The inadequacies of the photographic method stimulated the development of electric recording methods. Geiger-Muller counters have been extensively used for this purpose. In some cases, proportional counters have also been employed.

In the current practice of experimental physical research, scintillation methods are finding increasing application for measuring x-rays and γ-radiation.[3-7] This is explained by the fact that the scintillation method has a number of advantages over the ionization method. First, one must note the high efficiency of the scintillation method: x-ray radiations and γ-ray quanta of energies in the interval 5-80 kev have been counted with efficiencies attaining 100%, while in the case of quanta of energies up to 2 kev efficiencies of 80% have been reached. In view of the high efficiency of the scintillation method it should be feasible to record weaker lines (than now possible with GM counters) by means of this method; it should also allow of enhancing the accuracy and sensitivity of x-ray spectrum analysis.

Another major advantage of the scintillation method is the fact that it has almost zero inertia. The scintillation time of the luminophor crystals, which constitute the sensing element of a scintillation counter, is of the order of a fraction of a microsecond; for some organic phosphors the time is only 10^{-9} sec. Fluctuations in the build-up of the number of electrons in photomultipliers are of the order of 10^{-8}-10^{-9} sec. For this reason, the counting rate is currently limited only by the characteristics of the recording electronic circuit. Equipped with appropriate amplifying and counting circuits, a scintillation counter may give up to 1 million counts per second. Accordingly, employment of a scintillation counter for recording x-ray spectra should result in an appreciable acceleration of the measurement process.

In addition, the higher resolution in time of scintillation counters should permit of recording of greater intensities. In principle, the range of intensities which can be measured with a scintillation counter is appreciably wider than for GM counters.

It may be noted that a scintillation counter with an NaI(Tl) crystal has been successfully used for x-ray analysis.[6]

We investigated the feasibility of utilizing scintillation counters for recording characteristic spectrum lines for the purposes of x-ray chemical analysis.

In the spectral measurements with a scintillation counter of our own design, we tried various luminophors: NaI(Tl), CsI(Tl), KI(Tl), $CaWO_4$, thallan and stilbene. We measured the intensity of the $K\alpha_1$ and $K\alpha_2$ lines of a number of elements: Cu^{29}, Zn^{30}, Ge^{32}, Rb^{37}, Zr^{40}, Mo^{42} & Pd^{46}.

Equipment and Procedure

The first series of measurements was carried out on x-ray spectra, obtained by primary excitation, on our RSK-5 spectrograph (Fig. 1)*. The principal components of this instrument are a) the demountable x-ray tube 1 with a replaceable anode, b) a limiting diaphragm for separating the x-ray beam with the requisite angular divergence and a crystal-analyzer (both are mounted in the common housing 2), c) the recording assembly 3 with its receiving slit, moving over the focal circle (a scintillation or a gas counter can be mounted behind the slit for comparative tests), d) a kinematic arrangement for displacing the counter over the focal circle and, finally, the dial and pointer 4 serving to indicate the position of the recording unit on the focal circle.

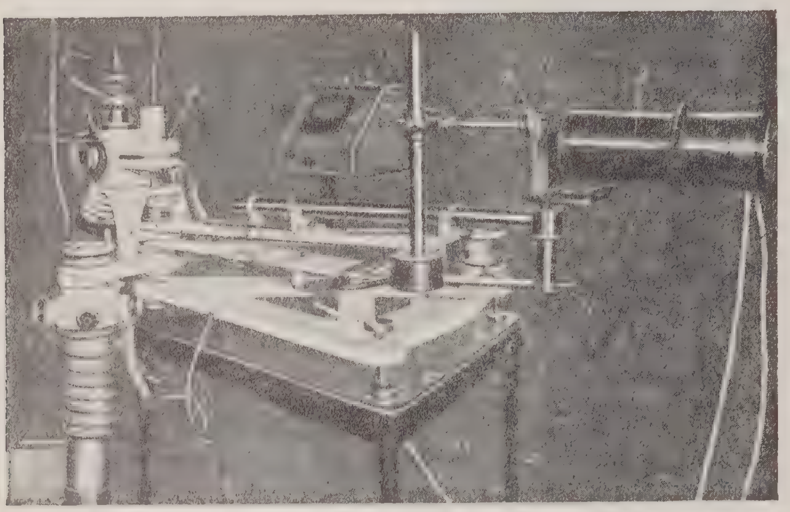

Fig. 1. RSK-5 spectrograph with scintillation counter: 1) demountable x-ray tube, 2) protective housing, enclosing the limiting diaphragm and the analyzer crystal, 3) recording assembly and 4) assembly position indicator.

The second series of measurements was made on x-ray spectra obtained by the fluorescence method. In this case the demountable x-ray tube of the RSK-5 spectrograph was replaced by a powerful sealed x-ray tube of the BFV-70 type.[9] The vertical beam of the primary x-ray radiation was incident on an inclined plate of the investigated element. The secondary x-ray radiation entered the crystal-analyzer and then the recording assembly: either a gas counter or our scintillation counter, which consisted of a crystal-phosphor, a photomultiplier and the associated electronic circuit. The electric pulses from the multiplier anode are fed into a one-stage preamplifier, designed about a 6Zh4 tube. The preamplifier is mounted inside the counter housing. Next, the pulses go to a wide-band amplifier, designed about 6Zh4 tubes, having high pass limit of 3.5 Mc and an amplification factor of 1000. The amplified pulses go to a discriminator, assembled about two 6Zh4 tubes, which suppresses pulses under a certain height (discriminator setting is adjustable). From the discriminator output, the pulses are transmitted to a scaler, built around 6N8 tubes and having a scaling ratio of 16 to 1, and thence to a standard scaling network (PS-64) and an electro-mechanical counter. As a whole, the scaling circuit allows of counting up to 10^5 pulses per sec. The maximum scaling factor was 1024.

The amplifier plate supply unit, designed about 6P3 and 6N8 tubes assured a uniform voltage with a stability coefficient of 0.1%. The high-voltage power-pack for the photomultiplier supplied stabilized potentials of up to 1.5 kv (stabilization coefficient 0.1%).

In view of the fact that NaI(Tl) crystals are highly hygroscopic, when the NaI(Tl) was being tested, the crystal was enclosed in a special packing, consisting of a rectangular container with a bottom of 1 mm thick glass and sidewalls of

---

*This instrument, designed by the writers, is an improved version of the RSK-3, which we have described in Ref. 8.

Plexiglass. The crystal measured 20 x 5 x 1 mm. The container was covered with a layer of 14 μ thick aluminum foil which also served as a reflector. The glass bottom was coated with vacuum grease and placed in contact with the multiplier photocathode.

All the other crystals were used without a packing; they were simply held in contact with the photocathode by means of a layer of vacuum grease. The photomultiplier was the domestic FEU-19 type, selected from among several dozen tubes on the basis of the best signal to noise ratio.

Experimental Results

1. The preliminary tests were carried out on spectra excited by the primary method. An NaI(Tl) crystal was used as the luminophor.

We used the height of the $K\alpha_1$ and $K\alpha_2$ lines above the background as the measure of counter efficiency. We recorded the $K\alpha_1$ and $K\alpha_2$ lines for Cu^{29} with the x-ray tube operated at 38 kv and 50 ma (Fig. 2) and for Ag^{47} with the tube operated at 35 kv and 15 ma (Fig. 3). The scaling ratio k in these measurements was 256. The counting time was 30 sec per point.

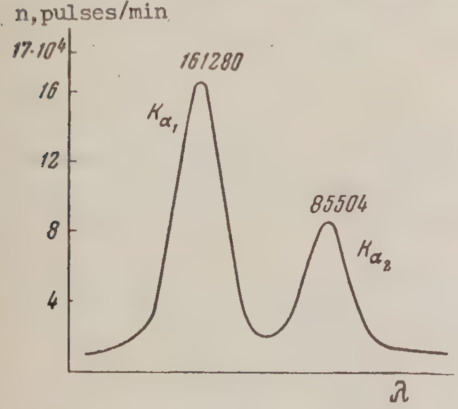

Fig. 2. K-spectrum of Cu^{29}, $n_{bkgr} = 19968$.

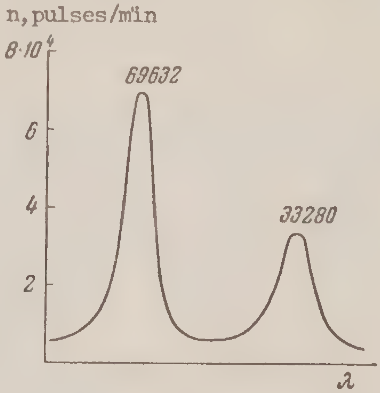

Fig. 3. K-spectrum of Ag^{47}, $n_{bkgr} = 6570$.

Analysis of the curves showed that the ratio $\frac{\alpha_2 - \text{background}}{\alpha_1 - \text{background}}$ equals 53% for Cu^{29} and 50% for Ag^{47}.

Thus it will be seen that a satisfactory value of the peak ratios was obtained. If the results are converted to the same x-ray tube operating regime (35 kv and 15 ma), we obtain the following values: for the Cu^{29} $K\alpha_1$ line - 44,550 pulses/min and for the Ag^{47} $K\alpha_1$ line - 69,600 pulses/min.

Thus the counting efficiency is one and one half times higher for silver.

An attempt to use a $CaWO_4$ crystal for recording the spectra failed to yield positive results. While it is feasible to record spectra by means of this crystal, the efficiency is very low.

2. The second series of measurements was carried out on secondary emission spectra. The x-ray tube was operated at 27 kv and 50 ma.

The experiments were carried out with different luminophors for the purpose of finding the luminophor yielding the highest recording efficiency. Here again the measure of efficiency was the maximum intensity of the spectral lines above the background. In addition the same lines were recorded under identical conditions by means of a gas counter. The efficiencies of the scintillation and gas counters were compared on the basis of $K\alpha_1$ line intensities, the intensity over the background (for each investigated element) obtained with the gas counter being taken as unity. The results of measurements for Ge^{32} and Rb^{37} are summarized in the accompanying table. The last column lists the ratio of the recording efficiency with the scintillation counter with different luminophors to the

Intensities of the $K\alpha_1$ and $K\alpha_2$ lines of Ge^{32} and Rb^{37} recorded by means of a gas counter and the scintillation counter with different luminophors

Luminophor	Line intensity, pulses/min		Bkgr, pulses/min	Intensity above bkgr pulses/min		$\frac{\alpha_2-\text{bkgr}}{\alpha_1-\text{bkgr}}$, %	$\frac{\alpha_1^{Sc}-\text{bkgr}}{\alpha_1^{Gas}-\text{bkgr}}$, %
	α_1	α_2		α_1–bkgr	α_2–bkgr		
K emission spectrum of Ge							
NaI(Tl)	60 160	38 400	17 280	42 880	21 120	49,3	5
KI(Tl)	660 800	481 600	284 800	376 600	196 800	52,3	43,5
Stilbene	27 520	24 328	21 920	5 600	2 408	43,0	0,65
Gas counter	9 472	4 320	832	8 640	3 488	41,0	1
K emission spectrum of Rb							
NaI(Tl)	33 536	26 272	18 496	15 040	7 776	51,5	6,7
CsI(Tl)	76 160	57 920	46 560	29 600	11 360	38,4	13,2
KI(Tl)	57 920	40 160	23 040	34 880	17 120	49	15,6
Thallan	25 600	24 720	23 040	2 560	1 680	65,5	1,14
Gas counter	2 384	1 280	144	2 240	1 136	50,06	1

recording efficiency with the gas counter.

The tabulated data for the $K\alpha_1$ and $K\alpha_2$ lines with the background subtracted for Ge^{32} are shown in Fig. 4 and for Rb^{37} in Fig. 5; the background in each case is listed in the captions. Similar curves were obtained for the other investigated elements: Zr^{40}, Cu^{29}, Zn^{30}, etc.

Analysis of the experimental data shows that a scintillation counter incorporating an inorganic crystal phosphor gives an appreciably higher recording efficiency than a gas counter. The highest efficiency was obtained with a KI(Tl) crystal.

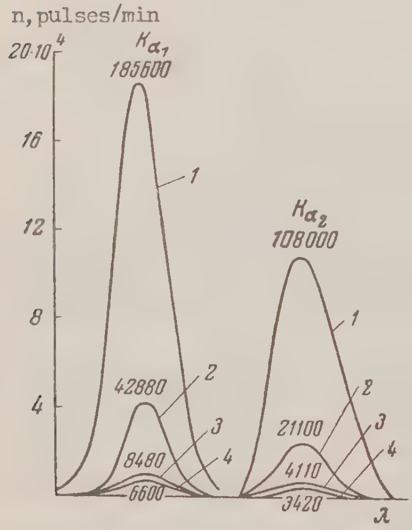

Fig. 4. K-spectrum of germanium recorded by means of the scintillation counter with different crystals (scaling ratio 1024): 1) KI(Tl), n_{bkgr} = 27,840; 2) NaI(Tl), n_{bkgr} = 17,280; 3) gas counter, n_{bkgr} = 832; 4) stilbene, n_{bkgr} = 6400.

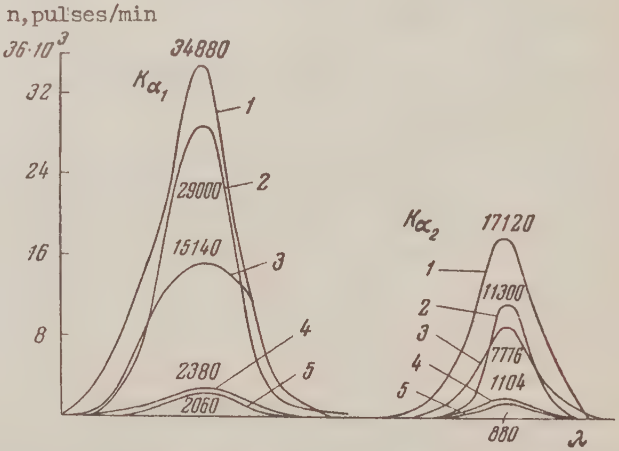

Fig. 5. K-spectrum of rubidium recorded by means of the scintillation counter with different crystals: 1) KI(Tl), n_{bkgr} = 23,040; 2) CsI(Tl), n_{bkgr} = 46,540; 3) NaI(Tl), n_{bkgr} = 18,496; 4) gas counter, n_{bkgr} = 152; 5) thallan, n_{bkgr} = 23,040.

The organic luminophors stilbene and thallan proved to be less efficient; in fact the efficiency of stilbene was lower than that of the gas counter.

3. The next series of experiments was carried out with a selected KI(Tl) crystal, characterized by the highest recording efficiency. In this series we recorded the $K\alpha_1$ and $K\alpha_2$ lines for different elements for the purpose of determining the energy dependence of the recording efficiency.

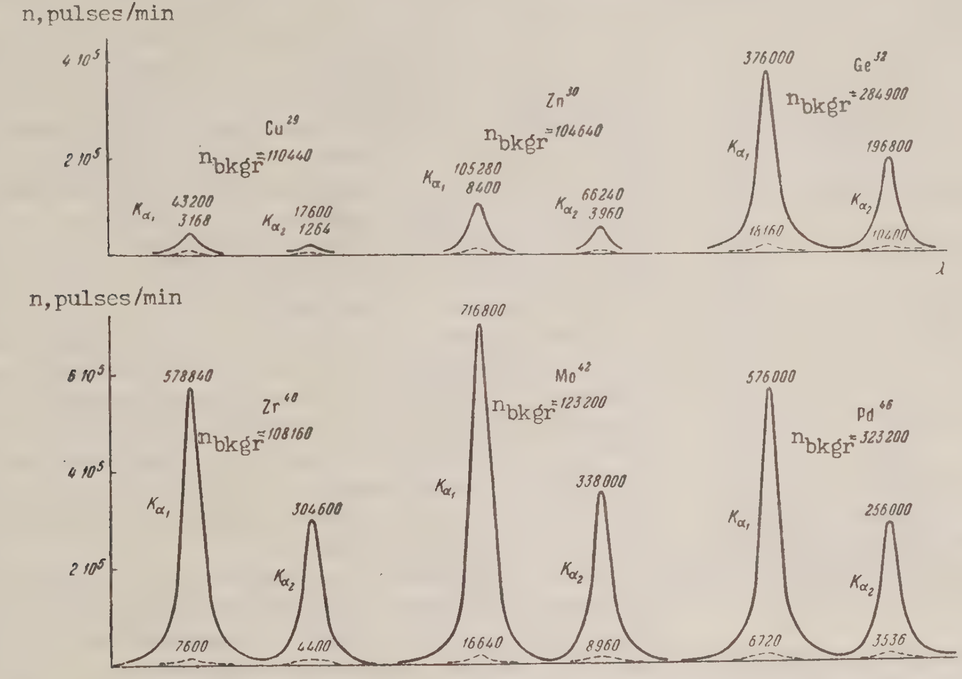

Fig. 6. K-spectra of different elements recorded by means of the scintillation counter with a KI(Tl) crystal; scaling factor 1024.

Fig. 6 shows a series of such curves obtained with the selected KI(Tl) crystal for Cu^{29}, Zn^{30}, Ge^{32}, Rb^{37}, Zr^{40}, Mo^{42} and Pd^{46}. The results show that the number of pulses increases with the line energy. The dash lines in Fig. 6 show the results obtained with a gas counter. The superiority of the scintillation counter is evident.

Use of a scintillation counter in investigating the fine structure of x-ray absorption spectra

After completion of the above tests, whose purpose was to determine the principal characteristics of scintillation counters as a means for recording x-ray quanta, we made an attempt to apply a scintillation counter to the investigation of the fine structure of x-ray absorption spectra. To this end we studied the K absorption spectrum of bromine in an aqueous solution of NaBr. By way of continuum source we utilized a BVF-80 x-ray tube with a tungsten anode. The analyzer was a concave quartz crystal, the radiation used being the reflections from the (1$\bar{3}$40) planes. The dispersion was 2.46 XE/mm; the slit width was 0.05 The tube was operated at 50 kv and 100 ma. The thin wall absorption cell containing the NaBr solution was located immediately behind the analyzer. In order to bring out the fine structure of the K-spectrum it was necessary to obtain at least 30 points at 0.1 intervals. As a first step we recorded the spectrum with a gas counter. In working with a gas counter satisfactory statistics could be obtained only by continuing the counting for at least 20 minutes for each point. During this interval approximately 10,600 pulses were recorded in the least intense part of the spectrum, the background count being 1600 ($I_{min} - I_{bkgr} = 9000$ pulses). Thus the recording of the entire absorption spectrum required about 12 hours. Then we used a scintillation counter with a KI(Tl) crystal under the same conditions. It was determined experimentally that the same statistical averaging is obtained in 5 minutes counting with a scintillation counter as a recording for 20 minutes with a gas counter. The following values were obtained: $I_o = 192{,}000$ pulses, $I_{min} = 77{,}000$ pulses, $I_{bkgr} = 68{,}000$ pulses ($I_{min} - I_{bkgr} = 9000$ pulses).

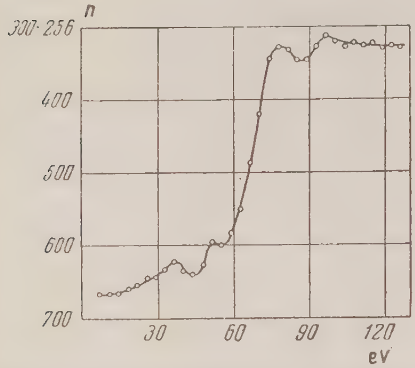

Fig. 7. K absorption spectrum of Br in an aqueous solution in NaBr recorded by means of the scintillation counter: $I_o = 748{,}256$; $I_{bkgr} = 265{,}256$.

The K absorption spectrum obtained in this manner is shown in Fig. 7. As regards the shape of the absorption maxima and minima this spectrum is identical with the one recorded by means of the gas counter. However, less than three hours were required to record the spectrum by means of the scintillation counter.

Thus the first practical application of a scintillation counter to the investigation of absorption spectra resulted in a four-fold saving of time. However, this is not the only consideration. The comparatively rapid recording made it possible to detect a hitherto undiscovered effect, namely, that the fine structure of the absorption spectra changes as a result of prolonged exposure of the absorbing substance to x-rays. A detailed discussion of this effect, however, is outside the scope of this report.

Our experiments on the use of scintillation counters for recording the intensity of x-ray spectra demonstrated the superiority of this type of counter as compared with gas counters. The following conclusions may be drawn on the basis of the experimental results.

1. By virtue of their higher recording efficiency (tens of times higher than that of gas counters) scintillation counters make it possible to enhance the sensitivity of x-ray analysis by at least an order of magnitude as compared with gas counters.

2. Of the six organic and inorganic luminophors tested, we can recommend the KI(Tl) crystals as having the highest efficiency and not requiring special protection.

3. The first practical use of a scintillation counter for recording the fine structure of x-ray absorption spectra gave satisfactory results and made it possible to reduce the overall recording time by about 75%.

4. In using a scintillation counter for the purpose of quantitative x-ray chemical analysis one must bear in mind the variation of the recording efficiency with the energy of the lines.

5. Scintillation counters can also be used in x-ray structural analysis, particularly where it is necessary to investigate chemically unstable complex crystals and prolonged exposure times are impractical.

Institute of Crystallography of the USSR Academy of Sciences
Institute of Geological Studies of the USSR Academy of Sciences
Moscow Engineering-Physics Institute

References

1. U.W.Arndt, Atomics, 4, 217 (1953).
2. KI.Narbutt, Izv. AN SSSR, Ser. fiz., 17, 249 (1953).
3. F.H.Marshall, J.W.Coltmen & A.I.Bennett, Rev. Sci. Instr., 19, 744 (1948).
4. J.P.Neissel & D.C.Moore, Phys. Rev., 78, 643 (1950).
5. H.I.West, Jr., W.E.Meyerhof & R.Hefstandter, Phys. Rev., 81, 141 (1951).
6. J.Brentano & I.Ladany, Rev. Sci. Instr., 25, 1028 (1954).
7. W.H.Robinson & W.Jentschke, Phys. Rev., 95, 1412 (1954).
8. K.I.Narbutt, A.B.Gil'barg, E.E.Vainshtein, L.M.Beliaev, Zavod. labor., 22, 1485 (1951).
9. K.I.Narbutt & E.M.Fridman, Izv. AN SSSR, Ser. fiz., 20, 136 (1956). (Trans. in Bulletin, Vol. 20, No.1, p. 123).

DETERMINATION OF THE DIFFUSION COEFFICIENT FROM SECONDARY X-RAY SPECTRA

- M.A.Blokhin, E.V.Timofeeva and G.Z.Chukhlov

In this investigation we applied quantitative analysis of secondary x-ray spectra to the evaluation of the diffusion coefficient of sulphur in steel and cast iron. The work was undertaken at the request of the Central Plant Laboratory of the Rostsel'mash Plant in connection with development of a method for increasing the wear resistance of steel and cast iron through surface saturation with sulphur (sulfiding). The Plant Laboratory is carrying on this development work in creative cooperation with Rostov State University. Specifically in this case, the x-ray laboratory of the University Plysics Department was assigned the problem of determining the distribution in depth of sulphur in metals sulfided by immersion in fused sulfur-containing salts.

The solution of this problem obviously required quantitative determinations of the sulfur content of successive metal layers. Chemical analysis, which was formerly commonly employed, requires an appreciable amount of analytic material. This is obtained in the form of chips cut off on a lathe from the face end of a sulfided cylinder. The thinnest layer which can be removed in this manner with sufficient accuracy is at least 50 μ thick.

Yet chemical analysis showed that practically all the sulfur entering the steel or cast iron was concentrated in the surface 50 μ layer. Consequently a more refined procedure was called for to determine the sulfur distribution in detail.

We applied x-ray analysis using secondary spectra. This method has a number of advantages over the chemical method as well as over x-ray analysis from primary spectra: first, such an analysis requires only a small amount of the substance; second, during analysis the metal is heated very little so that the specimen taken for analysis is not damaged; third, and most important, owing to the strong absorption of x-rays by sulphur in iron the effective thickness of the analyzed surface layer is very small - about 1 μ - which allows detailed study of the sulfur distribution in depth.

Accordingly, determination of the diffusion coefficient was based on layer-by-layer x-ray analysis, as successive layers were removed by grinding. The work was carried out on a long-wave x-ray fluorescence spectrometer designed by Blokhin. The x-ray tube was operated at 30 kv and 20 ma; the pulse counting time was 10 minutes. The dispersing element was a gypsum crystal. The use of gypsum, instead of the usual quartz crystal, was necessitated by the strong selective absorption of the analytical S $K\alpha$ line by silicon. The gypsum crystal, together with intensity determination by a counter tube and secondary spectrum excitation by the radiation from a silver anode, assured a sensitivity of analysis for sulfur close to 0.08%.

The method of calculating the diffusion coefficient employed in the study was that described in Ref. 1. This method requires knowing the sulfiding time and the ratio of the concentrations at two depths.

The sulfur content of the specimens was obtained by the external standard method, i.e., by comparison with an industrial alloy of iron and sulphur containing a known percentage of sulfur (16.5%). The first measurements showed that at a depth of approximately 5 μ there is practically no free sulfur. This indicated at once that x-ray analysis was eminently suitable for solving the assigned problem. However, it made it necessary to prepare the analytic samples in the shape of plane parallel plates (faces parallel within 1μ); the plates were checked on an optical comparator.

The external sulfided layer consists of a brittle, ~3 μ thick yellow-gray coating on the surface of the metal; the coating is readily scraped off. The yellowish color of the coating persists to a depth of 1μ, the color at a greater depth being black. If the entire coating is scraped off (for example, with a razor blade) a shiny black surface, having a burnished appearance, is revealed.

In this work we determined the concentration of sulfur which entered the metal from the sulfiding bath, in excess of the original sulfur content of the metal.

Results of the x-ray determinations of the distribution in depth of sulfur in cast iron and in St. 45 steel were virtually identical:

Layer		Sulfur Content
Yellow surface deposit		22%
Black layer on surface		18%
Burnished surface		11.5%
Under the burnished surface at a depth of	0.5 μ	7.4%
	1.5 μ	0.5%
	3.5 μ	$\leqslant$0.08%

In parallel with our work, Shuvaev carried out an x-ray structural analysis of the sulfided layer. He found that it contains a substantial amount of FeS and FeS_2; the FeS_2 is present only in the superficial (top 1 μ), yellow part of the brittle surface layer; the remaining, black part of the brittle layer contains mainly FeS.

Calculation of the diffusion coefficient in the metal below the burnished surface yielded the following value at a temperature of 220°:

$$D = (2.1 \pm 0.8)\cdot 10^{-13}\ \text{cm}^2/\text{sec}.$$

This result can be compared with the data given in Barrer's[2] book where the following equation is given for the temperature dependence of D:

$$D = 1.6\cdot 10^{-5}\ e^{-13350/T}. \qquad (1)$$

At 220°, this equation gives

$$D = 2.5\cdot 10^{-17}\ \text{cm}^2/\text{sec}.$$

The divergence from our value is explainable by the approximate character of equation (1) which, with the given numerical parameters, is approximately valid only in the temperature interval from 950 to 1050°, and is not applicable in a broader temperature range, as has been shown in Ref. 3.

In conclusion it can be said that the method described can be used for accurate and rapid determination of the diffusion of many elements through different solids.

"V.M.Molotov" Rostov State University

References

1. S.D.Gertsriken & V.G.Lozovik, Voprosy fiziki metallov (Problems of the Physics of metals), Kiev 1954.
2. R.Barrer, Diffusion in Solids, M. 1948.
3. A.Bramley, F.Haywood, A.Cooper & J.Watts, Trans. Faradey Soc., 31, 707 (1925).

X-RAY SPECTRAL STUDIES OF ALLOYS IN CONNECTION WITH THEIR MAGNETIC STATE

- S.M.Karal'nik, I.Ia.Dekhtiar, D.M.Konskii,
V.G.Chupryna and L.G.Nikolaeva

In recent years many authors have emphasized the importance of investigations of the fine-structure of the x-ray spectra of ferromagnetic materials. Thus Vainshtein[1] compared the variation of the index of asymmetry of the $K\alpha_{1,2}$ lines and the magnitude of the magnetic moment for elements of the iron group. In the course of x-ray studies of an alloy having the composition Ni_3Mn, one of us[2] investigated the dependence of the fine structure in the x-ray absorption spectra of the alloy on the degree of ordering in connection with changes in the magnetic state.

At about the same time Kazantsev,[3,4] studying alloys of the Fe-Cr system, came to the conclusion that there was a correlation between changes in the K_β emission lines of Fe and Cr and changes in the ferromagnetic state of their alloys. Recently other investigators (S.A.Nemnonov & N.G.Trapeznikov, N.D.Borisov and V.I.Kotliar) have undertaken studies of the variation of the atomic x-ray spectra incident to alterations of the magnetic state.

Originally we evaluated the changes in the magnetic state, as have other authors, in a crude qualitative way (by bringing the samples into the field of a magnet).

For subsequent investigations of the x-ray characteristics of ferromagnetic alloys incident to changes in the magnetic state, we felt it necessary, first, to select, from the diverse magnetic characteristics of the materials, the one most expedient to follow and, second, to obtain not just a qualititative but a quantitative measure of the chosen magnetic characteristic. We took the magnitude of the magnetic moment per atom to be the most suitable characteristic and determined it from the saturation magnetization.

We had at our disposal the following alloys of nickel and manganese with various amounts of tin: 1) 84.2% Ni + 13.8% Mn + 2% Sn, 2) 82.5% Ni + 13.8% Mn + + 3.7% Sn, 3) 78% Ni + 16.8% Mn + 5.2% Sn.

Inasmuch as the samples were small it was necessary to use a magnetometric procedure and build a special magnetometer for this purpose.*

By way of x-ray characteristics, we investigated the K absorption edges of the alloy components and partially the $K\beta_5$ line of Ni.

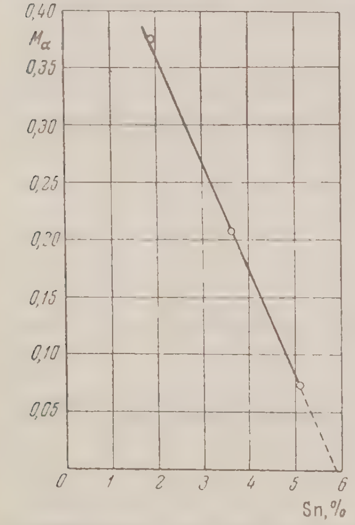

Dependence of the magnetic moment of Ni-Mn-Sn alloys on the tin content. Ordinates: magnetic moment per atom in Bohr magnetons.

Our experiments showed that the magnetic moment per atom decreases with increasing tin content (see accompanying figure). Extrapolating and, in the first approximation, ignoring the somewhat different manganese content of the third alloy, one can conclude that near an Sn content of ~6% the magnetic moment of the nickel will be completely suppressed. The K-edges of nickel in the absorption spectra of these alloys are all increasingly shifted to the side of shorter wavelengths with growing tin content (this shift amounts to several ev). In our opinion this shift may be interpreted as direct evidence for the transfer of tin valence electrons to the 3d-band of nickel, with a consequent suppression of the magnetic moment of the nickel. However, it if is assumed that an atom of tin can donate up to four electrons to fill the vacancies in the 3d-band of nickel in the alloy, then, taking the number of vacancies in the 3d-band to be 0.6 per atom and the nickel content of the alloy to be 80%, for complete quenching it is necessary to have not 6% (as our experiments indicated) but at least 12% tin in the alloy. Hence, if the experimental value is correct, it follows that to explain the quenching of the magnetic moment at the low tin concentration one must assume that the atoms of manganese (also a "defect" metal) likewise contribute to the quenching. If this were the case one would expect the K-edges of manganese in these alloys to be located at longer wavelengths than in the spectrum of the pure metal. However, our experiments showed that the K-edge of manganese in these alloys, like that of nickel, is displaced towards shorter wavelengths relative to its position in the pure metal.

---

*This was the thesis project of D.M.Komskii.

Our present experimental results are qualitative and it is necessary to accumulate more experimental material. Nevertheless, even the present data bring out some difficulties of principle. The way out may be sought in two directions: 1) in re-examining the assertion, purportedly established by experiment, that there is a direct correlation between changes in the magnetic state of the alloy and changes in the x-ray characteristics of the alloy components and 2) in a reconsideration of the presently accepted interpretation of the changes observed in x-ray spectra.

Let us take up the first point. In the experiments of Ref. 2 on Ni_3Mn it was found that the x-ray spectrum changed with alterations of the magnetic state of the alloy; but as is well known, such alterations are accompanied by order-disorder changes. Consequently, it is essential to determine the influence of ordering and that of the magnetic state separately. This is all the more necessary since the connection between ferromagnetism and ordering is often uncertain and correlations are not always reliable.[5]

The interpretation of Kazantsev's experimental data[3,4] also requires care. Indeed, in his work, changes in the x-ray spectra (broadening of the $K\beta_5$ iron line on the short-wave side and a narrowing of the $K\beta_5$ chromium line) appear to be equal, both incident to disappearance of ferromagnetism as a result of changes in component concentration and incident to going through the Curie point. This is the crux of the matter, for changes in the magnetic state in the two cases are presumably produced by quite different mechanisms. Even if, in connection with changes in alloy composition, it is still possible to speak about the transfer of electrons from atoms and the filling of the 3d-band of the ferromagnetics, the mechanism by which ferromagnetism vanishes incident to changes in temperature must be quite different.

Thus, instead of comparing changes in the x-ray spectra with changes in the magnetic state, it may be more logical to compare both with the variation of some other quantity. In our opinion this quantity is the strength of the interatomic bonds as it varies in alloys of different composition and in different states, for obviously the strength of the bonds between the atoms should affect the atomic x-ray spectra and the magnetic characteristics of the alloys, as well as some of their other physical attributes.

We note in passing (we intend to discuss this in detail elsewhere) that the changes in the x-ray spectra observed by Kazantsev can be interpreted from the point of view developed by one of us[6]; the interpretation is based on the hypothesis regarding the filling of the 3d-shell by the 4s-electrons of the same atom at high temperatures.[7,8]

Recently in collaboration with S.Litovchenko, we obtained new data on the x-ray spectra of alloys of iron and aluminum that show which of the two factors - ordering or changes in the magnetic state of the alloy - exerts the dominant influence on the x-ray characteristics of atoms in alloys. Among other results, it was established that specimens of the alloy containing 50% aluminum in the disordered state (there were no superlattice lines in the Debye patterns) possessed magnetic properties and that these properties are lacking in the ordered state of the alloy. At the same time the K absorption edge of iron has a shorter wavelength in the ordered alloy than in the disordered one. In the Ni_3Mn alloy the K absorption edge is again at a shorter wavelength for the ordered alloy, but in this case, in contrast to the preceding case, the alloy exhibits magnetic properties. Obviously, in such cases correlation should be sought between changes in ordering and changes in the x-ray spectra, and not between the latter and changes in the magnetic state.

We also note (on the basis of preliminary data obtained in x-ray studies of alloys of the cobalt-aluminum system) that it seems reasonable to compare the dependence of the atomic x-ray spectra on the component concentration with the dependence of the Curie point on the composition. This is in line with our assertion regarding the decisive influence of the strength of the interatomic bonds on the x-ray characteristics of the components of alloys comprising transition metals.

To sum up, we can draw the following conclusions. If, as is now commonly assumed, joint studies of the x-ray characteristics and magnetic properties of ferromagnetic metals and alloys can give valuable information about the nature of ferromagnetism, one must bear in mind in carrying out such investigations that the correlation is not as simple and direct as some workers have suggested. We feel that in order to explain the effects observed in the x-ray spectra it is necessary to adopt a point of view regarding the mechanism of changes in the x-ray spectra of alloys differing from the present one. We hope that this may throw light on the mechanism of interatomic bonds in alloys.

References

1. E.E.Vainshtein, Rentgenovskie spektry atomov v molekulakh khimicheskikh scedinenii i v splavakh. (X-ray spectra of atoms in the molecules of chemical compounds and in alloys) Izv. AN SSSR, 1950.
2. S.M.Karal'nik, Dissertation, Kiev State University, 1952.
3. M.A.Blokhin, Fizika rentgenovykh luchei (Physics of x-rays), 1953.
4. V.A.Kazantsev, Doklady AN SSSR, 101, 477 (1955).
5. C.S.Barrett, Structure of metals (In Russian trans. M. 1948).
6. S.M.Karal'nik, next article in present issue of Bulletin.
7. I.Ia.Dekhtiar, Doklady AN SSSR, 85, 583 (1952).
8. I.B.Borovskii, K.P.Gurov, S.A.Ditsman & V.A.Batyrev, Abstracts of reports presented at the Fifth All-Union Conference on the Application of X-rays, p. 9, Leningrad State University, L.1955.

X-RAY SPECTRA AND INTERATOMIC BONDS IN ALLOYS

- S.M.Karal'nik

Study of interatomic binding in metals and alloys is one of the important problems in metal physics. As is known, the strength of the bonds can be evaluated by studying such characteristics as the heat of sublimation, the activation energy for diffusion, the modulus of elasticity, the coefficient of thermal expansion, the characteristic temperature, the interatomic spacing and from data on the electron density obtained by x-ray diffraction analysis and in studying the thermal factor in x-ray scattering.[1,2]

In this article we wish to draw attention to some experimental facts concerning the x-ray absorption spectra of atoms of the transition elements and their alloys.

Dekhtiar[3] showed that as the chromium content of cobalt-chromium alloys is increased from 0 to 25% the wavelength of the K absorption edge of cobalt decreased. Sorokin[4] showed that when the aluminum content of manganese-aluminum is increased the K absorption edge of manganese is also displaced to the shortwave side. In our study[5] of a series of alloys of nickel with chromium and nickel with manganese and a series of the ternary alloys, it was established that the K-edges of the alloy components are displaced to the short wavelength side with respect to their positions in the pure metals. Analogous results were obtained by Nikolaeva for the K absorption edge of iron in the iron-chromium system. Data illustrating the above remarks are presented in the table below.

Displacements of the K-edges of metals in alloys relative to their positions in the pure metals.

Alloys	Concentration of 2nd comp., %	Shift of K-edge, ev First Component	Shift of K-edge, ev Second Component
Fe-Cr	8	0,8 ± 0,8**	
	16	1,3 ± 0,8	
	30	2,4 ± 0,8	
Co-Cr	5	0,6 ± 0,8	
	10	1,6 ± 0,8	
	25	4,1 ± 0,8	
Ni-Cr	7,5	0,8 ± 0,6	2,2 ± 0,7
	17,1	1,1 ± 0,6	2,2 ± 0,7
	20,6	1,7 ± 0,6	1,5 ± 0,7
Ni-Mn (disordered)	26	1,4 ± 0,6	4,3 ± 0,7
Ni-Mn (ordered)	26	3,9 ± 0,6	6,5 ± 0,7

**The uncertainties given are the maximum values.

On the other hand, it is known that in the enumerated alloys the interatomic bonds are stronger than in the pure metals. In view of this it would appear that strengthening of the interatomic bonds leads to a displacement of the K absorption edge of alloy components towards shorter wavelengths relative to their positions in the pure metals or in alloys with weaker bonds. One of our earlier observations[5] is of interest in this connection. The K-edges of nickel and manganese in alloys close to the Ni_3Mn stoichiometric composition appear at shorter wavelengths when the alloy is ordered than when it is disordered. It is safe to assume that the interatomic bonds are stronger in the ordered state than in the disordered one.

The connection between these facts can scarcely be fortuitous* and we therefore believe it merits further examination.

---

*Although it lies outside the field of the physics of alloys, we might mention here Kuntsl's empirical law which states that the displacement of the K-edge to the short-wave side increases with the valence of atoms in compounds, which in a sense also connotes strengthening of the atomic bonds (in the molecules, in this case).

We immediately encounter a number of difficulties, however. For example, the magnitude of the K-edge shift amounts to several electron volts (up to 5-6 ev), while the changes in binding energy on going from the pure component to an alloy do not exceed a fraction of an electron volt. Further, if, as assumed in current theories of x-ray spectra, the position of the K-edge corresponds to the value of the Fermi energy in the metal or alloy, then from the simple fact of a change in the strength of the bonds in the latter, we cannot deduce whether the K-edge will be displaced to the side of longer or shorter wavelengths.

From the viewpoint of the common interpretation of changes in the x-ray spectra of alloys it is difficult to explain the fact established in Ref. 5 that the displacements of the K-edges of all the alloy components are in the same direction (towards shorter wavelengths) on going over to alloys with enhanced interaction between atoms.

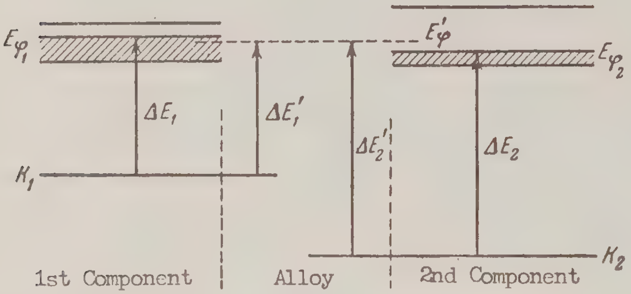

Fig. 1. Scheme of shifts of the K absorption edges of the components of alloys relative to their position in the pure metals.

Actually, the assumption that there is a common Fermi energy for the entire alloy would make it logical to expect the displacements of the K-edges of the alloy components to occur in different directions with respect to their positions in the pure metals. This follows from the scheme presented in Fig. 1.

In the scheme E_{φ} is the Fermi energy, K is the energy of the K level, ΔE is the energy corresponding to K-absorption; the indices 1,2, refer to the first and second components, and the primes signify the components in the alloy. It is obvious that according to this scheme the K-edge of the first component of the alloy should be displaced to the side of longer wavelengths, while that of the second component should be shifted to the short-wave side.

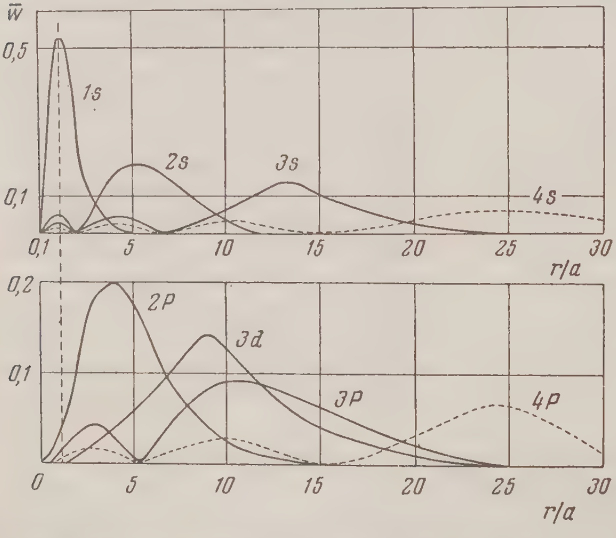

Fig. 2. The probability of finding an electron at different distances from the nucleus for the different states of the hydrogen atom.

It is also difficult to interpret the experimentally observed changes in the shape[6] and position[7] of the $K\alpha_{1,2}$ emission lines, which are associated with electronic transitions between deep-lying levels in the atoms and presumably not subject to the influence of the chemical bonds.

It seems to us that the above mentioned changes in the x-ray spectra of atoms in alloys can be explained if one takes into account the screening of the innter atomic electrons by the outer electrons and the changes in the degree of this screening incident to changes in the magnitude and character of the chemcal bonds between the atoms under different conditions.

Now the charge distribution for different atomic states can be found by quantum mechanics. The probabilities of finding an electron at different distances from the nucleus for various states of the hydrogen atom was worked out according to Ref. 8 and is shown in Fig. 2. The abscissae are distances from the nucleus in units of the Bohr radius for hydrogen; and ordinates give the probability ($\overline{w}$) of finding the electron between r and r + dr. The principal maximum for each state occurs at a distance equal to the radius of the corresponding Bohr orbit. At the same time there is a small but finite probability of finding the electron at ranges smaller than the radius of the Bohr orbit for the lowest states. In other words, there is some probability of an outer electron being inside the inner electron shells. In particular, there is a finite, though very small, probability of finding a 4s electron inside the 1s shell. The finite value of the electron density of the outer electrons inside the deep-lying inner shells leads to a screening of the interaction of the inner electrons with the nucleus. It is clear that the degree of screening will change with changes in the strength of the bonds of the atom with its neighbors, since the interatomic bonds are due to the outer electrons. Thus, there can be changes in the probability of screening of the inner electrons and, consequently, changes in the binding forces between the inner electrons and the nucleus. On the other hand, since the energy of the K-edge of the absorption spectrum of the atom corresponds to the binding energy of the K-electron with the nucleus, changes in this binding are reflected in the position of the K-edge of the absorption spectrum.

One can obtain an order of magnitude estimate of this effect from the following considerations. A complete localization of the inner electron inside the K-shell is in fact equivalent to reducing the charge of the nucleus by one unit. This would change the position of the K absorption edge of an element of the iron group, for example, by approximately 600 ev. The actual changes observed experimentally however amount to a few electron volts, apparently due to the low probability of finding an outer electron inside the K-shell.*

There should in principle be no objection to utilizing the charge density distribution in the hydrogen atom for interpreting processes occuring on complex atoms. In substantiation of this one can cite, for example, the analogous charge distributions in complex atoms deduced by the Hartree-Fock method by James[9] as well as other arguments.

In the light of these considerations, the difficult points mentioned above find at least a qualitative explanation. Thus, an increase in the strength of the atomic bonds due to participation in them of an outer electron - for example, a 4s electron - will lead to a decrease in the probability of the latter being within its parent atom and hence to a reduction of the screening by it of the 1s electrons. This, in turn, leads to an increase in the binding between the 1s electron and the nucleus with the result that the K absorption edge will be shifted to the side of shorter wavelengths (relative to its position when the interatomic bonds are weaker). Inasmuch as the binding between atoms is due to the participation of the electrons of both the interacting atoms, the K-edge of the other component atoms will also be displaced to the short-wave side.

The difficulty connected with the magnitude of the displacement (several electron volts) is also resolved, since according to the above interpretation the K-edge shift is determined by changes in the binding force between the inner electron and its atom rather than by the change in the interatomic bond energy per se. Changes in the inner electron-nucleus binding are only an indirect result of changes in the strength of the interatomic bonds. It is these small changes in the state of the 4s electrons or, more precisely, changes in the probability of their being localized in the region of the 1s shell incident to changes in the strength of the interatomic bonds that have a noticeable effect on the binding between the K-electron and the nucleus and this, in turn, is evinced in the position of the K-edge.

---

*According to an approximate evaluation by M.A.Krivoglaz, in the case of iron the probability for one electron is of the order of 0.01.

There are other interpretational possibilities inherent in this picture. In particular, we now have an explanation for the change in the shape of the $K\alpha_{1,2}$ lines. Since changes in the degree of screening of the inner electrons due to participation of the outer electrons in the interatomic bonds are manifested at the deep-lying levels, it is clear that such changes must affect the shape of these lines which are associated with electronic transitions between these deep levels.

Extending the concepts developed above, one can consider other possible redistributions of the electrons between atoms entering into bonds (including filling of the vacancies in the 3d-shells of the transition elements). However, space limitations preclude a detailed examination here. We can only note that one must also include in the consideration the data on the x-ray emission spectra of all the atoms comprising the alloy. This should make it feasible to obtain information not only on changes in the binding of the electrons with their own atoms but also on the possible further "localization" of the electrons as a result of changes in the binding forces between the atoms.

What is of paramount importance where this approach is concerned is that it makes it possible to obtain, through x-ray spectroscopic studies, additional information regarding the strength and mechanism of bonds in alloys, information not obtainable by any of the other methods mentioned at the beginning of this article. This approach also foreshadows the possibility of a single, consistent interpretation of the binding mechanism not only in alloys but in other substances as well.

In conclusion I wish to thank A.G.Lesnik for valuable discussions and G.S.Zhdanov for his interest in the investigation.

"T.G.Shevchenko" Kiev State University

References

1. V.K.Kritskaia, G.V.Kurdiumov & T.I.Stelletskaia, Doklady AN SSSR, 98, 63 (1954); G.V.Kurdiumov & N.T.Travina, Doklady AN SSSR, 99, 77 (1954).
2. V.I.Iveronova, Z.I.Kuz'mina, S.I.Futerlender & E.I.Detlaf, Izv. AN SSSR, Ser. fiz., 15, 44 (1951).
3. I.Ia.Dekhtiar, Zhur. eksp. i teor. fiz., 10, 499 (1940).
4. M.A.Blokhin, Usp. foz. nauk., 29, 125 (1946).
5. S.M.Karal'nik, Fizicheskii sbornik nauchnykh zapisok KGU (Physics collection from the Scientific Notes of Kiev State University), No.7, 105 (1955).
6. E.E.Vainshtein, Rentgenovskie spektry atomov v molekulakh khimicheskikh soedinenii i v splavakh (X-ray spectra of atoms in molecules of chemical compounds and in alloys), Izv. AN SSSR, L. 1950.
7. A.Z.Zhmudskii, Zhur. eksp. i teor. fiz., 11, 565 (1941).
8. D.I.Blokhintsev, Osnovy kvantovoi mekhaniki (Fundamentals of quantum mechanics), L. 1949.
9. R.M.James, Optical principles of the diffraction of x-rays. (In Russian trans. M. 1950).

ON INTERPRETATION OF DIFFRACTION PATTERNS OF AMORPHOUS MATERIALS BY THE RADIAL DISTRIBUTION METHOD

- T.M.Sereda

The method of radial distribution which permits of obtaining important information on the interatomic spacing directly from experimental data has great value in solving certain structural problems. In the field of electronographic structural analysis the application of this method to the investigation of amorphous materials, however, encounters a number of serious difficulties which have not yet been completely overcome. There has not yet been developed a precision method of Fourier analysis for determining the radial distribution functions for the purpose of studying systems consisting of atoms of several kinds.

There is no single theoretically validated approach to excluding the background in mathematical processing of microphotograms; consequently, related problems (on the correct answer to which the reliability of the results depends) are solved by different investigators in different ways on the basis primarily of success achieved in applying their procedure to individual cases.

The sector procedure of recording electronograms, whose purpose was to provide for automatic solution of the indicated problem, has not yet reached adequate development or general acceptance. Yet in electronographic analysis of the structure of amorphous materials we must frequently deal with very diffused electronograms, objective microphotometry of which does not allow of sufficiently accurate determination of the positions to say nothing of the intensity of the diffraction rings, which are readily discernible in the patterns by eye.

In view of this, there of necessity remains only the visual procedure of studying the diffraction patterns.

The simplified method of radial distribution originally proposed by Brockway and Pauling[1] for interpreting the electrograms of gas and vapor molecules, allows of circumventing the above mentioned difficulties to a considerable extent. The method is applicable both to the case of structures formed by atoms of one kind and in the case of systems consisting of atoms of several kinds. Being based only on the results of measurements of the diameters of the diffraction rings and evaluation of their relative intensities, the method does not necessarily require microphotometry of the patterns and thus can replace precision Fourier analysis in those branches of structural analysis in which application of Fourier analysis is still difficult or impossible.

However, efforts made by the writer[2] and other investigators[3] to utilize the simplified method of radial distribution for studying the structures of certain condensed solids did not yield satisfactory results: curves for D(r) plotted by means of this method failed to elucidate the interatomic distances corresponding to the first, in order of magnitude, radii of the coordination spheres. Nor can the method of Brockway and Pauling give the answer to the very important structural problem of the number of atoms separated by the distances given by the D(r) curve even in the simple case of materials consisting of atoms of one kind. The reason for these shortcomings of the simplified method of radial distribution does not lie in the use of the visual procedure upon which the method is based but is the result of inadequate mathematical development of the theory on which the originators based their method. The present investigation is therefore devoted to elucidating certain additional possibilities of the visual procedure for the purposes of structural analysis.

Let us limit our examination initially to a monoatomic liquid and let us see how one must modify, in view of application of the visual procedure, the expression given for the function $I(\mu)$ (Ref. 4) in the general theory of scattering by an arbitrary accumulation of scattering centers:

$$I_{\text{coh}}(\mu) = N\,|f|^2 \left\{1 - \int_0^\infty 4\pi r^2 \left[\rho_0 - \rho(r)\right] \frac{\sin \mu r}{\mu r}\, d\mu \right\}, \tag{1}$$

where

$$\mu = 4\pi \sin \vartheta / \lambda .$$

Let us proceed from the experience gained in utilizing the method of trial and error which has been extensively and successfully applied in structural analysis of amorphous materials. As diverse applications of the method of trial and error show, the curve I(μ) (Ref. 5) plotted on the basis of the relationship

$$I(\mu) = \frac{I_{\text{mol}}}{I_{\text{at}} + I_{\text{incoh}}} = \sum_{p \neq q}\sum Z_p Z_q \frac{\sin \mu r_{pq}}{\mu r_{pq}} \tag{2}$$

for testing the structural model "conveys a qualitatively correct picture of the maxima discernible by eye on the x-ray patterns" and can, therefore, be regarded as an approximate graphic representation of the pattern.

Having noted that the function I(μ) given by equation (1) determines the full value of the coherent scattering, the atomic component of which is expressed by the first term in $N|f|^2$, we readily find that transformation of expression (1) to the form (2) leads (taking into account the properties of incoherent scattering in equation (2) to the following expression for the function I(μ):

$$I(\mu) = \int_0^\infty 4\pi r^2 \left[\rho(r) - \rho_0\right] \frac{\sin \mu r}{\mu r}\, d\mu, \tag{3}$$

from which, applying the Fourier transform and leaving out the constant factors in view of the fact that selection of the unit for the intensity scale utilized in the visual procedure is arbitrary, we obtain

$$D(r) = \rho(r) - \rho_0 = k \int_0^\infty \mu^2 I \frac{\sin \mu r}{\mu r}\, d\mu. \tag{4}$$

Relationship (4) solves the given problem. The expression obtained for the function D(r) is an integral equation by means of which we specify the function D(r) in connection with the visual procedure of studying diffraction patterns.

The above definition (4) of the function D(r) makes it possible to obtain valuable information on the number of atoms at the distances brought out by the D(r) curve, a possibility which has not been mentioned in investigations devoted to the visual procedure in structural analysis. In the case of rigid dense packing of identical atoms of diameter S_o, the number of atoms separated by one of the possible distances (ms_0), is given by the following expression:

$$N_m = 4\pi r^2 \rho(r) = 4\pi m^2 s_0^2 \rho(r_m). \tag{5}$$

From this for the ordinate of the D(r) curve, according to (4), we have

$$D(r_m) = k'' \frac{N_m}{m^2} - \rho_0. \tag{6}$$

Then equation (6) for the first coordination sphere assumes the form

$$D(r_1) = k'' N_1 - \rho_0. \tag{7}$$

From (6) and (7), dividing term by term and neglecting the small quantity ρ_o (of the order of 10^{-2} atoms A^{-3}) and introducing the notation

$$\frac{D(r_m)}{D(r_1)} = L_m \text{ and } \frac{N_m}{N_1} = n_m,$$

we find the approximate relationship

$$n_m = L_m m^2. \tag{8}$$

If a certain degree of disorder is introduced into the rigidly packed aggregation of atoms, the concentration of possible atomic positions on the spheres of given radii becomes somewhat smeared out and the spectrum of the function $\rho(r)$ becomes continuous. The position of the maxima, as has been shown on the example of the melting of metals by V.I.Danilov, remains almost the same, there is only a slight displacement to the side of larger values of r and the equality (6), characterizing the height of the maxima in the D(r) curve, remains approximately valid in this case too.

In order to deduce the relationship determining the ordinates of the maxima in the D(r) curve in the general case of structures consisting of atoms of several kinds, let us investigate the function D(r) given by equation (4). Invoking (2), the integral equation (4) can be written in the following form:

$$D(r) = k\int_0^\infty \mu^2\left[\sum_{p\neq q}\sum Z_pZ_q\,\frac{\sin \mu r_{pq}}{\mu r_{pq}}\cdot\frac{\sin \mu r}{\mu r}\right]d\mu. \tag{9}$$

Integrating between the limits from 0 to the number +M, which if necessary can in what follows be assumed to tend to +∞, we obtain

$$D(r) = \frac{k}{r}\sum_{p\neq q}\sum \frac{Z_pZ_q}{r_{pq}}\left[\frac{\sin(r-r_{pq})M}{r-r_{pq}} - \frac{\sin(r+r_{pq})M}{r+r_{pq}}\right]. \tag{10}$$

Examining the properties of functions of the type (sin Mx)/x, we see that each term of the sum (10), having an appreciable magnitude at the point $r = r_{pq}$, becomes

$$d_{pq} = \frac{kZ_pZ_qM}{r_{pq}^2}, \tag{11}$$

and, consequently, the ordinate of the D(r) curve at $r = r_{pq}$ will be equal to

$$D(r_{pq}) = k'\Sigma\frac{Z_pZ_q}{r_{pq}^2}. \tag{12}$$

Here the summation is carried out for all the pairs of atoms separated by the distance r_{pq}.

The practical value of structural investigations of materials consisting of atoms of several kinds, whether carried out by means of equation (3) or by the precise method of Fourier analysis, is that these investigations, in addition to yielding the value of the interatomic distances, help select the most appropriate structural model by substantiating or invalidating the tentatively assumed structure.

The values of the coefficient k, necessary for the calculations, are obtained by means of equation (6) and our expressions (8) and (12) by substituting in them the numbers of atoms corresponding to the first coordination sphere for the assumed (tested) structure. Thus the simplified method of radial distribution is used as a trial and error method in solving structural problems.

For complete determination of the function D(r) given by expression (4) one can use one of the appropriate methods of approximate calculation of integrals, if the experimental curve I(μ) has been recorded. In the simplified method of radial distribution its purpose is served by a special computational relationship for D(r) replacing the integral formula for a finite sum, containing one term for each diffraction ring.

The writer in an earlier contribution, devoted to an investigation of the structure of amorphous aluminum oxides[2], showed that the shortcomings of calculations by the simplified method noted at the beginning of the present article can be appreciably attenuated if for calculating the D(r) curve one makes use of the following approximate equality:

$$D(r) = \int_a^b \mu I \frac{\sin \mu r}{\mu r}\, d\mu = k \sum_i \mu_i^2 I_i \frac{\sin \mu_i r}{\mu_i r}, \qquad (13)$$

which is mathematically identical with Chebyshev's expression for approximate calculation of definite integrals within the limits of its applicability ($i < 10$; $i \neq 8$).

Elets Pedagogical Institute

References

1. L.O.Brockway, Usp. fiz. nauk, 17, 173 (1937).
2. T.M.Sereda, Thesis, Inst. of Phys. Chem. of the USSR Ac. of Sci., 1953.
3. L.I.Tatarinova, Thesis, Inst. of Crystallography of the USSR Ac. of Sci., 1956.
4. Z.P.James, Optical principles of the diffraction of x-rays. (In Russian trans. M. 1950).
5. Z.G.Pinsker, Diffraktsiia elektronov (Diffraction of electrons), M.-L., 1942.

ELECTRON DIFFRACTION INVESTIGATION OF OXIDE FILMS FORMING ON MOLTEN ALUMINUM AND ITS ALLOYS

- M.V.Mal'tsev, Iu.D.Chistiakov & M.I.Tsypin

Whereas numerous investigations[1-5] in recent years have been devoted to films and coatings forming on solid metals, relatively little is known regarding the structure and properties of oxide films on liquid metals.[6] Yet data on the subject are of great practical interest in view of the current need for improvement of quality of metals in commercial production.

Nonmetallic inclusions in the form of oxide films forming on the surface of the metal bath are often carried into the ingot or casting thereby impairing its uniformity and lowering the quality of the product.

Determination of the nature of these films is the first step in developing processes for ridding metals of such oxide inclusions and also in understanding the protective and other properties of oxide films. The purpose of the present study was to investigate the structure and other attributes of oxide films forming on molten aluminum and its alloys. We studied the structure of oxide films skimmed at different temperatures from molten 99.99% pure aluminum and from the binary alloys Al-Cu, Al-Mg, Al-Zn, Al-Mn, Al-Si, Al-Fe and certain more complex commercial aluminum alloys: AMts, AMg, AV, D1, D16, D6, D3P, AK5, AK8, V95, AL1, AL3 and AL8 (АМц, АМг, АВ, Д1, Д16, Д6, Д3П, АК5, АК8, В95, АЛ1, АЛ3 and АЛ8).

In contrast to the procedures for obtaining oxide films employed in earlier investigations (evaporating aluminum under vacuum on a quartz plate and its subsequent oxidation) in the present investigation we worked with films skimmed directly off the melt by means of a nichrome wire loop. The film samples were taken at the following temperatures: 660, 670, 680, 690, 700, 800, 900, 1000 and 1100° C. The structure of the films was studied by transmission of electrons on an EM-4 electronograph. Our investigation showed that the oxide film forming on pure aluminum at temperatures below 670-680° has an amorphous structure as is evidenced by the absence of diffraction rings on the electron pattern (Fig. 1,a). At 680-690° there occurs a transition from the amorphous to the crystalline state and distinct lines, corresponding to the cubic lattice of aluminum oxide (γ-Al_2O_3) appear on the electron patterns (Fig. 1, b & c).

In addition there appear on the electronograms the lines of aluminum due to small amounts of the metal carried off in the process of skimming off the film. A distinctive feature of all the electronograms obtained of films skimmed off at temperatures up to 800° is the presence of maxima in the aluminum rings, which are evidence of a definite orientation (texture) of the aluminum grains in the oxide film. The appearance of texture is evidence of a definite generic relationship between the aluminum crystals and the particles of γ-Al_2O_3. When the film is skimmed off at a higher temperature the textured rings associated with aluminum disappear and the electron patterns exhibit only the lines of pure γ-Al_2O_3. In the case of films taken at temperatures above 1100° the γ-Al_2O_3 with a cubic lattice (a = 7.90 A) is transformed into a new modification of the oxide (corundum) with a rhombohedral lattice having a period $\underline{a} = 5.12$ A and $\alpha = 55^\circ 17'$.

An oxide film of γ-Al_2O_3 also forms on the binary alloys of aluminum with copper, zinc, silicon, manganese and iron as well as on the commercial alloy AMts (1.3% Mn, 0.3% Fe and 0.3% Si). In the case of some of these alloys (Al-Cu, Al-Mn, Al-Fe, and Al-Zn) there is a noticeable displacement of the γ-Al_2O_3 line, indicating a change in the period of the crystal lattice, with increasing content of the alloying component. The increase in the period of the lattice is connected with the formation of solid solutions of aluminum oxide with the corresponding metal oxides, solutions of the spinel type: $MeO \cdot Al_2O_3$, where Me is the corresponding metal atom. As in the case of the electronograms of the oxide films skimmed from pure aluminum, lines of metallic aluminum with pronounced texture maxima appear on the electron patterns of the films from the alloys.

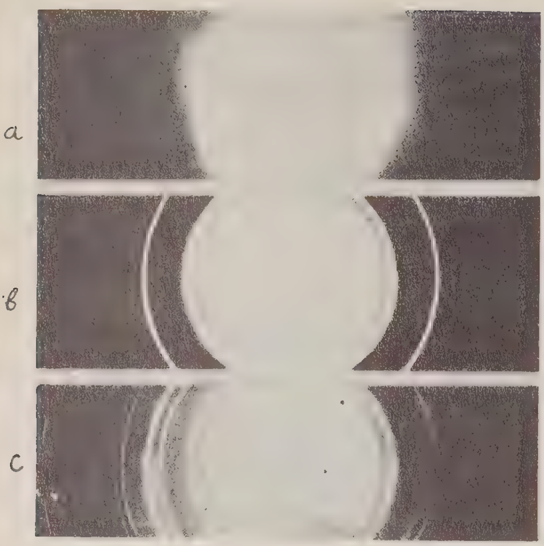

Fig. 1. Electronograms of oxide film skimmed from molten high purity (99.99%) aluminum at a) 670°, b) 700° and c) 760°.

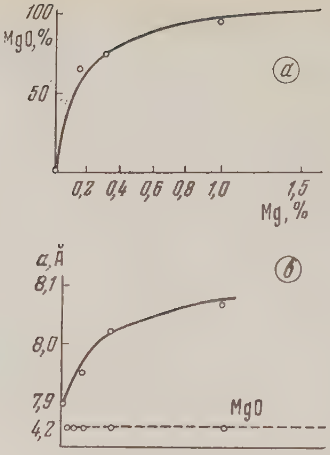

Fig. 2. Dependence of the lattice constant of solid solutions of MgO in γ-Al_2O_3 on the concentration of magnesium: a) MgO content in film, b) variation of the lattice period of spinel.

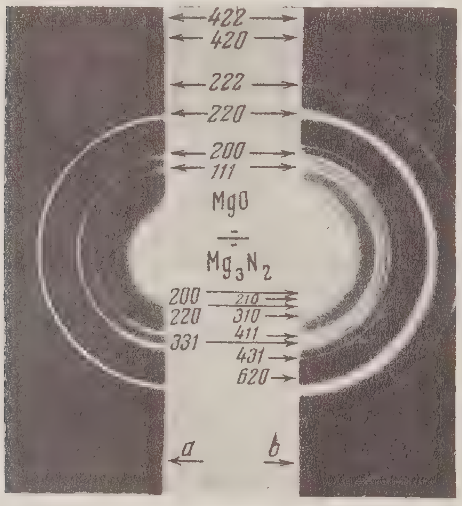
422
420
222
220
200
111
MgO
÷
Mg3N2
200
220
331
210
310
411
431
620
a
b

Fig. 4. Electronograms of oxide films from D16 alloy: a) at beginning of melting, b) after holding.

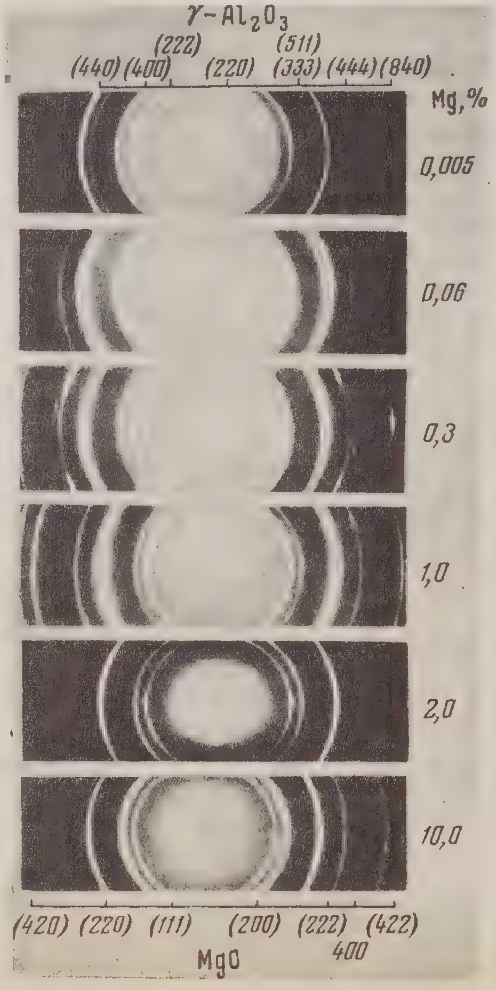
γ-Al2O3
(222) (511)
(440) (400) (220) (333) (444) (840)
Mg,%
0,005
0,06
0,3
1,0
2,0
10,0
(420) (220) (111) (200) (222) (422)
MgO
400

Fig. 3. Electronograms of oxide films from aluminum-magnesium alloys (spinel - $3MgO \cdot Al_2O_3$).

It is interesting to note that in the alloys the transition from the amorphous to the crystalline oxide occurs at lower temperatures than in pure aluminum. Thus, for example, in the case of Al-Mn alloys the oxide film exhibits crystal structure at a temperature of 660° whereas in the case of pure aluminum there are no indications of the crystal oxide at this temperature. A different picture emerges in the case of alloys of aluminum with magnesium: with a magnesium content of up to 0.01-0.02% the oxide film consists of a solid solution of magnesium oxide in γ-Al_2O_3 with a spinel structure. The lattice constant of the solid solution increases with increasing Mg content from 7.90 A (pure γ-Al_2O_3) to 8.09 A (spinel - $MgO \cdot Al_2O_3$) (Fig. 2). At Mg concentrations from 0.01-1% the oxide film consists of a mixture of spinel ($MgO \cdot Al_2O_3$) with magnesium oxide (MgO).

The heterogeneity of the film is clearly evident in the electron patterns shown in Fig. 3; as the amount of magnesium is increased the intensity of the spinel lines goes down, while the intensity of the magnesium oxide lines increases.

At Mg concentrations above 1% the oxide film consists of pure magnesium oxide. Evaluation of the intensity of the magnesium oxide lines showed that the intensity of the diffraction lines on the patterns does not conform with the predictions of theory: theoretically the most intense line should be that with the index (200), whereas on the electron patterns, the most intense is the (220) line. Some investigators[6] explain this divergence between the experimental intensity values and the theoretical ones by the regular orientation of the oxide crystals in the film. To check this we recorded a special series of patterns in which the oxide film was positioned at an oblique angle to the electron beam. Interpretation of the electronograms and calculations showed that the magnesium oxide crystals are oriented with the (111) planes parallel to the plane of the film (and, consequently, parallel to the surface of the melt) and form an axial texture which is responsible for the change in intensity in favor of the (220) lines.

After obtaining this substantiation of the oriented crystallization of the magnesium oxide grains in the film, we carried out a series of special experiments in which, before skimming off the film, the melt was thoroughly stirred so that the surface film was completely broken up and the orientation of the grains disturbed. The electron patterns of such films exhibited a normal distribution of line intensities.

Analogous regularities are observed in the formation of oxide films in case of complex commercial aluminum alloys containing magnesium. In the case of alloys containing up to 1% magnesium (AV, D1, AK5, D3P and D6) the oxide film consists of a mixture of spinel of the $MeO \cdot Al_2O_3$ type (where Me stands for Cu, Mn, Fe, etc) and magnesium oxide. In alloys containing more than 1% Mg (D16, AK8, AK6, V95, AL8, etc.) the film forming on the surface of the melt consists of magnesium oxide.

Additional lines, not associated with magnesium oxide, appear in the electronograms obtained after prolonged standing of some of these alloys (D16 and others) - Fig. 4.

Analysis showed that these lines closely resemble the lines of magnesium nitride (Mg_3N_4), however additional studies are required for a definitive identification. Actually, these lines may be associated with more complex structural formations of the spinel type, of spinel-like complexes formed by the oxides of aluminum, magnesium and other metals present in the alloy, either as components or impurities.

We also investigated the influence of the presence in the melt of a number of metals on the process of formation of the oxide film. Elements chemically more active than aluminum (lithium, beryllium, magnesium, calcium and strontium) exert a considerable influence (even when present in very small amounts) on the process of film formation. For example, beryllium present in the amount of only 0.005% in an aluminum-magnesium alloy yields clear BeO lines on the electron patterns. However, with a magnesium content of 5% in the alloy the principal lines in the patterns are those of magnesium oxide. When the beryllium content of the alloy is increased sufficiently, the magnesium oxide lines entirely disappear and the electron patterns of the oxide films show only the diffraction rings associated with beryllium oxide. An analogous picture is observed with other metals. However, Li_2O, CaO, and SrO form more complex associations with the principal-component metal oxides and interpretation of the resultant patterns becomes difficult.

Further, we established that the oxide film at certain concentrations of a more active metal has a two-phase structure and, depending on the nature of oxides, becomes either harder or, on the contrary, weaker and less uniform, thereby impairing the anticorrosion characteristics of the alloy.

Department of Metallurgy of the
"M.I.Kalinin" Moscow Institute of Nonferrous Metals and Gold

References

1. V.I.Arkharov, Zhur. tech. fiz., 7, 1584 (1937).
2. I.D.Dankov, D.V.Ignatov & N.A.Shishakov, Elektronograficheskoe issledovanie okisnykh i gidrookisnykh plenok na metallakh (Electronographic investigation of oxide and hydroxide films on metals), M.-L. 1953.
3. G.Preston & L.Bircumshau, Phil. Mag., 22, 706 (1935).
4. G.Preston & L.Bircumshau, Phil. Mag., 22, 54 (1936).
5. R.Buching, Phil. Mag., 22, 938 (1936).
6. G.Darbyshire & E.Cooper, Trans. Farad. Soc., 30, 1038 (1934).

MECHANISM OF TEXTURE FORMATION IN LAYERS CONDENSED ON A NEUTRAL BASE

- M.A.Rumsh & T.M.Zimkina

Electron diffraction studies of layers deposited by a molecular beam on a neutral base disclose the presence of a preferred orientation of the microcrystals. Usually there is observed a simple fibered or so-called axial texture. It is characterized by the fact that the crystals forming the layer are arranged with a given crystallographic axis parallel to a single direction; this direction is termed the texture (fiber) axis. It is the practice[1,2] to distinguish between texture with an axis directed along the normal to the mean surface of the layer and texture with an axis inclined to the base. Textures of the first type develop in the layers of substances whose atoms have a high mobility and manifest a strong tendency to crystallization. Even in the period of genesis, when only a monomolecular layer has formed, these substances are capable of giving two-dimensional atomic networks of the two-dimensional crystal nucleii type, distributed, naturally, over the surface of the base. Further increase in the thickness of the layer occurs through growth of the oriented nuclei as a result of which the reciprocal vector r^*_{hkl} in all the crystals of the layer is directed along the normal to the base. Textures of this type might be called genesis textures.

The behavior of substances with a low atomic mobility and a weak tendency to crystallization is entirely different. Substances incapable of two-dimensional crystallization crystallize in a three-dimensional layer, hence the orientation of the growing crystals is not connected with the geometry of the base and, consequently, the polycrystalline layer in the period of genesis is devoid of any preferred orientation. A preferred orientation does sometimes arise in the process of growth of the layer in thickness, but in this case the texture axis is related to the direction of the molecular stream from which the particles are deposited.

Certain definite views have been expressed regarding the mechanism of formation of textures of this type which might appropriately be called textures of growth. Burgers and Dippel[1] and Thomson[3] associate the origin of such textures with the ability of the material to migrate along the surface of the crystal in the direction of the crystal apices and edges and the tendency of the substance deposited on the crystal to become thick at the apices and edges. According to these investigators, newly arriving particles of the material are not assimilated by the natural faces but migrate to the corners and edges where they become attached. As a result of this alimentation of the crystals, these grow along the flat faces, with the rate of growth being proportional to the amount of particles or vapor incident on the face. Since the natural faces of the crystals that happen to be oriented normal to the direction of the incident molecular beam receive a larger amount of material compared with those at an angle to the beam, the crystals having faces normal to the beam grow at a faster rate. Expanding along the flat faces, these crystals with faces normal to the molecular beam shield or cover the crystals having other orientations and thus create conditions favoring their further development. As a result there develops a predominant orientation in the growing layer, that is, a preferred orientation with the natural faces normal to the molecular beam and the reciprocal vector parallel to the beam. The profile of the layer formed in this manner should have the appearance shown in Fig. 1.

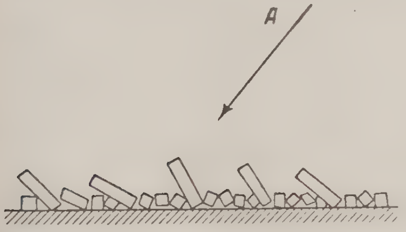

Fig. 1. Profile of a layer formed through the agency of the mechanism suggested by Burgers. Arrow A indicates the direction of the molecular beam.

Despite the simplicity and plausibility of the described mechanism, we cannot accept it for a number of reasons.

1. With the above mechanism, in the case of a molecular beam normal to the base, simultaneously with development of texture there should occur a leveling of the surface. As a result of this leveling a number of submicroscopic projections should decrease and electronographic investigation with a glancing electron beam should become increasingly difficult. Actually the contrary is the case: we have repeatedly observed for PbS that as the thickness of the layer increases electronograms obtained with a glancing beam become increasingly sharp and clear. The increase in the intensity of coherent scattering and a decrease in incoherent scattering indicate that in the process of growth, instead of becoming flatter and smoother, the surface is enriched with submicroscopic projections.

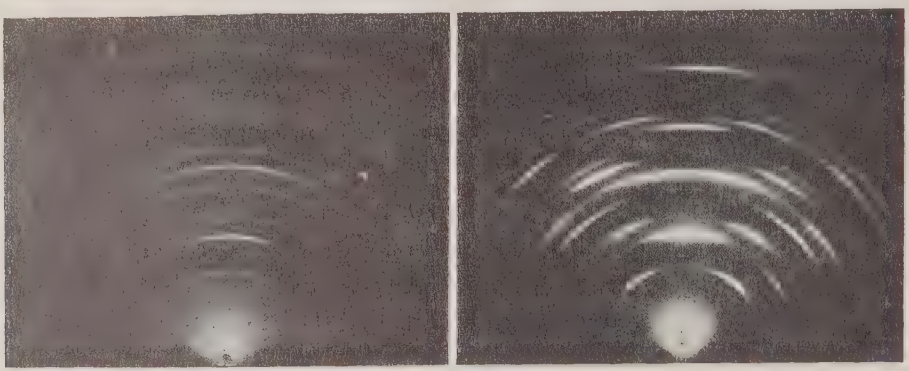
a b

Fig. 2. Electronograms of a layer of PbS taken at the beginning (a) and end (b) of deposition.

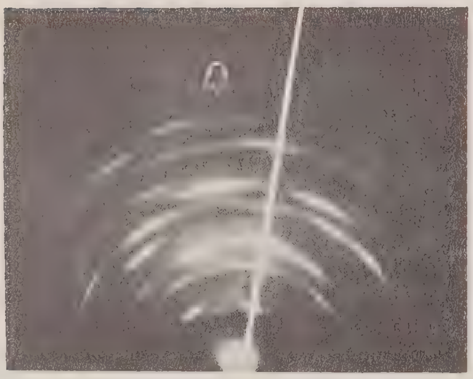
Fig. 3. Electronogram of a layer of PbS deposited by an oblique molecular beam.

Fig. 2 shows two electron diffraction patterns of the same specimen of PbS taken at the beginning and at the end of molecular deposition.

2. Electron diffraction data indicate that there is appreciable scattering by growth textures. Accordingly we must imagine the surface to be studded with lamella (into which the favored crystals have grown) inclined at slightly different angles to the surface (Fig. 1). Inasmuch as the coherent penetration of electrons is very small, the diffraction pattern in the electronograms is produced mainly by the salient parts of the surface, or in the case of the profile shown in Fig. 1, by the more erect lamella, the reciprocal vector r^{*}_{hkl} of which is close to the plane of the mean surface of the layer. This is why the electron diffraction patterns present an incomplete statistical record of the directions of preferred orientation. Analysis of the patterns should lead to the conclusion that the texture axis is at a smaller angle to the surface than the molecular beam, i.e., closer than it would appear to be if the directional statistics were complete. Actually, however, all the electronographic data$^{1-3}$ indicate the opposite. The texture axis as determined from electron patterns lies in the angle between the molecular beam and the normal to the surface; moreover, the greater the angle between the molecular beam and the normal to the surface, the closer the texture axis approaches the direction of the normal.

Fig. 3 shows an electron pattern of a layer of PbS deposited by a molecular beam incident at an angle of 45° to the base. In this case the angle between the texture axis in the pattern and the normal is only 15° (Ref. 4).

3. The hypothesis regarding the growth or expansion of the crystals along the flat faces is based on the assumption of migration of new material brought by the beam towards the apices and edges and its fixation there. However, such migration and fixation could occur only before the apices and edges are fully formed, only while there are rapidly growing faces at these points. However, when rapidly growing faces are absent, fixation of new particles at the apices and edges is energetically unadvantageous and there can be no migration towards them.

In view of the above considerations we feel that the mechanism suggested by Burgers et al is implausible. We propose a different mechanism for the formation of texture, a mechanism based on the well-known fact that not all the matter brought by the molecular beam is assimilated by the surface. It is known that a certain percent of the molecular beam material, characterized by the coefficient of accomodation, is reflected by the surface. The value of the accomodation coefficient depends on the properties and temperature of the surface. It is natural to expect, therefore, that the accomodation coefficient on different faces of the crystals will be different, that the coefficient will be greater on faces perpendicular to the beam and characterized by a relatively rapid rate of growth, and smaller on faces at an angle to the beam and characterized by a relatively slow rate of growth. Thus we assume that the preferred orientation of the microcrystals is produced as a result of the favored development of those crystals whose rapidly growing faces proved to be oriented initially perpendicular or nearly perpendicular to the incident molecular stream. Why the rapidly growing faces do not disappear, turn into a rib or apex is immaterial to the argument.

We suggest, therefore, that growth texture is generated by virtue of a dendritic development of selected orientations and results in a surface characterized by the profile shown in Fig. 4.

In the light of this hypothesis regarding the structure of the surface, the experimental facts noted under 1 and 2 above become understandable. The growth of the layer enriches the surface with submicroscopic projections, as a result of which coherent scattering in investigation with a grazing electron beam increases relative to incoherent scattering. The fact that the habit of the microcrystals is elongated in the direction of the texture axis explains why, in the presence of scattering, analysis of the electronograms leads to a systematic error as regards the orientation of the texture axis, i.e., to an apparent veering of the texture axis from the direction of the molecular beam towards the normal.

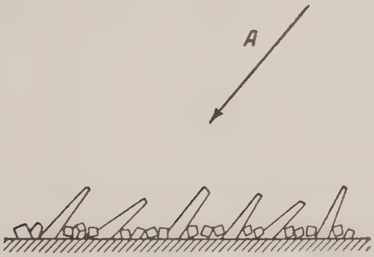

Fig. 4. Profile of a layer formed through the operation of the suggested dendritic mechanism. Arrow A indicates direction of molecular stream.

The texture axis in the layers of PbS according to x-ray diffraction data coincides with the direction of the molecular beam while from electronographic data the axis appears to be deflected to the side of the normal to the surface. The suggested mechanism of the development of texture is supported by our experimental results and those obtained by Berlaga et al.[5]

In conclusion we desire to thank A.A.Lebedev for his constant attention and discussion of the results.

"A.A.Zhdanov" Leningrad State University

References

1. W.G.Burgers & G.Dippel, Physica, 1, 549 (1934).
2. H.E.Wilman, Acta crystallogr., 5, 782 (1952).
3. G.P.Thomson & W.Cochrane, Theory and Practice of Electron Diffraction, p. 162, London, 1939.
4. M.A.Rumsh & T.M.Zimkina, Vestnik LGU (Leningrad State University Review) No. 4, 33, (1956).
5. R.Ia.Berlaga et al, Zhur. tekh. fiz., 25, 785 (1955).

ELECTRONOGRAPHIC INVESTIGATION OF THE NATURE OF PASSIVE FILMS

_ V.P.Batrakov & I.A.Ponizovskiia

Despite its great practical and theoretical importance the nature of passivity of metals and alloys, i.e., their transition under certain oxidizing conditions from a state of low chemical stability to a chemically unreactive state, has not yet been fully explored and no consistent theory characterizing the mechanism of the effect exists. Hence we felt it would be of interest to investigate by electron diffraction the structure of passive films forming on a number of commercially important metals and alloys.

Specifically we investigated the classical cases of passivity of the carbon steels St.10, St.45 and U8 (У8), the low alloy steel 30KhGSA (30ХГСА), a steel with 5% Cr, and the stainless steels EI457, EI268, EI401 and 1Kh18N9T (ЭИ457, ЭИ268, ЭИ401 & 1Х18Н9Т) as well as of pure commercial aluminum in solutions of HNO_3, $Na_2Cr_2O_7$ and $K_2Cr_2O_7$. It has been established in recent investigations[1-3] of corrosion of carbon, low-alloy and stainless steels in HNO_3 that the passive state is induced in the region of medium concentrations (45-60%); further increase in the concentration of the acid leads to an increase in the rate of corrosion, the most pronounced rise being observed at concentrations above 75% as the result of overpassivation. The curve characterizing the dependence of the rate of corrosion on the concentration of HNO_3 for steel at room temperature is shown in Fig. 1, a (Ref. 2).

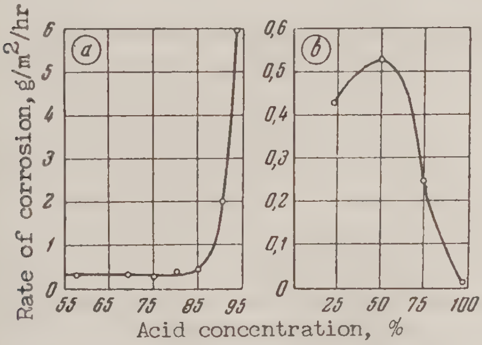

Fig. 1. Dependence of the rate of corrosion on the HNO_3 concentration for: a) 30 KhGSA steel, b) aluminum.

Fig. 1, b shows the rate of corrosion of aluminum determined in the present investigation. In contrast to steels, aluminum is passivated in concentrated solutions of HNO_3 and corrodes intensively in solutions of medium concentration. In view of this we studied the action of HNO_3 at medium and high concentrations.

We used specimens measuring 20 x 6 mm cut from sheet metal of different thicknesses and with surfaces worked in different ways. The specimens were kept for different lengths of time in the passivating solutions at room temperature or at 60° for the purpose of more intense oxidation. In order to remove all traces of acid from the specimens and prevent oxidation during their transfer to the electronograph we used the following procedure, which electronographic tests showed to be effective: washing with distilled water, three-fold washing in alcohol and drying with ash-free filter paper. In all the exposure to air of the specimens before registration of the electron diffraction patterns did not exceed 2 min. The electronograms of all the specimens were recorded by the method of reflection in an EM-4 electronograph with the exception of the stainless steels specimens, the patterns for which were obtained on a horizontal electronograph in the Institute of Crystallography of the USSR Academy of Sciences.

Results

1. Table 1 lists the determined structures of the surface layers of the carbon and alloy steels in the initial sandblasted state and after 10 hour immersion at room temperature in medium and high concentration HNO_3 solutions. There is some ferrite present on the surface of all the steels but in the case of chrome steels it was not detected electronographically in view of the closeness of the

Table 1

Structure of the surface layers of the investigated steels in the initial state and after 10 days immersion in HNO_3 solutions of different concentration at room temperature

Type of steel	Condition of surface		
	Initial state (sandblasted)	After immersion for 10 days in HNO_3	
		Medium concentration	High concentration
St.10	α-Fe & traces γ-Fe_2O_3	α-Fe & traces γ-Fe_2O_3	Amorphous structure
St.45	same	same	γ-Fe_2O_3 & γ-$Fe_2O_3 \cdot H_2O$ lines veiled
U8	same	same	same
30KhGSA	same	α-Fe, small amounts of γ-Fe_2O_3 and γ-$Fe_2O_3 \cdot H_2O$	Amorphous structure
12Kh5MA	same	Oxide and hydroxide phases	Hydroxide and oxide phases; veiled
1Kh18N9T	α-Fe	same	Oxide and hydroxide phases

Table 2

Structure of the surface layers of stainless steels after grinding and passivation for two hours in $K_2Cr_2O_7$ at 60°.

Type of steel	Heat treatment	Micro-structure	Structure of the surface layer after:	
			grinding	passivation in 3% solution of $K_2Cr_2O_7$ solution.
EI457	Normalization	Ferrite	α-Fe and traces of oxide phase with spinel structure	α-Fe and traces of oxide phase with spinel structure
EI268 (17% Cr, 2% Ni)	Quenching from 1050° in oil	Martensitic ferrite	same	same
EI401 (18% Cr, 9% Ni, 2% Mo)	Quenching in 1100° in water	Austenite	α-Fe and an appreciable amount of oxide phase with spinel structure	same
1Kh18N9T	same	same	α-Fe	same

atomic radii of Fe and Cr. The presence of ferrite on the sandblasted surface of the austenitic steel 1Kh18N9T and on the ground surfaces of steel 1Kh18N9T and EI401 (table 2) is explained by the phase transformation which occurs in the surface layer under the influence of working. In the case of the carbon steels there is no noticeable increase in the amount of the oxide phase on the surface (as compared to the initial state) after passivation in HNO_3 solutions of medium concentration, which indicates that the passivating mechanism is adsorptive. At high acid concentrations the complete absence of diffraction reflections or strong veiling (fogging) of the γ-Fe_2O_3 and γ-$Fe_2O_3 \cdot H_2O$ lines is evidence of the formation of an amorphous layer giving no protection. In the case of the 30KhGSA steel there is only a small amount of oxide phase formed in solutions of medium concentration which is also indicative of the adsorptive character of the passivity, just as in the carbon steels. In concentrated solutions of HNO_3 there is formed on the surface of this steel a thick, clearly discernible layer consisting of the amorphous product of corrosion, which is much thicker than that commonly observed on carbon steels.

There is observed on the surface of the alloy steels at all acid concentrations an oxide phase with spinel structure and a hydroxide phase with a rhombic lattice; the alloying elements undoubtedly participate in the formation of these phases.

The presence of an oxide phase film after passivation in medium concentration acid solutions is connected with the intense oxidation of the surface due to the presence in the steels of a large amount of chromium and the influence of concentrated HNO_3. However, this does not conflict with the hypothesis advanced by Akimov and Batrakov[4] regarding the presence of a phase-adsorptive film on stainless steels since it appears to be impossible to detect the adsorptive effect by electron diffraction under the given conditions.

On steel containing 5% Cr, upon passivation in a concentrated solution, there is still formed an amorphous film, which is not observed on steel with 18% Cr held for the same length of time in the passivating solution.

The results of our investigation of aluminum are listed in Table 3. In contrast to the case of steels, passivation of Al in HNO_3 solutions of high concentration occurs as the result of formation of a protective amorphous film and the quasi-insoluble compound $Al(NO_3)_3$, which is largely removed in washing. As the concentration of acid is reduced to 50%, the solution of the amorphous film and $Al(NO_3)_3$ is increased, corrosion is intensified and occurs even in the presence of a surface film. No discernible film is formed in a 23% solution of HNO_3.

Table 3

Structure of the surface layers of aluminum

In initial state (as delivered)	After immersion for 10 days in HNO_3 solutions		
	23%	50%	75% and higher
Al	Al	Amorphous structure	Two weak greatly veiled Al lines (amorphous structure)

2. In order to determine the influence of preliminary treatment on the structure of passive films we felt it would be of interest to investigate the process of formation of the passive layer on etched and, consequently, more active surfaces. To this end we investigated pickled carbon steels after passivation for a period of 10 min in 60% HNO_3 and 10 min and 24 hours in 0.1%, 10% and 60% aqueous solutions of $Na_2Cr_2O_7$. The results are listed in Table 4. After pickling in 10% hydrochloric acid the structure of the surface of all the

Table 4

Structure of the surface layers of St.10, St.45 and U8 steels after pickling in HCl solution and passivation in solutions of HNO_3 and $Na_2Cr_2O_7$ of different concentrations at room temperature.

Steel	Pickling in 10% HCl for 1 hour	Passivation in 60% HNO_3 for 10 min	Passivation on $Na_2Cr_2O_7$ solution					
			0.1%		10%		60%	
			10 min	24 hrs	10 min	24 hrs	10 min	24 hrs
St.10	α-Fe	γ-Fe_2O_3 and γ-$Fe_2O_3 \cdot H_2O$	α-Fe and two γ-Fe_2O_3 lines	α-Fe veiled	α-Fe and γ-Fe_2O_3	α-Fe veiled	α-Fe and two γ-Fe_2O_3 lines	α-Fe veiled
St.45	α-Fe & traces γ-Fe_2O_3	γ-Fe_2O_3& γ-$Fe_2O_3 \cdot H_2O$	α-Fe & traces γ-Fe_2O_3 slightly veiled	α-Fe & γ-Fe_2O_3 veiled	α-Fe slightly veiled	α-Fe & some γ-Fe_2O_3 and γ-$Fe_2O_3 \cdot H_2O$	α-Fe & some γ-Fe_2O_3 and γ-$Fe_2O_3 \cdot H_2O$	α-Fe veiled
U8	α-Fe & γ-Fe_2O_3	γ-Fe_2O_3& γ-$Fe_2O_3 \cdot H_2O$ veiled	α-Fe & traces γ-Fe_2O_3 slightly veiled	Two α-Fe lines			α-Fe & some γ-$Fe_2O_3 \cdot H_2O$	Two α-Fe lines
				Strongly veiled				

steels consisted mainly of α-Fe with a small amount of γ-Fe_2O_3, which increased with increasing carbon content of the steel. Passivation of the pickled steels in 60% HNO_3, in contrast to what has been noted above for sand-blasted surfaces, occurs as a result of formation on all the steels of a phase film consisting of γ-Fe_2O_3 and γ-$Fe_2O_3 \cdot H_2O$; this is explained by the more intense interaction of the steel surface with the oxidizing agent. After passivation in $Na_2Cr_2O_7$ the structure of the surface layer, as in the case of the sand-blasted surface, consists mainly of α-Fe. Preliminary etching in this case does not have an activating effect and the passivation mechanism is mainly adsorptive. Increasing the time of passivation at all concentrations of the dichromate leads to the formation of thin amorphous films which are protective. The thickness of these films increases with the carbon content in the steel.

3. The results of our investigation of the stainless steels EI457, EI268, EI401 and 1Kh18N9T passivated (after preliminary polishing with fine emery paper) in a 3% aqueous solution of $K_2Cr_2O_7$ for a period of 2 hours at 60° are shown in Table 2. On the 1Kh18N9T steel, which in the ground (polished) state has a ferrite structure, after passivation there appeared an oxide phase having a spinel structure which is evidence of a phase-adsorptive mechanism of passivation. An oxide phase is also observed, together with ferrite, on the other three stainless steels both after passivation and immediately after grinding which indicates that the passivation mechanism is primarily adsorptive under the given conditions.

References

1. V.P.Batrakov, Korroziia konstruktsionnykh materialov v agressivnykh sredakh (Corrosion of structural materials in agressive media), M. 1952.
2. V.P.Batrakov & G.V.Akimov, Doklady AN SSSR, 89, 321 (1953).
3. V.P.Batrakov, Doklady AN SSSR, 99, 97 (1954).
4. G.V.Akimov & V.P.Batrakov, Doklady AN SSSR, 45, 129 (1944).

ELECTRONOGRAPHIC INVESTIGATION BY MEANS OF AN EM-3 ELECTRON MICROSCOPE

- V.N.Vertsner

Electron diffraction studies can yield valuable supplementary information regarding the structure of materials being investigated by means of an electron microscope. In a number of cases such studies make it possible to amplify the data regarding the external shape of crystals, their size and orientation with information on the crystallographic structure. The electronographic procedure is applicable to the study of materials transparent to electrons and metallographic microsections as well as to a number of massive objects studied electron-microscopically by the replica procedure.

Any electron microscope can be utilized for electronographic studies. However, in the absence of special accessories only diffraction patterns formed by transmitted electrons can be registered. The electronograms obtained in this manner are of poor quality, have a limited number of reflections and in most cases are unsuitable for calculations. Yet if appropriate attachments are available, the electron microscope with its excellent optics and highly stable electric supply can be utilized as a fully satisfactory electronograph.

In view of the limited space available for attachments in the EM-3 electron microscope[1-3] we found it impossible to make a single universal attachment for both transmission and reflection electron patterns. Consequently, we developed two attachments: one for transmitted[4] and the other for reflected electron rays. (Ref. 5 & 6)

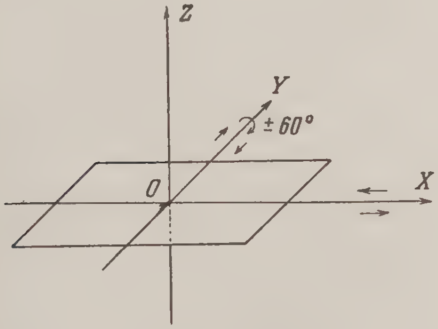

Fig. 1. Specimen displacements in transmission experiments.

The diagram of Fig. 1 shows the various displacements of the specimen provided for the case of investigation by transmitted rays. The direction of the electron beam is parallel to the OZ axis. The specimen is mounted in the plane XOY. For bringing any point of the specimen under the electron beam there is provision for translation along the OX and OY axes, while for investigating texture there is provision for rotation about the OY axis through angles up to ±60°.

The transmission attachment is pictured in Fig. 2. The specimens of the same type as those used for electron microscope studies are prepared on screen supports 2 mm in diameter (100 mesh per mm^2) and placed in the six nests of the stage 1; they are retained by the cover plate 2 which has appropriate apertures opposite each nest. Knobs 3, 4 and 5 permit translating and tilting the specimen and bringing the successive specimens into position under the beam. The knobs are equipped with appropriate scales and indexes.

The motions available for reflection investigations are shown in Fig. 3. The electron beam is directed parallel to the OZ axis. Let us assume that initially the specimen is in the plane ZOY. To bring it into or out of the beam the specimen is displaced along the OZ axis normal to its plane. The desired angle $\Delta\varphi$ of incidence of the beam is set by rotating the specimen about the OY axis (usually $\Delta\varphi$ equals a few degrees). The specimen, set at the desired angle $\Delta\varphi$, can be rotated (the full 360°) about the OX or OX' axis by which means one can realize the requisite orientation of the structural elements relative to the electron beam. By means of this rotation together with translation along the OY axis one can bring any point of the specimen under the beam. The angle at which the beam strikes the specimen remains unchanged in the process of rotation about the OX axis and translation along the OY axis.

A photograph of the reflection attachment is reproduced in Fig. 4. The

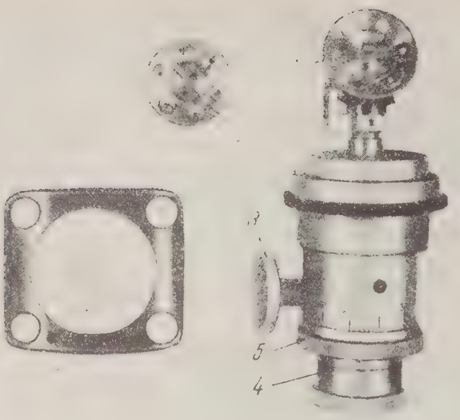

Fig. 2. Attachment for electron transmission studies: 1) stage, 2) cover plate with apertures, 3,4,& 5) knobs for displacement, tilting and indexing of specimens.

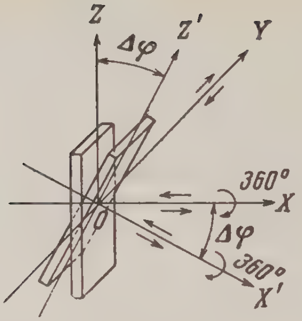

Fig. 3. Specimen motions in reflections experiments: Δφ - angle of incident beam relative to surface of the specimen.

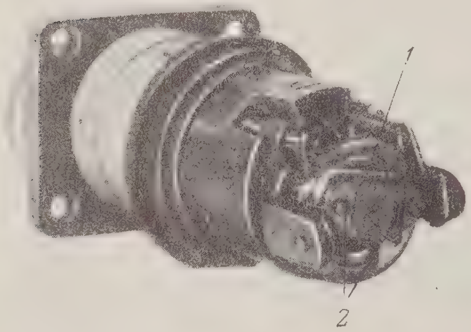

Fig. 4. Stage of reflection attachment: 1) stage for attaching specimens, 2) wedge-shaped clamps.

specimens measuring 10 x 15 mm and having a thickness from 0.5 mm to several millimeters, are attached to the stage 1 by means of two wedge-shaped clamps 2. The knobs of the attachment have appropriate scales indicating the rotation (in degrees) and displacement from center (in millimeters) of the specimen. A vacuum seal on the rods displacing the stage is provided for by double rubber gaskets coated with D-1 grease containing 20% graphite.

For use the diffraction attachments are mounted in front of the projection lens of the microscope in place of the mirror intended for observing the intermediate image. The objective holder and polepieces of the projection lens are removed. The optical components of the EM-3 microscope are activated as shown in the diagram of Fig. 5. In the arrangement a, the objective forms an image of the "neck" (smallest cross section) of the electron beam on the end screen; the condensor and projection lens are disconnected. In using the arrangement b, a reduced image of the electron source is obtained by means of the condenser lens and this turn is thrown by the objective lens on the final screen. At the same time the operating regimes of the microscope lenses are modified: the objective lens is operated at a reduced current (7-12 ma); this is accomplished by reconnecting the lens windings according to the diffraction hook-up provided for in the instrument. The condenser lens is connected to operate at maximum current.

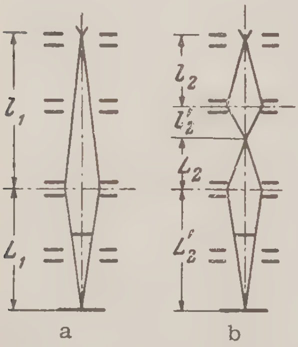

Fig. 5. Alternate arrangements for actuation of electron microscope optics for electron diffraction investigations.

As regards resolution ($\Delta d/d$), the EM-3 electron microscope operated as an electronograph is scarcely inferior to regular electronographs, in particular, to our domestic EM-4 electronograph (according to calculation for d = 1 A at 50 kv accelerating potential, $\Delta d/d$ is of the order of $1.5\cdot10^{-3}$; in practice, the attainable resolution is somewhat lower). Among the shortcomings of the EM-3 electron microscope used for electron diffraction studies is the somewhat low linear dispersion ($\Delta R/\Delta d \approx 21.6$ mm/A) due to the short specimen-to-photographic plate distance (350 mm) and the relatively small size of the obtainable patterns - 4.5 x 4.5 cm. Although the low dispersion does somewhat hamper measurements on the diffraction patterns, in view of the high resolution of the EM-3 this does not significantly limit the scope of diffraction studies with the instrument. In general, in electronographic investigations on different electronic microscopes, the specimens are placed either in front of the objective or in front of the projection lens. In either case the polepieces of the projection lens are removed and in some cases the polepieces of the objective as well. In contrast to the case in regular electronographs, in electron microscopes the diffracted electrons traverse weak magnetic fields due to the residual magnetism of the magnetic circuits of the objective and projection lenses. Deflection of the electron paths in these fields results in some displacement of the reflection spots on the patterns. Although these displacements are minor they still make it impossible to carry out accurate structural calculations.

The distortion of the diffraction pattern proves to be non-uniform over the field and varies depending on the magnitude of the residual field and the distance of the diffracted rays from the optical axis of the weak magnetic lens formed by this field. The effect is manifest even with precise centering of the electron beam relative to this lens. When the centering is off the annular reflections are distorted and become oval.

In order to eliminate the weak residual fields in the EM-3 electron microscope, we utilized a magnetic shield of Armco iron (one can also use a Permalloy shield). The shield was made in the form of a hollow cylinder with 4 mm thick walls. The length and outside diameter of the cylinder were determined by the dimensions of the projection lens polepieces. A brass diaphragm with a 5 mm diameter opening was mounted in the upper part of the magnetic shield.

Use of the magnetic shield made it possible to obtain undistorted electron diffraction patterns. For example, in the case of lead sulfide the error in determining the interplanar spacings was of the order of 2-3% in the absence of a shield and only about 0.5% with the shield in place.

Hence in using an electron microscope for electronographic investigations it is expedient to provide magnetic shielding along the path of the diffracted rays at all points of discontinuity of the magnetic circuit of the lenses. Without such shielding only qualitative studies can be made.

Furthermore difficulties often arise in analysis of reflection patterns since here in addition there is superimposed a certain inaccuracy in determining the center of the primary beam. In working with the EM-3 electron microscope this source of error can be virtually eliminated provided the optics of the microscope are focused so that the cross section of the primary beam is minimal at the final screen. In this case the "load" on the photographic plate at this point is so high that the emulsion layer is damaged at the point of incidence. The center of damage is readily identified and may be considered to be the center of the diffraction rings.

References

1. Elektronnaia mikroskopiia (Electron microscopy). Ed. by A.A.Lebedeva,M.-L.1954.
2. V.N.Vertsner, Zavod. labor. 13, 1364 (1947).
3. V.N.Vertsner, in "Sovremennye metody i tekhnika morfologicheskikh ussledovanii"(Modern methods and techniques of morphological investigations),L.1955.
4. V.N.Vertsner, Zavod. labor., 18, 1481 (1952).
5. V.N.Vertsner & N.G.Zandin, Zavod. labor., 20, 741 (1954).
6. V.N.Vertsner, in "Voprocy mikroskopii"(Problems of microscopy),M.-L.1956.

THE SECTOR METHOD IN ELECTRONOGRAPHY

- G.O.Bagdyk'iants

The intensity distribution of fast electrons scattered at different angles to the primary beam by an aggregation of atoms is characterized by the surposition of a background monotonously decreasing with increasing scattering angle; this background is due to independent scattering (coherent and incoherent) from individual atoms and to molecular scattering. The latter consists of a series of interference maxima and minima, deriving from functions of the form (sin x)/x, due to the interference of electronic waves scattered by atoms at identical distances.

Where determination of the molecular structure is concerned.only the latter form of scattering need be considered. However, as microphotometry of electron diffraction patterns of noncrystalline substances shows, molecular scattering is frequently masked by atomic scattering and appears as hardly discernible areas instead of as sharp maxima.

In order to eliminate the background due to atomic scattering, in investigating vitreous substances we utilized the method of equalizing the background by means of a special-cutout sector rapidly rotated in the path of the electrons in front of the photographic plate. Hitherto this method, known as the "sector method", has been used only for investigating gaseous substances.[1,2]

The contour of the sector cutout must be designed so that the values of the aperture angles φ_r for every angular zone of radius r will be such that the intensities of atomic scattering after passing through the different parts of the rotating sector will be equal. For consistent calculations of the sector aperture profile one must know the atomic scattering intensity distribution for the material in question.

For the intensity of incoherent scattering in the case when each electron in passing through the substance undergoes not more than one inelastic collision the following equation holds

$$I \approx \frac{1}{\mu^4}\ (\mu = 4\pi \sin \vartheta / \lambda).$$

Obviously where this expression is applicable,the angle of the cutout in the sector must be proportional to μ.[4] However, this expression is valid only in the case of passage of the electrons through a stream of gas at a pressure not exceeding a few millimeters Hg.

Commonly in investigations of scattering by gases the angle of opening of the sector cutout is taken proportional to μ^n, where n is taken equal to some value between 1 and 4. Sometimes the value of n is varied for different values of the scattering angle.

In the case of scattering by solids, design of the sector becomes more complicated, since even with a specimen thickness of 0.01 μ each electron undergoes several inelastic collisions and consequently the intensity of incoherent scattering varies more slowly than $1/\mu^4$. In view of this, we propose the following procedure for calculating the aperture profile; this method does not require knowing the intensity distribution and automatically excludes all forms of scattering resulting from surposition of an inhomogeneous background on the molecular scattering.

A series of microphotograms under identical experimental conditions,but with different exposures,is obtained from the substance for which the sector is being prepared. Then a straight line parallel to a base line,corresponding to equal blackenings is drawn through the microphotograms (see Fig. 1). From the points of intersection of this line with the background line of each microphotogram we can establish the ratio between the exposures in the different angular zones of the electronograms necessary for obtaining identical background densities and

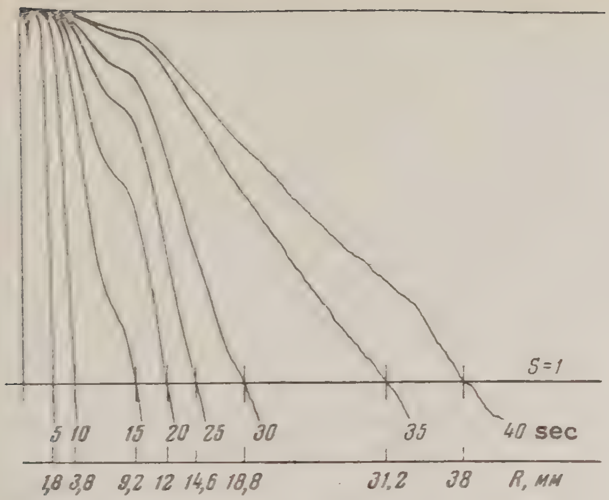

Fig. 1. Series of microphotograms for calculating the shape of the sector for molten silicon dioxide.

determine in this way the angle of opening of the sector for each value of its radius. In Fig. 1 we have drawn a line corresponding to a constant blackening density S = 1. The electronograms of the material obtained with the sector also had a background density close to unity.

In view of the fact that the intensity of scattering near the central ray is many times greater than towards the edges of the electronograms, replacement of the condition of equal intensity by the condition of equal blackening for the different zones may lead to the situation where on the electronograms obtained by means of a sector designed as described above the background line will somewhat deviate from the line parallel to the base line. In such cases corrections for the values of the angle of opening can be computed by means of the equality

$$\varphi' r = \frac{S'}{S_r} \varphi_r$$

where φ'_r and φ_r are the corrected and initial values of the angle of opening of the sector, respectively, S' is the corrected constant value of the density and S_r is the experimentally obtained density value with the initial design of the sector. The conformity of the sector to the calculated profile is checked by projecting an enlarged image (5 X) on the designed templet or drawing.

In order to detect invisible defects (nicks or projections) on the edges of the sector, which can give rise to the appearance of false rings due to greater or lesser blackening of the emulsion, we microphotometered photographic plates exposed through the rotating sector to an electron beam of uniform intensity over its entire cross-section.

The mechanism for rotating the sector, in our set-up, is enclosed in a cylindrical chamber (Fig. 2), mounted between the specimen chamber and the photographic camera of the EM-4 electronograph.[3] The sector is mounted on a special bearing which is rotated at high speed (over 600 rpm) by a motor mounted inside the vacuum section of the instrument. The center of the bearing is positioned to coincide exactly with the axis of the electron beam. The thin sheet metal sector is centered precisely (to within 0.03 mm) in a rigid angular frame fitting over the bearing. The centering of both the bearing and frame is accomplished by means of a microscope (magnification 150 X). By virtue of this sectors can readily be replaced (without further adjustment) through a special hatch in the sidewall of the chamber.

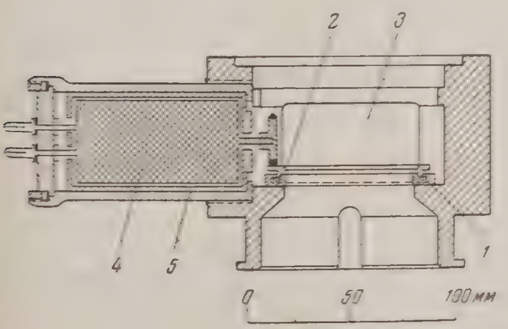

Fig. 2. Chamber housing sector mechanism: 1) bearing, 2) bearing seat, 3) axis hatch for changing sector, 4) motor, 5) screen.

To prevent excessive irradiation of the central portion of the photographic

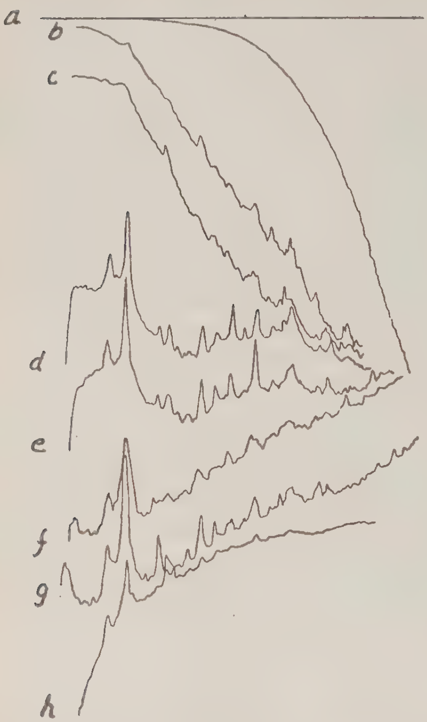

Fig. 3. Influence of sample thickness on the equalization of the background due to atomic scattering by means of the sector: a) scattering by residual air during prolonged exposures, b-h) scattering by finely dispersed specimens of crystalline quartz of increasing thickness.

plate by the unscattered electrons of the beam a cylindrical trap is provided at center of the sector. An opening in the bottom of the trap serves for checking the focusing with reference to the central beam (with the sector stationary). When the sector is rotating the opening is closed by a shutter actuated by centrifugal force.

Tests with solids showed that the requisite shape of the sector depends not only on the chemical composition of the specimen and the accelerating potential (as was initially assumed) but also on the thickness of the specimen. Fig. 3 shows a series of microphotograms obtained for finely dispersed crystalline quartz samples having different thicknesses (curve a was obtained from a photograph exposed for a prolonged time in the absence of a sample; the indicated scattering is due to residual gas in the instrument). It will be seen that for thin samples the equalization of the background is fairly satisfactory (curves b and c). As the thickness of the specimen is increased the equalization deteriorates and finally at a considerable thickness there is excessive "cutting off" of the background at small angles. This is explained by the fact that with very thin specimens electron scattering by the gas particles remaining in the electronograph has a relatively appreciable effect, while with a thick specimen incoherent scattering at large angles begins to play the dominant role.

Reduction of the intensity of atomic scattering by means of the rotating sector is accompanied by a proportional decrease in the interference maxima associated with the structure of the material: the central interferences are weakened to a greater degree, the peripheral ones to a lesser degree.

In view of this secondary effect, which has hitherto not received attention in investigations of gases, the following modifications in the rotating sector procedure are essential.

1. In order to obtain the true scattering intensity distribution associated with a given structure one must introduce appropriate scattering correction factors inversely proportional to the angles of opening of the sector.

2. All forms of scattering that are susceptible to reduction (scattering by residual air, incoherent scattering, etc.) should be minimized.

3. The thickness of the investigated layers (specimen) and the thickness of the layer used in designing the sector should not differ greatly.

In view of the fact that there is no great difference between the density (blackening) in the central and peripheral parts of the electronograms obtained with the sector, the sensitivity of the recording part of the microphotometer can be raised to the limit imposed by the grain of the photographic emulsion.

In order to reduce the influence of grain we rocked the electronograms during microphotometry, i.e., oscillated them in their plane through a small angle about an axis passing through the center of the electronogram (Fig. 4).

The arrangements for rotating the sector in the path of the electron beam in conjunction with the electronic optics of the EM-4 electronograph was also utilized for solving a problem that inevitably arises in connection with absolute

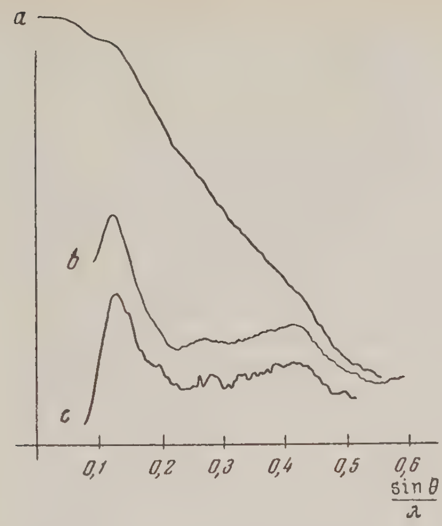

Fig, 4. Microphotograms obtained for molten silicon dioxide: a) without sector, b) with sector and rocking of the electronogram during microphotemetry, c) with sector but without rocking electronogram.

measurements of the intensity distribution of scattered electrons, namely, for determining the characteristic curve of the photographic emulsion.

In this case instead of a sector with a continuous change in the angle of opening we used a step sector, the angles of opening of which in the annular zones (a few millimeters wide) with different radii had values of 3, 6, 9, 18, 36, 72 and 144° and therefore produced exposures proportional to these annular values for the different zones of the photographic plate.

The second condition necessary in sensitometry - a uniform intensity over the entire cross section of the beam incident on the sector - was obtained by switching on, with no sample in the instrument, of the double electromagnetic lens with the current supply adjusted so as to obtain a shadow electron microscopic image.

The density of the electron beam on the photographic plate was computed as the total current of the beam incident on the plate divided by the irradiated surface of the plate. For measuring the full beam current incident on the plate the second lens of the electronograph was switched off and the beam having a cross section of less than 1 mm was intercepted by a collector connected to a DC amplifier circuit capable of measuring current values down to 10^{-13} amp.

The described procedure makes it possible to obtain a detailed electron scattering curve and thus offers new possibilities where investigation of the structure of noncrystalline materials is concerned.

Microphotograms of finely dispersed molten silica and of a collodion film obtained by means of the rotating sector are shown in Figs. 4 & 5. It will be seen that they comprise clear maxima, which are not discernible in curves obtained without the sector.

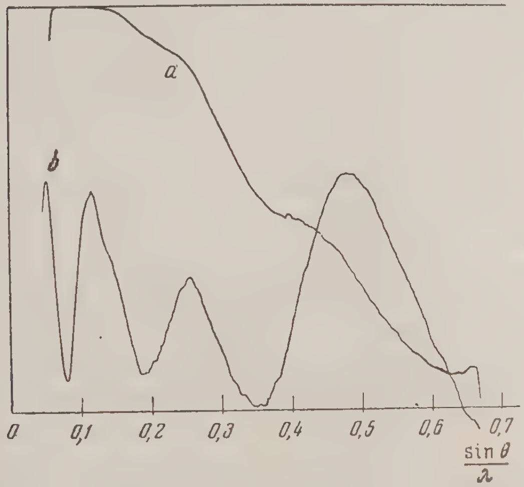

Fig. 5. Microphotograms of collodion film: a) without sector, b) with sector.

References

1. H.Finbak, Avhandl. Norske Videnkaps - Akad. Oslo, I. Math. -Naturw. Klasse, (1937).
2. P.P.Debye, Phys., ZS. 40, 66 (1939).
3. G.O.Bagdyk'iants, Izv. AN SSSR, Ser. fiz., 16, 255 (1953).

A SIMPLE METHOD OF OBSERVING THE PHOTOIONIZATION EFFECT OF X-RAYS AT ATMOSPHERIC PRESSURE

- M.E.Gurevich

Despite that fact that there exist numerous designs of dosimeters, the diverse requirements of roentgenologists are not fully satisfied by present day instruments. There is still urgent need for the development of new and inexpensive designs which would permit of dosimetric measurements under different conditions.

X-ray dosage is usually determined by their photoionization effect. In principle this effect can be observed at atmospheric pressure in a set-up similar to that utilized by Stoletov[1] in his experiments with ultraviolet radiation. The purpose of the present study was to develop for purposes of dosimetry an air unit (i.e., non-vacuum), converting the energy of x-ray radiation into electric energy.

Two metal plates measuring 30 x 30 cm were mounted 2-3 mm apart, parallel to each other and perpendicular to the x-ray beam. The plate closest to the x-ray tube was of aluminum, the other of copper or iron. The plates were connected to a mirror galvanometer having a sensitivity of about 10^{-9} amp per scale division.

There exists a natural contact difference of potential between the two plates: the aluminum plate is positive; the copper or iron plate, negative. When the x-ray tube is switched on the galvanometer connected to the plates records a photoionization current. The effect was readily detectable since with the parallel plates close to each other an appreciable part of the ions produced in the interelectrode gap is caught by the electrode of opposite charge. It may be assumed that the aluminum plate also served as a collector for the faster photoelectrons ejected from the copper or metal plate by the x-rays. At the same time the aluminum plate undoubtedly attenuated the primary x-ray beam and filtered out the long-wave part of the continuous spectrum.

The source of x-rays in the experiments was a deep-therapy tube with a tungsten anode. The tube was operated at voltages in the 120-180 kv range and at currents up to 15 ma.

In order to check the sensitivity of the set-up to variations in intensity, we investigated the dependence of the recorded photoionization current on the current through the x-ray tube with a constant potential on the latter. We found that the variation of the photoionization current obeys a parabolic law. At a dosage of some tens of roentgens per min, it was feasible to record 10% changes in intensity. The reproducibility was quite satisfactory provided the surface of the copper or iron plate was not subjected to mechanical or thermal treatment between tests.

An assembly of an aluminum and copper plate proved to be more sensitive than one made up of an aluminum and iron plate. This can readily be explained by the fact that the contact difference of potential between aluminum and copper is greater than between aluminum and iron.

In studying the dependence of the photoionization current on the voltage on the x-ray tube (with the current through the x-ray tube constant), we observed a linear increase in the photoionization current. This is due to the fact that the intensity of the continuous radiation from the tube is proportional to the square of the voltage while the strength of the photoionization current is proportional to the square root of the radiation intensity.

When the distance between the electrode plates is increased, the photoionization current falls off rapidly and at a separation exceeding 15 mm could no longer be detected with our initial set-up. The obvious reason for this was the decrease in the strength of the field between the electrodes and the consequent decrease in the number of ions taking part in the photoionization current.

When an additional potential from an outside source was applied to the electrode the photoionization current could be observed with an even greater separation of the plates.

Our set-up proved to be insensitive to large seasonal variations in atmospheric pressure and humidity; however, it did react strongly to changes in the state of the surface of the copper or iron plates: when the surface of the plate was cleaned off with emery paper the photoionization current fell off sharply (by a factor of about 1.5-2). After some days the photoionization current began to increase and reached its initial value after a period of about two weeks. It may be assumed that this effect is connected with destruction of the oxide film on the surface of the metal and with its subsequent regeneration.

Our research showed that the described simple system consisting of two plates of different metals connected to a galvanometer can serve for a rough evaluation of relative changes in dosage. By appropriate variation of the thickness of the aluminum plate (attenuating the primary x-ray beam to a greater or lesser extent), one can adapt the set-up for work in different intensity intervals. The sensitivity of the set-up can be increased by increasing the size of the plates, decreasing the distance between them or by applying a potential from an outside source to the electrodes (the last approach is not bery satisfactory since it requires careful and constant control of the external voltage source).

The described arrangement can also be used for gaging scattered radiation. In this case the plate should be rotated continuously or one can use an array of three sets of three plates each (two aluminum plates, one to each side of the copper one) set up at angles of 90° to each other.

With a constant-dosage source the described set-up can be used for studying certain changes on the surface of metals, the investigated surface in this case being one of the electrodes.

Kirghiz Agricultural Institute

References

1. A.G.Stoletov, Collected Works, Vol. 1, M.-L. 1941.

AN INSTRUMENT FOR MEASURING AND COMPARING DEBYE PATTERNS

- N.A.Ignat'ev

In the practice of x-ray analysis it is often necessary to compare two or more x-ray patterns and to evaluate visually the line intensities. Considerable difficulties are commonly encountered in comparing x-ray patterns. One of the simplest methods of comparison - laying one pattern over the other - permits of detecting only appreciable line displacements and precludes accurate quantitative measurements of such displacements. Weak lines, of course, cannot be observed at all.

Better results are obtained with a viewer in whose field one can simultaneously observe the two patterns side-by side. We developed an instrument of this type having certain advantages over present viewers and comparators. Its principle of operation is that, by means of an optical system similar to that used in visual photometers, the images of the two compared x-ray patterns are seen side-by-side in the field of view with half of each pattern being "cut off". Both the halves are joined at the "cut" edges and are examined through an eyepiece (Fig. 1). One can displace one half-pattern relative to the other by moving one of the patterns or by rotating a prism incorporated in the instrument.

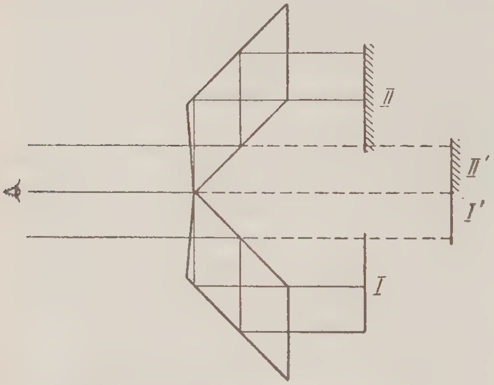

Fig. 1. Method of juxtaposing images of two x-ray patterns: I & II - two x-ray patterns, I' & II' - juxtaposed images of halves of patterns I & II.

All the components of the instrument are mounted on a heavy stand 1 (Figs. 2 & 3). The x-ray patterns are held on two glass plates mounted in metal frames 2 & 5. Frame 2 is fixed on the carriage 3 and can be displaced with it on the slide 4. The second frame 5 can be moved not only together with the carriage but also relative to it. The displacement of the carriage can be measured by means of the vernier scale 18 to within 0.1 mm. Displacement of the movable frame 5 relative to the carriage can be measured to within 0.01 mm by means of the micrometer knob 19 (Fig. 3) attached to the carriage 3.

The optical system of the instrument is shown in Fig. 3. The lighting assembly, consisting of automobile bulb 7, the prisms 8 and condensers 9, provides uniform illumination of the patterns 10. The images of the patterns are formed by the lenses 11 in the plane of the upper face of prism 12. The images are viewed through prism 13 and the eyepiece 14. To permit regulating the brightness of the images the objective lenses are equipped with calibrated diaphragms 15. These diaphragms can be used to equalize the density of the pattern if they are markedly different and to measure semi-quantitatively the blackening of the lines and background.

The diaphragm 16 serves to limit the field of view. The glass plate 6, located in the focal plane of the objective lenses, carries "sighting" reference lines. The instrument gives a 1.5-2-fold magnification.

The instrument can be used to measure the distance between symmetrical lines and the relative blackening of the lines and background on a given x-ray pattern, in addition carrying out qualitative and quantitative comparisons of two patterns.

The distance between symmetrical lines on one x-ray pattern is measured in the conventional manner: the pattern is mounted on frame 2 and the carriage displaced to bring the images of the successive lines under the reference line on

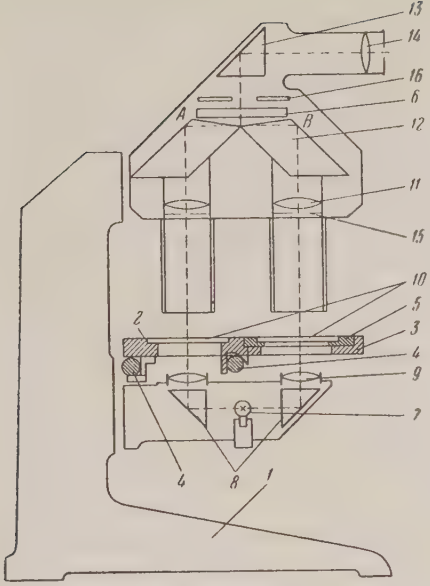

Fig. 2. Diagram of instrument: 1) stand, 2) frame for reference or standard x-ray pattern, 3) carriage, 4) slide for carriage, 5) movable frame for pattern being measured, 6) glass plate with reference marks, 7) bulb, 8) prisms, 9) condensing lens, 10) x-ray patterns, 11) lens, 12) prism, 13) eyepiece prism, 14) eyepiece, 15) calibrated diaphragms, 16) slit diaphragm limiting field of view.

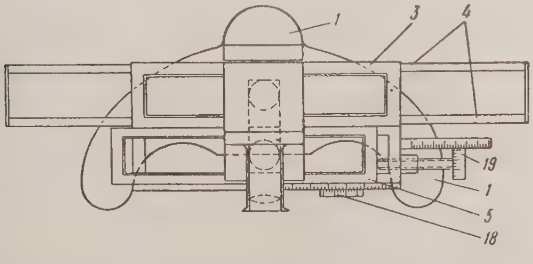

Fig. 3. Top view of instrument: 18) vernier scale, 19) micrometer knob for measuring the displacements of frame 5.

plate 6, the displacement of the carriage being read on scale 18 (Fig. 3).

The blackening of the lines in such cases can be measured by comparing them with a gray calibrating wedge mounted for this purpose in frame 5 or with the aid of a simple step plate, made of x-ray films exposed for different lengths of time, in combination with variation of the brightness by means of the calibrated diaphragms 15.

In order to minimize the influence of line shape and width on the accuracy of blackening measurements, the slit diaphragm 16 is used to frame narrow strips of the line maxima and the gray wedge; at the same time the magnification is increased to 5-6 X by replacing the usual eyepiece with a stronger one.

For comparison, the two x-ray patterns are placed on the glass plates and positioned thereon with reference to fiducial marks. Visual (qualitative) comparison can be made by matching the lines on one of the patterns with those on the other by appropriate displacement of the movable frame 5 relative to the carriage. If the patterns are characterized by different densities the compared lines or backgrounds can be equalized by means of the calibrated diaphragms 15. Such a qualitative comparison is often sufficient for the identification of many crystalline substances. In such cases one of the patterns is that registered for the investigated substance, while the other pattern is one recorded from a known material or may be a pattern plotted on the basis of known tabular values for the planar spacing.

In many cases it is important to determine with great accuracy changes in the interplanar spacing, i.e., to measure the "displacement" of the lines on one pattern relative to the lines on the other. Of course, the most accurate method of measuring such displacements consists in photographing the two patterns on the same film; however, this is not always feasible. Moreover, provided certain precautions are taken, patterns recorded on two separate films can fully satisfy all the requirements for precision measurement.

The primary purpose of our instrument is precisely measurement of such "displacements" in the two compared patterns. The procedure employed to this end is the following. After the patterns have been positioned with reference to the fiducial marks in their respective frames, the line of interest on one side of the patterns is brought into the field of view by moving the carriage. The movable frame is then displaced by means of the micrometer knob so as to bring the two half-lines into alignment. The indication of the micrometer knob is then noted. Next the carriage is moved to bring the other side of the compared patterns into view. If the distances between the symmetrical lines in the first and second patterns are not equal, the half-lines will appear displaced relative to each other. The micrometer knob is then rotated to bring them into alignment and the knob scale again read. The difference between the two readings will give the "displacement" of the line on one pattern relative to its position in the other. Thus on this instrument measurement of line displacement requires only two settings of the instrument as compared with four in working with a comparator. In view of this the error of measurement should be halved.

With any method of measuring the distance between lines the error in setting the instrument on the line is the main factor determining the accuracy of measurement. In most present instruments a crosshair or reference line is set over the lines in the pattern, while in our instrument in measuring displacement the "sighting" plate is not used: one line is set opposite the other. Tests of the instrument have shown that in comparing two lines of equal width the two half-lines can be matched with better accuracy (1.5-2 times) than a crosshair can be set over the center of a line in the pattern.

The writer has built a model of the proposed instrument and tested it. The model proved fully satisfactory for measuring and comparing Debye patterns. In order to facilitate rapid location of symmetric lines on both sides of the pattern, a second scale with the zero division in the center was mounted next to the carriage scale 18. With the pattern properly positioned on the carriage, symmetrical lines can be located rapidly by means of the "sight" 6 and the right and left hand scales.

X-ray patterns of ceramic materials having up to 90 lines have been successfully measured and compared on the model instrument; despite the great number of lines all the symmetrical lines were readily located and measured with adequate accuracy. Relative line "displacements" amounting to only 0.02-0.03 mm could readily be detected in comparing these x-ray patterns.

Voronezh State University

A NEEDLE ANODE X-RAY MICROPROJECTOR

- B.M.Rovinskii, V.G.Liuttsau & A.I.Avdeenko

In many fields of x-ray work it is highly desirable to have a "point" source of x-ray radiation. The use of tubes with a sharp focus in investigating the structure of materials by x-ray diffraction procedures enhances the resolution obtainable.[1] On the other hand, we now also have the possibility of using x-rays for shadow microscopy. In this case the size of the source of x-rays is one of the basic factors determining the resolution of the x-ray microscope.

Below we describe our new design for obtaining a small focus in an x-ray tube; this design differs from earlier proposed variants[2,3] and has been used by us for purposes of shadow microscopic radiography.

Conditions for obtaining an enlarged image in shadow radiography

If we accept that the human eye is capable of distinguishing diffused zones at the contours or boundaries of image details (i.e., half-shadows) having a width of 0.1 mm, then the maximum possible magnification that can be attained with a source of given size is given by the expression

$$r = \frac{R}{M-1} \qquad (1)$$

where r is the radius of the radiation source, R is the width of the half-shadow zone below the level of perception of the naked eye and M is the magnification.

From expression (1) it follows that with $R = 0.1$ mm, to obtain a "sharp" image of the specimen enlarged 100 times, we must have a source radius of 0.001 mm. A further condition is that the source must always be smaller than the investigated details.

A certain diffusion of the contours of the image details is also produced by the diffraction effect. The width of the diffraction "fringe" can be determined with sufficient accuracy from the expression deduced by the writers in Ref. 3:

$$p = (\lambda b)^{1/2} M \qquad (2)$$

where p is the width of the diffused zone at the detail contour in the enlarged image, M is the magnification, λ is the wavelength of the radiation employed and b is the source to specimen distance.

It follows from (2) that the sharpness of the image at a given magnification M will be maximal at minimal values of λ and b. However, in view of the conditions for obtaining an image with maximal contrast, it is advantageous to use long-wave radiation, while the distance b from the source to specimen can be reduced to the limit allowed by the design of the x-ray tube. Hence by selecting the most advantageous values of the quantities in expression (2) one can obtain the minimum value of p. Thus with $\lambda = 2$ Å, $b = 4$ mm and $M = 100$ the diffusion of the image contours p will be 0.09 mm, i.e., below the value perceived by the human eye.

On condition that $p \leqslant R \leqslant 0.1$ mm the minimal resolvable distance x in the specimen at a given magnification M is defined by the expression

$$x \approx \frac{2p}{M} \approx \frac{2R}{M} \approx \frac{0.2}{M} \text{ mm} \qquad (3)$$

Hence in designing an x-ray shadow microscope with high resolution the primary consideration is an x-ray source with the smallest possible focus.

Design of the microprojector

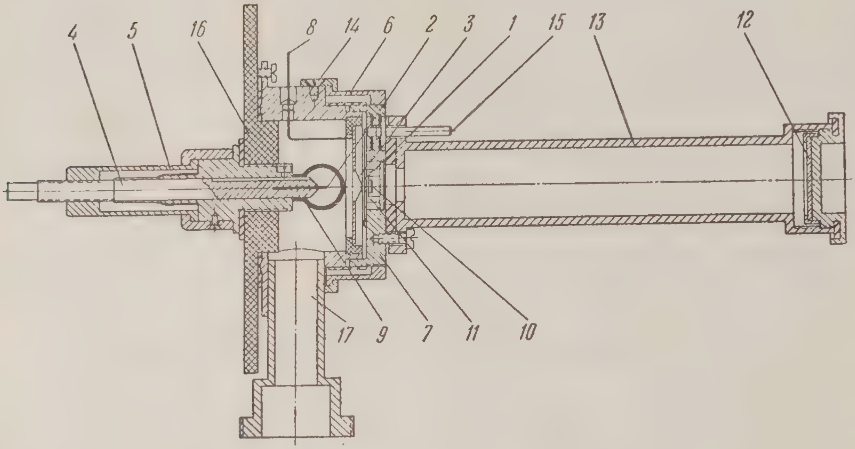

Fig. 1. Vertical section through needle x-ray microprojector (scale 1:4): 1) cathode, 2) anode, 3) diaphragm, 4) needle holder, 5) positioning and retaining nut, 6) ring, 7) cover, 8) lead for potential to diaphragm, 9) quartz cap, 10) specimen, 11) window for exit of x-ray, 12) cassette, 13) vacuum chamber (camera), 14) projector housing, 15) lead to cathode filament, 16) plexiglass insulator, 17) connecting sleeve to vacuum system.

The basic idea for obtaining a point x-ray source utilized in our instrument is rather simple.

The electrons emitted from an incandescent loop cathode are drawn by the accelerating electric field through the focusing diaphragm to the point of a fine metal needle utilized as the anode. If the tip of the anode needle is at the apex of the convergent electron beam, the x-ray radiation will be generated on the minimal area of the point. The size of the focal spot will be determined by the cross section of the electronic beam at the tip of the needle anode and the geometry of the needle tip (the radius of rounding near the point and the angle of the tip cone). The x-rays in the form of a divergent beam are emitted in the direction opposite to the motion of the electrons.

Fig. 1 shows a vertical section through the assembled x-ray microprojector. The cathode 1 is made of tungsten wire 0.07 mm in diameter and has the form of a loop 0.25 mm in diameter. The anode 2 consists of a thin metal needle with a rounding radius at the point of 0.1 μ and a solid angle at the cone tip of about 10^{o}. The needle point was formed in an electrolytic bath.

The primary focusing of the electron beam is realized by means of the diaphragm 3, made in the form of a disk of sheet nickel with a conical central aperture. At the apex of the cone there is a circular opening 0.05-0.1 mm in diameter. The diaphragm is insulated from the other parts of the tube and has its own lead 8 for applying the requisite potential.

The needle anode is mounted in the holder 4 and by means of the positioning nut 5 can be moved along the axis of the projector for bringing the tip to the focus of the convergent electron beam without disturbing the vacuum. Ring 6 serves to displace the cover 7, serving as the mount for the cathode 1, along the axis of the projector, i.e., to alter the position of the focus of the electron beam longitudinally.

For supplementary focusing of the electrons a hollow spherical quartz cap 9 with a 0.05-0.1 mm opening is mounted on the anode holder near the point of the needle. The cap is mounted so that the tip of the needle anode will be in the center of its opening and will not project through it. Nonfocused electrons striking the walls of the opening in the cap produce a negative field about the needle tip, enhancing the focusing.

The divergent x-ray beam emerges through the window 11. In case of photographing in air the window 11 is covered on the outside surface of cover 7 by a thin organic film sealed to the cover by a rubber ring and flange. In case of

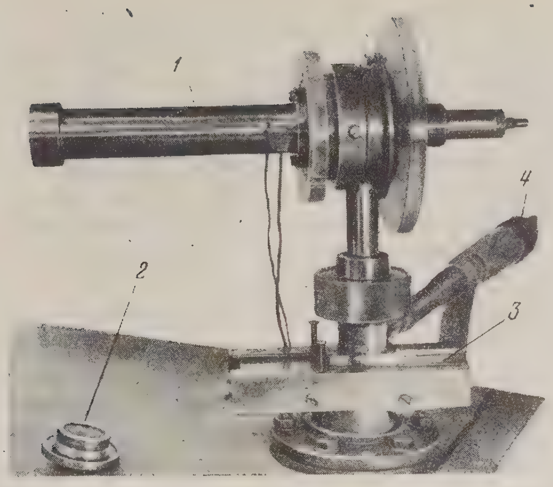

Fig. 2. External view of x-ray microprojector: 1) vacuum chamber (camera), 2) cassette, 3) vacuum valve (in setting for evacuating projector), 4) vacuum gage lamp. Projector shown 1/5th natural size.

photography in vacuum the film is removed and the flange is replaced by the vacuum chamber 13 which serves as the camera (the vacuum camera can also be used in photographing in air). The specimen 10 can be placed either in the window 11 or outside the tube.

The cathode current is supplied either from storage batteries or from an autotransformer through the leads 15, one of which is grounded through a microammeter. The anode part of the projector, which operates at high potential, is insulated from the housing 14 by the plexiglass insulator 16. With a light source beamed into the projector from the anode side the principal components of the tube can readily be adjusted, i.e., the needle and cathode loop centered. For adjustment the cassette 12 is removed and the tube of a long-focus microscope is introduced into the vacuum chamber 13.

Vacuum seals at the various joints are provided by rubber gaskets, periodically coated with vacuum grease. The instrument is evacuated through the connecting sleeve 17.

A photograph of the x-ray microprojector is reproduced in Fig. 2.

Results of tests

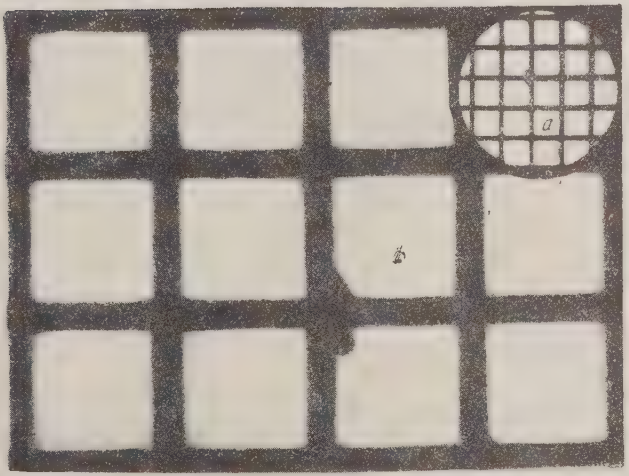

Fig. 3. Photograph of copper screen - 0.055 mm period and 5μ thick wires - made by means of the needle microprojector: a) direct 100X magnification; b) direct 100X x-ray magnification + subsequent 5X photographic enlargement = 500X total magnification.

Our primary purpose in testing the microprojector was to determine the size of the x-ray focal spot and the resolving power of the instrument. We determined the optimal conditions at which the dimensions of the focus are minimal and the resolution is maximal.

For evaluating the resolution obtained in shadow x-ray microscopy it is convenient to use fine metallic screens. By means of such screens one can determine the dimensions of the source, its shape and the geometric distortion of the image. We used a copper screen, prepared electrolytically, with a period of 0.055 mm and a filament thickness of 5 μ.

In the upper right hand corner of Fig. 3 is the direct 100X magnification photograph obtained by means of the x-ray microprojector. As may be seen the screen filament has sharp contours and the entire image is free of aberration. Examination of the image contours by means of a microphotometer showed that the diffusion zone R does not exceed 0.03 mm.

The reproduced photograph was obtained under the following conditions: cathode filament diameter 0.07 mm; cathode loop diameter 0.25 mm; filament current 1.2 amp; distance from plane of cathode loop to plane of diaphragm aperture 0.05 mm; aperture diameter 0.25 mm; diaphragm at ground potential; distance from plane of opening in diaphragm to tip of needle anode 1 mm; radius of rounding of needle point 0.1 μ; cone angle at tip 10°; needle made of tungsten wire; anode potential 8 kv, anode current 5 microamp; distance from tube focus to specimen (screen) 2.5 mm. The photograph was made in the vacuum camera: exposure 3 min on Agfa Lauefilm, developed as per recommendation of manufacturer.

Together with the direct print of the x-ray negative, Fig. 3 shows a 5X enlargement of the negative (i.e., total magnification 500X). It will be seen that in the enlargement the contours of the screen wires are still relatively sharp, although in this case the width of the diffused zone is about 0.2 mm. The fact that the diffusion of the vertical and horizontal wires is nearly the same indicates that the focal spot is circular. Substituting $M = 100$ and $R = 0.03$ in expression (1) we find a value of 0.6 μ for the diameter of the focal spot. Further substituting $b = 2.8$ mm, $\lambda = 1.5$ A and $M = 100$ in (2), we find that the width of the diffraction broadening does not exceed 0.01 mm. Hence the minimal resolution of the specimen detail as determined from expression (3) by substituting $R = 0.03$ mm therein is $x = 0.6$ μ.

Under optimal conditions the instrument can be operated for a long time. Thus the tungsten needles at a load of 0.03 watts did not melt even after 6-7 hours continuous operation. With a focus of about 0.5-0.6 μ and an emitting surface of about $3 \cdot 10^{-7}$ mm, the specific power is $\sim$100 kw/mm^2.

When needle anodes of lower melting point metals are used, the useful power is reduced. Thus in working with an iron needle the power is reduced to 0.02 watts. The needle anode can be replaced or resharpened in a matter of 15-20 min without stopping the vacuum pump.

Institute of Machine Design of the
Academy of Sciences of the USSR

References

1. B.Ia.Pines, Izv. AN SSSR, Ser. fiz., 16, 333 (1952).
2. V.D.Bezverkhii & B.Ia.Pines, Zhur. tekh.fiz., 17, 1341 (1947).
3. V.E.Kosslett & W.C.Nixon, J.Appl.Phys., 24, 616 (1953).

A CAMERA OBSCURA FOR SHADOW X-RAY MICROSCOPY

- B.M.Rovinskii & V.G.Liuttsau

The basic requirements that must be met by equipment for shadow x-ray microscopy (microradiography) were set forth in Ref. 1 (see preceding article). It was shown that the resolution of the x-ray microprojector is determined mainly by the size of the x-ray "point source". In the present report we describe a different type of microprojector, an instrument in the form of a camera obscura with a minute opening.

The camera obscura was invented[2] in the 16th Century by Leonardo da Vinci and Papnutio (Panuce) and subsequently exhaustively studied by Kepler (1604). In its time, the camera obscura was widely used as a simple optical instrument.

The discovery of x-rays in 1895 gave new impetus to practical application of the camera obscura.[3] At present it is commonly employed for studying the focus of x-ray tubes, in the form of a pinhole camera with a 0.1-0.2 mm diameter aperture.

Al'tshuler & Tzukerman[4] describe a set-up for investigating the distribution of chemical elements in surface layers by the x-ray fluorescence method. These authors used a camera obscura with a 0.1 mm diameter opening for obtaining microradiographs with a magnification of 4 X in the camera and a total enlargement of 12 X.

Conditions for obtaining an enlarged shadow image in a camera obscura

The necessary conditions for obtaining a sharp magnified image are simple. The x-rays from the wide focal spot of an x-ray tube in passing through a very small aperture emerge as a divergent beam. If the specimen is mounted in the path of this beam, the rays, being non-uniformly absorbed by the specimen, will form an enlarged shadow image - reproducing the inhomogeneities of the specimen - on a photographic plate set up behind the specimen. Just as in the microprojector described in Ref. 1, the enlargement obtained in the camera obscura is determined by the ratio of the distance from the aperture (replacing the point source) to the plate to the distance from the aperture to the specimen. Analogously, the resolution is determined by the diameter of the aperture (source).

The transmission factor or "relative aperture" of the camera is an important consideration since with a given source intensity it determines the exposure time. The relative aperture is proportional to d^2, where d is the diameter of the pinhole. Hence, in practice, the resolution which can be obtained with a camera obscura is limited by the power of the x-ray source available. We established in preliminary tests that with conventional x-ray tubes one can achieve acceptable exposure times only with pinholes not less than 0.5-1.0 μ in diameter. In view of this we used an aperture of this size in attempting to realize an x-ray camera obscura.

Technique of making very small openings

It is extremely difficult to make 0.5-0.1 μ diameter holes. By way of material for the diaphragm we selected gold because of its very high coefficient of linear absorption (the "half-thickness" for Fe Kα radiation is 0.9 μ) and its desirable mechanical properties. Tests showed that it was feasible to prick clean, small diameter holes in gold plates (foil) 0.02-0.03 mm thick, annealed at 500-600°, with a steel needle.

A PMT-3 microhardness tester was used to puncture the openings. The set-up employed is pictured in Fig. 1. A very sharp, electrolytically pointed, steel

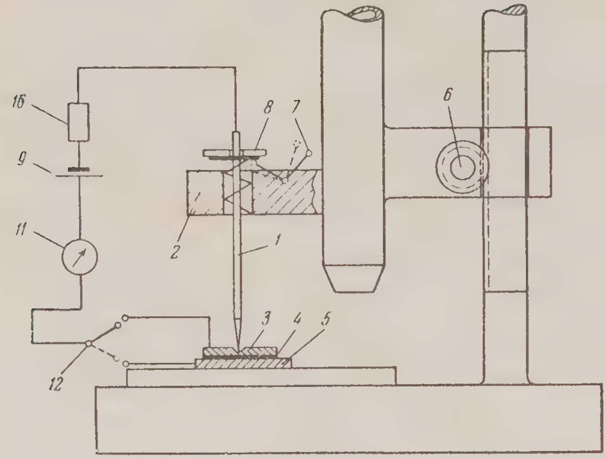

Fig. 1. Set-up employed for pricking very small diameter holes: 1) steel needle, 2) loading device, 3) gold plate (foil), 4) zapon lacquer layer, 5) lead support, 6) height adjustment screw, 7) catch, 8) weight, 9) battery, 10) high-value resistor, 11) galvanometer, 12) switch.

needle 1, having a 10-15° tip cone and a rounding radius near the point of 0.1-0.2 μ is mounted in the loading device of the PMY-3 tester in place of the usual diamond indentor. The annealed gold plate 3 is cemented by means of a very thin (~1 μ) coating of zapon lacquer 4 to the lead support 5, attached to the specimen table of the tester. The needle assembly is lowered by means of the height adjustment screw 6 until the needle point just touches the gold plate; the catch 7 is then released and the 2-3 gram weight 8 slowly forces the point of the needle through the gold plate.

The instant of contact of the needle with the gold plate and the instant of completion of perforation, i.e., emergence of the needle through the gold plate, are determined electrically. To this end one of the terminals of the 2 volt battery 9 is connected to the needle through the high resistance 10, while the other terminal is connected to the galvanometer 11 and through switch 12 either to the gold plate 3 or the lead support 5, which are insulated from each other by the zapon lacquer. Initially the gold plate is connected; when the needle touches the gold plate the galvanometer pointer is deflected, marking the instant of contact. The switch is then moved to the other position, breaking the first circuit. When the needle penetrates the gold plate and zapon layer and makes contact with the lead support, the galvanometer pointer is again deflected, indicating penetration. The weight 8 is then removed and the needle slowly withdrawn.

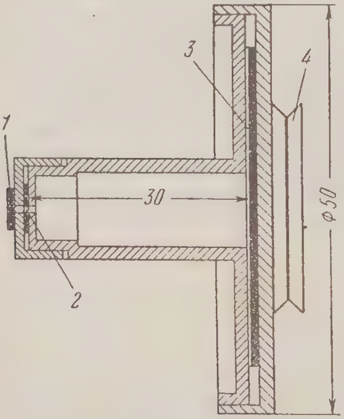

Fig. 2. Sectional view of camera obscura with < 1 μ diameter hole for microradiography: 1) specimen, 2) diaphragm with pinhole, 3) photographic plate, 4) pulley.

The resistance 10 is chosen so that the peak current through the circuit will not fuse the needle point. The penetration time depends on the weight 8 and in practice does not exceed 1-2 hours.

By means of the described procedure it is feasible to prick clean holes 0.5 μ and less in diameter; however, it must be admitted that it is difficult to determine the actual size of the apertures. The resultant holes are tapered to the extent of 10-15°, assuring an adequate divergence of the emerging beam and hence a sufficiently large "field of view". In view of the taper, the "effective" diameter of the aperture is some 10-20% greater than the minimal actual opening (at the side of emergence of the needle) and the edges of the emergent x-ray beam are somewhat diffuse.

Construction of the camera obscura and tests

In order to insure a sufficiently high magnification it is expedient to make the camera small.

A section through the model camera is shown in Fig. 2. The x-rays from the wide focus, demountable ion tube pass through the specimen 1, the camera diaphragm 2 (the specimen can be mounted outside the camera and in front of the diaphragm as shown in Fig. 2 or inside the camera) and finally fall on the photographic plate 3, recording the enlarged shadow image.

Generally the "brightness" over the focal spot of x-ray tubes is far from uniform. Hence to insure uniform blackening of the plate over the entire cross section of the conical beam our set-up has provision for continuous rotation of the camera obscura together with the specimen and photographic plate about the optical axis of the camera. The rotation is accomplished by means of a small 60 rpm synchronous motor with a variable speed drive to the pulley 4 (Fig. 2). A general view of the camera mounted in operating position on an ion tube is reproduced in Fig. 3.

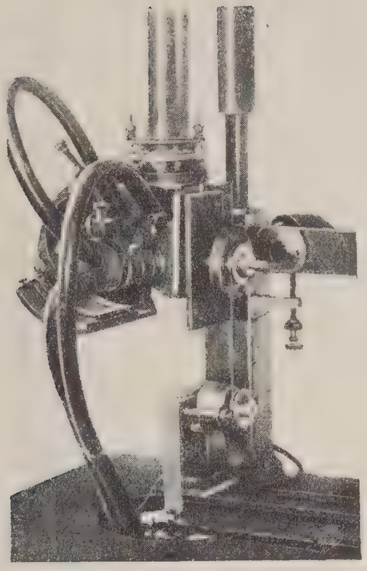

Fig. 3. General view of the camera-projector set up on a demountable ion tube.

With a specimen to pinhole distance of 0.3 mm the direct magnification obtained in the camera is 100 X. Thus, with a 10 X enlargement of the negative, the overall magnification is 1000 X.

In our tests we used the radiation from a cobalt anode with the x-ray tube operated at 15 kv and 5 ma. The exposures under the circumstances ranged from 30 min to 1 hour.

To check the resolution of the camera we photographed a 425 mesh screen woven of 23 μ diameter copper wire. A microradiogram of the screen is shown in Fig. 4 (direct magnification 50 X; overall enlargement 450 X). It will be seen that the image is fairly sharp; the diffused zone at the edges of the wires does not exceed 0.2 mm. According to the data of Ref. 1, it may be assumed that details 1 μ or less apart can be resolved.

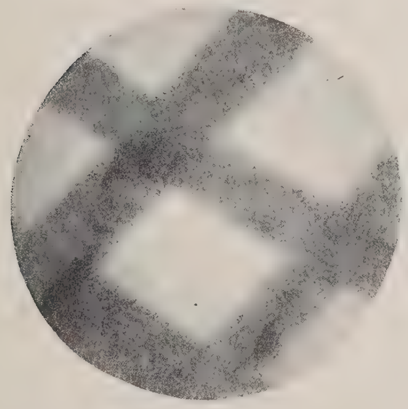

Fig. 4. Microradiogram of 425 mesh screen woven of 23 μ thick copper wire. Direct magnification 50 X; overall enlargement 450 X.

Institute of Machine Design of the
Academy of Sciences of the USSR

References

1. B.M.Rovinski, V.G.Liuttsau & A.I.Avdeenko, Article on page 771 of the present issue of the Bulletin.

2. "Camera obscura" in Fizicheskii slovar (Physics dictionary), Vol. 2. Pub. by "Sovietskaia entsiklopediia", M. 1937.

3. N.Uspenski, Phys. ZS., 15, 717 (1914).

4. L.V.Al'tshuler & V.A.Tsukerman, Zavod. labor., 5, 1278 (1938).

BULLETIN of the Academy of Sciences of the USSR - Physical Series
Vol. 20, No. 7, 1956 - Transactions of the Fifth Conference on the Application of X-Rays to the Investigation of Materials (Continued from Vol. 20, No. 6)

TABLE OF CONTENTS

Page

	Orig.	Trans.
Influence of heat and mechanical treatment on the thermal factor in scattering of x-rays by solid solutions - V.A.Il'ina, V.K.Kritskaia, G.V.Kurdiumov & T.I.Stelletskaia	723	659
On the intensity of x-ray scattering by solid solutions - V.I.Iveronova & A.P.Zviagina	729	664
X-ray investigation of structural changes in the surface layer of steel machined by turning - O.N.Shivrin	736	671
Refinement of the structural parameters of nickel triamino-dithiocyanogen (II) and cesium tetrachlorocobaltate by the method of differential Fourier synthesis on an electronic computer - M.A.Porai-Koshits	740	674
X-ray analysis of the molecular structure of the substance of coal and coke - V.I.Kasatochkin & L.L.Razumova	751	683
Application of x-ray structural analysis to investigation of oxide-coated cathodes - E.P.Ostapchenko	755	687
X-ray investigation of the dependence of the structure of a paladium catalyst on the conditions of its electrolytic preparation and heat treatment - V.D.Ruchkina	761	693
Possible use of x-ray analysis of polycrystals in geological studies - B.G.Erenburg	764	696
Recent advances of x-ray spectroscopy in the field of investigation of matter - M.A.Blokhin	770	701
On the nature of the fine structure in the K-edge of the absorption spectrum of germanium halide molecules - K.I.Narbutt	780	710
K series emission lines in the x-ray spectrum of titanium in the metallic state and in certain dielectric materials - E.E.Vainshtein, I.B.Staryi & M.N.Bril'	784	713
Investigation of the asymmetry and width of the $K\alpha_1$ lines of copper and manganese atoms in Heusler alloys by the fluorescence analysis method - B.I.Kotliar	790	718
A recording vacuum x-ray spectrograph (for the 20-300 A region) - A.I.Efremov & A.M.Tiutikov	794	721

	Page	
	Orig.	Trans.
A universal x-ray vacuum tubular spectrograph - I.B.Staryi	798	724
Experimental use of a scintillation counter for recording x-ray spectra - L.M.Beliaev, K.I.Narbutt, I.L.Stoliarova, I.E.Konstantinov, V.A.Alekseev, A.B.Gil'varg and I.S.Smirnova	801	727
Determination of the diffusion coefficient from secondary x-ray spectra - M.A.Blokhin, E.V.Timofeeva & G.Z.Chukhlov	809	734
X-ray spectral studies of alloys in connection with their magnetic state - S.M.Karal'nik, I.Ia.Dekhtiar, D.M.Konskii, V.G.Chupryna & L.G.Nikolaeva	811	736
X-ray spectra and interatomic bonds in alloys - S.M.Karal'nik	815	739
On interpretation of diffraction patterns of amorphous materials by the radial distribution method - T.M.Sereda	820	743
Electron diffraction investigation of oxide films forming on molten aluminum and its alloys - M.V.Mal'tsev, Iu.D.Chistiakov & M.I.Tsypin	824	747
Mechanism of texture formation in layers condensed on a neutral base - M.A.Rumsh & T.M.Zimkina	827	751
Electronographic investigation of the nature of passive films - V.P.Batrakov & I.A.Ponizovskiia	830	755
Electronographic investigation by means of an EM-3 electron microscope - V.N.Vertsner	834	759
The sector method in electronography - G.O.Bagdyk'iants	838	762
A simple method of observing the photoionization effect of x-rays at atmospheric pressure - M.E.Gurevich	843	766
An instrument for measuring and comparing Debye patterns - N.A.Ignat'ev	845	768
A needle anode x-ray microprojector - B.M.Rovinskii, V.G.Liuttsau & A.I.Avdeenko	848	771
A camera obscura for shadow x-ray microscopy - B.M.Rovinskii and V.G.Liuttsau	853	775

Translated in 1957 by
Columbia Technical Translations
5 Vermont Ave., White Plains, N.Y.

A PRECISION MAGNETIC α-SPECTROMETER

- L.L.Gol'din & E.F.Tret'iakov

Magnetic α-spectrometers are precision instruments. Their dimensions (of the order of a meter) are determined by α-particle $H\rho$ values, which are usually about $3\text{-}4\cdot10^5$ oersted-cm. The necessity for resolving closely spaced α-lines, sometimes having a separation of only 10-15 kev, determines the resolving power of spectrometers and makes the use of exceptionally strong magnetic fields impossible. For fields greater than 10 kilogauss, saturation of the polepieces leads to field configurations (and therefore also focusing) strongly dependent on the field strength.

At the present time interest is increasing in long-range α-particles, whose intensities amount to only some hundredths or even thousandths of a percent of the fundamental line intensity. At the same time the transmission factor of precision instruments having a high resolution remains quite low: about 10^{-4} of the 4π solid angle or less. The low transmission must be compensated for by extremely long exposure times, sometimes extending to several weeks of continuous operation.

In such cases the long-term stability of the spectrometer becomes extremely important. Efficient, reliable and economic design of the instrument and its power supply is therefore essential.

This article describes an α-spectrometer which has been in operation since 1952. Its resolution (peak width at half-height) is 7.5 kv at an α-energy of 5.3 Mev. The spectrum is recorded on photographic plates. This spectrometer has been successfully used to detect α-lines corresponding to a half-life of $5\cdot10^8$ years and has resolved lines 12 kev apart.

Magnetic Field

The α-particles are analyzed by means of a nonhomogeneous transverse axially symmetric magnetic field, assuring full spatial focusing at a deflection angle of 254°.[1]

In the central plane of the gap this field is given by

$$H_z = H_0\left[1 - \frac{1}{2}\cdot\frac{r-r_0}{r_0} + \beta\left(\frac{r-r_0}{r_0}\right)^2\right] \text{ and } H_r = H_\varphi = 0.$$

With $\beta = 1/8$, second order focusing is realized for angles of emission in a plane perpendicular to the magnetic field (Z axis). Such fields have been analyzed by the authors in Refs. 2 and 3, where it has been shown that a nonhomogeneous field has several advantages over a homogeneous one: a spectrometer with a nonhomogeneous field has twice the dispersion and one and a half times the transmission of an equivalent spectrometer with a homogeneous field.

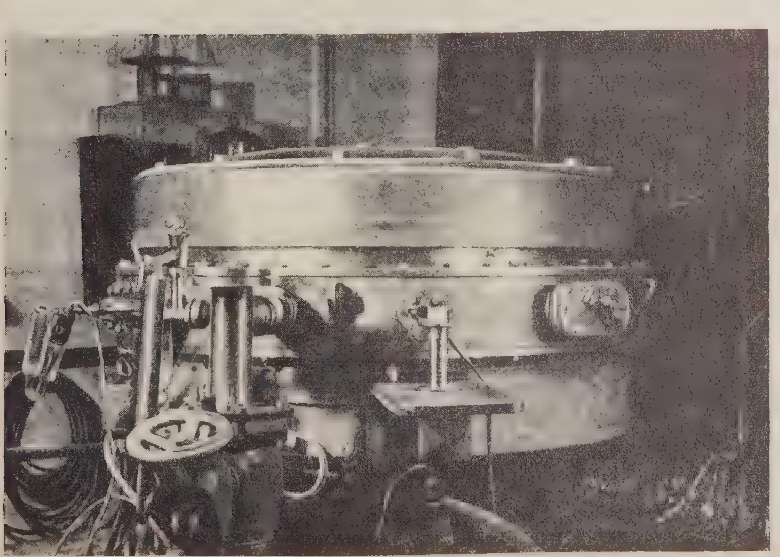

Fig. 1. External view of the α-spectrometer.

Magnetic fields with spatial focusing have been widely used in the past few years in high-intensity β-spectrometers: we were the first to use them in an α-spectrometer.

Design of the Electromagnet

The field is produced by an electromagnet with an annular gap. Fig. 1 shows an external view of the spectrometer; Fig. 2, a schematic cross section.

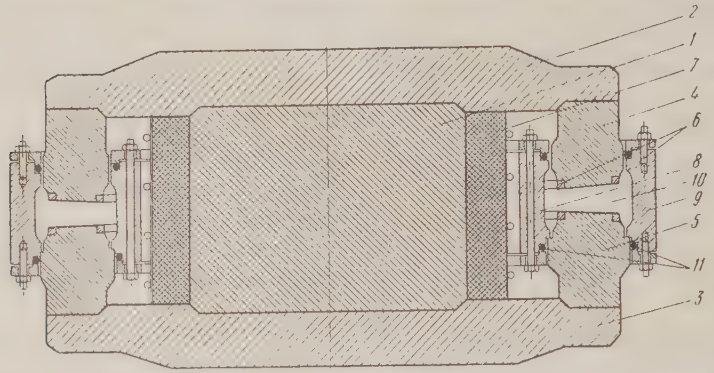

Fig. 2. Section through the magnet: 1) core, 2 & 3) covers, 4 & 5) polepieces, 6) shaped rings, 7) coil, 8 & 9) brass cylinders, 10) vacuum chamber, 11) rubber seal.

The magnetic circuit consists of a core 1, two covers 2 and 3, and polepieces 4 and 5. At the edges of the polepieces are located special shaped-section rings 6 which correct the field configuration in the gap.

The radius of the central α-particle trajectory is 50 cm; the width of the polepieces is 80 mm (together with the shaped rings it is 110 mm); and the height of the gap is 30 mm at its center.

In operation the central part of the gap, where the edge distortion of the poles is least pronounced, is employed. Depending on the resolution necessary, the beam width varies between 40 and 60 mm (the beam is limited by adjustable diaphragms).

The relatively large spectrometer radius makes it possible to use a field of only 6700 oersteds when working with α-particles from Po^{210} (5.3Mev). The weak field insures a magnetic field configuration independent of the field intensity through the whole energy range of α-particles ejected by natural α-emitters (we have never investigated long-range α-particles. The large radius is also desirable because with a given resolution, the width and, therefore, the total activity of the source is proportional to the radius. Owing to the fact that the weight of the magnet increases sharply with radius, we were limited to a 50 cm radius; the weight of the magnet is 4.5 tons.

Adjustment of the magnet necessitates replacement of the shaped rings, and therefore partial disassembly. Assembly-disassembly must not alter the geometry of the gap. This was insured by grinding the mounting surfaces and positioning the magnet parts relative to each other by means of tapered pins. Measurements with Johanson blocks showed that the magnet geometry remained constant after disassembly and assembly to within 0.01 mm.

The electromagnet coil 7 is located outside of the vacuum chamber and is water-cooled.

Fig. 2 shows the vacuum chamber 10, formed by the polepieces 4 and 5 and the two brass cylinders 8 and 9. The volume of the chamber is only 12 liters. The outer cylinder is easily removed, allowing ready access to the chamber and thus, facilitating replacement of the aluminum foil covering the polepieces. Periodic replacement of the foil is necessary to reduce the background due to contamination of the polepiece surfaces by radioactive material from the source.

Gap Geometry

The shape of the polepieces and the shaped adjustment rings is shown in

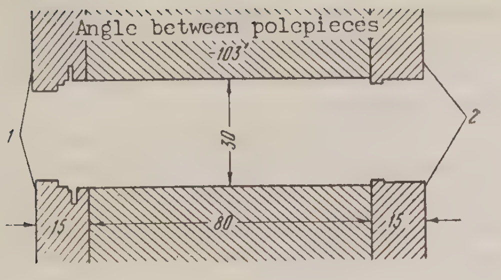

Fig. 3. Gap geometry: 1) outer shaped ring, 2) inner shaped ring.

Figs. 2 and 3. The pole surfaces form two cones with apex angles of 178°17'. This shape provides for a linear decrease of the field with increasing radius.[2] The shaped rings attached to the edges of the polepieces compensate for the edge effect of the magnet and give a quadratic term in the expression characterizing the dependence of the field on the radius. The shape of these rings was determined by calculation and tests on models.

First the field of a model magnet was measured with the initial calculated ring profile. Then the Green's function was calculated to determine the change in the magnetic field in the gap with changes in the dimensions of the rings at different points and the requisite alteration of the ring profile to obtain the desired field estimate. New rings were made and the whole procedure repeated.

Altogether four sets of shaped rings were made. The last one was designed on the basis of field measurements made on the full-scale magnet.*

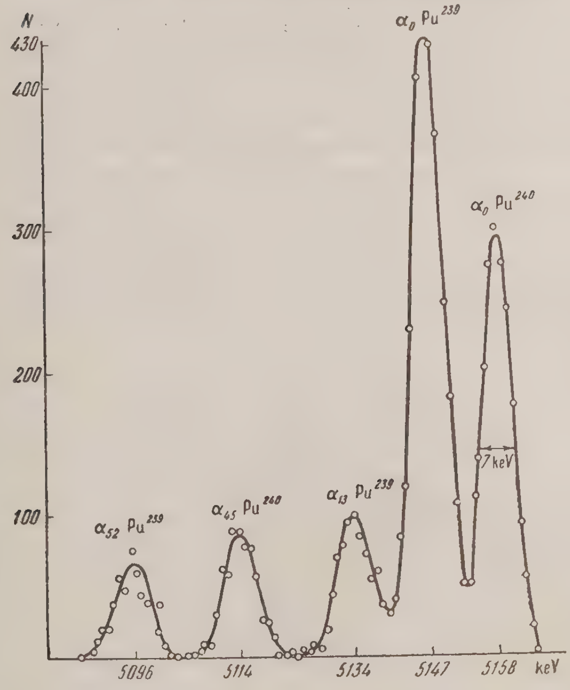

Fig. 4. α-Spectrum of a mixture of a Pu^{239} and Pu^{240}.

The final field measurements were made with an accuracy within $3 \cdot 10^{-3}\%$ at a field strength of 6500 oersteds along five radii of the magnet.

For $r - r_0 \leqslant 30$ mm, the deviation of the magnetic field from the prescribed values was no greater than $2 \cdot 10^{-4}$. The measurements were made with a "snatch" coil, which was moved in the gap in 4 mm jumps, and a ballistic galvanometer.

Use of the given type of focusing field and careful adjustment of the apparatus made it possible to obtain a high resolution (to 0.14%). As an illustration of the resolving power, the α-spectrum of a mixture of Pu^{239} and Pu^{240} is shown in Fig. 4.

Magnet Power Supply

A block diagram of the electric power supply, regulation, and current measurement is given in Fig. 5. The electromagnet winding 3 is supplied from the EMU-50 amplidyne 1, having a rating of 220 v at 20 amp. This current is sufficient for focusing α-particles of energies up to 9 Mev. Current regulation is obtained by varying the supply to the control winding of the amplidyne; this is accomplished by two electronic stabilizers, one for voltage (9) and one for current (8). A thermostatic resistor R_4, having a nominal rating of 0.3 ohm is connected in series with the magnet winding.

The potential across this resistor is applied to the voltage divider 6 and compared with a standard emf. The difference is applied to the input of a current amplifier which has excellent zero stability (better than 1 in 10^4), a high

---

*All the calculations were performed by F.M.Filler and A.S.Kronrod.

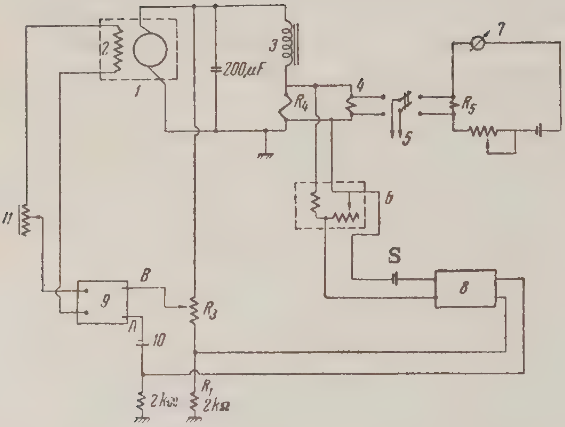
2
1
200μF
3
7
4
R4
R5
5
6
11
S
8
9
B
R3
Л
10
2kΩ
R1
2kΩ

Fig. 5. Block diagram of spectrometer power supply: 1) amplidyne, 2) excitation winding, 3) electromagnet winding, 4) potential divider, 5) to potentiometer, 6) field setting divider, 7) magnetic field meter, 8) current stabilizer, 9) voltage stabilizer, 10) comparison battery, 11) balancing variable resistance, S) standard emf cell.

amplification factor and a large time constant (about two minutes). This amplifier insures the necessary long-period stability of the spectrometer.

The amplidyne excitation is controlled directly by the voltage regulator 9, which has two inputs: to one of these is applied the voltage from the amplidyne terminals, while the other is connected to the current stabilizer. The voltage regulator has a relatively short time constant (about 10^{-3} seconds) and low long term stability. Its primary purpose is to compensate rapid voltage fluctuations associated with the supply line. In view of the high gain and large time constant of the current regulator, the short-period amplidyne excitation current is determined by the voltage fluctuations on its terminals; on the average, however, the excitation current depends only on the magnitude of the current flowing through the electromagnet winding.

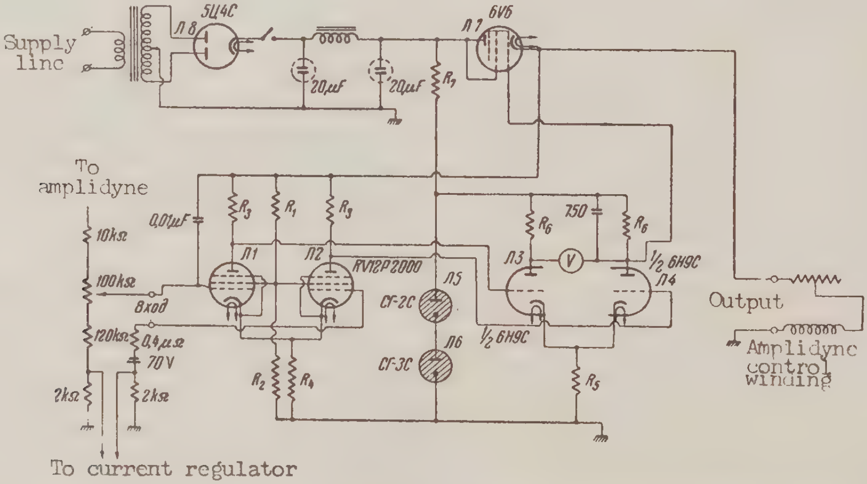
Supply line
5Ц4C
Л8
20μF
20μF
R7
Л7
6V6
To amplidyne
10kΩ
100kΩ
Вход
120kΩ
0.4μΩ
70V
2kΩ
2kΩ
0.01μF
R3
R1
R3
Л1
Л2
RV12P2000
Л5
CГ-2C
Л6
CГ-3C
R2
R4
R6
750
R6
Л3
V
1/2 6H9C
Л4
1/2 6H9C
R5
Output
Amplidyne control winding
To current regulator

Fig. 6. Voltage stabilizer circuit (R_1 = 130 k , R_2 = 80 kΩ, R_3 = 680 kΩ, R_4 = 330 kΩ, R_5 = 270 kΩ, R_6 = 500 kΩ, R_7 = 11 kΩ)

The voltage stabilizer circuit is shown in Fig. 6; that of the current regulator in Fig. 7. The voltage stabilizer is essentially a simple balanced dc amplifier. The current regulator is an amplifier with a high amplification factor; the dc voltage applied to its input is converted to ac by a vibrator operating at the line frequency. This signal is amplified by an ordinary low-frequency amplifier and is then rectified by a phase detector. During long exposures, the magnet current is checked every 30-40 minutes and is adjusted if necessary. The current drift over this interval seldom amounts to as much as 10^{-4} of the nominal value, and is usually very much less or entirely absent. The potential difference across the standard resistor terminals can be measured by a Disselhorst potentiometer.

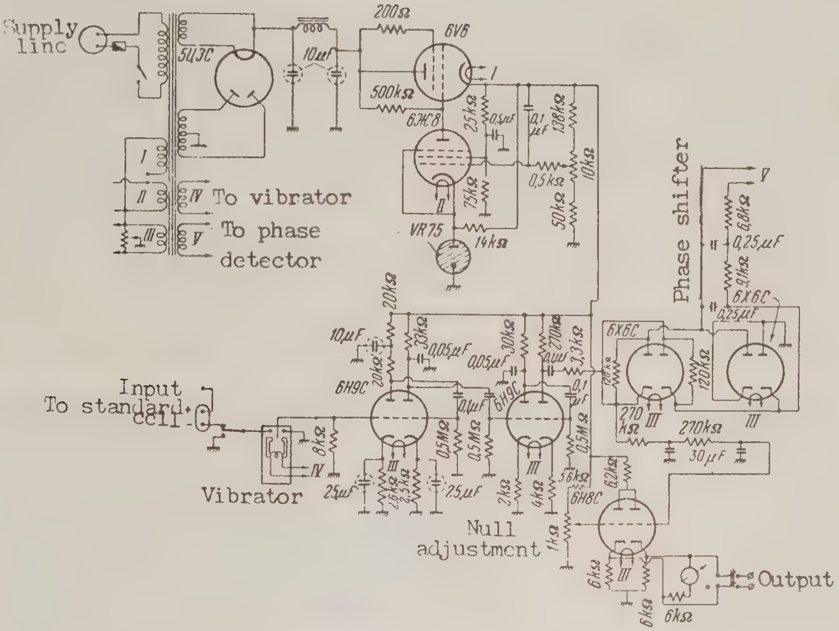
Supply line
5Ц3С
10μf
200Ω
6V6
I
500kΩ
6Ж8
25kΩ
0,5μf
0,1 μf
138kΩ
10kΩ
0,5kΩ
50kΩ
75kΩ
II
VR75
14kΩ
I
II
III
IV To vibrator
V To phase detector
Phase shifter
V
6,8kΩ
0,25μF
9,1kΩ
6X6C
0,25μF
20kΩ
10μF
33kΩ
0,05μF
0,05μF
30kΩ
270kΩ
0,1μF
3,3kΩ
6X6C
120kΩ
120kΩ
20kΩ
6H9C
6H9C
0,1μF
0,1 μF
Input
To standard cell
Vibrator
IV
8kΩ
25μF
III
2,6kΩ
2,5kΩ
25μF
0,5MΩ
0,5MΩ
2kΩ
4kΩ
III
0,5MΩ
5,6kΩ
270 kΩ
III
270kΩ
30μF
III
6,2kΩ
6H8C
Null adjustment
1kΩ
6kΩ
III
6kΩ
6kΩ
Output

Fig. 7. Current regulator circuit.

Measurement of the Magnetic Field Intensity

Measurement of the magnet current gives a good indication of the stability of the magnetic field, but not its magnitude. The magnetic field is measured (compared) by the field meter (Fig. 8), suggested by Shpinel. It consists of a light 9 mm diameter uncased coil 1 mounted in an unused section of the field at the center of the gap. The coil is suspended on horizontal phosphor-bronze filaments 7 (0.02 mm diameter), rolled into a ribbon. A current, measured by a Disselhorst potentiometer, is passed through the coil. The restoring torque is provided by the small weight 2 attached to the quartz arm 3. The angle of rotation of the coil is determined by the deflection of a light spot reflected by the mirror 4 cemented to the coil.

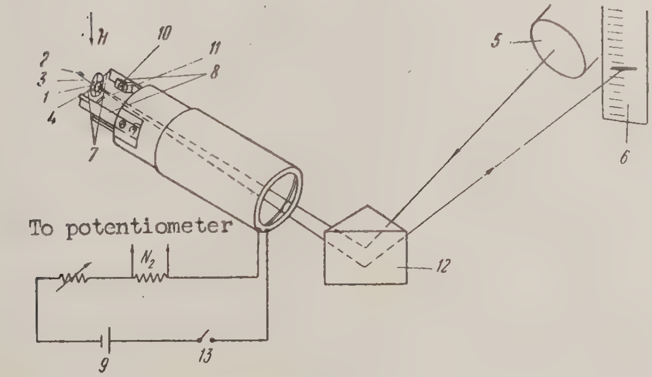
H
10
11
2
3
1
4
8
7
5
6
12
To potentiometer
N_2
9
13

Fig. 8. Magnetic field indicator: 1) coil, 2) weight, 3) quartz arm, 4) mirror, 5) light source, 6) scale, 7) flattened filaments, 8) springs, 9) 1.5 volt battery, 10) adjustment screw, 11) stop limiting rotation, 12) prism, 13) switch.

The sensitivity and short-term stability of the field intensity indicator makes it possible to compare magnetic fields with an accuracy of 1 part in 10^4. Its long-term stability is relatively low ($2 \cdot 10^{-3}$). As noted above, during exposures the magnetic field is stabilized by monitoring the magnet current.

Sources

At the present time the sources used are primarily α-emitters vacuum evaporated on glass supports. Special tests (accuracy within 0.5 kev) have shown that the glass does not become charged and the α-lines are not displaced.

The sources are prepared in the following manner. The chloride of the active substance is deposited on a tantalum ribbon through which an alternating current is passed. The glass disc onto which the evaporated substance is deposited is placed some 3-5 mm from the ribbon. The evaporation is performed in several stages onto different glass discs, which makes it possible to separate the investigated substance from any impurities present.

Only invisible layers (a few micrograms per cm^2) do not produce broadening of the α-lines. If necessary, thicker sources (100 μg/cm^2) can be obtained without the film pealing off. In this case the half-width of the lines increases to 50 kev.

When exposed to air, the sources deteriorate: not only the half-width, but also the low-energy background increases. In order to preserve the quality of the sources, they should be kept in vacuum.

The source-holder assembly is shown in Fig. 9. The effective source is the slit, behind which may be positioned either of two sources previously mounted on the holder. One of them is usually polonium (Po^{210}), used as the standard for energy measurements. An externally operated shutter covers the slit to end the exposure.

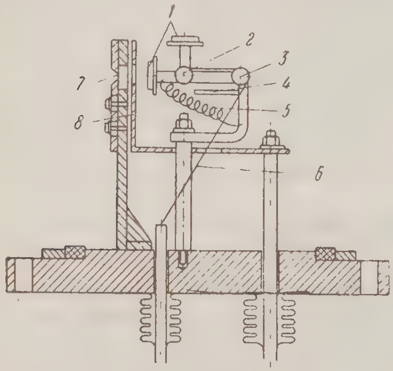

Fig. 9. Source-holder assembly: 1) sources, 2) rotating stand, 3) pulley, 4) stop, 5) spring, 6) wire, 7) slit, 8) shutter.

α-Particle Detectors

At present we are using photographic plates to record the α-particles. These have advantages over counters in that the spectrum can be investigated simultaneously over a large energy range, rather than point by point (in our spectrometer the recording range is 5 per cent of the energy of the α-particles being studied). The best α-sensitive material is A2 NIKFI plates. After immersion in a 10% glycerin solution and drying, the plates may be safely stored in vacuum (10^{-4} mm Hg) for two weeks.

Five 45 x 50 mm plates are loaded into the cassette at an angle of 45° to the direction of the α-particles. A mechanism controlled from the exterior makes it possible to expose any one of the five plates. Usually the substance being investigated is exposed on one plate and the standard on another.

The plates are processed in an amidol developer. After processing the plates are examined on an MBI02 microscope. The examination is usually made at a magnification of 400X in 0.2 mm-wide strips. Due to the fact that only those tracks are registered which have the correct angle of entry into the emulsion and a length and thickness in the set interval, the background is quite low.

The MBI-2 microscope is equipped with a special small motor that translates the plate in the slit direction. The eyepiece has a cross-hair. When an α-particle track comes under the cross-hair, the observer presses a button switch, which sends a pulse to the particle register and stops the motion of the plate. Travel of the plate resumes when the button is released. Experience has shown that this simple device reduces the number of errors and increases the speed of processing the plates. The complete scanning of a plate takes from 15 to 20 hours.

Calibration of the Photographic Plates

The intensity and shape of a line vary somewhat, depending on the location of the peak on the plate.

In order to process the results properly it is necessary to know the energy equivalent of a millimeter on the photographic plate and the dependence of the line shape and intensity on the coordinates of the peak.

For purposes of calibration the polonium α-line was moved to different points on the photographic plate by varying the magnetic field. It was discovered that the "transmission" of the instrument was maximal at the center of the plate and decreased towards the edges (by about 10%).

The following empirical expression was deduced for the energy of a line displaced from the center of the plate:

$$E = E_c\left[1 + (0.954 + 5.4\cdot10^{-4}x)10^{-3}x\right],$$

where E is the line energy, E_c is the energy corresponding to the center of the plate and x is the distance of the center of the line peak from the center of the plate in millimeters.

Use of this empirical formula makes it possible to determine the energy of unknown α-lines with reference to the standard with great accuracy. For example, the energy of the principal α-group of Pu^{239}, as determined from a series of three measurements, was found to be 5147.4 ± 0.3 kev (the uncertainty in the energy of the α-particles from the standard is not included in the possible error).

Processing the Results

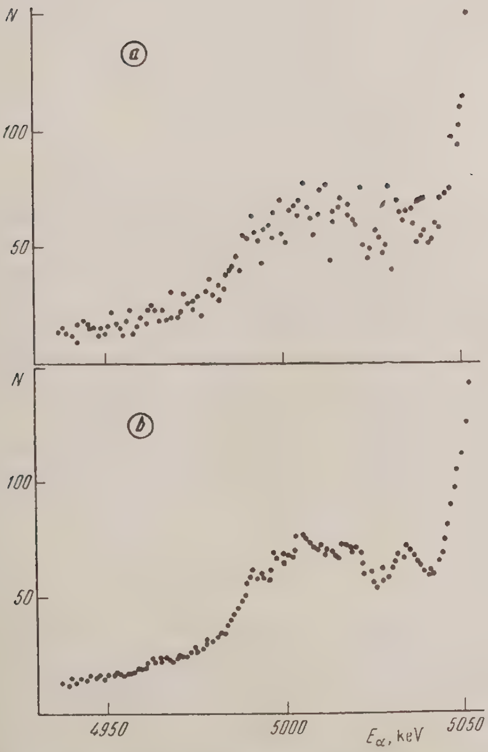

Fig. 10. The Pu^{240} α-spectrum in the 5 Mev region: a) before averaging, b) after averaging.

The energy and intensity of the α-lines were calculated from graphs on which the number of tracks in each strip were plotted as a function of the coordinates on the photographic plate.

In dealing with weak lines, the method of processing proved to have an appreciable influence on the accuracy and reliability of the results. Weak lines often contain 10-20 tracks per 0.2 mm wide strip with a background of 50-80%. Statistical fluctuations make the ordinary graphs of little value.

In order to facilitate the processing, we usually average the results, plotting the sum of the number of tracks in five or seven neighboring strips, rather than the number in the single strip corresponding to the given coordinate. The statistical spread is considerably reduced and the line peaks appear more clearly. This method is based on the following considerations. The only significant irregularities in the curve are those having a width equal to that of the principal peak. Thus it is legitimate to average over a number of strips small in comparison with the number of strips fitting into the line width (this averaging is equivalent to observing the α-line using a counter with a wide slit, successively moved by 1/5 or 1/7 of its width). In this case the extreme scatter or deviation of one or several points, after averaging, does not acquire the character of a peak. Provided the above condition regarding the number of totaled strips is satisfied, decreasing the statistical spread by averaging is definitely helpful.

By way of illustration, the α-spectrum of Pu^{240} in the 5 Mev region is shown in Fig. 10, before and after averaging.

In conclusion the authors gratefully acknowledge the help of I. I. Agapkin in adjusting the spectrometer.

References

1. N.Svartholm & K.Siegbahn, Ark. Mat., Astron. of Fys., 33A, 4, 21 (1947).
2. L.Gol'din, Thesis, 1953.
3. L.L.Gol'din, E.F.Tret'iakov & G.I.Novikova, Sessiia Akademii Nauk SSSR po mirnomu ispol'zovaniiu atomnoi energii. Zasedaniia OFMN (Session of the USSR Ac. of Sc. on the Peaceful Uses of Atomic Energy. Meetings of the OFMN), M.-L. 1955.

HIGHEST ROTATIONAL LEVELS OF CERTAIN NUCLEI. INTENSITY OF α-DECAY TO EXCITED ROTATIONAL LEVELS

- L.L.Gol'din, G.I.Novikova & E.F.Tret'iakov

Introduction

As is now well known, the lower energy levels of heavy nuclei for which the nucleon shells are far from closed, are rotational in character. The excitation energy for these levels is defined for even-even nuclei by

$$E_{\text{rot}} = \frac{\hbar^2}{2J} I(I+1) \tag{1}$$

and for odd nuclei by

$$E_{\text{rot}} = \frac{\hbar^2}{2J} [I(I+1) - I_0(I_0+1)], \tag{2}$$

where I is the nuclear spin in the given excited state, I_0 is the nuclear spin in the lowest state of the given rotational band, and J is the effective nuclear moment of inertia.

Rotational levels are clearly evidenced in α-decay. Until recently, however, no one succeeded in detecting more than three levels belonging to a single rotational band. Finally, in 1955, five α-lines associated with transitions to the levels of a single rotational band were observed in Am^{241} (Ref. 1).

It is of interest to determine at what excitation energies rotational lines of nuclei appear.

Recently attempts have been made to calculate the intensity of α-transitions to rotational levels. Bohr, Fröman & Mottelson[2] proposed the following expression for calculating the α-decay intensities for the α-lines of odd elements:

$$P = P_0(Z, E) \sum_{l=I-I_0}^{I+I_0} C_l \, | C_{II_0;\, l0}^{I_0 I_0} |^2, \tag{3a}$$

$$\lg P_0(Z, E) = C(Z) - \frac{D(Z)}{\sqrt{E}}, \tag{3b}$$

where P is the probability for α-decay to the given level, l is the angular momentum carried off by the α-particle, and the $C_{II_0;\, l0}^{I_0 I_0}$ are Clebsch-Gordan coefficients. Equation (3b) takes account of the dependence of the α-decay probability on the energy; C and D are parameters weakly dependent on Z and have been tabulated by the cited authors.[2] The quantities give the probability of α-emission with angular momentum l. They must be calculated on the basis of α-decay data of neighboring even-even nuclei.

Landau[3] has shown that for strongly elongated nuclei, for which practically all the α-particles are emitted into a narrow region near the major semi-axis, a simple expression may be used to give the relative intensities of α-decay to rotational levels. For even-even nuclei this expression is of the form:

$$P = C(2I+1) \exp\{-\alpha I(I+1)\}. \tag{4}$$

Here C is a normalizing factor, and α is a constant determined from experiment, which can be theoretically related to the dimensions and the degree of ellipticity of the nucleus. Landau asserts that equation (4) can be extended to odd nuclei. The Clebsch-Gordan coefficients do not enter into the expression.

Ter-Martirosian suggests a different formula for the intensity of α-decay of odd nuclei:

$$P = C \sum_{l=I-I_0}^{I+I_0} | C_{II_0;\, l0}^{I_0 I_0} |^2 (2l+1) \exp\{-\alpha_1 I(I+1) - \alpha_2 l(l+1)\}. \tag{5}$$

Here C is a normalizing constant, and α_1 and α_2 are experimentally determinable constants; the rest of the notation is the same as above. (See Ref. 5 for a more detailed discussion of these questions.)

In equation (5) the energy dependence of the probability of α-decay is given in terms of the parameter α_1, whereas in equation (3) it is assumed to be known. Actually, there is nothing to indicate that the intensity of α-decay to the levels of a rotational band has the same energy dependence as the decay-intensity to the ground states of different nuclei.

Equations (4) and (5) do not purport to describe high angular momentum α-emission with any accuracy, since they are deduced on the basis of approximations and contain only the first terms of the series in I and l.

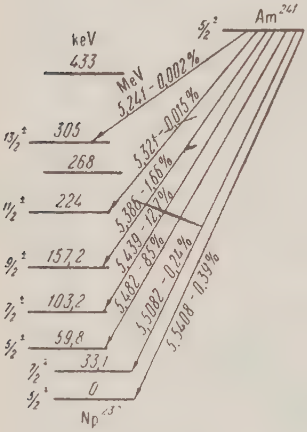

Fig. 1. α-Decay scheme for Am^{241} and the levels of Np^{237}.

It is clear from the above that it is of great interest to investigate as many levels as possible, belonging to a single rotational band.

We have investigated the fine structure of the Am^{241}, Pu^{240} and U^{233} α-spectra and compared the results with theory.

Experimental Part

We measured the α-spectra of Am^{241}, Pu^{240} and U^{233} on a precision magnetic α-spectrometer[1,4] with a resolution of 7.5 kev and a transmission factor of $2 \cdot 10^{-4}$ of 4π.

We determined the energies and intensities of seven lines in the Am^{241} α-spectrum. Definite values for the spins and parities have been assigned to all the Np^{237} levels resulting from α-decay of Am^{241}. These results have been published in Ref. 1. The α-decay scheme for Am^{241} and the levels of Np^{237} are shown in Fig. 1.

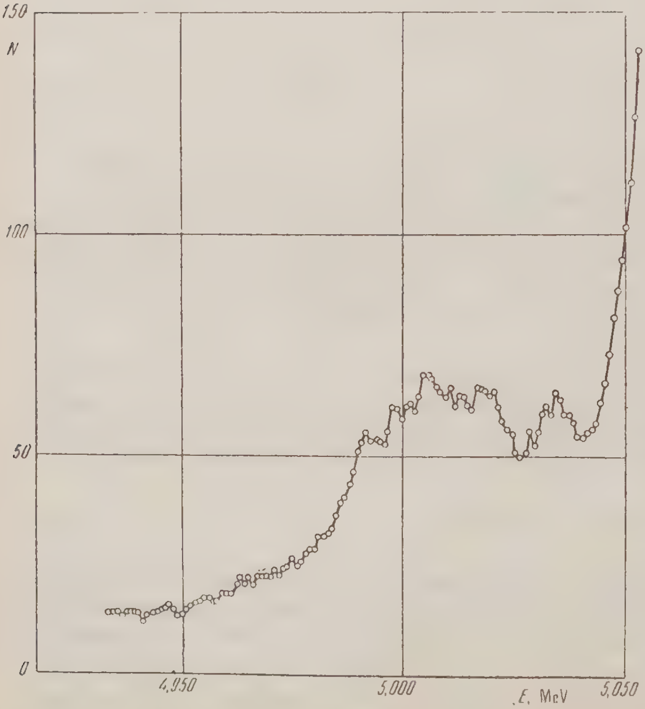

Fig. 2. α-Spectrum of Pu^{240} in the 5 Mev region (N is the averaged number of counts).

The Pu^{240} spectrum was investigated using a source consisting of 17% Pu^{240} and 79% Pu^{239}. In order to reduce statistical errors to a degree sufficient for detection of intermediate weakly excited levels, a thick source ($\sim$50 μg/cm^2) was used. The spectrum was measured for 100 hours with the slit and diaphragm of the spectrometer widened. The section of the spectrum in the 5 Mev region is shown in Fig. 2. A group of α-particles with an energy of 5.004 Mev and an intensity of 0.085 ± 0.015% associated with a transition to the second excited level of U^{236}, is clearly discernible. This level was first observed by Asaro and Perlman[6], but the transition intensity they give is only approximate, with no indication of the probable error.

The α-decay of Pu^{240} to the first excited level is familiar in

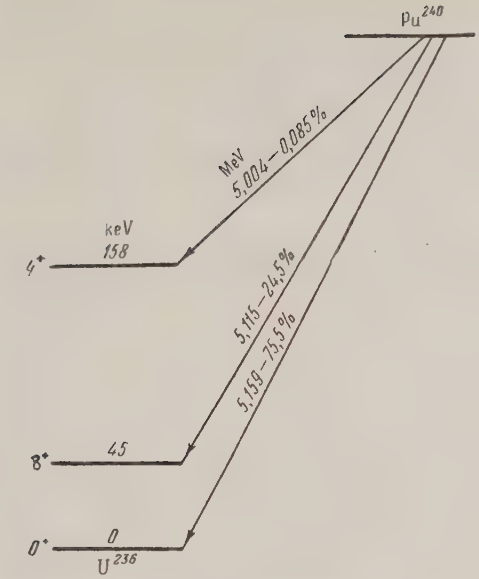
Pu^{240}
MeV
5,004—0,085%
keV
158
4$^+$
5,115—24,5%
5,159—75,5%
45
2$^+$
0
0$^+$
U^{236}

Fig. 3. α-Decay scheme for Pu^{240} and the levels of U^{236}.

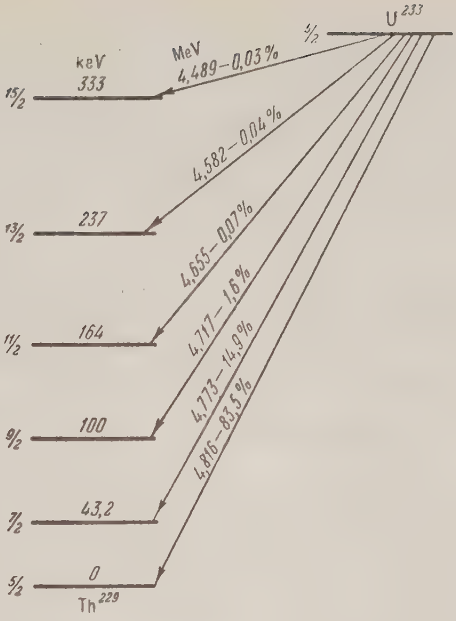
U^{233}
5/2
MeV
4,489—0,03%
keV
333
15/2
4,582—0,04%
237
13/2
4,655—0,07%
164
11/2
4,717—1,6%
100
9/2
4,773—14,9%
43,2
7/2
4,816—83,5%
0
5/2
Th^{229}

Fig. 5. α-Decay scheme for U^{233} and the levels of Th^{229}.

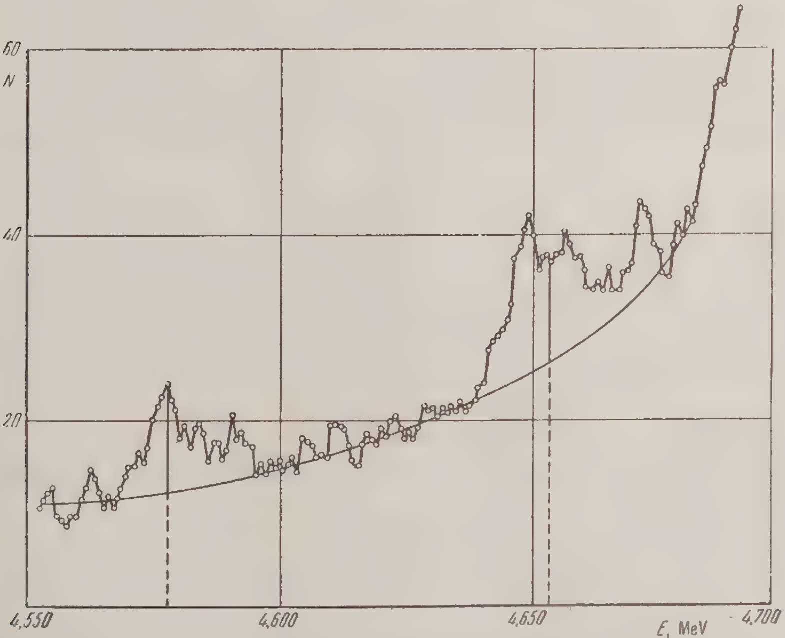

Fig. 4. α-Spectrum of U^{233} in the region near 4.6 Mev (N is the averaged number of counts).

the literature[7,1]. Fig. 3 shows the α-decay scheme for Pu^{240} and the level scheme for U^{236}. The equal parities of the levels, the systematic sequence of spins, and the ratios of the excited level energies are in full conformity with rotational transition rules for even-even nuclei.

We were not able to observe the 6$^+$ level, since the energy of the associated α-line is identical with that of the principal group of α-particles from Pu^{241}, an appreciable amount of which was present in our source.*

The main lines of the U^{233} α-spectrum are well known. Previously[1], in addition to the intense α-lines of energy 4.8157 Mev (83.5%), 4.7732 Mev (14.9 %), 4.7174 Mev (1.6%), the present authors have noted the presence of a weak

---

*Note added in proof: The 6$^+$ level of Pu^{240} was observed by L.M.Kondrat'ev, G.I.Novikova, Iu.P.Sobolev and L.L.Gol'din with a source containing 88% Pu^{240}, after presentation of the report at the Conference. Their article will be published in Zhur. eksp. i teor. fiz. (JETP), 31, No. 11, 1956).

4.489 Mev line (0.03%). In the present work we carefully investigated the region between the 4.7174 and 4.489 Mev lines. The experiments were performed using a source made by the electrolytic deposition of uranium on platinum from an alcohol solution of uranyl nitrate. As in the Pu^{240} experiments, we had to use a thick source and widen the entrance slit of the instrument (to 4 mm). Several exposures were made, each of which extended over about two weeks.

One of the spectra is shown in Fig. 4. In it can be seen the α-lines associated with transitions to the 164 kev (0.07 ± 0.04%) and 237 kev (0.04 ± 0.02%) levels.

Combining these results with those obtained earlier[1], we obtain the decay scheme shown in Fig. 5. The spin of the ground state of Th^{229} is 5/2. The level energies are in good agreement with equation (1):

the theoretical energy ratios are

$$1:2.28:3.86:5.72:7.85$$

and the experimental ones are

$$1:2.3:3.8:5.5:7.7.$$

Thus the rotational nature of the levels is definitely established; the excited states must be assigned the same parity and monotonically increasing spins: 5/2, 7/2, 9/2, 11/2, 13/2 and 15/2. The transition from the ground state of U^{233} (spin 5/2) to the 15/2 level is associated with α-particles which carry away an angular momentum $l \geqslant 6$. There has not previously been described in the literature any case with so complex a system of rotational levels.

Discussion of the Results

It is of interest to compare the α-line intensities for even-even nuclei with equation (4).

We undertook such a comparison for Pu^{240}, since the α-line intensities in the spectrum of this nucleus were measured with good accuracy. Selecting a value of 0.46 for α in equation (4), we find that the line intensities should be related as

$$1:5\cdot e^{-6\cdot 0.46}:9\cdot e^{-20\cdot 0.46}=1:0{,}32:0{,}9\cdot 10^{-3},$$

whereas experiment gives $1:0.32:1.1\cdot 10^{-3}$. In view of the approximate character of the theory, the agreement is surprisingly close.

In comparing equation (4) with experiment we must bear in mind that a deviation in the intensity of the α-line from decay to the 4^+ level even by as much as by a factor of 2 or 3 should not be considered in serious disagreement with theory.

Let us now turn to the α-decay of Am^{241} (Fig. 1).

The rotational band starts from the 59.8 kev level. The intensity of the successive α-lines should be in the ratio

$$1:0.15:1.9\cdot 10^{-2}:1.8\cdot 10^{-4}:2.5\cdot 10^{-5}.$$

The α-decay to the fundamental level of the rotational band is well described by equation (3b), i.e., according to the terminology of Bohr, Fröman and Mottelson[2], this is a favored transition. In such transitions, the spin and parity do not change[2]. Since the spin of the fundamental state of the rotational band[8] is 5/2, all the transitions involve α-particles which carry away three different even angular momenta: 0, 2 and 4 for the first level (59.8 kev); 2,4 and 6 for the second and third levels; and 4, 6 and 8 for the fourth and fifth levels.

Let us perform a comparison with equations (3). The coefficients C_l should be chosen on the basis of the α-decay of even-even nuclei. Bohr et al[2] recommend a value of 0.72 for C_2 and a value of 0.01 for C_4 in the case of Am^{241}. The values of C_6 and C_8 are not known; we shall set them equal to zero, which should not result in any appreciable error, since the contribution due to high angular momenta is small.

With the above assumptions, equations (3) give the following values for the successive α-line intensities:

$$1:011:1.6\cdot10^{-2}:1.5\cdot10^{-4}:1.3\cdot10^{-5}$$

which is in good agreement with experiment.

Even better agreement with experiment may be obtained from equation (5): taking $\alpha_1 = 0.050$ and $\alpha_2 = 0.364$ the α-line intensity ratios become

$$1:0.12:2.1\cdot10^{-2}:2.1\cdot10^{-4}:2.9\cdot10^{-5}.$$

Equation (4) gives

$$1:0.5:1.2\cdot10^{-2}:4.4\cdot10^{-4}:0.9\cdot10^{-5}.$$

This is in somewhat worse agreement with experiment, but, on the other hand, the expression is simpler and contains only one parameter to be determined by experiment.

Summing up, it must be acknowledged that the α-line intensities of Am^{241} vary in a regular way and are well described by several formulas. The experimental data does not allow of making a definitive choice between them. Such uniform agreement, however, is not always obtained.

Let us consider the two lowest levels of Np^{237} (Fig. 1): the first excited level at 33.1 kev is usually regarded as a rotational satellite of the ground level[9]; both these levels have a parity opposite to that of the Am^{241} ground state. Therefore only α-particles with odd angular momenta take part in the α-decay. The predominant role in both the transition to the ground level and that to the 33.1 kev level must be played by α-particles carrying away an angular momentum $l = 1$. Let us retain only the one term of the sum, corresponding to $l = 1$, in equations (3) and (5); then the relative intensities for decay to these levels should satisfy the relation

$$\frac{P_{33.1}}{P_0} < \frac{\left| C^{\,{}^5\!/_2\;{}^5\!/_2}_{\,{}^7\!/_2\,{}^5\!/_2,\;10} \right|^2}{\left| C^{\,{}^5\!/_2\;{}^5\!/_2}_{\,{}^5\!/_2\,{}^5\!/_2,\;10} \right|^2} = 0{,}3.$$

The experimental value for this ratio is 0.61.

There is thus significant disagreement with equations (3) and (5). Equation (4), which does not contain Clebsch-Gordan coefficients, does not conflict with the observed intensities. In order to arrive at more definite conclusions, however, it would be necessary to show more convincingly that the 33.1 kev level is actually a rotational satellite of the ground state.

Let us now consider U^{233}. The successive α-line intensities are related as

$$1:0.18:1.9\cdot10^{-2}:8\cdot10^{-4}:5\cdot10^{-4}:3.5\cdot10^{-4}.$$

The rapid and regular variation of the intensities of the first four lines becomes very weak for the succeeding ones. It is not difficult to describe the intensities of the first four lines by any one of the suggested theoretical equations. This can be shown by comparing the α-line intensities for U^{233} and Am^{241}. At the same time, none of the equations can explain the "plateau" for the last lines. It may be connected with the fact that the deviations from the theory which, as has already been mentioned, must necessarily be observed for the higher energy levels, are for some reason particularly pronounced in the case of U^{233}.

Conclusions

The experimental data now being accumulated should make it possible to test the theoretical descriptions of the α-line intensities belonging to a single rotational band. It is no less important to find the relation between the experimentally determined constants entering the descriptive equations and the geometrical nuclear parameters.

On the basis of a careful examination of the α-spectra of Pu^{240}, Am^{241} and U^{233} we have attempted the first comparison of the available theoretical equations with experiment. Equation (4), proposed by L.D.Landau, makes it possible to give a good description of α-decay intensities to various levels, at least for even-even nuclei. For odd nuclei, the picture remains cloudy.

The authors express their gratitude to L.D.Landau and K.A.Ter-Martirosian, who participated in discussions of the results, and to I.I.Agapkin, G.I.Grishuk and L.N.Kondrat'ev for their aid in carrying out the experiments.

References

1. L.L.Gol'din, E.F.Tret'iakov & G.I.Novikova, Sessiia Akademii Nauk SSSR po mirnomu ispol'zovaniiu atomnoi energii Zasedaniia OFMN (Session of the USSR Ac. of Sc. on the Peaceful Uses of Atomic Energy. Meetings of the OFMN), M.-L. 1955.
2. A.Bohr, P.Fröman & B.Mottelson, Dan. Mat. Fys. Medd., 29, 10 (1955).
3. L.D.Landau, Report at the Fourth Conference on Nuclear Spectroscopy in Moscow, January 1956.
4. L.L.Gol'din & E.F.Tret'iakov, Preceding article in the present issue of the Bulletin.
5. L.L.Gol'din, L.K.Pekar & G.I.Novikova, Usp. fiz. nauk, 59, 459 (1956).
6. I.Perlman & F.Asaro, Ann. Rev. Nucl. Sci., 4, 157 (1954).
7. F.Asaro & I.Perlman, Phys. Rev., 88, 828 (1953).
8. F.Asaro & I.Perlman, Phys. Rev. 93, 1423 (1954).
9. H.Jaffe, T.Passel, C.Browne & I.Perlman, Phys. Rev., 97, 142 (1955).

ON THE α-DECAY OF Np^{237}

- L.N.Kondrat'ev, G.I.Novikova, A.M.Vorob'ev
and L.L.Gol'din

Until very recently the α-spectrum of Np^{237} (half-life for α-decay $2.2 \cdot 10^6$ years) has remained virtually unknown. This is explained by the long lifetime of the isotope and the difficulty in obtaining it.

Np^{237} is the daughter nucleus of the α-emitter Am^{241}, whose α-spectrum is well known[1] and indicates the existence of a system of rotational levels in Np^{237}, mounting from a level at about 60 kev. Transitions from Am^{241} to the ground and first excited states of Np^{237} (33 kev) are realized by weak α-groups whose intensities are 0.39 and 0.24%, respectively, while the transition to the fundamental level of the rotational band has an intensity of 85%.

It has been noted in the literature[2] that α-decay of Np^{237} is attended by strong 87 kev γ-radiation, and the suggestion has been made that the most intense Np^{237} α-decay takes place, as for Am^{241}, not to the ground, but to an excited level of its daughter nucleus. For this reason it is of interest to examine the Np^{237} α-spectrum and to compare it with that of Am^{241}.

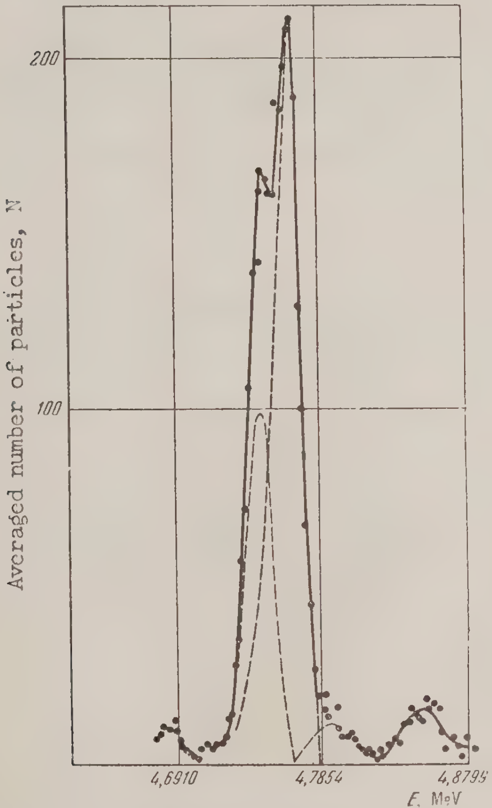

Np^{237} α-spectrum in the 4.8 Mev region.

The long lifetime of Np^{237} made use of a highly pure source imperative.

The neptunium was separated from plutonium by sublimation of the tetrachloride. Additional purification was carried out by means of a two-stage oxidizing-reducing cycle. Potassium bromate was used as the oxidizing agent.[3] The Pu^{239} content in the sample was 1.8% by activity, or 0.02% by weight. The total content of other impurities was under 0.01%. Neptunium chloride, obtained by dissolving neptunium peroxide in hydrochloric acid, was evaporated onto a glass plate under vacuum from a tantalum wire. Several exposures were made, each of which lasted about a week. A section of one of the Np^{237} α-spectra in the 4.8 Mev region is shown in the accompanying figure. The measurements were made on the magnetic α-spectrometer of the USSR Academy of Sciences.

The energy of the principal (54%) peak, determined with reference to Po^{210}, was found to be 4.781 ± 0.002 Mev. (The Po^{210} α-particle energy was taken as 5.2984 Mev.)

The results of the investigation of the Np^{237} α-spectrum are presented in the table on the following page.

A group of α-lines in the 4.643 Mev region was not resolved.

Let us compare the α-spectra of Np^{237} and Am^{241}. In both the most intense groups of α-particles correspond to transitions to the second excited level. Transitions to the ground and first excited levels in the Np^{237} α-spectrum are an order of magnitude more intense than in the Am^{241} α-spectrum. Whereas in the Am^{241} α-decay, the most intense transition is to the fundamental level of a wide rotational band, there is no indication that the excited levels of Np^{237} are rotational in character. For a nucleus as heavy as Np^{237} this is unexpected.

Table

Line	Line energy difference, kev	Line energy, kev	Intensity, %
α_o	---	0	2.5 ± 0.5
α_{64}	62.7	63.7 ± 5	3.4 ± 1
α_{86}	84.6	86.0 ± 2	54 ± 4
α_{105}	103.8	105.5 ± 3	29.5 ± 4
α_{166}	163.7	166.5 ± 3	2.3 ± 1
Group of lines	221	225 ± 10	8.3 ± 1

After our work was basically complete, there appeared a short communication[4] on the Np^{237} α-spectrum in the Bulletin of the American Physical Society. The spectrum was presumably measured by means of an ionization chamber. Nine separate lines in the Np^{237} α-spectrum are listed: 4.872 Mev (3.1%), 4.816 Mev (3.5%), 4.787 Mev (53%), 4.767 Mev (29%), 4.713 Mev (1.7%), 4.674 Mev (3.3%), 4.644 Mev (6.0%), 4.589 Mev (0.5%) and 4.52 Mev (0.02%). No experimental details are given.

Owing to its extreme weakness, we could not have detected the last line mentioned by the Americans. Three lines (4.674, 4.644 and 4.589 Mev) correspond to our unresolved "4.643 Mev" peak. The values for the remaining lines are in good agreement with our measurements.

In conclusion we gratefully acknowledge the aid given us by E.F.Tret'iakov, I.I.Agapkin, and G.I.Grishuk.

References

1. L.L.Gol'din, E.F.Tret'iakov & G.I.Novikova, Sessiia Akademii Nauk SSSR po mirnomu ispol'zovaniiu atomnoi energii Zasedaniia OFMN (Session of the USSR Ac. of Sc. on the Peaceful Uses of Atomic Energy. Meetings of the OFMN), M.-L. 1955.

2. D.Engelkemeir & L.Magnusson, Phys. Rev., 94, 1395 (1954).

3. I.Shvetsov & A.Vorob'ev, Reports of the Soviet Delegation at the International Conference on the Peaceful Uses of Atomic Energy. Investigations in the fields of geology, chemistry & metallurgy, M.-L.1955.

4. L.Magnusson, D.Engelkemeir, M.Freedman, F.Porter & F.Wagner, Bull. Am. Phys. Soc., 30, 7, 10 (1955).

INTERNAL CONVERSION ELECTRON SPECTRUM OF THE DEPOSIT FROM RaTh I

(In the $H\rho$ = 2600-10,300 gauss-cm region)

- E.M.Krisiuk, A.D.Vitman, V.D.Vorob'ev, G.D.Latyshev & A.G.Sergeev

This work was undertaken to obtain more accurate intensity and energy values for the conversion lines of the active deposit of RaTh.

Introduction

There are now a number of studies[1-6] in which the absolute values of the energy for several of the more intense conversion lines in this spectrum were determined with good accuracy (in the latest works[3-5], the relative error is of the order of 10^{-4}). These lines, specifically the A, B, F, I, L and X-lines (Ellis' notation[7]), are used as standards in β-spectroscopy for energy calibration of spectrometers. The accuracy with which energy values of the other conversion lines (and at present about 100 of them) are known is much lower. We felt it important to determine with greater accuracy the energies of all the lines of the conversion spectrum, since this would make it possible to determine the energies of the nuclear excited levels with higher precision (to within about 1 part in 10^4).

It is also of importance to know the number of conversion electrons per decay and, therefore, in carrying out this investigation we paid particular attention to accurate determination of the relative line intensities.

The measurements were performed on a magnetic spectrometer with improved refined focusing[8] at a resolution of 0.25%. The angle subtended by the spectrometer in the focal plane is 40°; the height of the diaphragm is 16 mm; the source slit and that in front of the first GM counter have dimensions 0.3 x 16 mm. The magnetic field was measured by the method of proton magnetic resonance.[9] The electrons were recorded by two self-quenching GM counters connected in coincidence. The results of the measurement are summarized in the table below. Figures 1 to 10 show the results of one of the five series of conversion line measurements (also see Fig. 3 in Ref. 10).

Sensitivity of the Method

Measurements of the internal conversion electron spectrum of the active deposit from RaTh have been made by Ellis[7,11] and Surugue[12,13] on a homogeneous magnetic field spectrometer with registration on a photographic plate. Flammersfeld[14], as well as Martin and Richardson,[17] measured this spectrum using GM counters to record the electrons.

A characteristic of the photographic plate method is its high sensitivity. Ellis was able to detect conversion lines having intensities only $7 \cdot 10^{-5}$ the intensity of the strongest line (the F-line). Surugue achieved a relative intensity of $5 \cdot 10^{-4}$. A shortcoming of the photographic plate method is the poor reliability of the line intensity determinations due to the necessity of introducing corrections for the spectral sensitivity of the photographic plates and for the dependence of the blackening on the radiation intensity. The use of counters to record the electrons makes it possible to determine the line intensity more accurately, though the sensitivity of the method is usually much lower.

Flammersfeld detected lines whose intensity was $3 \cdot 10^{-3}$ that of the F-line.

The use of the spectrometer with enhanced focusing made it possible to increase the sensitivity of the counter method: we were able to observe conversion lines whose intensity was only $7 \cdot 10^{-5}$ that of the F-line. Thus the sensitivity in our experiments was equal to that attained by Ellis and two hundred times better than that of Flammersfeld. However, the toilsomeness of the measurements precluded searching for new lines; we had to restrict our efforts to refining

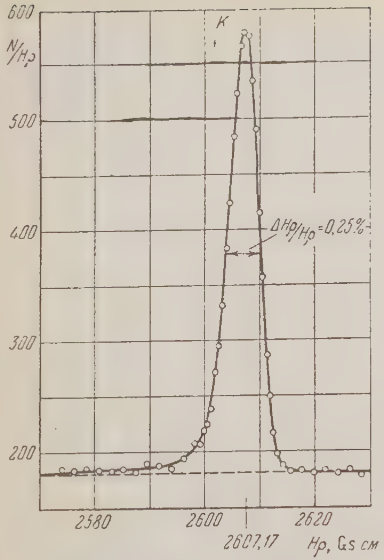

Fig. 1. L-line (the shape of this line was taken as the standard.

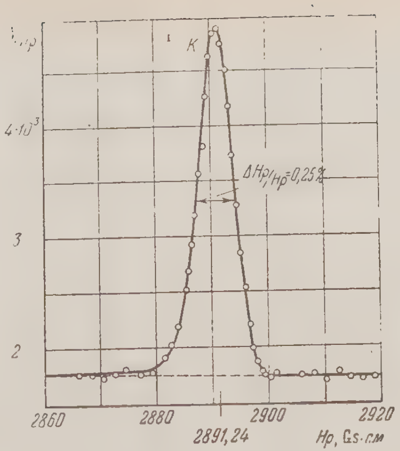

Fig. 2. M-line (this line is complex, but no broadening, within the limits of the experimental error, was observable).

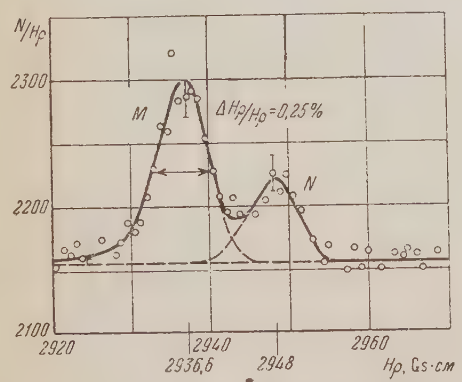

Fig. 3. Ma-line (this line was resolved into two).

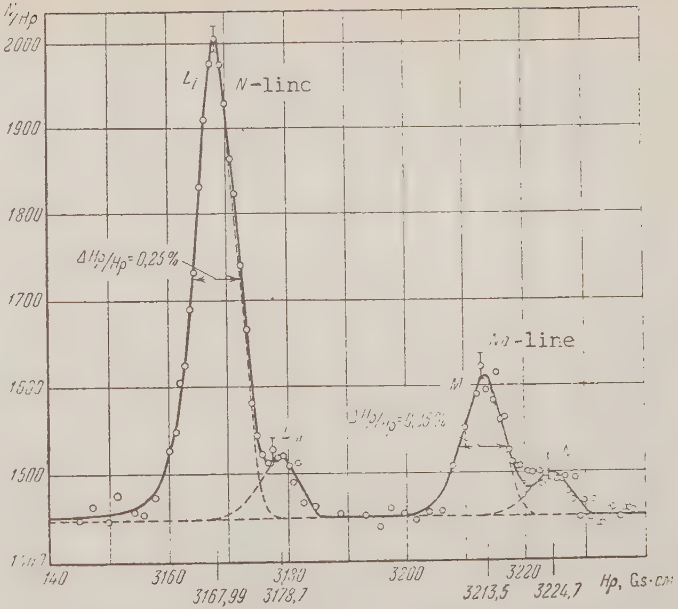

Fig. 4. N- and Na-lines (both lines were resolved into two).

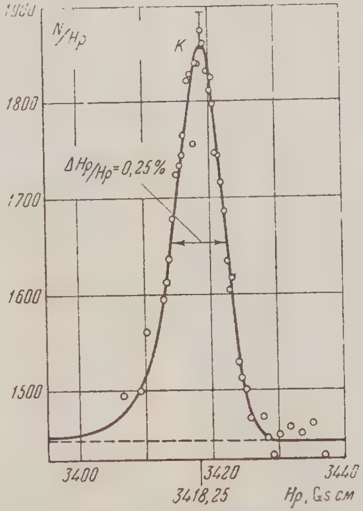

Fig. 5. O-line.

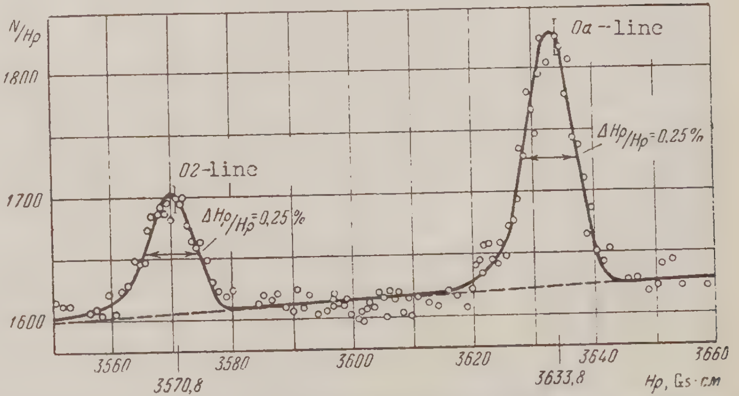

Fig. 6. O2- and Oa-lines (the O3-line, reported between these, was not detected in the present work).

Conversion spectrum of active deposit from radiothorium
($H\rho$ = 2600-10,300 gauss-cm region)

Designation according to Ellis	Our data								Ellis		Surugue		Flammersfeld		Martin & Richardson	
	$H\rho$	E, keV	Transition	Z	Level	E_γ, keV	I	$P\cdot\alpha\cdot10^2$	$H\rho$	I	$H\rho$	I	I	$P\cdot\alpha\cdot10^2$	I	$P\alpha\cdot10^2$
1	2	3	4	5	6	7	8	9	10	11	12	13	14	15	16	17
L	2607,17	422,84	$C''D$	82	*K*	510,84	1,000	0,612	2603,1	1,00	2607	1,0	1,00	0,76	1,000	0,688
M	2891,24	495,20	$C''D$ $C''D$	82 82	*L* *K*	511 583	0,888	0,544	2886,6	1,00	2891	1,0	0,78	0,59	0,897	0,617
Ma	2936,6	506,94	$C''D$	82	*M*	510,79	0,043	0,026	2934,6	0,03	2938	<0,07	—	—	—	—
	2948,0	509,9	$C''D$	82	*N*	511	0,016	0,010	—	—	—	—	—	—	—	—
*Ma*1	—	—	—	—	—	—	—	—	3033,3	—	3026	<0,07	—	—	—	—
N	3167,99	567,50	$C''D$	82	$L_{I}+L_{II}$	583,36	0,186	0,114	3163,7	0,18	3169	0,21	0,16	0,12	—	—
	3178,7	570,3	$C''D$	82	L_{III}	583	0,021	0,013	—	—	—	—	—	—	—	—
Na	3213,5	579,54	$C''D$	82	*M*	583,39	0,057	0,035	3210,4	0,04	3215	<0,07	—	—	—	—
	3224,7	582,5	$C''D$	82	*N*	583	0,018	0,011	—	—	—	—	—	—	—	—
O	3418,25	634,12	CC'	84	*K*	727,22	0,113	0,069	3415,2	0,18	3420	0,14	0,113	0,086	0,113	0,078
*O*1	—	—	—	—	—	—	—	—	3530,8	0,02	3539	<0,07	—	—	—	—
*O*2	3570,8	675,23	—	—	—	—	0,030	0,018	3566,1	0,02	3567	<0,07	—	—	—	—
*O*3	—	—	—	—	—	—	—	—	3594,1	0,006	3613	<0,07	—	—	—	—
Oa	3633,8	692,29	—	—	—	—	0,055	0,034	3629,0	0,06	3623	0,07	—	—	—	—
*Oa*1	3701,4	710,66	CC'	84	*L*	727,61	0,026	0,016	3700,1	0,02	3713	<0,07	—	—	—	—
*Oa*2	3748,7	723,3	CC'	84	*M*	727,4	0,005	0,003	3741,1	0,01	3753	<0,07	—	—	—	—
*Oa*3	—	—	—	—	—	—	—	—	3875,9	—	3895	<0,07	—	—	—	—
P	3927,13	772,46	$C''D$	82	*K*	860,46	0,160	0,098	3924,4	0,18	3931	0,14	0,113	0,086	0,142	0,098
Pa	4028,3	800,33	—	—	—	—	0,015	0,009	4010,7	0,01	4014	<0,07	—	—	—	—
*Pa*1	4188,2	844,61	$C''D$	82	*L*	860,47	0,028	0,017	4194,1	0,006	4199	<0,07	—	—	—	—
*Pa*2	4232	856,8	$C''D$	82	*M*	860,6	0,006	0,004	4224,8	0,006	4228	<0,07	—	—	—	—
*Pa*3	—	—	—	—	—	—	—	—	4272,4	—	4279	<0,07	—	—	—	—
X	9986,9	2526,33	$C''D$	82	*K*	2614,33	0,101	0,062	10000	0,21	10016	0,1	0,104	0,079	0,097	0,067
Xa	10231,1	2598,51	$C''D$	82	*L*	2614,37	0,0182	0,011	10260	—	10273	<0,07	—	—	—	—
*Xa*1	10273	2610,8	$C''D$	82	*M*	2614,7	0,0055	0,003	10300	—	10313	<0,07	—	—	—	—

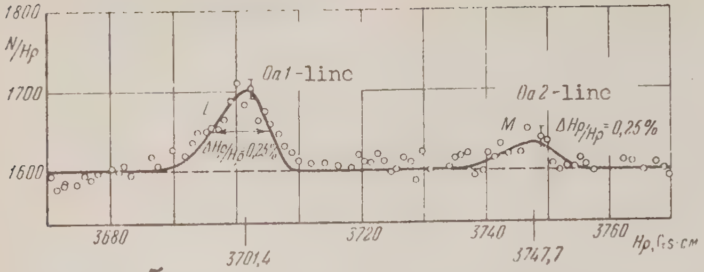

Fig. 7. Oa1- and Oa2-lines (the Oa2-line is at the limit of sensitivity of our spectrometer; the points on the low energy side of the Oa1-line depart from the standard line shape, probably owing to the influence of the L_{III}-line).

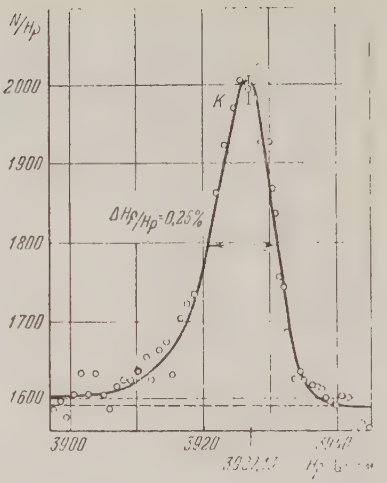

Fig. 8. P-line.

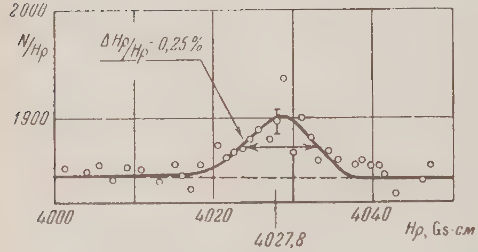

Fig. 9. Pa-line.

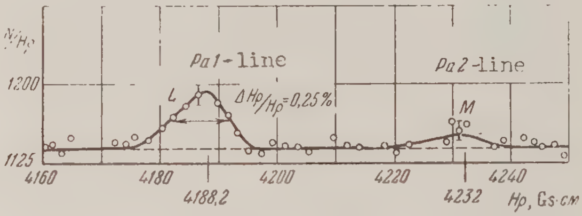

Fig. 10. Pa1- and Pa2-lines (the Pa2-line lies at the sensitivity limit of our apparatus).

the accuracy of the energy and intensity values of the already known lines. The new lines we have discovered are close to already known ones.

We are unable to observe five lines observed by Ellis and Surugue, three of which (Ma1, Oa3, Pa3) are so weak that neither of these authors was able to determine their intensities. It is possible that we were unable to detect them owing to their low intensities. The O3-line, according to Ellis' data, lies at the limit of sensitivity of our apparatus, and the fact that we were not able to observe it (see Fig. 6) would indicate that the intensity given for it by Ellis is an overestimate. The O1-line, according to Ellis' data, is three times stronger than the weakest line detected in our experiments. It may be that our failure to observe it is due to a large error in the $H\rho$ value in the tables of Ellis and Surugue.

Determination of $H\rho$ Values for the Conversion Lines

The instrument was calibrated in energy with reference to the $H\rho$ value for the L-line, which, according to Lindström[3], is 2607.17 ± 0.30 gauss-cm. Using this value, we obtained the $H\rho = 9986.9$ gauss-cm for the X-line on the assumption of strict linearity of the instrument in this region. This value is in very good agreement with Lindström's result for this line: $H\rho = 9986.7 \pm 1.5$ gauss-cm, which substantiates our assumption regarding the linearity of our instrument in this region of Hρ values and characterizes the accuracy of measurement. In addition, using the table for converting Hρ values to energy values and the table of binding energies for atomic electrons given in Siegbahn's book[15,16], it is possible to determine independently the γ-quanta energies from the K, L and M conversion lines. The results agree to within 30-50 ev, which is within the limits of our experimental accuracy. In view of this we may conclude that the relative error in the determination of the Hρ values for the conversion lines is determined primarily by the statistical scatter of the points; for the stronger lines it is of the order of 10^{-4} or less and somewhat greater for the weaker lines.

It is interesting to note that according to the above the absolute error is of the order of several tenths of a Hρ unit, whereas our data differ from those of Ellis and Surugue by several Hρ units on the average.

Determination of the Relative Line Intensities

In order to insure a more accurate determination of the relative intensities of the weak conversion lines, we studied the shape of the recorded strong lines. It turned out that there were no observable differences in the line shapes in the energy region above 100 kev. In view of this we determined the intensity of the weak lines on the basis of the area of the standard line drawn so that the sum of the distances from the points to the line should be equal for the points above and below the line, the sums being taken separately for the front and back edges of the line. In calculating the intensity of the X-line, a correction was made for the penetration of the knife-edges of the counter slit.[10]

The root mean square error, obtained from five series of measurements, was of the order of 1-2% for the strong lines and up to 10-20% for the weak ones. On the other hand, the difference between our results and those of earlier investigations averages 10-20% for the strong lines and 100% and more for the weak ones. The relative intensities of the weak lines are in good agreement with the data of Martin and Richardson[17]. The ninth column of the table gives the number of conversion electrons per ThB decay event. We obtained this figure on the basis of the value we obtained in the work of Ref. 10 for the ratio of the area under the L conversion line to the area of the total β-spectrum of Th(B+C+C''), taking account of the fact that the number of β-particles from Th(C+C'') is 1.106 times the number from ThB.

Department of Physics of
"V.N.Obraztsov" Leningrad Institute
of Railroad Transport Engineers

References

1. K.Siegbahn, Ark. Mat., Astron. og Fys., 30A, 20 (1944).
2. H.Graig, Phys. Rev., 85, 688 (1952).
3. G.Lindström, Phys. Rev., 83, 465 (1951).
4. G.Lindström, Phys. Rev., 87, 678 (1952).
5. D.Meyer & F.Schmidt, Phys. Rev., 94, 927 (1954).
6. K.Siegbahn, Beta- and Gamma-Ray Spectroscopy, p. 98.-Amsterdam, 1955.
7. C.Ellis, Proc. Roy. Soc., A 138, 318 (1932).
8. G.D.Latyshev, A.G.Sergeev, E.M.Krisiuk, L.A.Ostetsov, Iu.S.Egorov & N.M.Shishkov, Izv. AN SSSR, Ser. fiz., 20, 354 (1956). (Translation in Bulletin, Vol. 20, No. 3, p. 324).

9. A.G.Sergeev, G.D.Latyshev & V.D.Leonov, Izv. AN SSSR, Ser. fiz., 20, 369 (1956). (Translation in Bulletin, Vol. 20, No. 3, p. 337).

10. E.M.Krisiuk, A.D.Vitman, V.D.Vorob'ev, I.V.Vorob'ev, K.I.Il'in, G.D.Latyshev, M.A.Listengarten & A.G.Sergeev, Next article in the present issue of the Bulletin.

11. C.Ellis, Proc. Roy. Soc., A 143, 350 (1934).

12. J.Surugue, Ann. Phys., 8, 484 (1937).

13. J.Surugue, J. Phys. et Rad., 9, 438 (1938).

14. A.Flammersfeld, ZS. f. Phys., 114, 227 (1939).

15. K.Siegbahn, Beta- and Gamma-Ray Spectroscopy, p. 926.-Amsterdam, 1955.

16. K.Siegbahn, Beta- and Gamma-Ray Spectroscopy, p. 914.-Amsterdam, 1955.

17. D.Martin,& H.Richardson, Proc. Roy. Soc., A 195, 287 (1948).

INTERNAL CONVERSION OF THE 2615 kev TRANSITION IN Pb^{208}

- E.M.Krisiuk, A.D.Vitman, V.D.Vorob'ev, I.V.Vorob'ev,
K.I.Il'in, G.D.Latyshev, M.A.Listengarten & A.G.Sergeev

Introduction

Pb^{208} (ThD) forms in β-decay of Tl^{208} (ThC"). The Pb^{208} nucleus is produced in an excited state and its transition to the ground state is accompanied by γ-radiation, the highest intensity γ-line (the so-called "X" line[1]) being associated with the transition from the first excited level to the ground state. (Ref. 2 & 3). According to the latest measurements[4] the energy of these quanta is 2615 kev. The K, L and M conversion lines in the ThC"-ThD β-spectrum, which correspond to this γ-transition, are well known[1].

The most careful measurement of the K internal conversion coefficient for this 2615 kev transition was made in 1954 by Elliott et al.[4] They measured separately the number of gammas using a scintillation spectrometer and the number of K conversion electrons by means of a magnetic β-spectrometer, and obtained a value of $\alpha_K = (1.78 \pm 0.12)\cdot 10^{-3}$ for the 2615 kev transition. According to Rose's tables[5] of internal conversion coefficients, the theoretical α_K value for an electric octupole (E3), namely $1.86\cdot 10^{-3}$, lies closest to that obtained by Elliott. The angular correlation between the 2615 and 583 kev cascade γ-rays, also studied by the authors, is consistent only with the 0-3-5 spin assignment for the ground and first and second excited levels.

Thus the 2615 kev transition in Pb^{208} is an E3 transition.

It is interesting to note that the results of Elliott and co-workers are in conflict with many previous determinations of the multipole order of this transition. For a long time it had been accepted that this is an electric quadrupole transition. Various authors came to this conclusion, using different methods of investigation: determination of the internal conversion coefficient[6], measurement of the conversion coefficient with pair production[7,8], determination of the degrees of forbiddenness of β-transitions to various Pb^{208} levels[9], measurement of the γ-γ angular correlation[10], and measurement of the angular correlation and polarization of the gammas[11].

In view of this we undertook new measurements of the K internal conversion coefficient for the 2615 kev transition. We used a method differing somewhat from that of Elliott, and in comparing our experimental results with the theoretical values used the new table of conversion coefficients by L.A.Sliv[12], which were computed taking into account the finite dimensions of the nucleus and are therefore more accurate than Rose's coefficients.*

Instrument

For these measurements we used the Ketron type magnetic spectrometer, described in Ref. 13. The half-width of the conversion lines for the conditions of the experiment was 0.25%. The angle subtended by the instrument (Fig. 1) in the focal plane was 40°; the slit height was 16 mm.

The source was an aluminum foil 5μ thick, measuring 0.3 x 16 mm, activated on one side. The source was suspended from two fine wires exactly at the focus of the Ketron spectrometer. No slit was used in front of the source and all metal parts were moved as far as possible from it, so as to minimize the scattered electron background. Also, to this end, three diaphragms were set up as shown in Fig. 1, and these, together with the tungsten block, separated the spectrometer chamber into four quadrants. The central diaphragm (CD), separating quadrants 2 and 3 along the OY axis, defined the divergence of the electron beam. The two other diaphragms were set up along X-X, the line separating the homogeneous and nonhomogeneous regions of the magnetic field of the Ketron, i.e., between quadrants 1 & 2 and 3 & 4. The apertures in these diaphragms were made somewhat larger than the beam dimensions as defined by the central diaphragm. A 0.3 x 16 mm slit was installed in front of the first counter (C_1) at the focus of the apparatus.

---

*The authors express their gratitude to L.A.Sliv for allowing the use of his table prior to its publication.

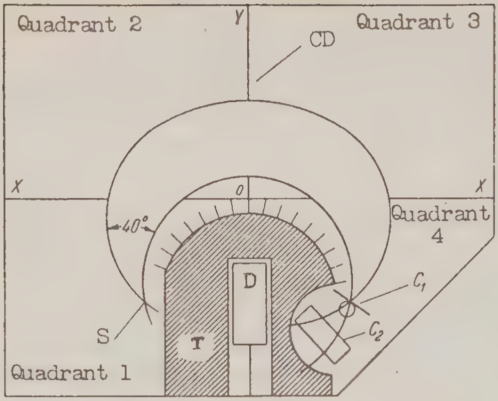

Fig. 1. Diagram of the magnetic spectrometer: S) electron source, X-X) separation line between homogeneous and nonhomogeneous magnetic field regions, CD) central diaphragm defining the electron beam, C_1 and C_2) electron counters, T) tungsten block, D) field indicator sensing element.

Measurements

Since the principal features of ThC"-ThD decay scheme are well known[2,3], we may assume that practically every decay is accompanied by a 2615 kev γ-quantum and that, therefore, the number of gammas with this energy equals the number of betas in the continuous ThC" β-spectrum, except that about 0.2% of the transitions involve conversion.

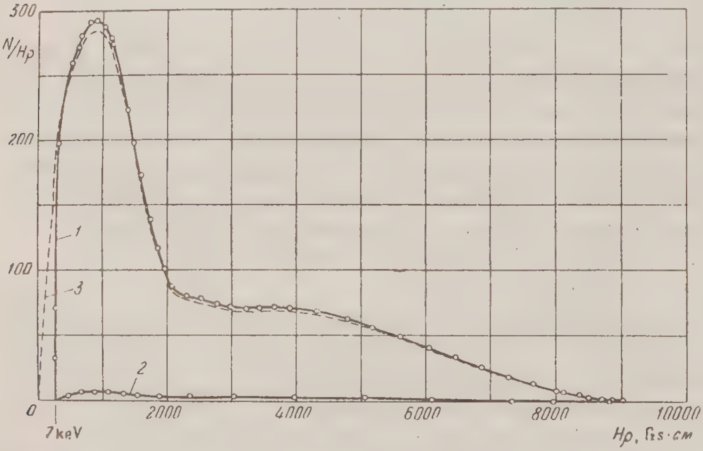

Fig. 2. Th(B+C+C") β-spectrum: 1) experimental curve, 2) background, 3) spectrum obtained after subtracting the background and correcting for absorption in the counter window.

A serious error could arise if a significant part of the decays were cross-over transitions from the second excited level at 3198 kev to the ground state, by-passing the 2615 kev level, as has indeed been assumed by several authors[14-16] who quote figures ranging from 1 to 12% for the intensity of this transition.

G.D.Latyshev, studying the recoil electrons and internal conversion positrons in lead, showed that if the 3200 kev line does exist, its intensity is no greater than a few hundredths of a percent[17]. Thus the probability of cross-over transitions may safely be neglected. This has since been substantiated by other investigators.[18,19]

In the present work we measured the ratio of the area under the ThC" L-line (423 kev) to that under the total β-spectrum of Th(B+C+C")(Fig. 2).

The ratio of the X and L line intensities was measured separately[20], since significant penetration of the counter slit edges was observed for the X-line. In order to exclude this effect, we measured the ratio of the X and L line intensities with the counter slits open to a greater width than the source image (source width - 0.3 mm; slits of both counters - 0.8 mm). The relative intensities were determined from the ratio of the heights of the conversion lines, since for the magnetic field corresponding to the X-line peak the entire electron beam is focused between the slit edges and therefore no penetration can occur.

The intensity ratio obtained was X/L = 0.101 ± 0.02, which is in good agreement with Flammersfeld's[21] data (X/L = 0.104) as well as that of Martin and Richardson[22] (X/L = 0.97).

The fraction of the total area in the Th(B+C+C") β-spectrum due to ThB and ThC is readily allowed for. It is known that the number of decays of ThC and ThC" can be expressed in terms of the number of ThB decays by the following formulas:

$$N_C = \frac{\lambda_C}{\lambda_C - \lambda_B} N_B = 1{,}104\, N_B,$$

$$N_{C''} = \frac{\lambda_C \lambda_{C''}}{(\lambda_C - \lambda_B)(\lambda_{C''} - \lambda_B)} 0{,}337\, N_B = 0{,}374\, N_B.$$

The coefficient 0.337 represents the fraction of ThC decays in the ThC" direction as obtained by Kovarik[23].

$$\begin{tikzcd}
 & & \mathrm{ThC''} \arrow[dr, "\beta"] & \\
\mathrm{ThB} \arrow[r, "\beta"] & \mathrm{ThC} \arrow[ur, "\alpha"] \arrow[dr, "\beta"'] & 3{,}1\,\mathrm{min} & \mathrm{ThD}\,(\mathrm{Pb}^{208}). \\
10{,}67\,\mathrm{hr} & 60{,}5\,\mathrm{min} & \mathrm{ThC'} \arrow[ur, "\alpha"'] &
\end{tikzcd}$$

The numerical values of the decay constants are taken from Refs. 24 & 25.

Corrections

The following corrections were made in the experimental value of the internal conversion coefficient:

1. A correction for absorption in the counter windows; this was based on the curves given by Lane.[26] The thickness of the zapon window of the first counter was determined from the cutoff energy: 7 kev (see Fig. 2). The correction was applied only to the points for which it was no greater than 20-30%. At the low energy end, the β-spectrum, converted to equal Hρ intervals, was extrapolated linearly to zero. The correction evaluated in this manner was 4.32% of the total β-spectrum area.

2. A correction for the energy dependence of the counter efficiency; this correction was evaluated according to McClure[27] and was found to be very small (0.03% of the ratio of the conversion line area to that of the continuous β-spectrum).

3. Corrections for the background:

a) the background due to cosmic rays and radioactive impurities was measured for ten hours, and the result, reduced to the appropriate time interval, was subtracted from all experimental points;

b) the γ-ray background was measured for H = 0 before each measurement of the spectrum, and after being corrected for decay, was subtracted from all the experimental points;

c) the background due to multiply scattered and Compton electrons produced in the walls of the apparatus and in the diaphragms; to take this background into account we investigated the spectrum with a source located at the bottom of the instrument. The direct electron beam was then cut off by the diaphragms, whereas γ-irradiation of the apparatus remained essentially unaltered. Thus the conditions for production of Compton electrons were the same. The electron bombardment conditions for quadrants 1 and 2 of the instrument were also little altered thereby, but with the source in its normal position multiple electron scattering should be greater due to electrons entering quadrants 3 and 4 directly from the source; therefore the result obtained (2.4%) can only be regarded as the lower bound of the background due to Compton and multiply scattered electrons. Although fewer scattered electrons are formed in quadrants 3 and 4 than in quadrants 1 and 2, the probability that electrons from 3 and 4 will reach the counters is greater than for those scattered in 1 and 2. It is difficult to evaluate the magnitude of this effect experimentally. In any case, it follows from the work of Owen and Cook,[28] that the background from scattered electrons cannot be very great with the three diaphragms in the instrument and with sufficient separation between the walls and the main beam. We have assumed that the additional background due to changing the irradiation conditions does not change the background by a factor of more than 2; this quantity (4.8%) was taken as the upper limit of the Compton and multiple scattering background, and consequently the background correction was taken as 3.6 ± 1.2%;

d) small-angle scattering from the edges of the diaphragms was taken into account by including the line "tails" in measuring the areas of the conversion lines.

4. A correction for escape of ThC" atoms from the source due to recoil in α-decay of ThC.

When a ThC atom α-decays, the ThC" atom acquires a recoil energy of the order of 100 kev and may escape from the source. In order to exclude this effect the source is usually covered by a film absorbing the recoil atoms. However, this gives rise to difficulties connected with evaluating the correction for absorption in this film. We decided not to cover the source, but rather to measure the number of ThC" atoms ejected from the source. For this purpose we measured the relative intensities of the G and H lines with and without the absorbing film over the source. The G line is associated with the decay of ThC"; the H line with the decay of ThB. Their energies are 190 and 210 kev, respectively. We found that in our experiments the intensity ratio of the G line to the H line with the source covered increased by 30.6% relative to the value with the source not covered. Thus the fraction of ThC" atoms leaving the source is 0.306. Since this correction must be made in the ThC" β-spectrum, the resulting correction for the internal conversion coefficient is 26.3 ± 2%.

5. Correction for penetration of the counter slit edges by electrons of the continuous spectrum.

To make this correction the hard region of the spectrum as obtained on the first counter was corrected on the basis of the spectrum recorded in counting coincidences; that is, we assumed that the electrons passing through the counter slit edges lose sufficient energy to prevent them from reaching the second counter. This correction was evaluated to be 3.0 ± 0.5%.

Evaluation of Errors

1. Seven series of measurements were made. The statistical error evaluated from these measurements was 1.43%. This error includes the possible instability of the apparatus and the uncertainty in determining the γ-background with H = 0.

2. The error in determining the area of the β-spectrum due to the inaccuracy in the correction for absorption in the first counter window was evaluated as 0.5%.

3. The error in the area of the β-spectrum due to inaccurate determination of the electron background was evaluated as 1.2%.

4. The error in measuring the ratio of the L and X line intensities equals 2%.

5. No error is given in Kovarik's[23] determination of the branching ratio in decay of ThC; we evaluated it at 1.4%.

6. The error in determining the number of recoil atoms leaving the source amounts to 2%.

7. The error due to inaccuracy in taking account of penetration of the counter slit walls equals 0.5%.

The resultant total root mean square uncertainty of our measurements is $\Delta\alpha_K/\alpha_K = 3.6\%$.

As will be seen below, the magnitude of the error is important where the deductions drawn from our experimental results are concerned.

Final Result and Comparison with Theoretical Data

We obtained the following value for the K internal conversion coefficient of the 2615 kev transition in Pb^{208}:

$$\alpha_K = (1.65 \pm 0.07)\cdot 10^{-3}.$$

This result was compared with Sliv's theoretical data.[12]

Sliv's calculations of the internal conversion coefficient differ from those of Rose[5], as we have already noted, in that Sliv takes into account finite nuclear size as well as screening on the K-shell for all energies (the latter correction, however, is not important at the given energy). According to Sliv, the values of the internal conversion coefficients differ appreciably from those of Rose. Thus, for a nuclear charge Z = 82 and energy $5.12\ m_oc^2$ (2615 kev), the difference is 35% for M1 and somewhat lower for other multipole orders.

The theoretical value closest to the measured internal conversion coefficient is $\alpha_K^{(3)} = 1.70\cdot 10^{-3}$ (E3), which is 8% lower than the value indicated by Rose. The theoretical coefficients for the other multipole orders differ greatly from the measured one: $0.93\cdot 10^{-3}$ for E2; $1.28\cdot 10^{-3}$ for M1; $2.8\cdot 10^{-3}$ for E4 and $3.1\cdot 10^{-3}$ for M2.

Thus from our results it follows uniquely that the 2615 kev transition in Pb^{208} is an electric octupole.

It can be seen, on the other hand, that the theoretical internal conversion coefficient of Rose ($1.86\cdot 10^{-3}$) is far outside the limits of the experimental error. Thus, while the necessity for taking account of finite nuclear size has already been demonstrated in the case of magnetic dipole radiation[29-31], our results show that agreement between theoretical and experimental data on the internal conversion coefficient for electric transitions, in particular for E3, can be obtained only when the theoretical computations take into account the finite dimensions of the nucleus.

Our experimental value of $\alpha_K = 1.65\cdot 10^{-3}$ for the 2615 kev transition in Pb^{208} does not differ greatly from those obtained in previous measurements: $1.8\cdot 10^{-3}$, $1.77\cdot 10^{-3}$ and $1.78\cdot 10^{-3}$ (Refs. 6, 32 & 4); we are disregarding the value $2.4\cdot 10^{-3}$ from Ref. 21 which is presumably erroneous. It should therefore be noted that assignments of different multipole orders to this line have been based on inaccurate theoretical data. Thus, the E2 assignment given in Ref. 6 is based on the incorrect theoretical data of Ref. 33; the M1 assignment of Ref. 34 is in agreement with the data of Rose[5], in evaluating which no account was taken of finite nuclear size.

As for the above mentioned determination of the multipole order from the internal conversion coefficient with pair production[7,8], comparison with theory in this case is very difficult because we have no calculations employing the exact relativistic wave functions for E3 and higher electric and M2 and higher magnetic multipoles. In any case, the best experimental value of $4.3\cdot 10^{-4}$ (Ref. 8) lies below the theoretical value of $4.6\cdot 10^{-4}$ (Ref. 35) for E2; however, it is difficult at present to determine how close this experimental value is to the theoretical one for E3.

The method based on the degree of forbiddenness of the β-spectrum[19] is of secondary significance in this case, since the spin of the mother nucleus Tl^{208} is not known with certainty and, by assigning it either the value 4 or 5, agreement can be obtained with multipole order assignments M1 (Ref. 36), E2 (Refs. 9 & 36) or E3 (Ref. 37) for the 2615 kev transition.

Finally, the early measurements of angular correlation in the 583-2615 kev cascade, in which Petch and Johns[10] obtained the assignment 0-2-4 for the first

Pb^{208} levels, i.e., E2 for the 2615 kev radiation, were performed without an accurate evaluation of the contribution to the correlation from other lines of the γ-spectrum, whereas in the work of Elliott[4] this effect is carefully accounted for and partially excluded. This would seem to explain the difference between the results of these two studies. In the second work on angular correlation[11], the results were not compared with the possible 0-3-5 assignment for the spins of the first levels.

Relative Probability of Conversion on the K-, L- and M-shells

In addition to measuring the K internal conversion coefficient, we also measured the intensity ratio of the K, L and M lines.

In many cases the determination of the multipole order from the probability ratio for conversion on the K- and L-shells (K/L) is most simple and accurate. The magnitude of this ratio for the 2615 kev transition in Pb^{208} was measured by Alikhanian and Nikitin[32]. They found K:L:M = 5:1:0.2. For high transition energies, however, the K/L values for different multipole orders are very close and at the limit ($h\nu \rightarrow \infty$) have the same value: 6.7:1 (Ref. 33). Thus, for comparison with theory to be of any value the K:L:M proportions for 2615 kev must be measured with extreme care.

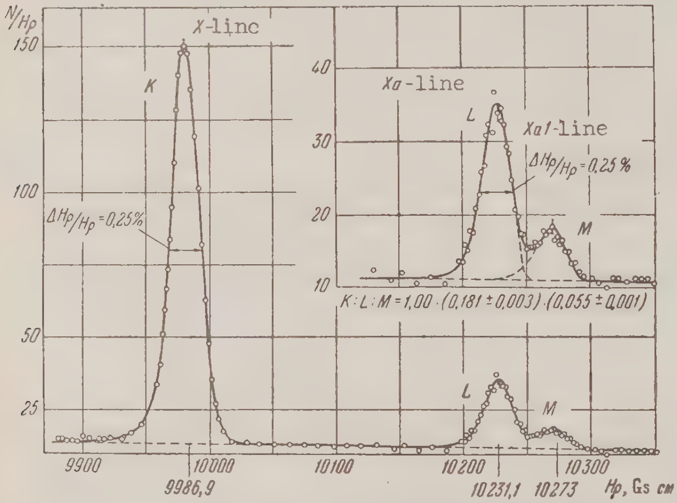

Fig. 3. X, Xa, and Xal-lines of ThD from conversion of 2615 kev γ-rays on the K, L and M-shells of Pb^{208}.

Our measurements were made with the same instrument parameters. The results are shown in Fig. 3.

We obtained the following value for the intensity ratio: $K:(L_I + L_{II} + L_{III}):(M_I + M_{II} + \ldots) = 1:(0.181\pm0.003):(0.055\pm0.001)$.

Unfortunately, we have at present no reliable theoretical data for energies greater than 1.5 m_0c^2 for conversion on the L-shell or for any energy on the M-shell; extant non-relativistic calculations are not applicable to heavy nuclei.

Nevertheless we may hope that the accuracy obtained in this work will make possible a definite multipole order assignment for the 2615 kev transition on the basis also of the intensity ratio obtained, as soon as the appropriate theoretical results are available.

In conclusion we note that Kraushaar and Goldhaber[11], having determined the spin value 2 for the 2615 kev level of Pb^{208}, consider this a substantiation of the empirically established regularity for the spins of the first excited levels of even-even nuclei[38, 39, etc.]. The fact that the spin of Pb^{208} (82 protons and 126 neutrons) is actually 3, rather than 2, serves to define the region of applicability of this rule and makes it possible to formulate a new regularity to the effect that the few exceptions[39] to the first rule are primarily nuclei with filled neutron and proton shells.

Department of Physics of
"V.N.Obraztsov" Leningrad Institute
for Railroad Transport Engineers

References

1. C.Ellis, Proc. Roy. Soc., A 138, 318 (1932).
2. F.Oppenheimer, Proc. Cambr. Philos. Soc., 32, 328 (1936).
3. J.Hollander, I.Perlam & G.Seaborg, Rev. Mod. Phys., 25, 469 (1953).
4. L.Elliott, R.Graham, J.Walker & J.Wolfson, Phys. Rev., 93, 356 (1954).
5. M.Rose et al, Phys. Rev., 83, 79 (1951).
6. H.Hulme, N.Mott, F.Oppenheimer & H.Taylor, Proc. Roy. Soc., A 155, 315 (1936).
7. A.Alikhanov, Izv. AN SSSR, Ser. fiz., No. 1, 33 (1938).
8. H.Slatis & K.Siegbahn, Ark. Fys., 4, 485 (1952).
9. R.Arnoult, Ann. de physique, 12, 241 (1939).
10. H.Petch & M.Johns, Phys. Rev., 80, 478 (1950).
11. J.Kraushaar & M.Goldhaber, Phys. Rev., 89, 1081 (1953).
12. L.A.Sliv & I.M.Band, Zhur. eksp. i teor. fiz., 31, 134 (1956).
13. G.Latyshev, A.Sergeev, E.Krisiuk, L.Ostretsov, Iu.Egorov & N.Shirshov, Izv. AN SSSR, Ser. fiz., 20, 354 (1956). (Trans. in Bulletin Vol.20, No.3, p.324).
14. A.Alikhanov & B.Dzhelepov, Doklady AN SSSR, 20, 113 (1938).
15. C.Ellis, Proc. Phys. Soc., 50, 213 (1938).
16. L.Simons & K.Zuber, Proc. Roy. Soc., A 159, 383 (1937).
17. G.Latyshev, Dissertation UFTI, Kharkov 1940.
18. R.Bell & L.Elliott, Canad. J. Research, A.26, 379 (1948).
19. G.Bishop, R.Wilson & H.Halban, Phys. Rev., 77, 416 (1950).
20. E.Krisiuk, A.Vitman, V.Vorob'ev, G.Latyshev & A.Sergeev, in present issue of the Bulletin, p. 797.
21. A.Flammersfeld, ZS. f. Phys., 114, 227 (1939).
22. D.Martin & H.Richardson, Proc. Roy. Soc., 195, 287 (1948).
23. A.Kovarik & N.Adams, Phys. Rev., 54, 413 (1938).
24. MCurie, A.Debirne, A.Eve, H.Geiger, O.Hahn, S.Lind, S.Meyer, E.Rutherford & E.Schweidler, Rev. Mod. Phys., 3, 427 (1931).
25. H.Buttlar, Naturwiss., 39, 575 (1952).
26. R.Lane & D.Zaffarano, Phys. Rev., 94, 960 (1954).
27. G.McClure, Phys. Rev., 90, 796 (1953).
28. G.Owen & C.Cook, Rev. Scien. Inst., 20, 768 (1949).
29. L.Sliv & M.Listergarten, Zhur. eksp. i teor. fiz., 21, 29 (1952).
30. E.Krisiuk, G.Latyshev, M.Listergarten, L.Ostretsov & A.Sergeev, Izv. AN SSSR, Ser. fiz., 20, 363 (1956). (Trans. in Bulletin, Vol.20, No.3, P.332).
31. A.Wapstra & G.Nijgh, Nuc. Phys., 1, 245 (1956).
32. A.I.Alichanian & S.J.Nikitin, Phys. Rev., 53, 767 (1938).
33. H.Hulme, Proc. Roy. Soc., A 138, 644 (1932); H.Taylor, N.Mott, Proc. Roy. Soc., A 138, 665 (1932).
34. D.Martin & H.Richardson, Proc. Phys. Soc., A 63, 223 (1950).
35. J.Jaeger,& H.Hulme, Proc. Roy. Soc., A 148, 708 (1935).
36. H.Richardson, Nature, 161, 516 (1948).
37. R.King, Rev. Mod. Phys., 26, 327 (1954).
38. M.Goldhaber & A.Sunyar, Phys. Rev., 83, 906 (1951).
39. M.Goldhaber, Phys. Rev., 90, 600 (1953).

β-SPECTRUM OF Pu^{241}*

- K.N.Shliagin

Introduction

In the process of β-decay there occurs a rearrangement of the electron shells due to the unit change in nuclear charge. The total binding energy of the electron shells increases with increasing nuclear charge. According to Foldy[2] the binding energy of the electron shells for heavy elements is equal to

$$E_Z = -32.64 \cdot Z^{7/5} \text{ev}.$$

If we know the electron shell binding energies for the mother and daughter atoms, E_Z and E_{Z+1}, we can determine the change-over energy for these shells, namely

$$\Delta E_{Z,Z+1} = E_{Z+1} - E_Z.$$

For elements at the end of the periodic system, $\Delta E_{Z,Z+1}$ attains a value of 15-25 kev. One may expect, therefore, that the change-over will have a noticeable effect on β-spectra whose end-point energies E_o are close to $E_{Z,Z+1}$.

In 1938 Hebb[3] suggested that the change-over energy of the electron shells is transferred to the β-particles, and that the neutrino, because of its weak interaction with the electrostatic field of the nucleus, receives no energy. In view of this it was assumed that the β-spectrum will be displaced as a whole by an amount $\Delta E_{Z,Z+1}$ into the high-energy region. This, however, is contradicted by the experimental data of several recent experiments. The present work was undertaken to solve this problem.

The β-spectrum of Pu^{241} was chosen for this investigation; its end-point energy had been roughly evaluated as E_o = 10-20 kev, and its half-life T = 10-14 years.[4]

Experimental Part

Apparatus

The first measurements of the Pu^{241} β-spectrum were performed on a magnetic β-spectrometer with a homogeneous field; the second repeat series of measurements was made in 1955 on a β-spectrometer with double focusing at an angle of $\pi\sqrt{2}$ (Ref. 5). The relative half-width of the conversion lines of Hg^{198}($h\nu$ = 411.8 kev) and Ba^{137}($h\nu$ = 661.6 kev) used for calibration and reference was about 1.5% in the former case, and 0.5% in the latter.

All necessary measures were taken to eliminate instrument distortions of the β-spectrum. Thin celluloid films were used both for the window of the GM counter and as the support for the radioactive source. In order to reduce effects due to absorption and back-scattering of electrons by the sources, these had a superficial density of 3 μg/cm^2 and less. The background due to scattered electrons was reduced by the installation of several aluminum baffles in the spectrometer and location of the β-source at a considerable distance from the chamber walls (> 5 cm).

The pressure in the instrument was about 10^{-5} mm Hg. A single GM counter was used to record the β-particles; its window had a tungsten filament screen and was covered with the above-mentioned 3 μg/cm^2 thick celluloid film. The GM counter was filled with a mixture of 90% argon and 10% ethyl alcohol vapor at a pressure of 30-50 mm Hg.

---

*This study of the β-spectrum of Pu^{241} was made mainly in 1950-1951 in conjunction with an overall investigation of Pu^{239}, Pu^{240} and Pu^{241} (Ref. 1).

Radioactive Source

The β-active isotope Pu^{241} was obtained by prolonged slow neutron bombardment of Pu^{239}. The successive neutron capture process involved is

$$Pu^{239}(n,\gamma)Pu^{240}(n,\gamma)Pu^{241}.$$

Specimens (mixtures of Pu^{239}, Pu^{240} and Pu^{241}) enriched in Pu^{241} were used in the investigation.

The radioactive source was prepared by depositing plutonium nitrate (from a water solution) on a thin celluloid film (surface density 5-10 μg/cm²). This was preceded by the application of a narrow strip (1-2 X 25-30 mm) of ethylene glycol or aquadag. The ethylene glycol wets the film and promotes uniform distribution of the radioactive material over the surface. The sources prepared with ethylene glycol were then metallized by vacuum evaporation of aluminum (thickness of coating ~1 μg/cm²).

Effect of Film over the Counter Window on the Shape of the β-spectrum

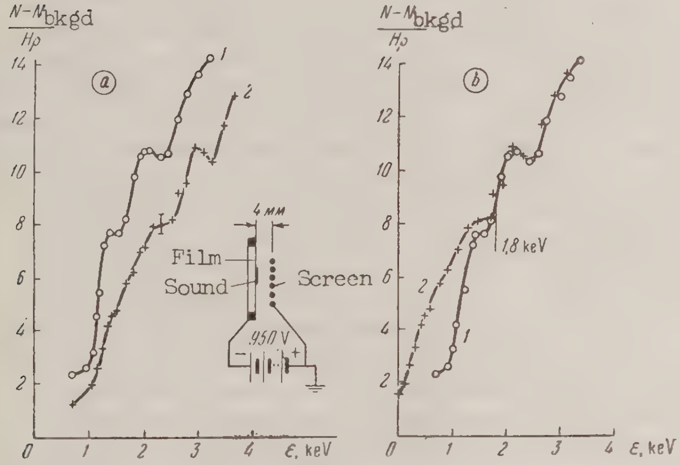

Fig. 1. The low-energy part of the Pu^{241} β-spectrum obtained on the magnetic β-spectrometer: 1) without potential on the source, 2) with an additional potential of -950 v; a) the spectra obtained separately, b) the spectra superposed.

Before beginning a study of the Pu^{241} spectrum, we performed an experiment to determine the effect of the finite thickness of the GM window film on the spectrum shape. The magnetic β-spectrometer with the counter window made of 3 μg/cm² thick celluloid film was used to measure the low-energy part of the Pu^{241} β-spectrum (0-5 kev) with and without a -950 v potential on the radioactive source. The spectra so obtained are shown in Fig. 1a. Fig. 1b, in which the two spectra are plotted superposed, shows that they have the same shape above a β-particle energy ~1.8 kev* (the 2 kev peak is apparently due to Auger electrons[1] from U^{235}). We may therefore assume that distortion of the spectrum due to scattering and absorption of electrons by the counter window film occurs only at electron energies <1.8 kev.

Results of Measurement

Figure 2 shows the Kurie plot of the Pu^{241} β-spectrum for sources of different superficial densities.**

These plots are constructed without taking into account the screening effect due to the atomic electrons, in view of the lack of accurate correction factors

---

*Calculations based on the formula given by Ross and Grazen[6] give a value of ~2 kev (for a film having a density of 3 μg/cm² and $\theta = 90^{\circ}$).

**The superficial densities of the sources were calculated taking the data on their α-activity into account. The α-emitters present were the Pu^{239} and Pu^{240}.

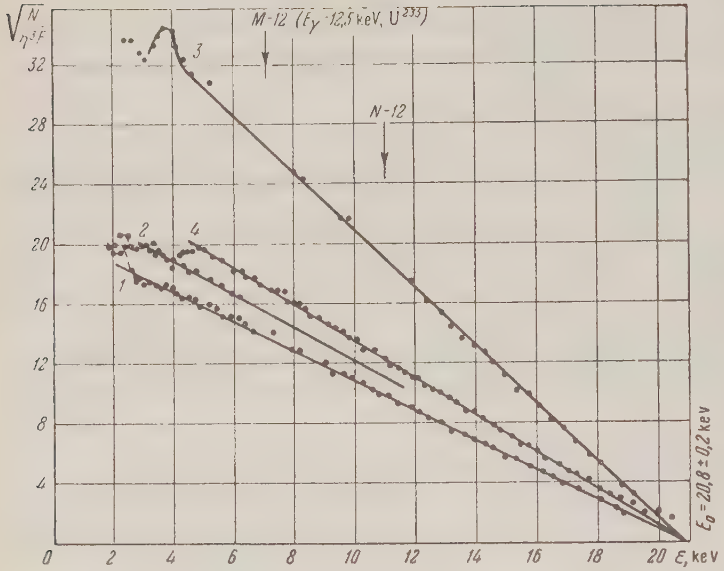

Fig. 2. Kurie plot of the Pu^{241} β-spectrum for sources with different superficial densities both of the source proper (t_1) and of the support (t_2): 1) $t_1 \approx 1$ μg/cm^2, 2) $t_1 = 1.3$ μg/cm^2, 3) $t_1 \approx 3$ μg/cm^2, 4) source (enriched to 85% Pu^{241} on aquadag coating over support) the support of the source for curve 1 had a thickness $t_2 \approx 5$ μg/cm^2 that for curves 2-4 had $t_2 \approx 10$ μg/cm^2.

for this effect. The linear character of the plots obtained may be taken as an indication of monotonic variation of the screening effect in the energy region in question (3→ 21 kev).

It can be seen from Fig. 2 that the thinner the source, the farther the rectilinear part of the plot extends into the low-energy region. The fact that there is little difference in the shapes of plots 1 and 2 for sources whose supports have superficial densities of 5 and 10 μg/cm^2 and nearly equal active-coating superficial densities shows that the back-scattering of electrons by these backings is small and does not alter the shape of the β-spectrum at energies above 3 kev. These plots have the longest rectilinear section (3-19 kev).

Plot 4 is constructed from the spectrum obtained with the double-focusing β-spectrometer (in 1955). The GM counter window had a thicker film than in the experiment described above. In addition, the source was deposited on a semi-transparent aquadag strip painted on the celluloid film. Apparently for these reasons the rectilinear part of the Kurie plot starts not at 3 kev, as previously, but at 5 kev.

In these experiments greatly Pu^{241}-enriched sources were used (85% Pu^{241} in the experiment of curve 4 as against 1% Pu^{241} in the sources characterized by curves 1, 2 & 3 in Fig. 2). Therefore the weak M12 and N12 conversion lines associated with γ-transitions of U^{235} (the α-decay product of Pu^{239}) with 12.5 kev energy[1] did not cause any significant distortion of the β-spectrum. This is particularly noticeable in the case of curve 4.

The end-point of the Pu^{241} β-spectrum, equal to 20.8 ± 0.2 kev, is determined by extrapolation of the linear part of the Kurie plot to its intercept on the abcissa.

Thus, within the limits of the measurement error, the experimental Pu^{241} β-spectrum agrees in the wide energy interval from 3 to 19 kev with the theoretical one for an allowed β-transition.

From the end-point energy of the Pu^{241} β-spectrum (20.8 kev)and the half-life (13 years), we calculated log(ƒt): The value obtained was 5.7.

The spins of the ground states of the mother and daughter nuclei have been determined by Bleaney et al[7] and Fred & Tomkins[8]: I = 5/2 for Pu^{241} and I = 5/2 for Am^{241}. Thus the ground states of Pu^{241} and Am^{241} have the same spin value (I = 5/2), i.e., ΔI = 0; however, the parities of these states are not known.

On the basis of the existing classifications of β-transitions according to the log (ƒt) values, the given transition with log (ƒt) = 5.7 may be either a first-order forbidden ΔI = 0 (yes) or an allowed ΔI = 0 (no) transition.

The results obtained in the present work are in agreement with the experimental data given by Freedman et al.[9] These investigators were able to study the Pu^{241} β-spectrum only in the 14-20 kev interval. Their spectrum also exhibits an allowed shape. The end-point energy is given as 20.5 kev.

Let us now return to the effect of the electron shell change-over on the shape of the β-spectrum. Calculations show that for the β-decay of Pu^{241} the change-over energy should be $\Delta E_{Z,Z+1} \approx 20$ kev. Therefore, if Hebb's[3] hypothesis were correct, the experimental β-spectrum of Pu^{241} should start not at zero energy, but at ~20 kev. As can be seen from Fig. 2, however, the β-spectrum starts at an energy close to zero,which would appear to invalidate Hebb's hypothesis.

Schwartz[10], Edwards[11], and Serber & Snyder[12] used a different approach. Theoretical calculations made by Schwartz show that atomic electron readjustment does not introduce any significant alteration in the form of the allowed β-spectrum and that the change-over energy of the shells is distributed between the β-particle and the neutrino in the same way as the β-decay energy of a nucleus stripped of its electron shells (bare nucleus).

According to the predictions of Schwartz's theory, the Pu^{241} β-spectrum should have an allowed shape. As we have shown, the experimental β-spectrum does in fact have this shape.

It must be assumed that if the end-point energy of the β-spectrum of Pu^{241} is 20.8 kev and the electron shell change-over energy $\Delta E_{Z,Z+1} \approx 20$ kev, the β-decay energy of the bare nucleus must be only ~0.8 kev. Apparently the possibility of β-transitions with even lower (perhaps even negative) decay energies may not be excluded.

In conclusion I want to thank S.N.Belen'kii for aid in performing the measurements and S.A.Baranov and V.N.Galitskii for discussion of the results.

References

1. K.N.Shliagin, Zhur. eksp. i teor. fiz., 30, 817 (1956).
2. L.L.Foldy, Phys. Rev., 83, 397 (1951).
3. M.H.Hebb, Physica, 5, 701 (1938).
4. G.T.Seaborg, R.A.Yames & L.O.Morgen, Rev. Mod. Phys., 20, 585 (1948).
5. S.A.Baranov & K.N.Shliagin, Pribory i tekhnika eksperimenta (Experimental instruments and techniques) No. 1, 3 (1956).
6. B.Rossi & K.Greisen, Interaction of Cosmic Rays with Matter. (In Russian translation, M. 1948).
7. B.Bleaney, P.Llewellyn, M.Pryce & C.Hall, Phil. Mag., 45, 991 (1954).
8. M.Fred,& F.Tomkins, Phys. Rev., 89, 318 (1953).
9. M.Freedman, F.Wagner & D.Engelkemeir, Phys. Rev., 88, 1155 (1952).
10. H.M.Schwartz, Phys. Rev., 85, 733 (1952); 86, 195 (1952).
11. R.R.Edwards, Sixth Southwest Regional Meeting, American Chemical Society, 1950.
12. R.Serber & H.Snyder, Phys. Rev., 87, 152 (1952).

INVESTIGATION OF THE CONVERSION ELECTRON SPECTRA OF THE ISOMERS Ba^{137*}, In^{113*} and In^{115*} IN A β-SPECTROMETER USING THICK-EMULSION PLATES

- I.A.Antonova

Introduction

Two basic methods are employed for recording electrons in modern β-spectroscopy: the first involves the use of gas-discharge or scintillation counters; the second, photographic plates.

The photographic method has the advantage that it can be used to study the electron spectra of extremely short-lived isotopes.

The sensitivity of the method based on the blackening of photographic plates is, however, quite low and makes it necessary to use highly active samples. At the same time, in order to decrease the self-absorption of electrons in the source, it is necessary to use very thin sources. Both these requirements can be satisfied only where sources having a high specific activity are available. Unfortunately, this is not always feasible in practice.

In addition, a serious disadvantage of the photographic method is the difficulty of measuring the relative electron line intensities, since the blackening density is not linearly dependent on the energy and exposure.

Development of Electron Recording by Thick-emulsion Plates

The above disadvantages of photographic recording may be avoided by using thick emulsions which are electron sensitive, and by determining the electron intensity directly by counting the number of electron tracks in the emulsion.

As became known after the present work was completed, thick emulsions were first used in β-spectroscopy for the investigation of the low-energy region of the RaE β-spectrum by Pnievski[1]. The difficulty of using this method in magnetic β-spectroscopy is that even in special emulsions the electrons give a relatively low grain density, and it is therefore not always easy to discern the tracks against the grainy background. In addition, due to strong scattering, the tracks of electrons in the ten to several hundred kev energy region appear in the form of complicated, tangled curves, which makes for difficulty in counting the number of electrons.

In the present investigation our purpose was to evaluate the possibility of using thick-emulsion photographic plates in β-spectroscopy, in particular, for studying conversion electron spectra. To this end we tested NIKFI type R (P) plates, which are sensitive to electrons, and type MR (MP) radiographic plates.

In the experiments with type R plates, emulsion thicknesses of 200, 100 and 50 μ were tested. The best results were obtained with R-50 plates (emulsion thickness, 50 μ). After processing and drying, the emulsion thickness of these plates amounted to only about 15-18 μ, but even such thin layers were found to be entirely sufficient for identification of electron tracks against the grainy background. The R-50 plates had the additional advantage that their photographic processing does not require much time or special equipment.

Good results were also obtained with MR type plates having a 10-15 μ thick emulsion. An electron track (i.e., the recorded section of a track) in these plates consisted of only 5-10 grains. In order to permit identification of such tracks, of course, the plates must meet enhanced quality requirements (low grainy background). Photographic processing of the MR plates is even simpler, being practically identical with that used in conventional photography.

Special attention was paid to the matter of exposure time for a given level of activity and the degree of magnification of the microscope used in scanning the plates. The relative exposure time was determined by the following considerations: on the one hand, the number of electron tracks should not be too great (otherwise they become tangled, and are hard to count), and on the other, it is desirable, in order to reduce the statistical straggling, that the number of electrons in the microscope field of view should not be too small. Tests showed that the best microscope magnification is between 300 and 450. It is desirable to adjust the exposure time so that there would be no more than 300 electron tracks in the microscope field of view. This number, however, may be increased by a factor of 1.5 if the examined plates are pre-soaked in a water solution of glycerin. In this swollen emulsion the electron tracks are elongated vertically and the microscope can be focused on track sections over which little scattering has had time to occur. Such tracks are easier to resolve and to count.

In this respect, the thin MR plates have a clear advantage. They allow of counting up to 500 tracks (in the dry form) with adequate accuracy. In addition, by virtue of their lesser emulsion thickness, the MR plates provide a better resolving power. In the thick emulsion R plates, the electron line width, as determined initially by the resolution of the β-spectrometer, will be increased due to electron scattering in the emulsion.

The electron tracks were counted on an MBI-2 binocular microscope with an ST-12 moving stage. To facilitate counting the eyepiece was provided with a reticle. The number of electrons was recorded by means of a manual tally register. With these simple devices, once-over inspection of a 10 cm long plate under the microscope took 2-3 hours.

In order to prove the practical usefulness of thick emulsions in β-spectroscopy, we investigated the conversion electron spectrum of Ba^{137*}.

We used a Danysz type 180° spectrometer and a homogeneous transverse magnetic field. The resolution of the instrument was 0.6-1%. The maximum electron trajectory radius was 14 cm. In order to investigate electrons whose energy was higher than 1 Mev, when the electrons tracks are almost straight lines, the instrument had provision for turning the plate holder to an angle of 30° or 60° relative to the plane of incidence of the electrons so that the projections of the tracks would appear in the emulsion.

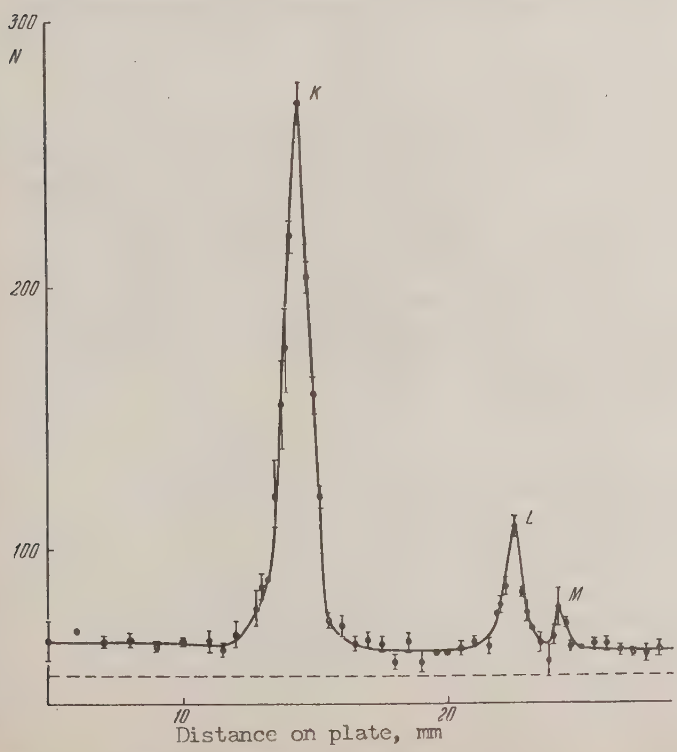

Fig. 1. The Ba^{137*} conversion electron spectrum.

A Cs^{137} sample in the form of the chloride was coated by evaporation onto a 0.28 mm diameter 40 mm long copper wire. The activity of the sample was 6 μcurie. The R-50 plates were exposed for 2.5 hours.

Fig. 1 shows the Ba^{137*} conversion electron spectrum obtained. The abcissae are coordinates of the plate, i.e., values proportional to $H\rho$ and the ordinates are the number of electron tracks in the microscope field of view at a magnification of 420 X. The curve is an average of four counts made from the same plate. For each new measurement, the plate was displaced somewhat vertically. This makes it possible to obtain good statistics from a single plate. As can be seen from Fig. 1, the experimental error with four times over counting is no greater than 5-8%, and can be reduced even further.

Study of a control plate from the same lot showed that 51 ± 1 electrons must be assigned to the background accumulated during storage. This background is indicated in Fig. 1 by the dash line. The rest of the electrons of the total background against which the K, L and M peaks stand out belong to the hard Cs^{137} β-spectrum, which accounts for only 8% of the total number of decays.

Table 1

Experimental internal conversion coefficients for Ba^{137*} γ-rays according to different investigators

Data	α_K/α_L	α_M/α_L	α_K/α_{L+M}
Our	$5,9 \pm 0,1$	$0,28 \pm 0,02$	$4,9 \pm 0,1$
Ref. 2	—	—	4,57
Ref. 3	—	—	4,64
Ref. 4	5,5	0,27	—
Ref. 5	$6,0 \pm 0,1$	$0,28 \pm 0,02$	—
Ref. 6	—	—	$4,52 \pm 0,07$
Ref. 7	—	—	4,7

A comparison of the areas under the K, L and M peaks reduced to equal $H\rho$ intervals gives the ratio of internal conversion coefficients for the Ba^{137*} γ-rays listed in Table 1. The experimental uncertainty given in Table 1 is the arithmetic mean of the results for 7 plates. Our results are in good agreement with the data of other authors[2-7], obtained on β-spectrometers with gas-counter recording of the electrons.

Thus, the example of the Ba^{137*} conversion electron spectrum may be considered a demonstration of the possibility of using thick-emulsion plates for β-spectroscopy.

In order to compare the exposure times necessary to give observable blackening of x-ray film and thick-emulsion plates, experiments were performed with the same Cs^{137} sample, whose activity was 2.65 m curie. It was found that for thick-emulsion plates a 10 sec exposure was sufficient, while one hour was needed for the x-ray film. These data show that the sensitivity (speed) of thick emulsions is 300-500 times greater than that obtaining with the blackening density method (x-ray film). This new method, therefore, makes it possible to investigate isotopes whose activity is only a few microcuries, which is practically impossible by any other method.

This increase in the sensitivity, together with the other advantages of this method, may be of importance in solving a number of problems in β-spectroscopy: for example, it makes it possible to investigate short-lived isotopes.

Investigation of the Isomeric Transitions of In^{113*} and In^{115*}

The above described method of recording electrons with thick emulsions was used to investigate the conversion electron spectra of In^{113*} and In^{115*}.

In^{113*} Spectrum

Table 2

Ratios of the K, L and M internal conversion coefficients of Ba^{137*}, In^{113*} and In^{115*}.

Isomer	T	$h\nu$, keV	Experimental		Theo. value α_K/α_L		Multipole order assignment
			α_K/α_L	α_M/α_L	$E5$	$M4$	
Ba^{137*}	2,3 мин	661,6	$5,9 \pm 0,1$	$0,28 \pm 0,02$	4,0	6,15	$M4$
In^{113*}	105 мин	393,3	$4,0 \pm 0,4$	$0,27 \pm 0,05$	3,15	8,70	$E5$
In^{115*}	4,5 час	337	$4,4 \pm 0,5$	$0,46 \pm 0,06$	2,65	5,85	$E5$, $M4$, $E5 + M4$

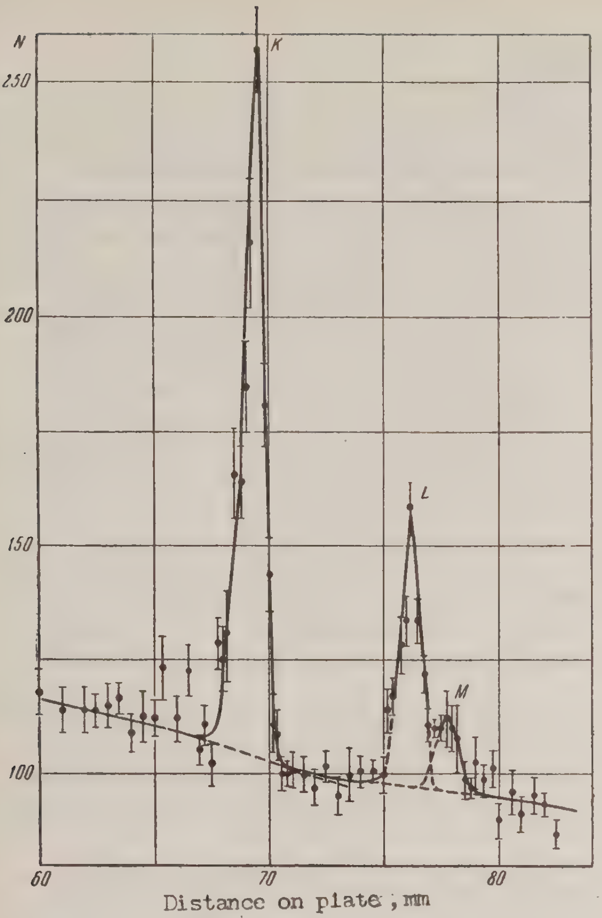

Fig. 2. The In^{113*} conversion electron spectrum.

A sample of In^{113*} (chemically separated from radioactive Sn$^{113+123}$ in the form of indium chloride*) was coated by evaporation on a copper wire 0.23 mm in diameter and 40 mm in length. The purity of the chemically separated indium was verified by the time variation of the γ- and β-activities. In all measurements both for the γ- and β-activities, only one half-life of 105 min, associated with In^{113*}, was observed. The activity of the sample was determined with the aid of a γ-counter of a known efficiency. In various series of measurements it varied between 4 and 7 µcuries. The R-50 plates used were from a fresh batch stored for less than 7 days. The exposure time was 3 hours.

Fig. 2 shows the In^{113*} conversion electron spectrum obtained from a 7 µcurie source. The curve is an average for nine curves taken from one plate. Control measurements showed that 31 ∓ 2 electrons should be assigned to the plate background.

Table 2 gives the results of our evaluations of the internal conversion coefficients on the K, L and M shells of the In^{113*} atom; these values are averages for fifteen curves taken from three plates. The table also gives the theoretical value of α_K/α_L obtained by extrapolation of the theoretical values of Rose et al.[8]

As can be seen from Fig. 2, the L and M peaks in the In^{113*} conversion electron spectrum were not entirely resolved, and therefore only the α_K/α_{L+M} values shown in Table 3 may be considered reliable. The value of α_K can be calculated on the basis of the total internal conversion coefficient of In^{113*}, which we have previously measured by an ionization method[9], and this value can be compared with the theoretical values of α_K for various multipole orders.[8]

Table 3

In^{113*} and In^{115*} internal conversion coefficients.

Isomer	Experimental			Theo. value α_K				Multipole order assignment
	α	α_K/α_{L+M}	α_K	$E4$	$M3$	$E5$	$M4$	
In^{113*}	$0{,}44 \pm 0{,}03$	$3{,}1 \pm 0{,}2$	$0{,}34 \pm 0{,}04$	0,102	0,104	0,338	0,460	$E5$
In^{115*}	$0{,}82 \pm 0{,}15$	$2{,}95 \pm 0{,}30$	$0{,}61 \pm 0{,}15$	0,22	0,24	0,68	0,88	$E5$

---

*The method of chemical separation of In^{113*} from Sn$^{113+123}$ was developed by Z.V.Pastukhova at the 2nd NIFI Chemical Laboratory of Moscow State University.

The experimental and theoretical values of α_K are shown in Table 3.

In^{115*} Spectrum

The In^{115*} sample was chemically separated* from Cd^{115}. An amount of In^{115*} too small to be weighed was deposited by evaporation in the form of indium chloride onto a copper wire 0.23 mm in diameter and 40 mm in length. The purity of the chemical separation was verified from the half-life for γ- and β-activities. In all the series of measurements both for γ- and β-activities only one half-life period of 4.5 hr, associated with In^{115*}, was observed. The activity of the In^{115*} sample was measured with a γ-counter and found to be 2-3 μcuries. The conversion electron spectrum was recorded on R-50 plates exposed for 3.5 hours. Two plates were obtained, and six series of measurements were made on these. Table 2 shows the values obtained for the ratios of the In^{115*} coefficients of internal conversion on the different shells.

On the basis of our previously obtained[9] value for the total In^{115*} internal conversion coefficient, we arrived at the value of α_K given in Table 3.

Multipole Order of the Radiative Transitions of Ba^{137*}, In^{113*} and In^{115*}

Comparison of the experimentally obtained values for α_K/α_L with the theoretical ones (Table 2) shows that for the isomeric transition of Ba^{137*}, the γ-radiation is M4. This conclusion is in complete agreement with that of other authors.[2-7]

Comparison of the experimental values of α_K and α_K/α_L for In^{113*} and In^{115*} with the theoretical ones (Tables 2 and 3) shows in both cases that the radiation is E5. True, this result is not very certain for In^{115*} since the experimental value of α_K/α_L is almost equally close to the theoretical values for both E5 and M4.

The results of the present work are not in conflict with nuclear shell theory, which allows both E5 and M4 transitions for In^{113*} and In^{115*}. It should be noted, however, that for excitation energies of 300 to 400 kev, when both E5 and M4 transitions are possible, the latter is the more probable.[10] This would seem to explain why all authors conclude on the basis of their experimental data, which are basically identical with ours, that the γ-radiation of In^{113*} and In^{115*} are M4.

The theoretical values of α_K should be somewhat lower than the ones in Ref. 8 for E5 and M4 radiations, when account is taken of the finite size of nuclei. For $Z = 49$ and excitation energies of the order of 300-400 kev, however, the difference is not over 5%. Therefore more exact calculations of α_K cannot change the above deductions regarding the probable multipole order of the isomeric transitions in In^{113*} and In^{115*}.

A similar situation is encountered in the case of nonspherical even-even nuclei. Recently Shapiro[12] carried out a theoretical investigation of such nuclei. He showed that there exist additional selection rules which in some cases may completely suppress magnetic transitions. Although Shapiro's results cannot be applied to In^{113*} and In^{115*}, since these are odd-odd nuclei, this example clearly shows that all the selection rules are not known at present.

Second Scientific Research Physical Institute
(2nd NIFI) of Moscow State University

---

*The method of separation of In^{115*} from Cd^{115} was developed under the direction of N.P.Rudenko in the 2nd NIFI Chemical Laboratory of Moscow State University.

References

1. J.Pnievski, Acta. Phys., Polon., 11, 3-4, 215 (1953).
2. W.Kelly, Phys. Rev., 85, 101 (1952).
3. A.Grawes, L.Langer & R.Moffat, Phys. Rev., 88, 344 (1952).
4. W.Bandel, F.Shore, & R.Becker, Phys. Rev., 87, 195 (1952).
5. B.Dolishniuk, G.Drabkin, L.Orlov & L.Rusinov, Doklady AN SSSR, 92, 1141 (1953).
6. R.Maerker & R.Birkhoff, Phys. Rev., 89, 1159 (1953).
7. M.Waggoner, Phys. Rev., 82, 906 (1951).
8. M.Rose, G.Goertzel, B.Spinard, J.Harz & P.Strong, Phys. Rev., 83, 79 (1951).
9. I.Antonova & I.Estulin, Izv. AN SSSR, Ser. fiz., 18, 79 (1953).
10. L.Gorishev & I.Shapiro, Spektroskopiia atomnykh iader (Spectroscopy of atomic nuclei), M.-L. 1952.
11. L.Sliv, Zhur. eksp. i teor. fiz., 21, 770 (1951).
12. I.Shapiro, Zhur. eksp. i teor. fiz., 30, 975 (1956).

A TWO-METER CURVED-CRYSTAL γ-RAY SPECTROMETER

- P. I. Lukirskii & O. I. Sumbaev

Recent years have seen marked advances in the technique of precise measurements of γ-radiation energy. Renewed interest in the matter was aroused by the investigations of the DuMond group,[1-6] carried out on a crystal spectrometer. Of particular interest was their work on the determination on the wavelength of annihilation radiation from which it is possible to calculate the mass of the positron.[1] Several subsequent investigations[2-5] were devoted to the development of procedures for precise determination of the wavelength on magnetic spectrometers as well.

The precision of modern measurements attains several hundredths and even thousandths of a percent[6] and comes close to the precision with which certain atomic constants are known. Thus, one can now speak of refining the values of certain universal constants by means of γ-spectroscopy.[3,7]

Most spectrometers must be calibrated before precise energy measurements can be made. This in turn makes it imperative to have accurately measured energy values for a number of lines over as large a range of wavelengths as possible. The availability of a large number of isotopes supplying such "reference points" makes it possible to carry out accurate calibrations using the most suitable source for any given case.

It is evident, finally, that instruments that can be used to measure γ-line energies precisely can also be employed for the study of new spectra. In many cases, a knowledge of the exact transition energy makes it possible to clarify the decay scheme.[8]

We built a two-meter focusing crystal diffraction γ-spectrometer of the DuMond type.[9] A diagram of the instrument is shown in Fig. 1. The γ-quanta from the source S fall on the quartz crystal C, curved along the arc of a 2 meter radius circle. The crystal is clamped between a convex and a concave steel cylindrical mirror; the two mirrors are ground with optical precision.

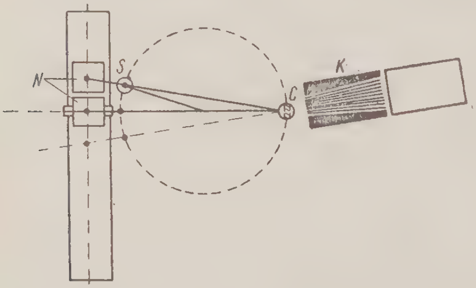

Fig. 1. Diagram of focusing crystal-diffraction γ-spectrometer: S) source, C) quartz crystal, K) collimator, N) carriages mounting the crystal and the source.

Before bending, the crystal has the form of a plane-parallel plate measuring 50 x 30 x 2 mm, cut from a quartz single crystal so that the working planes (in our case (3140) or (1124)) will be perpendicular to the large surface (face) of the plate. Gamma-quanta, having the wavelength for which the Bragg condition $\lambda = 2d \sin \theta$ is satisfied, form a diffracted beam, propagating at a small angle with the considerably more intense direct beam.

A multiple-slit collimator K is used to cut off the direct beam. The collimator consists of a system of twenty-six slits, 1 mm wide at the entrance and formed by radially-arranged brass plane-parallel plates. The total length of the collimator is 100 cm. The collimator passes 40-45% of the quanta arriving parallel to its axis, and greatly (by a factor of 10^5) attenuates the beam, propagating at an angle greater than 8' minutes relative to the collimator axis. The quanta passed by the collimator are recorded by a scintillation counter employing a CsI(Tl) crystal 50 mm in diameter and 20 mm high and a FEU-19 photomultiplier tube.[10] The effective transmission of the instrument could have been increased considerably by increasing the dimensions of the crystal to equal those of the collimator exit window (70 x 60 mm). By appropriate adjustment of the scintillation spectrometer to the energy interval of interest, the background can be reduced considerably without significant sacrifice of recording efficiency.

In studying spectra, the displacements of the quartz crystal and the source are correlated so that the spatial orientation of the diffracted beam remains unchanged. Hence the collimator scintillation counter can remain stationary. The source and crystal are moved by means of micrometer screws. Appropriate scales indicate the positions of the crystal and source carriages (N in Fig. 1) to within 0.01 mm. Thus there is no need to graduate the micrometer screws and the usual errors due to irregularities in the screws are eliminated. The readings on the scales are proportional to sin θ and, consequently, to the γ-radiation wavelength.

The existence of a plateau on the transmission characteristic of the collimator (dependence of the transparency on the angle relative to the collimator axis) makes it possible to move the source in steps of approximately 1 mm and to study the contour of an individual line with the source stationary.

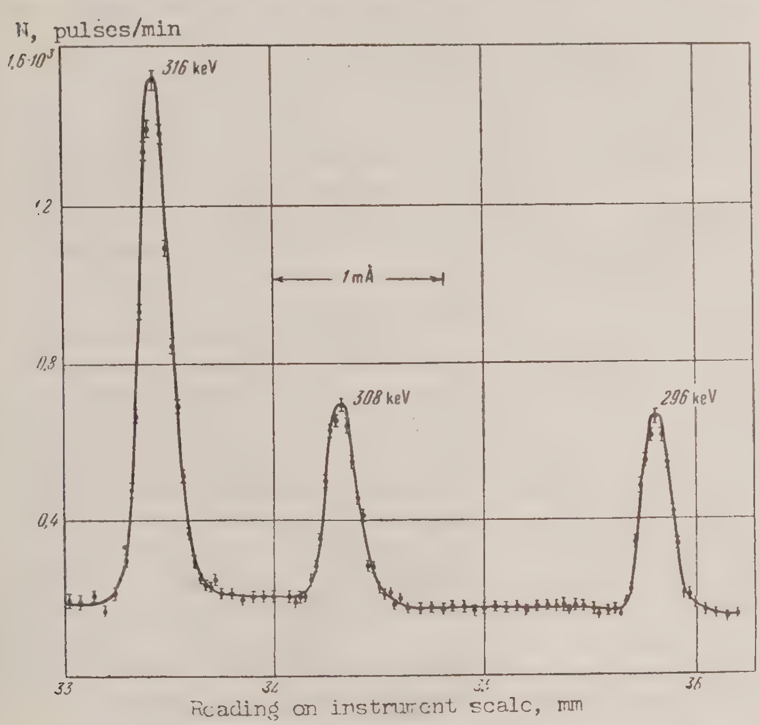

Fig. 2. Part of the γ-spectrum of Ir^{192} recorded by means of the focusing curved-crystal γ-spectrometer.

The instrument was adjusted optically and using x-rays.

The γ-spectrum of Ir^{192} was plotted to check the adjustment and to determine the basic parameters of the instrument. The source was 30 x 5 x 0.2 mm iridium foil, activated by neutron bombardment and mounted facing the crystal. The source activity just prior to the start of measurements was 1.2 curies. The 208, 296, 308, 316, 468, 485, 588, 604 and 612 kev lines were recorded. By way of illustration a portion of the spectrum is reproduced in Fig. 2. The width of the lines at half-height is 0.16-0.19 mm, which corresponds to the following energy dependence of the relative half-width:

$$\delta(\%) = (1.5\text{-}1.7)\cdot 10^{-3}E(\text{kev}).$$

The half-width in the 300 kev region is thus approximately 0.45%. It must be noted that the line width depends on lateral dimensions of the source; in our case, the effective width of the source is defined by the width of the slit in the lead diaphragm in front of the source (~0.12 mm). A certain broadening of the line with increasing energy (from 0.16 mm at 300 kev to 0.19 mm at 406 kev) can be explained by the penetration of the slit edges, resulting in an increase in the effective width of the source.

To evaluate the magnitude of the random measurement error, we made repeated determinations of the wavelength of the 316 kev line. The line was studied with the source shifted to the right and to the left of the crystal and the distance

Table 1

Results of measurements of the wavelength of the 316 kev γ-line of Ir^{192}

Series No.	$2l$	$2l - \overline{2l}$
1	66,415	0,007
2	66,384	—0,024
3	66,403	—0,005
4	66,396	—0,012
5	66,416	0,008
6	66,403	—0,005
7	66,397	—0,011
8	66,410	0,002
9	66,416	0,008
10	66,414	0,006
11	66,415	0,007
12	66,421	0,013
Average	$2l$=66,408	+0,051 —0,057

between such "mirror" lines was measured. The results of twelve series of such measurements are given in Table 1.

The root mean square error for a series of measurements proved to be ± 0.012 mm; and the root mean square error for the final result was ± 0.0035 mm; the mean distance between the mirror lines was $\overline{2l}$ = 66.408 mm.

It was assumed that the spectrometer scale would be linear without the need for any corrections. To check this assumption we calculated the instrument constant:

$$k = \lambda/\overline{2l} = 0.58987 \pm 0.00007 \text{ mA/mm}$$

where $\lambda = 39.172 \pm 0.004$ mÅ is the wavelength of the 316 kev line of Ir^{192} (Ref. 8) and $\overline{2l}$ = = 66.408 ± 0.04 mm is the distance between the mirror lines.

We next measured the distances between the mirror lines of energies 468, 308 and 296 kev (four measurements for each energy) and calculated their wavelength in accordance with the constant obtained. The results are given in Table 2.

Table 2

Comparison of the results for the wavelengths of four lines in the γ-spectrum of Ir^{192} obtained by the authors with DuMond's data.

E, keV	$2\overline{l}$, мм	λ, mÅ		Δλ
		Our data	DuMond's data	
468	44,897	26,483 ± 0,010	23,489 ± 0,004	—0,006
316	66,408	39,172	39,172 ± 0,004	0,000
308	68,135	40,191 ± 0,010	40,189 ± 0,004	0,002
295	71,026	41,896 ± 0,010	41,888 ± 0,000	0,008

As can be seen, our data agree well with those of DuMond. Thus, the non-linearity of the scale of our spectrometer in the investigated wavelength region does not exceed the limits of the statistical error (±0.01 mA).

Ir^{192} is one of the few isotopes for which the relative intensities of the γ-transitions are known from many investigations (Ref.s 11-13 & 8). These intensities are listed in Table 3.

Table 3

Relative intensities of γ-transitions in Ir^{192} according to the data of different investigators

E, kev [14]	[11]		[12]	[13]		[8]	
136,2	—		—	0,188		0,23	
174,0	—		—	0,058		—	
201,2	—		—	0,058		0,58	
205,4	0,27			0,25		4,35	
281,5	—			0,07		—	
295,8	3,0	14,1	9,09	1,88	9,77	22,0	105,2
308,4	3,1			2,02		21,4	
316,5	7,7			5,55		57,5	
374	—		—	0,036		—	
440	—		—	0,036		—	
467,8	4,1		4,58	4,1		17,4	
484,4	—		—	0,375		—	
588,7	0,33			0,46		0,64	
604,5	1,0	1,74	1,74	0,72	1,74	0,81	1,74
612,7	0,41			0,55		0,29	

In the investigations of Refs. 11 & 13, conversion electrons and photoelectrons were studied, while in the work of Ref. 12 recoil electrons were used. All these data are in good agreement with each other, but differ considerably from the results obtained on DuMond's crystal spectrometer.[8] It would be interesting to find out whether this divergence is due to mistaken theoretical assumptions in determining the spectral sensitivity curve for the curved-crystal spectrometer or to other factors.

We calculated the spectral-sensitivity curve in a manner analogous to that used by DuMond. As is known, DuMond's calculations allow for: (a) self-absorption in the source; (b) variation of the reflection coefficient from the curved crystal with the γ-ray wavelength (the reflection coefficient is assumed to be proportional to λ^2), and (c) the efficiency of the scintillation counter.

Our theoretical curve characterizing the dependence of the probability of the γ-quantum being recorded at the peak of the curve on the energy of the quantum is given in Fig. 3 (curve 1). The same figure shows the experimental points obtained by comparing the number of pulses at the line peaks obtained on our spectrometer with the relative intensities given in Ref. 13, and the relative intensities taken from DuMond's study (Ref. 8). As can be seen, the spectral sensitivity curve obtained by comparing our data with those of Ref. 13 (curve 2) agrees quite well with the theoretical one. Points associated with lines of nearly equal energies form close groups, indicating good accuracy for individual measurements. On the other hand, points obtained by comparison with DuMond's data (curve 3) do not fit a smooth curve and lie close to the theoretical spectral-sensitivity curve.

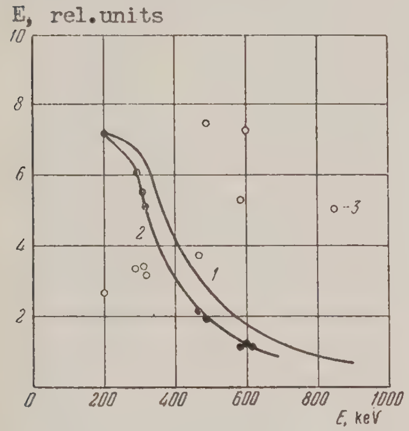

Fig. 3. Spectral sensitivity curves for our γ-spectrometer: 1) theoretical, 2) experimental (obtained using the relative intensities from Ref. 13), 3) results obtained using the relative intensities from Ref. 8.

Thus, using the calculated spectral-sensitivity curve, our results can be made to agree quite well with the data of Refs. 11, 12 & 13, but show no agreement with DuMond's data.[8]

In conclusion it must be noted that by virtue of the use of a collimator entirely different in design from that in the DuMond instrument, in our case the background does not rise with decreasing wavelength (as reported by DuMond). Measurements with a Ta^{182} source have shown that the background remains constant up to energies of at least 1.5 Mev.

We wish to thank Z.P.Balon, who spent much time and effort on developing the mechanical part of the spectrometer, Design Engineer V.S.Stepanov and the staff of the "Etalon" Plant, where the instrument was built.

"D.I.Mendeleev"
All-Union Scientific Research Institute of Metrology

References

1. J.DuMond, D.Lind & B.Watson, Phys. Rev., 75, 1226 (1949).
2. A.Hedgran & D.Lind, Phys. Rev., 82, 127 (1951).
3. G.Lindström, Phys. Rev., 83, 465 (1951).
4. G.Lindström, Phys. Rev., 87, 678 (1952).
5. MGraig, Phys. Rev., 85, 688 (1952).
6. J.DuMond & E.Cohen, Rev. Mod. Phys., 25, 691 (1953).

7. K.Siegbahn, Beta- and Gamma-ray Spectroscopy, p. 98. Amsterdam, 1955.
8. D.Muller, H.Hoyt, D.Klein & J.DuMond, Phys. Rev., 88, 775 (1952).
9. J.DuMond, Rev. Sci. Inst., 18, 626 (1947).
10. A.Konstantinov, O.Sumbaev & V.Chetkin, Izv. AN SSSR, Ser. fiz., 20, 347 (1956). (Trans. in Bulletin Vol. 20, No. 3, p. 318).
11. A.Bashilov, N.Anton'eva & B.Dzhelepov, Izv. AN SSSR, Ser. fiz., 16, 264 (1952).
12. M.Glazunov, D.Dzhelepov & Iu.Khol'nov, Izv. AN SSSR, Ser. fiz., 19, 294 (1955). (Trans. in Bulletin Vol. 19, No. 3, p. 267.)
13. M.Johns & S.Nablo, Phys. Rev., 96, 1599 (1954).

INVESTIGATION OF THE HARD γ-RADIATION FROM Ir^{192}* BY MEANS OF A SCINTILLATION SPECTROMETER

- N.N.Deliagin, G.A.Kuznetsova & V.S.Shpinel'

The decay scheme of Ir^{192} has been established on the basis of a number of studies[1-4] performed in 1951 and 1952. Recently new γ-transitions in Ir^{192} have been discovered[5-8] and this has made it possible to refine and supplement its decay scheme. The most comprehensive decay scheme is given by Jons and Nablo[6], who introduce two new excited Pt^{192} levels (1155 and 1359 kev). The 1359 kev level was deduced from the existence of several weak γ-transitions from this level to lower excited states of Pt^{192}.

In the present work we investigated the highest energy region of the Ir^{192} γ-spectrum, analyzed the relative transition intensities and compared them with the existing theoretical formulas.

The measurements were made on a scintillation spectrometer incorporating an NaI(Tl) crystal and FEU-19 photomultiplier and a single-channel differential discriminator. The relative half-width of the Cs^{137} 661 kev line obtained on our spectrometer was 9.5%. The spectrometer was provided with an automatic circuit stabilizing the position of the studied spectral line (the principle of operation of the stabilizing circuit is described in Ref. 9). The use of this circuit enabled us to exclude the possible influence of various instrument instabilities on the experimental results.

Difficulties are often encountered in interpreting complex γ-spectra obtained on a scintillation spectrometer due to overlapping of the pulse distributions from individual monochromatic γ-lines. In order to facilitate interpretation of the γ-spectrum, as well as to calibrate the spectrometer for energy, we performed a series of preliminary investigations of simple γ-sources: Hg^{203}, Au^{198}, Cs^{137}, Zn^{65}, Co^{60} and Na^{24}. The same sources were also used to calibrate the spectrometer as regards efficiency. This was done by measuring the absolute activities of the sources by means of a special calibrated Geiger counter (the calibration curve for the counter was based on the measurements of I.Estylin and I.Antonova). Then the γ-spectra were recorded on the scintillation spectrometer, and the total energy peak (photopeak) per unit activity was taken as the measure of the efficiency.

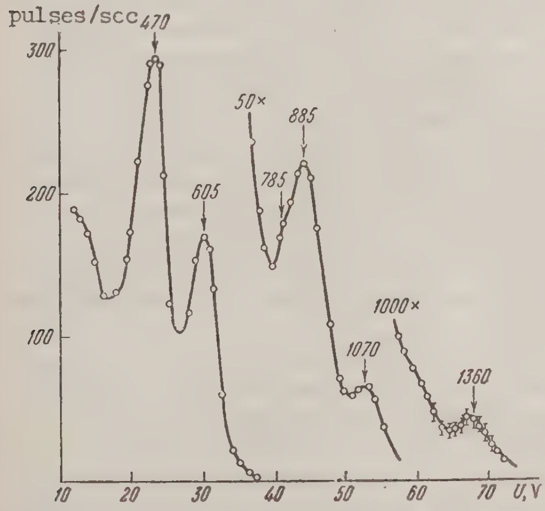

Fig. 1. γ-Spectrum of Ir^{192} as obtained on the scintillation spectrometer.

In our study we used an Ir^{192} source having an activity of 26 mcuries. In order to insure normal operation of the apparatus and to exclude the background due to gamma coincidences in the crystal, the soft and most intense part of the Ir^{192} γ-spectrum was attenuated by a 20 mm thick lead absorber.

The Ir^{192} γ-spectrum obtained is shown in Fig. 1. The most intense γ-transitions of energies 296, 308 and 316 kev are not visible in the spectrum obtained with the lead absorber. The 470 peak comprises contributions not only from the intense 468 kev transition, but also from the weak 484 and 440 kev transitions; the 605 kev peak is the sum of the 605, 613 and 589 kev transitions. In the higher energy region, in addition to the already known 785, 885 and 1070 kev lines, we observed a new

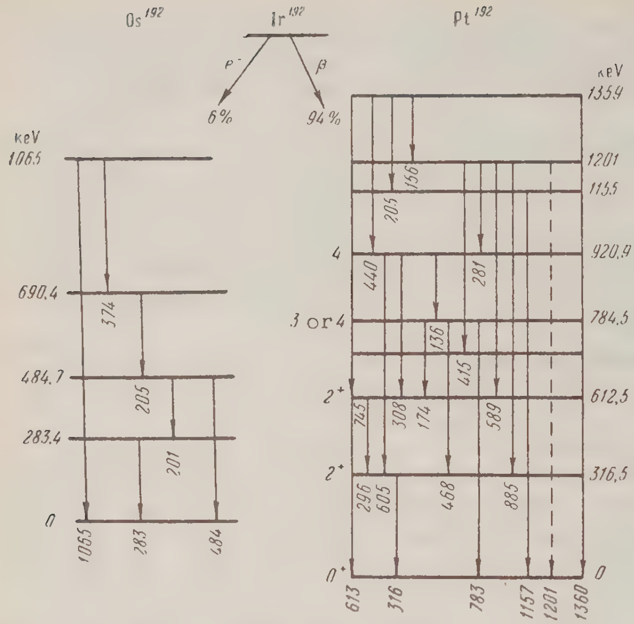

Fig. 2. Decay scheme for Ir^{192}.

transition having an energy of 1360 kev. The intensity of this transition is evaluated to be $(2.5 \pm 1.2) \cdot 10^{-4}$ relative to the 605 kev line and $(1.4 \pm 0.8) \cdot 10^{-4}$ relative to the 470 kev line. Using the data of Refs. 4, 6 & 7 on the intensities of the 470 and 605 kev peaks, one can calculate the intensity of the 1360 kev cross-over transition. This intensity is $6.3 \cdot 10^{-5}$ with a possible error of up to 80%, inasmuch as the 470 and 605 kev intensities are at present known to an accuracy of about 20%. The weak 1210 kev transition observed by Pringle et al[5] was not detected in our measurements. In the Ir^{192} decay scheme the 1360 kev transition represents a direct transition from the excited 1359 kev level to the ground state of Pt^{192}. In order to make sure that the 1360 kev photopeak is due to an actual transition and not to γ-coincidences in the crystal, we performed control measurements with various solid angles of the source viewed from the counter. It was established that the 1360 kev photopeak is due to a real transition. The Ir^{192} decay scheme as given in Ref. 4 & 6 is shown on Fig. 2 with the additional 1360 kev γ-transition.

The relative γ-transition intensities given in Refs. 4 & 6 were compared with the theoretical ones calculated according to Weisskopf's formula[10] which is based on the single-particle transition hypothesis. In the calculations we used spin values for the excited Pt^{192} states as determined by Taylor and Pringle[11] on the basis of γ-γ angular correlation. The parities of the first two excited Pt^{192} states may be considered positive, since it follows from data[4] on the conversion coefficients for the 296, 316 and 613 kev transitions that these transitions are E2. It must be noted, however, that the accuracy of the internal conversion coefficient measurements of Ref. 4 does not preclude the possibility of these being mixed E2 + M1 transitions.

Both a cross-over transition to the Pt^{192} ground state and a cascade transition are observed from the 613 kev excited level. According to Weisskopf's formula the intensity of the direct transition (E2) should be 50 times lower than that of the cascade transition (M1). Actually, however, the intensities differ by a factor of from 3.4 to 8, according to the data of different authors. This can be explained if we assume that the 296 kev transition is mixed (84-93% E2 + 7-16% M1).

The contradictions in principle with Weisskopf's formula are obtained in comparing the intensities for transitions from the higher excited Pt^{192} levels to the 316 and 613 kev levels, which have the same spins and parities. The data for the transitions from the 921 and 1200 kev levels are given in the table.

It will be seen that in reality transitions of lower energies have significantly higher intensities, whereas Weisskopf's formula predicts the opposite. Thus, if both the 308 and 605 kev transitions are quadrupole, the 605 kev transition should (theoretically) be 30 times as intense as the 308 kev one. Such disagreement with Weisskopf's formula indicates that in the present case the

Ratio of intensities of transitions from two high excited levels to lower levels according to the data of different authors.

Level, kev	Transitions compared	Experimental values according to various authors		Theoretical value
		Ref. 4 & 7	Ref. 6	
921	I_{308}/I_{605}	3.3	2.8	0.03
1200	I_{589}/I_{885}	10	7.1	<1

transitions are not single-particle transitions, but bear a different character. It would appear natural to relate the observed intensities to collective nuclear properties. An attempt was made to explain the disagreement with Weisskopf's formula by assuming that the transition is forbidden by the value of the quantum number K which determines the projection of the mechanical moment of the nucleus on the nuclear axis of symmetry[12]. Unfortunately, the now extant theoretical expressions were deduced only for strongly deformed nuclei, where K is a good quantum number. In the case of Pt^{192}, whose Z = 82 shell is almost filled, this apparently does not hold. Therefore calculations based on the formulas of Ref. 12 also did not yield agreement with the experimentally observed relative intensities.

Moscow State University

References

1. J.Cork, J.Leblanc, A.Sttoddard, W.Childs, C.Brangon & D.Martin, Phys. Rev., 82, 258 (1951).
2. D.Muller, H.Hoyt, D.Klein & W.DuMond, Phys. Rev., 88, 775 (1952).
3. V.Shpinel' & N.Forafontov, Zhur. eksp. i teor. fiz., 21, 1376 (1951).
4. A.Bashilov, H.Anton'eva & B.Dzhelepov, Izv. AN SSSR, Ser. fiz., 16, 264 (1952).
5. R.Pringle, W.Turchinetz & H.Taylor, Phys. Rev., 95, 115 (1954).
6. M.Jons & S.Nablo, Phys. Rev., 96, 1599 (1954).
7. M.Glazunov, B.Dzhelepov & Iu.Khol'nov, Izv. AN SSSR, Ser. fiz., 19, 294 (1955). (Trans. in Bulletin, Vol. 19, No. 3, p. 267).
8. F.Girard, L.Danguy & T.Franeau, J.Phys. et Rad., 16, 839 (1955).
9. H.Waard, Nucleonics, 13, 7, 36 (1955).
10. J.M.Blatt & V.F.Weisskopf, Theoretical Nuclear Physics. (In Russian trans. M.1955).
11. H.Taylor & R.Pringle, Phys. Rev., 99, 1345 (1955).
12. G.Alaga, R.Alder, A.Bohr & B.Mattelson, Dan. Mat. Fys. medd., 29, 9 (1955).

DECAY SCHEME OF Zr^{97} AND Nb^{97}

- N.N.Deliagin, A.A.Sorokin, N.V.Forafontov & V.S.Shpinel'

Introduction

The radioactive series $Zr^{97} \rightarrow Nb^{97} \rightarrow Mo^{97}$ has been investigated by several authors. A review of the data together with a bibliography will be found in Ref. 1. It is reliably established that Zr^{97} passes by β-decay to the 0.747 Mev isomeric state of Nb^{97}, which decays with a 60 sec half-life to the Nb^{97} ground state.

The Zr^{97} β-spectrum is a simple one with an end-point energy $E_\beta = 1.91$ Mev. Nb^{97} undergoes β-decay with $E_\beta = 1.267$ Mev; the process is accompanied by 0.665 Mev γ-rays. Shpinel' and Kuznetsova[1] using a $Zr^{97} + Nb^{97}$ source detected a soft β-spectrum with $E_\beta = 0.48$ Mev and hard γ-radiation of low intensity.

At the 1955 All-Union Conference on Nuclear Spectroscopy we reported on an investigation of the decay of these nuclei by the method of β-γ and γ-γ coincidences. By means of this procedure we were able to separate the low-energy Zr^{97} β-spectrum and the Nb^{97} β-spectrum from the total $Zr^{97} + Nb^{97}$ β-spectrum; in addition, γ-γ coincidences having an intensity of ~10% were observed from the same source. The energies of the cascade γ-quanta, as evaluated by absorption measurements, were ~0.7 Mev and >1 Mev. In order to obtain more accurate data, we repeated our measurements using improved equipment. The new results are described below.

Source

The radioactive Zr^{97} source was obtained by neutron irradiation of zirconium in a reactor for 10-24 hours. Samples prepared in this manner have a low specific activity in view of the low content of Zr^{96} (2.6%) in natural zirconium and the low activation cross section (0.1-0.2 barns). It is therefore necessary to pay particular attention to the purity of the initial material, particularly where investigations of low-intensity β- and γ-transitions are concerned. For most of the measurements, instead of starting with zirconium oxide as previously, we used metallic Zr prepared by the iodide method. The presence of about 1-2% hafnium and titanium impurities and the minor amount of Zr^{95} formed in the process of neutron bombardment do not affect the experimental results, since the half-lives of these isotopes are much greater than the period of Zr^{97}.

Possible surface contaminations (mainly sodium) were removed by rinsing in nitric acid after irradiation. In a number of control measurements the irradiated material was ZrO_3 powder, sixteen-fold enriched in Zr^{96}.

γ-Spectrum

The $Zr^{97} + Nb^{97}$ γ-ray spectrum was studied on a single-crystal scintillation spectrometer with a NaI(Tl) crystal coupled to FEU-19 photomultiplier. The 12 mm thick, 30 mm diameter sodium iodide crystal with a MgO reflector was hermetically sealed in an aluminum container. On the way to the crystal, the γ-rays passed through a 0.4 mm thick aluminum foil and a 1 mm magnesium layer. The measurements were performed without collimating the beam. Under these conditions the relative half-width of the Cs^{137} photoelectron line was 12%. Introduction of a lead collimator with a 3-7 mm diameter opening and a length of 40 mm reduces the line half-width to 9-10%. The linearity of the spectrometer's energy scale was checked with reference to γ-radiation from Hg^{203}, Au^{198}, Cs^{137}, Zn^{65}, Co^{60}, ThC'' and Na^{24}.

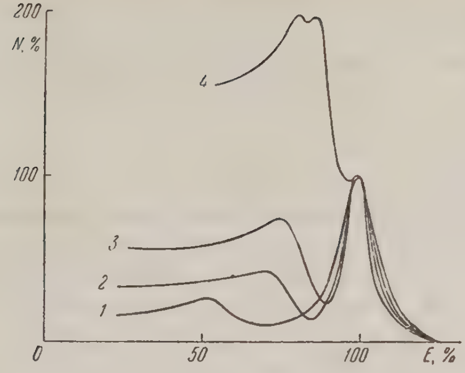

Fig. 1. Shapes of the Hg^{203}, Cs^{137}, Zn^{65} and Na^{24} γ-spectra as obtained on the scintillation spectrometer: 1) Hg^{203}, E_γ=0.279 Mev; 2) Cs^{137}, E_γ=0.661 Mev; 3) Zn^{65}, E_γ=1.118 Mev; 4) Na^{24}, E_γ=2.760 Mev.

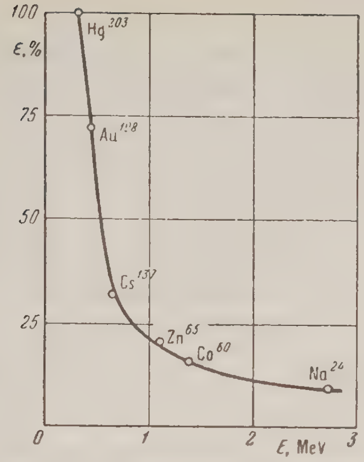

Fig. 2. Efficiency curve of the scintillation γ-spectrometer.

In interpreting the complex γ-spectrum obtained on the scintillation spectrometer, we resolved it into separate components using standard shapes obtained for known γ-lines. The shape of these standard spectra normalized to equal heights for the overall energy peaks (photopeaks) are shown in Fig. 1. Here the horizontal scale is laid off in percent of the photopeak energy. The intensities of the γ-lines were determined with reference to the area under the integral energy peak contour on the calibration curve for the relative efficiency of the spectrometer at various energies (Fig. 2). The method of obtaining the efficiency curve is described in Ref. 2. The error in determining the spectrometer efficiency is determined primarily by errors in measuring the absolute source activity (6%) and the uncertainty in measuring the photopeak areas (10-15%).

Fig. 3 shows the γ-spectrum of Zr^{97} + Nb^{97} obtained with the above-mentioned enriched source. It will be seen that in addition to the intense photopeaks due to the well known 0.665 and 0.750 Mev γ-rays of Zr^{97} and Nb^{97}, the spectrum comprises several peaks in the 1.0 to 2.6 Mev energy interval. Observation of the intensity decay rate of the hard part of the spectrum yielded a half-life of 17±1 hours (the period of Zr^{97} is 17 hours). The positions of these peaks correspond to the electron energies listed in the table below.

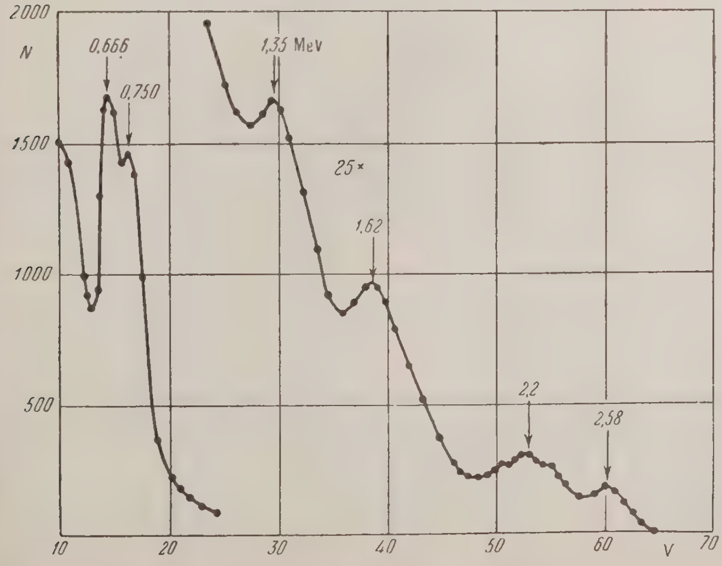

Fig. 3. γ-Spectrum of Zr^{97} and Nb^{97}

By successive subtraction of the standard spectrum shapes, starting with the highest energy line, one can deduce the origin of each peak. The results of such analysis, presented in the table, show that all maxima, with the exception of the hardest, are produced by the superimposition of the pulse distributions due to the individual monochromatic γ-lines whose energies and intensities are also given in the table. The intensities are given in percent of the total number of decays. Unfortunately, it must be noted that the interpretation of so complex a spectrum cannot be entirely unambiguous. We obtained additional information on the hard γ-radiation by investigating γ-γ coincidences.

Peaks in the γ-spectrum of $Zr^{97} + Nb^{97}$

Energy value of peak, Mev	Origin of peak	Energy of γ-line, Mev	Intensity of γ-line %
2.58	Ph_1*	2.58±0.05	$\leqslant 1$
2.3	C_1	---	---
2.2	Ph_2	2.2±0.05	~1 – 2
2.1	P_1	---	---
1.62	$Ph_3+P_1+P_2$	1.62±0.03	~ 1.5
1.35	Ph_4+K_3	1.35±0.05	~3 – 5
1.15	$C_4+P_3+P_2$	---	---

*Ph = photoelectron, C = Compton electron and P = pair peak.

Set-up for Investigating γ-γ Coincidences

The cascade γ-rays were studied on a scintillation coincidence spectrometer. This spectrometer is based on the fast-slow coincidence principle, which makes it possible to combine a short resolving time (about 10^{-8} seconds) with pulse-height analysis. A block diagram of the spectrometer is shown in Fig. 4. The detectors consist of standard model NaI(Tl) crystals, 30 mm diameter and 15 mm thick, and FEU-19 photomultiplier tubes. The pulses from photomultipliers 1 are fed to a fast coincidence circuit similar to that described in Refs. 3 and 5. These pulses are clipped by the pulse limiting 6Zh1P pentodes 5 and enter the variable delay line 6. This line consists of a series of 50 cm long sections of RK-50 cable (ρ = 150 ohms).

At the cable joints there is a sliding contact with a DGS-4 crystal diode 8, which selects the coincidences. By moving the diode mount along the line one can find the position corresponding to a maximum number of true coincidences or the position where only chance coincidences are counted. The resolving time of the coincidence circuit is determined mainly by the length of the shaping cable 7 (RK-1 cable, ρ = 77 ohms) and to some extent by the bias applied to the diode 8. The coincidence pulses passed by the crystal are amplified in the amplifier 9 (amplification factor 1000; 4 Mc passband) and enter the discriminator 10, which

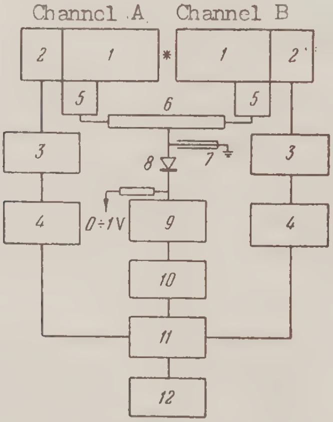

Fig. 4.

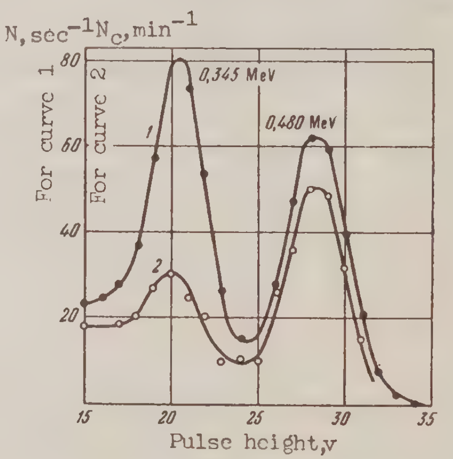

Fig. 5.

Fig. 4. Block diagram of set-up for investigating γ-γ coincidences: 1) counters and photomultipliers, 2) cathode followers, 3) linear amplifiers, 4) analyzers, 5) limiters, 6) variable delay line, 7) shaping cable, 8) crystal diode, 9) amplifier, 10) discriminator, 11) triple coincidence circuit, 12) scaling circuit.

Fig. 5. 1) Part of γ-spectrum of $Hf^{175} + Hf^{181}$ including the 0.345 and 0.480 Mev lines; 2) γ-spectrum of coincidences with the 0.132 and 0.135 Mev γ-quanta from Hf^{181}.

cuts off amplifier noise and individual pulses that leak through the parasitic capacity of the crystal diode. In order to insure maximum coincidence counting efficiency, the pulses leaving the photomultiplier should have the greatest possible height. With selected photomultiplier tubes, a non-uniform voltage divider and a supply voltage of 2.2 kv, the pulses at the photomultiplier output from Co^{60} γ-rays attain 100 v.

The pulses used for the pulse height analysis are taken from the 9th dynodes of the photomultipliers. In each channel these pulses go through the cathode followers 2 to the linear amplifiers 3 and single channel pulse height analyzers 4. The amplifiers are three-tube units with feedback[6] and have amplification factors of 100, 50 and 20 with a linear voltage output up to 100 v. The analyzers 4 and the discriminators 10 of the fast coincidence circuit are coupled to the triple-coincidence circuit 11 with a resolving time of $5 \cdot 10^{-7}$ sec. Thus the scaler 12 counts only coincidences between γ-rays of the particular energy selected by the pulse height analyzers.

The resolving time τ_0 of the fast coincidence circuit was chosen to be $(2.5\text{-}3) \cdot 10^{-8}$ sec. A test for coincidences between 0.058 Mev x-rays and 0.345 Mev γ-rays showed that even at such relatively low energies the coincidence counting loss did not exceed a few percent. Calibration of the spectrometer showed that its energy scale is linear up to the maximum measured energy: 2.76 Mev (Na^{24}). The half-width of the Cs^{137} line was 13-14% for both channels.

To check the operation of the set-up a series of control measurements of the coincidence spectra for several isotopes (Na^{24}, Co^{60} and Hf^{175} + Hf^{181}) were run. Fig. 5 shows the results for $Hf^{175+181}$. Curve 1 represents the part of the γ-spectrum of this isotope mixture comprising the 0.345 and 0.480 Mev lines (recorded in channel A). A great part of the intense 0.345 Mev peak is due to γ-radiation from Ta^{175}, since the intensity of the 0.345 Mev transition is 15.7% relative to the 0.480 Mev transition in Ta^{181} (Ref. 7). Curve 2 is the spectrum of γ-rays, coinciding with the 0.132 and 0.135 Mev Ta^{181} gammas, selected by the pulse height analyzer in channel B. As may be seen, the intensity of the 0.345 Mev line is appreciably weakened due to the exclusion of the Ta^{175} radiation which does not yield coincidences. An evaluation of the intensity of this line relative to the 0.480 Mev line, taking into account the internal conversion coefficients for the 0.132 and 0.135 Mev γ-transitions, gives a value of 15-20%, which is in agreement with the value cited above.

Spectrum of Zr^{97} + Nb^{97}

In measuring the γ-γ coincidences in the Zr^{97} + Nb^{97} spectrum we used the counter and source geometry shown in Fig. 6.

The 5 mm thick lead absorber shown in Fig. 6 was installed in front of the crystal in channel B in order to suppress coincidences due to scattering of gammas from one crystal to the other.

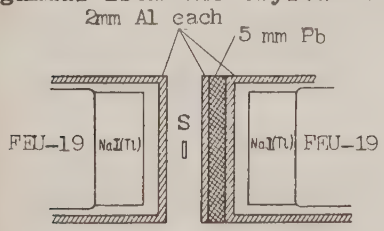

Fig. 6. Relative positions of the counters and source (S) in recording the γ-γ coincidences in the radiation from Zr^{97} + Nb^{97}. FEU-19 - photomultiplier.

The occurrence of cascade γ-radiation in the Zr^{97} + Nb^{97} spectrum is evident from curve 1 of Fig. 7, which gives the dependence of the fast-coincidence counting rate on the delay in the channels. For purposes of comparison, the analogous curve for Co^{60} (curve 3), characterizing the "resolution curve" of the set-up, is given in the same figure. The decrease of the γ-γ coincidence rate with time, as observed over a period of three days, corresponds to a half-life of 17 hours, thus indicating that the cascade radiation comes from Zr^{97} or Nb^{97}. In order to discover which of these nuclei is responsible for the coincidences, we performed analogous measurements on Nb^{97} chemically separated from the zirconium. The results (curve 2 in Fig. 7) show that there are no γ-γ coincidences in this case. We are therefore led to conclude that the observed cascade radiation comes from Zr^{97}.

Next we measured the energies of cascade γ-quanta. The results are given in Fig. 8.

Curve 1 in Fig. 8 gives the spectrum of γ-quanta, recorded in channel A, that coincided with all γ-rays of $E_\gamma > 0.250$ Mev registered in channel B, in which the integral analyzer output was used.

Curve 2 on Fig. 8 shows the spectrum obtained when channel B registered only γ-rays of $E_\gamma > 1$ Mev. The analyzer gate in the channel was increased to 2 volts (instead of the usual width of 1 volt) and the points on the spectra were taken at 2 v intervals. The results of this was that the spectra were not recorded in sufficient detail; however, it was necessary to do this in order to cut down the experiment time.

The background due to chance coincidences has been subtracted from all the experimental curves shown in the figures. In the low-energy part of the spectrum of Fig. 8 the chance background amounted to 20-25% (curves 1 and 2) of the number of true coincidences; in the high-energy part ($\geqslant$1 Mev) of this spectrum (curve 1) this background was much lower and could be safely neglected.

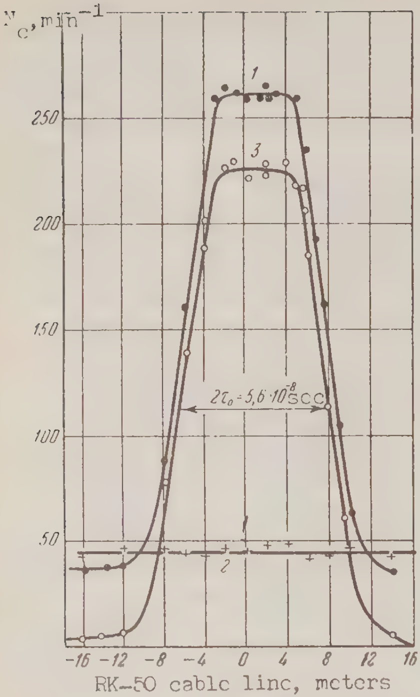

Fig. 7. The dependence of the number of γ-γ coincidences on the magnitude of the delay for the following sources: 1) $Zr^{97} + Nb^{97}$, 2) Nb^{97}, 3) Co^{60}.

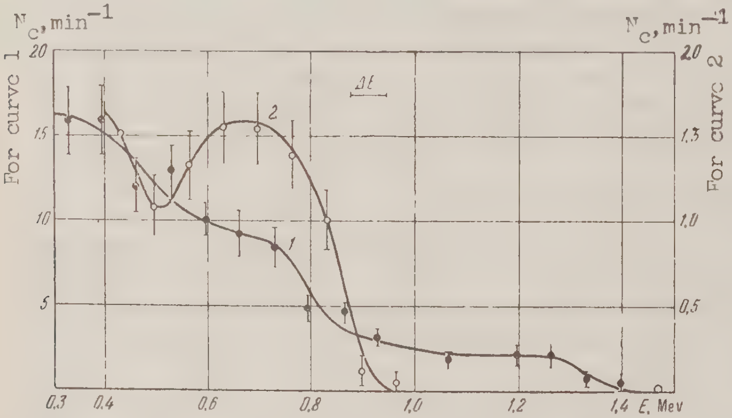

Fig. 8. The spectrum of γ-quanta coinciding with the γ-rays of energies 1) E_γ 0.250 Mev and 2) E_γ 1 Mev.

It will be seen from the above data that the energy of the most penetrating of the coincidence gammas is in the region of 1.3 - 1.4 Mev (Fig. 8, curve 1). These, clearly, are in cascade with the γ-rays whose spectrum is given by curve 2. This spectrum comprises a smeared out maximum in the 0.6-0.8 Mev region; this maximum is much wider than a normal photopeak due to a single γ-line. It may be assumed, therefore, that either:

1) there is only one γ-line, and the widening is due to instability of the set-up, manifested owing to the relatively long (10-12 hours) measurement time, and the large analyzer gate width; or

2) there exist two close lines which have not been resolved by the spectrometer.

In order to test these assumptions we performed the following control experiment.

The NaI(Tl) crystal in channel B was replaced by a tolane crystal covered only by a thin (surface density 1.6 mg/cm^2) aluminum foil.

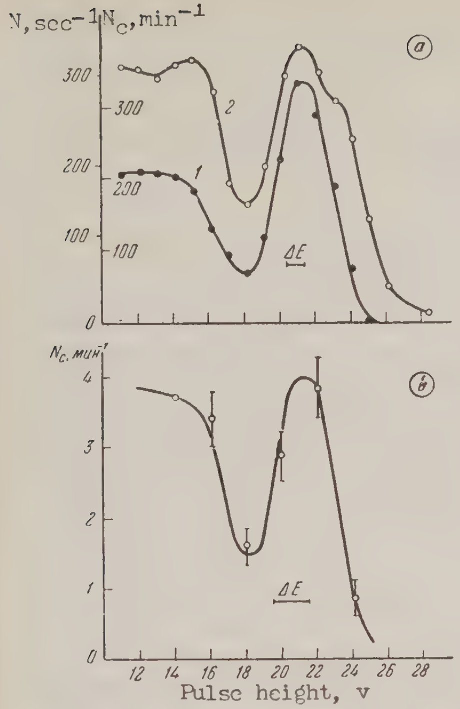

Fig. 9. a) Comparison of the β-γ coincidence spectrum (1) with the ordinary γ-spectrum of Zr^{97} + Nb^{97} (2); b) control measurement of β-γ coincidence measurements, yielding a spectrum identical with (1) in a) above.

In this case, there were recorded in this channel, in addition to the γ-quanta, electrons of the β-spectra with end-point energies $E_\beta =$ $= 1.910$ Mev from Zr^{97} and with $E_\beta = 1.270$ Mev from Nb^{97}. With this arrangement the set-up should record β-γ coincidences only between electrons of the β-spectrum with $E_\beta = 1.270$ Mev and the 0.665 Mev γ-rays from Nb^{97} (β-γ coincidences connected with the $E_\beta = 0.450$ Mev β-spectrum were cut off by an appropriate adjustment of the discriminator threshold in channel B). Thus, measurement of the spectrum of γ-rays giving β-γ coincidences should separate out the single 0.665 Mev line from the total γ-spectrum. The results of this measurement are presented in Fig. 9a, where the β-γ coincidence spectrum (1) is juxtaposed with the ordinary γ-spectrum of Zr^{97} + + Nb^{97} (2).

The discriminator threshold in channel B was then re-set so as to include the end region of the Nb^{97} β-spectrum. Most of the β-particles recorded in this case belonged to the β-spectrum of Zr. As a result, the coincidence counting rate was reduced by a factor of about 100 and amounted to a few pulses per minute. The analyzer gate in channel A was set at 2 v and the spectrum was measured at 2 v intervals. Thus the conditions approximated those obtaining in the γ-γ coincidence measurements. From the results shown in Fig. 9b, it can be seen that the 0.665 Mev line was quite sharply resolved. We conclude, therefore, that the more probable reason for the smearing out of the spectrum in Fig. 8 (curve 2) is the second of the two alternatives suggested.

The intensity of the cascade γ-rays was evaluated by comparing the number of γ-γ and β-γ coincidences recorded per unit time. In these measurements a tolane crystal was again used in channel B and a lead absorber installed in front of the crystal in channel A.

By adjusting the discriminator thresholds we obtained approximate equality of the counter efficiencies for the γ-rays from Cs^{137} and Co^{60}. For purposes of evaluation the efficiencies of the counters could then be considered equal for all γ-quanta participating in the coincidences. Assuming that the efficiencies of the counter in channel B in detecting the γ-rays from zirconium and niobium are the same, and neglecting β-γ coincidences connected with the 0.450 Mev β-spectrum, we can describe

the counting rate for β-γ coincidences by

$$N_{\beta\text{-}\gamma} = N_0 \varepsilon_\gamma^A \varepsilon_\beta^B$$

and the counting rate for γ-γ coincidences by

$$N_{\gamma\text{-}\gamma} = 2N_0 \varepsilon_\gamma^A \varepsilon_\gamma^B \cdot \delta.$$

The counting rates of γ-quanta and β-particles in channel B are, respectively,

$$N_\gamma^B = 2N_0 \varepsilon_\gamma^B,$$
$$N_\beta^B = 2N_0 \varepsilon_\beta^B.$$

Here ε is the efficiency of the given counter in detecting the γ- of β-rays (with the solid angle taken into account), N_0 is the activity of the source, and

δ is the intensity of the cascade radiation.

Under these assumptions, it can readily be shown that

$$\delta = \frac{1}{2}\,\frac{N_{\gamma\gamma}}{N_{\beta\gamma}}\,\frac{N_{\beta}^{B}}{N_{\gamma}^{B}},$$

wherein all the quantities are experimentally determined. The values of δ obtained from our measurements lie between 7 and 10%.

Set-up for Investigating Partial β-Spectra

The β-γ coincidences were investigated on a set-up consisting of a two-lens β-spectrometer[8] and a scintillation γ-spectrometer, connected to a coincidence circuit. A block diagram of the set-up is shown in Fig. 10. The electrons emitted by the radioactive source 2 are separated by the β-spectrometer 1 and recorded by the scintillation β-counter with a 3 mm thick, 10 mm diameter anthracene crystal 3, covered by a reflector made of an aluminized celluloid film having a superficial density not exceeding 0.1 mg/cm^2. The crystal is joined to the photocathode of the FEU-19 photomultiplier 5 by the 50 mm long Plexiglas light conductor 4.

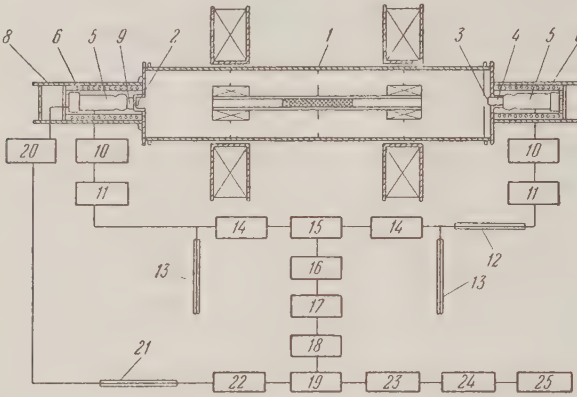

Fig. 10. Block diagram of set-up for measuring β-γ coincidences: 1) β-spectrometer, 2) radioactive source, 3) anthracene crystal, 4) light conductor, 5) FEU-19, 6) permalloy cylinder, 7) compensating coils, 8) photomultiplier housing, 9) NaI(Tl) crystal, 10, 17 & 20) cathode followers, 11) pre-amplifiers, 12) delay line, 13) shorted cable, 14) wide-band amplifiers, 15) coincidence circuit, 16) differential amplifier, 18) pulse height discriminator, 19) gating circuit, 21) delay line, 22 & 23) amplifiers, 24) differential discriminator, 25) PS-64.

The γ-radiation from the source is detected by the 15 mm thick and 30 mm diameter NaI(Tl) 9 in the previously mentioned container. The crystal is attached directly to the face of the FEU-19 photomultiplier 5 of the scintillation γ-spectrometer and is mounted in contact with the bottom of an aluminum cup with the source at its center. The crystal surface as viewed from the source subtends an angle of 15.2% of 4π. The photomultipliers are located in 3 mm thick permalloy cylinders, designed to shield them from the magnetic field of the β-spectrometer. Each cylinder has a helical compensating coil 7. The entire assembly, together with the photomultiplier, is encased in a cylindrical soft iron housing with 10 mm thick walls. With this shielding the counts of the photomultipliers in the β and γ channels did not change by more than 1.5% when the current in the spectrometer was varied from 0 to 8 amp (E ≈ 1.4 Mev).

The negative voltage pulses taken from the photomultiplier anodes are fed, through the cathode followers 10, to the pre-amplifiers 11 (amplification factor about 10) and are clipped to 2.5 v in the γ channel and to 1.7 v in the β channel. These clipped pulses are shaped by the 1.5 meter long section of shorted cable 13, after which their height is of the order of some hundredths of a volt. The β channel incorporates a delay 12, consisting of a 10 m length of cable.

The shaped pulses are again amplified by the wide-band amplifiers 14 with a 17 Mc passband and an amplification factor of about 15, and are applied to the bridge coincidence circuit 15 (see Ref. 9) designed about DGTs-9 germanium diodes.

The signals from the coincidence circuit go to the differential amplifier 16 and then the two-stage amplifier with the cathode follower 17 at its output. From the cathode follower the pulse is applied to the pulse height discriminator 18 (a modification of the Schmidt circuit) which selects the coincidences. From the discriminator, the coincidence pulses, having a width of 2 μsec and a height of 25 v, open the gating circuit 19. This gating circuit, suggested by A.A. Melioranskii, is characterized by a high stability, an amplification factor of about unity, a pedestal residue of 0.12 v, and linearity to 22 v; the maximum amplitude of the pulses getting through is 0.7 v. For height-analysis of the pulses in the γ-channel, positive pulses taken from the eleventh dynode of the photo-multiplier were applied to the gating circuit. These pulses, after passing through the cathode follower 20 and the 0.6 μsec delay line 21, are preamplified by the non-overloadable amplifier 22 (Ref. 10) which has a passband of about 8 Mc, an amplification factor of 10, and a linear characteristic to 20 v output. The pulses passed by the gating circuit are amplified by the amplifier 23 with a maximal output amplitude of 100 v and fed to the single-channel differential discriminator 24 and the Ps-64 scaler 25. During measurements, the load at each point in the β and γ channels was monitored by means of a decade scaling circuit with a scaling ratio of 1:10,000 (this is not shown in the block diagram).

An operational test of the γ-spectrometer, carried out with reference to the known γ-lines of Hg^{203}, Cs^{137} and Zn^{65} showed that the linearity of the energy scale and the shape of the spectra are not distorted by the gating circuit. Under the above-described conditions, the half-width of the Cs^{137} γ-line is 13%. The operation of the β-spectrometer with the scintillation counter was tested by recording known β-spectra.

The resolving time of the coincidence circuit was determined from the delay curve for β-γ coincidences recorded with a Co^{60} sample. On the basis of these measurements $\tau = 4 \cdot 10^{-8}$ sec, while the length of cable 12 corresponding to the maximum of the curve is 10 meters and is independent of the discrimination level in the γ channel. Frequent measurements taken over an extended period showed that the delay curve remains fairly stable as regards shape and position. The value of τ obtained is in good agreement with measurements of the accidental coincidence rate from two independent sources. That the shape of the β-spectra, being correlated with the γ-rays was being correctly recorded was verified by recording the β-spectrum of Co^{60} both by the β-γ coincidence method and directly with one β-counter. The β-spectra obtained by both methods were identical. The experimental points on a rectified plot of this β-spectrum (Fig. 11) fall on a straight line starting at an energy of about 0.1 Mev.

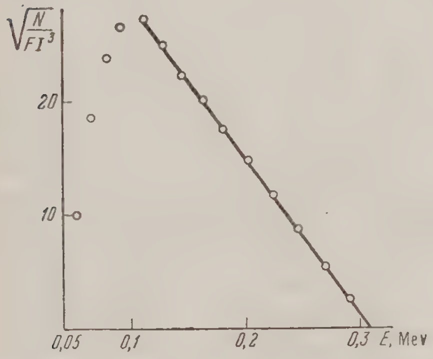

Fig. 11. Rectified plot of coincidence β-spectrum for Co^{60}.

Partial β-Spectra

The β-spectrum was studied using a source in the shape of an 8 mm diameter disc cut out of zirconium metal foil with a superficial density of 24 mg/cm^2. The rectified plot of the Zr^{97} + Nb^{97} β-spectrum obtained on our spectrometer using the β-counter alone is given by curve 1 in Fig. 12. The shape of this β-spectrum is in good agreement with the data of Ref. 1. The β-spectra with end-point energies 1.91 and 1.27 Mev pertain to Zr^{97} and Nb^{97}, respectively.

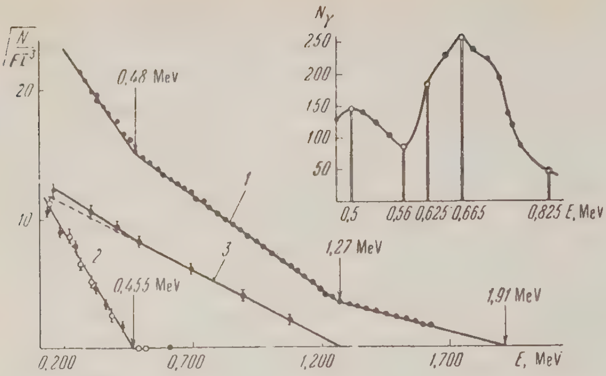

Fig. 12. Rectified plots of the β-spectra of Zr^{97} + Nb^{97}: 1) curve obtained on the β-spectrometer with one β-counter; 2) β-spectrum of coincidences with $E_\gamma > 1$ Mev (○) and $E_\gamma > 0.8$ Mev (●); 3) coincidence β-spectrum obtained with the discriminator gate set at the maximum of the photopeak ($E_\gamma = 0.665$ Mev).

The existence of a soft β-spectrum with an end-point energy of 0.48 Mev cannot be considered reliably established by earlier measurements with thick sources. In order to verify its existence we carried out β-γ coincidence measurements on the set-up described above. Two series of measurements were performed with an integral discriminator output. The discriminator threshold was first set so that coincidences with gammas of energy > 1 Mev would be recorded, and then, in order to increase the counting efficiency of the γ-quanta, the threshold was reduced to 0.8 Mev. The number of β-γ coincidences was measured at different values of the current in the β-spectrometer windings. The results of these measurements are also presented on Fig. 12 in the form of a rectified plot of the β-spectrum (curve 2). It can be seen that in both series of measurements a partial β-spectrum with end-point energy 0.45 Mev was resolved. At points beyond the end-point of this β-spectrum the counting rate fell to that for accidental coincidences. The number of accidental coincidences at each point was determined from the loads in the β and γ channels and in some cases was verified by introducing an additional delay in the β channel. For points in the low-energy part of the spectrum, the number of accidental coincidences was about one pulse per hour as compared with a true coincidence rate of about 30. The decrease in the true coincidence rate with time, investigated for one of the points of the spectrum, is in agreement with a 17 hour half-life.

It would appear from the data on the γ-γ coincidences that the low-energy β-spectrum should also correlate with the lower energy (0.6-0.8 Mev) γ-radiation which is in cascade with the higher energy γ-radiation. In order to verify this conclusion, we carried out measurements of β-γ coincidences with a differential discriminator output with a 2 v gate at five different points of the γ-spectrum in the interval from 0.5 to 0.82 Mev. The discriminator gate settings are shown in the upper right-hand corner of Fig. 12. The results of one of these measurements with the discriminator gate in the position corresponding to the peak of the photoelectron line (0.665 Mev) are again shown in the form of a rectified plot in Fig. 12 (curve 3). This plot shows the low-energy Zr^{97} β-spectrum and the Nb^{97} β-spectrum which correlates with the 0.66 Mev γ-rays accompanying it. If the low-energy β-spectrum did not yield coincidences with the γ-rays in the investigated energy interval from 0.5 to 0.8 Mev, the ratio of the intensity of the low-energy β-spectrum to that of the second β-spectrum over the whole interval would be constant within the limits of the experimental error. Actually, the relative intensity of the low-energy β-spectrum increases several-fold when the discriminator gate is positioned at the photoelectron line peak. This indicates that the low-energy β-spectrum is in coincidence with the γ-rays of energies equal or close to those of the intense Zr^{97} and Nb^{97} γ-lines.

Decay Scheme

A possible Zr^{97} and Nb^{97} decay scheme, including newly detected low-intensity transitions, is shown in Fig. 13. This scheme comprises new levels for Nb^{97}.

On the basis of the Zr^{97} decay energy, equal to 1.91 + 0.75 = 2.66 Mev, the partial β-transition with E_β = 0.45 Mev must proceed to a 2.2 Mev level. The existence of such an energy level is substantiated by the occurrence of γ-rays with an intensity of 1-2%, whose energy corresponds to a cross-over transition from this level to the ground state. The observed cascade γ-radiation whose total energy is close to 2.2 Mev and which yields coincidences with the electrons of the low-energy β-spectrum gives reason to assume that the 2.2 level also de-excites by cascade through an intermediate level. The location of this level cannot be indicated exactly in the decay scheme because the order of emission of the γ-rays is not known.

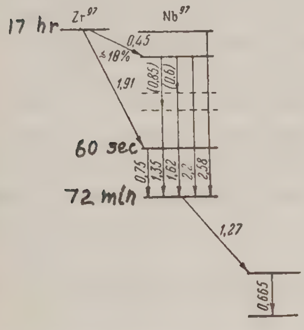

Fig. 13. Decay scheme for Zr^{97} and Nb^{97}.

Evidence in favor of the existence of two cascades is furnished by the γ-γ coincidence measurements which point to the presence of two γ-rays in the 0.6-0.8 Mev interval, γ-rays which give coincidences with the hard γ-rays, and by the observations with the scintillation spectrometer indicating the existence of 1.62 and 1.35 Mev γ-quanta. The 2.58 Mev level was introduced into the decay scheme solely on the basis of our observation of a γ-ray with this energy. The β-transition to this level could not have been observed in our experiments.

Second Scientific Research Physics Institute
of Moscow State University

References

1. V.Shpinal' & G.Kuznetsova, Zhur. eksp. i teor. fiz., 30, 231 (1956).
2. N.Deliagin, Thesis, Phys. Dept. Moscow State Univ. 1954.
3. R.Bell, R.Graham & H.Petch, Canad. J. Phys., 30, 35 (1952).
4. H.Waard, Physica, 18, 1151 (1952).
5. E.Berlovich, Izv. AN SSSR, Ser. fiz., 19, 343 (1955). (Trans. in Bulletin, Vol. 19, No. 3, p. 305.)
6. W.Jordan & P.Bell, Rev. Sci. Instr., 18, 703 (1947).
7. F.McGowan, Phys. Rev., 93, 163 (1954).
8. V.Shpinel', Zhur. eksp. i teor. fiz., 22, 255 (1952).
9. A.Landby, Rev. Sci. Instr., 22, 324 (1951).
10. R.Chase & W.Higginbotham, Rev. Sci. Instr., 23, 34 (1952).

GAMMA-RAY SPECTRUM OF Sb^{124}

- B.S.Dzhelepov, N.N.Zhukovskii, V.G.Nedovesov, I.F.Uchevatkin & V.G.Chumin

Introduction

In spite of the large number of investigations devoted to the β- and γ-spectra of Sb^{124}, the available data are inadequate for constructing the full decay scheme of this isotope. This is due to the fact that the Sb^{124} β- and γ-spectra are very complex. Five components have been detected in the β-spectrum. (Refs. 1-7). There is some arbitrariness involved in resolving such a spectrum into components, since the shapes of the elementary spectra are not known.

Over ten γ-lines are known to be present in the γ-spectrum of Sb^{124}. All these cannot be accommodated satisfactorily in any of the decay schemes proposed so far. The available β-γ and γ-γ coincidence data[7-10] are incomplete and sometimes contradictory; their interpretation is hampered by the fact that the energy intervals into which the spectrum is subdivided in experiments usually encompass more than one γ-line.

In this connection, in attempting to construct the Sb^{124} decay scheme it is highly important to know the relative γ-line intensities.

In 1952, the γ-radiation from Sb^{124} was investigated in our laboratory[12] on the Ritron[32].

In 1955 we undertook a re-examination of the Sb^{124} γ-radiation, using a γ-spectrometer with improved focusing, utilizing recoil electrons, namely, the Elotron[33].

Description of the Instrument

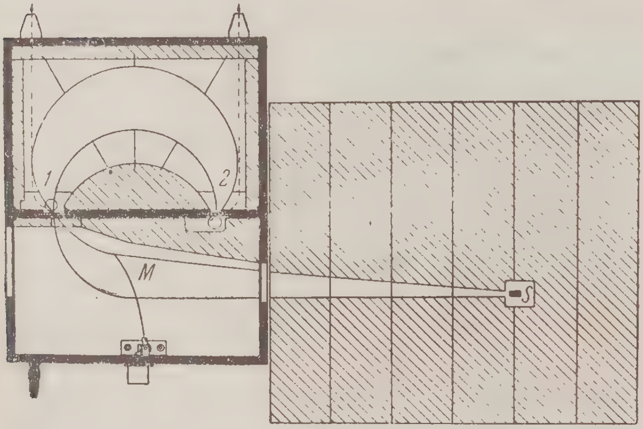

Fig. 1. The Elotron. Sectional view of the apparatus in the horizontal plane: S) source of γ-rays, M) target, 1 and 2) main defining diaphragms (slits).

A diagram of the instrument is shown in Fig. 1. γ-Rays from the source S, located in a lead collimator, knock out Compton recoil electrons from the cellophane target M.

The recoil electrons, ejected within a small solid angle about the incident direction of the gammas, are focused twice by the magnetic field on the defining slits 1 and 2. The use of a curved target[34] and a homogeneous magnetic field insures accurate focusing of the recoil electrons, moving in the direction of the γ-rays, on the first slit. Focusing on the second slit is accomplished by an inhomogeneous magnetic field of the same type as in the Ketron[35] with design radius $\rho = 100$ mm. Two GM counters with thin (1-2 μ) collodion film windows are located directly behind the slits in the path of the electron beam. The inside diameters of the counters are 15 mm. They are connected to a coincidence circuit with a resolving time of about 0.6 μsec.

The focused electron beam is defined by two brass (at the foci) and five aluminum diaphragms. The height and width of the diaphragm apertures can be varied. The target is fastened by caprone filaments to a duralumin frame which can be rotated by a special mechanism from the outside without disturbing the vacuum in the system. The background was measured with the target out of the beam.

Calibration of the Instrument

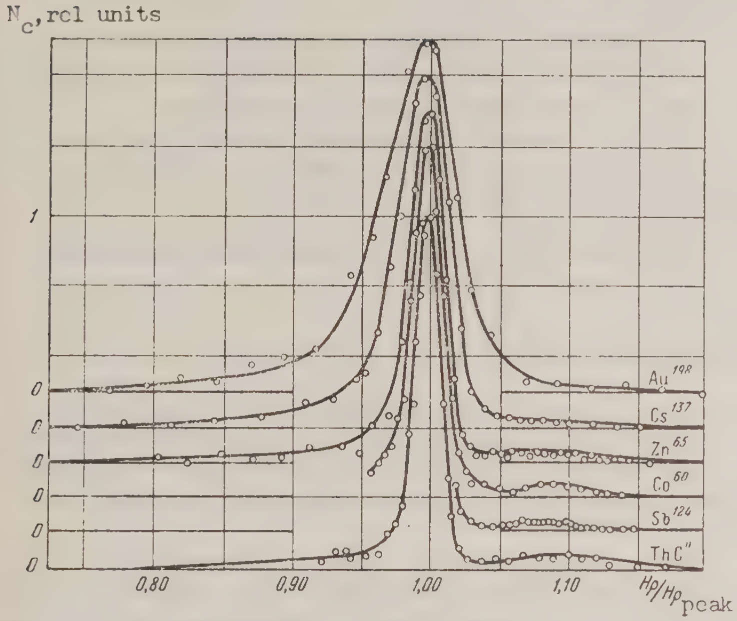

Fig. 2. Experimental γ-lines used for calibration, as recorded on the Elotron. The lines are normalized to the same height and are displaced vertically relative to each for clarity (the line energies are given in the text).

The γ-spectrometer was calibrated and the basic measurements were made under the following conditions: 1) source to the target distance - 400 mm; 2) cellophane target measuring 15 x 48 mm, having a superficial density of 2.15 mg/cm^2; 3) thickness of entrance window of instrument - 2 mm of brass; 4) slits dimensions - 2 x 15 mm (both); 5) instrument filled with a mixture of 98% He + 2% CH_4 to a pressure of 24 mm Hg, insuring a recording efficiency for electrons from 92.45% at $E_\beta \approx 0.3$ Mev to 83.50% for $E_\beta \geqslant 1$ Mev.

The following well-known γ-lines were recorded both to calibrate the instrument in energy and to determine the experimental line shape:

Au^{198} $h\nu$ = 0,4118 Mev
Cs^{137} $h\nu$ = 0,6616 »
Zn^{65} $h\nu$ = 1,118 »
Co^{60} $h\nu$ $\left\{\begin{array}{l} = 1,1715 \\ 1,3316 \end{array}\right.$ »
Na^{24} $h\nu$ = 1,368 »
ThC'' $h\nu$ = 2,6143 »
Na^{24} $h\nu$ = 2,753 »

They are shown, plotted in relative units, in Fig. 2.

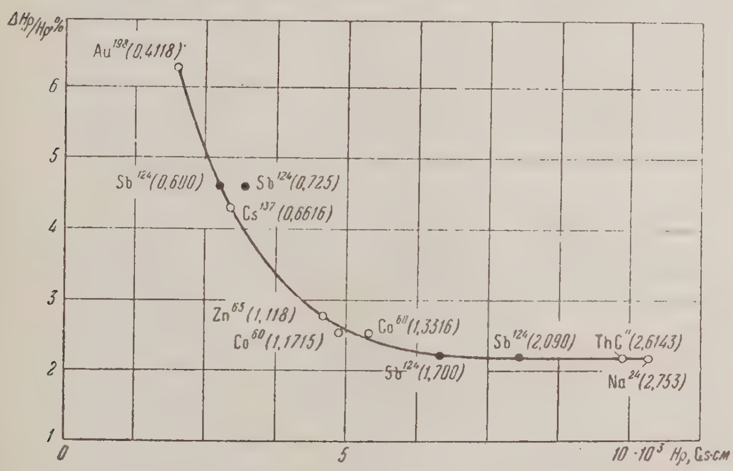

Fig. 3. The dependence of the relative half-width of the calibration lines on Hρ. The black dots give the half-width of the most intense Sb^{124} γ-lines.

Fig. 3 gives the dependence of the relative half-widths of the γ-lines on Hρ. At energies greater than 1 Mev, the half-width is 3.0-2.2%; the broadening of the lines in the low energy region is due to the presence of gas in the instrument.

The instrument line shape can be obtained by interpolation of this data (Figs. 2 and 3) for any energy in the interval from 0.4 to 2.8 Mev. This line shape is used in resolving complex γ-spectra into their separate components. The rather unusual descent of the line on the right side is due to inadequate collimation of the electron beam in front of the second counter. It was established in special experiments that the drop on the right side could be made steeper by means of additional baffles, although complete removal of the "tail" is impossible.

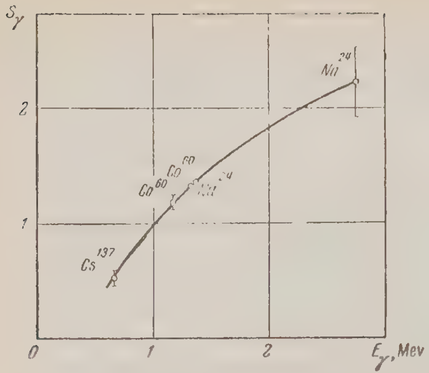

Fig. 4. The experimental spectral sensitivity of the Elotron.

The spectral sensitivity of the apparatus was determined by studying the following lines:

a) Compton lines from the γ-emitters Cs^{137} and Co^{60}, whose activity was determined calorimetrically by E.A.Khol'nova at VNIIM[36];

b) The Compton lines of Na^{24}, whose γ-spectrum, as is well known, contains two lines (1.38 and 2.76 Mev) of equal intensity.

Fig. 4 shows the spectral sensitivity S_γ obtained in this way; the ordinate scale is chosen so that the sensitivity $S_\gamma = 1$ for a γ-energy of 1 Mev.

The vertical segments give the experimental uncertainty.

Experimental Results

The Sb^{124} source was a 3 g sample of neutron-activated metallic antimony whose activity was about 4 curies. This source was placed in a glass tube having an inside diameter of 8 mm. The measurements were performed more than two months after the source was prepared, which insured the virtual absence of γ-lines associated with the short-lived isotope Sb^{122}.

Fig. 5 gives the experimental γ-spectrum of Sb^{124}. The instrument background (black dots) as a rule increases somewhat in the immediate vicinity of the spectral lines, but in general decreases monotonically in going to larger Hρ values. The background is due primarily to Compton scattering in the gas filling the instrument and to scattering of electrons in the first part of the spectrometer; the chance coincidence background was no greater than two pulses per hour. The statistical uncertainty is shown by vertical segments at the points; where not shown, it is less than the diameter of the point circle.

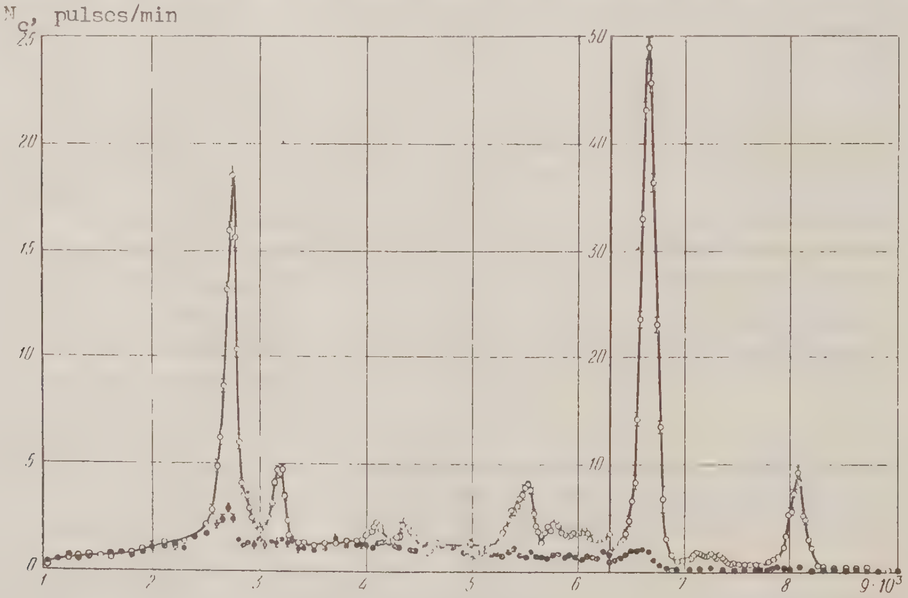

Fig. 5. Experimental curve for the γ-spectrum of Sb^{124}. Black dots = background (target out of the beam). The vertical scale on the left is for the soft part of the spectrum (up to the break); the scale on the right is for the hard part of the spectrum.

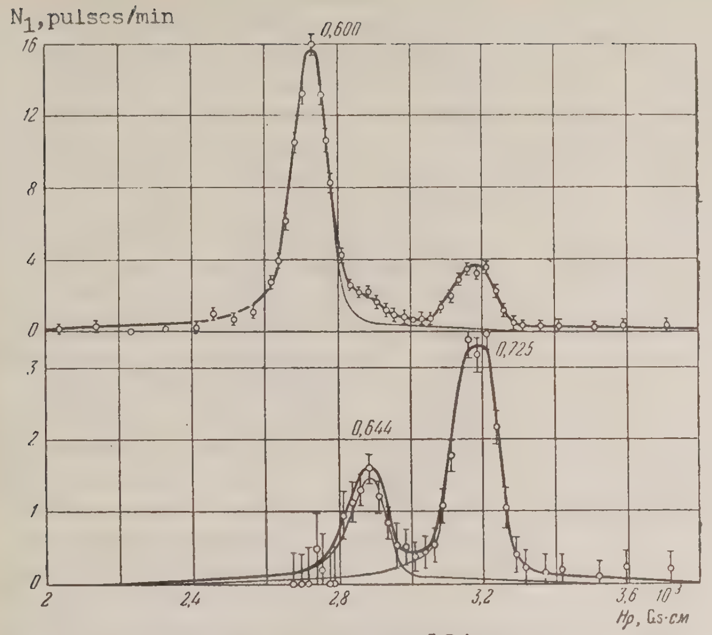

Fig. 6. Resolution of the Sb^{124} γ-spectrum into separate lines in the Hρ = 2000 to 3800 gauss-cm region. N_1 is the counting rate with the background subtracted.

After subtracting the background, the γ-spectrum was resolved into separate components taking into account the energy dependence of the instrument line shape as given in Figs. 2 and 3. The resolution for the Hρ = = 2000 to 6300 gauss-cm region is shown in Figs. 6, 7 & 8. The light lines give the separate components; the heavy line represents their sum. It will readily be seen that the total curve passes within the statistical uncertainty of the experimental points.

The figures at the line peaks are the line energy values in Mev on the basis of our calibration of the instrument.

The upper graph in Fig. 6 shows the section of the experimental spectrum from 2000 to 3800 gauss-cm with the instrument shape of the 0.6 Mev γ-line superimposed. To the right of this line can be seen a rise due to an excess of recoil electrons. The lower part of the same figure shows this rise after subtraction of the 0.6 Mev line. The resolution of this remainder into two γ-lines of energies 0.644 and 0.725 Mev is unambiguous. It should be noted that the 0.725 Mev line as here obtained is 0.6% wider than might be expected from Fig. 3. There is reason to suppose that this line is actually comprised of a 0.713 and a 0.725 Mev line, which have been detected by observing conversion and photoelectrons.[6]

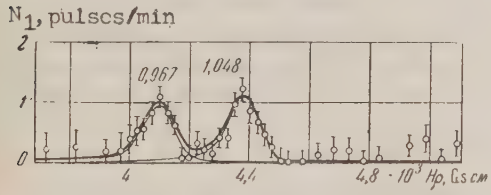

Fig. 7. Same as Fig. 6, but for Hρ = 3800 to 4500 gauss-cm.

Fig. 7 shows the spectrum from 3800 to 4500 gauss-cm; this section comprises two γ-lines having energies of 0.967 and 1.040 Mev. It is possible that the rises over the background in the regions from 3400 to 3800 and from 4600 to 5100 gauss-cm are due to the presence of weaker γ-lines.

The top of Fig. 8 shows the region from 5100 to 6300 gauss-cm. The light line represents the left side of the intense 1.7 Mev γ-line trailing out to about 5300 gauss-cm. The lower part of this figure shows the remainder after subtraction of this line. This remainder can be satisfactorily resolved into four γ-lines with $h\nu$ = 1.33, 1.37, 1.442 and (1.525) Mev. The resolution of the section of the spectrum above 6300 gauss-cm into two γ-lines of energies 1.7 and 2.09 Mev is not shown separately, since the lines are completely resolved. It should be noted that the rise over the background in the section between the two hardest γ-lines (Fig. 5) is due to the specific shape of the right side of the 1.7 Mev line. This can be seen clearly on Fig. 2, which shows this part of the spectrum plotted to a scale in which the unit height is that of the 1.7 Mev line (only the high-energy part of this line appears in Fig. 2).

Fig. 9 shows the final form of the γ-spectrum of Sb^{124}, plotted to a uniform energy scale after introducing the appropriate corrections for: a) γ-ray absorp-

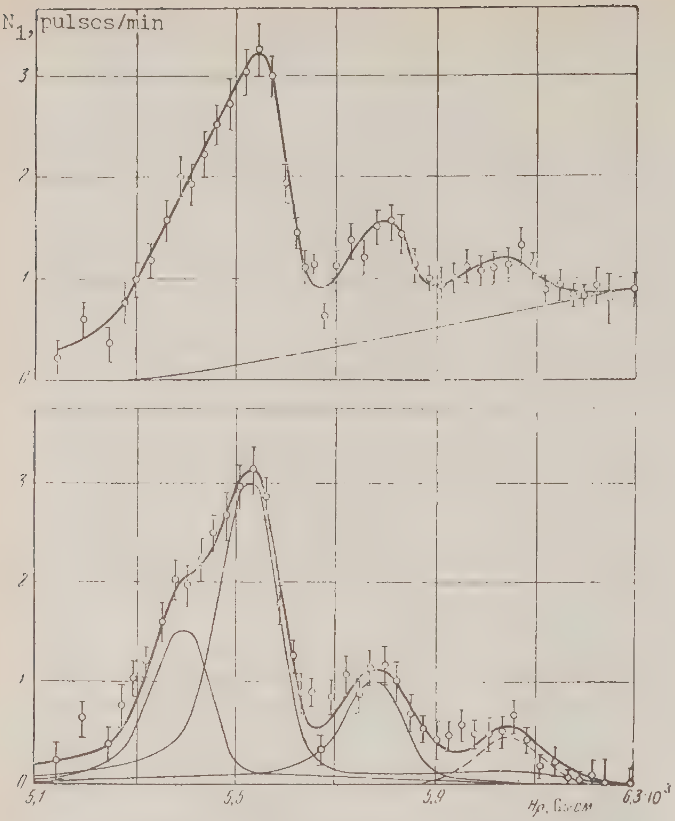

Fig. 8. Same as Fig. 6, but for Hρ = 5100 to 6200 gauss-cm.

tion in the entrance window of the instrument, b) absorption of γ-rays in the source, c) the counter efficiency, and d) the spectral sensitivity of the apparatus.

For clarity the region from 0.8 to 1.6 Mev is also shown enlarged.

The accompanying table lists the observed γ-lines and their relative intensities, as well as the results of other investigators. In addition to the already known γ-lines at 0.600, 0.644, 0.725, 0.967, 1.048, 1.330, 1.370, 1.700 and 2.090 Mev, we detected a 1.442 Mev γ-line; it is possible that there also exists a 1.525 Mev γ-line. Strictly speaking, the fact that these lines belong to Sb^{124} is not proven by our investigation, since no radiochemical analysis of our sample was performed. However, a second investigation of our sample after 80 days showed that the intensity drop over the entire spectrum corresponds, within the limits of the experimental error, to the 60 day half-life of Sb^{124}.

Energies and relative intensities of the γ-lines of Sb^{124}

Ref. 1 1948		Ref. 12 1952		Ref. 11 1954		Ref. 6 1956		Our data 1956	
E_γ, keV	Relat. inten.	E_γ, keV	Relat. inten.	E_γ, keV	Relat. inten.	E_γ, keV	Relat. inten.	E_γ, keV	Relative intensity
603	131	597	154	603	218,8	603	194	600	232 ± 30
650	11					646	12	644	20 ± 4
714	34	711	19	—	—	714	7,5	725	37 ± 5
						723	20,0		
—	—	958	6,6	990	11,8	970	5,0	967	$5{,}0 \pm 0{,}8$
—	—	1052	4,4	—	—	1047	4,0	1048	$4{,}8 \pm 0{,}8$
—	—	—	—	—	—	1298	2,5	1330	$4{,}5 \pm 1{,}5$
—	—	—	—	—	—	1326	4,0		
—	—	1347	17,0	1380	13,6	1361	6,0	1370	$8{,}7 \pm 2{,}2$
						1370			
—	—	—	—	—	—	—	—	1442	$2{,}6 \pm 0{,}6$
—	—	—	—	—	—	—	—	(1525)	$(1{,}1 \pm 0{,}7)$
1708	100	1691	100	1710	100	1691	100	1700	100
2062	8,6	2070	10,0	2110	21,7	2088	13,0	2090	$14{,}3 \pm 1{,}5$

The uncertainty in the relative intensities of the strong lines is determined primarily by the possible error in plotting the spectral sensitivity curve (± 13% for the 0.6 to 2.1 Mev range); for the weak lines the statistical uncertainty in subtracting the "tails" of neighboring lines and the error involved in resolving the spectrum into components must be added.

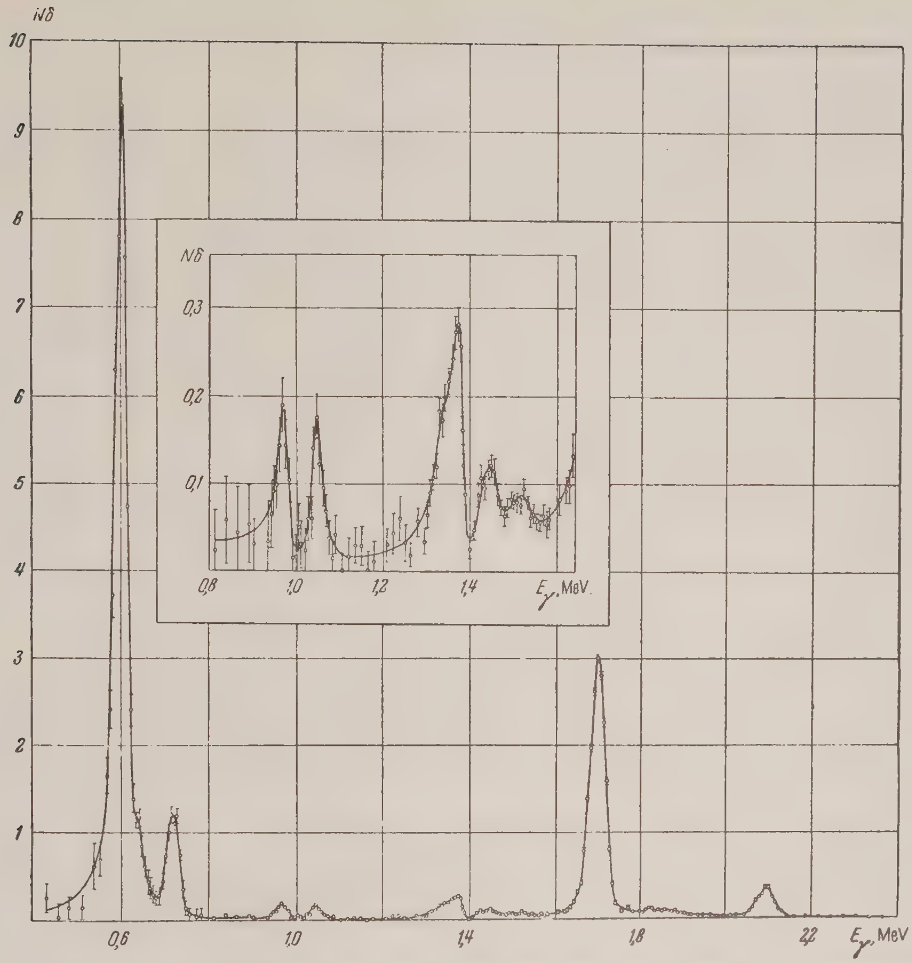

Fig. 9. The γ-ray spectrum of Sb^{124} after correction for γ-ray absorption in the entrance window of the instrument, self-absorption in the source, the variation in counter efficiency and the spectral sensitivity of the apparatus.

We are indebted to E.A.Khol'nova for the calorimetric measurements and to Iu.V.Khol'nov, V.P.Prikhodtseva and S.A.Shestopalova for valuable discussions of spectral sensitivity.

References

1. B.Kern, D.Zaffarano & A.Mitchell, Phys. Rev., 73, 1268 (1948); 73, 1142 (1948).
2. C.Cook & L.Langer, Phys. Rev., 73, 1268 (1948); 73, 1149 (1948).
3. E.Tomlinson, S.Ridgway & K.Gopalakrishnan, Phys. Rev., 91, 484 (1953).
4. J.Moreau, C.R., 239, 800 (1954).
5. T.Azuma, J. Phys. Soc., Japan, 10, 167 (1955).
6. A.Zolotavin, E.Grigor'ev & M.Abroian, Izv. AN SSSR, Zer. fiz., 20, 289 (1956). (Trans. in Bulletin, Vol. 20, No. 3, p. 271).
7. R.Moffat, N.Lazar & L.Langer, BAPS, 28, 3, U13 (1953); Phys. Rev., 91, 338, 485 (1953).
8. S.Almquist & S.Johanson, Nature, 170, 583 (1952); Ark. Fys., 5, 427 (1952).
9. L.Langer & J.Starner, Phys. Rev., 93, 253 (1954).

10. D.Lu, W.Kelly & M.Wiedenbeck, Phys. Rev., 95, 1533 (1954).

11. N.Lazar, Phys. Rev., 95, 292 (1954).

12. K.Gromov, Dzhelepov, Zhukovskii, Silant'ev & Khol'nov, Doklady AN SSSR, 86, 255 (1952).

13. A.Mitchell, L.Langer & P.McDaniel, Phys. Rev., 57, 1107 (1940).

14. G.Stanley Klaiber & G.Scharff-Goldhaber, Phys. Rev., 61, 733 (1942).

15. E.Hales & E.Jordan, Phys. Rev., 64, 202 (1943).

16. P.Kruger & R.Ogle, Phys. Rev., 67, 273 (1945).

17. L.Miller & L.Curtiss, Phys. Rev., 70, 983 (1946).

18. W.Rall & R.Wilkinson, Phys. Rev., 71, 321 (1947).

19. A.Wattenberg, Phys. Rev., 71, 497 (1947).

20. W.Meyerhof & G.Scharff-Goldhaber, Phys. Rev., 72, 273 (1947).

21. D.Hughes & C.Eggler, Phys. Rev., 72, 902 (1947).

22. S.Jnanananda, Phys. Rev., 72, 1124 (1947).

23. M.Wiedenbeck & K.Chu, Phys. Rev., 73, 1168 (1948).

24. M.Scherb & G.Mandeville, Phys. Rev., 73, 1268 (1948).

25. E.Jurney & A.Mitchell, Phys. Rev., 73, 1269 (1948); 73, 1153 (1948).

26. V.Feister & L.Curtiss, J. Res., NBS, 40, 315 (1948).

27. V.Meyers & A.Wattenberg, Phys. Rev., 75, 992 (1949).

28. F.Metzger, Phys. Rev., 86, 435 (1952).

29. D.Hutchinson & M.Wiedenbeck, Phys. Rev., 88, 699 (1952).

30. D.Alburger, Phys. Rev., 88, 1257 (1952).

31. R.Maerker & R.Birkhoff, Phys. Rev., 89, 1159 (1953).

32. B.Dzhelepov, N.Zhukovskii & Iu.Khol'nov, Izv. AN SSSR, Ser. fiz., 18, 599 (1954). (Trans. in Bulletin, Vol. 18, No. 5, p. 285.)

33. B.Dzhelepov, N.Zhukovskii, M.Karamian & S.Shestopalova, Izv. AN SSSR, Ser. fiz., 17, 518 (1953).

34. B.Dzhelepov, Doklady AN SSSR, 77, 389 (1951).

35. Dzhelepov & A.Bashilov, Izv. AN SSSR, Ser. fiz., 14, 263 (1950).

36. K.Aglintsev & E.Khol'nova, Doklady AN SSSR, 98, 360 (1953).

ON THE 0→0 TRANSITION IN RaC'

- B.S.Dzhelepov and S.A.Shestopalova

1. As long ago as 1930 Fowler[1] and Ellis and Aston[2] suggested that there exists in RaC' a transition between two spin-zero states. The suggestion was based on the following facts. Ellis and Aston observed an intense line of 1416 Kev energy in the conversion electron spectrum of RaC'. At the same time, this line could not be detected in the photoelectron spectrum, even with the most careful search (sensitivity <0.03 quanta per decay). It was assumed that this is a 0→0 transition, for which the emission of a single photon is forbidden, whereas a conversion transition is allowed (if the level parities coincide).

Measurement of the internal conversion ratios K/L and K/π could show whether this is actually a 0→0 transition. The first of these quantities has been measured three times: Ellis and Aston[2] found K/L = 7.1; Latyshev and co-workers[3] found K/L = 5.4; more recently Alburger and Hedgran[4] obtained K/L = 5.3 ± 0.3.

The theoretical value of K/L for the 0→0 transition in a pure Coulomb field is 5.5. However, comparison is hampered by the fact that the theoretical value for the internal conversion coefficients for 0→0 transitions is inexact, since it is not calculated for the actual field.

The ratio K/π has been measured by Latyshev and co-workers; they obtained the following values: 625 (Ref. 5), 550 and 440 (Ref. 3). Theory (Ref. 6) gives K/π = 420. While these results do not contradict the 0→0 assignment, they do not definitely substantiate it either, since the determination of α_π necessitates the resolution of the internal conversion positron spectrum of RaC' into many components, which cannot be done uniquely because their theoretical shape is not known. Thus the question of the 0→0 transition in RaC' was not resolved.

2. In studying the γ-ray spectrum of RaC', we were able to throw further light on the problem of this transition.

We discovered that in the recoil electron spectrum of RaC' there exists in the 1350-1450 kev energy region a line which is much wider than should be expected at this energy. This line is shown in Fig. 1. The normal half-width at this energy should be 2.8%; the experimental width is 4.7%. It may safely be assumed that we have here a group of lines. One of the components of this group is presumably the 1378 kev line which has been previously observed by various methods; energy of the other component or components is about 1410 kev.

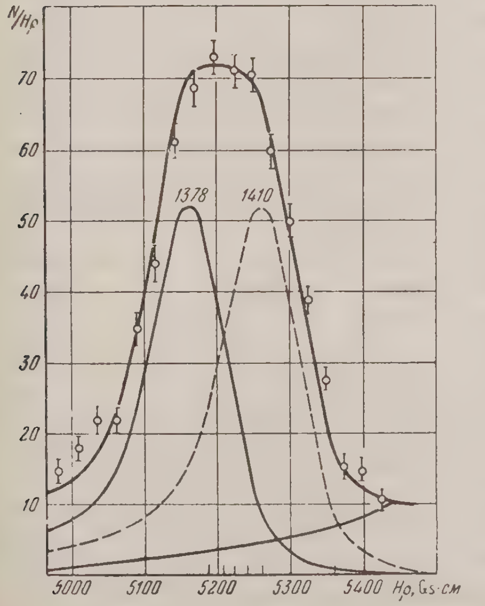

Fig. 1. Section of the γ-spectrum of RaC' from 1350 to 1450 kev.

If there exists even a weak 1416 kev γ-line, the assumption of 0→0 transition would have to be given up. Resolution of the curve (Fig. 1) into components of the standard shape shows that the excess of recoil electrons can be explained satisfactorily (though not only) by the presence of a 1410 kev line, but it cannot be explained by a single 1416 kev line. The situation became clearer when we analyzed the list of unidentified conversion lines given by Mladjenovic and Slatis[7]. We there found six conversion lines such that if their energies are added to the binding energy of the K-shell the following γ-line energies are obtained: 1385.3, 1391.1, 1396.5, 1401.7, 1408.0 and 1438.0 kev. Apparently these are the lines responsible for the above-mentioned electron excess.

At the Fifth Conference on β & γ Spectroscopy (1955) A.A.Bashilov showed a section of the

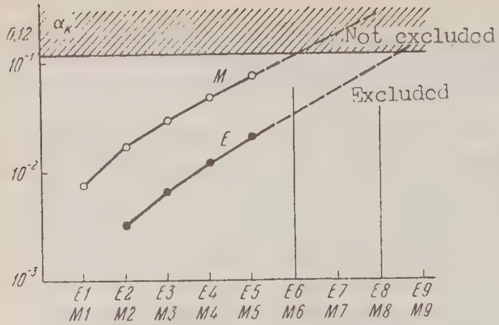

Fig. 2. Theoretical values of the K interval conversion coefficients for different multipole orders of the 1416 kev transition with Z = 84. Hatched area - experimental result.

photoelectron spectrum of RaC' in which a line having a peak at about 1406 kev was discernible. Probably the fifth of the abovementioned lines is the most intense and is the line detected in our experiments and those of Bashilov. This problem can be clarified only by careful measurements of the γ-spectrum with a resolution an order of magnitude better than in our experiments.

Let us now return to a consideration of the 0→0 transition in RaC'. On the basis of our experiments we can assert only that there are no more than 0.03 gammas with 1416 kev energy per decay. This is in agreement with the result of Ellis and Aston. Analysis shows that with existing data on internal conversion coefficients even this assertion is sufficient to invalidate all possible multipole order assignments other than this being a 0→0 transition.

In 1941 Konstantinov and Latyshev[8] measured the number of conversion electrons for this line; they obtained $p\alpha_K = 3.5 \cdot 10^{-3}$ electrons per decay. If the number of photons per decay is <0.03, the K conversion coefficient should be $\alpha_K > 0.12$.

Let us first consider the assumption that we are dealing with a transition of higher multipolarity. Fig. 2 shows the K-conversion coefficients for an energy of 1416 kev and Z = 84, as calculated by L.A.Sliv[9], taking into account finite nuclear size and screening of the atomic field. The figure shows that the requisite value of the conversion coefficient (> 0.12) can be obtained only for very high multipole orders; if the transition is electric, the multipolarity must be greater than E8, or if it is magnetic, the order must be greater than M6.

Let us now consider the experiments of Alburger and Hedgran[4], who studied the conversion ratios K/L_I, L_{II}/L_I and L_{III}/L_I for the 1416 kev transition in RaC' by means of a spectrometer with good resolving power; the first of these ratios was measured and the upper bounds were established for the second and third. Their results are shown in Figs. 3-5 (hatched areas). The same figures show the theoretical values for the three ratios. It will be seen from Fig. 3 that the experimental value of 5.3 ± 0.3 for K/L is not in contradiction with either a high multipole order or the assumption of a 0→0 transition.

Figs. 4 and 5, however, show that the upper limit for L_{II}/L_I obtained by Alburger and Hedgran excludes all electric multipoles higher than E4, while

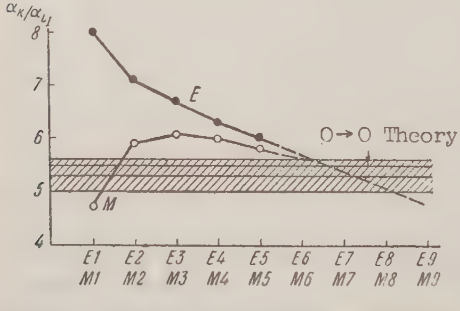

Fig. 3. Theoretical values for the K/L conversion ratio. Hatched area represents the experimental results of Alburger & Hedgran (Ref. 4).

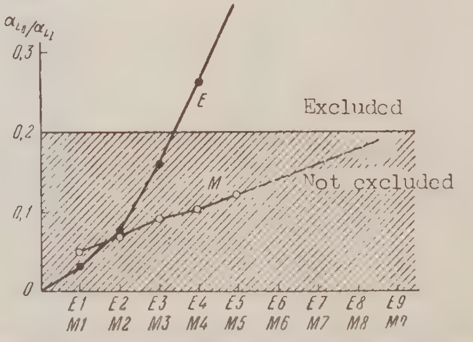

Fig. 4. Theoretical values for the L_{II}/L_I ratio. Hatched area from Ref. 4.

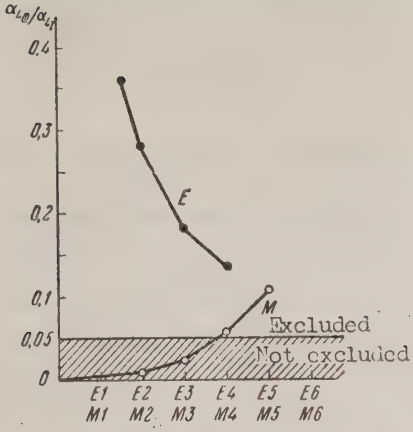

Fig. 5. Theoretical values of the L_{III}/L_I ratio. Hatched area from Ref. 4.

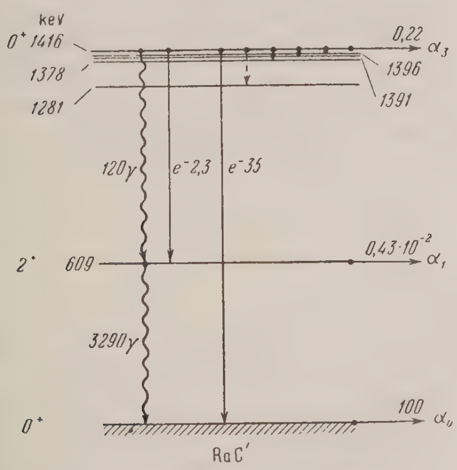

Fig. 6. The lower excited levels of RaC'. The figures at the letters identifying the type of decay denote the number of events per 10^4 decay.

the bound for L_{III}/L_I excludes all magnetic multipoles higher than M4. Hence, all multipolarities being excluded, the 1416 kev transition in RaC' must be 0→0.

3. Let us consider the lower excited levels of RaC'.

In all the decay schemes of RaC' so far proposed[10-13], the first excited level lies at 609 kev. There is no agreement as regards the height of the other levels; the following values have been given: 930, 1240, 1290 and 1410 kev (Demichelis and Malvano[10]); 934, 1120, 1282 and 1412 kev (Surugue[11]); 766, 934, 1120, 1282 and 1416 kev (Ellis[12]).

Shestopalova[13], having analyzed all the available data, concluded that the level sequence is the following: 1281, 1378, 1391, 1396 and 1416 kev. We shall adhere to this sequence, which is shown in Fig. 6.

The characteristics of three of the levels shown in Fig. 6 are known:

1) the ground state of RaC', as for all nuclei with even Z and A, is 0+;

2) the first excited level at 609 kev is 2+ for the same reason; the measurements of the conversion ratio for the transition from this level do not conflict with this assignment; a level at this energy is in good agreement with the empirical rule for the position of the first excited level of even-even nuclei, formulated by Scharf-Goldhaber[14];

3) in accord with what has been said above, the 1416 kev level is 0+.

An additional verification of these assignments can be obtained on the basis of the new experimental data[13] in the following way.

The transition from the 1416 to the 609 kev level should, according to this scheme, be of the 0+→2+ type, i.e., E2. The γ-ray intensity in this transition, according to Shestopalova[13], is 0.012 ± 0.008 photons per decay; the intensity of the conversion transition, according to Mladjenovic and Slatis[7], is $2.3 \cdot 10^{-4}$ electrons per decay. This gives $\alpha_K = 1.9 \cdot 10^{-2}$. This value is reasonably close to the theoretical value for an E2 transition, namely, $\alpha_K = 8.6 \cdot 10^{-3}$, if we take into account the large uncertainty in the experimental value.

4. Let us now consider the 1416 kev level. This level can decay by

1) a γ-transition to the 609 kev level, having an intensity of ~0.012 photons per decay[13],

2) a conversion transition to the same level with an intensity of $2.3 \cdot 10^{-4}$ electrons per decay[7],

3) a conversion transition to the ground state with an intensity of $3.5 \cdot 10^{-3}$ electrons per decay[8], and

4) the emission of long-range α-particles with an intensity of $2.2 \cdot 10^{-5}$ α's per decay[15].

In addition to the above modes of de-excitation, the 1416 kev level can probably decay by γ-transitions and conversion transitions to the 1281, 1378, 1391 and 1396 levels. In view of the small energy differences, however, these transitions could not be observed: even if they were E1 transitions, they would be weaker than the electric E2 with $h\nu = 806$ kev by a factor of more than 5000 and would occur less than once in 10^6 decays. Conversion transitions to these levels could be observed only if the intermediate levels had very high spin, which they presumably do not.

We may therefore restrict ourselves to a consideration of the above-mentioned four modes of de-excitation of the 1416 level.

In the theory of 0→0 transitions it is important to know the absolute probability of the conversion transition in question or, in other words, the partial lifetime of the 1416 kev level with respect to the conversion transition. This quantity has been determined several times, always by comparing the probability of the conversion transition with the probability of emission of long-range α-particles (α_3 group). The ratio of these probabilities can be written

$$\frac{\lambda_{e^-}}{\lambda_\alpha} = \frac{N_{e^-}}{N_{\alpha_3}}$$

where N_{e^-} is the number of conversion electrons and N_{α_3} is the number of α_3 group α-particles per decay.

Experiment gives the value $N_{\alpha_3} = 2.2\cdot 10^{-5}$ α's per decay[14] and $N_{e^-} = 3.5\cdot 10^{-3}$ electrons per decay[8]. Thus in order to determine λ_{e^-} we need only calculate λ_{α_3} or the lifetime of the 1416 kev level for α-decay. This quantity was determined on the assumption that the probability for α-decay from the ground state of RaC' and from the 1416 kev level differ only due to the penetrability of the barrier (the factors multiplying the exponentials were considered equal, and l was set equal to zero:

$$\lambda_{\alpha_3} = \lambda_{\alpha_0} e^{-(\Pi_3 - \Pi_0)}, \tag{1}$$

$$\Pi = 2\alpha \frac{c}{v} zZ(2U_0 - \sin 2U_0), \tag{2}$$

where λ_{α_0} is the probability for α-decay from the ground state of RaC' ($T = 1.55\cdot 10^{-4}$ sec), Π_3 and Π_0 are the values of Π for the α_3 and α_0 groups, α is the fine-structure constant, c is the velocity of light, v is the rate of divergence of the α-particles (i.e., the sum of their velocities), z and Z are the atomic numbers of the particles, $U_0 = \arccos (Qr_0/zZe^2)^{1/2}$; here Q is the total energy liberated in ergs and r_0 is the nuclear radius in centimeters.

Some support for the application of this formula is derived from the fact that both α-decays take place from spin zero levels and lead to the ground state of RaD, which also has spin zero; thus no factors connected with change of angular momentum are present.

In order to calculate $\Pi_3 - \Pi_0$ we must know the nuclear radius r_0.

The values of $e^{\Pi_1 - \Pi_0}$ for three different assumptions regarding nuclear radii are

$e^{\Pi_3 - \Pi_0} = 1998$ with $r_0 = 2.05\cdot 10^{-13} A^{1/3}$ (Bethe radii)
$e^{\Pi_3 - \Pi_0} = 2697$ with $r_0 = 1.50\cdot 10^{-13} A^{1/2}$ (conventional radii)
$e^{\Pi_3 - \Pi_0} = 3249$ with $r_0 = 1.20\cdot 10^{-13} A^{1/3}$ (new radii)

The values of $e^{\Pi_3 - \Pi_0}$ for the last two and more plausible assumptions regarding r_0 differ only slightly, hence the uncertainty in r_0 is unimportant in this case.

Inserting λ_{α_0} and $e^{\Pi_3 - \Pi_0}$ for the new radii into equation (1), we obtain

$$T_{e^-} = 3.0\cdot 10^{-10} \text{ sec}$$

There are two values of T_{e^-} in the literature obtained in this way:

a) Bethe's value[16] ($8\cdot 10^{-11}$ sec) which, when reduced to the new radii and to the new to the new value of N_{e^-} becomes

$$T_{e^-} = 3.5\cdot 10^{-11} \text{ sec};$$

b) the value of Drell and Rose[17],

$$T_{e^-} = 2.5\cdot 10^{-11} \text{ sec}.$$

The reasons for this divergence are not clear.

There are two objections to this method of calculating λ_{α_3}:

1) the extrapolation for the penetrability of the barrier extends over more than three orders of magnitude, and the result, therefore, can scarcely be accurate;

2) in the light of more recent concepts it would appear that the nucleus is not spherically symmetric, although it is not strongly deformed ($\Delta R/R \approx 0.2$, according to Sunyar[18]). The formulas used above were derived for a spherical potential well. There are no analogous expressions for deformed nuclei. Under these conditions extrapolation over several orders of magnitude is a doubtful procedure.

In view of the above, it is of interest to perform an independent evaluation of $_{e^-}$ based on a comparison of the probabilities λ_{e^-} and $\lambda_{\gamma_{806}}$

The 806 kev transition is E2. According to Weisskopf (Ref. 19; see also Siegbahn[20]) for single-particle E2 transitions

$$\gamma = 1.6\cdot 10^{8}\cdot A^{4/3}\cdot E_{\gamma}^{5} \text{ sec}^{-1}$$

In our 806 kev case $\lambda_{\gamma} = 6.9\cdot 10^{-10}$ and, therefore,

$$\lambda_{e^-} = \lambda_{\gamma}\, \frac{N_{e^-}}{N_{\gamma_{806}}}\, 2.0\cdot 10^{11} \text{ sec}^{-1},$$

and

$$T_{e^-} = 3.5\cdot 10^{-12} \text{ sec}.$$

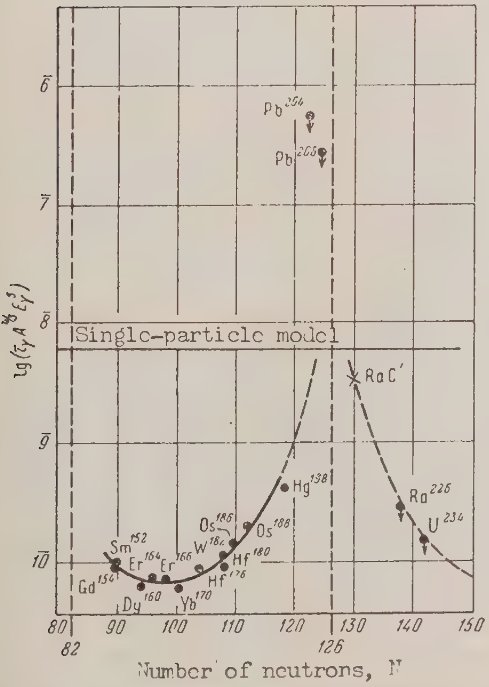

Fig. 7. Comparative lifetimes of isomers as a function of the neutron number N (according to Sunyar).
(See Phys.Rev. 98, p. 655. Trans.)

The corresponding overlap parameter of the wave functions is $\rho \approx 0.40$.

The following objection can be made to this calculation. The lifetimes for γ-transitions computed by Weisskopf's formulas are only approximate. It is known that for elements in the rare-earth region the lifetime of the first excited state of even-even nuclei is approximately 100 times shorter than that given by Weisskopf's formulas[19]. Sunyar[18] has noted that the deviation from the formulas shows a regular dependence on the number of neutrons in the nucleus: it reaches maximum values far from the magic numbers and decreases as closed orbits are approached. Sunyar's curve is presented in Fig. 7. Although plotting the dash-line sections of the curves in Fig. 7 (the dash-line through Ra^{226} and U^{234} is ours) is somewhat risky, it may serve for a rough evaluation of the lifetime of the first excited state of RaC'.

From the position of the cross (for RaC') on Fig. 7 one might expect the actual lifetime of the 609 kev state to be only

1.8 times shorter than that given by Weisskopf's formulas.

As was mentioned above, the 1416→609 kev transition in RaC' is a 0→2+ type transition, i.e., belongs to the same type as a 2+→0 transition. One cannot be sure, however, that the deviation from Weisskopf's formulas will be the same for the transition between the 1416 and 609 kev levels.

The ground state of RaC' and its first excited 609 kev state are probably similar in structure, since they belong in the same system of collective levels. The excited 1416 and 609 kev levels probably belong to different systems and may therefore be structurally different. The divergences from the theory, so clearly evident in Fig. 7, may be connected with just these structural factors.

It is therefore unclear whether one should use the correction factor 1.8 in calculating λ. We have not used this correction in the above value of T_{e^-}, but we believe that this determination may be uncertain by as much as a factor of 3. However, even within the wide limits of this uncertainty the value of T_{e^-} obtained does not agree with the evaluations of Bethe and Drell.

5. In connection with the above it is interesting to compare the probabilities for the two modes of de-excitation of the 609 kev level, namely γ-radiation and α-decay (α_1 group in the spectrum of long-range α-particles).

The lifetime with regard to γ-emission for the 609 kev level as given by Weisskopf's formula is

$$T_{\gamma_{609}} = 4.0 \cdot 10^{-11} \text{sec};$$

or, if we use the correction from Sunyar's empirical curve,

$$T_{\gamma_{609}} = 2.2 \cdot 10^{-11} \text{sec}.$$

The probability for α-decay from this state can be expressed in terms of the probability of α-decay from the ground state of RaC' and the ratio of the barrier penetrabilities (we assume, as before, that the factors in front of the exponentials are the same):

$$\lambda_{\alpha_1} = \lambda_{\alpha_0} e^{-\Pi_0+\Pi_1}$$

where Π_0 is calculated by equation (2) for Π and Π_1 is computed by the same formula, but with $l = 2$.

As a result we obtain

$$\lambda_{\alpha_1} = 9.5 \cdot 10^2$$

and, finally,

$$\lambda_{\gamma_{609}} : \lambda_{\alpha_1} = 1.8 \cdot 10^7.$$

Experiment, however, gives

$$\lambda_{\gamma_{609}} : \lambda_{\alpha_1} = 0.329 : 0.43 \cdot 10^{-6} = 7.6 \cdot 10^5.$$

The great difference between the experimental and theoretical values for this ratio shows that the probability for α-decay is affected by as yet unknown factors, possibly factors associated with the structures of the states involved.

The authors wish to thank L.A.Sliv for presenting the results of his calculations for the K-conversion coefficients in the relevant case, L.K.Peker for discussions of questions related to α-decay and V.A.Krutov for extrapolation of the conversion ratios from Rose's tables.

"D. I. Mendeleev" All-Union Scientific
Research Institute of Metrology

References

1. R.Fowler, Proc. Roy. Soc., A129, 1 (1930).
2. C.Ellis & G.Aston, Proc. Roy. Soc., A129, 180 (1930).
3. G.Latyshev, L.Sliv, IBarchuk & A.Bashilov, Izv. AN SSSR, Ser. fiz., 13, 340 (1949).
4. D.Alburger & A.Hedgran, Arc. f. Fys., 7, 423 (1954).
5. V.Gei, G.Latyshev & S.Tsypkin, Izv. AN SSSR, Ser. fiz., 12, 731 (1948); A.Alikhanov & G.Latyshev, Jour. of Phys. USSR, 3, 263 (1940).
6. A.Sakharov, Dissertation, FIAN, M.1948.
7. M.Mladjenovic & H.Slatis, Ark. f. Fys., 8, 65 (1954).
8. A.Konstantinov & G.Latyshev, Jour. of Phys. USSR, 5239 (1941); G.Latyshev, Zhur. eksp. i teor. fiz., 14, 65 (1944).
9. L.Sliv, Report at Fourth All-Union Conference on Nuclear Spectroscopy.
10. F.Demichelis & R.Malvano, Nuovo Cim., 12, 358 (1954).
11. J.Surugue, J. Phys. et Rad., 7, 358 (1946).
12. C.Ellis, Intern. Conference of Physics. -London, 1934.
13. S.Shestopolova, Dissertation, VNIIM, 1955.
14. G.Scharf-Goldhaber, Phys. Rev., 90, 587 (1953).
15. E.Rutherford, W.Lewis & B.Bowden, Proc. Roy. Soc., A 142, 347 (1933); E.Rutherford, C.Wynn-Williams, W.Lewis & B.Bowden, Proc. Roy. Soc., A 139, 617 (1933).
16. H.Bethe, Nuclear Physics, Part. 2. (In Russian trans. M.-L. 1948)
17. S.Drell & M.Rose, Prog. of Theor. Phys., 7, 125 (1952).
18. A.Sunyar, Phys. Rev., 98, 653 (1955).
19. V.Weisskopf, Phys. Rev., 83, 1073 (1951).
20. K.Siegbahn, Beta- and Gamma-Ray Spectroscopy, p. 391, Amsterdam, 1955.

INVESTIGATION OF THE NEUTRON CAPTURE γ-RAY SPECTRA OF Na^{23} AND Th^{232}

- N.A.Burgov and G.V.Danilian

When thermal neutrons are captured by nuclei, these are excited to energies equal to the neutron binding energy, i.e., to about 7-8 Mev. This excitation is removed primarily by the emission of one or several γ-rays. Knowing the γ-ray energies and intensities, on the one hand, and the nuclear level characteristics (spins and parities), determined from reactions with charged particles, on the other hand, we can make certain deductions regarding the multipolarities of the radiation, the radiation widths, etc. which can be used to test the validity of different nuclear models. Until recently such information was obtained mainly by studying the γ-rays accompanying β^{+}-decay, which limited investigators to the energy region up to 2-3 Mev. The development of nuclear reactors with large neutron fluxes has extended the region of investigation to 12 Mev.

Since 1948, Kinsey, Bartholomew, and Walker have been active in the investigation of neutron capture γ-radiation. They have studied the neutron capture γ-rays from many elements by means of a pair spectrometer and have obtained important results.

Groshev et al[1] have recently published the results of an investigation of neutron capture γ-rays with the aid of a spectrometer analyzing Compton electrons. The inherent characteristics of the "Compton" spectrometer make it a much more efficient instrument than the magnetic pair spectrometer.

In recent years scintillation γ-spectrometry has seen rapid development. A Canadian group[2] studied the γ-radiations emitted by boron and carbon under deuteron bombardment by means of a scintillation pair spectrometer. As regards both accuracy of the results obtained and the resolution, their instrument is nearly equal to magnetic spectrometers.

In the present investigation a magnetic pair spectrometer was used to study the γ-rays associated with neutron capture by nuclei.

Outline of Procedure

Fig. 1 is a schematic of the experimental geometry and the pair spectrometer.

The sample was placed into the horizontal exposure hole of the experimental heavy water reactor of the USSR Academy of Sciences. A 10 cm thick block of bismuth is located in front of the sample to absorb the γ-radiation from the reactor.

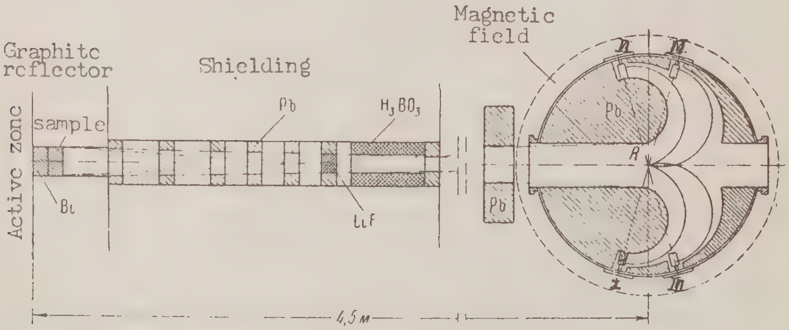

Fig. 1. Horizontal cross section of the pair γ-spectrometer and diagram of the geometry of the experiment: I - IV - groups of three miniature counters.

Next in line is a system of lead collimators. An LiF plug is placed into the opening of the last collimator to absorb neutrons. In addition, a collimating tube filled with boric acid is located at the exit of the exposure hole for the same purpose. The 50 mm diameter γ-ray beam, after passing an additional lead collimating diaphragm, falls on the radiator R at the center of the spectrometer chamber. This radiator is a lead foil 50 x 90 mm in area with a superficial density of 40 mg/cm^2. Thin-wall (0.05 mm) copper Geiger counters, 5 mm in diameter and 60 mm long, are mounted in special holders in planes oriented at 15° to the plane of the radiator.

It should be noted that these miniature counters were not sufficiently stable under heavy loads and required frequent replacement. Each of the four groups I - IV, arranged symmetrically with respect to the radiator comprised three counters. Each counter in groups I and III is connected in coincidence with each of the counters in groups II and IV. The resolving time of the coincidence circuit is 0.3 μsec. The pulses from the coincidence circuits were applied to counting channels corresponding to the given distance between the counters producing the coincidences.

The counting circuit consists of twenty mechanical counters, five for each of the four pairs of counter groups. Nine variants of the coincidences of the pulses from six counters of two groups gave five energy values for a given magnetic field strength. The magnetic field strength was determined from the current in the field winding of the magnet on the basis of the previously determined current dependence of the field and current. The absolute calibration of the field was effected with reference to the 2.756 Mev γ-line of Na^{24}. The current in the magnet winding was maintained stable within 0.05% by an electronic regulator. During the measurements the current was varied in steps of 0.05 amp, which correspond to 50 kev energy intervals on the average.

At each magnetic field strength, the mechanical register was read 3-4 times at 30 minute intervals. The results were then processed as follows.

From each reading of the mechanical register, a curve was plotted for the number of coincidences as a function of Hd, where d is the distance between the inner edges of the slits defining the two counters which gave the coincidences. Then the curves characterizing the coincidences between counters of the two groups were added graphically. It was not possible to add up all twenty curves, since the energy dependence of the efficiency and the shapes of the coincidence peaks for three geometric variants were different.

The γ-ray energies were calculated from

$$E_\gamma = 2\sqrt{\left[\frac{3\,(Hd)_0}{2\cdot 10^4}\right]^2 + (m_0c^2)^2},$$

where $(Hd)_0$ is the extrapolated coincidence peak boundary, and m_0c^2 = 0.511 Mev.

A theoretically computed correction for the so-called "tail" effect was made in the value of $(Hd)_0$. This correction varied from 0.5% for E_γ = 2.76 Mev to 1.2% for E_γ = 10.8 Mev. The relative line intensities were obtained from the heights of the coincidence peaks with the theoretical efficiency of the apparatus taken into account. The absolute value of ν(E), the number of γ-quanta per capture, was calculated by comparing the corrected height of the investigated peak with that of a known peak. In the investigation of Na the standard used was the 2.756 Mev γ-line which accompanies the β-decay of Na and thus has an absolute intensity of 1 photon per capture at saturation.

Under the operating conditions of our reactor, ν(2.756) was 0.9 γ-quanta per decay. It was found possible to evaluate, in the first approximation, the absolute efficiency of the instrument for E_γ = 2.756 Mev from the known capture cross section of Na and the number of nuclei, with self-screening taken into account. This figure was used to evaluate the absolute intensities of the γ-rays from Th.

It should be noted that due to the weak neutron flux (about $2.5\cdot 10^{11}$) and the low absolute efficiency of the instrument (about $0.8\cdot 10^{-8}$ coincidences per photon), the counting rate is so slow that in order to obtain reasonable results it was necessary to carry on the measurements for several hours at every value of the current (field). This forced us to double the radiator thickness to a superficial density of 40 mg/cm^2 and remove the slits from all the counter groups except IV (that under the highest electron load). These measures reduced the resolution by a factor of 2-3.

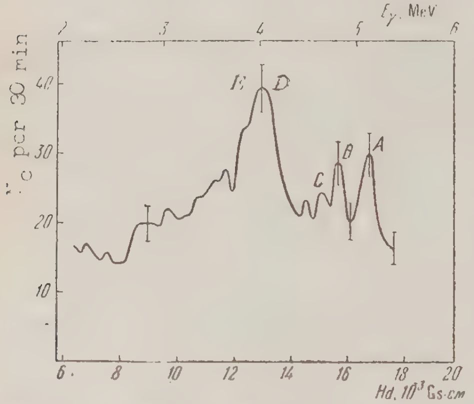

Fig. 2. The spectrum of the background due to γ-rays emitted in the reactor and penetrating partially through the bismuth block in the spectrometer (see also Table 1).

Results

Before describing the results of the investigation, we must briefly discuss the background.

The background comprised two entirely different components.

The first is the background due to the γ-rays from the reactor penetrating the bismuth block. We investigated this for our geometry and obtained the spectrum shown in Fig. 2; it contains several lines belonging to aluminum, carbon and bismuth.

The results of an analysis of the γ-ray background spectrum are presented in Table 1.

The second component of the background is due to chance coincidences. We made a special measurement of the number of chance coincidences between the counters of groups I & III and II & IV. The chance coincidence rate depends on the sample and is of the same order, on the average, as the intensity of the reactor γ-ray background.

This situation makes it difficult to subtract the background from the spectrum of a given element, and we found it necessary, in measuring the energies corresponding to the coincidence peaks, to extrapolate the upper bound of the peak to the level of the unresolved part of the spectrum. Often, however, it is not possible to determine this level unambiguously, and this introduces a fundamental contribution to the uncertainty in the energy measurements.

Table 1

Relative intensity and identification of the lines of the background spectrum due to γ-rays from the reactor penetrating the bismuth absorber block.

Line designation	E_γ, Mev	Relative intensity (arbitrary units)	Identification of line	Refs.
A	$5{,}25 \pm 0{,}05$	0,86	Al 5,21 MeV 3%	[3]
B	$4{,}96 \pm 0{,}05$	0,96	C 4,95 MeV	[4]
C	$4{,}73 \pm 0{,}05$	0,67	Al 4,79 MeV 9%	[3]
D	$4{,}27 \pm 0{,}10$	2,53	Bi 4,17 MeV	[5]
E	$4{,}06 \pm 0{,}10$	2,51		

Na^{24}

The sodium sample was 3.7 kg of NaF power in a thin-walled aluminum container 140 mm in diameter. The γ-spectrum was measured in the energy interval from 2 to 6.5 Mev. The best results were obtained from the coincidences between the counters of groups I and II, where, by virtue of the limited solid angle defined by the lead screens, the resolution was 140 kev. Due to the low transmission of the instrument, however, coincidences in these groups did not have a high enough rate for reliable measurement of weak γ-lines.

The distribution of coincidences between the counters of groups I and II is shown in Fig. 3. The results of the analysis of this spectrum are given in Table 2. For comparison, this table also gives the results of Groshev[1] and Kinsey[3]. All the lines detected with the pair spectrometer by Kinsey[3] were also observed by us. In addition, we found several other lines which coincide with lines reported by Groshev.[1] The statistics for these lines are insufficient, and therefore the energies and intensities given in parentheses in the table are

Table 2

A comparison of the data on neutron capture γ-spectrum of Na^{24} reported by different authors

Line designation	Our results		Kinsey		Groshev	
	E_γ, Mev	Intensity, %/capture	E_γ, Mev	Intensity, %/capture	E_γ, Mev	Intensity, %/capture
А	$6,42 \pm 0,03$	21	$6,41 \pm 0,03$	20	$6,40 \pm 0,03$	22
Б	$5,62 \pm 0,03$	5,7	$5,61 \pm 0,03$	7,5	$5,61 \pm 0,03$	6
В	$(5,35 \pm 0,05)$	(0,5)	—	—	$(5,30 \pm 0,05)$	(0,3)
Г	$(5,08 \pm 0,05)$	(1,2)	$5,13 \pm 0,03$	1,8	$(5,12 \pm 0,05)$	(0,8)
Д	$(4,91 \pm 0,07)$	(1,3)	—	—	$(4,90 \pm 0,05)$	(1,2)
Е	$(4,72 \pm 0,05)$	(1,3)	—	—	$(4,70 \pm 0,05)$	(0,9)
Ж	$(4,54 \pm 0,05)$	(1,3)	—	—	$4,50 \pm 0,04)$	2,1
З	$(4,29 \pm 0,05)$	(0,7)	—	—	$(4,30 \pm 0,05)$	(0,5)
И	$4,03 \pm 0,05$	14,6	$3,96 \pm 0,03$	20	$3,98 \pm 0,04)$	17,2
К			$3,85 \pm 0,03$	11	$3,86 \pm 0,04)$	5,9
Л	$3,64 \pm 0,05$	13,2	$3,60 \pm 0,03$	10	$3,60 \pm 0,03)$	18
М			$3,56 \pm 0,03$	20	$3,56 \pm 0,03)$	
Н	$(3,40 \pm 0,05)$	(2,3)	—	—	—	—
О	$(3,31 \pm 0,07)$	(5)	—	—	$3,30 \pm 0,02$	5
П	$(3,11 \pm 0,05)$	(8,2)	—	—	$3,08 \pm 0,02$	9,5
Р	$(2,36 \pm 0,05)$	(13,5)	—	—	$2,41 \pm 0,03$	10,5
С	$(2,20 \pm 0,05)$	(22,6)	—	—	$2,21 \pm 0,03$	7,5

only suggested, tentative values.

The fact that at the present time we have no analytic expression for the shape of the coincidence peak makes it impossible to resolve the doublets З, ИК and ЛМ. For the same reason we are not presenting the corrected spectrum. Analysis of the results for Na indicates that the data of Kinsey's group are not complete.

Th^{233}

The thorium sample was a stack of metal discs 2 mm thick cut out of pure sheet thorium and placed in an aluminum container. The weight of the thorium was 7.5 kg. The measurements were made in the energy interval from 2 to 5.5 Mev. The coincidence counting rate was so low that only coincidences between the counters of groups III and IV need be considered. This spectrum is shown in Fig. 4. The results of its analysis are presented in Table 3.

The most salient feature is the weak intensity of the lines in the energy region up to 2.5 Mev. The total line intensity in the region investigated is 15.4%. The unresolved parts of the spectrum may have the same order of intensity. Therefore about 70% of the γ-rays appear in the energy region be-2.5 Mev. This fact indicates a high level density and that the radiation is predominantly in cascade.

The second interesting feature is the presence of a 5.11 Mev γ-line (A). This line quite certainly does not belong to the background, as is evident from a comparison of the background and thorium spectra. The 5.25 and 4.70 Mev lines, which belong to aluminum, are present in both spectra.

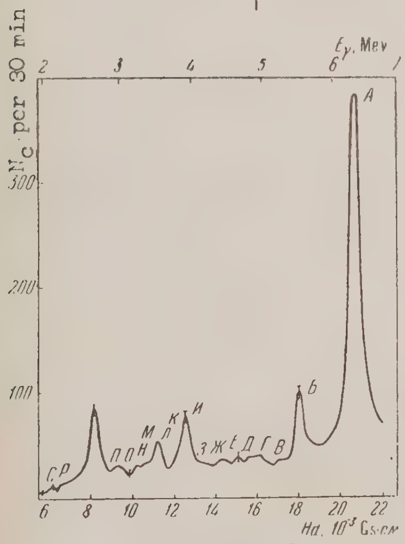

Fig. 3. Experimental γ-ray spectrum of Na^{24} (the unlabeled peak represents the 2.756 Mev γ-line accompanying the β-decay of Na^{24}).

Table 3

Neutron capture γ-spectrum of Th^{233} obtained on the pair spectrometer

Line designation	E_γ, Mev	Intensity, %/capture
	$5,25 \pm 0,05$	Al 3%
A	$5,11 \pm 0,05$	0,2
	$4,70 \pm 0,05$	Al 9%
C	$3,71 \pm 0,05$	0,4
D	$3,55 \pm 0,05$	3,4
E	$3,15 \pm 0,05$	1,6
F	$2,76 \pm 0,05$	4,2
G	$2,60 \pm 0,05$	5,6

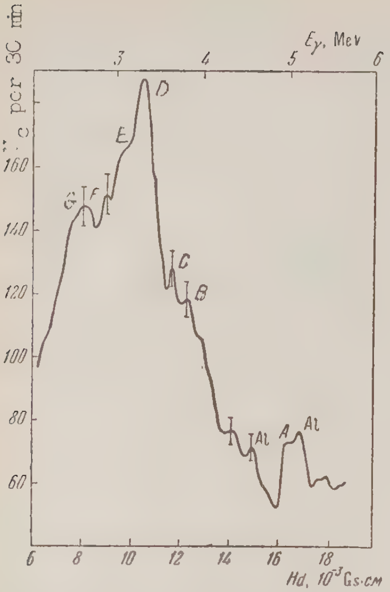

Fig. 4. Experimental γ-ray spectrum of Th^{233}.

From measurements of the d- and p—reactions, Harvey[6] gives the binding energy of the last neutron in Th^{233} as 4.9 ± 0.2 Mev, and states that this value is the lower bound.

Calculations[6,7] give the value 5.2-5.3 Mev for this energy, but in this mass region, the binding energy calculated from mass differences is generally an overestimate.

We feel it reasonable to assign the A line to a transition to the ground state of Th^{233}. Then the binding energy of the last neutron in Th^{233} comes out to be 5.11 ± 0.05 Mev. The presence of a transition to the ground state allows us to assume that this is a dipole transition. In this case the spin assignment for the ground state of Th^{233} can be $I = 1/2$ or $I = 3/2$, since the initial Th^{232} nucleus is even-even, and only S-neutrons are captured.

References

1. L.Gorshev, B.Al'iasevich & A.Demidov, Reports presented by the USSR at the International Conference on the Peaceful Uses of Atomic Energy at Geneva 1955, M.-L. 1955.

2. J.Sample, J.Neilson, G.Chadwick & G.Warren, Canad. J. of Phys., 33, 12 (1955).

3. B.Kinsey, G.Bartholomew & W.Walker, Phys. Rev., 83, 519 (1951).

4. G.Bartholomew & B.Kinsey, Canad. J. of Phys. 31, 1 (1952).

5. B.Kinsey, G.Bartholomew & W.Walker, Phys. Rev., 82, 380 (1951).

6. J. Harvey, Phys. Rev., 81, 353 (1951).

7. V.Kravpov, Usp. fiz. nauk, 47, 3 (1952).

A NEW METHOD OF IMPROVING THE FOCUSING CHARACTERISTICS OF A LENS SPECTROMETER

- B.S.Dzhelepov, No Sen Chan & P.A.Tishkin

Lens β-spectrometers do not as a rule have sharp focusing properties and therefore it is impossible to obtain a high resolution with adequate transmission in instruments of this type.

In spite of this great shortcoming, lens spectrometers are used in many laboratories for the reason that they have many positive qualities not possessed by the usual semicircular spectrometers. Among these qualities are the following:

1) the large solid acceptance angle obtainable (up to 11% of 4π - see Ref. 1);

2) the possibility of obtaining a high effective flux $L = \omega\sigma$, where σ is the area of the source (see the table in Ref. 2);

3) the possibility of calibrating the spectrometer with reference to a single conversion line (due to the absence of iron);

4) linearity of the calibration, which makes it possible to construct automatically recording β-spectrometers;

5) the fact that the source and counter can be located outside the magnetic field;

6) axial symmetry.

These positive qualities of lens spectrometers have led physicists to search for methods of improving their focusing. Various attempts have been made in this direction.

Two methods have been proposed for enhancing the focusing of short lens spectrometers:

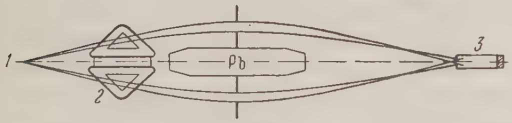

Fig. 1. Electron trajectories in the meridional plane of the lens spectrometer and positions of the correcting coils: 1) source, 2) coils correcting focusing, 3) counter.

1) Installation of an additional annular-slit diaphragm close to the focus. This method definitely yields a higher resolution at a given transmission factor; its theory has been worked out by Griwet[3]. Strictly speaking, this method does not improve the focusing characteristics of the instrument but merely insures obtaining the optimal focusing conditions. Hence its possibilities are limited.

2) A special coil, equivalent to a small coaxial lens, is installed inside the trajectories; the outside field of this coil corrects the focusing.[4,5] Shpinel'[4] obtained good results with this method: the half-width of the F conversion line was reduced by a factor of 1.5. However, the theory for this method has not been developed and its potentialities are obscure.

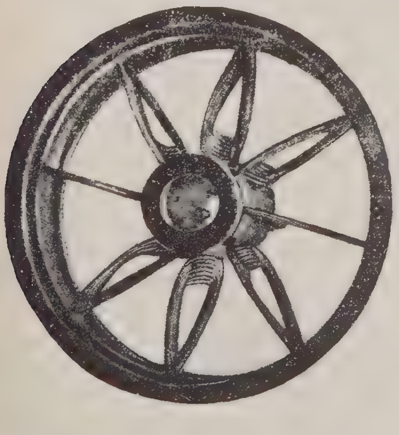

Fig. 2. General view of the system of correcting triangular coils.

Here we propose a third method, one based on the installation of a set of additional coils designed to produce a transverse correcting field.

Fig. 1 shows the electron trajectories in the rotating meridional plane (the plane which at all times passes through the moving electron and the main lens axis). The electrons on trajectories furthest from the axis are obviously over-focused.

The necessary correction can be effected by a weak toroidal transverse field. We produced this field by means of a system of flat triangular coils consisting of several turns each (Fig. 2). The coils are arranged symmetrically about the main lens axis. They are located at the point where the field of the main lens is weak and hence there is virtually no rotation of the meridional plane (see Fig. 1); this minimizes the electron scattering from the triangular coils.

Tests of the correcting coils were carried out on a lens spectrometer having the following characteristics: the source to focus distance is 100 cm; the cross sections of the focusing coils measure 32 x 10 cm with the midpoint of the cross section 18 cm from the axis of the lens (i.e., mean radius of coils = 18 cm). The slit of the defining diaphragm at the center of the lens passes trajectories having initial angles in the range from 10° 20' to 12° 53' relative to the lens axis; the instrument has no other diaphragms. The acceptance angle for a point source is 0.5% of 4π.

When a 2 mm diameter source and a counter with a 3 mm diameter window are used the relative width of the experimental F line at half-height is 3.2% (see curve at righ in Fig. 3). It will be seen from the above description that our spectrometer is of a rather common type and has no special features.

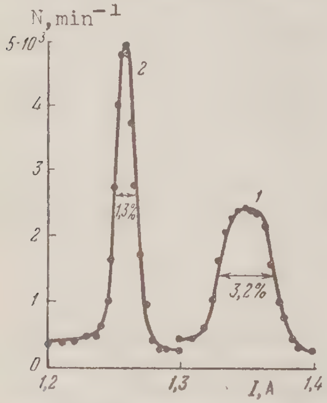

Fig. 3. F conversion line of a thorium active deposit as recorded on the lens spectrometer without (1) and with (2) the correcting field.

Among the different correcting coil assemblies tried, the best results were obtained with a system of 16 triangular single-layer coils, located at a distance of 15 cm from the source.

The effect of the system of correcting triangular coils on the focusing was studied by recording the F conversion line from a thorium active deposit with and without current through the correcting coils, all other conditions remaining the same.

The results of one of the series of test measurements are shown in Fig. 3. It will be seen that with the correcting coils activated the electron line is displaced to the side of weaker currents through the coils of the main lens. The half-width of the line is reduced by a factor of 2.5 (from 3.2% to 1.3%), while the counting rate at the peak is doubled.

The relative half-width of a line in a symmetric electric lens spectrometer, if spherical aberration is neglected, can be calculated by means of the following expression:[6]

$$\eta = \frac{d_s + d_w}{4D}$$

where d_s is the diameter of the source, d_w is the diameter of the counter window and D is in inside diameter of the annular slit. For our conditions we obtain $\eta = (2 + 3)/4 \cdot 140 = 0.9\%$, which is reasonably close to the experimental value of 1.3%. This indicates that the image obtained with the aid of the correcting coils is virtually free of aberration.

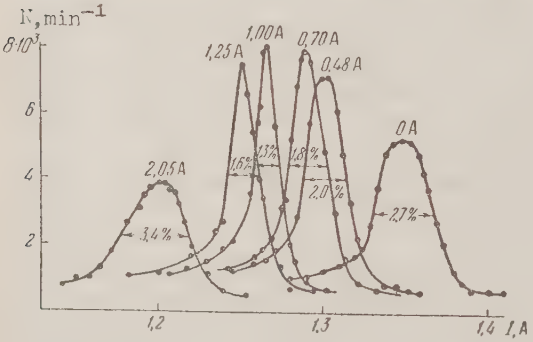

Fig. 4. Dependence of line shape and width on the current in the correcting coils. The figures at the peaks indicate the current through the correcting coils. Horizontal scale - current through the lens coils. These lines were recorded under conditions somewhat different from those obtaining during the measurement of the lines shown in Fig. 3.

In order to determine the optimum current through the correcting coils it is necessary to record a series of curves at different values of the current. One such series of measurements is shown in Fig. 4. The correcting coils are connected in parallel with the lens coils. It will be seen that as the current through the coils is increased the line at first becomes narrower and then again widens; in addition the line gradually shifts to the side of weaker currents through the lens coils.

When the optimal current has been determined, the number of turns in the correcting coils should be increased or decreased as necessary, so that these coils can be connected permanently in series with the main lens coils. In our case it was found that the proper number of turns for the correcting coils is 16.

The initial choice of a triangular shape for the correcting coils was purely empirical. There was therefore the possibility that the correcting effect differed for different sections of the beam. Moreover, it appeared desirable to check on the possible widening of the beam.

To this end we carried out a series of measurements with the same original system of coils but using diaphragms with different ennular slits. We used annular slits 10 mm wide limited by diaphragms of the following diameters:

Slit	Inside diameter, mm	Outside diameter, mm
I	16	18
II	14	16
III	12	14
IV	10	12
Full open	10	18

The results of these measurements are shown in Fig. 5. With the correcting coils inactive (the four curves I' - IV' at the right) the normal aberration of the instrument in the amount of about 5% is clearly evident: as the diameter of the annular slit is decreased the point at which the beam trajectories intersect the axis moves further out (see Fig. 1) and hence heavier currents are needed to record the full line.

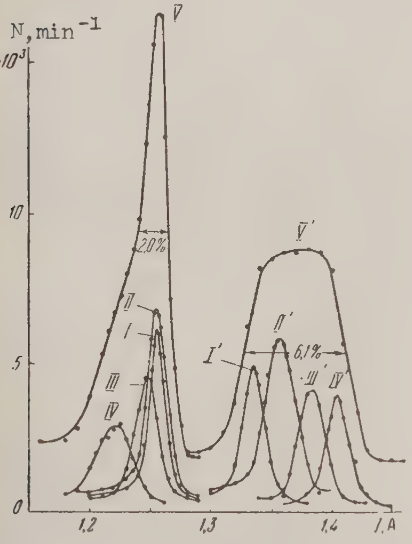

Fig. 5. Variation of the line position as a function of the distance r of the annular slit from the lens axis: I) r = 8.5 cm, II) r = 7.5 cm, III) r = = 6.5 cm, IV) r = 5.5 cm. The full-open curves V and V' were recorded with a different source.

When the correcting coils are switched on the picture changes radically: the relative half-width of the line recorded with the fully open slit goes down from 6.2 to 2.0%. The lines recorded with slits I and II appear at virtually the same main-lens current value, indicating that the correction with these slits is satisfactory. The line obtained with slit III is shifted slightly to the lower current side; the line recorded with slit IV is displaced appreciably more in the same direction. These displacements are evidence of minor but definite negative aberration.

By appropriate modification of the shape of the correcting coils it should be possible to make all the lines (I through IV) coincide and obtain even more exact focusing of the wide beam.

Scientific Research Physical Institute of
"A.A.Zhdanov" Leningrad State University

References

1. H.Agnew & H.Anderson, Rev.Sci.Inst.20,859(1949).
2. E.Persico & C.Geoffrion, " " " 21, 945 (1950).
3. P.Griwet, C.R., 230, 936 (1950).
4. V.Shpinel',Zhur.eksp.i teor.fiz.,22,255(1952).
5. P.Hubert, C.R., 233, 943 (1951).
6. K.Siegbahn,β- & γ-Ray spectroscopy, p.80, Amsterdam, 1955.

AN INVESTIGATION OF THE ANGULAR DISTRIBUTION OF PHOTONS FROM POSITRON ANNIHILATION IN VARIOUS SUBSTANCES

- K.A.Baskova & B.S.Dzhelepov

1. The process of slowing down and annihilation of positrons in matter is still unclear. Most of the positrons are, apparently, first slowed down to an energy of a few electron volts, and then annihilated. If a positron passes through a gas consisting of free electrons, then upon slowing down, it may be assumed to form a system similar to a hydrogen atom, i.e., positronium. Depending on the energy of both particles, positronium is formed in different excited states. Transitions take place quite rapidly from most of these states to one of the two positronium ground states; the singlet 1 $^1S_0$, or the triplet 1 $^3S_1$. The singlet state has a lifetime of about 10^{-10} seconds and the positronium decays into two gammas. In the triplet state its lifetime is about 10^{-7} seconds, and it decays into three gammas.

In two-photon annihilation of positronium, the gammas are ejected at an angle of 180° with each other if the decaying positronium is at rest. When the positronium is in motion, the angle departs from 180° and depends on the relative orientation of the positronium velocity vector and the directions of the gammas. It follows from conservation of momentum considerations that if the γ-rays are at an angle $(180^\circ - \theta)$, the velocity of the center of mass of the positronium is no less than

$$v \simeq \frac{h\nu}{m_0 c} \sin \frac{\theta}{2} .$$

This formula shows that in observing photons diverging at an angle less than 179°, we are witnessing a case of annihilation of positronium atoms having a velocity $v > 2.6 \cdot 10^8$ cm/sec, or an energy $E > 40$ ev. Thus an investigation of the angular distribution of annihilation radiation can give information on the energy of annihilated systems, when this energy lies in the region of about 1 to 100 ev.

The process of formation and the duration of existence of positronium in condensed systems are not clear; it is possible that positronium is continuously destroyed and re-formed, so that the positron interacts in turn with different electrons. The interaction, however, should be stronger with valence electrons (or conduction electrons in metals), since it is difficult for the positron to penetrate into deeper atomic shells due to electrostatic repulsion from the nucleus.

The angular distribution of photons from annihilation in condensed substances has been studied by many authors.[1-15]

In all these investigations the same basic set-up, similar to that shown in Fig. 1, was employed. As the measuring apparatus was refined, the angular distribution was found to be narrower and narrower, until in 1950 Vlasov and Dzhelepov[1] and DeBenedetti and co-workers[2] finally determined the "natural width" of the annihilation angular distribution. It was found that in a measurable number of cases the angle between the γ-rays is less than 180 - 0.6°. This means that cases of positronium energies greater than 14 ev were observed.

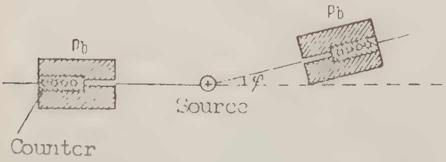

Fig. 1. Diagram of the experiment of Vlasov and Dzhelepov (not to scale).

Unfortunately it is difficult to deduce the energy distribution of the annihilating pairs from experiments employing the scheme of Fig. 1. In all of these experiments narrow but long slits were used, and therefore even when the apparatus was accurately aligned, photons at various angles (up to 176.8° in the experiments of Vlasov and Dzhelepov, and 178.5° in those of DeBenedetti et al) would be detected.

2. The use of scintillation counters and coincidence circuits with a resolving time of $5 \cdot 10^{-8}$ - 10^{-7} sec enabled us to make a more accurate study of the angular distribution.

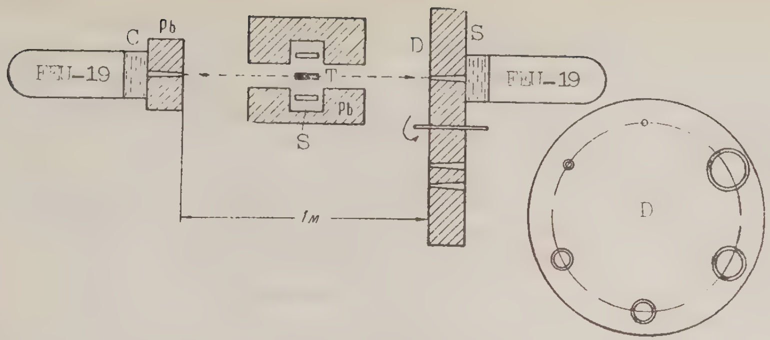

Fig. 2. Diagram of the experiment (not to scale): S) positron source (Cu^{64}), T) beryllium or lead target, D) diaphragm disc with annular apertures, C) NaI(Tl) crystal, FEU-19 - photomultiplier tube.

First we repeated the measurements obtained with the experimental scheme of Fig. 1, but with higher statistical accuracy and better angular resolution than in previous experiments. We replaced the usual GM counters by scintillation counters (NaI(Tl)). Our results agreed with those of Vlasov and Dzhelepov.

We then went on to experiments with a different geometry (Fig. 2). First we placed a radioactive source of Cu^{64} where the target T is shown in Fig. 2, and studied the angular distribution of annihilation γ-quanta. Those gammas leaving T towards the left were defined by a small circular aperture (diameter 2 mm) in the lead block; those moving towards the right were defined by the annular diaphragm, made by cutting six annular diaphragms of various diameters in the large lead disc D, as is shown at the right in Fig. 2. The different annular slits could be brought in front of the same crystal by rotating the disc.

The use of a small opening on one side and annular diaphragms on the other, makes it possible to separate photons in a well defined range of angles of departure from linearity. Since the solid angle increases with θ it becomes feasible to perform measurements at relatively large values of θ: from 0.6° to 2°.

Since different parts of the crystal are illuminated with the different annular diaphragms, the probability of recording a photon will not necessarily be the same with all the diaphragms. In order to exclude the ensuing error, we determined the effective area of the annular diaphragms from the counting rate for annihilation radiation as observed with the crystal when the given diaphragm was in the operative position.

The initial radioactive Cu^{64} source was in the form of powder enclosed in a lead container 0.2-0.3 mm thick. In this case the positrons were slowed down and annihilated in both the copper powder and the lead. The overall dimensions of the source did not exceed the dimensions of the circular collimator hole in front of the counter on the left (Fig. 2).

Moving the different diaphragms in turn in front of the counter on the right and measuring the number of coincidences, one can readily, taking the effective solid angles into account, plot the true angular distribution curve. A typical curve is shown in Fig. 3. Each point of this curve corresponds to the number of coincidences, recalculated for a unit solid angle, in the angular interval indicated by the hatching in the figure.

3. It may be assumed that variations in the velocity of the electrons participating in the annihilation should result in widening or narrowing of the angular distribution curve. In view of this, we felt it would be interesting to investigate positron annihilation in substances with different velocities of the valence electrons, since presumably these are the electrons involved in most of the annihilations. Hence we undertook measurements of the angular distribution curves for annihilation in Be and Pb.

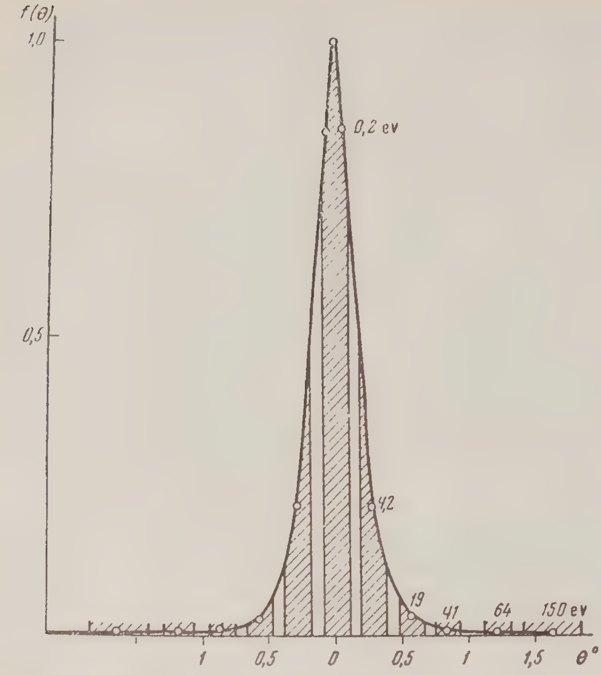

Fig. 3. Angular distribution curve of photons from positron annihilation in a lead ampoule containing Cu^{64}.

The measurements were performed on the apparatus diagrammed in Fig. 2. The investigated targets, in which the positrons were slowed down and annihilated, were prepared in the form of cylinders (5 mm in length and 1 or 2 mm in diameter, in accordance with the entrance of the collimator in front of the counter on the left.

The positron sources were placed on both sides of the target at a distance of 4-5 mm from it and were surrounded by a 5 cm thickness of lead to screen the scintillation counters from direct radiation. The positron sources were prepared of radioactive Cu^{64} in the form of 30-60 μ thick foil.

Even without the target, some coincidences were observed with all diaphragms; these were probably due to annihilation of slow positrons in the air in the region of the target. These coincidences were 3-4 times fewer than in the experiments with a target; they were treated as a background and were subtracted from the coincidences observed with the target.

The use of annular diaphragms made it possible to perform measurements with sufficient statistical accuracy to permit distinguishing between the angular distribution curves for annihilation in beryllium and lead. The angular distribution curves obtained are shown in Fig. 4. As can be seen, the angular distribution curve for beryllium is somewhat wider than that for lead. The difference in width exceeds the limits of the experimental error, as can be seen from Fig. 5, where the large-angle region is shown to an enlarged scale. At angles $\theta > 0.5^\circ$ the statistical error is smaller than the size of the point circles.

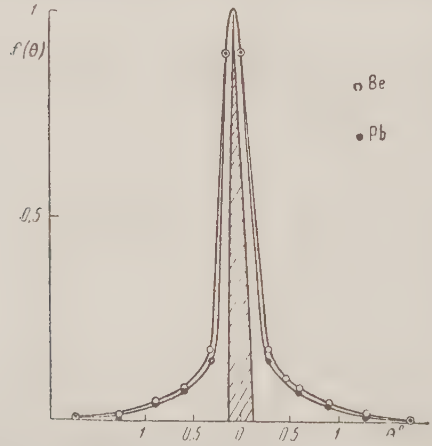

Fig. 4. Angular distribution of annihilation photons from beryllium and lead.

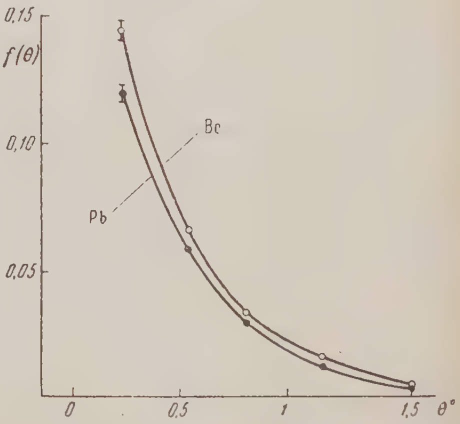

Fig. 5. The large θ region of the curves shown in Fig. 4, plotted to an enlarged scale.

Analogous results were obtained at about the same time by two groups of American physicists, namely Green & Stewart[3] and Lang, DeBenedetti & Smoluchowski[4]. In these experiments the angular distribution of annihilation photons was measured by the usual method of rotating one of the counters about an axis passing through the target with the other counter stationary, i.e., the method of Fig. 1. The results obtained by these investigators for beryllium and lead are in qualitative agreement with ours. The ratio of the beryllium and lead distribution curve widths is 1.20 in our work and 1.16 according to the Americans (although the curves themselves, as is evident from the above, pertain to different experimental conditions).

Green and Stewart evaluated the Fermi energies of electrons taking part in the annihilation from an analysis of their angular distribution curves. As the Fermi energy of the electrons in the metal increases, the width of the annihilation radiation angular distribution curve also increases; it is wider for beryllium than for the other metals investigated. This corresponds to a relatively high Fermi energy for the electrons in beryllium (14 ev). In potassium, sodium and lithium the Fermi energy is 2-4 ev; in lead it is about 10 ev.

The difference in the angular distributions indicates the role played by the velocity of the electrons participating in annihilation. The fact that there are cases in which the departure from colinearity is greater than 0.8°, which corresponds to positronium energy $>$ 25 ev, clearly indicates that part of the positrons are annihilated at high velocities of the center of mass of the positron + electron system.

The circuit for the coincidence amplifier was proposed by A.V.Kurashov; in adjusting the electronic circuits we were helped by V.B.Ustinov; A.S.Basina, student at the University, participated in the measurements. We express our gratitude to all of them.

Scientific Research Physical Institute of
"A.A.Zhdanov" Leningrad State University

References

1. N.Vlasov & B.Dzhelepov, Doklady AN SSSR, 60, 207 (1950).
2. S.DeBenedetti, C.Cowan, W.Konneker & H.Primakoff, Phys. Rev., 77, 205 (1950).
3. R.Green & A.Stewart, Phys. Rev., 98, 486 (1955).
4. G.Lang, S.DeBenedetti & R.Smoluchowski, Phys. Rev., 99, 596 (1955).
5. A.Alikhanian, A.Alikhanov & L.Artsimovich, Doklady AN SSSR, 1, 275 (1936).
6. R.Beringer & C.Montgomery, Phys. Rev., 61, 222 (1942).
7. N.Vlasov & E.Tsirel'son, Doklady AN SSSR, 59, 879 (1948).
8. N.Vlasov, Izv. AN SSSR, Ser. fiz., 14, 337 (1950).
9. P.Argyle & J.Warren, Canad. J. Phys., 29, 32 (1951).
10. G.Griffiths & J.Warren, Canad. J. Phys., 29, 325 (1951).
11. Maier-Leibnitz, ZS. f. Natur., 11, 665 (1951).
12. M.Ambrosino, J.Houbaut & P.Maignan, C.R., 237, 708 (1953).
13. L.Page, M.Heinberg, J.Wallace & T.Trout, Phys. Rev., 98, 206 (1955).
14. A.Stewart, Phys. Rev., 99, 594 (1955).
15. K.Erdman, Proc. Phys. Soc., A68, 304 (1955).

THE ROLE OF DEFORMATION IN THE FORMATION OF ISOMERIC STATES OF NUCLEI

- L.K.Peker

Developments in experimental technique have recently led to the discovery of many new isomeric states. Among these states, of particular interest are those in odd-A nuclei, since at present only such nuclei are susceptible of theoretical treatment within the framework of the existing nuclear models. The present particle is an attempt to analyze these states from the point of view of the generalized shell model.

In the modern literature the term isomer is applied to excited states with long lifetimes. The small decay probability of these states may be due to the large spin differences between them and the ground or lower excited states ($\Delta I \geqslant 3$).[1] It may also be taken as established that the probability of decay in general depends to a large extent on the nature of the levels involved in the transition. For example, in the case of Lu^{177}, Ta^{181}, Re^{187}, Pa^{231}, Pa^{233}, Np^{237}, Pu^{239} and certain other nuclei, the probability of γ-transitions from some levels is anomalously small (and the lifetime is large), although the spins of these levels differ from those of lower levels only by one or two units.[2]

However, we shall limit our examination to isomeric states whose long lifetimes are due primarily to spin differences $\Delta I \geqslant 3$.

In the description of the properties of such states, the single-particle shell model of the nucleus achieved the greatest success.[3-7]

According to this model, the multipolarity of isomeric γ-transitions should usually be M4, since these transitions occur between the states $g_{9/2} \rightleftarrows p_{1/2}$, $h_{11/2} \rightleftarrows d_{3/2}$ and $i_{13/2} \rightleftarrows f_{5/2}$, and occasionally E3 ($h_{11/2} \rightleftarrows d_{5/2}$ transitions).[5] This prediction is in fair agreement with the experimental data. Only in three or four cases (out of 90) are other types (M3, E4) of isomeric transitions observed.

The single-particle model also makes it possible to explain the clustering of isomers in the so-called islands of isomerism, since according to this model isomeric states can exist only in nuclei in which one of the above mentioned levels is in process of filling. This is true only for certain specific Z or N values $(39 \leqslant Z;\ N \leqslant 49;\ 63 \leqslant Z;\ N \leqslant 81;\ 93 \leqslant N \leqslant 125)$.[3,4]

Of the 90 known isomeric states in odd-A nuclei only three are found outside these islands: Ga^{65} (Ref. 8), Mo^{93} (Ref. 9) and Po^{211} (Ref. 10), and these are associated with a special excitation mechanism (the nuclear core rather than the last nucleon is excited).[11]

Where a more detailed analysis of isomeric states is concerned however, the single-particle model encounters several difficulties.

It is found that the islands of isomerism for odd-Z nuclei have, in general, different boundaries than those for odd-N nuclei. Thus, in nuclei with an odd number of neutrons, isomeric states are observed in the interval $63 \leqslant N \leqslant 81$, whereas in nuclei with an odd number of protons, they occur only in the $77 \leqslant Z \leqslant 81$ interval. No isomeric states are known for nuclei with $63 \leqslant Z \leqslant 75$.

In the next island, $93 \leqslant N \leqslant 125$, isomeric transitions that can be described by the single-particle model are observed only for $N > 113$ (there are ten such cases), whereas in nuclei with $93 \leqslant N \leqslant 115$, only five isomeric transitions of types E3, M3, E4 are observed. The single-particle shell model does not describe the E3 transitions which are observed for Z or N = 41, 43, 45, 47; this difficulty arises not only in describing the E3 multipole order (according to this model only M4 is possible), but also the transition probability. The E3 isomeric transition between the $p_{1/2} \rightleftarrows 7/2+$ levels is actually much less probable than might be expected on the basis of Weisskopf's single-particle equation.

It will be seen in Fig. 1 that the experimental curve for the lifetimes lies above the straight-line derived from the single-particle theory.[12]

Recently attempts have been made to overcome several of these difficulties.

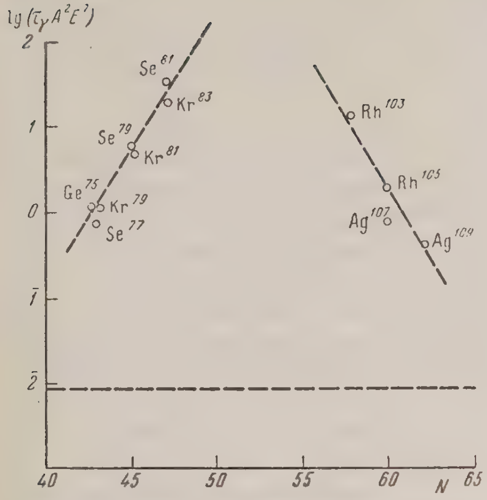

Fig. 1. Data on the probability of E3 γ-transitions between $7/2+ \rightleftarrows p1/2$ levels.[12] The ordinates are reduced lifetimes. The horizontal dash-line represents the theoretical evaluation for a rigorously single-particle E3 transition.

Mayer[5] called attention to a certain difference in the locations of the proton and neutron levels due to the influence of the Coulomb potential. Katz[13] showed that the absence of isomeric states in the $63 \leqslant Z \leqslant 75$ region can be explained by taking into account the different binding energies of protons and neutrons at the $h_{11/2}$ level. Scharff-Goldhaber[14] attempted to explain the same situation by the fact that in this region of Z, collective 2+ levels are very low-lying, being below the high-spin level. In view of this level distribution, decay of the high-spin level to the collective level becomes possible and the condition that $\Delta I \geqslant 3$, assumed to be necessary for the existence of isomeric states, need not be satisfied.

However, none of these attempts may be considered satisfactory, for they fail to yield a consistent explanation of all the experimental data.

We shall show below that taking account of the deformation of the nucleus allows of obviating all the above difficulties without introducing any additional assumptions.

From analysis of various experimental data (quadrupole moments, isotope shift, energy of the first excited levels of even-even nuclei, etc.) it follows that the deformation is small for nuclei at least one of whose shells (proton or neutron) is almost filled. For such nuclei it is possible in the first approximation to calculate the positions of the single-particle levels on the basis of a spherically symmetric potential of the same type as in the single-particle model; in consequence all the basic results of the single-particle model are retained, including the possibility of characterizing the levels by the pure quantum number j (total angular momentum of the odd nucleon) and l (orbital angular momentum), and describing them as $p_{1/2}$, $g_{9/2}$, $d_{5/2}$, $d_{3/2}$ or $h_{11/2}$ states. This essentially is the reason for the success of the simple single-particle model in explaining the existence of the islands of isomerism and the M4 and E3 multipole orders of the isomeric transitions in these islands.

However, when we go over to nuclei both of whose shells are far from filled, the situation changes radically.

The assumption of spherical symmetry of the nuclear potential becomes completely inapplicable. It becomes necessary to take into account the deformation, i.e., the aspherical shape of the nucleus. In the case of axial symmetry of the deformed nuclei, the projection of the angular momentum on the symmetry axis Ω rather than the angular momentum itself is the good quantum number;[15] this is what is measured directly by experiment ($I = \Omega$).

For isomerism to be observed, the ground state or the isomeric state must have high spin: $I = \Omega = 9/2, 11/2, 13/2$, etc. In weakly deformed nuclei, high spin values $I = j$ will be observed for all nuclei with an odd number of nucleons on the j level.

It can readily be shown that the number of nuclei in which the levels with $j = 9/2, 11/2, 13/2$ are filled is, respectively, 5, 6 and 7 (i.e., $(2j + 1)/2$ nuclei). At the same time, in nuclei with noticeable deformation, the highest spin value $I = \Omega = j$ is encountered only once, since only two nucleons can exist on a level with given Ω. Thus we may expect that levels with high spin values will be found in deformed nuclei much less often than is predicted by the single-particle model. Since deformation reduces the degeneracy of the energy levels with respect to the quantum number Ω, the number of such levels in strongly deformed nuclei is appreciably greater than in spherical ones. In view of this probability of two levels with very different spins ($\Delta I \geqslant 3$) lying next to each other is greatly reduced.

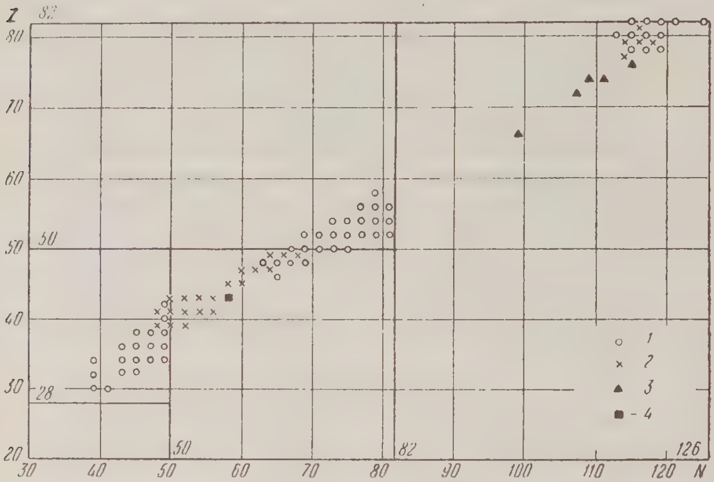

Fig. 2. Isomeric states in odd A nuclei. The straight-lines are drawn through points corresponding to nuclei with filled shells: 1) isomers with odd N, 2) isomers with odd Z, 3) isomers not explained on the basis of the single-particle shell model, 4) Tc^{101}.

Both of these factors lead to the situation where conditions in strongly deformed nuclei with $63 \leqslant Z \leqslant 75$ or $93 \leqslant N \leqslant 115$ are not favorable for the existence of isomeric states. Fig. 2, which gives all the known isomers with odd A, shows this quite clearly. It can be seen that the ordinary isomers are clustered about the horizontal and vertical lines corresponding to filled shells.

Thus the absence of ordinary isomers with M4 and E3 transitions in nuclei with $63 \leqslant Z \leqslant 75$ or $93 \leqslant N \leqslant 115$ is explained not by the distinctive characteristics of the individual proton or neutron levels, but by the deformation of the nuclear surface, due to all the nucleons (protons and neutrons) outside the filled shell.

Obviously, however, in this region of N and Z values there may also exist individual nuclei having isomeric states, but of a different type. At present five such nuclei are known; their characteristics are listed in Table 1. In order to describe such states we must make specific assumptions concerning the shape of the potential within the nucleus. If we make use of Nillsen's[16] single-particle level scheme, deduced on the basis of various assumptions regarding the magnitude of the nuclear deformation, we can find which deformed nuclei should have isomeric states and, also, determine the possible multipole orders of the isomeric γ-transitions. It is found that this group includes all five nuclei listed in Table 1, as well as a number of others (Er^{167}, Yb^{171}, Hf^{177}, etc.); not only the existence of the isomeric states per se but also the multipolarity of the isomeric transitions correctly predicted.

Table 1
Isomeric γ-transitions in the $99 \leqslant N \leqslant 115$ region

Nucleus	Spin & parity* of the isomeric & ground states	Multipole order of isomeric transition (experimental)	References
${}_{66}Dy^{165}_{99}$	$^{7}/_{2}{}^{+} \rightleftarrows {}^{1}/_{2}{}^{-}$	$E3$	[7]
${}_{72}Hf^{179}_{107}$	$^{9}/_{2}{}^{\pm} \rightleftarrows {}^{3}/_{2}{}^{\pm}$	$E3$ or $M3$	[7]
${}_{74}W^{183}_{109}$	$^{7}/_{2}{}^{\pm} \rightleftarrows {}^{3}/_{2}{}^{-}$	$E3$ or $M3$	[17]
${}_{74}W^{185}_{111}$	$^{9}/_{2}{}^{\pm} \rightleftarrows {}^{3}/_{2}{}^{-}$	$E3$ or $M3$	[17]
${}_{76}Os^{191}_{115}$	$^{9}/_{2}{}^{-} \rightleftarrows {}^{3}/_{2}{}^{-}$	$M3 + E4$	[18]

* *The spins and parities were deduced from analysis of different experimental data.*

In analyzing the experimental data, it should be borne in mind that in Nillsen's level scheme, as well as in Mayer's, levels may cross over, so that in some cases there may obtain a somewhat different level order than that given in Ref. 16. By using all of the experimental data, however, it is possible to establish the actual level sequence in every particular case.

On the basis of similar considerations it is possible to explain the absence of an isomeric state of Tc^{101}; no such state was found, although specifically searched for.[16] It will be seen in Fig. 2 that the point corresponding to Tc^{101} is further from the horizontal and vertical lines than any of the other points; therefore its nucleus is more strongly deformed than the others in this region and the effects associated with deformation affect this nucleus.

In analyzing isomeric states, in addition to determining the multipole order of the isomeric transitions, it is also very important to consider the level width or the probability of an isomeric γ-transition, since this makes it possible to clarify certain details of nuclear structure. Such examinations have already been undertaken several times[6,12,15,18,20], and it was shown that the probability for M4 γ-transitions is satisfactorily described by Weisskopf's single-particle formula.

The extant experimental data are summarized in Table 2 to show the extent to which Weisskopf's formula is substantiated by experiment. The factor F, which gives the deviation of the experimental value from the theoretical T_γ, is not very different from unity. According to Bohr and Mottelson, the deviation of F from unity can be explained by the somewhat different shape of the nucleus in the states between which the isomeric transition takes place.

Table 2

Probabilities for a number of isomeric M4 γ-transitions

Nucleus	F*	Nucleus	F	Nucleus	F
Zn^{69}	0,23	In^{113}	0,144	Xe^{131}	0,33
Kr^{85}	0,38	In^{115}	0,165	Xe^{133}	0,39
Sr^{87}	0,34	Sn^{117}	0,120	Xe^{135}	0,44
Y^{87}	0,22	Sn^{119}	0,90	Ba^{133}	0,21
Y^{89}	0,37	Te^{121}	0,31	Ba^{135}	0,46
Y^{91}	0,14	Te^{123}	0,33	Ba^{137}	0,32
Zr^{89}	0,35	Te^{125}	0,36	Pt^{195}	0,19
Nb^{91}	2,8	Te^{127}	0,31	Pt^{197}	0,20
Nb^{95}	0,23	Te^{129}	0,59	Hg^{197}	0,18
Nb^{97}	0,09	Te^{131}	0,90	Hg^{199}	0,20
Tc^{95}	0,17	Xe^{129}	0,21	Pb^{207}	0,32
Tc^{99}	0,22	—	—	—	—

* F is the ratio of the experimentally determined transition probability to that calculated by Weisskopf's formula with $R = 1.2 \cdot 10^{-13} A_{1/3}$ cm.

Recently several cases (Hg^{197}, Hg^{199}) of M4 isomeric transitions were observed with some admixture of E5 (Refs. 21 & 22), although according to the single-particle calculations, the admixture of E5 should be so small as to be undetectable ($E5/M4 \approx 10^{-4}$). This presence of the electric multipole in γ-radiation, according to Bohr and Mottelson, is due to collective effects, in particular, to an induced collective dynamic electric (E5) moment in a single-particle transition.[15,23] Since the whole nuclear surface takes part in producing this dynamic electric moment, it is much greater than the electric moment due to a single particle, and, consequently, the corresponding γ-transition becomes much more probable.

The situation with respect to $7/2+ \rightleftarrows p_{1/2}$ transitions is much more complicated. The 7/2+ level, which often appears in the $43 \leq Z, N \leq 47$ region, is not susceptible of description by the single-particle model. Goldhaber and Sunyar[6] have suggested that this level arises as a result of the interaction between 3, 5 and 7 nucleons in the $g_{9/2}$ state.

Fig. 1 shows how the probability of γ-transitions between the $p_{1/2}$ and 7/2+ levels depends on the degree to which the shells are filled. It is seen from the figure that this E3 transition is strongly suppressed and that the suppression increases as the state with the filled neutron shell given by N = 50 is approached.

This dependence of the probability can be qualitatively explained within the framework of the generalized shell model. For a pure configuration such as $(g_{9/2})^{3,5,7}_{7/2}$ single-particle E3 transitions should be entirely forbidden by the so-called j-forbiddenness.[15] For odd-neutron nuclei this forbiddenness is reinforced, since a neutral particle, whose interaction with the electromagnetic field of the radiation is extremely weak, participates in the transition.

Both of these restrictions, however, are eased by virtue of the appreciable coupling of the outer nucleons with the surface.[15] In the first place this interaction leads to a small admixture of the $g_{7/2}$ state, as a result of which ordinary single-particle E3 transitions become possible. The amount of this admixture depends both on the separation between the $g_{9/2}$ and $g_{7/2}$ levels and on the magnitude of the coupling between nucleons and the surface. As the filled shell is approached, on the one hand, the separation between $g_{9/2}$ and $g_{7/2}$ increases[24] and, on the other hand, the coupling between the outer nucleons and the surface is weakened. Both of these factors reduce the $g_{7/2}$ admixture and, consequently, lower the transition probability. Calculations show, however, that these factors taken alone do not fully explain the observed transition probabilities and that an important role is played by the induction of a collective dynamic E3 type moment in the transition.

Thus the difficulties encountered in attempting to explain the isomeric states in odd-A nuclei with the aid of the single-particle model are dissipated when we turn to the generalized shell model.

In conclusion I wish to thank L.A.Sliv, B.S.Dzhelepov and Aage Bohr for detailed discussion of the work.

References

1. C.Weizsäcker, Naturwiss, 24, 813 (1936).

D.Engelkemeir & L.Magnusson, Phys. Rev., 94, 1395 (1954); D.Strominger & J.Rasmussen, Phys. Rev., 100, 844 (1955); D.Engelkemeir & L.Magnusson, Phys. Rev. 99, 135 (1955); H.DeWaard, Phil. Mag., 46, 445 (1955); A.Sunyar, Phys. Rev., 90, 387 (1953); W.Barber, Phys. Rev., 80, 332 (1950).

3. L.Nordheim, Phys. Rev., 75, 1894 (1949).
4. E.Feenberg & K.Hammak, Phys. Rev., 75, 1877 (1949).
5. M.Mayer, Phys. Rev., 78, 16 (1950).
6. M.Goldhaber & A.Sunyar, Phys. Rev., 83, 907 (1953).
7. M.Goldhaber & R.Hill, Rev. Mod. Phys., 24, 179 (1952).
8. B.Grasemann, Phys. Rev., 93, 1034 (1954).
9. J.Kraushaar, Phys. Rev., 92, 318 (1953).
10. W.Jentschke, A.Juveland & D.Kinsey, Phys. Rev., 96, 231 (1954).
11. M.Goldhaber, Phys. Rev., 89, 1146 (1953).
12. M.Goldhaber & A.Sunyar, β- and γ-Ray Spectroscopy.-Ed: K.Siegbahn, Amsterdam, 1955.
13. R.Katz, Phys. Rev., 91, 1487 (1953).
14. G.Scharff-Goldhaber, Phys. Rev., 90, 587 (1953).
15. A.Bohr & B.Mottelson, Dan. Videnskab. selskab. Mat.-fys. Medd.,27,16(1953).
16. S.Nillsen, Dan. Videnskab. selskab. Mat.-fys. Medd., 29, 16 (1955).
17. A.Poe, Phil. Mag., 377, 611 (1955).
18. W.Mihelich, Bull. Am. Phys. Soc., 30, 46 (1955).
19. D.Wills, Phys. Rev., 93, 181 (1954).
20. W.Low, Bull. Res. Coun. Israel, 3, 4, 337 (1954).
21. H.Bolotin & R.Wilkinson, Bull. Amer. Phys. Soc., 30, 71 (1955).
22. F.Gimmi, E.Heer & P.Scherrer, Helv. Phys. Acta, 28, 470 (1955).
23. A.Bohr, B.Mottelson, β- and γ-ray Spectroscopy.-Ed: K.Siegbahn, Amsterdam, 1955.
24. L.Sliv & L.Peker, Doklady AN SSSR, 94, 849 (1954).

THE LEVELS OF NUCLEI WITH AN ODD NUMBER OF NEUTRONS AND Z = 11-28

- A.M. Demidov

Investigations performed in recent years on the energy and angular distribution of protons from (d,p) reactions, as well as further studies of $\beta\pm$ particles and γ-rays produced in (n,γ) reactions, have yielded much information on the energies, spins, and parities of certain excited states of nuclei with values of Z between 11 and 28.

The most detailed investigation has been made of the levels in even-odd (N odd) nuclei with Z = 11 to 20 by Holt and Marsham[1]. They investigated the angular distribution of protons and the cross section for the (d,p) reaction for various levels of these nuclei. Analyzing their data and assuming that the neutron is most likely to be captured at levels associated with single-particle excitation of the last neutron, they succeeded in establishing the characteristics of a number of levels of even-odd nuclei.

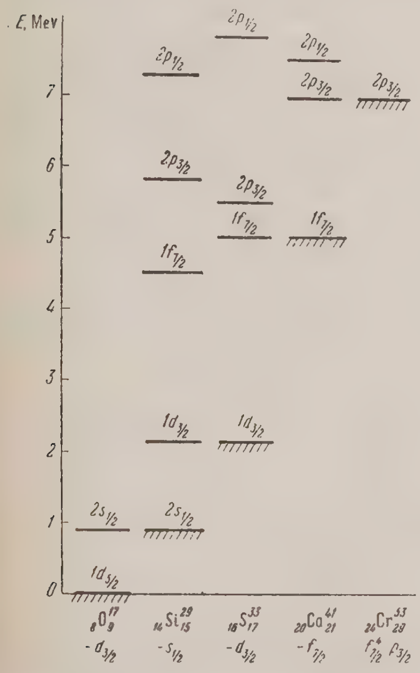

Fig. 1. Single-particle neutron levels of even-odd nuclei.

Fig. 1 is a schematic representation of the location of such single-particle neutron levels for several even-odd nuclei. For clarity this figure does not show other levels, and the ground state of each nucleus is plotted at the level of the preceding nucleus having the same characteristics.

It is interesting that the levels are distributed exactly in the order predicted by the nuclear shell model: $1d_{5/2}$, $2s_{1/2}$, $1d_{3/2}$, $1f_{7/2}$, $2p_{3/1}$, $1f_{5/2}$ and $2p_{1/2}$.

A further examination of the properties of these single-particle neutron states may be of interest. Below we shall show that certain additional data on such states can be obtained by analyzing the energy levels of nuclei with the same neutron configuration but a different number of protons. In particular, the case in which the number of protons differs by unity is of interest. In our analysis we shall compare the excited states of even-odd and odd-odd nuclei.

It has already been pointed out[2] that the interaction between the odd neutron and odd proton in an odd-odd nucleus can be weak, if they are in different orbits; it has been noted also that the states of odd-odd nuclei are characterized by the angular momenta and parities of the neutron and proton groups separately and that these groups have the same angular momenta and parities as observed in the neighboring odd-odd nucleus.

Obviously one may also expect that in odd-odd nuclei there may occur separate excitation of the neutron and proton configurations, i.e., one may expect that among the levels of an odd-odd nucleus there may also appear levels associated with a transition of the last neutron to a state predicted by the shell model ($1d_{5/2}$, $2s_{1/2}$, $1d_{3/2}$, etc.). However, upon closer examination of odd-odd nuclei, we find new factors connected with the nature of nuclear forces. In particular, it is possible that the interaction between the odd neutron and the odd proton may differ, depending on the mutual orientation of their angular momenta j_p and j_n; this may lead to splitting of those levels of odd-odd nuclei which correspond to fixed states of the neutron and proton. It then becomes necessary to consider several levels of the odd-odd nucleus corresponding to a given nucleon state. The parities of all these levels are the same (they are given by the sum of the

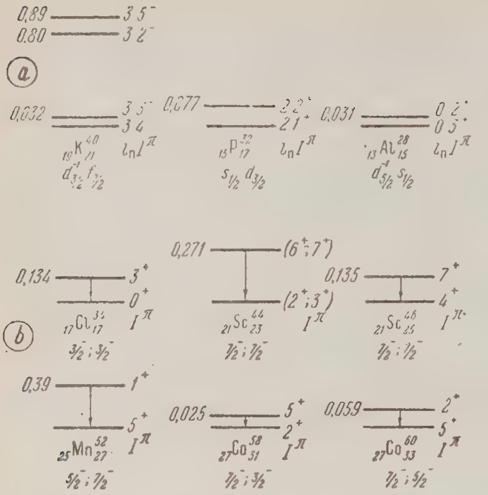

Fig. 2. a) multiplets for the ground states of K^{40}, Al^{28} and p^{32}; b) isomers of odd-odd nuclei with $Z < 28$.

parities of the neutron and proton states), while the total angular momenta of these states should vary from $|j_p - j_n|$ to $|j_p + j_n|$.

Unfortunately, at present the characteristics of only a few excited states of odd-odd nuclei are known. Therefore it is still impossible to give a completely satisfactory proof of the existence of multiplets of this kind. There do, however, exist several cases in which multiplet members can be identified with fair certainty. These cases involve mainly multiplets at the ground states of nuclei.

The above mentioned type of interaction can serve to explain, for instance, the appearance of the first three excited states of K^{40} (Fig. 2,a). The angular distribution of protons from the(d,p) reaction for the lowest of these three levels gives an orbital angular momentum $l_n = 3$ for the neutron.[3] This result gives reason to assume that these states correspond to the four possible mutual orientations of the angular momenta of the neutron in the $1f_{7/2}$ state and the proton in the $1d^{-1}_{3/2}$ state. The values of the total angular momenta of these states, as determined from the intensities of the proton groups, namely 4-, 3-, 3-, and 5-, respectively[4], are substantiated by data on the γ-transitions of the K^{40} nucleus after the (n,γ) reaction.

An analogous interpretation can be advanced for the first excited levels of Al^{28} ($1d^{-1}_{5/2}$ proton and $2s_{1/2}$ neutron) and p^{32} ($2s_{1/2}$ proton and $1d_{3/2}$ neutron) (Figure 2,a). The data on the orbital angular momenta of the neutron [3,1] and on the total angular momenta and parities[4,5] of the ground and first excited states of the Al^{28} and p^{32} nuclei give reason to assume that these states are due to different orientations of j_p and j_n in these nuclei.

It should be noted that this splitting of the levels can lead to isomerism in odd-odd nuclei if $j_p + j_n$ is much different from $|j_p - j_n|$.

Fig. 2,b lists the isomers of the odd-odd nuclei,

$$_{17}Cl^{34}_{17},\quad _{21}Sc^{44}_{23},\quad _{21}Sc^{46}_{25},\quad _{25}Mn^{52}_{27},\quad _{27}Co^{58}_{31}\ \text{и}\ _{27}Co^{60}_{33},$$

for which the data on the total angular momenta and parities of the ground and excited states make it possible to interpret their isomerism by this method. Under each level scheme we give the angular momenta and parities of the neutron and proton configurations in the nucleus. In all the cases shown, both the angular momenta and the parities of the states, comprising the isomer, can be deduced from the sum of the vectors j_p and j_n. In this connection it is interesting to note the following. According to the shell model, isomerism is associated mainly with the number of neutrons or protons in the nucleus: specifically the number of protons or neutrons must lie in the intervals 39-49 and 63-81, when the $2p_{1/2}$ & $1g_{9/2}$, and $1h_{11/2}$, $3s_{11/2}$ & $2d_{3/2}$ shells are being filled[6]. Yet, all the above-mentioned isomers of odd-odd nuclei have proton and neutron numbers in a region in which isomerism should not be expected according to the shell model.

All the above examples refer to multiplets at the ground states of odd-odd nuclei. Owing to the lack of data on the characteristics of the highly excited states of these nuclei it is almost impossible to demonstrate the presence of multiplets due to different orientations of the angular momentum of an excited neutron with respect to the angular momentum of the nonexcited proton. All the examples that can be cited are, therefore, necessarily hypothetical.

Let us compare, for instance, the spectra of the Al^{28} and Si^{29} nuclei, which

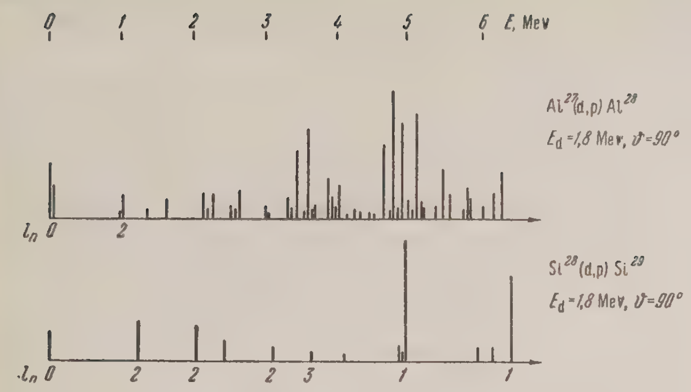

Fig. 3. The intensities of the proton groups from the $Al^{27}(d,p)Al^{28}$ and $Si^{28}(d,p)Si^{29}$ reactions.

have the same $2s_{1/2}$ neutron configuration. Fig. 3 shows dependences of the relative intensities of the proton groups from the $Al^{27}(d,p)Al^{28}$ and $Si^{28}(d,p)Si^{29}$ reactions on the energy of the levels of Al^{28} and Si^{28} nuclei.[7,8] Both nuclei were investigated at the same deuteron energy $E_d = 1.8$ Mev and at the same 90° angle of observation with respect to the incident deuteron beam.

The energies of the excited states can be read from the horizontal scale at the top of the figure; data concerning the orbital angular momenta of the neutron are given under the corresponding level observed in the (d,p) reaction. The length of the lines is proportional to the relative intensity of the proton groups from this reaction.

It will be seen that as regards the proton yield the 4.93 Mev energy level stands out sharply from the other of the Si^{29} levels. Holt and Marsham[1] characterized it as $2p_{3/2}$. In the case of Al^{28}, the outstanding four high proton group intensity levels are those with energies 4.67, 4.76, 4.90 and 5.13 Mev.

It may be assumed that these four Al^{28} levels correspond to the four possible mutual orientations of the $1d^{-1}_{5/2}$ unexcited proton and the $2p_{3/2}$ excited neutron. In this case their quantum characteristics should be 1-, 2-, 3- and 4-.

The Al^{28} nuclear state produced in thermal neutron capture is 2+ and 3+. If the probability for capture in one of these states is higher, intense (E1) γ-transitions will proceed only to three of the four above-mentioned levels. Kinsey and Bartolomew[9] have observed intense γ-transitions to the 4.67 and 4.90 Mev levels.

It is interesting to note that these outstanding Al^{28} levels have the same energy as the $2p_{3/2}$ level in Si^{29}. This may not be a coincidence, since in comparing other pairs of nuclei we encounter analogous situations. Data on the energy of the first excited level with $l_p = 1$ for two pairs of nuclei having the neutron configurations $1d_{3/2}$ and $1f_{7/2}$ in the nonexcited state are listed in the table below.

Energy of the first level with $l_p = 1$ and a large (d,p) reaction cross section, Mev	Nucleus	Neutron configuration
3.23 (Ref. 1)	S^{33}	$1d_{3/2}$
3.26 (Ref. 10)	P^{32}	
1.95 (Ref. 1)	Ca^{41}	$1f_{7/2}$
2.05 (Ref. 3)	K^{40}	

The above example, in which a multiplet is suggested for the excited state of the neutron is not the only one, but in the other cases, as in the given one, additional data on the level characteristics are necessary for certain identification of the multiplet components.

It must be noted that if the presence of multiplets in excited neutron states could be proved, this would make it possible to explain, at least partially, the high level density found in the (d,p) reaction on Al^{28} as compared with the density for the P^{32} nucleus.[11] In the case of the Al^{28} nucleus the 5/2 angular momentum of the proton should give more combinations in conjunction with the angular momentum of the excited neutron than the 1/2 angular momentum characteristic of the p^{32} proton. We are assuming here that the levels primarily participating (i.e., with the highest probability) in the (d,p) reaction are the levels corresponding to excitation of the neutron configuration.

Sc^{46}, whose odd proton and neutron in the ground state have the configuration $1f_{7/2}$, is characterized by an even higher level density than Al^{28}. Possibly this, as well as the presence of several neutrons outside the filled shell, affects the γ-spectrum emitted by Sc^{46} in the (n,γ) reaction.[12] The γ-spectrum of Sc^{46} differs sharply from those of its neighbor elements, and is reminiscent of the γ-spectra of heavy nuclei, the appearance of whose spectra is determined by their high level densities.

In conclusion, I wish to express my gratitude to L.V.Groshev for helpful suggestions and advice.

References

1. J.Holt & T.Marsham, Proc. Phys. Soc. (London), A 66, 249, 258, 467, 565 (1953).
2. A.DeShalit, Phys. Rev., 91, 1479 (1953).
3. I.Teplov, Dissertation, 1951.
4. H.Enge, Phys. Rev., 94, 730 (1954).
5. R.Sheline, N.Johnson, P.Bell, R.Davis & F.McGowan, Phys. Rev., 94, 1642 (1954).
6. M.Korsinskii, Izomeriia atomnykh iader (Isomerism of atomic nuclei), M. 1954.
7. H.Enge, W.Buechner & A.Sperduto, Phys. Rev., 88, 963 (1952).
8. D.VanPatter, W.Buechner, Phys. Rev., 87, 51 (1952).
9. B.Kinsey & G.Bartolomew, Canad. J. Pnys., 31 537 (1953).
10. B.Kinsey & G.Bartolomew, Phys. Rev., 93, 1260 (1954).
11. P.M.Endt,& I.C.Kluyver, Rev. Mod. Phys., 26, 95 (1954).
12. B.Kinsey & G.Bartolomew, Phys. Rev., 89, 375 (1953).

ON THE EXISTENCE OF OCTUPOLE ISOMERIC TRANSITIONS WITH PERIODS BETWEEN 10^{-4} AND 1 SEC IN ODD-A NUCLEI

- V.I.Gol'danskii and V.S.Evseev

On the basis of the correlations between the multipolarity, energy and lifetime of isomeric transitions[1,2], one can conclude that the overwhelming majority of transitions with half-lives $T_{1/2} = 10^{-4}$-1 sec are octupoles, and that for odd-Z nuclei the energy of these transitions lies in the range $\Delta E =$ = 150-700 kev, while for odd-N nuclei ΔE = 1-3 Mev.

Quadrupole transitions from levels with these lifetimes have energies of the order of 10 kev, while sixteen-pole transitions have energies of about 10 Mev, yet such separations between neighboring levels are almost never observed.[3]

When we consider the generally accepted shell-model distribution of states in the various shells (disregarding, for the moment, the sequence of these states), we conclude that octupole transitions can take place within a shell for far from all possible combinations of levels.*

This conclusion is illustrated in Figs. 1, 2 and 3. Here the + sign identifies combinations of pairs of low levels which can induce octupole transitions between some higher-lying level and one of the low ones, the $\triangle\!\!\!\!+$ sign denotes combinations for which octupole transitions are possible between the two low levels, and the ⊕ sign indicates combinations for which an octupole transition is possible between two of the higher-lying levels. Fig. 1 shows two possible variants for octupole transitions and Figs. 2 and 3 give three such variants each.

Variant a in all the figures corresponds to the order of filling of the nuclear shells in the simplest case of taking spin-orbit coupling splitting into account (see Ref. 4, for example). Variants b and c correspond to empirical** shell-filling orders; according to Klinkenberg[5], variant b corresponds to the filling of the proton shells, variant c to the filling of the neutron shells. The sequence in which the shells are filled is from left to right

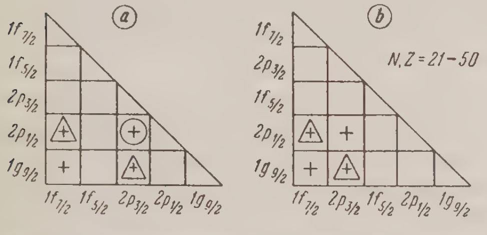

Fig. 1. Possible octupole transitions with N or Z = 21-50.

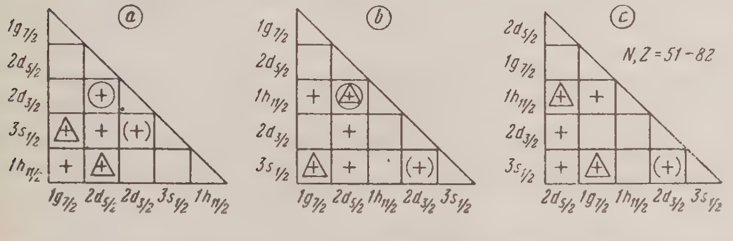

Fig. 2. Possible octupole transitions with N or Z = = 51-82.

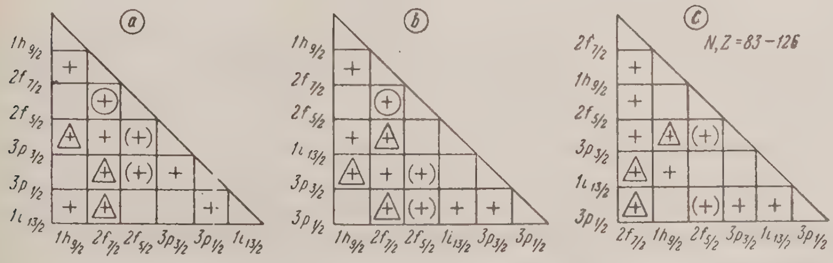

Fig. 3. Possible octupole transitions with N or Z = 83-126.

---

*We are not considering octupole transitions between levels of different shells, since we assume that the energies of such transitions would in general be much greater, so that $T_{1/2} \ll 10^{-4}$ sec.

**See new data on excited states of odd-A nuclei and Refs. 5-7.

along the horizontal axes and from the top down along the vertical.

Taking account of the order in which the various states are filled radically restricts the number of possible octupole transitions. Such transitions remain possible only for those combinations of two lowest levels which are indicated by the symbol ⊕ in Figs. 1-2 (the lowest level is found along the horizontal, and the second level along the vertical axis).

In the simplest case of the level order based on the spin-orbit splitting (variant a), the transitions of interest in odd-A nuclei can occur in filling of the $2p_{3/2}$ state in the IV shell (E3 transition $1g_{3/2} \rightarrow 2p_{3/2}$), the $2d_{5/2}$ state in the V shell (E3 - $1h_{11/2} \rightarrow 2d_{5/2}$) and the $2f_{7/2}$ state in the VI shell (E3 - $1i_{13/2} \rightarrow 2f_{7/2}$).

These states are filled, according to variant a, for odd Z or N values of 35 and 37 in the IV shell, 59, 61 and 63 in the V shell, and 93, 95, 97 and 99 in the VI shell.

Several cases of isomeric E3 transitions in nuclei with the above odd values of N have been observed: Pd^{109}_{63}, Cd^{111}_{63} and Dy^{165}_{99}; the energies of these transitions, however, are actually between 0.1 and 0.17 Mev, and their half-lives are of the order of minutes and even tens of minutes. A number of isomers with the above A and N values are reported to decay by quadrupole transitions (for instance, Rb^{85}_{48}, Eu^{153}_{90} and Zn^{67}_{37}).

The simplest level order, arrived at taking spin-orbit splitting into account (variant a), yields the largest number of possible isomeric octupole transitions; all additional considerations impose a reduction on this number (see, for instance, variants b and c in Figs. 1-3). It is therefore expedient to start here with the maximum list of isotopes in which octupole isomeric transitions may be expected according to variant a (later we shall introduce certain additional considerations which will reduce this list).

Among such stable or long-lived isotopes with odd Z are $Br^{79,81}_{44,46}$, Rb^{87}_{50}, Pr^{141}_{82} $Pm^{145,147}_{84,86}$ and Eu^{151}_{88}, as well as many isotopes of the transuranic elements Np, Am, Bk and E.

Among similar stable isotopes with odd-N are Gd^{157}_{93}, $Dy^{161,163}_{95,97}$ and Er^{167}_{99}.

Odd-N isomers decaying by octupole transitions (according to variant a) can also be produced by radiative capture of neutrons by the nuclei $Ni^{62,64}_{34,36}$, Zn^{64}_{34}, Mo^{100}_{58}, Ru^{102}_{58}, Pd^{106}_{60}, $Cd^{106,108}_{58,60}$, Sn^{112}_{62}, Sm^{154}_{92}, $Gd^{156,158,160}_{92,94,96}$, $Dy^{158,160,162}_{92,94,96}$, $Er^{162,164,166}_{94,96,98}$ and Yb^{168}_{98}.

If we use the empirical order in which the shells are filled, the number of possible octupole isomeric transitions is greatly reduced. For odd-Z isomers (variant b) such transitions become impossible for Z = 35 and 37, while for odd-N isomers (variant c) all such transitions are precluded in general.

Clearly, the existence or nonexistence of isomeric octupole transitions in the cases listed above can be used to choose among the possible variants of the level-filling order. The above conclusions would be exhaustive and fully valid only if the simple nuclear shell model were unconditionally applicable to all nuclei, i.e., if no excited levels except the single-nucleon shell levels existed.

Recently, however, it has been found that the new generalized shell model[6] gives a more correct and complete description of the atomic nucleus. In particular, it has been shown[7] that for deformed nuclei with odd A each of the single-particle states splits into $(2j+1)/2$ states with angular momenta j, $j-1$, ..., $1/2$ (where j is the angular momentum of the splitting single-particle state). This splitting is larger for nuclei with large quadrupole moments, or in general, for nuclei whose Z or N lies far from the "magic" numbers. Naturally, when such splitting takes place, the mean separation between neighboring nuclear levels becomes less than that for the unsplit single-particle state (~100 kev).

When this is taken into account, there should be no octupole transitions with $T_{1/2} = 10^{-4}$-1 sec for nuclei with Z or N = 93-99 (since nuclei with these Z or N values have large quadrupole moments*).

Thus on the basis of the generalized model (i.e., taking account of the splitting of the single-particle levels in deformed nuclei), one may conclude that the existence of octupole transitions with $T_{1/2} = 10^{-4}$-1 sec will be further restricted in odd-A nuclei (only the cases where Z = 59, 61 or 63 remain).

An examination of the experimental data on excited states of odd-A nuclei shows, however, that in addition to the levels forecast by the generalized model other, additional levels of a different type are also observed in some nuclei. Thus, for instance, in addition to single-particle, rotational levels are observed in many nuclei. Nuclei in this category apparently include Rh^{103} (Refs. 8,9), Ag^{107} (Refs. 3, 8-10), Ag^{108} (Refs. 3, 8-10), Eu^{153} (Refs. 11-13), Lu^{175} (Refs. 13-15) and Hf^{177} (Refs. 13-16).

Many of the levels which have previously been interpreted as "holes" may also turn out to be rotational.[17-19] Investigators have also reported the existence of levels which are neither single-particle nor rotational levels and which have not yet been satisfactorily explained. As examples of the occurrence of different types of levels in a single nucleus, one can cite the nuclei whose level schemes are shown in Figs. 4 and 5.

$\underline{Rh^{103}.}$ In this nucleus the 7/2+, 9/2+ ($1g_{9/2}$) and $1g_{7/2}$ levels are single-particle levels**, while the 3/2- and 5/2- levels are interpreted as rotational levels of the $2p_{1/2}$ ground state.[9] (Fig. 4)

$\underline{Lu^{175}.}$ The 9/2+ and 11/2+ states of this nucleus are rotational. The 9/2- level and one of the 5/2+ levels can be satisfactorily explained on the basis of splitting of the single-particle states[7] (Fig. 5).

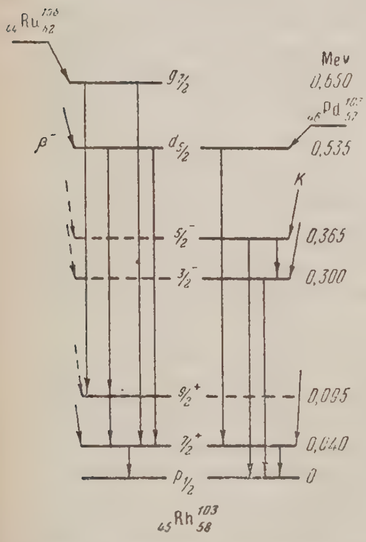

Fig. 4. Level scheme of the Rh^{103}_{58} nucleus.

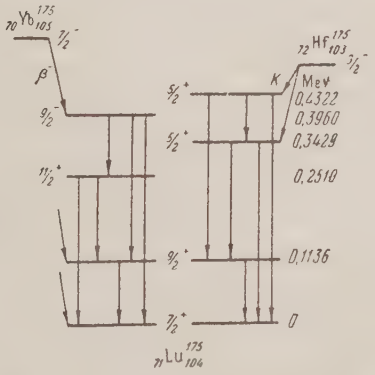

Fig. 5. Level scheme of the Lu^{175}_{103} nucleus.

The existence of levels other than those of the single-particle shell model may, in principle, lead to possible new octupole transitions, provided transitions between these levels are allowed. However, these could occur only in place of higher multipolarity transitions, i.e., instead of transitions that might be observed in the absence of these additional levels (among such transitions, perhaps, is the E3 transition $1h_{11/2} \rightarrow 5/2+$ in Au^{197}, which apparently appears instead of the M4 transition $1h_{11/2} \rightarrow 2d_{3/2}$ (see Fig. 6 and Ref. 20).

---

*The isomers decaying by octupole transitions predicted by L.K.Peker (see p. 864 of the present issue of the Bulletin) should have $T_{1/2} \approx 1$ sec in view of the small energy separation between the levels.

**The 7/2+ state is not purely single-particle, but is obtained as a result of interaction of the five protons in the $1g_{9/2}$ configuration with the nuclear surface.[6]

In view of the relatively low energy difference, such additional octupole transitions will hardly be characterized by half-lives in the 10^{-4}-1 sec interval. Thus, one should not expect an increase in the number of transitions with such half-lives whereas a decrease in their number due to the appearance of new quadrupole transitions is likely. Therefore, while the question of the over-all drop of transition multipolarities due to the presence of several types of nuclear levels requires further special examination, it is on the whole clear that this factor can explain only the rarer occurrence of octupole transitions with $T_{1/2} = 10^{-4}$-1 sec in odd-A nuclei.

Thus, consideration of all the conclusions deriving from the shell and generalized models, as well as of the new concepts of nuclear level structure, clearly indicates that isomeric transitions with $T_{1/2} = 10^{-4}$-1 sec in odd-A nuclei are extremely rare. Therefore any observation of isomerism of this type in odd-A nuclei would be of undoubted interest where verification and refinement of present nuclear models is concerned. Actually, such isomers can be formed only as a result of 1) a sharp divergence between the actual order in which the levels are filled and that predicted by a nuclear shell model, or 2) the existence of levels which are not predicted by the model (taking into account the level splitting due to nuclear deformation), i.e., levels which either replace predicted levels or coexist with them, without mutual transitions.*

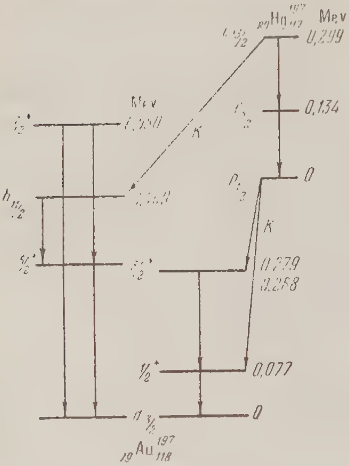

Fig. 6. Level scheme of the Au$^{197}_{118}$ nucleus.

Recently about ten radioactivities with lifetimes of the order of milliseconds have been discovered; these have been produced by bombarding various nuclei with Bremsstrahlung photons[20] of energies up to 22 Mev, and with protons[22] of energies of about 20 Mev.** It seems that most of these are in odd-A nuclei, i.e., odd-odd or even-even nuclei. However, the great diversity of the reactions taking place at these high energies makes reliable identification of the product isomers difficult. Since without such identification it is impossible to arrive at any definite conclusions regarding the nature of the isomeric transitions observed, we must emphasize the particular interest attached to observing isomers produced by the action of photons having energies below the threshold for the (γ,p) and (γ,n) reactions or under the influence of thermal neutrons.

Although the number of such isomers is limited (for instance, in the case of gamma irradiation the list is limited to isomers of stable isotopes and further depends on the existence of appropriate activation levels), the reliability of the isomeric identifications in such cases makes all the results thus obtained definite and valuable.

The author wishes to thank L.K.Peker for fruitful discussions.

"P.N.Lebedev" Physical Institute of the
Academy of Sciences of the USSR

---

* Presumably the second reason explains the recently established[21] existence of the 18 msec isomer $_{33}As^{75}$.

**See the article by O.I.Leipunskii, V.V.Miller, A.M.Morozov and P.A.Iampol'skii scheduled for publication in Izv. AN SSSR (Bulletin) Ser. fiz., Vol.20 (1956).

References

1. M.Goldhaber & A.Sunyar, Phys. Rev., 83, 907 (1951).
2. S.Moszkowsky, Phys. Rev., 89, 474 (1953).
3. J.Hollander, I.Perlman & G.Seaborg, Rev. Mod. Phys., 25, 469 (1953).
4. M.I.Korsunskii, Izomeriia atomnykh iader (Isomerism of atomic nuclei), M. 1954.
5. P.Klinkenberg, Ref. Mod. Phys., 24, 463 (1952).
6. A.Bohr & B.Mottelson, Dan. Vidensk. Selsk. Mat. -Fis. Medd., 27, 16 (1953).
7. B.Mottelson & S.Nilsson, Phys. Rev., 99, 1615 (1955); S.Nilsson, Dan. Vidensk. Selsk. Mat.-Fis. Medd., 29, 16 (1955).
8. B.Saraf.,Phys., Rev., 97, 715 (1955).
9. N.Heydenburg & G.Temmer, Phys. Rev., 95, 861 (1955).
10. L.Tagg, E.Wolicki, R.Bondeling, K.Dunning & S.Snyder, Phys. Rev., 100, 1299 (1955).
11. M.Lee & R.Katz, Phys. Rev., 93, 155 (1954).
12. N.Marty, C.R., 238, 2516 (1954).
13. M.Heydenburg & G.Temmer, Phys. Rev., 100, 150 (1955).
14. H.DeWaard, Phil. Mag., 46, 445 (1955).
15. J.Muze, M.Bunker & J.Starner, Phys. Rev., 100, 1390 (1955).
16. P.Marmier & F.Boehm, Phys. Rev., 97, 103 (1955).
17. L.Peker, L.Sliv & A.Zolotavin, Doklady AN SSSR, 88, 781 (1953).
18. L.Sliv & L.Peker, Doklady AN SSSR, 92, 227 (1953).
19. L.Peker & L.Sliv, Izv. AN SSSR, Ser. fiz., 17, 411 (1953).
20. S.Vegors & P.Axel, Phys. Rev., 100, 1238 (1955).
21. A.Schardt, Bull. Amer. Phys. Soc., 1, 2, D 1, 85 (1956).
22. S.Softky, Phys. Rev., 98, 736 (1955).

BULLETIN of the Academy of Sciences of the USSR - Physical Series
Vol. 20, No. 8, 1956 - Transactions of the Sixth All-Union Converence on
Nuclear Spectroscopy (Moscow, 26-30 January, 1956)

TABLE OF CONTENTS

	Page Orig.	Trans.
A precision magnetic α-spectrometer - L.L.Gol'din & E.F.Tret'iakov	859	781
Highest rotational levels of certain nuclei. Intensity of α-decay to excited rotational levels - L.L.Gol'din, G.I.Novikova & E.F.Tret'iakov	868	789
On the α-decay of Np^{237} - L.N.Kondrat'ev, G.I.Novikova, A.M.Vorob'ev & L.L.Gol'din	875	795
Internal conversion electron spectrum of the deposit from RaTh I (In the $H\rho = 2600\text{-}10{,}300$ gauss-cm region) - E.M.Krisiuk, A.D.Vitman, V.D.Vorob'ev, G.D.Latyshev & A.G.Sergeev	877	797
Internal conversion of the 2615 kev transition in Pb^{208} - E.M.Krisiuk, A.D.Vitman, V.D.Vorob'ev, I.V.Vorob'ev, K.I.Il'in, G.D.Latyshev, M.A.Listengarten & A.G.Sergeev	883	803
Beta-spectrum of Pu^{241} - K.N.Shliagin	891	810
Investigation of the conversion electron spectra of the isomers Ba^{137*}, In^{113*} and In^{115*} in a β-spectrometer using thick-emulsion plates - I.A.Antonova	896	814
A two-meter curved-crystal γ-ray spectrometer - P.I.Lukirskii & O.I.Sumbaev	903	820
Investigation of the hard γ-radiation from Ir^{192*} by means of a scintillation spectrometer - N.N.Deliagin, G.A.Kuznetsova & V.S.Shpinel'	909	825
Decay scheme of Zr^{97} and Nb^{97} - N.N.Deliagin, A.A.Sorokin, N.V.Forafontov & V.S.Shpinel'	913	828
Gamma-ray spectrum of Sb^{124} - B.S.Dzhelepov, N.N.Zhukovskii, V.G.Nedovesov, I.F.Uchevatkin & V.G.Chumin	925	838
On the $0 \to 0$ transition in RaC' - B.S.Dzhelepov & S.A.Shestopalova	933	845
Investigation of the neutron capture γ-ray spectra of Na^{23} and Th^{232} - N.A.Burgov & G.V.Danilian	941	852

A new method of improving the focusing characteristics of a lens spectrometer - B.S.Dzhelepov, No Sen Chan & P.A.Tishkin 947 857

An investigation of the angular distribution of photons from positron annihilation in various substances - K.A.Baskova & B.S.Dzhelepov 951 860

The role of deformation in the formation of isomeric states of nuclei - L.K.Peker 956 864

The levels of nuclei with an odd number of neutrons and Z = 11-28 - A.M.Demidov 962 869

On the existence of octupole isomeric transitions with periods between 10^{-4} and 1 sec in odd-A nuclei - V.I.Gol'danskii & V.S.Evseev 967 873

Translated in 1957 by
Columbia Technical Translations
5 Vermont Ave., White Plains, N.Y.

Transactions of the All-Union Conference on Cathode Electronics
(Kiev, 25-29 November 1955)

Opening Address

- A.A.Lebedev

Four and a half years have elapsed since the previous Conference on Cathode Electronics. This period was characterized by such a vigorous development of semiconductor electronics that many are now of the opinion that a radical metamorphosis of the radio industry is imminent, that an almost complete changeover to semiconductors may be expected in the near future. I believe this view of the situation is unjustified and that cathode electronics will long continue to be an important field. On the other hand, it is quite evident that a serious reorganization of the electronics industry is unavoidable. It therefore is imperative to press modernization of vacuum tubes, to make tube equipment commensurate in size with transistor equipment and to reduce the power expended on heating cathodes. As to dimensions, vacuum tubes of sufficiently small sizes have already been developed and are available, but these tubes still have power-consuming incandescent filaments.

It therefore becomes exceedingly urgent to eliminate the thermionic cathode and replace it with one in which electrons are produced in some other way, for example, by cold emission from sharp points. Recently, interesting work has been done in field emission; experimenters have obtained tremendous current densities, reaching hundreds of millions of amperes per cm^2 in pulses, but so far it has not been possible to produce stable cathodes of this type. A successful solution to this problem would not only greatly simplify the manufacture and operation of vacuum tubes, but would make it feasible to enhance the quality of electronic instruments employing narrow, high-density beam electron guns, as, for example, electron and x-ray microscopes, x-ray point spectrographs, electron diffraction cameras and television tubes, for in the final analysis the upper limit on the electron current density (even if focusing is employed) is imposed by the fact that the cathode emission current density cannot be increased beyond a certain point. To illustrate how important increasing the emission current density is, we might note that at the highest electron concentrations now available with heater cathodes one can obtain an x-ray emission from only a 1 μ^2 area of anode of sufficient intensity to record x-ray images. This means that it is possible to realize an x-ray microscope with a resolution of approximately 1 μ. The use of field emission, i.e., of cathodes in the form of sharp points, if made practical, would lead to a considerable increase in current density, and hence to a substantial increase in the resolution of x-ray microscopes, possibly bringing them to a par with electron microscopes in this respect. Similarly, the use of such cathodes in x-ray spectrographs for point spectral analysis would make it possible to reduce considerably the size of the investigated grains, probably to a fraction of a micron.

Thus the realization of stable field-emitters would not only give us heaterless vacuum tubes of small size, fully competative with transistors, but would also spur new important developments in vacuum-tube electronics. However, we have not paid enough attention to these problems, and in my opinion our conference should take note of the need for more intensive research in this direction.

I should like to touch upon still another very important problem, also, unfortunately, virtually neglected in the USSR, a problem which could probably best be solved by the methods and procedures of cathode electronics. I have in mind direct conversion of solar energy into electricity. In view of the fact that a square kilometer of the Earth's surface receives up to $1 \cdot 10^6$ kilowatts power, it is no wonder that so eminent a physicist as Joliot-Curie considers the utilization of solar energy more important than the utilization of atomic energy. The most direct way of transforming solar into electric energy is by means of one of the photoelectric effects, probably the external photoelectric effect.

There is no need to enumerate here the many and constantly increasing uses of cathode electronics in our industry and our daily life. The importance of electronics, in general, and of cathode electronics, in particular, where technical progress is concerned is well recognized; this makes even more surprising the paucity of investigations of the basic physics of cathode electronics and of the physical processes occurring in cathodes, although it is quite evident that without a clear understanding of the physics of these phenomena there can be no real progress even in the solution of purely engineering problems. This situation must be corrected as soon as possible and our Conference should forcibly express its authoritative opinion on this crucial matter.

A SURVEY OF RESEARCH ACCOMPLISHMENTS AND PROBLEMS IN THE FIELD OF CATHODE ELECTRONICS

- N.D.Morgulis

Introduction

This report naturally cannot claim to be exhaustive, and the agenda of our Conference will therefore include papers of approximately similar character but devoted to specific, important problems in this branch of physics. We trust that during the conference all aspects of cathode physics will be covered quite fully, and that this will serve as a solid basis for discussions in which, we hope, a large number of conferees will participate. The results of these discussions will mark the paths for further research and help coordinate our efforts towards the further development of both this branch of modern physics and the vacuum-tube industry, the demands of which have decisively stimulated research in the field of cathode electronics.

It is interesting to note certain features of the latest stage of development in this field, namely:

1) Initiation of extensive and exhaustive physical research projects, aimed at obtaining a most thorough physical description of the subjects of investigation, viz. specific cathodes.

2) Channeling of physical investigations towards the solution of concrete practical problems.

3) Rapid development of the physics of semiconductors (transistors and photoconductors) and their applications in fields previously served by vacuum-tubes.

4) Development of many new, highly-perfected and fruitful experimental procedures.

5) Accumulation of much experimental physical data on many problems, a considerable proportion of which is still inadequately analyzed. This means that the time has come to digest, collate and systematize the experimental material already on hand regarding many important problems. Incidentally, similar collation and generalization are also urgently needed where the practical experience gained by our vacuum-tube industry is concerned.

1. Thermionic Emission

Among the various problems of cathode physics, thermionic emission occupies a uniquely important place, for the thermionic cathode is the principal element of one of the most important and most extensively used classes of modern electronic devices, namely, diverse vacuum tubes of various types. This explains why so large a number of investigations in recent years have been devoted to the emission of thermionic cathodes (see, for example, Ref. 1). These investigations are characterized by

1) the great attention paid to investigation of the various physical properties and the further improvement of the familiar oxide-coated cathode, which remains to this day the best source of electrons for mass-produced electronic tubes;

2) the development and investigation of many new types of thermionic cathodes, often interesting as regards principle of operation, but still of limited application (unfortunately, we still have no better cathode suitable for mass production than the oxide-coated cathode);

3) renewed theoretical and practical interest in the old and once abandoned emission system consisting of a metal coated with active adsorbed films;

4) the widest employment of diverse new research procedures, most of which, it must be admitted, have so far yielded but scant results. Unfortunately, little theoretical research has been done in this field, so that to this day many old

and relatively primitive concepts, which in no way lead us forward, frequently continue to dominate.

Starting our review with the oxide-coated cathode, we must first note the great advances made as regards activating impurities added to the base material.[2] We know what particular characteristics are important in selecting the admixtures and how to compute (if only approximately) the activating ability of various impurity materials. These advances have led an appreciable improvement in the quality of oxide-coated cathodes.

Next, recalling that the oxide-coated cathode is essentially an impurity semiconductor, the emission of which depends decisively on the micro-components of the extraneous substances contained therein, we can readily understand the great importance of radioactive tracer procedures in studying the behavior of such cathodes. Significant progress has already been made in this field: investigators have measured the coefficients of diffusion in the active layer, the rate of diffusion of impurities from the base to the surface layer and the rate of evaporation of the cathode constituents. The groundwork has been laid for the formulation of a dynamic theory of oxide-coated cathodes. Other researchers have studied the different properties and characteristics of the oxide-coated cathode,[4] such as the conductivities of its individual elements, the thermal emf, the Hall effect, etc.

A distinctive feature of research on the oxide-coated cathode stems from the fact that structurally this cathode is a highly complicated system. Therefore, in attempting to elucidate the basic "pure" characteristics of the physical phenomena in the oxide-coated cathode, it is necessary as a first step to simulate the cathode with a model that is simple, yet close to reality. This correct approach was indeed chosen by many investigators, who used single crystals of barium oxide and who have accomplished extensive and interesting work.[5]

First, there were performed the many investigations needed to construct the energy diagram of barium oxide: the temperature dependence of conductivity and the optical absorption were determined for both pure and impurity-containing BaO crystals; the external and internal photoelectric effects and the luminescence were measured. The entire aggregate of its electric properties was thoroughly reviewed. The radioactive tracer method was used to measure the coefficient of diffusion of barium, etc. In addition, the equation for the thermal emission of such a crystal was modernized with the introduction of a factor allowing for polaron rather than electron type conduction.

All this resulted in an extensive assembly of experimental physical data. It has now become necessary and possible to draw general conclusions from these data and to evaluate their significance and usefulness where the emission from a real oxide-coated cathode is concerned.

Many questions also arise when we turn to the physics of a real oxide-coated cathode. At the present time it is customary to treat this cathode as an impurity semiconductor. Formerly only the donor impurity - the barium - was taken into account; subsequently, however, in view of experimental data on the thermal emf and the Hall effect, the possible presence of acceptor impurities - oxygen atoms (or Ba vacancies) - was also taken into consideration for the sake of generality. In this case a clear correlation should exist between the concentration of the atomic Ba impurity and the emission of the cathode. Yet even the most recent refined experiments disclose no such correlation.[6]

A recent new hypothesis utterly rejects the present firmly established concept of the activated oxide-coated cathode being a semiconductor with atomic Ba as the impurity, and assumes that this activator (barium) is present in the cathode in the form of minute colloidal metal particles.[7] It is too early to express an opinion on this problem, but it is of great importance that it be clarified as soon as possible and, if necessary, that a completely new theory of the thermionic emission from metal-semiconductor colloidal systems be formulated.

Another group of problems stems from the fact that oxide-coated cathodes frequently operate under conditions where one can no longer consider the emission as a pure evaporation effect. This applies even to the relatively high emission densities that are not uncommon at present.

First, it may turn out that the density of the emission current from the cathode may be comparable with the density of the disordered electron current inside the cathode; this would disturb the Maxwellian electron distribution in the surface layer of the cathode and, consequently, lead to a modification of the usual emission equation.

Second, a noticeable electric field, directed towards the surface, may develop in this layer of the cathode; such a field can exert a pronounced effect on the emission.[1] Let us recall, in connection with this, certain experiments on determination of the velocities of electrons escaping from pulsed oxide-coated cathodes; these experiments established that these velocities have high values and a discrete spectrum.[8] It is unfortunate that we still know so little about this phenomenon, for a systematic investigation of the velocity distribution of the electrons could throw light on many interesting problems, directly related to the nature of thermionic emission.

A third group of problems is connected with the inhomogeneity of the cathode structure. First, the oxide-coated cathode has a non-uniform cross section, which consists of at least three regions: the contact zone, where the depletion or barrier layer is usually located, the bulk zone or body of the cathode proper, and the surface zone; the nature of the latter is important where the emission characteristics are concerned. Second, the very structure of the cathode is in itself inhomogeneous, for the cathode consists of a sintered aggregate of individual minute crystals.

Attempts have recently been made to relate certain peculiarities of conductivity, thermal emf, and velocity distribution of the escaping electrons with the microcrystal size; however, these are still in the primitive stage.[8,9] In this connection it would be important to develop a sealed high-vacuum emission electron microscope with a useful magnification of 10^3-10^4, and a vacuum better than 10^{-7}mm, as required for the operation of activated cathodes.

Finally, we must note the importance of further search for other systems that might prove superior to the classic oxide-coated cathode. This may mean either replacing the barium oxide by other barium compounds, or else designing a cathode based, for example, on cesium or some other element. Unfortunately, the first attempt to see how well cesium (regardless of its high volatility) would serve as an activator in an oxide cathode has failed to yield any significant results; nevertheless this approach need not be abandoned.

Turning now to thermionic emission from metal-film systems, one can remark that this was investigated in considerable detail at an earlier stage of the development of cathode electronics. Later, when it appeared that these cathodes could not be of great practical importance, research on them was dropped. Recently, however, interest in such systems has been renewed, owing principally to the fact that porous and migration type cathodes of this class are assuming practical importance.[1] The revived researches are still in the early stages. We expect them to develop in the following directions:

1) Detailed study of the kinetics of adsorption phenomena (i.e., conditions under which active adsorbed films are formed and exist in a stable state on the surface of solids) as related to condensation and reflection, surface migration, evaporation, cathode sputtering, various chemical reactions, etc.

2) Research on the electronic properties of adsorbed films of various types (atomic or molecular) on bases of various types, and search for systems of practical value. For example, it is interesting to know why parallelism in the variation of the work function, the adsorption energy and other characteristics is observed for elements such as Cs, Ba and La, which occupy neighboring positions in the periodic table.

Most such studies must be carried out under high-vacuum (10^{-9}-10^{-10} mm Hg) conditions. The use of radioactive isotopes should also be quite useful in this field.

Attention must also be paid to ascertaining whether control can be exercised over such important characteristics as the work function of the surface film and its adsorption energy, for the relation between these quantities determines the quality of the surface as an electron source. We may attempt in this case to seek a suitable surface finish, to find advantageous surface coatings or merely to choose the "best" surface. We may also want to solve the reverse problem, namely, determine the principles of creating pure and smoothly finished surfaces that have a stable, high value of the work function. Such surfaces, for example, may be useful for the investigation of surface ionization, as well as for producing underlinings for low-work-function, electropositive coatings. Finally, we have the associated old, but still unsolved, problem of the nature and preparation of surfaces that will not themselves become activated when active films are deposited on them. The scant experimental data on hand at present (for example, data on gold coatings) are still puzzling. Thus there are opportunities here for interesting and important work, to say nothing of the necessary researches on the electronic properties of vacuum coated semiconductors.

Many new interesting cathode systems, the nature of which is still unclear, have been evolved in recent years. Among them are the following systems:

1) Boride cathodes, for example, LaB_6 (Ref. 10), which have emission properties commensurate with those of thoriated cathodes. According to the first investigations, this cathode is a compound having the unusual property of a "hole" metal; its emission is associated with the presence of an active monatomic layer of La on the surface.

2) Hollow cathodes,[11] i.e., hollow systems covered on the inside with an active oxide layer and emitting an electron beam of unusual properties through a small exit aperture.

3) Pure metal cathodes,[12] for example, of tungsten, heated by short pulses (on the order of 10^{-5} seconds) of very high density (10^7 amp/cm^2) current. Under these conditions the electron emission from the cathode reaches, in the case of tungsten, the tremendous density of $5 \cdot 10^4$ amp/cm^2, i.e., almost 100 times the emission from tungsten heated to its melting point. This striking result is undoubtedly worthy of attention and further study. This phenomenon is theoretically explained as ordinary thermionic emission, but with an electron temperature greatly exceeding the temperature of the metal lattice because the pulse time is too short for temperature equilibrium to be established between the electrons and the lattice. This interesting theory is quite similar to the theory of pulsed emission from oxide-coated cathodes,[13] which was the subject of a lively discussion at our previous Conference.

2. Field Emission

1. It can now be safely asserted that field emission is a very promising and important topic which involves a large, varied and very interesting group of physical problems (see Ref. 14).

An American group[15] has succeeded in obtaining very high stable field-emission densities of up to $40 \cdot 10^7$ amp/cm^2, thereby substantiating the Fowler-Nordheim theory at least to this current density value; deviations from the theory sometimes observed are attributed to space-charge effects.

Experiments performed some ten years ago in P.I.Lukirski's laboratory on the field emission of semiconductors (antimony-cesium cathodes) have now been extended to other photoconductive semiconductors, such as CdS and CdSe[16]. Illumination was found to have a strong influence on the field-emission current. However, this interesting effect has not been studied in detail. In fact, far too little is still known regarding the field emission of semiconductors in general.

There appears to be some immediate prospect of practical utilization of field-emission cathodes in extant electronic devices. In this connection we note two promising approaches.

First, a two-electrode tube, containing a conventional field-emission cathode in the form of a tungsten needle[14], has been already built and successfully tested. The tube operated under pulse conditions for 200 hours at 40 kv with a 0.2 amp. current. It can well be the prototype of many future electron tubes based on the field-emission principle. In fact, the same method can also be used to obtain a strong "point" electron source with an effective diameter of $\sim 0.3\ \mu$.

Second, attention may be called to a report published in the USSR back in 1950,[17] describing a Malter type cathode consisting of an aluminum base coated with a thin layer of a dielectric (aluminum oxide) which in turn is covered with a very thin metallic contact layer. When the entire cathode was placed in vacuum and a small (10-30 v) potential difference was applied to the aluminum-oxide layer, a noticeable ($\sim 10^{-7}$ amp) field emission current was observed from the aluminum oxide. The strength of this current was readily controlled by the potential difference. We have here the potentiality of obtaining a controllable, stable cold cathode. Obviously there are still many practical difficulties to overcome; among them are development of methods of producing long-lasting needle points, stable dielectric films and surface coatings for such point cathodes, etc.

2. Field emission in recent years has been employed mainly in various types of so-called projectors: electron point sources and special electron microscopes intended for the investigation of surface structures and processes occurring therein. An interesting feature of such investigations is the possibility of studying separately the emission and characteristics of the individual crystal faces of a polycrystalline metal needle. The potentialities of such electron instruments are noteworthy: for example, with an electric field of $5.4 \cdot 10^7$ v/cm (or 0.54 v/Å) one can obtain a resolution of 25 Å and a useful magnification of $5 \cdot 10^5$ X. One of the most interesting results of structural analysis by this method[18] was the detection of a work function of 6 ev for the (011) face of tungsten.

Instruments of this type can also be used in cases when the investigation calls for very strong local fields. An example of such an investigation is the determination of the polarization coefficients of free atoms and molecules.

An important step forward was the development of an ionic projector.[19] In this instrument, in contrast to the case in the old thermal ionization projector, (Ref. 20) the image of the investigated surface is formed by protons that are produced by the ionization of hydrogen in the tube, under the influence of a strong electric field at the surface of the sharp point. In one experiment, using a field of 2.8 v/A, a resolution of 2-4 Å was attained, i.e., a resolution about one order of magnitude better than obtained with a field-emission (electron) projector. It will be noted that this resolution is of the same order as the diameters of ordinary atoms and molecules, so that we need not stress the extraordinary possibilities of this method.

In addition there is also great interest in the physical problem of the nature of ionization of molecules in a strong electric field. Worthy of note in this connection is the interesting work on mass-spectrometric analysis of the products of similar ionization of hydrogen, deuterium and oxygen molecules in fields of varying intensity[21]. One can readily understand the potential value of such ionic-projector investigations to the theory of molecular forces. Incidentally, the case aptly illustrates the importance of research in the field of cathode electronics to other branches of physics.

3. Of great interest is the use of field-emission projectors for studying various molecular phenomena occurring on surfaces. Here we must touch on the possibility of "seeing" molecules and studying their structure. One must bear in mind that a resolution of 20—30 Å still precludes us from speaking of the

"detail" of such pictures. However, the question of what is the nature of the observed image is still unanswered: Is the observed image due to scattering of the field-emission electrons by individual elements of the molecule or is it related to the pattern formed by the electrons of the molecule itself, emitted due to ionization in the strong electric field?

Next, one should note the interesting work on the desorption of atomic films (Ba and others) from the surface of tungsten, also under the influence of strong electric fields of the order of 2-4 v/Å.[14] These experiments provide a partial answer to questions on the nature of the adsorption forces and their electrostatic component. Moreover, these experiments have shown that the critical field needed to detach the adsorbed atoms from the surface depends substantially on the crystallographic face forming the surface. The field-emission projector method was also used successfully to observe surface migration, for example, of Ba on W[22], and to determine the coefficients of this migration on each face separately. These experiments on migration and desorption, along with experiments on emission, etc., carried out by means of field-emission projectors, have demonstrated that the old procedure of employing polycrystalline surfaces to carry out physical investigations in these fields should be abandoned, since it yields only rough average values. The field-emission projector technique has also been used to study the elementary act of surface reaction of carbon with oxygen on tungsten[25], superficial ionization, etc.

4. Finally, a few words must be said on the importance of the physics of field emission to many problems connected with discharges in gases. Here we can do no more than list some of the problems and topics involved: 1) field emission in an important class of arc discharges (of the mercury type), produced by the field of an ionic space charge of very high density, reaching values of 10^5-10^6 amp/cm^2; 2) excitation of field-emission flashes, followed by an arc discharge at the contact point of a special dielectric ignitor and a liquid cathode; 3) the same phenomenon at the anode of an arc rectifier during the phase reversal, i.e., arc back (elimination of this effect is very important in the design of high-voltage mercury rectifiers); 4) disruptive discharges in vacuum, due to flash field emission. Although highly important, these effects are still little understood and investigation of them is only beginning.

3. Photoelectric Emission

Recent investigations in the field of photoelectric emissions (see Ref. 24) can be divided into two groups. Those in the first group are concerned with clarification of the physics of the photoelectric effect in general without any direct attempt at practical applications (this group could also include investigations utilizing photoelectric methods for determining energy diagrams). The second group comprises investigations of actual photocathodes for the purpose of determining their characteristics and evolving better cathodes.

Starting with the first group, it is of interest to mention studies devoted to the photoeffect in pure alkali metals. Here we might mention the full formation of the photoeffect manifested in films only three atoms thick and the interesting velocity distribution of photoelectrons from cathodes illuminated with far ultraviolet when, in addition to the usual fast electrons, groups of slow electrons appear.[25] This last effect is similar to that observed for non-metals and undoubtedly influences the kinetics and energy losses of excited electrons in solids. It would be of interest to combine investigation of this effect with studies of the depth-dependence of the photoeffect. Many interesting facts regarding the energy diagrams of different semiconductors have been obtained by optical methods and photoelectron delay curve measurements.[26]

Investigations of the photoeffect in certain non-metals under the influence of far ultraviolet radiation at wavelengths corresponding to the self-absorption limit has led to the conclusion that an exciton mechanism may be involved in this effect; the operation of this mechanism has also been observed in a cesium-antimony cathode.[27] If the exciton mechanism were the only mechanism involved, it might be possible to obtain a very efficient impurity photocathode, provided it were possible to concentrate the mechanism within the limits of the surface layer of photoelectron emergence. Unfortunately, available experimental data indicate that there exists in this surface region a photoelectrically passive, so-called "dead" layer. The latter, according to certain evaluations, has a depth of ~10 mμ, i.e., a depth somewhat inferior to that of the photoelectron escape zone.

As we already noted, a large number of investigations were carried out using barium oxide[5], particularly in the form of single crystals, both pure and with impurities. These photoelectric investigations, the results of which are similar to those obtained in the past for alkali-halide crystals, yielded valuable data characterizing the energy diagram of barium oxide.

Finally, we must mention a series of studies devoted to the photoeffect in different semiconductor compounds (CsIn, CsTe, CdS, etc.).[28] A secondary purpose of some of these studies was to investigate the possible existence of new photoelectrically efficient compounds; unfortunately, in this respect the results were negative.

Summarizing the results of this phase of recent research, we must note that we have here only the very beginning of investigation of the nature of absorption of light, a phenomenon of fundamental importance for photocathodes of homogeneous structure. Obviously without strong natural photoelectrically active absorption of light, such as is observed, for example, in the case of cesium-antimony cathodes, it is impossible to have an efficient cathode. However, the basic nature of such absorption is still far from clear: very often it is not accompanied by an appreciable photoelectric effect. Very little, too, is known regarding the characteristics and possibilities of the exciton mechanism, the kinetics of excitons or the relation between the internal and external photoeffects, to say nothing of the role of the kinetics of the excited electrons where the photoelectric effect is concerned. Paranthetically, we feel it is important to enlarge the number of investigated materials.

Let us turn back to the second group of investigations, devoted to actual photocathodes. In spite of the importance of the subject, relatively few serious contributions have appeared in recent years. Only two new photocathodes have been added to the list of efficient photocathodes: 1) a bismuth-silver-oxygen-cesium cathode[29], characterized by a relatively uniform spectral response over the entire visible spectrum and 2) a very recently described Sb-K-Na-Cs cathode[30], having a spectral characteristic similar to that of the cesium-antimony cathode but displaced upward and sidewise to 850 mμ so that it has an integral sensitivity 4.5 times greater than the usual cesium-antimony cathode.

High yields only in the ultraviolet region have been observed for a whole series of photocathode materials. As before, major problems are still the effective photoeffect in the long-wave region and fatigue of photocathodes, i.e., both their nature and method of controlling them. The failure to make progress here may easily result in partial "replacement" of the external photoeffect by the internal photoeffect in a number of important devices; to judge from the literature the changeover may soon take place in television pick-up tubes, converters and diverse photocells, particularly since far infrared radiation can be utilized in these devices.

One might assume that among the reasons for this research lag in the field of photocathode physics are the great complexity of the problem, inadequacy of the general physical theories and concepts and the lack of experimental procedures. Let us recall that the "armament" of experimenters is still largely limited to optical methods. While these made possible some progress in studying the relatively simple and homogeneous two-component cesium-antimony cathode, when we come to a three-component one, such as the silver-oxygen-cesium cathode, so far unsurmountable difficulties are encountered. One can expect similar or greater difficulties in the case of the multi-component antimony-multialkali cathode for which there is no observable correlation between the optical and photoelectric properties. It is safe to say that little progress in this field can be expected without a serious preliminary investigation of the structure of cathodes, such as that initiated by S.A.Vekshinskii before the war, investigations making a full use of electron and x-ray diffraction analysis, electron microscopy, turbidimetry, etc. It would be interesting to see the work on electron microscope investigation of photocathodes, begun under the leadership of A.A.Lebedev and reported on at our last conference, continued and developed further.

Turning to the first type of effective photocathodes - cesium-antimony photocathodes - we note that in this case we are dealing with the simplest, two-component system. This simplicity explains why any appreciable degree of success in the physical investigation of effective photocathodes has been attained only in this field.

First, as we know, there has been developed a full explanation and theoretical interpretation of the nature of the photoeffect in this cathode, which has at last made possible engineering design of cesium-antimony photocells.[31] Then the basic characteristics of its energy diagram were deduced from measurements of the optical absorption and the natural velocity distribution of the photoelectrons.[32] Incidentally, an interesting deduction follows from the last mentioned investigation (Ref. 32), a deduction which to some extent may be general: when photons of sufficiently high energy are used it is possible to obtain a noticeable secondary photoelectron emission, i.e., to observe excitation of secondary electrons by the impact of fast primary photoelectrons.

Second, we should take note of a whole series of investigations of the electric properties of the cesium-antimony photocathode[33], such as the conductivity (both ordinary and in magnetic fields), thermal emf, Hall effect, carrier mobility, electrolysis, etc.

Unfortunately, the results of these investigations are isolated from those of photoelectric studies so that we still do not know which of these parameters influence the photoeffect and to what extent. In view of this our understanding of the principle of operation of even this cathode is still not nearly deep enough.

This leads us to the need for clarifying what might be termed "second order of importance" questions of the physics of cesium-antimony photocathodes, for example, questions having to do with 1) the relationship between the photoelectric characteristics and the structural and electric properties, 2) the nature of the natural and photoelectrically active absorption of light, particularly in connection with the possible exciton mechanism involved and 3) the relative importance and role of primary excitation of electrons in the body of the cathode. In this connection it may prove useful to study the transition to the "elementary" photoeffect at coating thicknesses greatly inferior to the effective full-emission thickness and to make accurate determinations of the natural velocity distribution of the electrons, the probabilities of photoexcitation, etc.

Investigation of the last problem may be expediently combined with study of the photoconductivity in view of the interesting experimental discovery that introduction of an excess of cesium into a normally p-conducting cesium-antimony coating (which transforms it into an n-conducting state) suppresses the conductivity but does not noticeably influence the external photoeffect.[34]

The situation is considerably worse as regards the second important type of photocathode - the silver-oxygen-cesium cathode - which is particularly valuable in the long-wave region. While there has been much work on this cathode in recent years, it has been predominantly of a technological nature, i.e., on a purely engineering level. As regards the physics of this cathode, we know little more now than we did 10-15 years ago; this despite the fact that this cathode is still the only useful one for the long-wave region even though its efficiency leaves much to be desired. Perhaps the principle reason for this sad situation is that so far little attention has been paid to studying the structure of this photocathode, which is supposed to consist of a mixture of colloidal silver particles and cesium oxide crystals covered on all sides by cesium atoms.

If this is the case investigation might disclose a number of new and unexpected effects in the field of colloid physics. For example, it might be shown that as regards certain properties colloidal metallic particles are not similar to a metal with its continuous band of electric states but are rather reminiscent of a semiconductor, for, as calculations and experiments show, aggregations of colloidal metallic particles are characterized by selective absorption of light and photoemission in a given region of the spectrum[35] and that these properties are dependent on the size, number, shape and nature of the metal particles.

On the other hand, while there is a complete absence of any kind of correlation between the spectral characteristics of the photoeffect and the optical absorption, the cathode under certain conditions may exhibit a rather sharp interference pattern, characteristic of small deviations from homogeneity.[35] Furthermore, even with the improved technology of manufacture now used individual cathodes may vary greatly as regards physical characteristics although most will have nearly identical values of photoelectric efficiency. While all this makes investigation of this cathode difficult, it is nevertheless imperative to press studies aimed at clarifying the nature of its photoeffect and enhancing its efficiency.

4. Secondary-electron emission

Secondary electron emission and efficient cathodes of this type, which attracted much attention in pre-war years, are no longer of interest to many investigators. Neither this nor the fact that engineers now have available a number of very efficient secondary emission cathodes must be taken to mean that everything worthwhile is known regarding the physics of this effect.

The few investigations that have been reported in recent years (see Ref. 36) have been, for the most part, carried out in the middle range of primary potentials (100-2000 v) and have been limited largely to determining the dependence of the secondary emission coefficient and occasional measurement of the velocity distribution. Yet it will readily be admitted that these data are insufficient for an understanding of the physics of secondary emission. For example, what can be deduced from comparing the results for such different systems as the cesium oxide and the silver-oxygen-cesium cathode which have virtually equal secondary emissions? Questions having to do with the nature of secondary emission, in general, and emission efficiency, in particular, are very complex and surely merit more extensive and intensive study.

Returning to investigations of secondary emission in the range of medium primary energies, we shall here note only a few of the high points inasmuch as a complete discussion of this matter will be presented by L.N.Dobretsov. First, we have a discovery of an entirely new form of the dependence of the secondary emission coefficient on the primary energy for NaCl single crystals: the curve has a long horizontal plateau[37]. This unexpected result is the first exception to the usual dependence characterized by a maximum and, in fact, may require a new approach to the interpretation of the effect.

We would also like to note the systematic comparative investigation of the distribution in energy of secondary electrons for whole series of metals and compounds.[38] This investigation substantiated the earlier discovered fact that this distribution exhibits fine structure. This fine structure is interpreted as a result of the Auger effect and can be used for determining the coefficient of absorption of secondary electrons, a very important quantity where secondary emission is concerned. Some attention has been paid to secondary emission from thin films in connection with the problem of the effective depth of escape of the electrons.[39] This, of course, is not a complete list of the researches in this field.

However, we still have no satisfactory solution of the old and basic problem: what are the respective roles in the secondary emission process of primary excitation of electrons in the emitter material, on the one hand, and of the kinetics of their motion, on the other hand.

Obtaining an answer to this question - an answer which may or may not be generally applicable - naturally calls for experiments in which the influence of these factors can be separated. In this connection one might recommend all around investigation of "elementary" secondary emission from metals and nonmetals (to eliminate the effect of Coulomb interaction) in the region of very small emitter thicknesses, well below the usual effective thickness which is of the order of 100 mμ for semiconductors.

One should always strive for complete localization of electron excitation in this region since this leads to an increase in the emission yield; however, this can also result in accelerated exhaustion of this layer of the emitter due to decomposition of the molecules of the semiconductor compound under electron impact. Having determined the absolute yield, i.e., the probability of excitation and the distribution in velocity of the secondary electrons under these "elementary" conditions, a monotonic layer of some element sharply reducing only the work function should be applied to the emitter and the measurements repeated. In this way we should be able to determine a number of important characteristics. It must be admitted that in practice such experiments will be far from simple, particularly in connection with the necessity of taking into account the influences of the base.

On the other hand, similar experiments with free-standing thin films should also be of value[40]. The old and often discussed question of the regularity of secondary emission from films transparent to electrons has as yet not been seriously investigated in view of the difficulty of taking into account the influence of microholes which cannot be eliminated. Still one can express the hope that eventually a method of preparing continuous, holefree thin films will be developed and investigation of secondary emission from them made possible.

Recently, through the application of a new electron-optical principle,[41] it has proved possible to study the kinetics of motion and the discrete energy losses of electrons in solids with high accuracy. At a primary electron energy of 30 kv, discrete energy losses on the order of 1 volt can be measured, i.e., the resolving power of this method is $3 \cdot 10^{-5}$. The method has been successfully tested on a number of metals and compounds and the energy losses in these determined. There are also indications that this method can be used for a new type of chemical analysis. Thus, this special electron microscope procedure supplements the usual optical and thermal procedures for determining the energy diagrams of solids and indicates that even slow secondary electrons excited in a solid may undergo energy losses. In order to evaluate the latter factor fully, it is necessary to have a more complete determination both of the energy loss spectrum and the cross-sections involved, particularly in the range of low electron energies.

In the region of low primary energies the individual characteristics of the investigated surface will probably evince a greater influence. In view of the probable influence of the state of the surface on the results, in working in this region experimental cleanliness is particularly important; one should use a very high vacuum and preferably the surfaces of single crystals.

Very interesting results have been obtained on inelastic scattering of slow electrons by NaCl and KCl single crystals; the discrete energy losses were found to be multiples of about 10 v.[42] This value is appreciably greater than the value for non-metals found in the above mentioned experiments, but correlates well with the value following from the selection rule for momentum. There have been other measurements of the energies of inelastic transitions in a number of compounds and attempts to correlate the observed values with optical absorption data. Of course, all this is important where investigation of the discrete losses of secondary electrons and excited photoelectrons are concerned. On the other hand, nothing significant has been done to establish the beginning and effectiveness of Coulomb interaction with free conduction electrons; something along this line might be accomplished with the aid of methods analogous to those used for determining the attenuation of electron beams in the plasma of a gas discharge.

Nor should we neglect the necessity of further investigations in the field of the physics of electronic memory devices.[36] Here we refer to investigation of the necessary conditions for producing and maintaining a given potential "map" on the surface of a dielectric by either electron bombardment or illumination. From the physics point of view this is connected with the interesting problem of surface energy states, with changes in the surface layer to a depth of the order of the screening depth and, in particular, with surface conduction. This problem has already been investigated experimentally for the case of alkali-halide crytals and certain semiconductors. However, a fundamentally new approach to the problem is necessary in the field of vacuum electronics.

Finally, in this section of our survey we should mention a) the Malter cathode (we have touched upon it briefly in the section on field emission) and b) induced conduction. The latter merits special attention in connection with the case of bombardment of a dielectric with fast electrons having velocities of the order of a megaelectronvolt. It will be recalled that the first atomic battery, converting nuclear energy directly into electric energy, was realized in this manner; it utilizes the 0.7 mev β-particles from Sr^{90} (half-life, 20 years) and a crystalline silicon wafer in which the electron multiplication takes place.[43] We are faced with the problem of studying the effect and increasing the yield of the excited electrons producing the induced emf. We must also study the structural changes occurring in the materials utilized for such devices (nuclear batteries). The few experiments made so far only highlight these effects which are obviously of great potential importance.

5. Effects associated with bombardment by heavy particles

In this section we shall examine a group of diverse effects having in common the fact that they are produced in the interaction of heavy particles (atoms and ions) of different energies with the surface of a solid; the interaction often occurs under gas discharge conditions. Here we must consider a) energy transfer in the event of such impact and subsequent scattering of the bombarding particle, b) disintegration of the bombarded solid surface, c) electron exchange, i.e., surface neutralization of ions and, on the contrary, the formation of positive or negative ions and d) emission of secondary electrons under heavy particle bombardment.

There is comparatively little in the literature on energy transfer and scattering incident to the impact of heavy particles on a solid surface. We have only scattered data pertaining mainly to alkali ions, for a considerable proportion of these remains ionized after impact, i.e., in a state susceptible of measurement.

In connection with investigations of the energy balance, it has been found that an appreciable number of heavy particles interact with the atoms of the surface in accord with the classical law for elastic collisions.[44] However, one cannot generalize from this particular case for the region of medium energies, since in the general case we cannot now evaluate the accomodation coefficient in impact by an ion, especially if its energy is not particularly high and this coefficient cannot be computed from the theory of pair collision of free elastic bodies. The same observations apply to the transfer of neutralization energy.

All these problems, that are so important in our field, seem to have dropped from view. In experimenting in this field it would also be useful to utilize the smooth surfaces of single crystals. If such experiments could be carried out with ions tagged with radioactive isotopes, they could be supplemented by determinations of both the angular scattering of the ions (regardless of the degree of neutralization) and their penetration into the target. It might then prove useful to continue the old investigations on the experimental (thermal) determination of the accomodation coefficient in the impact of ions of different velocities, etc.

There has been a noticeable but unjustified loss of interest in the physics of cathode sputtering (see, for example, Ref. 45). Some recent experimental investigations utilizing electron microscopy have elucidated the changes in the structure in the disintegrated surface under the influence of different secondary factors (reverse diffusion, surface migration, etc.); as a result, it has been suggested that cathode sputtering can be used as a practical method of gas etching of metal surfaces.[46] However, this only emphasizes the urgent need of repeated careful experimental investigation of this phenomenon in its primary, uncomplicated form over a wide range of target materials and bombarding ion energies. Here, too, the use of radioactive tracers should prove worthwhile.

The theory of cathode sputtering is also behind the times: use is still made of outdated concepts regarding thermal flashing, equilibrium expressions for evaporation that are inapplicable in the case of high ion energies and elastic collision formulas that are not valid at low energies. True, very recently there have been some attempts to apply some of the concepts of nuclear physics to interpretation of this phenomenon.[47]

On the other hand, great interest had been displayed in past years in electron exchange on metal surfaces, primarily in connection with surface ionization effects. However, the interest died down once the list of obvious alkali elements and pure surfaces of high melting point metals was exhausted; in general, the extant theories of the effect were substantiated. Still it should be of interest to extend the investigation into the realm of less readily ionizable atoms, for which purpose it is necessary to learn how to produce surfaces with an enhanced work function.

In one of the more detailed investigations[48] in this field use was made of tungsten coated with platinum for which, according to thermionic data, the work function is 5.4 ev. However, when an attempt was made to detect the ionization of sodium, which should be complete on this surface, the results were negative. This is difficult to understand unless we assume that platinum in the heated state reacts chemically with sodium (which is not impossible). A different result was obtained in this field when, as mentioned in the previous section, it was found by the field emission method[18] that the (011) face of tungsten has a work function of 6 ev; it was also found that one can obtain on the surface of a polycrystalline filament a noticeable (~10%) ionization of aluminum atoms, the ionization potential of which is also equal to 6 ev. It is strange that nothing of the kind has hitherto been observed by any of the numerous experimenters working in this field who unanimously report a low degree of ionization on polycrystalline tungsten even for sodium and barium, elements which have a much lower ionization potential (5.1-5.4 ev) than aluminum. In any case this entire complex of problems deserves attention. Experiments should be carried out with single crystal filaments, for example, of tungsten, and with surfaces with an elevated work function. We also hope to see studies of the surface of vacuum semiconductors regarding which we know virtually nothing at present. We have no time here to more than mention the complex problem of negative ionization surfaces.

Experiments have continued on secondary emission from surfaces bombarded with heavy particles[44,49]; in these experiments the investigators have striven to obtain ever cleaner surfaces of pure metals. It was shown that the coefficient of secondary emission from thoroughly clean metal surfaces becomes very small. An investigation by Hagstrum[50] merits a special mention in view of the refined experimental procedures employed. The investigation was concerned with secondary emission from exceptionally pure tungsten under bombardment by not only singly but also multiply charged noble gas ions (for example, Kr^{4+} and Xe^{5+}). The ion charge has an appreciable influence on investigated effect. The experimental results for the electron yield and distribution in energy of the electrons are interpreted from a new point of view, i.e., as Auger ejection.

Conclusions

Our survey, incomplete though it is, clearly indicates the great amount of work still to be done in the field of physical cathode electronics. Research work should be aimed at developing the theoretical physical base necessary for directed consistent improvement of the old methods and creation of new methods of obtaining electron currents and their utilization in electronic and ionic devices. In this work we must make the fullest possible use of all the new and improved experimental procedures. Hence one of the important tasks of our conference will be a thorough discussion of plans for the development of investigations in the field of cathode electronics and of coordination of our joint efforts directed towards their realization.

Institute of Physics of the
Academy of Sciences of the Ukrainian SSR

References

1. N.Morgulis, Usp. fiz. nauk., 53, 501 (1954); Rapports des travaux du Congrès international du cinquantenaire de la cathode â oxydes., Le Vide, 51-55, (1954-55).

2. E.Rittner, Philips Res. Rep., 8, 184 (1953).

3. J.Debiesse, L'onde électrique, 30, 351 (1950); W.Leverton & W.Shepherd, J. Appl. Phys., 23, 787 (1952); R.Redington, Phys. Rev., 87, 1006 (1952); R.Bever, J.Appl. Phys., 24, 1008 (1953); N.Morgulis & Iu.Ptushinskii, Zhur. tekh. fiz., 25, 1157 (1955).

4. N.Morgulis & V.Iagovdik, Doklady AN SSSR, 59, 247 (1948); N.Morgulis & Ia.Zingerman, Doklady AN SSSR, 81, 783 (1951); P.Zel'tsman, N.Morgulis & V.Iagovdik, Zhur. tekh. fiz., 21, 1035 (1951); E.Pell, Phys. Rev., 87, 457 (1952); L.Nedgaard, RCA Rev., 13, 464 (1952); J.Young, J. Appl. Phys., 23, 1129 (1952); J.Sparks, H.Philipp, J. Appl. Phys., 24, 453 (1953); R.Forman, Phys. Rev., 96, 1479 (1954).

5. R.Sproull, W.Dash, W.Tyler & A.Moore, Rev. Sc. Instr., 22, 410 (1951); A.Kane, J. Appl. Phys., 22, 1214 (1951); Phys. Rev., 94, 1439 (1954); E.Pell, Phys. Rev., 87, 457 (1952); R.Redington, Phys. Rev., 87, 1006 (1952); N.Morgulis & K.Tolpygo, Zhur. eksp. i teor. fiz., 25, 718 (1953); W.Dash, Phys. Rev., 92, 68 (1953); W.Tyler & R.Sproull, Russian trans. in "Poluprovodnikovye materialy" (Collection of articles on "Semiconductor materials"), M. 1954.

6. G.Moore, L.Wooten & J.Morrison, Phys. Rev., 96, 840 (1954); J. Appl. Phys., 26, 943 (1955).

7. J.Ortusi, Le Vide, 52-53, 100 (1954).

8. C.Jansen, K.Loosjes & K.Compaan, Philips Res. Rep., 9, 241 (1954).

9. E.Hensley, J. Appl. Phys., 23, 1122 (1952); J.Young, J. Appl. Phys., 23, 1129 (1952); R.Forman, J. Appl. Phys., 26, 1187 (1955).

10. J.Lafferty, J. Appl. Phys., 22, 299 (1951).

11. M.Babcock, D.Holzhouser & H.VonFoerster, Phys. Rev., 91, 755 (1953); B.Klumpfer & H.Brett, Conv. Rec. of I.R.E., III 66 (1954).

12. S.Lebedev & S.Khaikin, Zhur. eksp. i teor. fiz., 26, 723 (1954); L.Borodovskaia & S.Lebedev, Zhur. eksp. i teor. fiz., 28, 96 (1955); V.Ginzburg & V.Shabanskii, Doklady AN SSSR, 100, 445 (1955).

13. S.Levitin, Zhur. tekh. fiz., 23, 1700, 2166 (1953); S.Lehovec, Phys. Rev., 96, 921 (1954).

14. F.Llewellyn-Jones, Nature, 175, 244 (1955); W.Dyke, Proc. I.R.E., 43, 162 (1955).

15. J.Barbour a. oth., Phys. Rev., 92, 45 (1953).

16. L.Apker & E.Taft, Phys. Rev., 88, 1037 (1952).

17. M.Vudynskii, Zhur. tekh. fiz., 20, 1306 (1950).

18. E.Muller, J. Appl. Phys., 26, 732 (1955).

19. E.Muller, ZS. f. Phys., 131, 136 (1951); A.Komar & Iu.Selitskii, Doklady AN SSSR, 96, 957 (1954).

20. N.Morgulis, Zhur. eksp. i teor. fiz., 10, 168 (1940).

21. M.Ingram & R.Gomer, J. Chem. Phys., 22, 1279 (1954); ZS.Naturforsch, 10a, 863 (1955).

22. M.Drechsler, ZS. f. Elektrochemie, 58, 340 (1954).

23. R.Klein, J.Chem. Phys., 21, 1177 (1953).

24. W.Kluge, ZS. angew. Phys., 7, 302 (1955).

25. J.Dickey, Phys. Rev., 81, 612 (1951).

26. L.Apker & E.Taft, Phys. Rev., 82, 814 (1951); 96, 827 (1954); Meyer-Schutzmeister, ZS. f. Phys., 129, 148 (1951; I.A.Arsen'eva-Geil', Zhur. tekh. fiz., 25, 1544 (1955).

27. L.Apker, E.Taft, Phys. Rev., 81, 698 (1951); M.Hebb, Phys. Rev., 81, 702 (1951); P.Borziak, Trudy IFAN USSR (Transactions of the Institute of Physics of the Ukrainian SSR Ac. of Sci.), No. 4, 28, 1953.

28. E.Taft & L.Apker, J.O.S.A., 43, 81 (1953); N.Schaetti, W.Baumgartner & C.Flury, Helv. Phys. Acta, 24, 609 (1951).

29. A.Sommer, Photoelectric tubes, London, 1951.

30. A.Sommer, Rev. Sc. Instr., 26, 725 (1955).

31. P.Borziak, Dissertation, Institute of Physics of the Ukrainian SSR, Ac. of Sci., 1954.

32. N.Morgulis, P.Borziak & B.Diatlovitskaia, Izv. AN SSSR, Ser. fiz., 12, 126 (1948); B.Diatlovitskaia, Zhur. tekh. fiz., 22, 84 (1952); P.Borziak, Trudy IFAN USSR (see 27), No. 2,3 (1952); L.Apker, E.Taft & E.Dickey, J.O.S.A.,43,78 (1953).

33. T.Sakata, J.Phys.Soc.Japan, 8, 125, 272, 723, 793 (1953); 9, 141, 1030, 1031 (1954); H.Mijasawa & S.Fukuhara, J.Phys.Soc.Japan, 7, 645 (1952).

34. P.Borziak, Doklady AN SSSR, 31, 547 (1941).

35. P.Borziak & N.Morgulis, Doklady SSSR, 61, 625 (1948); P.Borziak, Trudy IFAN USSR (see 27), No. 4, 11 (1953); N.Dykman, Trudy IFAN USSR, No.5, 94 (1954).

36. H.Bruining, Physics and Applications of Secondary Emission.-London, 1954; S.Rodda, Nature, 175, 1112 (1955).

37. L.Dobretsov & A.Titkov, Doklady AN SSSR, 100, 33 (1955); A.Shul'man, Zhur. tekh. fiz., 25, 2150 (1955).

38. J.Lander, Phys. Rev., 91, 1382 (1953).

39. B.Diatlovitskaia, Doklady AN SSSR, 63, 641 (1948); N.Morgulis & N.Nakhodkin, Doklady, AN SSSR, 94, 1029 (1954); I.Bronshtein & T.Smorodina, Zhur. eksp. i teor. fiz., 29, 500 (1955).

40. W.Berger, Ann. d. Phys., 15, 394 (1955); H.Mendelowitz & L.Marton, Phys. Rev., 98, 1168 (1955).

41. G.Mollenstedt, Optik, 5, 499 (1949); L.Leder, Phys. Rev., 95, 1345 (1954); L.Marton & L.Leder, Phys. Rev., 94, 203, 777 (1954).

42. A.Shul'man & S.Fridrikhov, Zhur. tekh. fiz., 25, 1344 (1955).

43. P.Rappaport, Phys. Rev., 93, 246 (1954); W.Pfaun & W.vanRoosboeck, J.Appl. Phys., 25, 1422 (1954); W.Shorr, Nuclear Batteries, Report No. 171, International Conference on the Peaceful Uses of Atomic Energy, Geneva, 1955.

44. U.Arifov, Dissertation, LFTI AN SSSR, 1954.

45. N.Morgulis, Usp. fiz. nauk, 28, 202 (1946).

46. G.Spivak, I.Prilezhaeva & O.Savochkina, Zhur. tekh. fiz., 23, 225 (1953); 24, 2090 (1954).

47. F.Keywell, Phys. Rev., 87, 160 (1952); D.Harrison, Phys. Rev., 93, 652 (1954).

48. Kim Khen Bon & I.Sokol'skaia, Vestnik LGU (Review, Leningrad State Univ.) 12, 67 (1952).

49. M.Eremeev, Dissertation LPI (Leningrad Pedagogical Inst.), 1953.

50. H.Hagstrum, Phys. Rev., 96, 325, 336 (1954).

EMISSION OF ELECTRONS FROM COMPLEX SURFACES (Abstract)

- P.V.Timofeev

The quantitative theory of complex emitters, prepared of alkali or alkaline-earth metals and their compounds with oxygen or other elements, is still in the initial stage and the development of these emitters continues mainly on the basis of experimental investigations.

Experimental studies have shown that the electron emission depends on the structure of the surface layer and, in particular, on the amount of free alkali or alkaline-earth metal contained therein.

Under certain conditions, positive charges may form on the surface of complex emitters in the process of electron emission. These positive charges influence the emission with a resultant increase in the secondary emission coefficient and give rise to the anamolous effects observed in field-emission from cesium oxide photocathodes, and are responsible for a number of other effects such as fatigue of cesium oxide cathodes. As is known, fatigue is due to the appearance of positive cesium particles adsorbed on the surface layer of the cathode.

The electron energy level distribution in the surface layer of a complex emitter with an inhomogeneous surface is quite different from the distribution inside the bulk of the emitter.

The thickness of the surface layer from which electron emission occurs seldom exceeds 10^{-6} cm; consequently, the emission from complex emitters must be determined primarily by the energy level distribution in the superficial layer.

In view of this one cannot accept for a complex emitter the concept of an emission mechanism, based on an energy level scheme valid for the interior of the emitter. In particular, we must reject certain deductions regarding the emission properties of emitters deriving from measurements of their electric conductivity.

It was established that with a steep electric field gradient at the surface complex emitters of the cesium oxide type can emit positive ions at room temperature.

"V.I.Lenin" All-Union Electrotechnical Institute.

SECONDARY-ELECTRON EMISSION

(Present State and Future Prospects)

- L.N. Dobretsov

The familiar conceptions regarding the mechanism of secondary-electron emission were largely formulated in the Nineteen Thirties. In the present report I should like to discuss how our views and ideas have been modified in recent years.

Secondary-electron emission can be thought of as consisting of three stages: 1) excitation of the electrons in the emitter by the primary electrons, 2) movement of the excited electrons from the site of excitation to the emitter surface and 3) escape of the electrons through the emitter boundary to the outside. Accordingly, the following equation is usually written for the secondary-electron-emission coefficient

$$\sigma = \int_0^L w(x) W(x) P(l, E_0)\, dl, \tag{1}$$

where $P(l, E_0)\, dl$ is the number of electrons excited along an element dl of the primary electron path at a distance l from the beginning of the path, where the primary energy was E_0 (Fig. 1); $W(x)$ is the probability of an electron, excited at a depth x, reaching the surface and $w(x)$ is the probability of escape to the outside for an electron that has reached the surface; the integral is taken over the entire effective primary-electron path L (i.e., the ionization range).

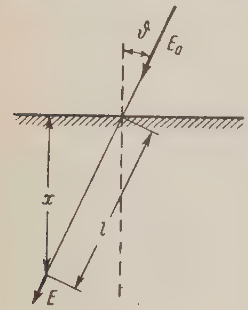

Fig. 1

It is easy to show, first, that expression (1) presupposes the possibility of localization of the excitation site within a sufficiently small volume; and, second, that inasmuch as W and w depend on the distribution in momentum of the excited electrons, the fact that we write $W(x)$ rather than $W(E(x))$ implies that only the number of excited electrons depends on on the energy of the primary electron, and that the velocity distribution of the excited electrons at the site of excitation is independent of the primary-electron energy. Let us examine the function $P(l, E_0)$. The number p of transitions, i.e., the number of electrons excited in a given solid, along the path element dl depends only on the energy E of the primary electron at this element; however, this energy depends on the initial energy E_0 and the energy loss dE/dl in the given substance, i.e., $E = E(l, E_0)$; consequently, also $P = P(l, E_0)$. Many theoretical investigations are devoted to the determination of the form of the function $p(E)$.

Let us denote the wave vectors of the primary electron and the electron of the solid (emitter) in their initial states (i.e., prior to their interaction) by $\mathbf{K}_1$ and $\mathbf{K}_2$ respectively, the energies in these states by $E_1 = E_1(\mathbf{K}_1)$ and $E_2 = E_2(\mathbf{K}_2)$, respectively, and the corresponding quantities after interaction by $\mathbf{K}_1'$, $\mathbf{K}_2'$, $E_1' = E_1'(\mathbf{K}_1')$ and $E_2' = E_2'(\mathbf{K}_2')$.

Quantum-mechanical analysis shows that as a result of the interaction between this pair of electrons transitions to the states $\mathbf{K}_1'$ and $\mathbf{K}_2'$ are possible provided the two conservation laws (see Ref. 1):

and

$$\left.\begin{aligned} E_1 + E_2 &= E_1' + E_2' \\ \mathbf{K}_1 + \mathbf{K}_2 + \frac{2\pi}{a}\mathbf{g} &= \mathbf{K}_1' + \mathbf{K}_2' \end{aligned}\right\}, \tag{2}$$

apply (here g is a vector with integer components (in a simple cubic crystal) and a is the lattice constant). The second of these conservation laws represents the quantum-mechanical analogue of the law of conservation of momentum, and the term $\frac{2\pi}{a}g$ takes into account the momentum acquired by the electron of the solid from the crystal lattice; this momentum can, in certain particular cases, equal zero. When $g \neq 0$, the initial and final states of the electron of the solid correspond to two different Brillouin zones ("interzonal transition", according to Viatskin[2]); when $g = 0$ both states of the solid-body electron are within a single zone ("intrazonal transition"). For "free" electrons of the Sommerfeld model of the metal, only transitions with $g = 0$ are possible; the second conservation law becomes simply the classical conservation of momentum law. Naturally, the Pauli principle allows intrazonal transitions only within unfilled zones, i.e., only in metals. Interzonal transitions are possible in dielectrics or semiconductors as well as in metals; in the latter conduction band electrons can also accomplish these transitions.

In the general case, when both types of transitions are possible, $p(E)$ will be the sum of $p_{\mathrm{B}}(E)$, due to intrazonal transitions, and $p_{\mathrm{M}}(E)$, due to interzonal transitions:

$$p(E) = p_{\mathrm{B}}(E) + p_{\mathrm{M}}(E).$$

Intrazonal transitions for "free" electrons were studied by Kadyshevich[3], and subsequently by Baroody[4] from the classical mechanics point of view, and by Viatskin[2] from the quantum mechanical point of view for weakly bound electrons. Dekker and van der Ziel[1] used the Coulomb potential $U = e^2/|\mathbf{R}-\mathbf{r}|$ to evaluate the interaction between the primary electrons and the electrons of the solid, while van der Ziel[5] later used the screened Coulomb potential:

$$U = \frac{e^2}{|\mathbf{R}-\mathbf{r}|}\, e^{-\lambda |\mathbf{R}-\mathbf{r}|}.$$

They[1] concluded that for sufficiently fast primary electrons

$$p_{\mathrm{B}}(E) \approx \frac{1^*}{E} \tag{3}$$

(for the classical treatment this was proven by Hachenberg in Ref. 6) and that the distribution of the excited electrons with respect to excitation energy ΔE is

$$p_{\mathrm{B}}(\Delta E) \approx \frac{1}{(\Delta E + a)^2}, \tag{4}$$

where $a = \frac{\hbar^2}{2m}\lambda^2 \approx 5$ ev (or zero for the unscreened Coulomb potential); the distribution in ΔE is independent of E. If the primary electron expended its energy only for such excitations, the loss law would have the form:

$$-\frac{dE}{dl} = \frac{A}{E} \tag{5}$$

(Widdington's law), where A is a constant; whence the ionization range of the primary electron would be $L \approx E_0^2$.

In the case of normal incidence of the primary beam, excitations of this type do not yield electrons with sufficient additional momentum in the direction of the emitter surface to allow their escape; in view of this, excitations of this type were excluded by Fröhlich from consideration in the theory of secondary emission. The assertion that interactions of primary electrons only with the bound electrons of the metal with $g \neq 0$ play a part in secondary emission is found in many books on the subject (for example, S.Iu.Luk'ianov, "Fotoelementy" (Photocells) and L.N.Dobretsov, "Elektronnaia i ionnaia emissiia" (Electronic

---

* More accurately:

$$p_{\mathrm{B}} \approx E^{-1} \ln E/c.$$

In (3) and the subsequent equations the slowly varying factors are assumed to be constant.

and ionic emission)).

Kadyshevich and Baroody took into account the changes in the direction of the momentum of the excited electron as a result of subsequent phonon collisions and showed that it is feasible to construct a theory taking excitations of this type into account.

The interzonal transitions are, naturally, beyond the scope of classical mechanics. They were analyzed quantum-mechanically, in the weakly bound lattice electron approximation by Wooldridge (1939), Viatskin[2] and Dekker & van der Ziel[1]. The second of the conservation laws (2) can be rewritten as

$$\Delta K_2 = K_2' - K_2 = \frac{2\pi g}{a} + q, \qquad (2')$$

where $q = K_1 - K_1'$ is the momentum acquired by the electron of the solid from the primary electron. At large values of K_1 we have $|q| \ll \frac{2\pi}{a}|g|$.

Calculations made in the above investigations, in which q was considered to be negligible compared with $\frac{2\pi}{a} g$ led to the conclusion that

$$\frac{dp_M}{dE} = 0, \qquad (6)$$

and that, if the primary electron loses energy only through such excitations,

$$-\frac{dE}{dl} = \text{const}, \qquad (7)$$

whence the ionization range of the primary electron $L \approx E_0$.

However, it was shown by van der Ziel[5] and van der Ziel and Dekker[1], that in the strongly bound electron approximation

$$p_M \approx \frac{1}{E}.$$

An important question in secondary-electron emission from metals is how each of these two types of excitation affects both the value of the secondary-emission coefficient σ, as well as the character of the energy loss by the primary electron. Viatskin's calculations[2] show that although the intrazonal transitions play the dominant role in the production of secondary electrons in metals, inasmuch as $p_B > p_M$ the energy losses, which are proportional to $\overline{\Delta E} \cdot p$, are determined by the interzonal transitions, since $\overline{\Delta E_B} \ll \Delta E_M$ and, consequently, the energy loss in metals is described by (7).

Marshall[7] showed in a work published in 1952 that neglecting the quantity q in (2') leads not only to $dp_M/dE = 0$, but also to $p_M = 0$. Interzonal transitions can occur essentially only if $q \neq 0$. If this is taken into account, the calculations based on the weakly bound electron approximation yield $p_M \neq 0$ and, for sufficiently large values of K lead to

$$p_M \approx \frac{1}{E}. \qquad (3')$$

An evaluation of the relative magnitudes of $p_B(E)$ and $p_M(E)$ in this case leads to a considerably stronger inequality $p_B(E) \gg p_M(E)$, particularly if the screened potential is used. In view of this, one must assume (see, also, Refs. 5 & 6) that in metals both the excitation of the secondary electrons and the energy loss by the primary electrons are associated primarily with intrazonal transitions of the conduction electrons. In this case the energy loss will be characterized by equation (4) for sufficiently high energies. This naturally does not mean that interzonal transitions are wholly absent. The emission of characteristic x-rays serves as evidence of interzonal transitions from deep-lying zones to the conduction zone.

Lender's investigations[8] demonstrated the presence of Auger electrons among the secondaries, but their number is very small compared with that of "ordinary" secondary electrons. Hence interzonal transitions of conduction electrons inside the conduction zone are also possible provided the latter is formed by wuperposition of several Brillouin zones.

As noted, interzonal transitions are the only ones possible in dielectrics. According to Marshall, at high energies, their rate, as that of intrazonal transitions is characterized by the law of (3).

What law applies in the region of middle energies ($100 < E < 5000$ ev) for metals and dielectrics we do not know. The strongly bound electron approximation does not yield the answer for this energy interval, for with this approximation the dependence (3') is deduced only for high energies.[1] Furthermore, while this approximation probably correctly describes the states of the electrons in the normally filled zone, it does not satisfactorily describe their states in the conduction band.

One can, however, extend the region of applicability of equation (3) for both metals and dielectrics in the following manner. It is evident that for very low energies, $p(E)$ must go to zero, i.e., that $p(E)$ must be a function with a maximum (Fig. 2). It follows that in the region of deviation from 1/E, this function must vary more slowly with E than 1/E. One of the simplest functions of this type, which in the region of high values of E goes over into 1/E is

$$p(E) = \frac{A}{E+B} \tag{8}$$

where B is a constant for the given type of transitions and given material. Naturally, this expression will not be correct at very low values of E. However, it gives us a single expression that is applicable in a wider range of energy values than (3); that is, deviations of the actual $p(E)$ from (8) will become evident at lower values of E than the deviations from (3) and (3').

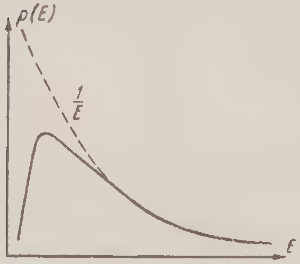

Fig. 2

As indicated above, to determine the function $P(l, E_0)$, it is necessary to know not only $p(E)$, but also the law characterizing the energy loss dE/dl. It is commonly assumed that

$$-\frac{dE}{dl} \approx p(E). \tag{9}$$

This presupposes, first, that the mean energy expended by a primary electron on excitation of an electron of the solid is independent of E and, second, that if the primary electrons expend any of their energy on any processes in addition to raising electrons to the conduction band, the ratio of the excitation loss to all the other losses is also independent of E. It is safe to say that (9) is valid for metals, for here, as emphasized above, we have one energy loss process (intrazonal transitions) predominating over all the possible primary energy loss processes. For such processes $p(\Delta E)$ according to (4) is independent of E, i.e., $\overline{\Delta E}$ is also independent of the energy. Hence for metals, expression (5) is valid in the region of high energies and the equation

$$-\frac{dE}{dl} = \frac{A}{E+B} \tag{8'}$$

is applicable in a wider energy range.

The situation is different in dielectrics. Here, in addition to excitation of electrons from the ground zone to the conduction zone, excitation of excitons is possible. Moreover, the dependences of the number of excitations to the conduction zone and the number of exciton excitations need not be the same. Since the transitions from all the filled bands of the dielectric are of the same type (interzone transitions), there is no reason to assume that, say, excitation of the electrons from the nearest filled band predominates over their excitation from the deeper-lying bands. Hence if the function $S\ p_{MS}(E)$ differs for different zones (for example, if the values of B_S in (8) are different for different zones) then

$$\overline{\Delta E} = \frac{\sum\limits_S \overline{\Delta E}_S p_{MS}(E)}{\sum\limits_S p_{MS}(E)}$$

will obviously depend on E, inasmuch as the mean energy loss $\overline{\Delta E_S}$ of the primary electron will not be the same for all zones. For example, if $p_{MS}(E)$ is taken from (8), then

$$\overline{\Delta E} = \frac{\sum\limits_S \Delta E_S \frac{A_S}{E+B_S}}{\sum\limits_S \frac{A_S}{E+B_S}}$$

and if B_S is larger for deeper-lying zones (i.e., for larger values of $\overline{\Delta E_S}$), $\overline{\Delta E}$ will obviously increase with increasing E.

There is in fact experimental evidence that in NaCl $p(E)$ is not directly proportional to dE/dl. If the path of the primary electron in the emitter is rectilinear (and it can be shown that in NaCl at E = 200-1000 ev it is), then

$$x = l \cos \vartheta.$$

Since $w(x)W(x)$ is a function that decreases with increasing x, the angular dependence is evidently connected with the increase of $w(x)W(x)$ in equation (1) for all values of l with increasing angle of incidence ϑ of the primary electrons. In the E_0 region, where $d\sigma/d\vartheta$ is small, $w(x)W(x)$ is almost constant for all sections of the path making a noticeable contribution to σ, and we can write

$$\sigma = w(0)W(0)\int\limits_0^L P(E_0,\ l)\,dl = w(0)W(0)N,$$

where N is the total number of excited electrons. If $p(E)$ is proportional to dE/dl, N becomes proportional to E_0 and we have $\sigma/E_0 = \text{const}$.

It was shown in Ref. 9 that in the region $E_0 < \sim 600$ ev, where $d\sigma/d\vartheta = 0$, the ratio σ/E_0 diminishes with growing E_0. This means that the mean energy per electron excitation increases with increasing E, and that $p(E)$ is not proportional to dE/dl. Thus, it is virtually impossible at present to justify theoretically any of the suggested forms of the function $P(l, E_0)$ for dielectrics.

Let us now turn to the variable $W(x)$. We must note that, in general, owing to the presence of $W(x)$ and $w(x)$ in (1) we cannot judge of the relative importance of the different excitation processes in the solid, i.e., evaluate $p_S(E)$ for these different processes, on the basis of the relative yields of electrons produced by these processes. If, for example, one of the processes produces $p_1(E)$ excited electrons with an energy distribution for which the corresponding emergence probability is $w_1(x)W_1(x)$, and a second process produces $p_2(E) < p_1(E)$, electrons but with higher energies, then $w_2(x)W_2(x) > w_1(x)W_1(x)$, and the proportion of the electrons, produced by the second process, in the flow of electrons out of the solid (i.e., in the stream of emitted electrons) will be greater than the relative fraction of these electrons in the total number of secondaries produced in the solid. In particular, it appears to us that elastic and inelastic scattering processes can direct electrons toward the surface of the body with a considerable energy and can thus be responsible for a noticeable fraction of the emitted secondary electrons,[10] even though the probability of these processes is low compared with the probability of excitation of electrons of the solid.

The probability that an excited electron will reach the surface depends on the nature of the interactions occurring in the emitter: a) interactions with conduction electrons, b) with phonons, c) with lattice defects, d) with electrons of lower-lying zones and e) recombination interaction. Interactions with deeper-lying zone electrons apparently do not play a noticeable role in either metals or dielectrics.

In metals, σ is independent of temperature, and this indicates that in metals phonon collisions do not affect $W(x)$ to any appreciable extent. The role of these collisions amounts to little more than changing the direction of the velocity of the excited electrons towards the surface of the metal (according to Kadyshevich). The principal type of interaction that determines $W(x)$ in metals is interaction with the conduction electrons.

Unlike electrons with large values of E (primary electrons), which lose only a small fraction of their energy in a single interaction ("collision") with a conduction electron, the excited electrons, which have much lower energies, lose a considerable fraction of their energy in a "collision". Shul'man and Miakinin[22] reached this conclusion regarding energy losses by excited electrons in studying secondary-electron emission at low primary energies, as did Dickey[11] in connection with an investigation of the photoemission from Na and K at large values of $h\nu$. Wolff arrived at the same conclusion by theoretical analysis;[12] according to Wolff, an electron of energy $E < \sim 50$ ev loses about half its energy incident to a "collision".

Since according to both Kadyshevich and the calculations based on the weakly bound electron approximation, the excitation probability diminishes (approximately as $1/(\Delta E)^2$) with increasing energy for intrazonal transitions, the major fraction of the electrons initially excited to a state with sufficient energy to escape from the metal ("internal secondary electrons") can lose their ability to escape as the result of a single encounter with a conduction electron.

Hence the result of such interaction of the internal secondary electrons will be in effect a single-event "relaxation" of the electron, or what might be termed an "absorption" of the internal secondary electron. The probability that a secondary electron will travel over a length of path s without undergoing "absorption" will be

$$W(s) = e^{-\gamma s} \tag{9'}$$

where $\gamma = 1/\lambda_p$; here λ_p is the mean "relaxation" path of the internal secondary electron in the given metal. Since for $E \gg \Delta E$ the distribution in energy of the internal secondary electrons is independent of E and, hence, also of E_0, according to both Kadyshevich and the weakly bound electron approximation, γ will be independent of E_0. This explains the variation of $W(s)$ in metals assumed in many secondary-electron-emission theories (Refs. 13-16).

It has been commonly believed that (9') leads to $W(x) = e^{-\gamma x}$ only under the assumption that the mean relaxation path λ_p is considerably shorter than the phonon-collision free path λ_Φ. We succeeded in showing for the case of one-dimensional motion that the exponential variation of $W(x)$ is retained in the form*

$$W(x) = \sqrt{1 + \frac{\lambda_\Phi}{\lambda_p}} \left(\sqrt{1 + \frac{\lambda_\Phi}{\lambda_p}} - \sqrt{\frac{\lambda_\Phi}{\lambda_p}} \right) \exp\left\{ -\frac{x}{\lambda_p} \sqrt{\frac{\lambda_p}{\lambda_\Phi} + 1} \right\} \tag{10}$$

for all relative values of λ_p and λ_Φ, assuming that slowing down in phonon collisions is small.

With $\lambda_p \ll \lambda_\Phi$ this expression becomes

$$W(x) = \frac{1}{2} e^{-x/\lambda_p} \tag{11}$$

---

*The complicated expression for $W(x)$ in the form of an infinite sum of multiple integrals was simplified to (10) by G.A.Grinberg, whom I take this occasion to thank.

Translator's note: The subscript Φ stands for "phonon".

and with $\lambda_\Phi \ll \lambda_p$,

$$W(x) = e^{-x/\sqrt{\lambda_p \lambda_\Phi}}. \tag{12}$$

We thus obtain for metals and the case of large values of E equation (3) for $p(E)$, equation (5) for dE/dl and equation (10) for $W(x)$. These equations were postulated a priori by Lukianov[13], Salov[14], Bruining[15] and Jonker[16] in developing their semi-phenomenological secondary emission theories.

The semi-phenomenological theories of secondary electron emission lead to expressions for σ that contain two quantities characterizing the emitter: the constant A of equation (5) and the constant γ of equation (10). These theories lead to a "similarity rule" for the relationship

$$\sigma/\sigma_{max} = F(E_0/E_{max}), \tag{13}$$

where σ is the value of the secondary emission coefficient in any metal at a primary energy E_0, σ_{max} is the maximum value of this coefficient for the same metal, E_{max} is the energy of the primary electrons at which $\sigma = \sigma_{max}$, and F is a theoretically determined function, which is the same for all metals.

The "similarity rule" holds approximately in practice for many metals, however, the experimental plot of the function F differs considerably from the theoretical one.

If we carry out all the calculations of the semi-phenomenological theory (after Jonker), using (8') in lieu of (5), then, through appropriate selection of B, we arrive at a theoretical function F_1 different from F, that yields good agreement with the experimental curve σ/σ_{max} vs E_0/E_{max}. Fig. 3 shows plots of the function F_1 as calculated for several values of $\beta = B/E_{max}$ (the curve with $\beta = 0$ is a plot of the function F and corresponds to dE/dl from (5). The crosses mark the experimental values of σ/σ_{max} for several values of E_0/E_{max}, pertaining to the true secondary electrons in Ni. It can be seen that for $\beta = 1.3$ (i.e., B = 600 ev) there is good agreement between the theoretical and experimental curves. The "similarity rule" will hold if B/E_{max} is constant for all metals.

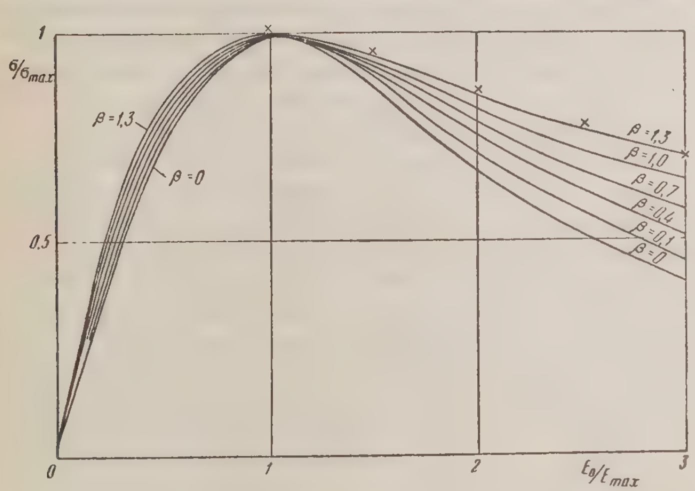

Fig. 3

The semi-phenomenological theories yield a dependence of σ on the angle of incidence ϑ of the primary beam that is in good agreement with experiment in the region of medium and high primary energies.

If equation (4) is used for the excitation-energy distribution and it is assumed that the angular distribution of the "internal secondary electrons" arriving at the surface of the solid (emitter) is spherically symmetrical, then the semi-phenomenological theory gives a distribution in energy for the true secondary electrons that is in good agreement with experiment.

In dielectrics, interaction between the excited electrons and conduction electrons plays no significant part in secondary electron emission. Here the factors determining $W(x)$ are interactions with phonons, recombination and interactions with lattice defects.

It is known from theory (see, for example, Ref. 17), that the average energy $\Delta\varepsilon$ lost by an excited electron in a phonon collision and phonon-collision mean free path λ_Φ for an electron having an energy ε relative to the bottom of the conduction zone, are given by the following expressions:

$$\Delta\varepsilon = \frac{h\nu}{2n+1} \tag{14}$$

and

$$\lambda_\Phi = \frac{a\varepsilon}{2n+1}, \tag{15}$$

where

$$n = n(T) = (e^{h\nu/kT} - 1)^{-1}, \tag{16}$$

and ν is the lattice vibration frequency; $\Delta\varepsilon$ is thus independent of ε, while λ_Φ is proportional to ε; the temperature dependence of $\Delta\varepsilon$ and λ_Φ, given by $n(T)$ is the same for $\Delta\varepsilon$ and λ_Φ.

It can be deduced from (15) that the preponderant majority of electrons with energies $E_0 > \sim 100$ ev travel in straight lines in the surface layer, which is the source of most of the secondary electrons. An electron excited at a given depth can come to the surface after completing a varying number of collision paths $\varkappa$ (i.e., after experiencing a varying number of phonon collisions). It can be shown that the probability of an electron, excited at a depth equal to f phonon-collision free paths reaching the surface by diffusion is highest when the number of these free paths $\varkappa = f^2/3$. On the other hand, the length of the straight-line path of the primary electron depends on its phonon free path λ_{Φ_1}. If, for example, $E_0 \approx 400$ ev and $\bar{\varepsilon} = 8$ ev, the phonon free path of the primary electron is approximately 50 times greater than that of the excited electron, i.e., within the length of the primary's free path the excited electrons will experience $(50)^2/3 \approx 800$ phonon collisions. In spite of the low value of $\Delta\varepsilon$ ($\Delta\varepsilon \approx 0.01$ ev for NaCl at 300° K), the probability is great that an excited electron will lose all its energy in excess of the thermal energy, equal to kT above the bottom of the conduction zone, and will be unable to emerge as a secondary electron (if the electron affinity of the crystal $\chi > kT$).

Mechanisms of the escape of excited electrons from dielectrics based on consideration of only phonon collisions have been proposed by Hachenberg[18] and Dekker[19]. According to Dekker, an internal secondary electron, moving towards the surface and undergoing phonon collisions, will be slowed down; when its energy becomes less than the electron affinity of the crystal, it will cease being a true internal secondary electron. If $\bar{\varepsilon}_0$ is the mean internal secondary electron energy in the conduction zone at the instant of excitation and χ is the electron affinity, the average number of "relaxation" collisions is $\frac{\bar{\varepsilon}_0 - \chi}{\Delta\varepsilon}$, and the average relaxation free path $\lambda_p = \frac{\bar{\varepsilon}_0 - \chi}{\Delta\varepsilon}\lambda_\Phi$, and according to (14) and (15) is independent of the temperature. However, the average "relaxation depth" $\bar{x}_p$ in the case of diffusion type motion does not equal the relaxation free path, since after $\frac{\bar{\varepsilon}_0 - \chi}{\Delta\varepsilon}$ individual relaxation paths the displacement of the electron towards the surface will be

$$\bar{\lambda}_\Phi \sqrt{\frac{\bar{\varepsilon}_0 - \chi}{\Delta\varepsilon}},$$

i.e., from (14) and (15)

$$\bar{x}_p \approx (2n+1)^{-1/2} \tag{17}$$

Translator's note: The subscript p stands for "relaxation".

and, according to (16), will depend on the temperature.

In his analysis, Dekker assumes that the escape probability of an internal secondary electron as a function of the depth of the point excitation has the form shown in Fig. 4. This function is not deduced but is simply postulated by Dekker. We note that several other investigators employ a function $W(x)$ of the same form, but we failed to find in the literature any justification of a function of this form based on a plausible escape micromechanism.

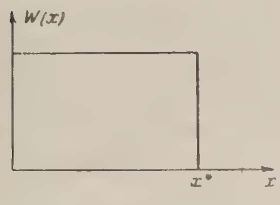

Fig. 4

Assuming that the limiting depth of escape x^* equals the relaxation depth, Dekker concludes that for the high primary energy range the temperature dependence of σ will be given by equation (17). This conclusion is in good agreement with the experimental results for MgO (according to the data of Ref. 19) and for NaCl and other alkali-halide crystals (according to the data of Ref. 9 and 20).

The above examination of the behavior of excited electrons in dielectrics is clearly far from being complete. It is evident that in the stationary state the number of electrons excited into the conduction band should equal the number of recombinations of electrons with "holes" in the lower zones (probably through "traps", as is customarily assumed in the case of photoconduction). According to Dekker, it is apparently necessary to assume that this removal of the electrons from the conduction zone occurs at the expense of electrons with $\varepsilon < \chi$, but if recombination occurs for electrons with $\varepsilon < \chi$, it should also take place for internal secondary electrons. Naturally, the recombination (absorption) range λ_a for the slower electrons with $\varepsilon < \chi$ will be shorter than the range for the faster internal secondary electrons. However, the relative role of relaxation and combination in the "absorption" of internal secondary electrons is determined not by the ratio between the absorption ranges of the internal secondary electrons and the slower electrons, but by the ratio between the lengths of the relaxation path λ_p and the recombination path λ_a for the internal secondary electrons. The failure of Dekker to take recombination into account is equivalent to an assumption that $\lambda_p \ll \lambda_a$, something that is not evident a priori and that is not proved in Dekker's work.

Some evidence against this assumption, in the case of alkali-halide salts, can be deduced from the data on secondary-electron velocity distributions in such salts, obtained by Shul'man[21], and from data on the angular dependence of σ. For $E_o > \sim 100$ ev, the distribution of the secondary electrons in velocity does not vary with E_o. But if the slowing down of the electrons by phonon collisions on their way towards the surface does play an important part, the distribution in velocity of the internal secondary electrons at the surface (and, consequently of the escaping secondary electrons) should depend on the depth from which they arrived at the surface.

Inasmuch as the ionization range of the primary electron increases with increasing E_o, the fact that the distribution is independent of E_o brings us to two alternatives:

a) either the ionization range L of the primary electron with $E_o > \sim 100$ ev is already greater than the relaxation and absorption ranges ($L > \lambda_p, \lambda_a$), for then at all energies $E_o > \sim 100$ ev the secondary electrons will come out of one and the same layer of the emitter, or

b) the slowing-down through phonon collisions within the emitter layer from which most of the secondaries escape is unimportant.

However, the experimentally proved fact that σ is independent of the angle of incidence ϑ at $E_o < \sim 600$ ev and room temperature,[9] shows that alternative "a" is improbable, at least at low temperatures.

Thus, for example, if $L = 2\lambda$, increasing ϑ from 0° to 60° would result in electrons emerging not from the depth of one half the ionization range of the primary electron, but from the depth of the full ionization range, i.e., would yield a noticeable increase in σ.

We are therefore inclined to assume that alternative "b" is more likely for alkali-halide crystals and that the probability of an internal secondary electron reaching the surface is determined not by relaxation, but by recombination, i.e., that $\lambda_a < \lambda_p$.

If we accept this, then, as indicated above, we obtain equation (10) for the function $W(x)$. It can be shown that for large values of E_0, for which one can assume that $P(l)$ is constant in the layer making the greatest contribution to the secondary emission (as is also assumed by Dekker), one can obtain the experimentally substantiated temperature dependence of σ given by (17). The assumption that $P(l) = \text{const} = C$ for $W(x)$ as described by (10) is equivalent to saying that $W(L) \ll 1$, and we can then write for $\vartheta = 0$:

$$\sigma = \int_0^L w(x) W(x) P(x,\ E_0)\, dx = C w_0 \int_0^\infty W(x)\, dx$$

(in view of the fact that the slowing down is small on the way to the surface, $w(x) = \text{const} = w_0$). Inserting $W(x)$ from (10), we get

$$\sigma = C w_0 \lambda_\Phi \left(\sqrt{\frac{\lambda_a}{\lambda_\Phi} + 1} - 1 \right),$$

and if $\lambda_a \gg \lambda_\Phi$,

$$\sigma = C w_0 \sqrt{\lambda_\Phi \lambda_a}, \tag{18}$$

i.e., $\sigma \approx \sqrt{\lambda_\Phi} \approx (2n+1)^{-1/2}$, as obtained by Dekker.

Let us consider the probability $w(x)$ of escape of an electron through the potential barrier χ at the surface of the solid. To leave the solid, an electron with energy ε must approach the surface at an angle such that the energy ε_n, associated with the normal component of the velocity, is not less than χ. Upon emerging from the solid, this electron will have an energy $\varepsilon' = \varepsilon - \chi$. If the directional distribution of all electrons having an energy ε at the surface is characterized by spherical symmetry, then the probability of ε_n being equal to or greater than χ is

$$\frac{1}{2}\left(1 - \sqrt{\frac{\chi}{\varepsilon}}\right) = \frac{1}{2}\left(1 - \sqrt{\frac{\chi}{\varepsilon' + \chi}}\right),$$

and hence, for a single incidence on the boundary of the solid,

$$w(\varepsilon') = \frac{1}{2}\left(1 - \sqrt{\frac{\chi}{\varepsilon' + \chi}}\right)(1 - \bar{R}_\varepsilon), \tag{19}$$

where $\bar{R}_\varepsilon$ is the quantum-mechanical reflection coefficient for electrons of energy ε, averaged over all directions of incidence, satisfying the condition $\varepsilon_n \geqslant \chi$.

Expression (19) determined the escape probability of an electron arriving at the boundary with an energy ε, if one excludes repeated arrivals of the electron on the boundary, for example, if $\lambda_a \ll \lambda_\Phi$ — a condition that is fulfilled in metals. If repeat arrivals at the boundary are possible, then $w(\varepsilon)$ is greater than given in (19). In particular, with $\lambda_a \gg \lambda_\Phi$, an electron arriving at the boundary with $\varepsilon > \chi$ and striking the boundary repeatedly at diverse angles is bound to escape in the long run. In this case

$$w(\varepsilon) = \left. \begin{array}{l} \nearrow 1 \text{ with } \varepsilon > \chi \\ \searrow 0 \text{ with } \varepsilon < \chi \end{array} \right\}. \tag{20}$$

We note that if $w(\varepsilon)$ is determined by (19), then the total-energy distribution curve for the secondary electrons will have a maximum at a certain value

$\varepsilon' > 0$, even if the number $\nu_i(\varepsilon)$ of electrons arriving at the surface with $\varepsilon > \chi$ decreases monotonically with increasing ε (as follows from (4)). Actually, the number of electrons escaping from the solid will be

$$\nu_a(\varepsilon') = \nu_i(\varepsilon' + \chi)\, w(\varepsilon')$$

where, as can be seen from (19), $w(\varepsilon') = 0$ at $\varepsilon' = 0$.

To determine $w(x)$ it is necessary to know the distribution in momentum of the electrons arriving from a depth x; this obviously depends on the distribution at the site of excitation and on the energy losses on the way to the surface. In those cases when the slowing down of the internal secondary electrons can be neglected and the distribution of the excited electrons can be assumed to be independent of the primary energy, the distribution in momentum of the secondary electrons at the surface will be independent of x and, consequently, we will have

$$w(x) = w_0$$

(under this condition R_ε, averaged over all ε's, will also be independent of x).

This is, apparently, the case for metals.

Leningrad Physical-Technical Institute of the
Academy of Sciences of the USSR

References

1. A.Dekker & A.van der Zeil, PSF* No. 3, 159 (1954). Probably a translation of Phys. Rev., 86, 755 (1952)
2. A.Ia.Viatskii, Zhur. eksp. i teor. fiz., 20, 557 (1950).
3. A.E.Kadyshevich, Zhur. eksp. i teor. fiz., 9, 930 (1939).
4. E.M.Baroody, PSF*, No. 1, 153 (1953).
5. A.van der Zeil, Phys. Rev., 92, 35 (1953).
6. O.Hachenberg, W.Brauer, Fortschr. d. Phys., 1, 9-10, 439 (1954).
7. J.Marshall, PSF*, No. 3, 172 (1954).
8. J.Lander, Phys. Rev., 91, 1382 (1953).
9. L.N.Dobretsov, A.S.Titkov, Doklady AN SSSR, 100, 33 (1955).
10. E.J.Sternglass, Phys. Rev., 95, 345 (1954).
11. J.Dickey, PSF*, No. 1, 102 (1953).
12. P.A.Wolff, Phys. Rev., 95, 56 (1954).
13. S.Iu.Luk'ianov & V.N.Bernatovich, Zhur. eksp. i teor. fiz., 7, 856 (1937).
14. W.Salow, Phys. ZS., 41, 434 (1940).
15. H.Bruining, Physica, 3, 1047 (1936).
16. J.Jonker, PSF*, No. 3, 173 (1954).
17. N.Mott & R.Gurney, Electronic Processes in Ionic Crystals (in Russian trans.) M. 1950.
18. O.Hachenberg, Ann. d. Phys., 2, 7/8, 404 (1948).
19. A.Dekker, Phys. Rev., 94, 1179 (1954).
20. A.R.Shul'man, B.P.Dement'ev, Zhur. tekh. fiz., 25, 2256 (1955).
21. A.R.Shul'man, see present issue of the Bulletin.
22. A.R.Shul'man & E.I.Miakinin, Doklady AN SSSR, 91, 1075 (1953).

* PSF = "Problems of Modern Physics" (A collection of translations).

DISCUSSION

N.G.Nakhodkin: Do you think that the conduction band is the principal source of secondary electrons in metals?

L.N.Dobretsov: Yes. However, this does not exclude interzonal transitions.

N.G.Nakhodkin: Will the secondary-electron emission be proportional to the filling of the conduction band?

L.N.Dobretsov: Yes, it will, other conditions being equal. It should, however, be noted that this is not usually realized.

I.M.Dykman: What is the "bottleneck" in the theory — the fact that we do not know the excitation function or the probability of the escape of the electrons from the emitter material?

L.N.Dobretsov: It is difficult to answer this question. The excitation function for large energies is known more or less accurately, but only approximately for middle energies. The probability of escape is known satisfactorily for metals, but not for dielectrics.

I.M.Dykman: I assume that it is simpler to analyze the motion of the electrons by the kinetic-equation method. This will take into account the electron recombination events.

N.D.Morgulis: Why do you not take account of discrete losses?

L.N.Dobretsov: I agree that they should be taken into account, but discrete losses lie beyond the scope of this analysis.

L.N.Iasnopol'ski: How do the deductions of the theory of secondary emission and of the excited conductivity in the high-energy regions agree with the experimental data?

L.N.Dobretsov: The agreement is good in the high-energy region.

P.V.Timofeev: Secondary-electron emission occurs from the surface layer, but the theory does not specifically take the surface layer into account.

L.N.Dobretsov: The theory does not take into account all the fine points. I will not undertake to explain the experiments that confirm the role of the surface layers.

I.M.Dykman: Couldn't the angular independence of the secondary emission be attributed to scattering of the primary electron? I have the phonon mechanism in mind.

L.N.Dobretsov: If the primary electron is assumed to be scattered by phonons, it can be shown that its path will be a straight line inside the emitter in that layer from which practically all the secondary electrons escape.

N.L.Iasnopol'skii: The corrections you propose for the Thompson losses lead to results that are in conflict with those of Diatlovitskaia's experiments. How can this be explained?

L.N.Dobretsov: I cannot explain this.

A.I.Piatnitskii: What will be the angular distribution of secondary electrons from a thin film?

L.N.Dobretsov: The distribution will be the same as from bulk metal.

A.I.Piatnitskii: Experiments with cesium-antimony films show that the thinner the film, the narrower the angular distribution of the escaping electrons.

N.G.Nakhodkin: One can hardly agree with L.N.Dobretsov when he states that in metals intrazonal transitions of conduction electrons play the predominant role both in the excitation of secondary electrons and in the energy loss by the primary electrons. From this point of view it is impossible to explain the variation of the maximum value of the secondary emission coefficients of various substances with their atomic number observed by us back in 1952* (see diagram). We plotted this dependence using especially-determined values of δ_{max} for 12 substances (Ag, Cu, Zn, Sb, Te, Tl, Pb, Bi, In, Ge, Cr, and Ce) and the most reliable values of δ_{max} for 42 substances found in the literature.

In contrast with earlier attempts to obtain such a dependence, we plotted our curve using only the experimental data for δ_{max}, without any processing that might involve additional errors. For example, Sternglass** subtracted from the

---

*N.G.Nakhodkin, Transactions of the Tenth Scientific Session at Kiev State University, 1953.

**E.I.Sternglass, Phys. Rev., 80, 924 (1950); 85, 391 (1952).

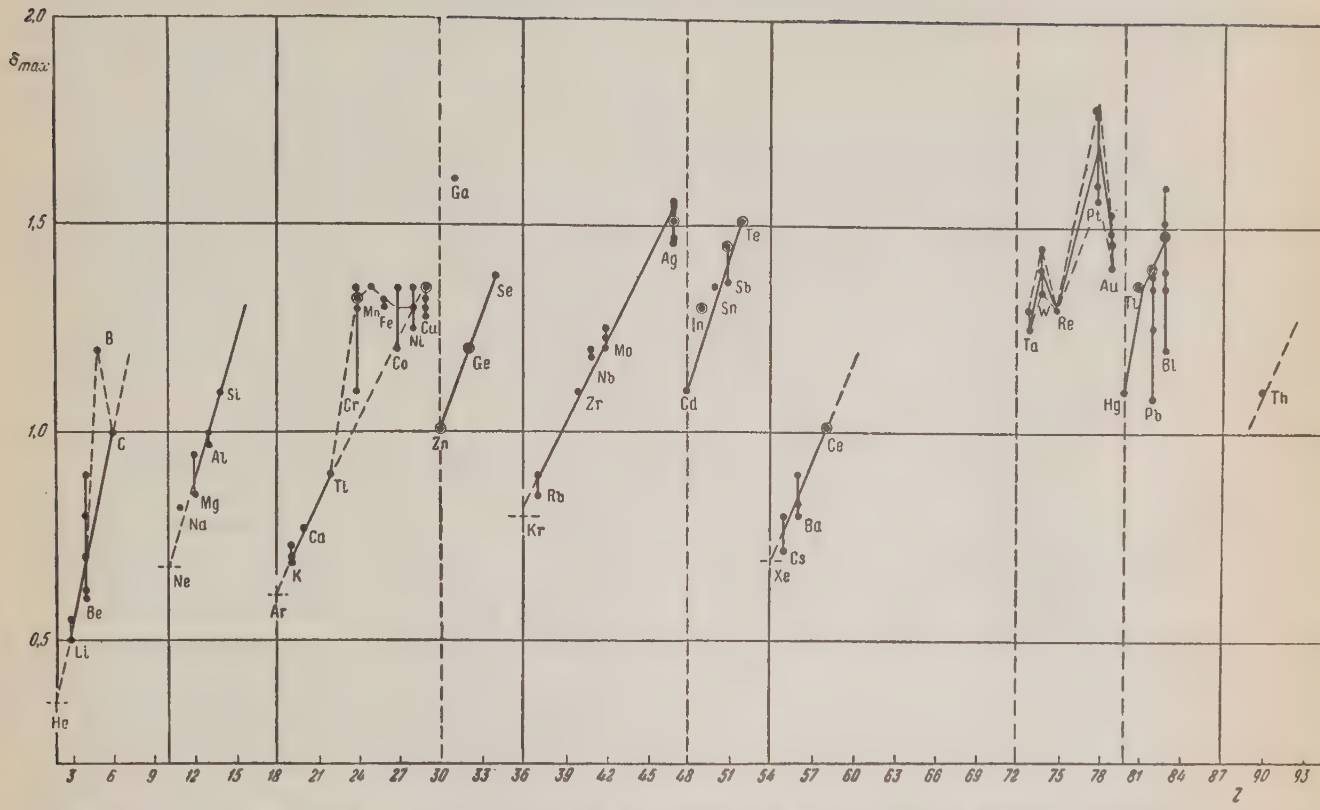

experimental value of δ_{max} the function η, which is supposed to represent those electrons in the secondary beam that are produced by the scattered primary electrons diffusing in the reverse direction; Sternglass himself stated in a subsequent article that this function was only approximate.

It will be seen from the figure that δ_{max} varies periodically with the atomic number. Within each period it increases monotonically until the electron shell is filled. Once the shell is filled and a noble gas type structure is formed, δ_{max} drops abruptly and then starts rising again as the next shell fills. Jumps are observed to Na, K, Rb and Cs, and also in going from Cu to Zn, from Ag to Cd and from Au to Hg, since the d- and s-shells are filled in zinc, cadmium and mercury. The difference between going from K to Ca, when the value of δ_{max} increases monotonically, and going from Cu to Zn, when δ_{max} falls off abruptly, can apparently be explained by the fact that inside the outer s-electron orbit K has a filled p-shell (noble gas configuration), the electrons of which ionize with difficulty, whereas Cu has a filled d-shell, whose electrons are readily ionized, as is evidenced by the bivalence of copper. In zinc the d- and s-shells are filled. However, in contrast with copper, the d-shell in zinc lies deeper and its electrons are less readily ionized, as indicated by the fact zinc never has a valence of three or more. This explains the drop in δ_{max} in going from Cu to Zn, from Ag to Cd, etc. The values of δ_{max} for Tl, In, Te and Sn predicted from the plotted dependences were within 7% of the subsequently measured values. The observed regularities in the variation of δ_{max} with atomic number, the similarity of the secondary emission characteristics as the same electron shell (but with different quantum numbers) in different elements is filled and the monotonic transitions from metal to semiconductors are all arguments against the hypothesis that only conduction electrons participate in secondary emission. We must assume valence electrons originating from overlapping of outer p-, d- and perhaps even f-shells also take part in the secondary emission process.

SECONDARY-ELECTRON EMISSION OF DIELECTRICS AND METALS

- A.R.Shul'man

Introduction

Over the past several years the Electronics Laboratory of Leningrad Polytechnical Institute has been engaged in research on the secondary emission properties of certain substances. Use of the method of single pulses, described in Ref. 1, made it possible to study the materials in different forms and states, including single crystals at room temperature and to exclude the influence of secondary effects arising incident to bombardment of non-metallic emitters: surface charge and changes in the composition or structure of the target.

The present report is devoted to a description and discussion of the results obtained with the active participation of Dement'ev, Mar'in, Miakinin and Fridrikhov, students of the Institute.

Dependence of σ on U_p and the slowing down of primary electrons.

Detailed investigation of the dependence of the coefficient of secondary-electron emission σ on the primary energy U_p in a number of substances established the following two facts.

1. The $\sigma = f(U_p)$ curves exhibit fine structure in the region of rising values of σ. The curves can be regarded as smooth only in the first approximation. The dependence of σ on U_p for NaCl in the region of small values of U_p is shown in Fig. 1; the points have been recorded at 10 v intervals. It will be seen that the assumption of a monotonic increase in σ in this region of U_p values is only a very rough approximation. An analogous curve for KBr is shown in Fig. 2.

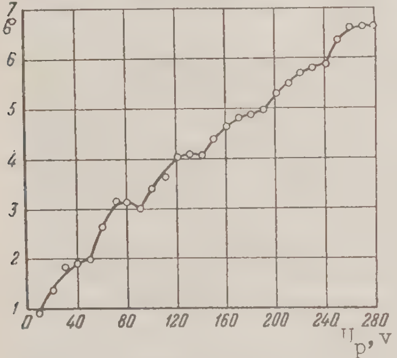

Fig. 1. Dependence of the secondary emission coefficient σ on the energy U_p of the primary electrons for artificial crystals of NaCl.

It will be seen that the curve characterizing the dependence of σ on U_p has a noticeable fine structure. A characteristic feature of these curves is the periodicity of the fine structure. Thus in the case of NaCl sharp increases in σ occur at 50, 90, 140, 190 and 240 v; in the case of KBr, at 60, 120 and 180 v.

These curves are fully reproducible. Different specimens of the same substance yield similar curves (see Fig. 3, for example). Although the values of σ for different specimens differ somewhat, the general character of the curve is the same and the values of U_p at which the rapid increases in σ occur coincide.

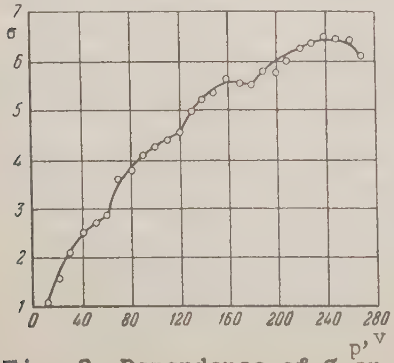

Fig. 2. Dependence of σ on U_p for artificially grown KBr single crystals.

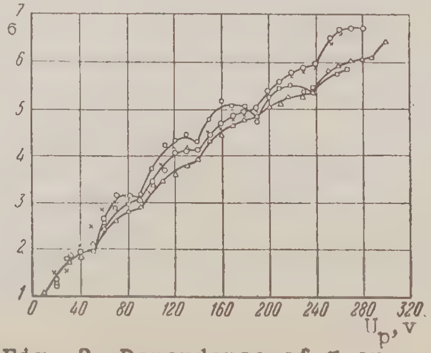

Fig. 3. Dependence of σ on the primary energy for four different specimens of NaCl.

The fine structure of the σ vs U_p curves for metals has been detected in a number of earlier investigations. As far as we know, however, the effect has not hitherto been observed for non-metallic targets. In the case of dielectrics the fine structure is appreciably more pronounced than in the case of metals; where metals are concerned the character of the fine structure is strongly dependent on the previous heat treatment of the target.

It may be asked whether the peaks in the curve are not due to apparatus errors or errors of measurement. The principal argument against this is the fact that each of the investigated substances has a definite, characteristic periodicity of the fine structure, which of course would not be the case if the peaks were due to experimental errors. The assumption that the peaks are of a diffractional nature must also be rejected in light of analysis of the experimental conditions in conjunction with the numerical values characterizing the fine structure and its periodicity.

If we consider that the presence of fine structure is due to the fact that there occur preferred transitions of the lattice electrons from one state to another, it may be assumed that there occur excitations of the secondary electrons from zones located below the highest, completely filled band (for example, in the case of NaCl from the zone located below the $3P_{Cl}$-band).

For metals it has proved possible by taking certain precautions to obtain in some cases a correlation between the positions of the maxima and the width of the energy levels for soft x-rays. Such matching could not be carried out in the case of the investigated dielectrics since data for these substances in the soft x-ray spectral region of interest are lacking. Thus we do not have sufficient data for unique interpretation of the fine structure of the σ vs U_p curves for dielectric targets; this aspect of the problem requires further investigation.

2. It has hitherto been assumed that the dependences of σ on U_p are essentially similar for metallic and non-metallic emitters. Thus in a recent survey[2] devoted to secondary electron emission the authors write that (the curves for $\sigma = f(U_p)$ for semiconductors and dielectrics are analogous to the curves for metals". Our experiments have shown, however, that the basic emission characteristic, i.e., the curve $\sigma = f(U_p)$ differs in appearance for different substances.

According to our data substances may be divided into three groups according to the form of dependence of σ on U_p at medium values of U_p:

A. Dielectrics with a sharply pronounced maximum in the emission vs primary energy curve. Such curves are obtained for substances having a large amount of impurities or defects of the crystal lattice and for amorphous glass; they are also characteristic of alkali-halide compounds and aluminum oxide when water is present in the surface layers. Curves of this type are shown, for example, in Ref. 3.

B. Dielectrics characterized by a constant value of σ over an appreciable range of U_p. Such curves are obtained for a number of crystal dielectrics (Refs. 4 & 5). We can speak of a constant value of σ within the limits of experimental error, i.e., within 5% (at high temperatures the experimental accuracy can be enhanced by using short periodic pulses). It may be that there is actually some variation in the value of σ, i.e., that the $\sigma = f(U_p)$ curve does have a low rise (flat maximum), but it is impossible to establish this experimentally. If there is a variation in σ it must be a second order effect. We note that attainment of a saturation value of σ has been substantiated by the investigations of Refs. 6 & 7. With further increase in U_p after the plateau in the $\sigma = f(U_p)$ curve we come to a region of decreasing values of σ.

C. Metals occupying an intermediate position between the above-mentioned two groups of dielectrics. The form of the primary-energy dependence of σ is determined mainly by two factors: the law characterizing the slowing down of the primary electrons and the processes of interaction of the secondary electrons with electrons of the lattice, phonons, lattice defects and so on, as a result of which there may occur changes both in the number and energy of the secondary electrons. In view of this one cannot judge of the influence of these factors separately from the general appearance of the $\sigma = f(U_p)$ curve. However, from an examination of the individual sections of the curve one can draw certain conclusions regarding the regularity characterizing the slowing down of the primary electrons. This applies in particular to sufficiently large values of U_p when the depth of penetration of the primary electrons exceeds the limiting depth for the emergence of the secondary ones.

The hypothesis that there exists a certain limiting depth for the emergence of secondary electrons was advanced some time ago. It has been shown in two recent investigations[8,9] that there exists a measureable effective depth of secondary emission, i.e., a certain limiting depth ξ beginning with which the probability of escape of secondary electrons becomes so small that it does not effect the value of σ.

Above a certain high value of U_p, the secondary electrons will emerge from one and the same space zone even with further increases in U_p. The variations in σ occurring in this case will be determined primarily by variations in the number of secondary electrons produced in this zone. At the same time there can be variations in the relative number of secondary electrons produced at different depths within the limits of this zone and in consequence some variation in the number of secondary electrons escaping from the emitter. However, regardless of the nature of the law governing the slowing down of primaries at high values of U_p, this effect is negligible and for the first approximation can be disregarded.

Thus at sufficiently high values of U_p when x_0, the depth of penetration of the primary electrons, is greater than ξ the form of the corresponding section of the $\sigma = f(U_p)$ curve is determined primarily by the law governing the slowing down of the primary electrons. The yield of secondary electrons with the primary beam incident normal to the surface of the emitter is characterized by

$$\sigma = \int_0^{x_0} \frac{dn}{dx}\, dx \int^{\varphi_0} f(x, \varphi)\, d\varphi \tag{1}$$

where dn/dx is the number of secondary electrons produced per unit path of the primary electron, $f(x, \varphi)$ is the probability of escape of a secondary electron, φ is the angle between the direction of motion of the secondary electron and the normal to the emitter surface and φ_0 is the limiting angle at which the normal component of the electron velocity is sufficient for overcoming the barrier at the emitter surface.

At sufficiently large values of U_p, when $x_0 > \xi$ (1) can be written in the form

$$\sigma = \int_0^{\xi} \frac{dn}{dx} F(x)\, dx, \tag{2}$$

inasmuch as when $x_0 > \xi$, $F(x)$ tends to zero.

If in the energy interval in question there is no appreciable change in the relative number of electrons ejected from different energy zones of the emitter and the losses due to excitation of excitons can be neglected, it may be assumed, as is usually done, that the number of secondary electrons produced per unit path of the primary is proportional to the specific energy loss of the primary electron:

$$\frac{dn}{dx} \approx \frac{dU}{dx}. \tag{3}$$

Let us examine the two limiting cases.

In the case of a square slowing down law substituting the expression for energy loss in explicit form in (3) and then substituting (3) in (2) we get

$$\sigma \approx \int_0^{\xi} \frac{F(x)\, dx}{\sqrt{U_p^2 - \beta x}}. \tag{4}$$

With $x_0 > \xi$ this expression is simplified (see Ref. 10):

$$\sigma \approx \frac{1}{U_p}\int_0^{\xi} F(x)\,dx. \qquad (5)$$

In the case of a linear slowing down law, substituting (3) in (2) we obtain

$$\sigma \approx \int_0^{\xi} F(x)\,dx. \qquad (6)$$

As was noted above the integration limit ξ does not depend on the energy U_p. The magnitude of $F(x)$ is a function of the coordinates of the site of genesis of the electrons and their energy, i.e., $F(x)$ is not a function of U_p or is at most a slowly varying function of this quantity. Hence we can say that the dependence of σ on U_p is expressed in explicit form in (5) and (6).

Thus in light of the above assumptions, if the square slowing down law obtains, at sufficiently high values of U_p we would have

$$\sigma = \frac{\text{const}}{U_p}. \qquad (7)$$

Or, if the linear law holds

$$\sigma = \text{const}. \qquad (8)$$

Let us now examine the available experimental data and attempt to draw a qualitative deduction regarding the form of the slowing down law.

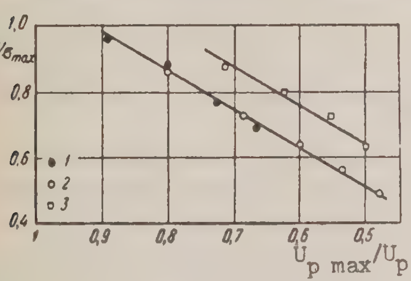

Fig. 4. Dependence of σ/σ_{max} on $U_{p\,max}/U_p$: 1) glass No.46, 2) aluminum oxide with an admixture of molybdenum, 3) grade No.2 aluminum oxide.

For amorphous dielectrics as well as for crystalline ones with an appreciable concentration of impurities and lattice defects or in the presence of water in the surface layer, the section of the $\sigma = f(U_p)$ curve for values of U_p exceeding the value $U_{p\,max}$ corresponding to the maximum in the curve is satisfactorily described by expression (7). It will be seen from Fig. 4 where data for a number of substances in this class are plotted, that in this region, despite the great difference in the actual values of σ for these emitters, in all cases $\sigma \approx 1/U_p$. It may therefore be concluded that the secondary emission of these substances, in any case in the region $U_p > U_{p\,max}$ may be described by means of the square law for the slowing down of primary electrons.

The virtual stability of σ in an appreciable primary energy interval for alkali halide crystals, aluminum oxide and thorium oxide is in accord with expression (8). Hence the presence of saturation in the $\sigma = f(U_p)$ curve for crystalline dielectrics may be interpreted to mean that at least in this interval of primary energy values the linear slowing down law obtains.

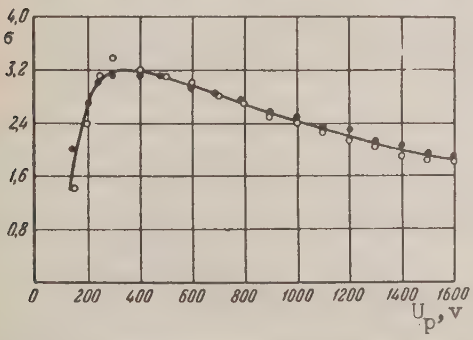

Fig. 5. Dependence of σ on the primary energy at 290°K for the No. 1 sample of mica.

Let us examine the data for mica from this viewpoint. If the above division of dielectrics into two groups is correct, we should expect to find a plateau in the σ curve for mica. Actually, however, the curve has a distinct maximum (see Fig. 5).

If we plot this dependence for mica in dimensionless units, as we did for the dielectrics of the first group in Fig. 4, we obtain the curve of Fig. 6. It will be seen

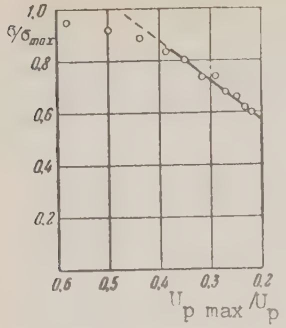

Fig. 6. Dependence of σ/σ_{max} on $U_{p\,max}/U_p$ for the mica sample.

from a comparison of the figures that the regularities of emission for mica are different from those for the dielectrics of the first group. The transition to the square slowing down law in mica occurs appreciably later than in the dielectrics of the first group. In this respect mica is rather similar to the dielectrics of the second group. As regards its emission characteristics mica either belongs to the substances of the second group or occupies an intermediate position between the first and second groups. The presence of the maximum in the curve for mica only indicates that the region of operation of the linear law is not great.

Let us examine the obtained results from the point of view of current theories of secondary electron emission. According to Baroody[11] the emission of metallic emitters can be characterized by the universal formula:

$$\frac{\sigma}{\sigma_{max}} = 1{,}85\,F\left(0{,}92\,\frac{U_p}{U_{p\,max}}\right), \qquad (9)$$

where

$$F(y) = e^{-y^2}\int_0^y e^{z^2}\,dz. \qquad (10)$$

Later the same author[12] showed that if the necessary corrections are made in Wooldridge's theory, we obtain

$$\frac{\sigma}{\sigma_\infty} = 1 - e^{-\gamma x_0}. \qquad (11)$$

The first formula (9) is based on the square, the second (11) on the linear slowing down law.

Juxtaposition of the experimental data for metals with the curves calculated according to these formulas shows appreciable deviation of the experimental data from the theoretical curves: the experimental points fall above the theoretical curve based on the square law and below the curve based on the linear law. Chachenberg and Brauer[2] note that if the reflected electrons are excluded from the examination, the experimental points approach the curve based on the square law. However, even with this correction it is impossible to make the experimental data fit the theoretical curve perfectly.

If we nevertheless consider it justifiable to draw any conclusions regarding the form of the slowing down law on the basis of comparison of theoretical and experimental data, we must conclude that in the case of metals we have either simultaneous operation of both laws (taking into account free and bound electrons) as has been suggested by Viatskin[13] or that the effective law is intermediate between the linear and square one.

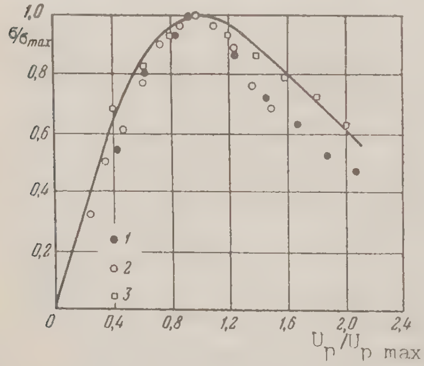

Fig. 7. Dependence of σ/σ_{max} on $U_p/U_{p\,max}$. Curve calculated according to expression (9); designation of points same as in Fig. 4.

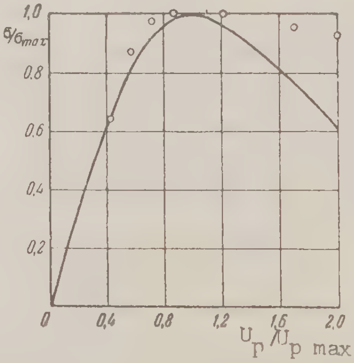

Fig. 8. Same curve as in Fig. 7 and experimental points obtained for a mica specimen.

In the case of dielectrics of the first group the correspondence between the computed curve and the experimental points is appreciably better than in the case of metals (Fig. 7). This apparently is connected with the fact that in the case of dielectrics of the first group the square law better describes the actual slowing down of the primaries than in the case of metals.

It will be seen from Fig. 8 showing the theoretical curve and the data for mica that the formula based on the square law is not suitable for describing the secondary emission of this material. This substantiates our view that mica cannot be classed with dielectrics of the first group.

In our opinion the impossibility of describing the secondary electron emission of crystalline dielectrics by means of the square slowing down law is significant where elucidating the mechanism of emission is concerned.

At high primary electron speeds the experimental data in all cases are satisfactorily described by the square law.

The question of the boundaries of applicability of the linear slowing down law has not received proper attention in the theory of secondary emission. Marshall[14] considers that the square law is valid for primary energies above several hundred electronvolts. Viatskin in a recent contribution[15] indicates that the region of operation of the linear extends to several kev. Obviously the electrons cannot be retarded according to the square law right up to a certain speed and then according to the linear law at higher speeds. The square and linear laws are clearly limiting cases. With this qualification in mind we can say that if it is justifiable to determine the intervals of applicability of the two limiting laws from the shape of the $\sigma = f(U_p)$ curve for crystalline dielectrics, the experimental data appear to indicate that the region of applicability of the linear law for alkali halide compounds extends to 1.5 kev or higher.

Distribution in energy of secondary electrons

When the single pulse method is employed the retarding potential curves do not have a part corresponding to electrons with "insufficient" speeds, the appearance of which is due to secondary effects.[5] This makes it possible to compare the distribution in energy of secondary electrons in dielectric emitters with their distribution in metallic emitters. Simultaneous determination of the distribution curves for metals and dielectrics under identical conditions and over a wide range of U_p values may help in clarifying the difference in the secondary electron yields of metals and dielectrics.

Let us examine the available data on the position and width of the maxima of the distribution in energy curves for slow true secondary electrons. It has been shown in a number of investigations among which that of Becker[16] is one of the first, that the spectral composition of secondary electrons is virtually independent of their energy. At the same time, it was shown for non-metallic targets that the energy maximum is displaced with changes in depth of emergence of the secondary electrons or temperature[17,18]; Vudynskii[19] also indicates that the number of fast electrons increases slightly with increasing U_p.

In order to clear up the uncertainty in this respect we carried measurements of the distribution in energy of secondary electrons from metallic and dielectric targets in a wide range of primary energies. The measurements with metals were carried out using a thoroughly cleaned nickel target maintained at a high temperature during the experiment. The experimental conditions for dielectric targets are described in Ref. 4.

As was shown in Ref. 20, at primary energies below the work function of the metal true secondary electrons are absent; this is also evident from the curve of Fig. 9.

The distributions in energy of secondary electrons at small values of U_p (but greater than the work function) are shown in Figs. 10, 11 and 12. The characteristics of the maxima are listed in Table 1.

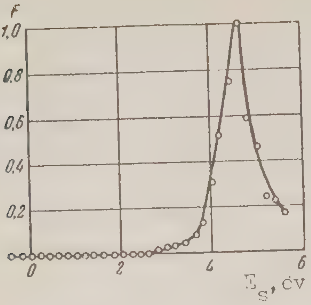

Fig. 9. Distribution in energy of secondary electrons from a clean nickel sample at U_p = 4.56 v.

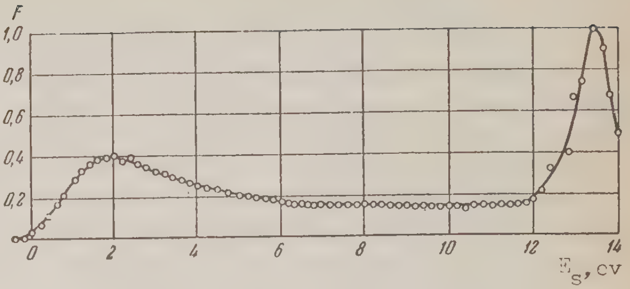

Fig. 11. Same as Fig. 9 but for U_p = 13.58 v.

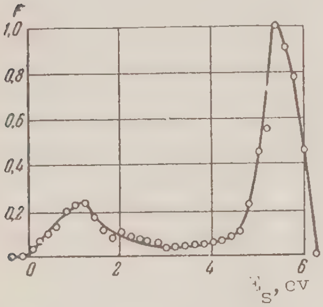

Fig. 10. Same as Fig. 9 but for U_p = 5.8 v.

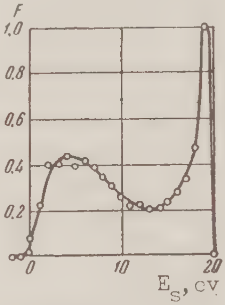

Fig. 12. Same as Fig. 9 but for U_p = 18.58 v.

Table 1

Positions and widths of maxima in the distribution in energy curves of secondary electrons emitted by nickel at low values of U_p

U_p, v	Value of U_c corresponding to the maximum	Half-width of maximum, ev
5,8	—1,2	1,4
8,8	—1,1	1,4
10,8	—1,5	2,0
13,5	—2,0	4,2
18,5	—4,0	10,0

It will be seen from these data that at values of U_p up to about 18 v the position and width of the maximum depend on the primary energy. As U_p is increased, the maximum is shifted to the side of larger primary energies and the half-width increases. Beginning with U_p = 18 v the maximum in the distribution curve exhibits all the characteristics peculiar to the distribution maxima in the curves for metallic targets; with further increase in U_p both the position and half-width of the maximum change insignificantly or not at all. The data for U_p = 500 v are given in Fig. 13. No significant alterations in the position and half-width of the maximum were detected up to U_p = 1600 v.

It was shown in Ref. 4 that in the case of alkali-halide crystals and in the interval of medium values of U_p it is impossible to detect any significant change in the form of the I_e-U_c curve (in the region corresponding to the maximum in the distribution curve) with changes in U_p. This has been found to hold for mica as well. A typical curve characterizing the distribution in energy of secondary electrons for NaCl is reproduced in Fig. 13.

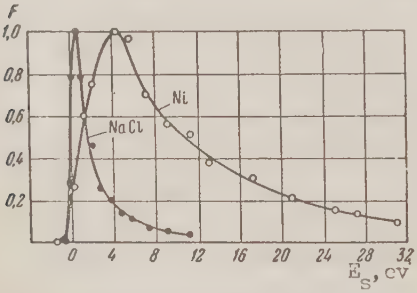

Fig. 13. Comparison of the distributions in energy of secondary electrons from NaCl and Ni. Curves recorded under identical conditions with U_p = 500 v.

Changes in the I_e-U_c curve were observed in two limiting cases: in going over to higher and lower values of U_p. In going over to higher values of U_p the change in the I_e-U_c curve is relatively minor (see Ref. 4).

Changes in the energy distribution with changes in U_p are particularly evident in the

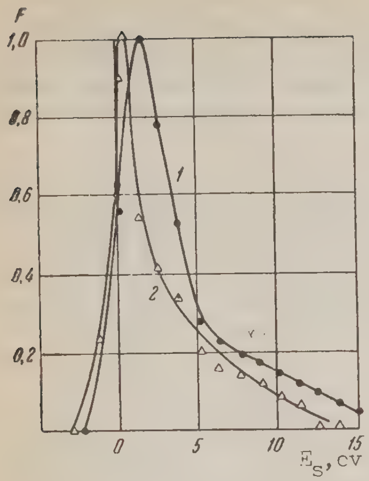

Fig. 14. Distribution in energy of secondary electrons for mica sample No. 2: 1) U_p = 150 v, 2) U_p = 400-1500 v.

region of low values of primary energy. At low values of U_p, for dielectrics the maximum corresponding to true secondary electrons is relatively wide and located at a value of U_c on the order of a few electron volts. Thus in the case of NaCl, with U_p = = 50 v the maximum is located at U_c = 2.5 ev, while the half-width of the maximum equals 2.5-3 ev. Values of the same order of magnitude were obtained for the other investigated dielectrics.

As U_p is increased, the width of the maxima begins to decrease and at the same time the maxima shift to the side of lower energies. This is clearly seen in Fig. 14 for mica and in Fig. 15 for NaCl. With further increase in U_p the position and width of the maximum for NaCl remain constant. The same thing is true for mica. The data on position and width of the maxima for NaCl and mica are summarized in Table 2.

The relatively small displacement of the maxima at large values of U_p compared with that previously noted is apparently due to the contact difference of potential inasmuch as the curves were recorded in different set-ups. In a series of control experiments on the same set-up the position of the maximum for NaCl remained unchanged at U_p greater than 200 v. It follows from the cited data that the distribution in energy of secondary electrons for dielectrics differs from that for metals.

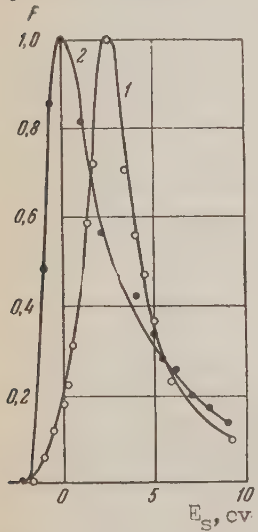

Fig. 15. Distribution in energy of secondary electrons from NaCl sample: 1) U_p = 30 v, 2) U_p = = 100 v.

Table 2

Position and width of maxima in the distribution in energy curves for secondary electrons from NaCl and mica at different values of U_p

Substance	U_p, v	Value of U_c corresponding to the maximum	Half-width of maximum, ev
NaCl	30÷50	—2,5	3,0
	100	0,0	3,5
	200	0,0	2,8
	400÷1800	—0,4	1,8÷1,4
Mica	150	—1,5	4,3
	400÷1600	—0,4÷0,5	1,9÷2,3

1. The distribution in energy of secondary electrons from metallic targets is independent (within the limits of the experimental error) of the primary electron energy in a wide range of primary energy values (for nickel from 18.5 to 1600 v). The distribution curves for dielectric targets change noticeably with U_p in the region of small values of U_p (approximately 200-400 v) and to a lesser extent in the region of high primary energies (beginning from 1600 v).

2) Comparison of the secondary electron energy spectra for metals and dielectrics obtained under identical conditions for medium values of U_p shows that the maximum pertaining to true secondary electrons is appreciably narrower for dielectrics as compared with metals. This is clearly evident from Fig. 13 from which it can be seen that the half-width of the maximum for nickel equals approximately 10 ev, whereas for NaCl the half-width equals about 1.4 ev.

Kollath[21] noted that the maximum corresponding to true secondary electrons emitted by a cesium antimonate cathode is appreciably more pronounced than the maxima for a number of metallic emitters studied by this investigator. Our ex-

---

U_c = collector (retarding) potential. Translator periments showed that this is the case for all the investigated dielectric targets and also for non-degassed metallic targets. From this it may be concluded that a narrower (as compared with metals) maximum of the distribution curve is a common attribute of non-metallic targets.

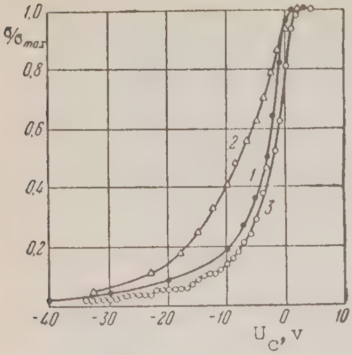

Fig. 16. Characteristic curves for nickel and NaCl samples (at U_p = 100 v): 1) nickel sample before heating, 2) nickel sample after heat treatment, 3) NaCl sample.

3. At medium values of U_p the most probable energy of the secondary electrons emitted by metallic targets is of the order of several electron volts (for example, about 4 ev for nickel), while in the case of dielectric targets the speed of most secondary electrons escaping from the emitter is close to zero.

The difference between the distribution in energy curves for metals and dielectrics diminishes and the curves for metals approach those for dielectrics when the surface of the metallic target is not clean.

The energy spectrum of secondary electrons emitted by metallic targets depends appreciably on the condition of the surface of the target. The effect of contaminants is particularly strong at relatively low values of U_p. The curves for a nickel target before and after heating for 10 hours at 1000° are juxtaposed in Fig. 16. After degassing or cleaning of the target surface the curve is displaced to the side of higher energies.

The curve for the distribution in energy of secondary electrons obtained by differentiating curve 1 of Fig. 16 for a non-degassed nickel sample is shown in Fig. 17. It will be seen that the maximum corresponding to true secondary electrons is located at a value of $U_c \approx 1$ ev and that the maximum is relatively narrow. It will be readily noted that this energy spectrum is very similar to those for dielectrics (Fig. 16, curve 3).

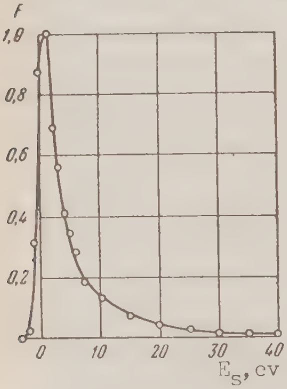

Fig. 17. Distribution in energy of secondary electrons from a non-degassed nickel sample (U_p = 100 v).

In discussing the energy spectra of secondary electrons emitted by metals we must bear in mind that in all probability the laws governing the scattering of low energy electrons in matter differ from those applying to high energy electrons. It may be assumed that at low energies the scattering is characterized by spherical symmetry and that in most cases the energy of colliding electrons after the interaction will be equal to half the sum of their energies prior to the encounter. This hypothesis has been advanced in our earlier contribution[20] and subsequently substantiated by the calculations of Wolf[22].

In the light of the above hypothesis one can explain the shift of the maximum in the distribution in energy curve to the side of higher energies in the region of small values of U_p in metals: the energy imparted by the primary electron to the secondary electron will increase with increasing U_p. The shift of the maximum with increasing U_p will continue to the point where the electron energy transfer law changes. From this viewpoint and in the light of the experimental data, it may be assumed that the electron energy transfer law changes at an energy level of about 30 v ($U_p + W_a$). We note that a result of his calculations Wolf came to the conclusion that the change should occur at an energy on the order of 50 v.

The hypothesis also helps explain the energy independence of the distribution in energy of secondary electrons emitted by metallic targets in a wide range of primary energies. When a primary electron of medium energy interacts with a

---

U_c = collector (retarding) potential. Translator.

lattice electron only a small part of the energy is transferred to the generated secondary electron. This slow secondary electron in turn also interacts with lattice electrons. Using the common notation for energy levels in metals, we can write for the most probable energy of the electrons after interaction:

$$eU = \frac{\mathcal{E} + W_i + W_a}{2} \tag{12}$$

where $\mathcal{E}$ is the energy acquired by the secondary electron from the primary one. For the secondary electron to be able to emerge from the metal after interaction with a lattice electron the energy transferred to it by the primary electron must satisfy the condition $\mathcal{E} > 2e\varphi$ (where φ is the work function).

If the secondary electron receives from the primary an amount of energy inferior to 2 $e\varphi$, then an elastic collision with a lattice electron will "eliminate both partners from the game", i.e., preclude escape of this secondary electron. In view of this, the increase in depth of genesis of secondary electrons incident to an increase in U_p will only alter the number of escaping electrons but will not change their energy (assuming that the mean energy transferred by a primary electron to a secondary one is, in the first approximation, independent of U_p at small values of U_p).

We must therefore conclude from the fact that the position of the maximum is independent of U_p that most secondary electrons receive from the primary an energy lower than 2 $e\varphi$, i.e., inferior to about 10 ev in nickel.

If the above assumption is valid, it must be admitted that the curve for distribution in energy of secondary electrons, or at least the part of it corresponding to slow true secondary electrons, also characterizes the distribution in energy of secondary electrons as produced inside the metal, with the difference that the electron momentum component normal to the surface is smaller than the initial value by the amount of energy expended on overcoming the potential barrier W_a.

Thus we feel that the distinctive characteristics of secondary electron emission from metallic targets at not very low primary energies (i.e., the relatively low values of σ, the relatively high energy of the secondary electrons and the primary energy independence of the secondary electron spectrum) are explained by the fact that the dominant role in the process of electron emergence is played by the decrease in the number of electrons, while the energy loss of the escaping electrons is negligible. The secondary emission coefficient σ for metals is not large because the number of interactions with the electrons of the conduction band is comparatively great. The emerging electrons are characterized by higher energies than in the case of dielectrics because in this case energy losses play a minor role. For the same reason the secondary electron energy spectrum does not change in a wide range of primary energy values.

The mechanism of emergence of secondary electrons in dielectrics differs from the mechanism in metals. Interaction of the secondary electrons with electrons of the conduction band, which in the case of metals is a decisive factor, can be neglected in the case of dielectrics. In dielectrics the predominant role is played by interactions with phonons and lattice defects. As a result of these interactions the number of escaping secondary electrons may be reduced both due to absorption of the electrons and to reduction of their energy.

In the case of crystalline dielectrics, at low primary energies the distribution in energy of secondary electrons approaches, to a certain extent, the distribution for metals. With increasing U_p, i.e., with increasing depth of penetration of the primaries and consequently increasing depth of emergence of the secondaries (inasmuch as $x_0 < \xi$), the proportion of slow electrons escaping increases with U_p. The change in the secondary electron spectrum in this case indicates that in dielectrics (in contrast to metals) there occur interactions in which the energy of the secondary electron is altered. Such interactions can, for example, be collisions with phonons. At medium primary energies the secondary electron energy spectrum in dielectrics, as in metals, is independent of U_p. From this it was concluded in Ref. 4 that the predominant role here is played by absorption of secondary electrons. This conclusion would be correct if any law except the linear obtained for slowing down of the primary electrons. If the linear law obtains then with $x_0 > \xi$ the secondary electron spectrum should not change inasmuch as the emission occurs from one space zone and a number of electrons excited at different depths does not vary.

However, whereas in the case of mica changes in the secondary electron spectrum continue up to a value of U_p corresponding to the maximum in the $\sigma = f(U_p)$ curve, which is in agreement with the above hypothesis, the data for NaCl would appear to invalidate it. The variation of the spectrum for NaCl continues to several hundred volts, while saturation value of σ is attained appreciably later. Hence it must be assumed that either the limiting depth of emergence of secondary electrons from NaCl does not exceed x_0, corresponding to approximately 200 ev, or there exists yet another mechanism influencing the escape of secondary electrons. At present we do not have sufficient data to resolve the question.

The observed decrease in a relative number of fast electrons at high values of U_p may be explained on the assumption that the square law for the slowing down of primary electrons comes into effect at these high values of U_p; in consequence, with increasing U_p there occurs a redistribution in the relative number of secondary electrons produced at different depths and with it an increase in energy losses. This is a second order effect and hence the experimentally observed change in the secondary electron spectrum is minor.

The difference in the distribution in energy of secondary electrons for metals and dielectrics at medium values of U_p is due to the fact that in the case of dielectrics there emerge from the emitter electrons which have already lost part of their energy (which is not the case in metals).

We would like to suggest that the differences between the secondary emission characteristics of metals and dielectrics (in metals σ is small, while the energy of the secondary electrons is relatively high; in dielectrics σ is large, while the energies of the secondary electrons are low) are partially explained by the above mentioned difference in the conditions of emergence of the electrons.

We have not touched here on the possible role of impurities and lattice defects. Under certain conditions, i.e., at sufficiently high impurity concentrations, the predominant role is apparently played by electron absorption as is evinced by the fact that σ is virtually independent of the temperature in such cases (see Ref. 3). As was noted above, a very high concentration of lattice defects affects not only the conditions of escape of the secondary electrons but of their excitation as well.

Conclusions

1. The measuring procedure in determining the secondary-electron emission from non-metallic materials is important where investigation of the effect is concerned. We have developed a method for measuring secondary emission which excludes the secondary effects arising incident to bombardment of non-metallic targets: surface charge and changes in the composition or structure of the emitter.

2. As regards the secondary emission characteristics, specifically as regards the form of the σ vs U_p curve, the investigated materials can be divided into three groups: a) crystalline dielectrics with a high concentration of impurities and lattice defects and amorphous dielectrics, b) crystalline dielectrics with a relatively low concentration of defects and c) metals. Thus the emission characteristics of dielectrics are related to their composition or structure.

3. Widdington's law for the slowing down of primary electrons may be said to apply to all materials only at high primary energy values. At medium and low values of U_p other approximations are indicated.

4. In the case of very slow electrons (under ~30 ev) moving in a metal the most probable interactions of these electrons with conduction electrons are interactions as a result of which the energy of both electrons will equal half the sum of their energies prior to the encounter.

This may serve to explain a number of the distinctive characteristics of secondary emission from metals: a) the existence of an emission threshold equal to the work function φ[20], b) the increase in the relative number of fast electrons with increasing U_p from φ to about 15 v and c) the invariance of secondary electron spectrum in a wide range of primary energies.

5. In the range of medium primary energies the law for the slowing down of the primaries apparently differs in all three groups of materials. In the dielectrics of the first group the slowing down law is described or at least approximated by Widdington's formula. To describe the emission of crystalline dielectrics one must first use the linear slowing down law and assume that it subsequently transforms to the square law with increasing primary energy. Lastly metals occupy an intermediate position between the two groups of dielectrics.

6. The invariance of the secondary electron spectrum in a wide interval of primary energies and the relatively high values of the secondary electron energy in the case of metals indicate that the secondary electrons emerge from metallic emitters without undergoing a loss of energy.

In the case of crystalline dielectrics changes in the secondary electron spectrum continue up to primary energies of the order of several hundred volts and the low secondary energies at large values of σ indicate that in dielectrics secondary electrons undergo energy losses prior to emergence.

"M.I.Kalinin" Leningrad Polytechnical Institute

References

1. A.R.Shul'man & V.L.Makedonskii, Zhur. tekh. fiz., 22, 1542 (1952).
2. O.Chachenberg & W.Brauer, Fortschr. d. Phys., 1, 439 (1954).
3. A.R.Shul'man, V.D.Makedonskii & I.D.Iaroshetskii, Zhur. tekh. fiz., 23, 1152 (1953).
4. A.R.Shul'man & B.P.Dement'ev, Zhur. tekh. fiz., 25, 2256 (1955).
5. A.R.Shyl'man, Zhur. tekh. fiz., 25, 2150 (1955).
6. L.N.Dobretsov, A.S.Titkov, Doklady AN SSSR, 100, 33 (1955).
7. V.N.Lepeshinskaia & Iu.L.Kleiman, Trudy LPI (Transactions of Leningrad Polytechnical Institute), 181, 195 (1955).
8. N.D.Morgulis & N.G.Nakhodkin, Doklady AN SSSR, 94, 1029 (1954).
9. I.M.Bronshtein & T.A.Smorodina, Zhur. eksp. i teor. fiz., 27, 215 (1954); 29, 495, 500 (1955).
10. A.J.Dekker, Phys. Rev., 94, 1179 (1954).
11. E.Baroody, Phys. Rev., 78, 780 (1950).
12. E.Baroody, Phys. Rev., 86, 915 (1952).
13. A.Ia.Viatskin, Zhur. eksp. i teor. fiz., 20, 547, 557 (1950).
14. J.Marshall, Phys. Rev., 88, 416 (1952).
15. A.Ia.Viatskin, Zhur. tekh. fiz., 25, 1155 (1955).
16. A.Becker, Ann. Phys., 78, 228 (1928).
17. N.D.Morgulis & A.T.Nagorskii, Zhur.eksp.i teor.fiz., 8, 1159 (1938).
18. B.I.Diatlovitskaia, Doklady AN SSSR, 63, 641 (1948).
19. M.M.Vudynskii, Zhur. tekh. fiz., 9, 1583 (1939).
20. A.R.Shul'man & E.I.Miakinin, Doklady AN SSSR, 91, 1075 (1953).
21. R.Kollath, Ann. Phys., 1, 357 (1947).
22. P.A.Wolf, Phys. Rev., 95, 56 (1954).

DISCUSSION

P.G.Borziak: Would you please clarify the difference between the secondary electron energy distributions for metals and dielectrics?

A.R.Shul'man: In the case of metals we have high losses as regards number of particles (electrons) and small losses as regards the energy of the particles emerging into the vacuum; for dielectrics the opposite holds.

P.V.Timofeev: Did you observe changes in the charge on the target with changes in the current density?

A.R.Shulman: The charge depends on the capacity of the target; in our case the charge was small as evinced by invariance of the pulse shape. The computed absolute value of the charge did not exceed 0.1 v which is entirely permissible.

U.A.Arifov: How good was the reproducibility of the dependence of the secondary emission coefficient on the temperature for different types of glass?

A.R.Shul'man: The reproducibility for a series of samples of the same type of glass was satisfactory. It was not checked for other types of glass.

K.B.Tolpygp: Would the curves for the dependence of the secondary emission current on the retarding potential in the region of the primary energies be similar if these curves were normalized?

A.R.Shul'man: We did not try normalizing the curves.

A.A.Mostovskii: Do the relative positions of the elastic and inelastic maxima in the retarding potential curve remain constant at different primary energy values?

A.R.Shul'man: I do not know.

A.A.Zhigarev: How do you explain the presence of fine structure in the curve for $\sigma = f(U_p)$?

A.R.Shul'man: It is apparently to be explained by electronic transitions from lower bands.

N.D.Morgulis: Did you carry out measurements on single crystals?

A.R.Shul'man: The alkali-halide salt measurements were made on single crystals. The aluminum oxide was investigated in the form of a cataphoretic film.

G.V.Spivak: How did the pulse repetition rate and shape of the pulses affect the results?

A.R.Shul'man: We used single pulses. This obviated the effect of target charge. The width of the pulse front amounted to about 15% of the pulse duration.

G.V.Spivak: How do you explain the invariance of σ as a function of the temperature for glass?

A.R.Shul'man: By the presence of a great number of lattice defects which of course do not depend on the temperature.

D.V.Zernov: How do you explain the differences between your evaluation of the role of energy losses by primary electrons in metals and dielectrics and that given by L.M.Dobretsov?

A.R.Shul'man: This may be attributed to differences in points of view. In metals the electrons undergo interaction with the electrons of the conduction band; the energy loss in each interaction is appreciable. In dielectrics the secondary electrons interact either with phonons or lattice defects; the energy loss per interaction is smaller but the number of interactions is greater.

K.B.Tolpygo: It seems to me that there is another explanation for the difference in the variation of the current for metals and dielectrics. The difference stems from the fact that in dielectrics, in addition to phonon losses, there are also discrete losses for the formation of pairs or excitons.

N.L.Iasnopol'skii: All present theories are based on the Born approximation. This is not applicable in the region where experimentors are now working. In view of this, the researches of B.I.Diatlovitskaia, who studied the energy loss law in the 100-1000 ev interval, are of great interest.

REFLECTION OF SLOW ELECTRONS FROM PURE METAL AND COATED METAL SURFACES

(Abstract)

-D.A.Gorodetskii

The value of the coefficient of reflection of slow electrons from a metal surface depends on the form of the potential barrier at the metal-vacuum interface. By studying the dependence of the reflection coefficient on the primary electron energy we can judge of the variation of the potential in the vicinity of the surface of the metal and of changes in the potential barrier incident to increase or decrease of the work function. Such investigations are of value in connection with development work on metal-film coated cathodes.

We investigated the coefficient of reflection of slow (2-10 ev) electrons from the surface of tungsten subjected to intense heating under vacuum, from layers of barium and silver vacuum sputtered on tungsten and from tungsten coated with thin films of barium and oxygen. The target was bombarded with a beam of slow electrons produced by an electron gun. The reflected and secondary electrons were caught by a collector surrounding the target. The coefficient of reflection was determined from the curve characterizing the current on the collector. The focusing of the primary beam was checked by special experiments with a sectioned target.

Particular attention was paid to cleanliness of the investigated surfaces. The experiments were carried out in sealed-off tubes at pressures of $3\text{-}5\cdot10^{-9}$ mm Hg as determined by an Alpert ionization gage. Measurements of the absorbed part of the residual gas by the flash method yielded pressure values of the order of $10^{-10}\text{-}10^{-11}$ mm Hg.

It was found that the coefficient of reflection of electrons of energies under 4 ev is very sensitive to the state of the metal surface. Formation of a film of residual gas on the surface of the metal increases the reflection by a factor of 2-3; at the same time there is no significant change in the work function. For this reason the experiments were carried out with the tungsten target heated to 1700°K or immediately after sputtering on the barium or silver coating. The results of these measurements were in agreement with the results obtained with a cold target immediately after heating. In view of this and the results of direct measurements of the time of formation of absorption films by the flash method it can safely be asserted that we were dealing with clean surfaces.

The variation of the reflection coefficient with the primary electron energy for pure tungsten does not agree with the theoretical curve computed on the basis of the potential corresponding to the image field. The reflection grows with increasing energy. Inasmuch as the specimen was polycrystalline we felt that the presence of spot fields could affect the result; we therefore made an attempt to crystallize a tungsten ribbon by appropriate heat treatment. Although we succeeded in increasing the size of the tungsten crystals appreciably this had no noticeable effect as regards the variation of the reflection coefficient with primary energy. We plan to make measurements on a tungsten single crystal in the near future.

When a heavy coating of barium or silver is deposited on the tungsten target the variation of the coefficient of reflection with the primary electron energy changes markedly: there is a decrease in reflection with increasing energy, which is in qualitative agreement with theory.

The application of a thin layer of barium on the tungsten lowers the work function and simultaneously increases the reflection in the region of low energies. The coefficient of reflection for slow electrons passes through a maximum as the degree of covering of the surface is increased. This maximum lies in the coating interval corresponding to a minimal work function. This result is in agreement with the hypothesis regarding the building up of a maximum potential barrier as the work function decreases. Application of an oxygen film on the surface of the tungsten leads to an increase in the work function by 1.7 ev and an increase in reflection. The variation of the coefficient of reflection with the primary energy, however, is not altered.

At a certain primary electron energy there appears among the electrons leaving the target a group of electrons with energies below the primary. It was noted that the energy at which this group appears coincides with the work function and varies with the value of the latter. Apparently this effect marks the secondary emission threshold.

"T.G.Shevchenko" Kiev State University

DISCUSSION

I.M.Bronshtein: How many anodes did your electron gun have?

D.A.Gorodetskii: One anode; after passing this the electrons were slowed down by a retarding field.

I.M.Bronshtein: Did you measure the diameter of the electron beam?

D.A.Gorodetskii: No, but we carried out measurements with a second anode which made it possible to evaluate qualitatively the diameter of the beam. It was found that this had an acceptable size.

I.M.Bronshtein: How do you explain the divergence between the results obtained by A.R.Shul'man and yourself?

D.A.Gorodetskii: It may be because the vacuum conditions were inferior in Shul'man's experiments.

I.M.Bronshtein: Your curve for the coefficient of reflection is similar to the corresponding curve for non-degassed molybdenum target obtained by A.R.Shul'man.

D.A.Gorodetskii: Shul'man obtained a reflection coefficient four times greater than ours. It is better to compare our results with the data of Mayers.

I.M.Bronshtein: At a primary electron energy of 10 ev you found that the fraction of electrons reflected is 0.3. This seems very high. What values did you find for other metals?

D.A.Gorodetskii: For silver the value of the coefficient of secondary electron emission was about 0.15.

K.B.Tolpygo: Why is there an increase in the coefficient of reflection with the appearance of an oxygen film? What is the form of the barrier on the metal-adsorbed film-vacuum boundary?

D.A.Gorodetskii: Oxygen increases the work function. The form of the barrier for the O-W system is not known.

CERTAIN ANOMALOUS CHARACTERISTICS OF THE SECONDARY-ELECTRON EMISSION OF MAGNESIUM ALLOYS

-V.N.Lepeshinskaia

Studies of the distribution in energy of secondary electrons can yield valuable information on the mechanism of secondary emission. The distribution in total energy curves are usually obtained by the classical method of a retarding field in a spherical capacitor, proposed by Lukirski.[1] However, the results obtained under these conditions can be regarded as reliable only provided the secondary electron velocities are not distorted in the process of measurement by external factors, primarily surface charge. Hence to obtain undistorted emission curves for dielectrics one must work under conditions insuring the absence of charge, for example, by the method of single pulses.[2] In this case if one uses pulses of a few microseconds duration the emission curves (current-voltage curves: $I_s = f(V_c)$) level off, i.e., attain a saturation value, at relatively low collector potentials.

The emission-collector potential curves for metals can also be recorded under a static regime, in which case the beginning of saturation is connected only with the contact difference of potential between the collector and target.

Thus both for metals and for dielectrics the true distribution in energy of the secondary electrons can be obtained by differentiating the emission curves.

In studying the secondary emission of alloys of copper with magnesium (and also of Ag-Mg and Al-Mg alloys) which have a high coefficient of secondary emission after appropriate treatment, it was found[3] that the emission curves recorded under static conditions at low current values level off only at relatively large collector potentials. The point of beginning of saturation was displaced to higher potentials in proportion to the magnitude of coefficient of secondary emission σ of the given specimen and at $\sigma_{max} = 12$ attained a value of $+V_c = 40$ v. It was found that the emission curves did not depend on the primary current density, which could be varied by two orders of magnitude, and were also independent of the primary electron energy in the range from 300 to 1200 ev. Heating of the target at the time of measurement to 400° made it possible to obtain normal emission-voltage curves with the beginning of saturation at about 1-1.5 v regardless of the value of σ_{max} characteristic of the specimen (the magnitude of σ_{max} was not affected by the heating). It must be noted that the process in all cases was reversible; when the target was cooled, the point of beginning of saturation again moved into the region of higher collector potentials. Varying the dimensions of the target also affected the emission curves: increasing the target size resulted in displacement of the saturation point to the side of larger values of $+U_c$.

It might be supposed that charges, distorting the experimental curve, develop on the activated surface of the alloy (which apparently consists of magnesium oxide) under the static measurement conditions. In order to clarify this matter we undertook the studies reported on in the present article. We recorded the emission curves for an alloy of copper with magnesium characterized by different degrees of activation (i.e., having different values of σ_{max}) by four different methods: the static, the periodic pulse, the single pulse and the thermal (heated target) method.

The measurements were carried in a spherical capacitor with a 170 mm diameter collector and in most cases with a 15 mm diameter target. A diagram of the setup is shown in Fig. 1. The square waveform pulses of 2.5 microsec duration were supplied by an I-26 pulse generator. The primary and secondary current pulses were measured with an EO-6 cathode-ray oscillograph with a driven sweep. The frequency of the periodic pulses was 50 cps. During the single-pulse measurements any residual charge was dissipated by heating between measurements.

The curves obtained by all three methods of measurement including the single

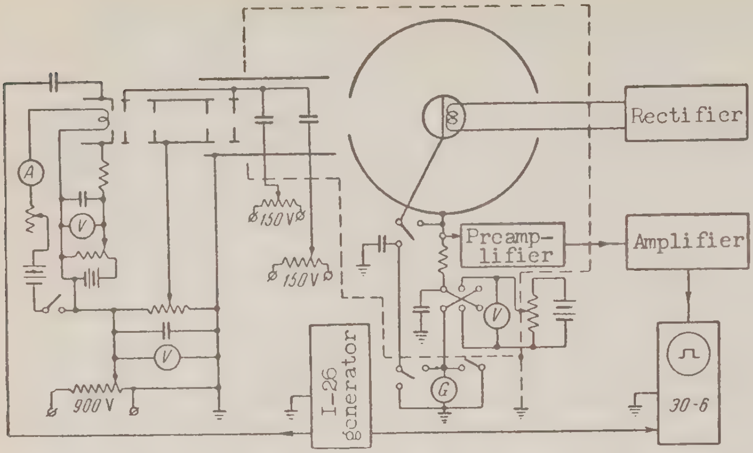

Fig. 1. Diagram of set-up allowing of static or pulse measurements.

pulse one are similar, with saturation at high values of $+V_c$. The location of the saturation point in all cases depended on the value of σ_{max} of the specimen. The curves for the $\sigma_{max} = 4$ and $\sigma_{max} \approx 7$ are shown in Fig. 2.

As in the previous investigation[3] the secondary electron emission spectrum was found to be independent of the primary current density and of the primary electron energy.

With the thermal method of measurements the curves level off at +1 v, the secondary electron emission coefficient σ remains unchanged. Cooling of the specimen led to reappearance of the low energy tail.

With a view to determining the invluence of target size, we prepared targets in the form of hollow spheres 6.5, 10, 15, and 20 mm in diameter. Emission curves were recorded by the static and periodic pulse procedures. The spheres were chosen with as nearly equal values of the secondary emission coefficient as possible inasmuch as the influence of σ_{max} on the beginning of saturation is stronger than the influence of target size. As may be seen from Fig. 3, the beginning-of-saturation potential decreases with decreasing target size. Nevertheless the saturation voltage in all cases is fairly high: for example, with $\sigma_{max} \approx 7$ and d = 10 mm saturation is attained only at $V_c = 7$ v.

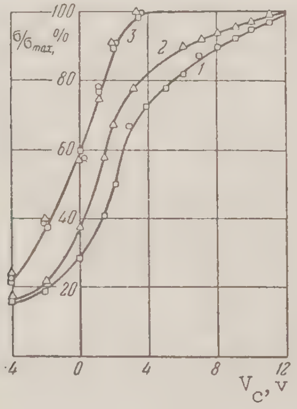

Fig. 2. Curves for $\sigma/\sigma_{max} = f(V_c)$ recorded for Cu-Mg alloy by three methods: 1) periodic 2.5 microsec pulses at a frequency of 50 cps, alloy activated to $\sigma_{max} = 6.7$; 2) static regime, alloy activated to $\sigma_{max} = 6.4$; 3) alloy activated to $\sigma_{max} = 4$. The results obtained under the static regime, with 2.5 microsec periodic pulses at a frequency of 50 cps and with single pulses of the same duration for the $\sigma_{max} = 4$ specimen, all fell on the same curve (curve 3). (V_c = collector potential).

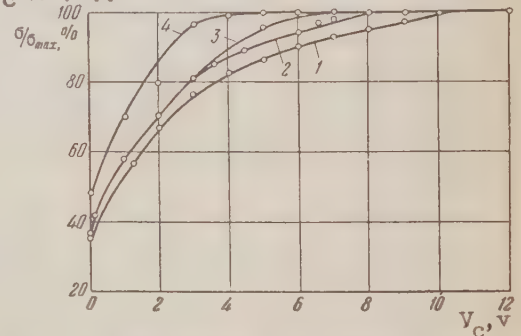

Fig. 3. Influence of target diameter on the emission vs collector potential curves for Cu-Mg alloy: 1) $d_t = 20$ mm, $d_c/d_t = 8.5$, $\sigma_{max} = 6.7$, $V_c = 12$ v; 2) $d_t = 15$ mm, $d_c/d_t = 11$, $\sigma_{max} = 6.15$, $V_c = 9$ v; 3) $d_t = 10$ mm, $d_c/d_t = 17$, $\sigma_{max} = 6.95$ mm, $d_c/d_t = 26$, $\sigma_{max} = 6.0$, $V_c = 5$ v. (t = target; c = collector).

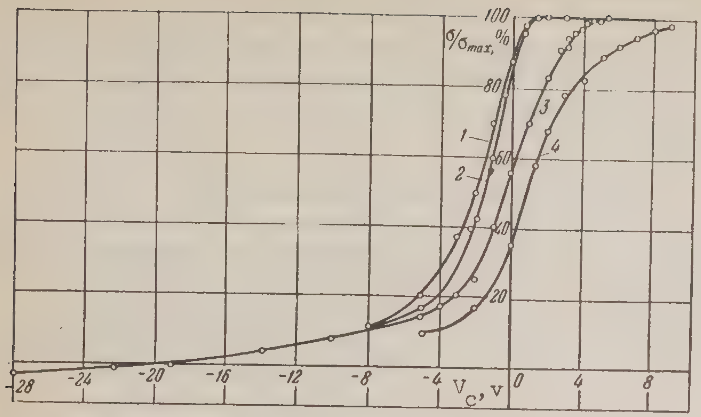

Fig. 4. Control curves showing the variation of σ/σ_{max} as a function of V_c for the Cu-Mg alloy under different conditions: 1) non-activated alloy; 2) alloy activated to $\sigma_{max} = 7.6$, measurements made at 350°; 3) alloy activated to $\sigma_{max} = 4$, measurements at 20°; 4) alloy activated to $\sigma_{max} = 7.6$, measurements at 20°.

In order to explain the experimental results it must be assumed that there exists an external field which holds back the escaping secondary electrons and prevents them from reaching the collector. The experiments with targets of different size furnish direct evidence of this. However it might also be assumed that the distortions of the emission curves are due to a systematic measurement error, for example, to the presence of secondary electrons on the collector, which in our experiments was silver coated.

In order to check this we recorded the control curves for σ/σ_{max} vs V_c shown in Fig. 4. Curve 1 was recorded for the non-activated alloy (when it has purely metallic properties), curve 2 was recorded with the alloy activated to a secondary emission coefficient of 7.6 and heated to 350°. Both curves reached saturation value at $V_c = 1$ v. This is evidence of normal operation of our experimental set-up and the absence of any external factors affecting the position of the saturation points. The same alloy activated to $\sigma_{max} = 7.6$ yields curve 4 at room temperature. Curve 3 was recorded with a specimen activated to $\sigma_{max} = 4$ at room temperature and was extended to appreciable negative collector potentials; it will be seen from this curve that the number of tertiary electrons is small.*

The fact that the curves recorded by the single pulse method coincide with the static regime curves indicates that there is no surface charge under the beam.

It might be supposed that the activated alloy surface has a spotty microstructure with different sections characterized by different values of the work function. This would give rise to a potential "relief" which would be present even when the target is not irradiated. In this case, when the target is bombarded with primary electrons, the secondary electrons escaping at points where the work function $\varphi < \overline{\varphi}$ emerge into a field tending to retain them at the surface. This effect would explain the independence of the current-voltage characteristics as regards primary current strength and their dependence on the target size.

The appreciable influence of the magnitude of σ, i.e., of the degree of activation of the surface, on the character of the current-voltage curve suggests that the potential microrelief is altered in the process of activation. It is more difficult to explain the influence of temperature and particularly the reversibility of the effect. We might assume that in the process of heating there occurs a migration of the magnesium atoms over the surface leading to a more uniform distribution, with the result that the retarding potential of the spot fields disappears. However, this hypothesis does not explain why the original curve is reproduced when the temperature is reduced to the initial value (20°).

---

*Note added in proof. Supplementary experiments carried out after the close of the conference indicated that the number of tertiary electrons actually was not very small and their presence may result in distortions of the emission curves.

Before one can attempt to interpret the variation of the experimental curves, it is essential to obtain additional experimental data on the structure of the surface layer and its variation with temperature. The present investigation was carried out in collaboration with B.A.Golubev, student, in the Department of Electronics of Leningrad Polytechnic Institute.

References

1. P.I.Lukirskii, ZhRFKhO (Journal of the Russian Physical Chemical Society) (Physics Section), 7, 5/6, 459 (1925).
2. A.R.Shul'man, V.L.Makedonskii, Zhur. tekh. fiz., 22, 1540 (1952).
3. V.N.Lepeshinskaia, V.M.Tumorin, Zhur. tekh. fiz., 24, 1933 (1954).

SECONDARY-ELECTRON EMISSION OF NICKEL-BASE ALLOYS

- B.S.Kul'varskaia

Introduction

For a long time the mechanism of emission from alloys has remained obscure and searches for new efficient emitters have been carried out by the empirical method of testing series of alloys with new components.[1]

Now, however, electron diffraction analysis of the surface structure of emitters of Ag-Mg, Cu-Be and Cu-Mg alloys, which has yielded evidence of the formation of oxide layers on the surface of the oxidized (activated) alloys,[2-5] has made it possible to determine the role played by the individual components.

One of the alloy components, the so-called active component (Mg, Be or other), present in the alloy in a minute amount and having a strong affinity for oxygen, upon activation of the alloy diffuses to the surface and combines with oxygen with the resultant formation of a thin oxide layer, whose properties determine the emission. The second component, present in a far greater amount in the alloy, plays the role of a medium, which, in order to obtain an efficient emitter, must not hinder diffusion of the active component to the surface and its oxidation.

The new understanding of the mechanism of formation of efficient emitters has made it possible to elucidate and specify the basic requirements that must be satisfied by the alloy components in order to obtain new emitters having desirable characteristics, specifically good air- and temperature-stability.

In the present article we shall attempt to formulate these requirements and also list the secondary emission characteristics of a number of emitters of nickel-base alloys satisfying these requirements.

Certain physical-chemical characteristics of alloy components determining the stability of the emitter

1. In developing alloy emitters resistant to the influence of residual air one must select an active component which in addition to having a high affinity to oxygen also forms an oxide stable in air. Among the metals having stable oxides are aluminum, beryllium and chromium and a few others.

As is known the thinnest film of oxide (~50 Å) on the surface of these metals can effectively protect the metal from further oxidation; this protective property is not exhibited, for example, by the oxides of barium, calcium and cerium, even though in themselves these oxides are stable compounds.

Hence it is logical to use beryllium, aluminum, zirconium and similar metals as the active components in developing air-stable emitters.

2. In developing temperature-stable emitters, one must utilize high melting point components having the lowest possible vapor tension at the proposed operating temperature. From this point of view, Cu-Be alloy and particularly Ni-Be alloy emitters must be more temperature-stable than emitters of magnesium alloys inasmuch as the vapor tension of beryllium is much lower than that of magnesium. Consequently, destructive evaporation of the active element begins at a much higher temperature for beryllium alloys as compared with magnesium ones.

3. The results of our electron diffraction analyses show that in the process of prolonged electron bombardment the oxide coating is destroyed due to dissociation of oxide molecules into the metal and gaseous oxygen. Consequently, free metal accumulates in the surface layer in the process of bombardment and hence the more firmly the metal atoms are held by the oxide coating the more stable will be the emitter of the given alloy. For if the free metal is retained in the surface layer, regeneration through oxidation by the residual gases is possible.

Inasmuch as the degree to which the free metal is retained depends on the adsorption energy Q, in attempting to develop more stable emitters one should try alloying metals characterized by a maximal value of Q.

As is known, the heat of adsorption Q is given by

$$Q = \frac{1}{2}\sqrt{L_a L_c}$$

where L_a is the heat of the evaporation of the adsorbent and L_c is the heat of evaporation of the adsorbing medium.

Where reliable data regarding the heat of evaporation of the proposed components are not available, approximate calculations can be made by taking advantage of Trouton's rule and using boiling points in °K absolute instead of the heat of evaporation.

Evaluations of the heats of adsorption showed that the value of Q is greater for beryllium layers as compared, for example, with magnesium coatings.

Thus in view of the above described requirements, which should be used as a guide in seeking more temperature-stable and air-stable alloy emitters, it would appear expedient to go from emitters of magnesium alloys (Ag-Mg and Cu-Mg) to beryllium alloys (Cu-Be) and further to emitters of nickel-base alloys: Ni-Be, Ni-Ti, Ni-Zr, etc.

Nickel-beryllium emitters

The first emitters of Ni-Be alloy were prepared by Gille[1] and Matthes[6] in the early 1940ies. More thorough investigations of Ni-Be emitters were carried out only years later by Bobenrieth[7], Millet[8] and the writer[9].

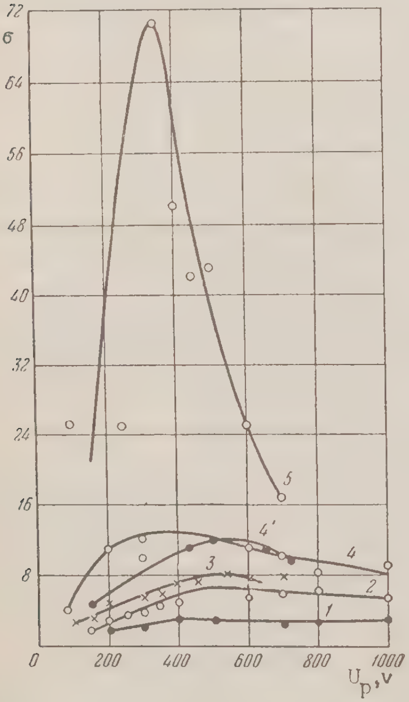

Fig. 1. Variation of the coefficient of secondary emission σ on the primary electron energy for Ni-Be alloy at different stages of oxidation: 1) non-oxidized specimen; 2,3,4 & 5) specimens oxidized to increasingly greater depths.

A distinctive characteristic of Ni-Be alloys is their higher formation temperature as compared with magnesium alloys: the process of formation occurs fairly rapidly (in the course of a few minutes) at ~800°.

In order to determine the optimum value of the coefficient of secondary emission of Ni-Be emitters and to establish the volume of oxygen necessary for activation, we carried out measurements of the secondary emission coefficient σ at different stages of oxidation of the alloy.

A typical series of curves giving the dependence of σ on the primary voltage U_p for Ni-Be alloys at different stages of oxidation is given in Fig. 1. Curve 1 pertains to the initial state of the alloy (prior to activation); curves 2 and 3 pertain to the initial stages of oxidation, stages preceding the attainment of optimum values of σ ($\sigma_{max} = 6.5-8$). After repeat oxidation in the process of which over 10 μg of oxygen are absorbed per cm^2 of the surface the $\sigma = f(U_p)$ curve lies appreciably higher and σ_{max} attains a value of ~12 (curves 4 and 4' for different specimens).

With further oxidation of the alloy there is an appreciable increase in the emission largely due to the Malter effect. Curve 5 in Fig. 1 is for a layer with a maximum coefficient equal to approximately 70 at U_p = 350 v (at U_p = 100 v, $\sigma \approx 25$).

Thus as a result of stepwise formation of Ni-Be alloy emitters, we invariably observe a gradual increase in the value of σ starting from 9-13 at the initial stages of oxidation and a sharp increase of the emission at the final stages of deep oxidation due to the Malter effect.

It will be seen that curve 5 in Fig. 1 has a sharp maximum corresponding to a primary energy of 300 v. The precipitate falling off of the electron current at higher values of U_p may be explained by the fact that fast primary electrons produce an appreciable "induction" conductivity of the surface layer which leads to a reduction of the potential gradient of the electric field in the coating and a consequent decrease of the Malter emission. It may be noted that an analogous character of the secondary emission curves in the presence of Malter emission has been observed by Zernov and Kul'varskaia for KCl films[9].

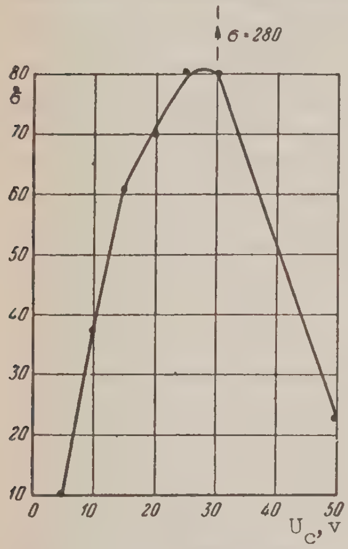

Fig. 2. Variation of the secondary emission coefficient with the collector potential at anomalously high values of σ for the Ni-Be alloy.

The variation of the secondary-electron emission coefficient with the collector potential for the Ni-Be alloy is interesting. For coatings having a value of σ = 9-13, at a collector potential U_c = 60-70 v the emission current attains a saturation value, while in the case of deeper oxidation (specimens with a higher value of σ) saturation is absent and an increase in U_c within certain limits leads to a sharp increase in the value of the emission coefficient. Thus in the case illustrated in Fig. 2, σ attains a value of ~80 at U_c = 30 v (in some cases σ goes up as high as 280). As the collector potential is further increased σ falls off, dropping to 23 at U_c = 50 v. This falling off of σ is apparently due to break down of the active layer on the Ni-Be alloy under the influence of steep potential gradients in the surface layer.

We carried out measurements of the secondary emission as a function of the primary current I_p for coatings having an exceptionally high value of σ. The results of one such series of measurements are shown in Fig. 3. It will be seen that initially the curve falls off rapidly and then beginning with I_p = 1-1.5 microamp becomes almost flat; in the range from 2.0-10 microamp the emission coefficient equals approximately 6.7.

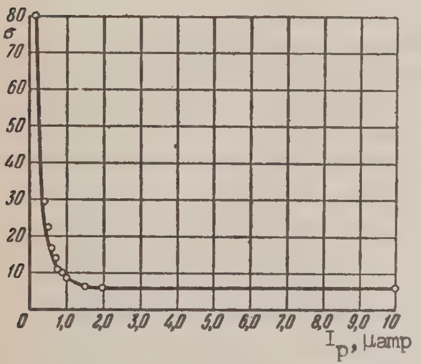

Fig. 3. Dependence of the secondary-electron emission on the primary current at anomalously high values of σ (U_p = 800 v, U_c = 30 v).

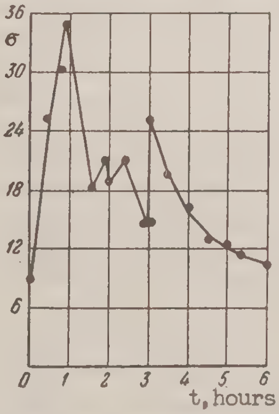

Fig. 4. Curve characterizing the variation in the anomalously high values of σ under prolonged electron bombardment (I_p = 0.1 μa. U_p = 80 v & U_c = 200 v).

The curves for σ as a function of I_p for the Ni-Be alloy are very similar to the curves obtained earlier for [Al]—Al_2O_3—Cs_2O. However, they differ from the corresponding curves for KCl coatings inasmuch as the latter according to Zernov and Kul'varskaia[10] are characterized by a rising section in the interval of I_p values under 0.2 microamp.

The different nature of the variation of σ as a function of U_p, U_c and I_p and the data to be cited below on the inertness of the secondary emission current obtained for Ni-Be alloy at different stages of observation, i.e., for specimens with $\sigma = 9\text{-}13$ and with $\sigma = 70\text{-}80$, indicate that in the former case we have a true secondary-electron emission, while in the latter we have cold emission of electrons from the metallic core.

The curve of Fig. 4 shows the characteristic variation with time of the emission from an Ni-Be alloy specimen subjected to deep oxidation under continuous electron bombardment at $I_p = 0.1$ microamp and $U_p = 80$ v; the initial value of σ (35) after approximately 6 hours continuous bombardment is reduced to 10. It must be noted that after a short rest period (following 3 hours operation), there was observed some increase in σ relative to the last value, after which the emission again fell off.

When an emitter of Ni-Be alloy with an anomalously high value of σ was heated to 800-850°, the secondary-electron emission fell off sharply and σ at these temperatures proved equal to 4-5 ($U_p = 400$ v). However, after cooling to room temperature σ returned to its initial value. In tests involving multiply repeated heating and cooling of Ni-Be specimens with anomalously high values of σ, we invariably observed the reproducibility of the original values of σ. It follows therefore that heating to $\sim 850°$ is not accompanied by any irreversible alterations of the coating.

Prolonged (40 hours) contact with air of a specimen of activated Ni-Be alloy did not result in breakdown of the coating and its secondary emission remained unaffected.

Finally we must mention the inertness of the formation and attenuation of the electron emission of Ni-Be alloys with an anomalously high σ observed when the primary current is switched on. The primary current was initiated by the application of a sinusoidal voltage on the control electrode. With a primary current pulse duration of the order of a fraction of a millisecond (up to 1 msec), the secondary-electron current does not have time to attain its peak value. In the case of longer pulses (over 1 msec) the inertness was not evinced and we observed secondary current pulses of maximum height. It is interesting to note that approximately the same shaping time for the secondary current ($1.3 \cdot 10^{-3}$ sec) was determined by Jacobs et al[12] for the case of MgO coatings having an emission coefficient $\sigma = 70$.

It was established by electron diffraction analysis that the emission of Ni-Be alloy is due to a superficial layer of BeO.

Nickel-zirconium emitters

In view of the very low vapor tension of zirconium, its comparatively high heat of adsorption and the air-stability of zirconium oxide coatings, the use of zirconium as the active component in a nickel-base alloy should yield emitters having temperature-stability characteristics superior to those of beryllium alloys. Below we give the results of our investigations of the secondary-electron emission of specimens of Ni-Zr alloy containing ~2% Zr.

We developed a special activating procedure for these alloys differing from the earlier described activation technique for such emitters by the use of a higher temperature (~900°). The criterion for completion of the activation process, as usual, was the drop in oxygen pressure to a stable value. Initially, we recorded the dependences of σ on U_p for the Ni-Zr alloy at different stages of oxidation. Optimum oxidation results in a coefficient σ_{max} equal to 3.5-4 at $U_p = 800\text{-}1000$ v. With deep oxidation of the Ni-Zr alloy, just as in the case of the Ni-Be alloy, there is a sharp increase in the secondary-electron current due to Malter effect emission. Curve 4 in Fig. 5 illustrates the typical dependence of the anomalously high electron emission coefficients on the primary energy.

Fig. 6 shows the variation of σ with increasing and decreasing U_p for a specimen of Ni-Zr alloy having the anomalously high value of $\sigma \approx 140$ at $U_p = 600$v.

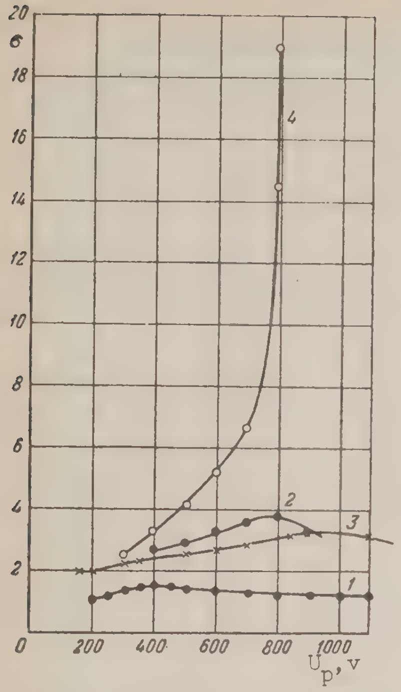

Fig. 5. Dependence of the secondary-electron emission coefficient on primary electron energy at different stages of oxidation of the Ni-Zr alloy: 1) non-oxidized specimen; 2,3 & 4) specimens with increasing depths of oxidation.

Investigation of the temperature-stability of emitters of Ni-Zr alloy showed that heating to 1000° or higher does not lead to any irreversible changes and does not result in appreciable evaporation of the alloy component. Brief exposure to air also has no noticeable effect on the emission characteristic of the Ni-Zr alloy.

Both zirconium oxide and nickel oxide were detected on the surface or activated Ni-Zr alloy specimens.

Nickel-titanium emitters

Like Ni-Zr alloys, Ni-Ti alloys containing ~2% Ti should also have fairly satisfactory stability characteristics.

The technology of activating these alloys differs little from that for activating nickel-zirconium alloys.

A typical secondary-electron emission vs primary energy curve for an Ni-Ti alloy is shown in Fig. 7. Curve 1 pertains to the alloy before oxidation. The maximum secondary emission coefficient for Ni-Ti emitters after oxidation equals 3 at U_p = = 1200 v (curve 2).

With an increase in the depth of oxidation, σ falls off to 1.7-2. When the temperature of a deeply oxidized specimen of Ni-Ti alloy is raised to 700-800°, the emission coefficient rises to approximately 2.2.

Like Ni-Zr alloy emitters, Ni-Ti emitters do not break down when heated to 1000° or even higher.

Nickel-barium emitters

When activated Ni-Ba alloys containing about 2% Ba have a higher secondary-electron emission coefficient than corresponding titanium alloys. The $\sigma = f(U_p)$ curve shown in Fig. 8 is rather flat and has no pronounced maximum.

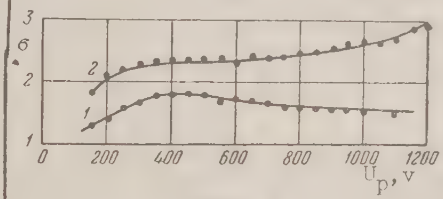

Fig. 7

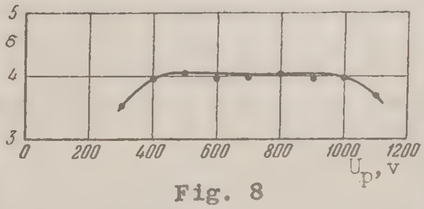

Fig. 8

Fig. 7. Variation of secondary-electron emission coefficient with primary electron energy for Ni-Ti alloy: 1) before oxidation, 2) after oxidation.

Fig. 8. Variation of secondary-electron emission coefficient with primary electron energy for Ni-Ba alloy.

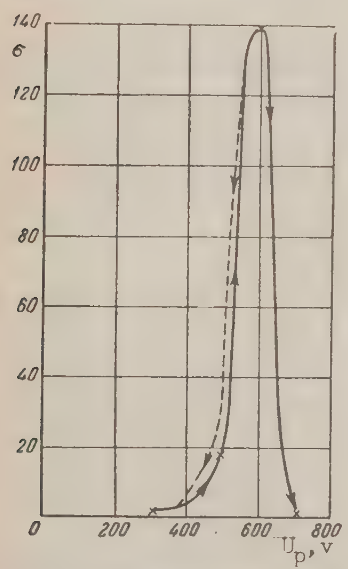

Fig. 6. Dependence of the secondary-electron emission coefficient on primary electron energy for specimens of Ni-Zr alloy with anomalously high values of σ (solid line - variation with increasing primary voltage; dash line - reverse process, shown only from maximum.

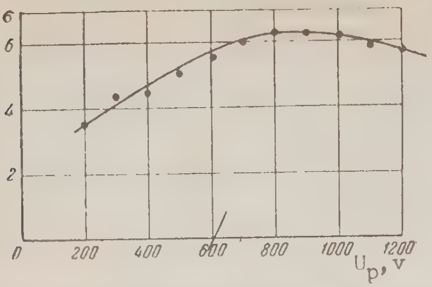

Fig. 9. Variation of secondary-electron emission coefficient with primary electron energy for Ni-Mg alloy.

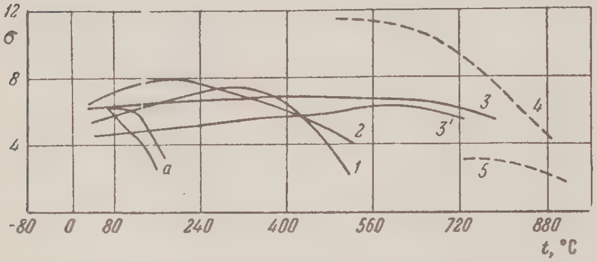

Fig. 10. Temperature dependence of the secondary-electron emission coefficients for the investigated alloys: 1) Ag-Mg; 2) Cu-Mg; 3 & 3') two different specimens of Cu-Be; 4) Ni-Be; 5) Ni-Zr; a) cesium emitter (Ag-O-Cs). The maximum operating temperatures are 960° for Ni-Be & Ni-Mg and 1040° for Ni-Zr.

The highest value of σ obtained for Ni-Ba emitters was ~ 4.2. This alloy was also investigated by Farnsworth and Lun.[11]

In contrast to the case of emitters of Ni-Be and Ni-Zr, the Malter effect was not detected in Ni-Ba alloys.

Nickel-magnesium emitters

We activated our specimens of Ni-Mg alloy containing 1% Mg at 800°. The value of σ_{max} of the activated specimens was 6.3 at U_p = 800 v (Fig. 9).

When an Ni-Mg alloy emitter is heated to 700°, σ_{max} falls off to 3.5. After cooling σ returns to its initial value or sometimes increases slightly.

The activated surface of Ni-Mg alloys acquires a golden hue.

After repeated heating σ increases to 10 and the target becomes bronze colored. No evaporation of Mg at this temperature was observed; this is presumably due to the formation of the compound NiMg and free magnesium in the alloy.

Upon deep oxidation of the Ni-Mg alloy there is observed a noticeable increase in the secondary-electron emission due to the Malter effect.

It must be emphasized that our data on Ni-Ba and Ni-Mg alloy emitters are of a preliminary character.

Conclusions

As our tests have shown the formation of efficient emitters of different nickel-base alloys (magnesium, beryllium, zirconium, etc.) can be realized by the use of a more or less identical activation procedure. In all cases the emitter formation procedure was monitored by the volume of oxygen absorbed by the alloy. The principal difference between the activation procedures used for the different alloys is the temperature range: the temperature limits increase in going from magnesium alloys (lower limit ~300-400°) to beryllium alloys and then to Ni-Ti and Ni-Zr alloys (900°).

From a study of the temperature-stability of emitters of the different alloys and of the nature of the variation of σ with the temperature, it was possible to determine the optimum temperature regions for the operation of the different emitters. It is known that for magnesium alloys containing 3% Mg the limiting operating temperature is about 500-550°; under prolonged heating at higher temperatures the alloy begins to break down due to evaporation of the magnesium. Emitters of copper-beryllium alloys can withstand prolonged heating at ~750°; nickel-beryllium emitters are capable of prolonged operation at 900-1000°; nickel-zirconium emitters at 1000° or higher.

The variation of σ with temperature for some of the investigated alloys is shown in Fig. 10. Curves 4 and 5 (for Ni-Be and Ni-Zr, respectively) are tentative inasmuch as the values of σ only at room temperature and at 800-900° were determined. For purposes of comparison we also give the temperature dependence of σ for cesium emitters (a), the upper operating temperature limit for which is about 180°.

Appreciable heating of the emitter may occur in the process of electron bombardment. In cases when the current load results in heating of the alloy above the indicated limiting temperature, the alloy begins to break down due to evaporation of one of the components.

Where the effect of exposure to air (air-stability) are concerned, beryllium alloy emitters are superior to magnesium alloy ones.

Our measurements of the secondary emission characteristics of a series of emitters of different alloys have shown the validity of the approach to the development of more stable emitters based on analysis of the physical-chemical properties of the individual alloy component and studies of the mechanism of formation of alloy emitters. The stability of efficient alloy emitters increases in going from magnesium alloy (Ag-Mg and Cu-Mg) to nickel-beryllium alloys and on to nickel-titanium and nickel-zirconium alloys.

In view of their appreciable temperature-stability the investigated nickel-base alloys (ni-Be and others) can be presumably employed for the cathodes of low power magnetrons, in which cathodes may be heated to 1000° or higher during operation.

stitute of Radio Engineering and Electronics of the
cademy of Sciences of the USSR

References

1. C.Gille, ZS. techn. Phys., 22, 228 (1941).
2. Oshida Arisumi, J.Appl.Phys., Japan, 12, 269 (1943).
3. G.Honjo, J. Phys. Soc., Japan, 8, 1 (1953).
4. S.Yoshida, J.Takeda, Y.Ygarashi & H.Arata, J. Phys. Soc., Japan, 8, 318 (1953).
5. B.S.Kul'varskaia & B.K.Vainshtein, Trudy Instituta kristallografii (Proceedings of the Institute of Crystallography of the USSR Ac. of Sci., 1955.
6. Y.Matthes, ZS. techn. Phys., 22, 232 (1941).
7. A.Bobenreith, J.Millet & S.Teszner, C.R., 14, 239 (1954).
8. J.Millet, Le Vide, 10, 96 (1955).
9. B.S.Kul'varskaia, Thesis, Institute of Radio Engineering and Electronics of the USSR Ac. of Sci., 1955.
10. D.V.Zernov & B.S.Kul'varskaia, Zhur. tekh. fiz., 16, 71 (1946).
11. H.E.Farnsworth & M.Y.Lun, J. Appl. Phys., 22, 77 (1951).
12. H.Jacobs, J.Martin & F.Brand, Phys. Rev., 85, 441 (1952).

DISCUSSION

A.A.Zhigarev: At what potentials did you observe anomalously high secondary emission?

B.S.Kul'varskaia: At approximately 300 v.

P.V.Timofeev: Did you observe inertness of secondary emission?

B.S.Kul'varskaia: There are data indicating persistence of the emission of Ni-Be emitters.

P.V.Timofeev: What was the temperature of activation and how much oxygen was used in the process?

B.S.Kul'varskaia: The Cu-Mg emitters were activated at temperatures exceeding 400°. At these temperatures MgO is formed on the surface of the alloy; at lower temperatures Cu_2O is formed. The maximum secondary-electron emission is obtained upon absorption of 15-20 ml of oxygen per cm^2 of surface.

ELECTRON MULTIPLIERS FOR RECORDING CORPUSCULAR AND HARD ELECTROMAGNETIC RADIATION

(Abstract)

-T.M.Lifshits

In recording corpuscular as well as ultraviolet and x-ray radiations it is sometimes expedient to employ special electron multiplier tubes with cathodes and emitters of pure metals or alloys.

Such multipliers have a high amplification factor and are not harmed by periodic contact with air and, consequently, make it possible to dispense with special entrance windows in measuring low energy corpuscular radiation. In addition, these multipliers are not sensitive to visible light, which is an advantageous feature where detection and measurement of ultraviolet radiation is concerned. Finally, the extremely low thermionic emission of metal and alloy surfaces at room temperature makes it possible, despite the relatively low sensitivity of metallic cathodes to ultraviolet and x-rays, to record weaker fluxes of ultraviolet and x-rays with a better signal to noise ratio than is possible with conventional photomultipliers.

In the electron multipliers developed by the writer the emitter is made of a Cu-Al-Mg alloy. This emitter is readily activated (the activating procedure consists of heating at 450° in an atmosphere of oxygen) and provides a high and stable value of the secondary emission coefficient $\sigma = 6-7$ at a primary energy $U_p = 300$ v.

The 13-stage multipliers, the amplification factor was of the order of 10^9-10^{11} at an operating potential of 4 kv. The number of "dark" pulses with the multiplier operating at this amplification did not exceed 5-8 per minute.

When air is let into the multiplier, its amplification factor is reduced on the average by half after each 100 hours exposure to air. However, the initial amplification factor is fully reestablished after heating the electrode assembly in vacuum at 450°.

For recording ultraviolet radiation the electrode assembly of the multiplier was enclosed in a suitable envelope with a quartz window and the first electrode was made of carefully degassed platinum or tantalium. The prototype multipliers proved capable of recording ultraviolet radiation in the 3000-1900 A interval. The minimal detectable ultraviolet flux at $\lambda = 2500$ A was $2.5 \cdot 10^3$ photons/sec, which corresponds to an energy of $1.6 \cdot 10^{15}$ watt.

Photomultipliers with cathodes of heavy metals and alloy emitters have been successfully used for recording x-ray radiation, specifically in radiomateriological equipment.

Institute of Radio Engineering and Electronics of the
Academy of Sciences of the USSR

DISCUSSION

V.L.Granovski: What is the greatest current you can obtain at the multiplier output?

T.M.Lifshits: There is noticeable fatigue with 10 ma at the output; hence lower currents are recommended.

V.L.Granovski: What is the spread of the parameters characterizing different multipliers?

T.M.Lifshits: In a lot of one hundred multiplier tubes the amplification factor varied between 10^9 and 10^{11}.

DISTINCTIVE CHARACTERISTICS OF THE PHOTOEFFECT IN CESIUM-OXIDE-SILVER PHOTOCATHODES

- P.G.Borziak, V.F.Bibik & G.S.Kramerenko

1. Although the history of the cesium-oxide-silver (hereinafter "c-o-s") photocathode dates back a full quarter of a century and it has long been widely employed in practice, its nature as a photoelectron emitter is still not definitively established. The view of De Boer[1] was long commonly accepted and still has many adherents among physicists.

However, certain criticisms[2], recent advances in the physics of semiconductors and the results of investigations of the cesium-antimony semiconductor photocathode have furthered the tendency to regard the c-o-s photocathode as a semiconductor one.[3] However, it must be noted that both views are based mainly on analogies and not on direct experimental evidence. Investigators have studied effects in other materials and have then postulated, sometimes arbitrarily, that the observed effects and characteristics are also proper to the c-o-s cathodes and determine its behavior as a photo-electron emitter.

Where De Boer postulated that the c-o-s cathode consists of a film of cesium atoms adsorbed on an "intermediate" dielectric layer and entirely neglected the presence of silver, later investigators[3] postulate that the c-o-s cathode is essentially an impurity semiconductor (cesium oxide) coating and that its photoelectric properties are due to the Cs and Ag impurity atoms. It is assumed in this interpretation that the sensitivity of the c-o-s cathode in the region of its longwave maximum (750-850 mμ) is due to the excitation of electrons from local centers formed by the cesium atoms. Similarly the shortwave maximum in the near ultraviolet (~360 mμ) is assumed to be due to atomic silver serving as the impurity. This view has been argued in a number of monographs and is currently gaining acceptance.

It is known that a c-o-s cathode consists of a mixture of microparticles of silver and cesium oxide. Hence the first step should be to clarify the role of these structural components in the behavior of the photocathode. In both the hypotheses mentioned above it is assumed that the silver particles have no direct bearing on the properties of the photocathode and that the role of silver is confined to that of an atomic impurity in the cesium oxide. In order to determine the part played by each of these structural components in the behavior of the c-o-s cathode, we deemed it desirable first to investigate each of them separately and only then study a cathode composed of them.

2. Separate microcrystalline silver particles can readily be obtained by condensing a small amount of silver vapor on a glass support. By such condensation on glass one can attain a wide range of coating thicknesses ranging from very thin microformations to a continuous, solid film of "bulk metal".[4] In the present investigation we studied some of the optical and photoelectric properties of such films in the ultra-violet region of the spectrum with a view to supplementing the data obtained in the investigation of Ref. 5 for the longer wavelength region. The silver films were condensed on the inner surface of a cylindrical envelopes of uviol (ultraviolet transmitting) glass. The red limit of the photoeffect for silver lies at about 260 mμ, while we were able to use the spectral region up to only $\lambda \approx 250$ mμ. Hence in order to shift the red limit and to approach the actual conditions under which silver particles are present in a c-o-s cathode we investigated films with cesium adsorbed thereon. Control tests showed that the adsorption of cesium has no noticeable effect on the optical properties of the silver film.

First we measured and plotted curves for the optical transparency distribution over the area of the films

$$D = f(l),$$

where l is the distance along the surface of the film in the direction of its thickness gradient from an arbitrarily selected reference point.

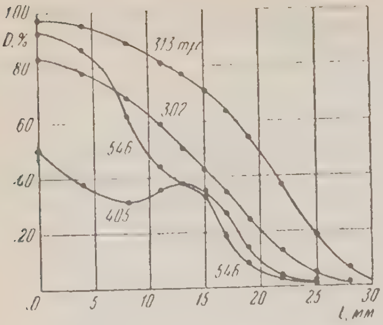

Fig. 1. Optical density distribution $D = f(l)$ over a silver film of variable "thickness" with cesium atoms adsorbed thereon for light of different wavelengths (as indicated in mμ at the curves). The film "thickens" with increasing distance l from the arbitrarily selected reference point.

Typical results of such measurements for a number of wavelengths are shown in Fig. 1. The curve for $\lambda = 405$ mμ has the characteristic shape from which one can readily determine the region at which the transition from a solid film of silver to its dispersed state begins.[4] The anomaly, i.e., the maximum, in the variation of the transparency of the coating or "thickness" of the film with l is associated with this transition from the continuous film to the dispersed state. This maximum in the transparency curve, as Morozov and Butslov[4] showed, disappears for long wavelengths.

It might be assumed that this anomaly is connected with mechanical inhomogeneity of the film (discontinuities between individual spots or areas), i.e., that the dimensions of the inhomogeneities are small compared to the long wavelengths and hence are not evinced with such radiation. However, Morozov and Butslov also showed that there is mirror reflection of light (absence of scattering) at every point of a variable thickness silver film both for long and short (visible) wavelengths. Hence it must be assumed that the inhomogeneities are small even compared to the short wavelengths. In addition, as may be seen from Fig. 1, in going to still shorter wavelengths ($\lambda < 316$ mμ) the maximum in the transparency distribution curves again disappears. All this is probably an indication that in going from the solid silver film to the dispersed the apparent change in optical properties is not due simply to changes in the "effective" values of the optical constants, but, as we have noted in Ref. 5, is connected with true variation of the actual optical properties. The fact that the character of the transparency curves changes in going through the transparency band for silver, i.e., incident to an obvious change in the nature of the optical absorption of silver, is further evidence in support of our conclusion.

On the basis of data of the type shown in Fig. 1 we obtained the spectral transparency characteristics

$$D = f(\lambda)$$

for different sections of the films corresponding to different values of l.

The family of such characteristic curves for the same film, whose thickness distribution is given in Fig. 1, is shown in Fig. 2. The numbers at each curve indicate the corresponding value of l. The curve for $l = 22$ mm characterizes the solid silver film and portrays a characteristic optical property of silver, namely, the presence of a transparency band with a maximum at $\lambda = 316$ mμ.

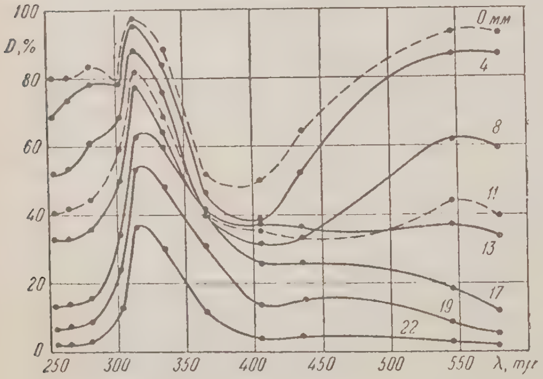

Fig. 2. Spectral transparency characteristics $D = f(\lambda)$ of sections of the film whose thickness distribution is given in Fig. 1. The figures at the curves indicate the values of l from Fig. 1.

Inasmuch as in going to microcrystals one can expect to observe a change in the optical characteristics[6], it is important to know whether the above discussed spectral characteristics persist for small silver formations. The evidence of Fig. 2 is affirmative. The characteristic curves plotted in Fig. 2 are generally similar to the curves given by Asao[2] except for the variation in the shortest wavelength part of the investigated region.

Since the absorbing power of substances is usually related to their reflecting power, i.e., since reflection usually decreases with decreasing absorption, we can deduce the probable optical influence of the silver particles in a thick cathode coating on the spectral characteristics of the photoeffect. In the spectral region near 316 mμ the silver particles reflect less of the incident light than in neighboring spectral regions. Consequently less light of this wavelength penetrates into the superficial, electron-emitting cathode layer. In general, the silver base-layer under the cathode coating also plays a similar role. Consequently, one might expect a more or less pronounced minimum in the region near 316 mμ in the spectral curve for the photo-effect from silver containing cathodes; this is substantiated by experiments on c-o-s cathodes.

As the next step we recorded the photoelectric emission characteristics of the same variable thickness silver coatings with adsorbed cesium. Fig. 3 shows the photosensitivity distribution curves for a number of different wavelengths over the film characterized in Figs. 1 & 2. The sharp falling-off of the curves to the side of small film "thicknesses" is connected with a decrease in conductivity over the film due to the dispersion of silver.[4]

It is interesting to note that in going from λ > 316 mμ to λ < 316 mμ, the nature of the distribution curves changes: the maximum in the region of $l \approx 13$ mm disappears. This may be connected with a change in the nature of light absorption in going through the transparency band or with the transition from one structure of the silver coating to another.

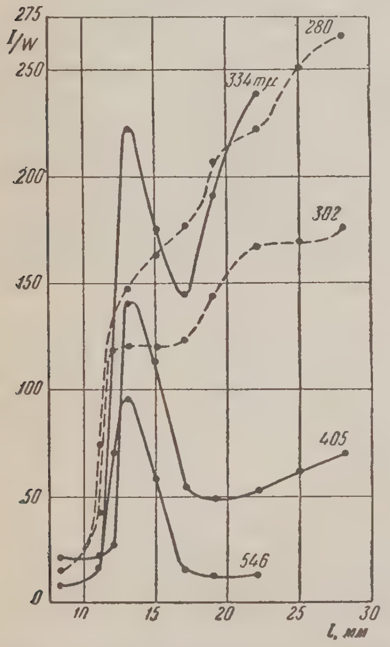

Fig. 3. Distribution of photosensitivity I/W = f(l) over the film characterized in Fig. 1 for light of different wavelengths (given in mμ at the curves).

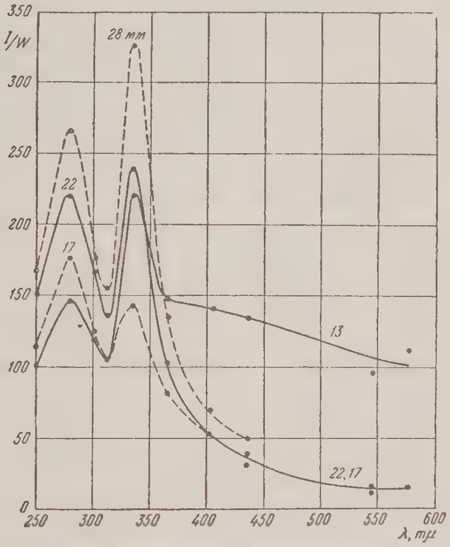

Fig. 4. Spectral characteristics of the photosensitivity I/W = f(λ) for sections of the same film (figures at the curves give the values of from Figs. 1 & 3.

The spectral characteristics of the photoeffect plotted for the different sections of the film identified by different values of l are shown in Fig. 4. Unfortunately, due to the absence of a layer of conduction silver over the entire film surface, the spectral characteristics for all the sections with different particle sizes cannot be obtained by the conventional method. Of the curves shown in Fig. 4, curve 13 pertains to the film of minimal "thickness", that is, to the "thickness" at which the film is dispersed but there still remains sufficient contact between the grains to provide conduction. The l = 28 and 22 curves already characterize continuous films of different thickness.

A distinctive feature of all the spectral characteristics is the presence of a minimum connected with a maximum transparency of the silver near 316 mμ. This minimum is explained by the fact that, although less light is reflected in this spectral interval, still less light is absorbed in the effective silver layer from which the photoelectrons can emerge. By virtue of this minimum there appears in the curves, which generally have a tendency to rise in going from long to short wavelengths, a maximum in the vicinity of 340 mμ. Another interesting feature of the curves is their rise to a peak below 316 mμ.

When we come to the dispersed section of the film (curve 13) we see that the spectral characteristic of the photoeffect noticeably deviates from the variation of the other properties in the long-wave region. This can be taken as evidence in favor of the hypothesis that the transition to fine metallic formations can influence the characteristics of the photoeffect.[6] In going from Ag-Cs to Ag-Cs-O-Cs films, we still obtain spectral characteristics of the photoeffect analogous to those shown in Fig. 4 (Ref. 5).

3. In order to study the properties of the second structural component of the c-o-s cathode we prepared films of cesium oxide in similar uviol glass envelopes. First, a film of cesium was condensed on the inner surface of the envelope and this was then oxidized to Cs_2O_4 (Ref. 7). Next, the oxide film was heated in cesium vapor at a temperature above 150° to convert it to the photosensitive cesium oxide coating. Previously, in the work of Ref. 7, it was noted that cesiation of a homogeneous Cs_2O_4 coating resulted in the formation of finely dispersed turbid Cs_2O films. However, in the present investigation we succeeded in obtaining homogeneous Cs_2O films of satisfactory optical quality. The spectral transparency characteristics $D(\lambda)$ were determined using such films.

Curve 1 in Fig. 5 shows the spectral transparency characteristic $(1 - D) = f(\lambda)$ recorded for one of the Cs_2O_4 coatings prior to the cesium vapor treatment; curve 2 gives the characteristic for the final cesium oxide film. In the first approximation, $(1 - D)$ characterizes the absorption of the film.

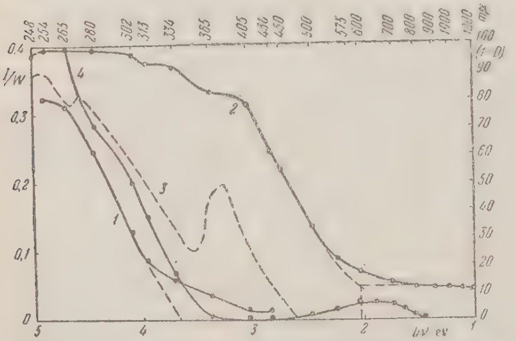

Fig. 5. Spectral characteristics of the optical absorption $(1 - D) = f(h\nu)$ and of the external photoeffect $I/W = \varphi(h\nu)$ of cesium oxide films. Absorption: 1) Cs_2O_4 coating, 2) Cs_2O film obtained by reduction of the Cs_2O_4 coating, 3) Rauch's[8] data for Cs_2O film, 4) characteristic of the external photoeffect for the Cs_2O film.

It must be noted that our results for the optical absorption characteristics of Cs_2O films are not in agreement with the data of Rauch[8] who determined the spectral dependence of the coefficient of absorption for Cs_2O. His curve in arbitrary units is shown by curve 3 in Fig. 5. It is not clear from Rauch's short article exactly what procedure he used in preparing the films. After stating that the cesium was deposited on a quartz support cooled with liquid air, Rauch merely mentions that "finally the film was oxidized by atomic oxygen". There is no data on the dosage of the components. Hence there is some question regarding the chemical composition of Rauch's films since one can rarely obtain a pure Cs_2O film simply by oxidation of cesium. Rauch gives neither the thermoelectronic nor the photoelectronic attributes of his film. It is also not clear how he determined the thickness of his films for calculating the absorption coefficients. In any case, his characteristic resembles neither our characteristic for Cs_2O_4 nor our characteristic for Cs_2O, but occupies an intermediate position and is distinguished by the presence of a sharp peak at $\lambda \approx 376$ mμ. It is probable that Rauch's data pertains to an oxidized film of cesium which is neither a Cs_2O_4 nor a Cs_2O coating.

From curve 2 of Fig. 5 we deduced that Cs_2O films are characterized by strong self-absorption in the ultraviolet region, the long-wave edge of which extends into the visible range of the spectrum (this explains the yellow color of the coating). From these data one can approximately estimate the optical self-absorption limit and the corresponding width of the so-called forbidden zone in our semiconductor film (the width is approximately 2 ev). The analogous absorption characteristic for Cs_2O_4 is appreciably shifted to the short-wave side relative to that for Cs_2O; the Cs_2O_4 characteristic indicates that self-absorption limit for this film lies well inside the ultraviolet region, which explains why Cs_2O_4 films appear entirely transparent in visible light.

We also recorded the spectral characteristics of the photoeffect. The result for the film, whose absorption is given by curve 2, is shown by curve 4. In the ultraviolet region we have an intense photoeffect due to optical self-absorption, while in the visible range of the spectrum we obviously have an impurity photoeffect.

From the difference in the positions of the red boundaries of the photoeffect and self-absorption one can evaluate the height of the potential barrier over the bottom of the conduction band: in this case, about 1 ev. This so-called "external work function" varies from specimen to specimen, attaining a value of about 0.5-0.6 ev in the "best" cases. Accordingly, the sensitivity of such "best" samples is appreciably higher and in the 250 mμ region may even exceed the sensitivity of cesium-antimony cathodes.

The high sensitivity of cesium oxide coatings in the ultraviolet suggests that the sensitivity of c-o-s cathodes to ultraviolet is due primarily to the cesium oxide. This deduction is substantiated by the experimentally established fact that the sensitivity of dispersed silver films (with a lower work function) is appreciably lower.

Ratios of spectral sensitivities of Cs_2O (I_1) and Ag-Cs (I_2) films

λ, mμ	I_1/I_2	λ, mμ	I_1/I_2
546	0,5	313	36,4
435	0,9	302	44,8
405	2,3	280	26,7
365	7,3	265	20,4
334	15,8	254	21,0

The relative sensitivities of Cs_2O (I_1) and Ag-Cs (I_2) coatings at different wavelengths are shown in the accompanying table.

With further change of the work function of silver, incident to going to more complex coatings (Cs-O-Cs, etc.), the sensitivity of the cathode changes greatly in the long-wave region[5] and relatively little in the ultraviolet. Hence while the introduction of silver particles into the cesium oxide can be expected to greatly enhance the sensitivity of the cathode in the long-wave region, in the ultraviolet region it can only bring it down by reducing the effective emitting area of the more sensitive cesium oxide.

4. Next we compared the properties of cesium oxide cathodes without silver with the properties of such cathodes after the introduction of silver.

Fig. 6 shows the characteristics $(1 - D) = f(\lambda)$ for the initial cesium oxide film (curve 1), for the same film after the application of a small amount of silver at

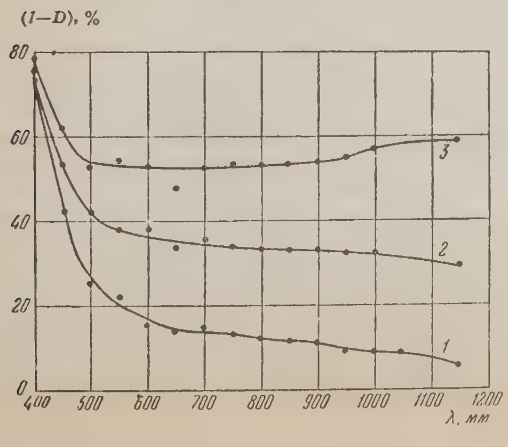

Fig. 6. Change in the optical absorption of Cs_2O coatings as the result of introduction of silver: 1) absorption of the initial Cs_2O film, 2) after sputtering on a small amount of silver at room temperature, 3) after sputtering on the optimal amount of silver and subsequent heating of the cathode.

room temperature (curve 2) and after sputtering on additional silver to the optimal amount and subsequent heating of the cathode (curve 3). It will be seen that with the introduction of silver the absorption of the film increases sharply in the longwave region. In going over to shorter wavelengths the additional absorption due to the silver decreases and, finally, in the ultraviolet region the introduced silver has very little effect on the high initial absorption of the coating.

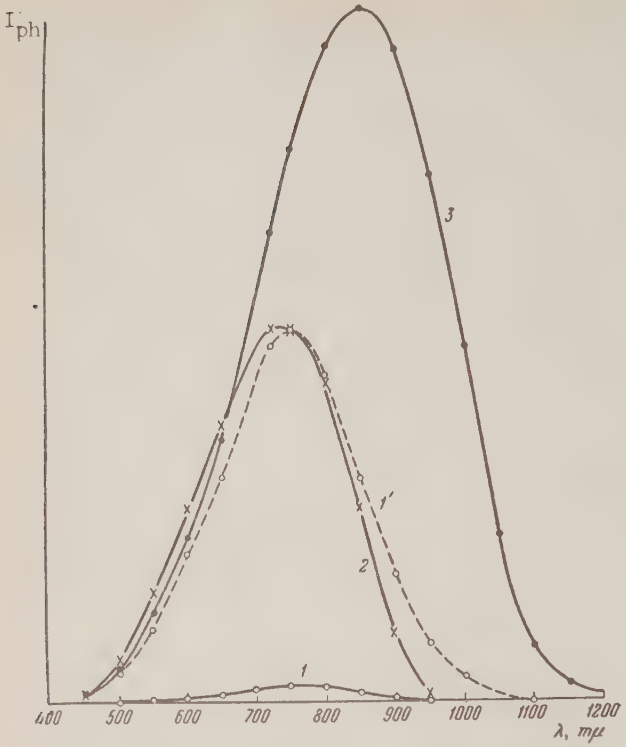

Fig. 7. Changes in the photosensitivity of a cesium oxide cathode in the longwave region resulting from the introduction of silver: 1) spectral characteristic of the external photoeffect for the initial Cs_2O coating, 2) after introduction of a small amount of silver at room temperature, 3) after introduction of the optimal amount of silver with subsequent heating of the cathode (current values not recalculated per unit incident light energy).

The changes in the photoelectric properties of cesium oxide cathodes resulting from the introduction of silver are shown in Figs. 7 & 8. The former characterizes the changes in the visible and infrared regions. Curve 1 in Fig. 7 shows the dependence of the photocurrent (not recalculated for equal incident energies) on the wavelength of the incident light for the initial cesium oxide coating. Curve 2 shows the same dependence obtained after sputtering a certain amount of silver on the film at room temperature (this curve corresponds to curve 2 in Fig. 6). Curve 1' represents curve 1 recalculated to have a maximum value equal to that of curve 2. Curve 3 was obtained after sputtering on the optimal amount of silver and subsequent heating of the cathode (this curve corresponds to curve 3 in Fig. 6).

Comparing curves 1 & 2, we see that sputtering silver on the cesium oxide cathode even at room temperature leads to a very appreciable increase in the longwave sensitivity. To what may this increase be due? A number of authors have suggested[3] that the longwave sensitivity of c-o-s cathodes is due to the presence of impurity cesium atoms in the Cs_2O. However, it is obvious that sputtering silver on the surface of the cathode could not increase the amount of cesium impurity. It might be assumed that the longwave sensitivity, erroneously associated with cesium, may actually be due to atomic silver.

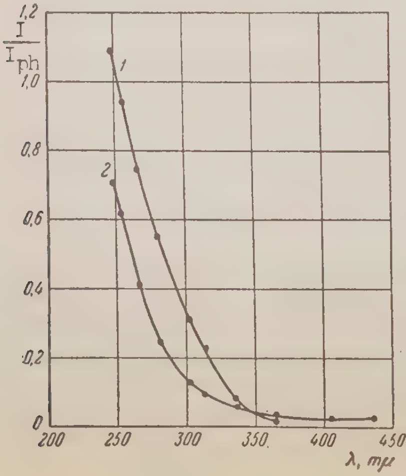

Fig. 8. Changes in the photosensitivity of a cesium oxide cathode in the ultraviolet region with the introduction of silver: 1) characteristic of relative (compared to a cesium-antimony photocathode) sensitivity of a Cs_2O cathode, 2) same characteristic after introduction of the optimal amount of silver.

This is doubtful, however, since it is difficult to see how the silver could diffuse rapidly into the cesium oxide lattice at room temperature.

On the other hand, it is obvious that the sputtered-on silver does not simply form a continuous silver film over the surface since this would reduce rather than increase the response. Clearly, even at room temperature there is some dispersion or breaking up of the silver film, as has been established to be the case for glass and other supports (see Ref. 4).

Apparently the free cesium present in the initial cathode coating is better adsorbed on the silver than on the cesium oxide; this leads to migration of the free cesium from the exposed cesium oxide spots to the silver and to the shift of the red limit of the photoeffect to the short-wave side (as may be seen from a comparison of curves 1' and 2). Curve 2, therefore, pertains not to a film of cesium oxide but primarily to silver particles with a reduced work function. True, it is not clear just how this reduction of work function is realized. Coating of the silver with only cesium atoms is not sufficient[5] for obtaining the spectral response characterized by curve 2; for this one must obtain a more complex coating on the silver, a film reducing the work function to a greater degree than a film of Cs.

If we assume, however, that between the cesium oxide and the silver there act molecular interaction forces commensurable with the strength of the cesium oxide lattice, we can see where, during formation of the silver microcrystals, cesium oxide particles can be broken off and "contaminate" the silver microcrystals. If this is true, comparison of curves 2 and 3 would indicate that heating of the cathode results in an envelopment of the silver grains by an active film, lowering the work function.

Clearly, at room temperature the process of aggregation of the silver does not go to completion,[4] while raising the temperature favors completion of the process as well as of the process of coating of the silver grains with cesium oxide, which leads to the displacement of the photoeffect threshold to the long-wave side. In any case it will be seen from a comparison of curves 1 and 3 in Fig. 7 that the difference in spectral sensitivity of the films is so great that it is more meaningful to speak of the formation of a new cathode rather than of enhancement of the properties of the original one.

Turning to Fig. 8, where the dependence of the photocurrent is given in terms of the ratio of the photocurrent I of the investigated cathode to the photocurrent I_{ph} from the cesium-antimony photocell monitoring the light flux from the monochromater, we see that in the given case we can speak of the decrease in the sensitivity of the initial cathode. As we expected, introduction of silver reduces the sensitivity of the cathode in the ultraviolet region. This is apparently due to the surface of the cathode being partially occupied by silver particles characterized by a poor sensitivity in this spectral interval. Incidentally this is also evidence that the silver does not diffuse into the depth of the cathode but rather aggregates and remains primarily on the surface.

Our data indubitably prove that the c-o-s photocathode cannot be regarded simply an impurity semiconductor coating, as some authors[3] have suggested. Let us turn to Fig. 9 showing the wavelength dependence of the ratio of the sensitivity of the cathode after sputtering on silver (I_2) to the sensitivity prior to sputtering (I_1). Curves 1 & 2 pertain to two different cases of sputtering of silver on a cesium oxide cathode with subsequent heating; curve 1 corresponds to the case of curve 3 in Fig. 7. Curve 3 characterizes the case of sputtering silver on a cesium oxide cathode without subsequent heating (this curve corresponds to curve 2 in Fig. 7). If the role of silver were limited to the formation of local impurity centers in the Cs_2O lattice, centers presumably responsible for the photoelectron emission in the 350-400 mμ region, the introduction of silver should not enhance the sensitivity in the region near 800 mμ, for example, where it is supposed to be associated with impurity cesium atoms. Actually, however, we find an entirely different order of sensitivity. On the other

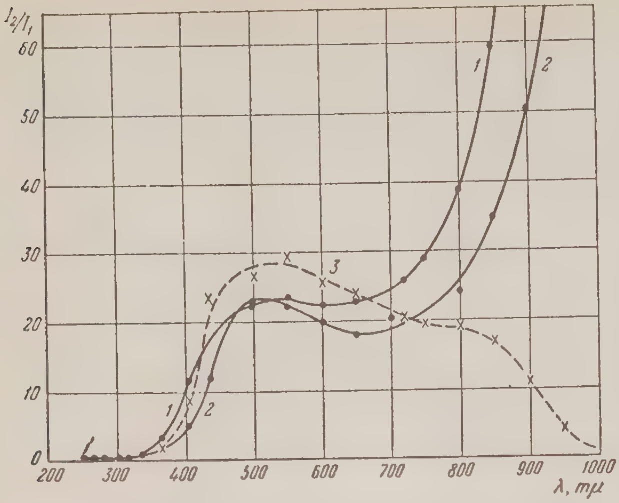

Fig. 9. Spectral characteristics of the change in sensitivity of cesium oxide cathodes resulting from the introduction of silver: 1 & 2) characteristics for two different specimens obtained after introduction of approximately the optimal amount of silver with subsequent heating of the cathode, 3) characteristic for a specimen with a smaller than optimum amount of silver sputtered on at room temperature.

hand, the addition of silver should lead to a selective increase in the sensitivity in the 350-400 mμ region, which in fact we do not observe.

It would be more logical to think of the c-o-s photocathode as a composite one, additively made up of two cathodes of different kinds: 1) a semiconductor cesium oxide cathode, determining the sensitivity in the ultraviolet region and 2) a dispersed-metallic (Ag particles coated with cesium oxide) cathode, determining the sensitivity of the composite cathode in the longwave region.

5. We observed the variation of the photocurrent with time under strong illumination for both the initial cesium oxide cathodes and for the same cathodes sputtered with silver. The results for two samples are shown in Fig. 10. The dash-line curves pertain to cathodes without silver; the solid line curves to the same cathodes after sputtering. The initial photocurrents in each case have been converted to equal ordinate values, peculiar to the given cathode.

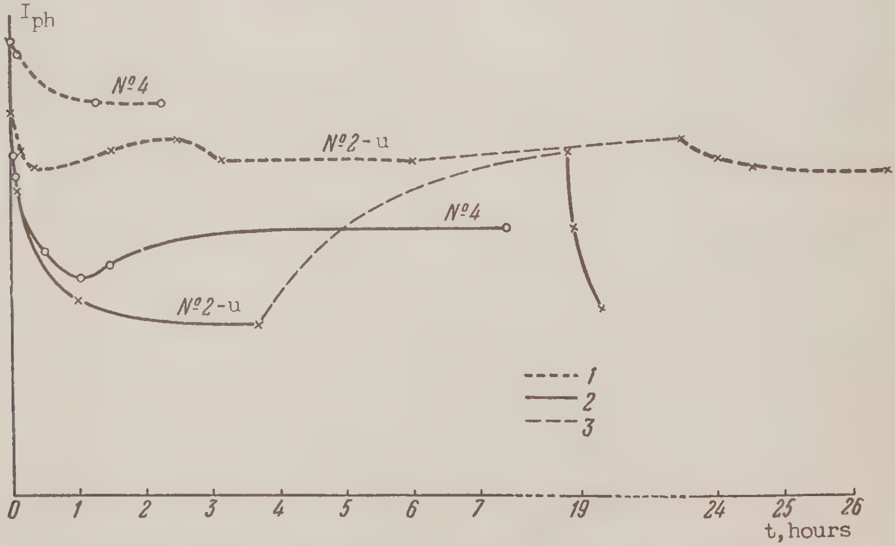

Fig. 10. Fatigue characteristics of cesium oxide photocathodes: 1) cathodes without silver, 2) same cathodes after sputtering on silver, 3) curves corresponding to dark-time intervals.

It will be seen from the curves that the introduction of silver does not eliminate fatigue. Hence the views regarding the nature of fatigue held by many investigators are not supported by the experimental evidence: the entire problem manifestly calls for a new approach.

Institute of Physics of the
Academy of Sciences of the Ukrainian SSR

References

1. J.H.De Boer, Electron emission and adsorption effects. (In Russian trans.) M.-L., 1936.

2. P.Borziak, Zhur. tekh. fiz., 9, 1380 (1939); S.Asao, Proc. Phys. Math. Soc., Japan, 22, 488 (1940); N.S.Khlebnikov, Zhur. tekh. fiz., 16, 745 (1946).

3. N.S.Khlebnikov, Zhur. tekh. fiz., 16, 745 (1946); L.N.Dobretsov, Elektronnaia i ionnaia emissiia (Electronic and ionic emission), p. 204, M.-L., 1952; N. O.Chechik, S.M.Feinshtein & T.M.Lifshits, Elektronnye umnozhiteli (Electron multipliers), p. 40, M.-L., 1954.

4. P.M.Morozov & M.M.Butslov, Zhur. tekh. fiz., 16, 857 (1946); R.S.Sennet & G.D.Scott, JOSA, 40, 203 (1950).

5. P.G.Borziak, Trudy IFAN USSR (Proceedings of the Physics Institute of the Ukrainian SSR), No. 4, 11, 1953.

6. I.M.Dykman, Trudy IFAN USSR, No. 5, 94, 1954.

7. P.G.Borziak, Zhur. tekh. fiz., 20, 928 (1950).

8. W.Rauch, ZS. f. Phys., 116, 652 (1940).

DISCUSSION

V.L.Granovski: In what form is the silver in the superficial layer?

P.G.Borziak: I believe it is primarily in the form of microcrystals.

A.A.Mostovski: What is the quantum yield of photoelectrons in the ultraviolet?

P.G.Borziak: The absolute quantum efficiency was not determined, we only compared the spectral sensitivities of the investigated cathodes with the cesium-antimony ones. The sensitivity of the studied cathodes came to about 50% of that of the reference cathode in the spectral region near 250 mμ. Obviously, there were deviations to both sides.

A.A.Mostovski: Does not the structure of Cs_2O change incident to the introduction of silver and does this not affect the maximum in the 750 mμ region?

P.G.Borziak: We did not investigate structural changes and hence I have not information on this point.

N.A.Sobolev: Did you evaluate the amount of silver brought into the layer, in particular did you compare the amount of Ag with the amount of Cs_2O?

P.G.Borziak: We carried out tests on the sputtering of silver films of different thickness onto cesium oxide cathodes. We determined the areas of optimal sensitivity on c-o-s cathodes prepared in this manner and the amount of silver deposited on such optimal sensitivity areas. These amounts in the case of thick cesium oxide films were of the same order of magnitude as Asao reports for the case of thin films.

V.M.Agranovich: Did you compare the absorption of silver in the coating with the absorption of pure silver?

P.G.Borziak: No. In general there is no reason for the absorption to be equal, in view of the different conditions of crystallization and the difference in the optical media.

K.B.Tolpygo: Did you compare the work functions of a c-o-s cathode and a cesium oxide cathode with sputtered on silver?

P.G.Borziak: The work function for the latter was higher.

A.I.Piatnitski: Do you disagree with the results of Kluge?

P.G.Borziak: He associated the sensitivity at the long-wave maximum with adsorbed cesium atoms; we believe it is due to silver microcrystals with a reduced work function.

"EXCESS" VELOCITIES IN THE ENERGY SPECTRUM OF PHOTOELECTRONS FROM A CESIUM-ANTIMONY CATHODE (Abstract)

- N.M.Politova

The present study is devoted to a detailed investigation of the distribution in energy curves of photoelectrons from a non-sensitized cesium-antimony cathode at different wavelengths of the incident light (4000-6300 Å). The distribution in energy of the photoelectrons was studied by the method of a retarding field in a spherical capacitor. The photocells were made so that it was feasible to investigate the different replaceable cesium-antimony cathodes under identical conditions. The investigated cathodes differed from each other as regards the thickness of the antimony layer or the nature of base material and were compared with reference metallic cathodes.

It was found that the work function computed according to the Einstein equation (from the value of the maximum retarding potential and the energy of the quanta) is not equal to the photoelectric work function determined from the red limit of the photoeffect. The photoelectric work function of the investigated cesium-antimony cathodes proved to be the most constant parameter of these cathodes and equal to 1.8 ± 0.02 ev, while the work function computed from Einstein's equation was appreciably smaller and varied between 1.3 and 1.6 ev. The latter work function is different for different cesium-antimony cathodes and depends on the energy of the incident photons. As the wavelength is decreased from 6200 to 4000 Å, this work function increases by approximately 0.2 ev.

For metallic cathodes investigated in the same set-up and under the same conditions the values of the work function determined in the two described manners are equal.

Thus, electrons emitted from a cesium-antimony cathode have an "excess" velocity, i.e., a velocity greater than follows from Einstein's equation when one substitutes the photoelectric work function therein and this excess velocity decreases with decreasing wavelength of the light absorbed by the cathode.

A possible explanation of this effect from the viewpoint of the hypothesis regarding surface states in cesium-antimony cathodes is suggested. According to this viewpoint, there should form near the surface of the cathode a double electric layer consisting of a positive surface charge and a negative volume charge extending to a depth of approximately 10^{-5} cm. The light-excited electrons coming under the influence of this accelerating electric field acquire an additional energy and, as a result, there is observed in the spherical capacitor a wider photoelectric energy spectrum than would be observed if there were no double electric layer.

Institute of Radio Engineering and Electronics of the
Academy of Sciences of the USSR

DISCUSSION

V.N.Lepeshinskaia: At what temperature were the measurements made?

N.M.Politova: Mainly at room temperature. Some characteristics were recorded at the temperature of dry ice.

A.A.Mostovski: Is there a difference between the retarding potential curves for metallic and cesium-antimony cathodes?

N.M.Politova: In the case of cesium-antimony cathodes there are obtained excess velocities due to the field of the positive surface charge.

A.A.Piatnitski: How was the contact of the coating with the base realized?

N.M.Politova: The cathode consisted of a small cube or plate coated with layers of different thickness. Contact was realized by deposition on glass plates. The dimensions of the cube were one tenth those of the sphere. This is fully sufficient in the case of metals to obtain good retarding potential curves.

INFLUENCE OF ELECTRON BOMBARDMENT ON THE PHOTOEMISSION OF COMPLEX PHOTOCATHODES*

- L.N.Bykhovskaia

Introduction

Influence of electron bombardment on the photoelectric and thermionic emission of different cathodes has been studied by a number of investigators. Thus Kushnir[1] observed an increase in the photocurrent from an opaque cesium oxide cathode after irradiation with slow electrons. Dember[2] discovered that the limit of the photoemission effect in aluminum is displaced from the ultraviolet to the visible region of the spectrum under the simultaneous influence of light and electrons. These effects are explained by the formation of a surface charge by the slow electrons and their subsequent removal by the light quanta. There have been reports of an increase in the thermal current in oxide-coated cathodes under electron bombardment or irradiation with light.[3-5] This effect has been explained by the transition of electrons from the filled band to the conduction band, due to the energy brought in by the primary electrons or photons, and the subsequent escape of the electrons from the conduction band.

The purpose of the present study was to investigate the influence of electron bombardment on the photoelectron emission of complex photocathodes. The measurements were carried out by two methods: the electron-optical, i.e., by observing the photoelectron images of the cathodes, and the method of measuring the photocurrents before and after electron bombardment.

Electronoptical Investigations of the Influence of Electron Bombardment On the Photoemission of Complex Photocathodes

Experimental equipment and procedure

A special emission microscope (Fig. 1) was developed for the electron-optical investigations of the photoelectric and secondary-electron emissions of complex photocathodes. The microscope consisted of a sealed glass tube enclosing the photocathode 1, prepared on a movable glass plate, and a movable cylindrical anode 6. The electrons emitted by the photocathode were accelerated by the electric field, focused by the magnetic lens 12 and, after deflection in the homogeneous magnetic field by the yoke 13, fell on the fluorescent screen 9. The source of the bombarding electrons was a special long-focus gun 8 with a tungsten cathode and a condenser lens 14.

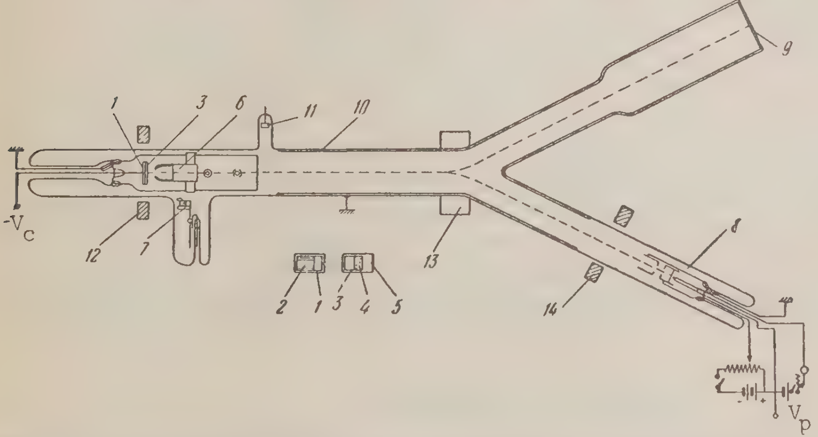

Fig. 1. Microscope for investigating photocathodes: 1) holder with photocathode, 2) photocathode on glass plate, 3) frame with fluorescent screen (4), serving for adjustment of the primary electron beam, 5) protective cover for the fluorescent screen, 6) movable anode, 7) movable vaporizer, 8) long-focus gun, 9) fluorescent viewing screen, 10) conducting layer, 11) getter, 12) magnetic lens, 13) magnetic deflecting system, 14) condenser lens.

---

*The report was presented to the Conference by N.A.Soboleva

With an appropriate negative bias on the control electrode, the gun formed a narrow and homogeneous electron beam (a narrow beam was necessary because with a wide beam there appeared on the microscope screen a background due to electrons scattered from the electrodes and tube walls). The gun and the fluorescent screen for observing the cathode image were located in two lateral off-shoots of the tube, branching at 25^0 to the optical axis of the magnetic lens. The primary electron beam was deflected in a homogeneous magnetic field and fell on the microscope cathode at an angle of incidence of 90^0. The requisite stabilized high voltages for the cathodes of the gun and microscope were supplied by two separate and independent rectifiers; the anodes were grounded.

The speed of the primary electrons was set by the potential difference between the cathodes of the gun and microscope and could be varied from 100 volts to several kilovolts. The magnetic lens 12 focused the primary electrons on the surface of the cathode, forming a reduced image of the primary beam. The diameter of the focal spot depended on the velocity of the primary electrons and at $V_e =$ $= 180$ v was approximately 0.5 mm.

During adjustment of the instrument the investigated cathode was covered by a retractable nickel shielding screen coated with a luminescent conducting layer of sublimated zinc oxide.* This shield-screen protected the photocathode against the influence of electrons and at the same time made it possible to check the focusing of the primary beam. The microscope was adjusted with reference to the secondary electron image of the screen.

In addition to photocathodes, the microscope could also be used for investigating different secondary emitters. In this case the gun and cathode assembly were mounted in separate envelopes connected to the main tube by ground glass joints. The parameters of the microscope are the following: electron magnification up to 50 X, separation resolved in secondary electron images 4-5 μ, anode voltage in sealed tubes with photocathodes 5-6 kv, in tubes with ground glass joints up to 10 kv. The screen was photographed from the outside.

By way of illustration of the results obtained with our microscope a secondary-electron image of etched transformer iron and thermionic and secondary-electron images of an oxide-coated cathode are reproduced in Figs. 2 & 3.

We investigated thick cesium oxide and cesium-antimony cathodes by means of the microscope. The cesium oxide cathodes were prepared on layers of silver with a transparency of ~10%; the integral sensitivity of these cathodes was 7-8 μa/ /lumen (without the addition of silver or oxygen sensitization). The sensitivity of the tested cesium-antimony cathode was 40 μa/lumen. The photoelectron images of the cathodes were observed before and after electron bombardment. The cathodes were illuminated from an incandescent lamp through different wide-band and interference light filters. To permit comparison of the photoelectric emission of the cathode before and after electron bombardment half the area of the cathode in the field of view of the microscope was not subjected to electron bombardment. The secondary electron images of the cathode were observed during the bombardment.

Experimental results

Our experiments showed that the sensitivity of thick cesium oxide cathodes increases in the spectral region above 600 mμ after bombardment with 100-1300 v electrons at a current density of several microamperes per cm^2. The greatest increase in sensitivity (in individual cases by a factor of 20) was observed in the long-wave part of the spectrum. Some time after cessation of electron bombardment the sensitivity of the cathode falls off to its initial value.

The photoelectron images of a cesium oxide cathode with a non-uniformly emitting surface before and after 3 minutes bombardment with 1000 volt electrons at a current density of several microamperes per cm^2 are reproduced in Fig. 4, a, b and c. The cathode was illuminated with light having a wavelength $\lambda > 820$ mμ. The dark spots are areas characterized by a large work function.

---

*These luminophor screens were developed and prepared by V.V.Golubtsov.

It follows from microphotometric measurements of the photographs that the current from the bombarded section of the cathode increased by a factor of 20 in the $\lambda > 820$ mμ region (Fig. 4,b). Six minutes after cessation of bombardment the emission of the irradiated section was still three times greater than the initial (Fig. 4, c). The secondary emission produced by the bombardment with 1000 v primary electrons was uniform despite the variation of the work function of different individual sections of the surface (Fig. 4, d).

In order to determine the changes in the spectral sensitivity after electron bombardment the cathode was irradiated through interference light filters by light of different wavelengths. The result is shown in Fig. 5. The sensitivity of the cathode increased in the $\lambda > 600$ mμ spectral region.

The greatest relative increase in the photocurrent was observed for $\lambda = 1007$ mμ. The bombarded section of the cathode when illuminated with 1007 mμ light yielded a photocurrent sufficient for observing and photographing the electron image, whereas the nonbombarded section had virtually no emission (Fig. 5, a).

The relative increase in photocurrent after electron bombardment in the case of illumination with $\lambda = 908$ mμ light was appreciably smaller (Fig. 5, b).

The increase in cathode sensitivity was found to depend on the duration of bombardment, the current density and the energy of the primary electrons. The optimal bombardment time varied for different cathodes from 2-3 min to a few seconds, depending on the electron bombardment conditions. With increasing bombardment time and current density the sensitivity of the cathodes at first increased and then, after passing through a maximum, fell off to the initial value. In fact, prolonged bombardment of the cathodes with a high current density ultimately resulted in a decrease of the sensitivity in the long-wave region. In such cases the initial emission was re-established several hours after cessation of bombardment. The optimum value of the primary electron potential varied for different cathodes from a thousand to a few hundred volts.

As a rule the secondary emission from the cesium oxide cathodes was uniform over the surface of the cathode. In the case of cathodes with different values of the work function for different sections of the surface, the secondary emission was found to be uniform for primary electron speeds up to 1000 v; at higher primary potentials non-uniform secondary emission was observed in some cases (Fig. 6).

As noted above the microscope was also used to investigate a non-sensitized cesium-antimony cathode. Both the photoelectric and secondary-electron emissions were uniform. After electron bombardment there was no noticeable change in the photoelectric emission in the 500 mμ $< \lambda >$ 600 mμ region.

Investigation of the Influence of Electron Bombardment on the Photoelectric Emission of Complex Cathodes by the Method of Measuring Photocurrents

Experimental equipment and procedure

In order to determine the quantitative dependence of changes in the photoemission of cathodes on the conditions of electron bombardment, we developed two types of special sealed glass tubes with appropriate measuring circuits.

In the tube of the first type (Fig. 7, a) the photocathode was prepared on the end wall. The electron source for bombarding the photocathode 1 was a four-electrode gun 2 with two anodes and an annular tungsten cathode producing a uniform current-density electron beam. The size of the beam was monitored by means of the movable nickel screen 3 coated with sublimated zinc oxide.

The tube circuit is shown in Fig. 7, b. The potential from the two rectifiers B_1 and B_2 was applied to the cathode K of the gun and the first anode A_1. The second anode A_2 was grounded. A control bias voltage from the battery D_1

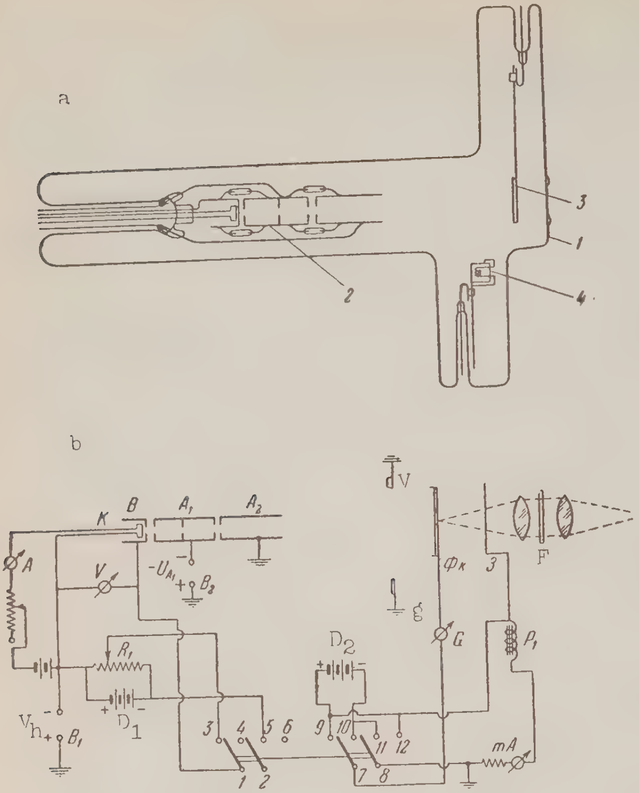

Fig. 7. a - tube for measuring the photocurrent and the parameters of the electron beam: 1) photocathode, 2) four-electrode gun, 3) movable screen for preliminary adjustment of the beam, 4) movable vaporizer; b - circuit diagram of tube: K) cathode, A_1 & A_2) anodes, B_1 & B_2) rectifiers, B) control electrode, D_1) bias battery, ϕ_K) photocathode.

Fig. 2. Secondary-electron image of a) transformer iron (magnification: electronic 25 X, photographic 2 X, overall 50 X); b) fluorescent zinc oxide screen (magnification: 50 X, 2 X and 100 X resp.).

Fig. 3. Oxide-coated cathode: a) thermionic emission (magnification: electronic 30 X, photographic 2 X, overall 60 X); b) secondary-electron emission (the protective ring about the cathode is discernible in the photograph) (magnification: 16 X, 2 X and 32 X resp.).

Fig. 4. Photoelectron images of a thick cesium oxide cathode illuminated with 820 mμ light: a) before electron bombardment, b) immediately after 3 min bombardment of the left section of the cathode with 1000 v electrons, c) 6 min after electron bombardment, d) secondary-electron image of section of cathode obtained during bombardment with 1000 v electrons. Magnification: electronic 50 X, photographic 1.5 X, overall 75 X.

Fig. 5. Change in the photoelectric emission of a thick cesium oxide cathode after 6 min bombardment of the left part by 600 v electrons with the cathode illuminated by a) 1007 mμ and b) 908 mμ light. Magnification: electronic 50 X, photographic 1.5 X, overall 75 X.

Fig. 6. Secondary-electron image of a thick cesium oxide cathode. Primary electron voltage 1260 v. Magnification: electronic 50 X, photographic 2 X, overall 100 X.

was applied to the control electrode B.

The circuit design allowed of simultaneously cutting off the electron beam and turning on the light flux, which made it possible to measure the magnitude of the photocurrent immediately after cessation of bombardment.

With the switch in the left position (Fig. 7, b) the electron gun is activated, the electron beam falls on the photocathode, the circuit to the electromagnetic relay P_1 is closed, and the screen 3 shields the photocathode from the light source. A potential of +80 v (relative to the ground) is applied to the cathode. In this case the electric field between the photocathode and the grounded anode A_2 stops the secondary electrons ejected by the primary beam from the photocathode and returns them to the cathode. The galvanometer G measures the primary current to the photocathode. With the selector switch in the right position, a -80 v blocking bias from the battery D_2 is applied to the control electron of the gun, the circuit to the relay P_1 is open and the shutter 3 is retracted allowing the light flux to fall on the photocathode. A potential

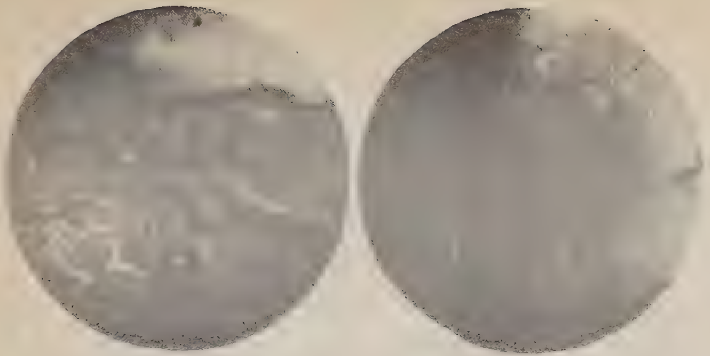
Fig.2

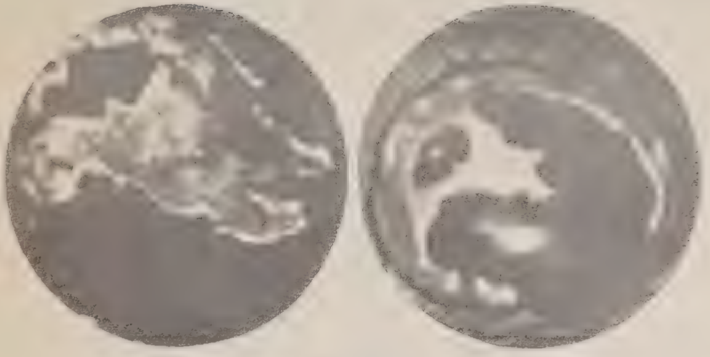
Fig.3

Fig.6

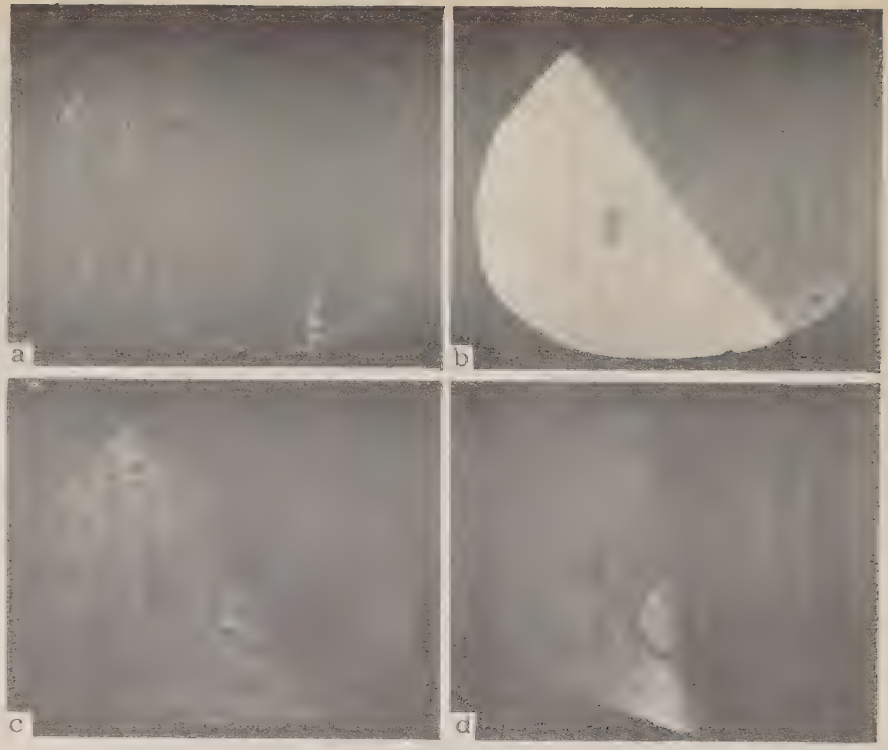

Fig.4

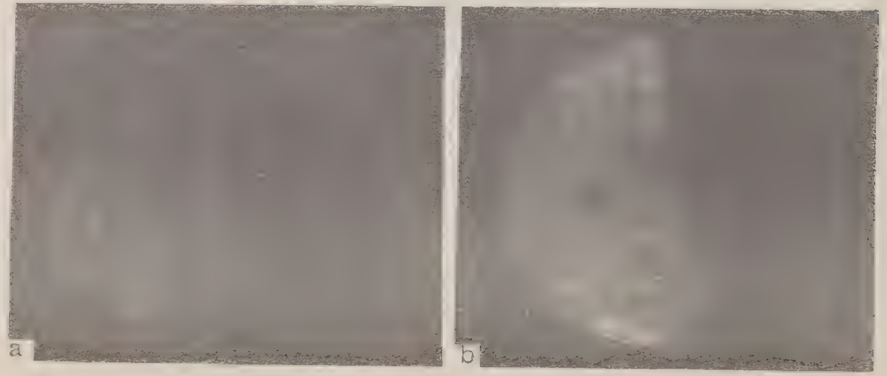

Fig.5

of -80 v relative to the ground is applied to the photocathode from D_2. The galvanometer G in this case measures the photocurrent flowing to the anode A_2. The energy of the primary electrons was varied from 200-2000 v. The diameter of the primary beam was regulated by adjusting the voltage ratio on the second and first anodes and was approximately 18 mm at all electron energies. The tube design allowed of varying the speed of the primary electrons, while maintaining a constant current density.

The photocathodes were illuminated, as in the first part of the study, from an incandescent lamp through different glass lightfilters.

A shortcoming of tubes of this type was the gradual falling off of the sensitivity of the cesium oxide cathode due to the influence of residual gases, evolved, despite the presence of a getter, during operation. In order to obviate this effect we developed the tubes of the second type (Fig. 8). These tubes had two photocathodes which were prepared simultaneously. Cathode ϕk_2 served as the source of electrons for bombarding cathode ϕk_1. The grounded screen accelerating electrode C (Fig. 8) could be moved in and out of position between the photocathodes. The fluorescent screen Э was lowered into the beam path between the cathodes during adjustment of the tube.

The operation of the measuring circuit was analogous to that of the circuit shown in Fig. 7, b. The investigated photocathode ϕk_1 was illuminated by an incandescent lamp through a 3 mm diameter aperture. The photocathode ϕk_2, serving as the electron source, could be illuminated by the incandescent bulb L2.

With both types of tubes, we measured the photocurrent from the same section of the cathode before and after electron bombardment, the primary electron potential, the beam current and the bombardment time. Using tubes of the first type, we investigated one solid and a number of semi-transparent cesium oxide cathodes as well as a cesium-antimony cathode; in tubes of the second type, we investigated only semi-transparent cesium oxide cathodes. The cathodes were prepared in the conventional manner (Refs. 6 & 7). The sensitivity of the semi-transparent cesium oxide cathodes ranged from 14 to 24 μa/lumen.

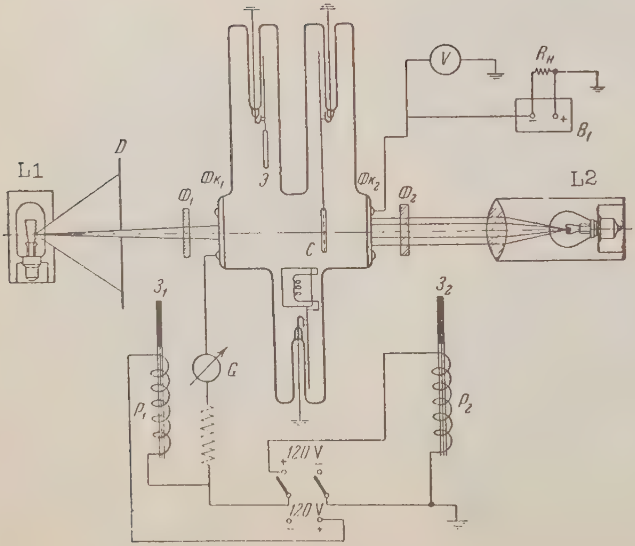

Fig. 8. Tube with two photocathodes.

Experimental results

The photocurrent measurements confirmed and supplemented the results obtained from the electron-optical investigations of thick cesium oxide cathodes. We established the electron bombardment conditions producing an increase in the photoelectric emission of semi-transparent and solid cesium oxide cathodes having a sensitivity of up to 20 μa/lumen. As in the previous experiments the greatest increase in sensitivity was observed in the infrared region of the spectrum. In the case of illumination with light of λ> 820 mμ, the sensitivity fell off to its initial value only several hours after cessation of electron bombardment. Under the influence of blue light (< 500 mμ) the cathodes returned to their initial state in a few seconds. This effect was made use of in our measurements of the dependence of the photocurrent increment on the parameters of the electron beam.

The results of our investigations of a thick cesium oxide cathode with a sensitivity of 13 μa/lumen, prepared on a layer of silver having a transparency of ~10%, are shown in Figs. 9, 10 & 11. The vertical axes are laid off in terms of the ratio of the photocurrents before and after electron bombardment

As the density of the primary current was increased from 0.25 to 6 $\mu a/cm^2$ there was a noticeable increase in the photocurrent in the λ > 820 mμ region after electron bombardment (Fig. 9).

The curve giving the dependence of the photocurrent increment in the λ > 820 mμ region on the electron bombardment time shows clear evidence of saturation (Fig. 10, a). We established that the increase in the photocurrent is proportional to the amount of electric charge Q received by the cathode during bombardment; saturation for the given cathode occurs at $Q = 1.68 \cdot 10^{-3}$ $a \cdot sec/cm^2$. The variation of the photocurrent increase after electron bombardment with the wavelength of the incident light shows a sharp maximum in the value of I_{ϕ_2}/I_{ϕ_1} at λ = 950 mμ (Fig. 10, b; the curves

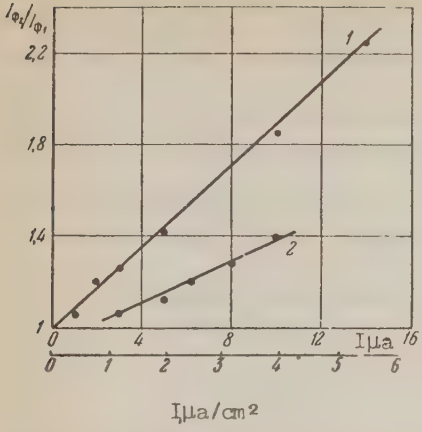

Fig. 9. Dependence of the increment in photocurrent from a thick cesium oxide cathode in the λ > 820 mμ spectral region (1 min electron bombardment time) on the primary current density. 1) electron potential V_e = 270 v; 2) V_e = 440 v.

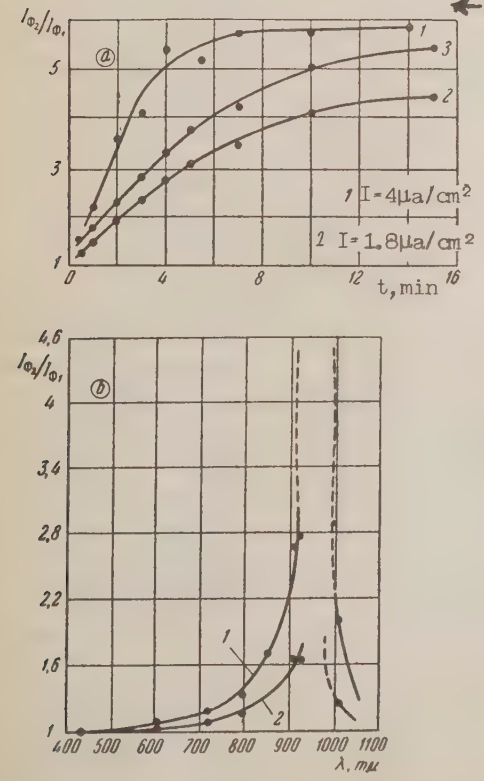

Fig. 10

Fig. 10. Dependence of the photocurrent increment from thick cesium oxide cathode a) on the electron bombardment time in the λ > 820 mμ spectral region at V_e = 260 v (curve 2 was recorded at a greater value of the photocurrent I_{ϕ_1} than curve 1; curve 3 was obtained by calculating the ratio I_{ϕ_2}/I_{ϕ_1} for the value of I_{ϕ_1} corresponding to curve 1) and b) on the wavelength of the incident light after 3 minute electron bombardment at a current density I_e = 4 microamp/cm²: V_e = 260 v (curve 1) and V_e = 430 v (curve 2).

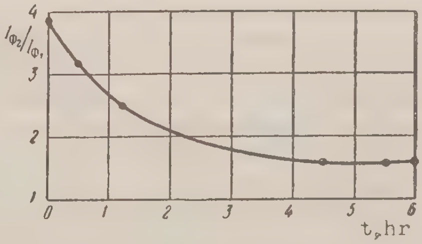

Fig. 11. Decrease of the photocurrent from a thick cesium oxide cathode after cessation of electron bombardment. Cathode illuminated with λ > 820 mμ light.

were recorded using interference filters). The decrease in the photocurrent in the $\lambda > 820$ mμ region after cessation of electron bombardment is characterized in Fig. 11 (the cathode was bombarded beforehand for 5 minutes with 260 v electrons at a current density of 1.85 μa/cm^2).

In a number of cases a decrease in sensitivity in the cathodes was observed after prolonged bombardment with electrons having speeds above 600 v at current densities of 1-4 μa/cm^2.

The greatest decrease in sensitivity was observed in the long-wave region. The sensitivity of the cathodes returned to the initial value approximately one hour after cessation of electron bombardment.

A number of semi-transparent cathodes were investigated in tubes of the first type. The typical results are given in Figs. 12 & 13. Immediately after preparation the characterized cathode had an integral sensitivity of 24 μa/lumen; during adjustment of the tube the sensitivity fell off to 16.5 μa/lumen.

The sensitivity of the cathode increased after bombardment with 200-2000 v electrons. The greatest increase in the sensitivity in the cathodes (up to 34 times) was observed in the long-wave region of the spectrum ($\lambda > 900$ mμ). The change in the sensitivity of the cathode as a function of the electron bombardment time is shown in Fig. 12, a.

The increase in the photocurrent was proportional to the electric charge transferred to the cathode during bombardment. The amount of charge required for the onset of saturation for the given cathode was $Q = 0.84 \cdot 10^{-4}$ a·sec/cm^2, i.e., one order of magnitude lower than in the case of a thick cesium oxide cathode. The sensitivity of the semi-transparent cathode before and after bombardment with 478 v electrons at a current density of 0.2 μa/cm^2 is shown in Table 1. The bombardment was continued to the onset of saturation.

With illumination by $\lambda > 870$ mμ light, the sensitivity dropped to its initial value after several hours (Fig. 12 b). In the case of $\lambda >$ 500 mμ light, the

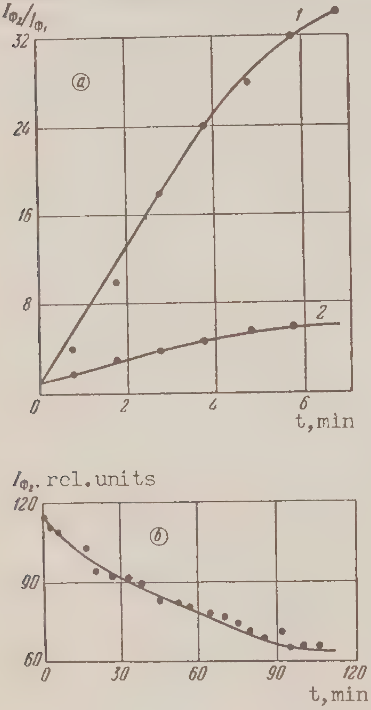

Fig. 12. a - Dependence of the increment in photocurrent from a semi-transparent cesium oxide cathon the electron bombardment time ($V_e = 476$ v, $I_e = 0.2$ μa/cm^2): 1) $\lambda > 900$ 2) $\lambda > 820$ mμ. b - Decrease in the photocurrent from the semi-transparent cesium oxide cathode after cessation of electron bombardment with the cathode illuminated with $\lambda > 870$ mμ light. $I_{\phi_1} = 8$ relative units.

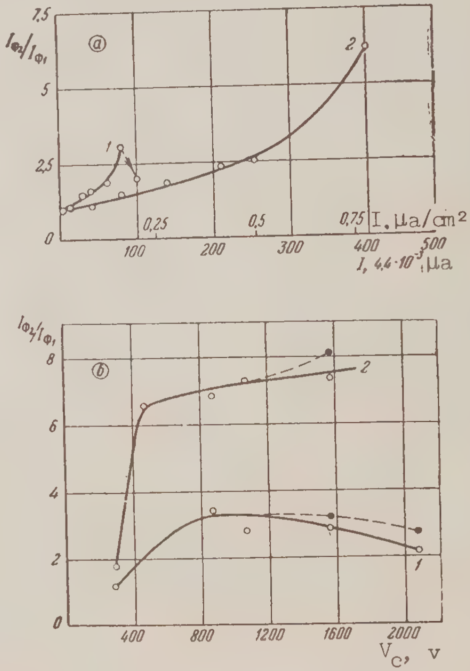

Fig. 13. Dependence of the increment in photocurrent from a semi-transparent cesium oxide cathode in the $\lambda > 870$ mμ spectral region a) on the primary current density ($V_e = 480$ v): 2 min bombardment - curve 1; 1 min bombardment - curve 2, and b) on the potential of the primary electron (bombardment time - 1 min): $I_e = 0.2$ μa/ /cm^2 - curve 1; $I_e = 0.39$ μa/cm^2 - curve 2.

sensitivity returned to its initial value in a few seconds after cessation of bombardment, just as in the case of the opaque (thick) cesium oxide cathode.

The photocurrent in the $\lambda > 870$ mμ region increased in proportion to the current density up to 0.5 μa/cm^2 with a bombardment time of 1 min. With current densities above 0.5 μa/cm^2, there was a sharper increase in the photocurrent (Fig. 13, a, curve 2). In the case of 2 minute bombardment, increase in the primary current density first caused a strong rise in emission; however, beginning with $I_e = 0.17$ μa/cm^2 the photocurrent fell off sharply.

The dependence of the photocurrent increment in the $\lambda > 870$ mμ region on the speed of the primary electrons differed for different current densities (see Fig. 13, b): with $I_e = 0.2$ μa/cm^2 the maximum increase in photocurrent was observed at electron potentials of 900-1000 v; with I_e 0.39 μa/cm^2 the photocurrent continued to increase even at primary energies of 1600 v. At electron speeds above 1000 v the photocurrent I_{ϕ_2} continued to increase over a period of several minutes after cessation of bombardment, rising to a value I'_{ϕ_2}. The values of the ratio I'_{ϕ_2}/I_{ϕ_1} are shown in Fig. 13, b by the dash lines.

Table 1

Sensitivity of a semitransparent cesium oxide cathode before and after bombardment with 478 v electrons (sensitivity in μa/lumen)

Sensitivity	Before Bombardment	After Bombardment	I_{ϕ_2}/I_{ϕ_1}
Integral	16.5	22.5	1.36
Spectral region $\lambda > 820$ mμ	0.55	3.25	5.9
$\lambda > 900$ mμ	0.028	0.94	34.0

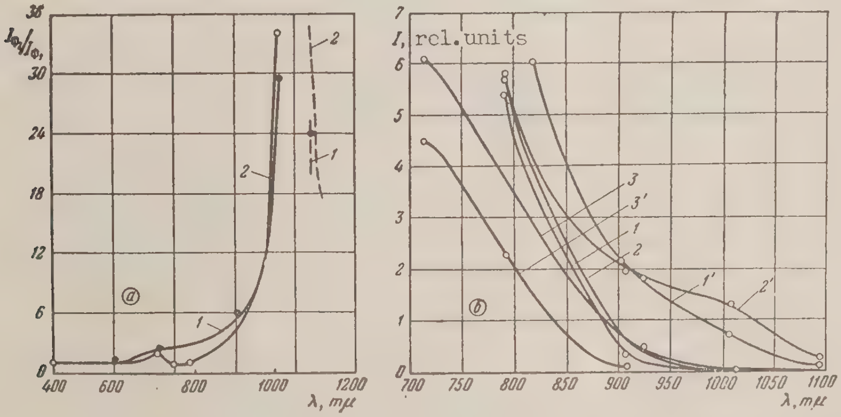

Fig. 14. a - Increase in the photocurrent from a semi-transparent cesium oxide cathode with an initial sensitivity of 16.5 μa/lumen in different regions of the spectrum after bombardment with electrons at a potential of 460 v and $I_e = 0.2$ μa/cm^2. Bombardment times: 1) 3 min, 2) 7 min. b - Spectral sensitivity curves for two semi-transparent cesium oxide cathodes in the long-wave region before (curves 1, 2 & 3) and after (curves 1', 2' & 3') electron bombardment. Curves 1 & 1' and 2 & 2' were obtained for a cathode with a sensitivity of 16.5 μa/lumen after 3 min bombardment (curve 1) and 7 min bombardment (curve 2'). Curves 3 & 3' were obtained for a cathode having a sensitivity of 14 μa/lumen.

The dependence of the bombardment induced increase in photocurrent on the wavelength of the incident light is characterized by a sharp maximum in the vicinity of $\lambda = 1005$ mμ (Fig. 14, a). After some 6-7 min bombardment there appears a second maximum at $\lambda = 714$ mμ. The spectral sensitivity curves for semi-transparent cathodes obtained by using interference filters show that the greatest increase in photocurrent due to bombardment also occurs in the near infrared region (Fig. 14, b).

The long-wave part of the spectral sensitivity curve is shifted to the right as a result of electron bombardment. The greatest relative increase in photocurrent corresponds to the wavelength at which the spectral sensitivity of the cathode before bombardment is close to zero and rises to an appreciable value after bombardment.

The next series of experiments were carried out in tubes of the second type with two semi-transparent cesium oxide photocathodes. It was established that the increase in the photocathode current after electron bombardment decreases with increasing initial sensitivity of the cathode. Data on the increase in the sensitivity of different cathodes as a result of electron bombardment are given in Table 2. In each case bombardment was carried on to beginning of saturation.

Table 2

Sensitivity of semi-transparent cesium oxide cathodes before and after electron bombardment (sensitivity in μa/lumen)

Cathode	Sensitivity	Before Bombardment	After Bombardment	I_{ϕ_2}/I_{ϕ_1}	Bombardment Conditions
No. 1	Integral	14.6	17.2	1.18	V_e = 600 v
	Spectral region λ > 820 mμ	2.13	2.94	1.38	
	Spectral region λ > 870 mμ	0.88	1.54	1.75	I_1 = 0.66 μa
No. 2	Integral	19.0	21.9	1.15	
	Spectral region λ > 820 mμ	2.06	4.12	2.0	V_e = 220 v
	Spectral region λ > 870 mμ	0.8	1.93	2.41	I_1 = 0.66 μa
No. 3	Integral	19.4	19.4	1	
	Spectral region λ > 820 mμ	3.52	3.82	1.08	V_e = 600 v
	Spectral region λ > 870 mμ	1.62	1.84	1.135	I_1 = 0.66 μa

It follows from the data for cathodes Nos. 2 & 3 that with equal integral sensitivities the greatest increase in the photocurrent under the influence of electron bombardment is observed for the cathode with the lowest initial sensitivity in the infrared region. The dependences of the increment of photocurrent from these three cathodes on the density of the primary current, the bombardment time and the wavelength of the incident light are analogous to those for the semi-transparent cathode having a sensitivity of 16.5 μa/lumen described above. By way of illustration, the increase in the photocurrent from cathode No. 2 in different spectral regions after electron bombardment is shown in Fig. 15. The main long-wave maximum in the photocurrent increment curve is located at 1100-1150 mμ, while the small rise occurs as usual at ~700 mμ.

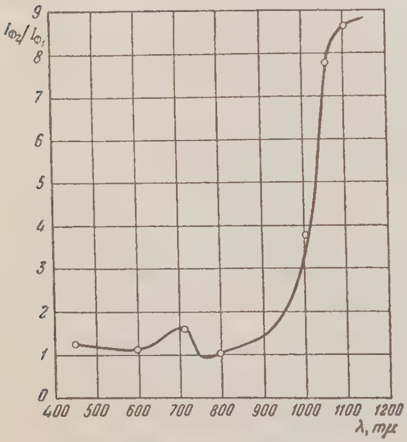

Fig. 15. Increase in the photocurrent from the No.2 cesium oxide photocathode, having an initial integral sensitivity of 19 μa/lumen, in different regions of the spectrum after bombardment with electrons at a potential of 180 v.

Electron bombardment of semi-transparent cesium oxide cathodes with an integral sensitivity above 20 μa/lumen produces a decrease in the photoelectric emission in long-wave spectral region (see Table 3). The initial sensitivity is reestablished only after a long rest period.

The sensitivity of the cathode characterized in Table 3 decreased after bombardment with 180-500 v primary energy electrons at current densities from 0.35 to 0.56 μa/cm^2. The sensitivity loss was greater for higher current densities and longer bombardment periods.

Table 3

Sensitivity of a semitransparent cesium oxide cathode before and after bombardment (sensitivity in μa/lumen)

Sensitivity	Before Bombardment	After Bombardment	Ratio
Integral	20.8	20.6	0.99
Spectral $\lambda > 820$ mμ	4.12	2.5	0.607
region $\lambda > 870$ mμ	1.91	1.18	0.618

It was established by special experiments, in which the sensitivity of the cathodes was gradually reduced under the influence of residual gases, that the increase in the emission of oxygen-cesium cathodes after electron bombardment is connected with the presence of cesium oxide of their surface. The test cathode was gradually poisoned by the oxygen of the residual gas evolved during heating of a vaporizer spiral in the sealed tube. We measured the photoelectric sensitivity before and after the electron bombardment as well as the secondary emission coefficient σ for four states of the cathode (Table 4). The experiments were carried out in a two-photocathode type experimental tube. The primary current i_1 was measured in the conventional manner. To determine the secondary current i_2 we measured the current $i' = i_1 - i_2$ with a negative potential of 120 v relative to the grounded screen C applied to the investigated cathode. The primary electron potential was 580 v.

Table 4

Variation of the sensitivity (in μa/lumen) of a semi-transparent oxygen-cesium cathode under the influence of electron bombardment at different stages of oxidation

Stage of Measurement	Sensitivity	Before Bombardment	After Bombardment	I_{ϕ_2}/I_{ϕ_1}	σ
Immediately after preparation	Integral	19.1	19.1	1	
	Spectral $\lambda > 820$ mμ	3.6	3.82	1.06	
	region $\lambda > 870$ mμ	1.62	1.765	1.09	
After first drop in sensitivity	Integral	17.65	19.7	1.12	
	Spectral $\lambda > 820$ mμ	2.55	3.99	1.5	3.5
	region $\lambda > 870$ mμ	1.08	1.91	1.63	
After second drop in sensitivity	Integral	13	15.15	1.17	
	Spectral $\lambda > 820$ mμ	1.61	2.5	1.55	3.15
	region $\lambda > 870$ mμ	0.58	1.08	1.86	
After third drop in sensitivity	Integral	8.1	14.1	1.74	
	Spectral $\lambda > 820$ mμ	0.15	2.13	14.5	
	region $\lambda > 870$ mμ	0.037	1	30	2.75

The relative increase in the sensitivity of the cathode grows with the amount of cesium oxide (the greatest relative increase was 30-fold in the infrared region). However, the maximum sensitivity of the cathode after electron bombardment does not as a rule rise above the initial (immediately after preparation) value. The secondary emission coefficient decreased after the exposure to oxygen.

We also investigated the dependence of the secondary emission coefficient σ on the primary electron energy for an oxidized cathode with an initial sensitivity of 8.1 μa/lumen. The speed of the primary electrons was first gradually increased and then decreased (Table 5). The secondary emission coefficient rose as the electron potential was increased from 200 to 1200 v. In addition, a small increase in σ was observed during electron bombardment. In connection with this, measurements of σ, as the primary potential was reduced from 1200 to 220 v, yielded values greater than the initial ones.

Table 5

Dependence of the secondary emission coefficient on the primary electron potential

V_c	220	420	580	730	1020	1200	1020	680	580	220
σ	2	2.4	2.6	2.8	2.67	2.8	2.88	2.9	2.91	2.2

When investigating a cesium-antimony cathode we detected no increase in the photocurrent after electron bombardment.

Conclusions

The study established the conditions of electron bombardment producing an increase in the sensitivity of semi-transparent and thick cesium oxide cathodes with an initial sensitivity up to 20 μa/lumen. The emission of these cathodes increases in the spectral region above 600 mμ. The greatest increase in photocurrent (up to 30 times) is observed in the $\lambda > 900$ mμ region. The dependence of the increment in photocurrent after electron bombardment with the wavelength of the incident light is characterized for all cathodes by a sharp maximum in the 950-1150 mμ region and, in addition, for semi-transparent cathodes, by a small maximum at $\lambda \approx 700$ mμ. The location of the long-wave maximum in the photocurrent increment curve depends on the position of the red boundary of the photoeffect for the given cathode. The sensitivity of cathodes increases with bombardment time, up to a certain saturation value, in proportion to the amount of the electric charge Q received by the cathode. In the case of semi-transparent cathodes saturation occurs at $Q \approx 0.84 \cdot 10^{-4}$ a·sec/cm^2; in the case of thick cathodes - at $Q = 1.68 \cdot 10^{-3}$ a·sec/cm^2.

It must be noted that the amount of additional electric charge given up by the cathode after cessation of bombardment in the form of an increased photocurrent is at least an order of magnitude greater than the charge received by the cathode. The amount of electric charge given up by the cathode was determined from the curves characterizing the falling off of photocurrent to its initial value after cessation of electron bombardment. The maximum increase in sensitivity of semi-transparent cathodes as a result of bombardment was observed at electron speeds of 700-1000 v and current densities of 0.2-0.4 μa/cm^2.

Under the influence of red light the sensitivity of the cathode returns to its initial value only several hours after cessation of bombardment. Under the influence of blue light ($\lambda > 500$ mμ) the cathodes returned to their initial state in a matter of a few seconds.

Electron bombardment of semi-transparent cesium oxide cathodes with an initial integral sensitivity above 20 μa/lumen does not produce an increase in the photocurrent.

It was established that the increase in the emission of cesium-oxide cathodes after electron bombardment is connected with the presence of excess cesium oxide on the cathode surface. The greatest relative increase in photocurrent was observed for normally prepared cathodes subjected to additional oxidation after preparation. However, the maximum sensitivity of such cathodes after electron bombardment was still generally lower than the initial sensitivity immediately after preparation (i.e., before oxidation).

It may be assumed that in electron bombardment of a cathode containing an excess of cesium oxide, in addition to the ejection of secondary electrons, there occurs a transfer of energy to the electrons in the filled band or on local impurity levels. As a result these electrons can go over into the conduction band or to local levels of higher energy, which favors the rise in photosensitivity in the long-wave spectral region. Another possible explanation of the observed effect may be found in the influence of positive ions forming on the surface of the photocathode as the result of electron bombardment. We must emphasize that the above are only suggested, tentative explanations and that a satisfactory and reliable interpretation must await further investigations.

In practice the increase in photocurrent under the influence of electron bombardment can be utilized for re-establishing the sensitivity of oxygen-cesium cathodes.

The subject of the present investigation was suggested by Iu.A.Kushnir. The writer wishes to thank Iu.M.Kushir and A.A.Lebedev for their valuable advice and constant interest in the work.

References

1. Iu.M.Kushnir, Zhur. eksp. i teor. fiz., 6, 964 (1936).
2. H.Dember, Phys. ZS., 33, 529 (1925).
3. I.Johnson, Phys. Rev., 83, 49 (1951).
4. T.Hibi & K.Ishikawa, Phys. Rev., 83, 659 (1951).
5. T.Hibi & K.Ishikawa, Phys. Rev., 84, 1252 (1951).
6. S.Iu.Luk'ianov, Fotoelementy (Photocells), M. 1948.
7. P.Herlich, Photocells, (In Russian trans. M. 1948).

DISCUSSION

N.D.Morgulis: Would you say that electron bombardment is a practical method for improving photocathodes?

N.A.Soboleva: This method can be utilized for regenerating fatigued photocathodes.

N.D.Morgulis: What is the reason for the difference between the results obtained by Bykhovskaia and those reported by Japanese investigators?

N.A.Soboleva: Bykhovskaia discovered the absence of non-additivity in the case of cesium-antimony and cesium oxide photocathodes.

P.G.Borziak: Is it not possible that the electron beam shifts or disturbs the chemical equilibrium which is then reestablished?

N.A.Soboleva: It is possible that electron bombardment results in "recesiation" of the cathode.

P.V.Timofeev: It is strange that fatigue was not observed in the case of the cesium-antimony cathodes; a great number of photocells with single stage amplification has been produced and they all exhibit fatigue.

N.A.Soboleva: It is possible that the absence of fatigue is connected with the short bombardment times used in our experiments.

THE PHOTOELECTRIC EFFECT IN OXYGEN-SENSITIZED CESIUM-ANTIMONY CATHODES

(Abstract - Complete report in Zhur. tekh. fiz., 25, 2264 (1955)

- B.I.Diatlovitskaia

The investigation concerned the optical properties of extremely thin cesium-oxide films (on the order of the depth of emergence of photoelectrons, i.e., ~20 mμ) before and after their activation with oxygen to the optimal photosensitivity in the spectral region from 400 to 740 mμ. It was found that sensitization which results in a great increase in photosensitivity does not have any noticeable effect on the optical properties of such cesium-antimony coatings. Consequently, the change in sensitivity is not connected with the formation of a new substance on the surface of the cathode but is due only to a process lowering the work function.

The reduction of the work function as a result of optimal sensitization, as determined from the displacement of the red limit of the principal photoeffect, is of the order of 0.1 ev.

The coefficient of sensitization K_s slowly increases with the wavelength λ in the range from 400 to 600 mμ from ~ 1.2 to ~ 2; beginning with $\lambda \approx 580$-600 mμ, however, the K_s (λ) curve rises sharply attaining a value of ~ 25 at $\lambda \approx 640$ mμ. So sharp a change in K_s indicates that, after the lowering of the potential barrier as a result of sensitization, numerous new photoemission centers begin to participate in the photoelectric process in the spectral region above 600 mμ: for example, in the case of $\lambda \approx 630$ mμ ($h\nu \approx 2$ ev), these may be electrons from the filled band.

In accord with this the red limit of the principal photoeffect, which lies at $h\nu_0 \approx 2$ ev prior to sensitization, shifts to $h\nu_0 \approx 1.9$ ev after sensitization.

The flat section in the K_s (λ) curve is explained, in the light of the concept of the diffusional nature of the motion of photoelectrons inside the cathode, by an increase in the number of electrons having sufficiently high "normal energies" to overcome the low surface potential barrier.

The results of the investigation are described in detail by the author in her dissertation.[1]

Institute of Physics of the
Academy of the Ukrainian SSR

References

1. B.I.Diatlovitskaia, Dissertation, Kiev State University, 1952.

INFLUENCE OF ADSORPTION OF DIPOLE BARIUM OXIDE MOLECULES ON THE PHOTOELECTRIC EMISSION OF A CESIUM-ANTIMONY CATHODE

(Abstract - Complete report in Zhur. tekh. fiz., 25, 2469 (1955).

- V.M.Gavriliuk

An attempt was made to control the work function and photoelectric emission of a semiconductor cesium-antimony cathode by adsorption of dipole molecules of barium oxide on its surface. It was established that the adsorption of barium oxide molecules at the optimal concentration leads to a reduction of the work function by about 0.1 ev and an increase in the photocurrent by a factor of approximately 1.5.

Comparison of our results with those of Diatlovitskaia[1] substantiated the conclusion reached by Morozov[2] and Diatlovitskaia that the mechanism of sensitization of cesium-antimony cathodes with oxygen consists in the formation of dipole cesium oxide molecules on the cathode surface.

Institute of Physics of the
Academy of the Ukrainian SSR

References

1. B.I.Diatlovitskaia, Zhur. tekh. fiz., 25, 2264 (1955).
2. G.A.Morozov, Zhur. tekh. fiz., 9, 2012, 2018 (1939).

DISCUSSION

P.V.Timofeev: Why do you exclude the possibility of adsorption of gas on the barium oxide?

V.M.Gavriliuk: We do not reject the possibility.

Question: What were the sensitivity values obtained?

V.M.Gavriliuk: The sensitivity rose by a factor of 1.5-2 relative to the initial value common to such cathodes. Absolute determinations of the sensitivity were not made.

ON THE PHYSICS OF POROUS METAL-FILM CATHODES

(Abstract - Complete report in Zhur. tekh. fiz., 26, 536 (1956)

- N.D.Morgulis

1. The report gives the results of a correlated series of investigations of the different physical properties of porous metal-film cathodes with a pure barium carbonate filler carried out by the laboratory staff of the Institute of Physics of the Academy of Sciences of the Ukrainian SSR.

2. The report introduces the concept of the optimal type cathode on the surface of which the barium forms a film of optimal thickness corresponding to the maximum emission, while the Ba loss occurs only by desorbtion. The optimal vapor pressure and rate of evaporation of the barium were evaluated for such optimum type cathodes. An equation was deduced for determining the rate of diffusion of Ba through the sponge of the tungsten cathode, a process which involved the parallel operation of two mechanisms: Knudsen flow through the cathode sponge pores and migration of the Ba over the surface of these pores. On the basis of this one can evaluate the pressure differential across the sponge layer, i.e., the optimal Ba vapor pressure inside the envelope enclosing the cathode.

3. Experimental determinations were made of the vapor pressure of Ba and Sr (the latter by the method of radioactive isotopes) both over cathodes with different degrees of porosity and in the case of free evaporation. Analysis of our data and the results published by other authors leads to the conclusion that in our specific case the loss of active Ba occurs primarily by Knudsen flow through the sponge pores. This indicates that in the given case the barium is utilized with low efficiency.

4. For the purpose of clarifying the influence of residual gases in the tube on the emission of such cathodes we carried out a mass-spectrometric determination of the composition of these gases over a period of over 100 hours operation of a cathode in a laboratory set-up, successively in under zero emission and measurable emission conditions. It followed from these measurements that both the poisoning influence of the active components of these gases and the disintegration of the cathode by ion bombardment may have a very appreciable effect on the cathode emission (over and above that due to evaporation of the adsorbed Ba film).

5. Calculations were carried out for the dimensions of the effective emission zone on the surface of the cathodes; to obtain a quantitative result it is necessary to know both the coefficient of surface diffusion and the lifetime of the Ba atom in the adsorbed state, regarding which there are no reliable experimental data. Calculations on the basis of arbitrarily assumed likely values of these quantities leads to the conclusion that this emission zone is usually much thinner than the grain size, i.e., that the emission of cathodes must be highly nonuniform over the surface.

6. From an examination of the kinetics of the thermochemical reaction of barium carbonate and its decomposition products with the tungsten sponge it is concluded that this reaction must also occur on the exterior of the cathode; hence the cathode surface must consist of a system: metal + semiconductor compound layer + film of adsorbed Ba atoms. This conclusion is substantiated by 1) direct electron diffraction analysis of the composition of the outer surface of the cathode, which indicates the presence of barium tungstenate, and 2) the fact that these cathodes exhibit a marked tendency to sparking.

ELECTRON EMISSION OF POROUS METAL-FILM THERMIONIC CATHODES
(Abstract)

- Ia.P.Zingerman

The work, which consisted of two parts*, was devoted to experimental investigation of the thermionic emission of porous metal-film cathodes - so-called "L" cathodes - initially filled with pure barium carbonate.

In the first part of the work we investigated (in a plane diode system) the electron emission of the porous cathode in retarding and accelerating electric fields with the cathode operating at low temperatures : ~600-900°K. In this temperature region the dependence of log I_a on V_a in the retarding field proved to be rigorously linear in a very wide range of plate currents (over 6-7 orders of magnitude), i.e., the distribution of electron velocities was Maxwellian. The electron temperature determined from the slope of this dependence agreed within 5-10% with the temperature of the cathode as measured directly with a thermocouple. The current voltage characteristics measured in the same low temperature region in an accelerating electric field ($E \lesssim 1.5 \cdot 10^4$ v/cm) indicated the presence of an anomalous Schottky effect. Analysis of these characteristics by the method of Becker made it possible to evaluate the degree of inhomogeneity in the distribution of the work function over the surface of the porous metal-film cathode. The size of the individual spots proved to be $\sim 10^{-4}$ cm, while the amplitude of the variation of the work function $1/2\ \Delta\varphi \approx 0.3$-$0.35$ ev. The mean value of the work function as evaluated from the slope of the Richardson plots was 2.1 ev.

In the second part of the work we investigated the cause of the anomalous saturation of the current-voltage characteristics as observed at high emission current densities in the region of ~1300-1500°K. Through analysis of the current-voltage characteristics recorded at a rigorously constant cathode temperature but at different values of the interelectrode distance d, it was shown that regardless of the value of d, I_a depends uniquely on the magnitude of $V_a^{3/2}/d^2$ not only in the region of the variation of V_a, where the emission from the entire surface of the cathode is limited by the space charge, but also over an appreciable part of the region where anomalous saturation obtains. This indicates that the reason for the anomalous saturation lies in the gradual saturation of the emission current on the surface of the thermionic cathode, nonuniform as regards the work function, rather than with the Schottky effect as was assumed earlier. Using the previously proposed method[1] for analyzing the current-voltage characteristics in the region of their anomalous saturation, we determined the magnitude of the inhomogeneities in the distribution of the emission current density over the surface of a porous metal-film cathode. In one of the investigated cases, at ~1100°K and a mean plate current density ~8.5 a/cm^2, the true current density on the cathode surface was found to vary between the 3.5 and 28 a/cm^2, which is evidence of marked emission inhomogeneity of actual porous metal-film cathodes.

Institute of Physics of the
Academy of Sciences of the Ukrainian SSR

References

1. Ia.P.Zingerman, Dissertation, IFAN USSR (Institute of Physics of the Ukrainian SSR Ac. of Sci.) Kiev, 1950; Trudy IFAN (Transactions of the Institute of Physics of the Ukrainian SSSR Ac. of Sci.) No. 2, 57 (1952).

---

*The report on the first part of the work is published in Trudy IFAN USSR (Transactions of the Institute of Physics of the Ukrainian SSR Ac. of Sci., No. 7,24 (1956); that on the second part in Ukr.fiz.zhurn.,(Ukrainian Physics Journal), 1, 134 (1956).

INFLUENCE OF ADSORBED FILMS OF DIPOLE MOLECULES ON THE WORK FUNCTION OF METALS

(Abstract - Complete report published in Zhur. eksp. i teor. fiz., 30,149 (1956)

- N.D.Morgulis & V.M.Gavriliuk

1. An experimental study was made of the influence of an adsorbed film of dipole molecules (CsCl) on the work function of tungsten. Distinctive features of the investigation were 1) use of the "wedge" method which allowed of obtaining films in a wide and continuous range of densities, 2) use of CsCl tagged with radioactive Cs^{134}, which made it possible to determine the amount of adsorbed molecules with high accuracy, and 3) use of a very high vacuum ($p \approx 10^{-9}$ mm, $p_{cond} \approx 10^{-10}$ mm Hg, a condition under which the influence of adsorption of the residual gases can be neglected.

2. The dependence of the work function on the amount of adsorbed CsCl molecules was determined experimentally. A comparison of the observed dependence for the CsCl-W system with the corresponding dependences for the Cs-W, BaO-W and Ba-W systems, taken from the literature and found in our previous investigations (Refs. 1-3), brings to light interesting differences. The fact that dipole films of CsCl and BaO always reduce the work function of the base metal is interpreted as an indication of the presence on the surface of the metal of an electric field orienting the dipole molecules. By applying Langevin's equation to a film with infinitely low density one can deduce that the strength of this field is between 10^6 and 10^7 v/cm. However, this does not exclude the possibility that in this case changes of the charge density in the double surface layer may also play a certain role.

Institute of Physics of the
Academy of Sciences of the Ukrainian SSR

References

1. J.Taylor & I.Langmuir, Phys. Rev., 44, 423 (1933).
2. G.Moore & H.Allison, Phys. Rev., 77, 247 (1950).
3. V.Gavriliuk, Trudy IFAN USSR (Transactions of the Institute of Physics of the Ukrainian SSR Ac. of Sci.), No. 5, 87 (1954).

DISCUSSION

A.R.Rumiantsev: What was evaporated from the vaporizer and at what temperature?

V.M.Gavriliuk: The vaporizer temperature was about 350°; the substance evaporated was CsCl.

A.R.Rumiantsev: Was the coefficient of reflection of the neutral molecules taken into account?

V.M.Gavriliuk: Yes, it was taken into account. We plotted a curve of the dependence of the coefficient of reflection on the concentration of the adsorbed CsCl molecules.

A.R.Rumiantsev: What were the absolute values of the work function and how were they determined?

V.M.Gavriliuk: The work function of tungsten under our high-vacuum conditions was assumed to be 4.5 ev and we determined the variation of the work function of the base with adsorption of CsCl molecules. Absolute measurements of the work function were not made.

INFLUENCE OF ADSORBED FILMS OF BARIUM ATOMS AND POLAR BARIUM OXIDE MOLECULES ON THE WORK FUNCTION OF TUNGSTEN, GOLD AND GERMANIUM

- V.M.Gavriliuk

Investigation of the influence of adsorbed films of atoms and dipole molecules on the thermionic emission of different solids is of particular interest at present in view of the increasing industrial use of new types of metal-film cathodes as well as of anti-emission coatings. Moreover, there now exist improved experimental techniques for investigating adsorption effects.

In the present work we investigated the range of variation of the work function of tungsten, gold and germanium under the influence of active adsorbed films of atomic barium and barium oxide as the components of the products of evaporation from oxide-coated cathodes.

We developed an appropriate procedure and a suitable platinum evaporator for obtaining the Ba and BaO films.[1] In the first case, the evaporator cup was charged with barium aluminate getter; in the second case with $BaCO_3$. We could judge of the absence of Ba impurity atoms from the BaO molecular beam both on the basis of results of investigation of the systems BaO-W and Ba-W (see below) and on the basis of special experiments, carried out in our laboratory by L.S. Zaitseva (whom we take this occasion to thank), on the evaporation from a similar evaporator of SrO molecules tagged with radioactive Sr^{89}; the proportion of Sr atoms in the evaporated material was determined by the method of Berdennikova[8]. These experiments showed that the admixture of Sr atoms in the SrO molecular beam did not exceed 1-2%.

1. Barium and barium oxide films on tungsten and gold*

The experiments were carried out using the specially developed procedure described in Ref. 1. The adsorbed film was obtained in the form of a "wedge", i.e., had a different gradually varying concentration of atoms or molecules over the length of the coating. The concentration at each point of the wedge was determined by means of the familiar formulas for the amount of atoms or molecules condensing from a molecular beam, taking into account the coefficient of condensation and utilizing the method of amperometric titration. The change in the work function under the influence of the film was determined at different points of the "wedge" by the electron beam method by means of a movable electron gun. This method does not require heating of the base which is very important since heating may produce irreversible changes in the film, seriously distorting the results.

The experiments were carried out under very high vacuum ($\sim 10^{-9}$ mm Hg).

In investigating the Ba-W system, we established that the dependence of the work function $\varphi = \varphi_W - \Delta\varphi$ of the system on the concentration n of adsorbed atoms is of the same character as reported in most classical investigations (see, for example, Ref. 2), i.e., the work function at first falls off sharply, passes through a minimum ($\varphi_{min} \approx 1.6$ ev) at concentrations $n \approx 3.5 \cdot 10^{14}$ cm^{-2} and then increases to the values common to metallic barium (see table below).

Investigation of the BaO-W system showed that adsorption of BaO molecules leads to a sharp decrease in the work function of tungsten. The work function of the system attains 2 ev at $n \approx 1 \cdot 10^{14}$ cm^{-2} and then remains steady. Heating the system at $\sim 900°$ for a few seconds leads to a decrease of the work function over the entire "wedge". A minimum forms in the curve for $\varphi(n)$ and φ_{min} attains a value of 1 ev at $n \approx 1 \cdot 10^{14}$ cm^{-2}. The mechanism of adsorption of dipole BaO molecules has been examined in Ref. 3 on the assumption of the presence of an orienting field at the surface of the metal and the possibility of electron exchange interaction of the molecules with the metal.

---

*The report on this part of the investigation is given here in condensed form; the full report appears in Ukr.fiz.zhur., (Ukrainian Physics Journal), 1,73(1956).

An investigation of the Ba-Au and BaO-Au systems was undertaken in view of the fact that gold is the material used for anti-emission coatings in sector electron tubes.

Our experiments showed that the barium film reduces the work function of gold, but that the dependence of the work function on n for this case is entirely different from that of the BaW system. The curve for $\varphi(n)$ does not have a minimum and hence the lowest work function of such a system equals the work function of metallic barium ($\varphi \approx 2.4$ ev), i.e., is much higher than φ_{min} for the BaW system. The monotonic character of this dependence and the high value of φ_{min} lead us to conclude that the anti-emission effect of gold is determined by the fact that the work function of this system cannot be less than 2.4 ev, particularly since under the actual operating conditions of a gold-plated grid in a vacuum tube (where it is operated at a temperature of $\sim 500^{\circ}$, which favors strong diffusion of the barium through the gold layer and evaporation of it from the surface) the work function of the system must be appreciably greater than 2.4 ev. Here one may assume the formation of a compound of gold with barium, as was observed in the experiments of P.G.Borziak.

The adsorption of BaO molecules on the gold surface leads to an insignificant reduction of the work function ($\varphi \approx 3.7$ ev) (see table below). Heating to $\sim 900^{\circ}$ leads to an additional decrease in the work function by approximately 1 ev as in the case of the BaO-W system. The high value of the work function of the BaO-Au system indicates that the thermionic emission of such a system at the operating temperatures of vacuum tube grids will be virtually nil.

2. Atomic barium and barium oxide films on germanium

The number of investigations devoted to the influence of adsorbed films on the emission characteristics and the work function of semiconductors is woefully inadequate. In this connection we would like to mention the researches of Lashkarev and Liashenko,[4] who studied the influence of adsorption of mainly organic molecules under low-vacuum conditions.

At first we made an attempt to investigate the influence of the adsorption of BaO molecules on the work function of a semiconductor - a cesium-antimony cathode - under high vacuum.[5] However, this choice proved unsuitable for, as we later found out, the work function of such cathodes is always depressed beforehand by the adsorbed film of cesium atoms.

Borziak[6] undertook a series of experiments in our laboratory on the influence of the products of evaporation of BaO from a platinum wire on the work function and photoelectric emission of germanium. The description of the evaporating procedure Borziak used and the limiting value of the work function obtained by him (close to the normal value of 2.4 ev), lead us to believe that due to dissociation of the BaO an appreciable number of Ba atoms was also lost through evaporation.

As part of the present series of experiments we investigated the influence of adsorbed films of atomic Ba and dipole BaO molecules on the work function of germanium. The basic procedure was similar to that employed in our previous investigations.[1,5] The germanium surface was prepared by evaporation of spectroscopically pure germanium (current carrier concentration $\sim 10^{14}$ cm^{-3}) onto a metallic base. During the evaporation process the work function was checked periodically.

We started our real experiments with Ba and BaO only when the value of the work function, changing gradually from the value corresponding to the base metal to that for solid germanium, attained a stable value. The determined differences between the values of the work function of germanium and of the base metal (for example, with a tungsten base $\Delta\varphi = 0.4$ ev) lead to a value of 4.8-4.9 for the work function of germanium, which is in agreement with the data of other investi-

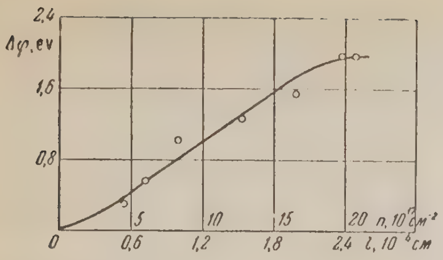

Fig. 1. Dependence of the work function of a base with φ_0 = = 2.8 ev on the thickness of the germanium coating sputtered on its surface.

gators.[7] In order to know the actual thicknesses of the germanium coatings involved we carried out measurements of the dependence of the work function of the germanium film on its thickness. For convenience of measurement we used a base with a low work function for these experiments. The thickness of the coating was determined by the method of tagged atoms, using radioactive Ge^{71}.

The results of these experiments are shown in Fig. 1. It will be seen that the limiting work function corresponding to solid germanium (flattening of the $\Delta\varphi$ curve) is attained at a film thickness of about $2.5 \cdot 10^{-4}$ cm. From this we evaluated the Debye screening length for our film to be $\sim 5 \cdot 10^{-5}$ cm. Knowing the Debye screening length makes it possible to evaluate the concentration of curve carriers in the germanium film, which proved to be equal to about 10^{14}-10^{15} cm^{-3}, and a number of other useful parameters.

The investigation of the influence of adsorbed barium atoms and barium oxide molecules on the work function of germanium was carried out at a vacuum of $\sim 10^{-8}$-10^{-9} mm Hg. The results of this experiment are shown in Fig. 2. The curves in this figure give the dependence of the work function of germanium - assumed initially equal to 4.8 ev - on the duration of sputtering of barium (curve I) or barium oxide (curve II) on its surface.

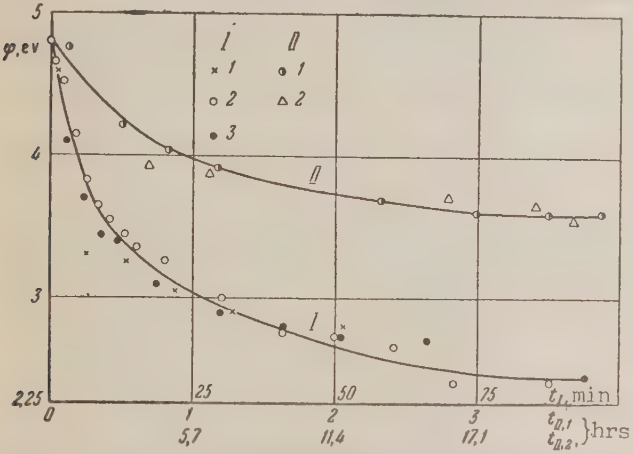

Fig. 2. Variation of the work function of germanium film on the duration of sputtering on barium or barium oxide: I) barium; II) barium oxide. The differently identified points correspond to different experiments.

The basic physical parameters characterizing both the Ba-Ge and the BaO-Ge systems, as well as the other systems investigated, are listed in the table. It will be seen from the table and Fig. 2 that the adsorption of barium atoms on the surface of germanium leads to an appreciable decrease of the work function of the latter ($\varphi_{min} \approx 2.4$ ev); this value of φ_{min} is of the same order of magnitude as that obtained by Borziak.

The curve for $\varphi(n)$ for the Ba-Ge system has no minimum: the work function decreases monotonically with increasing barium atom concentration all the way to the value corresponding to metallic barium. The character of the $\varphi(n)$ curve and the limiting value of the work function are the same as for the Ba-Au system.

The adsorption of dipole BaO molecules on the surface of germanium leads to a lesser decrease of its work function ($\varphi_{min} \approx 3.6$ ev) than in the case of the Ba-Ge system. The $\varphi(n)$ curve also has no minimum and is similar to the corresponding curve for the BaO-Au system in the absence of heating. Thus, in this

Emission characteristics of tungsten, gold and germanium coated with a film of Ba or BaO

System	φ_{min}, ev	φ_{∞}, ev	$n_{min} \cdot 10^{-15}$ cm^{-2}	$p_{n \to 0} \cdot 10^{18}$, CGS
Ba — W . . .	1,6	2,4	0,35	12
BaO — W . . .	1,0	—	0,08	9,4
Ba — Au . . .	2,4	2,4	5,0	0,4
BaO — Au . .	3,2	—	0,35	—
Ba — Ge . . .	2,4	2,4	—	—
BaO — Ge . .	3,6	—	—	—

case, just as in the case of the BaO-Au and Ba-Au systems, the influence of the dipole BaO molecules on the work function proves to be weaker than the influence of adsorbed Ba atoms; this is in marked contrast to the case of the BaO-W and Ba-W systems, wherein the influence of adsorbed atomic barium is weaker than that of BaO molecules. All these facts indicate that in the case of germanium we are apparently dealing with an adsorption mechanism and an electronic interaction of Ba atoms and BaO molecules with the metal base different from those obtaining in the case of tungsten. Apparently, however, the mechanism of adsorption on gold is similar to that of adsorption on germanium.

In attempting an interpretation of the similarity of the cases of germanium and gold one should bear in mind the possibility of chemical reaction of barium with these metals and the possible formation of intermetallic compounds.

In conclusion the the writer desires to thank N.D.Morgulis for his constant attention and valuable advice.

Institute of Physics of the
Academy of Sciences of the Ukrainian SSR

References

1. V.M.Gavriliuk, Trudy IFAN USSR (Transactions of the Institute of Physics of the Ukrainian SSR Ac. of Sci.) No. 5, 87 (1954).

2. J.De Boer, Electronic emission and adsorption effects (In Russ. translation, M. 1936); A.L.Riemann, Thermionic emission (In Russian trans. M.-L. 1940); B.M.Tsarev, Kontaktnaia raznost' potentsialov (Contact potential difference), M.-L. 1954.

3. D.N.Morgulis & V.M.Gavriliuk, Zhur. eksp. i teor. fiz., 30, 149 (1956); present issue of the Bulletin.

4. V.E.Lashkarev & V.I.Liashenko, Sb., posviashchennyi 70-letiiu Akad. A.F. Ioffe(Symposium dedicated to the 70th anniversary of Academician A.F.Ioffe) M.-L. 1950; V.I.Liashenko & I.I.Stepko, Izv. AN SSSR, Ser. fiz., 16, 211,1952; W.Brattain & J.Bardin, Bell-Syst. Techn. J., 32, 1 (1953).

5. V.M.Gavriliuk, Zhur. tekh. fiz., 25, 2469 (1955); present issue of the Bulletin.

6. P.G.Borziak, O.G.Sarbei, Ukr. fiz. zhurn., (Ukrainian Physics Journal) 1, 3 (1956).

7. E.Mitchell & J.Mitchell, in "Poluprovodnikovye materialy" (Semiconductor materials), M. 1954.

8. N.N.Berdennikova, Tekhnika zav. "Svetlana" (Technology of the "Svetlana" Plant), Ser. 3, Issue 2, No. 6, Gosenergoizdat, M., 1934.

DISCUSSION

V.L.Granovskii: Why did you want to know the thickness of the Ge film?

V.M.Gavriliuk: In order to be sure that the base was not affecting the results

L.N.Dobretsov: Does the curve characterizing the dependence of the work function of germanium on the thickness of the germanium film exhibit saturation?

V.N.Gavriliuk: Saturation was always observed. The curve shown is rather unsatisfactory; it gives the data pertaining to the experiment with radioactive germanium.

S.A.Vekshinskii: Were the variations in the work function of germanium you obtained stable?

V.M.Gavriliuk: Yes, they were stable.

D.G.Bulyginskii: At what thickness of the Ba film does the work function stop changing with increasing thickness?

V.M.Gavriliuk: At a thickness of 3-5 monatomic layers without taking into account the reflection of barium atoms during adsorption from the molecular beam.

K.B.Tolpygo: Can one compare the obtained experimental data with my theory?

V.M.Gavriliuk: We could not make a comparison since your formulas are valid only for semiconductor thicknesses smaller than the screening radius.

A.R.Rumiantsev: Was not the barium coating oxidized by the residual oxygen in the tube?

V.M.Gavriliuk: Apparently not, inasmuch as the observed value of the work function remained stable for a prolonged period.

V.N.Lepeshinskaia: What was the pressure in the tube?

V.N.Gavriliuk: About 10^{-9} mm Hg; the pressure of the condensing component was even lower.

A.R.Rumiantsev: How did you obtain the Ba and BaO films and how could you be sure you had vaporized BaO in one case and Ba in the other?

V.M.Gavriliuk: The barium films were obtained by evaporating Ba from aluminum-barium getter at 400°. The work function of the barium films had a value identical with that reported in the literature. The barium oxide films were obtained by evaporation of BaO from a platinum vaporizer. Initially the vaporizer was loaded with $BaCO_3$ which was transformed into BaO by heating. According to G.Ia.Pinkus, this process proceeds rapidly at the temperature employed and goes to completion. In order to make sure that the molecular BaO beam was not contaminated with atomic barium we periodically oxidized the material in the evaporator during the process of evacuation, leaving the set-up at forevacuum pressure for a number of hours. Thus we obviated the possible formation of Ba as a result of the thermochemical reaction of BaO with impurities in the platinum and the $BaCO_3$. Furthermore, as we noted in our report, Zaitseva in our laboratory carried out a special series of experiments with strontium oxide using radioactive Sr^{89}. These experiments showed that the amount of Sr atoms in the molecular beam of SrO does not exceed 1-2%.

S.A.Tiktin: Why in selecting the material for anti-emission coatings of vacuum tube grids must one know the shape of the $\varphi(n)$ curve?

V.M.Gavriliuk: In the case of a monotonic curve such as that characteristic of the Ba-Au system the minimal work function is large, about 2.4 ev. Furthermore, under the actual operating conditions of a gold-plated grid, that is, at a temperature of about 500°, there is a certain equilibrium value of the concentration of barium on the gold surface. This equilibrium value depends on the rate of arrival of barium at the grid surface and the rate of its removal due to diffusion into the gold coating and evaporation. Probably this equilibrium value of the concentration is lower than the value corresponding to the limiting φ. In this case the work function can only be greater than 2.4 ev and, consequently, any noticeable thermionic emission will be impossible. In the case of a $\varphi(n)$ curve with a minimum such as that typical of the Ba-W system the above mentioned processes would probably lead to a reduction of the work function and, consequently, to an increase of the thermionic emission.

CHANGE IN THE WORK FUNCTION DURING ADSORPTION OF DIPOLE MOLECULES ON A METAL SURFACE

(Abstract - Complete report in Ukr.fiz.zhurn(Ukrainian Physics Journ.)1,81(1956))

- I.M.Dykman

The change in the work function of a metal due to adsorption on its surface of atoms or molecules depends not only on the interaction of the adsorbed molecules with the adsorbing metal but also on the interaction of the molecules with each other. In the case of physical adsorption, when the molecules in the adsorbed state have a certain dipole moment, the decrease in the work function can be explained by preferred orientation of the molecular dipoles.

It is assumed in the investigation that there exists at the metal surface an electric field effective over a short range and directed from the metal to the vacuum. Account is taken of electrostatic interaction of the adsorbed molecules with each other. The dependence of the decrease in the work function on the concentration of the adsorbed molecules for the case of a monomolecular layer is deduced from statistical considerations. The curve characterizing this dependence has a maximum.

The results of the theoretical calculations were applied to the case of adsorption of BaO and CsCl molecules on tungsten and compared with the appropriate experimental data of Morgulis and Gavriliuk. The values of the electric field E determined from a comparison of the theoretical and experimental data in the two cases proved to be in as close agreement as might be expected in view of the simplifying assumptions made in deducing the theoretical formulas.

Institute of Physics of the
Academy of Sciences of the Ukrainian SSR

DISCUSSION

S.D.Gvozdover: Langevin's theory requires a homogeneous field. To what extent is your theory which utilizes Langevin's expressions valid if the field at the surface is not uniform?

I.M.Dykman: In our case the field must be homogeneous only within the limits of the effective dimensions of the molecular dipole adsorbed on the surface. This condition is approximately satisfied.

S.D.Gvozdover: What is new or different in your calculations as compared with the familiar examination of the change in work function due to adsorption of n dipoles with a momentum P?

I.M.Dykman: In our calculations account is taken of the interaction of the adsorbed molecules with each other. It is precisely taking this interaction into account that leads to the nonmonotonic variation in $\Delta\varphi$ with n and to the appearance of the maximum. Without taking this interaction into account the maximum in the variation of $\Delta\varphi$ cannot be explained.

BULLETIN of the Academy of Sciences of the USSR - Physical Series
Vol. 20, No. 9 - Transactions of the All-Union Conference on Cathode Electronics
(Kiev, 25-29 November 1955)

TABLE OF CONTENTS

	Page Orig.	Page Trans.
Opening address - A.A.Lebedev	975	881
A survey of research accomplishments and problems in the field of cathode electronics - N.D.Morgulis	977	883
Emission of electrons from complex surfaces (Abstract) - P.V.Timofeev	993	898
Secondary-electron emission (Present state and future prospects) - L.N.Dobretsov	994	899
Secondary-electron emission of dielectrics and metals - A.R.Shul'man	1008	912
Reflection of slow electrons from pure metal and coated metal surfaces (Abstract) - D.A.Gorodetskii	1023	925
Certain anomalous characteristics of the secondary-electron emission of magnesium alloys - V.N.Lepeshinskaia	1025	927
Secondary-electron emission of nickel-base alloys - B.S.Kul'varskaia	1029	931
Electron multipliers for recording corupscular and hard electromagnetic radiation (Abstract) - T.M.Lifshits	1038	938
Distinctive characteristics of the photoeffect in cesium-oxide-silver photocathodes - P.G.Borziak, V.F.Bibik and G.S.Kramerenko	1039	939
"Excess" velocities in the energy spectrum of photoelectrons from a cesium-antimony cathode (Abstract) - N.M.Politova	1050	948
Influence of electron bombardment on the photoemission of complex photocathodes - L.N.Bykhovskaia	1052	949
The photoelectric effect in oxygen-sensitized cesium-antimony cathodes (Abstract) - B.I.Diatlovitskaia	1065	962
Influence of adsorption of dipole barium oxide molecules on the photoelectric emission of a cesium-antimony cathode (Abstract) - V.M.Gavriliuk	1066	963

On the physics of porous metal-film cathodes (Abstract) - N.D.Morgulis	1067	964
Electron emission of porous metal-film thermionic cathodes (Abstract) - Ia.P.Zingerman	1068	965
Influence of adsorbed films of dipole molecules on the work function of metals (Abstract) - N.D.Morgulis & V.M.Gavriliuk	1069	966
Influence of adsorbed films of barium atoms and polar barium oxide molecules on the work function of tungsten, gold and germanium - V.M.Gavriliuk	1071	967
Change in the work function during adsorption of dipole molecules on a metal surface (Abstract) - I.M.Dykman	1076	972

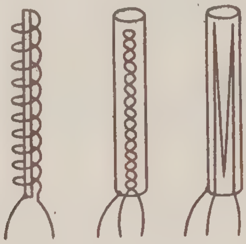

Translated in 1957 by
Columbia Technical Translations
5 Vermont Ave., White Plains, N.Y.

Transactions
# of the
All-Union Conference on Cathode Electronics

(First Conference continued from Vol.20, No.9)

(Kiev, 25-29 November 1955)

NON-UNIFORMITY OF THE WORK FUNCTION OF OXIDE-COATED CATHODES

- D.G.Bulyginskii

In many papers devoted to the physics and preparation of the oxide-coated cathode, this cathode is assumed to be a system having uniform emissive properties. Actually, however, it is known that the cathode surface has a non-uniform work function and, consequently, is characterized by non-uniform distribution of the emission over the surface. The assumption of uniformity is a common simplification which, under certain circumstances, can lead to erroneous deductions. The non-uniformity of the work function can be quantitatively specified either in terms of a surface distribution function of the work function $\varphi(XY)$ or a distribution function of the cathode area according to the values of the work function $\beta(\varphi)$, the latter being defined so that $ds = \beta(\varphi)d\varphi$ represents the total area of all elements characterized by a work function in the interval from φ to $\varphi + d\varphi$.

Until now there has been no satisfactory quantitative procedure for studying the non-uniformity of the work function that would allow of determining of the form of either of these functions.*

The purpose of the present investigation was to develop an experimental method of determining the area distribution function for an oxide-coated cathode according to the work function, i.e., $\beta(\varphi)$.

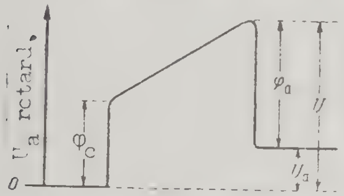

Fig. 1. Potential distribution in a system consisting of a plane oxide-coated cathode and a plane anode to which a retarding potential is applied.

The method is based on the following considerations. Let us assume we have a diode system consisting of a plane oxide-coated cathode of unit area and of a plane anode parallel to it. If a certain retarding potential is applied to the anode, the potential distribution in the system will be as shown in Fig. 1, where the ordinates are values of the retarding potential above the level of the electrochemical potential of the cathode.

It can readily be seen that, if the cathode and anode were completely homogeneous as regards work function and if, in addition, ideal conditions for the passage of current obtained, the current-voltage characteristic of the diode would have the ideal form indicated by curve a in Fig. 2.

In going from a retarding field to an accelerating one, we have a sharp transition from the exponential increase law to saturation. Under actual conditions this transition occurs gradually, i.e., extends over a certain interval of anode potentials (curve b in Fig. 2). This is due to a number of causes, among which are: distortion of the field in the gap between the electrodes, non-uniformity of the potential drop in the oxide layer, non-uniformity of the work functions of the cathode and anode, space charge and geometrical irregularities of the electrode surfaces. If by improving the technique

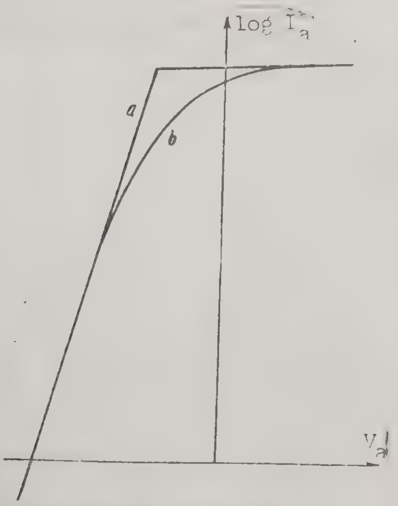

Fig. 2. Diode current-voltage characteristic: a) for a uniform cathode and anode and ideal conditions for current flow, b) under actual tube conditions.

---

*A method of investigating the non-uniformity of the work function by analysis of the current-voltage characteristics under anomalous saturation conditions was first proposed by Ia. P. Zingerman, Trudy (Transactions) of the Ukrainian SSR Ac. of Sci. No. 2, p. 57 (1952).

of obtaining the current-voltage characteristic, we succeed in eliminating all these factors except the non-uniformity of the work function, we should be able to deduce the nature of the non-uniformity of the cathode work function from the shape of the current-voltage curve and its deviation from the ideal shape.

This can be accomplished in the following way. Let the voltage applied to the anode be such that its surface potential U (above the electrochemical potential of the cathode) has a value intermediate between the maximum and minimum values of the work function of the different parts of the cathode. Then the current I_a flowing to the anode can be viewed as consisting of two parts. The current from all parts having a work function less than U will have everywhere the same density, i.e., the density given by the ideal characteristic:

$$j_1 = AT^2 e^{-eU/kT}.$$

The current coming from the remaining areas will have a density determined at every point by the local work function. Therefore

$$I_a = AT^2 e^{-eU/kT} \int_0^U \beta(\varphi)\, d\varphi + AT^2 \int_U^\infty e^{-e\varphi/kT} \beta(\varphi)\, d\varphi.$$

Differentiating this expression with respect to U, we obtain

$$\frac{dI_a}{dU} = -\frac{e}{kT} AT^2 e^{-eU/kT} \int_0^U \beta(\varphi)\, d\varphi.$$

Noting that the expression in front of the integral is the derivative of the ideal current-voltage characteristic with respect to the current density, we can write:

$$\frac{dI_a}{dU} = \frac{dj_1}{dU} \int_0^U \beta(\varphi)\, d\varphi.$$

or

$$\int_0^U \beta(\varphi)\, d\varphi = \frac{dI_a}{dU} \Big/ \frac{dj_1}{dU}.$$

Differentiation of the last expression yields the function $\beta(\varphi)$ characterizing the distribution of the cathode area according to values of the work function.

Our investigation of the non-uniformity of the work function of oxide-coated cathodes was based on this approach.

A great deal of attention was given to analysis and elimination of various factors capable of distorting the current-voltage characteristic. To eliminate the effects of space charge, a grid carrying a sufficiently high positive potential was introduced between the cathode and anode. In the first approximation, introduction of a grid does not produce any distortion of the current-voltage characteristic since the flow of current is still determined by the anode potential. However, when a grid with an accelerating potential is involved, it is necessary to take the "micro-optics" into account, i.e., to allow for the deviation of the electron trajectories from linearity in the vicinity of the grid filaments. We obviated the influence of this factor by using a sufficiently fine mesh screen for the grid.

In order to avoid the distorting influence of the potential drop in the oxide layer we were forced to keep the upper limit of the experimental temperature range some 200-250° below the usual operating temperature of an oxide-coated cathode.

A number of other possible causes of distortion of the current-voltage characteristic were examined and methods found for eliminating them. However, in addition to systematic distortions, which we believe we succeeded in making insignificantly small, there remain chance errors - statistical scattering of

the points - which may be considerable and the effect of which increases incident to differentiation of the experimental curve and particularly in the case of double differentiation. In order to evaluate the effect of such errors on the final shape of the β(φ) curves we carried out the following control experiment.

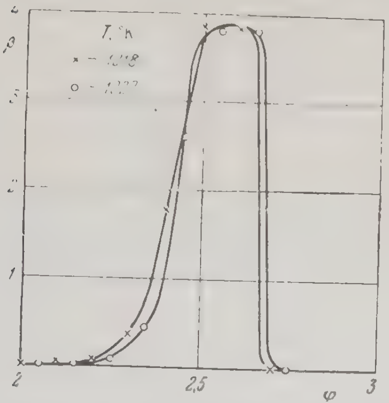

Fig. 3. Pair of β(φ) curves for a cathode activated at 900°.

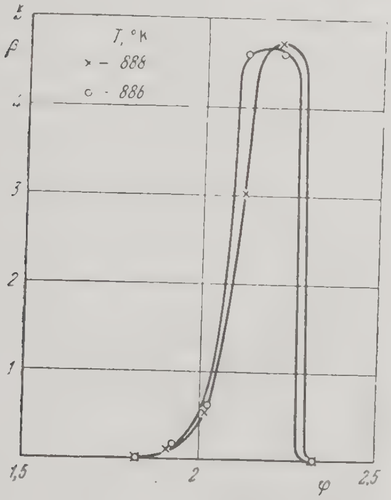

Fig. 4. Same as Fig. 3 but for a cathode activated at 1000°.

We recorded pairs of current-voltage characteristics for the same cathode at different temperatures and processed these to obtain the corresponding β(φ) curves. Some of the curves so obtained are reproduced in Figs. 3 & 4. It will be seen that the resultant accuracy is not sufficient to justify our speaking of the precise shape of the curve, but we feel that the method does allow of determining such quantitative parameters as the position of the β(φ) curve and the maximum and minimum values or spread of the work function.

The measurement section of our apparatus is shown in Fig. 5. The cathode 1 is a nickel cup; the oxide coating was applied to the bottom face of the cup. The thermocouple 2 which served to measure the temperature of the cathode was attached to the edge of this bottom face. The guard disc 3 mounted in the plane of the cathode served to maintain uniformity of the field. Opposite the cathode were the two grids 4 & 5 (connected together and maintained at the same potential) and the anode 6 in the form of a glass plate coated with a layer of silver evaporated from the vaporizer 7. The introduction of the second grid and drift gap was dictated by the necessity of locating the anode at a sufficient distance from the cathode to obviate the possibility of silver atoms falling on the cathode during the sputtering of the anode with resultant additional activation (or deactivation) of the cathode. The heater 8 was double-wound to obviate magnetic effects from the heater current.

The electric circuit, which was of conventional design for such measurements, is shown in Fig. 6.

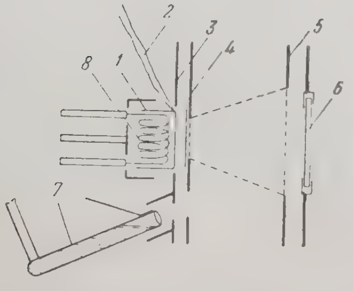

Fig. 5. Measurement section of apparatus used for investigating the areal distribution of an oxide-coated cathode according to values of the work function: 1) nickel cup, 2) thermocouple, 3) guard disc, 4 & 5) grids, 6) anode, 7) vaporizer for evaporating silver coating on the anode, 8) heater.

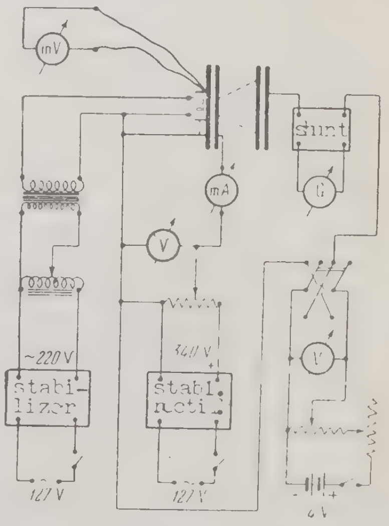

Fig. 6. Electric diagram of the experimental apparatus.

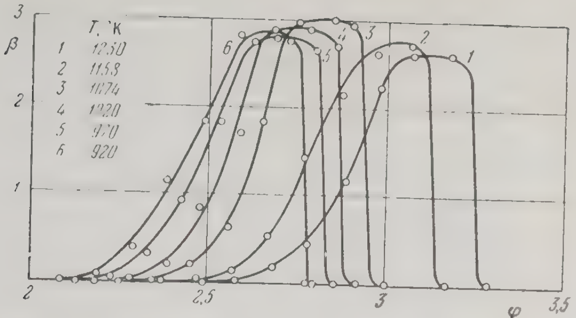

Fig. 7. Dependence of the areal distribution of an oxide-coated cathode activated at 850° according to values of the work function on the operating temperature of the cathode.

In the main part of the investigation we studied the dependence of the areal distribution according to values of work function on the degree (temperature) of activation and the operating temperature of a cathode with a coating of BaO·SrO on a base of nickel-silicon alloy.

The dependence of β on the operating temperature of a poorly activated cathode is shown in Fig. 7. It will be seen that without changing its shape beyond the limits of the experimental error the curve is displaced to the side of higher work function values with increasing cathode temperature.

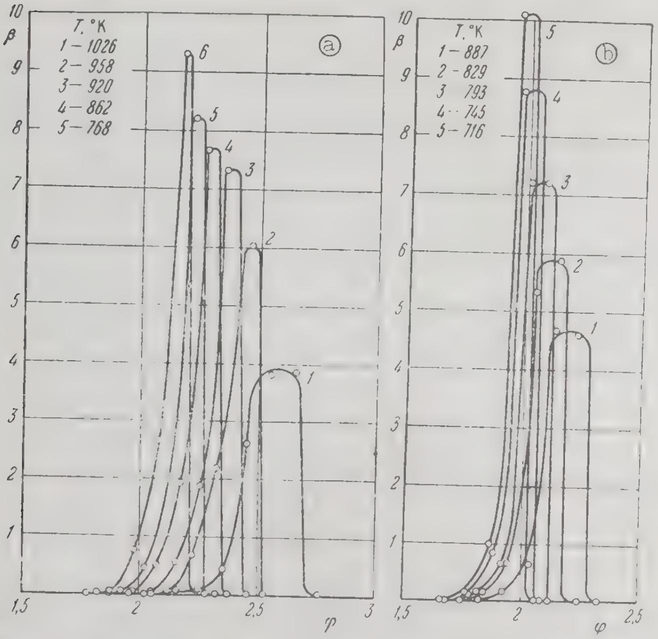

Fig. 8. Same as Fig. 7 but a) for a cathode activated at 900° and b) a cathode activated at 1000°.

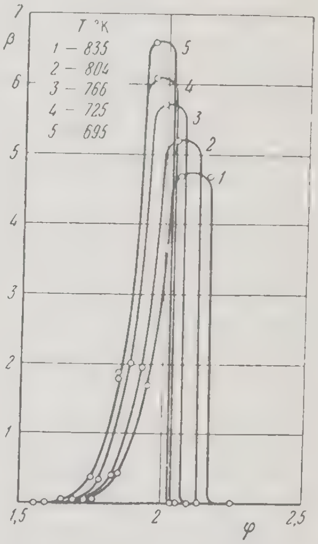

Fig. 9. Same as Fig. 6 but for a cathode superactivated at 1200°.

The results of our determination of the variation of β with the cathode temperature for cathodes activated at a number of other temperatures are shown in Figs. 8 & 9; the cathode of Fig. 9 was in the "superactivated" state. It will be seen that with increasing operating temperature we have not only a shift of the curve but also a broadening of the work function interval. In other words, the changes are such as would occur if each of the local work functions were characterized by a positive temperature coefficient proportional to the magnitude of the given work function. In general this kind of dependence can be understood from the viewpoint of the theory of the work function of donor semiconductors which gives the following familiar expression:

$$\varphi = \chi + \frac{E_1 - E_д}{2} + \frac{kT}{2e} \ln \left(\frac{g}{h^3 n_д} (2\pi m^* kT)^{3/2} \right).$$

It will readily be seen from this equation that the temperature coefficient of the work function will be greater for lower donor concentrations, i.e., for larger values of the work function.

The fact that the data for the poorly activated cathode are not consistent with the general scheme, i.e., are out of line with the regularities observed for the better activated cathodes, is an indication that under-activated cathodes cannot be regarded as purely donor semiconductors and that the above formula is not applicable to them.

There is little point in attempting a more detailed comparison of theory with experiment since a) the accuracy of our experiments hardly justifies this and b) the donor concentration n_d in the above equation can scarcely be assumed to be entirely temperature independent. As a matter of fact the concentration is known to vary with the temperature, although the reasons for the variation are still obscure.

Leningrad Physico-Technical Institute
of the Academy of Science of the USSR

DISCUSSION

Question: What was the grid voltage?

D.G.Bulyginskii: 100 v.

Question: How significant a role could reflection of electrons from the anode play in the measurement?

D.G.Bulyginskii: The role of reflection is insignificant.

Question: How large an error is introduced by differentiation of the curve?

D.G.Bulyginskii: Not over 25%.

K.B.Tolpygo: Your equation is based on the assumption that the currents from different areas of the cathode are independent; actually in view of surface inhomogeneities there may be an intereffect.

D.G.Bulyginskii: This was excluded by appropriate selection of the voltage.

K.B.Tolpygo: What was the grid to cathode distance?

D.G.Bulyginskii: 5 mm.

B.N.Popov: Did you carry out experiments with pure metals?

D.G.Bulyginskii: No.

N.D.Morgulis: Did you determine the electron temperature?

D.G.Bulyginskii: It was found to be higher than the temperature of the lattice.

G.A.Tiagunov: Were experiments aimed at verifying the experimental procedure or in investigating a particular cathode?

D.G.Bulyginskii: Both. We used standard commercially produced cathodes.

G.A.Tiagunov: It would be desirable to carry out analogous experiments with a pure metal.

D.G.Bulyginskii: I agree that this would be of interest.

N.N.Iakimov: What was the current density?

D.G.Bulyginskii: 0.5 ma/cm^2.

I.M.Bronshtein: There should be a dynode effect on the grid. Was it observed?

D.G.Bulyginskii: The decrease in plate current due to this effect was negligible.

K.B.Tolpygo: Since the cathode was not homogeneous over the surface, contact fields associated with spots could influence the results. Your procedure is not capable of taking into account inhomogeneities smaller than 10^{-6} cm.

D.G.Bulyginskii: The grid obviated the influence of spot contact fields.

MASS-SPECTROMETRIC STUDIES OF OXIDE-COATED CATHODES DURING PROLONGED OPERATION

- G. Ia. Pikus

1. In recent years mass spectrometry has found wide application in physical research. In addition to a large number of studies involving the analysis of organic mixtures, investigations of the interaction of electrons with gas molecules and so on, there have been a number of studies devoted to the oxide-coated cathode. Most of these studies were made by means of a more or less modified Nier[1] type continuously pumped glass-metal mass spectrometer.

Aldrich[2] mounted a metal tape with deposits of the carbonates of Ba, Sr and Ca in the ionization chamber and investigated the dependence of the rate of vaporization of the various components of the coating on the base material and the temperature. A more detailed investigation of the same type was made by Pelchowitch[2].

Plumlee & Smith[4] investigated the vaporization products of an oxide-coated cathode; in their work the cathode region was partitioned from the ionization region by a special slit diaphragm which served to separate the charged particles from the neutral ones. Stier[5], as well as Plumlee & Smith, analyzed, with the aid of a mass spectrometer, the gases evolved during the activation process.

A number of studies[4,6,8] have been devoted to certain problems associated with the emission of negative ions during activation as well as over the first few hours of operation. Two other investigations concerned with negative ion emission are distinguished by the use of somewhat different mass-spectrometric tubes: a demountable metal tube with 180° deflection[9] and a glass tube with a bellows and slip connections[10]. One should also mention an attempt by Blears[11] to employ a Nier type spectrometer for studying certain problems of high-vacuum physics.

2. We used the mass-spectroscopic method in our laboratory for studying the evolution of gas and emission of negative ions from oxide-coated[12] and metal-sponge[13] cathodes, the vaporization products from L-cathodes [porous metal-film type cathodes], the activation of oxide-coated cathodes[14] and the chemical combination and binding of residual gases incident to the operation of an ionization gage[15].

In contradistinction to most of the studies mentioned above, in all our investigations we employed a sealed analyzer tube, which made it feasible to work in the normal range of vacuum-tube pressures (10^{-7}-10^{-8} mm Hg).

The tube and the associated electric circuits constituting the apparatus are shown in Fig. 1. The central part of the tube, consisting of a section of 12 mm diameter tubing curved to a radius of 100 mm over a 60° arc, was located in the sector-shaped magnetic field.

The principal components of the positive ion source are the ion chamber 1 in the form of a cylindrical box, the extracting 2 and accelerating 3 slit diaphragms and the tungsten cathode 4 enclosed in the Wehnelt cylinder 5. All these parts were made of 0.2 mm thick nickel sheet; for the sake of strength the slit diaphragms were made of a double thickness of the sheet.

The dimensions of the slits and the inter-electrode distances are listed in Fig. 1. The slit diaphragms and the chamber were mounted on four ceramic tubes by means of appropriate supporting fittings. The assembled source was set on the 10-terminal mount 6, two leads from which were insulated for high voltage. Prior to being sealed in the tube, the entire assembly was centered by means of braces attached to the mount.

The ions forming in the chamber 1 through ionization of the residual gas by 140 ev electrons were extracted by the slit 2 and then accelerated to 800 ev. To minimize scattering of the ion beam, the inside surface of the spectrometer tube was coated with a layer of aquadag 7 which was maintained at the potential of the

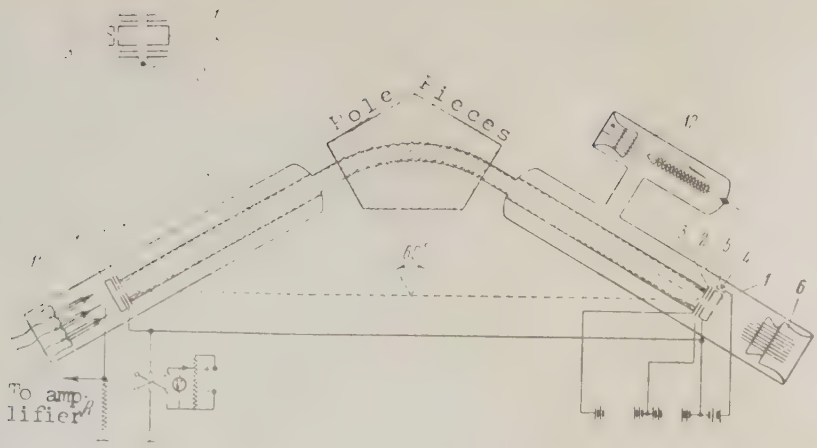

Dimensions of (slits)mm	
in 1	8x1.5
in 2	8x1.5
in 3	8x0.5

Distances between electrodes	
1-2	1mm
2-3	2mm
8-9	1mm
9-10	1mm

Fig. 1. Design of the mass spectrometer used in studying oxide-coated cathodes: 1) ion chamber, 2) extracting slit diaphragm, 3) accelerating slit diaphragm, 4) tungsten cathode, 5) Wehnelt cylinder, 6) mount, 7) aquadag, 8) defining slit, 9) antidynatron slit, 10) ion collector, 11) mount, 12) ionization pressure gage. Insert at upper left shows modification of ion source used for investigating the gases in the tube during operation of the cathode: 1) ion chamber, 2) cathode, 3) control grid, 4) anode, 5) slit diaphragm.

accelerating slit diaphragm 3. The receiving assembly, consisting of the defining 8 and antidynatron 9 slits and the ion collector 10 in the form of a Faraday cup, was mounted on the well insulated 3-contact mount 11. The ion current in the collector circuit was measured by means of a dc amplifier, having a sensitivity of $\sim 10^{-15}$ amp, employing a Bart bridge circuit assembled about an 1E1P (or EM-3) tetrode[16].

The theoretical resolution of our set up, as given by

$$\frac{\Delta m}{m} = \frac{d_1 + d_2}{R},$$

where m is the mass number, d_1 and d_2 are the respective widths of the entrance and exit slits and R is the radius of the ion trajectories, was of the order of 0.01, which is adequate for investigating masses in the 0 to 50 range (mass range of the evolved gases) and in 0 to 150 range (mass region of the products of evaporation from the cathode).

The tube was equipped with a modified Alpert[17] ionization gage 12, which served both for measuring the vacuum and for lowering the pressure in the tube.

Current for the spectrometer was supplied from dry cells and storage batteries, thereby insuring stable and dependable operation of the equipment. The power supply, amplifiers and collector section of the tube were shielded to minimize interference.

The cross section of the magnet pole pieces and their location relative to the tube are shown in Fig. 1. The gap between the pole pieces is 13 mm which makes it possible to obtain magnetic fields of sufficient intensity for the analysis of $m \approx 200$ ions with a relatively moderate current through the magnet windings. The current for the magnet windings was supplied by a lead-acid battery, which insured adequate stability of the magnetic field.

The magnetic field intensity was measured by means of a bismuth spiral located in the gap between the pole pieces and calibrated beforehand by means of

an IMI-1 magnetic induction indicator. A suitable source of Na^{23}, K^{39} and Rb^{85} positive ions was used for mass calibration of the instrument in the higher range. The reference points for the calibration curve in the low mass region were the lines of H_1^+, H_2^+ and He^+, obtained by ionization of these gases in the tube. Two additional reference points were given by the more intense lines of the nitrogen and water vapor, present in the tube during pumping.

In order to be able to study the composition of the residual gases in the tube with the cathode operating under normal conditions we modified the design of the ion source as shown in the insert in Fig. 1. In this design the cathode (oxide-coated or metal-sponge) assembly, comprising the cathode 2, the control grid 3 and the anode 4, is mounted immediately next to the ionization chamber 1 on the same support. The cathode system is separated from the ion source by a special slit diaphragm 5 which, being connected to the cathode, makes it possible to obviate ionization of the residual gas by the electrons from the cathode (this arrangement is analogous to that used by the authors of Ref. 4). This simple arrangement can also be used for investigating negative ions formed in the cathode system by changing the polarity of the voltage on the ion source.

3. We used a similar spectrometer tube for analyzing the gases liberated by an oxide-coated cathode during activation.[14] However, unlike the tube described above, this tube was not sealed but was continuously evacuated by an MM-40 oil diffusion pump. In addition the mass spectrometer was connected to another demountable tube by means of two capillaries with different transmission capacities; the different tested standard oxide-coated cathodes of the 6-volt series were successively installed in this second tube, which was evacuated by a separate MM-40 pump. The pressure in this tube was measured by a thermocouple type gage and an ionization gage. This arrangement made it possible to investigate the gases liberated from the cathode during activation according to the standard factory procedure, something that could not be done in earlier investigations (see Ref. 4, for example) in which the cathode was sealed in the spectrometer tube.

The pressure of the gases evolved during activation, particularly during its initial stages, is so great (10^{-4}-10^{-1} mm Hg) that the spectrometer cannot function properly. In order to determine the composition of the gases evolved at a given temperature one must first outgas the cathode at this temperature for a considerable time; obviously the composition of the gases may change in the interval.

The system employed for admitting the evolved gases to the mass-spectrometer tube is shown in Fig. 2. With the valve in the large transmission capacity capillary closed, the tube 2, containing the cathode 4, communicated with the mass spectrometer only through the fine capillary 3 whose transmission capacity was one tenth that of capillary 1. With this arrangement the pressure in the mass spectrometer did not exceed $1 \cdot 10^{-5}$ mm Hg despite variations of the pressure in tube 2 from 10^{-1} to 10^{-4} mm Hg. As a result of thorough preliminary evacuation of the entire system the pressure in the mass spectrometer before the beginning of measurements was $3\text{-}5 \cdot 10^{-7}$ mm Hg, while the pressure in tube 2 after it was cut off from the pump by closing the stopcock 5 did not rise above $2 \cdot 10^{-5}$ mm Hg over a period of ten minutes.

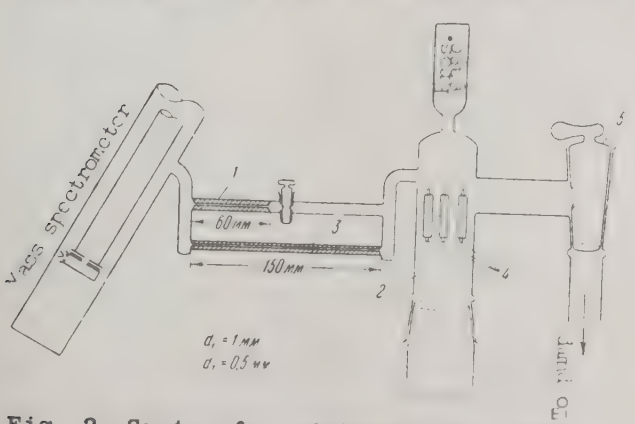

Fig. 2. System for admitting the gases evolved during activation of an oxide-coated cathode into the mass spectrometer: 1) high transmission capacity capillary, 2) tube for activating cathodes, 3) low transmission capacity capillary, 4) investigated cathodes, 5) stopcock.

After obtaining a qualitative mass spectrogram of the gases evolved during heating of the cathode, the mass spectrometer was adjusted for one of the gaseous components and the variation in the height of the selected line peak was observed at different stages of activation of the oxide-coated cathode. To this end the tube 2 was cut off from the pump by closing the stopcock 5 and the cathode in the first stage of decomposition of the carbonates and binder was heated to a certain temperature; at the end of a minute's exposure the maximum height of the peak associated with the investigated component was noted and this subsequently served as the measure of the amount of this component. Then the stopcock 5 was opened, tube 2 evacuated and the entire procedure repeated but for a different cathode temperature, on up to T = 1400° K (V_f = 12 v). During the second stage, when the cathode was activated with current being taken off the plate, the stopcock 5 was closed at 3-5 min intervals for 1 min and the height of the peak associated with the given component determined. Such measurements were repeated many times and showed fully satisfactory reproducibility.

In order to be able to determine the quantitative proportions between the various components from the heights of the respective peaks, these first readings were normalized both with respect to the relative pressure drop over the two capillaries used and with respect to the ionization probability of the different components[18]. It must be noted that the amounts of gas determined in this way during the first activation stage are not equilibrium quantities but merely characterize the activation procedure employed. However, this does not detract from the value of the data, for these are the conditions obtaining in the process of formation of oxide-coated cathodes in actual vacuum tubes. Since the results of these studies are described in Ref. 14 we will not dwell upon them here.

As mentioned above, in investigating the negative ions forming in the oxide-coated cathode system during its activation, the cathodes were mounted directly in the mass-spectrometer tube.

4. As has now been definitely established, one of the factors determining the quality of operation and useful service life of an oxide-coated cathode is the residual gas in the tube.[19] The presence of residual gas leads to disintegration of the active layer by ion bombardment and to chemical binding of the free barium in the coating. In order to evaluate the effect of residual gases one must know not only the total pressure but also their amount and composition in an actual operating vacuum tube. Yet despite the practical importance of this problem it has received little attention until now.[4] In view of this we applied the above described mass-spectroscopic procedure to the investigation of the gas content in a sealed-off tube with an operating oxide-coated cathode. The first results obtained for a specific case are described in Ref. 12. In the present investigation the studies were extended to the more general case of oxide-coated cathodes operating under conditions approximating those encountered in actual tubes. The specific subject of investigation was a commercial cathode for a type 6N8 tube with a silicon-nickel base and a binary carbonate coating.

In the general case the composition of the residual gases must depend to an appreciable extent on the type of tube and the technology of its fabrication. However, by reducing to a minimum the evolution of gas from the metal components and gas envelope by thorough pumping and outgassing, one can investigate the specific characteristics of the gases evolved during operation of the oxide-coated cathode, i.e., study the factors common to all vacuum tubes employing oxide-coated cathodes.

In our experiments, after heating the glass envelope at 450° for several hours and the metallic components by high-frequency currents, the oxide-coated cathode was activated in the usual manner. Then the barium getter was vaporized and the tube sealed off. The pressure after sealing was 10^{-6}-10^{-7} mm Hg. The vacuum in the tube was further reduced to about 10^{-8} mm Hg by means of an ionization gage. At this point a mass spectrogram of the residual gas was recorded; this spectrogram was thereafter regarded as the background.

In order to determine the effect of electrolytic processes in the oxide-coated cathode and electron bombardment of the anode on the gas content the tubes were mounted on a test stand where they were operated at the normal filament temperature (1100°K) in one of the following regimes:

1) zero emission, i.e., $I_a = 0$;

2) 4-volt ($V_a = 4$ v, $I_a = 7$ ma which corresponds to $i = 15$ ma/cm^2); under these conditions there is no dissociation;

3) 240-volt ($V_a = 240$ v, $I_a = 7$ ma).

The experimental procedure consisted of periodically recording the mass spectrograms of the residual gas, determining its total pressure and measuring the emission of negative ions and the emissivity of the cathode while underheated ($V_f = 1.2$ v, $V_a = 4$ v). During the pressure measurements the pressure gage was cut off for 10-15 sec to avoid possible chemical binding of the gas[15].

It must be emphasized that the mass spectrogram of the gas obtained under these conditions characterizes a certain state of dynamic equilibrium determined, on the one hand, by evolution of gas from the oxide-coated cathode and the metallic supports and leads and, on the other hand, by removal of the gases through combination with the getter and the walls of the tube. A typical early-stage mass spectrogram, obtained 1/2 hour after switching on the cathode in tubes operated in the zero emission or 4-volt regime is shown in Fig. 3. The shaded areas in the peaks indicate the background typical for all the investigated tubes. Noteworthy features are the rise above the initial background of the m = 2 (H_2) and m = 28 (mixture of N_2 + CO) peaks and the appearance of the m = 35 and 37 peaks associated with chlorine. For evaluating the proportions of N_2 and CO in their mixture one can utilize the fact that in the ionization of CO by electrons there are formed appreciable and approximately equal quantities of C^+ and O^+ ions.[20] Special control experiments substantiated this. From Fig. 3 it will be seen that the C^+ peak (M = 12) is only a small fraction of the height of the m = 16 peak, from which it may be concluded that the m = 28 peak is due primarily to N_2. The group of peaks in the m = 13-16 interval is apparently due to remains of organic compounds (in particular, methane). This conclusion is supported by the fact that the spectrum of methane ionized by ~100 ev electrons comprises four peaks having relative heights of 1.9: 4.3: 41: 49 in this mass interval[21]. The ratio of the peak heights in Fig. 3 is almost the same, except for the m = 14 peak which is partially due to nitrogen atoms.

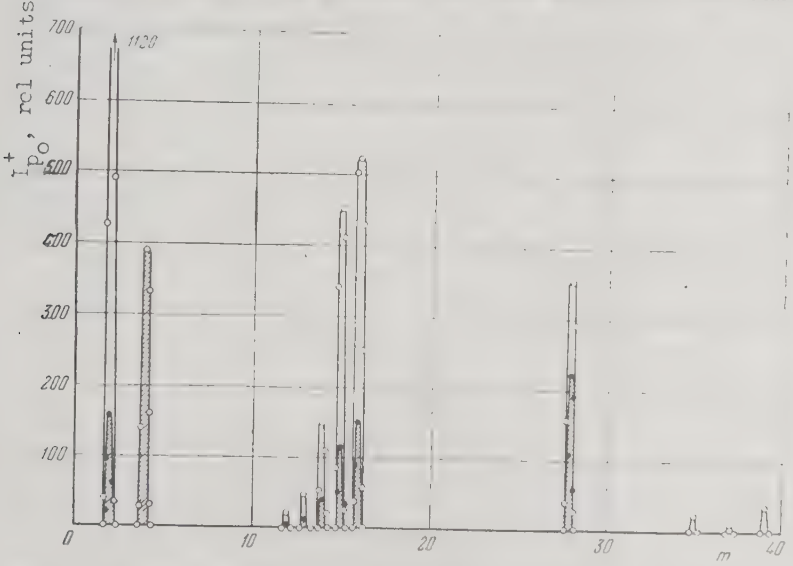

Fig. 3. Mass spectrogram of gases evolved from an oxide-coated cathode during the initial 30 minutes in tubes operated in the zero emission and 4-volt (anode voltage) regimes. Hatched peaks indicate the typical background for such tubes.

The mass spectrograms of the gas in tubes operated with a 240 v potential on the anode differ from that shown in Fig. 3 by the appreciably greater height of the peaks, particularly the H_2 peak and the group in the m = 13-16 interval, and the appearance of a peak at m = 18, apparently associated with water vapor. In the case of our first tubes[12] whose cathodes were prepared in our laboratory, the spectrograms also comprised a noticeable peak associated with molecular oxygen.

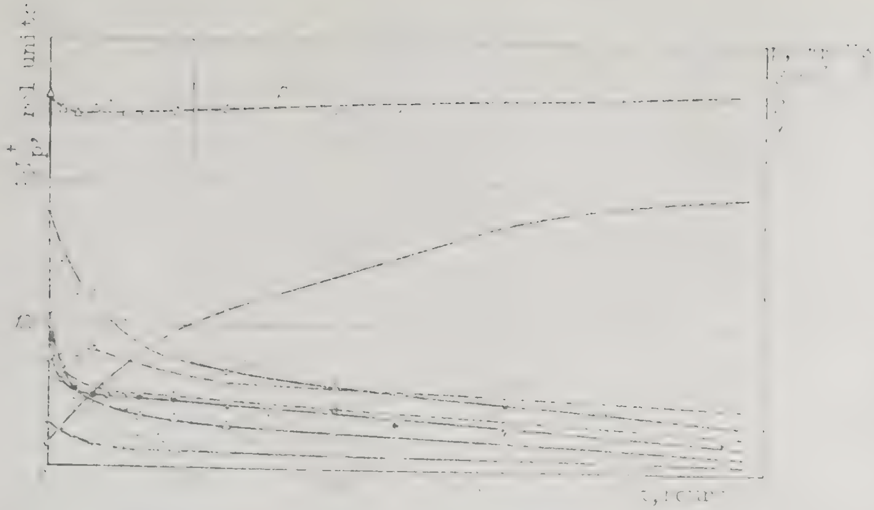

Fig. 4. Variation of the height of the peaks associated with the principal components of the residual gas in tubes operated in the zero emission regime (V_a = -10 v, I_a = 0) with the operating time from the initial instant of switching on the cathode.

The typical variations with time of the heights of the peaks associated with the principal components of the residual gas in tubes operated at the three regimes over a period of about 500 hours are shown in Figs. 4, 5 and 6. It will be seen that the removal (binding) of the different gases present differs, but that the principal changes in the gas content occur during the first 100 hours of operating. The mass spectrograms of the residual gas and the variations in peak height with time are almost the same for tubes operated in the 4-volt and zero emission regimes; from which it may be concluded that electrolytic processes in the oxide-coating have virtually no effect on the residual gas content in the tube.

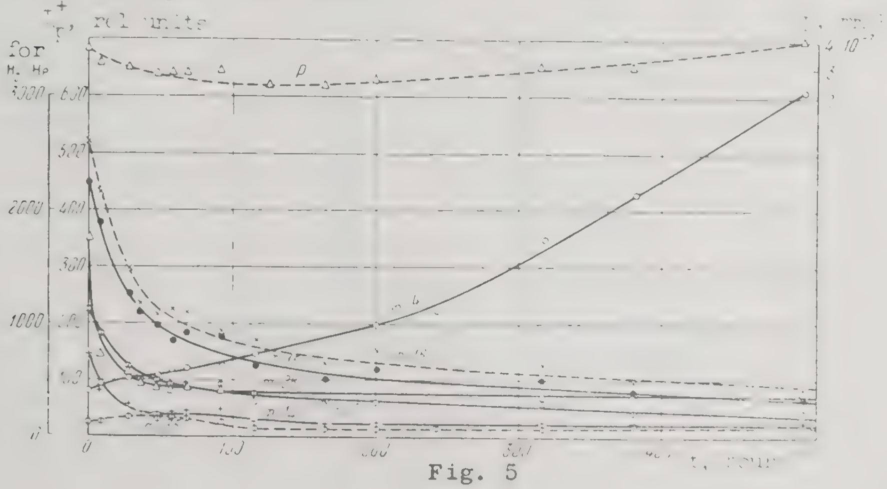

Fig. 5

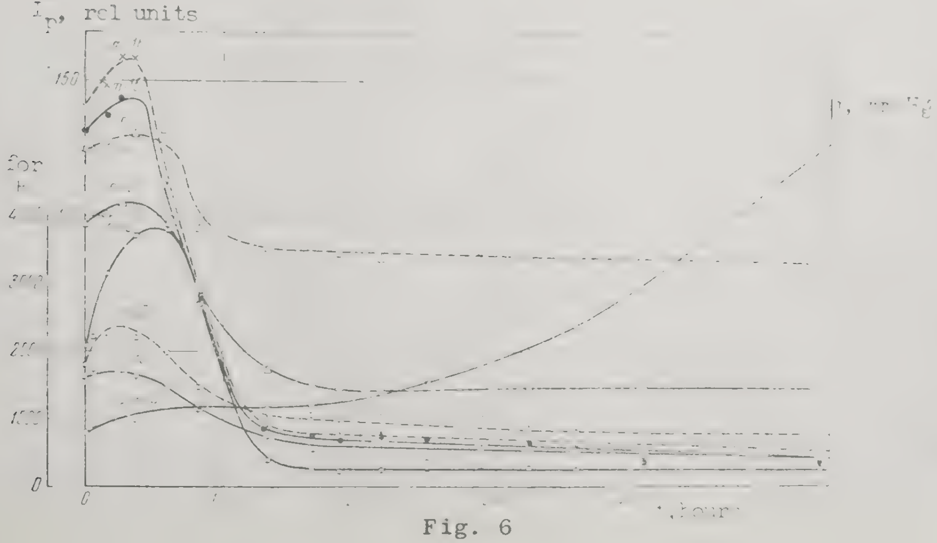

Fig. 6

Fig. 5. Same as Fig. 4 but with tube operated in the 4-volt regime (V_a = 4 v, I_a = = 7 ma).

Fig. 6. Same as Fig. 4 but with tube operated in the 240-volt regime (V_a = 240 v, I_a = 7 ma).

An entirely different picture appears in the case of tubes operated in the 240-volt regime, where during the first 100-150 hours of operation instead of a monotonic decrease in the amount of gas we see a rapid rise in the gas content followed by a gradual decrease as in the other two cases. Further, it is interesting to note, that if a tube which has been operated for 550 hours in the 4-volt regime is then switched to the 240-volt regime, the observed variation in time of the spectrograms is similar to that shown in the initial part of Fig. 6. Inasmuch as the 240 v anode voltage regime differs from the 4 v anode voltage regime only as regards intensity of the electron bombardment of the anode, it may safely be concluded that the increased pressure in the 240 v case is due to active evolution of gas from the anode under electron bombardment. Hence the major part of the residual gas present in the case of electron bombardment is due to liberation of gases from the anode event if it has been thoroughly outgassed in the process of preparation. A major fraction of the evolving gases is hydrogen H_2.

In order to evaluate the influence of the cathode base and heater on the gas content, we prepared a similar tube containing only the base and heater, i.e., no oxide coating. The initial mass spectrogram of the residual gas and the background (hatched peaks) obtained for such a tube are shown in Fig. 7 from which it can be seen that the role of the base where gas formation is concerned is minor compared to that of the coating. This is substantiated by the variation with time of the mass spectrograms: after some 10-20 hours of operation the mass spectrogram of the gas becomes indistinguishable from the background spectrogram.

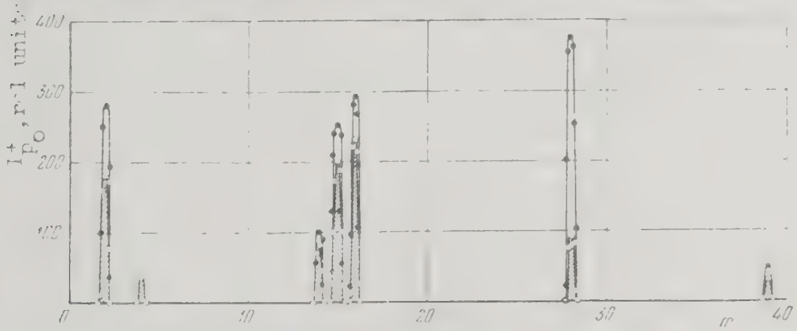

Fig. 7. Mass spectrogram of gases evolved from a bare base cathode (no oxide-coating) 30 minutes after switching on the tube. Hatched peaks indicate background characteristic of the tube.

Of considerable interest is the variation in time of the He content. As may be seen from Figs. 4-6, the amount of helium in the tube increases continuously over the entire period of the test, attaining a value tens of times greater than the initial one at the end of 500 hours. This can be explained only by continuous diffusion of helium into the tube from the atmosphere.[22] Obviously this diffusion limits the minimal value of the residual gas pressure in tubes with a glass envelope (molybdenum glass).

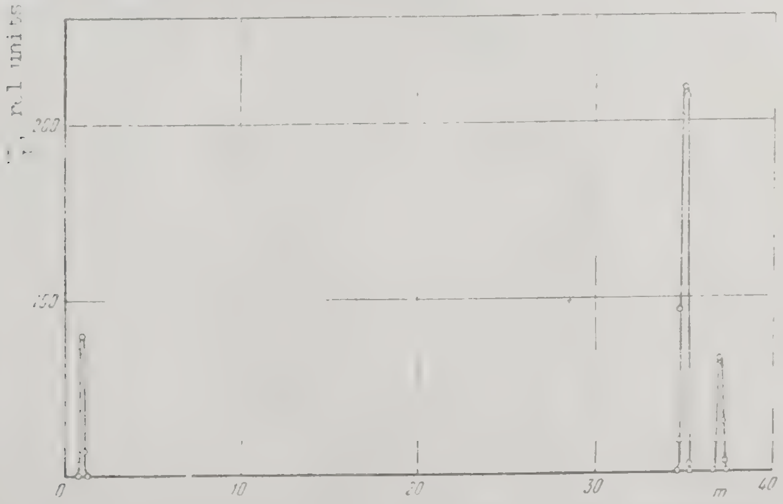

Fig. 8. Negative ion mass spectrum typical of tubes with an oxide-coated cathode. Emission current I_e = 10 a.

One of the important results of our investigation is that we have shown

that in a high-vacuum tube with an oxide-coated cathode there may be present over a prolonged period noticeable amounts of chemically active gases, namely, chlorine and oxygen. The partial pressures of these gases, according to our evaluation, are of the order of 10^{-9} mm Hg, i.e., relatively high from the point of view of possible chemical poisoning of the oxide-coated cathode in the process of operation.

On the other hand, during the course of operation of the tube the composition of the gas in it changes so that after several hundred hours helium (chemically inert) and hydrogen make up the major part (90% or over) of the gases present. Bombardment of the oxide-coated cathode by fast ions of these gases can also lead to noticeable deterioration of its emission characteristics in service.

Thus, in addition to disintegration of the cathode coating by ion bombardment, there may also occur noticeable chemical poisoning of the coating. However, it is difficult to evaluate the relative importance of the different possible poisoning mechanisms on the basis of our data. The related problem of the mechanism of poisoning of oxide-coated cathodes by oxygen at low pressures is discussed in a report to be presented to this conference by Kulik and Nakhodkin[23] (see next article).

Concurrently with the above described investigation of the residual gas content we carried out some measurements of the emission of negative ions forming in the cathode system. The problem of negative ion emission is important in itself. Fig. 8 shows the negative ion mass spectrum typical of most of the investigated tubes; it consists mostly of H_1^- ions and chlorine isotopes. In some cases we also observed low peaks associated with atomic and molecular oxygen.

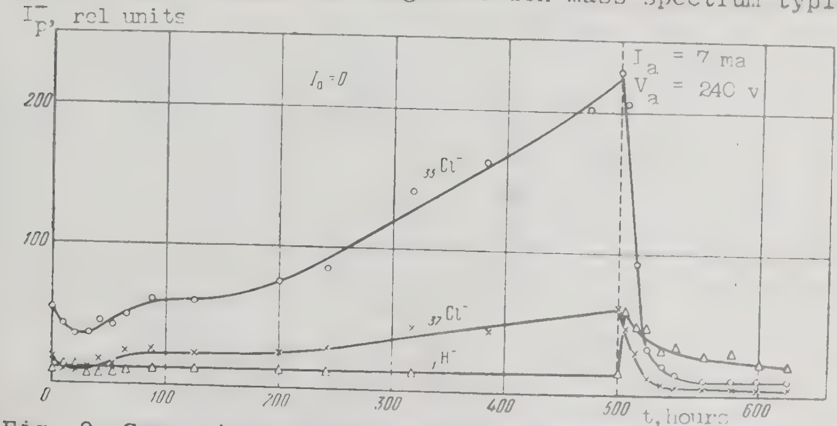

Fig. 9. Comparison of the variation in emission of chlorine ions and atomic hydrogen ions by an oxide-coated cathode with the operating time of the cathode with (at right) and without (at left) emission.

In the case of tubes operated with current taken off the plate (4-volt and 240-volt regimes) the negative ion emission fell off continuously, dropping to a very small value after a few hundred hours of operation. An entirely different picture is observed in the case of zero emission operation. In this case, after a small decrease during the first hours of operation, there begins a continuous increase in the emission of chlorine ions (see left side of Fig. 9) although the electron current taken off the cathode at the instant of measurement remained the same (5 ma). At the same time the H_1^- ion current remained virtually constant. Switching the cathode to an emission regime (i.e., applying a plate voltage) leads to a rapid falling off of the Cl^- ion emission (Fig. 9 at right) as in the case of tubes operated in the emission regime from the very beginning. This is probably connected with the increase in the potential gradient in the oxide layer during operation

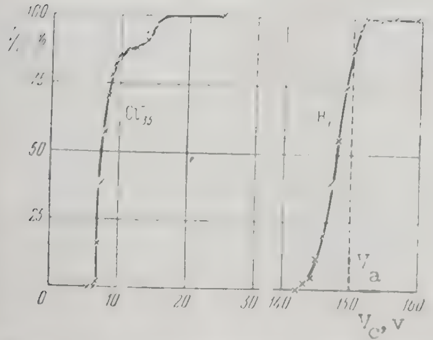

Fig. 10. Current-voltage characteristics of the current of negative chlorine and oxygen ions to the collector in a retarding field relative to the cathode.

of the cathode in the zero emission regime, leading to accelerated diffusion of the Cl^- ions to the surface.

In order to determine the point of origin of the observed negative ions we recorded the current-voltage characteristics of their current to the collector in a retarding field relative to the cathode; the results are shown in Fig. 10. It will be seen that the Cl^- ions originate on the cathode and undergo thermal evaporation from its surface, while the H_1^- ions form at the anode, for the collector potential at which the H_1^- ion current begins to fall off is equal to the anode potential. This is apparently connected with ionization of the hydrogen liberated in appreciable amounts in electron bombardment of the anode.

It will be seen that employment of the mass-spectrometric procedure has made it possible to obtain much valuable information essential to an understanding of the operation of oxide-coated cathodes in modern high-vacuum electron tubes and the process of their operation under different conditions.

In conclusion the writer desires to thank N.D.Morgulis for his constant interest and guidance in the work.

"T.G.Shevchenko" Kiev State University

References

1. A.Nier, Rev. Sci. Inst., 18, 398 (1947).
2. L.Aldrich, J. Appl. Phys., 22, 1168 (1951).
3. J.Pelchowitch, Philips Res. Rep., 9, 42 (1954).
4. R.Plumlee & L.Smith, J. Appl. Phys., 21, 811 (1950).
5. P.Stier, Phys. Rev., 83, 877 (1951).
6. A.Shepherd, Brit. J. Appl. Phys., 4, 70 (1953).
7. F.Vick & C.Walley, Proc. Phys. Soc., B 67 (1954).
8. W.Grattidge & A.Shepherd, Proc. Phys. Soc., B 67, 177 (1954).
9. R.Sloane & C.Watt, Proc. Phys. Soc., 61, 217 (1948).
10. H.Schaefer & W.Walcher, ZS. f. Phys., 121, 679 (1943).
11. J.Blears, J.Sci.Instr., 7, 36 (1951).
12. N.D.Morgulis & G.Ia.Pikus, Doklady AN SSSR, 102, 1103 (1955).
13. N.D.Morgulis, Zhur. tekh. fiz., 26, 536 (1956).
14. N.D.Morgulis & G.Ia.Pikus, Zhur. tekh. fiz., 26, 1174 (1956).
15. N.D.Morgulis, Zhur. tekh. fiz., 25, 1667 (1955).
16. A.M.Bonch-Bruevich, Primenenie elektronnykh lamp v eksperimental'noi fizike (Applications of electron tubes in experimental physics), M. 1950.
17. R.Bayard & D.Alpert, Rev. Sci. Instr., 21, 571 (1950).
18. N.A.Kaptsov, Elektricheskie iavleniia v gazakh i vakuume (Electrical phenomena in gases and vacuum); A.Engel & M.Steinbeck, Fizika i tekhnika elektricheskogo razriada v gazakh (Physics and technology of electric discharges in gases) [Probably translation from German] Vol. 1, M.-L., 1935
19. G.Metson, S.Wagener, M.Holms & M.Child, Proc. IEE, 99, 69 (1952).
20. H.Hagstrum & J.Tate, Phys. Rev., 59, 354 (1941).
21. L.Smith, Phys. Rev., 51, 262 (1937).
22. S.Dushman, Scientific foundations of vacuum tachniques (In Russian trans. M. 1950); D.Alpert & R.Buritz, J.Appl.Phys., 25, 202 (1954).
23. A.E.Kulik & N.G.Nakhodkin, in present issue of the Bulletin - next article.

INFLUENCE OF OXYGEN AT LOW PRESSURES ON THE EMISSION OF AN OXIDE-COATED CATHODE

- A.E.Kulik & N.G.Nakhodkin

1. Numerous investigations of the oxide-coated cathode show that the atmosphere surrounding it has a strong influence on the emission characteristics of the cathode. In conventional vacuum tubes this atmosphere consists of residual gases at pressures under 10^{-6} mm Hg. It is essential to investigate how the cathode behaves in an atmosphere of these gases at such low pressures since it is impossible to deduce the behavior of the cathode from a knowledge of its properties in the range of higher gas pressures.[1]

In a special series of experiments Morgulis and Pinkus[2] determined that in a vacuum tube with an oxide-coated cathode, even after good evacuation and proper aging, there is a certain amount of oxygen present in the residual gases during the initial hours of operation of the tube. Since with the exception of chlorine, which is present in very minute amounts, oxygen is the most active of the residual gases present, we felt it would be of interest to investigate its influence on the emission characteristics of oxide-coated cathodes.

The influence of oxygen on the emission of oxide-coated cathodes has been studied by a number of investigators[3-6]; however, most of these were more interested in the regeneration of a poisoned cathode than in studying the properties of the cathode in the process of poisoning and in measuring the oxygen pressure in the course of the poisoning process. Only Wagener[1] in his comprehensive investigation studied the oxide-coated cathode both in the process of poisoning and in the process of subsequent regeneration at oxygen pressures of 10^{-7}-10^{-5} mm Hg. To evaluate the pressure in his experimental tube Wagener employed an ionization pressure gage with the investigated oxide-coated cathode serving as the source of electrons. This obviously introduced a certain error into the measurements inasmuch as they were carried out in the presence of a constant dc component. Hence Wagener did not succeed in obtaining any definitive results regarding the influence of the constant component of the emission current on the behavior of the cathode in the process of its poisoning and regeneration.

2. In the present investigation the pressure was measured with an ionization gage having a separate tungsten cathode so that the picture of the changes in the characteristics of the cathode in the process of poisoning and regeneration was not obscured by the influence of the constant component which always slowed down the rate of poisoning and increased the rate of regeneration of the emission of the cathode.

For our investigation we chose the oxide-coated cathode of the 6Zh2P (6Ж2П) tube prepared and activated under the usual industrial conditions and the cathode of tubes 2192 and 2190 (glass-envelope variants of tubes 6P9 (6П9) and 6Zh4 (6Ж4)). For the purposes of the investigation we developed a procedure for opening the tubes in a special vacuum container in which it was feasible to maintain the desired oxygen pressure ($5 \cdot 10^{-7}$-$5 \cdot 10^{-6}$ mm Hg) for a prolonged time by admitting the requisite amounts of oxygen through a capillary.* The selected degassing regime does not impair the emission properties of the cathode: tests showed that the emission and transconductance did not change when the tube was opened. The oxygen was prepared by thermal decomposition of thoroughly degassed potassium permanganate.

The emission was measured under the conditions of "single" exponential pulses of 100-150 microsec duration, having a frequency of several pulses per minute. A diagram of the set-up is shown in Fig. 1. As may be seen from the figure, the set-up permitted of regulating the magnitude of the constant dc component of the emission current by adjustment of the plate and control grid voltages. Inasmuch as we were interested only in the chemical action of the oxygen, the grid and

---

*The tubes were opened by local heating of a scratch, filed beforehand in the glass envelope.

plate voltages were kept below 5 v, i.e., not only below the ionization potential of the residual gases usually present but also below the dissociation potential of the oxides of barium, strontium, etc.

In order to obtain reproducible results the measurements were made sometime after switching on the pulse generator since it was noted that when the pulser is first cut in and also for a few seconds after turning on the dc component there occurs a decrease in emission, which appears to be more rapid at higher temperatures.

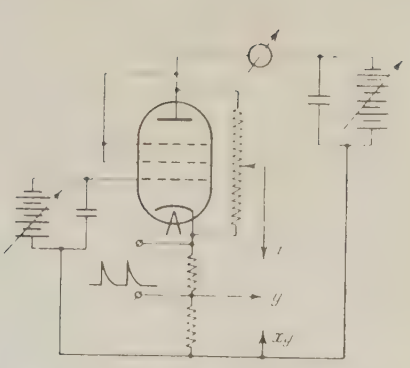

Fig. 1. Diagram of set-up for measuring the emission of oxide-coated cathodes.

After opening a fresh tube and before beginning of measurements, oxygen at a pressure of $8\cdot10^{-7}$–$1\cdot10^{-6}$ mm Hg was admitted several times into the working volume and then evacuated to complete restoration of the emission. It was found, as may be seen from Fig. 2, where the relative emission current is plotted against time from the instant of admission of oxygen, that two successive admissions were sufficient to obtain reproducible results (during the third admission) even at higher oxygen pressures. In Fig. 2, curves 1, 2 and 3 pertain to three successive admissions of oxygen at a pressure of $8\cdot10^{-7}$ mm Hg (the pressure gage was calibrated using air). Apparently three successive admissions of oxygen are sufficient for the mounting components and getter to be saturated with oxygen since even at higher pressures ($1.1\cdot10^{-6}$ mm Hg - see curves 4 & 5 in Fig. 2) two successive admissions of oxygen lead to reproducible results.

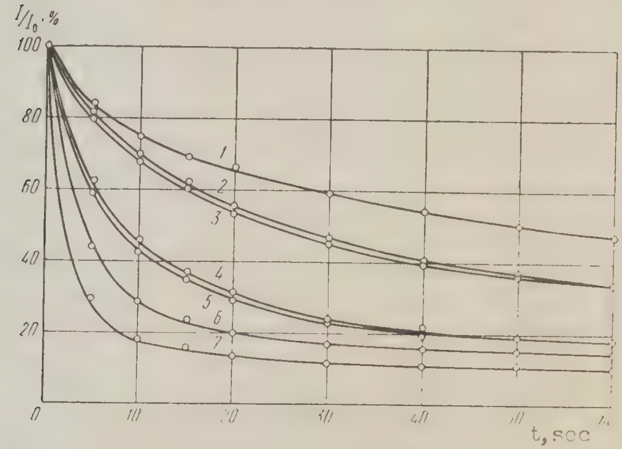

Fig. 2. Variation of the ratio of the emission current of an oxide-coated cathode to the initial value of the current with time from the instant of admission of oxygen at different pressures p: 1, 2, 3) $p = 8\cdot10^{-7}$ mm Hg, 4, 5) $p = 1.1\cdot10^{-6}$, 6) $p = 1.3\cdot10^{-6}$, 7) $p = 1.7\cdot10^{-6}$.

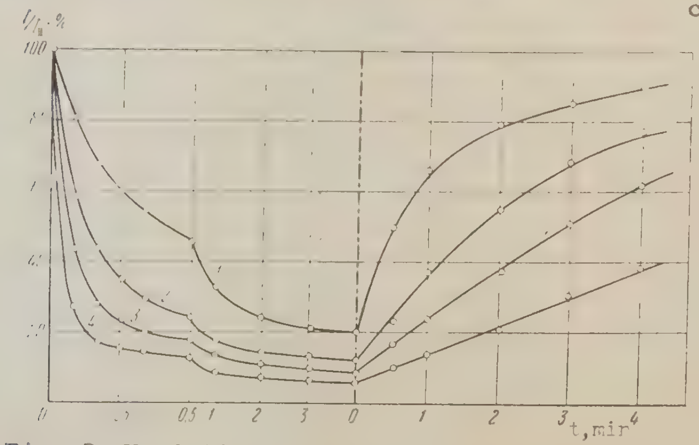

Fig. 3. Variation with time of the ratio of the saturation emission current of an oxide-coated cathode to the initial value of the current in the process of poisoning and regeneration of the cathode at different oxygen pressures: 1) $8\cdot10^{-7}$, 2) $1.1\cdot10^{-6}$, 3) $1.3\cdot10^{-6}$, 4) $1.7\cdot10^{-6}$ mm Hg.

We measured the variation in time of the saturation emission current at the given instant to its initial value ($I/I_0 = f(t)$) during the course of the processes of poisoning and regeneration of the cathode. The measurements were carried out at different oxygen pressures from $5\cdot10^{-7}$ to $5\cdot10^{-6}$ mm Hg (Fig. 3) and at different filament voltages $V_f = 6$ to 4.5 v (Fig. 4). The lower limit of the selected pressure range was determined by the residual pressure of the gases in the set-up ($3\cdot10^{-7}$ mm Hg) and also by the fact that at pressures under

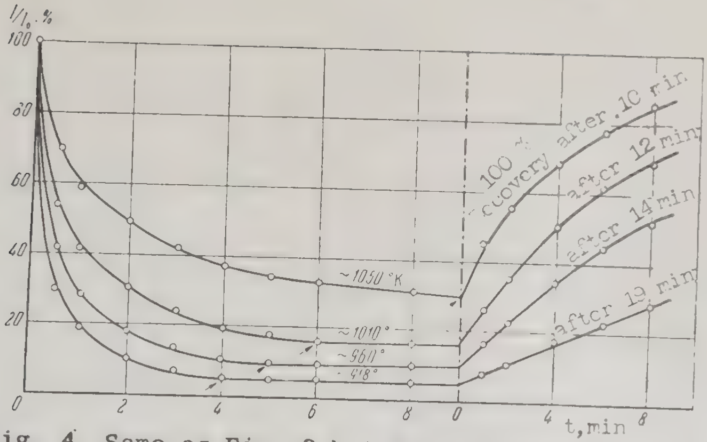

Fig. 4. Same as Fig. 3 but for different temperatures (different V_f).

$4 \cdot 10^{-7}$ mm Hg virtually no poisoning of the oxide-coated cathode is observed at the usual operating temperatures. The upper pressure limit of $5 \cdot 10^{-6}$ mm Hg was determined by the fact that at higher pressures a poisoned cathode does not fully recover its emission without an appreciable increase in temperature.

The temperature interval (V_f = 6-4.5 v, equivalent to 1050-918° K) was selected so that the cathode after poisoning would fully recover its initial emission and so there would be no sparking during regeneration. It was impractical to use higher temperatures since at higher temperatures the emission current does not reach a saturation value.

First we checked to make sure that the application of a pulse voltage has no influence on the poisoning and regeneration of the cathode. To this end the voltage pulses were applied singly at intervals. It was found that the resultant $I/I_0 = f(t)$ curve is identical with that obtained with continuous operation of the pulse generator.

The results of measurements on different tubes are shown in Figs. 2, 3 & 4; very similar curves were obtained for almost all the investigated tubes. It must be emphasized that the curves reproduce very well if the oxygen pressure is accurately duplicated. It will be seen from an examination of the experimental $I/I_0 = f(t)$ curves that after a certain time from the beginning of admission of oxygen the ratio I/I_0 no longer changes with t, i.e., attains an equilibrium value I_∞/I_0 for given values of p and T (cathode temperature). We shall term this interval the poisoning time and the time reckoned from the instant of evacuation of the oxygen the regeneration time. The regeneration times at underheat temperatures were always several times greater than the poisoning times. Hence it may safely be asserted that poisoning is the more rapid process. However, with increasing filament temperature the poisoning time increases, while the regeneration time decreases, so that at some point the latter may become equal to or even shorter than the poisoning time. Hence one cannot ignore the effect of regeneration processes in considering the poisoning in any given range of temperatures and pressures.

The poisoning time appears to be little dependent on the oxygen pressure (see Fig. 3), whereas the regeneration time increases noticeably with increasing oxygen pressure. If it be assumed that poisoning in the given interval of temperatures and pressures occurs only due to adsorption of oxygen on the exposed surface of the cathode (as suggested in Ref. 6), then the poisoning time should depend substantially on the oxygen pressure, i.e., should decrease with increasing p and T. This is not substantiated by experiment.

It might be assumed that the oxygen acts not only on the exposed surface but also diffuses into the cathode. If this is the case the poisoning curves should have the same appearance for cathodes of different thickness and the poisoning time should clearly depend on the thickness of the cathode. Tests carried out with 6Zh2P, 2192 and 2190 tubes, the cathodes of which are 30, 80 and 65 μ thick, respectively, showed that the general shape of the poisoning curves is the same and that the poisoning time increases in direct proportion to the square of the thickness of the oxide layer. The coating thicknesses were measured in the conventional manner by means of an MIS-11 microscope; the measure-

ments were made after opening the tubes. Thus apparently the dependence $d^2 \sim Dt$, where D is the diffusion coefficient, is apparently satisfied.

However, the fact that the poisoning time increases with the temperature instead of decreasing as the relationship $d^2 \sim Dt$ would require (since the coefficient of diffusion increases with temperature) shows that other - reactivation - processes are involved.

The variations with time of I/I_0 in the process of regeneration at different oxygen pressures and cathode temperatures are also shown in Figs. 3 & 4. It will be seen that during the initial stage of recovery I/I_0 increases almost linearly with time, the linearity being more pronounced at lower temperatures and higher pressures. The rate of regeneration, as characterized by the slope of the curves, increases with increasing temperature and decreasing pressure. The regeneration time noticeably decreases with increasing T and decreasing p. The dependence of the regeneration time on the thickness of the oxide-coated cathode is somewhat indeterminate. However, it must again be emphasized that in the investigated range of oxygen pressures and cathode temperatures the emission always climbed back to its initial value without additional heating of the cathode and without the application of a dc plate voltage.

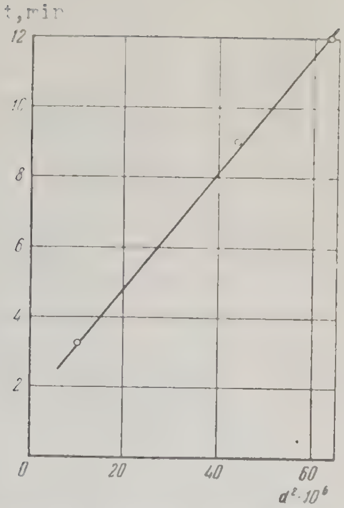

Fig. 5. Dependence of the poisoning time on the thickness of the oxide-coated cathode.

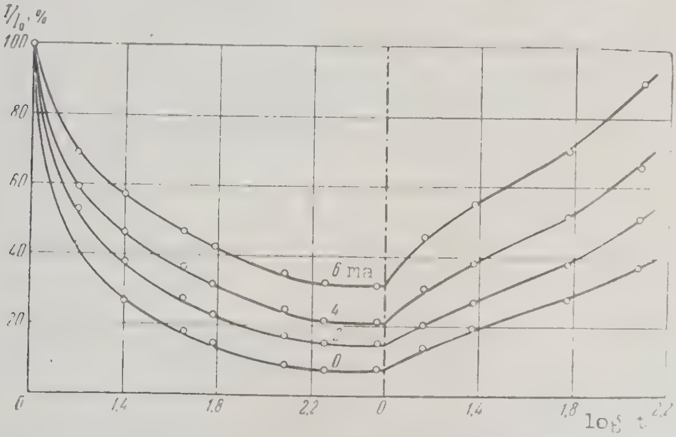

Fig. 6. Same as Fig. 3 but for different values of the constant dc component of the emission current.

In the second part of the investigation we studied the influence of the constant component of the emission current (plate current) on the poisoning and regeneration of our cathodes. It was established that there is no additional evolution of gas when a dc current is taken off the plate. The results of these measurements are shown in Fig. 6. The upper limit of the current was set by the selected grid and anode voltages (<5 v).

We found that initially, prior to admission of oxygen, turning on the dc component depresses the emission for several seconds so that in order to obtain reproducible results one must measure the initial current (which is then used as the reference value I_0) some seconds after starting to take off the dc component. If one then plots the values of the saturation current at different instants relative to I_0, as has been done in Fig. 6, it will be seen that the presence of the constant dc component slows down the poisoning. The greater the dc component, the slower the poisoning and the more rapid the subsequent regeneration of the cathode. The character of the influence of the constant component is virtually the same at other temperatures and pressures.

3. In order to explain the observed regularities, it may be assumed that the oxygen acts primarily on the surface of the oxide-coated cathode. It is adsorbed on the oxygen vacancies which may be localized both on the outer and inner surfaces of the individual oxide crystals. That such vacancies exist has been

demonstrated by Redington[7].

Wagener[1] estimates that the surface concentration of such oxygen-barium vacancies is ~1%. Oxygen, adsorbed on these vacancies, may form less stable compounds with the excess barium than barium oxide. When the oxygen is pumped out these compounds readily decompose in the investigated temperature interval. The authors of Ref. 6 suggest, for example, that such compounds may be formed through polar linkages of Ba with atomic oxygen ions O^-; such ions, according to these authors, form more simply than the molecular oxygen ions O_2^- that are needed for the formation of barium oxide. In fact Shepherd[5] showed that in regeneration of oxygen-poisoned oxide-coated cathodes primarily O^- ions are liberated. This may serve to explain the 100% reversibility of the poisoning process in the investigated range of temperatures and pressures. This is also in conformity with the experimental fact[1] that the poisoning and regeneration of oxide-coated cathodes does not depend on the base material.

However, dependence of the poisoning time on the thickness of the oxide coating shows that the volume properties of the cathode also play a certain role. We feel that the volume plays the role of a medium into which the oxygen diffuses over the surface of the individual oxide grains.

Thus if we examine the one dimensional problem, the concentration of barium atoms in a certain surface layer would be determined by the reaction of the combining of Ba with O^-. Let us denote through n_{Ba} the concentration of barium atoms at the instant t, through n_{O_2} the concentration of oxygen molecules, and through $n_{0\mathrm{Ba}}$ the concentration of barium atoms prior to the beginning of poisoning (at t = 0). If we assume that only the linked atoms of barium and oxygen decompose, the concentration of atoms participating in the decomposition process would be

$$n_{0\mathrm{Ba}} - n_{\mathrm{Ba}};$$

then

$$\frac{dn_{\mathrm{Ba}}}{dt} = k_2 (n_{0\mathrm{Ba}} - n_{\mathrm{Ba}}) - k_1 n_{O_2} n_{\mathrm{Ba}}, \tag{1}$$

where k_2 is the rate of the decomposition reaction and k_1 is the rate of combination of barium and oxygen.

The amount of oxygen will be determined by two processes: adsorption from the surrounding atmosphere and diffusion into the depth of the cathode. Inasmuch as the time of formation of the adsorbed layer is short compared with the time for diffusion, it may be assumed in the zeroth approximation that there is formed on the surface of the cathode in a matter of seconds an equilibrium adsorbed layer, the number of atoms in which depends exponentially on the temperature and is directly proportional to the pressure, i.e., $Ape^{Q/kT}$, where p is the oxygen pressure and Q is the heat of adsorption.

The number of oxygen molecules diffusing into the depth of the oxide layer per second through a unit area of the surface is βn_{O_2}, where β is a quantity depending on the coefficient of diffusion and on the geometric dimensions of the layer. Then for times appreciably shorter than time for diffusion of the oxygen through the entire thickness of the cathode, expression (1) can be written in the form

$$\frac{dn_{\mathrm{Ba}}}{dt} = k_2 (n_{0\mathrm{Ba}} - n_{\mathrm{Ba}}) - k_1 n_{\mathrm{Ba}} Ape^{Q/kT} (1 - \beta). \tag{2}$$

the solution of which for small values of t will be:

$$\frac{n_{\mathrm{Ba}}}{n_{0\mathrm{Ba}}} = 1 - k_1 Ape^{Q/kT}(1 - \beta)\, t. \tag{3}$$

Inasmuch as for a well-activated cathode[3]

$$I / I_0 \approx (n_{\mathrm{Ba}} / n_{0\mathrm{Ba}})^{1/2}, \tag{4}$$

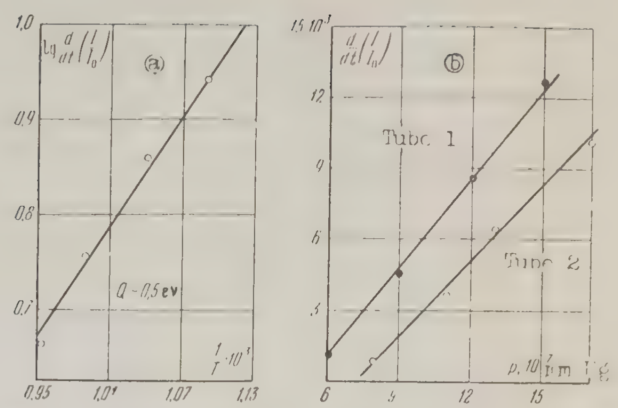

Fig. 7. Dependence of the slope of $(I/I_0)^2 = f(t)$, at small values of t, a) on the temperature, b) on the pressure.

this expression makes it possible to explain the experimentally observed regularities. The slope of the function $(I/I_0)^2 = f(t)$ at small values of t depends linearly on the pressure and exponentially on the temperature for an activation energy Q = 0.5 ev, as may be seen in Fig. 7.

An expression analogous to (1) can be written for the process of regeneration. If we then assume that the amount of oxygen in the surface layer of thickness h (where h is of the order of the screening radius) is determined by the diffusion of the oxygen from the depth of the cathode at zero concentration at the surface, equation (1) can be written in the form

$$\frac{dn_{\mathrm{Ba}}}{dt} = k_2 (n_{0\mathrm{Ba}} - n_{\mathrm{Ba}}) - k_1 n_{\mathrm{Ba}} n_{\mathrm{O}_2\infty} \frac{h}{2\sqrt{\pi D}} t^{-1/2}, \qquad (5)$$

where $n_{\mathrm{O}_2\infty}$ is the oxygen concentration at equilibrium poisoning.

Inasmuch as for a poisoned cathode it may be assumed[3] that $I/I_0 = n_{\mathrm{Ba}} / n_{0\mathrm{Ba}}$, the solution of (5) is obtained in the form

$$\frac{\frac{I}{I_0} - \frac{I_\infty}{I_0}}{1 - \frac{I_\infty}{I_0}} = \left[k_2 - \frac{1}{1 - \frac{I_\infty}{I_0}} \cdot \frac{h}{\sqrt{\pi D}} t^{-1/2}\right] t, \qquad (6)$$

where the subscript ∞ indicates the equilibrium condition at the end of poisoning. Comparison of this expression with experiment shows agreement for small values of t. The left side of equality (6) depends almost linearly on t with a slope which increases with the temperature and decreases with increasing pressure. The deduced value of k_2 is of the order of 10^{-2}-10^{-3} sec^{-1}.

In order to evaluate the poisoning time we must attempt to solve equation (1) for large values of t. We assume that in this case the principal source of oxygen is its diffusion into the oxide layer. Then for n_{O_2} in (1) we must substitute solution of the diffusion equation for sorption by a plate at constant pressure:[8]

$$n_{\mathrm{O}_2} = 1 - \frac{2d}{\pi^2} \sin \frac{\pi x}{d} e^{-\pi^2 Dt/d^2}. \qquad (7)$$

Averaging the obtained value over x within the limits of the surface layer of thickness h participating in the emission and bearing in mind that the instant of attainment of equilibrium is characterized by the condition

$$\frac{dn_{\mathrm{Ba}}}{dt} = 0,$$

we obtain

$$\frac{\pi^2 D t_{\mathrm{pois}}}{d^2} = 2.3 \lg \frac{h}{\pi\left(1 - \frac{k_2 \left|1 - \frac{I_\infty}{I_0}\right|}{k_1 \frac{I_\infty}{I_0} A p e^{Q/kT}}\right)}. \qquad (8)$$

The deduced expression, despite the very rough approximations used in deriving it, is in agreement with experiment. First, it relates the value of I_∞/I_0

with the pressure, i.e., shows that I_∞/I_0 decreases with increasing p. Then, from expression (8) one can readily obtain the experimentally observed dependence (see Fig. 5) $t_{pois} = f(d^2)$ since the logarithm in the right side of the equation remains unchanged with changes of d. The order of magnitude of D obtained from the slope of the curve in Fig. 5 proves to be 10^{-8} cm^{-2} sec^{-1}. This value as regards order of magnitude agrees with the data of Redington[7] for the coefficients of surface diffusion of Ba over barium oxide.

From equation (8) one can also deduce the temperature dependence of the poisoning time if we assume an appropriate value of k_2, all the other quantities being taken from experiment. Let us take $k_2 \approx 2 \cdot 10^{-2}$ at 1050°K and $\approx 4 \cdot 10^{-3}$ at 918°K, i.e., let us assume that the decomposition energy Q_2 equals 1.9 ev; then the right hand parts of equation (8) will be in the ratio of 3:1, i.e., we will have $D_{1050} t_{pois1050} / D_{918} t_{pois918} \approx 3$. If, after Redington[3], we take $Q_D \approx 0.2$ ev, then $D_{1050}/D_{918} \approx 1.2$ and $t_{pois1050}/t_{pois918} = 2.5$, which, as may be seen from Fig. 4, is in agreement with experiment.

To explain the results of the experiments with a constant dc component of the emission current we need only assume, as a working hypothesis, that the constant component of the electronic current is always accompanied by an ionic component, i.e., that there occurs electrolytic reduction of the cathode. According to Faraday's law, the number of barium atoms transferred per second in electrolysis is proportional to the magnitude of the ionic and, consequently, of the electronic current. Hence in expression (1) and in all the following equations including (5) for the case of regeneration there will appear a term $\gamma I_c/n_{0Ba}$, where γ is a proportionality coefficient and I_c is the constant component of the current. The slope of the $(I/I_0)^2 = f(t)$ curves will decrease since the above new term will be subtracted from it. Actually as experiment shows the difference between $(I'/I_0)^2$ at $I_c \neq 0$ and $(I/I_0)^2$ at $I_c = 0$ is proportional to the magnitude of the constant component of the emission current. The dependence $(I'/I_0)^2 - (I/I_0)^2 = f(I_c)$ is characterized by a straight line passing through the origin and having the slope $\gamma/n_{0Ba} = 0.02$ ma^{-1}. If we assume that the ionic current amounts to $5 \cdot 10^{-2}$ % of the electronic current, the concentration of excess barium at the initial instant proves to be equal to 10^{16}-$10^{17} cm^{-3}$. In the case of regeneration, the term $\gamma I_c/n_{0Ba}$ also appears in the equations and acts to accelerate the regeneration of the cathode during evacuation of the oxygen, which is also in agreement with experiment. Thus the presence of a constant dc component (i.e., taking off a plate current) will increase the poisoning time and reduce the regeneration time, effects which can readily be explained in the light of currently accepted concepts.

Conclusions

1. We developed a procedure which makes it possible to investigate the influence of different gases on the emission of the cathodes of standard industrial glass-envelope tubes. The developed procedure was used for determining the influence of oxygen at pressures from $5 \cdot 10^{-7}$ to $1 \cdot 10^{-5}$ mm Hg on the emission of the oxide-coated cathodes of 6Zh2P (6Ж2П), 2190 and 2192 type tubes.

2. We found that in the investigated ranges of pressures and temperatures (V_f = 6 to 4 v) the oxygen-poisoned cathode is fully regenerated when the oxygen is evacuated, without the need for raising the temperature. At oxygen pressures under $5 \cdot 10^{-7}$ mm Hg virtually no poisoning is observed.

3. The poisoning time proved to depend linearly on the square of the thickness of the oxide coating. From this we deduce that not only the surface of the cathode but also its volume plays a part in the poisoning process. However, the fact that the poisoning time increases with temperature indicates that we have here not only diffusion of oxygen into the cathode but also continuously acting reactivation processes, which become more intense with increasing temperature.

4. In order to explain the observed regularities, we propose a qualitative theory in which it is assumed that the emission of a well-activated cathode is proportional to the square root of the concentration of excess barium atoms, while the emission of a poorly activated cathode is proportional directly to the Ba atom concentration. The amount of excess barium during poisoning decreases due to combination of the barium with oxygen with the formation of compounds less stable than barium oxide, compounds which readily decompose when the oxygen is evacuated. The concentration of oxygen in the surface oxide layer (which is primarily responsible for the emission from the cathode) is determined by processes of diffusion of the oxygen into the depth of the cathode and vice versa and processes of adsorption of the oxygen on the surface.

5. We found that a constant dc component of the emission current (a plate current) has an activating effect on the cathode both in the process of poisoning and in the process of regeneration, the effect increasing with the magnitude of the component. This substantiates the commonly accepted view that the flow of plate current is accompanied by electrolytic processes leading to an increase in the amount of free barium in the oxide layer.

In conclusion we wish to thank N.D.Morgulis for his interest in the work and E.D.Maiborode for undertaking to check our calculations.

"T.G.Shevchenko" Kiev State University

References

1. S.Wagener, Proc. Phys. Soc., B 67, 369 (1954).
2. N.D.Morgulis & G.Ia.Pikus, Doklady AN SSSR, 103, 1103 (1955).
3. T.Arizumi & S.Narita, J. Phys. Soc. Japan, 3, 356 (1948).
4. G.Metson, Nature, 164, 540 (1949).
5. A.A.Shepherd, Brit. J. Appl. Phys., 4, 70 (1953).
6. G.Herrmann & S.Wagener, Oxide-coated cathode (In Russian trans., M.1949).
7. R.W.Redington, Phys. Rev., 87, 1066 (1952).
8. R.M.Barrer, Diffusion in and through solids (In Russian trans., M.1948).

X-RAY INVESTIGATION OF THE SYSTEMS OF BINARY AND TERNARY CARBONATES AND OXIDES OF THE ALKALINE EARTH METALS

- E.P.Ostapchenko

In spite of the great number of investigations of the oxide cathode and the physical and chemical processes occurring therein, we still lack definitive answers to a number of questions relating to the theory of its operation and capable of explaining the experimentally observed effects leading to premature failure of such cathodes. To an extent this may be explained by the inadequate number of systematic investigations of the physics of the oxide-coated cathode and the physical-chemical phenomena occurring at the temperatures of its preparation and operation. We still lack adequate information on the crystal state of the binary and ternary carbonates and oxides of barium, strontium and calcium, the processes occurring during the decomposition of the carbonates and oxides, the changes taking place in the crystalline state of the coating during service, etc.

A number of reports[1-4] published abroad on the use of x-ray and electron diffraction for investigating oxide-coated cathodes yield some information on the subject but most of these investigations were of an incidental character and led to conflicting results. In view of this we carried out an x-ray structural investigation of the systems of binary and ternary carbonates and oxides of the alkaline earth metals; some of the results are set forth in the present report.

Crystal structure of jointly precipitated binary and ternary carbonates of barium, strontium and calcium

We investigated the structure of alkaline earth metal carbonates jointly precipitated with soda at about 90°C. The x-ray patterns were recorded by the powder method in 57.4 and 143.25 mm diameter cameras using radiation from copper or cobalt anodes. To check the identity of the structures a number of carbonate mixtures were also precipitated with ammonium carbonate. The carbonates of barium and strontium, whether precipitated by soda or ammonium carbonate, crystallized in a rhombic lattice of the aragonite type; when precipitated with soda calcium carbonate crystallizes in the same lattice, while when precipitated by ammonium carbonate it crystallizes in a rhombohedral lattice of the calcite type.

When jointly precipitated with soda the carbonates of barium and strontium form solid solutions having the same structure with lattice parameters varying monotonically from $BaCO_3$ (Table 1). In the case of joint precipitation of the carbonates of barium and calcium at all concentrations of the components there are also formed solid solutions of the two carbonates in each other; however, in the case of precipitation of 80-100% $BaCO_3$ + 20-0% $CaCO_3$, there is formed a solid solution of the aragonite type; when the $BaCO_3$ concentration is under 55%, there is formed a solid solution with a calcite structure, while in the intermediate 55-80% $BaCO_3$ range two solid solutions are present in the precipitate: one with a structure of the aragonite type and the other with a calcite structure.

The x-ray patterns for a number of jointly precipitated carbonates of barium and calcium are shown in Fig. 1; their lattice parameters are listed in Table 2.

Table 1

Lattice parameters of solid solutions of the binary carbonates $(Ba,Sr)CO_3$

Molar composition	Argonite type rhombic lattice		
	a, Å	b, Å	c, Å
100% $BaCO_3$	5,25	8.82	6,42
86% $BaCO_3$—14% $SrCO_3$	5.22	8.76	6.40
72.3% $BaCO_3$—27,7% $SrCO_3$	5.20	8.71	6.35
61.3% $BaCO_3$—38.7% $SrCO_3$	5.19	8.69	6.33
50,4% $BaCO_3$—49.6% $SrCO_3$	5,17	8.62	6,26
40.4% $BaCO_3$—59,6% $SrCO_3$	5,16	8,58	6,18
30% $BaCO_3$—70% $SrCO_3$	5,14	8,56	6,14
20.8% $BaCO_3$—79.2% $SrCO_3$	5.13	8.49	6.09
15.3% $BaCO_3$—84,7% $SrCO_3$	5,13	8,46	6,09
7.0% $BaCO_3$—93.0% $SrCO_3$	5.11	8.40	6.05
100%—$SrCO_3$	5.10	8.36	6.03

Table 2

Lattice parameters of the solid solutions of the binary carbonates $(Ba,Ca)CO_3$

Molar composition	Argonite type rhombic lattice			Calcite type rhombohedral lattice	
	a, Å	b, Å	c, Å	a, Å	α
100% $BaCO_3$	5,25	8,82	6,42		
90% $BaCO_3$ — 10% $CaCO_3$	5,22	8,88	6,40		
80% $BaCO_3$ — 20% $CaCO_3$	5,19	8,72	6,39		
70% $BaCO_3$ — 30% $CaCO_3$	5,16	8,70	6,40	6,59	45°36′
60% $BaCO_3$ — 40% $CaCO_3$	5,15	8,69	6,39	6,60	45°39′
55% $BaCO_3$ — 45% $CaCO_3$				6,67	44°54′
50% $BaCO_3$ — 50% $CaCO_3$				6,62	44°57′
40% $BaCO_3$ — 60% $CaCO_3$				5,58	45°06′
30% $BaCO_3$ — 70% $CaCO_3$				5,53	45°12′
20% $BaCO_3$ — 80% $CaCO_3$				6,48	45°27′
100% $CaCO_3$				6,35	45°57′

An analogous picture is observed for the jointly precipitated carbonates of strontium and calcium (the region of formation of the two-phase solid solution lies in the 20-45% $SrCO_3$ content interval). When jointly precipitated with soda the ternary carbonates at relatively low concentrations of $CaCO_3$ (20-40%) form a solid solution with an aragonite type lattice; at higher (over 45-50%) $CaCO_3$ contents there is formed a solid solution with a calcite structure; in the intermediate $CaCO_3$ concentration range two solid solution phases are formed: one with an aragonite type structure, the other with a calcite structure (Fig. 2).

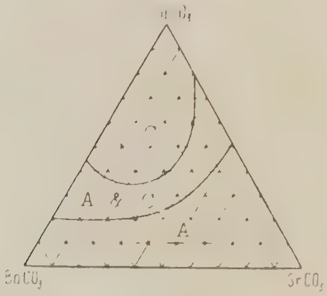

Fig. 2. State diagram of jointly precipitated ternary carbonates $(Ba,Sr,Ca)CO_3$. A- aragonite; C - calcite.

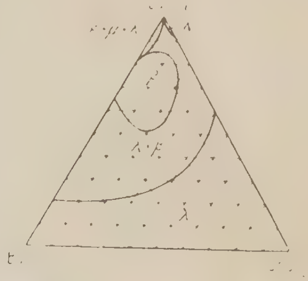

Fig. 3. State diagram of jointly precipitated ternary carbonates $(Ba,Sr,Ca)CO_3$ according to Terada[6]: λ - aragonite, β - calcite, μ - waterite.

Decomposition of the carbonates into oxides

The process of decomposition of carbonates applied to a heater core of pure nickel 1.14 mm in diameter was investigated in special experimental tubes without plates. The cathode temperature was monitored by means of a chromyl-aluminum thermocouple.

At different stages of decomposition the tube was taken off the vacuum-pump line and opened in an atmosphere of thoroughly purified and dried nitrogen. The filament was cut off the support and dipped briefly into molten wax, after which it was mounted in the x-ray camera. Special tests showed that the wax protects the cathode coating from chemical changes under the influence of atmospheric air and yields only two x-ray diffraction lines that can readily be allowed for in the subsequent analysis.

Investigation of the decomposition of binary carbonates of equimolar composition showed that in both the case of jointly precipitated carbonates and the case of mechanical mixtures of carbonates of barium and strontium decomposition begins after ten minutes heating at a temperature of 600° and that the time of decomposition decreases rapidly with increasing temperature. The carbonates are fully decomposed in 5 minutes at 700° or 2 minutes at 745°, forming, in the case of jointly precipitated carbonates, two-phase solid solutions (compositions ap-

proximately: 95% SrO + 5% BaO and 73% BaO + 27% SrO); in the case of an initial mechanical mixture of the carbonates, separate oxides of barium and strontium are formed. Further, whereas in the first case there is formed a single phase solid solution of the oxides after 5 minutes heating at 745°, in the latter case (mechanical mixture) there form two phases which become a one-phase solid solution only after further prolonged heating.

Thus the formation of a single phase solid solution of the oxides occurs much faster and at lower temperatures in the case of jointly precipitated carbonates of Ba and Sr.

An analogous situation is observed as regards decomposition of the ternary carbonates (we investigated jointly precipitated and mechanical mixtures having the compositions $BaCO_3$: $SrCO_3$: $CaCO_3$ = 50:45:5 and 40:20:40). However, in this case the temperatures requisite for obtaining the final decomposition product are higher than in the case of binary carbonates. Moreover, these temperatures differ for the two investigated ternary compositions. Thus in preparing oxide coatings of the carbonates of Ba, Sr and Ca one must select the appropriate heat treatment for each individual proportion of components.

Crystalline states of jointly heated binary and ternary oxides of barium, strontium and calcium

The procedure employed in investigating the oxides of barium, strontium and calcium forming from the carbonates under the influence of heat was similar to that described above for the binary compounds.

As is known, separately barium, strontium and calcium oxide crystallize in a face-centered cubic lattice characterized by the parameters 5.524, 5.145 and 4.801 Å, respectively.[7] In the case of joint heating of the carbonates, the oxides of barium and strontium form mixed crystals with a lattice constant varying linearly as a function of the composition. The lattice parameters of different solid solutions are listed in Table 3 and the variation of the lattice parameter with the composition of the solid solution is shown graphically in Fig. 4.

Table 3

Lattice parameters of solid solutions of the binary oxides (Ba,Sr)O

Molar percent		a, Á	Molar percent		a, Å
BaO	SrO		BaO	SrO	
100	—	0,524	30,0	70,0	5,253
86,0	14,0	5,465	20,8	79,2	5,221
72,3	27,7	5,416	15,3	84,7	5,198
61,3	38,7	5,371	7,0	93,0	5,164
50,4	49,6	5,332	—	100	5,144
40,4	59,6	5,295			

A similar picture is observed in the case of oxides of strontium and calcium, but in this case the linearity of the variation of the lattice parameter breaks down at about 60% BaO content. Furthermore, in a number of cases (specifically in our control experiments) we observed the formation of two phases of the solid solution in this concentration region.

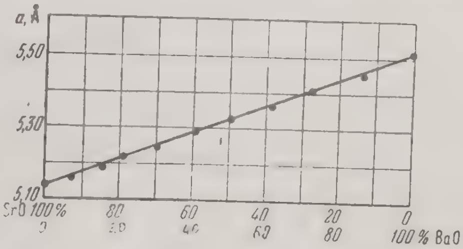

Fig. 4. Variation of the lattice parameter a of the solid solutions of BaO and SrO with the molar composition.

The oxides of barium and calcium do not form mixed crystals at any proportions of the components or any heating temperatures from 1050-1100° (Fig. 5).

Investigation of the ternary oxides obtained by decomposition of jointly precipitated carbonates presented the greatest experimental difficulties. As noted above, ternary carbonates of different compositions require different heat treatments for complete transformation into solid solutions of the oxides. Naturally, one could not expect all compositions to form a single-phase solid solution. On

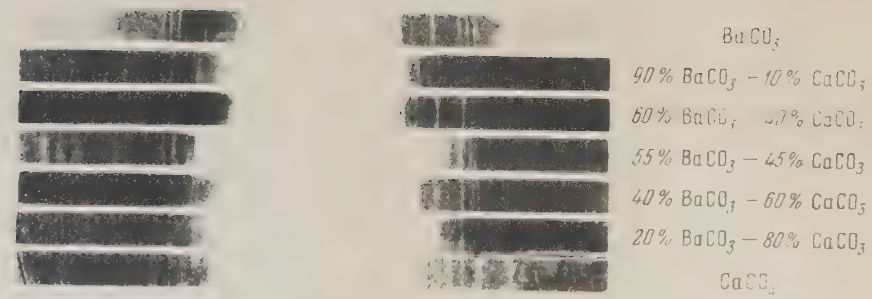
BaCO3
90% BaCO3 - 10% CaCO3
60% BaCO3 - 40% CaCO3
55% BaCO3 - 45% CaCO3
40% BaCO3 - 60% CaCO3
20% BaCO3 - 80% CaCO3
CaCO3

Fig. 1. X-ray patterns of jointly precipitated binary carbonates $(Ba,Ca)CO_3$ of different composition.

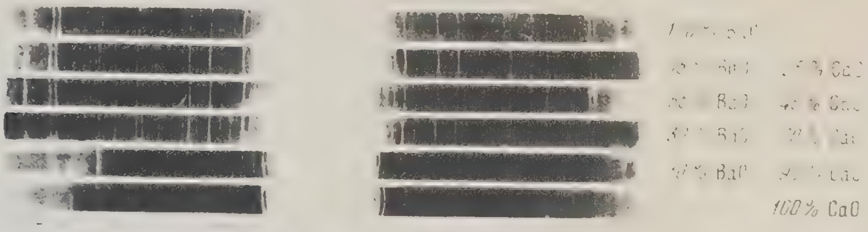

Fig. 5. X-ray patterns of jointly heated binary oxides of barium and calcium.

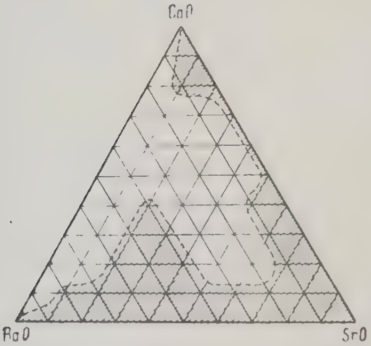

Fig. 6

the other hand, appreciable overheating of the cathodes would undoubtedly result in evaporation of the more volatile component (BaO), which would, of course, impair the accuracy of the results. Nevertheless, we found it necessary to raise the heating temperature to about 1100° if only for a short time.

The results of this part of the investigation are shown in Figs. 6 & 7. A two-phase solid solution forms at most concentrations; a single phase solid solution is observed only at low (under ~12%) concentrations of CaO and also in a narrow range of BaO and CaO concentrations (under 40%). In the latter case there is also probably present a second phase, as evinced by the measured values of the lattice parameters, but in amounts too small to be detected on the x-ray patterns.

The variation of the lattice parameters is not regular in all directions over the diagram, which is evidence of the possible formation of different mixed

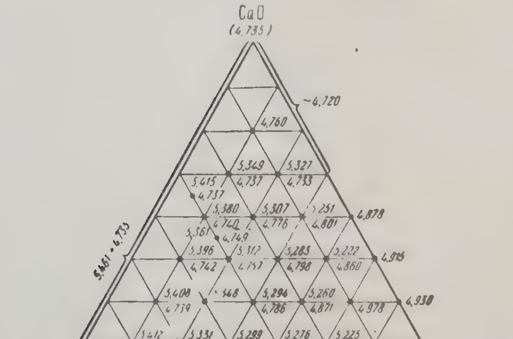
CaO
(4,733)
~4,720
4,760
5,349
5,327
4,878
4,915
4,938
5,000
5,061
BaO
(5,481)
5,407
5,347
5,306
5,266
5,229
5,191
5,160
5,130
5,099
SrO
(5,077)

Fig. 7

Fig. 6. Formation of ternary oxide solid solutions in the BaO + SrO + CaO system (hatched area - region of formation of single phase solid solution).

Fig. 7. Lattice parameters in the BaO + + SrO + CaO system.

Discussion of results and conclusions

Even in the light of the experimental data obtained the question of the influence of the crystallographic structure of the carbonates (i.e., the structure of their crystal lattice rather than the shape and size of the particles, which are often referred to as the "structure" in the literature) still remains largely unclear; but it can be safely asserted that the crystallographic structure does exert a certain influence on the rate of decomposition of the carbonates into oxides, on the formation of the oxide solid solution and, probably, on the final degree of homogeneity of the oxides as regards composition. Comparison of the results of x-ray investigation with the emission characteristics and work functions of different coatings (Fig. 8) shows, however, that the formation of mixed (Ba,Sr)O crystals leads to a reduction of the work function and, consequently, an increase in the emission as compared with pure BaO or SrO. The formation of mixed (Sr,Ca)O crystals also reduces the work function. In the case of a mixture of BaO + CaO, which does not form a solid solution, there is observed only a small reduction of the work function (~0.07 ev), probably due to the fact that where both the external and internal work functions are concerned interaction of the barium atoms with CaO is more advantageous than their interaction with BaO.

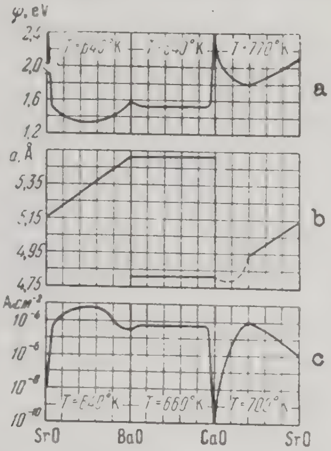

Fig. 8. Variation with the composition of the work function, the lattice parameter a and the density of the emission current for different binary oxide coatings.

Changes of the lattice constant as a function of the composition of the oxide solid solution may also exert an appreciable influence on the emission characteristics of mixed crystals, i.e., for example, closer packing due to the addition of SrO to BaO may be the reason for the decrease in the work function observed for mixed crystals. The tighter packing of the BaO lattice resulting from the addition of strontium oxide may substantially reduce the rate of diffusion of barium, which would naturally change the equilibrium concentration of free barium and lead to an appreciable change in the work function. This tentative hypothesis is in need of experimental verification, since we have, unfortunately, no specific data relative to the rate of diffusion of barium in mixed (Ba,Sr)O crystals.

In selecting new compositions of ternary oxides for cathode coatings, one must bear in mind the possible formation of mixed crystals. Thus, our experiments showed that a coating consisting of the jointly precipitated ternary carbonate having the composition 47% $BaCO_3$ + 46% $SrCO_3$ + 6.5% $CaCO_3$, after a brief heating at about 1050°, exhibits a sharp increase in emission. According to the x-ray diffraction data there is first formed in this case a two-phase solid solution of the three oxides which subsequently goes over into a single-phase solid solution.

The higher emission from ternary oxides, as compared with the emission from (Ba,Sr)O, observed by Grey[8] in pulsed emission, can probably be explained as follows. At sufficiently high temperatures (above about 1000-1050°), there readily develop defects in the oxide lattice in connection with the increased rate of diffusion; this effect occurs under conditions of rapid elimination of BaO. One can hardly expect to detect the appearance of lattice defects in the case of binary and ternary oxides by means of x-rays since, after heating at about 1050°, the broadening of the x-ray diffraction lines produced by changes of composition proves to be so appreciable that it becomes impossible to judge of possible disturbances of the lattice. It is known, however, that in complex solid solutions there is an appreciably greater degree of disordering than in

the case of pure components. When the ternary oxides form a single phase solid solution, the number of imperfections in the lattice forming as the result of heat treatment may be even greater than in the case of a single-phase binary solution; the disordering may be assumed to be maximal on the boundary of the diagram region corresponding to the formation of single-phase solid solutions (10-12% CaO).

In addition to the role played by such lattice defects, changes in the value of the coefficient of diffusion of barium in ternary oxide crystals may have an appreciable effect on the emission characteristics of the coating. Formation of a single phase solid solution of the ternary oxides probably changes the rate of diffusion of barium, reducing it even below the rate characteristic of binary oxides; this also serves to explain the observed enhanced emission from ternary oxides.

Furthermore, the addition of a certain amount of calcium oxide to a (Ba,Sr)O coating probably inhibits the evaporation of barium to a greater degree than the addition of an equal amount of strontium oxide. This assumption is substantiated by the results of Kovtunenko's[9] determinations of the equilibrium concentration of free barium in oxide coatings of different composition. In the case of the ternary oxide with 5% BaO, i.e., clearly in the region of the single phase structure, the equilibrium concentration of barium was found to be one order of magnitude lower than its value for the binary equimolar oxide. Moreover, according to the results of Pelchowitch's[10] investigation of the evaporation of the oxides of alkaline earth metals from different materials, even in the case of highest purity nickel and platinum, barium oxide evaporates in the form of the oxide, while the oxides of strontium and calcium evaporate primarily in the form of the pure metals, i.e., the thermal dissociation of the oxides of Ca and Sr begins much earlier than that of barium oxide, apparently at temperatures within the range commonly employed in treating cathodes. Thus, in the case of a ternary oxide coating dissociation of the CaO, leading to evolution of pure calcium, can result in activation of the coating due to reduction of the barium oxide by the free calcium.

In addition we must briefly mention the recently published article by Ferada[11] devoted to the results of x-ray investigations of the ternary oxides of barium, strontium and calcium. Ferada asserts that in practically all cases there are formed three types of solid solution crystals: (Ba,Sr)), (Sr,Ca)O and (Ca,Sr)O (in the latter case the solid solution presumably consists primarily of calcium oxide with a small admixture of strontium oxide). These results were obtained after 2 hours heating of the cathode at 900°. Actually, as our experiments on the decomposition of the ternary carbonate solutions showed, this temperature is not sufficiently high for the formation of a single-phase solid solution of the oxides. Further, Ferada asserts that one cannot judge of the formation of a single-phase solid solution of the oxide at higher temperatures in view of the appreciable evaporation of BaO at 1000-1100°. While it is true that evaporation of BaO does occur at these temperatures, our investigations showed that there is no need to heat the cathode for 3 hours at 1100° (the procedure reported by Ferada): 1-2 minutes heating at ~1050° is sufficient. In view of this all the "transitions" of the components from one type of solid solution to others described by Ferada have no practical significance where the actual operating conditions of an oxide-coated cathode are concerned.

In our experiments, we never observed the formation of three phases in the solid solution of the oxides, while measurements of the lattice parameters indicate the possibility of formation of (Ba,Sr,Ca)O crystals even in the region of the two-phase solid solution.[12]

We hope that more accurate x-ray structural data on the BaO + SrO + CaO system can be obtained with the aid of ionization recording. We plan in the near future to undertake such an investigation in conjunction with a parallel careful measurement of the emission properties of the different crystals.

In conclusion the writer takes this occasion to thank B.M.Tsarev for his interest and help in the present investigation.

References

1. W.Burgers, ZS. f. Phys., 80, 352 (1933).
2. N.Benjamin & H.Rooksby, Phil. Mag., 15, 810 (1933).
3. A.Einstein, J.Appl.Phys., 17, 434 (1946).
4. E.Jamaka, J.Appl.Phys., 22, 1087 (1951); 23, 498, 937 (1952).
5. E.P.Ostapchenko, Otchet NII MRTP (Report, Scientific Research Institute of the Ministry of the Radio Engineering Industry), 1953.
6. J.Terada, Nature, 171, 517 (1953).
7. Handbook of Chemistry and Physics, 1939.
8. L.Grey, Nature, 167, 522 (1951).
9. P.V.Kovtunenko, Dissertation MKhTI (Moscow Institute of Chemical Technology), 1954.
10. J.Pelchowitch, Philips Res. Rep., 9, 42 (1954).
11. J.Ferada, J. Phys. Soc. Japan, 10, 555 (1955).
12. E.P.Ostapchenko, Dissertation, NII MRTP (see Ref. 5) 1955.

INVESTIGATION OF THE EMISSION CHARACTERISTICS OF OXIDE-COATED CATHODES WITH BASES OF NEW NICKEL ALLOYS

- V.S.Parkhomenko, M.A.Chistiakova, G.A.Vostrov & G.M.Kudriasheva

Introduction

The development and investigation of new and better materials for the sleeves of oxide-coated cathodes continues to be important in view of the continuing necessity of improving the quality of such cathodes. The commonly employed base materials fail to meet the new, more exacting requirements as regards dependability and longevity. The most suitable base material, as we know, is standard grade "A" nickel containing 0.15-0.25% silicon.

Work on the development of new alloys has been going on for several years. Our laboratory has taken an active part in this work and, in particular, has investigated the emission characteristics of oxide-coated cathodes employing these new alloys as the base. A distinctive feature of the tests carried out in our laboratory was the systematic investigation of the electric parameters of a large number of vacuum tubes, both experimental and production models, over the course of a prolonged period of service (~ 10,000 hours).

The ultimate purpose of these investigations was to make available to the vacuum tube industry better nickel alloys for use as the base material for oxide-coated cathodes. To this end we studied sleeves of different diameters made of the alloys of the following composition:

Designation of alloy	Alloying components, %					
	Si	Fe	Ca	Sr	W	Other
Ni-Ca	--	To 0.05	0.15-0.2	--	--	0.1
Ni-Sr	--	" 0.05	--	0.15	--	0.1
Ni-W	0.01	" 0.05	--	--	2.55-4.0	0.1

Preparation of experimental lots of tubes and testing

The investigation of the emission characteristics of cathodes with different bases was carried out in an experimental diode and in industrial tubes of the following types: 6P9-E, 6Zh4-E, 6Zh8-E, 12S3S, 5Ts9S, 6Zh8, 6K7 (6П9-Е, 6Ж4-Е, 6Ж8-Е, 12С3С, 5Ц9С, 6Ж8, 6К7) and others.

The experimental diode of cylindrical design was assembled of a minimal number of standard parts. In developing the procedure for fabricating the diodes, stress was laid on obtaining as uniform a product as possible and excluding the influence of all extraneous factors on the emission characteristics of the cathode. As a result of the measures taken, the only varying element in the diode was the cathode itself. A three-carbonate coating containing 12%$CaCO_3$ was used on all the cathodes of the experimental diodes.

In the investigations using commercial tubes, the oxide coating regularly used by the manufacturing plant for the given type of tube was retained.

To obtain a complete picture of the emission characteristics of different cathodes, both the experimental lots of diodes and the industrial tubes were tested for prolonged service.

In the longevity tests the diodes were operated at $V_h = 6.3$ v and $V_a = 22$ v which corresponds to a theoretical current density i = 65 ma/cm^2.

The commercial tubes were tested at three different operating conditions: 1) the normal operating condition appropriate to the given type of tube, 2) stand-by conditions ($V_h = 6.3$ v, $I_a = 0$), and 3) "forced" stand-by conditions ($V_h = 8$v, $I_a = 0$).

In determining the emission characteristics of the different cathodes, in addition to the usual static parameters, we measured a number of additional parameters. Among the latter, the more interesting are a) the pulse emission (τ = 1.5 microsec, V_a = 1000 v) indicative of the peak emission capability of the cathode, b) the resistance of the substratum or intermediate layer - R_k, c) the emission ability of the cathode when markedly underheated (V_h = 1.2 v, V_a = 4.5 v), d) the high-frequency and low-frequency noise levels, and e) the pulse emission with a constant dc plate current.

Test Results

The alkaline earth elements Ca and Sr are active reducing agents where barium oxide is concerned. Previous investigations of the emission characteristics of cathodes with an Ni-Ca alloy base in the experimental diode substantiated the high reducing power of Ca. The use of this alloy for the cathodes of the 6P9-E type tube made possible the excellent emission parameters and service life (5000 hours) now specified for this tube.

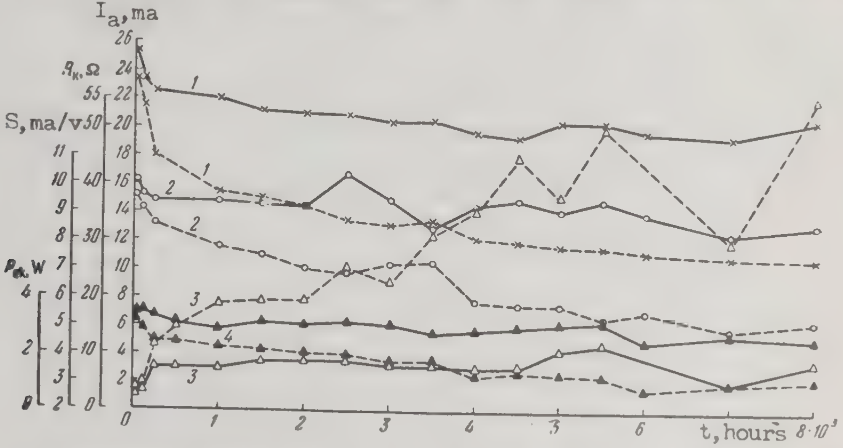

Fig. 1. Variation with time of the plate current I_a (1), transconductance S (2), resistance of the intermediate layer R_k (3) and output power P_{ek} (4) of a 6P9-E type tube. Solid lines - tube with a cathode having an Ni-Ca base; dash lines - tube with a cathode having an Ni-Si alloy base.

Curves characterizing the variation of plate current, the transconductance, the output power and the resistance of the intermediate layer with time for 6P9-E tubes are shown in Fig. 1. The tubes were tested over a period of over 8000 hours under normal operating conditions. From a comparison of the curves it will be seen that the tube with a base of Ni-Ca alloy has higher and far more stable parameters than the older version of the tube with the standard Ni-Si alloy (i.e., grade "A" nickel) cathode base. Moreoever, it will be noted that the characteristics of the Ni-Si alloy base tube fell below the minimal acceptable values towards 4000 hours of service, whereas the Ni-Ca alloy base tube was still serviceable after 8000 hours of operation.

The probable reason for the early failure of tubes with cathodes having bases of Ni-Si is the growth of the resistance of the intermediate layer (Ba_2SiO_4): towards 4000 hours of operation the resistance of the interlayer in these tubes attains 40 ohms, while in the tubes with the Ni-Ca base this resistance is less than 15 ohms.

The time dependences of the plate current, the transconductance and the resistance of the interlayer for 6Zh4-E tubes when operated under the two standby regimes and with V_h = 8 v are shown in Figs. 2 & 3.

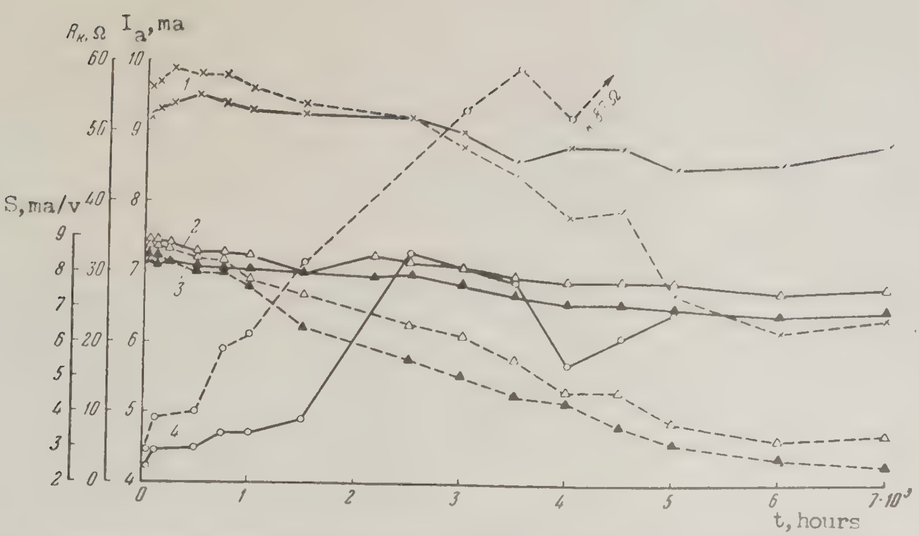

Fig. 2. Variation with time of plate current (1), transconductance with $V_h = 6.3$ v (2), transconductance with $V_h = 5.5$ v (3) and resistance of the intermediate layer (4) for a type 6Zh4-E tube. Solid lines- tube with Ni-Ca base cathode; dash lines - tube with Ni-Si base cathode.

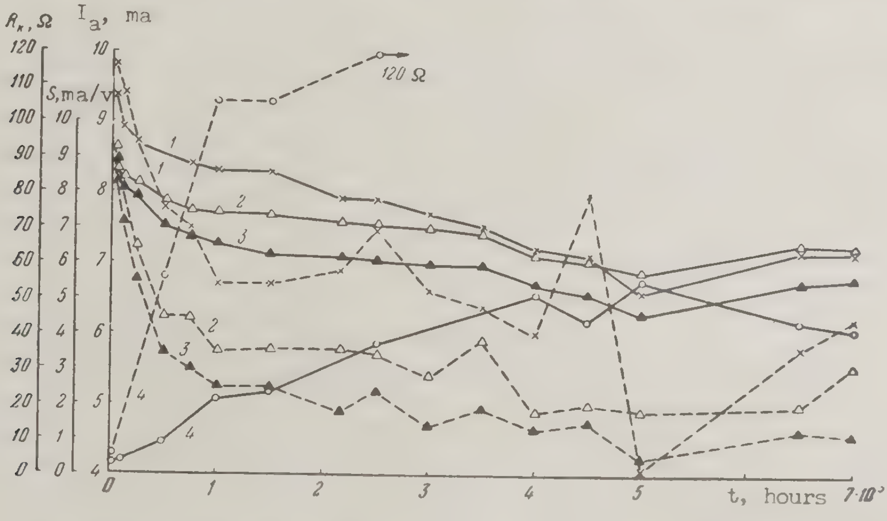

Fig. 3. Variation with time of plate current (1), transconductance with $V_h = 8$ v (2), transconductance with $V_h = 5.5$ v (3) and resistance of the intermediate layer (4) for a type 6Zh4-E tube. Solid lines - tube with Ni-Ca base cathode; dash lines - tube with Ni-Si base cathode.

It will be seen that the variations of the static parameters are in general accord with the variation of the resistance of the intermediate layer. It will be seen from the curves that test operation at an elevated temperature ($V_h = 8$ v) with no plate current promotes a more intense growth of the interlayer; because of this the characteristics of the tubes with the Ni-Si base fell below the rated values towards 500 hours of operation (with R_k reaching 50-60 ohms). In the case of tubes tested at $V_h = 6.3$ v and $I_a = 0$, the resistance of the interlayer increased more slowly and these tubes remained serviceable for up to 3500 hours.

It will be seen from the same figures that tubes with Ni-Ca alloy base

cathodes retained satisfactory characteristics for the full 7000 hours of the test even at the elevated (V_h = 8 v) cathode temperature.

From a critical comparison of the test results for the tubes with Ni-Ca and Ni-Si base cathodes we can draw the following conclusions:

1) The parameters of the tubes with Ni-Ca base cathodes are appreciably higher than the corresponding parameters of the tubes with grade "A" nickel bases.

2) The stability of the parameters of tubes with an Ni-Ca base cathode assures a longer satisfactory service life (according to our tests up to 7000-8000 hours); however, a serious shortcoming of the Ni-Ca alloy, which limits its application, is the enhanced conductivity between the heater and the cathode base.

The cathode-heater leakage current amounts to 1-100 μa which is 100-1000 times greater than the leakage current in the case of grade "A" nickel (Ni-Si) bases. The values of the cathode-heater leakage current for a 6P9-E tube before the start of the service life test and after 2500 hours of operation are shown in Fig. 4.

The mechanism of formation of the enhanced conductivity has not yet been elucidated, but there can be no doubt that it is associated with the presence of Ca. The presence of Sr in the base material has the same effect as that of Ca on the emission characteristics of the oxide-coated cathode.

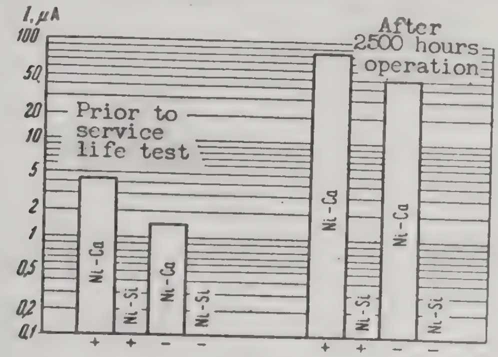

Fig. 4. Values of the cathode-heater leakage current for a 6P9-E tube.

The curves showing the variation with time of the plate current density, the transconductance and the pulse emission for the experimental diode are shown in Figs. 5-7. From a comparison of the curves for I_a and S it will be seen that the static parameters of diodes with bases of Ni-Sr are higher than the corresponding parameters of diodes with Ni-Si bases. The pulse emission of Ni-Sr base cathodes is more than twice as large as than from Ni-Si base cathodes.

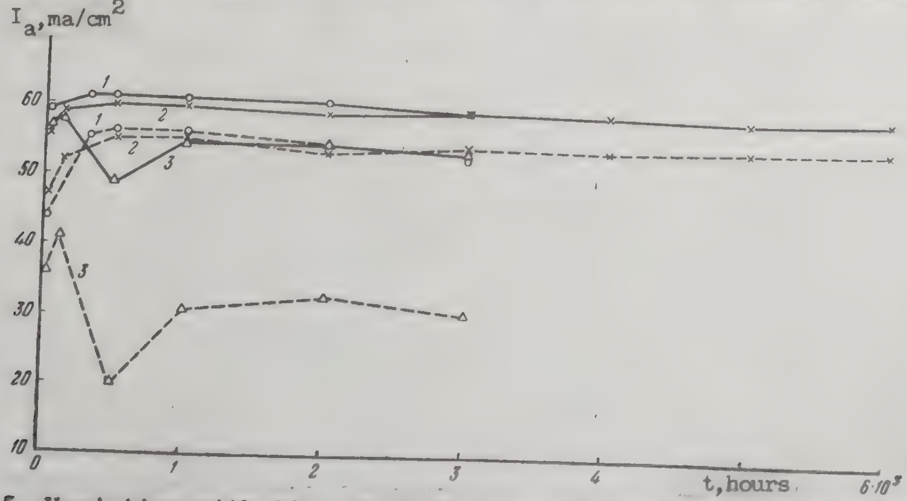

Fig. 5. Variation with time of plate current density for three lots of experimental diodes having bases of the following materials: 1) Ni-Sr alloy with 0.15% Sr, 2) Ni-W-Si alloy with 42% W and 0.01% Si, and 3) grade "A" nickel. Solid lines - V_h = 6.3 v; dash lines - V_h = 4.5 v.

Measurements of the plate current with V_h = 4.5 v yielded analogous results. In addition, use of the Ni-Sr alloy insures more uniform parameters, i.e., smaller departures from the mean value of the transconductance (see Fig. 8).

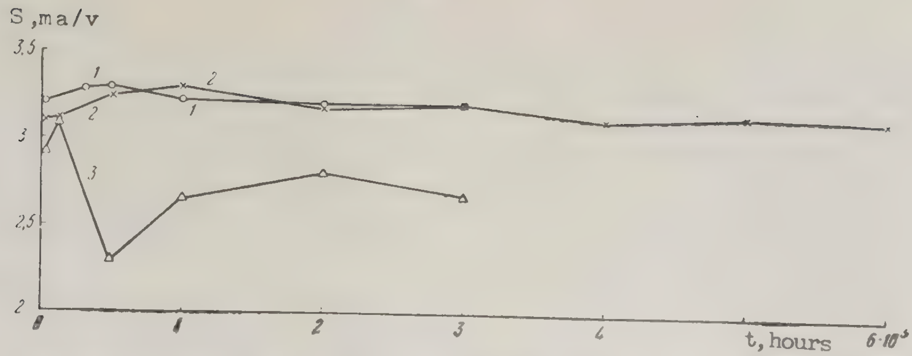

Fig. 6. Variation with time of the transconductance for the three cathodes listed in Fig. 5 but with normal heater current (6.3 v).

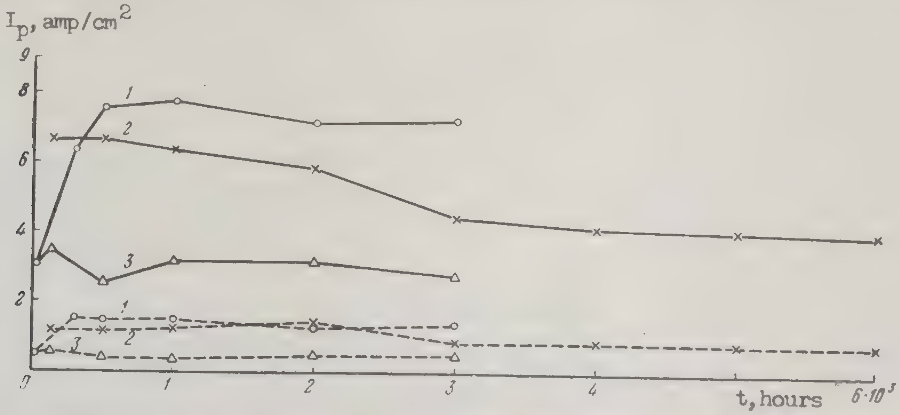

Fig. 7. Variation with time of the pulse emission (τ = 1.5 microsec) for the diodes listed in Fig. 5.

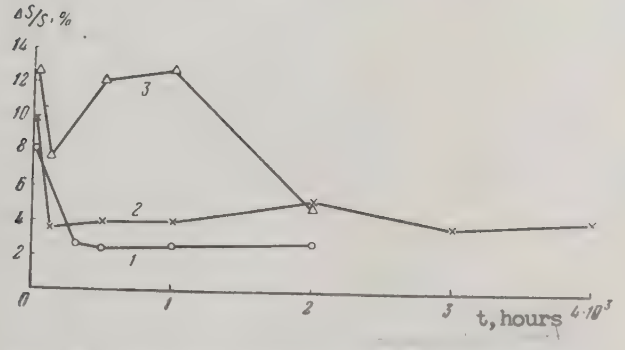

Fig. 8. Variation with time of the relative deviation from the mean value of the transconductance for the diodes listed in Fig. 5, but with normal heater voltage.

However, cathodes prepared of the Ni-Sr alloy, just as cathodes with an Ni-Ca alloy base, are characterized by an elevated conductivity between the heater and the cathode base. In view of this elevated conductivity (leakage) the use of Ni-Ca and Ni-Sr bases can be recommended primarily for tubes in which the cathode can be shorted to the heater.

Since the activating ability of the two alloys is the same, while the Ni-Sr alloy is less expensive to produce, the latter will doubtless be given preference in practice.

There are conflicting opinions in the literature regarding the activating ability of admixtures of tungsten. Some investigators[1] are of the opinion that W is a poor activator where barium oxide is concerned. Other investigators[2], on the contrary, put tungsten in the group of active reducing agents of barium oxide.

Our results show that the presence of tungsten impurity in the cathode base has a positive effect on the emission characteristic of the oxide-coated cathode both during the initial hours of operation of the tube and, particularly, over a prolonged period.

The high values of the parameters and their stability in the case of bases containing tungsten may be explained by the fact that the activation process

continues of the entire period of operation and by the very low resistance of the intermediate layer ($BaWO_3$ or/and Ba_3WO_6). The nature of the activation process in this case is not entirely clear. Furthermore, addition of tungsten to the base material increases its mechanical strength of the sleeve.

The cathode to heater conductivity in tubes with bases of Ni-W is of the same order of magnitude as in the case of bases of grade "A" nickel (Ni-Si).

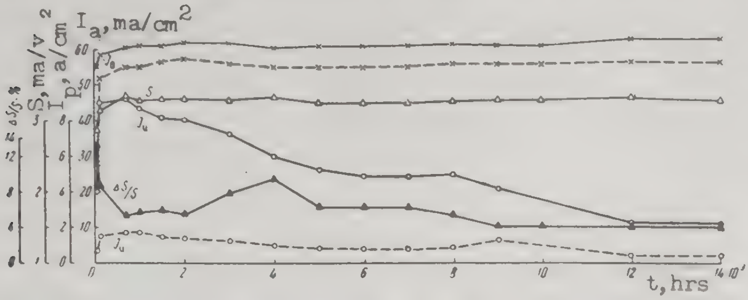

Fig. 9. Variation with time of the principal parameters of a lot of experimental diodes with Ni-W base cathodes. Solid lines - V_h = 6.3 v; dash lines - V_h = 4.5 v.

Fig. 9 shows the time dependence of the parameters of the experimental diode with a cathode base of Ni-W as determined over a prolonged period of operation (14,000 hours). The parameters of a similar lot of diodes with bases of Ni-Si fell off sharply towards 4000 hours so that the longevity test was stopped at this point and the data for these diodes are not shown in Fig. 9. In the course of the longevity tests on the experimental diodes with cathode bases of Ni-W, it was found that they have exceptionally stable parameters and a very high value of plate current at V_h = = 4.5 v. The decrease with test time of the pulse emission from diode cathodes with a Ni-W base is much smaller than the decrease from cathodes having other bases.

For the purpose of checking the results obtained for the lot of diodes with Ni-W alloy bases, we recently carried out a series of repeat tests on another lot of diodes. The results of the measurements, shown in Figs. 5-8, substantiate our earlier results.

The final step in our investigation of the Ni-W alloy consisted of testing commercial 6P9-E, 6Zh4-E, 12S3S, 6Zh8-E, 5Ts9S, 5Ts8S and other tubes fabricated with bases of this alloy.

The results of test on the 12S3S tubes prepared with cathode bases of Ni-W and Ni-Ca are shown in Fig. 10. The characteristics of the 12S3S tubes with cathodes of "V" ("B") (the standard material now used) fall below the minimum rated values before the expiration of the guaranteed service life (when operated at V_h = 10.8 v and P = 210 milliwatts), while the lots of tubes with cathode bases of Ni-W and Ni-Ca satisfied the pertinent Technical Specifications over a period exceeding the guaranteed operating life. As may be seen from Fig. 10, use of the Ni-W alloy appreciably increases the oscillating

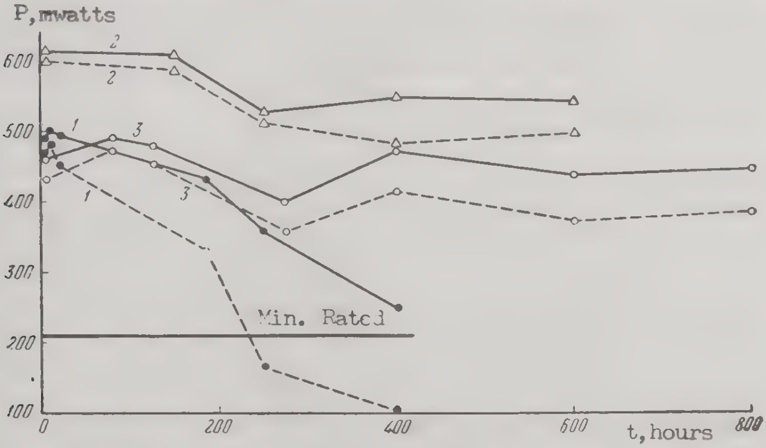

Fig. 10. Variation with time of the oscillating power for 12S3S (12C3C) tubes with cathodes having the following bases: 1) grade "V" ("B") nickel, 2) Ni-W alloy, 3) Ni-Ca alloy. Solid lines - V_h = = 12.6 v; dash lines - V_h = 10.8 v.

power output of the tube (particularly when underheated - $V_h = 10.8$ v).

The only material that will insure the electrical characteristics and service life called for by the Technical Specifications for the 12S3S tubes is the Ni-W alloy.

Our tube plants are now going over to the use of the Ni-W alloy for the production of 12S3S tubes and have been using it for 6P9-E tubes for some time.

Use of the nickel-tungsten alloy appreciably improves the quality not only of heater cathodes but also of filamentary cathodes. Thus, for example, the change-over in 1954 to the Ni-W alloy in the production of 6S4S (6C4C) tubes entirely eliminated defective production as regards burned out filaments and resulted in a substantial improvement in the static parameters and longevity of the tubes.

Conclusions

The following conclusions may be drawn from the results of our all-around investigation of the emission characteristics of oxide cathodes with different bases both in experimental diodes and in industrial type tubes:

1. The emission characteristics of cathodes with bases of Ni-Ca, Ni-Sr and Ni-W alloys are appreciably higher than those of cathodes of standard silicon-nickel alloy and of nickel with the addition of magnesium.
2. The resistance of the intermediate layer in all cases is lower for bases of the new alloys as compared with that for bases of Ni-Si (grade "A" nickel).
3. Tubes with cathode bases of the new alloys are superior to tube with bases with grade "A" nickel as regards high-frequency and low-frequency noise, pulse emission and other characteristics.
4. A shortcoming of bases containing Ca or Sr as the alloying material is the increased conductivity between the heater and cathode which limits their use to certain applications.
5. In view of the fact that the Ni-Sr alloy is cheaper than the Ni-Ca alloy preference should be given to the former in planning the industrial production of vacuum tubes.
6. In developing new and redesigning present dependable long-lived tubes it is advisable to use the Ni-W alloy as being the most active and insuring high and stable cathode parameters.
7. Investigation of the emission of oxide cathodes with other active alloying elements in the base should be continued for the purpose of finding the most active and economical material suitable for mass production of vacuum tubes.

References

1. E.S.Rittner, Philips Res. Rep., 8, 184 (1953).
2. A.M.Bounds & T.H.Briggs, Proc. IEE, 39, 788 (1951).

MECHANISM OF THE FORMATION OF ELECTRONMICROSCOPE IMAGES OF THERMIONIC CATHODES

- D.P.Vinogradov

We all know that the processes occurring on the surface of cathodes can be studied by means of an emission electron microscope, the principal component of which is an immersion lens. Emission microscopes used hitherto have employed glass optics. Despite the inadequacy of such systems, investigators have succeeded in observing a number of phenomena occurring on the surface of operating cathodes.[1] Among others oxide-coated cathodes have been studied and there have been obtained emission images of such cathodes, consisting of bright spots on a dark background. The appearance of these spots has been attributed to non-uniform emission of the oxide-coated cathode, i.e., it has been assumed that some sections of the cathode surface are characterized by a very appreciable emission, while other sections emit virtually no electrons. The bright sections have been called "emission centers".

Electric "microlenses" on the cathode surface

In discussions of the mechanism of formation of the emission image it is usually assumed that the cathode surface is smooth and that the electric field over the cathode is homogeneous. Actual oxide-coated cathodes, of course, have a rough surface with a pronounced "accidented relief". The degree of roughness depends on the technology of applying the oxide-coating; the height of the elevations or projections in such coatings may be of the order of several tens of microns. The electric field over such a cathode will naturally not be homogeneous. The equipotential surfaces in the immediate vicinity of the cathode will follow the convolutions of the cathode surface. Thus, there is formed over the surface of the cathode a system of converging and diverging "microlenses", lenses which deflect the electrons escaping from the cathode. It is obvious, therefore, that the distribution of electrons in a plane at a certain distance from the cathode will differ to a greater or lesser extent from the distribution of the emission current over the plane of the cathode. This difference will depend on the degree of inhomogeneity of the electric field near the surface of the cathode and on the distance of the said plane from the cathode surface. Such a rough surface, giving rise to "microlenses", and the approximate paths of the electrons are shown schematically in Fig. 1.

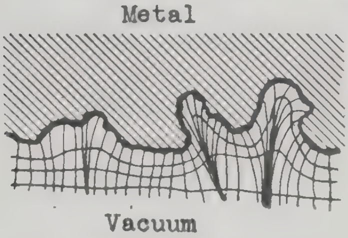

Fig. 1. Schematic section through a rough cathode surface and the adjacent vacuum. The lines indicate the approximate paths of the electrons in the vacuum and the sections through the equipotential surfaces in the vicinity of the cathode surface.

In order to check the above reasoning one must focus the microscope lens on planes at different distances from the cathode surface. Since, as noted, the height of the projections is of the order of tens of microns, the displaçement of the lens relative to the cathode surface should be of the same order of magnitude.

Experimental observations of the "microlens" effect

It proved feasible to realize such displacements only in the all-metal EEM-75 electron emission microscope.[1] This instrument which is essentially the first commercial emission microscope produced in the Soviet Union, has high quality optics and a precision mechanical regulating mechanism. For the experiments in question the cathode and focusing electrode of the objective lens were shorted

to each other and hence the lenses operated as a bipolar system. Focusing on different planes was realized by changing the distance between the cathode and the focusing electrode. The potential applied to the anode was 20 kv and the distance between the cathode and the anode was 4 mm. The approximate magnification of the emission images obtained on the microscope screen was 150 X.

On the present investigation we used cathodes prepared for electron-beam tubes with coatings applied by means of an atomizer. The pressure in the microscope column was $2 \cdot 10^{-5}$ mm Hg. The cathodes were activated at a filament voltage of 9 v. The cathodes were held at the maximum temperature for 1-2 min.

At a filament voltage of 6.5 v the density of the current from the cathode was 1-1.5 ma/cm^2; emission images of the cathode were obtained at a filament voltage of 5-5.5 v.

It was found that the emission pattern is greatly dependent on the location of the plane on which the immersion lens is focused relative to the surface of the cathode. Thus the four photographs reproduced in Figs. 2-5 were made of the same section of an oxide-coated cathode under identical vacuum and temperature conditions. The distance between the limiting positions of the focused-on plane (Figs. 2 & 5) was 150 mμ.

A comparison of these photographs shows that the influence of inhomogeneity of the electric field over the cathode is so great that it is impossible to establish any correspondence between the individual sections of the extreme-position photographs (Figs. 2 & 5). As the distance between the cathode and the focusing electrode is changed the image on the microscope screen varies continuously: some spots gradually merge into one, while other spots break up into several sections; at the same time the spots change in size and shape. This is to be explained by the fact that the "microlenses" gather the escaping electrons into beams, the directions of which in the immediate vicinity of the cathode do not coincide with the direction of the optical oxis of the microscope lens. Obviously these beams can converge, intersect or diverge so that the distribution of electrons in any plane perpendicular to the optical axis of the objective lens will depend on its distance from the surface of the cathode.

Our hypothesis is further substantiated by the two photographs made of an oxide-coated cathode in the surface of which a few 20-30 μ deep grooves were scratched (Figs. 6 & 7). These photographs were made of the same section of the cathode but whereas five bright stripes are visible in one, six stripes are discernible in the other. The very great brightness of the scratches compared with the general background is apparently due to more intense emission of electrons from the scratches.

Thus it may safely be asserted that the picture observed when we examine an oxide-coated cathode with an emission microscope is largely due to the focusing influence of the microlenses. Hence the hitherto current idea that the picture on the microscope screen shows the actual distribution of emission centers over the surface of the cathode is entirely erroneous. A non-uniform emission pattern will be obtained even with an entirely homogeneous emission from the surface if the adjacent field is inhomogeneous.

Naturally, the above observations concerning the mechanism of formation of the emission image apply equally to other types of cathodes and other forms of emission.

On the observations of true emission centers

Observation of the true emission structure is possible when the size of the uniformly emitting section of the cathode is appreciably greater than the size of the irregularities of its surface. In some cases observation of the emission structure of the cathode with commensurate dimensions of the surface irregularities and the emission centers may be possible, but for this one must have additional information regarding the structure of the cathode, information which

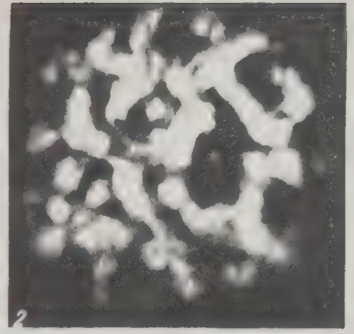

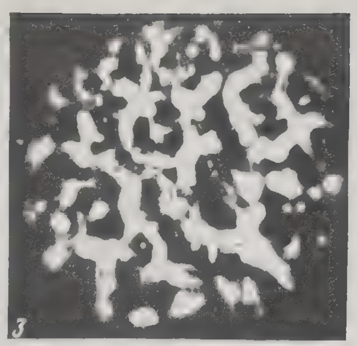

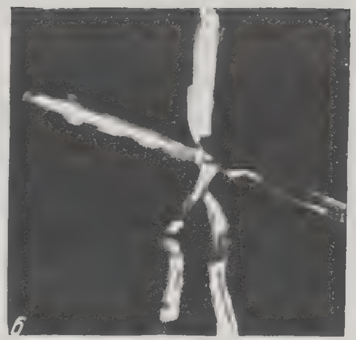

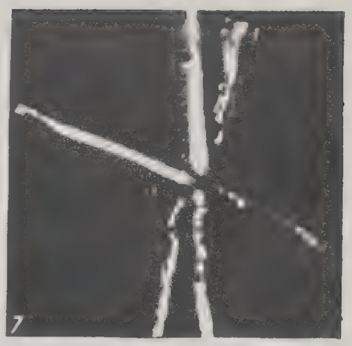

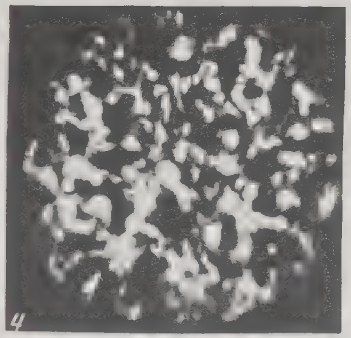

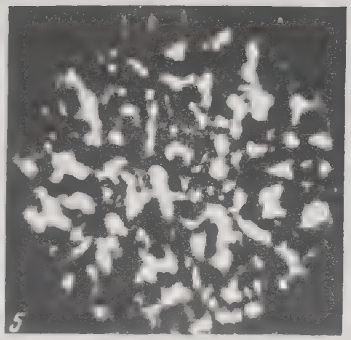

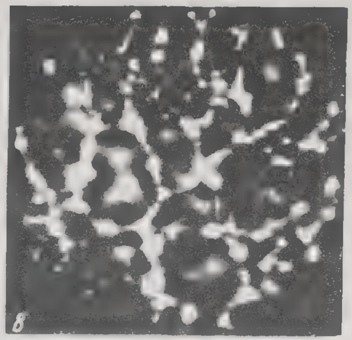

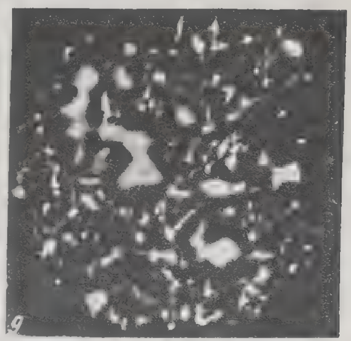

Figs. 2-5. Photographs of the emission images obtained from the same section of an oxide-coated cathode under identical vacuum and temperature conditions in the EEM-75 emission microscope. The images were obtained with different depths of focus (the distance between the extreme focused-on planes - Figs. 2 & 5 - was 150 μ). Magnification ~150 X.

Figs. 6 & 7. Photographs of the emission image of the same section of an oxide-coated cathode on the surface of which a few 20-30 μ deep scratches were made. The number and shape of the stripes depends on the distance between the plane focused upon and the cathode surface.

Fig. 8. Photograph of the surface of a porous metal-film cathode obtained with the emission microscope. Magnification 500 X.

Fig. 9. Photograph of the same cathode as in Fig. 8 obtained with the immersion lens backed off 10 μ. Same magnification.

would enable us to determine upon what surface the immersion lens is focused. This is possible, for example, in investigating L-cathodes (porous base metal-film cathodes). Comparison of the photographs of Figs. 8 & 9 made by means of an emission microscope with the picture observed in examining the surface of the same cathode under an optical microscope shows that the photograph of Fig. 8 was made with the immersion lens focused approximately on the surface containing the openings of the pores into the depth of the cathode. Hence this photograph, made at a magnification of 500 X, roughly pictures the emission structure of an L-cathode.

In conclusion I desire to thank G.V.Spivak in whose laboratory and under whose guidance the present investigation was carried out and A.M.Rozenfeld for his advice regarding the use of the emission microscope.

Physics Department of
Moscow State University

References

1. Elektronnaia mikroskopiia (Electron microscopy), A.A.Lebedev, editor, Chapter 6, Moscow, 1954.

DISCUSSION

Question: Did you investigate oxide-coated cathodes having different degrees of roughness?

D.P.Vinogradov: Yes, we did. Moreover, as I mentioned, we made a number of scratches on the surface of an oxide-coated cathode, but as you can see one cannot even tell the number of scratches from the photographs.

D.G.Bulyginskii: How did the picture change for different field intensities?

D.P.Vinogradov: The observed pattern is independent of the field strength.

N.D.Morgulis: If, as you say, the emission microscope cannot be utilized for investigating the oxide-coated cathode, can one not employ an electron projector (projection tube) for this purpose?

D.P.Vinogradov: The roughness or irregularities of the surface will undoubtedly distort the picture in this case also.

THERMODYNAMIC CALCULATION OF SOME REACTIONS OF REDUCTION OF BaO

- L.S.Zaitseva

Cathodes of the barium oxide type are complex systems whose physical and chemical properties are still the subject of extensive investigations. The oxide-coated cathode is essentially an impurity semiconductor with excess barium in its volume and on its surface.[1] According to present-day concepts, the emission characteristics of the cathode are largely determined by the concentration of free barium. One of the ways of producing free barium in the bulk of the oxide is by chemical reduction of the barium oxide by different additives, introduced into the base material of the oxide cathode or in the case of a porous metal-film L-cathode directly into its volume. The physical-chemical problem can be analyzed by the method of classical thermodynamics.

As Epstein[2] notes, in the simplest case

$$BaO + Me \rightleftharpoons MeO + Ba\ (gas); \tag{1}$$

when only one gaseous product is formed in the reaction, the equilibrium vapor pressure of the given substance will be equal to the equilibrium constant for the reaction:

$$P_{Ba} = K. \tag{2}$$

The eqilibrium constant can readily be calculated by means of the equation:

$$\log K = - \frac{\Delta F^o}{RT}, \tag{3}$$

where the free energy change, according to the Gibbs-Helmholz equation, is

$$\Delta F^o = \Delta H(T^o) - T\Delta S(T^o) + f(C_p, T), \tag{4}$$

The ^{o} sign indicates that all the substances are taken in the standard state. The values of the heat content $H(T^o)$, entropy $S(T^o)$ and heat capacity C_p can be found in chemical handbooks.

In a contribution published in 1949, White[3] gave calculations of the pressure of Ba vapor over certain reactions of reduction of barium oxide by different activators. In his calculations White took into account the last term in equation (4). However, first, for many substances the specific heats are not known or are known only in a narrow temperature range and, second, the values of the heat content and entropy are tabulated in reference books with a far greater relative error than is introduced by the last term of equation (4). Moreover, there is appreciable divergence between the data given by different authors: for example, the values for ΔH_{298^o} of BaO listed in Refs. 4 & 5 differ by 7.2 Kcal/mole, while the values ΔH_{298^o} of Ba(g) given in Refs. 4 & 6 differ by 8 Kcal/mole.

In order to determine how important it is to take the heat capacity into account in the thermodynamic calculations, we carried out calculations taking and not taking C_p into account for the tabular values of ΔH and S taken from Ref. 6 ($\Delta H_{298^o BaO}$ = - 133 Kcal/mole) and calculations taking C_p into account but using the value of -126.1 taken from Ref. 5.

Comparison shows that the divergence of the results obtained taking and not taking C_p into account is of the same order of magnitude as the divergence obtained when using the values of -133 and -126.1 Kcal/mole for ΔH_{BaO}.

Thus for the reduction of BaO by beryllium at 1000^o we obtained:
P_{Ba} = 2 mm Hg (ΔH_{BaO} = -133 Kcal/mole taking C_p into account),

P_{Ba} = 2 mm Hg (ΔH_{BaO} = -133 Kcal/mole without taking C_p into account),
P_{Ba} = 30 mm Hg (ΔH_{BaO} = -126.1 Kcal/mole taking C_p into account).

For the reduction of BaO by gaseous magnesium we obtained:
P_{Ba} = 6.2 mm Hg (ΔH_{BaO} = -133 Kcal/mole taking C_p into account),
P_{Ba} = 2.5·10 mm Hg (ΔH_{BaO} = -133 Kcal/mole without taking C_p into account),
P_{Ba} = $4\cdot 10^{-1}$ mm Hg (ΔH_{BaO} = -126.1 Kcal/mole taking C_p into account).

Thus it will be seen that there is no point in taking C_p into account.

In 1953 Rittner[7] published thermodynamic calculations for a number of reactions of the reduction of barium oxide without taking C_p into account. Since his initial data were taken from Ref. 4 (ΔH_{BaO} = -126.1 Kcal/mole) Rittner's results differ from those obtained by White.

In view of the importance of the problem where the physics of oxide-coated and porous metal-film cathodes are concerned, we carried out similar calculations for a series of analogous reactions, taking C_p into account where values for the heat capacity were available. There are no data for $S_{298°}$ for many substances. Hence we evaluated the approximate entropy of La_2O_3, ThO_2 and ZrO_2 according to Latimer's rule.[8] We evaluated the entropies of $BaSiO_3$ and Ba_2SiO_4 on the basis of the statement in Ref. 9 that the entropy of silicates is equal to the sum of the entropies of the oxides. The value of the entropy of barium monoaluminate $BaO\cdot Al_2O_3$ was evaluated on the basis of the analogy of the structure and properties of aluminates and silicates.[9]

Our evaluation of the entropy of Ba_3WO_6 was considerably rougher: from a comparison of the tabular data for various alloys of solid oxides one can conclude that in this case the entropy of the complex compound is equal to the sum of the entropies of the oxides; in view of this we estimated the entropy of Ba_3WO_6 on the assumption that $S_{Ba_3WO_6} = S_{WO_3} + 3S_{BaO}$. Then the value of $\Delta H_{298°}$ of Ba_3WO_6 was evaluated very roughly on the basis of the following considerations. Since the reaction of formation of this compound occurs only at high temperatures[10], the heat evolved in the process is small and one can therefore assume that

$$\Delta H_{Ba_3WO_6} = \Delta H_{BaWO_4} + 2\Delta H_{BaO}.$$

Calculations were carried out for the case when the activator is solid or liquid and for the case when it is gaseous. The first case occurs in L-cathodes when the activator is introduced directly into the oxide; the second case obtains in an oxide-coated cathode when the activator, introduced as an admixture into the base material, gradually diffuses, entering the oxide layer in the form of individual atoms, which may be considered analogous to the gaseous state. The results of the calculations for a temperature of 1273°K are given in the accompanying table (see next page).

It must be emphasized that regardless of how the calculations are carried out (with or without taking C_p into account) the results give only the possible yield of the substance and the upper bound of the vapor pressure. From the practical viewpoint what is more important is the rate with which the reaction proceeds[11] rather than the possible extent of conversion of the reacting substances; hence in practice one must give preference to kinetic rather than to thermochemical investigations which are only the preliminary step.

The results of the cited calculations should be applied to actual cathodes with caution inasmuch as, first, the actual conditions obtaining in a cathode are not equilibrium ones and, second, the character of the actual contact between the grains of BaO and the activator will have a decided influence on the value of the yield of barium. Consequently, the data obtained through such calculations are of value mainly for comparison purposes.

In conclusion I wish to thank N.D.Morgulis for suggesting the subject and for his guidance in carrying out the investigation.

Values of the equilibrium constant of the reaction and the vapor pressure of barium at 1273° K

Reaction			K	P_{Ba}, mm Hg
3 BaO(T) + 2 Al(l)	$\rightleftharpoons Al_2O_3(s)$	+ 3Ba(g)	$3.14 \cdot 10^{-13}$	$5 \cdot 10^{-2}$
3 BaO(T) + 2 Al(g)	$\rightleftharpoons Al_2O_3(s)$	+ 3Ba(g)	$1.45 \cdot 10^{-2}$	$7 \cdot 10^{-3}$(K); $1 \cdot 10^{-2}$(D)
4 BaO(T) + 2 Al(l)	$\rightleftharpoons BaOAl_2O_3(s)$	+ 3Ba(g)	$2.6 \cdot 10^{-12}$	$1 \cdot 10^{-1}$
4 BaO(T) + 2 Al(g)	$\rightleftharpoons BaOAl_2O_3(s)$	+ 3Ba(g)	$2.75 \cdot 10^{-3}$	$4 \cdot 10^{-3}$(K) $8 \cdot 10^{-3}$(D)
BaO(T) + Be(s)	$\rightleftharpoons BeO(s)$	+ Ba(g)	$2.5 \cdot 10^{-3}$	2;
BaO(T) + Be(g)	$\rightleftharpoons BeO(s)$	+ Ba(g)	$1.45 \cdot 10^{4}$	$8.2 \cdot 10$(K)
BaO(T) + C(sgr)	$\rightleftharpoons CO(g)$	+ Ba(g)	$3.14 \cdot 10^{-13}$	$4 \cdot 10^{-4}$
BaO(T) + C(g)	$\rightleftharpoons CO(g)$	+ Ba(g)	$5.6 \cdot 10^{9}$	$1 \cdot 10^{-6}$(K); $5 \cdot 10^{-4}$(D)
2 BaO(T) + C(sgr)	$\rightleftharpoons CO_2(g)$	+ 2Ba(g)	$2.5 \cdot 10^{-27}$	$1 \cdot 10^{-6}$
2 BaO(T) + C(g)	$\rightleftharpoons CO_2(g)$	+ 2Ba(g)	$1.7 \cdot 10^{-4}$	$3 \cdot 10^{-8}$(K); $3 \cdot 10^{-6}$(D)
BaO(T) + Ca(l)	$\rightleftharpoons CaO(s)$	+ Ba(g)	$7.7 \cdot 10^{-1}$	$5.8 \cdot 10^{2}$
BaO(T) + Ca(g)	$\rightleftharpoons CaO(s)$	+ Ba(g)	$2.2 \cdot 10$	$6 \cdot 10$(K); $3 \cdot 10^{2}$(D)
3 BaO(T) + 2 La(s)	$\rightleftharpoons La_2O_3(s)$	+ 3Ba(g)	5.5	$1 \cdot 10^{3}$
3 BaO(T) + 2 La(g)	$\rightleftharpoons La_2O_3(s)$	+ 3Ba(g)	$4 \cdot 10^{18}$	$4 \cdot 10^{3}$(D)
BaO(T) + 2 Li(l)	$\rightleftharpoons Li_2O(s)$	+ Ba(g)	$3.5 \cdot 10^{-4}$	$2 \cdot 10^{-1}$
BaO(T) + 2 Li(g)	$\rightleftharpoons Li_2O(s)$	+ Ba(g)	$1.5 \cdot 10^{-2}$	$2 \cdot 10$(K); $3 \cdot 10$(D)
BaO(T) + Mg(l)	$\rightleftharpoons MgO(s)$	+ Ba(g)	$4.4 \cdot 10^{-2}$	$3.3 \cdot 10$
BaO(T) + Mg(g)	$\rightleftharpoons MgO(s)$	+ Ba(g)	$2.3 \cdot 10^{-2}$	6(K); $1.1 \cdot 10$(D)
BaO(T) + Ni(s)	$\rightleftharpoons NiO(s)$	+ Ba(g)	$1.26 \cdot 10^{-16}$	10^{-13}
BaO(T) + Ni(g)	$\rightleftharpoons NiO(s)$	+ Ba(g)	$1.26 \cdot 10^{-9}$	$2 \cdot 10^{-16}$(K)
2 BaO(T) + Th(s)	$\rightleftharpoons ThO_2(s)$	+ 2Ba(g)	$3.7 \cdot 10^{-1}$	$4 \cdot 10^{2}$
2 BaO(T) + Th(g)	$\rightleftharpoons ThO_2(s)$	+ 2Ba(g)	$4 \cdot 10^{22}$	$2 \cdot 10^{6}$(D)
4 BaO(T) + W(s)	$\rightleftharpoons BaWO_4(s)$	+ 3Ba(g)	$4 \cdot 10^{-29}$	$2 \cdot 10^{-7}$
4 BaO(T) + W(g)	$\rightleftharpoons BaWO_4(s)$	+ 3Ba(g)	2.2	$1 \cdot 10^{-6}$(K); $4 \cdot 10^{-6}$(D)
6 BaO(T) + W(s)	$\rightleftharpoons Ba_3WO_6(s)$	+ 3Ba(g)	$1 \cdot 10^{-29}$	$1 \cdot 10^{-7}$
6 BaO(T) + W(g)	$\rightleftharpoons Ba_3WO_6(s)$	+ 3Ba(g)	$5.3 \cdot 10^{-1}$	$7 \cdot 10^{-7}$(K)
2 BaO(T) + Zr(s)	$\rightleftharpoons ZrO_2(s)$	+ 2Ba(g)	$5.9 \cdot 10^{-8}$	$2 \cdot 10^{-1}$
2 BaO(T) + Zr(g)	$\rightleftharpoons ZrO_2(s)$	+ 2Ba(g)	$2 \cdot 10^{4}$	$1 \cdot 10^{-2}$
3 BaO(T) + Si(s)	$\rightleftharpoons BaSiO_3(s)$	+ 2Ba(g)	$2 \cdot 10^{-12}$	$1 \cdot 10^{-2}$
3 BaO(T) + Si(s)	$\rightleftharpoons BaSiO_3(s)$	+ 2Ba(g)	$5 \cdot 10^{-5}$	$1 \cdot 10^{-2}$
2 BaO(T) + Si(s)	$\rightleftharpoons SiO_2(s)$	+ 2Ba(g)	$3.16 \cdot 10^{-16}$	$1 \cdot 10^{-5}$
2 BaO(T) + Si(g)	$\rightleftharpoons SiO_2(s)$	+ 2Ba(g)	$1.25 \cdot 10^{-9}$	$4 \cdot 10^{-6}$
4 BaO(T) + Si(s)	$\rightleftharpoons Ba_2SiO_4(s)$	+ 2Ba(g)	$8 \cdot 10^{-12}$	$2 \cdot 10^{-3}$
4 BaO(T) + Si(g)	$\rightleftharpoons Ba_2SiO_4(s)$	+ 2Ba(g)	$4.8 \cdot 10^{-5}$	$1 \cdot 10^{-3}$

Note: (s) = solid, (l) = liquid, (g) = gas and (sgr) = graphite; (K) and (D) indicate that the vapor pressure of the gaseous activator (Al, Be, C, Ca, La, Li, etc.) was calculated according to the data of Kubachewski[5] or Dushman[12], respectively.

Institute of Physics of the
Academy of Sciences of the Ukrainian SSR

References

1. G. Herrmann & S.Wagener, OxideOcoated cathodes (In Russian trans., M.-L. 1949).

2. P.S.Epstein, Textbook of Thermodynamics (In Russian trans., M.-L., 1948).

3. A.H.White, J. Appl. Phys., 20, 856 (1949).

4. W.M.Latimer, Oxidation potentials (In Russian trans, M. 1954).

5. O.Kubaschewski & E.L.Evans, Metallurgical thermochemistry (In Russian trans., M. 1954).

6. Termicheskie konstanty neorganicheskikh veshchestv (Thermal constants of inorganic substances) edited by A.F.Kapustinski & E.V.Britske, M.-L., 1949.

7. E.S.Rittner, Philips Res. Rep., 8, 184 (1953).

8. W.M.Latimer, J. Am. Chem. Soc., 43, 818 (1921).

9. A.I.Avgustinik & O.P.Mchedlov-Petrosian, ZhPKh (Journal of Applied Chemistry) 20, 584 (1947).

10. R.C.Hughes, P.P.Coppola & H.T.Evans, J.Appl.Phys., 23, 635 (1952).

11. R.R.Wenner, Thermochemical calculations (In Russian trans. M. 1954).

12. S.Dushman, Scientific foundations of vacuum techniques (In Russian trans., M. 1950).

INVESTIGATION OF THE DYNAMICS OF FORMATION OF THE BARRIER LAYER IN AN OXIDE-COATED CATHODE BY THE RADIOACTIVE TRACER METHOD

(Abstract - Complete report in Zhur. tekh. fiz., 26, 232 (1956).)

- Iu.G.Ptushinskii

The radioactive tracer method was used to study the dynamics of growth in thickness of the intermediate layer of Ba_3WO_6 developing in the zone of contact between the coating of an oxide-coated cathode and its base of Ni-W alloy. It was shown that the growth in thickness of this layer and the inflow of W-activator from the base ceases after the first 100-150 hours of operation of the cathode. The concentration of excess barium evolved in the process of reaction between BaO and W at the normal operating temperature of 800° remains sufficient for normal operation of the cathode over a period of about 10,000 hours, which serves to explain the long service life of such cathodes. At 1000° the tungsten impurity in the oxide coating does not migrate more than 5 μ over a period of 200 hours. The intermediate Ba_3WO_6 layer exerts a retarding effect on the diffusion of the Co impurity from the base into the oxide coating.

Institute of Physics of the
Academy of Sciences of the Ukrainian SSR

DISCUSSION

L.N.Dobretsov: Available data indicate that the tungsten cannot reduce BaO. What tungstates were taken into account in the investigation? Does the speaker know of the work of Rittner who has a different view regarding the role of tungsten?

Iu.G.Ptushinskii: I understand from certain reports published abroad that the intermediate layer consists of Ba_3WO_6. I am also aware of the x-ray investigation of Steward substantiating this. On the other hand, the observed growth in thickness of the intermediate layer under operating conditions after activation of the cathode, in the course of which there occurs a complete decomposition of the carbonates (according to the mass spectroscopic data of Pinkus), is evidence in favor of a possible reaction between BaO and W.

L.N.Dobretsov: Could it be that there initially forms a compound with a lower content of tungsten?

Iu.G.Ptushinskii: This does not follow from the data in the literature.

Question: The resistance of the intermediate layer was measured in our laboratory. We found that it changes somewhat with time.

Iu.G.Ptushinskii: The overall resistance of the intermediate layer can change not only due to changes in thickness of the layer but also due to changes in its specific conductivity.

EXPERIMENTAL INVESTIGATION OF THERMIONIC AND SECONDARY-ELECTRON EMISSION FROM COPPER AND GERMANIUM IN TRANSITION FROM THE SOLID TO THE LIQUID STATE

- V.G.Bol'shov

Measurements show that the values of the work function of different faces of crystals differ: according to recent measurements, for instance, the difference between the work function of different faces for tungsten is of the order of one electronvolt. This difference in work function is due to the different arrangement of the atoms on the surface of the different faces. Hence it was natural to expect that during disintegration of the crystal lattice incident to melting there should occur a radical change in the arrangement of the atoms on the surface of an emitter and that this should lead to a change in the work function which should be manifested in an abrupt change in the thermionic emission at the melting point. Actually early investigators[1,2] reported such changes in emission incident to transition of metals from one state to another. However, the data of different investigators working with the same substances are contradictory.

The influence of the state of aggregation on the secondary-electron emission has been studied by a number of authors.[3,4] As a result of investigations carried out on Sn, Pb and Bi, Morozov[3] established that the coefficient of secondary emission changes with a jump incident to melting of these substances. In more recent experiments carried out on Bi, Pb, Hg and Ga, Brophy[4] found no substantial difference between the coefficients of secondary emission for the solid and liquid states. Thus, here again we have disagreement between the data of different investigators working with the same substances. In view of this we felt it would be of interest to repeat the experiment on the thermionic and secondary-electron emission of substances in different states under better vacuum conditions and utilizing purer materials.

The choice of materials to be investigated was limited by the following considerations: 1) the vapor pressure had to be sufficiently low over the molten substance, 2) it had to be possible to measure the thermionic emission from the substance at temperatures near its melting point, 3) the substance had to have a low solubility for the crucible material and 4) the melting point had to be in the range of accessible temperatures. One of the substances chosen was copper as a typical representative of metals; the coordination number of copper does not change in melting. The other substance chosen was germanium which is of interest because its coordination number is doubled as a result of melting (4 in the solid state and 8 in the liquid).

The first experiments were made with Kyshtym electrolytic copper, but the final measurements were carried out on 99.995-99.999% pure copper. The germanium samples were cut from an n-type single crystal, the number of current crriers in which was of the order of 10^{14} per cm^3. Conductivity measurements on the samples showed that after the experiments the germanium changed its conductivity from n to p and the final number of current carriers did not exceed 10^{15} per cm^3. The crucibles for the copper were stamped in the form of cups from molybdenum sheet; the crucibles for the germanium were prepared from spectroscopically pure graphite or pure quartz. The temperature of the samples was measured by means of a W-Ta thermocouple, graduated beforehand in vacuum with reference to the melting points of a number of metals; the indications of the thermocouple were further checked on the basis of the melting point of the investigated materials.

The experimental set-up is shown in Fig. 1. The important dimensions of the measurement section of the apparatus are indicated in the insert. The apparatus had no demountable joints, i.e., was entirely sealed. Prior to the experiments the apparatus was evacuated continuously for a week with the traps kept filled with liquid nitrogen.

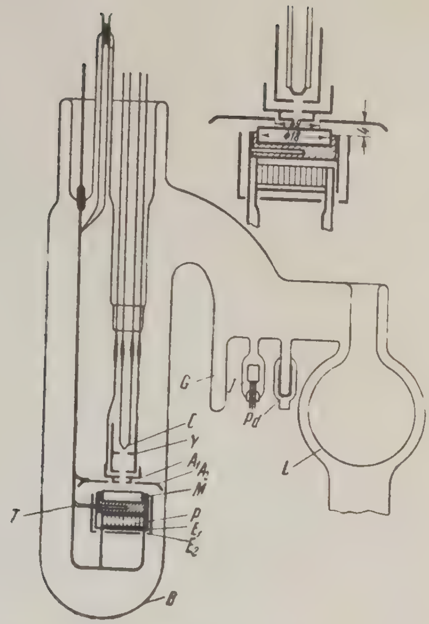

Fig. 1

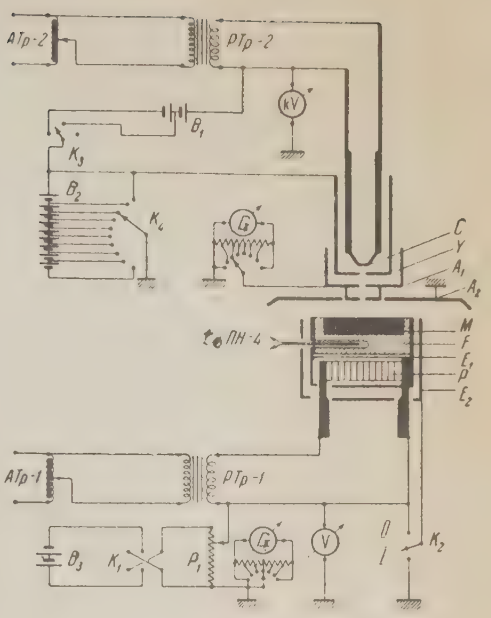

Fig. 2

Fig. 1. Diagram of vacuum apparatus for investigating the thermionic and secondary-electron emission: B) vacuum flask, G) getter, Pd) palladium cylinder for hydrogen, I) pressure gage tube, L) liquid nitrogen trap, M) crucible for investigated material, P) heater spiral, E_1 & E_2) heat shields, A_1 & A_2) guard and measuring electrodes, T) thermocouple, C,Y & A_2) components of electron gun. Insert: detail of measurement section.

Fig. 2. Measurement circuit diagram.

To insure the highest purity and cleanliness of the investigated materials we utilized all the advanced techniques available to us in preparing the equipment: washing all components in pure reagents, heating by high-frequency currents to get rid of most of the impurities and metal oxides and partially degas the specimens even before mounting them in the apparatus, annealing in hydrogen to get rid of oxides, and high-frequency heating of the assembled measurement section before sealing it in the vacuum flask.

Particular attention was paid to cleansing the crucibles before loading the investigated materials. The molybdenum crucibles were first cleansed by electrolytic etching and then by prolonged boiling in triple-distilled water and finally prolonged high-frequency heating in an atmosphere of hydrogen and in vacuum at temperatures above 2000°. The graphite crucibles were washing in distilled hydrochloric acid to eliminate all traces of iron left by the shaping cutter, then boiled in triple-distilled water and repeatedly heated for a day by high-frequency currents in vacuum at 2500-3000°. The quartz crucible was washed in hydrofluoric acid, boiled in triple-distilled water and heated in vacuum.

After being sealed to the vacuum system the apparatus was further cleansed and degassed by heating in vacuum and in an atmosphere of hydrogen. The latter was carried on over a period of 10-15 hours (necessary for copper; not necessary for germanium), with the specimen maintained at about 800° and periodically raised to a temperature a few degrees below the melting point. The getter was vaporized with all the parts heated and a vacuum better than 10^{-7} mm Hg. Actual measurements, using the conventional circuit shown in Fig. 2, were started after the third day when the vacuum in the system with the specimen at a temperature slightly below the melting point remained somewhat below the sensitivity of the vacuum meter, i.e., better than $5 \cdot 10^{-8}$ mm Hg.

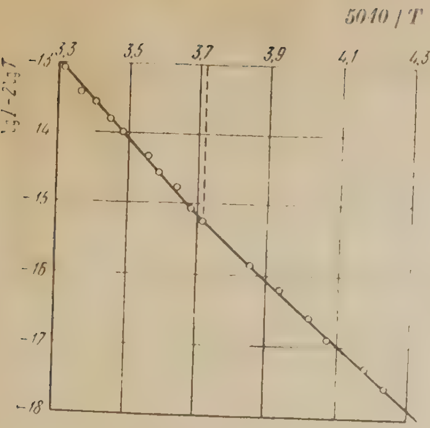

Fig. 3. Temperature dependence of the thermionic current for pure copper.

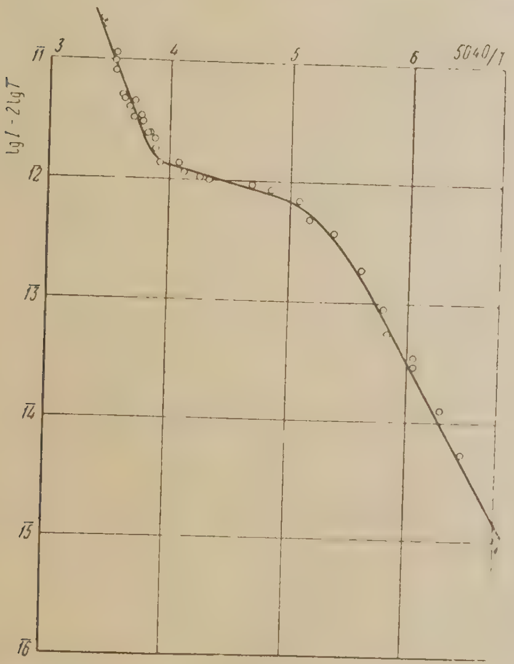

Fig. 4. Temperature dependence of the thermionic current for a germanium sample.

First, the electron emission of the material in the solid state was repeatedly measured as the temperature was gradually increased and decreased. After making sure that fully reproducible results were obtained for the solid state, the temperature was raised above the melting point and the thermionic emission of the substance in the liquid state was measured. The current-voltage characteristics of the current from the specimen were recorded at the maximum attainable experimental temperatures; these showed that the measured currents were saturation currents. Next the temperature was reduced below the melting point and solid state measurements repeated; the results for pure germanium and pure copper were in good agreement with the results obtained prior to melting. In the case of Kyshtym copper not annealed in hydrogen, we obtained results similar to those reported by Ameiser[1] and Goetz[2], i.e., the thermionic emission at the melting point exhibited a jump. The magnitude of the current jump and sometimes its sign depended on the number of times the sample had been melted. Preliminary annealing of the copper in hydrogen appreciably reduced the magnitude of this jump, but we were unable to obtain reproducible (before and after melting) data for the Kyshtym copper.

The temperature dependence of the thermionic current from pure copper is shown in Fig. 3. The corresponding curve for germanium is shown in Fig. 4. As may be seen from the curves, the thermionic emission from copper and germanium does not exhibit a jump at the melting point, only the slope of the emission curve changes at this temperature. It will be seen from Fig. 4 that for germanium the section of the curve corresponding to emission in the solid state is not rectilinear. The curves characterizing the variation of the secondary emission coefficient σ with the primary voltage for the solid and liquid states of copper and germanium are given in Figs. 5 & 6. It will be

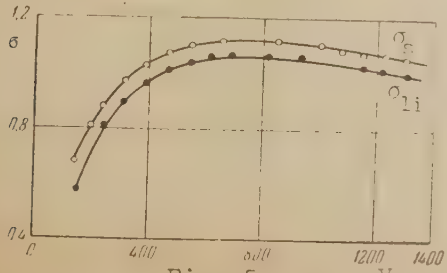

Fig. 5

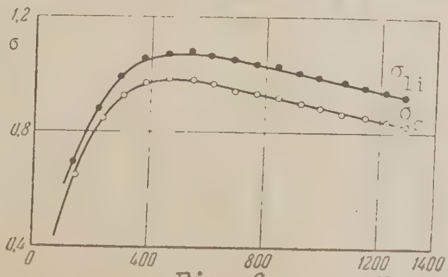

Fig. 6

Fig. 5. Variation of the secondary emission coefficient with the primary electron energy for samples of pure copper in the solid and liquid states.
Fig. 6. Same as Fig. 5 but for germanium.

seen that the secondary emission coefficient of both substances changes abruptly in melting, as was found by Morozov[3]. In the case of copper it drops 5-6%, while in the case of germanium it increases 9-10%. The magnitude of the jump $\Delta\sigma$ with $V_p > 100$ v is independent of the primary electron energy.

We note that under the conditions of our secondary emission measurements the state of the surface does not change incident to melting (as evinced by the steady value of the thermionic emission). It may therefrom be concluded that modifications of the long-range order incident to melting exert a small but definite influence on the magnitude of the secondary-electron emission of germanium and copper.

At first the absence of a jump in thermionic emission incident to melting seemed surprising and unexpected. However, we feel that there is a perfectly natural explanation for the absence of a jump.[5] The arrangement of the atoms in the two surface layers of the metal does not remain constant and ordered as the temperature is raised particularly in the vicinity of the melting point. Part of the atoms forming the ordered face of the crystal may leave the lattice sites and migrate to positions above this face, leaving behind vacant sites, as shown schematically in Fig. 7. It may be reasonably assumed that increasing the temperature of a crystal leads to a gradual increase in the degree of disorder in the arrangement of the surface atoms. It can readily be imagined that at temperatures near the melting point the degree of disorder becomes so great that the structure of the surface layers and the arrangement of the atoms therein undergo no further change incident to breakdown of the long-range order, i.e., incident to melting.

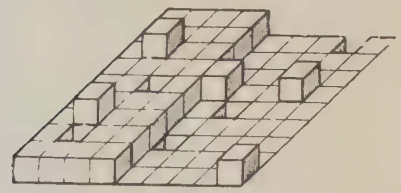

Fig.7. Schematic representation of the two surface layers of a metal on the ordered face of a crystal; some of the atoms have left their lattice sites, leaving vacancies, and migrated to the surface of the face as a result of heating of the crystal to a temperature close to the melting point.

This interpretation suggests one reason for the change in work function of a given face of a crystal with temperature, a reason which, to the best of our knowledge, has not been taken into account in theoretical treatments of the variation of the work function with temperature. This reason is the change in the structure of the surface of the crystal face due to the increase in disorder with increasing temperature. This factor may likely play a very important role at temperatures near the melting point.

It also follows from our interpretation that changes in the volume structure of the crystal incident to melting (provided the surface structure remains unchanged) do not alter the work function. This indicates that the work function does not depend on the volume structure of the crystal and is determined only by the structure of its surface layers, despite assertions of certain authors on the contrary (see Ref. 6, for example).

Using the measured values of the thermionic current and the equation

$$j = A_0 (1 - \bar{R}) T^2 e^{-e\varphi(T)/kT}, \qquad (1)$$

we can readily calculate the work function of copper and germanium under our experimental conditions. In making the calculations we will assume that $(1 - \bar{R}) = 1$ (if we assume a different value for $(1 - \bar{R})$, not greatly different from unity, the value of $\varphi(T)$ will not change substantially; for example with $(1 - \bar{R}) = 0.7$, it will be reduced by approximately 0.03 ev at 1273°K). The value of the work function calculated in this manner for copper is close to the value given in the accompanying table.

State	A_2, amp cm^{-2} degree^{-2}	φ^*_0, ev	φt_{melt}, ev	α, ev/degree
Liquid	64	4.5	4.6	$5 \cdot 10^{-5}$
Solid	$3.5 \cdot 10^4$	5.3	4.6	$-6 \cdot 10^{-4}$

*φ_0 is the effective work function determined from the slope of the Richardson plot.

The values of the true work function for germanium calculated according to equation (1) are shown in Fig. 8. It will be seen that the work function of germanium in the solid state changes gradually from 2.4 to 3.5 v as the temperature is increased from 400 to 959°.

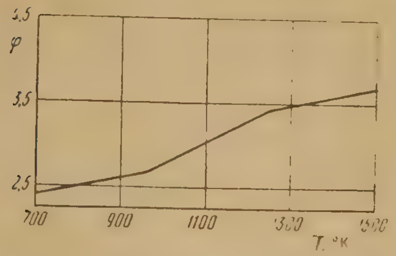

Fig. 8. Temperature dependence of the work function of germanium.

There is a considerable divergence between our data on the work function of germanium and the data in the literature. According to Smith[7] the work function of germanium does not change in the indicated temperature range. According to the data of different authors the value of the work function varies between 4 and 4.8; however, all investigators emphasize that their data are not characteristic for the pure material (for example, in the experiments of Shul'man and Pisarevskii[8] intrinsic conductivity begins at a temperature above 400°) and pertain to certain specific vacuum conditions.

As is known, the work function of impurity semiconductors depends on the temperature because of the temperature dependence of the position of the electrochemical potential level. In our samples the number of current carriers after the experiment did not exceed 10^{15} per cm^3 and was even less before the experiments. At this concentration of current carriers, germanium is an intrinsic semiconductor even at room temperature and its electrochemical potential level at all higher temperatures will lie in the middle of the forbidden band. Consequently, the observed temperature dependence of the work function is connected with changes in the electron affinity of germanium and can be explained either by rearrangement of the structure of the surface or by the influence of some impurities. The latter might conceivably be due to adsorption of residual gases on the surface of the investigated sample or to comtamination of the germanium by the material of the crucible.

Measurements of the thermionic emission of germanium in vacuums from 10^{-5} to better $5 \cdot 10^{-8}$ mm Hg and measurements of thermionic emission in a stream of hydrogen at the same pressures showed no noticeable difference between the I(T) curves. It may therefore be assumed that adsorption of residual gases did not play any appreciable part in our experiments. Contamination of the germanium by the material of the crucibles as a result of repeated melting also appears to be improbable in view of the fact that the values of the thermionic emission from the samples tested in graphite and quartz crucibles proved to be identical within the limits of the experimental error. Moreover, as noted above, measurements of the electric conductivity of the germanium samples after the experiments showed that the number of current carriers in them did not exceed 10^{15} per cm^3.

A difference in the values of the work function determined by the contact potential method and from the emission current could arise due to incorrectly taking into account the reflection coefficient in using the "field-free emission current" method. The value of R does not enter into the evaluation in the contact difference of potential method. It can readily be shown that if we take $(1 - \bar{R}) < 1$, this will decrease the value of the work function as determined by the "field-free current" method.

Although our measurements of the conductivity of the specimens showed that the concentration of impurities in the volume of the sample is low, it might be

suspected that their concentration at the surface is appreciably higher due to enrichment (according to Gibbs) of the surface layer by dissolved impurities when these lower the surface tension. However, it must be noted, first, that even if all the impurities present in our high purity materials collected on the surface the resultant impurity coating would be less than monatomic and, second, those impurities which can concentrate on the surface evaporate more intensively than the base material, since their enhanced concentration in the surface layer is due to weaker bonds between the impurity atoms and the lattice as compared with the bonds between the lattice and the base material atoms. Further, in view of the fact that most of the substances soluble in germanium have very low diffusion coefficients their rapid evaporation from the surface must actually result in purification of the surface layer, i.e., lead to a lower impurity concentration in the surface layer as compared with the bulk of the material. Moreover, if we assume the possibility of contamination of the investigated surface in our experiments, one must admit to a like or greater contamination in all the other investigations devoted to determinations of the work function.

Thus our examination of the principal causes which might under the conditions of our experiment result in an appreciable distortion of the determined value of the work function fails to explain the large divergence between our values and the values in the literature.

Leningrad Physico-technico Institute of the
Academy of Sciences of the USSR

References

1. I.Ameiser, ZS.f.Phys., 69, 111 (1931).
2. A.Goetz, ZS.f.Phys., 43, 531 (1927).
3. P.M.Morozov, Zhur.eksp.i teor.fiz., 11, 410 (1941).
4. I.I.Brophy, Phys.Rev., 83, 534 (1951).
5. V.G.Bol'shov & L.N.Dobretsov, Doklady AN SSSR, 97, 193 (1954).
6. C.Herring & M.Nichols, Thermionic emission (in Russian trans. M.1950).
7. A.H.Smith, Phys.Rev., 75, 953 (1949).
8. A.R.Shul'man & A.N.Pisarevskii, Zhur.tekh.fiz., 25, 1547 (1955).

DISCUSSION

N.D.Morgulis & P.G.Borziak: In view of your concluding statement, how do you explain the large difference between the values of the work function obtained by you and the data of other investigators?

V.G.Bol'shov: By the greater cleanliness and purity in our experiments. As noted the current carrier concentration was 10^{15} per cm^3 or less.

P.G.Borziak: Did you try to determine the work function of germanium by other methods?

V.G.Bol'shov: This would be difficult in our apparatus.

K.B.Tolpygo: How do you explain the change in the work function of germanium by a value greater than the width of the forbidden band?

V.G.Bol'shov: We worked in the region where the chemical potential level must lie in the middle of the forbidden band. The changes in the work function may possibly be explained by changes in the electron affinity of the material.

N.D.Morgulis: What are the vapor pressures at the melting points of Cu and Ge?

V.G.Bol'shov: About 10^{-5} mm Hg for Cu and about 10^{-9} mm Hg for Ge.

P.G.Borziak: Does the value of the work function of germanium depend on the vacuum conditions, i.e., on gas adsorbed on the sample?

V.G.Bol'shov: The samples were thoroughly degassed before measurements, adsorption of nitrogen, hydrogen and even oxygen at the temperatures of our experiments did not have any appreciable effects on the results.

L.N.Dobretsov: The purpose of this investigation was to determine the work function at the melting point. The data for germanium may appear surprising but we guarantee the accuracy of the measurements. We will be grateful if anyone can point to experimental errors.

N.D.Morgulis: To do so one must study the experimental procedure in detail. It would be desirable to check the value of the work function of Ge by the contact potential method.

FIELD EMISSION AND FIELD-EMISSION CATHODES

(Abstract - Complete report in Radiotekhnika i elektronika, 1,5 (1956).

- D.B.Zernov

The report examines the principal stages in the development of theoretical and experimental investigations of field emission from metals and semiconductors. It is noted that experimental studies in this field - in contrast to studies of thermo-, photo- and secondary-electron emission - have had as their primary aim verification of the predictions of theory, rather than practical advances. The problem of utilizing field emission in vacuum tubes and similar equipment has not yet been solved since field-emission cathodes are at present characterized by instability and a relatively short life.

The report describes the latest results obtained in theoretical and experimental investigations of thermo-field emission (i.e., field emission at an arbitrary cathode temperature) and of field emission at high current densities. These investigations have shown agreement of experiment with the deductions of quantum-mechanical theory of field emission in a wide range of temperatures (0-2000°K) and current densities (from a few amperes to $4 \cdot 10^7$ amp/cm^2).

The report outlines the principal conclusions of Stratton's recently published theory of field emission of semiconductors and lists some of the results of the very small number of experimental studies that have been made in this field. The report examines the possibility of realizing practical, stable long-lived field-emission cathodes and lists the potential advantages and disadvantages of such cathodes as compared with thermionic ones. Possible ways of eliminating some of the shortcomings are suggested.

It is concluded that the present stage of development is characterized by a) a well developed quantum-mechanical theory of field emission from pure metals which has been satisfactorily verified by experiment, b) a more or less advanced theory of field emission from semiconductors which has so far received little substantiation through experimental studies and c) considerable progress in the development of procedures for preparing long-lasting and relatively stable field-emission cathodes. All this gives reason to hope that it may be possible to utilize such cathodes in certain vacuum tubes in the not too distant future.

Institute of Radio Engineering and Electronics of the
Academy of Sciences of the USSR

DISCUSSION

G.V.Spivak: What can you say regarding the field emission of metal-film cathodes?

D.V.Zernov: In my opinion cathodes with an adsorbed film are not promising in view of migration of the atoms in the coating and the possibility of their being knocked out by bombardment. This should result in instability of such cathodes.

G.V.Spivak: What has been accomplished in the search for stable materials for field-emission cathodes?

D.V.Zernov: There are a number of materials little subject to cathode sputtering. Such materials are purified by a combination of heating and washing with certain gases.

L.N.Dobretsov: Are you not unduly optimistic in evaluating the present state of theory of field emission?

D.V.Zernov: The problem has been satisfactorily solved for metals. The agreement with experiment is very good.

S.I.Pekar: Is a well developed relief of the cathode surface taken into account in comparing theory with experiment?

D.V.Zernov: The field at the cathode surface has been calculated on the basis of cathode geometry, i.e., on the assumption that it is a hyperboloid. Accidented surface relief has not been taken into account.

S.I.Pekar: Cold cathodes are characterized by anisotropy of the work function. Smoothing of the point due to local fusion does not necessarily remove the anisotropy. In measurements we may be dealing with the mean value of the work function, which may explain the apparent agreement of theory with experiment.

I.L.Sokol'skaia: Our experiments with a single crystal point gave no indication of non-uniformity of the work function.

P.V.Timofeev: In your opinion what is the reason for the sharp bend in the theoretical curve for field emission from semiconductors in the presence of surface levels?

D.V.Zernov: The surface levels screen the external field. When these levels are filled we have the case examined by Morgulis, i.e., the case when the external field penetrates into the semiconductor.

P.V.Timofeev: Do you consider it inexpedient to use complex cathodes? I understand the operation of such cathodes has been studied.

D.V.Zernov: There is reason to think that complex cathodes will be unstable in time.

EXPERIMENTS WITH AN ELECTRON AND ION PROJECTOR TUBE

- A.P.Komar & Iu.N.Talanin

A characteristic common to recent investigations[1-6] involving electron projectors (projection tubes) is the striving to obtain as high a vacuum as possible. This was attained either by using sealed tubes with an appropriate getter (usually atomized tantalium) or by means of the evacuating effect of an ionization pressure gage[8]. The pressures obtained were of the order of 10^{-11} mm Hg.

In studies involving verification of the laws of field emission[3], determinations of the work function of pure metals[2,4 & 7] and investigations of the process of adsorption of different substances[5,6] this striving for high vacuum is fully justified. However, in a number of cases working with electron projectors it is sufficient to have a vacuum of 10^{-7}-10^{-8} mm Hg, a vacuum which can be obtained more simply and more rapidly, for example, by continuous evacuation with oil diffusion pumps. Such relatively "poor" vacuum conditions are adequate for the study of

1) the process of recrystallization of a polycrystalline needle point, leading to the formation of a single crystal,

2) the influence of different impurities and heat treatments on the shape of a single crystal point both in the presence of a strong electric field and in the absence thereof,

3) the reasons for the appearance of images of "individual molecules", etc.

The continuous evacuation procedure facilitates the investigation of adsorption of different gaseous substances in view of the ease with which one gas can be replaced with another. The electron projector can readily be converted to an ion gun by the admission of hydrogen.

The pictures obtained on the screen of the projector under conditions of not very good vacuum are sometimes very complex, but often they are of particular interest from the point of view of crystallography or physical chemistry of surface phenomena.

In the present article we shall describe some of the results obtained in working with an electron projector with a tungsten point under conditions of relatively "poor" vacuum with continuous evacuation of the tube by means of two TsVL-100 oil diffusion pumps connected in series. The oil vapor was frozen out by two liquid nitrogen traps also connected in series. The vacuum obtained in this manner was 10^{-7}-10^{-8} mm Hg.

The image of a tungsten point commonly observed in an electron projector (Fig. 1) corresponds to a single crystal bounded on one side by a more or less hemispherical surface with a certain number of flats formed by the crystal faces. A point of this shape is obtained as a result of prolonged heating at 2500-2700° in the absence of an electric field. It is usually described as a smooth or rounded point.

The picture of such a rounded point as observed in the projector under our conditions (Fig. 1, b) differs from the picture obtained under high (10^{-10}-10^{-11} mm Hg) vacuum conditions[6] in that it is less stable and the edges of the faces are more diffused. The apparent dimensions of the (011) and (001) faces are reduced while those of the (112) face are increased. However, the general character of the image in both cases is similar, which indicates that the orientation of the crystal at the tip of the point is the same.

The shape of the crystal is reminiscent of the shape observed in the initial stage of facetting of spheres ground out from certain single crystals,[9,10] when flats begin to appear and grow on the spherical surface. Microscopic examination shows that the areas between the flats are rough. The roughness is due to small step-like formations associated with nascent faces. This shape is not an equilibrium one, i.e., it is not characterized by a minimal free surface energy in

the vapor saturating the space above the crystal.

The analogous rounded point is therefore also only relatively smooth. The fine "shingly" roughness of the areas between the larger faces is the reason for the uniform luminosity of the image on the projector screen.

Sometimes instead of the usual rounded point picture, we observe a pattern like that shown in Fig. 2. A point yielding a picture of this type is known as a "ribbed" or "carbon contaminated" point. Under our conditions, images of points of this type were frequently observed. The image obtained on the screen in such cases is very stable and does not change even when the point is heated to a rather high temperature. The image characterizes the appearance of a single crystal. The light areas in the photograph are due primarily to projections above the surface of the needle point, while the dark areas correspond to flats on the surface. That the light or dark areas are not connected with adsorption of electropositive or electronegative impurities is evidenced by the image of the same point obtained in the projector operated as an ion gun (Fig. 3). If the picture obtained in the electron projector were associated with adsorption of impurities changing the work function, the image of the same point obtained in the ion projector would be a negative of the electron-projector image, since in the electron projector the emission is maximal from areas with a small work function, while in the ion projector the emission from such areas is minimal.[11]

From an analysis of the photographs obtained with the electron and ion projectors, we deduced the probable shape of the tungsten single crystal and constructed the model pictured in Fig. 4. This shows both the position of some of the more important faces and the arrangement of the atoms thereon. Obviously, this model is only a very rough approximation to reality: it does not show the true proportions between the different faces or the step-like, rough character of some of their surfaces. Nevertheless, it helps form some idea of the shape of the observed crystal and can be of help in interpreting the images observed by means of the projectors.

Our study of the "ribbed" point convinced us that in the given case we are dealing with the single crystal shape most frequently encountered in crystallization of tungsten under ordinary conditions. This is substantiated by the experimental data on the growth of tungsten single crystals from the gaseous phase (Fig. 5)[12], by electron microscope examinations of the crystals in tungsten powder[13] and by Stranski and Honigmann's[14] experimental investigation of the growth of an urotropine single crystal (molecular body-centered cubic lattice).

The indicated shape is the one closest to the equilibrium shape, characterized by minimal free surface energy.

Stranski's theory[15], which establishes a direct connection between the presence of the different faces on the equilibrium shape and the lattice structure and the range of the forces acting between the component particles, shows that for substances crystallizing in a body-centered lattice (provided the binding forces acting between the particles are inversely proportional to the distance between them to the sixth power, which is true for metallic lattices as well as for molecular lattices with van der Waals binding forces) the equilibrium form is a rhombododecahedron whose corners and edges are cut by the (001) faces of a cube, the (111) faces of an octahedron and the (112) faces of a tetragonal tri-octahedron, i.e., a polyhedron with the faces observed on the "ribbed" point.

In the case of the "ribbed" point the (001) cube faces are very strongly developed compared with the (011) faces of the rhombododecahedron, which is presumably connected with the particular conditions under which it is formed (influence of the support, its small dimensions, possible contaminations, etc.).

Tungsten crystals of the form close to the equilibrium one are almost never observed if the heat treatment of the tungsten point is carried out under high vacuum conditions. Nor can this shape be obtained by evaporation of tungsten on

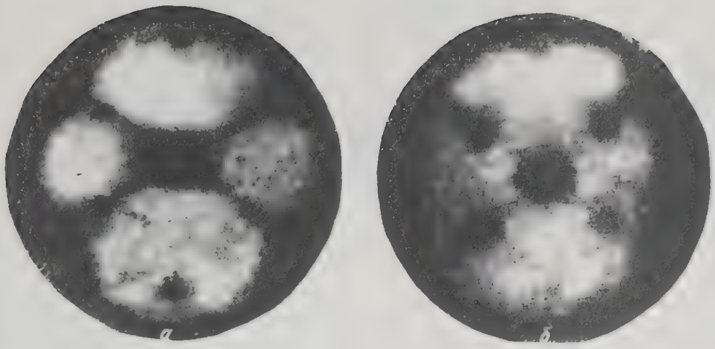

Fig. 1. Image of a "smoothed" or rounded tungsten point obtained in an electron projector: a) at a vacuum of 10^{-11} mm Hg (Ref.6); b) at a vacuum of 10^{-7} mm Hg (our experiments).

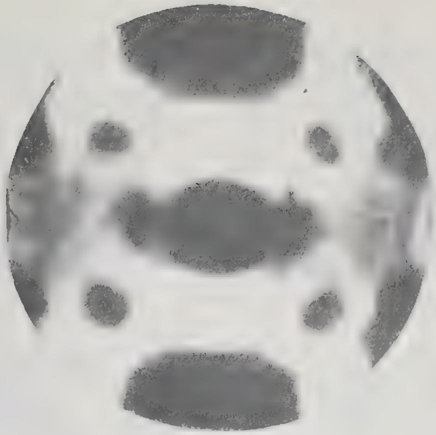

Fig. 2. Image of a "ribbed" single crystal point obtained in the electron projector.

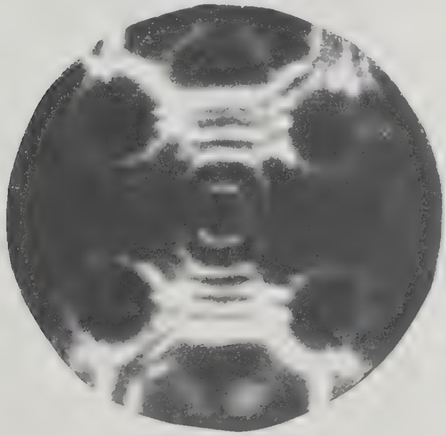

Fig. 3. Image of the same point as in Fig.2 obtained in the ion projector.

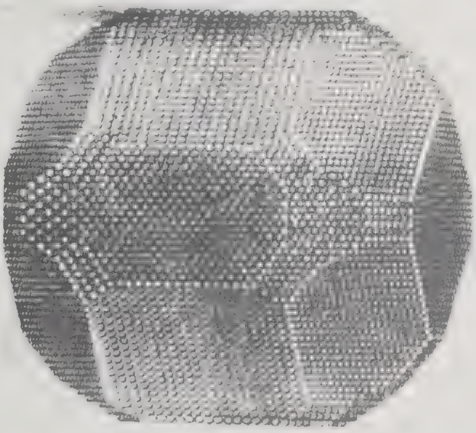

Fig. 4. Schematic model of a "ribbed" tungsten single crystal.

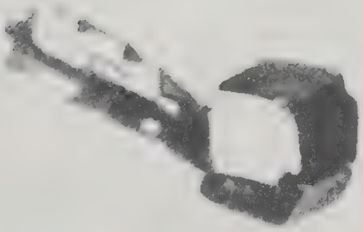

Fig. 5. Shape of tungsten single crystal grown from the gaseous phase (after Schmidt[12]).

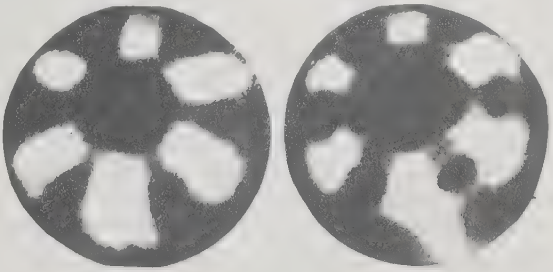

a b

Fig. 6. Formation of point shape corresponding to the hexagonal structure as a result of heating to 700-800° (tungsten carbide on tungsten).

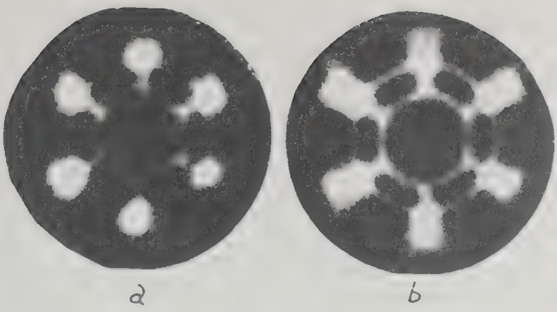

Fig. 7. Same as Fig. 6 but for molybdenum (molybdenum carbide on molybdenum).

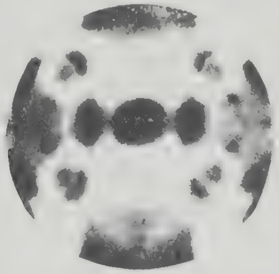

Fig. 10. Moving film in the region of the triad axis (t ≈ 600°).

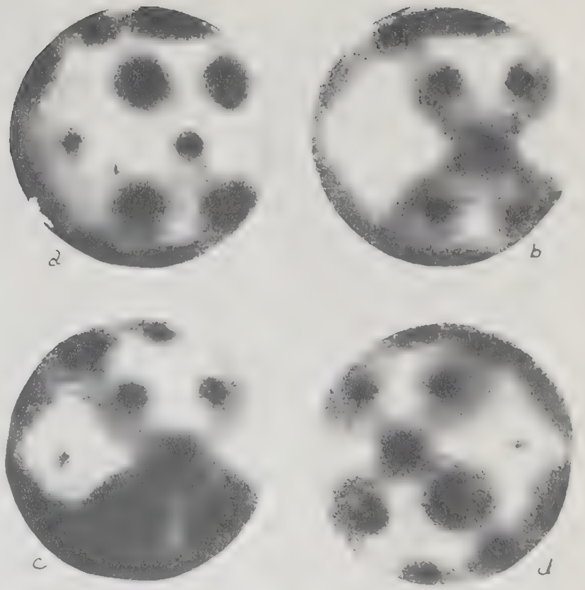

Fig. 9. Moving film in the region of the tetrad axis: a) t = 0°; b,c & d) t ≈ 600°.

tungsten since in the process it is impossible to obtain uniform distribution of the supersaturated tungsten vapor over the surface of the point.

However, the well facetted form is frequently obtained when the point is contaminated with carbon.[6] The fact that this shape is readily formed under our conditions indicates that our points were probably contaminated with carbon. The sources of the carbon could be the oil vapor and the more volatile products of its decomposition. In this case the carbon, present on the surface of the crystal, without altering the structure of the tungsten itself apparently aided the change in its shape, approaching it to the equilibrium one.

The alteration of the form of the crystal usually observed in an electron projector is due partly to evaporation and mainly to migration of the surface atoms. Primarily this applies to the more weakly bound atoms, located at the corners and edges of the crystal. Removal of the atoms from the corners and edges leads to the formation of the rounded shape commonly observed.

Carbon on the surface of the tungsten apparently acts on the weakly bound "corner" atoms enhancing their cohesion with the crystal. As a result the migration and rearrangement of the atoms is hindered which leads to the formation of a regularly facetted crystal. With considerable contamination of the point surface (mainly with carbon), we succeeded in observing the formation of the different crystal forms characteristic of crystals with a hexagonal structure. Crystals of this kind form both on tungsten (Fig. 6) and on molybdenum (Fig. 7) points. It may be assumed that the respective carbides (W_2C or Mo_2C) form on the surface.

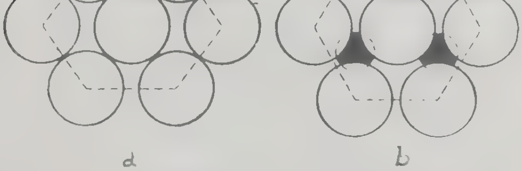

Fig. 8. Arrangement of atoms in the (011) plane of tungsten (a) and the (0001) plane of tungsten carbide (b).

It should be noted that the (0001)

basal plane of the carbide coincides with the (011) plane of the tungsten (or molybdenum) single crystal. This is explained by the fact that both these planes are the most closely packed and that the closest correspondence for the plane networks of the body-centered cubic and hexagonal structures obtains for these planes (Fig. 8).

Aside from carbon, the surface of the tungsten point under "poor" vacuum conditions can be contaminated with residual gases and their different compounds with carbon. In some cases the different impurities on the tungsten surface may be in the form of an amorphous phase. The mobility of the surface layer increases rapidly with increasing temperature. The presence of a mobile amorphous phase, which may be thought of as two-dimensional gas or liquid on the surface of the crystal, greatly facilitates the different possible surface reactions, which explains the diversity and complexity of the pictures observed under conditions of relatively "poor" vacuum.

In the electron projector one can frequently observe anisotropic spreading of the impurities in the form of films moving over the surface of the single crystal. Most frequently the movement of the films occurs in the direction of the tetrad or triad crystal axis.

The photographs of Fig. 9 show the successive stages of the motion of the film in the direction of the tetrad axis during heating of the point. The movement of the film begins from the periphery of the (001) face and terminates at its center. The motion of the film is apparently due to its partial evaporation and the influence of the forces of surface tension.

Similar films are observed in the region of the (111) plane of the octahedron (Fig. 10). As the film is pulled towards the center of the (111) face one can observe the displacement of its boundary over the (112) face. When observing the image visually one can readily see that the film boundary is somewhat ragged (the reproduced photograph is slightly retouched). In this case the contaminating material apparently consists of two-dimensional crystals which become a two-dimensional liquid upon heating. In cases when the amount of surface impurities is particularly large one can observe how the heated films move off in successive layers over an appreciable period of time. As the surface becomes clean the movement of the films slows down and finally ceases. It is difficult to record the movement of such films by means of a conventional photographic camera. We plan to make a motion picture record of this interesting phenomenon in the near future.

Leningrad Physico-technico Institute
of the Academy of Sciences of the USSR

References

1. I.LSokol'skaia, Zhur. tekh. fiz., 22, 1301 (1952).
2. B.G.Smirnov & G.N.Shuppe, Zhur. tekh. fiz., 22, 973 (1952).
3. I.S.Andreev, Zhur, tekh. fiz., 22, 1428 (1952).
4. R.Asadullin & G.N.Shuppe, Zhur. tekh. fiz., 24, 205 (1954).
5. N.A.Gorbatyi & G.N.Shuppe, Zhur. tekh. fiz., 25, 1364 (1955).
6. E.W.Miller, Ergebn. exakt. Naturwiss., 27, 290 (1953).
7. E.W.Miller, J. Appl. Phys., 26, 732 (1955).
8. D.Alpert, J. Appl. Phys., 24, 860 (1953).
9. A.V.Shubnikov, Kak rastut kirstally (How crystals grow), M.-L., 1935.
10. P.I.Lukirskii, Doklady AN SSSR, 46, 300 (1945).
11. L.N.Dobretsov, Zhur. tekh. fiz., 23, 417 (1953).
12. R.W.Schmidt, ZS. f. Phys., 120, 69 (1942).
13. A.M.Reshetnikov, P.I.Sal'nikov & B.M.Tsarev, Zhur. tekh. fiz., 25, 414 (1955).

14. I.N.Stranski & B.Honigmann, ZS. phys. Chem., 194, 180 (1950).
15. I.N.Stranski, ZS. phys. Chem., B38, 451 (1938).

DISCUSSION

N.D.Gabovich: How long did the picture remain stable? Was it reproducible after heating and removal of the impurities?

Iu.N.Talanin: The picture was not stable; it diffused after 2-3 min. We did not purposely contaminate the points; the impurities were formed by the oil vapor and it was impossible to eliminate them entirely.

L.N.Dobretsov: Did you observe twins or quadruplets on the (110) face?

Iu.N.Talanin: Twins and quadruplets were observed on all the faces in the case of a highly contaminated point.

L.N.Dobretsov: What prevents the carbon from penetrating into the tungsten?

Iu.N.Talanin: Possibly this is connected with the fact that the carbon is a surface-active substance. When present in small amounts it does not change the surface structure. The hexagonal structure appears only when a large amount of carbon is present, when it enters into the lattice.

I.L.Sokol'skaia: The carbon is not incorporated in the tungsten lattice properly speaking since the lattice expands.

N.D.Morgulis: What can you say regarding the pictures obtained with the ion projector?

Iu.N.Talanin: The hydrogen was admitted through a paladium capillary. The resultant picture was usually very dark and it was often impossible to photograph it.

A.P.Komar: In working with the ion projector one obtains a picture more sensitive to the surface relief, but image detail is lost when the field gradient at the point is increased.

WORK FUNCTION OF THE (110) FACE OF A TUNGSTEN SINGLE CRYSTAL AND POSITIVE SURFACE IONIZATION OF SODIUM ON THIS FACE

- G.N.Shuppe, E.P.Sytaia & R.M.Kadyrov

Analysis of all the available data on the emission from tungsten single crystals shows that we can speak with reasonable confidence regarding the value of the work function of only the more strongly emitting surfaces: the work function of the (111), (113) and (116) faces apparently lies between 4.3 and 4.4 ev; the work function of the (100) tungsten single crystal face is 4.6 ev. However, as may be seen from table 1, the data in the literature regarding the work function of the most closely packed (110) face are conflicting.

Table 1

Values of the work function of the (110) tungsten single crystal face according to the data in the literature

Investigators	Work function, ev	Emission and method
Nichols[1]	4.68	Thermionic emission; Richardson plots
Müller[2]	6.0	Electrostatic emission
Smirnov & Shuppe[3]	5.5±0.2	Same
Drechsler & Müller[4]	5.70±0.15	Same
Andreev[5]	4.60±0.08	Electrostatic emission with utilization of its dependence on the emitter temperature
Wilkinson[6]	~4.7	Electrostatic emission. On the basis of the brightness of the spots on the screen of a spherical electron projection tube.
Dyke, Trolan, Dolan & Grundhauser[7]	5.0-5.5	Same
Becker[8]	>4.9	Same
Smith[9]	1) 4.72 2) ~5.3	1) Thermionic emission; Richardson plots. 2) Value obtained by rather arbitrary evaluation of experimental data
Hutson[10]	5.70-5.99	Thermionic emission. From analysis of distribution in energy curves for electrons emitted from the different surfaces it was found that $\varphi_{110} - \varphi_{111} = 0.71$ ev.
Müller[11]	1) 5.70-5.99 2) >5.99	1) Electrostatic emission (assuming that the work function of polycrystalline tungsten ~4.5 ev). 2) On the basis of surface ionization of aluminum ($V_i = 5.96$ v).

There are a number of reasons for this great divergence in the values of the work function of the (110) face. For one thing in view of the preparation procedures used the (110) face in all the experiments was not uniform, i.e., undoubtedly had structural dislocations and "patches" of other crystal faces. In the investigations of Refs. 2 & 4, the electric field in the spherical projector was unjustifiably[3] assumed to be hyperbolic. The assumptions made regarding the field in Ref. 6 fail to take into account the shape of the cathode point and form of the electrodes. The assumptions regarding the configuration of the field in Ref. 7 are also arbitrary. In Ref. 11 the field is evaluated on the basis of a number of simplifying assumptions. Smirnov & Shuppe[3] assume that the tip of the emitter is smoothly rounded (the same assumption is made in Refs. 2, 4, 6, 7 & 8) and that the field intensity is constant over a certain section of the emitter

surface. Furthermore in the experiments of Smirnov & Shuppe[3] there could have occurred more or less significant changes in the intensity of the electron beam incident to focusing the beam from individual spots on the collector.

In comparing the emission from the (110) face with the emission from the other faces this effect in addition to that due to scattered electrons apparently depressed the value of $\varphi_{(110)}$. There can be no doubt that scattered electrons filled the apparatus and enhanced the brightness of the screen in the investigations of Refs. 6, 7 & 8. It may be assumed that secondary electrons of different origins reduced the value of $\varphi_{(110)}$ in the experiments of Refs. 1 & 9 as well. Special procedures were employed in connection with the measurements of Ref. 9 to evaluate the influence of these secondary electrons; the validity of these procedures is questionable.

Although measurement of the electrostatic emission from a heated emitter (1000-1300°K - Ref. 5) makes it possible to eliminate the field strength from the equations, such heating is accompanied by changes in the shape of the emitter and rearrangement of the faces due to migration of atoms over the surface. Such migration over the surface of a tungsten single crystal in the case of strong fields becomes noticeable[8] even at an emitter temperature of about 800°K while its influence on the microstructure of the facet surfaces is still unknown.

Direct measurements[1 & 9] of the thermionic emission from the different faces of a tungsten single crystal lead to a work function difference $\Delta\varphi_{max} = (\varphi_{max} - \varphi_{min})$ amounting to about 0.3-0.4 ev.

For other, previously investigated metals we have $\varphi_{(100)} - \varphi_{(\bar{1}\bar{1}\bar{1})} = \varphi_{(111)} = 0.463$ ev (Ref.13) or 0.73 ev (Ref.14) for copper; $\varphi_{(111)} = 0.36$ ev for bismuth (Ref.15). According to our earlier evaluation[16] $\Delta\varphi_{max}$ for nickel is appreciably greater than 0.3 ev.

Even minor inhomogeneity in the structure of the (110) face in the case when only one form of electron emission (photo-, thermo- or field-emission) is used for the measurements can distort the true value of the work function of the face and result in an underestimate of $\varphi_{(110)}$. In the course of such measurements it is essential to evaluate the inhomogeneity of the face, i.e., to check for the presence of spots or areas with a different work function. Hence, in general, it is desirable to use a combination of methods, one of which would permit evaluating the emission from the part of the face having the lower work function and the other the emission from the remaining area characterized by a higher work function. In the specific case of the (110) face of a single crystal of tungsten, a desirable combination, in our opinion, would be measurement of the electron emission, which comes mainly from areas where $\varphi = \varphi_{min}$, and of the emission of positive sodium (or lithium) ions, which form by surface ionization mainly at points where $\varphi = \varphi_{max}$.

Equipment and preparation of specimens

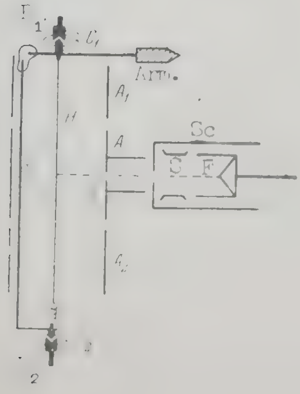

Fig. 1. Apparatus used for measuring the work function of different faces of a tungsten single crystal: A, A_1 & A_2) cylinders, R) rotor frame, H) tungsten filaments, Arm) armature, B_1 & B_2) bearings, C_1 & C_2) shunting spirals, S & Sc) shielding cylinders, F) Faraday cup.

Our apparatus (Fig. 1) was similar, in principle, to that used by Nichols[1] and Smith[2]: the tungsten filament H was suspended in the frame P along the center line of the three coaxial cylinders A_1, A & A_2; the filament in its frame could be rotated by means of a magnet acting on the iron armature Arm.

To obviate arcing in the bearings B_1 & B_2 incident to the passage of a heavy filament current these were shunted by the spirals C_1 & C_2 which did

not interfere with the rotation. The presence of the guard cylinders A_1 & A_2 made it possible to collect the full emission from the central portion of the filament H on the main cylinder A. The emission in the individual crystallographic directions was measured on the Faraday cup F. The shielding cylinder S served to cut off scattered and secondary electrons. The diameter of cylinder A was 40 mm; with the entry aperture for the electron beam having a diameter of 1 mm, we obtain an angular resolution of about 2.9°. Investigations of the field in the central portion of the apparatus by means of an electrolytic bath showed that within the limits of about 220° the field about the aperture O was not noticeably distorted by the frame P.

After prolonged (several days) aging of the tube, accompanied by heating of the glass at 450° and heating of the metallic parts by high-frequency current, the tube was sealed off. The pressure at this stage was measured by an ionization pressure gage: the vacuum in all the tubes used in the experiments was never worse than 10^{-8} mm Hg (in the absence of sodium vapor). The filament current was measured by a vacuum-tube electrometer with a sensitivity of 10^{-15} amp per scale division.

Numerous specimens of brand VCh, VK and VA (ВЧ, ВК and ВА) tungsten wire, ranging from 40 to 190 μ in diameter, were subjected to recrystallization by intense heating under high vacuum and in an atmosphere of hydrogen with a moveable mercury contact[1]. To eliminate drawing die marks, before installation in the apparatus, the filaments were ground on a special device using fine emergy and then polished with emergy cloth.*

Spectroscopic analysis fails to show any appreciable difference as regards purity of the tungsten between the enumerated wires. Studies in a cylindrical electron projection tube showed that large single crystals (5 cm or more in length) readily grow under heat treatment in brand VK and VA wires (a somewhat higher temperature was used for the brand VA wires), while in brand VCh (and apparently VT (ВТ)) wires the size of the crystals does not exceed 1-2 mm. To eliminate all traces of drawing a rather thick layer (up to 15% of the diameter) had to be ground off all the wires; this is a rather greater thickness than was removed from the wires in the investigations of Ref. 1 & 9.

Alternating current was used for heating. In heating with dc current a distinctive structure tends to form on a number of faces, particularly the (110) face of the recrystallized wire.[17] This effect is called the "dc etch". However, even with ac heating, contrary to the hopeful predictions expressed by Herring and Nichols[18] there can, under certain conditions, form on some of the faces, including the (110) face, a special structure which might from the appearance of the surface be called "grainy structure".

A photograph of a brand VA tungsten wire (190 μ in diameter) crystallized over its entire length with this structure on the (110) face is reproduced in Fig. 2,a. This wire was heated for 22 hours at 2400°K and 20 hours at 2500°K. A number of damaged facets can already be distinguished in Fig. 2,b. Structure of this type was less pronounced on grade VK wire; however, this is insufficient evidence to judge of the relative mobility or volatility of the atoms of brand VA and VK wires. After prolonged heating with either ac or dc, the initially cylindrical wires become facetted (Fig. 3: due to the shallow depth of focus, the facetting at the break is not clearly discernible in the photograph; however, optical examination shows six faces; the form of the cross section correlates with the surface energy of the faces). The flat sections may form either over the entire wire or only on some parts of its surface.

If during intense heating the wire is subjected to vibration - mechanical, due, for example, to the operation of the fore pump, or electrical, associated

---

*It was noted that the use of grinding powders containing boron carbide leads to permanent contamination and alteration of the emitter surface (brittleness, etc.); the effect is accompanied by an increase of emission.

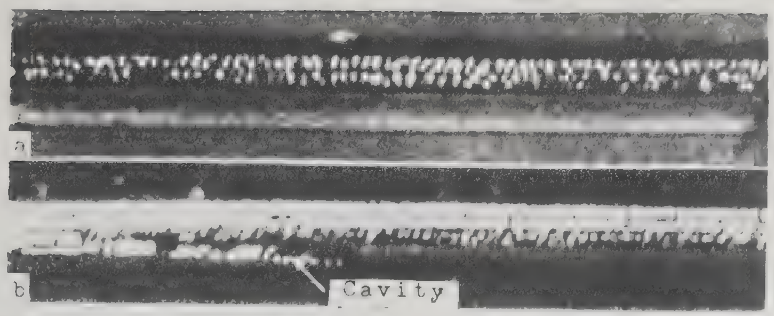

Fig. 2. Photographs of crystallized brand VA tungsten wires after heating for 22 hours at 2400° and for 20 hours at 2500°K (magnification ~70 X): a) grainy structure of the (110) face, b) grainy structure with defects.

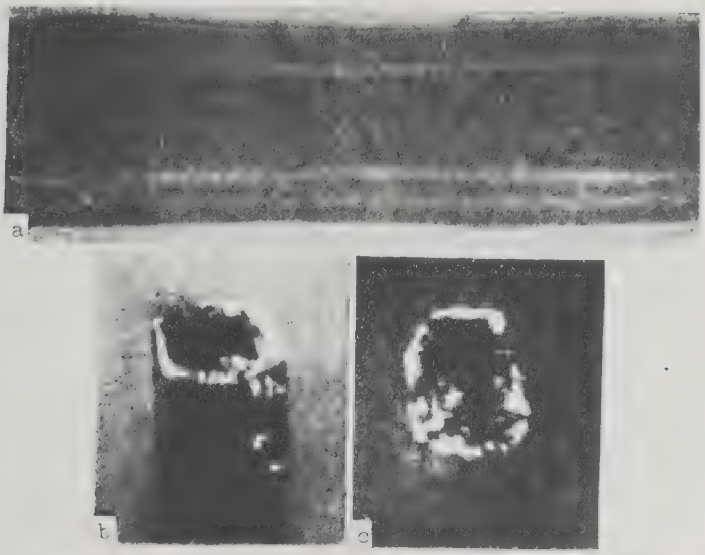

Fig. 3. Recrystallized tungsten wires: a) brand VK; transformation from cylindrical to facetted shape; b & c) brand VA; cross sections of wire at break.

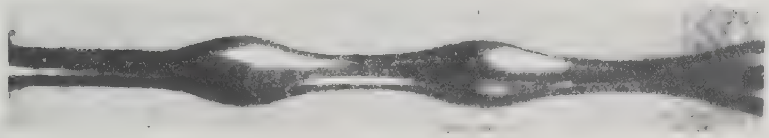

Fig. 4. Photograph of brand VK tungsten wire showing necks and beads formed as the result of heating under the influence of vibration.

with ac passing through the wire and the tension spring - there form in the wire necks (in some cases facetted) and thickened sections in the form of beads. A section of VK wire having an initial diameter of 120 μ with this formation is shown in Fig. 4; the diameter of the neck is about 90 μ; that of the beads about 160 μ. Obviously, in resistance heating the temperature at the bead and at the neck differs. The number of beads forming varies depending on the tensile stress in the wire, its length, the magnitude of the current and the applied voltage. Apparently, under the influence of vibration, the tungsten atoms migrate over the surface from the antinodes to the nodes of the standing waves to form beads at these points.

Aside from the above described "macro-changes" of the surface in heating with either ac or dc, there form on the facets "micro-ulcerations" due to local variations in volatility; these disturb the atomic packing on the faces and leads to the formation of steps, cavities, etc. Such dislocations and deformations result in the reduction of the work function of the (110) and (112) faces of the tungsten single crystal.

With a sufficiently high resolution of the instrument, directional variations in the emission can be observed even for a non-recrystallized (but degassed) wire. The emission diagram obtained from a 160 μ diameter brand VCh wire is reproduced in Fig. 5 ($T = 2100^\circ$K; for convenience of comparison the curves are plotted to different scales). Whereas in curve I the emission peaks and dips are randomly distributed, i.e., correspond to the random distribution of the crystals on the surface of the polycrystalline wire, curve IV, recorded after more than ten hours of heating, already exhibits a certain symmetry in the distribution of the peaks, a distribution

which begins to reflect the symmetry of the cubic system in which tungsten crystallizes.

Fig. 6 shows the angular variation of the electron emission from a recrystallized brand VK wire 190 μ in diameter subjected to heating for 183 hours at 1900-2000°K. The crystallographic directions were identified from considerations of symmetry of the emission pattern, i.e., as is commonly done in the case of field emission from a tungsten point. The deduced orientation of the axes was substantiated by analysis of Laue diffraction patterns obtained from three of the specimens.

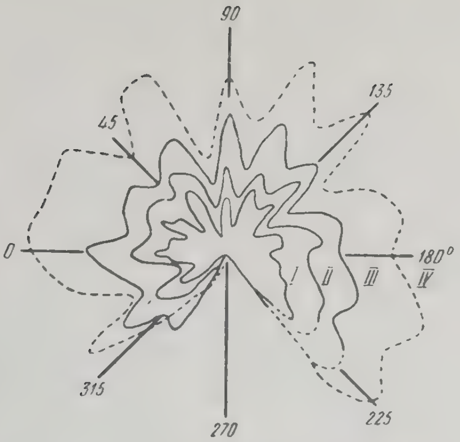

Fig. 5. Polar diagram of electron emission from a brand VCh tungsten wire at 2100°K at different stages of heat treatment: I - III) after heating for only a few hours, IV) after prolonged heating over a period of tens of hours.

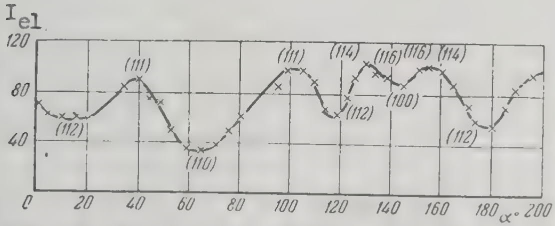

Fig. 6. Variation of the electron emission from a recrystallized brand VK tungsten wire with the angle of rotation in the apparatus of Fig. 1.

Measurements of the emission from single-crystal specimens

The values of the electron work function of brand VK wire, as determined on the basis of the total emission to the cylinder A, fall off as a result of recrystallization from 4.60-4.65 ev to 4.45-4.50 ev. Different sections of wire from the same spool yield values of the work function differing by as much as 0.15 ev, depending not only on the heat treatment procedure but also on wholly indeterminable conditions inside the wire during recrystallization. The values of the work function determined from the electron emission, both the mean values and, particularly, the specific values for individual faces, depend on the previous history of the sample and can readily be changed by further heat treatment. Hence the work function determined in this manner for a given polycrystalline surface, even though the surface is thoroughly cleaned and degassed, can be considered accurate only within a few percent, i.e., must be understood as a characteristic particular to the given emitter rather than common to all metallic emitters of the given type.

In view of this in many cases there is no point in attempting to refine the measurement procedure beyond a certain point with a view to enhancing the accuracy of measurement. As will be seen from the diagram of Fig. 5 the surface of an emitter changes continuously: the area and type of patches present vary constantly.

The Richardson plot for a polycrystalline surface or the non-uniform surface of a specific face is not a straight line but a broken line or curve, not because of experimental errors or theoretical considerations (see Ref. 18), but simply because the surface of the emitter is not stable at high temperatures. It must be emphasized that the time factor is particularly important at high temperatures. In view of the observed changes in the appearance and form of the surface (formation of grains, cavities, flat areas, excrescences, etc.) measured values of the Richardson constant A and, of course, of the Schottky form factor (slope) S must be regarded as particular values peculiar to the given specimen. Thus for the form factor S we found it necessary to indicate the date of measurement (i.e., the number of hours of heating of the wire).

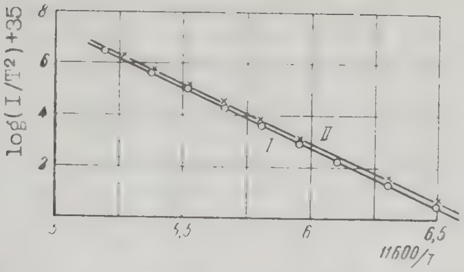

Fig. 7. Richardson plot for the (112) face of a specimen at V_a = 2000 v and V_s =-80 v as a function of the time: I) φ = 4.68 ev, A = 94 amp cm^2 $degree^{-2}$; II) φ = 4.65 ev, A = 100 amp $cm^{-2}degree^{-2}$.

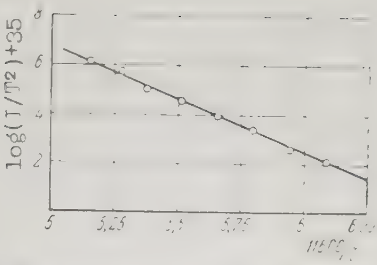

Fig. 8. Richardson plot for the (110) face with V_a = 2200v, V_s = 80 v, φ = = 4.61 ev, A = 86 amp cm^{-2} $degree^{-2}$.

[V_s= retarding potential. Trans.]

For example, our laboratory notes in connection with determinations of the S values for the (110) face of one of the samples read as follows: 10 Oct. 1954 - S = 30, 21 Oct. 1954 - S = 39, etc., whereas the theoretical value of S (for bulk material) is 22.

Fig. 7 shows the Richardson plots for the (112) face of a specimen characterizing the change in the electron work function over a few hours of heating (0.03 ev decrease).

For the (110) face after prolonged heating we were able to obtain a value of 4.61 ev (Fig. 8) for the so-called apparent work function[18] (for other specimens the value ranged to 4.8 ev). The slit system leading to the Faraday cup F and the shielding of the cylinder itself and its leads obviated the influence of different interfering currents at any rate in making measurements in the direction of strong emission. In the case of weak emission from the (110) face the results conceivably could be influenced by secondary electrons, ejected, for example, from the inside wall of cylinder A, penetrating into the cup F through the slit system. However, this can only partially explain the low value obtained for the work function of the (110) face. A number of procedures can be used for investigating the decisive factor (changes of the initially uniform surface of the face and the appearance of spots, patches and other defects thereon) responsible for the depressed work function:

1) examining the surface with an optical or electron microscope or by means of an electron or ion projection tube;

2) on the basis of deviations of Richardson's constant from its theoretical value of 120 amp $cm^{-2}degree^{-2}$;

3) on the basis of the presence of an anomalous Schottky effect (provisionally neglecting the possible influence of space charge on the shape of the Schottky plots at low potentials[19]).

In investigating inhomogeneities of the surface by means of a projection tube, depositing a coating of extraneous atoms on the emitter, greatly helps bring out the plateaus, steps and other complex features of the surface structure[20]. The above mentioned three procedures, however, admit of drawing only qualitative conclusions regarding the degree of non-uniformity of the face surface. Consequently, we employed yet a fourth possible procedure, namely, that based on measuring the difference between the values of the work function φ_{el} determined on the basis of the electron emission and the work function φ_{ion} determined by means of surface ionization of sodium atoms.

In order to determine φ_{ion} the apparatus with the rotatable tungsten single-crystal wire was filled with sodium vapor and the ion currents in the different directions were measured. The temperatures used in these measurements were above the temperature of adsorption of sodium on tungsten but under ~2200°K, when the

photo-emission current from the collector begins to interfere with the measurements. The filament was heated to above this temperature between each series of measurements. The repeatedly redistilled metallic sodium, the purity of which was checked chemically, spectroscopically and on a mass spectrograph, was placed in a branch tube of the apparatus. The apparatus was surrounded by a heating chamber capable of maintaining temperatures up to 250° (the actual working temperatures were between 120 and 170°). The number N of sodium atoms striking 1 cm^2 of the wire surface at a vapor temperature T could be approximated from the number n of particles per cm^3 of vapor^{21}:

$$\log n = -\frac{5573}{T} - 1.68 \log T + 28.71.$$

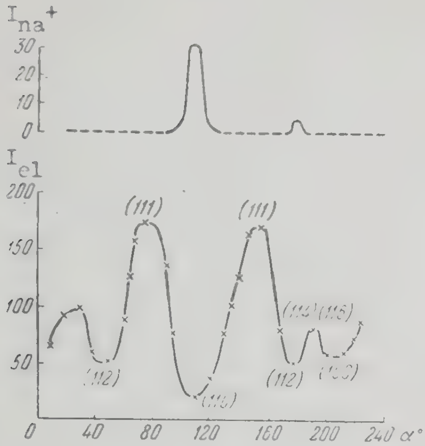

Fig. 9. Angular distribution of ion and electric currents from a recrystallized brand VK tungsten wire.

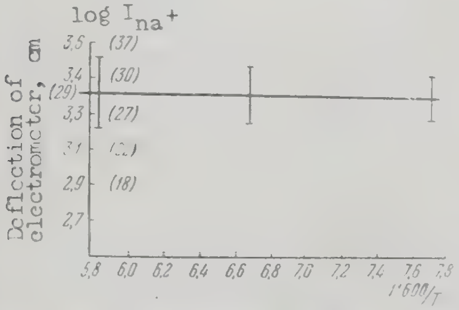

Fig. 10. Variation of the ion current from the (110) face with the temperature of the recrystallized brand VK tungsten wire. Sensitivity of the electrometer $2 \cdot 10^{-14}$ amp/cm.

The ion current maxima occurred at the points of minimum electron current for the two (110) faces present on the wire.

The electron and ion currents near one of the (110) faces are shown in Fig. 9 (temperature in apparatus 140°, temperature of wire 1500°K). The small ion current peak on the (112) face present on this specimen could be due to residual (110) faces of the original rhombododecahedrons of the tungsten grains.

Fig. 10 shows the temperature dependence of the ion current from a (110) face. We note that Fig. 9 showing the ion current peaks in the [110] directions is in a sense a cross section through Figs. 2, e-3 in Ref. 20 (electrostatic emission from a tungsten single crystal activated by a layer of sodium on the (110) face). We note further that an admixture of potassium, for example, in the sodium used would give a strong background in all directions. Contamination with oxygen would produce the same result. No such background was observed; hence it may be assumed that the sodium used was actually of high purity.

Discussion of results

The ionization potential of sodium is 5.14 v. From the values in Fig. 10, we find according to the Saha-Langmuir formula that $V_i - \varphi_{(110)} = 0$, i.e., that $\varphi_{110} \approx 5.14$ ev.

The work function calculated for the (110) face on the basis of the electron current was 4.8 ± 0.1 ev for the given specimen. For the mean work function of the section of wire enclosed in the collector cylinder A we obtained from the dependence of log I^+ on 1/T a value of $\bar{\varphi}_{ion} \approx 4.9\text{-}5.0$ ev. This indicates that patches with a large work function are present on the investigated surface. Like the dependence of log I^- on 1/T, the dependence of log I^+ on 1/T can, in principle, be a broken or curving line not only for the polycrystalline surface but also for a single face if the wire is intensely heated during the measurements with a resultant change in the percentage of the area occupied by different patches or spots. Inasmuch as $\varphi_{(110)} \gg \varphi_{\text{other faces}}$, the second term in the sum

$$\overline{I}^{+}_{(110)} = I^{+}_{\text{undamaged area}} + \sum I^{+}_{\text{damaged sections}}$$

can, if the ulceration of the (110) face is not very great, be neglected (or if we take the view that positive ions of alkali metals can form only on areas where $\varphi \geqslant V_i$, the second term in the case of ionization of sodium or lithium should be discarded). Hence our results should be regarded as the lower bound for $\varphi_{(110)}$.

One can roughly evaluate the uniformity of the (110) face on the basis of the magnitude of the electron and ion currents, taking into account the geometry of the apparatus and the sodium vapor pressure. In the case of the sample in question the undamaged area of the (110) face in the [110] direction was less than 50%. If $\varphi_{(110)}$ were appreciably greater than 5.14 ev (for example, 6 ev) the plot of Fig. 10 would exhibit a discernible slope even with the given degree of defectiveness of the (110) face. Hence we feel that in measurements employing electrostatic emission, i.e., in the investigations of Refs. 2, 4, 7 & 11 and our study of Ref. 3, the results were affected by ribbing or shingling of the "rounded" point, that is, by flat areas on the (110) face, whose presence on such tungsten points, as has been established by adsorption in Ref. 20, reduces the field emission in this direction.

Further, we feel that there is good reason to question the validity of the Fowler-Nordheim field emission equation which was deduced for a mirror-smooth surface without taking into account the atomic structure of the surface, penetration of the field (10^7-10^8 v/cm) into the conductor and its influence on the outer crystal layers and similar factors (see, for example, Refs. 4, 20 & 22).

An analogous ionization procedure was employed in the investigation of Ref. 11, published after completion of the present experiments. In this investigation, aluminum (V_i = 5.96 v) was sputtered on a polycrystalline tungsten surface. In the process of evaporation about 10% of the aluminum atoms left the tungsten surface in the form of ions. One cannot conclude from this, however, there were present on the tungsten patches with a work function greater than 5.96 ev in view of the following considerations:

1) there is no indication in Ref. 11 regarding the purity of the aluminum (i.e., regarding the possible content of oxygen, aluminum oxide, etc.);

2) there exist convincing data regarding noticeable ionization on tungsten of atoms with even higher ionization potentials[23];

3) the Saha-Langmuir equation can be applied with reasonable certainty only to alkali metal atoms;

4) in order to determine the electron work function one must measure the temperature dependence of the ion current in as much as the Saha-Langmuir equation in addition to the exponent also contains a coefficient.

L.V.Reshetnikova, laboratory technician, and D.N.Vasil'kovskii, graduate student, participated in the present investigation.

"V.I.Lenin"
State University of Central Asia

References

1. M.Nichols, Phys. Rev., 57, 297 (1940).
2. E.Müller, ZS.f.Phys., 120, 261 (1943).
3. B.G.Smirnov & G.N.Shuppe, Zhur. tekh. fiz., 22, 973 (1952).
4. M.Drechsler & E.Müller, ZS.f.Phys., 134, 208 (1953).
5. I.S.Andreev, Zhur. tekh. fiz., 22, 1428 (1952).
6. M.Wilkinson, J.Appl.Phys., 24, 1203 (1953).
7. W.Dyke, J.Trolan and others, J.Appl.Phys., 25, 106 (1954).
8. J.Becker, BellSyst.Techn.J., 30, 907 (1951).
9. G.Smith, Phys.Rev., 94, 295 (1954).

10. A.Hutson, Phys.Rev., 98, 889 (1955).
11. E.Müller, J.Appl.Phys., 26, 732 (1955).
12. G.V.Spivak & A.Gil'berg, Doklady AN SSSR, 94, 455 (1954).
13. B.Rose, Phys.Rev., 44, 585 (1933).
14. N.Underwood, Phys.Rev., 47, 502 (1935).
15. H.Kurzke, J.Rottgardt, ZS.f.Phys., 100, 718 (1936).
16. R.Asadullin & G.N.Shuppe, Zhur.tekh.fiz., 24, 205 (1954).
17. R.Schmidt, ZS.f.Phys., 120, 69 (1942).
18. C.Herring & M.Nichols, Thermionic emission (In Russian trans. M.1950).
19. H.Ivey, Phys.Rev., 76, 554 (1949).
20. N.A.Gorbatyi & G.N.Shuppe, Zhur.tekh.fiz., 25, 1364 (1955).
21. N.A.Kaptsov, Elektricheskie iavleniia v gazakh i vakuume (Electrical phenomena in gases and vacuum), M.-L., 1950.
22. G.M.Avakiants, Trudy FTI AN UzSSSR, 6, 43, 1955.
23. S.V.Starodubtsev & Iu.I.Timokhina, in Sbornik, posviashchennyi 70-letiiu akad. A.F.Ioffe (Symposium dedicated to the 70th anniversary of Academician A.F. Ioffe), M.-L., 1950.

DISCUSSION

L.N.Dobretsov: Did you verify the fact that the degree of ionization was far from 100%. In my opinion, the absence of a temperature dependence shows that $\varphi_{(110)}$ is equal to or greater than 5.14 ev.

G.N.Shuppe: On the basis of the admittedly doubtful formula for the pressure of sodium vapor it can be shown that the ion current was less than the theoretical value. It follows from our experiments only that $\varphi_{(110)}$ is not smaller than 5.14 ev; it can, of course, be larger.

B.M.Tsarev: What can you say regarding your earlier data and the data of Müller?

G.N.Shuppe: I feel that our data as well as those of Smirnov and Müller indicate that the tungsten point in these experiments was not truly rounded and that therefore the determined values of the work function of the (110) face were not true values. I think that $\varphi_{(110)}$ can be somewhat greater than 5.14 ev, but not 6 ev.

N.D.Morgulis: How is one to understand the noticeable ionization of aluminum atoms reported by Müller?

G.N.Shuppe: I cannot answer this question since Müller's experimental conditions are not adequately described in his article.

L.N.Dobretsov: To what extent is the magnitude of the ion current constant?

G.N.Shuppe: To within 10-15%.

K.A.Michurina: In what brands of wire is recrystallization best observed?

G.N.Shuppe: Wires of brands VK and VA (BK and BA) recrystallize readily.

K.A.Michurina: What was the length of the wires?

G.N.Shuppe: Not less than 12-13 cm.

SURFACE MIGRATION IN AN ELECTRIC FIELD AND THE BINDING ENERGY OF TUNGSTEN ATOMS

(Abstract)

- I.L.Sokol'skaia

When heated, the submicroscopic single-crystal tungsten points, which serve as emitters in electron projection tubes, acquire a rounded shape that is not the equilibrium shape for tungsten single crystals. When the heating is carried out in a strong electric field there occurs a rearrangement of the point structure as a result of which the point acquires a rounded form. This process occurs through surface migration of the atoms which, moving to new equilibrium positions, arrange themselves in an ordered manner completing the flat surfaces of the faces. The rate of change or rearrangement increases with increasing temperature and field strength but is independent of the direction of the field. This means that the migrating tungsten atoms acquire a dipole moment and move in the field as dipoles in the direction of increasing gradient. In very strong fields the atoms do not have time to arrange themselves in ideal order and pile up into "heaps", as is evinced by the emission image obtained in such cases. The incoherent rearrangement process is accompanied by an increase in the field emission current (at a constant field potential) by virtue of the formation of edges and corners in the proximity of which the field intensity is naturally greater than at the rounded surface. The emission approaches a constant, saturation value as the process nears completion. In the case of the inverse process - smoothing out of the surface - the emission current decreases.

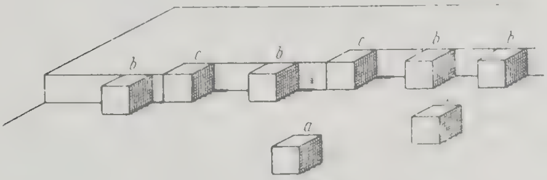

The kinetics of the process can be characterized as follows.[1] The smooth surface has an atomic-step structure comprising three phases: a plane-condensed phase c, a linear-adsorbed phase b, and a plane-adsorbed phase a (see figure). Equilibrium is determined primarily by b ⇄ a transitions since the number of atoms in the c positions is much smaller than the number of atoms in the b positions. Atoms in the a positions can move with almost no expenditure of energy. The b → a transitions, on the contrary, require an appreciable energy and these are the transitions which determine the temperature dependence of the rearrangement process.

The energy of the b → a transition can be computed by the method of Stranski & Suhrmann[2] by computing the change in the number of neighbor atoms incident to this transition for different faces. According to the data of Stranski & Suhrmann[2] the number of neighbors changes appreciably only for the (011) planes for which the change in detachment energy amounts to $(3/2)\varphi_1$ (φ_1 is the break-away energy for two nearest neighbors in the tungsten lattice).

Having determined the temperature dependence of the rate of rearrangement, one can find U, the energy of activation of this process, which must be equivalent to the above computed energy of the b → a transition ($(3/2)\varphi_1$).

Our experiments were carried out in a conventional projection tube with a tungsten point, equipped with a tantalum getter and an Alpert pressure gage.[3] The pressure in the sealed off tubes was $< 10^{-9}$ mm Hg; the correctness of the measured pressure was substantiated by the invariance of the emission picture over a period of more than a day.

The parameter selected to characterize quantitatively the rearrangement process was t_{max}, the time required for the emission current to reach a constant value, i.e., the value characteristic of the rearranged point. The magnitude of $1/t_{max}$ is a measure of the rate of the process. In order to obviate contamination of the point by gases evolved incident to electron bombardment of the screen and overheating of the point by the emission current, the rearrangement

process was carried out in a "reverse" field. The direct or "forward" field was turned on only for the short period necessary for measuring the current and observing the emission picture.

The activation energy U of the rearrangement process can be determined from a semilogarithmic plot of the observed temperature dependence of $1/t_{max}$. The average value of U for three projection tubes and different values of applied voltage was found to be 2.36±0.10 ev.

Since, as noted above, $U = (3/2)\varphi_1$, we have

$$\varphi_1 = 1.6 \pm 0.10 \text{ ev/atom.}$$

The value of φ_1 can also be determined from the heat of sublimation of tungsten[2,4], equal to 8.9 ev/atom $\approx 5.5\varphi_1$, whence

$$\varphi_1 = 1.6 \text{ ev/atom.}$$

The agreement of the results obtained from independent experiments substantiates our hypothesis regarding the mechanism of the process.

"A.A.Zhdanov" Leningrad State University

References

1. Ia.I.Frenkel', Zhur.eksp.i. teor.fiz., 16, 39 (1946).
2. I.N.Stranski & R.Suhrmann, Ann.Phys., 1, 153 (1947).
3. D.Alpert, J.Appl.Phys., 24, 7 (1953).
4. E.W.Müller, ZS.f.Phys., 126, 643 (1949).

DISCUSSION

N.D.Morgulis: What is the significance of the fact that the effect is independent of the polarity?

I.L.Sokol'skaia: It means that the migrating atoms are free two-dimensionally adsorbed atoms.

N.D.Morgulis: How does the value of U depend on the field intensity?

I.L.Sokol'skaia: U was independent of the field intensity in the range of fields employed.

PROPERTIES OF A COLD CATHODE WITH A FIRING DEVICE IN PULSE DISCHARGES AT LOW PRESSURES*

- E.M.Reikhrudel', A.G.Zimelev & A.V.Kustova

Introduction

In pulsed operation hot cathodes are capable of emitting very appreciable electron currents. The current density from oxide-coated and L-cathodes** may be as great as 350 amp/cm^2. However, the common shortcomings of such cathodes - sensitivity to contamination, consumption of energy for heating and a relatively short service life - persist even in pulsed operation.

Particularly unfavorable conditions for cathodes obtain when it is necessary to work at high voltages and large current densities. Under such conditions the surface of the cathode rapidly breaks down as the result of bombardment by fast ions. In such cases it is expedient to employ a cold cathode with a firing electrode.

The cathodes we tested with a peak pulse voltage of 100 kv yielded currents of the order of 1200 amp with an effective cathode area of 7 mm^2. One of these cathodes withstood about $1 \cdot 10^6$ pulses without an appreciable change in its characteristics. Evidently the service life of such a cathode extends to a much greater number of pulses.

In the present report we describe some of the results obtained in our study of a cathode with a firing electrode in the range of initial voltages from 3 to 100 kv and pulse currents from 3 to 1200 amp at low gas pressures.

The study comprised three parallel lines of investigation: 1) microscopic observation of the cathode surface, 2) oscillographic recording of the currents and voltages in the igniter gap and in the main discharge, and 3) measurement of the x-ray focus on the anode surface. The microscopic observations made it possible to determine the character and distribution of the emission over the cathode surface. The oscillographic measurements brought out the high emission characteristics of the cathode. Observation of the x-ray focal spot on the anode helped clarify the electron-optical properties of the cathode and demonstrated the possibility of controlling the high density electron beam in pulsed operation.

Microscopic observation of the surface of the working cathode

A special tube with a sealed-in flat window (Fig. 1) was used to permit microscopic study of the erosion of the surface and edges of the cathode. The main cathode K_1 and the flat igniter cathode K_2 were mounted on a special rotatable support passing through a vacuum-tight sleeve. Rotation through 90° brought the cathode and electrode directly under the microscope window thus making it possible to photograph different sections of their surfaces after every pulse without opening the tube and exposing them to the deleterious influence of air, i.e., without disturbing the conditions obtaining in

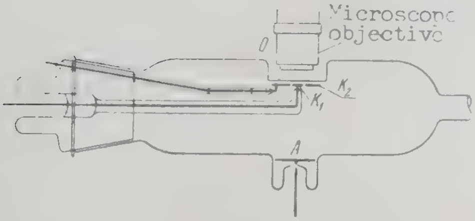

Fig. 1. Experimental tube for microscopic observation of the cathode: A) anode, K_1) cathode, K_2) firing electrode, O) observation window (in the actual tube the plane of the anode was perpendicular to the plane of the window).

---

*B.M.Berezovskii, I.D.Anisimova & T.F.Loginova participated in the experiments and discussions of the results; the authors take this occasion to thank them.

**Porous metal-film cathodes, such as Ba-filled W cathode. Trans.

the tube.

Various metals (molybdenum, nickel and others) were used for the electrodes K_1 and K_2; however, in the experiments described below both electrodes were made of nickel. The electrode K_1 - the cathode - was a flat disc 3 mm in diameter; the electrode K_2 was a disc 20 mm in diameter with a 4 mm diameter central opening. Consequently, the width of the annular gap - the firing gap - was 0.5 mm. The anode A was a tantalum disc 20 mm in diameter. The electrode surfaces were polished.

The high-voltage source was an Arkad'ev-Marx[1] cascade (voltage multiplier) generator. The parameters of the generator were the following: $C = 0.017\ \mu f$; charging resistance $R = 200$ kilohm; the number of multiplication cascades varied. The voltage was varied from 10 to 100 kv. A second generator, employing a similar circuit, permitted reducing the initial voltage to 3 kv.

The first series of observations was carried out with non-outgassed electrodes; in the second series of experiments, the electrodes were thoroughly outgassed in order to determine the role of adsorbed gases.

Microscopic investigation of the cathode surface after single pulses and series of pulses showed that a number of factors are involved in the changes taking place in the surface and edges of the cathode: electroerosion due to bombardment by positive ions, cathode sputtering, etching of the surface between metal grains, strong local fusion of microscopic inhomogeneities, liberation and absorption of gasses, etc.

One can distinguish two principal types of cathode disintegration (Figs. 2 a,b and c): 1) the marks left by a powerful discharge (fused spots, craters, etc.) and 2) comparatively weak "working over" or alteration of the surface by discharges.

The first type of disintegration appears after each pulse on a small area ($\sim 10^{-5} cm^2$) of the surface of the cathode K_1. This damage appears at the edge of the cathode at the point where the spark breaks through the discharge gap. Disintegrations of the second type extend over the entire surface of the cathode, being somewhat more intense in the regions adjacent to the edge, but they become noticeable only after many pulses (Fig. 2,b and c). At the magnification used in our experiments disintegrations of this type have the appearance of very small pits or craters.

The appearance of the surface is analogous to that of a cathode subjected to the prolonged influence of a glow discharge with ionic etching.[2] Figs. 2 b and c are microphotographs of the same section near the edge of the cathode after a different number of pulses (see page 1049). Observations showed that each successive pulse results in a disintegration of the first type at a new spot on the cathode edge. This is due to successive degassing and smoothing out of the microprojections on the surface of the metal.

Spectroscopic investigation of the radiation * from the discharge region in the vicinity of the cathode showed that the intensity of the lines characteristic of the cathode metal is appreciably greater in the case of a cathode not subjected to preaging compared to the line intensity for a cathode operated for a prolonged period (over 200,000 pulses). In addition, it was noted that after degassing of the cathode the current amplitude is somewhat reduced. This suggests that degassing of the cathode should lead to a reduction of disintegration and hence greater stability and longer life of the cathode. This assumption was substantiated by the results of the second series of experiments carried out with twelve degassed electrodes.

For purposes of degassing an additional tungsten spiral was mounted in the tube. The electrodes were heated by electron bombardment to red heat. The de-

---

*At low pressures (10^{-3}-10^{-4} mm Hg) the spectrum of the radiation in the visible and ultraviolet regions can be recorded only as a result of a large number (about 100,000) pulses.

gassing was repeated several times at a pressure of 10-6 mm Hg until the liberation of gas from the electrodes became insignificant.

After such preliminary treatment the tube was connected to the pulse voltage source in the usual manner and the erosion of the electrode surfaces again observed. The general character of the disintegration was found to be the same but the size of the affected regions was reduced.

Tests were run both with single pulses of voltages ranging from 3 to 100 kv and with periodic pulses having frequencies from 2 to 100 cps and voltages from 3 to 25 kv.

Tests with cathodes of different metals showed that where a longer service life is concerned it is advantageous to use high melting point metals (W, Mo & Re). The current amplitude is changed very little, only the degree of disintegration of the cathode is reduced, when a low melting point metal is replaced by a high melting point one. As noted above, such a pulse-degassed cathode withstood about 1 million pulses without serious deterioration.

Current oscillograms

Earlier oscillographic studies[1] of the crest value of the current I_o and the time τ of discharge formation in the main gap showed that as the initial pressure is increased in the range from 10^{-4} to 10^{-1} mm Hg, I_o increases while τ decreases. Increasing the applied voltage also leads to an increase in I_o and a decrease in τ. In the present series of experiments the range of experimental voltages and pressures was extended. In addition, we made simultaneous oscillographic records of the current and voltage both in the firing gap and in the main discharge. The current recording circuit is shown in Fig. 3.

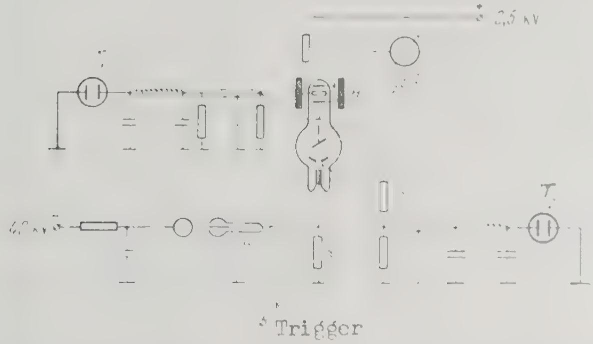

Fig. 3. Circuit for oscillographic recording of the current in the main discharge and the firing gap: I) ion pump, H) pump solenoid.

In these experiments we used a VEI2KO-20 pulse oscillograph with sweep rates from 1 to $1 \cdot 10^{-3}$ microsec/mm. The oscilloscope traces were recorded on aerial films having a speed rating of 800 GOST units. The pressure in the tube was monitored and controlled by an ion pump with cold electrodes.[3]

Fig. 4 shows the dependence of the current amplitude on the initial value of the anode voltage V_a. It will be seen that through appropriate selection of the circuit parameters (C, V_a and R_1) it is feasible in pulsed operation to obtain from a cold cathode currents of several amperes at initial voltages of 3-8 kv and up to 1000 amp at voltages of 100 kv (at low pressures of the order of 10^{-5}-10^{-2} mm Hg).

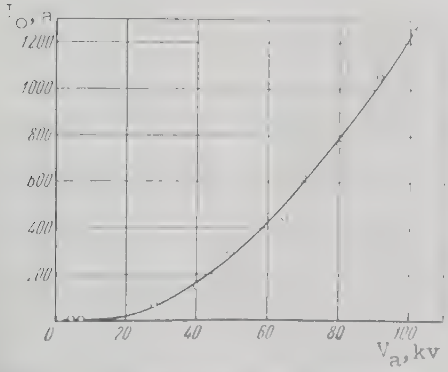

Fig. 4. Variation of the current amplitude with the initial voltage at an initial pressure of $5 \cdot 10^{-3}$ mm Hg.

In earlier experiments[4,5] the voltage was brought up to 450 kv (up to 700 kv in individual tests). The peak current in such cases attained 2000-3000 amp at very low pressures in the tube.

The crest values of the current I_o and the formation time τ as functions of the pressure are shown in Fig. 5. In the low (10^{-6}-10^{-5} mm Hg) pressure range I_o is nearly independent of the

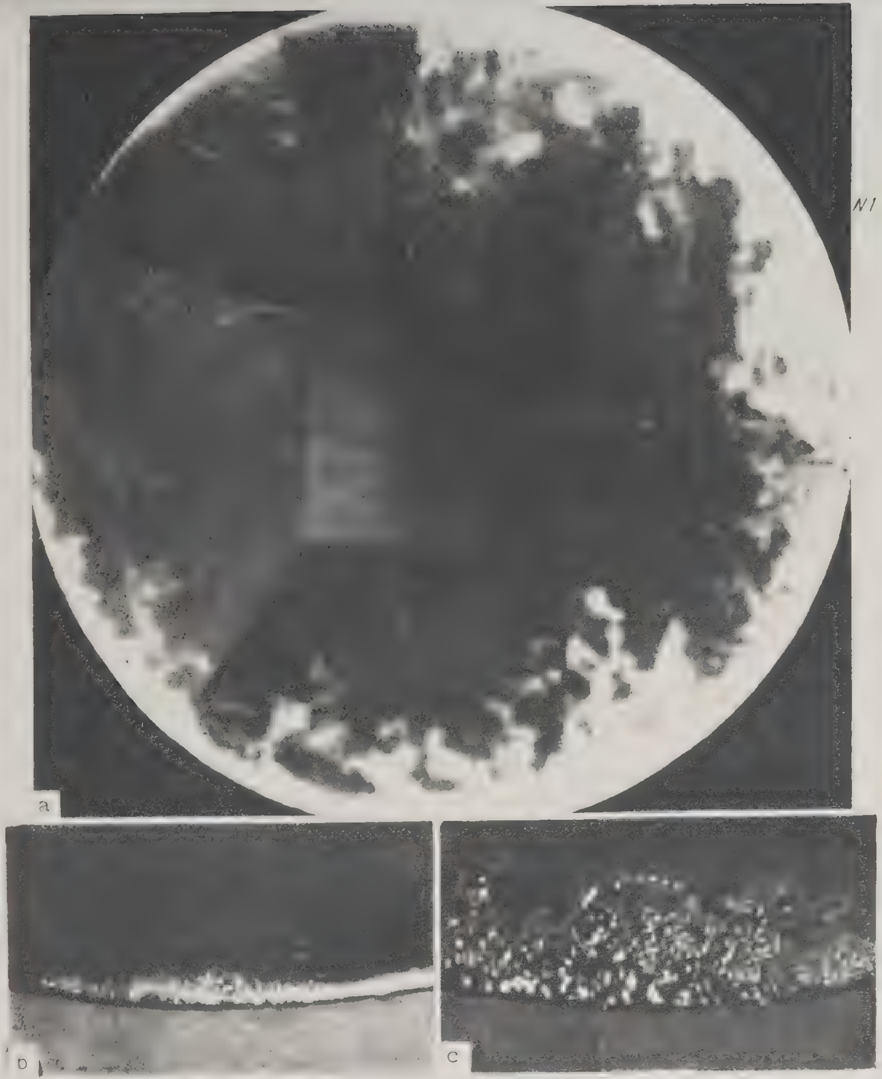

Fig. 2. a) Surface of cathode after 500 pulses; magnification 40 X. Edge of cathode b) after 10 pulses, c) after 480 pulses; magnification 180 X.

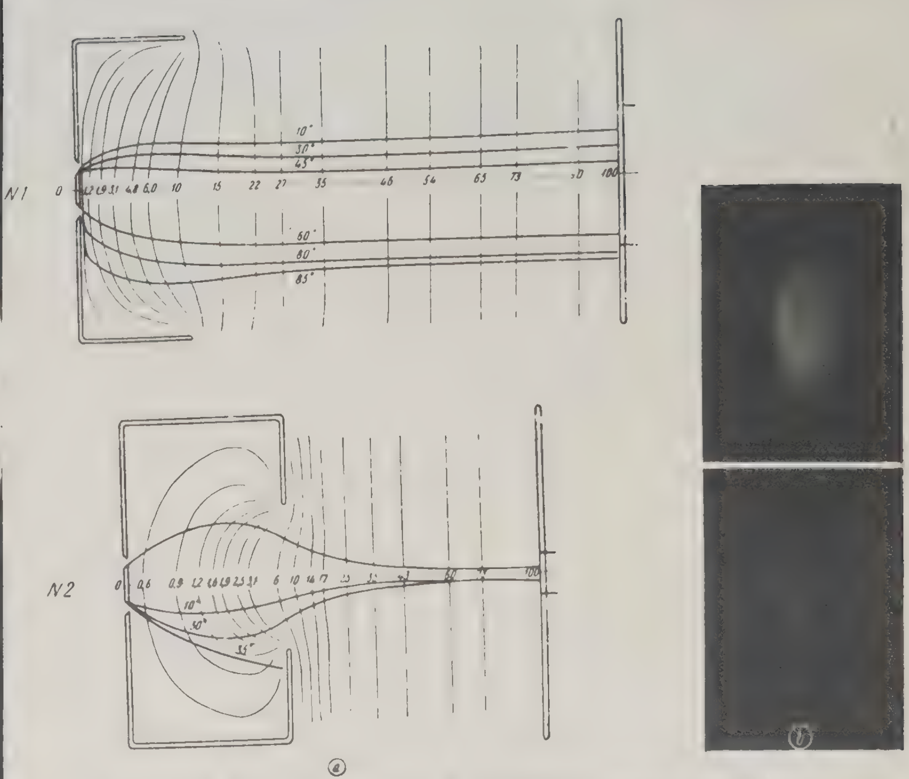
N1
0
10
15
22
27
35
46
54
65
73
100
10°
30°
45°
60°
80°
85°
N2
0
0,6
0,9
1,2
6
10
60
100
10°
50°
55°
a
b

Fig. 9.a) Distribution of external electric field for two cathodes (No.1 & No.2) and calculated electron trajectories for different escape angles; the horizontal marks on the anode indicate the dimensions of the actual experimental beam; V_a = = 100 kv. The firing electrode of cathode No.1 was a cylindrical cap 30 mm in diameter and 10 mm deep; the firing electrode of cathode No.2 was a cylindrical cup 30 mm in diameter and 13 mm deep with a 13 mm diameter aperture. b) x-ray pinhole camera photographs of the focal spots on the anode. Magnification 1.3 X.

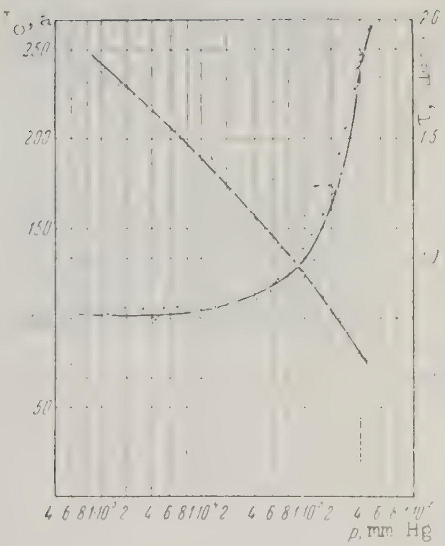

Fig. 5. Dependence of the current amplitude and discharge formation time in the initial pressure at an initial voltage of 40 kv.

initial pressure. The value of I_o in this region is apparently determined not by the pressure of residual gasses but by the density of the metal vapor and gases liberated during operation of the cathode. The value of τ depends on the conditions obtaining in the tube and varies with the pressure from 0.6 to 1.8 microsec.

The oscillographic studies showed that changing the initial pressure does not affect the amplitude of the current I_g in the firing gap. This may be explained by the fact that the width of the gap is appreciably smaller than the length of the mean free path of the electrons in the initial stages of the discharge. Measurements of the dimensions of the fused areas on the cathode and the pressures in the tube after individual pulses showed[6] that a local pressure of the order of 1 mm Hg is produced in the region of the firing gap during a pulse.

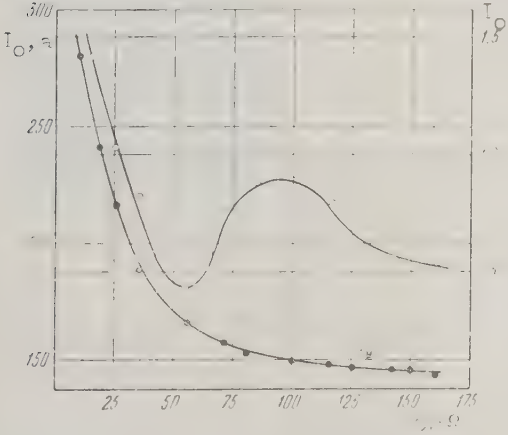

Fig. 6. Dependence of I_o and I_g on the resistance R_2 at an initial voltage of 50 kv and an initial pressure of $1 \cdot 10^{-2}$ mm Hg.

The parameters of the external circuit have an appreciable influence on the peak current in the firing gap. I_g increases with increasing pulse voltage. Decreasing the resistance R_2 (Fig. 3), which serves to limit the current in the gap, also leads to an increase in the current through the gap and, consequently, to enhanced emission. However, an excessive current in the gap leads to a reduction of the current in the main discharge due to redistribution of the currents in the corresponding circuits. The optimal value for R_2 under our experimental conditions (V_a = 50 kv, R_1 = 2 MΩ, $p = 10^{-3}$ mm Hg) proved to be 100 kilohm (Fig.6).

Fig. 7 shows oscillograms of the currents, recorded simultaneously under the above described conditions, in the main discharge (a) and in the firing gap (b). The time scales of the two oscillograms are the same, while the current (vertical) scales are different. It will be seen that the discharge in the firing gap first passes through a spark stage and then through a glow discharge stage (rectilinear part of trace). Development of the main discharge leads to a decrease of the gap current I_g, which falls off to its minimal value when the current in the main discharge attains its crest value.

Differences in current amplitude for cathodes of different materials are within the limits of the accuracy of measurement. The process of development of the discharge is virtually the same for cathodes of different materials.

Fig. 8 shows oscillograms of the voltage between the cathode K_1 and the anode (a) and between the firing electrode K_2 and the anode (b). On the basis of the above-described microscopic and oscillographic observations we can draw the following conclusions regarding the operation of a cathode with an igniting device.

When a pulse voltage is applied to the electrodes of the tube, field emission is initiated between the electrodes at the points where the potential gradient is the steepest. Because of the high current densities obtaining, there is

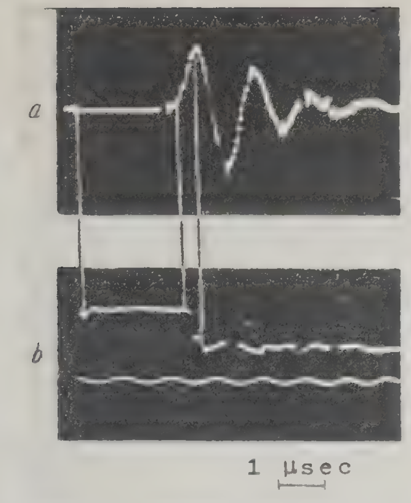

Fig. 7. Oscillograms of current: a) in main discharge, $I_o = 73$ amp, b) in firing gap, $I_g = 0.35$ amp.

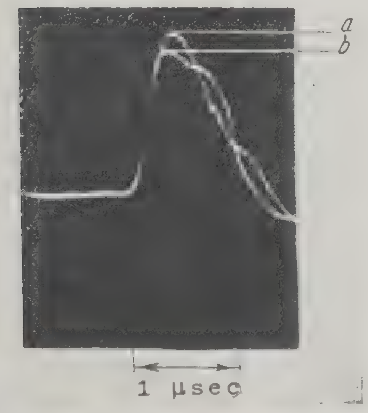

Fig. 8. Oscillograms of voltage: a) between K_1 and A, b) between K_2 and A (see Fig. 1).

strong heating of the edges of the electrode K_1 and local fusion of micro-inhomogeneities on its surface.* Spark breakthrough of the gap occurs; this is evinced by a bright flash between the electrodes K_1 and K_2. This stage is characterized by a rapid increase of the current in the firing gap (Fig. 7,b). As may be seen from the oscillograms, this growth continues for $5 \cdot 10^{-8}$-$1 \cdot 10^{-7}$ sec.

The spark discharge results in liberation of the adsorbed gases and cleansing of the surface over a small area. Consequently, the conditions for a repeat breakthrough at the same point are impaired and with succeeding pulses the spark breakthrough is displaced along the edge of the cathode. The marks of erosion of the cathode initiated by the breakthrough spark and aggravated with the further development of the main discharge are clearly discernible in microphotographs (Fig.2).

Approximate evaluation of the energy of the positive ions in the spark breakthrough stage and in the glow discharge stage, based on the oscillographic records of the currents and voltages yields a value of ~17 for the ratio W_1/W_2. Thus the energy transferred by the positive ions to the surface of the cathode in the spark stage is much greater than the energy evolved during the glow discharge. The current during the glow discharge stage does relatively little harm to the cathode surface; its effect is similar to ion etching.

Development of the discharge in the main gap limits the development of the discharge in the firing gap and, as I_o reaches its maximum value, I_g falls off almost to zero.

The development of the discharge in the main gap, i.e., between the electrodes K_1 and K_2 and the anode A, is determined by the initial conditions obtaining in the region of the cathode, namely:

a) the presence of a source of emission: highly heated spots at the edges of electrodes K_1 and K_2;

b) the presence of a cloud of metal vapor at a relatively elevated pressure near the surface of the cathode, which facilitates the passage of heavy currents, hundreds of times greater than the value "allowed" by the 3/2 law (due to compensation of the negative space charge by positive ions);

c) the presence of a strong electric field formed in the first phase of the discharge (this field is due to the cathode drop of potential at the surface of the combined K_1 and K_2 cathode); this field furthers enhanced electron emission over the entire surface of the cathode.

The joint influence of the fields associated with the cathode drop of potential at the cathode K_1 and the firing electrode K_2 (made in the form of a cylinder or cup) leads to satisfactory focusing of the electron beam. This is important where practical utilization of pulse discharges at low pressures is con-

---

*It has been shown in a number of recently published investigations[7] that the transition to field emission in a vacuum arc occurs at current densities of 10^7-10^8 amp/cm^2.

cerned, and, in particular, in developing sharp-focus x-ray pulse tubes and other devices wherein it is necessary to obtain electron (or ion) beams with a current density of the order of 10^5-10^6 amp/cm^2.

Electron-optical properties of the cathode

The studies of the mechanism of formation of the electron beam by a cathode with a firing electrode were carried out at voltages from 50 to 110 kv and initial pressures from 10^{-4} to 10^{-6} mm Hg.

The experimental tube with the movable anode has been described earlier (Ref. 1). The distance between the electrodes was varied from 1 to 17 cm. A special slip joint made it possible to change the shape of the cathode and the firing electrode.

The structure of the electron beam and the distribution of electron density over the cross section of the beam in the first phase of the discharge were determined by means of an x-ray pinhole camera with a 0.2 mm diameter aperture. These x-ray photographs were then photometered. As a preliminary step, we compared the image of the electron beam obtained by means of the pinhole camera for a large number of pulses (20-50) with the image of the beam trace for a single pulse, obtained on a fluorescent screen. This comparison showed that the structure and electron distribution in the beam given by the pinhole camera correspond to the electron optical picture of the beam due to a single pulse obtained on a fluorescent layer applied directly to the tube anode.

The formation of the electron beam is determined by the electric field distribution in the vicinity of the cathode. In the light of our studies, one can distinguish two fields responsible for this distribution: an "internal" field and an "external" field. The former is due to the cathode drop in the gap; it is localized in the vicinity of the electrode K_1. After passing through the "internal" field the electrons acquire high radial velocities with which they then enter the "external" field. The configuration of the "external" electric field is determined by the geometry of the firing electrode and corresponds to the field in the vacuum during the initial instants, i.e., before the positive space charge forming in the process of development of the discharge distorts the field.

The motion of the electrons of the main beam in the external field is subject to the laws of electron optics. Hence, the electron-optical properties of a cathode with a firing device are determined by the optical geometry of the cathode drop (the internal field) and the electron optics of the external field and can, therefore, be approximately evaluated.

Calculations of the focusing action of a cathode with a firing electrode were carried out for two types of cathodes (Fig. 9): cathode No.1 had the form of an open cylindrical cap, while cathode No.2 was in the form of a closed cup with a central 13 mm diameter aperture.

In carrying out the calculations we assumed that the internal field does not affect the distribution of the external field. The effect of the internal field is to impart high radial velocities to the electrons so that they enter the external field at large angles.

In order to evaluate the maximum energy $\mathcal{E}$ acquired by an electron in the internal field and the angle of emergence φ we measured the diameter of the focal spot on the anode for the case of a flat firing electrode.

If the initial velocity of the electrons, i.e., the velocity with which the electrons enter the external field, has only a radial component, the electron trajectories in a homogeneous electric field will have the form of parabolas[8] whose angle of divergence is given by

$$\varphi = 2 \text{ arc tan}(\mathcal{E}/V_a)^{1/2}$$

where ε is the initial energy of the electrons in volts.

Under our conditions $\varphi = 34^\circ$ which corresponds to $\varepsilon = 10$ kv.

The distribution of the external field was measured in an electrolytic bath. The limiting electron trajectories were calculated by the conventional trigonometric method. The calculations were carried out for different angles of emergence of the electrons from the cathode for the case of motion in vacuum. In our calculations we did not take into account distortion of the field by negative space charge and electrostatic interaction of the electrons in the beam. Nor did we take into account gas focusing, which is significant only at higher pressures.[9] The calculated field distributions and trajectories are shown in Fig. 9 a, where the actual beam diameters are also indicated.

The experimentally observed focal spots under these conditions are shown in Fig. 9 b. In view of the simplifying assumptions made in the calculations, the agreement may be considered satisfactory.

The influence of the geometry of the discharge gap and the voltage on the electrodes were studied with different separations between the cathode and anode. It was found that as the distance between the electrodes is increased the radius of the electron beam increases slowly at first (3-5 cm) and then more rapidly. Calculations show that this increase is due to electrostatic repulsion between the electrons of the beam.

Reduction of the voltage by 35% decreases the beam diameter by only 10%. At the same time, however, the intensity of the x-ray radiation falls off by a factor of more than two. This change in intensity is due not only to the decrease in beam current but also to the quadratic dependence of the radiation intensity on the voltage applied to the tube.

This weak dependence of the focusing characteristics of a cathode with an igniter electrode on the magnitude of the voltage is important where employment of such cathodes in pulse equipment is concerned, for it means that the diameter of the electron beam is not greatly affected by the shape of the voltage pulses.

In designing cathodes with a firing electrode it is also important to bear in mind that the position of the cathode K_1 in the opening in the firing electrode K_2 can materially affect the external field distribution and consequently the focusing properties of the system.

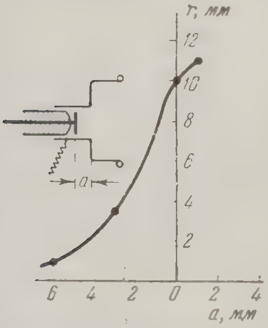

Fig. 10. Dependence of the electron beam radius on the depth d of recessing the cathode K_1 in the "neck" of the firing electrode K_2. V = 100 kv; cathode to anode distance = 4.6 cm = const.

We investigated the influence of the geometry of the firing device on the diameter of the electron beam using the electrode arrangement shown in Fig. 10. The depth a to which the cathode K_1 is recessed into the neck of the firing electrode K_2 was varied from -2 mm (protrusion) to 6 mm. The distance between the cathode K_1 and the anode A was kept constant at 4.6 cm.

The curve in Fig. 10 shows the variation of the radius of the main electron beam at the anode with a. It will be seen that the radius of the beam decreases as the cathode is moved deeper into the neck of the electrode K_2.

This decrease in beam diameter is due to changes in the distribution of the external field at the cathode surface. The principal focusing field in this case is produced by the neck of the firing electrode.

Conclusions

1. Cathodes with a firing electrode are capable of yielding large (~1000 amp) pulse currents. The current density in the beam may attain 10^5-10^6 amp/cm^2. Such cathodes can operate in a wide range of voltages (10-300 kv) and pressures (10^{-2}-10^{-6} mm Hg) both with single and periodic pulses. In the case of relatively low initial voltages (3-8 kv), the firing gap becomes

shorted by a metal bridge after about 300,000 pulses. The tube can be brought back into operating condition, i.e., the shorting bridge burnt out, by passing a heavy current through the firing gap. In practice this can be realized either by applying a higher voltage or by shorting out the limiting resistance R_2.

2. The electron-optical characteristics of a cathode with a firing electrode are determined by two electric fields: an internal and an external one. The internal field is produced by the cathode potential drop in the gap between K_1 and K_2. Its influence is localized in the vicinity of the surface of the cathode K_1. The electrons of the main beam acquire a high radial velocity in this field. The effective focusing field is the external field, the configuration of which is determined mainly by the geometry of the firing electrode.

3. We have established experimentally that it is feasible to control the intensity of electron beams with a peak pulse current of the order of 1000 amp and have suggested an electron-optical method of calculating the beam diameter in cold cathode tubes of this type.

4. The experiments have shown that the focusing characteristics of a cathode with a firing device are little dependent on the voltage on the tube.

5. In special experiments we have clarified the effect of the additional focusing field produced when the cathode K_1 is recessed into the neck of the firing electrode K_2.

6. The excellent emission characteristics, stability at large current densities and high voltages and economy of cold cathodes with a firing electrode and the possibility of focusing the high density pulsed beam produced by such cathodes gives reason to think that such devices will find wide application in the near future.

Physics Department of
Moscow State University

References

1. E.M.Reikhrudel', A.V.Kustova & A.G.Zimelev, Zhur.tekh.fiz., 24,1179 (1954).

2. G.V.Spivak, I.N.Prilezhaeva & E.A.Gruz, Izv. AN SSSR, Ser. fiz., 15, 409 (1951).

3. E.M.Reikhrudel', G.V.Smirnitskaia & A.I.Borisenko, Radiotekhnika i elektronika (Radio engineering and electronics), 1, 253 (1956).

4. E.M.Reikhrudel', A.A.Sanin & T.A.Titova, Zhur. tekh. fiz., 21, 746 (1951).

5. E.M.Reikhrudel' & T.A.Titova, Trudy Soveshchaniia po katodnoi elektronike (Transactions of the Conference on Cathode Electronics), Ukrainian SSSR Ac. of Sci., Kiev, 1951.

6. B.M.Berezovskii, Thesis, Moscow State University, 1952.

7. W.Dyke & J.Trolan, Phys. Rev., 89, 799 (1953); W.Dolan, W.Dyke, Phys. Rev., 95, 327 (1954).

8. E.Bruke & A.Rakhandel, Elektronnye pribory (Electronic tubes), M. 1949.

9. A.V.Kustova & E.M.Reikhrudel', Zhur.tekh.fiz., 24, 2183 (1954).

EFFECTS OCCURRING ON ELECTRODES DURING HIGH-ENERGY ELECTRIC BREAKTHROUGH IN A HIGH VACUUM

(Abstract - complete report in Zhur.tekh.fiz., 26, 489 (1956)).

- N.B.Rozanova & V.L.Granovskii

The report is devoted to an investigation of high-energy electric breakthrough in a high vacuum. Here breakthrough is understood to mean the initiation of a self-sustaining current having a falling current-voltage characteristic in the final stage of the process. We restricted our examination to gaps between solid, chemically simple (not activated), well outgassed electrodes with an approximately equal field intensity on both.

The initial and final stages of the breakthrough process in vacuum are essentially different. There appears to be little difference of opinion regarding the nature of the last stage: it is an arc in the vapor of the electrode material, accompanied by melting, evaporation and transfer of the material in the form of vapor and minute particles. There is still no unanimous opinion regarding the nature of the initial stage of the process (Refs. 1-6).

The experiments were carried out with gaps having the following configuration: cathode - hemispherical 10-12 mm in diameter; anode - flat; both electrodes polished; the distance d between the electrodes was varied from 0.1 to 3.0 mm. The measurements were made after evacuation and freezing out of the mercury vapor following prolonged heating of the electrodes by electron bombardment. The pressure of the residual gasses did not exceed $1 \cdot 10^{-5}$ mm Hg. The voltage was applied to the gap either over a prolonged period (in which case it was measured by means of a conventional sphere gap) or in short pulses (in which case the voltage was determined oscillographically.

To check the validity of the procedure we recorded the dependence of the breakthrough voltage V_{bt} on d with electrodes of iron and molybdenum; the electrode separation d was varied from 0.3 to 3 mm, V from 50-160 kv. It was found that $V_{bt} \approx K\sqrt{d}$, which agrees within the limits of the experimental error with the dependence found by Cranberg[5] in analyzing the data of different authors.

We investigated 1) the dependence of the breakthrough voltage on the material of the anode for which purpose we compared the values of V_{bt} for gaps differing only as regards the material of the anode and 2) the intensity of the x-ray radiation from the gaps in the pre-breakthrough stage. The anodes were made of Cu, Fe, Ni, W, Mo, Al and graphite. The measurements showed that V_{bt} increases for different anode materials in the following order: graphite, Al, Cu, (Fe,Ni), Mo and W. This sequence remains the same regardless of the material of the cathode and the width of the gap. The sequence of the tested anode materials as regards increasing yield of x-ray radiation per unit current (at a given voltage) is the following: graphite, Cu, Fe, Mo and W. The values of the radiation yield from graphite and tungsten anodes differed by an order of magnitude.

It follows that the electric strength of a vacuum gap does not decrease but, on the contrary, increases with increasing x-ray radiation yield in the pre-breakthrough stage. Inasmuch as increase of the x-ray radiation does not facilitate the breakthrough, it must be assumed that the x-ray radiation is not a causitive factor but merely an effect accompanying development of the breakthrough.

The increase in the electric strength of the gap is paralleled by the increase in the mechanical strength of the anode material as characterized by Young's modulus. This can be reconciled with Cranberg's hypothesis[5] regarding the formation of discharges in vacuum only if we make the additional assumption that particles of material are torn off the anode by the electric field.

"V.I.Lenin" All-Union Electrotechnical Institute

References

1. L.B.Snoddy, Phys. Rev., 37, 1678 (1931).
2. C.F.Bareford, Phil. Mag., 20, 825 (1935).
3. F.Bertein, C.R., 222, 64 (1946).
4. I.G.Trump & R.I.Van de Graaf, J.Appl.Phys., 18, 327 (1947).
5. L.Cranberg, J.Appl.Phys., 23, 518 (1952).
6. W.P.Dyke & J.K.Trolan, Phys.Rev., 89, 799 (1953).

DISCUSSION

N.D.Morgulis: Is there any guarantee that the results depend on the material of the electrode and not on the condition of the surface left by machining or treatment?

N.B.Rozanova: All the cathodes were prepared the same way. What is significant is that the values of the breakthrough voltage vary in a similar manner for different anode materials with the gap length d.

A.Z.Shakirov: What were the actual values of the breakthrough voltage?

N.B.Rozanova: Discharges across a 2 mm gap occurred at 85 to 121 kv depending on the anode material.

A.I.Vishnevskii: What kind of voltages did you use?

N.B.Rozanova: We tried both pulse and steady dc voltages.

M.A.Bruk: Did you determine the dependence of the breakthrough voltage on the temperature of the electrodes?

N.B.Rozanova: We did not make a special study of the temperature dependence, but we observed no significant temperature dependence up to the temperature of yellow heat.

G.V.Spivak: Can the breakthrough voltage of a gap be increased by coating the electrodes with another metal, for example by chrome-plating its surface?

N.B.Rozanova: We did not investigate the influence of thin coatings. It must be borne in mine that in such cases the degree of adhesion of the coating to the base metal may plan an important part.

V.L.Granovskii: It would be erroneous to assume that the breakdown mechanism is the same under all conditions. The decisive factor in one case may play only a secondary part in another case. For example, in gaps having the configuration of the field-emission projector (the cathode - a point, the anode - a sphere of large radius) the breakdown occurs as a result of heating of the cathode by the cold emission current. In this specific case, when the field at the anode is several orders of magnitude weaker than at the cathode, tearing out of particles from the anode by the electric field is obviously negligible. In the case of gaps having the ordinary configuration but a very short separation ($\ll 1$ mm) the principal cause of the breakthrough is apparently cold emission from the cathode and heating of the opposed areas of the anode with evaporation of the anode material. Obviously, here particles can be torn out of both electrodes by the field and in some cases may form a "bridge" between the electrodes. However, the process cannot lead to the formation of a vapor cloud in this case since the full voltage over such short gaps is too small. In both the noted cases the condition of breakdown is $E_c \approx 10^6$ v/cm = const. This condition does not hold for longer gaps. The value of E falls to $1 \cdot 10^5$ v/cm at the separation of about 1 cm. Calculations show that such fields are sufficient to detach particles from the surface of the metal and accelerate them to energies sufficient for their complete evaporation.

INVESTIGATION OF SECONDARY EMISSION FROM METALS UNDER BOMBARDMENT BY POSITIVE IONS OF ALKALI ELEMENTS

- U.A.Arifov & A.Kh.Aiukhanov

Introduction

There have been numerous investigations of secondary emission under the influence of positive ions. In these investigations the values of the coefficients of secondary ion-electron emission (γ) and secondary-ion emission (K) have been determined as functions of the nature, energy, ionization potential and angle of incidence of the primary ions and of the state and the temperature of the target. Investigators have studied the thresholds of these emission as well as the maximum energy and the distribution in energy of the secondary particles. Until recently there has been no doubt that secondary ion-electron emission does occur from "pure" metal surfaces.

Most investigators[1-10] assert that there exists a definite relationship between γ and the primary ion energy. Many authors[3-5,9-13] report observing a dependence of γ on the number of atoms adsorbed on the target surface or a decrease of γ with increasing temperature of the target. On the other hand, some authors[6] assert that γ is temperature independent, while others state that γ increases with the target temperature[14].

The question of the threshold of secondary ion-electron emission from pure metals is still unresolved. According to Ref. 14 this threshold lies near a bombarding ion energy of 10-20 ev; according to the data of Ref. 1 the threshold is as high as 100-200 ev; according to Ref. 9, γ is less than 1% at an ion energy of $\sim$1000 ev; according to Ref. 10 there is no emission at primary energies under several kev.

Actually there are no reliable data on the absolute values of the secondary-ion emission coefficient K in the literature. Some authors[1,13-17] assert that K is not greater than 10% for any pair of colliding particles. It is noted in recent reports[10,18] that this coefficient may be as large as 20%, but according to our data[9,19] K $\approx$ 40% at primary ion energies of $\sim$200 ev.

The question of the dependence of K on the temperature of the target has also not been clarified. For example, some authors[10,18] imply that the temperature of the target is a decisive factor, while others[6,9,20] assert that K is independent of the temperature.

Furthermore, there is still room for argument regarding the dependence of K on the energy of the primary ions. Many authors[1,6,10,12,13,18] consider this coefficient to be independent of the primary ion energy; Pavlov and Dobroliubski[5] assert that there is a direct dependence, while we[9] consider, on the contrary, that the dependence is an inverse one. Further, there are still no reliable data on the influence of the ionization potential (V_i) of the bombarding ions, the work function (φ) of the surface or the relative masses of the colliding particles on the value of K.

No one has investigated separately secondary emission proper and surface ionization which apparently accompanies it at high temperatures. Nor has there been an adequate study of the neutralization and absorption of the bombarding ions in connection with surface ionization, cathode sputtering and evaporation of particles from the target surface. Very little is known regarding the penetration of the bombarding ions into the depth of the target and their possible diffusion back to the target surface, depending on the parameters of the colliding particles.

In fact, there is yet no clear-cut definition of the term "ion-ion emission". All ions leaving the surface of the target at the instant of impact of the bombarding ions, regardless of the conditions of interaction, are generally called "secondary ions" or reflected ions[10,18].

The fact that different investigators studying secondary emission from pure metals under the influence of positive ion bombardment have come up with such divergent results suggests the existence of uncontrolled or unknown factors that become manifest in different ways under different experimental conditions.

It can be assumed that among such factors are the degree of purity and cleanliness of the investigated surfaces. Both the method of initial purification and cleaning of the target and impurities forming during the experiments (through adsorption of residual gases and vapors from the vacuum and even adsorption of the primary ions) could obviously seriously influence the secondary emission characteristics of the investigated surface. Obviously, the secondary emission parameters determined under such conditions may differ appreciably from the true parameters for ideally clean surfaces of pure metals. It must be noted, too, that there is a time factor involved where contamination with residual gases and the primary ions is concerned. With no control over the degree of contamination of the surface it is not surprising that different investigators have obtained different results for the targets of the same material.

The present report is devoted to the results obtained in experimental investigations by galvanometric and oscillographic methods of the values of γ and K for relatively pure tungsten, tantalum and molybdenum targets under bombardment by Li, Na, K, Rb and Cs ions of energies in the range from 150 to 1000 ev.

Galvanometric Measurement Procedure

All the galvanometric and oscillographic measurements were made in the tube shown in Fig. 1.

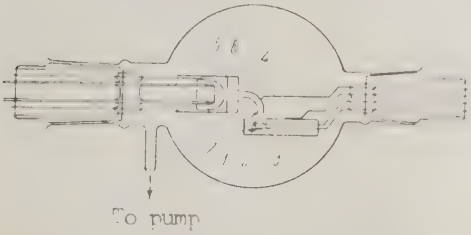

Fig. 1. Diagram of the vacuum tube: 1) spiral, 2) cup with alkali-halide salt, 3) slit, 4) cylindrical condenser, 5) shielding cylinder with two apertures, 6) collector, 7) target.

The apparatus comprised a source and a receiving section. The ion source consisted of the incandescent spiral 1 located above the cup 2 holding the alkali-halide salt. The ions produced by surface ionization on the spiral of the salt vapor were accelerated by the spiral-to-case field. The ion beam having passed through the slit was separated from the neutral particles, focused and directed to the target by the cylindrical condenser 4. The receiving section of the apparatus consisted of the shielding cylinder 5 with two apertures for entry of the primary ion beam, the collector 6 for receiving the secondary current and the target 7. The target was a strip of the investigated metal measuring about 30 x 5 x 0.03 mm.

Throughout the experiments we paid particular attention to cleanliness of the target surface. The tube was evacuated by means of a two-stage rotary forevacuum pump and a two-stage oil diffusion pump. The vacuum was checked by means of an ionization pressure gage. After evacuation to 10^{-6} mm Hg, usually accompanied by heating of the glass parts of the tube and degassing of the metallic parts by high-frequency current, we proceeded to cleaning of the target. To this end the target was heated to a high temperature by passing a current through it. The heating continued for several days with the vacuum traps always kept filled with liquid notrogen.

The criteria for cleanness of the target were 1) obtaining a definite reproducible value for the secondary-ion emission coefficient K at a given primary ion energy (for example, obtaining a value K $\approx$ 30% for almost all alkali ions bombarding W, Ta and Mo at a primary energy of 400 ev) and 2) the absence of electron emission from the surface of the cold or heated (to just under the thermionic emission threshold) target under bombardment with positive alkali metal ions.

If the surface is not sufficiently well cleaned, K under the above described

conditions remains below 20% and a noticeable secondary-electron emission is observed. After adequate cleaning of the target, K becomes equal to about 30% and remains stable at this value no matter how long the cleansing of the target at high temperatures is continued. However, if the target is allowed to cool even for a short time, the conditions on the surface of the target quickly change as a result of adsorption of part of the bombarding ions and the residual gas and vapor in the vacuum and, consequently, the coefficient of secondary-ion emission decreases and noticeable secondary-electron emission from the adsorbed films develops.

In view of the impossibility of eliminating the influence of adsorption of gas and vapor from the vacuum and ions from the primary beam at low temperatures of the target, all the secondary emission measurements from clean surfaces in all of the galvanometric experiments were carried out at a temperature near the threshold of thermionic emission for the given target material.

After the above described preparation of the target, the ion beam was energized only during the actual measurements, i.e., during an interval not exceeding a few periods of the galvanometer. Prior to each measurement (i.e., prior to obtaining each experimental point) the target was heated to about 2500°K at first for 3-4 minutes and then immediately before each measurement several times for brief periods. Then, having lowered the temperature of the target to the requisite level and initiated the beam by applying the appropriate potential to the outer "plate" of the cylindrical capacitor, we measured the current.

The measurements were made by means of a mirror galvanometer having a sensitivity of $6 \cdot 10^{-10}$ amp/mm/m with a period of 5 sec and an electrometer having a sensitivity of 10^{-12} amp/mm/m. The secondary and total currents were measured using the conventional galvanometric circuit for studying secondary processes.

Influence of Adsorbed Films on the Secondary Emission

In the processing of measuring K for a cold tungsten target we found that the application of a small (30-50 v) potential between the target and the collector at the beginning of the experiment, when the target is still clean, was not sufficient to completely stop the secondary ions. A galvanometer connected into the collector circuit at first continuously shows a current of positive ions, the magnitude of which decreases with increasing ion-retarding field. With the passage of time the current gradually passes through zero and with a retarding potential of 10-20 v between the target and collector the electron current attains saturation.

Evidently during the experiment there occurs on the surface of the initially clean target some process which leads to a reduction of the energy of the secondary ions and at the same time to the appearance and growth of a secondary-electron current. To study this effect we recorded the variation with time of the secondary-electron emission at different temperatures of the target. The primary ion beam was applied to a thoroughly cleaned (by prolonged and repeated heating at high temperatures) target kept at the temperature of the experiment. A field completely stopping the secondary ions was applied between the target and the collector (the experimentally determined value of the field was such that the galvanometer connected into the collector circuit showed no ion current at the initial instant of initiation of the primary ion beam).

Measurements of the secondary-electron emission showed that for all the investigated ions and targets the electron emission increases with time. The time-curves for secondary electron emission from a tantalum target bombarded with cesium ions at different temperatures are shown in Fig. 2. As may be seen from the figure all the curves exhibit saturation, with a definite saturation-current value corresponding to each temperature. It will be noted that the value of γ in the region of saturation at first increases with the temperature, then decreases. There is an optimum temperature - in this case 870°K (corresponding

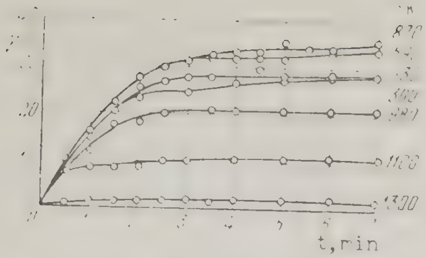

Fig. 2. Variation with time of the secondary-electron emission from adsorbed cesium films forming on initially clean tantalum bombarded with positive Cs ions at different temperatures of the target.

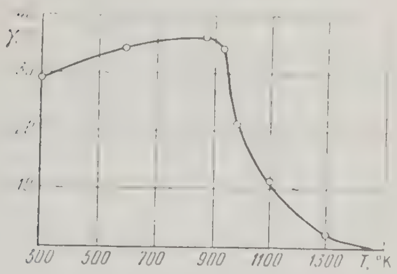

Fig. 3. Target-temperature dependence of the saturation secondary-electron current from the equilibrium films formed on the surface of a tantalum target under bombardment with positive Cs ions (curve based on the data of Fig.2).

to the optimal density of the adsorbed cesium film) - at which maximum emission is attained.

In Fig. 3 the values of γ in the region of saturation of the secondary emission (taken from Fig. 2) are plotted against the target temperature. This curve shows that at temperatures near the threshold of thermionic emission (~1350°K) the secondary-electron emission from a tantalum target is negligibly small ($\gamma < 1\%$). Thus, it can safely be asserted that the principal reason for secondary-electron emission from this target is the presence of an adsorbed film on the target surface. The fact that the emission is negligibly small at high temperatures of the target leads us to conclude that the emission of electrons by metals under the influence of bombardment by positive ions is not a property of these metals per se but is due to the formation of adsorbed films on their surface.

Observation of the variation with time of the secondary-ion currents from adsorbed coatings shows that the presence of such adsorbed films also influences the magnitude of the secondary-ion emission. However, in this case the regularities are more complex (they have been examined by us in Refs. 9 and 19).

The cited experimental data clearly indicate that in order to study the secondary emission characteristics of metals one must have them in highly pure form and take appropriate measures to preclude the formation of adsorbed films on the investigated surface. The most favorable conditions as regards prevention formation of such films obtain at high target temperatures, for under these conditions the "lifetime" of the adsorbed atoms is very short[21,22] and, consequently, the equilibrium coatings on the surface will be negligibly thin.

Calvanometric Investigation of the Secondary Emission from Metallic Surfaces at High Temperature

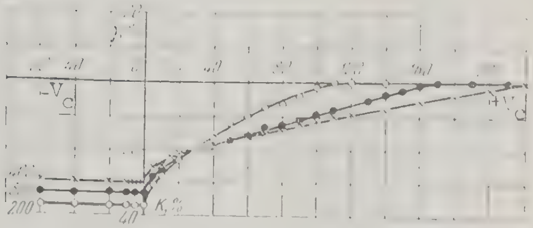

Fig. 4. Family of curves analogous to the current-voltage characteristics of the secondary emission from pure tantalum, heated to 1350°K, and bombarded by positive Na ions having primary energies of 200, 300 and 400 ev.

To study the secondary emission effects at a high temperature of the target we recorded the current-voltage characteristics in the cases of bombardment of a clean tantalum target held at 1350°K with Na, K, Rb and Cs ions of different energies.

The family of curves shown in Fig.4, characterizing the secondary emission from a tantalum target bombarded with 200, 300 and 400 ev sodium ions are analogous to the current-voltage characteristics since the ordinates are proportional to the secondary currents. It will be seen from the figure 1) that the secondary ion-electron emission at a target temperature of 1350° is negligibly small

($\gamma < 1\%$) and 2) that there is a linear dependence of the limiting energy of the secondary ions on the primary ion energy. However, the proportionality coefficients for ions of the different alkali metals proved to be different and showed a certain dependence on the mass of the bombarding ions. The family of curves obtained in bombarding a tantalum target heated to ~1350° by Na, K, Rb and Cs ions of 400 ev energy are shown in Fig. 5. As may be seen the limiting (maximum) energy of the secondary ions decreases with increasing mass of the bombarding ions. Measurements show that this dependence of the limiting secondary-ion energy on the energy and mass of the primary ions (Figs. 4 & 5) - as was noted earlier in Refs. 9, 10 & 19 - agrees within the limits of the experimental error with the familiar expression for elastic collision of ions with individual atoms of the target.

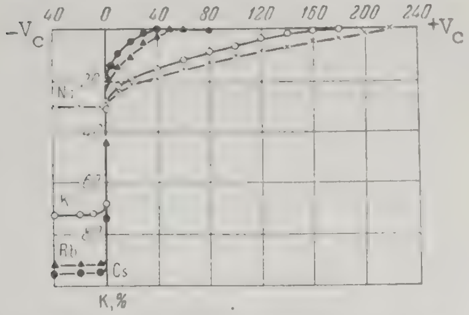

Fig. 5. Curves characterizing the secondary emission from a pure tantalum target, heated to 1350°K, bombarded with 400 ev positive Na, K, Rb and Cs ions.

These curves also give us some idea of the distribution in energy of the secondary ions. As may be seen from Fig. 5, part of the secondary ions have a continuous energy spectrum ranging from thermal energies to the maximum values determined by the elastic collision law. This distribution is difficult to explain if it is assumed that the secondary ions are scattered only by single collisions with the surface atoms of the target. On the contrary, the continuous distribution in energy indicated by experiment gives reason to assume that the primary atoms mainly undergo multiple collisions with atoms of the target located at a depth of several atomic layers.

It will also be seen from the curves of Fig. 5 that the values of K for bombardment of tantalum with all the different alkali metal ions at the same primary energy are nearly identical and equal to ~30%. It will also be noted that at high temperatures of the target the secondary-ion emission incident to bombardment with K, Rb and Cs ions (but not Na) is large, but differs from the different ions (about 72% for K, 91% for Rb and 96% for Cs). These "secondary" ions produced at a high temperature of the target have only thermal speeds. When the target temperature is reduced below a certain point these "secondary" thermal ions disappear entirely.

The variation of the coefficient of secondary emission from pure (clean) tungsten with the temperature of the target under bombardment by sodium and potassium ions is shown in Fig. 6. It follows from the character of these curves that up to about 1100°K the ionic emission consists largely of scattered primary ions (~30%); above this point there is a noticeable increase in secondary-ion emission with rising target temperature for potassium but virtually no increase for sodium.

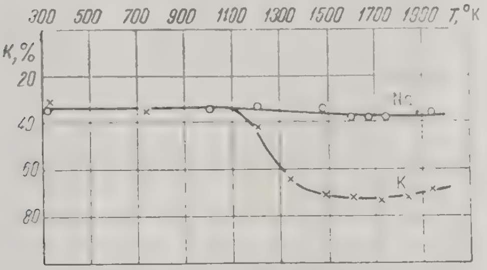

Fig. 6. Temperature dependence of K for pure tungsten bombarded with 560 ev Na and K ions.

Comparing the curves of Figs. 5 & 6, we conclude that at high temperatures of the target the secondary-ion emission produced by bombardment with K, Rb and Cs ions comprises a group of "secondary" ions with thermal speeds; the number of such ions is determined by the ratio between the work function φ of the target and the ionization potential of the bombarding ions and depends on the temperature of the target.

It may logically be assumed that some of the bombarding ions rebound from

the target, expending part of their energy on the process, while the rest of the ions lose all their initial energy and are adsorbed on the target. At high temperatures of the target these adsorbed atoms will evaporate in the form of ions and neutral atoms. The evaporating ions will have a) thermal speeds and b) a certain "inertia" (time lag) with respect to the primary ion beam since the statistical lifetime of the adsorbed atoms, which is determined by the heat of adsorption and the temperature of the target, will vary with the temperature from a fraction of a microsecond to many hours.

Thus it may be asserted that high target temperatures when $V_i < \varphi$ the secondary ion emission consists of scattered and evaporated ions.

Oscillographic Investigations of the Secondary Emission from Metallic Surfaces

As was shown by the above-described experiments, in order to obtain a true picture of the secondary processes occurring on clean, pure metals under the influence of positive ion bombardment it is essential to provide appropriate conditions insuring cleanliness of the investigated surface. Hence, in addition to using highly pure metals and degassing them under high vacuum by intense heating and utilizing an ion beam free of any admixture of neutral particles, it is also important to prevent contamination of the investigated surfaces through adsorption of bombarding ions and residual gases from the vacuum during the course of the experiments. This can be achieved by improving the vacuum condition and carrying out the measurements at a high temperature. At low temperatures of the target there will always be some contamination of its surface by the ions of the primary beam. In order to minimize this contamination at low temperatures one can either reduce the magnitude of the primary ionic current or shorten the bombardment and measuring time; this can be done by using an inertialess (electronic) device with automatic recording for making the measurements. The latter procedure (sharply reducing the bombardment time) proved to be not only more convenient from the experimental viewpoint but preferable in principle.

The method of double modulation[2], developed by the authors in collaboration with Starodubtsev for investigating secondary processes, is applicable to the case in question and permits of making rapid determinations of the distribution in energy of secondary particles and the coefficients of secondary ion, ion-electron and electron emissions under identical experimental conditions. By means of this method one can also separate the inertial (lagging) components of the secondary currents from the inertialess (instantaneous) components, modulated secondary currents from non-modulated ones and thus obtain oscillograms more fully characterizing the principal parameters of the secondary effects.

Briefly, the double modulation method may be described as follows: the primary ion beam (obtained by surface ionization of the appropriate molecules or from a gas discharge) accelerated by the source field enters the cylindrical condenser, where it is separated from neutral atoms and then modulated in intensity by a square-wave generator having a frequency of 500-1000 cps (first modulation) and then impinges on the target. The secondary emission current from the target is collected by a collector, the potential of which relative to the target is modulated by a sawtooth pulse generator having a frequency of 25 cps (second modulation). This current is applied to the input of the vertical-deflection amplifier of the oscillograph; the horizontal sweep of the oscillograph is synchronized with the sawtooth voltage generator.

If the process of secondary emission is inertialess (i.e., if there is no delay in the response) each primary ion-beam pulse will yield a corresponding secondary-current pulse which will produce an upward or downward (depending on whether the current is electronic or ionic) deflection of the oscillograph beam proportional to its magnitude. Inasmuch as commonly the frequency of the square-wave pulse is made several times greater than the frequency of the sawtooth pulses, we will have a number of secondary-current pulses during the period of each sweep. Obviously the envelope of the pulse crests will characterize the

dependence of the secondary current on the voltage between the target and collector. The horizontal straight line, corresponding to the sweep of the beam in the absence of primary current on the target, will be the null line separating the values of the secondary ion current from those of the secondary electron current. Hence we automatically obtain on the screen a stationary current-ampere characteristic of the secondary emission.

Fig. 7 shows an oscillogram characterizing the secondary emission from an equilibrium adsorbed film of rubidium on tantalum under bombardment by positive 400 ev Rb ions with the target at a temperature of 300°K.

Investigation of the secondary emission at low target temperatures.

In employing the galvanometric measurement procedure, before recording the indications of the instrument for each point of the $\gamma(V_c)$ and $K(V_c)$ curves it was necessary to carefully clean the target by heating it to a high temperature. Since in the time required to obtain the data for one point by the galvanometric procedure one can record several complete curves by the oscillographic method, we cleaned and outgassed the target (following the procedure described in the preceding section) only once prior to recording the entire oscillographic curve.

If we take a target coated with an adsorbed film, i.e., a target yielding a current-voltage characteristic such as that shown in Fig. 7, clean it by heating and then immediately after cooling record the characteristic of its emission, we obtain an entirely different picture. An oscillogram obtained for a clean cold tungsten target bombarded with 300 ev Rb ions is shown in Fig. 8. It will be seen that there is no secondary-electron emission from such a cold pure metal surface and that the secondary ions have a continuous energy spectrum ranging from thermal to the maximum values.

Thus for low target temperatures, provided the surface is sufficiently clean, we have the same regularities as were established by the galvanometric experiments at high temperatures of the target.

In contrast to the experiments carried out at high temperatures, when these regularities obtained over the entire time of the experiment, at low temperatures they are manifested only at the very beginning of the experiment, that is, so long as there is only negligible contamination of the surface. With time, various impurities accumulate on the cold surface and the shape of the oscillogram changes. Fig. 9 shows a series of oscillograms recorded at intervals (not equal) during continuous bombardment of an initially clean cold surface of a tungsten target with Rb ions, i.e., in the course of the process of development of an adsorbed film of Rb and residual gases on the initially clean tungsten surface. The oscillograms show that, whereas there is virtually no electron emission from the clean tungsten surface (Fig. 9,a), with the passage of time such emission appears and grows with increasing thickness of the adsorbed film (Fig. 9,b,c & d).

We could also readily obtain evidence of the reverse process: starting with a contaminated target, yielding oscillograms analogous to those of Fig. 9,b and Fig. 7 and gradually raising its temperature, we obtained an inverse sequency of curves terminating in one similar to that shown in Fig. 9,a. Thus it can be asserted that our oscillographic experiments with relatively cool targets have shown that intense secondary-electron emission is not an inherent property of pure metals. Such emission is due to the formation on the initially clean metal surface of impurity films by adsorption of primary ions and possibly residual gases from the vacuum.

Investigation of secondary emission at high target temperatures.

The double-modulation oscillographic method can be used for investigating secondary effects at high target temperatures as well. By means of this method one can investigate the dependence of the number of scattered ions and the energy

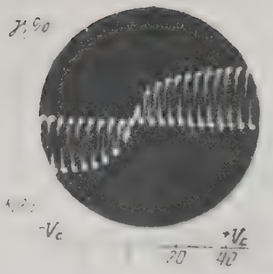

Fig. 7.

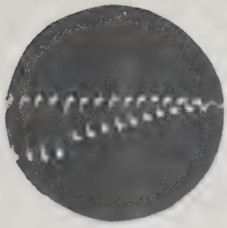

Fig. 8.

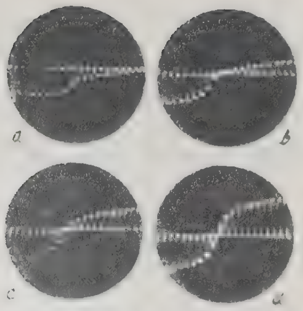

Fig. 9.

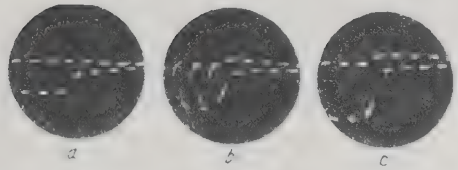

Fig. 10.

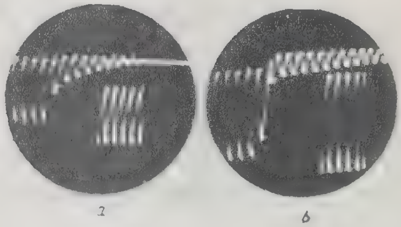

Fig. 12.

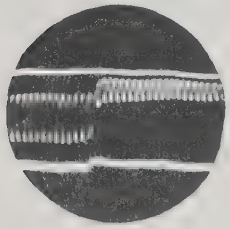

Fig. 11.

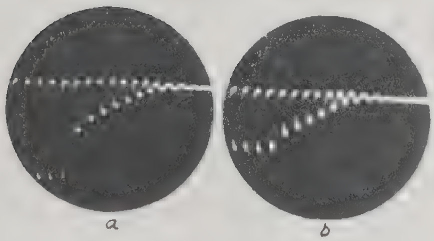

Fig. 13.

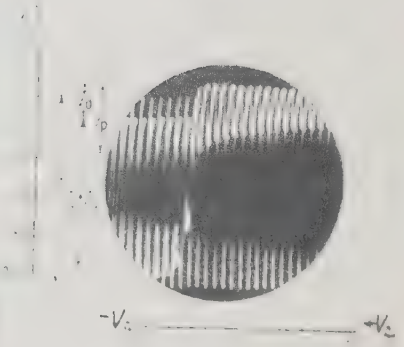

Fig. 14.

Fig. 7. Oscillogram of secondary emission from equilibrium Rb films adsorbed on a clean cold (300°K) tantalum target bombarded by positive 400 ev Rb ions.

Fig. 8. Oscillogram of secondary emission from a clean cold tungsten target bombarded with 300 ev Rb ions.

Fig. 9. Variation of the oscillograms characterizing the secondary emission from an initially cleaned and cooled (to 300°K) tungsten surface bombarded with 300 ev Rb ions with changes in the density of the coating of Rb atoms on the target surface.

Fig. 10. Oscillograms of secondary emission from pure tungsten bombarded with 400 ev Rv ions at target temperatures of 300°(a), 1100°(b) and 1350°K (c).

Fig. 11. Three successive oscillograms of the secondary current from a clean tungsten target (bombarded at a temperature of 1350°K by 600 ev K ions); these show the presence in the secondary-ion emission of ions forming as the result of diffusion of atoms from the depth of the target to the surface. Upper oscillogram recorded before incidence of the potassium ion beam on the target; middle spectrogram recorded with ion beam incident on the target; lower oscillogram recorded immediately after cutting off beam.

Fig. 12. Oscillograms of secondary emission from clean tantalum heated to 1300°K under bombardment with Cs ions of different energies: a) 170 ev and b) 570 ev.

Fig. 13. Oscillograms of secondary emission from clean tantalum under bombardment by 170 ev Rb ions at different temperatures of the target: a) 1300° and b) 300°K.

Fig. 14. Oscillogram of secondary emission from clean tantalum bombarded with 400 ev Rb ions with the target at 1300°K.

distribution in the secondary-ion emission on the target temperature and elucidate the inertial (response time) characteristics of the secondary ions.

In this part of the investigation the target was kept continuously heated to a certain temperature (constant filament current). The conditions of modulation of the primary beam and the operation of the horizontal sweep were identical with those described above. In Fig. 10 we reproduce three oscillograms obtained in bombarding a clean tungsten surface with Rb ions at room temperature (a), at $\sim 1100^{\circ}$K (b) and at $\sim 1350^{\circ}$K (c). The right-hand sides of these oscillograms represent the integral distribution in energy of the secondary (scattered) ions; it will readily be seen that they show no change despite an increase of more than 1000° in the temperature of the target. Hence the amount of back scattering of the primary ions is virtually independent of the target temperature.

From the results obtained in our investigation of secondary effects with the target at room temperature it follows that part of the ions of the primary beam ($K \approx 30\%$ at $E = 400$ ev) are elastically scattered (Fig. 5) while the rest ($\sim 70\%$) are neutralized. One can advance two hypotheses regarding the neutralized part of the primary ions: 1) they are also scattered with the capture of an electron or 2) having lost all their energy they are adsorbed on the target surface.

Leaving aside for the moment the question of the possibility of scattering of the neutralized part of the ions with capture of an electron, let us assume simply that part of the bombarding ions rebound without loss of momentum from the target surface, while the remaining part is adsorbed.

Now let the target be heated to a temperature high enough for the alkali metal atoms adsorbed on the surface to evaporate. The adsorbed atoms will evaporate partly in the form of ions and partly in the form of neutral atoms. The statistical "lifetime" of the adsorbed atoms will depend on their heat of adsorption and the temperature of the target.

In any case, however, the process of evaporation of the ions from the adsorbed layer will take a much longer time than a single collision of a primary ion with atoms of the target.

There can be no doubt that part of the ions rebounding virtually instantaneously from a heated target will have appreciable velocities and will synchronously repeat the modulation of the primary beam, i.e., will yield square-wave pulses on the oscillograph screen. On the other hand, the ions adsorbed on the target and transformed into adsorbed atoms will produce (as a result of thermal ionization) ion currents over some period of time, i.e., even during the intervals when no primary beam is incident on the target. When the primary pulse is

cut off, these surface ionization currents will decay exponentially distorting the square-wave pattern of the modulated signal on the oscilloscope. The resultant deformation of the curve will be different for different target temperatures; on the basis of this we can separate the instanteneously rebounding particles from the temporary "trapped" ones, i.e., from the ions, initially adsorbed and subsequently evaporating even in the absence of ion bombardment.

Let us examine the right-hand parts of the oscillograms reproduced in Fig. 10. They show that the secondary ions emitted from a cold clean target (Fig. 10, a), when there is no evaporation of adsorbed ions, comprise only scattered ions leaving the surface of the target with appreciable energies and with no delay; that is, the secondary emission faithfully duplicates the shape of the square-wave pulses of the modulated primary ion beam. As the temperature is increased the total secondary-ion current rises and at the same time a unique delay appears; an ion current, that falls off almost exponentially, persists after the primary beam is cut off (b). At high target temperatures the "lifetime" of the adsorbed atoms on the surface becomes very short and the entire evaporation process ends so quickly that the oscillograph pattern again becomes a square one (c). However, the height of the pulses at this temperature is greater and this increase is due to ions with thermal energies, which is clear evidence of the existence of a comparitively large group of secondary particles formed as the result of evaporation of adsorbed atoms in the form of ions, i.e., by surface ionization. Thus oscillographic investigation shows that the secondary ions produced by bombardment of a pure metal target at high temperatures with positive alkali element ions, in the case when $V_i < \varphi$, comprises two groups of ions: 1) scattered ions from the primary beam and 2) ions formed by surface ionization of initially adsorbed atoms.

Further analysis of the oscillograms obtained for targets at high temperatures shows that despite the apparently complete evaporation for the adsorbed part of the primary ions, the ion currents from the target do not entirely disappear during the first instants of the absence of the primary ion beam. In going from positive potentials on the collector to negative ones, the zero horizontal line of the current-voltage characteristic always jumps (shifts), indicating the presence of a non-modulated positive current with negative voltages on the collector.

Fig. 11 shows three successive oscillograms recorded on the same film with the tungsten target at $\sim 1350^{\circ}K$: a) with no ion beam impinging on the target (upper straight line), b) with a modulated potassium ion beam incident on the target (middle pattern) and c) after cutting off the ion beam (lower line with break). As may be seen from the patterns, in going from positive values of the potential on the collector to negative ones (middle and lower oscillograms), there appears a non-modulated ion current which was not in evidence prior to initiation of the primary beam and which persists some 3-4 seconds after the beam is cut off.

Thus at high target temperatures we have evidence of evaporation of ions with unusually long lifetimes. This is clearly not the evaporation of ordinary adsorbed atoms inasmuch as such atoms have a "lifetime" of the order of a fraction of a micro-second at such high target temperatures.

We ran a series of control experiments to get at the causes of this effect. The experiments showed that this effect occurs only at high values of the primary ion energy and target temperatures above $1000^{\circ}K$, as well as in the case when the value of the ionization potential of the bombarding ions is smaller than the work function of the bombarded target ($V_i < \varphi$).

We carried out measurements to determine the dependence of this effect on the energy of the primary bombarding ions, the temperature of the target and the value of ($V_i - \varphi$). Two oscillograms recorded at the same target temperature ($\sim 1300^{\circ}K$) with the tantalum target bombarded with 170 ev and with 570 ev Cs ions are reproduced in Fig. 12. It will be seen from the oscillograms that the

evaporation of the ions with a long lifetime occurs only at the high primary ion energy (b) and is virtually absent at a primary energy of 170 ev (a).

Fig. 13 shows two oscillograms recorded at the same energy (170 ev) of the primary Rb ions but with the clean tantalum target at different temperatures: $\sim 1300^{\circ}$ and 300°K. As may be seen from the left-hand oscillogram, at $\sim 1300^{\circ}$K the ion component of the secondary current consists of scattered and evaporated ions. The characteristic shift associated with high energy ions is not observed at this temperature. At a target temperature of 300°K, the secondary ion current consists only of scattered ions (b). The shift of the current-voltage characteristic occurring under bombardment with high energy primary ions and at high temperatures in cases when $V_i < \varphi$ is no longer observed under the same conditions when $V_i > \varphi$. For example, in the case of bombardment of W, Ta or Mo targets with Li or Na ions of energies under 1000 ev one can hardly distinguish between the oscillograms obtained at high temperatures of the target and those obtained at room temperature.

In seeking an explanation of this phenomenon it is useful to examine the general distribution in energy of the secondary ions. The fact that the secondary scattered ions are characterized by continuous spectrum, i.e., have all possible energy values from thermal to the maximum possible ones determined by elastic collision of the bombarding ions with the atoms of the target, forces us to assume that the scattering occurs not only as the result of single collisions with surface atoms but also a result of multiple collisions with atoms located down to a depth of several atomic layers.

In this case the decrease of the energy of the primary ions to values less than the heat of evaporation will occur not only on the surface of the target but also when the ions are at a depth of several atomic layers. Consequently, the evaporation of these ions will be determined not by the "lifetime" of ordinary adsorbed atoms but by the rate of diffusion of these ions from the given depth to the surface.

These "secondary" ions are obviously ions of the primary beam that have penetrated deep into the target. Their emergence to the surface is determined by the rate of ordinary thermal diffusion which, as we know, is relatively slow.

Thus investigation by means of the double-modulation oscillographic method shows that at high temperatures of the target the secondary-ion emission comprises, in addition to scattered and evaporated ions, yet a third component: "secondary" ions which appear as a result of diffusion back to the surface of primary ions initially penetrating into the depth of the target. Hereinafter we shall call these "diffusion ions".

Another advantage of the double-modulation procedure is that it allows of simultaneously recording the entire complex of secondary processes occurring at a given temperature and condition of the target surface and given value of the total primary-ion current. Recording the total current is accomplished by shorting the collector to the target and photographing the total current trace on the same film with the oscillogram giving the $K(V_c)$ curve.

Such a combined oscillogram obtained for a clean tantalum target bombarded at $\sim 1300^{\circ}$K by 400 ev Rb ions is reproduced in Fig. 14. One can readily see the absence of secondary-electron emission, the distribution in energy of the secondary ions, the presence of three different groups of ions (scattered - I_p, evaporated - I_u and diffusion - I_d) in the secondary ion emission and, finally, the total ion current I_{Σ} incident on the target. From this oscillogram one can evaluate the relative intensities of the individual secondary components. One can distinguish between these components on the basis of their specific characteristics.

The ions of the primary beam scattered as the result of single and multiple collisions with atoms of the target almost instantaneously repeat the modulation of the primary beam and their energy spectrum extends from zero to the values determined by the elastic collision law (right-hand sides of Figs. 10 & 14).

The ions adsorbed by the lattice and remaining on the surface in the form of

adsorbed atoms will partially evaporate in the form of ions, presumably in accordance with the Saha-Langmuir formula; the kinetics of their evaporation imposes a relatively short "lifetime", the exact value depending on the heat of adsorption and the temperature of the target. Depending on the conditions obtaining and their "lifetime" on the surface these ions may either instantaneously repeat the modulation of the primary beam (Fig. 10,c) or may be manifested in the form of rising and falling exponential curves (Fig. 10,b).

The existence of the third group of ions - the diffusion ions - is evidenced by the presence of a non-modulated current of positive ions which shifts the modulated current pattern by an amount equal to the value of this constant current and which appears whenever the collector potential becomes negative.

Conclusions

1. It has been established by the galvanometric and oscillographic measurements that the secondary-electron emission from clean pure metals (W, Ta & Mo) under bombardment with positive ions is small ($\gamma < 1\%$). The value of the secondary-electron emission coefficient γ depends on the density of the coating formed by the adsorbed atoms; the density of the coating in turn depends on the temperature of the metal and the rate of arrival of "impurities". Thus the temperature, which determines the equilibrium thickness of the adsorbed film, also determines the value of γ. There exists an equilibrium density of the film at which the electron-ion emission is maximum. The secondary electrons have a continuous energy spectrum extending to several tens of electron volts. It must be concluded therefore that the secondary-electron emission from W, Ta and Mo observed by many investigators is due primarily to a surface film of adsorbed atoms.

2. Our investigations have shown that the secondary-ion emission from heated metal targets in the case when the mass of the target atoms is greater than the mass of the bombarding ions and $V_i < \varphi$ comprises three groups of different ions: a) scattered, b) evaporated (i.e., initially adsorbed in the form of atoms and almost immediately ionized and evaporated) and c) diffusion (i.e., ions penetrating to some depth and then diffusing back to the target surface).

We found that in the case of a clean metal surface the scattered ions are characterized by an almost linear continuous energy distribution from zero to the limiting value set by the law of elastic collisions and we established that the number of scattered ions is virtually independent of the target temperature.

Oscillographic recording of the distribution in energy of the evaporating and diffusing ions showed that the ions of these groups have only thermal energies and that the magnitudes of the respective ion currents depend on the temperature of the target, the ionization potential of the bombarding atoms and the work function of the target surface. Our studies showed that necessary conditions for the appearance of the group of diffusion ions are a high target temperature ($>1000^{\circ}$K) and an appreciable energy ($>$250-300 ev) of the primary ions.

3. We developed a procedure for obtaining oscillographic records of the complex of simultaneously occurring secondary processes and recorded such oscillograms. Through analysis of these oscillograms, it is possible to evaluate the relative magnitude of each group of secondary ions at different temperatures and surface conditions of the target.

In conclusion the writers desire to thank S.V.Starodubtsev for his interest in the work and discussion of the results.

Physical-Technical Institute of the
Academy of Sciences of the Uzbeck SSR

References

1. N.Campbell, Phil. Mag., 29, 783 (1915).
2. A.L.Klein, Phys. Rev., 26, 800 (1925).
3. W.J.Jackson, Phys. Rev., 28, 524 (1926).
4. P.B.Moon, Proc.Cambr.Phil.Soc., 27, 570 (1931).
5. V.I.Pavlov & A.N.Dobroliubskii, Uchenye zapiski LGU, Seriia fizich. (Scientific records of Leningrad State Unversity, Physical Series) 1, 65 (1934).
6. V.I.Pavlov & S.V.Starodubtsev, Zhur.eksp.i teor.fiz., 7, 409 (1937).
7. L.M.Nemenov & A.S.Fediurko, Zhur.eksp.i teor.fiz., 9, 532 (1939).
8. M.E.Gurtovoi, Zhur.eksp.i teor.fiz., 10, 483 (1940).
9. U.A.Arifov & A.Kh.Aiukhanov, Doklady (Reports) of the Academy of Sciences of the Uzbek SSR), 4, 12 (1951).
10. M.A.Eremeev, Doklady AN SSSR, 79, 5 (1951).
11. W.L.Cheney, Phys. Rev., 10, 325 (1917).
12. W.J.Jackson, Phys. Rev., 30, 473 (1927).
13. M.L.Oliphant, Proc.Cambr.Phil.Soc., 24, 451 (1928).
14. V.I.Pavlov & S.V.Starodubtsev, Zhur.eksp.i teor.fiz., 7, 424 (1937).
15. J.Koch, ZS.f.Phys., 100, 685 (1936).
16. W.Weith, Ann.d.Phys., 29, 800 (1937).
17. H.Paetow & W.Walcher, XS.f.Phys., 110, 69 (1938).
18. M.A.Eremeev & E.V.Shestukhina, Zhur.tekh.fiz., 22, 1262, 1268 (1952); M.A.Eremeev & V.G.Iur'ev, Zhur.tekh.fiz., 22, 1290 (1952); M.A.Eremeev & T.L. Matskevich, Zhur.tekh.fiz., 22, 1296 (1952).
19. U.A.Arifov & A.Kh.Aiukhanov, Zhur.eksp.i teor.fiz., 27, 87 (1954).
20. U.A.Arifov, A.Kh.Aiukhanov & S.V.Starodubtsev, Zhur.eksp.i teor.fiz., 26, 714 (1954).
21. S.V.Starodubtsev, Zhur. eksp.i teor.fiz., 19, 215 (1949).
22. U.A.Arifov, V.M.Lovtsov & A.Kh.Aiukhanov, Doklady (Reports) of the Academy of Sciences of the Uzbek SSR, 10, 7 (1949).

SECONDARY-ELECTRON EMISSION UNDER THE INFLUENCE OF POSITIVE IONS AND NEUTRAL PARTICLES

- V.G.Tel'kovskii

Most investigators studying secondary-electron emission did not use targets with an ideally clean surface; consequently it is impossible to compare the results of their measurements. Only a few investigators employed procedures calculated to insure an atomically pure target surface. Hagstrum[1], for example, heated his target in vacuum for a prolonged time and effected his measurements of the emission from the cold target within an interval shorter than the time necessary for the formation of a monatomic layer of gas on its surface.

Other investigators measured the emission from hot targets (Oliphant[2] at 1000°; Eremeev et al[3] at 900°), but in all cases the temperature was relatively low, since at higher temperatures thermionic emission makes accurate secondary-emission measurements impossible. In addition to "decontamination" by heating, a number of investigators resorted to renewing the target surface by deposition of the same material on the target surface between measurements (Schwartz[4]).

However, the results of even these painstaking studies are contradictory: for example, Oliphant reports observing an appreciable number of electrons from a nickel target bombarded with potassium ions, while according to Eremeev et al potassium ions eject no electrons at all from metal targets. The ion energy intervals in both investigations were almost identical. On the basis of their measurements of the emission from tantalum, tungsten and other metals Eremeev[2] and Arifov & Aiukhanov[5] conclude that there is no secondary-electron emission from pure metals. On the other hand, Hagstrum[1] working with the same materials and in the same energy ranges but bombarding his targets with noble gas ions obtained large coefficients of secondary emission.

It might be assumed that this divergence can be explained not only by different degrees of cleanliness of the target surface but also by the presence in the secondary emission of negative ions which none of the above mentioned investigators took into account.

It must be noted that most measurements were made with primary ions of low energy (up to 2-3 kev) and only a few with high-energy ions (above 50 kev). There have been virtually no experiments with clean targets in the interval of medium energies.

Accordingly, the purpose of the present investigation was to determine the fundamental regularities of secondary-electron emission from ideally clean metal surfaces in the range of medium bombarding-ion energies.

Our apparatus was essentially a large mass spectrometer having a length of about 4 meters and a beam deflection angle of 25°. The slit assembly limited the angle of divergence of the ions to ±3°. The target was located near the focus of the convergent ion beam.

The positive ion beam was produced by a source employing an arc discharge in a magnetic field. The ions were extracted from the source by the magnetic field. The ion current density at the point of emergence of the ions from the gas-discharge chamber attained 100 ma/cm^2. The apparatus was evacuated by two N2T pumps and one N5T pump. The differential evacuation system made it possible to maintain a 1:1000 pressure difference between the sections of the apparatus housing the source and the measurement chamber.

Contamination of the target with oil from the diffusion pump and other condensing substances was obviated by the use of traps and protective baffles maintained at the boiling point of nitrogen. The residual gas pressure in the vicinity of the target at the time of measurement did not exceed $3 \cdot 10^{-8}$ mm Hg. The design of the apparatus provided for heating the target to 2300-2800° prior to making measurements. The temperature at which the measurements were made was selected so that the thermionic emission would be considerably lower than the

secondary-electron emission. For most metals the measurement temperature range was from 1300 to 1500°. The use of the 200-500 oersted magnetic field directed perpendicularly to the ion beam in the measurement chamber, in conjunction with an extracting electric field, wholly prevented any negative ions emitted by the target from arriving at the secondary-electron collector.

The neutral particles were obtained by resonance neutralization of positive ions. The neutralization chamber was equipped with a system of apertures that made it possible to maintain a 1 to 500 pressure differential; the angle of emergence of particles was limited to ±0.5° by an appropriate aperture. This made it possible to obtain monoenergetic beams of neutral particles while maintaining the requisite high vacuum in the measurement section. The neutral particles were separated by a magnetic field which deflected the non-neutralized ions. Since the intensity of the beam could vary during the time of the experiment, the number of neutral atoms was measured by the method of recording the momenta of the particles. The set-up employed allowed of measuring the particle flux density (10^{13}-10^{14} cm^{-2} sec^{-1}) in the experimental energy interval with an accuracy of a few percent. Preliminary experiments showed that even with minor contamination of the target surface with extraneous atoms (on the order of a monolayer) the secondary-electron emission coefficient loses all significance as a physical constant, inasmuch as in such cases it depends on the flux density of the bombarding ions or neutral atoms. This effect was utilized in our experiments for checking the state (cleanliness) of the target surface. The target was assumed to be ideally clean only if the secondary-electron emission coefficient remained constant within the limits of the measurement error (±1%) through a 1 to 1000 change in the ion current density (from 10^{-7} amp/cm^2 to 10^{-4} amp/cm^2).

Our measurements showed that prolonged heating alone does not result in complete cleaning of the surface. Chemical and spectroscopic analyses of specimens of molybdenum and other metals established that they contain non-volatile compounds (carbides, nitrides, silicides, etc.). The ions of the beam may also be a source of contamination. An ideally clean surface is obtained only after etching the target with argon ions.

In our secondary-electron emission experiments we used the targets of Mo, Zr, Ni, Ta, Cu and graphite. The targets were bombarded with H, He, N, Ne, Ar and Mo ions and neutral inert gas ions. The best reproducibility was obtained with molybdenum and zirconium targets since the cleaning and degassing were most effective for these metals. The other materials yielded the same regularities but with a somewhat greater scattering of the experimental points.

A study of the influence of the target angle showed that in the investigated angular interval (20 to 90°) the magnitude of the secondary-electron emission coefficient is approximately inversely proportional to the sine of the angle of incidence of the beam. The dependence of the secondary-electron emission on the ion energy is best shown graphically in speed coordinates, for in this case it is characterized by a straight line. The variation of the secondary-electron emission from a molybdenum target as a function of the velocity of different bombarding ions is shown in Figs. 1 & 2.

It will be seen that the coefficient of secondary-electron emission for all the investigated ions and metallic targets increases linearly with the ion velocity up to $v = 2 \cdot 10^8$ cm/sec. With further increase in the speed of the bombarding ions (the experimental data in this region were obtained only with

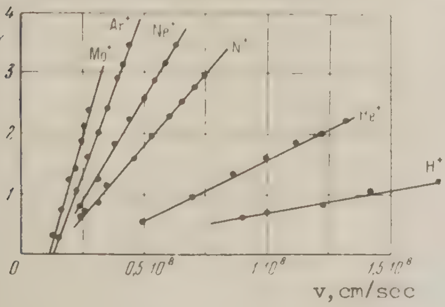

Fig. 1. Dependence of the coefficient of secondary-electron emission on the velocity of the ions bombarding a molybdenum target.

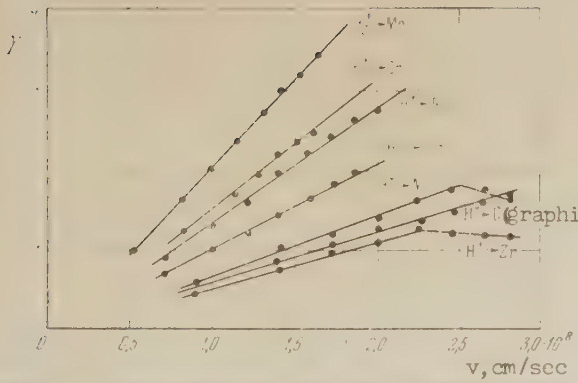

Fig. 2. Dependence of the coefficient of secondary-electron emission on the velocity of the hydrogen ions bombarding targets of molybdenum, zirconium and carbon.

proton beams) there is observed a flat maximum in the region of $2.5 \cdot 10^8$ cm/sec, followed by a gradual decrease which can be explained by increasing penetration of the ions into the depth of the target. The electron emission from graphite under the influence of protons increases monotonically with increasing energy. The absence of a maximum in this case is presumably connected with the lower concentration of electrons in graphite.

All the experimental curves show evidence of a fairly definite threshold of secondary-electron emission. There is no clear correlation between the magnitude of the ion velocity corresponding to the threshold and the material of the target or the type of ions. In the investigated cases, the threshold velocities lie in the interval from $0.5 \cdot 10^7$ to $2 \cdot 10^7$ cm/sec. Experiments showed that at argon and molybdenum ion speeds of $1 \cdot 10^7$ cm/sec (energies of 4 and 6 kev respectively) there is no measureable (accuracy 0.1%) secondary emission from a molybdenum target.

We studied the velocity distribution of the secondary electrons by the method of retarding potentials. The design of our apparatus permitted of measuring only the velocity component directed along the lines of force of the magnetic field oriented perpendicularly to the ion trajectories. In order to evaluate the influence of the magnetic field we carried out measurements of the electron velocity distribution with an ordinary spherical collector for the case of a low negative ion emission under bombardment of the target with ions of different energies. The results showed that the magnetic field does not distort the shape of the distribution. The characteristic retarding potential curves plotted on a semilogarithmic scale are shown in Fig. 3.

It will be seen that the characteristics are straight lines; consequently, the velocity distribution of the secondary electrons is Maxwellian. The mean energy of the secondary electrons, which one might call the "temperature" of the secondary electrons, does not depend on the energy of the bombarding ions. It varies little for all the investigated ions and targets and always lies in the interval from 5 to 8 ev.

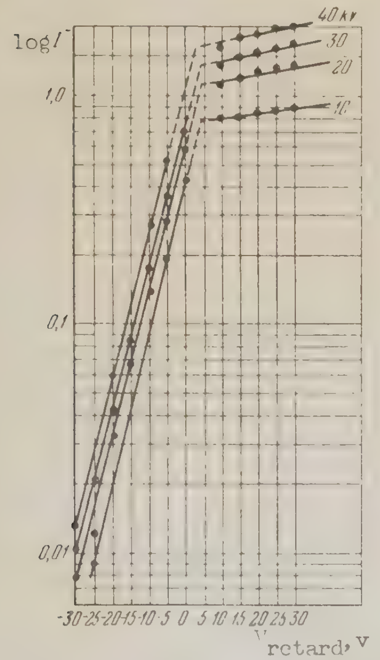

Fig. 3. Log I vs retarding potential curves characterizing secondary-electron emission from targets bombarded with ions of different energies.

The coefficient of secondary-electron emission for molecular ions, as for atomic ions, is proportional to their speed (Fig. 2). At equal ion speeds the secondary-electron emission is proportional to the mass of the bombarding molecular ions. Analogous dependences were obtained for the secondary-electron emission from Ta, Ni, Cu, Mo and graphite under bombardment with molecular and atomic nitrogen ions. The rigorous proportionality between the coefficient of secondary-electron emission and the number of particles comprising the molecular ions leads us to conclude that the molecular ions break up into their constituent particles

at the metal boundary and that the disintegration products interact with the metal analogously to single ions or atoms having the same velocity.

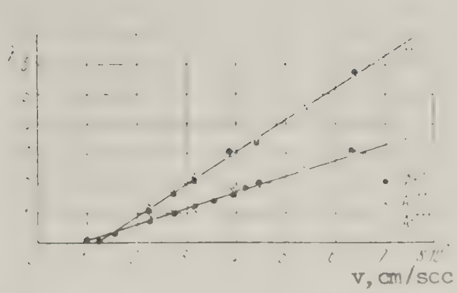

Fig. 4. Dependence of the secondary-electron emission coefficients on the velocity of argon ions with different charges bombarding molybdenum and zirconium targets.

Fig. 4 shows the dependence of the secondary-electron emission from molybdenum and zirconium targets on the velocity of bombarding argon ions with different values of charge (the maximum ion speeds corresponded to an energy of 120 kev for molybdenum and 80 kev for zirconium).

It will be seen that for both targets the secondary-electron emission coefficients are virtually identical for Ar^+, Ar^{++} and Ar^{+++} ions having the same velocities. Obviously, the secondary-electron emission is determined only by the energy of the bombarding particle and not by the magnitude of its charge.

To verify further the independence of the secondary-electron emission coefficient on the particle charge we carried out comparative measurements of the emission produced by bombardment with ions and neutral atoms of helium, nitrogen and argon. The results showed that under the same experimental conditions the secondary-electron emission under the influence of neutral atoms is equal, within the accuracy of measurement, to the secondary-electron emission under the influence of ions. Hence the theory of potential-ejection of secondary electrons is not applicable to pure metals.

Conclusions

Our investigation of the basic regularities of secondary-electron emission from ideally clean metal surfaces established the following:

1) secondary-electron emission is a volume effect (rather than simply a surface effect);

2) the secondary-electron emission is proportional to the velocity of the bombarding ions and has a threshold at velocities in the neighborhood of $1 \cdot 10^7$ cm/sec;

3) molecular ions split into their constituent particles (ions or atoms) at the target surface;

4) the velocity distribution of the secondary electrons is Maxwellian;

5) the secondary-electron emission is determined only by the energy of the bombarding particles and is independent of their charge.

The author desires to thank L.A.Artsimovich, I.N.Golovin, S.Iu.Luk'ianov and G.Ia.Shchepkin for suggesting the subject, valuable discussions and support and encouragement in carrying out the investigation. The author also desires to acknowledge his obligation to B.V.Panin for aid in carrying out the experiments and discussion of the results and T.I.Morozov and D.P.Ivanov, former graduate students at Moscow State University, for their active participation in developing procedures for obtaining and detecting neutral particles.

References

1. H.Hagstrum, Phys.Rev., 89, 244 (1953); 91,543 (1953); 96,325 (1954).
2. M.Oliphant, Proc. Roy. Soc., 127,373 (1930).
3. M.A.Eremeev and others, Zhur.tekh.fiz., 22, 1262, 1290 (1952).
4. M.Schwartz & P.L.Copeland, Phys. Rev., 96, 1466 (1954).
5. U.A.Arifov & A.Kh.Aiukhanov, Trudy Soveshchaniia po katodnoi elektronike (Transactions of the Conference on Cathode Electronics) Ukrainian SSR Ac. of Sci., Kiev, 1952.

DISCUSSION

N.D.Morgulis: To what do you attribute the appearance of the threshold of secondary ion-electron emission?

V.G.Tel'kovskii: I am unable to answer this question at present.

N.D.Morgulis: We know from the literature that in experiments of this kind there is observed a clear dependence of the secondary emission on the ion charge for low ion energies; I understand you observed no such dependence.

V.G.Tel'kovskii: We did not carry out measurements at low ion energies.

N.D.Morgulis: How do you explain the break in the $\gamma(v)$ curves?

V.G.Tel'kovskii: I believe the breaks are due to penetration of the bombarding particles into the depth of the target.

N.D.Morgulis: Did you investigate disintegration of the target under the influence of the bombarding ions?

V.G.Tel'kovskii: We did. The disintegration is strongly dependent on the material of the target and independent of the beam density.

A.P.Komar: How did you obtain a clean surface in the case of Zr?

V.G.Tel'kovskii: We cleaned it by cathode sputtering. In other words, preparation of the targets included not only heating but cathode sputtering of their surface.

L.N.Dobretsov: How did you record the retarding potential curves?

V.G.Tel'kovskii: We recorded these curves both with a magnetic field and in its absence; the difference was minor.

A.R.Rumiantsev: It is known that if the ion beam is incident on the target at an angle some ions may be reflected at an angle close to that of mirror reflection. Could not some of these reflected ions fall on the collector?

V.G.Tel'kovskii: Mirror reflection is observed at small angles of incidence. In our case the ions were incident at an angle of 45° and, furthermore, the measurement chamber was maintained at a potential of 150 v.

M.E.Gurtovoi: How do you interpret the fact that the effect does not depend on the ion charge? At low ion energies there must be ejection of electrons by the incident ions as has been shown by Hagstrum whose experiments were carried out under conditions of very high vacuum.

V.G.Tel'kovskii: I do not agree with you. Hagstrum's work was not carried out with ideally clean surfaces despite the high vacuum conditions provided.

PROCESSES OCCURRING ON METAL SURFACES DURING CATHODE SPUTTERING

- G.V.Spivak, V.E.Iurasova, I.N.Prilezhaeva & E.K.Pravdina

One can distinguish several stages in the alterations taking place on the surface of a metallic cathode in the course of sputtering[1]: 1) cleansing or decontamination of the surface, 2) ionic etching during which the grain boundaries are brought out, 3) formation of a crystal structure inside the grains and 4) fusion of the figures formed in the preceding stages. The rate at which these stages follow each other and their duration depend on the sputtering conditions.

Ionic etching has recently been used for investigating the structure of metals and alloys.[2] This method has a number of advantages as compared with chemical etching and evaporation under vacuum to bring out the structure[3]. Under ion bombardment no oxide film forms on the metal surface as in chemical etching; in contrast to the other methods, sputtering can be carried out in a wide range of temperatures; finally, ion bombardment is apparently a universal "etchant" suitable for bringing out the structure not only of metals but of dielectrics as well.[4]

Quantitative Investigation of the Depth of Etching of Grain Boundaries in Cathode Sputtering*

The material selected for investigation was commercial copper because samples of this material are easily prepared and sputter rapidly. The copper samples were polished mechanically and washed in alcohol. The sputtering was effected by bombardment with neon ions in the special tube shown in Fig. 1. During the sputtering the samples were cooled with running water to insure a constant temperature. This precaution was taken because the intensity of certain processes accompanying cathode sputtering (recondensation of the dispersed metal, migration, etc.) are known to depend on the temperature.

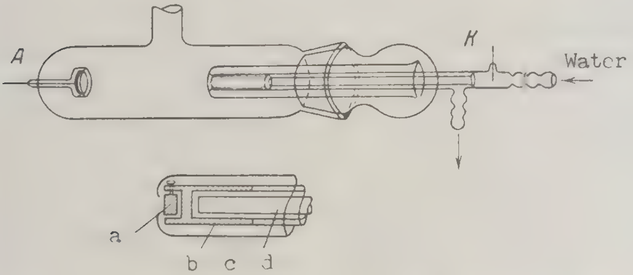

Fig. 1. Tube used for cathode sputtering: a) specimen, b) copper specimen-holder, c) copper-glass seal, d) tube for cooling water.

After ionic etching single-stage quartz replicas were made of the specimens. Stereograms were then made of the replicas at angles of +6° and -6° relative to the optical axis in an UEM-100 electron microscope. The parallel measurements were made on a STD-3 precision stereometer. The orientation of the photographic plates in the stereometer was determined from the maximum parallax or with reference to a third photograph made at some intermediate angle.[5]

A stereopair obtained from a specimen subjected to sputtering for 45 min at a neon pressure of $2.1 \cdot 10^{-1}$ mm Hg and a voltage of 2.3 kv is reproduced on Fig. 2. Measurements showed that the depth of etching over the boundaries of an individual grain varies widely. Hence for comparing the relief of specimens sputtered under different conditions it was necessary to take a certain mean depth of etching over the grain boundaries for each case. This value was determined as the arithmetic mean of the depths of etching over the boundary between the grains in several stereopairs recorded from different sections of the same specimen.

Fig. 3,a shows the dependence of the mean depth δ of etching of the bound-

---

*T.F.Filippova & A.I.Klenova participated in this part of the work; the authors take this occasion to thank them.

aries between the grains of commercial copper on the sputtering time at a constant accelerating potential of 2.3 kv and a neon pressure of $4.3 \cdot 10^{-2}$ mm Hg. It will be seen that at first δ increases rapidly with etching time. However, the rate of increase of the depth falls off, so that after one and a half hours sputtering there is little further change in δ. It may be concluded that the optimal etching time is between 45 min and 1 hour; at the end of this period the grain boundaries are clearly discernible. The curves characterizing the dependence of the depth of etching on the neon pressure and on the accelerating potential are shown in Fig. 3,b and c. It will be seen that the etching depth is virtually independent of the gas pressure in the range from 10^{-2} to 10^{-1} mm Hg and that the depth of etching of the boundaries increases almost linearly with the accelerating potential.

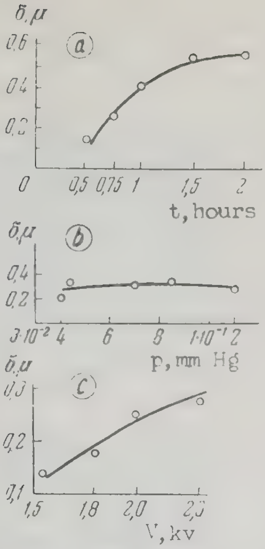

Fig. 3. Dependence of the mean depth of etching of the copper grain boundaries a) on the sputtering time t at a neon pressure p = $= 4.3 \cdot 10^{-2}$ mm and accelerating potential U = 23 kv, b) on the neon pressure at U = = 2.3 kv and t = 45 min and c) on the accelerating potential U at $p = 1.6 \cdot 10^{-1}$ mm Hg and t = 45 min.

Thus the optimum conditions for ionic etching in our case are the following: voltage between electrodes 2.0-2.5 kv, gas pressure $3 \cdot 10^{-2}$-$2 \cdot 10^{-1}$ mm Hg and sputtering time 45 min to 1 hour.

In the future we plan to measure the depth of etching of the grain boundaries for other metals and alloys and to investigate the influence of a wider range of accelerating potentials.

Use of Ion Bombardment to Bring Out the Granular Structure of Alloys not Revealed by Chemical Etching

When chemical etching is employed to bring out the structure of a material it is necessary to select the etching agent and etching conditions appropriate to the particular metal or alloy. This is often difficult particularly in dealing with new alloys and alloys resistant to chemicals.

We used cathode sputtering to bring out the grain boundaries of a number of alloys for which chemical etching failed to give satisfactory results. In Fig. 4 we reproduce a series of photographs of an aluminum base alloy containing magnesium: photograph a was taken after chemical etching, b was taken after ionic etching at approximately room temperature and c was taken at room temperature of an alloy sputtered at 350°. The samples were sputtered for 1 hour at a potential of 2.0 kv, a current density of 2 ma/cm^2 and a neon pressure of $8 \cdot 10^{-2}$ mm Hg. Ionic etching not only brings out the structure better but is easier to use since selection of the cathode sputtering conditions is obviously not critical.

Microrelief developing on the surface of pure metals during cathode sputtering

As was noted in earlier reports[6] crystal formations appear on metallic surfaces after prolonged ion bombardment. In working with pure metals (aluminum, magnesium, zinc, cadmium, tin and bismuth) in a number of cases we observed clearly defined faceted figures, which had one shape in some grains and a different shape in other grains. By way of illustration, we reproduce in Fig. 5 photographs of two neighboring grains of aluminum subjected to cathode sputtering for 1.5 hours at a pressure of $8 \cdot 10^{-2}$ mm Hg, a potential of 2.0 kv and a current density of 0.8 ma/cm^2. Fig. 6 shows the surface of polycrystalline cadmium subjected to sputtering for 20 min under the same conditions; in some cadmium grains the crystal figures have the appearance of pyramids, while in others they resemble steps.

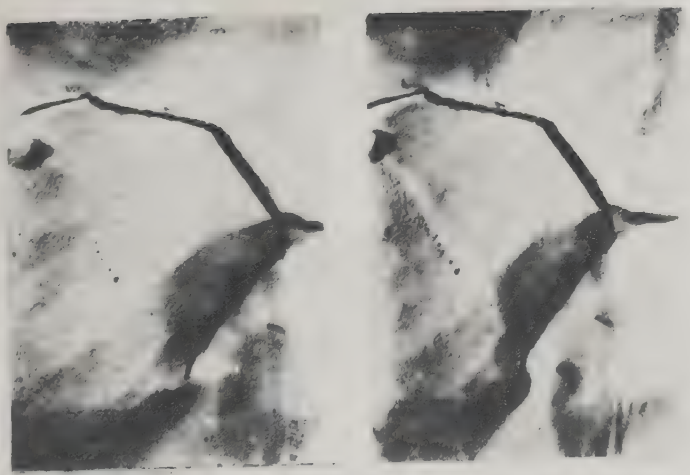
Fig. 2. Stereoscopic photograph of the grain of commercial copper made by means of an electron microscope from a quartz replica. Magnification 8500 X.

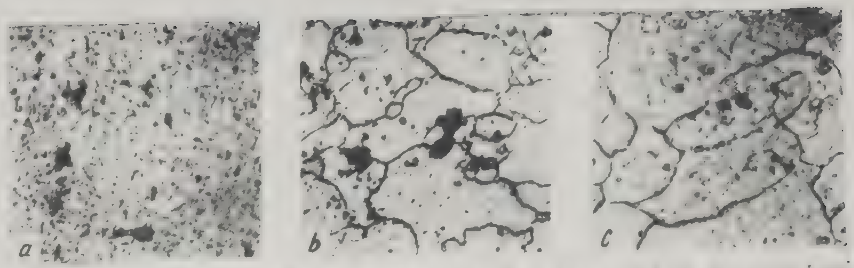

Fig. 4. Photographs of an aluminum alloy with magnesium (Magnification 300 X): a) after chemical etching, b) after ionic etching at about room temperature, c) after ionic etching at 350°.

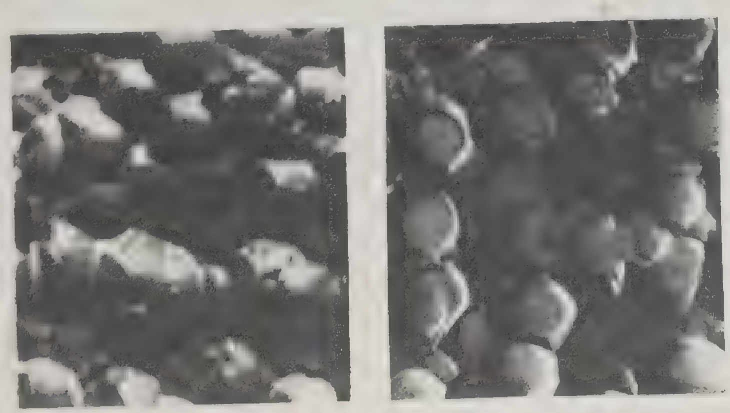
Fig. 5. Photographs of the surfaces of two neighboring grains of pure aluminum after cathode sputtering. Magnification 1000 X.

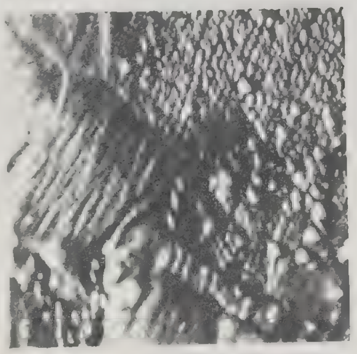
Fig. 6. Surface of polycrystalline cadmium after cathode sputtering. Magnification 600 X.

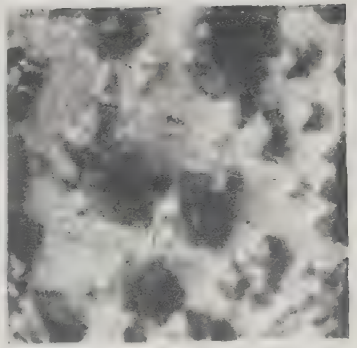
Fig. 7. Photograph of the (0001) cleavage plane of a bismuth single crystal subjected to cathode sputtering. Magnification 1000 X.

The crystal formations in the photographs are indentations, i.e., are negative crystals. In some cases, however, protruding "humps" appear on the surface (see, for example, Fig. 7).

These crystal formations bear a strong resemblance to the so-called "etch figures" that are obtained in chemical etching of crystal surfaces.[7] It is known that the etch figures are characterized by the same symmetry as the faces on which they form. Hence, study of etch figures is one of the simplest methods of determining the symmetry of crystal faces and is frequently employed in crystallography.

Hence one may well ask whether the figures obtained in cathode sputtering do not have the same attributes, i.e., whether they do not follow the symmetry of the face upon which they are formed?

To check this it was obviously necessary to subject to ion bombardment a definite crystal face having a known symmetry. For this purpose we selected the (0001) cleavage face of a bismuth single crystal containing a sixth order symmetry axis. As was expected, six-sided pyramids formed on this face after sputtering (Fig. 7).

Thus we found that one can use cathode sputtering for obtaining etch figures for the purpose of determining the symmetry of faces on the metal surface. Here again cathode sputtering has the same advantages over chemical etching.

If bombardment with fast ions is continued for a prolonged period, in some cases the crystal relief on the metal surface is formed of the equilibrium planes characteristic of the given type of crystal lattice. For example, in sputtering aluminum (face-centered cubic lattice) in neon we frequently observed the $\{111\}$ octahedron planes (Fig. 9). On the other hand, in the case of zinc (hexagonal lattice), we observed sections of the (0001) faces on the sputtered surface.

Kossel and Stranski[8] showed that one can determine the group of equilibrium planes for a given crystal from the structure of the lattice. Where formation of the faces of a slowly growing or dissolving crystal is concerned, an influential factor is the difference in atom-lattice binding energy for different positions on the incomplete atomic planes (at the center of the plane, at the end of an atomic chain, etc.). Fixation of atoms is most probable at positions with strongest binding to the crystal lattice and this leads to the formation of the equilibrium planes during the crystal growth. For the growth of convex homeopolar crystals (and the form of solution or disintegration of negative homeopolar crystals) theory predicts the predominance of the (111) octahedron plane for the case of a face-centerd cubic lattice and of the (0001) plane and its zone for a hexagonal lattice. In a number of cases these faces do form the relief of sputtered metallic surface.

The appearance of the equilibrium planes as a result of prolonged bombardment with fast ions, however, cannot be explained solely by preferred removal of atoms from positions where their binding with the crystal is minimal. The energy of fast ions is appreciably greater than the threshold value for removal, while the difference between the lattice-atom binding energies in different positions on the crystal is relatively minor.

It must be borne in mind that the energy transferred by a fast ion to the crystal is distributed among a group of lattice sites.[9] It is probable that in the process some of the atoms receive a sufficient amount of energy for them to move (migrate) over the surface. Theoretical analysis of the formation of crystal surfaces in the case of migration of surface atoms[10] showed that the process proceeds in the direction of thermodynamic equilibrium on the surface and leads to the growth of sections of equilibrium faces. In the case of cathode sputtering growth of the equilibrium faces can also occur due to recondensation of the metal vapor on the surface of the specimen, for in this case too, the atoms tend to attach themselves in positions of strongest lattice-atom binding.

Recondensation sometimes leads to the growth of convex crystals on the metal surface (Fig. 8). The number and size of the crystals increase when the specimen

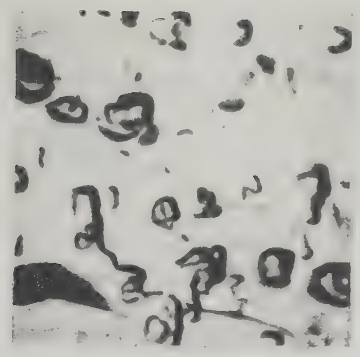

Fig. 8. Photograph of the surface of aluminum sputtered in neon. The surface is covered with microscopic crystals. Magnification 10,000 X.

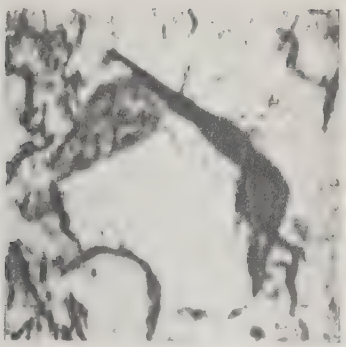

Fig. 9. Photograph of a section aluminum surface with (111) faces, subjected to cathode sputtering in neon. Magnification 8000 X.

temperature is lowered and when the gas pressure is increased, i.e., under conditions of enhanced recondensation.

Thus the formation of faceted figures during cathode sputtering can be characterized as follows: 1) when the metal is bombarded with slow ions the coefficient of sputtering (disintegration and removal) depends on the crystallographic direction;[11] the crystal formations in this case develop due to preferred disintegration of certain faces; 2) at higher bombarding ion energies a significant part may also be played by recondensation of the vaporized material and surface migration of the metal atoms. The intensity of both these processes depends on the binding energy of the atom with the lattice (i.e., on the crystallographic direction); both processes lead to the formation of oriented figures.

Influence of Surface Relief on the Intensity of Cathode Sputtering*

It may be assumed that the intensity of sputtering of a given section of the surface will depend on the density of the ion current incident upon it. The ion current at a given element of the surface, in turn, will be modulated by the density of secondary electrons emitted from the given element.

Where the specimen has a cavity or recess, the slow secondary electrons will be focused on its axis of symmetry owing to distortion of the equipotential surfaces in the vicinity of the cavity, i.e., owing to the formation of a "microlens". The effect of such microlenses will persist even in the presence of a positive space charge. This is substantiated, for example, by the light-and-dark-field image of cold cathodes obtained in gas filled electron microscope, where such ion-focusing of the beam obtains.[12] Enhancement of the electron density along the axis of the cavity must lead to increased ionization, i.e., to an increase in the ion current density in the vicinity of the cavity. Hence sputtering (disintegration) must be more intense in depressions as compared with smooth level sections of the cathode.

Observations have shown that at the beginning of sputtering the depth of depressions and scratches on the cathode actually does increase rapidly. Subsequently, however, removal of metal from these sections slows down. This may be

---

*The authors acknowledge with thanks the assistance of N.A.Pereverzentsev in this part of the investigation.

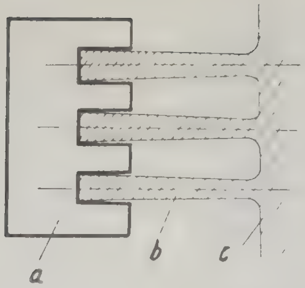

Fig. 10. Schematic cross section of cathode surface and region of cathode dark space and beginning of glow in the presence of cavities in the cathode: a) cathode, b) region of enhanced luminosity, c) beginning of luminous glow.

due to the increasing effect of recondensation as it becomes more difficult for the metal vapor to diffuse out of the ever deeper recesses.

The superiority of cathode sputtering as compared with chemical etching in bringing out the grain boundaries may in part be due to the above electron optical influence of the surface relief on the process of metal removal.

Because of experimental difficulties the above assumptions could be checked only on cathodes with cavities 2-2.5 times smaller than the width of the cathode dark space (recess diameter 1.5 mm; p = 0.03-0.05 mm Hg). Narrow, intensely luminous regions passing through the cathode dark space to the region of luminous glow were observed over the cavities (Fig. 10). Microscopic examination of the surface of the cavities and surrounding areas showed that sputtering was more intense in the cavities. Photometric measurements of the cathode dark space and the region of luminous glow showed a noticeably enhanced brightness over the cavities. The effect was observed over both rectangular and cylindrical cavities.

However, it would be imprudent to assume that the results of this experiment hold in toto for sputtering from recesses 0.1 mm or less in diameter, since in the case of our larger cavities we may have been dealing with the hollow cathode effect.[13]

Influence of the Purity of the Gas on Cathode Sputtering

It has been held that the structure of metals brought out by ion bombardment in an inert gas differs substantially from the structure obtained with ion bombardment in air.[6] Thus, for example, it was assumed that the surface relief forming as a result of prolonged sputtering in neon (cones on aluminum and terraces on zinc) cannot be obtained by etching in air.

In order to check this, we sputtered zinc, aluminum, cadmium and 30KhGSA steel samples in neon and air. The surface of zinc etched in neon is shown in Fig. 11,a; the surface sputtered in air in Fig. 11,b. It will be seen that similar patterns with characteristic terraces were obtained in both cases. Photographs of the surfaces of 30KhGSA steel obtained after ion bombardment in neon and in air are reproduced in Fig. 12. The sputtering in neon and in air was carried out at the same pressure and equal current densities and accelerating potentials. However, the duration of sputtering in neon and air differed; 10 hours sputtering in air were required to obtain the same picture as obtained after 1.5 hours sputtering in neon.

The requisite sputtering time in air is presumably increased owing to the formation of an oxide coating which slows down the process. This factor was not taken into account in earlier investigations; the specimens were subjected to ion bombardment in neon and air for the same period[6] and naturally exhibited a different surface relief.

Thus the structure of a metal can be brought out satisfactorily by sputtering either in an inert gas or in air. The admixture of air to the inert gas only prolongs the requisite sputtering time.

Physics Department of
Moscow State University.

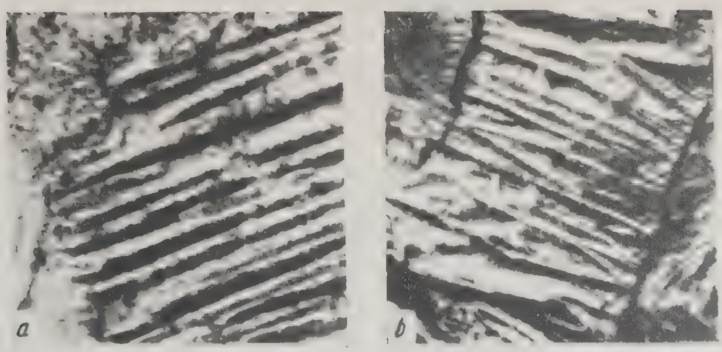

Fig. 11. Photographs of the surface of zinc subjected to sputtering a) in neon, b) in air.

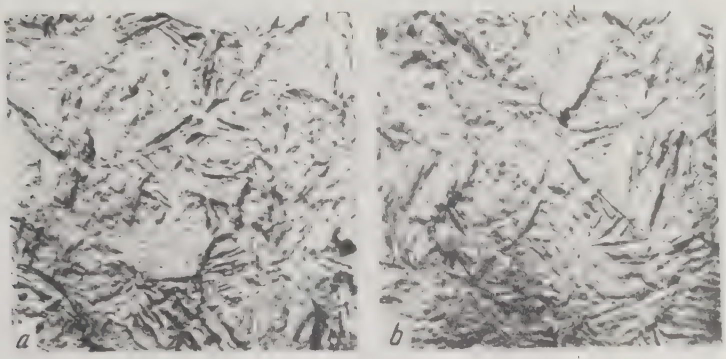

Fig. 12. Photographs of 30KhGSA (30XГCA) steel subjected to sputtering a) in neon, b) in air.

References

1. G.V.Spivak, I.N.Prilezhaeva & O.I.Savochkina, Zhur.tekh.fiz., 23, 225 (1953).

2. McCutcheon, Metal Progress, 56, 674 (1949); T.R.Padden & J.R.Cain, Metal Progress, 66, 108 (1954); I.I.Papenova & A.I.Fromer, Zavod.labor. (The Factory Laboratory), 4, 432 (1955).

3. I.A.Oding & M.T.Lozinskii, Izv. AN SSSR, Otd.tekh.nauk., 7, 1035 (1953).

4. G.V.Spivak, A.I.Krokhina & L.V.Lazareva, Doklady AN SSSR, 104, 579 (1955).

5. Müller, Koll.ZS., 99, 6 (1942).

6. G.V.Spivak, I.N.Prilezhaeva & E.A.Gruz, Izv. AN SSSR, Ser.fiz., 15, 409 (1951); A.M.Shemaev, A.I.Frimer & I.I.Sil'vestrovich, Izv.AN SSSR, Ser.fiz., 15, 413 (1951).

7. H.E.Buckley, Crystal growth (In Russian trans. M, 1945).

8. V.D.Kuznetsov, Kristally i kristallizatsiia (Crystals and crystallization) M.-L, 1953.

9. N.D.Morgulis, Usp.fiz.nauk., 28, 202 (1946).

10. Ia.I.Frenkel', Zhur.eksp.i teor.fiz., 16, 39 (1946).

11. K.Wehner, J.Appl.Phys., 26, 1056 (1955); Phys.Rev., 102, 690 (1956).

12. "Elektronnaia mikroskopiia" (Electron microscopy) Collection of articles. A.A.Levedeva, editor. M.-L., 1954.

13. A.Engel & M.Steinbeck, Fizika i tekhnika elektricheskogo razriada v gase (Physics and technique of electric discharges in gases - Probably trans. from German Trans.) M.-L., 1936.

ON THE THRESHOLD FOR CATHODE SPUTTERING OF METALS

- N.D.Morgulis & V.D.Tishchenko

The problem of determining the threshold energy for sputtering has always occupied a rather special place in investigations of this effect.[1] This is due to the fact that attempts to determine the threshold are hampered by the lack of dependable methods for measuring low values of the sputtering coefficient μ in the prethreshold region. As a consequence, we frequently encounter the use of rather arbitrary and ill-founded procedures in studies in this field.

By way of example, one can cite attempts to determine the threshold energy V_o by measuring the dependence of the coefficient μ on the energy V_p of the sputtering primary ions in the region of medium and high energies and subsequent linear extrapolation to $\mu = 0$ on the basis of the empirical dependence $\mu = A(V_p - V_o)$.

As a result, even in recent literature we encounter diverse and sometimes obviously absurd values for V_o; yet a knowledge of the threshold energy is very important for understanding the nature of this interesting effect. Even the latest attempts at determining sputtering threshold energies, made by investigators using advanced and more accurate techniques[2 & 3], failed to yield convincing results. Probably the most reliable data in the field are those obtained some years ago[1,4] on the value of V_o for effective film cathodes since a very accurate method of monitoring the electron emission or detecting a noticeable contact potential was employed in these investigations.

Thus, cathode sputtering in the prethreshold region and the thresholds for sputtering have remained "unexplored areas" in this field of cathode electronics. Yet modern experimental physics furnishes us with a new effective method - that of radioactive indicators - which in principle can readily be applied in this field. In view of this we undertook a new investigation of cathode sputtering in the prethreshold region; the experimental procedure and preliminary results have already been described in Ref. 5. In the present report we shall summarize the results obtained to date for the threshold energies for sputtering of different metals under bombardment by ions of different inert gases. We shall not discuss here the dependence of the sputtering coefficient on the ion energy in the prethreshold region and allied problems; these will be considered in a future publication.

Briefly, as described in Ref. 5, the experimental procedure was based on using a gas-rectifier type discharge in the appropriate gas, the ions of which bombarded the investigated metal; the target of this metal served as the probe. The sputtered metal together with an admixture of its radioactive isotope was deposited on a metallic collector located at a certain distance from the target. The values of the sputtering coefficient μ (atoms per ion) at different bombarding ion energies were calculated from the known specific activity of the sputtered metal and the measured total activity of the deposit taking into account the counting efficiency, the geometry of the system, the strength of the sputtering ion current and other factors. Having thus obtained $\mu = f(V_p)$ in the prethreshold region we could readily evaluate the threshold energy V_o with a fair degree of reliability.

We studied the following metals tagged with their radioactive isotopes: Co^{60}, Zn^{65}, Zr^{95}, Ag^{110}, Sb^{124}, Ta^{182}, W^{185}, Ir^{192} and Tl^{204}. These were selected because they had a sufficiently high activity and different other physical properties. Before making measurements the target surfaces were cleaned by ion bombardment. For sputtering we used argon and helium atoms which have substantially different masses (m = 40 and m = 4) and neutralization potentials $V_n = (V_i - \varphi)$, where V_i is the ionization potential (15.7 and 24.5 ev, respectively) and φ is the work function of the investigated metal. We introduced an additional correction for the coefficient of secondary emission of the second kind; here

we provisionally assumed $\gamma \approx 0.1$ and 0.2 for Ar and He, respectively. We excluded sputtering with mercury ions from our main program in view of the possible masking effect of surface films of Hg (see Ref. 5); this effect is absent in the case of inert gases.

An example of the experimental dependence of $\mu = f(V_p)$ in the prethreshold region in the case of sputtering of Ir^{192} in Ar and the determination of the threshold energy V_o (insert on the large scale) are shown in Fig. 1. One can readily see why the above mentioned procedure for determining V_o by linear extrapolation to $\mu = 0$ from the region of high and medium values of V_p is inadmissable.

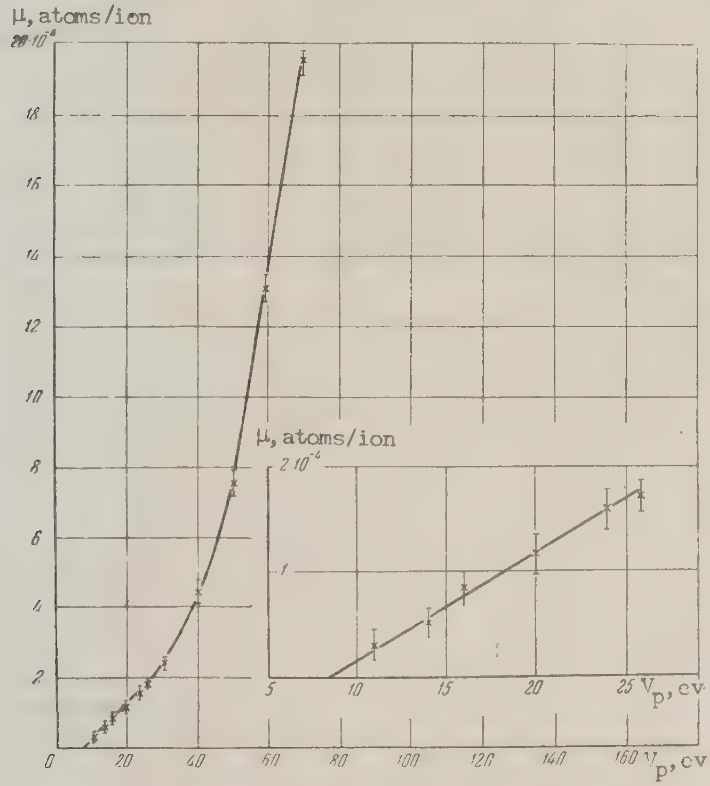

Fig. 1. Dependence of the coefficient of sputtering for an Ir^{192} target on the energy of the bombarding Ar ions. Insert: initial section of curve plotted to an enlarged scale.

As follows from elementary considerations[1], the threshold energy for sputtering must be directly related with both the heat of evaporation (sublimation) Q of the sputtered metal and with the energy transferred to the metal by the incident ion, i.e., the accomodation (elastic) constant α. In this case $\alpha V_o = Q$; or more accurately speaking $\alpha\beta V_o = Q$ where $\beta < 1$ is an efficiency coefficient characterizing the efficiency of utilization of the transferred energy for sputtering. On the other hand, in the optimum case of "rigid", central pair elastic collisions the accomodation coefficient $\alpha = 4mM/(m + M)^2$ where m and M are the masses of the sputtering ion and the sputtered metal atom, respectively.

In the general case, if, as in the present experiment, relatively slow ions are involved, the impact will be "soft" and the value of α may prove to depend (in addition) on the velocity v_p of the ion, the velocity c of propogation of deformation (i.e., sound) in the metal lattice, etc.[6] However, under all circumstances we must first seek the basic relationship between the threshold energy V_o and the heat of sublimation Q (see below).

Turning to the results obtained in the present investigation, we must emphasize that in conformity with the statements in Ref. 5, the absolute values of the threshold energy for sputtering are actually rather small ($V_o \approx$ 3-20 ev) i.e., considerably smaller than the values of ~30-140 ev very recently published by Wehner[7]. Our experimental values for V_o are shown in Fig. 2 in the form of the dependence of V_o on the sublimation energy Q (see above); the values of Q were taken from Dushman[8]. The two important curves in the figure are those obtained for sputtering in Ar and He; no great significance can be attached to the third curve, pertaining to sputtering in Hg, in view of the reasons set forth in Ref. 5. Hence in the present experiments we limited ourselves mainly to sputtering Co^{60}, but for purposes of comparison we also show in the figure the results obtained earlier[4] on the sputtering of active surface films of thorium on thoriated cathodes (point T.K. on the curve) and barium on oxide-coated cathodes (O.K. on

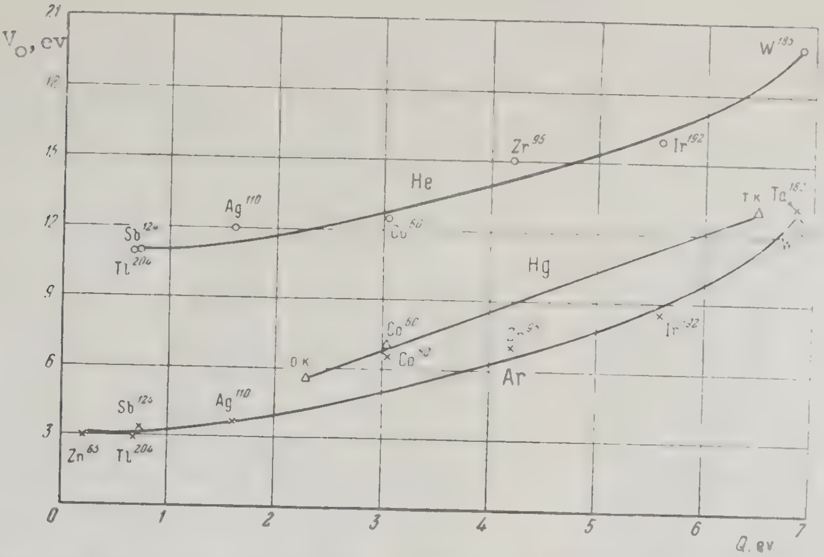

Fig. 2. Dependence of the threshold energy for sputtering of a number of metals on their heat of sublimation under bombardment of the metals with He, Ar and Hg ions.

the curve). It may be noted that the values of V_o obtained in the present case by means of the radioactive indicator method (for Co^{60}) correlate well with the values obtained earlier by monitoring the emission from thoriated cathodes (T.K.) and by detecting their cathode potential (O.K.).

Viewing the curve shown in Fig. 2, we note 1) that, as pointed out above, the absolute values of V_o are relatively small and 2) that, other conditions being equal, there is a definite correlation between the increase in V_o and the growth of Q. Thus, on the basis of extensive experimental data, we have brought to light one of the important regularities in the variation of the energy threshold for cathode sputtering.

Turning now to the role of the coefficient of accomodation, i.e., in the first place the influence of the magnitude of M and m, we see that the dependence of V_o on the mass M of the atoms of the sputtered metal is somewhat less obvious, largely because it is difficult to select appropriate experimental conditions for clarifying it. We could do this only from a comparison of the results for Sb^{124} and Tl^{204} in the same gas (i.e., from results obtained with equal values of m and approximately equal values of V_n) since both these metals, differing substantially as regards M (124 and 204, respectively) are characterized by almost equal values of Q. It will be seen from Fig. 2 that for sputtering of these metals in Ar and He, we obtained almost identical values for V_o; this suggests that the value of V_o is very little dependent on M. If this interesting fact is substantiated in further experiments, it would mean that each of the curves of Fig. 2 gives us a unique dependence of V_o as a function of Q. At present we can say nothing new or definite regarding the role of the other properties of the sputtered metal (for example, the sound velocity c) entering our equation through the empirical parameter $\beta < 1$.

Lastly, we see from Fig. 2 that there is another possible factor affecting the value of V_o, i.e., we see that V_o depends on the nature of the sputtering gas ion. The role of the last can, in principle, be evinced through the values of m, V_n or v_p. From Fig. 2 it follows that in going from Ar to He, when the mass m sharply decreases while the value of V_n increases somewhat, the magnitude of V_o still rises appreciably. Thus it would appear that the dominant role belongs to the mass m of the sputtering ion, i.e., that in qualitative accord with the variation of the accomodation coefficient α, V_o increases with decreasing mass m.

In view of this it is not without interest to compare the experimental values of the effective accomodation coefficient determined as $\alpha_e = Q/V_o$ with its theoretical value $\alpha_t = 4mM/(m + M)^2$ obtaining in the simplest case of a "rigid" central pair elastic collision. This comparison for sputtering by Ar and He ions is shown in Fig. 3 in the form of the dependences $\alpha = f(M)$. We see here not only

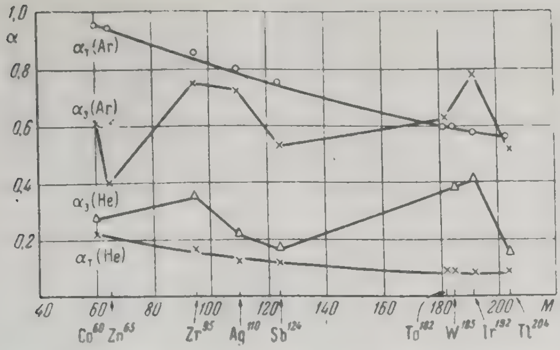

Fig. 3. Variation of the experimental and theoretical values of the accomodation coefficient for a number of pure metals on their mass number in the case of bombardment of these metals by He and Ar ions.

the complete absence of any sign of correlation between the variation of the curves for α_e and α_t but, on the contrary, a rather surprising monotonic variation of α_e as a function of M. Possible reasons for the disparity between the values of α_e and α_t may be 1) the admitted possible inaccuracy in our experimental determinations of V_0 and hence of α_e (we shall examine this question at a later date), 2) the inadmissability of using the above very simplified expression for determining α_e and 3) the necessity of taking into account (to what extent we cannot tell) that in the event of sputtering by the impact of a slow ion some portion of its neutralization energy may also be utilized. Some of the deductions regarding the regularities involved in the variation of V_0 advanced by Wehner and Guntherschulze[7] appear to us to be arbitrary or based on fortuitous coincidences. We hope to be able to clarify some of the doubtful questions in the near future.

"T.G.Shevchenko" Kiev State University

References

1. N.Morgulis, Usp.fiz.nauk., 28, 202 (1946).

2. G.Wehner & G.Medicus, J.Appl.Phys., 23, 1035 (1952); 25, 698 (1954); G.Wehner, Phys.Rev., 93, 633 (1954).

3. R.Bradley, Phys.Rev., 93, 719 (1954).

4. N.Morgulis & M.Bernadiner, Zhur.tekh.fiz., 5, 1231 (1935); N.Morgulis & Ia.Liubarskii, Fiz.zap.AN USSR (Physics Records of the Ukrainian SSSR Ac. of Sci.) 9, 233 (1941); in "Sbornike statei po tekhnicheskoi fizike" (Collection of articles on technical physics), Pub. USSR Ac. of Sci., M.-L., 1947.

5. N.Morgulis & V.Tishchenko, Zhur.eksp.i teor.fiz., 30, 54 (1956).

6. Ia.Frenkel', Usp.fiz.nauk, 20, 84 (1938).

7. G.Wehner, Phys.Rev., 93, 633 (1954); A.Guntherschulze, ZS.f.Phys., 141, 346 (1955).

8. S.Dushman, Scientific foundations of vacuum techniques (In Russian trans. M. 1950).

DISCUSSION

G.V.Spivak: What was the initial state of the metal surfaces?

N.D.Morgulis: The specimens were ordinary pieces of metal , the surfaces of which were cleaned before measurements by cathode sputtering with inert gas ions.

G.V.Spivak: In such investigations it is necessary to take into account the microrelief of the surface. Was this taken into account in the experiment?

N.D.Morgulis: Our results are averaged values.

V.L.Granovskii: How would you describe the mechanism of the effect at low ion velocities?

N.D.Morgulis: The principal difference between sputtering at high and low velocities is that in the case of low velocities one must regard the collisions with the solid as "soft" and, apparently, to some extent take into account the neutralization energy of the ions.

G.V.Spivak: Why were not the properties of structure of the surface of the target taken into account? Even reverse diffusion alone should noticeably change the target surface.

N.D.Morgulis: The mean free path of the sputtered atoms in our experiments is appreciably greater than the distance between the target and collector.

V.G.Bol'shov: To what extent was the ionic composition of the plasma homogeneous?

N.D.Morgulis: We used ordinary discharges at a pressure 10^{-2} mm Hg, at which singly charged ions predominate.

V.G.Tel'kovskii: How did you check or control the state of the surface? The presence of diverse surface films could obviously affect the sputtering coefficient. Did you study the sputtering of active coatings on cathodes?

N.D.Morgulis: Prior to each experiment the target was cleaned by cathode sputtering. The sputtering of active coatings was studied in our pre-war experiments.

ELECTRON MICROSCOPIC INVESTIGATION OF PHOTOCATHODES SUBJECTED TO THE INFLUENCE OF A GAS DISCHARGE

(Abstract - Complete article in Zhur.tekh.fiz., 26, 549 (1956))

- A.I.Frimer, E.M.Belavtseva & A.M.Gerasimova

1. The structure of the cathodes was investigated by the method of "etching" the cathode surface by means of non-selfsustaining and glow discharges in an inert gas (argon).

2. Mainly cesium-antimony and cesium-bismuth photocathodes were subjected to the influence of gas discharges since the structure of these cathodes is readily reproduced, which makes it possible to check the changes in structure produced by the discharge. Concurrently with our investigation of the structural changes we measured the sensitivity of the photocathodes.

The experimental tube containing the cathode was filled with argon to different pressures ranging from $5 \cdot 10^{-3}$ to $1 \cdot 10^{-3}$ mm Hg. The dc voltage on the electrodes was varied in different experiments from 75 to 1400 v.

The structure of the cathodes after exposure to the discharge was investigated in an electron microscope by the method of quartz replicas.[1]

3. Three series of experiments were carried out; these were aimed at determining the influence of a) a non-selfsustaining discharge, b) a glow discharge and c) a glow discharge with simultaneous illumination of a small section of the cathode.

4. The results where gas discharges are concerned show that the nature of the destruction of the cathode surface and the change in cathode sensitivity depend on the discharge conditions, the duration of exposure to the discharge and the type of photocathode.

a) In the case of cesium oxide cathodes, exposure to the action of a gas discharge results in a change of both the structure and sensitivity of the cathode. Non-selfsustaining discharges produce an insignificant change in structure and a 40-50% reduction in sensitivity. Glow discharges result in pronounced disintegration of the surface and a complete loss of sensitivity.

b) Cesium-antimony photocathodes subjected to the action of non-selfsustaining discharges exhibit only minor changes in surface structure and sensitivity. After subjection to a glow discharge the surface of the cathode has a pronounced dendritic structure similar to that of an insufficiently treated cesium-antimony cathode; the sensitivity of such a cathode falls to zero.

c) In the case of cesium-bismuth cathodes, exposure to the influence of gas discharges leads to entirely different results as regards both structure and sensitivity. Non-selfsustaining discharges produce a finer crystal structure and an enhanced sensitivity, the increase in sensitivity is observed at low pressures (a few mm Hg). Glow discharges, in addition to the breaking up of the crystals, result in etching and partial fusion of the crystals; illuminated sections are more strongly affected than non-illuminated ones.

The structure of a cesium-bismuth cathode after exposure to a glow discharge resembles the structure of an ordinary cesium-antimony photocathode and the sensitivity of the cathode approaches that characteristic of a cesium-antimony cathode. At electrode potentials of 1200-1500 v there is strong sputtering of the cathode material. The sputtered particles settling on the walls of the tube form a highly dispersed photocathode with a rather high sensitivity.

5. The structural changes of photocathodes subjected to the influence of gas discharges can be due to sputtering of the cathode material, redeposition of the sputtered particles on the cathode and migration of atoms over the cathode surface.

In the case of cesium-antimony cathodes, the disintegration produced by the

discharge is tantamount to removal of the upper active layer and the sensitivity is reduced accordingly. The sharp increase in the sensitivity of the cesium-bismuth cathode after exposure to discharges is apparently due to pulverization of compounds of bismuth with cesium under the impact of bombarding ions, resulting in additional sensitization of the cathode.

The experimental procedure employed in the investigation can be used for studying the changes occurring in the surface of cathodes in gas phototubes.

References

1. A.I.Frimer, A.M.Gerasimova, Zhur.tekh.fiz., 26, 726 (1956).

BULLETIN of the Academy of Sciences of the USSR - Physical Series
Vol. 20, No.10 - Transactions of the All-Union Conference on Cathode Electronics
(continued from Vol.20, No.9)

TABLE OF CONTENTS

	Page Orig.	Page Trans.
Non-uniformity of the work function of oxide-coated cathodes - D.G.Bulyginskii	1079	975
Mass-spectrometric studies of oxide-coated cathodes during prolonged operation - G.Ia.Pikus	1085	980
Influence of oxygen at low pressures on the emission of an oxide-coated cathode - A.E.Kulik & N.G.Nakhodkin	1096	989
X-ray investigation of the systems of binary and ternary carbonates and oxides of the alkaline earth metals - E.P.Ostapchenko	1105	997
Investigation of the emission characteristics of oxide-coated cathodes with bases of new nickel alloys - V.S.Parkhomenko, M.A.Chistiakova, G.A.Vostrov & G.M.Kudriasheva	1112	1004
Mechanism of the formation of electronmicroscope images of thermionic cathodes - D.P.Vinogradov	1120	1011
Thermodynamic calculation of some reactions of reduction of BaO - L.S.Zaitseva	1123	1015
Investigation of the dynamics of formation of the barrier layer in an oxide-coated cathode by the radioactive tracer method - Iu.G.Ptushinskii	1127	1019
Experimental investigation of thermionic and secondary-electron emission from copper and germanium in transition from the solid to the liquid state - V.G.Bol'shov	1128	1020
Field emission and field-emission cathodes - D.B.Zernov	1135	1027
Experiments with an electron and ion projector tube - A.P.Komar & Iu.N.Talanin	1137	1029
Work function of the (110) face of a tungsten single crystal and positive surface ionization of sodium on this face - G.N.Shuppe, E.P.Sytaia & R.M.Kadyrov	1142	1035
Surface migration in an electric field and the binding energy of tungsten atoms - I.L.Sokol'skaia	1151	1044
Properties of a cold cathode with a firing device in pulse discharges at low pressures - E.M.Reikhrudel', A.G.Zimelev & A.V.Kustova	1153	1046

Effects occurring on electrodes during high-energy electric breakthrough in a high vacuum - N.B.Rozanova & V.L.Granovskii 1162 1055

Investigation of secondary emission from metals under bombardment by positive ions of alkali elements - U.A.Arifov & A.Kh.Aiukhanov 1165 1057

Secondary-electron emission under the influence of positive ions and neutral particles - V.G.Tel'kovskii 1179 1070

Processes occurring on metal surfaces during cathode sputtering - G.V.Spivak, V.E.Iurasova, I.N.Prilezhaeva & E.K.Pravdina 1189 1075

On the threshold for cathode sputtering of metals - N.D.Morgulis & V.D.Tishchenko 1190 1082

Electron microscope investigation of photocathodes subjected to the influence of a gas discharge - A.I.Frimer, E.M.Belavtseva & A.M.Gerasimova 1195 1087

Translated in 1957 by
Columbia Technical Translations
5 Vermont Ave., White Plains, N.Y.

PARAMAGNETIC RESONANCE

(A Survey and Review)

- E.K.Zavoiskii, S.A.Al'tshuler & B.M.Kozyrev

Paramagnetic resonance (hereinafter - PR) was discovered by one of the authors[1] in Kazan in 1944. The history of this discovery is the following. Since 1936 the Dutch school of physicists, headed by Gorter, had been engaged in studies of paramagnetic absorption in parallel and perpendicular fields.[2] It became clear that in the case of a mutually perpendicular orientation of the constant and alternating magnetic fields the absorption must have a resonance character. However, despite numerous attempts, Gorter did not succeed in establishing the resonant nature of paramagnetic absorption. The reasons for the failure of these attempts were, first, that Gorter carried out his measurements at frequencies under 100 Mc and, second, that he used the relatively insensitive direct calorimetric method of measuring the energy absorbed by the paramagnetic substance. Gorter's ideas were utilized by Rabi[3] in developing a method of determining nuclear magnetic moments in molecular beams on the basis of changing the orientation of the spins under conditions of magnetic resonance. It must be noted that this method is very complicated and has only a limited range of application.

The author of Ref. 1 succeeded in greatly expanding the range of alternating field frequencies and, what is more important, developed new highly sensitive methods for investigating paramagnetic absorption; he abandoned the calorimetric method and went over to indirect electric procedures for measuring the energy dissipated in the paramagnet. The simplicity and sensitivity of the method employed for controlling the r-f generator - substantially improved soon after its inception by employing modulation of the constant magnetic field[4] - insured success. These developments not only allowed detection of PR but also made it possible to expand the range of investigations of paramagnetic relaxation in parallel fields.

What exactly is paramagnetic resonance absorption? The effects consist in a transfer of energy from the radio frequency field having a frequency ν to the paramagnetic material as a result of magnetic dipole transitions between energy sublevels produced by the constant magnetic field H. Resonance absorption occurs when an energy quantum of the r-f field is equal to the energy interval between the magnetic sublevels. In the simplest case the resonance condition has the form

$$g\beta H = h\nu, \tag{1}$$

where g is the spectroscopic splitting factor and β is the Bohr magneton. In the overwhelming majority of cases the probability of magnetic dipole transition in the first approximation is nonzero only when the constant and alternating magnetic fields are mutually perpendicular.

At first PR was investigated in detail by one of the authors[1] in salts of elements of the iron group. He also initiated study of PR in solutions of paramagnetic salts in metals[1,5]. A natural further step in the investigation of PR due to the magnetic moments of electrons was the discovery in 1946 by Purcell[6] and Bloch[7] and their coworkers of nuclear magnetic resonance. Further, in the field of PR we have the discovery of ferromagnetic resonance, made by Griffiths[8,*], but theoretically predicted back in 1935 by Landau and Lifshits[9]. It may be noted that on the basis of the discovery by Arkad'ev[10] of selective absorption of the energy of an alternating electromagnetic field by ferromagnets, Dorfman[11] back in 1923 conjectured the existence of magnetic resonance.

---

*Griffiths discovered this effect in ferromagnets in the presence of strong external magnetic fields; Arkad'ev observed the same phenomenon back in 1911-13 in the same substances but in the absence of an applied field.

PR offers a means for determining the positions of the energy levels of magnetic particles; in view of this, investigations of this effect are an indispensable part of spectroscopy. On the other hand, this effect is closely connected with magnetic cooling and with paramagnetic relaxation, inasmuch as both these phenomena have to do with the kinetics of magnetization processes.

The numerous experimental and theoretical investigations of magnetic resonance carried out during the past decade have opened new approaches in physics, have extended and enriched our knowledge regarding the magnetic properties of matter and have greatly influenced the development of theories of the solid and liquid states. Thus magnetic resonance is an important part of the modern theory of magnetism which has developed as the result of the transition from investigation of the static magnetic properties of bodies to investigation of magnetization in alternating fields.

Whereas in investigations of paramagnetism in constant fields the important quantity is the static susceptibility χ_0, in alternating fields the susceptibility becomes a complex quantity: $\chi = \chi' - i\chi''$. The fundamental problem in theories of paramagnetic dispersion and absorption is investigation of the dependence of χ' and χ'' on the frequency ν and strength H of the r-f field. It is well known that the magnetic properties of solid and liquid paramagnets depend on the internal electric field in the material, on the magnetic and exchange interactions between the atoms.

These internal forces determine the PR effect inasmuch as in the overwhelming majority of cases the effect is investigated in condensed systems.

First, by virtue of these internal forces the paramagnet as a whole absorbs the r-f field energy. The alternating field with equal probability stimulates both forced radiation and absorption of energy. For processes of the latter type to predominate there must exist a mechanism insuring re-establishment of thermodynamic equilibrium by continuous transfer of magnetic energy to the thermal motion of the atomic particles. The dependence of the internal forces, acting on the paramagnetic particles, on the thermal motion is responsible for what is called the "spin-lattice" interaction.

Second, the internal forces determine the shape of the PR lines. The inherent width of the lines lying in the radio frequency range is negligibly small. Hence the line shape can depend only on the thermal motion and interaction of magnetic particles with each other and with diamagnetic particles.

Third, these internal forces have an appreciable influence on the appearance of the PR spectrum, i.e., on the number and position of the absorption lines.

It follows from the above that experimental and theoretical investigation of PR may proceed in three directions: 1) determination of PR spectra in different substances, 2) determination of PR line shapes and 3) evaluation of the magnitude of spin-lattice interaction.

With the aid of PR one can measure the mechanical and magnetic moment of atoms and atomic nuclei more accurately than was possible by other methods. The most effective methods of obtaining oriented atomic nuclei are based on paramagnetic resonance. Further investigation of PR makes it possible to draw certain conclusions regarding the fine structure of crystals and liquids and, finally, to solve certain chemical problems.

In recent years there have been published several surveys[12-13] on PR that adequately describe the studies in this field carried out by physicists abroad. Hence we shall concentrate our attention in the present report on investigations carried out in the Soviet Union. We shall divide our brief survey in accord with the three principal categories of PR studies mentioned above.

Let us start with PR spectra.

The first observations of PR were made in polycrystalline specimens of salts of the iron group elements. In all cases there was detected one sharp peak whose position corresponded to pure spin magnetism of the atoms.

The appearance of the resonance absorption spectrum in paramagnetic salts depends primarily on the intensity and symmetry of the electric field of the crystal. In salts of elements of the iron group the influence of the electric field of the crystal is much stronger than that of spin-orbital coupling. In fields characterized by a low degree of symmetry the orbital levels will be single and consequently nonmagnetic. This explains why the electric field "freezes" the orbital motion of the electrons, "suppresses" orbital magnetism.

If the magnetism of the atoms is due only to electron spins, then, since the probability of magnetic dipole transitions differs appreciably from zero only for neighboring energy sublevels, the spectrum of paramagnetic absorption must comprise only one line, as was indeed established in the very first experiments. If the electron spin is greater than 1/2, taking higher order approximations into account may lead to two kinds of consequences.

First, there must then exist weak lines corresponding to transitions with $\Delta M > 1$, where M is the magnetic quantum number characterizing the electron spin. Zavoiskii[15] in 1947 succeeded in detecting this effect in a number of salts.

Second, the PR lines may develop fine structure due to minor splitting of the ground energy level even in the absence of an external magnetic field. Such fine structure was experimentally detected by Zavoiskii[16] in chrome alum powders and theoretically interpreted by Weiss[17]. For purposes of detailed investigation of the fine structure, measurements must be made on single crystals of solid solutions of paramagnetic salts.

Interesting results relating to single crystals of artificial ruby[18,19] and beryl[20] were recently obtained by Zaripov and Shamonin in Kazan and by Prokhorov and Manenkov in Moscow.

After solid paramagnetic salts, next in order of importance where PR investigations are concerned are liquid solutions of these salts. A detailed investigation of PR in such solutions was undertaken in the Kazan Branch of the USSR Academy of Sciences.[21,22]

The hyperfine structure of PR lines is now being intensively studied. The first to establish the influence of the spin of atomic nuclei on the appearance of PR spectra were Al'tshuler, Kozyrev and Salikhov[22]. Their first experiments (1948) were carried out on aqueous solutions of manganese salts at relatively low frequencies (~100 Mc). Subsequently, extensive investigations of the influence of the nuclear spin on the form of the PR spectrum in solid salts at high frequencies were undertaken by Penrose and Bleaney[23] in Oxford. Interesting results on the hyperfine structure of PR lines in liquid solution were obtained at high frequencies by Garif'ianov and Kozyrev[24].

Recently Zaripov and Garif'ianov[25] completed an experimental and theoretical investigation of the hyperfine structure of PR in copper salts at low frequencies. There is reason to assume that investigations at low frequencies should make it possible to determine more accurately certain physical constants, for example, the quadrupole moments of atomic nuclei.

Recently Zaripov[26] developed a theory of the fine structure of PR on single electronic levels. His calculations show that PR due to transitions between such hyperfine sublevels must be susceptible of observation in a number of salts whose paramagnetic ions have an even number of electrons. This effect may be regarded as intermediate between purely electron and purely nuclear PR.

At first PR was studied only in paramagnetic salts. Soon, however, the range of investigation was broadened. In 1947 Salikhov and one of the present writers[27] pioneered in establishing the existence of PR in free organic radicals. Subsequent investigation of different organic substances led to the detection of "latent" paramagnetism in some of them[28]. It may safely be asserted that magnetic resonance will soon become one of the important methods of investigation in the field of organic chemistry. Of particular interest is investigation of PR in different forms of free carbon. The effect has already been studied in anthracite and certain other substances containing free carbon by Garif'ianov and one of the present writers.[29]

In concluding this list of investigated paramagnetic substances we must mention metals; the investigation of PR in these is of great interest but is hampered by serious experimental difficulties.

The effect must be most intense in the rare earth metals, which occupy a special place inasmuch as their magnetic properties are determined by deep-lying electrons. The PR spectra in metallic Ce, Pr and Nd were measured by Salikhov[30]. One of the present authors[31] carried out a theoretical examination of PR spectra for all the rare earth metals.

Up to this point, in speaking of PR we had in mind only paramagnetic absorption, but paramagnetic absorption is always accompanied by dispersion of the magnetic susceptibility. Paramagnetic dispersion in the resonance region was first studied by Zavoiskii[32] in 1947. He developed a new method for investigating this effect and, working at high frequencies, obtained a complete dispersion curve for one manganese salt. It must be recalled that in optics investigation of dispersion in the resonance region, where it is anomalous in character, presents appreciable difficulties. Subsequently, Romanov[33] successfully investigated the dispersion of susceptibility in a series of salts of elements of the iron group at low frequencies. He noted a number of distinctive features characterizing the effect. Measurements of dispersion at high frequencies have been made by Kozyrev, Salikhov and Shamonin[34] and, more recently, by Neprimerov[35] who studied the effect in a large number of different salts. There is an intimate connection, satisfactorily explained by the theory, between dispersion of susceptibility and absorption.

Let us now turn to line shape in paramagnetic resonance. In the region of optical frequencies the line width is always very small compared to the fundamental frequency. In the r-f region, on the other hand, the relation between these quantities is entirely different since the interactions producing line broadening may be of the same order of magnitude in the energy scale with the splitting determining the resonance frequencies. Hence in PR the line width is often comparable with the fundamental frequency and can be measured with great accuracy. But these same circumstances lead to great difficulties in attempts to construct a quantitative theory of PR line shape.

The first theoretical interpretation of the results of PR experiments was proposed by Frenkel'.[36] He deduced expressions defining the line shape on the assumption that the line broadening is due to the interaction of spins with the thermal vibrations of the lattice, which interaction was formerly treated as a kind of friction.

On the basis of an analysis of experimental data, the present authors[37] in 1947 established a number of regularities relative to the line shape in PR, regularities which were in clear conflict with the theory of Frenkel'. The empirical regularities established by the present authors were explained by the fact that spin-lattice interaction does not effect the PR line shape and that the line width is determined by the interaction of the magnetic ions with each other. The authors showed that purely magnetic interaction cannot explain the observed values of line width; hence they postulated that exchange forces and the internal electric fields of the material must have an appreciable influence on the line width.

The idea of narrowing of the absorption lines under the influence of exchange forces was developed by Gorter and Van Vleck[38]; subsequently, Van Vleck[39] carried out quantitative calculations by means of the method of moments. He calculated the second and fourth moments of the absorption lines and found that the second moment is independent of the exchange forces.

In order to determine whether the developed theory was adequate for explaining the observed narrowing of the lines it was necessary to know yet another moment containing the exchange integral. Glebashev[40] carried out exceptionally laborious calculations to determine the sixth moment of the absorption line. He showed that within the limits of the experimental error the agreement with theory is fully satisfactory. Furthermore, using the method of moments, Glebashev examined the question of the dependence of the line shape on the temperature[41] and on the dilution of paramagnetic ions by diamagnetic particles[42].

In a number of cases PR is studied in substances containing two different paramagnetic components, having an identical g-factor but different spins. The appropriate generalization of theory for such cases was carried out by Al'tshuler and Odintsov[43]. An interesting experimental investigation of the dependence of the line width on exchange interactions was performed by Kashaev[44] by measuring PR in solid solutions having different concentrations.

Rigorous theoretical examination of the line width is feasible only by means of the method of moments. However, this method suffers from a number of serious shortcomings and, in addition, is applicable only to a restricted group of paramagnetic materials. Hence there was need for a phenomenological theory, the development of which we owe to Shaposhnikov[45]. This theory, obviously, does not fully resolve the problem since the relation between the spin-spin relaxation time, introduced by this theory, and the actual interactions producing line broadening remains unclear.

In view of the impossibility of developing a rigorous theory of line broadening, general relationships relative to the shape of the PR curves are of particular value. Such relationships were established by Kramers[46]. Unfortunately these relationships imply the assumption that experiment directly gives the dependence of the absorption (or the dispersion of susceptibility) on the frequency of the alternating field, whereas actually PR measurements are made at a constant frequency but a varying static magnetic field, i.e., with varying inherent frequencies.

One of the present authors[46] found relationships analogous to those of Kramers and applicable to cases realizable in practice. These relationships were cerified and utilized in the investigations of Romanov[33], Kozyrev, Salikhov & Shamonin[34], Rivkind[48] and Neprimerov[35].

Let us now turn to spin-lattice interaction. Experimental investigation of spin-lattice interaction was initiated by the Dutch school by measuring PR in parallel fields. The highly sensitive procedures for measuring paramagnetic losses, introduced by Zavoiskii[1], enabled him and a number of other investigators to obtain a series of new results, made it possible to effect measurements at room temperature[49] and led to detection of the effect in liquid solutions of paramagnetic salts[50]. Where the theory of paramagnetic relaxation is concerned, the work of Shaposhnikov[51] merits special mention. In the thermodynamic theory of Casimir & Du Pré[52] account was taken only of spin-lattice relaxation; it is assumed that the spin system is in a state of thermal equilibrium. Shaposhnikov, utilizing the methods of Mandel'shtam & Leontovich[53] developed for the theory of accoustic relaxation effects, constructed a general thermodynamic theory including spin-spin relaxation. Shaposhnikov's formulas have been well substantiated by experiment. Rivkind[48] carried out absolute measurements at low frequencies and determined the spin-spin relaxation times for a number of substances. These measurements confirmed the validity of Shaposhnikov's theory for weak magnetic fields. In the region of higher frequencies, where the role of spin-spin relaxation predominates, Shaposhnikov's theory was first substantiated by Garif'ianov[54]. Subsequently Sitnikov[55] carried out a series of measurements which made it possible to determine the magnetic heat capacities of many salts. Investigations of solid solutions of paramagnetic salts carried out in parallel fields by Sitnikov are of particular interest. The results of his experiments make it possible to clarify the role of different types of interaction in determining the spin-lattice relaxation and magnetic heat capacity.

Side-by-side with the development of the phenomenological theory of PR various investigators have contributed to the development of the quantum theory of spin-lattice interaction. The investigations of Waller, Kronig and Van Vleck and of Akhiezer & Pomeranchuk[56] have thrown light on the nature of different relaxation mechanisms and made it possible to calculate the spin-lattice interaction for certain salts of iron-group elements. Al'tshuler[57] carried out calculations of the spin-lattice interaction for salts of the rare earth elements. Al'tshuler[58] also extended Waller's theory to include the case of arbitrary spin on the assumption that in addition to magnetic forces there also act exchange forces. Finally, there have been examinations of salts, the magnetic ions of which are in the s-state.

In recent years there have been published reports on investigations of certain new effects closely related to paramagnetic resonance. For example, the Faraday effect in paramagnets at centimeter wavelengths and resonance absorption of sound in paramagnetic materials have been investigated in Kazan University.

The first of these effects was examined theoretically by Kastler[59] and experimentally discovered in 1948 by Wilson and Hull[60] in two magnesium salts. Further attempts at experimental investigation of this phenomenon have failed to yield substantial results.

Neprimerov[61] carried out measurements of the rotation of the plane of polarization of centimeter waves under the influence of a constant magnetic field in a large number of paramagnetic salts. Substantially modifying the method used by previous investigators, he designed a set-up characterized by a high sensitivity. Neprimerov's measurements showed that there is a close relation between the Faraday effect in paramagnetics and the dispersion of susceptibility in the resonance region. The idea of possible resonance absorption of ultrasound in paramagnets was first advanced by Zavoiskii. Al'tshuler[62] developed the theory of this effect. This new phenomenon can be regarded as an inverse PR effect: the energy of the elastic vibrations, excited by the ultrasound, is transferred by virtue of spin-lattice interactions to the system of magnetic particles, when the quantum of the lattice vibrations proves equal to the difference of the magnetic level energies. Detailed calculations have been carried out for different types of paramagnets on the assumption of different spin-lattice coupling mechanisms. It follows from these calculations that both electronic and nuclear acoustic paramagnetic resonances can in certain cases be observed experimentally.

In conclusion we would like to note that, in addition to the various applications mentioned above, paramagnetic resonance is the basis of one of the most effective methods of obtaining oriented nuclei.

References

1. E.K.Zavoiskii, Ph.D.Thesis, FIAN (Phys. Inst. of the USSR Ac. of Sci.), M., 1944; Journ of Phys. USSR, 9, 245 (1945).
2. C.J.Gorter, Paramagnetic Relaxation (In Russian trans., M.-L., 1949).
3. J.Rabi, Phys. Rev., 51, 652 (1937).
4. E.K.Zavoiskii, Journ. of Phys. USSR, 9, 245 (1945).
5. E.K.Zavoiskii, Zhur.eksp.i teor.fiz., 15, 345 (1945).
6. E.M.Purcell, R.V.Pound & N.S.Torrey, Phys. Rev., 69, 37 (1946).
7. F.Bloch, W.W.Hansen & N.Paccard, Phys.Rev., 69, 127 (1946).
8. J.Griffiths, Nature, 158, 670 (1946).
9. L.D.Landau & E.M.Lifshits, Sow.Phys., 8, 153 (1935).
10. V.K.Arkad'ev, ZhRFKhO (Journal of the Russian Physical and Chemical Society), 45, 103 (1913).
11. Ia.G.Dorfman, ZS.f.Phys., 17, 98 (1923).
12. B.Bleaney & K.W.H.Stevens, Rep.Progr.Phys., 16, 108 (1953).
13. K.D.Bowers & J.Owen, Rep.Progr.Phys., 18, 304 (1955).
14. J.R.Weiss, Phys.Rev., 99, 829 (1955).
15. E.K.Zavoiskii, Doklady AN SSSR, 57, 887 (1947).
16. E.K.Zavoiskii, Journ. of Phys.USSR, 10, 170 (1946); 11, 197 (1947).
17. P.R.Weiss, Phys.Rev., 74, 470 (1948).
18. M.M.Zaripov & Iu.Ia.Shamonin, Zhur.eksp.i teor.fiz., 30, 291 (1956).

19. A.A.Manenkov & A.M.Prokhorov, Zhur.eksp.i teor.fiz., 28, 762 (1955).

20. M.M.Zaripov & Iu.Ia.Shamonin, Present issue of the Bulletin.

21. B.M.Kozyrev, Doklady AN SSSR, 103, 53 (1955); N.S.Garif'ianov, Doklady AN SSSR, 103, 41 (1955).

22. S.A.Al'tshuler, B.M.Kozyrev & S.G.Salikhov, Doklady AN SSSR, 71, 855 (1950).

23. B.B.leaney & R.P.Penrose, Proc.Phys.Soc., 60, 83, 395, 540 (1948).

24. N.S.Garif'ianov & B.M.Kozyrev, Doklady AN SSSR, 98, 929 (1954).

25. M.M.Zaripov & N.S.Garif'ianov, Zhur.eksp.i teor.fiz., 28, 629 (1955).

26. M.M.Zaripov, Present issue of the Bulletin.

27. B.M.Kozyrev, Doklady AN SSSR, 81, 427 (1951).

28. B.M.Kozyrev, Doklady AN SSSR, 81, 427 (1951).

29. N.S.Garif'ianov & B.M.Kozyrev, Zhur.eksp.i teor.fiz., 30, 272 (1956).

30. S.G.Salikhov, Zhur.eksp.i teor.fiz., 26, 447 (1954).

31. S.A.Al'tshuler, Zhur.eksp.i teor.fiz., 26, 439 (1954).

32. E.K.Zavoiskii, Zhur.eksp.i teor.fiz., 17, 155 (1947).

33. I.M.Romanov, Uch.zap.Kazanskogo un-ta (Scientific notes of Kazan University), 113, 187 (1953).

34. B.M.Kozyrev, S.G.Salikhov & Iu.Ia.Shamonin, Zhur.eksp.i teor.fiz., 22, 56 (1952).

35. N.N.Neprimerov, Izv. AN SSSR, Ser.fiz., 18, 360 (1954) (Translation in Bulletin, Vol.18, No.3, p.55).

36. Ia.I.Frenkel', Zhur.eksp.i teor.fiz., 15, 409 (1945).

37. S.A.Al'tshuler, E.K.Zavoiskii & B.M.Kozyrev, Zhur.eksp.i teor.fiz., 17, 1121 (1947).

38. C.J.Gorter, J.H.Van Vleck, Phys. Rev., 72, 1128 (1947).

39. J.H.Van Vleck, Phys. Rev., 74, 1168 (1948).

40. G.Ia.Glebashev, Zhur.eksp.i teor.fiz., 30, 612 (1956).

41. G.Ia.Glebashev, Uch.zap.Kazanskogo un-ta (Scientific notes of Kazan University), 116, 121 (1956).

42. G.Ia.Glebashev, Zhur.eksp.i teor.fiz., 31, 1 (1957).

43. S.A.Al'tshuler, M.G.Odintsov, Izv.Kazanskogo filiala AN SSSR, Ser.fiz.-tekhn. (Bulletin of the Kazan Branch of USSR Ac.ofSci., Phys.tekh.series) 3,39(1953).

44. S.Kashaev, Doklady AN SSSR, 110, 362 (1956).

45. I.G.Shaposhnikov, Ph.D.Thesis, FIAN, M., 1949.

46. H.A.Kramers, Atti del Congresso Intern.del Fisici, Como, 2, 545 (1927).

47. S.A.Al'tshuler, Zhur.eksp. i teor. fiz., 20, 1047 (1950).

48. A.I.Rivkink, Izv. AN SSSR, Ser.fiz., 16, 541 (1952).

49. B.M.Kozyrev, Uch.zep.Kazanskogo ped. un-ta (Scientific notes of Kazan Pedagogical Institute), 1, 83 (1947).

50. E.K.Zavoiskii, Journ. of Phys. USSR, 8, 377 (1944).

51. I.G.Shaposhnikov, Zhur.eksp.i teor.fiz., 18, 533 (1948).

52. H.Casimir, F.Du Pre, Physica, 5, 507 (1938).

53. L.I.Mendel'shtam & M.A.Leontovich, Zhur.eksp.i teor.fiz., 17, 438 (1937).

54. N.S.Garif'ianov, Zhur.eksp.i teor. fiz., 25, 359 (1953).

55. K.P.Sitnikov, Dissertation, Kazan University, 1954.

56. A.I.Akhiezer & I.Ia.Pomeranchuk, Zhur.eksp.i teor.fiz., 14, 342 (1944); Doklady AN SSSR, 87, 917 (1952).

57. S.A.Al'tshuler, Zhur.eksp.i teor. fiz., 24, 681 (1953).

58. S.A.Al'tshuler, Present issue of the Bulletin, following article.

59. A.Kastler, S.R. 228, 1640 (1949).

60. Wilson, Hull, Phys. Rev., 74, 711 (1948).

61. N.N.Neprimerov, Izv. AN SSSR, Ser.fiz., 18, 368 (1954) (Translation in Bulletin, Vol.18, No.3, p.63)

62. S.A.Al'tshuler, Doklady AN SSSR, 85, 1225 (1952); Zhur.eksp.i teor.fiz., 28, 38 (1955); Zhur.eksp.i teor.fiz., 28, 49 (1955).

ON THE THEORY OF PARAMAGNETIC SPIN-LATTICE RELAXATION

-S.A.Al'tshuler

1. Introduction

In the earliest theory of paramagnetic spin-lattice relaxation, which was proposed by Waller[1], it was assumed that energy is transferred from the spin system to the lattice vibrations because of the changes in the magnetic spin interaction caused by these vibrations. Waller's calculations, however, gave values of the relaxation time several orders of magnitude higher than the experimental values. Particularly great disagreement between theory and experiment was observed in the case of titanium-cesium alum. Therefore, Kronig[2] and Van Vleck[3] suggested a different relaxation mechanism. Waller's mechanism may, however, play a fundamental role in many cases. Waller's calculations were carried out for a paramagnet whose magnetic particles have spin S = 1/2. Yet the probability of spin reorientation of a particle under the influence of the oscillations of the magnetic forces acting on it is proportional to the fourth power of the magnetic moment of the particle. In addition, this probability is inversely proportional to r_0^6 where r_0 is the equilibrium separation between two neighboring atoms of the crystal, which have magnetic moments. Often there are several such atoms in a single cell of the crystal. It is easy to see that in this case a more accurate result will be obtained if r_0 is taken not as the average, but as the shortest distance between neighboring particles possessing magnetic moments. It is clear, therefore, that the magnetic forces may determine the spin-lattice interaction in substances whose atoms have high magnetic moments and whose density of particles having magnetic moments is high.

It should also be noted that Waller considered the relaxation due to reorientation of the spin of a single particle by lattice vibrations, assuming that all other spin directions remain constant. As we shall see, however, there is a high probability for the simultaneous reorientation of the spins of two neighboring particles, which should reduce the relaxation time considerably. In Section 2 we shall refine and generalize Waller's theory.

Recent investigations of the properties of paramagnets in static and alternating magnetic fields and, in particular, studies of paramagnetic resonance have shown that exchange interaction between particles having magnetic moments is of great importance. Therefore there arises the question of the influence of exchange forces on spin-lattice coupling. Section 3 is devoted to an examination of this question.

Lastly, in Section 4 we shall consider paramagnetic spin-lattice relaxation in salts whose magnetic ions are in the s-state. The electric field of the crystal produces only minor splitting of the ground energy level of the magnetic particle (of the order of 1 cm^{-1}). The question arises whether modulation of the crystal field by lattice vibrations can lead to the experimentally observed spin-lattice interaction.

2. Relaxation Produced by Magnetic Interactions

For cases in which the orbital magnetism is not suppressed by the electric field of the crystal, modulation of the given crystal field by lattice vibrations plays the dominant role in the mechanism of spin-lattice relaxation. Good examples of this are the salts of rare earth elements.[4] We shall, accordingly, consider here substances with pure spin magnetism. Most salts of the iron group elements belong to this class. As a model of a paramagnet, we shall take a simple cubic lattice; with the magnetic particles having a spin S located at the lattice sites. We shall use the usual expression for the magnetic dipole interaction operator of two particles:

$$U = g^2\beta^2 \left[\frac{\mathbf{s}_1\mathbf{s}_2}{r_{12}^3} - \frac{3(\mathbf{s}_1 r_{12})(\mathbf{s}_2 r_{12})}{r_{12}^5} \right]. \tag{1}$$

Let us first consider first-order processes (single-phonon processes). We shall start with the expression derived by Waller for the transition probability from the magnetic level E_α to E_β, namely,

$$A_{\alpha\beta} = \frac{8\pi^3 Z}{3h^4} \cdot \frac{E_{\alpha\beta} r_0^2}{\rho v^5} \cdot \frac{e^{E_{\alpha\beta}/kT}}{e^{E_{\alpha\beta}/kT} - 1} \sum_{q=x,y,z} |(U_q)_{\alpha\beta}|^2, \tag{2}$$

where $U_q = \frac{\partial U}{\partial q}$, $E_{\alpha\beta} = E_\alpha - E_\beta$, ρ is the density of the paramagnet, v is the mean velocity of sound, Z is the number of closest neighbors, and T is the temperature. We shall use the representation in which s_{1z} and s_{2z} are diagonals. Let us use M_1 and M_2 to denote the magnetic quantum numbers of the respective atoms. The operator U_q will contain various expressions involving $s_{1q}s_{2q'}$, whose nondiagonal matrix elements are nonzero only in the following cases:

$$\left.\begin{aligned} (s_{1x}s_{2z})_{M_1,\,M_2;\,M_1+1,\,M_2} &= \frac{1}{2}\sqrt{s(s+1) - M_1(M_1+1)}\,M_2 \equiv t, \\ (s_{1y}s_{2z})_{M_1,\,M_2;\,M_1+1,\,M_2} &= it; \end{aligned}\right\} \tag{3}$$

$$\left.\begin{aligned} &(s_{1x}s_{2x})_{M_1,\,M_2;\,M_1+1,\,M_2+1} = \\ &= \frac{1}{4}\sqrt{s(s+1) - M_1(M_1+1)} \cdot \sqrt{s(s+1) - M_2(M_2+1)} \equiv p, \\ &(s_{1x}s_{2y})_{M_1,\,M_2;\,M_1+1,\,M_2+1} = (s_{1y}s_{2x})_{M_1,\,M_2;\,M_1+1,\,M_2+1} = ip, \\ &(s_{1y}s_{2y})_{M_1,\,M_2;\,M_1+1,\,M_2+1} = -p. \end{aligned}\right\} \tag{4}$$

Let us first consider the relaxation associated with transitions with $\Delta M_1 = 1$ and $\Delta M_2 = 0$. We use Eqs. (1), (3) and (4) to obtain the sum of the square moduli of the matrix elements of U_q:

$$\sum_{q=x,\,y,\,z} |(U_q)_{M_1,\,M_2;\,M_1+1,\,M_2}|^2 = \frac{9g^4\beta^4}{r_0^{12}}[r_0^4 + 6r_0^2 z_0^2 - 5z_0^4] \cdot \frac{1}{4}[s(s+1) - M_1(M_1+1)]\,M_2^2. \tag{5}$$

Averaging over different directions of the radius vector r_0 and over all possible values of M_1 and M_2, we obtain

$$\overline{\sum_q |(U_q)_{M_1,\,M_2;\,M_1+1,\,M_2}|^2} = \frac{18g^4\beta^4}{r_0^8} \cdot \frac{1}{36}\,s(2s+1)(s+1)^2. \tag{6}$$

Thus bearing in mind that $E_\alpha - E_\beta = g\beta H$, we obtain the transition probability in the form

$$A_1 = \frac{4\pi^3 Z}{3h^4} \cdot \frac{(g\beta)^3}{\rho v^5} \left(\frac{g^2\beta^2}{r_0^3}\right)^2 \frac{e^{g\beta H/kT}}{e^{g\beta H/kT} - 1}\,s(2s+1)(s+1)^2 H^3. \tag{7}$$

In the case of double transitions ($\Delta M_1 = 1$ and $\Delta M_2 = 1$)

$$\sum_{q=x,\,y,\,z} |(U_q)_{M_1,\,M_2;\,M_1+1,\,M_2+1}|^2 =$$

$$= \frac{9g^4\beta^4}{r_0^{12}}(r_0^2 - z_0^2)(13r_0^2 - 5z_0^2) \cdot \frac{1}{16}[s(s+1) - M_1(M_1+1)] \times [s(s+1) - M_2(M_2+1)]. \tag{8}$$

Averaging gives

$$\overline{\sum_{q=x,\,y,\,z} |(U_q)_{M_1,\,M_2;\,M_1+1,\,M_2+1}|^2} = \frac{72g^4\beta^4}{r_0^8} \cdot \frac{1}{36}(2s+1)^2(s+1)^2, \tag{9}$$

and, hence, the probability for double transitions is

$$A_2 = \frac{16\pi^3 Z}{3h^4} \cdot \frac{(2g\beta)^3}{\rho v^5} \left(\frac{g^2\beta^2}{r_0^3}\right)^2 \frac{e^{2g\beta H/kT}}{e^{2g\beta H/kT} - 1}(2s+1)^2(s+1)^2 H^3. \tag{10}$$

We see that the probability for double transitions proves to be much greater than A_1; thus, for $s = 1/2$, for instance, we have $A_2/A_1 \approx 64$. If we note also that double transitions are associated with the transfer of twice the amount of energy, $E_{\alpha\beta} = 2g\beta H$ to the lattice vibrations, we find that the relaxation time is reduced by a factor of approximately 10^2 as a result of these transitions.

For second-order processes (combined phonon scattering) the transition probability is given by[1]

$$A_{\alpha\beta} = \frac{\pi^3 Z}{18} \cdot \frac{r_0^4}{\rho^2 v^{10}} e^{E_{\alpha\beta}/kT} I_6 \sum_{q,\, p=x,\, y,\, z} \left|(U_q)_{\alpha\beta}\right|^2, \tag{11}$$

where

$$U_{q,p} = \frac{\partial^2 U}{\partial q\, \partial p}, \qquad I_n = \int\limits_0^{k\theta/h} \frac{\nu^n e^{h\nu/kT}}{(e^{h\nu/kT} - 1)^2} d\nu,$$

and θ is the Debye temperature. Calculation and averaging of the matrix elements yield

$$\left.\begin{aligned} \overline{\sum_{q,p} \left|(U_{q,p})_{M_1,\, M_2;\, M_1+1,\, M_2}\right|^2} &= 434 \frac{g^4\beta^4}{r_0^{10}} \cdot \frac{1}{36} s\,(2s+1)\,(s+1)^2, \\ \overline{\sum_{q,p} \left|(U_{q,p})_{M_1,\, M_2;\, M_1+1;\, M_2+1}\right|^2} &= 2366 \frac{g^4\beta^4}{r_0^{10}} \cdot \frac{1}{36} (s+1)^2\,(2s+1)^2. \end{aligned}\right\} \tag{12}$$

From this we obtain the transition probabilities:

$$\left.\begin{aligned} A_1 &= \frac{2\pi^3}{3} \cdot \frac{Z}{\rho^2 v^{10}} \left(\frac{g^2\beta^2}{r_0^3}\right)^2 e^{g\beta H/kT} I_6 \cdot s\,(2s+1)\,(s+1)^2, \\ A_2 &= 3{,}16\pi^3 \frac{Z}{\rho^2 v^{10}} \left(\frac{g^2\beta^2}{r_0^3}\right)^2 e^{2g\beta H/kT} I_6\, (2s+1)^2\,(s+1)^2. \end{aligned}\right\} \tag{13}$$

If the temperature of the paramagnet is appreciably higher than the Debye temperature, the probability for double transitions becomes

$$A_2 = 15{,}8\pi^3 \frac{Z}{\rho^2 v^{10}} \left(\frac{g^2\beta^2}{r_0^3}\right)^2 (s+1)^2\,(2s+1)^2 \left(\frac{kT}{h}\right)^2 \left(\frac{k\theta}{h}\right)^5. \tag{14}$$

Sitnikov[5] measured the spin-lattice relaxation time at room temperature in manganese solid solutions. The manganese in $MnSO_4 \cdot 4H_2O$ was replaced by diamagnetic magnesium. It was established that the relaxation time increases linearly with decreasing manganese concentration. This is readily explained if we assume that the spin-lattice coupling is accomplished by magnetic forces; on the other hand, it is hard to understand if we postulate any other relaxation mechanism. Unfortunately, not all the constants in Eq. (13) are known for the given substance; if plausible values are taken for these constants, however, the relaxation time for the undiluted salt is $\tau \approx 10^{-5}$ sec, while experiment gives $\tau \approx 10^{-7}$ at room temperature. The agreement may be considered satisfactory.

Hence we conclude that in many substances paramagnetic lattice relaxation is determined by the magnetic interactions of the atoms.

3. Relaxation Produced by Exchange Forces

It is known that in substances with high densities of magnetic ions, exchange forces significantly alter the static susceptibility and the line width of paramagnetic resonance. It is obviously of interest to clarify the influence of these forces on spin-lattice interaction. Usually the exchange interaction operator is given the isotropic form $A(r_{12})\,(s_1, s_2)$. This matrix has no nondiagonal elements and, consequently, isotropic spin forces can have no direct influence on the spin-lattice interaction.* However, the anisotropic exchange forces[6] encountered in certain paramagnetic materials may have an appreciable effect. Let us assume, as was done by Ollom and Van Vleck[7] in interpreting the magnetic properties of $NiSiF_6 \cdot 6H_2O$, that the exchange interaction operator has the dipole form

---

*See footnote next page.

$$v = A(r_{12})\,[(\mathbf{s}_1\mathbf{s}_2) - 3r_{12}^{-2}(\mathbf{s}_1 r_{12})(\mathbf{s}_2 r_{12})]. \tag{15}$$

The calculations will then be entirely similar to those we performed for magnetic forces. We need only know the dependence of the exchange integral A on the separation between the atoms. Let us make the logical assumption that $A(r) = A_0(r_0)\,e^{-r/R_0}$, where $R_0 \sim r_0$; then the expression $\left(\frac{2}{r_0} + \frac{1}{R_0}\right)$ enters into the perturbation matrix element. If we assume that it is equal to $3/r_0$ and if we introduce the notation $v_x = \frac{\partial v}{\partial x_0}$, $v_{xy} = \frac{\partial^2 v}{\partial x_0 \partial y_0}$ & $A(r_0) = A$,then proceding as in the previous section, we arrive at

$$\left.\begin{aligned} \sum_{q=x,\,y,\,z} \left|(v_q)_{M_1,\,M_2;\,M_1+1,\,M_2}\right|^2 &= \frac{24}{7} \cdot \frac{A^2}{r_0^2} \cdot \frac{1}{36}\, s(s+1)^2(2s+1), \\ \sum_{q=x,\,y,\,z} \left|(v_q)_{M_1,\,M_2;\,M_1+1,\,M_2+1}\right|^2 &= \frac{432}{7} \cdot \frac{A^2}{r_0^2} \cdot \frac{1}{36}(s+1)^2(2s+1)^2. \end{aligned}\right\} \tag{16}$$

$$\left.\begin{aligned} \overline{\sum_{p,q} \left|(v_{q,p})_{M_1,\,M_2;\,M_1+1;\,M_2}\right|^2} &= 105\,\frac{A^2}{r_0^4} \cdot \frac{1}{36}\, s(s+1)^2(2s+1). \\ \overline{\sum_{p,q} \left|(v_{q,p})_{M_1,\,M_2;\,M_1+1;\,M_2+1}\right|^2} &= 2147\,\frac{A^2}{r_0^4} \cdot \frac{1}{36}(s+1)^2(2s+1)^2. \end{aligned}\right\} \tag{17}$$

For direct processes, inserting (16) into (2), we obtain the transition probabilities

$$A_1 = \frac{16\pi^3}{63} Z\, \frac{(g\beta)^3}{h^4} \cdot \frac{A^2}{\rho v^5} \cdot \frac{e^{g\beta H/kT}}{e^{g\beta H/kT} - 1}\, s(2s+1)(s+1)^2 H^3, \tag{18}$$

$$A_2 = \frac{32\pi^3}{9} Z\, \frac{(2g\beta)^3}{h^4} \cdot \frac{A^2}{\rho v^5} \cdot \frac{e^{2g\beta H/kT}}{e^{2g\beta H/kT} - 1}(2s+1)^2(s+1)^2. \tag{19}$$

For second-order processes, substitution of (17) in (11) gives

$$A_1 = \frac{\pi^3}{6} Z\, \frac{A^2}{\rho^2 v^{10}}\, e^{g\beta H/kT} I_6\, s(2s+1)(s+1)^2, \tag{20}$$

$$A_2 = \frac{10}{3}\pi^3 Z\, \frac{A^2}{\rho^2 v^{10}}\, e^{2g\beta H/kT} I_6 (2s+1)^2(s+1)^2. \tag{21}$$

An exhaustive comparison of the experimental data on paramagnetic resonance with the results of theoretical calculations, carried out by Glebashev,[8] showed that the exchange integrals attain values of 10^{-18}-10^{-17} ergs. This means that the exchange integral A and the energy of magnetic interaction $g^2\beta^2/r_0^3$ are of the same order of magnitude. Therefore anisotropic exchange forces may play a decisive role in the mechanism of spin-lattice relaxation.

---

*(See previous page) The mean internal magnetic field of the crystal depends strongly on the isotropic exchange forces. Therefore, indirectly these forces may have a weak influence on spin-lattice relaxation. Moreover, we are not considering here processes of energy transfer from the spin system to lattice vibrations which are not accompanied by spin reorientation; more exactly, we are not considering processes connected with variations in exchange interactions that do not affect the overall magnetization of the paramagnet.

4. Relaxation in Salts with Magnetic Ions in s-States

Salts containing Mn^{++}, Fe^{+++}, Eu^{++} and Gd^{+++} ions occupy a special place among paramagnets. The magnetic ions of these salts are in s-states, as a result of which there is only insignificant splitting of the energy ground level by the electric field of the crystal. The total splitting is usually no more than 1 cm^{-1}. Hence it is of interest to determine the nature of the relaxation mechanism in these salts, i.e., to elucidate whether the decisive factors are the magnetic and exchange interactions considered in Sections 2 and 3 or whether the spin-lattice coupling due to modulation of the electric field of the crystal by lattice vibrations plays the dominant role.

We shall therefore use the case of salts containing trivalent iron ions for a detailed calculation of the paramagnetic relaxation time, assuming that the spin-lattice coupling is due to the electric interactions. It is known from investigations of paramagnetic resonance that the splitting of the Fe^{+++} ion ground level by the crystal field and the external magnetic field H applied in the [100] direction is given by a spin Hamiltonian[9] of the form

$$H = \frac{1}{6} D \left[s_x^4 + s_y^4 + s_z^4 - \frac{1}{3} s(s+1)(3s^2 + s - 1) \right] + g\beta H s_z. \tag{22}$$

For iron-rubidium alum, D = 0.0134 cm^{-1} (Ref. 10). Noting that the ground state of Fe^{+++} is $^6S_{5/2}$, we can use Eq. (22) to find the following eigenvalues and wave functions:

$$\left.\begin{aligned}
E_a &= -\frac{1}{2} D - \frac{1}{2} G + \sqrt{(D-2G)^2 + \frac{5}{4} D^2}, & \psi_a &= a_1 \Phi_{-5/2} + a_2 \Phi_{3/2};\\
E_b &= -\frac{1}{2} D + \frac{1}{2} G + \sqrt{(D+2G)^2 + \frac{5}{4} D^2}, & \psi_b &= b_1 \Phi_{-3/2} + b_2 \Phi_{5/2};\\
E_c &= D - \frac{1}{2} G, & \psi_c &= \Phi_{-1/2};\\
E_d &= D + \frac{1}{2} G, & \psi_d &= \Phi_{1/2};\\
E_f &= -\frac{1}{2} D - \frac{1}{2} G - \sqrt{(D-2G)^2 + \frac{5}{4} D^2}, & \psi_f &= f_1 \Phi_{-5/2} + f_2 \Phi_{3/2};\\
E_g &= -\frac{1}{2} D + \frac{1}{2} G - \sqrt{(D+2G)^2 + \frac{5}{4} D^2}, & \psi_g &= g_1 \Phi_{-3/2} + g_2 \Phi_{5/2}.
\end{aligned}\right\} \tag{23}$$

Here $G = g\beta H$ while the coefficients $a_1, a_2, b_1, \ldots, g_2$ are somewhat complicated functions of D and g; the values of these coefficients for simple cases will be given below.

The matrix elements of the spin-lattice interaction operator can be calculated with the aid of the wave functions of (23). We have already performed these calculations in investigating acoustical paramagnetic resonance (see Eq. 27 in Ref. 11). The calculations were carried out on the assumption that the magnetic ion is situated at the center of the octahedron at whose vertices are the sites of the water molecules. The influence of the crystal field on the magnetic ion is determined primarily by its charge e, the dipole moment μ of water, the distance R between the metal ion and a water molecule, and, finally, by the mean distance $\overline{r}$ of the 3d-electron from the center of the atom.

We shall first consider the spin-lattice coupling due to first-order (single-phonon) processes. In order to avoid cumbersome calculations, we shall consider only the following particular cases which are of the greatest practical interest:

1. Relaxation in weak magnetic fields. This means that the splitting of the energy levels due to application of the magnetic field is assumed to be much smaller than the splitting due to the electric field of the crystal or, in other words, $g\beta H \ll 3D$.

2. Relaxation in strong magnetic fields. This means that $g\beta H \gg 3D$.

In the case of weak magnetic fields

$$a_1 = b_2 = -f_2 = -g_1 = \sqrt{\frac{5}{6}} \text{ and } a_2 = b_1 = f_1 = g_2 = \frac{1}{\sqrt{6}}. \tag{24}$$

Using these coefficients to determine the matrix elements of the spin-lattice perturbation by means of Eq.(27) of Ref.11 and continuing the calculations in the usual way, we obtain the following expressions for the transition probability between a pair of sublevels α and β:

$$A_{\alpha,\beta} = \gamma_{\alpha,\beta} \frac{\pi^3}{h^4 \rho v^5} E^3_{\alpha,\beta} \left(\frac{e\mu}{R^2}\right)^2 \Big/ \left(1 - e^{-E_{\alpha\beta}/kT}\right), \tag{25}$$

where

$$\left.\begin{aligned} \gamma_{ac} = \gamma_{db} &= 155\left(\frac{\overline{r^2}}{R^2} + \frac{45}{32}\cdot\frac{\overline{r^4}}{R^4}\right)^2, & \gamma_{ad} = \gamma_{bc} &= 65\left(\frac{\overline{r^2}}{R^2} + \frac{45}{16}\cdot\frac{\overline{r^4}}{R^4}\right)^2, \\ \gamma_{af} = \gamma_{bg} &= 540\left(\frac{\overline{r^2}}{R^2} - \frac{9}{64}\cdot\frac{\overline{r^4}}{R^4}\right)^2, & \gamma_{bf} = \gamma_{ag} &= 1460\left(\frac{\overline{r^2}}{R^2} - \frac{9}{64}\cdot\frac{\overline{r^4}}{R^4}\right)^2, \\ \gamma_{cf} = \gamma_{dg} &= 1485\left(\frac{\overline{r^2}}{R^2} + \frac{45}{32}\cdot\frac{\overline{r^4}}{R^4}\right)^2, & \gamma_{fd} = \gamma_{cg} &= 480\left(\frac{\overline{r^2}}{R^2} - \frac{9}{64}\cdot\frac{\overline{r^4}}{R^4}\right)^2. \end{aligned}\right\} \tag{26}$$

Inserting these expressions for the transition probabilities into Gorter's[13] formula for the coefficient of heat transfer between the spin system and the lattice and assuming that the heat capacity of the spin system is determined by its magnetic interactions, we obtain the following expression for the limiting value of the relaxation time when H = 0:

$$\tau = 4\cdot 10^{-7}\frac{h^4 \rho g^2 \beta^2 H_i^2 v^5 s(s+1)}{D^4 \left(\frac{e\mu}{R^2}\right)^2 kT}. \tag{27}$$

The values of the coefficients γ were calculated on the assumption[12] that

$$\overline{r^2} = 4{,}4a_0^2, \quad \overline{r^4} = 30a_0^4, \quad R = 2\cdot 10^{-8} \text{ см}, \tag{28}$$

where $a_0 = \frac{\hbar^2}{me^2}$.

In order to calculate the relaxation time from Eq.(27), one must take the following considerations into account. The interaction energy of the magnetic ion with a water molecule is of order $e\mu/R^2$. The effect of the electric field of the crystal on an ion in the s-state is much weaker than in other cases. We shall take this into account by assigning an appropriately lower value to the dipole moment μ. In iron-rubidium alum the crystal field produces an energy-level splitting smaller by a factor of about 10^6 compared to the splitting in similar salts with a different cation. Thus, if we assume $\mu \sim 10^{-24}$ and assume for the other quantities in Eq.(27) the values given by Van Vleck[3] for other alums, the relaxation time we obtain for T = 1°K is $\tau \approx 10^3$ sec.

In a strong magnetic field the energy levels are best characterized in terms of the magnetic quantum number M. For the transition probability between sublevels with magnetic quantum numbers M and M' we again obtain Eq.(25), but since in this case

$$a_1 = b_1 = f_2 = g_2 = 0 \text{ and } a_2 = b_2 = f_1 = g_1 = 1, \tag{29}$$

the coefficients $\gamma_{MM'}$ will now be

$$\left.\begin{aligned} &\gamma_{5/2,\,3/2} = \gamma_{-3/2,\,-5/2} = 50\left(\frac{\overline{r^2}}{R^2} - \frac{9}{64}\cdot\frac{\overline{r^4}}{R^4}\right)^2, \quad \gamma_{5/2,\,-3/2} = \gamma_{3/2,\,-5/2} = 92\left(\frac{\overline{r^4}}{R^4}\right)^2, \\ &\gamma_{5/2,\,1/2} = \gamma_{-1/2,\,-5/2} = 100\left(\frac{\overline{r^4}}{R^4}\right)^2, \quad \gamma_{3/2,\,1/2} = \gamma_{-1/2,\,-3/2} = 8\left(\frac{\overline{r^2}}{R^2} + \frac{45}{128}\cdot\frac{\overline{r^4}}{R^4}\right)^2, \\ &\qquad\qquad \gamma_{5/2,\,-1/2} = \gamma_{1/2,\,-5/2} = 390\left(\frac{\overline{r^2}}{R^2} + \frac{45}{32}\cdot\frac{\overline{r^4}}{R^4}\right)^2, \\ &\gamma_{3/2,\,-1/2} = \gamma_{1/2,\,-3/2} = 125\left(\frac{\overline{r^2}}{R^2} + \frac{45}{32}\cdot\frac{\overline{r^4}}{R^4}\right)^2, \quad \gamma_{5/2,\,-5/2} = \gamma_{3/2,\,-3/2} = \gamma_{1/2,\,-1/2} = 0. \end{aligned}\right\} \tag{30}$$

Whence we obtain the relaxation time

$$\tau = \frac{7h^4\rho v^5}{\pi^3 (g\beta)^2 \left(\frac{e\mu}{R^2}\right)^2 kT} \cdot \frac{1}{\sum\limits_{M>M'} \gamma_{MM'} (M-M')^2 \frac{H^2+\frac{1}{2}H_i^2}{(H^2+H_i^2)^2}}. \qquad (31)$$

The commonly accepted values for the quantities entering this equation with T = 1°K and H = 1000 oersteds, give $\tau \approx 10^2$sec. Thus the relaxation time changes little on going from weak to strong fields. The change is even smaller where relaxations due to second-order processes are concerned. Hence in turning to an examination of the spin-lattice interaction due to combined phonon scattering we shall consider only relaxation in strong fields.

In this case we need not perform new calculations. Trivalent iron and cerium ions have the same total angular momentum quantum numbers 5/2. Consequently, the calculations of the relaxation time for cerium salts previously made by the author[4] can be utilized. These calculations gave the following expressions for the transition probability between energy sublevels of the metal ion under the influence of lattice vibrations:

$$A_{fg} = 10(4\pi)^4 \frac{h^2}{\rho^2\Delta^4 v^5}\left(\frac{e\mu}{R^2}\right)^4\left(\frac{\overline{r^2}}{R^2} - \frac{9}{64}\cdot\frac{\overline{r^4}}{R^4}\right)\left[\left(\frac{\overline{r^2}}{R^2} + \frac{27}{32}\frac{\overline{r^4}}{R^4}\right)^3 + \right.$$
$$\left. + \frac{3}{16}\left(\frac{\overline{r^2}}{R^2} - \frac{95}{32}\cdot\frac{\overline{r^4}}{R^4}\right)^2 \cdot \frac{9}{16}\left(\frac{\overline{r^2}}{R^2} + \frac{45}{32}\cdot\frac{\overline{r^4}}{R^4}\right)\right]\cdot I_8, \qquad (32)$$

$$A_{ab} = \frac{32}{5}\pi^4 \frac{1}{h^2\rho^2 v^5}\left(\frac{e\mu}{R^2}\right)^4\left(\frac{\overline{r^2}}{R^2} + \frac{45}{16}\cdot\frac{\overline{r^4}}{R^4}\right)^2\left[144\left(\frac{\overline{r^2}}{R^2} + \frac{45}{32}\cdot\frac{\overline{r^4}}{R^4}\right)^2 + \left(\frac{\overline{r^2}}{R^2} + \frac{27}{32}\cdot\frac{\overline{r^4}}{R^4}\right)^2\right] I_4. \qquad (33)$$

Similar expressions are obtained for other pairs of sublevels.

The transition probability between sublevels a and b will be very small, since the effective dipole moment of water enters to the fourth power in Eq.(33), and we have seen that in our case μ is 10^6 times less than for the salts of other elements. Eq.(32) contains the ratio of μ to $\Delta = g\beta H$ and these quantities are approximately proportional to each other. Hence we can evaluate the relaxation time by means of Eq.(32). Numerical computations show that the relaxation time is about 10^{-4}sec at the temperature of liquid oxygen.

In conclusion it should be noted that in many substances the hyperfine splitting of the energy levels exceeds the splitting due to the crystal field. This pertains particularly to manganese salts. In such cases the hyperfine structure of the energy levels may have a considerable influence on the actual spin-lattice relaxation time.

"V.I.Ul'ianov-Lenin" Kazan State University

References

1. I.Waller, ZS. f. Phys., 79, 370 (1932).
2. K.Kronig, Physica, 6, 33 (1939).
3. J.H.Van Vleck, Phys. Rev., 57, 426 (1940).
4. S.A.Al'tshuler, Zhur.eksp.i teor.fiz., 20, 1047 (1950).
5. K.P.Sitnikov, Dissertation, Kazan State University, 1954.
6. W.Opechowski, Physica, 14, 234 (1948).
7. J.P.Ollom & J.H.Van Vleck, Physica, 17, 225 (1951).
8. G.Ia.Glebashev, Zhur.eksp.i teor.fiz., 31, 1 (1957).
9. K.W.H.Steevens, Proc.Roy.Soc., A 214, 237 (1952).
10. B.Bleaney & R.S.Trenam, Proc.Phys.Soc., A 65, 560 (1953).
11. S.A.Al'tshuler, Zhur.eksp.i teor.fiz., 28, 38 (1955).
12. J.H.Van Vleck, JournChem.Phys., 7, 72 (1939).
13. C.J.Gorter, Paramagnetic Relaxation (In Russian trans.) M., 1949.

SOME REMARKS CONCERNING THE PROCESSING OF EXPERIMENTAL DATA ON NUCLEAR PARAMAGNETIC ABSORPTION

- R.A. Zhitnikov

In his first theoretical work devoted to nuclear induction, Bloch[1] showed that it should, in principle, be feasible to utilize radiofrequency nuclear paramagnetic resonance for purposes of isotopic analysis.

The magnitude of the nuclear paramagnetic resonance absorption effect, when sweeping slowly through resonance, is given by the expression[1]

$$v = \frac{n\gamma^2 I(I+1)\hbar^2 H_0}{3kT} \cdot \frac{|\gamma| H_1 \tau_2}{1 + (\tau_2 \Delta\omega)^2 + (\gamma H_1)^2 \tau_1 \tau_2}, \tag{1}$$

where n is the number of nuclei of the analyzed-for isotope in the given sample, I is the spin of these nuclei, γ is their gyromagnetic ratio, τ_1 and τ_2 are the longitudinal and transverse relaxation times, H_1 is the amplitude of the radiofrequency magnetic field, ω is its frequency, H_0 is the strength of the constant magnetic field, and $\Delta\omega = |\gamma| H_0 - \omega$.

It has been experimentally demonstrated several times that Eq.(1) gives the correct expression for nuclear paramagnetic absorption in low-viscosity liquids provided the absorption line does not exhibit a complex structure. Thus, it has been shown[2,3] that for such samples the shape of the absorption line and the dependence of the absorption on the amplitude of the radiofrequency field H_1 satisfy Eq.(1).

According to Eq.(1), other conditions remaining equal, the resonance absorption effect is proportional to n, the number of nuclei of the given isotope in the sample. This obviously offers a way of determining the isotope content of a sample.

The magnitude of this effect, however, depends strongly on the relaxation times τ_1 and τ_2. These relaxation times vary within wide limits depending on the type of chemical compound, the composition and structure of the sample, its physical state, temperature, purity, etc. It is therefore desirable in certain cases to eliminate the relaxation times from the results. This may be accomplished, apparently, in the following manner.

Experimental methods for investigating nuclear paramagnetic resonance absorption make it possible to obtain the resonance curve (1) on an oscilloscope screen[4,5] and to determine the area S under this curve, its width $2\Delta\omega_{1/2}$ at half-height and the magnitude v_m of the maximum absorption effect, corresponding to expression (1) with $\Delta\omega = 0$. In addition, with the aid of a recording or indicating instrument at the output of the apparatus[6,7] one can obtain the dependence of the derivative $\frac{\partial v}{\partial H_0}$ on $\Delta\omega$ and find its maximum value $\left(\frac{\partial v}{\partial H_0}\right)_m$ and the corresponding $\Delta\omega = \Delta\omega_m$.

Let us form the following expressions from these quantities:

$$R_1 = \frac{v_m \Delta\omega_{1/2}}{H_1} = \frac{n\gamma^2 I(I+1)\hbar^2 H_0}{3kT} |\gamma| [1 + (\gamma H_1)^2 \tau_1 \tau_2]^{-1/2}, \tag{2}$$

$$R_2 = \frac{\left(\frac{\partial v}{\partial H_0}\right)_m \cdot \Delta\omega_m^2}{H_1} = \frac{\sqrt{3}}{8} \cdot \frac{n\gamma^2 I(I+1)\hbar^2 H_0}{3kT} \gamma^2 [1 + (\gamma H_1)^2 \tau_1 \tau_2]^{-1/2}, \tag{3}$$

$$R_3 = \frac{v_m^2}{\left(\frac{\partial v}{\partial H_0}\right)_m \cdot H_1} = \frac{8\sqrt{3}}{9} \cdot \frac{n\gamma^2 I(I+1)\hbar^2 H_0}{3kT} [1 + (\gamma H_1)^2 \tau_1 \tau_2]^{-1/2}, \tag{4}$$

$$R_4 = \frac{S}{H_1} = \frac{1}{H_1} \int_{-\infty}^{\infty} v \cdot d(\Delta\omega) = \pi \frac{n\gamma^2 I(I+1)\hbar^2 H_0}{3kT} |\gamma| [1 + (\gamma H_1)^2 \tau_1 \tau_2]^{-1/2}. \tag{5}$$

The validity of these expressions for strong magnetic fields ($H_0 \approx 10^3$-10^4 oersted) can readily be verified by means of expression (1). The left sides of equations (2)—(5) contain experimentally obtainable quantities, while the right sides are proportional to n and depend on τ_1 and τ_2 in the same way, i.e., τ_1 and τ_2 are present only in the brackets. The right sides of these equations can clearly be made independent of the relaxation times if the measurements are performed in one of the following ways.

1. From Eq.(1) it is seen that if H_1 is varied, v_m attains a maximum value when

$$H_1 = \frac{1}{|\gamma|(\tau_1, \tau_2)^{1/2}} = H_{1m}. \tag{6}$$

In this case the expression in the brackets of Eqs.(2)—(5) becomes equal to 2 and the right sides are independent of τ_1 and τ_2. The value of H_1 corresponding to the condition (6) can be determined by observing v_m as H_1 is varied.

2. It also follows from Eq.(1) that $\left(\frac{\partial v}{\partial H_0}\right)_m$ attains its maximum value when

$$H_1 = \frac{1}{\sqrt{2}|\gamma|(\tau_1\tau_2)^{1/2}} = H_{1n}, \tag{7}$$

the value at which the expression in brackets in Eqs.(2)—(5) becomes equal to 3/2 and the right sides become independent of the relaxation times.

3. If the amplitude of the radiofrequency field is chosen so that

$$H_1 \ll \frac{1}{|\gamma|(\tau_1\tau_2)^{1/2}}, \tag{8}$$

Eqs.(2)—(5) again become independent of the relaxation times.

If all of the measurements are made satisfying one of the conditions (6), (7) or (8), the number n' of nuclei in the sample can be determined if there is available a standard sample for which the number n'' of nuclei of the same isotope is known.

Using one of equalities (2)—(5), we obtain

$$n' = n''\left(\frac{R_i'}{R_i''}\right). \tag{9}$$

Here R_i' and R_i'' are the left sides of one of Eqs.(2)—(5), as obtained under the conditions defined by (6)—(8), for the sample being investigated and the standard, respectively.

Eqs.(2)—(5) can also be used, when conditions (6)—(8) are satisfied, to determine the unknown spin I_a of an investigated nucleus from the resonance absorption effect. If I_b is the known spin of another isotope, then by using Eq.(3), for example, we obtain

$$I_a(I_a+1) = I_b(I_b+1)\left(\frac{\gamma_b}{\gamma_a}\right)^4\left(\frac{n_b}{n_a}\right)\left(\frac{R_{2a}}{R_{2b}}\right), \tag{10}$$

where all quantities with the subscript a pertain to the isotope under investigation, and those with the subscript b pertain to the known isotope.

$I_a(I_a+1)$ is found in a similar way from Eqs.(2), (4) or (5).

It is assumed here that the field H_0 is the same for the measurements on both isotopes, and that the frequency is changed. However, if the frequency is kept constant in the measurements, and the field is changed, H_0 in Eqs.(2)-(5) should be eliminated and ω introduced by the condition $H_0 = \omega/|\gamma|$. Equations such as (9) and (10) assume the same radio amplification in the measurements with the isotope under investigation and the standard, as well as the same depth of modulation of the field in measuring $\left(\frac{\partial v}{\partial H_0}\right)_m$.

4. If all the experimental data are first obtained at a r-f amplitude H_1 and then the same quantities are measured with an amplitude which differs from

the first by a factor p (where p is greater or smaller than unity), then in using, for instance, Eq.(5), we obtain

$$[1+(\gamma H_1)^2\tau_1\tau_2]^{1/2} = \frac{1}{p}\sqrt{\frac{1-p^2}{\left(\frac{S}{S_p}\right)^2-1}} = D_4, \tag{11}$$

where S is the area of the resonance curve corresponding to the amplitude H_1 and S_p is the area of the resonance curve corresponding to the amplitude pH_1. Multiplying the left side of Eq.(5) obtained with a r-f amplitude of H_1 by the right side of Eq.(11), we obtain a quantity independent of the relaxation times.

In using Eqs.(2)—(4), the area S in expression (11) is replaced by $v_m\cdot\Delta\omega_{1/2}$, $\left(\frac{\partial v}{\partial H_0}\right)_m\cdot\Delta\omega_m^2$ or $\frac{v_m^2}{\left(\frac{\partial v}{\partial H_0}\right)_m}$ respectively. The corresponding expressions such as (11) obtained by substitution of one of these quantities shall be denoted by D_i.

By using relationships such as (11) and one of the Eqs.(2)—(5), we can find the number n' of nuclei in the isotope under investigation. If n'' is the known number of nuclei of this isotope in the standard, then

$$n' = n''\left(\frac{R_i'}{R_i''}\right)\left(\frac{D_i'}{D_i''}\right). \tag{12}$$

Eq.(11) can also be used to determine an unknown nuclear spin I_a. If I_b is the known spin of another isotope, then using Eq.(3), for example, we obtain

$$I_a(I_a+1) = I_b(I_b+1)\left(\frac{\gamma_b}{\gamma_a}\right)^4\left(\frac{n_b}{n_a}\right)\left(\frac{R_{2a}}{R_{2b}}\right)\left(\frac{D_{2a}}{D_{2b}}\right). \tag{13}$$

Again it is assumed here that the measurements for both isotopes are made with the same constant field H_0.

All the remarks made above about Eqs.(9) and (10) apply equally to Eqs. (12) and (13).

From Eq.(1) it follows that the expression for the half-width $\Delta\omega_{1/2}$ of the resonance curve for nuclear paramagnetic absorption is of the form

$$\Delta\omega_{1/2} = \sqrt{3}\,\Delta\omega_m = \frac{1}{\tau_2}\,[1+(\gamma H_1)^2\,\tau_1\tau_2]^{1/2}. \tag{14}$$

Measurement of $\Delta\omega_{1/2}$ or $\Delta\omega_m$ when one of conditions (6)—(8) is satisfied can be used to determine the relaxation time τ_2.

Having measured the quantities on the left side of one of Eqs.(2)—(5) at two r-f amplitudes H_1 and pH_1, and making use of an equation such as (11), we can compute τ_2 according to Eq.(14):

$$\tau_2 = \frac{D_i}{\Delta\omega_{1/2}} = \frac{D_i}{\sqrt{3}\,\Delta\omega_m}. \tag{15}$$

In this case the measurements can also be performed under condition of partial saturation, when the magnitude of the r-f field is greater than that given by (6) or (7). Having found τ_2, Eq.(11) or (14) can be used to evaluate τ_1.

In the above discussions regarding the determination of the relaxation times τ_1 and τ_2, it is assumed that the resonance line width is determined not by the inhomogeneity of H_0, but by condition (14).

If the values of D_4 of expression (11) are found both for a standard sample with known relaxation times τ_1 and τ_2 and for the sample under investigation, it is possible to determine the product $\tau_1\cdot\tau_2$ for the latter even if the inhomogeneity of the constant field produces widening of the line over and above its natural width as given by (14).

Attempts to satisfy conditions (6) or (7) in determining the isotope content, nuclear spin and relaxation time are bound, in most cases, to result in poor accuracy. This is due primarily to the fact that the functions $v_m = f_1(H_1)$ and

$\left(\frac{\partial r}{\partial H_0}\right)_m = f_2(H_1)$ have very flat maxima, so it is difficult to maintain the conditions in question accurately. Variations in the conditions lead to errors in determining H_{1m} and H_{1m} and these errors in turn introduce uncertainties into the right sides of Eqs.(9), (10) and (14). Moreover, satisfying (6) or (7) for many samples involves both variation of the r-f current over a wide range and accurate measurement of the r-f field, which makes for certain experimental difficulties.

It may be difficult to fulfill condition (8) in the case of large relaxation times; attempting to satisfy this condition also leads to a reduction of the r-f power absorbed, since the r-f field in this case is far below the optimal values available with (6) and (7).

The use of two r-f amplitudes H_1 and pH_1 and relations such as (11) is free of the above disadvantages associated with attempting to satisfy the conditions of (6)—(8). This procedure should give the best accuracy and is easier to use in practice, since the values of the r-f fields H_1 and pH_1 used in this case are largely arbitrary and need not be determined with great accuracy. It is sufficient for H_1 and pH_1 to have the same values for the sample under investigation and the standard. Therefore H_1 and pH_1 can be chosen close to the values defined by (6) or (7), which makes it possible to effect the measurements at optimal conditions.

All the considerations presented above, of course, are valid only when Eq. (1) hold, i.e., when the absorption line is devoid of structure due to quadrupole interaction or nuclear spin interaction, and only on condition of slow variation through resonance.

Eqs.(2), (3) and (4) can presumably be used only when the degree of homogeneity of the field is such that the shape and width of the resonance line are determined by Eqs.(1) and (14), respectively, rather than by the homogeneity of the field in the volume of the sample. This condition is not obligatory when use is made of expression (5).

After the present article was already written, there were published Refs. 3 and 8 describing investigations in which the measurements were made satisfying condition (8) and relationship (10) was used to determine the nuclear spins of Ca^{43}, Ti^{47} and Ti^{49}.

As has been noted by Proctor and Yu[9], the reliable determination of spins equal to or greater than 5/2 necessitates enhanced accuracy of measurement and processing of the experimental data. The use of Eq.(10) by Jeffries[3,8] is related to this latter requirement. However, in determining nuclear spins, relations such as (11) and (13), whose advantages have been mentioned above, would also seem useful.

Arnold, Dharmatti and Packard[5] compared the areas under the resonance curves for protons from various organic-compound radicals to determine the number of protons responsible for the different resonance curves and discover which resonance peak is associated with which radical. It was found that proton resonance curves have different widths for different radicals of the same compound. This indicates that the relaxation times are different in different radicals of the same compound. Therefore more reliable results, such as those given by Pound and Knight[7], can probably be obtained in some cases if, in addition to Eq.(5), use is also made of Eqs.(11) and (12), and the relaxation times are entirely eliminated from results.

Kazan State Pedagogical Institute

References

1. F.Bloch, Phys. Rev., 70, 460 (1946).
2. F.Alder & F.C.Yu, Phys. Rev., 81, 1067 (1951).
3. C.D.Jeffries, Phys. Rev., 90, 1130 (1953).
4. N.Bloembergen, E.M.Purcell & R.V.Pound, Phys. Rev., 73, 679 (1948).
5. J.T.Arnold, S.S.Dharmatti & M.E.Packard, Journ. Chem. Phys., 19, 507 (1951).
6. W.G.Proctor, Phys. Rev., 79, 35 (1950).
7. R.V.Pound & W.D.Knight, Rev. Sci. Instr., 21, 219 (1950).
8. C.D.Jeffries, Phys. Rev., 92, 1262 (1953).
9. W.G.Proctor & F.C.Yu, Phys. Rev., 81, 20 (1951).

HYPERFINE SPLITTING OF ELECTRON LEVELS IN PARAMAGNETS

- M.M. Zaripov

Introduction

In recent years the methods of nuclear and electron paramagnetic resonance have come to be widely used for determining the spins of atomic nuclei. In investigating nuclear magnetic resonance one observes r-f resonance absorption lines associated with reorientation of the nuclear spin relative to an applied constant magnetic field. Nuclear resonance is usually studied in diamagnetic substances. It can also be studied in paramagnets when the nucleus under investigation belongs to an atom which has no electronic magnetism. If, however, the nucleus belongs to a paramagnetic atom, the interaction of the given nucleus with the magnetic moment of the electrons leads to extreme complexity of the phenomenon of paramagnetic resonance (hereinafter - PR) and in most cases makes the effect unobservable.

The spins of nuclei may be determined with the aid of electron resonance by means of studying the hyperfine structure (hereinafter - hfs) of the absorption lines. Until now, in electron PR investigations, studies have been confined to lines, which are due to transitions between magnetic sublevels, occurring as a result of splitting of degenerate or quasidegenerate electron energy levels in a constant external magnetic field. By quasidegenerate levels we mean levels separated, in the absence of an external magnetic field, by an interval no greater than 1-2 cm^{-1}, so that transitions between them correspond to radiofrequencies.

The present work is devoted to the theory of PR due to transitions between hfs sublevels of single electron energy levels of paramagnetic ions. This case may be considered intermediate between nuclear and electronic magnetic resonance. The essence of the problem is the following. It is well known[1] that the mean magnetic moment of an atomic electron shell is zero in a state which is nondegenerate in the absence of a magnetic field. If the spin of the nucleus is taken into account, the energy level becomes degenerate and, in the first approximation, the magnetism of the atom is determined by the nuclear magnetic moment. The influence of the other electronic levels on the level under consideration leads to the magnetic moment of the single electron level not being purely nuclear in the second approximation. The magnitude of the additional magnetic moment μ' depends on the hfs and on the separation between electron levels. The order of magnitude of μ' can be evaluated from

$$\mu' \approx \frac{A}{\Delta E}\beta$$

where A is the hfs constant and ΔE is the interval between electron levels. In many cases $A \approx 5\cdot10^{-2}cm^{-1}$ and $\Delta E < 5cm^{-1}$, so that the magnetic moment has a value intermediate between the electronic and nuclear values, i.e., $\mu' \approx 0.01\beta$. It follows that as regards both the position and intensity of the resonance lines, the effect we are considering will be intermediate between the electronic and nuclear PR phenomena.

It is well known that single electron energy levels arise when the number of unpaired electrons of the paramagnetic ion is even.[2] Hence our calculations will pertain only to triply charged ions of rare earth elements with an even number of valence electrons.

Of the iron group elements we shall consider Cr^{++} and V^{+++}, for which it is known from experimental data that the singlets are not distant from the other electron energy levels. The case of Ni^{++} is analogous to that of V^{+++}.

Spin Hamiltonian for Calculating the Hyperfine Structure of Simple Levels of Rare Earth Ions; Selection Rules for Magnetic Dipole Transitions Between Hfs Sublevels

On the basis of the general theory of PR spectra of the crystals of rare earth compounds,[3] the Hamiltonian of our problem can be written

$$\mathcal{H} = \lambda(\mathbf{LS}) + V + a(\mathbf{NI}) + \beta\mathbf{H}(\mathbf{L}+2\mathbf{S}) + P\left[I_z^2 - \frac{1}{3}I(I+1)\right] - \gamma\beta_N\mathbf{HI}, \qquad (1)$$

where λ is the spin-orbit interaction constant, V is the energy of the ion in the electric field of the crystal, and P is the quadrupole interaction constant.

It is well known that the width of the multiplet in rare earth salts is greater than the splitting due to the electric field of the crystal. Therefore, following perturbation theory, in solving Eq. (1), we should first consider the splitting due to spin-orbit interaction, and then take account of the crystal field. We shall consider the splitting of the lowest multiplet level of the free ion in an electric field with symmetry C_{3h} (rare earth ethyl sulfates, bromates, nitrates and formates). In this case the influence of the neighboring multiplet level is negligibly small. We shall derive the Hamiltonian for calculating the hfs of simple rare earth levels in the same way as for the iron group ions in which the lowest Stark level is not split in the first approximation of spin-orbit interaction.

Taking the axis of symmetry of the electric field as the Z axis, it can be shown that the desired spin Hamiltonian is of the form

$$\begin{aligned}\mathcal{H}_{\text{spin}} = {} & a^2(\langle J\|N\|J\rangle)^2(C_{ZZ}-C_{XX})I_z^2 + 2aC_{ZZ}\beta\langle J\|N\|J\rangle H_Z I_Z + \\ & + 2a\langle J\|N\|J\rangle\langle J\|\lambda\|J\rangle\beta C_{XX}(H_X I_X + H_Y I_Y) + \\ & + P\left[I_Z^2 - \frac{1}{3}I(I+1)\right] - \gamma\beta_N\mathbf{HI},\end{aligned} \qquad (2)$$

where

$$C_{ZZ} = \sum_{n\neq 0}\frac{|\langle 0|J_Z|n\rangle|^2}{W_0 - W_n}, \qquad C_{XX} = \sum\frac{|\langle 0|J_X|n\rangle|^2}{W_0 - W_n},$$

$$\langle J\|N\|J\rangle, \qquad \langle J\|\lambda\|J\rangle, \qquad a = \frac{2\gamma\beta\beta_N}{r^3}$$

are constants characterizing the given ion, and $\langle 0|$ is the wave function of the individual energy level. We cannot look for eigenvalues of this Hamiltonian with the aid of perturbation theory if we take the unperturbed Hamiltonian as the interaction with the constant magnetic field, since with the magnetic field strengths currently assumed, all of its terms have approximately the same order of magnitude. Therefore this problem must be solved by taking account of all terms of the Hamiltonian simultaneously. It can readily be seen that for an arbitrary direction of the magnetic field with respect to the Z axis the problem reduces to solving an irreducible secular equation of order 2I + 1. We shall therefore consider the case in which the magnetic field vector is parallel to the Z axis. Then Eq. (2) becomes

$$\mathcal{H}_{\text{spin}} = \alpha I_Z^2 + \delta\beta H I_Z + P\left[I_Z^2 - \frac{1}{3}I(I+1)\right] - \gamma\beta_N H I_Z. \qquad (3)$$

Here

$$\alpha = a^2(\langle J\|N\|J\rangle)^2(C_{ZZ}-C_{XX}), \quad \delta = 2a\langle J\|N\|J\rangle\langle J\|\lambda\|J\rangle C_{ZZ}.$$

The further calculations involved essentially finding the coefficients α and δ, since it is a trivial problem to find the eigenvalues of Eq. (3).

Calculation of the magnetic dipole transition probabilities between energy levels given by the Hamiltonian of (2) leads to the following selection rules: if the alternating magnetic field is directed along the Z axis, it will excite no dipole transitions between hfs sublevels; if, on the other hand, the alternating magnetic field is directed along the X axis, transitions between neighboring hfs sublevels are allowed. In the first approximation these selection rules do not depend on the direction of the constant magnetic field relative to the symmetry axis of the electric field.

The talbe presents the calculated values of the coefficients of the spin Hamiltonian of (3), as well as the relative magnetic dipole transition probabilities mentioned above.

Values of the coefficients α and δ and transition probabilities.*

Ion	Height of the single level above ground state, cm^{-1}	$\alpha \cdot 10^{-3}$, см$^{-1}$	$\delta \cdot 10^{-3}$, см$^{-1}$	Relative transition probability
Pr^{+++}	98	$-0{,}096$	$-1{,}97$	1**
	277	$0{,}096$	0	1
	332	$-0{,}0023$	$1{,}97$	1
Eu^{+++}	$^6F_0$	$-0{,}015$	$-0{,}26$	1/3
Tb^{+++}	0	$0{,}1\,\mu_N^2$	$-6{,}8\,\mu_N$	10
	34	$-0{,}24\,\mu_N^2$	$-13\,\mu_N$	10
	58	$0{,}21\,\mu_N^2$	$13\,\mu_N$	10
Ho^{+++}	0	$0{,}29\,\mu_N^2$	$-8\,\mu_N$	100
	50	$-0{,}23\,\mu_N^2$	$-2{,}6\,\mu_N$	100
	75	$-0{,}12\,\mu_N^2$	$-3{,}1\,\mu_N$	100
	85	$0{,}04\,\mu_N^2$	$8{,}7\,\mu_N$	10
	189	$-0{,}17\,\mu_N^2$	$3{,}1\,\mu_N$	100
Tm^{+++}	0	$-0{,}53\,\mu_N^2$	$-0{,}10\,\mu_N$	10
	26	$-1\,\mu_N^2$	$-0{,}013\,\mu_N$	10
	30	$0{,}013\,\mu_N^2$	$-0{,}012\,\mu_N$	30
	51	$2{,}8\,\mu_N^2$	$0{,}013\,\mu_N$	10
	138	$-7{,}1\,\mu_N^2$	$0{,}01\,\mu_N$	30

---

*Detailed calculations for the coefficients and transition probabilities can be found in Ref. 4.

**The transition probability four times greater than the probability for nuclear resonance is taken as unity here.

Our calculations for the iron group elements V^{+++} and Cr^{++} are based on the results obtained by Ono et al[5] in investigating the fine structure of the PR spectra. It was found that as regards both the intensity of the resonance lines and their positions, the effect in question differs little from nuclear magnetic resonance.

Conclusions

In conclusion we want to touch on certain distinctive features of paramagnetic resonance associated with transitions between hfs sublevels of simple electron energy levels, and examine the possibility of its experimental detection.

In investigating PR in ions with integral spins (an even number of valence electrons) there always arise difficulties related to the Jahn-Teller effect[6]. Van Vleck[7] has treated this effect in crystals. He showed that in rare earth elements the splitting of degenerate energy levels due to the given effect is small (of the order of 0.01 cm^{-1}), but it must be noted that this is the splitting which is of great significance for radiospectroscopic investigations. In addition to the Jahn-Teller effect, there may be other factors which cause deviations from the basic symmetry of the electric field. For instance, in rare earth ethyl sulfates such deviations can be caused by the structure of the ethyl sulfate radical. Therefore the interpretation of PR spectra of rare earth salts with an even number of electrons is extremely difficult.

It is clear that the above difficulties will not be overcome by considering the effect discussed in the present article.

Comparison of the experimentally obtained values of α, δ and P with the calculated ones should make it possible to evaluate the magnetic dipole and electric quadrupole moments of nuclei.

The detection of the effect discussed here depends not only on the intensity of the absorption line, whose magnitude we took into consideration in each specific case, but also on the line width. The width of a PR line is determined by the spin-spin and spin-lattice interactions. Since only a small magnetic moment is associated with the single electron energy levels herein considered, it may be expected that both the spin-spin and spin-lattice relaxation times will be intermediate between their pure nuclear and pure electron values. It follows that experimental observation of this effect should present no particular difficulties.

The further development of the theory of this question must be correlated with detailed calculations of the widths of the absorption lines due to spin-spin interactions and evaluation of the spin-lattice relaxation times.

Lastly, we note that a similar effect can take place in compounds of elements belonging to other transition groups.

"V.I.Ul'ianov-Lenin" Kazan State University

References

1. L.Landau & E.Lifshits, Kvantovaia mekhanika (Quantum Mechanics), M.-L., 1948.
2. H.Bethe, Ann. de Phys., 3, 133 (1929).
3. R.J.Elliott & K.W.Stevens, Proc.Roy.Soc., A218, 553 (1953).
4. M.M.Zaripov, Dissertation, Kazan State University, 1955.
5. K.Ono, S.Koide, H.Seiyama & H.Abe, Phys.Rev., 96, 38 (1954).
6. H.A.Jahn & E.Teller, Proc.Roy.Soc., A161, 220 (1937).
7. J.H.Van Vleck, J.Chem.Phys., 7, 72 (1939).

ELECTRONIC PARAMAGNETIC RESONANCE IN NATURAL BERYLLIUM CRYSTALS

- M.M.Zaripov & Iu.Ia.Shamonin

In the course of investigating paramagnetic resonance in five natural beryllium single crystals at a frequency of 9655 Mc we detected and recorded the paramagnetic resonance absorption spectra. We found that the character of the spectrum – the number of lines and their relative positions and intensities – depends greatly on the direction of the constant magnetic field H relative to the crystal axes. The general appearance of the spectrum obtained for sample No.2 is shown in the accompanying figure.

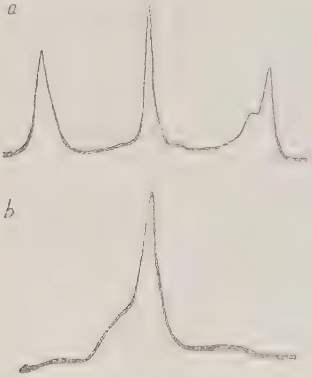

Dependence of the paramagnetic resonance absorption spectrum of a beryllium single crystal on the direction of the magnetic field relative to the optical axis of the crystal: a) field parallel to the optical axis, b) perpendicular to the optical axis.

The measurements were made using the conventional procedure[1] at room temperature. The strength of the constant magnetic field was determined by the proton resonance technique to within 0.1%. The resonance values of the magnetic field as measured for the parallel and perpendicular orientations of the field relative to the optical axis of the crystal, are listed in the accompanying table. It must be noted that the accuracy of determination of the resonance values of H in most cases depends on the line width and hence here the accuracy is appreciably inferior to 0.1 %. There is good reason to assume that the line width in the investigated specimens is determined by spin-lattice interaction. It should be possible to verify this by measurements at very low temperatures, for at low temperatures it should be feasible to determine the positions of the resonance absorption lines much more accurately.

Pure beryllium ($Al_2Be_3(SiO_3)_6$) itself does not comprise paramagnetic atoms, hence the appearance of the paramagnetic absorption spectrum is due to the absorption of r-f energy by paramagnetic impurities incorporated in the beryllium lattice. From an analysis of the observed spectrum one can conclude that it is associated with Fe^{+++} ions which can isomorphously replace Al^{+++} ions in the beryllium lattice. Optical spectrum analysis, carried out by Stolov, confirms the presence of iron in our beryllium crystals.

Resonance values of the constant magnetic field (in oersteds) for beryllium single crystals

Sample No.	Field parallel to optical axis of crystal					Field perpendicular to optical axis of crystal				
	1	2	3	4	5*	1	2	3	4	5*
1	2852	—	3436	3962	4040	2982	3329	3446	—	—
2	2868	—	3437	3945	4040	3010	3329	3446	—	3854
3	2848	—	3439	3974	4056	2982	3306	3445	—	3844
4	2861	—	3439	3969	4050	2977	3325	3447	—	—
5	2860	—	3437	—	4033	—	—	3439	—	—
Averages	2856	—	3437	3962	4044	2988	3320	3445	—	3849
Calculated	2856	2922	3437	3962	4048	3017	3341	3433	3517	3891

*Consecutive line numbers

Beryllium crystals have hexagonal symmetry. The nearest neighbors of the aluminum atoms are oxygen atoms, which are located at the vertices of an octahedron; just as in the ruby lattice[2], in the beryllium lattice the aluminum atoms are not at the center of the octahedron but are displaced along its trigonal axis which is the optical oxis of the crystal. Hence the paramagnetic Fe^{+++} ions are under the influence of an electrostatic field having trigonal symmetry.

Calculation of the fine structure of the paramagnetic resonance spectrum consists of determining the splitting of the ground state of the paramagnetic ion under the influence of the electric field of the crystal and the constant applied magnetic field and in establishing the selection rules for magnetic dipole transitions between the spin sublevels. Such calculations for the Fe^{+++} ion in alum were carried out by Bleaney & Trenam[3]. As is known the paramagnetic ion in alums is under the influence of an electric field having trigonal symmetry; hence in interpreting the observed spectrum we will use the results obtained by Bleaney & Trenam.

For computing the constants a, D and F, entering into the spin Hamiltonian and characterizing the coupling of the paramagnetic ion with the internal electrostatic field of the crystal, we made the following identification. In the case when the magnetic field is parallel to the optical axis of the crystal, the first absorption line is associated with the transition $M = 3/2 \leftrightarrow 1/2$, the third line with $M = 1/2 \leftrightarrow -1/2$ and the fourth line with $M = -5/2 \leftrightarrow -3/2$. Using the resonance values of H, averaged for all five specimens, we obtained a = 152 oersted, D = 178 oersted and F = 8 oersted. The spectroscopic splitting factor g can, with good accuracy, be assumed to be equal to 2.00, inasmuch as we are dealing with the ^6S-state. Having the values of the constants, one can readily evaluate the energy separations between the three Kramers doublets into which the ground state of Fe^{+++} in beryllium is split by the electric field. The separations proved to be 0.058 cm^{-1} and 0.050^{+0}_{-5} cm^{-1}.

In addition to the three absorption lines mentioned above, calculations indicate the existence of two more lines. The position of one of these lines, associated with $M = -3/2 \leftrightarrow -1/2$ transitions, coincides closely with the position of the fifth observed line. The resonance value of the constant magnetic field for the line associated with the $M = 5/2 \leftrightarrow -3/2$ transition is 2922 oersted. The asymmetry of the first absorption line is apparently due to this transition.

Calculation of the spectrum in the case when the constant magnetic field is directed perpendicular to the optical axis of the crystal shows that in this case the spectrum must consist of five absorption lines. In this case, in view of the great width and overlapping of the last two lines it is impossible to fix the position of the fourth line. The somewhat poor (as compared with the parallel field case) agreement between the experimental and calculated resonance values of H for the other lines can also be explained by the greater width and overlapping of the lines.

The results of this investigation show that in some cases one can use the method of paramagnetic resonance for qualitative analysis of minerals for their paramagnetic inclusion content.

"V.I.Ul'ianov-Lenin" Kazan State University

References

1. M.M.Zaripov & Iu.Ia.Shamonin, Zhur.eksp.i teor.fiz., 30, 291 (1956).
2. B.F.Ormont, Strutury neorganicheskikh veshchestv (Structures of inorganic substances) M.-L., 1950.
3. B.Bleaney & R.S.Trenam, Proc. Roy. Soc., A223, 1 (1954).

ON THE SIGNAL SHAPE IN NUCLEAR MAGNETIC RESONANCE IN THE CASE OF MEDIUM RELAXATION TIMES

- N.M. Ievskaia

In magnetic resonance of atomic nuclei the behavior of the magnetization vector, associated with nuclear magnetism, is influenced not only by the external magnetic field (static and high-frequency), but also by the internal fields due to the interaction of the nuclei with each other and with other component elements of the surrounding substance and characterized by the longitudinal and transverse relaxation times.[1-7] Thus through observation of magnetic resonance of atomic nuclei and investigation of the shape of the r-f signals appearing on the oscilloscope screen one can determine not only the nuclear magnetic moment but also the longitudinal and transverse relaxation times, the values of which in turn yield information on the structure of the medium surrounding the nucleus. In the present investigation we studied the shape of the dispersion and absorption signals appearing in weak and strong r-f fields with sinusoidal modulation of the longitudinal magnetic field in the case of medium relaxation times, i.e., in the case when the period of T_m of the modulating magnetic field and the relaxation times (longitudinal - τ_1 and transverse - τ_2) are comparable in magnitude. By definition a weak r-f field is a field for which the magnetization vector at the instant of resonance deviates very little from its equilibrium position; a strong r-f field is one for which the magnetization vector at resonance undergoes strong perturbation and turns over.

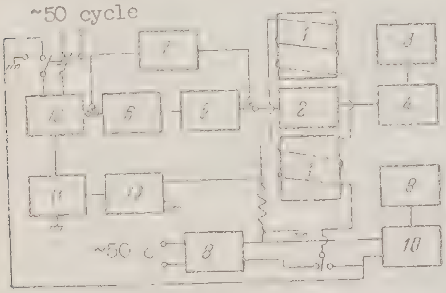

Fig. 1. Block diagram of apparatus: 1) electromagnet, 2) circuit component containing the specimen 3) r-f generator, 4) power amplifier, 5) i-f amplifier, 6) detector, 7) receiver unit, 8) transformer, 9) audio generator, 10) power amplifier, 11) oscillograph, 12) vertical phase shifter and 13) horizontal phase shifter.

For observing the signals we developed and built the special set-up diagramed in Fig. 1. To allow of separate observation of the dispersion and absorption signals the set-up incorporated a circuit with two perpendicular coils with electric compensation[8]. The specimen was placed in the gap between the pole pieces of the electromagnet 1. The circuit component 2, containing the specimen, was connected to the r-f generator 3 and the power amplifier 4. The signals were amplified and detected either by means of the i-f amplifier 5 and detector 6 or the receiver unit 7. Modulation of the magnetic field was accomplished by means of an additional winding of the electromagnet fed either from the power line through the transformer 8 or from the audio generator 9 through the power amplifier 10. For viewing the signal on the oscillograph screen we used an elliptical time base, realized by applying a voltage synchronized with field modulating voltage to the vertical and horizontal inputs of the oscillograph through the phase shifters 12 and 13.

The experimental conditions were the following: frequency of the r-f magnetic field f = 12.6 Mc, half-full amplitude of the r-f magnetic field H_1 = 0.01 — 1 oersted, intensity of the constant magnetic field H_o = 2960 oersted, frequency of the modulating magnetic field f_m = 50-500 cps, amplitude of the modulating magnetic field H_m = 1-35 oersted, volume of the investigated specimen 0.5-0.[illegible] cm^3.

In all the experiments we studied proton resonance. The investigated materials included distilled water, water solutions having different concentrations of copper sulfate and ferric nitrate, paraffin, glycerin and different types of synthetic rubber.

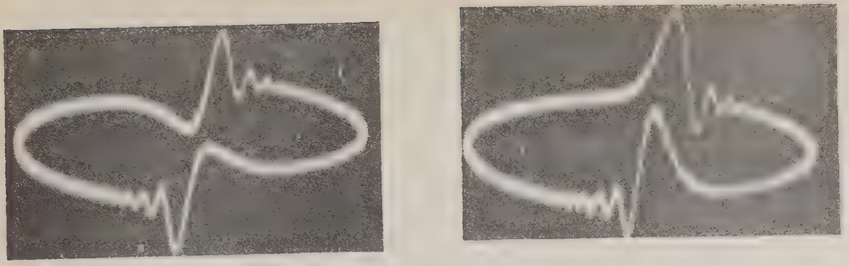

a

б

Fig. 2. Shape of dispersion (a) and absorption (b) signals in a weak r-f magnetic field with non-adiabatic sweep through resonance. The oscillograms are for a 0.5 molar aqueous solution of $CuSO_4$ recorded under the following conditions: $f_m = 50$ cps, $H_m = 2.38$ oersted, $H_1 = 0.1$ oersted.

As was noted above, the shape of the dispersion and absorption signals appearing on the oscillograph screen depends on the values of the longitudinal and transverse relaxation times and on external conditions which include the intensity of the r-f magnetic field, the amplitude and frequency of the modulating field and the time interval between signals.

Oscillograms of the dispersion and absorption signals in a weak r-f magnetic field with non-adiabatic variation through resonance are reproduced in Fig.2.

A procedure for determining the transverse relaxation time τ_2 was developed on the basis of analysis of the shape of the dispersion signal appearing in the case of a weak r-f magnetic field when $T_m/\tau_2 > 1$ (Ref. 9). We calculated the dependence of the distance between the first and second extrema of the dispersion signal on the transverse relaxation time and modulation rate. This is shown in Fig. 3, where

$$\Delta r = \sqrt{\frac{|\gamma| H_m \omega_m}{2}}\,\Delta t \quad \text{and} \quad \frac{\alpha}{2} = \frac{1}{\tau_2}\cdot\frac{1}{\sqrt{2|\gamma| H_m \omega_m}}, \qquad (1)$$

here Δt is the separation in time between the first and second extremum points (maximum and minimum) and γ is the gyromagnetic ratio.

The determination of the dependence of Δr on $\alpha/2$ was reduced through solution of a transcendental equation derived from Bloch's equation. Thus having measured the separation between the first maximum and first minimum of the dispersion signal one can by means of the computation curve of Fig.3 and the cited equations determine the transverse relaxation time τ_2.

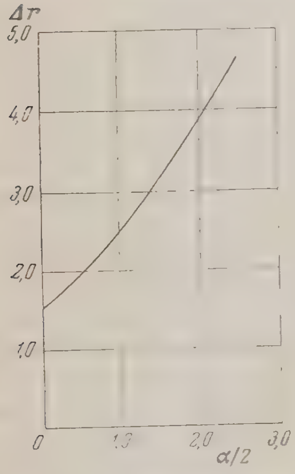

Fig. 3. Dependence of the separation between the first and second extremum points of the dispersion signal in a weak r-f magnetic field on the transverse relaxation time for the condition $T_m/\tau_2 > 1$.

Analysis of the shape of the signal appearing when a strong r-f magnetic field is applied in a case of medium relaxation times is of great interest, for this situation is frequently encountered in experiments. A general solu- for the shape of the signal in strong r-f magnetic fields for the case of arbitrary relaxation times with symmetric modulation is given in Refs. 1 & 10. However, this solution is given in the form of an integral which does not reduce to tabulated functions and hence at present cannot be used for analysis of the shape of signals for the purpose of determining the relaxation times.

An approximate solution by the method of numerical integration was obtained for the shape of the dispersion signal in the case of a strong r-f magnetic field with symmetric or asymmetric modulation for medium relaxation times.

In the case of symmetric modulation the solution is of the form

$$u(x) = u(x_\tau)\frac{g(x_\tau)}{g(x)}\exp\{f(x_\tau) - f(x)\}, \qquad (2)$$

where

$$f(x) = \nu x + \frac{\mu - \nu}{\sqrt{1+k^2}} \operatorname{arc\,tg}\left(\sqrt{1+k^2}\,\operatorname{tg} x\right), \qquad g(x) = \left[1 + k^2 \sin^2 x\right]^{1/2},$$

$$x = \omega_m t, \quad \nu = \frac{1}{\omega_m \tau_1}, \quad \mu = \frac{1}{\omega_m \tau_2}, \quad k = \frac{H_m}{H_1},$$

t is the time, x_τ is the instant when, as resonance is approached, the signal attains half its maximum value $(u(x_\tau) = 0{,}5\,u_{max})$. The limits of applicability of this approximate solution for two values of k are shown in Fig. 4. If with the given value of k the values of μ and ν lie inside the corresponding shaded area, the shape of the dispersion signal is described by expression (2) with an accuracy of 10% or better.

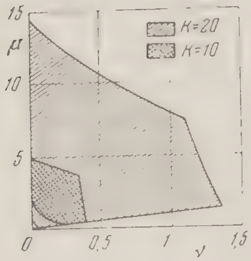

Fig.4. Region of applicability of the approximate solution for the shape of the dispersion signal in a strong r-f magnetic field for two values of k.

Under conditions when the constant magnetic field to which the modulating magnetic field is applied differs from the resonance value the signals are displaced off center on the oscillogram.

An approximate solution for the shape of the dispersion signal with asymmetric modulation was obtained in the following form

$$u(x) = u(x_\tau)\frac{G(x_\tau)}{G(x)} \exp\left\{F(x_\tau) - F(x)\right\}, \tag{3}$$

where

$$F(x) = \nu x + \frac{\mu - \nu}{p} \operatorname{arc\,tg}\left[p(x + \psi)\right], \quad G(x) = \left[1 + k^2(\varkappa + \sin x)^2\right]^{1/2},$$

$$p = k\cos\psi, \quad \psi = \arcsin\varkappa, \quad \varkappa = \frac{H_c}{H_m},$$

and H_c is the constant displacement imposed on the resonance value of the constant magnetic field.

Analysis of Eqs.(2) and (3) shows that the dispersion signal has a somewhat deformed bell-like shape. The width and deformation of the signal depend on the relaxation times, the amplitude of the r-f and modulating fields, the frequency of the modulating field and the position of the signal on the oscillogram.

When the r-f field is homogeneous one can determine the amplitude of the r-f magnetic field and the transverse relaxation time from the shape of the signal.

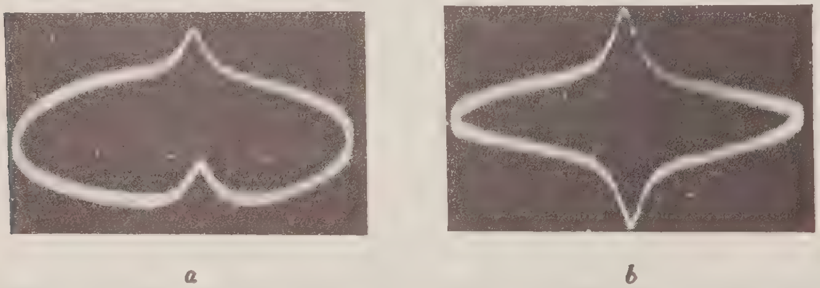
a b

Fig.5. Shape of dispersion signals in a strong r-f magnetic field under conditions when the approximate solution is applicable. The oscillograms were obtained for aqueous solutions: a) 0.001 M $CuSO_4$, b) 0.02 M $Fe(NO_3)_3$, under the following conditions f_m = 50 cps, H_m = 19 oersted, H_1 = 1 oersted (for a, ν = 0.0035 and μ = 6.9; for b, ν = 0.57 and μ = 10).

Experiments substantiate the deductions of theory regarding the bell-like shape of the signal. Oscillograms of dispersion signals in a strong r-f magnetic field obtained under conditions when the approximate solution is valid are reproduced in Fig.5.

Procedures, based on the method of envelopes and on the method of inversion points, have been developed for determining the longitudinal relaxation time τ_1 for the case when the dispersion signal in a strong r-f magnetic field is bell-shaped.[11]

It is known that the magnitude of the signals is proportional to the magnitude of the longitudinal component of the magnetization M_z at the instant of beginning of resonance. During the period of modulation the signal appears twice. If the separation between the signals is varied by varying the constant magnetic field, the amplitude of the second signal can be used as a sort of "probe" by means of which one can obtain the curve characterizing the variation of M_z. In cases when the envelope of the signals yields a sufficiently large section of the exponential curve, i.e., when the condition $T_m/\tau_1 \geqslant 1$ is fulfilled, the envelope can be utilized for determining the longitudinal relaxation time τ_1.

We developed a procedure for processing the signal envelope for the purpose of obtaining τ_1 by the method of least squares:

$$\tau_1 = \frac{1}{\omega_m} \cdot \frac{n \sum_{i=1}^{n} (y_i)^2 - \left(\sum_{i=1}^{n} y_i \right)^2}{\sum_{i=1}^{n} \alpha_i \sum_{i=1}^{n} y_i - n \sum_{i=1}^{n} \alpha_i y_i}, \tag{4}$$

where

$$\alpha_i = \ln \frac{(u_{i+1} - u_i)}{(y_{i+1} - y_i)}, \qquad y_i = \eta_i - \Delta_i,$$

u_i and u_{i+1} are the amplitudes of the i-th and (i+1)-th dispersion signals (two upper or two lower peaks), η_i is the separation in time between the peaks of the upper and lower i-th signals and Δ_i is the width of the i-th signal.

The procedure for determining the longitudinal relaxation time τ_1 by the inversion point method is the following. From the theory of magnetic resonance we have the following formula[6,11] relating τ_1 with the magnitude of the inversion coefficient, the distance to the inversion point and the width of the signal:

$$R = \frac{1 - e^{z_2}}{1 - e^{-z_1}}, \tag{5}$$

where

$$z_1 = \nu(2\pi - \eta_0 - \Delta), \quad z_2 = \nu(\eta_0 - \Delta), \tag{6}$$

R is the coefficient of inversion, η_0 is the distance from the upper signal to the inversion point of the lower signal. (The coefficient of inversion is understood to be the ratio of the longitudinal component of the magnetization at the end of the resonance region to the longitudinal component of the magnetization at the beginning of the resonance region. The point of inversion is the instant of time when the second, "probing" signal does not appear.)

It follows from the theory that with a constant amplitude and frequency of modulation the inversion coefficient and the distance from the upper signal to the point of inversion must increase with increasing amplitude of the r-f magnetic field. As was shown in Ref.11, beginning with a certain value of the r-f field H_1 the distance to the inversion point virtually does not change with increasing amplitude of H_1, which can occur only in the case when the inversion coefficient is close or equal to -1.

Curves characterizing the dependences of z_2/z_1 on z_2, satisfying Eq.(5) with R = -1 and R = -0.9 are given in Fig.6. Thus under the conditions when the distance to the inversion point virtually does not change one can, having experimentally measured $\frac{z_2}{z_1} = \frac{\eta_0 - \Delta}{2\pi - \eta_0 - \Delta}$, determine by means of the curves of Fig.6 and Eq.6 the longitudinal relaxation time τ_1.

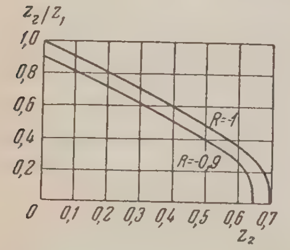

Fig.6. Positions of the inversion point in a strong r-f magnetic field for two values of the inversion coefficient R.

The developed procedures for determining the longitudinal and the transverse relaxation times were verified experimentally. The values of τ_1 and τ_2 obtained for aqueous solutions containing different concentrations of copper

Results of measurements of the longitudinal and transverse relaxation times in SKB (butadiene) synthetic rubber of different compositions

Sample	$\tau_1 \cdot 10^2$, sec		$\tau_2 \cdot 10^4$, sec	
	not vulcanized	vulcanized	not vulcanized	vulcanized
SKB	1.7	-	2.7	-
SKB 200 p.w. Sulfur 5 p.w.	1.6	1.5	2.2	1.7
SKB 200 p.w. Sulfur 5 p.w. Captax 2 p.w.	1.4	1.1	1.6	1.3
SKB 200 p.w. Sulfur 5 p.w. Captax 2 p.w. Carbon bl.120 p.w.	1.2	1.1	1.4	1.2
SKB 200 p.w. Thiuram 6 p.w.	1.7	1.5	2.0	1.8
SKB 200 p.w. Thiuram 6 p.w. Carbon bl.120 p.w.	1.5	1.5	1.7	1.4

Note: p.w. = parts by weight

sulfate and ferric nitrate agree within the limits of the experimental error with the data in the literature.

The proposed procedures differ from those described in the literature by their greater simplicity and the possibility they offer of performing the relaxation time measurements in a nonstabilized constant magnetic field.

An example of the potentialities of the procedure is furnished by the measurements of the longitudinal and transverse relaxation times in SKB synthetic rubber carried out in the Physics Department of Moscow State University by Graduate Student I.A.Loginova (see accompanying table).

As is known the molecules of pure rubber are long straight chains consisting of different hydrocarbon radicals having a large number of degrees of freedom. The high mobility of the molecules must reduce the influence of internal fields and, consequently, the shape of the signals from protons in the rubber should not differ greatly from the shape of the signals from protons in liquids.

As may be seen from the table the addition of such substances as sulphur and carbon black leads to a decrease of the longitudinal and transverse relaxation times, which is undoubtedly a consequence of reduction of the mobility of the synthetic rubber molecules. Comparison of the relaxation times for raw samples of synthetic rubber with the times for samples of the same composition but vulcanized shows that vulcanization reduces the longitudinal and transverse relaxation times. This is explained by the fact that as a result of vulcanization the number of bonds between the molecules is increased and internal interactions are enhanced. These experimental results are in agreement with the data of Holroyd et al[12] who studied different types of natural and synthetic rubber.

In conclusion the writer desires to thank S.D.Gvozdover for his valuable advice in connection with the investigation.

Department of Physics of
Moscow State University

References

1. F.Bloch, Phys.Rev., 70, 460 (1946).
2. K.V.Vladimirskii, Doklady AN SSSR, 58, 1625 (1947).
3. N.Bloembergen, Nuclear Magnetic Relaxation, Hague, 1948.
4. Ia.G.Dorfman, Manitnye svoistva atomnogo iadra (Magnetic Properties of the atomic nucleus), M.-L., 1948.
5. B.A.Jacobsohn & R.K.Wangsness, Phys.Rev., 73, 942 (1948).
6. S.D.Gvozdorer & A.A.Magazanik, Zhur.eksp.i teor.fiz., 20, 705 (1950).
7. R.K.Wangsness & F.Bloch, Phys.Rev., 89, 728 (1953).
8. S.D.Gvozdover & N.M.Ievskaia, Zhur.eksp.i teor.fiz., 25, 435 (1953).
9. S.D.Gvozdover & N.M.Ievskaia, Zhur.eksp.i teor.fiz., 29, 227 (1955).
10. S.D.Gvozdover & N.M.Pomerantsev, Vestnik (Review) Moscow State University, 9, 79 (1953).
11. S.D.Gvozdover & N.M.Ievskaia, Zhur.eksp.i teor.fiz., 29, 637 (1955).
12. L.V.Holroyd, R.C.Codrington, B.A.Mrowca & E.Guth, J.Appl.Phys., 22, 696 (1951).

ON PARAMAGNETIC ABSORPTION IN PARALLEL FIELDS AT SUPER-HIGH FREQUENCIES

- A. I. Kurushin

1. In their investigations Garif'ianov[2] and Sitnikov[3] used Zaikovskii's grid current method for studying paramagnetic absorption in parallel fields at frequencies of the order of $6 \cdot 10^8$ cps with constant fields ranging up to 6000 oersteds. They investigated several salts in which spin absorption predominates in these frequency and field-strength regions. On the basis of their results, they established certain empirical regularities for spin absorption. Their experimental dependences of the absorption on the constant field strength at a given alternating field frequency are in good agreement with Shaposhnikov's formula for spin absorption provided the isothermal spin relaxation time τ_s of the magnetization, which enters into this formula, is assumed independent of the constant field strength. This agreement made it possible to use Shaposhnikov's formula to obtain an experimental value for the internal field constant b/C (where b is the magnetic specific heat, and C is the Curie constant).

2. Shaposhnikov's formula for spin absorption in parallel fields is

$$\chi'' = \chi_0 \frac{(1-F)^2 \tau_s \nu}{1+(1-F)^2 \tau_s^2 \nu^2}, \tag{1}$$

where $F =$ [illegible] χ'' is the imaginary part of the complex magnetic susceptibility, χ_0 is the isothermal equilibrium susceptibility, ν is the alternating field frequency, and H is the constant field strength. This formula, as can be seen from Eq.(1), gives a dependence of the Debye type for χ'' as a function of the alternating field frequency for a given constant field strength, with a maximum which moves towards higher frequencies as the constant field strength is increased; in weak fields this maximum lies in the range corresponding to τ_s^{-1}. The above-mentioned experiments[2,3] were performed at frequencies much lower than τ_s^{-1}, when Eq.(1) assumes the simpler form

$$\chi'' = \chi_0 (1-F)^2 \tau_s \nu. \tag{2}$$

Thus these experiments yield satisfactory but only partial substantiation of Shaposhnikov's formula and the assumption that τ_s is independent of H. In order to study spin absorption in more detail and compare experiment with theory more thoroughly, it was obviously desirable to carry out experiments in parallel fields at frequencies such that $\tau_s \nu$ is of the order of unity. This was the purpose of the present investigation.

3. In order to achieve this purpose, it was necessary to construct an apparatus which could be used to measure paramagnetic absorption in parallel fields in the centimeter wavelength region. Here the grid current method is no longer applicable.

The assembled set-up consisted of an oscillator unit using a reflex klystron, operating at a frequency $\nu = 9.15 \cdot 10^9$ cps, a cylindrical resonator, and an indicator section, all connected to each other by coaxial waveguides. The indicator unit consisted of a section of coaxial line with a detector head. The detected signal was applied to a mirror galvanometer. A difference between our apparatus and others described in the literature is that ours can be used for experiments both in parallel and in perpendicular fields in the microwave region. It was found convenient to use the H_{011} mode in the cylindrical resonator. It is known that the magnetic field of this mode possesses axial symmetry, and that the magnetic lines of force along the axis of the cylinder are parallel to it, so that close to the center of the resonator the field is practically homogeneous. Parallel alignment of the constant and r-f fields is realized by orienting the cylinder so that its axis is parallel to the lines of force of the constant field. To obtain perpendicular fields, it is only necessary to rotate the resonator through

90°. For this purpose, the coaxial waveguide connecting the resonator to the generator was provided with a rotating connector.

The paramagnetic substance in the form of the powder was placed into a small thin-walled cylindrical polystyrene capsule about 4 mm in diameter and 6 mm long. The capsule was attached to the bottom of the cavity so that the paramagnetic substance was at the center of the resonator. Such symmetrical placement of an extraneous object does not seriously distort the field pattern. This was experimentally verified by filling the capsule with a substance giving a strong effect in perpendicular fields (paramagnetic resonance), but no effect in parallel fields at the given frequencies (for example, $MnSO_4$). If the presence of the loaded capsule distorted the field pattern, then with the resonator oriented for parallel fields a paramagnetic resonance effect should have been observed due to the appearance of a perpendicular field component. Such an effect was observed only when capsules of larger size were tried; there was no observable effect with capsules of the dimensions given above.

As is well known[5], for relative measurements and a square-law detector, the imaginary part of the magnetic susceptibility is proportional to $\sqrt{(\alpha_e/\alpha_m)} - 1$, where α_e and α_m are the galvanometer readings in the absence of and with magnetic losses, respectively. The value of α_e was obtained on the assumption that a sufficiently strong constant field perpendicular to the alternating one almost entirely eliminates magnetic losses[4]. In order to exclude the influence of the real part of the magnetic susceptibility on the galvanometer indications, before each measurement of α_m the resonator was tuned by means of an end piston.

4. Using this set-up, we measured the paramagnetic absorption in a number of salts, primarily those of elements of the iron group, and found that increasing the constant field leads to a monotonic decrease in the absorption of r-f energy by the samples. This means that the effect in parallel fields is detectable only in substances which have a sufficiently large initial absorption (i.e., at H = 0) at these frequencies. In most of the substances investigated, the initial absorption was found to be so small that it was impossible to make reliable observations of any decrease in absorption as the field was increased (to 9000 oersteds). For a few paramagnetic salts, however, the initial absorption proved to be sufficiently large, and it was therefore feasible to record the full curve of the absorption as a function of the constant field strength at the given r-f field frequency. The most reliable results were obtained for $Gd_2(SO_4)_3 \cdot 8H_2O$ and $MnCl_2 \cdot 4H_2O$.

The experimental curves were compared with those obtained from Shaposhnikov's theoretical formula (1). This was done as follows: experiment gives $d = a\chi''$ as a function of H, where a is a calibrating constant determined by the design and adjustment of the apparatus. Taking χ'' from (1), we obtain

$$d = a\chi_0 \frac{(1-F)^2 \tau_s \nu}{1 + (1-F)^2 \tau_s^2 \nu^2}. \qquad (3)$$

If b/C and τ_s for the given substance are known from other data, then taking the experimental values of d for H = 0, we can find $a\chi_0$ from Eq.(3) and then plot the theoretical curve for $d(H)$ so that it coincides exactly with the experimental curve of $d(H)$ at the point H = 0. If the theory is in agreement with experiment, this fit will be obtained for all values of H. According to Garif'ianov[2] for $Gd_2(SO_4)_3 \cdot 8H_2O$, $\tau_s = 0.22 \cdot 10^{-9}$ sec and $b/C = 3.82 \cdot 10^6$ oersteds^2, so that $\tau_s \nu \approx 2$. In the accompanying figure the solid line I gives the theoretical curve; the points indicate the experimental values. As may be seen, the experimental points fit the theoretical curve well within the limits of experimental error (about 6%). In a similar way, we obtained the curve shown in the figure for $MnCl_2 \cdot 4H_2O$, for which we took $\tau_s = 0.24 \cdot 10^{-9}$ sec and $b/C = 19.3 \cdot 10^6$ oersteds^2 from Ref. 3. In this case the theoretical curve agrees with experiment up to fields of the order of 6000 oersteds; in stronger fields the experimental points fall somewhat below the theoretical curve.

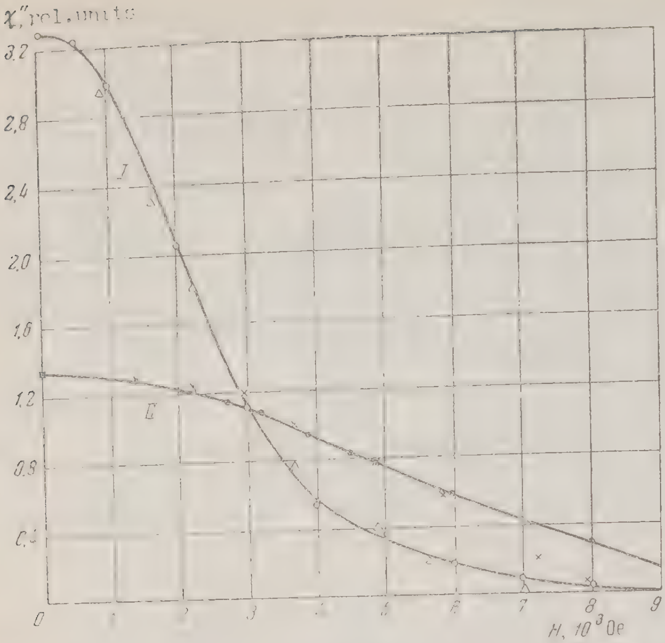

Variation of the paramagnetic absorption of $Gd_2(SO_4)_3 \cdot 8H_2O$ (curve I) and $MnCl_2 \cdot 4H_2O$ (curve II) powders with the magnetic field. Solid lines - theoretical curves; points X and △ - experimental values (τ = 20°); points ○ and ● - values calculated according to Shaposhnikov's theoretical formula.

5. Thus our results, in conjunction with the earlier data from Refs.2 and 3 give reason to assume that Shaposhnikov's phenomenological theory of spin relaxation with the assumption of constant field-independence of the isothermal spin relaxation time τ_s is in good agreement with experiment over the entire ranges of frequencies and fields of practical interest.

6. Assuming, in view of the above, that Eq.(1) is valid, let us now evaluate the experimental possibilities for determining various parameters of interest.

Taking the experimental values of d for three arbitrary values of H, we obtain a set of three equations for the variables b/C, τ_s and a. For example, if we take d_1 at H = 0, $d_2 = d_1/2$ at the appropriate field H_2, and $d_3 = d_1/3$ at H_3, solution of the resultant set of equations leads to the following expressions for b/C, τ_s and $\chi''(H) = d(H)/a$:

$$\frac{b}{C} = \frac{1}{2} \cdot \frac{H_3^4 - 2H_2^4}{2H_2^2 - H_3^2}, \tag{4}$$

$$\tau_s = \frac{\sqrt{H_2^4 + 2\frac{b}{C}H_2^2 - \left(\frac{b}{C}\right)^2}}{\frac{b}{C}\nu} \tag{5}$$

and

$$\chi'' = \chi_0 \frac{\left(\frac{b}{C}\right)^2 \tau_s \nu}{H_2^4 + 2\frac{b}{C}H_2^2} \cdot \frac{d(H)}{d_1}. \tag{6}$$

Here $d(H)$ is the value of d obtained from experiment at any value of H, the value of b/C inserted in Eqs.(5) and (6) is that given by Eq.(4), and the value of τ_s entering into Eq.(6) is that given by Eq.(5).

Thus experiments in parallel fields in the appropriate frequency and field strength regions should make it possible to determine b/C, τ_s and χ''. It can be shown that when the experiments are performed[2,3] at frequencies corresponding to the condition $\tau_s \nu \ll 1$, when Eq.(2) is applicable, one can find only b/C, since τ_s and a enter into the corresponding set of equations only in the form of their product $\tau_s a$.

The writer desires to express his deep gratitude to I.G.Shaposhnikov for suggesting the topic and for aid in the work.

"A.M.Gorikii" Molotov State University

References

1. I.G.Shaposhnikov, Dissertation, Molotov State University, 1949.
2. N.S.Garif'ianov, Zhur.eksp.i teor.fiz., 25, 360 (1953).
3. K.P.Sitnikov, Dissertation, Kazan State University, 1954.
4. E.K.Zavoiskii, Dissertation, FIAN (Phys. Inst. of the USSR Ac.of Sci.), 1944.
5. R.L.Cummerow, D.Halliday & G.E.Moore, Phys.Rev., 72, 1233 (1947).

EXPERIMENTAL VERIFICATION OF AN EXPRESSION FOR RESONANCE PARAMAGNETIC ROTATION

- N.N.Neprimerov

In an earlier contribution[1] the writer gave an expression for the dependence of the angle of rotation of plane polarized microwaves on the magnetic field. Although certain admittedly rough simplifying assumptions were made in deducing this expression, these were based on extensive experimental data. A rigorous quantum-mechanical derivation carried out by Shekun[2], showed that this expression can be applied in the resonance region if the half-width of the absorption line is appreciably smaller than the value of the resonance field.

A new expression for the angle of rotation derived by Shekun[2] is valid for all frequencies provided the shape of the absorption curve is close to the Lorentz shape. The expression derived by Tsirul'nikova & Shaposhnikov[3] on the basis of a phenomenological examination of resonance paramagnetic rotation is fully equivalent to the expression obtained by Shekun and hence hereinafter we will use the common expression:

$$\varphi = \frac{2\pi\omega\sqrt{\varepsilon}}{c}\cdot\frac{\chi_0}{2}\left\{\frac{\omega_0\tau^2(\omega_0-\omega)+1}{\tau^2(\omega_0-\omega)^2+1}-\frac{\omega_0\tau^2(\omega_0+\omega)+1}{\tau^2(\omega_0+\omega)^2+1}\right\}, \tag{1}$$

where φ is the angle of rotation per unit length, ω is the oscillator frequency, $\omega_0 = g\beta H/\hbar$, τ is the relaxation time, c is the velocity of light, ε is the dielectric constant and χ_0 is the static magnetic susceptibility of the material.

Where experimental verification of the theory[2,3] is concerned, in addition to direct comparison of the theoretical and experimental data, it is of interest to follow the divergence between the resonance rotation curve and the curve characterizing the dispersion of magnetic susceptibility of the material for different values of $\omega\tau$:

$$\chi' = \frac{\chi_0}{2}\left\{\frac{\omega_0\tau^2(\omega_0-\omega)+1}{\tau^2(\omega_0-\omega)^2+1}+\frac{\omega_0\tau^2(\omega_0+\omega)+1}{\tau^2(\omega_0+\omega)^2+1}\right\}. \tag{2}$$

Case 1. $\omega\tau \gg 1$. In this case the magnitude of the second, non-resonance terms in Eqs.(1) & (2) becomes small compared with the magnitude of the first terms and the two curves become virtually indistinguishable as regards shape. All the experimental data on the dispersion of susceptibility and resonance rotation given in Ref.1 pertain to this case ($3.5 \leqslant \omega\tau \leqslant 36$). In view of the relatively low accuracy of measurements of dispersion of susceptibility and the smallness of the effect in weak fields, in most cases it is difficult to detect any difference in the field dependence of the two quantities in the vicinity of $H = 0$. At the same time the external magnetic fields used in the investigation of Ref.1 were not sufficiently strong to bring out the divergence of the curves in the region of very strong fields $H \longrightarrow \infty$.

Of the investigated paramagnetic materials $MnCl_2 \cdot 4H_2O$ has the widest absorption curve ($\omega\tau = 3.5$). The theoretical curves and experimental points for the dispersion of susceptibility and resonance rotation in this substance are shown in Fig.1. The latter curve is inverted to facilitate comparison. The parameters and measurement procedure used to obtain the data of Fig.1 are described in Ref.1. The value of τ was computed from the absorption curve. As may be seen, there is good qualitative as well as quantitative agreement.

Case 2. $\omega\tau < 1$. At present it is impossible to find a paramagnetic material with $\omega\tau < 1$ in the 9100 Mc frequency region. In view of this the most interesting fact of the change of sign of the rotation from positive to negative with $\omega\tau < 1$ can be illustrated only on magnetodielectric specimens, using such substances as powdered iron carbonyl, nickel, permally, Alcifer, and transformer & dynamo steels (particle size $\leqslant 100\ \mu$) as fillers for parrafin.' All these powdered substances give similar, very broad absorption lines and a large negative rotation. By way of illustration the curves for permalloy (5% by volume in paraf-

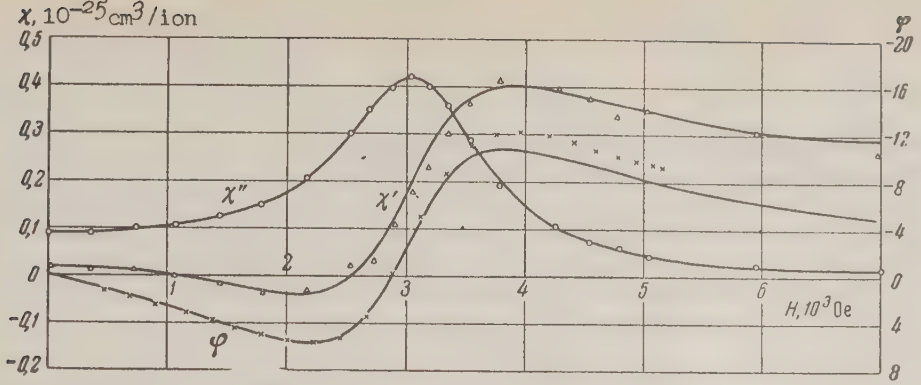

Fig. 1. Resonance paramagnetic rotation (φ), dispersion of susceptibility (χ') and absorption (χ'') for powdered $MnCl_2 \cdot 4H_2O$ at $\lambda = 3.3$ cm, calculated according to Eqs.(1) & (2) (with $\omega\tau = 3.5$, $\epsilon = 9.6$, $\chi_0 = 0.24 \cdot 10^{-25}$ cm^3 ion^{-1}). Solid lines - theoretical curves; points - experimental values.

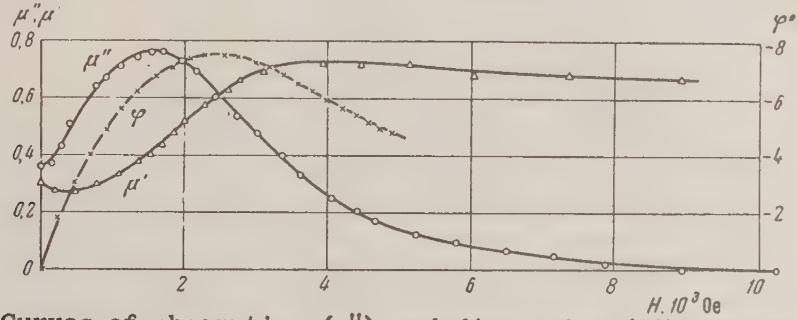

Fig. 2. Curves of absorption (μ'') and dispersion (μ') of permeability and resonance rotation (φ) for permalloy powder in paraffin ($C_v = 5\%$) at $\lambda = 3.33$ cm.

fin) are given in Fig.2.

There is reason to hope that at a frequency of 3000 Mc, at which some investigations[4] have already been performed, it may be possible to observe purely negative rotation in paramagnets as well.

"V.I.Ul'ianov-Lenin" Kazan State University

References

1. N.N.Neprimerov, Izv. AN SSSR, Ser. fiz., 18, 368 (1954). (Translation in Bulletin, Vol. 18, No. 3, p. 63).
2. L.Ia.Shekun, Present issue of the Bulletin.
3. L.M.Tsirul'nikova & I.G.Shaposhnikov, Present issue of the Bulletin.
4. I.Soutif-Guicherd, C.R., 231, 1460 (1950); 240, 2126 (1955).

INVESTIGATION OF PROTON MAGNETIC RESONANCE

- N.M. Pomerantsev

1. In an earlier investigation we used a self-oscillating system for observing the signals of nuclear magnetic resonance.[1] After a series of tests with different oscillator circuits we selected the one shown in Fig.1. This circuit is distinguished by its simplicity and the convenience of regulating the amplitude. The circuit consists essentially of a cathode follower, which with an appropriate load can have a negative input impedance.

The input impedance of a cathode follower is given by[2]

$$Z_{\text{in}} = Z_{\kappa} + \frac{1 + SZ_{\kappa}}{i\omega C_g}, \tag{1}$$

where Z_k is the complex impedance of the load, S is the transconductance of the tube and C_g is the grid-cathode capacitance.

A necessary condition (following from Eq.(1)) for the input impedance of the circuit pictured in Fig.1 to be negative is

$$SR_kC_k > C_g \tag{2}$$

where C_k and R_k are the load capacitance and resistance.

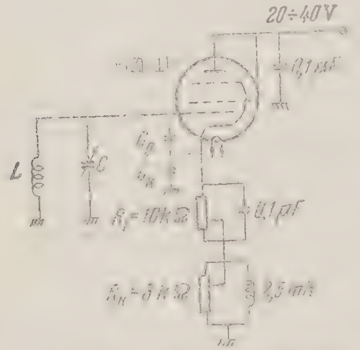

Fig.1. Circuit of generator for observing nuclear magnetic resonance signals.

In the circuit of Fig.1, C_k is the capacitance of the wiring. The choke connected in parallel with R_k serves to take off the dc component of the plate current. It has a high inductance and plays no part in exciting the oscillations. The resistance R_1, shunted by the 0.1 μf capacitor, serves for applying a negative bias on the grid and thereby select the operating point. The transconductance of the tube is controlled by varying the plate voltage V_a. Thus by regulating R_1, R_k and V_a one can readily attain the operating regime at which the oscillations are smoothly excited and the amplitude can easily be maintained at the requisite level.

The high-frequency signal from the generator was applied to an amplifier and, after detection, fed to the input of an oscillograph, the sweep of which was synchronized with the modulation of the magnetic field. The complete circuit of the set-up is shown in Fig.2. The amplifier had a 12.5-13.2 Mc passband which could be regulated by appropriate tuning of the circuits. The amplification factor of the amplifier was $3 \cdot 10^3$. The passband of the low frequency part of the amplifying channel, including the the load of the diode detector and EO-4 oscillograph amplifier, extended from 2 c to 150 kc. The amplifier noise of the set-up was negligibly small and practically unnoticeable. Consequently the principal factor determining the

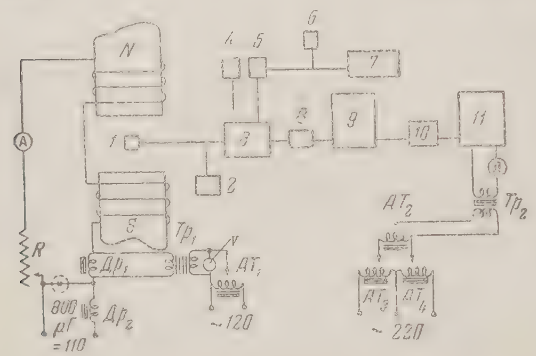

Fig.2. Diagram of set-up for investigating nuclear magnetic resonance: 1) specimen coil, 2) generator, 3) r-f amplifier, 4) cathode voltmeter, 5) Type 527 heterodyne wavemeter, 6) IV-4 output meter, 7) ICh-5 frequency meter, 8) detector, 9) EO-4 oscillograph, 10) power amplifier, 11) electrodynamic wattmeter, AT_1-AT_4) LATR-1 autotransformers, Tp_1 and Tp_2) OSO-0.1 transformers, $Дp_1$ and $Дp_2$) chokes, A) 5 amp ammeter.

sensitivity of the set-up was the generator noise. In the case of weak signals, for the sake of suppressing noise we used synchronous detection by means of an electrodynamic wattmeter, the indications of which were proportional to the integral of the product of the currents flowing through its coils. A description of this part of the set-up is given in Ref.3.

We observed the changes in the frequency of the generator at the onset of resonance by means of a frequency meter which measured the beat frequency between the oscillations of the generator and a heterodyne wavemeter. An output meter was used to check the indications of the frequency meter; this was necessary inasmuch as the latter does not give a correct reading when the amplitude on its input is less than 0.5 v. By way of illustration of the results obtained with the circuit, an oscillogram of the signal from the protons in a unimolar solution of $CuSO_4$ is reproduced in Fig.3.

2. We discussed the theory of the operation of an oscillating system in the presence of an emf from nuclear magnetic resonance in an earlier contribution.[4]

The basic system of equations is

$$\left.\begin{aligned} &\frac{d^2U}{dt^2}+\omega^2U=F\left(U,\frac{dU}{dt}\right)-A\frac{dM_x}{dt},\\ &\frac{dW}{dt}+\left[\frac{1}{\tau_2}+i\gamma H_z\right]W-i\gamma BM_z\frac{dU}{dt}=0,\\ &\frac{dM_z}{dt}+\frac{M_z-M_0}{\tau_1}=\frac{i\gamma B}{2}\left(W\frac{dU^*}{dt}-W^*\frac{dU}{dt}\right).\end{aligned}\right\} \qquad (3)$$

Here U is the voltage on the capacitor of the circuit, ω is the self-resonant frequency of the circuit, γ is the gyromagnetic ratio, τ_1 and τ_2 are the relaxation times, $W=M_x+iM_y$, M_x, M_y and M_z are the components of the resultant nuclear magnetization vector, M_0 is the equilibrium value of the component M_z, A and B are constants dependent on the parameters of the oscillating circuit, and $F\left(U,\frac{dU}{dt}\right)$ is a function determined by the damping of the circuit and the action of the electron tube thereon.

We used the method of slowly changing amplitudes in combination with the method of perturbation to solve this system of equations. In this way we solved the problem of small perturbations of the stationary amplitude and phase of the oscillations under the influence of the nuclear resonance emf.

The solution has the form

$$U=U_{st}\left[1+C\int_{-\infty}^{t}e^{\alpha(\eta-t)}v(\eta)\,d\eta\right]\cos\left(\omega t+C\int_{-\infty}^{t}u(\eta)\,d\eta\right), \qquad (4)$$

where $v(\eta)$ and $u(\eta)$ are functions defined by the expressions:

$$v(\eta)=-\int_{-\infty}^{\eta}M_ze^{\frac{1}{\tau_2}(\xi-\eta)}\cos\left[f(\eta)-f(\xi)\right]d\xi, \qquad (5)$$

$$u(\eta)=\int_{-\infty}^{\eta}M_ze^{\frac{1}{\tau_2}(\xi-\eta)}\sin\left[f(\eta)-f(\xi)\right]d\xi, \qquad (6)$$

$$f(\eta)-f(\xi)=\int_{\xi}^{\eta}(|\gamma|H_z-\omega)\,dt'. \qquad (7)$$

In Eq.(4) $\alpha=-\left[\frac{\partial\Phi}{\partial\rho}\right]_{\rho=U_{st}}$ is a parameter characterizing the stability of the system, while C is a constant that depends on the geometry of the oscillating circuit coil.

If $\alpha\gg n\omega_m$, where $n\omega_m$ is the the highest multiple frequency of the signal (which is always the case in practice) the expression for the voltage on the oscillating circuit becomes

$$U = U_{\mathrm{st}}\left[1 + \frac{C}{\alpha} v(t)\right] \cos\left[\omega t + c \int_{-\infty}^{t} u(\eta)\, d\eta\right]. \qquad (8)$$

Expression (8) shows that the amplitude of the oscillations is modulated by the signal $v(t)$, and the frequency is modulated by the signal $u(t)$.

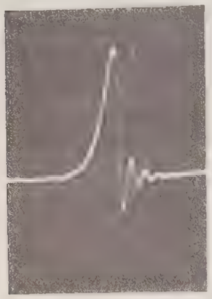

Fig. 3. Oscillogram of signal from protons in 0.7 cm^3 of 1M solution of $CuSO_4$. Amplitude and frequency of modulation - 0.6 oersted and 50 cps, respectively. Effective inhomogeneity of field in the volume of the specimen - 0.015 oersted.

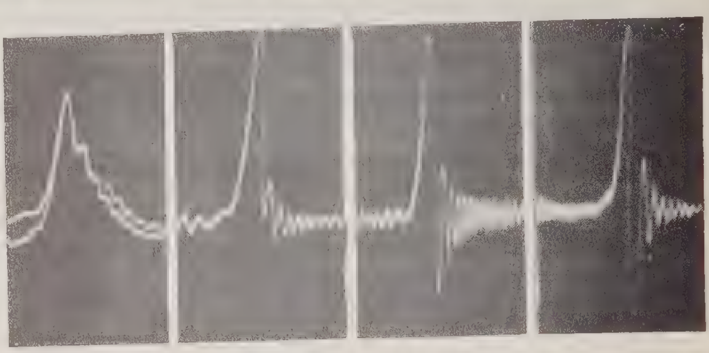

Fig. 4. Oscillograms of signals from protons in glycerin with different degrees of stability of oscillation. The oscillogram at the right is for a stable oscillating regime; the remaining photographs are for gradually deteriorating stability.

The above deductions from theory are well substantiated by experiment. At small values of α, as follows from Eq. (4), there must be distortion of the signal corresponding to its passage through the R-C filter, the determining factor here being the value of $1/\alpha$. The oscillogram of four signals obtained with different degrees of stability of oscillation, other conditions being equal, are shown in Fig. 4. These are oscillograms of the signal from protons in glycerin. The oscillogram at the right corresponds to stable oscillation; the one at the left for the least stable operation. The gradual change in the shape of the signals with deteriorating stability of the system is clearly evident. Observations of the variation in frequency of the generator by the methods described above showed that in case of slow variation of the magnetic field intensity (modulation was not used in this case) the frequency of oscillation near resonance shifts first to one side and then to the other, as is evident from the appearance of the dispersion curve (expression (6) for slow passage through resonance). Frequency drifts of the order of 100 c were observed.

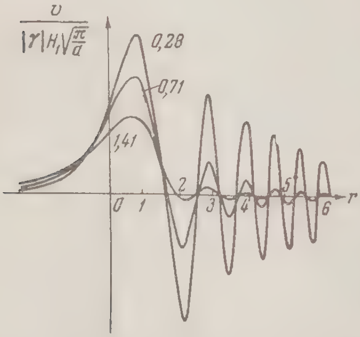

Fig.5. Curves of the function $v(t)$ determining the shape of the absorption signal. The figures at the curves are values of the parameter $\alpha = \sqrt{2/a}\,\frac{1}{\tau_2}$

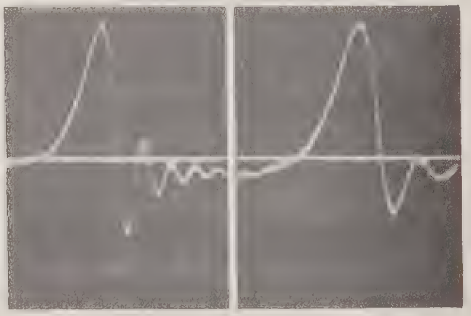

Fig.6. Oscillograms of signal with base line from protons in 0.7 cm^3 of $Fe(NO_3)_3$: a) 0.06 M solution, b) 0.12 M solution.

3. The procedure for measuring the transverse relaxation time

τ_2 is based on the fact that the ratio of the magnitudes of the first and second extrema (maxima - minima) of the absorption signal depends strongly on a parameter that is determined by the rate of change of the magnetic field and the relaxation time τ_2.

Curves of the function $v(t)$ are shown in Fig. 5. These curves differ from the analogous curves of Jacobsohn and Wangsness as regards choice of parameters used in plotting. It will be seen from the curves that the ratio of the amplitudes of the first and second extrema of the signal depends strongly on the parameter α, which with a constant rate of modulation depends only on the relaxation time τ_2. Using (5), one can calculate this ratio of the extrema as a function of τ_2 and then from the experimentally measured value of Z (see Eq.(9)) determine τ_2.

In order to have an accurately positioned base line, the signal before being applied to the oscillograph was passed through an electronic commutator which blocked the oscillograph input for 1/2 period. As a result for 1/2 period we had the observable signal and for the other 1/2 period the cathode-ray beam traced the base line. Typical oscillograms obtained under these conditions are shown in Fig.6. The method of determining the ratios Z of the extrema is illustrated in Fig.7. Due to the presence of transient capacitances the dc component of the signal is lost. Consequently Z measured experimentally will be

$$Z = \frac{v(t_1) - v_0}{v(t_2) + v_0} = f\left(\frac{\partial H_z}{\partial t}, \tau_2\right), \tag{9}$$

where v_0 is the dc component of the signal

In order to obtain Z as a function of τ_2, we carried out a tabulation of the function $v(t)$ giving the shape of the absorption signal. To this end the functions $v(t)$ and $u(t)$ were reduced to the tabulated functions[6]:

$$v(r) = -\frac{1}{2}|\gamma|H_1\sqrt{\pi/a}\,[V(x, y) + U(x, y)], \tag{10}$$

$$u(r) = \frac{1}{2}|\gamma|H_1\sqrt{\pi/a}\,[V(x, y) - U(x, y)], \tag{11}$$

where $U(x, y)$ and $V(x, y)$ are, respectively, the real and imaginary parts of the complex function

$$W(z) = U(x, y) + iV(x, y) = e^{-z^2}\left(1 + \frac{2i}{\sqrt{\pi}}\int_0^z e^{t^2}dt\right), \tag{12}$$

$$z = x + iy = \frac{1}{\sqrt{2}}\left(\frac{\alpha}{2} + r\right) + \frac{i}{\sqrt{2}}\left(\frac{\alpha}{2} - r\right),$$
$$r = \sqrt{a/2}\,t,\quad \alpha = \sqrt{2/a}\,\frac{1}{\tau_2},\quad a = |\gamma|\frac{dH_z}{dt}. \tag{13}$$

The determined dependence of τ_2 on Z for different modulation amplitudes is shown in Fig. 8. It is assumed that sinusoidal modulation is employed, but inasmuch as the signals are damped out before the beginning of the next modulation period, in the calculations one may assume the modulation to be linear. The curves are computed for a modulation frequency of 50 cps.

Measurements of the relaxation time by the proposed method are carried out as follows. Three horizontal lines are drawn on the oscillograph screen so that the distance between them will correspond to a certain predetermined ratio of the extrema (from the curves of Fig.8 it will be seen that the best as regards sensitivity will be a ratio between 3 and 4). Then by varying the modulation amplitude the upper and lower edges of the signal are aligned with the lines on the screen. Finally the sought value of τ_2 corresponding to the said modulation amplitude is picked off the appropriate curve.

It will be seen that the procedure is experimentally simple and rapid.

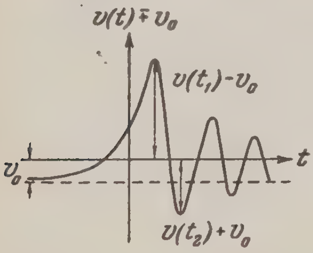

Fig. 7. Method of measuring the parameters of the signal v(t); $v(t_1)$ and $v(t_2)$ are the absolute values of the function v(t) at the instant t_1 and t_2.

4. In employing the above described method it is necessary to take into account the influence of inhomogeneities of the magnetic field. The shape of the signal in the presence of field inhomogeneities is determined by the following expression[5]:

$$F(r) = \frac{-v + iu}{|\gamma| H_1 \sqrt{a/2}} \int_{-\infty}^{r} \exp\{\alpha(\xi - r) + i(r^2 - \xi^2)\}\, \theta \, d\xi, \tag{14}$$

where $\theta = \theta(r - \xi)$ is the characteristic function

$$\theta = \int_{-\infty}^{\infty} \varphi(\Delta H) \exp\left\{i \frac{|\gamma|}{\sqrt{a/2}} (r - \xi)\, \Delta H\right\} d(\Delta H), \tag{15}$$

and $\varphi(\Delta H)$ is the field inhomogeneity distribution function.

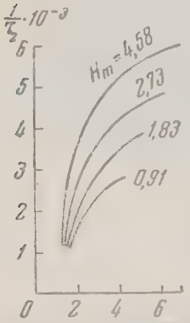

Fig. 8. Curves giving the dependence of the value of $1/\tau_2$ on the ratio Z of the extrema at different modulation amplitudes H_m.

For a Lorentz distribution

$$\varphi(\Delta H) = \frac{1}{\pi} \cdot \frac{\Gamma}{(\Delta H)^2 + \Gamma^2} \tag{16}$$

and

$$\theta = \exp\left\{-\frac{|\gamma|\Gamma}{\sqrt{a/2}} (r - \xi)\right\}. \tag{17}$$

For a Gaussian distribution

$$\varphi(\Delta H) = \frac{1}{2\pi\sigma} \exp\{-(\Delta H)^2/2\sigma^2\} \tag{18}$$

and

$$\theta = \exp\left\{-\frac{\gamma^2\sigma^2}{a} (r - \xi)^2\right\}. \tag{19}$$

If we assume that the Lorentz distribution obtains, the effect of the inhomogeneities will amount to reduction of the relaxation time τ_2 and the experimentally observed relaxation time will be given by

$$\frac{1}{\tau_2^*} = \frac{1}{\tau_2} + |\gamma|\Gamma, \tag{20}$$

where Γ is the effective magnitude of the field inhomogeneity (half-width of the Lorentz curve). The suggested method of determining the inhomogeneity of the magnetic field consists of measuring the relaxation times for protons in specimens containing different numbers of paramagnetic ions. Plotting a curve of the dependence of $1/\tau_2^*$ on the concentration and extrapolating it to zero concentration we obtain the value of $1/\tau_2^* = |\gamma|\Gamma$ which gives us the effective inhomogeneity of the field in the volume of the specimen.

By way of illustration the experimentally determined dependences of $1/\tau_2^*$ on the molar concentration of paramagnetic Fe^{+++} and Ni^{++} ions in solutions of iron nitrate and nickel nitrate are plotted in Fig.9. It will be seen that both the straight lines intersect the vertical axis at the same point where $1/\tau_2^* = 0.65 \cdot 10^3$, which corresponds to an effective magnetic field inhomogeneity of 0.025 oersted.

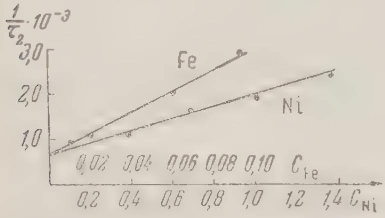

Fig. 9. Experimentally determined dependence of $1/\tau_2^*$ on the molar concentration of paramagnetic Fe^{+++} and Ni^{++} ions in solutions of iron and nickel nitrate.

Conclusions

1. We tested a simple and experimentally convenient r-f generator circuit for observing the signals of nuclear magnetic resonance. In this circuit the specimen is placed directly inside a coil in the generator circuit. The oscillograms reproduced above show that a very good signal to noise ratio can be

obtained in this set-up.

2. We examined the theory of operation of an oscillating system in the presence of a nuclear magnetic resonance emf. It is shown that the amplitude of the oscillations of such a system is modulated by the signal $v(t)$ and the frequency by the signal $u(t)$. The deductions drawn from theory were substantiated experimentally.

3. We propose a method for determining the transverse relaxation time τ_2, based on measuring the amplitude of the first and second extrema (peaks) of the absorption signal. Experimental verification of the method showed that it is simple and convenient.

4. We propose a method for determining the effective inhomogeneity of the magnetic field in the volume of the specimen; the method is based on measuring the relaxation times in samples with different concentrations of paramagnetic ions. The suggested procedure was also verified experimentally.

Department of Physics of
Moscow State University

References

1. F.Bloch, Phys. Rev., 70, 460 (1946); N.M.Pomerantsev, Usp.fiz.nauk, 55, 3 (1955).
2. K.Schlesinger, Proceedings IRE, 33, 843 (1945).
3. N.M.Pomerantsev, Vestnik (Review) Moscow State University, 8, 57 (1955).
4. N.M.Pomerantsev, Vestnik (Review) Moscow State University, 2, 47 (1955).
5. B.A.Jacobsohn & R.K.Wangsness, Phys. Rev., 73, 942 (1948).
6. S.D.Gvozdover, N.M.Pomerantsev & A.L.Poliakova, Zhur.eksp.i teor.fiz., 28, 584 (1955).

ON THE SPIN-SPIN RELAXATION TIME IN NICKEL FLUOSILICATE IN THE ABSENCE OF A STATIC MAGNETIC FIELD

- V. Ia. Kharanen

1. The paramagnetic resonance method of studying the properties of paramagnetic materials is now widely employed. The use of this method, however, is frequently hampered by poor resolution of the absorption spectra. These resolution difficulties are usually due not to inadequacy of the experimental equipment but to the inherent width of the spectral lines. The width of the lines is determined primarily by two factors: first, the interaction between the magnetic moments of the ions (spin system) and thermal vibrations of the lattice and, second, the interactions between the magnetic moments of the ions themselves. These two types of interaction give rise to two relaxation processes, characterized by two distinct relaxation times: the spin-lattice relaxation time τ_L and the spin-spin relaxation time τ_s. The former characterizes the rate at which thermal equilibrium is established between the spin system and the lattice. The latter characterizes the rate at which the magnetization adiabatically approaches its equilibrium value, which corresponds to the instantaneous values of the temperature of the spin system and the external magnetic field.[1] The spin-spin time τ_s is temperature independent, decreases only a little with increasing values of the external constant field[1], and is of the order of 10^{-9}-10^{-10} sec in a wide range of fields for all common paramagnetic substances. The spin-lattice time τ_L, although also only weakly dependent on the field, does depend on the temperature - as the temperature is reduced, τ_L increases rapidly - and has a wide range of values for different paramagnetic substances and different temperatures. Therefore the most suitable experimental conditions for obtaining resonance spectra are those at which $\tau_L \gg \tau_s$, i.e., when the paramagnetic ions are much more weakly coupled to the lattice vibrations than to each other; under these conditions the width of the spectral lines is determined primarily by spin-spin relaxation. The spin-lattice relaxation times should not, however, be too great, since if it is the absorption will be unobservable due to saturation effects.[2] In a number of paramagnets, mainly those in which the paramagnetism is due to ions with unfilled 3d-shells, the condition $\tau_L \gg \tau_s$ is satisfied at room temperature. In the case of other paramagnetic materials the experiments must be carried out at low temperatures in order to obviate the line broadening due to spin-lattice interaction. However, the line broadening due to spin-spin interaction is also, of course, a hindrance where obtaining well resolved spectra is concerned. This difficulty can be alleviated to some extent by applying an appropriate constant external magnetic field, for the effect of this is to spread out the lines. In order to specify the intensity of the applied magnetic field one must know the spin-spin relaxation time. In addition, a knowledge of this time is important where elucidation of the interaction mechanism with the spin system is concerned.

2. In the present investigation we used the method of moments[3,4] to deduce a theoretical expression for τ_s in the absence of a constant external magnetic field for a nickel fluosilicate ($NiSiF_6 \cdot 12H_2O$) single crystal. This substance has a hexagonal crystal structure[5]. Each unit cell contains one paramagnetic doubly ionized Ni^{++} ion, surrounded by six dipole water molecules, forming a slightly distorted octahedron. Therefore the electric field acting on the Ni^{++} ion possesses almost cubical symmetry[2]. The deviations from ideal cubical symmetry are characterized by trigonal symmetry. The axis of the trigonal field, which is weak compared to the cubic one, is aligned with the hexagonal crystal axis. The paramagnetism of the Ni^{++} ion is due to the unfilled 3d-shell, which contains 8 electrons. According to Hund's rule,[6] the ground state of the free ion will be $^3F_4$. The energy spectrum of the Ni^{++} ion in fluosilicate crystals has been investigated by Becquerel and Opechowski[7]. The cubic field splits the

F-state into a singlet and two triplets, with the lowest triplet state about 10,000 cm^{-1} above the singlet. If we take account of the combined effect of the weak trigonal field and spin-orbit interaction, the lowest orbital level, which is triply degenerate because its spin S = 1, splits into two sublevels: a singlet and a doublet, with a separation of δ = 0.5 cm^{-1}. If the hexagonal axis is taken as the Z axis for quantization, the upper and lower sublevels will correspond to the states with $S_z = 0$ and $S_z = \pm 1$, respectively. At room temperature, in view of the Boltzmann distribution, only this spin triplet of the lowest orbital level will be populated; and it may be assumed that the three spin sublevels are equally occupied.

3. In order to find τ_s, let us use the expressions for the imaginary part χ'' of the complex magnetic susceptibility as given (for our case, when the constant external field is absent and the adiabatic and isothermal spin-spin relaxation times are identical[1]) by Shaposhnikov's phenomenological theory[8] and quantum theory (see, for example, Ref.3). The first of these expressions is

$$\chi'' = \chi_0 \frac{\tau_s \nu}{1 + \tau_s^2 \nu^2}, \tag{1}$$

where χ_0 is the isothermal equilibrium susceptibility, and ν is the frequency of the alternating external field (Shaposhnikov[8] uses $\omega = 2\pi\nu$ instead of ν, and thus his value of τ_s is equivalent to our $\frac{1}{2\pi}\tau_s$). The second expression is

$$\chi'' = \frac{\pi\nu}{2kT} f(\nu); \tag{2}$$

here T is the lattice temperature, k is Boltzmann's constant, and $f(\nu)\Delta\nu = \sum_{\nu, \Delta\nu} |M_{nn'}|^2$, where $M_{nn'}$ is the matrix element of the component of the magnetic moment of the spin system, directed along the external magnetic field, in the representation of the spin-system Hamiltonian not taking into account the interactions with thermal lattice vibrations. The summation is taken over all pairs of eigenfunctions of this Hamiltonian for which $\frac{|E_n - E_{n'}|}{h}$ (where h is Planck's constant) lies within the interval between ν and $\nu + \Delta\nu$.

Equating (1) and (2) for frequencies which are small in the sense that $\tau_s \nu \ll 1$, we obtain

$$\tau_s = \frac{\pi}{2kT\chi_0} f(0), \tag{3}$$

where $f(0)$ is an approximation for f at a sufficiently low frequency.

Thus the problem reduces to determining $f(0)$. It is not possible to find the exact analytic expression for $f(\nu)$ because of the extreme complexity of the eigenvalue problem for the spin-system Hamiltonian. One may, however, use a different approach. As has been shown by Broer[3], the qualitative variation of $f(\nu)$ can be predicted. When the crystal field does not completely remove the degeneracy, as is true in our case, $f(\nu)$ will have several maxima, one of which will lie close to the origin, and the next one at a distance δ/h from the origin, where δ is the separation between the spin sublevels of the ion (see section 2). We wish to determine $f(\nu)$ in the neighborhood of $\nu = 0$; the corresponding part of the $f(\nu)$ curve is usually called the aperiodic line. For this line, we can calculate the moments of various orders by making use of the invariance of traces[9]. Let us consider the even-order moments

$$\int_0^\infty \varphi(\nu)\, d\nu \equiv \langle \nu^0 \rangle, \quad \int_0^\infty \nu^2 \varphi(\nu)\, d\nu \equiv \langle \nu^2 \rangle, \quad \int_0^\infty \nu^4 \varphi(\nu)\, d\nu \equiv \langle \nu^4 \rangle, \ldots;$$

here $\varphi(\nu)$ denotes that part of $f(\nu)$ which corresponds to the aperiodic line. If we know these moments of $\varphi(\nu)$, we can obtain an approximation for it in the form of an analytic function, and the more moments we know, the more accurate will be our approximation[9].

4. The total Hamiltonian of the spin system corresponding to N identical ions can be written (without taking the interaction with thermal lattice vibrations into account):

$$\mathscr{H} = \sum_{i=1}^{N} W_i + \sum_{i>j} A_{ij} (\mathbf{S}_i \mathbf{S}_j) + \sum_{i>j} \frac{g^2\beta^2}{r_{ij}^3} \left[(\mathbf{S}_i \mathbf{S}_j) - \frac{3}{r_{ij}^2} (\mathbf{S}_i \mathbf{r}_{ij}) (\mathbf{S}_j \mathbf{r}_{ij}) \right], \tag{4}$$

where $W_i = -\delta S_{zi}^2$ is the energy operator of the i-th ion[10], $\mathbf{S}_i$ is the spin operator of the i-th ion, $\mathbf{r}_{ij}$ is the radius vector from the i-th to the j-th ion, β is the Bohr magneton, is the usual g-factor, and A_{ij} is the exchange coefficient for the i-th and j-th ions. The second and third terms in the right side of (4) characterize exchange interactions and dipole magnetic interactions, respectively, within the spin system. In view of the absence of orbital degeneracy, the values of A_{ij} may be assumed to be equal for equally separated ions (isotropic exchange)[2]. Let us take external magnetic field, that induces transitions between energy levels of the spin system whose Hamiltonian $\mathscr{H}$ is given by Eq.(4), as directed along the hexagonal Z-axis (the field is assumed to be sinusoidal). Then the probability of dipole transitions will be given by the square moduli of the matrix elements of the operator $S_z = \sum_{i=1}^{N} S_{zi}$ in the diagonal representation of the Hamiltonian $\mathscr{H}$. The moments of the aperiodic line can be approximated in the form

$$\left.\begin{aligned} \langle \nu^0 \rangle &= g^2\beta^2 \sum_{n,n'}{}' \, |S_{znn'}|^2 = g^2\beta^2 \,\mathrm{Sp}\, \overline{S}_z^2 , \\ h^2 \langle \nu^2 \rangle_{\text{пр}} &= \frac{\sum_{n,n'}' (H_{nn} - H_{n'n'})^2 \, |S_{znn'}|^2}{\sum_{nn'} |S_{znn'}|^2} = - \frac{\mathrm{Sp}\,(\overline{H}\overline{S}_z - \overline{S}_z\overline{H})^2}{\mathrm{Sp}\,\overline{S}_z^2} , \\ h^4 \langle \nu^4 \rangle_{\text{пр}} &= \frac{\sum_{n,n'}' (H_{nn} - H_{n'n'})^4 \, |S_{znn'}|^2}{\sum_{n,n'} |S_{znn'}|^2} = \frac{\mathrm{Sp}\,(\overline{H}U - U\overline{H})^2}{\mathrm{Sp}\,\overline{S}_z^2} , \end{aligned}\right\} \tag{5*}$$

where $U = \overline{H}\overline{S}_z - \overline{S}_z\overline{H}$. Here the symbol $\langle\,\rangle_{\text{пр}}$ indicates that the corresponding moment is divided by $\langle \nu^0 \rangle$ and the prime on the sums indicates that the pairs of states n and n' over which the summation is taken must be only such that $|E_n - E_{n'}| \ll \delta$ (which corresponds to considering only one aperiodic line). In addition, a bar over an operator in Eq.(5) has the following meaning: the sums over the pairs entering into Eq.(5) (with the above selection of the pairs of states) can be represented approximately by traces of operators obtained by means of operators H and S_z, in accordance with (5). The operators $\overline{H}$ and $\overline{S}_z$ should be taken as those parts of H and S_z which commute with the single-ion energy operator $\sum_{i=1}^{N} W_i$ (Ref. 11); these parts of operators are usually called their semidiagonal parts. In the case of our aperiodic line, the operators $\overline{S}_z$ and S_z are identical, since the latter commutes with $\sum_{i=1}^{N} W_i$.

Let us calculate the traces in the expressions for the moments in the representation. The semidiagonal part of the Hamiltonian is

$$\overline{H} = -\delta \sum_{i=1}^{N} S_{zi}^2 + \sum_{i>j} \overline{T}_{ij}, \tag{6}$$

---

*Translator's note. The Russian subscript пр presumably stands for approximate; Wright[0] uses the subscript Av throughout. The translator wishes to remain impartial.

where T_{ij} is the operator of the exchange and magnetic dipole interaction of the ions. Introducing the projection operators A_i and B_i , respectively, for the singlet and doublet levels of the i-th ion, $\overline{T}_{ij}$ can be written

$$\overline{T}_{ij} = A_iA_jT_{ij}A_iA_j + B_iB_jT_{ij}B_iB_j + A_iB_jT_{ij}A_iB_j + A_iB_jT_{ij}B_iA_j + B_iA_jT_{ij}B_iA_j + B_iA_jT_{ij}A_iB_j. \quad (7)$$

Having thus found $\overline{H}$ we can calculate the moments of interest by means of Eq.(5).

For the zeroth moment we obtain

$$\langle \nu^0 \rangle = \frac{2}{3} N (2S+1)^N, \quad (8)$$

where S is the spin of a single ion. If the electric field of the lattice does not entirely remove the degeneracy, and there is no constant magnetic field (our case), the zeroth moment of the whole $f(\nu)$ curve proves equal to $kT\chi_0$ (see Ref.3). On the other hand, in our case the zeroth moment of the whole $f(\nu)$ curve is virtually identical with the zeroth moment of the aperiodic line, as follows from the first of Eqs.(5), taking into account that $\overline{S}_z = S_z$. Thus

$$\langle \nu^0 \rangle = kT\chi_0. \quad (9)$$

After a series of simple, though somewhat cumbersome, calculations, we obtain

$$h^2 \langle \nu^2 \rangle_{\text{ап}} = 3g^4\beta^4 \sum_{j\neq i} (1-\gamma_{ij}^2)^2 r_{ij}^{-6}, \quad (10)$$

where γ_{ij} is the cosine of the angle between the hexagonal Z axis and the radius vector r_{ij}. The exchange coefficient did not enter into the expression for the second moment because the exchange operator commutes with S_z.

Assuming the Ni^{++} lattice to be cubic with a lattice constant d = 6.21 A, and using the lattice sums for a simple cubic lattice[10], namely,

$$\sum r_{ij}^{-6} = 8{,}50d^{-6}, \quad \sum_{j\neq i} (\lambda_{ij}^4 + \mu_{ij}^4 + \nu_{ij}^4)\, r_{ij}^{-6} = 7{,}25d^{-6},$$

$$\sum_{j\neq i} (\lambda_{ij}^2\mu_{ij}^2 + \mu_{ij}^2\nu_{ij}^2 + \nu_{ij}^2\lambda_{ij}^2)\, r_{ij}^{-6} = 0{,}625d^{-6},$$

where λ_{ij}, μ_{ij} and ν_{ij} are the direction cosines of r_{ij} in the coordinate system in which the edges of the cube form the coordinate axes, we obtain

$$n^2 \langle \nu^2 \rangle_{\text{ап}} = 12{,}15g^4\beta^4 d^{-6}. \quad (11)$$

Since the exchange interaction can strongly influence the shape of the $f(\nu)$ curve[4], in order to allow for it we must calculate higher order moments of the aperiodic line. Calculation of fourth moment involves elementary but very cumbersome computations. If we take into account the exchange interaction only for nearest neighbors, we obtain

$$h^4 \langle \nu^4 \rangle_{\text{ап}} = 198g^4\beta^4A^2d^{-6} + 213g^8\beta^8d^{-12} \pm 0{,}3\cdot 10^{-68}\,\text{erg}^4, \quad (12)$$

where A is the exchange coefficient for neighbor ions. In order to calculate this moment, we calculated the following lattice sums, which may also prove useful in solving other problems relating to crystals with a cubic lattice

$$\sum_{\substack{j\neq i_0 \neq l\\ j\neq l}} \frac{\lambda_{il}^2\lambda_{jl}^2}{r_{il}^3 r_{jl}^3} = 4{,}740d^{-6}, \quad \sum_{\substack{j\neq i_0 \neq l\\ j\neq l}} \frac{\lambda_{il}^2\nu_{jl}^2}{r_{il}^3 r_{jl}^3} = 2{,}155d^{-6}, \quad \sum_{\substack{j\neq i_0 \neq l\\ j\neq l}} \frac{\lambda_{il}\nu_{il}\lambda_{jl}\nu_{jl}}{r_{il}^3 r_{jl}^3} = 0{,}472d^{-6}, \quad (13)$$

where the summation is taken over the 400 nearest neighbors of the i_o-th ion.

5. By way of our function having second and fourth moments, we can choose the function:[9]

$$\varphi_4(\nu) = \varphi_2(\nu) + \frac{1}{4!}\left(\langle\nu^4\rangle_{\text{пр}} - \int\limits_0^\infty \nu^4\varphi_2(\nu)\,d\nu\right)\frac{d}{d\nu^4}\varphi_2(\nu), \tag{14}$$

where

$$\varphi_2(\nu) = \langle\nu^0\rangle\left(\frac{2}{\pi\langle\nu^2\rangle_{\text{пр}}}\right)^{1/2} e^{-\nu^2/2\langle\nu^2\rangle_{\text{пр}}}. \tag{15}$$

Inserting $\varphi_1(0)$ in (3) and making use of Eq.(9), we obtained the relation between τ_s and A. According to Ref.10, $g = 2.36$. Unfortunately, there is no data in the literature on the value of τ_s in nickel fluosilicate. If such data existed, the results of our calculations would make it possible to evaluate the exchange coefficient A. An evaluation of this constant by Ishiguro et al[10] on the basis of the shape of the Larmor absorption line in nickel fluosilicate yielded $|A| \approx 8\cdot10^{-18}$ erg, which is clearly too high a value compared with $|A| \approx 5\cdot10^{-18}$ erg obtained by Benzie & Cooke[12] from measurements of the specific heat of the spin system at extremely low temperatures. It may be that this high value was due to inhomogeneities of the strong external magnetic field used in the paramagnetic resonance experiments. Experiments to determine τ_s on the basis of Eq.(1) would be free of this shortcoming and should therefore make it possible to obtain a more accurate value for $|A|$. It would, unfortunately, be impossible to determine the sign of A from such experiments, since terms proportional to the first power of A in the expression for $\langle\nu^4\rangle_{\text{пр}}$ give a smaller contribution than the error with which the other terms are calculated (for this reason we have not included terms containing the first power of A on the right side of Eq.(12)). Taking $|A|$ equal to $5\cdot10^{-18}$ erg, Eqs.(11) and (12) lead to

$$\left.\begin{aligned}\langle\nu^2\rangle_{\text{пр}} &= (1{,}10 \pm 0{,}02)\cdot10^{18}\ \text{сек}^{-2},\\ \langle\nu^4\rangle_{\text{пр}} &= (12 \pm 1{,}5)\cdot10^{36}\ \text{сек}^{-4}.\end{aligned}\right\} \tag{16}$$

From this we get $\langle\nu^4\rangle^{1/4}_{\text{пр}}/\langle\nu^2\rangle^{1/2}_{\text{пр}} = 1.78$, whereas for a Gaussian shape of the curve (which is acceptable when the contribution due to exchange is small) this ratio is 1.32. Thus it is seen that the exchange interactions have a strong influence on the shape of the curve, although they do not affect the magnitude of the second moment. As has been shown by Van Vleck, the fact that the above ratio is greater than its value for a Gaussian curve indicates that the curve drops less rapidly at the edges of the line than in the Gaussian case and that it peaks more rapidly at the maximum (exchange narrowing).

Finally, using Eqs.(3), (14), (15) and (16), we obtain for the spin-spin relaxation time

$$\tau_s = 2.2\cdot10^{-9}\ \text{sec} \tag{17}$$

I take this opportunity to express my gratitude to I.G.Shaposhnikov and S.A.Al'tshuler for their constant interest in the work and helpful discussions.

"A.M.Gor'kii" Molotov State University

References

1. I.G.Shaposhnikov, Present issue of the Bulletin.
2. B.Bleaney & K.W.H.Stevens, Rep.Progr.Phys., 16, 108 (1953).
3. L.J.F.Broer, Physica, 10, 801 (1943).
4. J.H.Van Vleck, Phys. Rev., 74, 1168 (1948).
5. L.Pauling, ZS.Kristallogr. 72, 345 (1930).

6. F.Hund, ZS.f.Phys., 33, 855 (1925).
7. J.Becquerel & W.Opechowski, Physica, 6, 1039 (1939).
8. I.G.Shaposhnikov, Zhur.eksp.i teor.fiz., 17, 824 (1947).
9. A.Wright, Phys.Rev., 76, 1826 (1949).
10. E.Ishiguro, K.Kambe & T.Usui, Physica, 17, 310 (1951).
11. E.Ishiguro, K.Kambe & T.Usui, Phys.Rev., 82, 680 (1951).
12. R.J.Benzie & A.H.Cooke, Proc.Phys.Soc., A 63, 213 (1950).

TOWARDS A PHENOMENOLOGICAL THEORY OF RESONANCE PARAMAGNETIC ROTATION

- L.M.Tsirul'nikova & I.G.Shaposhnikov

1. In 1948 it was discovered[1] that when electromagnetic waves in the microwave region propogate through a paramagnet in the direction parallel to the constant external magnetic field, their plane of polarization is rotated. This effect was called the r-f Faraday effect (more recently it has also been called the resonance paramagnetic rotation effect), although it is only remotely analogous to the ordinary Faraday effect for visible light. In view of the fact that the macroscopic magnetic moment has a relaxation time of the order of the period of microwave (this relaxation is due to interactions among the magnetic moments of paramagnetic ions), and is therefore much greater than the period of visible light, the mechanisms of these two effects are entirely different. Only the electrical anisotropy of the medium produced by the magnetic field is of importance in the ordinary Faraday effect, whereas paramagnetic rotation of the plane of polarization of radio waves is due to magnetic anisotropy produced by the constant magnetic field, while electrical anisotropy is of no importance.

The most thorough experimental investigation of the rotation of the plane of rotation of microwaves is that of Neprimerov[2]. As far as we know, there exists no complete, consistent theory for this effect.

In the present work we make an attempt to construct a phenomenological theory of paramagnetic rotation for waves in the microwave region. In accord with what has been said above, the paramagnetic medium is considered electrically isotropic and the constant external magnetic field is assumed to cause only magnetic anisotropy.

2. In order to obtain an expression for the specific angle of rotation of the plane of polarization of an r-f wave, having an angular frequency ω, as a function of the constant external magnetic field, we use Fresnel's formula

$$\vartheta = \frac{\omega}{C} \cdot \frac{\gamma_- - \gamma_+}{2}, \tag{1}$$

where γ_+ and γ_- are the real parts of the complex indices of refraction for the left and right circularly polarized waves, respectively. We shall express γ_+ and γ_- in the usual way in terms of the components of the magnetic susceptibility tensor, which we shall find on the basis of Shaposhnikov's[3] phenomenological theory of the magnetization of a normal paramagnet with pure spin magnetism in perpendicular fields.

Let us make use of Shaposhnikov's equation for the time dependence of the magnetization:

$$\dot{\mathrm{M}} = -\varkappa \left\{\frac{\partial \Phi}{\partial \mathrm{M}}\right\} + g\,[\mathrm{MH}], \tag{2}$$

where Φ is the nonequilibrium thermodynamic potential, given by

$$\Phi = -\frac{a}{2T} - \mathrm{HM} + \frac{M^2 T}{2b}, \tag{3}$$

and $\vec{\mathrm{H}} = \mathrm{H}_0 + \vec{\eta}$ is the external magnetic field with a constant component H_0 directed along the z- axis and an r-f component η directed along the x- axis. In Eqs.(2) and (3) T is the temperature of the spin system (which differs from the temperature T_0 of the lattice), g is the gyromagnetic ratio, $\varkappa$ is an unknown function of T_0 and H_0, b is the Curie constant, and a is the magnetic specific heat.

The braces in the right side of Eq.(2) indicate linearization of the expression within them with respect to the following small quantities: $\theta \equiv T - T_0$, the components of $\vec{\eta}$ and the components of the variable part of the magnetization $\vec{\xi} = \mathrm{M} - \mathrm{M}_0$, where $\mathrm{M}_0 = \frac{b}{T_0} \mathrm{H}_0$. After performing this linearization, invoking the first law of thermodynamics for the spin system and replacing $\varkappa$ by the isothermal spin relaxation time $\tau_s = \frac{b}{T_0\varkappa}$ of the magnetization[4], we obtain for $\vec{\xi}$ the equation

$$\left(i\omega + \frac{1}{\tau_s}\right)\vec{\xi} + g\,[\mathbf{H}_0\vec{\xi}] = \frac{\chi_0}{\tau_s}\vec{\eta} + g\,[\mathbf{M}_0\vec{\eta}], \tag{4}$$

where $\chi_0 = \frac{b}{T_0}$ is the isothermal equilibrium magnetic susceptibility. The solution of Eq.(4) can be written

$$\vec{\xi} = \chi\vec{\eta} + i\,[\vec{\delta}\,\vec{\eta}], \tag{5}$$

where $\vec{\delta}$ is directed along H_0,

$$\chi = \frac{\chi_0\left[\frac{1}{\tau_s}\left(i\omega + \frac{1}{\tau_s}\right) + \omega_0^2\right]}{\left(i\omega + \frac{1}{\tau_s}\right)^2 + \omega_0^2} \tag{6}$$

and

$$\delta = \frac{\chi_0\omega\omega_0}{\left(i\omega + \frac{1}{\tau_s}\right)^2 + \omega_0^2}, \tag{7}$$

wherein $\omega_0 \equiv gH_0$. Inserting (5) into (4), we find the complex susceptibility tensor

$$\{\chi\} = \begin{Bmatrix} \chi & -i\delta & 0 \\ i\delta & \chi & 0 \\ 0 & 0 & \chi \end{Bmatrix}, \tag{8}$$

whose components are thus functions of the cyclic frequency ω of the alternating field of the magnitude H_0 of the constant magnetic field. We note that here, as in Ref.3, the magnetic susceptibility tensor is understood as the tensor relating the variable part of the expression for the magnetization with the variable part of the expression for the external magnetic field.

Let us now turn to Maxwell's equations, having in mind dielectric paramagnets to which Neprimerov's[2] experiments pertain:

$$\left.\begin{aligned} \operatorname{rot}\mathbf{E} &= -\frac{1}{c}\dot{\mathbf{B}}, \\ \operatorname{rot}\mathbf{H} &= \frac{1}{c}\dot{\mathbf{D}}. \end{aligned}\right\} \tag{9}$$

Since the paramagnetic substance is considered electrically isotropic, we can write

$$\mathbf{D} = \varepsilon\mathbf{E}, \tag{10}$$

where the dielectric constant ε is a scalar. Let us denote the variable part of H by $\vec{\eta}'$, and the variable part of B by $\mathbf{b}$. The variable part of the magnetization $\vec{\xi}$ is related to the variable part of the external magnetic field $\vec{\eta}$ in terms of the tensor of Eq.(8) by Eq.(5). In view of the low polarizability of paramagnetic substances, we shall assume that the same tensor gives the relation be- $\vec{\xi}$ and $\vec{\eta}'$, then

$$\mathbf{b} = (1 + 4\pi\chi)\,\vec{\eta}' + 4\pi i\,[\vec{\delta}\,\vec{\eta}']. \tag{11}$$

Using Eqs.(10) and (11) and eliminating E from (9), we obtain an equation for $\vec{\eta}'$:

$$\nabla(\nabla\vec{\eta}') - \nabla^2\vec{\eta}' + \frac{\varepsilon}{c^2}\{(1+4\pi\chi)\ddot{\vec{\eta}}' + 4\pi i[\vec{\delta}\ddot{\vec{\eta}}']\} = 0. \tag{12}$$

It can readily be shown that this equation has two solutions in the form of left and right circularly polarized waves, whose complex indices of refraction are

$$n_{\pm}^2 = \varepsilon(1 + 4\pi\chi \pm 4\pi\delta). \tag{13}$$

In experimental investigations of resonance paramagnetic rotation (see Ref. 2), the conditions are such that $\tau_s\omega$ is not very much different from unity and that ω_0 lies close to ω. On the other hand, $\chi_0 \sim 10^{-6}$ Thus χ and δ are very small compared with unity, and with sufficient accuracy Eq.(13) yields

$$\gamma_{\pm} = \sqrt{\varepsilon}(1 + 2\pi\chi' \pm 2\pi\delta'), \tag{14}$$

where χ' and δ' are the real parts of χ and δ. Eqs.(1) and (14) then lead to

$$\vartheta = -\frac{2\pi\omega\sqrt{\varepsilon}}{c}\delta'. \tag{15}$$

Eq.(15) shows that the specific angle of rotation of the plane of polarization of r-f waves in paramagnets substances is determined by the real part of the so-called gyration vector $\vec{\delta}$. Finally, invoking Eq.(7), we obtain

$$\vartheta = -\vartheta_0 \frac{\omega^2\omega_0\tau_s^2[1 + \tau_s^2(\omega_0^2 - \omega^2)]}{[1 + \tau_s^2(\omega_0^2 - \omega^2)]^2 + 4\tau_s^2\omega^2}, \tag{16}$$

where

$$\vartheta_0 \equiv \frac{2\pi\sqrt{\varepsilon}\chi_0}{c}. \tag{17}$$

As can be seen from (16) and (17), the angle of rotation depends on the frewuency of the alternating field and on the magnitude of the constant field. The frequency enters explicitly into the expression for ϑ whereas the constant field enters both indirectly (through ω_0) and in general through the isothermal spin relaxation time τ_s of the magnetization. From the experiments of Garif'ianov[5], Sitnikov[6], and Kurushin[7] it follows that τ_s is virtually independent of the magnitude of the constant field, so that the formula we have obtained gives a direct and unambiguous dependence of the angle of rotation on magnitude of the constant field.

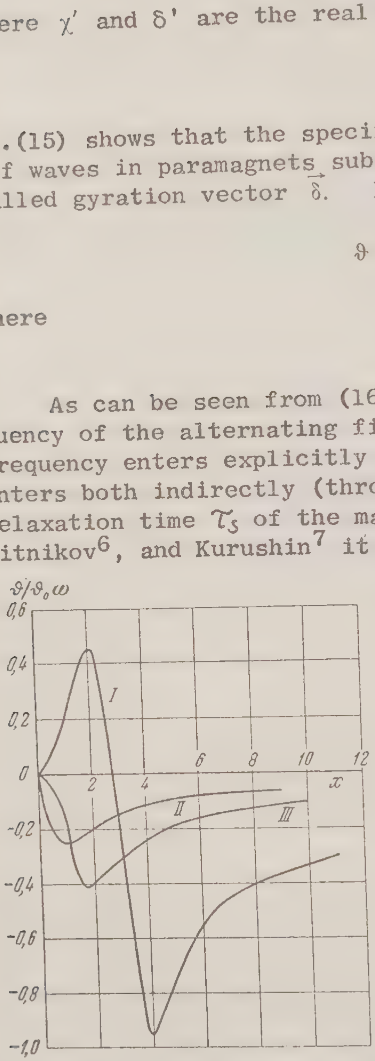

Theoretical curves for resonance paramagnetic rotation at three different values of a:
I) 3, II) 0.5, III) 1.

3. Introducing the notation $\tau_s\omega \equiv a$ and $\tau_s\omega_0 \equiv x$, Eq.(16) leads to

$$\vartheta(x) = \vartheta_0 \frac{a\omega x[a^2 - 1 - x^2]}{4a^2 + [1 - a^2 + x^2]^2}, \tag{18}$$

into which H_0 enters through x.

The shape of the $\vartheta(x)$ curve depends strongly on the value of the parameter a. This can be seen from the curves for three values of a ($a < 1$, $a = 1$ and $a > 1$) shown in the accompanying figure. It is found that the shape of this curve is altogether different in the case when the alternating field frequency is greater than $1/\tau_s$ as compared with the case when the frequency is lower than this value. All the experiments with which we are familiar pertain to the first of these two cases. Comparison of our theoretical results with the experimental data of Neprimerov[2] shows that the theory is in good agreement with experiment as regards both the order of magnitude of the effect and the general shape of the curve characterizing the variation of the angle of rotation with the constant field strength at a given r-f field frequency.

In conclusion we note that the extrema of the functions giving the angle of rotation occur approximately at

$$x = a \pm 1. \tag{19}$$

This makes possible a new experimental determination of the isothermal spin relaxation time τ_s.

"A.M.Gor'kii" Molotov State University

References

1. M.C.Wilson & G.F.Hull, Phys.Rev., 74, 711 (1948).
2. N.N.Neprimerov, Izv.AN SSSR, Ser.fiz., 18, 368 (1954).(Translation in the Bulletin, Vol.18, No.3, p.63.
3. I.G.Shaposhnikov, Dissertation, Molotov State University, 1949.
4. I.G.Shaposhnikov, Following article in the present issue of the Bulletin.
5. N.S.Garif'ianov, Zhur.eksp.i teor.fiz., 25, 359 (1953).
6. K.P.Sitnikov, Dissertation, Kazan State University, 1954.
7. A.I.Kurushin, Present issue of the Bulletin.

ON THE MEANING OF SPIN-SPIN RELAXATION TIME IN PARAMAGNETIC SUBSTANCES

- I.G.Shaposhnikov

1. In this article we shall consider only nonresonance paramagnetic relaxation phenomena, that is, effects which take place only in the absence of a constant external magnetic field or when this field is directed parallel to the r-f field[1].

Works on the phenomenological theory of paramagnetic relaxation in the nonresonance case have been devoted to dielectric paramagnetic crystals with pure spin electronic magnetism. Paramagnetic relaxation effects in such substances lead to two types of relaxation processes in the system composed of the magnetic moments of the particles that comprise the paramagnetic material. These magnetic moments are responsible for the magnetic properties of the paramagnet and interact both with each other and with surrounding medium. The system of magnetic moments is ordinarily called the spin system of the paramagnet. The two relaxation processes are 1) the relaxation due to internal interactions in this system (the relaxation of the magnetic moment to its equilibrium value corresponding to the instantaneous temperature of the spin system and the intensity of the external magnetic field), called spin-spin relaxation, and 2) the relaxation of this system due to its interactions with other elements of the paramagnetic substance, such as its lattice (relaxation of the temperature of the spin system to the lattice temperature), called spin-lattice relaxation.

The first phenomenological theory of paramagnetic relaxation was given by Casimir and du Prè[2] in 1938 for spin-lattice relaxation in parallel fields, and was subsequently modified by other authors[1]. Later Shaposhnikov[3] gave a more general phenomenological theory which treated both spin-lattice and spin-spin relaxations. Finally, Khutsishvili[4] recently undertook a more general phenomenological treatment of relaxation processes (in the more restricted sense of this word, i.e., in a constant external magnetic field) in paramagnetic substances, a treatment based on the Onsager principle, and showed, among other things, under what assumptions one obtains the relationships deriving from Shaposhnikov's theory.

2. The theory of Casimir and du Prè treats only spin-lattice relaxation; accordingly, it is assumed that the spin system goes through a state of complete internal equilibrium, although it is not in equilibrium with the lattice. In this theory, the quantity τ_ℓ, which characterizes the rate at which thermal equilibrium is established between the spin system and the lattice, is called the spin-lattice relaxation time.

In a large number of cases the theory of Casimir and du Prè gives entirely satisfactory agreement with experiment[1]. However, at sufficiently high frequencies of the alternating field and moderate values of the constant field there have been observed significant divergences between theory and experiment[1]. Soon after the discovery of these divergences, Gorter suggested that at frequencies and in fields where the spin-lattice relaxation theory no longer agrees with experiment, spin-spin relaxation becomes significant. To take account of this effect he suggested adding the term

$$\chi''_s = \chi_0(1-F)\tau'\omega \qquad (1)$$

to the imaginary part of the complex magnetic susceptibility given by spin-lattice relaxation theory. Here χ_0 is the isothermal equilibrium susceptibility, F is a known function of the strength of the constant field (for normal paramagnetic substances F increases monotonically from zero to unity as the argument increases), ω is the frequency of the alternating field, and τ' is the quantity which is an empirical function of the constant field strength and should in some sense characterize the rate at which equilibrium is established within the spin system as a result of interactions within it; this quantity τ' has come to be called the spin-spin relaxation time. The addition of the empirical expression (1) to the theory of Casimir and du Pre made it possible to obtain satisfactory agreement with experiment although convincing theoretical interpretation of this expression was not advanced. In particular, the exact sense in which τ' characterizes the rate at which equilibrium is established in the spin system remained unclear.

3. Shaposhnikov's theory takes account of the fact that the spin system passes through nonequilibrium states. The basic assumption is made that these states are partial equilibrium states, which can be completely specified by the temperature of the spin system, the external field strength and the magnetization, whose instantaneous value is here no longer determined by the instantaneous values of the temperature and field. Shaposhnikov's development utilizes Leontovich's[5] determination of the thermodynamic characteristic functions for nonequilibrium states. The theory of Shaposhnikov contains, in addition to the quantity τ_ℓ, which has the same meaning as in the Casimir-du Prè theory, a quantity τ_s which characterizes the rate at which the magnetization isothermally approaches its equilibrium value as a result of internal interactions within the spin system. This quantity τ_s has also been termed the spin-spin relaxation time (just as τ' in Eq.(1)), although for clarity it would be preferable to call it the isothermal spin-spin relaxation time of the magnetization, which is more descriptive.

From Shaposhnikov's theory it follows that in the field-strength and frequency region in which experiment begins to deviate appreciably from the Casimir-du Prè theory, the role of the spin-spin relaxation can indeed by approximated by the addition in (1) of the term suggested by Gorter. Since Shaposhnikov's formula for the complex magnetic susceptibility becomes identical with that of Casimir and du Prè when $\tau_s = 0$, it is natural to suppose that in the above-mentioned field strength and frequency region $\tau_s\omega \ll 1$ for the paramagnetic substances commonly used in experiments. On the other hand, as has been shown by experiment[1], for these substances, $\tau_\ell\omega$ is always greater, and often much greater than unity in this field-strength and frequency region. If we take both these circumstances into account (by the way, this also leads us to the conclusion that $\tau_s \ll \tau_\ell$) and expand the expression for the imaginary part χ'' of the complex magnetic susceptibility, as given by Shaposhnikov's theory, in powers of small values of $\tau_s\omega$ and $1/\tau_\ell\omega$, we find that the first terms of this expansion are linear in $\tau_s\omega$ and $1/\tau_\ell\omega$. Thus in the first approximation, the contributions to χ'' from the spin-lattice and spin-spin relaxations are additive, and the spin-spin relaxation contribution is

$$\chi_s'' = \chi_0(1-F)^2\tau_s\omega. \qquad (2)$$

4. Comparison of Eqs.(1) and (2) shows that the quantity τ' entering into Gorter's empirical expression is $\tau_s(1-F)$. In order to clarify the meaning of this quantity in the most frequent case of normal paramagnetic substances, let us consider spin system of such a paramagnetic substance isolated from the lattice (in practice, such isolation will virtually obtain at frequencies large in the sense that $\tau_\ell\omega \gg 1$ when the paramagnetic relaxation effects will be determined by spin-spin relaxation alone). Let the external magnetic field have only a constant component H_0. Let us denote the temperature of the spin system at the initial time $t = 0$ by T_0, the equilibrium value of the magnetization M, corresponding to H_0 and T_0 by M_0, and the deviation of M_0 from M by ϵ. Let the initial value of ϵ be $\epsilon(0)$, such that $\epsilon(0) \ll M_0$. By using the basic equations of Shaposhnikov's theory, specialized to the case under consideration, we easily obtain the time variation of ϵ. It is found (see Ref.6) that in the approximation linear with respect to $\epsilon(0)/M_0$ (which corresponds to linearity of Shaposhnikov's theory with respect to the deviations of all quantities from their equilibrium values), as t increases, ϵ tends to the limit $\epsilon(\infty)$ that gives the equili-

brium magnetization for H_0 and T (∞); ε approaches this value according to the e^{-t/τ_s^*} law, where $\tau_s^* \equiv \tau_s(1-F)$. Since processes taking place in the spin system isolated from the lattice are adiabatic, τ_s^* may logically be called the *adiabatic spin-spin relaxation time* of the magnetization. Thus the meaning of the quantity entering into Eq.(1) becomes clear: $\tau' = \tau_s^*$.

If we take into account the fact that the adiabatic equilibrium susceptibility of the paramagnetic substances we are considering is given by $\chi_0^* = \chi_0(1-F)$ (see Ref.6), Eq.(2) for the spin-spin part of χ'' at frequencies such that $\tau_\ell\omega \gg 1$, but $\tau_s\omega \gg 1$ can, according to Shaposhnikov's theory, be written as

$$\chi_s'' = \chi_0^* \tau_s^* \omega. \qquad (3)$$

If we do not consider the frequency to be low in the sense that $\tau_s\omega \ll 1$, the theory gives an expression, equivalent to the Debye expression, for the complex susceptibility of a spin system isolated from the lattice and having an equilibrium susceptibility χ_0^* and relaxation time τ_s^*. From this expression, Eq.(3) is obtained in the special case when $\tau_s\omega \ll 1$.

5. Thus in phenomenological treatments of nonresonance paramagnetic relaxation phenomena the same term, spin-spin relaxation time, is used for two different quantities. These quantities τ_s and τ_s^* characterize, respectively, the isothermal and adiabatic rates at which the magnetization of the paramagnetic substance approaches its equilibrium value due to internal interactions in its spin system. Obviously, in some cases this causes confusion. Thus Shaposhnikov asserted in Ref.3 that Gorter's empirical expression (1) is not entirely correct; elsewhere[7,8] this expression has been called erroneous and in conflict with experimental facts. Khutsishvili[9], on the contrary, states that it is incorrect to replace (1-F) (see Eq.(1)) by $(1-F)^2$ (see Eq.(2)) in the expression for χ_s''. It is hoped that the above analysis will serve to clear away the confusion.

"A.M.Gor'kii" Molotov State University

References

1. C.J.Gorter, Paramagnetic Relaxation (In Russian trans.) M., 1949.
2. H.Casimer & F.du Prè, Physica, 5, 507 (1938).
3. I.G.Shaposhnikov, Zhur.eksp.i teor.fiz., 18, 533 (1948).
4. G.R.Khutsishvili, Zhur.eksp.i teor.fizika, 29, 329 (1955).
5. M.A.Leontovich, Vvedenie v termodinamiku (Introduction to Thermodynamics), M.-L. 1951.
6. A.S.Kuznetsov, Dissertation, Molotov State University, 1954.
7. N.S.Garif'ianov, Zhur.eksp.i teor.fiz., 25, 359 (1953).
8. K.P.Sitnikov, Dissertation, Kazan State University, 1954.
9. G.R.Khutsishvili, Soobshcheniia AN Gruz. SSR (Reports of the Georgian SSR Ac. of Sci.), 16, 351 (1955).

TOWARDS A GENERAL THEORY OF RELAXATION PHENOMENA

- I.G.Shaposhnikov & A.S.Kuznetsov

1. Since the discovery of paramagnetic relaxation phenomena[1] much attention has been devoted to the kinetics of magnetization of paramagnetic substances. The theoretical quantum-mechanical treatment of the problem was started in 1932 by Waller[2] even before paramagnetic relaxation had been experimentally observed. Waller considers a very rough model of a paramagnet, but the problem is stated in a very general way; relaxation is not assumed a priori but follows from the theory. Waller was not, however, able to proceed far along the path he had indicated due to the complexity of his deduced expression for the paramagnetic magnetization. As for the fundamental question of the asymptotic behavior of this expression for long relaxation times, Waller advanced only some preliminary rough considerations. The many subsequent works on the quantum theoretical treatment of paramagnetic relaxation phenomena (we have in mind both nonresonance effects in parallel fields or with no constant field and paramagnetic resonance in perpendicular fields) are devoted primarily to solving individual particular problems involving these effects in diverse specific paramagnetic substances (Refs.3 & 4). Thus many existing general questions of the kinetics of paramagnetic magnetization remained unclarified. Recently attempts have been made to analyze several of these problems[5-7]. One of these attempts, undertaken by one of the present authors[7], is a continuation of the general investigation started by Waller[2]. In the present note we review some of the results arrived at in Ref. 7. These results are of a general character and go beyond the scope of the original specific magnetic problem[7]. In order to simplify the presentation, however, we shall continue to use the terminology of Ref.7.

2. Let us consider the spin system of a dielectric paramagnetic crystal with normal pure spin magnetism; the spin system is isolated from the lattice and interacts with an external magnetic field directed along the Z-axis (see Ref.7). Let E be the internal interaction operator in the spin system, η the intensity of the external magnetic field, and μ the operator of the Z-component of the magnetic moment of the spin system; then the Hamiltonian of the spin system is

$$H = E - \eta\mu. \tag{1}$$

Let us consider the following problem. Let us assume that prior to the instant t = 0 there was no external field and that the spin system was in equilibrium at a temperature T. At time t = 0 the external field is applied, with η being given as a function of t. Our problem is to determine how the magnetization ξ of the paramagnet, i.e., the Z-component of the macroscopic magnetic moment of the spin system, will vary with time. We shall consider this problem in the case when for $t \geqslant 0$ the condition

$$\eta(t) = \eta_0 \sin \omega t \tag{2}$$

obtains and when η_0 is sufficiently small for ξ to be considered proportional to η_0.

We shall attempt to find a solution for ξ by means of the formula

$$\xi = \mathrm{Sp}\,(w\mu), \tag{3}$$

where w is the statistical operator of the spin system (density matrix) for which we have the equation

$$ihw = Hw - wH \tag{4}$$

(where h is Planck's constant divided by 2π). In accord with the formulation of the problem, Eq.(4) should be solved with the initial condition

$$w(0) = Z^{-1}e^{-E/kT}, \tag{5}$$

where

$$Z = \mathrm{Sp}\, e^{-E/kT} \tag{6}$$

(where k is Boltzmann's constant).

Waller[2] writes Eq.(4) in the matrix form in the E-representation, and solves it for different forms of η as a function of t in the approximation linear with respect to η_0. For $\eta(t)$ as given by Eq.(2), the solution for ξ can be brought to the form

$$\xi = 2\eta_0 G^{-1}(kT)^{-1} \sum_{j>k} (j,k)\,|\mu_{jk}|^2 \frac{\omega_{jk}}{\omega_{jk}^2 - \omega^2} (\omega_{jk} \sin \omega t - \omega \sin \omega_{jk} t), \tag{7}$$

where G is the number of eigenfunctions of the operator E, and μ_{jk} and ω_{jk} are the matrix elements of the operator μ and the quantum frequencies of $h^{-1}(E_i - E_k)$; the eigenvalues E_r of E are ordered according to increasing magnitude, so that all the ω_{jk} in (7) are positive.

3. For what follows we need certain information regarding the quantum frequencies ω_{jk}. Since the number of possible spin orientations is finite, G is also finite, and the spectrum of E is bounded both above and below. Therefore the $|\omega_{jk}|$ lie between a lower bound ω_0 and an upper bound ω_1. Let us consider the case in which E may be taken as the magnetic dipole spin interaction operator. Then Sp E = 0, and ω_1 is determined by the order of magnitude of the largest of the $|E_j|$. Not being able to solve the equation for the eigenfunctions and eigenvalues of the operator E, let us turn to a rough evaluation based on classical concepts. The dipole magnetic interaction in the spin system is often characterized[1] by the quantity H, called the internal magnetic field constant and introduced as the root mean square of the magnetic field strength within the spin system at a point occupied by an arbitrary spin, and produced by all the other spins, the average being taken over all possible orientations of all the spins except the one being considered, on the assumption that these orientations are equally probable and independent. It is found that H depends very weakly on the particular spin being considered and is determined primarily by ten to a hundred of its closest spin neighbors; for different paramagnetic substances[1], H varies between 10^2 and 10^3 oersteds. As a rough evaluation of the largest of the quantities $|E_j|$, we may take NβH, where N is the total number of spins, and β is the Bohr magneton. Then

$$\omega_1 \sim N\beta H h^{-1} \sim 10^9 \div 10^{10} N \text{ radian/sec.} \tag{8}$$

If we take account of other than dipole interactions within the spin system, the value of ω_1 may be raised. As for ω_0 for a paramagnet of macroscopic dimensions the spectrum of E is almost continuous, so that we may consider $\omega_0 = 0$. In fact, the number of points in this spectrum is of the order of $G = m^N$, where m is the number of possible orientations of a single spin, and the width of the interval in which all these points lie increases with N at a much slower rate (in the case of dipole magnetic interaction alone it may roughly be evaluated as NβH - see above). It is clear that ω always lies within the interval 0 to ω_1. The number R of values of $|\omega_{jk}|$ within this interval is given by

$$R \sim G^2 = m^{2N}. \tag{9}$$

4. Let us now return to Eq.(7) for the magnetization. Let us rewrite it in the form

$$\xi = \eta_0 [\chi'(t) \sin \omega t - \chi''(t) \cos \omega t], \tag{10}$$

where

$$\chi'(t) = 2G^{-1}(kT)^{-1} \sum_{j>k} (j, k)\,|\mu_{jk}|^2 \frac{\omega_{jk}}{\omega_{jk}^2 - \omega^2}\,[\omega_{jk} - \omega\cos(\omega_{jk} - \omega)\,t], \tag{11}$$

$$\chi''(t) = 2G^{-1}(kT)^{-1} \sum_{j>k} (j, k)\,|\mu_{jk}|^2 \frac{\omega_{jk}}{\omega_{jk}^2 - \omega^2}\,\omega\sin(\omega_{jk} - \omega)\,t. \tag{12}$$

Experiment shows that a sufficiently long time (in practice, almost immediately) after the external magnetic field is turned on the magnetization is given by Eq.(10) with χ' and χ'' being time independent, and corresponding to the real and imaginary parts of the complex magnetic susceptibility which determines the paramagnetic relaxation effect. But according to Eqs.(11) and (12) χ' and χ'' are almost periodic functions of time. Thus our theoretical treatment based on the fundamental quantum mechanical Eq.(4) would appear not to give relaxation. However, in discussing the question of the degree to which our results correspond to experiment, one must bear in mind that relaxation is a specifically macroscopic phenomenon. Therefore we should investigate the properties of the right sides of Eq.(11) and (12), which are valid for any value of N, in the specific case of a paramagnet of macroscopic size when N is extremely large.

5. For a macroscopic paramagnet the spectrum of E is quasicontinuous, as a result of which the numbers ω_{jk}, entering into Eqs.(11) and (12) are extremely close to each other (see Eqs.(8) and (9)). This means that if t is not too large, the terms in the sums appearing in Eqs.(11) and (12) are also very close to each other. In order to see how this situation effects Eqs.(11) and (12), let us replace the sums by integrals. A formal replacement[7] leads to

$$\chi'(t) = 2G^{-1}(kT)^{-1}\int_0^{\omega_1} f(\omega')\,\frac{\omega'}{\omega'^2 - \omega^2}\,[\omega' - \omega\cos(\omega' - \omega)t]\,d\omega', \tag{13}$$

$$\chi''(t) = 2G^{-1}(kT)^{-1}\int_0^{\omega_1} f(\omega')\,\frac{\omega'}{\omega'^2 - \omega^2}\,\sin(\omega' - \omega)\,t\,d\omega', \tag{14}$$

where $f(\omega')\,d\omega'$ is the sum of all $|\mu_{jk}|^2$, for which $\omega' \leqslant \omega_{jk} < \omega' + d\omega'$ (in general the μ_{jk} may differ for the same ω_{jk} but different j and k). This formal replacement will be meaningful only if the properties of f are such that the integrals in (13) and (14) exist. Further, the behavior of these integrals as t increases, which is what we are concerned with, can be found only when we know enough about the function f. In order to find f we would need to know the eigenfunctions and eigenvalues of E. This problem, however, is not solved, and is so complex that one can hardly hope to solve it. It is interesting, however, to see whether it is possible to make reasonable assumptions concerning f such that when they are fulfilled the integrals of (13) and (14) exist and are practically time independent for large times. It has been shown in Ref.7 that the following assumptions will do: the function f is continuous, has a continuous first derivative, and a finite number of maxima in its region of definition 0 to ω_1. With these assumptions Eqs.(13) and (14) for χ' and χ'' for large enough times can be replaced by[7]

$$\chi' = 2G^{-1}(kT)^{-1}P\int_0^{\omega_1} f(\omega')\,\frac{\omega'^2}{\omega'^2 - \omega^2}\,d\omega', \tag{15}$$

$$\chi'' = \pi G^{-1}(kT)^{-1}\omega f(\omega), \tag{16}$$

where P denotes the Cauchy principal part of the integral about the point $\omega' = \omega$. As for the time at which one may make this replacement, all one can say is that it depends to a significant extent on the explicit form of f.

Thus when the above-mentioned assumptions concerning f are fulfilled, the theory based on Eq.(4) points to the existence of relaxation in the spin system, isolated from the lattice, of a dielectric paramagnetic crystal with normal pure spin magnetism, provided the times being considered are not too long. A rough evaluation of the time to which our considerations are valid may be made as follows. In order to replace the sums of (11) and (12) by integrals it is necessary not only that the numbers ω_{jk} be close to each other, but also that the numbers $\omega_{jk}t$ be close, i.e., that $\frac{\omega_1 t}{R} \ll 1$ (see section 3); whence we obtain

$$t \ll \frac{R}{\omega_1}. \tag{17}$$

Using Eqs.(8) and (9) and setting $N \approx 10^{23}$ we find that Eq.(17) is satisfied for any time intervals that may be of practical interest. Thus the fact that the right sides of Eqs.(11) and (12) are almost periodic is of no practical significance.

It follows from the character of our analysis that our results pertain not only to the spin system of paramagnets of the given type, but also to all linear macroscopic systems, i.e., all those which respond linearly to external forces, if the interactions within the system are such that the assumptions we have made with respect to f are valid.

The A.M.Gor'kii Molotov State University

References

1. C.J.Gorter, Paramagnetic relaxation (In Russian trans. M. 1949).
2. J.Waller, ZS.f.Phys., 79, 370 (1932).
3. A.Cooke, Rep.Progr.Phys., 13, 276 (1950).
4. B.Bleaney & K.Stevens, Rep.Progr.Phys., 16, 108 (1954).
5. R.Wangsness & F.Bloch, Phys. Rev., 89, 728 (1953).
6. B.V.Semakov, Thesis, Molotov State University, 1954.
7. A.S.Kuznetsov, Dissertation, Molotov State University, 1954.

ON THE ROTATION OF THE PLANE OF POLARIZATION OF MICROWAVES IN PARAMAGNETIC SUBSTANCES

- L. Ia. Shekun

Magneto-optical phenomena in dielectrics are determined in general by the dielectric and magnetic permeabilities ϵ and μ. It is known that in the optical region μ may be regarded as a scalar, so that magneto-optical effects, including rotation of the plane of polarization, are entirely determined by the tensor ϵ.[1] The situation is entirely different in the radio-frequency region. Here ϵ may be considered a scalar (real or imaginary) with sufficient accuracy, so that magneto-optical effects will then depend on the tensor μ. Thus in order to explain the dependence of the rotation of the plane of polarization on the constant magnetic field and the radiation frequency we must know how the complex magnetic susceptibility tensor X depends on these quantities.

There exists no general quantum mechanical theory of X for paramagnets. In order to explain the basic regularities of the microwave Faraday effect, we shall consider paramagnetic substances for which the theory of this susceptibility has been sufficiently well developed, namely paramagnetic gases. In this case we may use the results of Karplus and Schwinger[2], who have performed a quantum mechanical investigation of the behavior in an external magnetic field of a gas whose atoms have dipole moments.

If a plane r-f wave of amplitude F and frequency ω propagates through such a gas, so that

$$\mathbf{F}(t) = \mathrm{Re}\,(\mathbf{F}\,e^{-i\omega t}),$$

this wave will induce a dipole moment

$$\mathbf{p}(t) = \mathrm{Re}\,(\mathrm{X}\mathbf{F}e^{-i\omega t}). \qquad (1)$$

Karplus and Schwinger found that if the atomic energy levels are not degenerate, the mean dipole moment of an atom will be

$$\mathbf{p}(t) = \sum_{m,n} \mathbf{p}_{nm}(\mathbf{p}_{mn}\mathbf{F})\,e^{-i\omega t}\left(1 - \frac{\omega}{\omega - \omega_{mn} + i/\tau}\right)\frac{\rho_n^{(0)} - \rho_m^{(0)}}{2\hbar\omega_{mn}} +$$

$$+ \sum_{m,n} \mathbf{p}_{mn}(\mathbf{p}_{nm}\mathbf{F})\,e^{i\omega t}\left(1 - \frac{\omega}{\omega - \omega_{mn} - i/\tau}\right)\frac{\rho_n^{(0)} - \rho_m^{(0)}}{2\hbar\omega_{mn}}. \qquad (2)$$

Here the indices m and n indicate the energy levels, $\rho_k^{(0)}$ is the relative degree of occupation of the k-th level in the absence of the alternating field $(k = m, n)$, $\mathbf{p}_{mn}$ is the dipole moment matrix element, τ is the mean time between collisions of atoms in the gas, and $\hbar$ and ω_{mn} have their usual quantum mechanical meanings. An explicit expression for the components of X can be found by writing (2) in the form of Eq. (1).

In view of its complexity, Eq. (2) is not convenient for purposes of analysis. Therefore we shall consider the simplest case, when the atoms have no orbital magnetism and the spin is 1/2. When such an atom is placed in a constant magnetic field H_0, it will have two energy levels and its intrinsic frequency spectrum reduces to the single frequency $\omega_0 = g\beta H_0/\hbar$ where g is the Landé factor and β is the Bohr magneton. Choosing the z-axis along H_0 and using Pauli matrices to calculate the components of the dipole moment, we obtain

$$\mathrm{X} = \begin{pmatrix} \chi & -i\delta & 0 \\ i\delta & \chi & 0 \\ 0 & 0 & \chi \end{pmatrix}. \qquad (3)$$

The quantities χ and δ are given by

$$\chi = \chi' - i\chi'', \quad \delta = \delta' - i\delta'',$$

where

$$\chi' = \chi'_1 + \chi'_2, \ \delta' = \chi'_1 - \chi'_2, \quad \chi'' = \chi''_1 + \chi''_2, \ \delta'' = \chi''_1 - \chi''_2,$$

$$\chi'_1 = \frac{\chi_0}{2} \cdot \frac{\omega_0(\omega_0 - \omega) + 1/\tau^2}{(\omega_0 - \omega)^2 + 1/\tau^2}, \quad \chi'_1 = \frac{\chi_0}{2} \cdot \frac{\omega/\tau}{(\omega_0 - \omega)^2 + 1/\tau^2}, \tag{4}$$

$$\chi''_2 = \frac{\chi_0}{2} \cdot \frac{\omega_0(\omega_0 + \omega) + 1/\tau^2}{(\omega_0 + \omega)^2 + 1/\tau^2}, \quad \chi''_2 = \frac{\chi_0}{2} \cdot \frac{\omega/\tau}{(\omega_0 + \omega)^2 + 1/\tau^2}.$$

Here χ_0 is the static atomic susceptibility. It can be seen from Eqs. (4) that when the constant magnetic field is zero, the nondiagonal elements of the tensor X vanish, which corresponds to complete isotropy of the medium.

The propagation of microwaves in gyrotropic media has been considered by many authors[3]. In the case of greatest practical interest, when the wave propagates along the constant magnetic field, we may describe the physical situation as follows. A plane linearly polarized wave enters a medium whose properties are described by the tensor of Eq. (3). The wave becomes elliptically polarized and its "plane of polarization" is rotated. Due to absorption, the amplitude of the wave falls off as it penetrates into the medium. The absorption coefficient is proportional to χ''. The wavelength also changes, this change being determined by the dispersion of χ'. If χ and δ are much smaller than unity, as is true for all paramagnetic substances, the ellipticity will be negligible and the angle of rotation per unit path length will be $\varphi = -(2\pi\omega\sqrt{\varepsilon}/c)\,\delta'$ (where c is the velocity of light), or $\varphi = -\varphi_0(\chi'_1 - \chi'_2)$, where $\varphi_0 = 2\pi\omega\sqrt{\varepsilon}/c$.

The shape of the curve characterizing the rotation is determined by the three parameters ω, ω_0 and τ. In most experiments ω remains constant and ω_0 is varied (by varying the constant magnetic field). The dependences of χ'', χ' and the quantity $\chi'_1 - \chi'_2$, which determines the rotation, on ω_0 for different values of $\omega\tau$ are shown in the accompanying figure.

Unfortunately, it is impossible to subject our theory to rigorous experimental test, since the microwave Faraday effect in gases has not been studied. However, the deduced formulas may be considered applicable with some degree of approximation to solids. In this case τ should be understood as the characteristic time determining the width of the absorption line, i.e., as a rule τ is the spin-spin relaxation time. For lines that are not extremely wide, $\omega\tau$ may be considered equal to $2\omega/\Delta\omega_0$, where $\Delta\omega_0$ is the half-width.

Several experimental investigations have been devoted to the microwave Faraday effect in solid paramag-

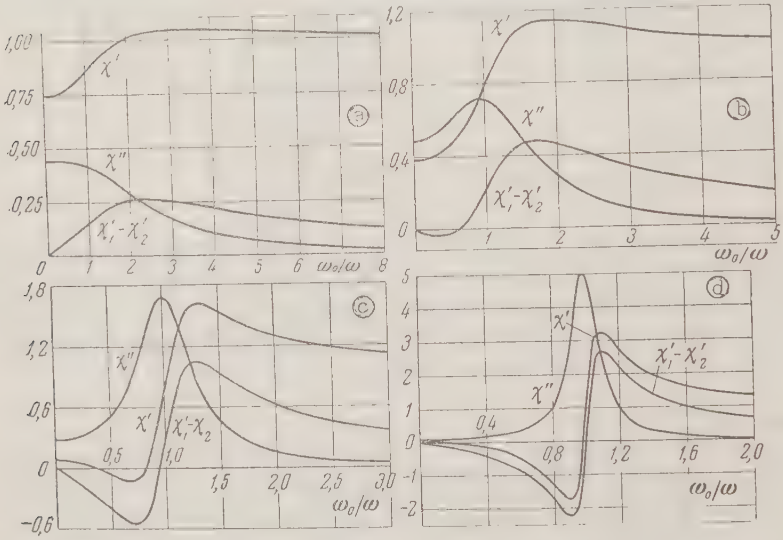

Dependences of the absorption (χ''), dispersion (χ') and rotation of the plane of polarization ($\chi'_1 - \chi'_2$) in a paramagnetic gas on the constant magnetic field for different values of $\omega\tau$. The values of $\omega\tau$ are a) 0.59, b) 1.25, c) 3.33, and d) 10.0. Vertical axis scaled in units of χ_0; horizontal axis in units of ω_0/ω.

netic substances (see bibliography in Ref. 4). The most accurate and thorough quantitative results for paramagnetic salts are those of Neprimerov[4]. He has shown that for salts whose absorption line does not exhibit structure one can obtain good agreement with experiment if the angle of rotation is calculated by the formula which in our notation is $\varphi = -\varphi_0 \chi'$ and which is rigorously speaking incorrect even if only because $\chi' \neq 0$ when $\omega_0 = 0$. From the standpoint of our theory this result is entirely understandable, since for large values of $\omega\tau$ (the region of Nepreimerov's experiments) the dispersion and rotation curves lie close to each other (see d in the figure) so that calculations according to $\varphi = -\varphi_0 \chi'$ and $\varphi = -\varphi_0 (\chi' - \chi_2')$ yield almost equal values. We may thus consider Neprimerov's experiments to be in quantitative agreement with our theory.

It would be interesting to perform experiments under conditions of low values of $\omega\tau$, i.e., on paramagnetic salts in the ten-centimeter region. It should also be noted that although the condition $\omega\tau \lesssim 1$ is fulfilled for many ferromagnets in the centimeter region, our theory is invalid here, since μ is of the order of unity and the conditions $\chi \ll 1$ and $\delta \ll 1$ are not satisfied and hence one should not expect quantitative agreement with experiment. However, the fundamental characteristics of the effect should, presumably, be the same for both paramagnetic and ferromagnetic materials.

"V.I.Ul'ianov-Lenin" Kazan State University

References

1. H.A.Kramers, Proc.Acad.Amsterdam, 33, 959 (1930).
2. R.Karplus & J.Schwinger, Phys.Rev., 73, 1020 (1948).
3. A.L.Mikaelian, Usp.fiz.nauk, 51, 205 (1953); I.G.Shaposhnikov, L.M.Tsirul'nikova, Present issue of the Bulletin.
4. N.N.Neprimerov, Izv. AN SSSR, Ser.fiz., 18, 368 (1954). (Translation in Bulletin, Vol. 18, No.3, p.63).

RELATION BETWEEN PARAMAGNETIC RESONANCE ABSORPTION AND PARAMAGNETIC RESONANCE ROTATION

- L. Ia. Shekun

Magneto-optical phenomena, the absorption of energy and dispersion of susceptibility in paramagnetic substances in the microwave region, are closely related to each other, inasmuch as they are all determined by the same magnetic susceptibility tensor[1] X. Furthermore, the Kramers-Kronig formulas[2] make it possible to establish integral relations between the real and imaginary parts of certain components of X. Since, however, the integration in these relations is taken over the frequency, the expressions are inconvenient for experimental use because as a rule experiments are performed at a constant frequency, with the magnetic field (essentially the intrinsic frequency of the system) being varied. In 1950 Al'tshuler[3] deduced an integral relation between the imaginary and real parts of the susceptibility (χ'' and χ'), in which the integration is over the field. In using these relations, however, it is necessary to make certain arbitrary assumptions with respect to the shape of the curves. We shall show that the imaginary part of the susceptibility is uniquely related to the paramagnetic resonance rotation φ in a way involving no arbitrary quantities.

Using the results of our preceding article[1], let us write the formulas for the imaginary and real components of the susceptibility and the resonance rotation in a paramagnetic gas:

$$\chi'' = \chi''_1 + \chi''_2, \quad \chi' = \chi'_1 + \chi'_2, \quad \varphi = -\varphi_0 (\chi'_1 - \chi'_2), \tag{1}$$

where

$$\varphi_0 = 2\pi\omega \sqrt{\varepsilon}/c,$$

$$\chi''_1 = \frac{\chi_0}{2} \cdot \frac{\omega/\tau}{(\omega_0 - \omega)^2 + 1/\tau^2}, \qquad \chi''_2 = \frac{\chi_0}{2} \cdot \frac{\omega/\tau}{(\omega_0 + \omega)^2 + 1/\tau^2},$$

$$\chi'_1 = \frac{\chi_0}{2} \cdot \frac{\omega_0(\omega_0 - \omega) + 1/\tau^2}{(\omega_0 - \omega)^2 + 1/\tau^2}, \qquad \chi'_2 = \frac{\chi_0}{2} \cdot \frac{\omega_0(\omega_0 + \omega) + 1/\tau^2}{(\omega_0 + \omega)^2 + 1/\tau^2}.$$

Here χ_0 is the static susceptibility, τ is the relaxation time, ω is the radiation frequency and ω_0 is the intrinsic frequency. The magnetic field is related to the frequency by the expression $\hbar\omega = g\beta H$ where g is the Landé factor and β is the Bohr magneton. Al'tshuler[3] established integral relations between χ'_1 and χ''_1, as well as between χ'_2 and χ''_2. In our notation these relations are

$$\chi''_1(H_0) = \frac{1}{\pi} \int_{-\infty}^{\infty} \frac{\chi'_1(H)}{H - H_0} dH, \qquad \chi'_1(H_0) - \chi'_1(\infty) = -\frac{1}{\pi} \int_{-\infty}^{\infty} \frac{\chi''_1(H)}{H - H_0} dH,$$

$$\chi''_2(H_0) = -\frac{1}{\pi} \int_{-\infty}^{\infty} \frac{\chi'_2(H)}{H - H_0} dH, \quad \chi'_2(H_0) - \chi'_2(\infty) = \frac{1}{\pi} \int_{-\infty}^{\infty} \frac{\chi''_2(H)}{H - H_0} dH.$$

It can be seen that by adding and subtracting these expressions, we can obtain the relation between either χ'' and $\chi'_1 - \chi'_2$, or χ' and $\chi''_1 - \chi''_2$. Before the discovery of paramagnetic resonance rotation, neither of these relations could be used without additional assumptions. Thus, for instance, the relation between χ' and $\chi''_1 - \chi''_2$ could be written as one between χ' and $\chi'' - 2\chi''_2$ and, by postulating a definite form for χ''_2, used for conversion from absorption to dispersion[3]. If, however, we note that $\chi'_1 - \chi'_2$ is proportional to φ, the $\chi'' \longleftrightarrow (\chi'_1 - \chi'_2)$ expressions will yield the exact relation between the rotation and absorption. Let us write these expressions in full:

$$\chi''(H_0) = \frac{1}{\pi} \int_{-\infty}^{\infty} \frac{\chi'_1(H) - \chi'_2(H)}{H - H_0} dH,$$

$$\chi'_1(H_0) - \chi'_2(H_0) - \chi'_1(\infty) + \chi'_2(\infty) = -\frac{1}{\pi} \int_{-\infty}^{\infty} \frac{\chi''(H)}{H - H_0} dH.$$

Introducing the angle of rotation φ and noting that φ (∞) = 0, after some simple operations, we obtain these relations in the more convenient form for calculation,

$$\left.\begin{aligned}\chi''(H_0) &= -\frac{1}{\pi\varphi_0}\int_0^\infty \frac{\varphi(H_0+H)-\varphi(H_0-H)}{H}\,dH,\\ \varphi(H_0) &= \frac{\varphi_0}{\pi}\int_0^\infty \frac{\chi''(H_0+H)-\chi''(H_0-H)}{H}\,dH.\end{aligned}\right\} \qquad (2)$$

Thus if we know the experimental curve for φ(H), we can find the absorption curve χ''(H) and vice versa. Since in calculating the integrals, we need to know χ'' and φ for negative values of H, we must bear in mind that $\varphi(-H)=-\varphi(H)$ and $\chi''(-H)=\chi''(H)$.

Expressions (2) may be useful in finding the absolute values of χ'' since it is simpler to measure φ in terms of absolute quantities.

Finally, it should be noted that the application of Eqs.(2) to nongaseous paramagnetic substances is more justified than the direct use of Eqs.(1). This is true because Eqs.(2) are valid not only when χ'', χ' and φ are described by Eqs.(1). In order for these relations to hold, it is necessary only that the susceptibility can be separated into two such components that one can be obtained from the other by changing the sign of ω_0. This requirement is apparently satisfied for all paramagnetic substances[3].

It would also be interesting to verify experimentally to what extent Eqs.(2) are applicable to ferromagnets.

"V.I.Ul'ianov-Lenin" Kazan State University

References

1. L.Ia.Shekun, Preceding article in the present issue of the Bulletin.
2. C.J.Gorter, Paramagnetic resonance (In Russian trans. M., 1949).
3. S.A.Al'tshuler, Zhur.eksp.i teor.fiz., 20, 1047 (1950).

FERRITE DISC IN A COAXIAL LINE
II. METHOD OF ACTIVE AND REACTIVE LOADS*

- Ia.N.Kolli

1. In an earlier contribution[1] attention was called to the basic shortcomings of the common method of determining the four parameters of a doubly-complex medium ($\mu = \mu_1 - j\mu_2$, $\epsilon = \epsilon_1 - j\epsilon_2$) filling a section of coaxial line, i.e., of the open circuit and short circuit impedance measurement method. This method may be appreciably improved if the determinations of the input impedances Z_x and Z_k, corresponding to an open circuit and a short circuit at the termination of the line containing the specimen are made on the basis of a series of measurements.

It is known that when the modulus of the load impedance is varied, the points representing the values of the input impedances in the complex impedance diagram fall on the circumference of a circle. By varying the reactive load one can obtain a circle which will be the locus of the input impedance values with a reactive load. By varying the active (resistive) load one can obtain an analogous circle for the values of the input impedances with a resistive load. Obviously the point Z_x and Z_k will be the points of intersection of these circles.

The circle $Z_{in} = f(jX_H)$, where X_H is the reactive load impedance (reactance), can be plotted on the basis of a large number of experimental points inasmuch as a variable reactive load is readily realized by means of a lossless line terminated by a moveable short-circuiting piston. Having plotted the circle diagram on the basis of the entire series of experimental points, one can identify and winnow out the questionable points (points comprising incidental measurement errors).

In practice realization of an active load in the centimeter wave length range is difficult. Of all the possible resistive loads in this range one can easily check only one: $R_H = Z_{ma}$ (here Z_{ma} is the matched load equal to the characteristic impedance of the line beyond the obstacle). Thus for the entire active-load impedance circle we can know with a certainty only one point and for plotting the entire circle diagram we need additional conditions which can be obtained from an examination of the general relationships in a quadripole network (see Appendix).

The use of the circle diagram $Z_{in} = f(R_H)$ in addition to the circle diagram $Z_{in} = f(jX_H)$ may serve as justification for calling this method the method of reactive and active loads. With an accurately matched load available, the point $Z_{in} = f(Z_{ma})$ can be measured directly. It can also be plotted on the basis of the circle diagram for the values of the input impedance with a reactive load. This method of plotting was recently proposed by Deschamps[2].

From an analysis of the expressions for a quadripole network one can obtain the following conditions, which must be observed in plotting the circle $Z'_{in} = f(R_H)$:**

1) the sought circle must be orthogonal (see Appendix) with respect to the circle $Z'_{in} = f(jX_H)$;

2) the sought circle must pass through the given point $Z'_{in} = Z_o = f(Z_{ma})$;

3) the following condition must be satisfied

$$\frac{\rho_{Im}}{\rho_{Re}} = \frac{|y_1|}{x_2}, \qquad (1)$$

here ρ_{Im} is the radius of the circle defined by the values of the input impedances with a reactive load, ρ_{Re} is the radius of the circle given by the values of the input impedances with a resistive load, y_1 is the ordinate of the center of the reactive load impedance circle and x_2 is the abscissa of the center of the resistive load input impedances circle.

---

*The first part of this study is Ref. 1.

**Here and below the primes (') designate normalized impedances.

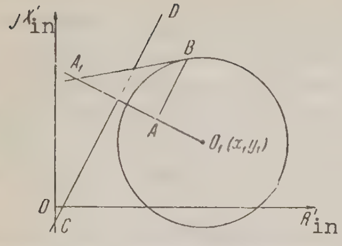

Fig. 1. Construction of the line of centers with a resistive load.

The solution must determine the coordinates of the center and radius of the sought circle.

The graphic method of solving this problem consists in the following (Fig.1).

1. In view of the orthogonality of the given and sought circles, the sought circle must pass not only through the point $A = Z_0 = f(Z_{ma})$, but also through the point A_1 symmetric to it relative to the given circle.^{3} We can employ the following construction to locate point A_1: draw a line from O_1 through A, erect a perpendicular AB at A and finally draw a tangent to the circle at the point of intersection of the line AB with the circle $f(jX_H)$. The point of intersection of this tangent and the extension of O_1A is the sought point A_1.

2. The center of the sought circle $Z'_{in} = f(R_H)$ must lie on the line CD perpendicular to the segment AA_1 at its midpoint. For our further construction let us make use of the similarity of the plotted figures.

From (1) it follows that:

$$\frac{x_2}{\rho_{Re}} = \frac{|y_1|}{\rho_{Im}}. \tag{2}$$

Inasmuch as y_1 and ρ_{Im} are known, when the center of the sought circle is moved along CD, the radius ρ_{Re} must change so that the ratio x_2/ρ_{Re} remains constant and equal to y_1/ρ_{Im}.

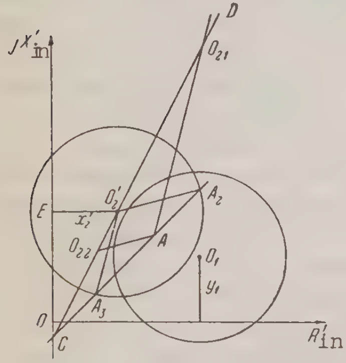

Fig. 2. Construction for locating the centers of the circles with a resistive load.

Accordingly we can proceed as follows. Let us select on CD a point O'_2, the abscissa of which x'_2 is equal to the ordinate y_1 of the center of the given circle (i.e., of O_1). Here ρ_{Re} must be taken equal to ρ_{Im}. Using the center O'_2 found in this manner (Fig.2), let us draw a circle of radius ρ'_{Re}. This circle will intersect the line CA at points A_2 and A_3. For the sought circle to pass through point A we must redraw it so that it will go through point A_2 or A_3, modifying the construction so that it will remain similar to the initial one. To this end we must increase all the dimensions by a factor CA/CA_3 or reduce them by a factor CA/CA_2. The simplest graphic procedure is to draw through point A straight lines parallel to the radii O'_2A_2 and O'_2A_3. The points of intersection of these lines with CD - O_{21} and O_{22} - are the possible centers of the sought circle, the possible radii of which are $O_{21}A$ or $O_{22}A$ (Fig.3). Circles with these radii give two pairs of points of intersection with the given circle $Z_{in} = f(jX_H)$, namely, Z_{k_1}, Z_{x_1} and Z_{k_2}, Z_{x_2}.

In the case of a distortion-free line ($\arg Z_c = 0$), we have $y_1 = 0$. In view of Eq.(2), with $y_1 = 0$, $x_2 = 0$, i.e., O_1 lies on the R'_{in} axis, while the center of the sought circle lies on the jX'_{in} axis; in this case we have a unique solution.

In some cases we can discard the extraneous solution on the basis of physical considerations. One of these is evaluation of the modulus of the characteristic impedance. All now know magnetodielectrics are characterized in the centimeter range by a modulus of magnetic permeability $|\mu|$ much smaller than the modulus of the dielectric constant $|\epsilon|$. Consequently, the modulus of the normalized

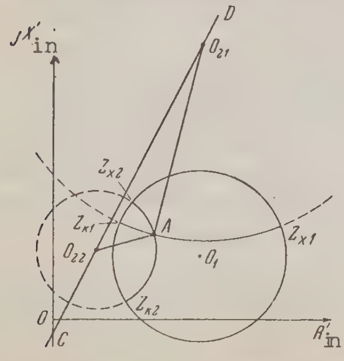

Fig. 3. Determination of the input impedances corresponding to short circuit and open circuit conditions.

characteristic impedance $|Z_c'|$ of these materials must be smaller than unity.

Thus the described method makes it possible to find Z_x and $Z_к$ of the investigated coaxial line if we know 1) the circle forming the locus of the values of the input impedance of the line for one resistive load ($Z_н = Z_{ma}$). In addition, in the general case, it is necessary to know the approximate position of the point corresponding to $Z_н = 0$ or $Z_н \to \infty$ in order to discard the extraneous solution.

Having found Z_x and $Z_к$ we can readily compute μ and ϵ by means of familiar equations.

Everything that has been said above is obviously applicable not only to a coaxial line but to a waveguide as well. The only difference in the calculations will be in the form of the equations relating μ and ϵ with Z_x and $Z_к$.

2. The experimental verification of the described measurement procedure and method of processing the data was carried out on type 0-400 nickel-zinc ferrite specimens. The specimens, which were obtained from the laboratory headed by N.N.Shol'ts, were in the form of discs 16 mm in diameter with a central aperture 5 mm in diameter. The thickness of the discs (effective length of the line with specimen) was 3.7 mm. The results of the input impedance measurements for one of these specimens carried out at a frequency of $2.92 \cdot 10^3$ Mc are shown in Fig.4.

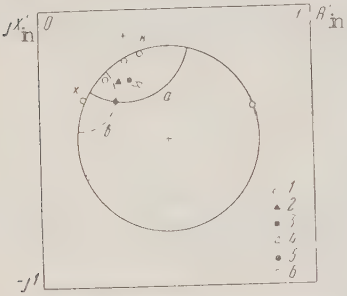

Fig. 4. Circle diagram of the input impedance values of an 0-400 ferrite disc at λ = 10.24 cm ($\nu = 2.92 \cdot 10^3$ Mc); thickness of disc = length of line = 0.37 cm: 1) experimental points, 2) Z_c' determined by the method of three reactive loads with $\Delta x = \lambda/8$, 4) same as 3 but with $\Delta x = 2.00$ cm, 5) input impedance with matched load, 6) Z_c' determined by the method of resistive and reactive loads.

The reactive load input impedance circle was plotted on the basis of the experimental points 1 (Fig.4). The values of points "k" and "x", taken respectively as the short circuit and open circuit points, were used to calculate the value of the normalized characteristic impedance Z_c' (point 2). In addition, Z_c' was determined by the method of three reactive loads (Ref.1) with $\Delta x = \lambda/8$ (point 3) and with $\Delta x = 2.00$ cm (point 4). The input impedance was also measured with $Z_н = Z_{ma}$ (point 5); the two arcs a and b of the circle $Z_{in}' = f(jX_H)$ were drawn through this point. Arc a was taken to be the correct solution since only in this case do the points 3 and 4 lie in the region of input impedance corresponding to $X_H < 0$ (Z_c' may be regarded as the input impedance of the disc with $Z_н' = Z_c$, inasmuch as for arg $Z_c < 0$, $X_H = \operatorname{Im}(Z_c') < 0$). The figure shows the relative inaccuracy of the determination of Z_c' in this case when made by the open and short circuit method. The good agreement of the results for Z_c' obtained by the method of three reactive loads and by the method of resistive and reactive loads (point 6) gives reason to assume that this value is the correct one.

The propagation constant γ was calculated on the basis of the circle parameters (Ref.1, Eqs.(20) & (21). The final results of the computations were $Z_c' = 0.44 \angle -36^\circ$; $\gamma = 2.08 + j\,2.80$; $\mu = 0.72 - j\,2.4$; and $\epsilon = 13 - j\,0.038$.

The values of μ and ϵ computed on the basis of the experimental data agree as regards order of magnitude with the data in the literature. Thus Rado, Wright and Emerson[4] give the following data for ferramic A: $\mu \approx 0.23 - j\,1.05$ at a frequency of 3000 Mc; ϵ has a constant value of 8.5 ± 10% over the frequency range from 50 to 10,000 Mc, while ϵ_2 is small and does not exceed 0.7.

Analysis of the Results of Measurement for Specimens with Low Attenuation

The method of resistive and reactive loads and the method of three reactive loads are based on constructing a circle diagram of the input impedance in Cartesian coordinates. With a reactive load and low attenuation the size of the circle increases greatly and the experimental points fall near the imaginary component axis. Hence determination of the coordinates of the center of the circle a and φ and the radius ρ_{Im} becomes inaccurate.

By way of illustration the experimental points obtained in investigating one type of magnetodielectric are shown in Fig.5. In such cases it is expedient to go over to the circle diagram of the coefficient of reflection Γ; on such a diagram all the possible values of the reflection coefficient lie inside a circle of unit radius (Fig.6 - this circle diagram is constructed in polar coordinates). The same experimental points as in Fig.5 have been plotted on this reflection-coefficient circle diagram. It will be seen that the possible accuracy of determination in this case is much better than in the preceding case.

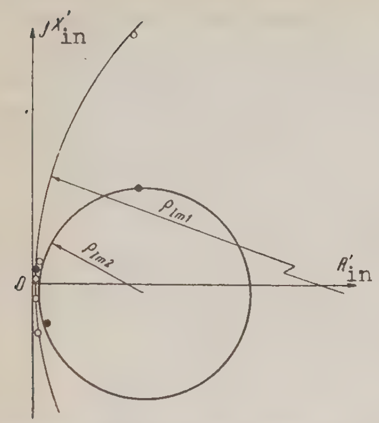

Fig.5. Circle diagram of values of input impedances with low attenuation in a magnetodielectric specimen.

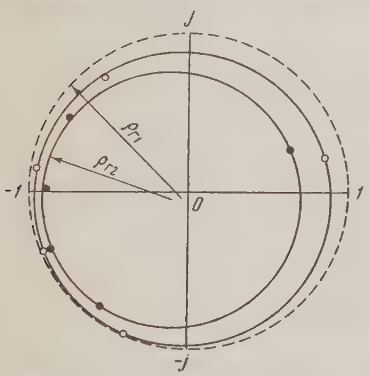

Fig.6. Circle diagram of reflection coefficient.

The relationship between the input impedance Z'_{in} and the reflection coefficient Γ is given by the familiar expression

$$Z'_{in} = \frac{1+\Gamma}{1-\Gamma}. \tag{3}$$

Making use of this expression one can readily find the radius ρ and the coordinates a and φ of the center of the input impedance circle diagram from the radius ρ_Γ and the coordinates K and ξ of the reflection-coefficient circle diagram. The equations relating ρ, a and φ with ρ_Γ, K and ξ, can readily be derived on the basis of the properties of a fractional-linear transformation wuch as expression (3). The derivation of these expressions for the general case is given in Smirnov's book[3]. For the given case we obtain

$$\rho = \frac{2\rho_\Gamma}{D} \tag{4}$$

and

$$ae^{j\varphi} = \frac{2(1-Ke^{-j\xi})}{D}, \tag{5}$$

where

$$D = 1 + K^2 - 2K\cos\xi - \rho_\Gamma^2.$$

Appendix

Relation between the input impedance circle diagram for a quadripole network with reactive and resistive loads

The following dependences of the circle-diagram parameters on the parameters of the quadripole network have been established (see, for example, Ref.1, Appendix 1).

1. With a variable reactive load:

$$\mathbf{Z}_{in} = \mathbf{Z}_x + \mathbf{Z}_{rev.\,x}\frac{\mathbf{Z}_\text{н} - \mathbf{Z}_x}{2R_{rev.\,x}}\left(1 + e^{-j2\psi_1}\right), \tag{1.1}$$

where

$$\psi_1 = \operatorname{arc\,tg}\frac{X_\text{н} + X_{rev.\,x}}{R_{rev.\,x}}$$

($Z_{\text{rev.x}}$ is the input impedance looking into the quadripole network from the output side with the input terminals open and X_H is the alternating load); the radius of the circle

$$\rho_{\text{Im}} = \left| \frac{Z_{\text{rev. x}}(Z_{\text{н}} - Z_{\text{x}})}{2R_{\text{rev. x}}} \right|; \tag{1.2}$$

the coordinates of the center of the circle

$$x_1 + jy_1 = Z_{\text{x}} + Z_{\text{rev. x}} \frac{Z_{\text{н}} - Z_{\text{x}}}{2R_{\text{rev. x}}}. \tag{1.3}$$

2. With a variable resistive load:

$$Z_{\text{in}} = Z_{\text{x}} + Z_{\text{rev. x}} \frac{Z_{\text{н}} - Z_{\text{x}}}{2jX_{\text{rev. x}}}(1 - e^{j2\psi_2}), \tag{1.4}$$

where

$$\psi_2 = \operatorname{arc\,tg} \frac{R_{\text{н}} + R_{\text{rev. x}}}{X_{\text{rev. x}}},$$

the radius of the circle with a resistive load is

$$\rho_{\text{Re}} = \left| \frac{Z_{\text{rev. x}}(Z_{\text{н}} - Z_{\text{x}})}{2jX_{\text{rev. x}}} \right| \tag{1.5}$$

and the coordinates of its center are

$$x_2 + jy_2 = Z_{\text{x}} + Z_{\text{rev. x}} \frac{Z_{\text{н}} - Z_{\text{x}}}{2jX_{\text{rev. x}}}. \tag{1.6}$$

From (1.2) and (1.5) we find

$$\frac{\rho_{\text{Im}}}{\rho_{\text{Re}}} = \frac{|X_{\text{rev. x}}|}{R_{\text{rev. x}}} = \operatorname{tg} |\varphi_{\text{rev. x}}|. \tag{1.7}$$

From (1.3) and (1.6) we can write expressions for y_1 and x_2:

$$y_1 = \frac{X_{\text{rev. x}}(R_{\text{н}} - R_{\text{x}}) + R_{\text{rev. x}}(X_{\text{н}} + X_{\text{x}})}{2R_{\text{rev. x}}}, \tag{1.8}$$

$$x_2 = \frac{X_{\text{rev. x}}(R_{\text{н}} + R_{\text{x}}) + R_{\text{rev. x}}(X_{\text{н}} - X_{\text{x}})}{2X_{\text{rev. x}}}. \tag{1.9}$$

3. For a symmetric quadripole network

$$Z_{\text{rev. x}} = Z_{\text{x}} \tag{1.10}$$

and Eqs.(1.8) and (1.9) simplified to:

$$y_1 = \frac{R_{\text{x}} X_{\text{н}} + R_{\text{н}} X_{\text{x}}}{2R_{\text{x}}}, \tag{1.11}$$

$$x_2 = \frac{R_{\text{x}} X_{\text{н}} + R_{\text{н}} X_{\text{x}}}{2X_{\text{x}}}. \tag{1.12}$$

Consequently, for a symmetric quadripole network we have

$$\frac{y_1}{x_2} = \frac{X_{\text{x}}}{R_{\text{x}}} = \operatorname{tg} \varphi_{\text{x}}. \tag{1.13}$$

Comparing (1.7) and (1.13) we obtain for the condition (1.10):

$$\frac{\rho_{\text{Im}}}{\rho_{\text{Re}}} = \frac{|y_1|}{x_2} = \operatorname{tg} |\varphi_{\text{x}}|. \tag{1.14}$$

We can draw the following deductions on the basis of the above analysis:

1. As the reactive load impedance is increased from $-\infty$ to $+\infty$ the point

representing the input impedance of the quadripole network moves clockwise around the circle (see Eq.(1.1) & Fig.7).

2. As the resistive load impedance is increased from 0 to +∞, the point representing the input impedance of the quadripole network moves counterclockwise around the circle if $X_{rev.x} > 0$ and clockwise if $X_{rev.x} < 0$ (see Eq.(1.4) & Fig.7).

3. The relation between the radii of the input impedance circles with reactive and resistive loads is given by expression (1.7).

4. For a symmetric quadripole network the relation between the coordinates of the centers of these circles is characterized by expression (1.13), analogous to (1.7).

5. The familiar expression for the input impedance of a quadripole network

$$Z_{in} = \frac{AZ_{\text{н}} + B}{CZ_{\text{н}} + D} \qquad (1.15)$$

(where Z_H is the alternating load) is a fractional-linear function of the form

$$w = \frac{az + b}{cz + d}. \qquad (1.16)$$

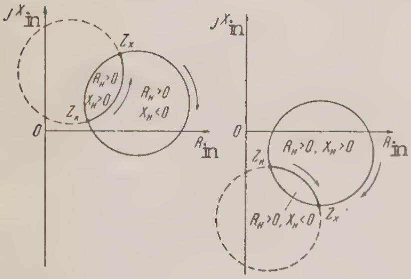

Fig. 7. Circle diagram with resistive and reactive loads.

As is known, the function (1.16) effects the transformation of mutually perpendicular straight lines in plane z into orthogonal circles in plane w. Consequently Eq.(1.15) transforms the straight lines R_H = var. and X_H = var. into the orthogonal circles $Z_{in} = f(R_H)$ and $Z_{in} = f(jX_H)$. In the transformation the points of intersection of the straight lines R_H = var. and X_H = var. with $Z_{\text{н}} = 0$ and $Z_{\text{н}} = \infty$ become, respectively, the points of intersection of the circles $Z_{in} = f(R_H)$ and $Z_{in} = f(jX_H)$ with $Z_{in} = Z_{\text{к}}$ and $Z_{in} = Z_{\text{х}}$.

With $R_H \geqslant 0$ all possible values of $Z_{\text{н}}$ lie to the right of the ordinates of the plane $Z_{\text{н}}$, including the axis itself. Upon the transformation (1.15) the straight line X_H = var. - ordinate axis of the $Z_{\text{н}}$ plane - becomes the circle $Z_{in} = f(jX_H)$ in the Z_{in} plane (Fig.7). Then all the values of Z_{in} corresponding to $R_H > 0$ can lie either outside the circle or inside it. If it is assumed that (1.15) effects the transformation of the semiplane $R_H > 0$ into the region lying outside the circle $Z_{in} = f(jX_H)$, then at certain values of $R_H > 0$ and X_H we will obtain $R_{in} < 0$. This is obviously devoid of physical significance. Consequently all the values of Z_{in}, corresponding to $R_H > 0$ must lie inside the circle $Z_{in} = f(jX_H)$.

Deductions 3, 4 & 5 above enable us to construct the resistive load circle from the reactive load circle and one of the points on the resistive load circle, and vice versa. Deductions 1 & 2 enable us to determine which of the two points of intersection of the circles is the short-circuit point and which the open-circuit point.

If the points of intersection of the circles lie in the same quadrant, the points representing $Z_{\text{к}}$ and $Z_{\text{х}}$ will be located as shown in Fig.7 (the arrows indicate the direction of displacement with increasing R_H and X_H).

If the points of intersection of the circles lie in different quadrants, then to identify the points $Z_{\text{к}}$ and $Z_{\text{х}}$ one must first determine the direction of displacement of $Z_{in} = f(R_H)$ around the circle. For this it is sufficient to measure the input impedance at two different values of R_H, and thus find out which is larger.

"V.M.Molotov" Moscow Power Engineering Institute

References

1. Ia.N.Kolli, K.M.Polivanov, Izv. AN SSSR, Ser. fiz., 18, 382 (1954). (Translation in Bulletin, Vol.18, No.3, p.78.)

2. G.Deschamps, J.Appl.Phys., 24, 8, 1046 (1953).

3. V.I.Smirnov, Kurs vysshei matematiki (Course in Higher Mathematics), Vol.3, Part 2, M.-L., 1950.

4. G.T.Rado, R.W.Wright & W.H.Emerson, Phys. Rev., 80, 273 (1950).

FREQUENCY CHARACTERISTICS OF MAGNETODIELECTRICS

- V.V.Kuznetskii

The purpose of the study was to investigate the magnetic and electric properties of the nickel-zinc ferrites designated 0-2000 and 0-1000 (Oxifer series) in the radiofrequency range from 0.1 to 50 Mc.

The experiments were conducted and the experimental results processed according to Polivanov's[1] method of two measurements, which makes it possible to obtain the two values of μ and ϵ at any frequency.

Ferrites, as a rule, in addition to a high magnetic permeability μ also have a high permittivity (dielectric constant) ϵ.

Substances in which the course of electromagnetic processes is determined both by the permeability and the permittivity can be classed as magnetodielectrics regardless of the specific factors determining their properties.

In evaluating the electromagnetic fields in such materials one must take into account not only the conduction currents but also the displacement currents.

Hence Maxwell's first equation, which must be solved for certain boundary conditions in order to elucidate the demagnetizing role of eddy currents, must be written in the complete form:

$$\operatorname{rot} \dot{\mathrm{H}} = (\sigma + j\omega\varepsilon\varepsilon_0)\, \dot{\mathrm{E}} = \sigma_{\text{п}}\dot{\mathrm{E}},$$

where $\sigma_{\text{п}} = \sigma + j\omega\varepsilon\varepsilon_0$ is the admittance.

In this case one cannot compute the permeability μ by means of the familiar formulas excluding the influence of the skin effect in metallic ferromagnets, inasmuch as for this one must know the complex specific admittance σ_{π} or the complex dielectric constant ϵ_{π}, which, in turn, are functions of the frequency.

For solving the given problem, i.e., for determining the complex permeability, one must have the data not from one but from two independent experiments since the results of each experiment yields only one complex equation containing two unknown complex quantities (μ and σ_{π}).

Polivanov's method of two measurements makes it possible to exclude the demagnetizing effect of eddy currents due to the admittance, and enables us to determine the values of the permeability and the dielectric constant at any frequency. To evaluate μ and ϵ_{π} we must know the values of the impedances Z_M and Z_E of the specimen obtained from two experiments, a magnetic and an electric, carried out under appropriate conditions.

The requirements of the method of two measurements used for investigating our toroidal specimens of 0-2000 and 0-1000 ferrites dictated our experimental conditions. In the magnetic experiment we measured the impedance Z_M introduced by the ferrite toroid when mounted in a section of coaxial line; in the electric experiment we measured the impedance Z_E of a cylindrical capacitor in which the dielectric was the ferrite specimen.

In the first experiment the cylindrical surface of the specimen was covered with conducting shields which obviated the penetration of the magnetic field in the radial direction; this made it possible to assume that only plane electromagnetic waves penetrate from the face side of the specimen.

In this case

$$Z_{\text{M}} = j\omega \frac{\mu\mu_0}{\pi\gamma} \ln \frac{r_2}{r_1} \operatorname{th} a\gamma,$$

where r_1 is the inside and r_2 is the outside radius of the ferrite toroid, a is the half-thickness of the specimen and $\gamma = \sqrt{j\omega\mu\mu_0\sigma_{\text{п}}}$ is the propagation constant of the electromagnetic waves in the ferrite.

The second, electric experiment was carried out in rigorous conformity with the first, namely, the electric field was directed along the radius exactly as in the first, magnetic experiment. To this end the current was brought in to the cylindrical generatrices of the specimen, which was covered with conducting shields.

In this case

$$Z_E = \frac{\ln \frac{r_2}{r_1}}{4\pi\sigma_\Pi a} \cdot \frac{a\gamma}{\operatorname{th} a\gamma}.$$

Having found Z_M and Z_E one can readily obtain one equation from their product:

$$Z_M \cdot Z_E = \frac{\left(\ln \frac{r_2}{r_1}\right)^2}{4\pi^2} \cdot \frac{j\omega\mu\mu_0}{\sigma_\Pi},$$

and another equation from their ratio:

$$\frac{Z_M}{Z_E} = 4 \operatorname{th}^2 a \sqrt{j\omega\mu\mu_0\sigma_\Pi}.$$

Through simultaneous solution of these equations, we obtain the values of the complex quantities μ and σ_Π.

The measurements were carried out with the aid of the familiar and widely used instrument - a Q-meter. In order to extend the range of measurement of the Q-meter, a VKS-7 (BKC-7) cathode-ray voltmeter was connected in parallel to the calibrated capacitor of the instrument. The usual input microameter of the cathode-ray voltmeter was replaced by a more sensitive one. After this replacement the full-scale displacement of the voltmeter equaled 0.3 v. By means of this instrument it was possible to determine the parameters of the measuring circuit of the Q-meter with a Q-factor of the system of the order of several units. It may be noted that the Q-factors of the investigated specimens were generally less than unity.

The formulas used for processing the Q-meter data were deduced from the general theory of resonance circuits.

The voltage supply to the Q-meter was stabilized by means of a ferroresonance voltage regulator. To insure attainment of thermal equilibrium the entire instrument was preheated for 1-1.5 hours.

In measurements at high frequencies the matter of correctly taking into account the influence of the windings on the results presents great difficulties since the distributed capacitance of the turns may be the cause of natural oscillations in the windings. In our case the influence of the winding at frequencies from 0.1 to 50 Mc was eliminated inasmuch as the measurements were carried out with one turn - a shorted section of coaxial cable.

Two sets of measurements were made at each frequency: first, we measured the inductance of the system with the specimen and then the inductance without the specimen, which enabled us to eliminate the influence of the measuring system on the results. An analogous procedure was used at each frequency in determining the capacitance of the specimens.

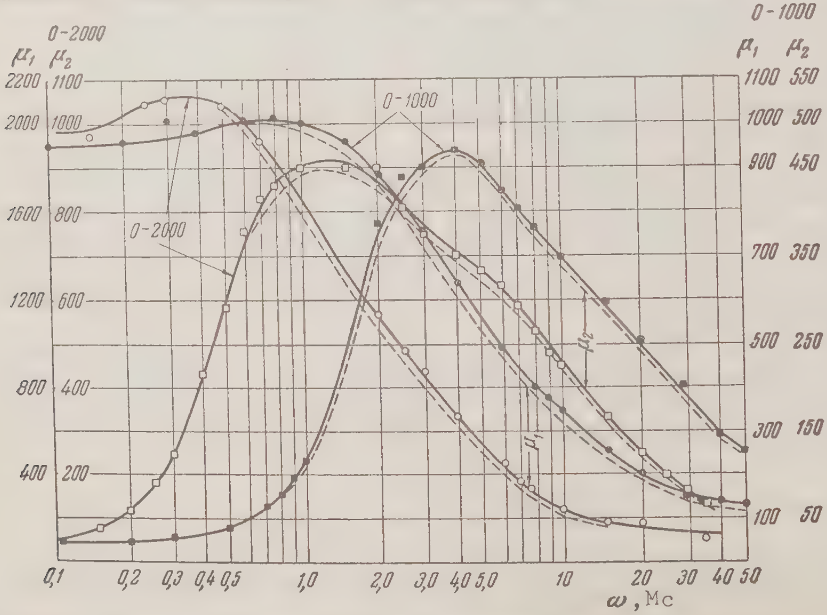

Fig.1. Characteristics of the permeability of the 0-2000 and 0-1000 ferrites. The dash lines indicate average values.

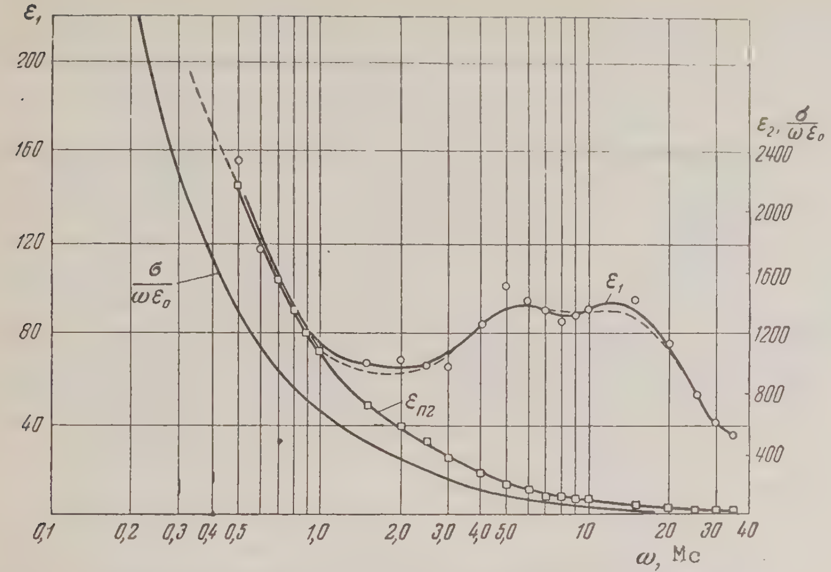

Fig.2. Characteristic of the dielectric constant of 0-2000 ferrite ($\sigma = 3.84 \cdot 10^{-4}$ ohm^{-1}cm^{-1}).

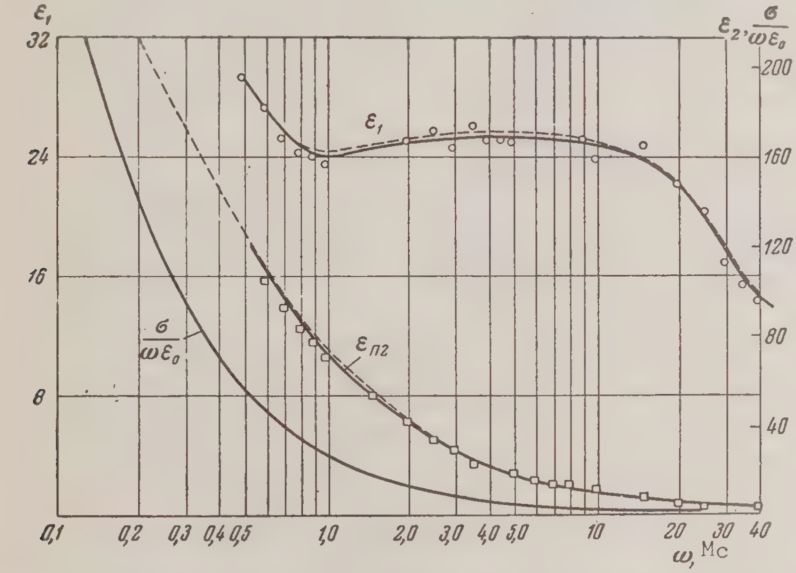

Fig.3. Characteristic of the dielectric constant of 0-1000 ferrite ($\sigma = 1.54 \cdot 10^{-5}$ ohm^{-1}cm^{-1}).

As a result of the experiments and subsequent calculations we obtained the frequency characteristics of the permeability and dielectric constant of the 0-2000 and 0-1000 ferrites shown in Figs. 1-3.

Our determinations of the values of μ and ϵ by the method of two measurements, which excludes the influence of the skin effect, showed that the skin effect in nickel-zinc ferrites in the frequency range in question is extremely small.

Our measurements also showed that volume resonance (dimensional effect) is also virtually absent; this effect can occur when the length of the electromagnetic waves is commensurate with the geometric dimensions of the specimen. In our case the wavelength in the material was much greater than the specimen dimensions. Thus at a frequency of 40 Mc the wavelengths in the two ferrites were λ_{0-2000} = 12.55 cm and λ_{0-1000} = 20 cm, whereas the maximum thickness of these specimens was 8 mm with a ring thickness of 11 mm.

That the skin effect and volume resonance were absent or negligible in our case is further substantiated by the fact that the curves obtained by recalculation of the experimental data by the method of two measurements differ very little (by not more than 3-5%) from the curves for the mean values of μ and ϵ (dash lines in Figs.1-3) computed directly on the basis of the same test data.

As may be seen from Fig.1 the curves characterizing the real part of the permeability show a slight rise at relatively low frequencies (0.1-1.5 Mc) and then fall off precipitately. This falling section corresponds to a strong increase in magnetic losses. The fact that the real part of the permeability becomes greater at a certain frequency than the permeability in a constant field indicates that in this frequency range oscillatory rather than relaxation effects predominate.

The mechanism of the dispersion of permeability can be explained by a resonance effect associated with movements of the spontaneous magnetization domain walls. The possibility of this effect was first suggested by Döring[2] who proved that a moving domain wall acquires an additional kinetic energy proportional to the square of the speed of displacement of the wall, which is equivalent to acquisition of an effective inert mass by the domain wall.

As noted above, in addition to the permeability, we investigated the dielectric properties of the 0-2000 and 0-1000 ferrites. The real component of the dielectric constant, which determines the capacitive properties of the ferrites proved to be negligibly small in the investigated range of frequencies (0.5-50 Mc). The imaginary part of ϵ, which determines the absorption in the material, as a rule was greater than the real part for both types of ferrites; this is equivalent to a low Q-factor ($Q = \epsilon_1/\epsilon_{\text{п}2}$, where $\epsilon_{\text{п}2} = \epsilon_2 \div \sigma/\omega\epsilon_0$) or a large tan δ ($\tan \delta = 1/Q$). Tan δ attains a value of up to 4 in the case of the 0-1000 ferrite and 16 in the case of the 0-2000 ferrite. Obviously at such ratios of the components of ϵ, the principal (dominant) characteristic of the material will be the imaginary component of the dielectric constant. It is due not only to the dielectric losses but also to the dc conductivity.

The conductivity σ was determined experimentally; this made it possible to evaluate its role in the variation of $\epsilon_{\text{п}2}$ as a function of the frequency (Figs.2 & 3). To determine σ, the resistance of the specimens was measured in a dc bridge using the same mounts as in the capacitance measurements.

As regards their electrical attributes the investigated ferrites are essentially semiconductors with pronounced capacitive properties.

"V.M.Molotov" Moscow Power Engineering Institute

References

1. K.M.Polivanov, Elektrichestvo (Electricity), No.3, 19 (1954).
2. W.Döring, ZS.Naturforsch., 3a, 373 (1948).

INVESTIGATION OF THE PARAMETERS OF FERRITES

- L.K.Mikhailovskii

A rigorous solution of the electrodynamic problem of determining the shape of the electromagnetic field in a finite (bounded) gyromagnetic medium with transverse magnetization* is predicated on the solution of the wave equation. No solution for the last having yet been found, it is impossible to obtain a rigorous solution of the above mentioned electrodynamic problem. Hence until now it has only been possible to assume that in the case of bounded gyromagnetic media, just as in the case of infinite media, there appears in the medium in the case of transverse magnetization an ordinary and an extraordinary wave.

In the present report we shall describe the results of theoretical and experimental investigations of the structure of the electromagnetic field in a waveguide filled with a medium characterized by a magnetic permeability tensor of the form[1]:

$$\mu_{ik} = \begin{vmatrix} \mu_x & 0 & 0 \\ 0 & \mu & jk \\ 0 & -jk & \mu \end{vmatrix}, \qquad (1)$$

where $\mu_x = \mu'_x - j\mu''_x$, $\mu = \mu' - j\mu''$ and $k = k' - jk''$.

As a result of these investigations we found that there can exist in a bounded gyromagnetic medium subject to transverse magnetization both waves dependent on and waves virtually independent of the magnetizing field (i.e., extraordinary and ordinary waves).

1. Theoretical considerations

Utilizing Maxwell's equations for the case of a gyromagnetic medium with transverse magnetization, we can establish for the general case (without imposing boundary conditions or any other limitations) the relation between the transverse and the longitudinal components of the electromagnetic field propagating in the Z direction with a constant magnetizing field directed along the X-axis.

It is possible to divide the deduced expressions into expressions characterizing waves with a weak dependence on the constant magnetic field H (waves having a propagation constant γ_1) and expressions characterizing waves with a strong dependence on H (waves having a propagation constant γ_2),**

$$h_x = \frac{1}{\omega^2\varepsilon\mu + \gamma_1^2}\left(j\omega\varepsilon\frac{\partial E_z}{\partial y} - \gamma_1\frac{\partial h_z}{\partial x}\right). \qquad (2)$$

The expressions for waves of the first type (ordinary) were obtained in the form:

$$E_y = \frac{1}{\omega^2\varepsilon\mu_x + \gamma_1^2}\left(-\gamma_1\frac{\partial E_z}{\partial y} + j\omega\mu_x\frac{\partial h_z}{\partial x}\right). \qquad (3)$$

Similarly for waves of the second type (extraordinary) we have:

$$h_y = -\frac{1}{\omega^2\varepsilon\mu + \gamma_2^2}\left(j\omega\varepsilon\frac{\partial E_z}{\partial x} + \gamma_2\frac{\partial h_z}{\partial y} + j\omega^2\varepsilon k h_z\right), \qquad (4)$$

$$E_x = -\frac{1}{\omega^2\varepsilon\mu + \gamma_2^2}\left(\gamma_2\frac{\partial E_z}{\partial x} + j\omega\mu\frac{\partial h_z}{\partial y} + \gamma_2\omega k h_z\right). \qquad (5)$$

---

*The lines of force of the magnetizing field are assumed to be straight lines perpendicular to the axis of the waveguide.

**The influence of H on the relationship between the transverse and longitudinal components of the field is manifested mainly through μ and k.

For isotropic media these expressions reduce to a form familiar in electrodynamics. As a particular case one can also obtain a relation for the fields of the ordinary and extraordinary waves in an infinite gyromagnetic medium. These last relations are identical with the expressions following from the formulas found by other authors (see, for example, Ref.2).

In the case of bounded gyromagnetic media, prior to solution of the wave equation, i.e., determination of γ_1 and γ_2, the deduced relationships (2)-(5) may be regarded as substantiation of the possibility of the existence of ordinary and extraordinary waves in such media.

2. Experimental part

Thus if ordinary and extraordinary waves do exist in bounded gyromagnetic media their presence must be manifested through the volume (dimensional) resonance effects.*

The purpose of our experiments was to obtain results that after appropriate processing would make it possible to separate in pure form the fraction of the loss of electromagnetic energy in the gyrotropic medium, due exclusively to the volume resonance effect.

Further theoretical processing of these results, as will be shown below, in turn makes it possible to deduce the dependence of the wavelength in the gyromagnetic medium on the magnetizing field.

To obtain the desired data ferrite discs of different thickness were inserted into a circular waveguide with a TM_{01} mode; the dependence of the electromagnetic energy loss through the disc on the strength of the external magnetizing field (directed perpendicularly to the waveguide axis) was determined for each of the discs.

Then having computed the internal field equivalent to the external one for each disc, we determined the dependence of the losses in the disc on its thickness for a number of different values of the internal field. In other words, we regarded the ferrite disc as an ordinary cylindrical cavity tuned successively to all the different types of waves present in this cavity (disc), the tuning being accomplished by varying the thickness of the disc (length of the resonance cavity); at the same time the external magnetizing field is always "adjusted" so that the internal field in the disc would remain constant and equal to a preselected value.

Thus the loss maxima arising incident to changes in the thickness of the disc due to volume resonances of the gyromagnetic waves must appear with a certain definite regularity; the separation between two similar maxima associated with the same type of wave must characterize the half-wavelength of the given wave in the disc.

The ferrite discs were prepared of type Oxifer-400 ferrite; their diameter was equal to the internal diameter of the circular waveguide (26.8 mm). The thickness of the discs was varied from 8.3 to 0.96 mm by successively grinding down the faces of the disc (precision ±0.005 mm). The disc was cemented into the waveguide by means of polystyrene lacquer so that its faces were perpendicular to the walls of the waveguide.

The electromagnetic energy losses in the disc were calculated to within ±0.1 db on the basis of measurements of the power passing through the disc and reflected from it.[4]

The measurements were carried out at a frequency of 9590 Mc maintained with an accuracy of ±(30-50) kc. Through special tests we established that the influence of the parasitic H_{11} wave on the experimental results was negligibly small.

---

*The volume or dimensional effect has been noted and observed by many investigators[3] and its existence may be considered firmly established.

3. Results and discussion

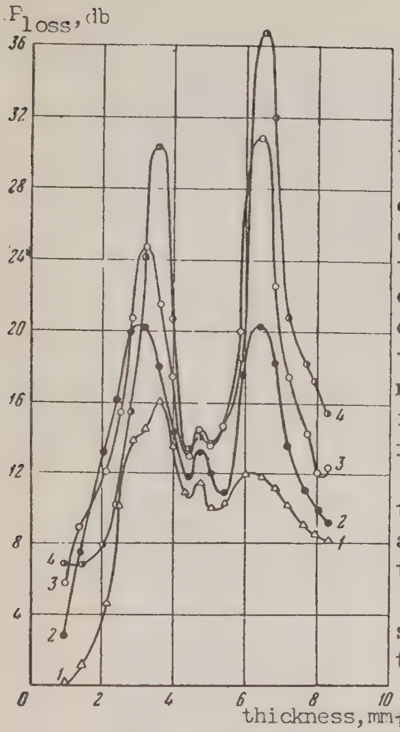

Fig.1. Variation of the losses in the ferrite disc with its thickness at different constant values of the internal field H_{in}: 1) 3250, 2) 3350, 3) 3390 and 4) 3420 oersted.

As was noted above, we determined experimentally the dependence of the loss of electromagnetic energy in the ferrite disc on the strength of the magnetizing field and on the thickness of the disc.

This experimental data was used to plot the family of curves shown in Figs.1 & 2 (for clarity not all the experimental curves are given in the figures), characterizing the variation of the loss in the disc with changes in its thickness for a number of values of the effective internal field. The relation between the external field and effective internal magnetizing field, needed for calculating the latter, was determined taking into account the demagnetizing factor, the anisotropy field and the damping.[5]

The curves of Fig.1 give the losses corresponding to internal fields weaker than the gyromagnetic resonance field; the curves of Fig.2 are for fields stronger than the resonance field.

A glance at the figures shows a physically understandable increase in the losses with increasing disc thickness at every value of the internal field.

As expected, however, there are superimposed on these "main" losses additional losses having a pronounced resonance character. Noting that the losses due to gyromagnetic resonance incident to changes of the internal field in this case can only change the slope of the mean level of the loss curves, we can readily separate the additional losses due exclusively to volume resonance. Examining the additional losses in Figs. 1 & 2, we readily note that the positions and magnitudes of part of the maxima and inflection points depend on the intensity of the internal field, while the other part of the maxima and inflection is virtually field independent. This can only be explained by assuming that the first type of abosrption is due to volume resonance at a wavelength, the value of which depends on the intensity of the internal field (extraordinary waves), while the second type of absorption occurs as the result of volume resonance at a wavelength which is virtually independent of the field (ordinary waves). This also explains why the intensity of volume resonance absorption in the first case falls off and in the second case remains practically unchanged as the internal field intensity departs from the value corresponding to the frequency of gyromagnetic resonance.

Inasmuch as the distance between similar internal field-dependent "main" loss maxima defines the half-wavelength of the fundamental type of gyromagnetic wave, we can readily plot the variation of this wavelength in the investigated range of internal fields. This has been done in Fig.3.

The variations of the length of the fundamental type of gyromagnetic wave relative to its mean value (see Fig.3) and of the total electromagnetic power loss in a ferrite disc 0.96 mm thick with the intensity of the internal magnetic field are plotted in Fig.4.

Conclusions

1. We have substantiated that there can exist in a bounded (finite) gyromagnetic medium with transverse magnetization waves that are dependent on and waves that are virtually independent of the intensity of the external magnetiz-

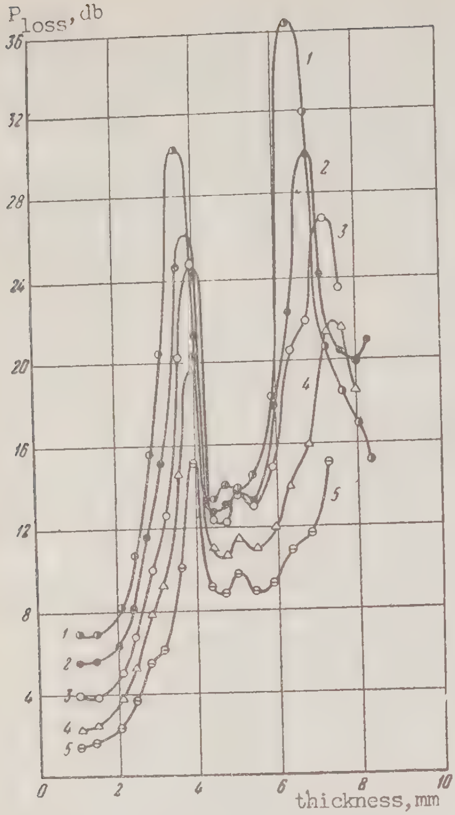

Fig. 2. Same as Fig.1 but in stronger fields: 1) 3420, 2) 3440, 3) 3460, 4) 3500 and 5) 3550 oersted.

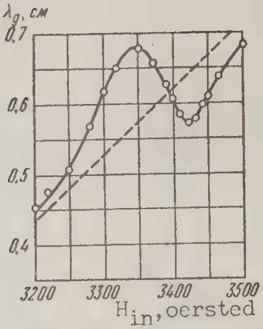

Fig. 3. Variation of the length of the gyromagnetic wave of the fundamental type in the investigated range of internal fields.

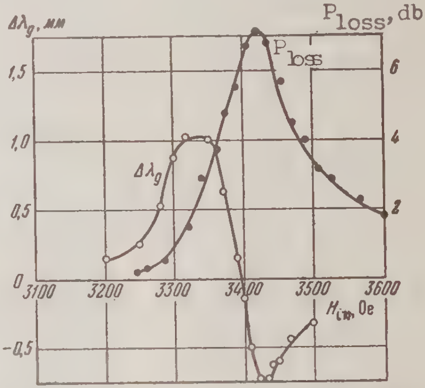

Fig.4. Relative change in the length of the gyromagnetic wave and the total power loss in a ferrite disc 0.96 mm thick in the resonance region.

ing field.

2. We have proposed a method for practical utilization of the volume (dimensional) resonance effect.

We desire to thank K.M.Polivanov for his aid in carrying out the investigation.

"V.M.Molotov" Moscow Power Engineering Institute

References

1. D.Polder, Phil. Mag., 40, 99 (1949).

2. A.L.Mikaelian & A.A.Pistol'kors, Radiotekhnika, 3, 14 (1955); F.K.Du Pré, Philips Res.Rep., 10, 1 (1955).

3. K.M.Polivanov, Trudy MEI (Transactions of the Moscow Energetics Institute) No.14, p.166 (1953); W.A.Yager, J.K.Galt, F.R.Merrit & E.A.Wood, Phys.Rev., 80, 744 (1950); F.G.Brockman, P.H.Dowling & W.G.Steneck, Phys.Rev., 77, 85 (1950); L.Goldstein, M.Gilden & J.Etter, Conv.Rec.I.R.E., Part 10. Microwaves, 58,(1953); J.Rowen, Bell Syst. Techn. Journ., 32, 6, 1333 (1953); C.Hogan, Rev. Mod. Phys., 25, 1,253 (1953); G.T.Rado, R.W.Wright & W.H.Emerson, Phys. Rev., 80, 273 (1950).

4. "Izmereniia na sverkhvysokikh chastotakh" (Measurements at super-high frequencies). Trans. from English, V.B.Shteinshleiger, editor. M.1952.

5. C.Kittel, Phys.Rev., 73, 155 (1948); C.Hogan, Bell Syst. Techn. Journ., 31, 1, 1 (1952); J.R.Macdonald, Proc. Phys. Soc., 64, 968 (1951); J.B.Birks, Phys. Rev., 74, 988 (1948).

Translator's note: A number of the above references are cited as appearing in Russian translation in "Ferromagnetic Resonance", a collection of articles edited by S.V.Vonsovskii.

INFLUENCE OF INHOMOGENEOUS DEMAGNETIZING FIELDS ON FERROMAGNETIC RESONANCE

- A.I.Pil'shchikov

Study of ferromagnetic resonance, which was discovered by Arkad'ev[1,2] in 1911-1913, is of great interest now both from the viewpoint of practical application of ferromagnetic materials in the field of high-frequency radio engineering and for the investigation of physical effects in ferromagnets. Experimental and theoretical investigations carried out in recent years have made it possible to establish the fundamental regularities of ferromagnetic resonance in weak high-frequency magnetic fields.[3-5]

One of the most important problems in studying ferromagnetic resonance is the question of the width of the resonance absorption line, which is determined by the transverse relaxation time. A number of investigators have suggested a number of different theoretical interpretations of broadening and attempted to compute the absorption line width[5]; however, many of the calculations yield either an incorrect temperature dependence or a much smaller line width than is indicated by experimental data. It must be noted that all calculations of the absorption line width have been carried out for ideal (hysteresis-free, unstrained and homogeneous) single crystals. On the other hand, most of the experimental data have been obtained for polycrystalline specimens for which the absorption line width is determined to an appreciable extent by the nonuniform conditions of ferromagnetic resonance in different parts of the specimen; this nonuniformity is due to different orientations of the crystallographic axes relative to the external constant magnetic field, to inhomogeneity of the internal demagnetizing fields, to the presence of varying elastic stresses, etc.

One of the more important causes of line broadening is the presence of inhomogeneous demagnetizing fields in the specimen. The demagnetizing field is uniform only for a homogeneously magnetized ellipsoid, while the specimens used in experiments with metallic ferromagnets are usually in the form of plates, discs or more complex geometric shapes, which obviously leads to the appearance of non-uniform demagnetizing fields.

In the present work we investigated the influence of nonuniform demagnetizing fields in the specimen on the shape of the absorption and dispersion curves and on the values of the gyromagnetic ratio (γ), the splitting factor (g) and the relaxation time (τ) which are determined from experimental data.

The influence of nonuniform demagnetizing fields on ferromagnetic resonance was investigated using metallic ferromagnetic materials. The specimens in the form of very thin-walled cylinders were mounted on a special polystyrene insert inside the cavity of a cylindrical resonator in which an E_{010} mode was excited. The cylindrical cavity was mounted between the pole pieces of an electromagnet so that the constant field was perpendicular to the high-frequency field. The necessary values of the demagnetizing factor for the specimens were obtained by appropriate selection of the ratio between the thickness of the walls $\underline{a}$ and the height (length) of the specimen $\underline{c}$ (Fig.1).

The principal measured quantities were the resonance frequency and the Q-factor of the cavity with the specimen for different values of the constant magnetic field. The depth of penetration of the field into the ferromagnet was appreciably smaller than the thickness of the specimen, consequently the Q-factor and the correction to the resonance frequency due to the ferromagnet were determined from the relations[6]:

$$\frac{1}{Q} = \sqrt{\mu_{\text{к}}}\,\frac{1}{Q_\infty}, \tag{1}$$

and

$$\frac{2\Delta f}{f} = \pm\sqrt{\mu_{\text{п}}}\,\frac{1}{Q_\infty}^{*}, \tag{2}$$

---

*In Eq.(2) the + sign holds in the region where $\mu < 0$, while the - sign holds in the region where $\mu > 0$.

where Q is the quality factor of the hollow resonator determined by the losses in the ferromagnet; Δf is the correction to the resonance frequency of the resonator due to the ferromagnet (f is the resonance frequency of the hollow resonator); $\mu_к$ is the effective magnetic permeability from the damping factor; $\mu_п$ is the effective magnetic permeability from the index of refraction.

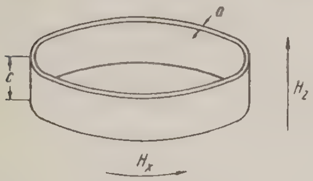

Fig. 1. Orientation of annular band specimen relative to the constant field H_z and the high-frequency magnetic field H_x.

If the complex magnetic permeability of the material $\mu' = \mu - jp'$, then[7]:

$$\mu_к = \sqrt{\mu^2 + \rho'^2} + \rho', \tag{3}$$

$$\mu_п = \sqrt{\mu^2 + \rho'^2} - \rho', \tag{4}$$

and

$$\frac{1}{Q_\infty} = d_0 \frac{\int\limits_S H^2 dS}{\int\limits_V \mu_1 H^2 dV}, \tag{4a}$$

where d_0 is the depth of penetration of the field into the ferromagnet with $\mu' = 1$, S is the surface area of the ferromagnet, V is the volume of the cavity, μ_1 is the magnetic permeability of the medium filling the resonator cavity and H is the amplitude in the cavity of the high-frequency magnetic field.

As follows from (1) and (2) the dependences of Q and the resonance frequency of the cavity on the constant magnetic field enable us to judge of the behavior of $\mu_к$ and $\mu_п$ in the region of ferromagnetic resonance. The measurements were carried out in the ten centimeter wavelength range on the set-up diagramed in Fig.2.

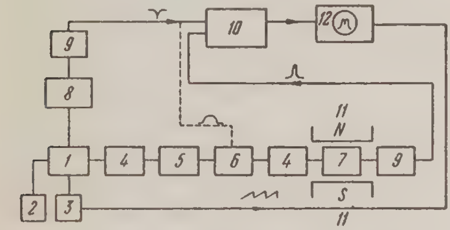

Fig.2. Block diagram of the experimental set-up: 1) klystron, 2) klystron power supply, 3) modulation and sweep unit, 4) matcher, 5) attenuator, 6) monitoring detector, 7) measurement cavity, 8) wavemeter, 9) detector head, 10) summing amplifier, 11) pole pieces of electromagnet, 12) oscilloscope.

For determining the parameters of the hollow resonator we utilized the oscillographic method based on comparing the resonance curves of the measurement resonator with those of a high-Q cavity wavemeter[8]. The source of frequency modulated oscillations was a klystron to the reflector plate of which we applied a dc and a sawtooth voltage. The high frequency oscillations were fed through one channel to the input of the measurement cavity and through another to the input of the wavemeter. Detectors having square-law characteristics were installed at the outputs of the measurement cavity and the wavemeter. With a pure resistance load on the detector the voltages had the shape of resonance power curves. The signals from the outputs of the measurement cavity and the wavemeter were applied in opposite phase to the separate inputs of the summing amplifier, in which they were added and amplified to the value necessary for observation on the oscilloscope. The sawtooth modulation voltage also served to activate the oscilloscope sweep; this insured complete synchronization of the signal and sweep. Thus on the screen of the oscilloscope we observed the resonance curve of the measurement cavity, from which the resonance curve of the wavemeter was subtracted. The changes in the appearance of the resonance curves of the measurement cavity with a ferromagnetic specimen with changes in the intensity of the constant magnetic field are shown in Fig.3. These oscillograms were recorded under the following conditions: at the maximum value of the constant field the resonance frequencies of the measurement cavity and the wavemeter were matched by appropriate tuning of the wavemeter. After this only the intensity of the field was changed, while the amplification and the adjustment of the wavemeter remained the same; consequently, the resonance curve of the wavemeter in all the oscillograms corresponds to the resonance frequency of the measurement cavity at the maximum magnetic field intensity. Changes in the height and relative width of the resonance curves enable us to judge of the changes in the Q-factor of the measurement cavity, while displacement of the peak relative to the peak of the wavemeter resonance curve characterizes the change in the resonance frequency of the cavity resonator. At the upper left in Fig.3 we have the oscillogram corresponding to $H = H_{max}$; the succeeding oscillograms (from left to right) pertain to gradually decreasing values of the constant field. From the series of oscillograms one can readily follow the variation of Q and the resonance frequency with the intensity of the magnetic field.

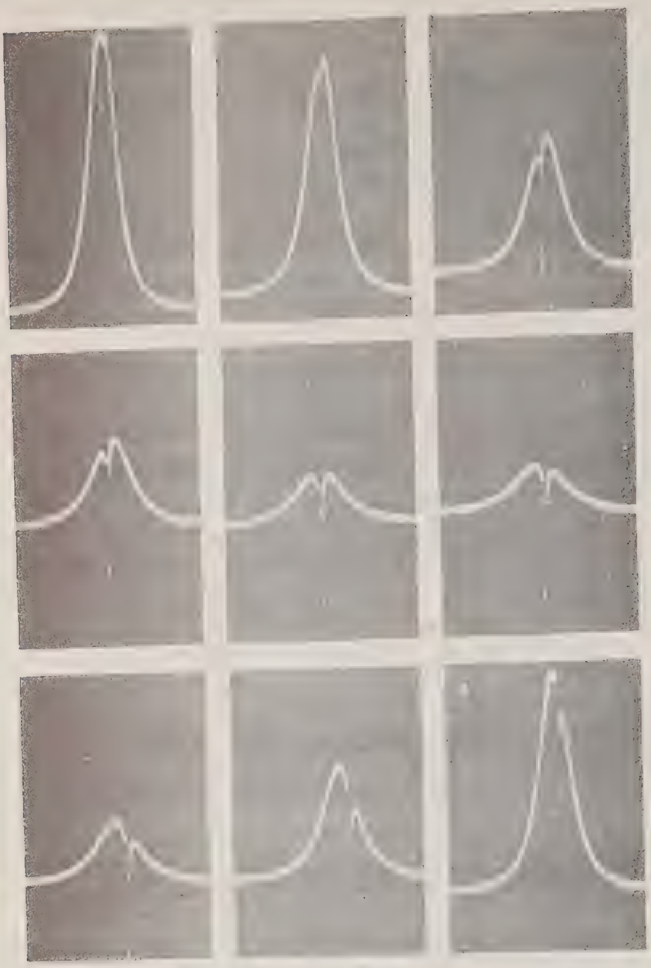

Fig.3. Oscillograms of resonance curves of the measurement cavity plus specimen at different values of the external constant magnetic field from H_{max} (upper left) down to H_{min} (lower right).

The procedure where measurement of the resonance frequency of the measurement cavity was concerned amounted to tuning the voltmeter so that its resonance curve would appear at the peak of the resonance curve of the cavity, i.e., so that the left and right peaks of the resultant curve would have the same height.

To determine the Q of the measurement resonator we measured the width of the resonance curve at the level of half the maximum power. In order to obviate errors in measurement due to amplitude modulation, the frequencies at the points corresponding to half-power were measured by the "submersion" method described by Sproull & Linder[8].

Satisfactory accuracy of measurement is assured provided the following conditions are satisfied:

1) the channels carrying the high-frequency power to the resonator and wavemeter must pass the entire excitation range (i.e., the passband of the channels must be wider than the tuning range of the klystron);

2) the Q-factor of the wavemeter must not change incident to retuning of the wavemeter within the frequency range of the width of the cavity resonance curve;

3) the detectors at the outputs of the measurement cavity and wavemeter must have rigorously square-law characteristics;

4) the Q of the wavemeter must be appreciably higher than that of the measurement cavity.

The use of [illegible] lines for coupling the units and appropriate absorbing attenuators and [illegible] ensured the requisite wide passband. One of the methods of checking the effective passband of the channels was comparison of the excitation regions obtained from a control detector and from the detector coupled into the klystron circuit. The invariance of the wavemeter Q during retuning was checked by comparing the excitation region with the resonance curve of the wavemeter. To this end the excitation signal from the detector in the klystron circuit was applied to one of the amplifier channels instead of the resonance signal from the cavity. The height of the signal from the wavemeter was adjusted by regulating the amplification so that with coincidence of the signal with the maximum of the excitation range its peak would just touch the basal line of the region. During retuning of the wavemeter the peak of the signal always just touched the basal line and departed only slightly from this line towards the edges of the region. There was no detectable deviation of the wavemeter signal peak from the basal line in the part of the region where the resonance curve of the measurement cavity was located during the measurements. This verification procedure not only showed that the Q of the wavemeter remained constant but also proved that the wavemeter channel had a sufficiently wide passband.

The square-law characteristic of the measurement cavity detector and the reliability of the Q-factor measurements were verified by determining the Q of the measurement cavity on the basis of the width of the resonance curve at different heights. This check showed that the average scatter of the Q values as measured at different heights lay within the limits of the measurement error in determining the Q-factor with reference to the half-power (3-4%) and was entirely independent of the height. This verification justified our assumption that our Q measurement was accurate within 3-4%. During the measurements the resonance curve of the cavity was set in the region of the maximum of the excitation range, which insured correct determination of the resonance frequency drift. Each of the two channels of the summing amplifier had one stage of preamplification and a cathode follower. The amplification in the channels was controlled separately at the input to the cathode followers. From the cathode follower the signal was fed to the two-tube summing stage and then to three stages of amplification. The signal from the symmetrical output of the amplifier was applied to the vertical deflection plates of the oscilloscope. The input resistance of the amplifier channels was 700 ohm, the maximum amplification was $5 \cdot 10^5$; the frequency characteristic was verified by undistorted amplification of square pulses (pulse repetition rate - 50 kc and 200 c per sec; duty factor 1/2). Careful measurements of the characteristics showed that the amplification factor is constant in the interval from 150 c to 400 kc and then falls off to 50% at 700 kc. The passband of the amplifier was checked with reference to the wavemeter signal (the shortest of all the pulses used). Through measurements of the modulation frequency it was established that the height of the wavemeter signal remains constant up to a frequency of the order of 1000 c and that it begins to decrease noticeably only at 1200 c. The measurements were made at modulation frequency of 500-900 cps or well within the range insuring satisfactory accuracy.

By way of wavemeter we utilized an echo box type cavity resonator with a Q-factor not less than 10^4 (the maximum Q of the measurement cavity was 2500). The constant magnetic field was produced by an electromagnet with 140 mm diameter pole pieces. The field throughout the volume of the specimen was uniform to within one oersted in the entire range of field values employed (up to 2300 oersted). All measurements were made starting with the demagnetized state of the electromagnet. The measurements were made on two permalloys: NKhS-80 (НХС-80) "chrome" (80% Ni) and 50-N (50-II) (50% Ni) permalloy. The magnetic characteristics of the permalloys (after appropriate annealing) are listed in Table 1.

The specimens, initially in the form of bands, were bent to a cylinder on a special mandrel of Armco iron and fastened by means of strips or wires of the same permalloy. The mandrel was of the same diameter as the polystyrene insert on which the specimens were subsequently inserted into the cavity of the hollow resonator. The specimens were annealed under vacuum while still on the mandrel. After annealing the retaining wire and upper layer of permalloy were carefully removed and the specimen was shifted onto the polystyrene insert and fastened on it by means of varnished cambric (Fig.4). This method of preparation made it possible to give the specimens the requisite shape prior to annealing and thus avoid deformation incident to transferring the specimens onto the insert.

Table 1

Magnetic characteristics of the investigated permalloys

Type of permalloy	Thickness of band, mm	Initial permeability μ_a, gauss/oersted	Max. permeability μ_{max}, gauss/oersted	Coercive force H_c, oersted	$4\pi J_s$*, gauss	Resistivity, ohm·cm·m^{-1}
NKxS-80	0.05	20000	100000	0.03	6850	0.61
NKhS-80	0.15	24000	125000	0.02	6850	0.62
50-H	0.12	3500	28000	0.22	15000	0.45

*J_s = saturation magnetization

The demagnetizing factor was calculated according to the approximate formula for a strongly elongated flattened ellipsoid with $a \ll c$ (Fig.1):

$$N_z = 4\pi \frac{a}{a+c}. \qquad (5)$$

This expression is a close approximation for thin plates and its use for our hollow cylinders is justified by the fact that the radius of the cylinders was appreciably greater than the wall thickness. Measurements of the resonance field for NKhS-80 permalloy cylinders 50 and 60 mm in diameter with 0.15 mm thick walls yielded the same value for the field. This shows that the demagnetizing factor for the selected cylinder size (60 mm diameter) is independent of the radius of curvature.

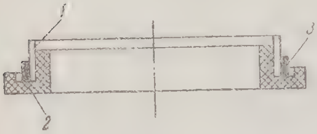

Fig.4. Polystyrene insert with specimen: 1) specimen, 2) polystyrene insert, 3) varnished cambric.

The dimensions of the specimens and the values of the demagnetizing factor are listed in Table 2.

Table 2

Values of the demagnetizing factor for the permalloy specimens

Type of permalloy	No. of specimen	Dimensions		N_z
		a, MM	c, MM	
HXC-80	1	0,05	10	0,063
HXC-80	2	0,15	10	0,188
HXC-80	3	0,15	5	0,377
50-H	—	0,12	10	0,15

The resonator, the metallic parts of the high frequency channel fittings and the detector head were made of brass. Before making measurements with specimens, we undertook a preliminary check of the influence of the magnetic field on the parameters of the hollow resonator with the polystyrene insert in place. These measurements showed that within the range of the fields employed the resonance frequency and the Q of the resonator without the specimen are independent of the constant magnetic field. These measurements also established that the field had no noticeable effect on the crystal detector located near the electromagnet pole pieces.

As the result of measurements on three specimens of NKhS-80 permalloy we obtained the dependences of the resonance line width and resonance frequency of the hollow resonator with specimen on the constant field intensity. The experimental dependences of the deviation in resonance frequency (Δf) and the change in the half width of the resonance line $(\delta f-\delta f_o)/2$ (referred to their respective values at the maximum field) on the strength of the external magnetic field are shown in Fig.5. The dependences of these qualities on the effective field $H - N_z J_s$ are shown in Fig.6.

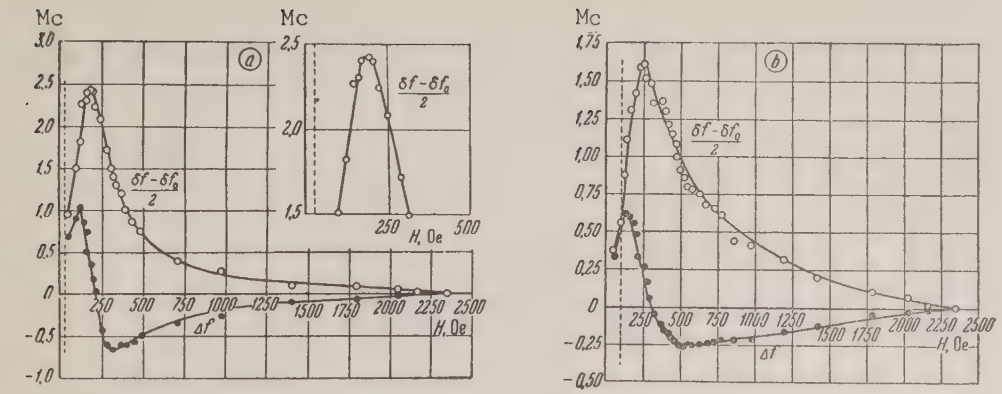

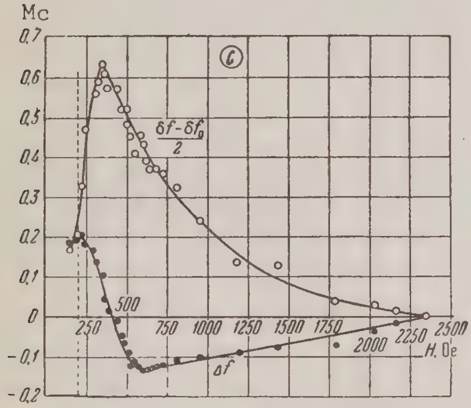

Fig.5. Experimental dependences of the damping and deviation of the resonance frequency of the measurement resonator on the external magnetic field for chrome permalloy (NKhS-80): a) specimen No.1, $N_z = 0.063$, $g = 2.16$, $1/T = 5.0\cdot10^9$ sec^{-1}; b) specimen No.2, $N_z = 0.188$, $g = 2.10$, $1/T = 8.5\cdot10^9$ sec^{-1}; c) specimen No.3, $N_z = 0.377$, $g = 2.12$, $1/T = 9\cdot10^9$ sec^{-1}.

The ferromagnetic resonance parameters (γ, g, and T) were evaluated with reference to the values of the constant magnetic field corresponding to the maximum and minimum effective permeabilities[9], i.e., H_o - the field corresponding to the maximum for μ_H (the peak in the resonator attenuation curve) and H_2 - the field corresponding to the second maximum of μ_π (i.e., the minimum in the resonance frequency deviation curve).

In calculating the ferromagnetic resonance parameters we also utilized the values of the demagnetizing factor computed according to Eq.(5), the values of $4\pi J_s$ listed in Table 1 and the values of the resonance frequency ω of the measurement resonator. A method of computing the resonator parameters from the values of the constant magnetic field corresponding to the extremum values of the magnetic permeability was developed in Ref.9. This method makes it possible to carry out the calculations in the case when suppression of ferromagnetic resonance is not attained experimentally. The method does not require calculating Q (see Eq.(4a)) and consequently it can be applied in the case of a complex shape of the specimen when the exact structure of the high-frequency field in the cavity of the measurement resonator is not known.

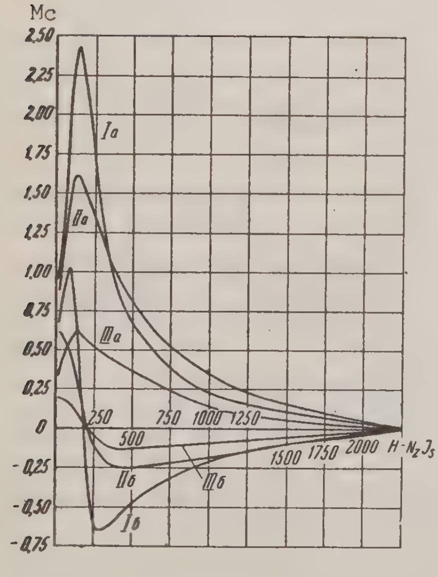

Fig.6. Experimental dependences of the damping (curves a) and deviation of resonance frequency (curves b) on the effective field ($H - N_zJ_s$) for the three specimens of chrome permalloy: I) specimen No.1, $N_z = 0.063$; II) specimen No.2, $N_z = 0.188$, III) specimen No.3, $N_z = 0.377$.

The gyromagnetic ratio and the relaxation frequency were calculated by means of the equation from Ref.9:

$$\gamma^2 = -\frac{q}{2p^2} + \frac{1}{p}\sqrt{\frac{q^2}{4p^2} + \omega^2}, \tag{6}$$

$$\frac{1}{T} = \gamma^2 p, \tag{7}$$

where

$$p = \frac{(H_2 - H_0)\,[H_2 + H_0 + (N_x + N_y - 2N_z)\,J_s]}{2\sqrt{3}\,\omega}, \tag{8}$$

$$q = [H_0 + (N_x - N_z)\,J_s]\,[H_0 + (N_y - N_z)\,J_s], \tag{9}$$

N_x, N_y and N_z are the demagnetizing factors along the respective axes (the z-axis is in the direction of the constant magnetic field; the x-axis in the direction of the high frequency field), and $\omega = 2\pi f$ is the angular frequency of the r-f field.

Usually the relation

$$\gamma = \frac{\omega}{\sqrt{q}}. \tag{6a}$$

is used for evaluating γ. However, this relation can be used only when $\omega^2 \gg 1/T^2$. In the case of our specimens this condition was not fulfilled and in evaluating γ it is necessary to take into account the term $1/T^2$ in the expression for the resonance absorption frequency[6]:

$$\omega^2 = \gamma^2 q + 1/T^2. \tag{10}$$

Consequently, in our calculations we used Eq.(6) taking into account the $1/T^2$ term in (10).

The Landé splitting factor g was calculated from $\gamma = 8.79 \cdot 10^6$ g. Eq.(7) for calculating the relaxation frequency is an approximate one and hence, in accord with what has been said in Ref.9, the following correction was introduced

$$\frac{1}{T} = \frac{1}{T'}\left(1 - 4{,}25\,\frac{\omega}{\omega_{1k}^2 T'}\right), \tag{11}$$

where $1/T'$ is the value of the relaxation frequency calculated according to Eq.(7),

$$\omega_{1k}^2 = \omega_1^2|_{H=H_0},$$

and

$$\omega_1^2 = 4\pi\gamma^2 J_s\,[H + (N_y - N_z)\,J_s]. \tag{12}$$

The experimental data and the results of our calculations are shown in Table 3. The last column lists the values of the splitting factor g_1 calculated according to Eq.(6a).

An experimental curve analogous to that of Fig.5 was also obtained for 50-N permalloy are also listed in Table 3.

Before turning to a comparison of the experimental results with theory, we would like to call attention to some of the distinctive characteristics of the recorded curves.

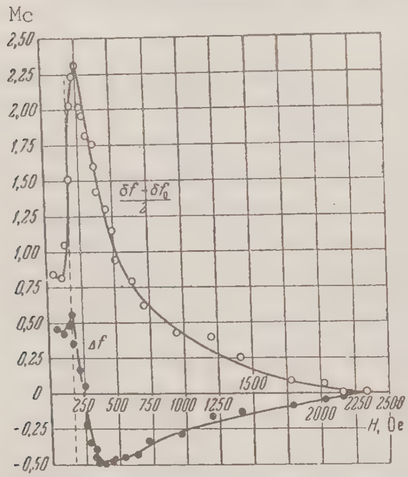

Fig.7. Same as Fig.5 but for 50-N permalloy: $N_z = 0.15$, $g = 2.04$, $1/T = 10.3 \cdot 10^9$ sec^{-1}.

Table 3

Experimental data for calculating the ferromagnetic resonance parameters and the values of these parameters for specimens of NKhS-80 and 50-N permalloys

Specimen No.		N_z	N_zJ_s, Gs	$\omega\cdot10^{-10}$, rad/sec	H_1, Oe	H_0, Oe	H_2, Oe	$H_0-N_zJ_s$, Oe	H_0-H_1, Oe	H_2-H_0, Oe	$\gamma\cdot10^{-6}$, Hz Oe^{-1}	g	$1/T\cdot10^{-9}$, sec^{-1}	g_1
HXC-80	1	0,063	35	2,04	125	190	325	155	65	135	19	2,16	5,0	2,23
	2	0,188	105	2,04	125	245	505	140	120	260	18,4	2,10	8,5	2,35
	3	0,377	205	2,05	220	340	610	135	120	270	18,6	2,12	9,0	2,40
50-H		0,15	180	2,04	170	245	400	65	75	155	17,7	2,04	10,3	2,35

Relatively sharp absorption peaks, well defined by the experimental points, were obtained for all the specimens. The values of the effective field $(H_0 - N_ZJ_S)$ change very little with changes in the demagnetizing factor. There is a noticeable broadening of the resonance absorption curves with increasing demagnetizing factor N_Z (Fig.6). Specimens Nos.1 & 2 differed only as regards thickness of the walls; consequently, the effective surface of the specimens was the same, and hence the attenuation curves directly characterize the ratio of the changes in μ_H for these specimens. From Fig.6, in particular, it will be seen that the specimen with the smallest change in demagnetizing factor is characterized by an appreciably greater change in μ_H.

The shape of the curves giving the dependence of the resonance frequency deviation (Δf) of the cavity resonator with values of the demagnetizing factor changes much more. It will be seen from Fig.6 and Table 3 that in going from a specimen with a relatively small N_z to specimens with a large N_z the minimum in the resonance frequency deviation curve is markedly displaced to the side of stronger magnetic fields and $H_2 - H_0$ increases. With increasing demagnetizing factor the curves broaden, while the range over which the resonance frequency of the resonator changes becomes narrower.

The noted broadening of the attenuation and frequency deviation curves with increasing N_Z and the displacement of the frequency deviation maximum to the side of stronger effective fields are responsible for the increase in the relaxation frequency obtained in Table 3. All the experimental resonance frequency deviation curves exhibit a maximum in weak fields (the first μ_n maximum). The values of the constant field H_1 corresponding to these maxima are listed in Table 3. It will be seen from the experimental curves and data of Table 3 that the maximum of the resonance frequency deviation curve lies appreciably closer to the absorption maximum than the minimum in this curve; also the maximum is appreciably sharper than the minimum. However, it must be borne in mind that the maxima of the resonance frequency deviation curves lie in the range of fields where magnetization of the specimen to saturation cannot be assured; this is clearly evident from the position of the maxima relative to the vertical dash-lines plotted for $H = N_ZJ_S$ (see Figs.5 & 7). In the field region of the resonance frequency deviation minimum the ferromagnetic specimen is more uniformly magnetized, hence in all the calculations we used the field value corresponding to this minimum.

In order to clarify the nature of the influence of inhomogeneous demagnetizing fields on the shape of the experimental curves we carried out a comparison of the theoretical and experimental curves. The theoretical values of μ and ρ' were calculated according to the formulas[6]:

$$\mu = \frac{\omega_1^2(\omega_0^2 - \omega^2)}{(\omega_0^2 - \omega^2)^2 + \frac{4\omega^2}{T^2}} + 1 \qquad (13)$$

and

$$\rho' = \frac{\omega_1^2 \frac{2\omega}{T}}{(\omega_0^2 - \omega^2)^2 + \frac{4\omega^2}{T^2}}, \tag{14}$$

while $\mu_{\text{к}}$ and $\mu_{\text{п}}$ were computed according to Eqs.(3) & (4). In computing μ and ρ' we used the experimental values for γ and 1/T listed in Table 3.

For finding the experimental values of $\mu_{\text{к}}$ and $\mu_{\text{п}}$, we used the following relationships deriving from Eqs.(1) & (2):

$$\sqrt{\mu_{\text{к}}} = A(\delta f - \delta f_0) + \sqrt{\mu_{\text{к}_0}}, \tag{15}$$

$$\sqrt{\mu_{\text{п}}}\begin{cases} = B\Delta f - \sqrt{\mu_{\text{п}_0}} & \text{for } H < H_0, \quad (16)\\ = -B\Delta f + \sqrt{\mu_{\text{п}_0}} & \text{for } H > H_0, \quad (17)\end{cases}$$

where

$$A = \frac{\sqrt{\mu_{\text{к}max}} - \sqrt{\mu_{\text{п}_0}}}{\delta f_{max} - \delta f_0},$$

$$B = \frac{\sqrt{\mu_{\text{п}_0}} - \sqrt{\mu_{\text{п}max}}}{\Delta f_{max}};$$

here $\mu_{\text{к}_0}$ and $\mu_{\text{п}_0}$ are the theoretical values of $\mu_{\text{к}}$ and $\mu_{\text{п}}$ at the maximum magnetic field ($H = H_{max}$), $\mu_{\text{к}max}$ is the maximum theoretical value of $\mu_{\text{к}}$, $\mu_{\text{п}max}$ is the theoretical value of $\mu_{\text{п}}$ for the second maximum ($H = H_2$), δf is the width of the resonance curve of the measurement resonator, Δf is the deviation of the resonance frequency of the measurement resonator relative to the resonance frequency at $H = H_{max}$; $\delta f_0 = \delta f|_{H=H_{max}}$; $\delta f_{max} = \delta f|_{H=H_0}$; $\Delta f_{max} = \Delta f_{H=H_2}$. The theoretical curves for $\sqrt{\mu_{\text{к}}}$ and $\sqrt{\mu_{\text{п}}}$ as functions of the constant magnetic field for the investigated specimens are shown in Fig. 8. The points in the figure are the experimental values for these quantities.

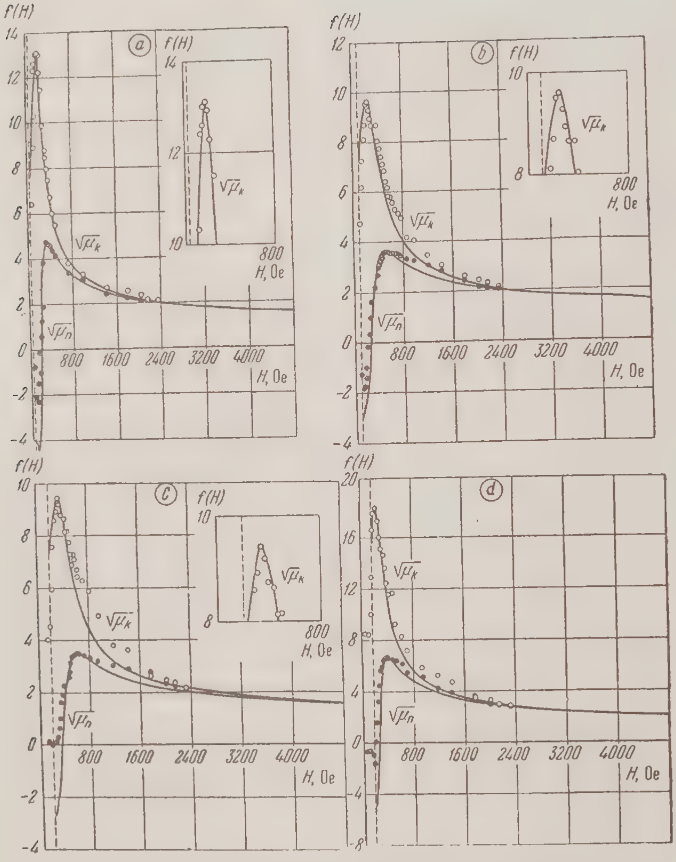

Fig.8. Comparison of the theoretical curves characterizing the dependence of $\sqrt{\mu_{\text{к}}}$ and $\sqrt{\mu_{\text{п}}}$ on the constant magnetic field with the experimental data (points) for the chrome NKhS-80 permalloy (a - specimen No.1, b - specimen No.2, c - specimen No.3) and for the 50-N permalloy (d). Values of N_z, g & 1/T - same as for specimens of Figs.5 & 6.

For fields $H < H_0$ the curves for $\sqrt{\mu_{\text{п}}}$ are plotted in the negative region, since it proved impossible to determine experimentally the points corresponding to $\mu_{\text{п}} = 0$ with sufficient accuracy. The influence of demagnetizing fields on the resonance absorption and dispersion curves can be deduced from the results obtained for the specimens of NKhS-80 permalloy. For specimen No.1 with the lowest demagnetizing factor (Fig.8,a), the experimental points fit the theoretical curves over the entire range of constant magnetic fields; the only noticeable deviation is for $\sqrt{\mu_\pi}$ in the region of the minimum in this curve. In the case of specimens Nos.2 & 3 characterized by large values of demagnetizing factor (Fig.8, b & c), there is a regular deviation of the experimental points from the theoretical curves: for $\sqrt{\mu_K}$ the experimental points lie below the theoretical curve in the region of field $H < H_0$, while in the region where $H > H_0$ the points lie above the curve. For specimen No.1 the deviation of the experimental points from the theoretical curve is insignificant, while for specimens Nos.2 & 3 these deviations are appreciable. As regards the $\sqrt{\mu_\pi}$ curves there is also a noticeable broadening of the experimental curves as compared with the theoretical ones for $H > H_2$ and an appreciably smaller deviation for fields $H_0 < H < H_2$. In the vicinity of the minimum in the $\sqrt{\mu_\pi}$ curves the deviation of the experimental points from the theoretical curves increases rapidly with increasing demagnetizing factor, so that at a high value of the demagnetizing factor there is an appreciable disagreement as regards both position and magnitude of the minimum of μ_π.

It must be noted that the broadening of the experimental curves for $\sqrt{\mu_K}$ (for $H > H_0$) and $\sqrt{\mu_\pi}$ is appreciably greater than the broadening of the theoretical curves attributable to the growth in relaxation frequency. It will be evident from a comparison of curves a, b & c in Fig.8 that the maximum value of the effective magnetic permeability decreases with increasing demagnetizing factor.

Comparison of the theoretical curves and experimental points for the 50-N permalloy, given in Fig.8,d, substantiates the above noted influence of demagnetizing fields on the experimental absorption and dispersion curves.

The change in the shape of the experimental absorption and dispersion curves and the increase in the relaxation frequencies deduced from the experimental data can be explained in the light of an examination of the distribution of the demagnetizing fields in the specimens.

The demagnetizing fields in the specimen, obtaining in the present investigation, were not homogeneous; actually the demagnetizing factor N_z as computed according to Eq.(5) determined the demagnetizing field for the middle part of the specimen (mid-point along c in Fig.1). The sections of the specimen lying closer to the ends were situated in stronger demagnetizing fields. In consequence of this demagnetizing field distribution conditions for resonance in different parts of the specimen occurred at different values of the external magnetic field. For the central section, which comprised the greater portion of the specimen, resonance conditions set in at weaker fields than for the end sections. This explains why the experimental resonance absorption and dispersion curves recorded under our conditions differ appreciably from similar curves recorded under uniform resonance conditions throughout the entire specimen. There are two basic reasons for the distortion of the experimental curves for specimens with an inhomogeneous demagnetizing field. The experimental resonance absorption and dispersion curves are essentially the result of superposition of the corresponding curves for the individual sections of the specimen with different resonance conditions. The broadening of the experimental curves is also due to the interaction of these end and middle sections with each other. Such interaction of the different sections in a ferromagnet must be appreciable in view of the high magnetization and is apparently equivalent to the influence of additional high-frequency fields (having a frequency close to the frequency of precession of the magnetic moment of the electrons in the external constant magnetic field) on the precessing electrons. Obviously the presence of these additional electric fields led to broadening of the resonance absorption and dispersion curves and, consequently, to an increase in the relaxation frequency of each section of the specimen. It may be noted that at different values of the constant magnetic field additional fields of different intensity acted on the same section of the specimen, depending on the state or condition of the neighboring sections of the specimen. When the constant field was varied from weak to strong fields, resonance conditions set in first for the the middle section of the specimen and the initial parts of the absorption and dispersion curves were determined primarily by this section wherein the demagnetizing fields are most uniform. Here, the end sections of the specimen, being in stronger demagnetizing fields, were relatively far from resonance and exerted a negligible influence on the shape of the curves. With further increase in the strength of the constant field conditions for resonance set in for sections located closer to the ends; thus the greater the constant field, the closer to the ends of the specimen are the sections for which conditions of resonance are satisfied and the greater the influence of the additional fields on the electrons of the middle section. Consequently, our first factor - the superposition of the curves for individual sections - leads to broadening of the curves to the side of stronger fields, while our second factor - the interaction of the sections with different resonance conditions - leads to broadening of the curves in both directions, but primarily to broadening of the curves associated with the middle section again to the side of stronger fields.

The variation of the experimental and theoretical curves shown in Fig.8 can readily be understood in the light of the specific characteristics of ferromagnetic resonance discussed above. The displacement of the experimental points for $\sqrt{\mu_к}$ to the side of stronger fields relative to the theoretical curve in the $H > H_0$ region and of the points for $\sqrt{\mu_п}$ in the $H > H_2$ region is a result of the superposition of the curves for the different sections of the ferromagnetic specimen and the interaction of different sections of the specimen with different resonance conditions. The appreciably smaller broadening of the experimental curve for $\sqrt{\mu_п}$ in the $H < H_2$ region is apparently due primarily to the interaction of the different sections and only partly to the superposition of the dispersion curves of these sections. In weak field $H < H_0$ the character of the experimental curves is apparently determined mainly by the middle section of the specimen with the end sections exerting only a negligible influence. In such weak fields ferromagnetic resonance occurs under more uniform conditions, corresponding to a lower relaxation frequency, in consequence of which the experimental points fall below the theoretical curve. The relaxation frequency as determined from the experimental curve on the basis of the position of the maxima and minima (fields H_0 and H_2) is a more or less average relaxation frequency value. This value correctly defines the positions of the maxima in the curves for $\mu_к$ and $\mu_п$; however, it is less than the value necessary for a correct description of the resonance absorption curve (for $H > H_0$) and the dispersion curve. At the same time it is greater than the relaxation frequency value corresponding to the absorption curve for $H < H_0$. It is obvious that one cannot define the experimental curves in terms of one value of the relaxation frequency and one value of the demagnetizing factor, for, as noted above, these curves are affected by the inhomogeneity of the resonance conditions for different parts of the specimen and the interaction between different parts of the specimen; hence any formula correctly describing these curves must take these factors into account as well.

The decrease in the magnetic permeabilities with increasing demagnetizing factor, noted above in connection with a comparison of the theoretical and experimental curves, is also explained by the fact that with increasing N_z the demagnetizing fields and their inhomogeneity also increase (to a certain point) and this leads to a greater difference in conditions for resonance in the different sections of the specimen, i.e., to a decrease of the total magnetic moment and, consequently, of the magnetic permeabilities. The data listed in Table 3 and in Figs. 8, a, b & c show that the relaxation frequency and the deviation of the experimental points from the theoretical curves increase much more in going from specimen No.1 to specimen No.2 compared with going from No.2 to No.3, there being relatively little difference in the experimental data for the last two. This feature of the results is apparently associated with the fact that the influence of the demagnetizing fields is determined not only by their magnitude but also by their degree of inhomogeneity: in going from specimen No.2 to specimen No.3 the demagnetizing field increases by 100 oersted while in going from No.1 to No.2 it increases only by 70 oersted but apparently the inhomogeneity of the fields in specimens Nos.2 & 3 differs little whereas in specimen No.1 the demagnetizing field is much more homogeneous than in specimen No.2. This is substantiated by the good fit of the experimental points with the theoretical curves for specimen No.1. Analysis of the experimental data and comparison of these data with the theoretical curves together with an examination of the conditions for ferromagnetic resonance in the presence of inhomogeneous demagnetizing fields leads us to conclude that the most reliable data for the chrome permalloy were obtained with specimen No.1. The average results for five series of measurements on this specimen were

$$H_0 = 190 \pm 2 \text{ oersted}$$

$$H_2 = 325 \pm 5 \text{ oersted}$$

The uncertainty in measuring ω is less than 0.5%; that in determining $4\pi J_s$ is of the order of 1%. As a result we obtain:

$$g = 2.6 \pm 0.05$$

$$1/T = (5.0 \pm 0.5)\cdot 10^9 \text{ sec}^{-1}.$$

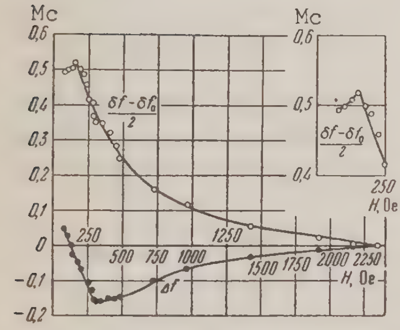

Fig.9. Same as Fig.5 but for electrolytic nickel: $N_z = 0$, $g = 2.20$, $1/T = 5.4\cdot 10^9$ sec^{-1}.

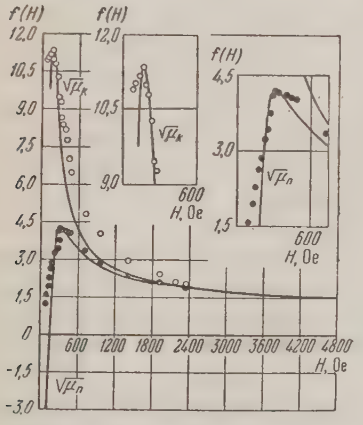

Fig.10. Same as Fig.8 but for electrolytic nickel: $N_z = 0$, $g = 2.20$, $1/T = 5.4\cdot 10^9$ sec^{-1}.

The character of the above noted influence of inhomogeneous demagnetizing fields on the shape of the absorption dispersion curves - primarily broadening of the curves to the side of stronger fields - differs from the influence of other factors giving rise to nonuniform conditions of resonance in different sections of the specimen. By way of illustration of the influence of nonuniform elastic stresses let us examine analogous results for electrolytic nickel. The experimental data were obtained on the same set-up with a cylindrical resonator; the layer of nickel was deposited electrolytically on the side wall of the resonator. Mechanical polishing after deposition brought the thickness of the nickel layer down to 0.03 mm ($N_z = 0.009$). The experimental data obtained and the corresponding theoretical curves are plotted in Figs.9 and 10.

A characteristic feature of Fig.10 is the broadening of the experimental curve for $\sqrt{\mu_K}$ to both sides of the maximum in the theoretical curve. The experimental dispersion curve is also appreciably wider than the theoretical curve, the spread again being to both sides of the maximum. Such broadening of the experimental curves is associated with the presence of nonuniform elastic stresses in the specimen, i.e., with different resonance conditions in different sections of the specimen. The basic form of the experimental curves is apparently determined by sections of the specimen with a certain "average" level of elastic stresses. For sections having smaller or greater elastic stresses, conditions for resonance are attained in external fields correspondingly smaller or greater than the resonance field for the principal average-value section. The superposition of the absorption curves for these lower and higher stress sections to the left and right of the curve for the principal section results in the broadening of the experimental curve to both sides. Another factor contributing to the broadening of the experimental curves is the interaction of sections with different resonance conditions. For electrolytic nickel we obtained:

$$g = 2.20 \pm 0.05,$$
$$1/T = (5.4 \pm 0.5)\cdot 10^9 \text{ sec}^{-1}.$$

Conclusions

One can draw the following conclusions on the basis of the experimental data, comparison of the data with the theoretical curves and analysis of the conditions for ferromagnetic resonance in the presence of inhomogeneous demagnetizing fields:

1. The presence of inhomogeneous demagnetizing fields leads to a pronounced distortion of the resonance absorption and dispersion curves. This distortion is characterized broadening of the curves mainly to the side of stronger fields.
2. The range of variation of the magnetic permeabilities decreases sharply with increasing strength of the demagnetizing fields.
3. The relaxation frequency increases with increasing demagnetizing field strength.
4. The splitting factor g remains virtually constant (within the limits of experimental accuracy) for specimens with different values of demagnetizing factor.
5. The experimental curves for specimens with inhomogeneous demagnetizing fields cannot be characterized by the usual parameters of ferromagnetic resonance, specifically, by a single value of the relaxation time and a single value of the demagnetizing factor.
6. The experimental data show that in comparing the theoretical and experimental values of the relaxation times it is essential to analyze and take into account the experimental conditions and, in particular, the presence of nonuniform conditions for resonance in different parts of the specimen.
7. The distortion of the absorption and dispersion curves is determined not only by the magnitude of the demagnetizing fields but also by the degree of their inhomogeneity. The distortions become noticeable when the demagnetizing fields are commensurate with the resonance field. Obviously, in working with a material for which the maximum value of μ_Π (the effective permeability based on the index of refraction - see Eq.(4)) can be obtained, these distortions will be manifest if the demagnetizing fields are commensurate with the field corresponding to this maximum.
8. Many applications of ferrites in super-high frequency radio engineering are based on utilization of ferromagnetic resonance. In a number of devices it is important to have the greatest possible range of variation of the magnetic permeability of the ferrite component and a maximum rate of change of these permeability of the ferrite component and a maximum rate of change of these permeabilities with changes of the external magnetic field. The data obtained in the present investigation show that to obtain the optimum results with a given ferrite, the ferrite component must be given a shape for which the inhomogeneity of the demagnetizing fields is minimal.

The present investigation was carried out under the guidance of S.D.Gvozdorev whom the writers take this occasion to thank.

Department of Physics of
Moscow State University

References

1. V.K.Arkad'ev, ZhRFKhO (Journal of the Russian Physical and Chemical Society) 44, 165 (1912).

2. V.K.Arkad'ev, ZhRFKhO (Journal of the Russian Physical and Chemical Society) 45, 302 (1913).

3. C.Kittel, Phys.Rev., 73, 155 (1948).

4. C.Kittel, J. de phys. et rad., 12, 291 (1951).

5. J.H.Van Vleck, Physica, 17, 234 (1951).

6. N.Bloembergen, Phys.Rev., 78, 572 (1951).

7. V.K.Arkad'ev, Elektromagnitnye protsessy v metallakh (Electromagnetic processes in metals), Part II, Moscow, 1938.

8. R.L.Sproull & E.G.Linder, Proceedings IRE, 34, 5 (1946).

9. A.I.Pil'shchikov, Zhur.eksp.i teor.fiz., 29, 6 (1955).

FERROMAGNETIC RESONANCE UNDER NONUNIFORM CONDITIONS

- A.I.Pil'shchikov, Z.D.Trishina & T.A.Zvereva

1. Introduction

Theoretical evaluations[1,2] of the conditions for ferromagnetic resonance in single crystals have made it possible to allow for the influence of magnetic crystalline anisotropy, homogeneous elastic stresses and uniform demagnetizing fields and have shown the substantial dependence of resonance conditions on these factors.

The influence of magnetic anisotropy and uniform demagnetizing fields on resonance conditions have been studied in a number of experimental investigations[1,3 & 4], the results of which are in good agreement with the predictions of theory.

In the case of polycrystalline specimens the orientation of the crystallographic axes relative to the external magnetic field, the internal demagnetizing fields and the elastic stresses are not the same for different parts of the specimen. This gives rise to nonuniform resonance conditions through the volume of the specimen with the result that the shape of the resonance absorption and dispersion curves and the experimental values of the ferromagnetic resonance parameters are substantially modified.

Investigation of the influence of nonuniform conditions helps clarify the distinctive characteristics of ferromagnetic resonance in polycrystalline specimens, refine our concepts of the mechanism of the effect and determine the nature of the factors affecting the resonance absorption line width.

The presence of nonuniform demagnetizing fields in the specimen is one of the causes responsible for heterogeneous resonance conditions. The investigation of Ref.5 threw light on the influence of demagnetizing fields on the shape of the resonance absorption and dispersion curves, on the experimental values of the splitting factor and on the relaxation times. It was shown that the absorption and dispersion curves broaden, extending primarily to the side of stronger fields, with increasing demagnetizing factor. The increase in the experimentally determined value of the relaxation frequency is associated with this broadening. No clear dependence of the splitting factor, as determined from the experimental data, on the demagnetizing factor was observed in the investigation. The range of variation of the magnetic permeabilities in the region of ferromagnetic resonance decreases with increasing demagnetizing factor.

The above mentioned characteristics of ferromagnetic resonance must be taken into account in comparing experimental data with the results of theoretical calculations as well as in designing equipment incorporating ferromagnetic materials (in particular super-high frequency equipment employing ferrites).

The first experimental results on the influence of inhomogeneous demagnetizing fields were obtained on three specimens of NKhS-80 (HXC-80) permalloy[5] (see preceding article). These specimens were prepared of bands of different thicknesses and had different magnetic properties in static magnetic fields. In view of the fact that only three specimens with different magnetic properties were studied, it was impossible to establish definitely the dependence of the ferromagnetic resonance parameters on the demagnetizing factor. Hence one of the purposes of the present study was to investigate the influence of inhomogeneous demagnetizing fields in specimens with identical properties for the purpose of establishing the character of the dependence of the ferromagnetic resonance parameters on the demagnetizing factor and observe in more detail the changes in the absorption and dispersion curves with the demagnetizing factor.

In the presence of inhomogeneous demagnetizing fields the behavior of the absorption and dispersion curves in the region of fields weaker than the resonance one has a number of distinctive characteristics[5]: in such weak fields the broadening of the curves is appreciably less than in strong fields, the minimum of the dispersion curve is appreciably sharper and lower than the maximum, and the slope of the absorption curve is appreciably steeper than on the side of strong fields. These distinctive features of ferromagnetic resonance are connected with the fact that in weak fields the shape of the absorption and dispersion curves is determined primarily by the middle sections of the specimen with the most uniform resonance conditions. In such weak fields the end sections of the specimen are far from resonance and their influence on the middle section is virtually negligible.

A second factor affecting the appearance of the curves in weak fields is that the ferromagnetic material in these fields is not magnetized to saturation.

A result of the first factor (the predominant influence of the middle section) is that the shape of the ferromagnetic resonance curve for this field interval corresponds to a lower relaxation frequency than in the case of strong fields. Elucidation of the influence of the second factor calls for investigation of resonance in ferromagnets magnetized to below saturation, investigation of which is also of intrinsic interest. Investigation of ferromagnetic resonance in the presence of inhomogeneous demagnetizing fields stronger than the resonance field makes it possible to clarify certain characteristics of the effect in ferromagnets below saturation. This question is more conveniently investigated in materials with a high magnetizability since one can then realize strong demagnetizing fields with acceptable specimen dimensions.

The present study was carried out on specimens of NKhS-80 (НХС-80) and 50-N (50-Н) permalloys. The NKhS-80 permalloy has a relatively low saturation magnetization (for it $4\pi J_s = 6770$ gauss); hence one can prepare from it a series of specimens with demagnetizing fields ranging from relatively weak ones (appreciably weaker than the acting resonance field) to fields commensurate with the acting resonance field. Specimens of NKhS-80 permalloy were used for the measurements intended to refine the experimental results of Ref.5 regarding the influence of inhomogeneous demagnetizing fields on the shape of the ferromagnetic resonance curves and determining the dependence of the experimental values of the splitting factor and the relaxation frequency on the demagnetizing factor.

The influence of strong demagnetizing fields was investigated using specimens of 50-N permalloy which has a higher saturation magnetization (for it $4\pi J_s =$ $= 15$ kilogauss).

The measurements were made on specimens in the form of thin wall cylinders. The specimens were mounted coaxially in the cavity of a cylindrical resonator in which an E_{010} mode was excited. The basic quantities measured were the change in the Q-factor and resonance frequency of the measurement resonator with the specimen in it as a function of the constant magnetic field. The experimental set-up, measurement procedure and method of processing the experimental data are described in Refs. 5 & 6.

2. Experimental Results

NKhS-80 Permalloy

The dimensions of the investigated specimen and the values of the demagnetizing factor for them are listed in Table 1.

All the specimens except No.1 were cut from the same band and all were annealed together under vacuum.[5] Specimen No.1 with the lowest demagnetizing factor was made from thinner material since with a thickness of 0.05 mm too great a cylinder height was necessary to obtain $N_z = 0.025$. This specimen was used as a control. The basic experimental data for specimens Nos.2 & 5 in the form of the variation of the change in the half-width of the resonance curve $(\frac{\delta f - \delta f_0}{2})$ and the deviation of resonance frequency (Δf) of the measurement resonator relative to their respective values at the maximum field with the intensity of the constant magnetic field are shown in Fig.1. The vertical dash line in the figures corresponds to $H = N_z J_s$. The dependences of these same quantities on the effective field ($H - N_z J_s$) for all the NKhS-80 permalloy specimens are shown in Fig.2.

Table 1

Values of the demagnetizing factor for the investigated specimens of NKhS-80 permalloy

Sample No.	Dimensions		N_z
	a, мм	c, мм	
1	0,02	10	0,025
2	0,05	10	0,063
3	0,05	6	0,105
4	0,05	4	0,155
5	0,05	2	0,305

---

a is the wall thickness of the cylindrical specimen, c is the height of specimen and N_z is the demagnetizing factor along the z-axis of the specimen (the direction of the constant magnetic field).

The values of the ferromagnetic resonance parameters (γ, g and T) were calculated from the field values corresponding to the maximum attenuation and minimum deviation of the resonance frequency. The following formulas were used[6]:

$$\gamma^2 = -\frac{q}{2p^2} + \frac{1}{p}\sqrt{\frac{q^2}{3p^2} + \omega^2}, \tag{1}$$

$$\frac{1}{T} = \gamma^2 p, \tag{2}$$

where

$$p = \frac{(H_2 - H_0)\,[H_2 + H_0 + (N_x + N_y - 2N_z)\,J_s]}{2\sqrt{3}\,\omega}, \tag{3}$$

$$q = [H_0 + (N_x - N_z)\,J_s]\,[H_0 + (N_y - N_z)\,J_s]. \tag{4}$$

In computing the relaxation frequency we introduced the correction:

$$\frac{1}{T} = \frac{1}{T'}\left(1 - 4{,}25\,\frac{\omega}{\omega_{1k}^2 T'}\right),$$

where $1/T'$ is the value of the relaxation frequency calculated according to Eq.(2),

$$\omega_{1k}^2 = \omega_1^2 /_{H = H_0},$$

and

$$\omega_1^2 = 4\pi\gamma^2 J_s\,[H + (N_y - N_z)\,J_s].$$

In the above equations and in what follows we use the following notation: ω is the angular frequency of the high-frequency magnetic field, J_s is the saturation magnetization, H_0 is the value of the external constant magnetic field corresponding to the maximum attenuation (maximum $\mu_к$), H_1 and H_2 are the values of the external magnetic field corresponding, respectively, to the maximum and minimum deviation of the resonance frequency (first and second maxima of $\mu_п$), γ is the ferromagnetic ratio, g is the splitting factor, T is the transverse relaxation time, $\mu_п$ is the effective magnetic permeability based on the absorption coefficient, $\mu_к$ is the effective magnetic permeability based on the index of refraction, $\mu' = \mu - j\rho'$ is the complex magnetic permeability of the investigated material and N_x, N_y and N_z are the demagnetizing factors along the corresponding axes (the

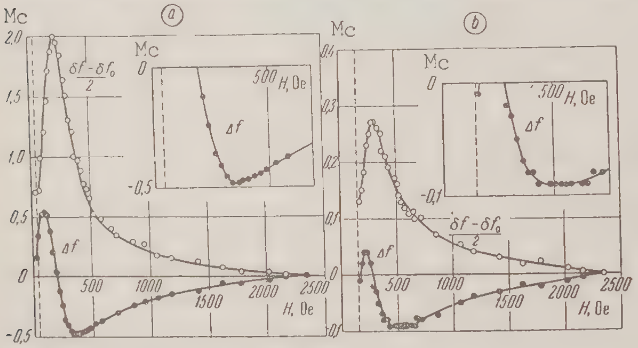

Fig.1. Experimental dependences of the attenuation and deviation of resonance frequency of the measurement resonator with specimens of NKhS-80 permalloy on the external field: a) specimen No.2 (N_z = 0.063), b) specimen No.5 (N_z = 0.305).

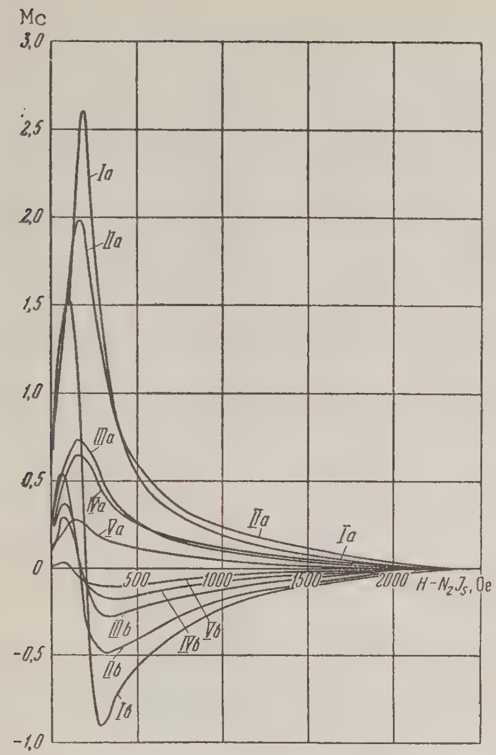

Fig.2. Experimental dependences of the attenuation and deviation of resonance frequency of the measurement resonator on the effective field ($H - N_zJ_s$) for five specimens of NKhS-80 permalloy. The Roman numbers at the curves correspond to the Arabic number designation of the specimens in Table 1; a - attenuation curves; b - resonance deviation curves.

z-axis coincides with the direction of the constant magnetic field, the x-axis with the direction of the high-frequency field).

The basic experimental data and the results of computations of the ferromagnetic resonance parameters are listed in Table 2. Comparison of the experimental curves of Figs. 1 & 2 and the data given in Table 2 shows that with increasing values of demagnetizing factor the absorption and dispersion curves broaden primarily to the side of stronger fields. The maximum of the attenuation curve is displaced to the side of stronger fields, but, as is evident from Table 2, the effective field ($H - N_zJ_s$) decreases with increasing N_z. The minimum of the frequency deviation curve is displaced to the side of stronger fields to an appreciably greater extent than the attenuation maximum and the difference $H_2 - H_o$ increases. The attenuation curves for specimens Nos. 4 & 5 are steeper in fields $H < H_o$ than with fields $H > H_o$. In the region of the minimum the resonance frequency deviation curves in weak fields $H < H_2$ are also steeper than in strong fields $H > H_2$. The maxima of the resonance frequency deviation curves are appreciably sharper than the minima.

The broadening of the absorption and dispersion curves and the greater displacement of the minimum of the resonance frequency deviation to the side of stronger fields as compared with the displacement of the absorption maxima characterizes the growth of the relaxation frequency with increasing demagnetizing factor (Table 2).

All these changes in the shape of the experimental curves with increasing demagnetizing factor agree with the analogous results obtained in the investigation of Ref.5. The results of the present work bring out more clearly the changes in the effective field with increasing N_z.

Table 2

Basic experimental data and results of calculations of the parameters of ferromagnetic resonance for specimens of NKhS-80 permalloy

Sample No.	N_z	N_zJ_s, Oe	$\omega\cdot10^{10}$, rad/sec	H_1, Oe	H_0, Oe	H_2, Oe	$H_0-H_zJ_s$, Oe	H_0-H_1, Oe	H_2-H_0, Oe	$\gamma\cdot10^{-6}$, Hz Oe^{-1}	g	$\frac{1}{T}\cdot10^{-6}$, sec^{-1}
1	0,025	13	2,04	125	195	293	182	70	98	17,9	2,05	3,0
2	0,063	34	2,03	100	195	352	161	95	157	18,4	2,10	5,3
3	0,105	56	2,05	145	208	385	152	63	177	19,0	2,15	6,3
4	0,155	84	2,05	145	232	448	148	87	216	19,2	2,20	7,7
5	0,305	165	2,05	245	304	530	139	59	226	19,3	2,20	8,1

Note: For the investigated specimens $4\pi J_s = 6770$ gauss.

We computed the theoretical values of μ, ρ', $\mu_{\text{п}}$ and $\mu_{\text{к}}$ for different values of the constant magnetic field on the basis of the experimental values of γ and T. The theoretical curves for $\sqrt{\mu_{\text{п}}}$ and $\sqrt{\mu_{\text{к}}}$ are juxtaposed with experimental data for specimens Nos.2, 4 & 5 in Fig.3. Whereas the experimental points for specimens Nos.1 & 2 fit the theoretical curves well except in the region of the dispersion curve minimum, for the other specimens there is an appreciable divergence: where the absorption curves are concerned the experimental points in fields $H > H_0$ lie above the theoretical curves, while for fields $H < H_0$ they lie below; in the $H_0 < H < H_2$ interval the experimental points for specimens Nos.3 & 4 lie closer to the theoretical dispersion curve than in fields $H > H_2$. There is a noticeable displacement of the experimental points to the side of stronger fields relative to all the theoretical curves.

The range of variation of magnetic permeabilities decreases with increasing demagnetizing factor.

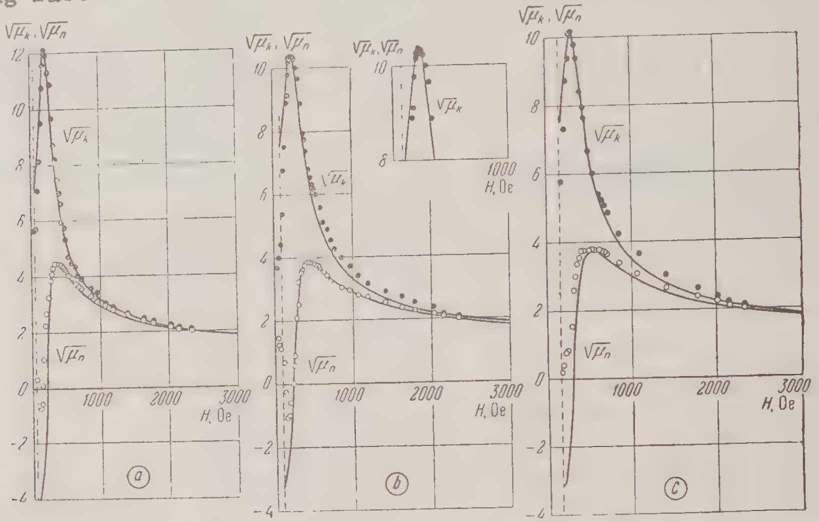

Fig.3. Comparison of experimental values of $\sqrt{\mu_{\text{п}}}$ and $\sqrt{\mu_{\text{к}}}$ (points) with the theoretical curves for the three specimens of NKhS-80 permalloy: a) specimen No.2, $N_z = 0.063$, $g = 2.10$, $1/T = 5.3 \cdot 10^9$ sec^{-1}; b) specimen No.4, $N_z = 0.155$, $g = 2.20$, $1/T = 7.7 \cdot 10^9$ sec^{-1}; c) specimen No.5, $N_z = 0.305$, $g = 2.20$, $1/T = 8.1 \cdot 10^9$ sec^{-1}.

In Ref.5 the noted distinctive characteristics of ferromagnetic resonance curves were explained by the dissimilar resonance conditions in the specimen, conditions due to the presence of inhomogeneous demagnetizing fields. The sections near the middle of the specimen are presumably in weaker demagnetizing fields than the sections near the ends of the specimen. As a result, conditions for resonance in the middle sections are attained in weaker fields as compared with the end sections, which leads to broadening of the curves to the side of stronger fields. The curves are also broadened due to the interaction of the different sections with different resonance conditions.

Taking these circumstances into account, one of the present authors gave (in Ref.5) a qualitative explanation of the distortion of the shape of the experimental curves, the increase in the relaxation frequency and the decrease in the range of variation of the magnetic permeabilities with increasing demagnetizing factor; the arguments are fully applicable to the results summarized in Fig.3 of the present article.

It must be noted that the experimental and theoretical curves for specimen No.5 have certain distinctive features. In the vicinity of the $\sqrt{\mu_{\text{к}}}$ maximum there is relatively good fit of the experimental points to the theoretical curve, while in the region of strong fields the experimental points, just as in the case

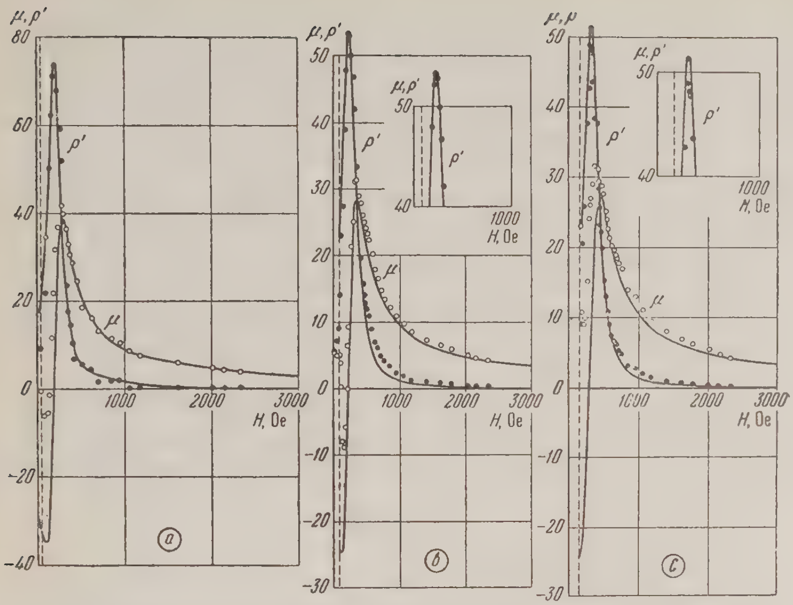

Fig.4. Comparison of the experimental values of the magnetic permeabilities μ and ρ' with the theoretical curves for the same specimens of permalloy as in Fig.3.

of other specimens, lie above the curve. In the region of the $\sqrt{\mu_{\text{п}}}$ maximum, the experimental points form a curve that is broadened both to the side of stronger and to the side of weaker fields.

The theoretical curves and experimental points for the magnetic permeabilities of the material μ and ρ' determined for specimens Nos. 2, 4 & 5 of the chrome NKhS-80 permalloy are shown in Fig.4. Just as in the case of effective permeabilities, the experimental points here fit the theoretical curves for specimens Nos.1 & 2 characterized by a small demagnetizing factor. It will be seen that for specimens with a larger demagnetizing factor (specimens Nos.3 & 4) there is an appreciable displacement of the experimental points to the side of the stronger fields. The deviations of the experimental points from the theoretical curves for both the effective magnetic permeabilities ($\mu_{\text{п}}$, $\mu_{\text{к}}$) and the permeabilities of the material (μ, ρ') are similar in character.

In the case of specimen No.5, which has the highest demagnetizing factor, the experimental points for μ to the left of the maximum are displaced to the side of weaker fields to an appreciably greater extent than the points to the right are displaced to the side of stronger fields. The reasons for these distinctive results obtained for specimen No.5 will become clear when we examine the data obtained for the 50-N permalloy.

The data obtained with the NKhS-80 permalloy specimens enable us to establish the character of the dependence of the relaxation frequency on the demagnetizing factor. The curve characterizing this dependence, based both on our data and the data obtained in the investigation of Ref.5, is shown in Fig.5. Comparison of the results obtained in the present investigation with those obtained in the investigation of Ref.5 shows that they yield a similar variation of the relaxation frequency with the demagnetizing factor. As may be seen from Fig. 5 the relaxation frequency increases rapidly with increasing demagnetizing factor in the region of small values of the factor and that beginning with $N_Z \approx 0.15$ the growth in relaxation frequency slows down. To understand the reasons for this N_Z-dependence of the relaxation frequency one must bear in mind that the influence of demagnetizing fields on ferromagnetic resonance is determined not only by the magnitude but

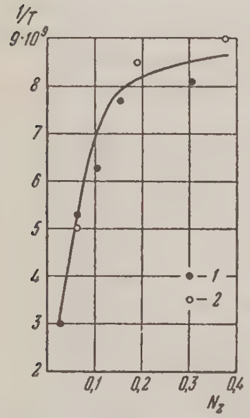

Fig.5. Dependence of the relaxation frequency on the demagnetizing factor for NKhS-80 permalloy: 1) experimental points obtained on the basis of the results of the present investigation; 2) points obtained on the basis of the results of Ref.5.

also by the degree of inhomogeneity of these fields. The most important conclusion that can be drawn from the curve of Fig.5 is that the presence of even relatively weak demagnetizing fields has a strong effect on the relaxation frequency. Thus, for specimens Nos.1, 2 & 3, while the demagnetizing fields are appreciably weaker than the effective field, the relaxation frequency increases rapidly with increasing N_z. This is apparently connected with an appreciable increase in the degree of inhomogeneity of the demagnetizing fields. The rise in the relaxation frequency in going from specimen No.3 to specimen No.4 is apparently connected with increases in both the intensity and the inhomogeneity of the demagnetizing fields. In going from specimen No.4 to No.5 the value of N_z increases by a factor of almost 2 (in both cases the demagnetizing field is commensurate with the effective field), but the relaxation frequency increases only slightly. Apparently, although the demagnetizing fields increase in strength, their inhomogeneity changes little and this results in a relatively minor increment in the relaxation frequency.

The splitting factor g of the specimens changes appreciably less with N_z, but, as can be seen from Table 2, there is evident a tendency towards growth of the experimental values of g with increasing demagnetizing factor. The reason for this tendency is obscure.

50-N Permalloy

Table 3

Values of the demagnetizing factor for the 50-N permalloy specimens

Sample No.	Dimensions		N_z
	a, MM	c, MM	
1	0,11	10	0,14
2	0,22	10	0,275
3	0,21	5	0,505

We used specimens of 50-N permalloy to study the influence of very strong demagnetizing fields $N_zJ_s > (H_o - N_zJ_s)$, for specimens of this material could be prepared with a high demagnetizing factor (see Table 3). This made it possible to obtain resonance conditions in specimens magnetized to less than saturation.

In Fig.6 we give the experimental curve for two of the specimens (Nos.2 & 3) and in Table 4 the basic experimental data and results of calculations of the ferromagnetic parameters.

The shape of the experimental curves for 50-N permalloy changes with increasing demagnetizing factor in the same way as the shape of the curves for the chrome NKhS-80 permalloy. However, the curves for the specimen with the greatest value of the demagnetizing factor ($N_z = 0.505$) differ somewhat from the curves for the other specimens: the absorption curve has a sharper maximum than might be expected from the trend of the curve in strong fields, while the minimum of the resonance frequency deviation curve is very diffused. The experimental value of the splitting factor for this specimen is appreciably less than 2 (g = 1.50).

Table 4

Basic experimental data and results of calculations of the ferromagnetic resonance parameters for the 50-N permalloy specimens

N_z	N_zJ_s, Oe	$\omega \cdot 10^{-10}$, rad/sec	H_0, Oe	H_2, Oe	$H_0 - N_zJ_s$, Oe	$H_g - H_0$, Oe	$\gamma \cdot 10^{-8}$, Hz Oe^{-1}	g	$\frac{1}{T} \cdot 10^{-9}$, sec^{-1}
0,14	167	2,04	205	420	38	215	18,1	2,06	15,0
0,275	325	2,04	337	595	12	258	18,6	2,12	18,5
0,505	602	2,05	614	1150	12	536	13,2	1,50	19,0

Just as for the NKhS-80 permalloy specimens, we calculated the theoretical values of μ, ρ', $\mu_п$ and $\mu_к$ for the 50-N specimens on the basis of the values of γ and T listed in Table 4. The experimental values of $\sqrt{\mu_п}$ and $\sqrt{\mu_к}$ are compared with the theoretical curves in Fig.7. Whereas for the specimens with $N_z = 0.14$ and 0.275 the deviations of the experimental points from the theoretical curve are similar to those of the NKhS-80 permalloy specimens (Fig.3), the deviations are appreciably different for the specimen with $N_z = 0.505$. It will be evident from Fig.7,b that the experimental points for fields $H > H_0$ near the absorption maximum lie below the theoretical curve and that they come above the curve only for $H > 1000$ oersted. In the region of the maximum in the dispersion curve for $H < H_2$ the experimental points are sharply displaced to the side of weaker fields relative to the theoretical curve. To the right of this maximum the experimental points lie close to the theoretical curve.

The experimental values of the magnetic permeabilities μ and ρ' are plotted against the theoretical curves in Fig.8. For specimens Nos.1 & 2 experimental points for ρ' (with $H > H_0$) and for μ (with $H < H_2$) are displaced to the side of stronger fields. For specimen No.3 (Fig.8,b) the experimental points for μ and ρ' are displaced to the side of weaker fields in the field interval $H_0 < H < H_2$ and to the side of stronger fields in the range $H > H_2$. The experimental maximum of μ is displaced to the side of weaker fields relative to the maximum of the theoretical curve. Analogous divergences between the experimental and theoretical data were observed for specimen No.5 of the NKhS-80 permalloy (Figs.3,b and 4,b). The similarity of the divergences is particularly striking in the region of the maxima in the dispersion curves for $\sqrt{\mu_{\text{п}}}$ and μ. This kind of deviation of the experimental points from the theoretical curve is explained by the fact that in fields weaker than that corresponding to the maxi-

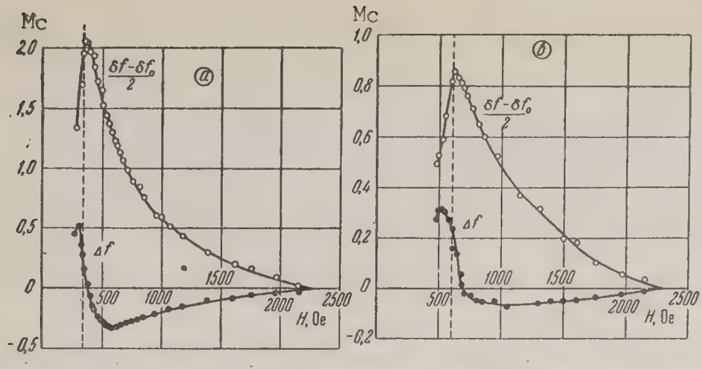

Fig.6. Experimental dependences of the attenuation and deviation of resonance frequency of the measurement resonator with specimens of 50-N permalloy on the external magnetic field: a) specimen No.2, $N_z = 0.275$; b) specimen No.3, $N_z = 0.505$.

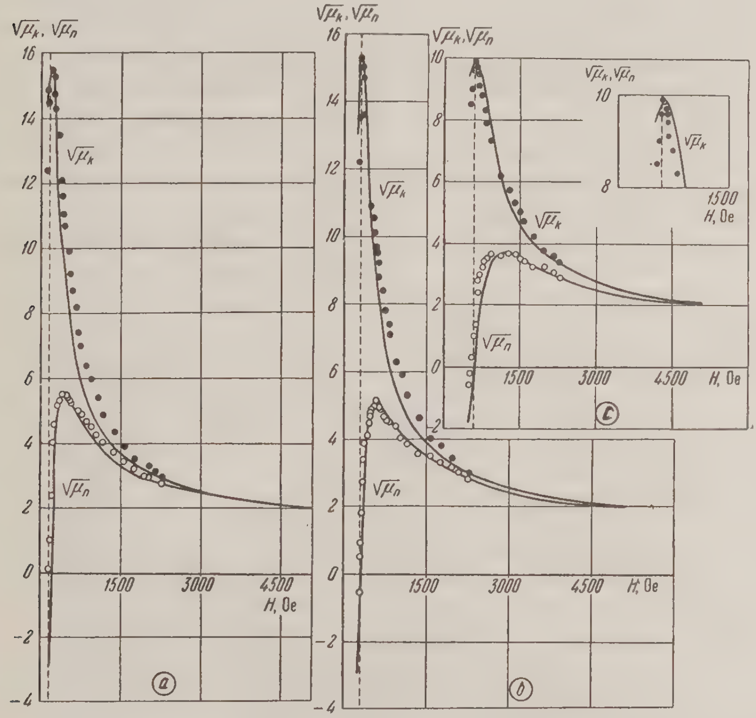

Fig.7. Comparison of the experimental values of $\sqrt{\mu_{\text{п}}}$ and $\sqrt{\mu_{\text{к}}}$ with the theoretical curves for the 50-N permalloy specimens: a) specimen No.1, $N_z = 0.14$, $g = 2.06$, $1/T = 14.9 \cdot 10^9$ sec^{-1}; b) specimen No.2, $N_z = 0.275$, $g = 2.12$, $1/T = 18.5 \cdot 10^9$ sec^{-1}; c) specimen No.3, $N_z = 30.505$, $g = 1.5$, $1/T = 18.9 \cdot 10^9$ sec^{-1}.

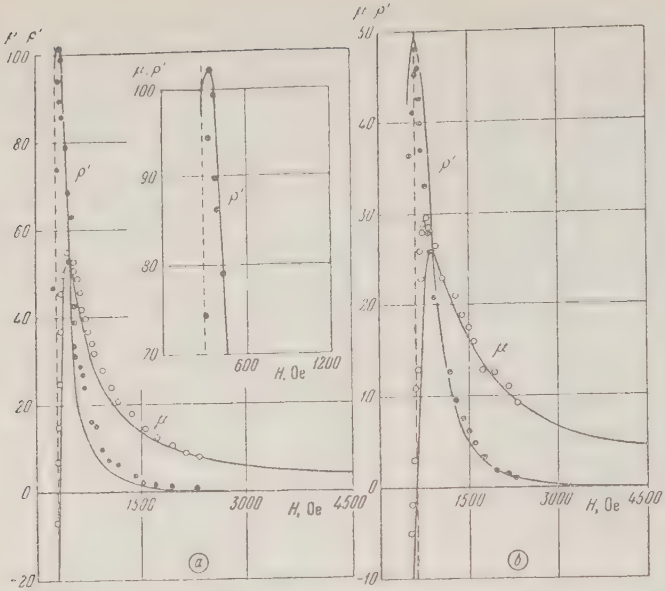

Fig.8. Comparison of the experimental values of the magnetic permeabilities of the material μ and ρ' (points) with the theortical curves for the specimens of 50-N permalloy: a) specimen No.2, $N_z = 0.275$, $g = 2.12$, $1/T = 18.5 \cdot 10^9$ sec^{-1}; b) specimen No.3, $N_z = 0.505$, $g = 1.5$, $1/T = 18.9 \cdot 10^9$ sec^{-1}.

mum of the dispersion curve the specimen is not magnetized to saturation.

The theoretical curves were calculated on the assumption that for all fields $H > N_z J_s$ saturation was attained ($J = J_s$). Consequently, for a given external field the theoretical value of the effective field ($H - N_z J_s$) was smaller than the true value of the effective field actually obtaining in the specimen during measurement. In plotting the theoretical curves and experimental points the values of the magnetic permeabilities, computed and experimental, were referred to the same value of the external field, whereas the effective fields were actually different. Moreover, in the range of fields $H < H_2$ the magnetization does not remain constant but decreases with decreasing external field. In view of this the experimental values of magnetic permeabilities turn out to be smaller than the theoretical ones and fall off more rapidly.

For fields $H_0 < H < H_2$ the magnetization of the specimen changes relatively little, hence the displacement of the experimental points is determined primarily by the divergence between the theoretical and experimental values of the effective field. In fields $H < H_0$ changes in the magnetization of the specimen play a substantial role. Because of this the experimental points $\sqrt{\mu_{\text{к}}}$ and ρ' in this field region fall below the theoretical curves, while the experimental values of $\sqrt{\mu_{\text{п}}}$ and μ are smaller than the theoretical values as regards absolute magnitude. It should be noted that the experimental values of the magnetic permeabilities were obtained by means of calculations in which the experimental values of the corresponding effective magnetic permeabilities were equated to the theoretical ones at two points. These points are the maxima of the curves and the points corresponding to the maximum value of the external magnetic field. By virtue of this the maxima of the theoretical and experimental curves coincide as regards height, whereas actually they should differ inasmuch as the actual magnetization of specimens is not equal to saturation magnetization.

For a more conclusive comparison of the experiment and theoretical data one must have and make use of the magnetization curve for the specimen, or, more accurately, of the dependence of the magnetization on the external field with magnetization of the specimen along its longitudinal axis. In the analysis of the dispersion curves for NKhS-80 permalloy obtained in the present investigation and that of Ref.5 it was noted that the minimum in the dispersion curve is sharper than the maximum and that the absolute value of the magnetic permeability is lower at the minimum than at the maximum. As follows from the above examination, this is due to the fact that saturation magnetization of the ferromagnet is not attained in these fields.

The exceptionally low value of the splitting factor for specimen No.3 of 50-N permalloy is to be explained by the fact that it was calculated on the assumption that $J = J_s$, whereas the position of the absorption maximum was determined for $J < J_s$.

With fields $H > H_2$ the specimen was apparently magnetized to saturation and the displacement of the experimental points to the side of stronger fields relative to the theoretical curve is explained by the presence of inhomogeneous demagnetizing fields just as for the other specimens. Moreover, although the experimental maxima, as noted above, are lower than the theoretical ones they were equated to the theoretical values and because of this all the points of the experimental curves lie higher than they should.

Department of Physics of
Moscow State University

References

1. G.Kittel, Phys. Rev., 73, 155 (1948).
2. J.R.Macdonald, Proc. Phys. Soc., 64, 968 (1951).
3. A.F.Kip & R.D.Arnold, Phys. Rev., 75, 1556 (1949).
4. L.R.Bickford, Phys. Rev., 78, 449 (1950).
5. A.I.Pil'shchikov, Preceding article in present issue of the Bulletin.
6. A.I.Pil'shchikov, Zhur.eksp.i teor.fiz., 29, 6 (1955).

GENERAL PROPERTIES OF LINEAR SYSTEMS

- E.M.Polivánov & V.V.Kuznetskii

The dependence of the permeability or susceptibility on the frequency is a very important characteristic of magnetic materials (or bodies) both because it allows us to judge the physical processes occurring therein (relaxation times, natural frequencies, etc.) and because knowing the frequency characteristic we can determine the effective permeability and losses at a given operating frequency; moreover, knowing the frequency characteristic we can determine the transient conditions in any given pulse field.

The practical importance of requency characteristics has greatly increased in the last decade in connection with the widespread employment of pulse and high-frequency equipment and the development of magnetic materials for use therein.

Analysis of frequency characteristics plays an important part not only in the relatively narrow field of magnetic phenomena: different methods of frequency characteristic analysis are extensively used in different branches of physics, in electrical and radio engineering, in the theory of automatic control and in the theory of dynamic systems.

The relation between the quantities determined by the real and imaginary components of the permeability, in the case of the simplest relaxation and oscillatory processes, has long been known in optics and has been analyzed in detail for the case of magnetic media by Arkad'ev[1].

However, the general analytic expressions characterizing the relation between the real and imaginary components of the permittivity or the magnetic susceptibility (permeability) were first formulated by Kramers[2] in 1927.

These general expressions are:

$$\chi_1(\nu') - \chi_1(\infty) = \frac{2}{\pi}\int_0^\infty \frac{\nu\chi_2(\nu)}{\nu^2-\nu'^2}\,d\nu \tag{1}$$

and

$$\chi_2(\nu') = -\frac{2\nu'}{\pi}\int_0^\infty \frac{\chi_1(\nu)-\chi_1(\infty)}{\nu^2-\nu'^2}\,d\nu. \tag{2}$$

Here $\chi_1(\nu)$ and $\chi_2(\nu)$ are the dependences of the real and imaginary components of the magnetic susceptibility on the frequency ν of the applied sinusoidal field and ν' is the frequency at which the value of the real or imaginary component of the susceptibility $\chi_1(\nu')$ or $\chi_2(\nu')$ is determined.

Al'tshuler[3] and Romanov[4] have published contributions devoted to the relation between the real and imaginary parts of analogous characteristics under somewhat different conditions.

Kramers' work did not become widely known in electrical engineering circles; it may have been thought that his conclusions applied only to linear polarizable media. Independently and twenty years after the publication of Kramers' contribution, Bode[5] deduced the same formulas for the frequency characteristics of linear electric networks. Bode also developed simple graphic methods of constructing one characteristic from the other, experimentally recorded characteristics.

Subsequently, thanks to the successful mathematical development of operational calculus and establishment of its connection with the Laplace transform and Fourier's integral, the entire theory of frequency spectra became much clearer and at present the basic relationships between the frequency characteristics (Kramers' formulas) can be derived in a clear and direct manner (see for example Kontorovich[6], Solodovnikov[7] and Gonorovski[8]).

The expressions characterizing the relationship between the real and imaginary components of the magnetic permeability can be written:

$$\mu_1(\omega_1) - \mu_1(\infty) = \frac{2}{\pi} \int_0^\infty \frac{\omega \mu_2(\omega)}{\omega^2 - \omega_1^2}\, d\omega, \tag{3}$$

$$\mu_2(\omega_1) = -\frac{2\omega_1}{\pi} \int_0^\infty \frac{\mu_1(\omega)}{\omega^2 - \omega_1^2}\, d\omega, \tag{4}$$

where $\mu_1(\omega)$ and $\mu_2(\omega)$ are the frequency dependences of the real and imaginary parts of the magnetic permeability, respectively, ω is the angular frequency of the sinusoidal magnetic field and ω_1 is the frequency at which the value of $\mu_1(\omega_1)$ or $\mu_2(\omega_1)$ is determined.

In Eq. (4) there is no second term in the numerator of the fraction under the integral, which distinguishes this equation from that of Kramers (2). It can readily be shown that this does not affect the result, inasmuch as

$$\int_0^\infty \frac{\mu_1(\infty)}{\omega^2 - \omega_1^2}\, d\omega = 0, \tag{5}$$

if we have in mind the principal value of the integral.

It is generally difficult to utilize these formulas for the practical purpose of determining one characteristic from the other, since usually the analytic expression for the function is not known and only an experimentally determined curve for one of the characteristics is available.

The graphic analysis method proposed by Bode greatly simplifies constructing one characteristic on the basis of the other and thereby makes it possible to utilize the relation between the frequency characteristics of linear systems in a great number of cases. Bode's method was used by the present authors for determining the frequency characteristic of the imaginary part of the permeability from the characteristic of the real component.

In most cases encountered in practice one can interchange the even and odd components of the frequency characteristic by multiplying or dividing both quantities by $j\omega$. Hence in the discussion below we will use only Eq. (4) which serves to determine the imaginary component from the real one.

Let us give Eq. (4) a different form by carrying out integration by parts. Bearing in mind that*

$$\frac{d}{d\omega} \ln \left| \frac{\omega - \omega_1}{\omega + \omega_1} \right| = \frac{2\omega_1}{\omega^2 - \omega_1^2}, \tag{6}$$

we obtain:

$$\mu_2(\omega_1) = -\frac{1}{\pi} \int_0^\infty \mu_1(\omega)\, d \ln \left| \frac{\omega - \omega_1}{\omega + \omega_1} \right| = \frac{1}{\pi} \mu_1(\omega) \ln \left| \frac{\omega + \omega_1}{\omega - \omega_1} \right| \Bigg|_0^\infty - \frac{1}{\pi} \int_0^\infty \ln \left| \frac{\omega + \omega_1}{\omega - \omega_1} \right| d\mu_1(\omega). \tag{7}$$

But the first term in the right-hand part equals zero, if $\mu_1(\omega)$ remains limited with $\omega = 0$ and $\omega = \infty$.

Hence we can write

$$\mu_2(\omega_1) = -\frac{1}{\pi} \int_0^\infty \ln \left| \frac{\omega + \omega_1}{\omega - \omega_1} \right| \frac{d\mu_1(\omega)}{d\omega}\, d\omega. \tag{8}$$

The last equality shows that the imaginary frequency characteristic is proportional to the slope of the real characteristic. However, inasmuch as the integration is carried out over the entire frequency range, the imaginary characteristic of any point depends on the slope of the real characteristic over the entire range of frequencies (from 0 to ∞). The relative effect of the slope in different parts of the frequency range is determined by the factor $\ln \left| \frac{\omega + \omega_1}{\omega - \omega_1} \right|$.

---

* $\ln(-x^2) = \ln x^2 + j\pi$. The derivative of a logarithm does not depend on the sign of the argument.

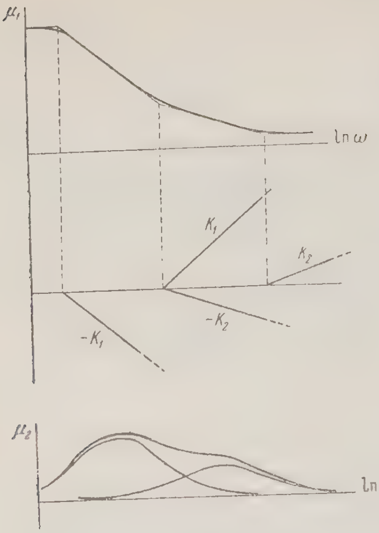

Fig.1. Derivation of the imaginary component $\mu_2(\omega)$ of the permeability from the real component $\mu_1(\omega)$.

Let us plot the dependence $\mu_1(\omega)$ in the logarithmic scale of frequencies $\lambda = \ln \omega$ and then replace the resultant curve by a series of rectilinear sections (Fig.1). Then for each i-th rectilinear section (i.e., the sections represented by horizontal lines $k = 0$ in Fig.1), we will have

$$\frac{d\mu_1(\omega)}{d\lambda} = k_i = \text{const} \tag{9}$$

Let us express the derivative $\frac{d\mu_1(\omega)}{d\omega}$ in terms of the slope k_i:

$$\frac{d\mu_1(\omega)}{d\omega} = \frac{d\mu_1(\omega)}{d\lambda} \cdot \frac{d\lambda}{d\omega} = \frac{k_i}{\omega}. \tag{10}$$

Substituting this value in (8), we find that we must integrate the function

$$\ln\left|\frac{\omega + \omega_1}{\omega - \omega_1}\right| \frac{d\omega}{\omega} = \ln\left|\frac{x+1}{x-1}\right| \frac{dx}{x} = L(x)\,dx, \tag{11}$$

where

$$x = \omega / \omega_1.$$

Let us use ω_{k_i} to designate the frequency corresponding to the beginning of the section for which the slope is characterized by k_i. The relative frequency corresponding to these points will be $x_{k_i} = \omega_{k_i} / \omega_1$.

Returning to the integral (8) and substituting (10) and (11) therein, we find that in the case of two sloping sections:

$$\mu_2(\omega) = -\frac{1}{\pi}\left\{k_1 \int_{x_{k_1}}^{x_{k_2}} L(x)\,dx + k_2 \int_{x_{k_2}}^{x_{k_3}} L(x)\,dx\right\}, \tag{12}$$

or, representing the curve by a series of semi-infinite inclined straight lines:

$$\mu_2(\omega) = -\frac{1}{\pi}\left\{k_1 \int_{x_{k_1}}^{\infty} L(x)\,dx - k_1 \int_{x_{k_2}}^{\infty} L(x)\,dx + k_2 \int_{x_{k_2}}^{\infty} L(x)\,dx - k_2 \int_{x_{k_3}}^{\infty} L(x)\,dx\right\}. \tag{13}$$

An advantage of the last expression is that all the integrals in it are identical functions of their lower limit:

$$I(x_k) = I\left(\frac{\omega_k}{\omega_1}\right) = \int_{x_k}^{\infty} \ln\left|\frac{x+1}{x-1}\right| \frac{dx}{x} \tag{14}$$

The integral (14) can readily be calculated by expanding the functions under the integral in a power series.[9] We get

$$I(x_k) = \frac{\pi^2}{2} - 2\left[x_k + \frac{x_k^3}{3^2} + \frac{x_k^5}{5^2} + \ldots\right] \text{ with } x_k < 1 \tag{15}$$

and

$$I(x_k) = 2\left[\frac{1}{x_k} + \frac{1}{3^2 x_k^3} + \frac{1}{5^2 x_k^5} + \ldots\right] \text{ with } x_k > 1. \tag{16}$$

It will be seen from these expressions that the sum of the functions $I(x_k)$ for the reciprocal values of the relative frequency equals $\pi^2/2$, i.e., that

$$I(x_k) + I\left(\frac{1}{x_k}\right) = \frac{\pi^2}{2}. \tag{17}$$

Hence to construct the entire function it is sufficient to know its value only in the region $x_k \leqslant 1$ or only in the region $x_k \geqslant 1$.

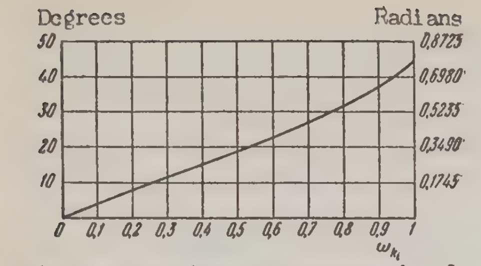

Fig.2. Imaginary component of the magnetic permeability corresponding to the semi-infinite straight line with unit slope.

After the values of the integral $I(x_k)$ have been found, the sought imaginary component of the frequency characteristic can be found as the sum of the imaginary characteristics obtained for each of the semi-infinite sloping straight lines.

A detailed plot of $\frac{1}{\pi} I\left(\frac{1}{x_k}\right)$ for $x_k > 1$ taken from Bode's book^5 is reproduced in Fig.2. Knowing the slope of each semi-infinite straight line we can find the imaginary characteristic corresponding to this straight line. In order to obtain this characteristic we need only multiply each ordinate of the curve in Fig.2 (which is plotted for a semi-infinite straight line with a unit slope between the limits $0 < 1/x_k < 1$) by the slope k and then draw in the second part of the characteristic, which is a symmetrical continuation of the curve thus obtained, approaching $k\pi/2$ at infinite frequency.

Thus to obtain the imaginary characteristic from an available real characteristic one must:

1) approximate the experimental (available) curve by a series of semi-infinite straight lines;

2) construct the component of the imaginary characteristic for each section: to this end we plot the imaginary characteristic for the semi-infinite straight line having the given slope at the beginning of the section and then the same characteristic at the end of the section; the difference between these gives the sought component;

3) sum the curves so obtained.

Of even greater practical interest is the possibility of recording the frequency characteristic of the modulus of the permeability and then determining the phase characteristic from it.

As noted above, the magnetic permeability at any frequency will be a complex quantity:

$$\mu(j\omega) = \mu_1(\omega) - j\mu_2(\omega) = \mu(\omega)\, e^{-j\delta(\omega)}, \tag{18}$$

where $\mu(\omega)$ is the frequency dependence of the modulus of the permeability and $\delta(\omega)$ is the frequency dependence of the phase of the permeability (loss angle).

Taking the logarithm of (18), we obtain

$$\ln\left[\mu(\omega)\, e^{-j\delta(\omega)}\right] = \ln \mu(\omega) - j\delta(\omega). \tag{19}$$

Eqs.(3) & (4), relating the real and imaginary components of permeability, were derived on the assumption that all the singularities of the function $\mu(p)$ are located in the left half-plane of the complex variable $p = \sigma + j\omega$. Analogously, the expressions relating the logarithms of the function $\mu(\omega)$ and the phase $\delta(\omega)$

$$\delta(\omega_1) = -\frac{2\omega_1}{\pi} \int_0^\infty \frac{\ln \mu(\omega)}{\omega^2 - \omega_1^2}\, d\omega \tag{20}$$

and

$$\ln \mu(\omega_1) - \ln \mu(\infty) = \frac{2}{\pi} \int_0^\infty \frac{\omega\, \delta(\omega)}{\omega^2 - \omega_1^2}\, d\omega \tag{21}$$

will be valid only provided the function $\ln \mu(p)$ does not have any singular points in the right half-plane, the imaginary axis $j\omega$ included.

Bearing in mind that zero for function $\mu(p)$ is equivalent to infinity for its logarithm, i.e., a singularity for the function $\ln \mu(p)$, the condition for the absence of singularities of the function $\ln \mu(p)$ in the right half-plane reduces the requirement that the function $\mu(p)$ must have not only no poles but also no zeros in the entire right half-plane including the imaginary axis.

It is not difficult to show that this requirement is fulfilled in our case.

Thus knowing the variation with frequency of $\ln \mu$ and applying the above described procedure for determining the imaginary component of the frequency characteristic from the real component, one can easily find the phase characteristic $\delta(\omega)$. Knowing the modulus and the phase one can readily calculate the real and imaginary components of the permeability.

For determining the modulus $\mu(\omega)$, it is essential to obtain the frequency dependence of the modulus of the impedance of the specimen. The circuit necessary for investigating specimens in this case can be assembled in any electronics laboratory. Voltage from an appropriate high-frequency source is applied to the specimen, the magnetizing winding on which is connected in series with a suitable thermoelement recording the magnitude of the current flowing through it; a cathode-ray voltmeter, designed for the frequency range in question, is connected in parallel with the specimen. Obviously, knowing the voltage and current from direct measurements, one can readily determine the impedance of the specimen.

The graphic analysis method of obtaining one characteristic from the other was used by the writers for analyzing the frequency dependence of the magnetic permeability of ferrites.

Good agreement of the experimental and calculated curves was obtained both in determining the frequency characteristic of the imaginary component of the permeability from the characteristic of the real component and in determining the phase characteristic from the amplitude characteristic.

Comparison of calculated values with experimental data shows that the suggested procedure can be used in the region of weak fields for measurements in the wide range of frequencies, a range extending to the region where the permeability drops off sharply.

Examples of determination of the imaginary characteristic from the real one and the phase characteristic from the amplitude characteristic for 0-2000 and 0-1000 (Oxifer-2000 and Oxifer-1000) ferrites are shown in Figs.3-6.

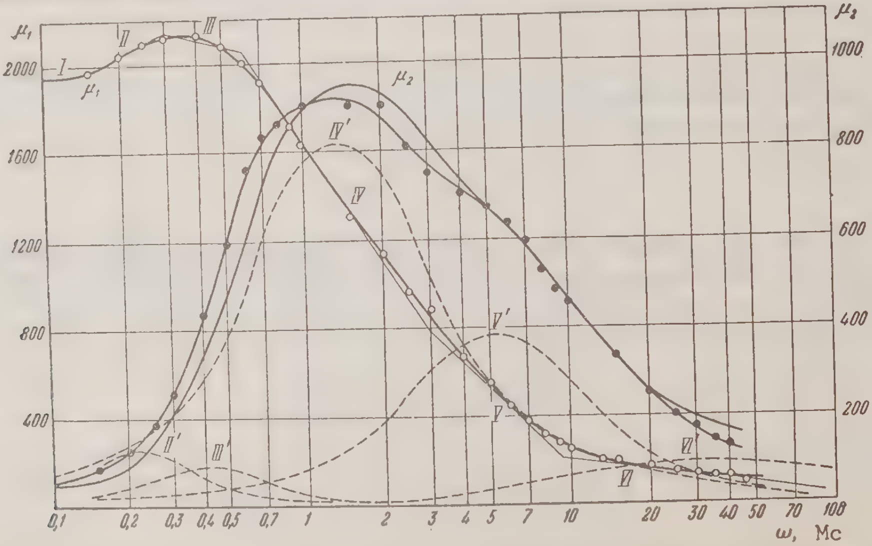

Fig.3. Frequency dependence of the real and imaginary components of the permeability of 0-2000 ferrite.

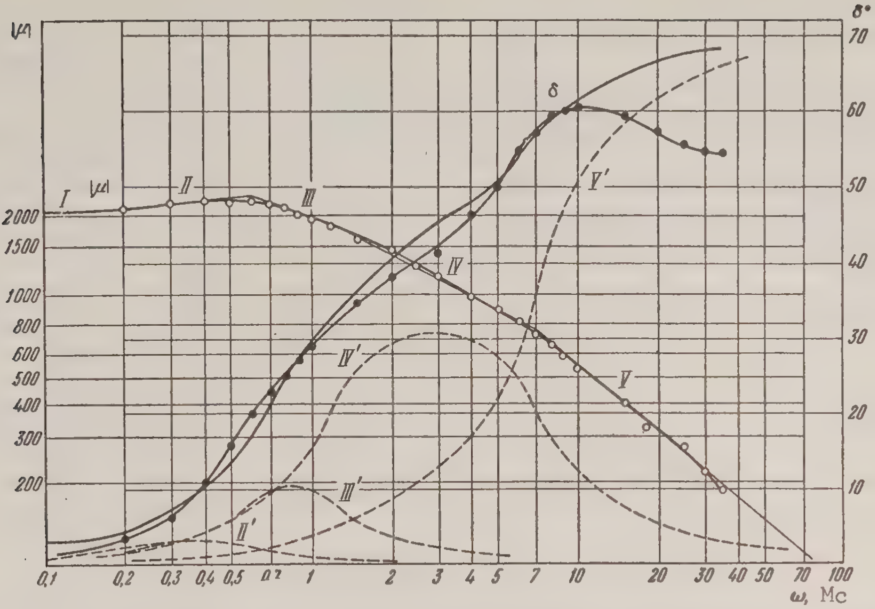

Fig.4. Frequency dependence of the amplitude and argument of the permeability of 0-2000 ferrite.

By way of illustration, let us examine the procedure for obtaining the characteristic of the imaginary component of the permeability from the characteristic of the real component for 0-2000 ferrite. The frequency characteristic of the real component $\mu_1(\omega)$ (Fig.3), obtained experimentally, was approximated by a broken line of six rectilinear sections. For each section we found the corresponding component of the imaginary characteristics (dash line curves), the value of which depended on the slope of the corresponding section and its length. Then all the components were summed. It will be seen that the resultant $\mu_2(\omega)$ curve agrees fairly well with the curve drawn through the experimental points.

In Fig.4 the amplitude characteristic $\mu(\omega)$ plotted to a logarithmic scale, was approximated by a broken line consisting of four sections. Then the corresponding component of the phase characteristic was found for each section (dash line curves) and the components added.

It will be seen that towards the end of the frequency range in question the calculated and experimental values for the phase characteristic diverge to some extent (the experimental curve is drawn through the points). The last section of the linear representation of the $\mu(\omega)$ curve is only partially plotted on the basis of the experimental data, while at the same time the trend of the curve in this section has an appreciable effect on the phase characteristic. In view of the fact that the actual shape of the experimental curve in the higher range of frequencies is not known, the linear extrapolation in this range comprises a source of possible error. This explains the divergence of the computed and experimental curves at the high end of the frequency range.

An analogous procedure was followed in plotting the curves for 0-1000 ferrite shown in Figs.5 & 6.

Good agreement of the experimental and calculated curves was also obtained in processing the results obtained by other investigators for different ferrmagnetic materials.

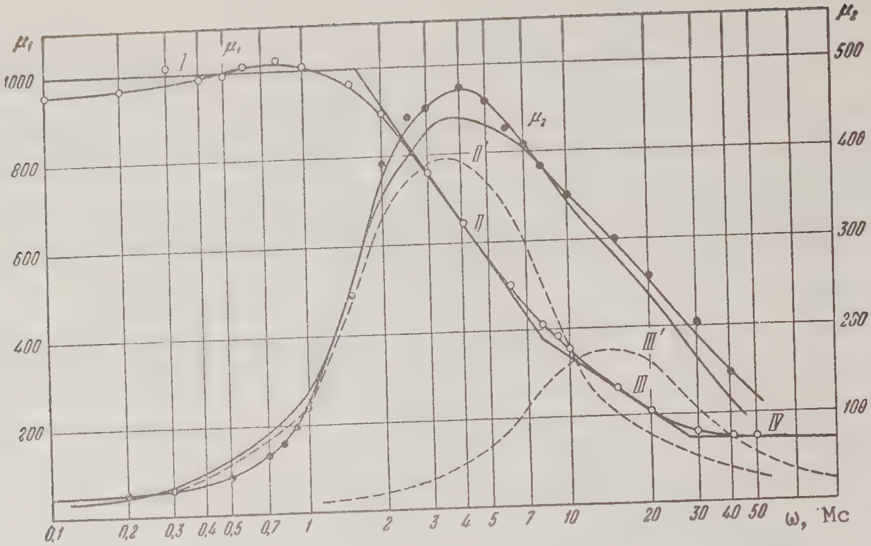

Fig.5. Same as Fig.3 but for 0-1000 ferrite.

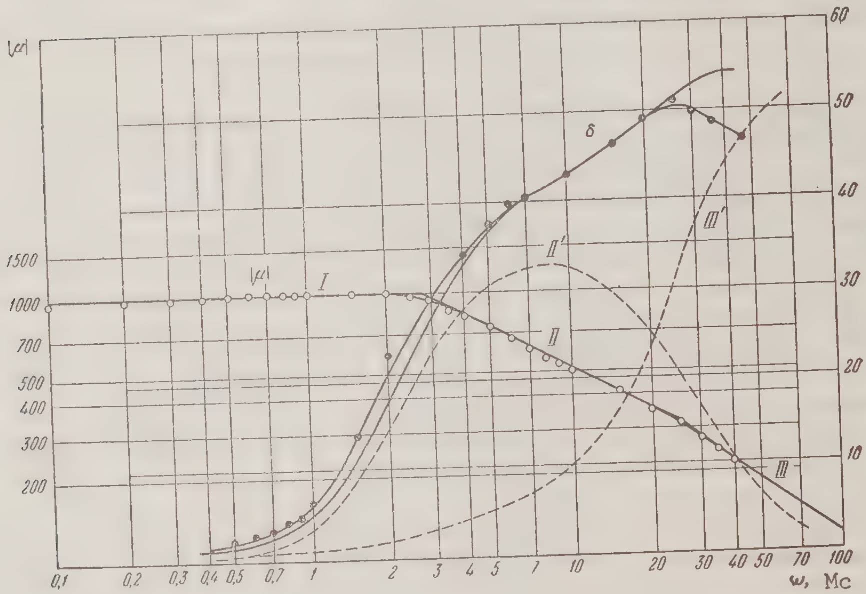

Fig.6. Same as Fig.4 but for 0-1000 ferrite.

"V.M.Molotov" Moscow Power Engineering Institute

References

1. V.K.Arkad'ev, Elektromagnitnye protsessy v metallakh (Electromagnetic processes in metals) Part II, M.-L., 1936.

2. H.A.Kramers, Atti del Congresso Internationale del Fisici, Como, v.2, p.545, 1927.

3. S.A.Al'tshuler, Zhur.eksp.i teor.fiz., 20, 1047 (1950).

4. I.M.Pomanov, Uch.zapiski Kazanskogo universiteta (Scientific Notes, Kazan University), 1953.

5. G.V.Bode, Teoriia tsepei i proektirovanie usilitelei s obratnoi sviaz'iu (The theory of circuits and the design of amplifiers with feedback), M.,1948.

6. M.I.Kontorovich, Operatsionnoe ischislenie i nestatsionarnye iavleniia v elektricheskikh tsepiakh (Operational computations and transient phenomena in electric circuits), M.-L., 1949.

7. V.V.Solodovnikov, Vvedenie v statisticheskuiu dinamiku sistem avtomaticheskogo regulirovaniia (Introduction to statistical dynamics of automatic control systems), M. 1952.

8. I.S.Gonorovskii, Radiosignaly i perekhodnye iavleniia v radiotsepiakh (Radio signals and transient phenomena in radio circuits), M. 1954.

9. G.B.Dwight, Tables of integrals and other mathematical formulas (M.1948).

SOME PROBLEMS IN THE THEORY OF GYROTROPIC MEDIA

- V.A.Fabrikov

Phenomenological Treatment of the General Case of a Gyrotropic Linear Electrodynamic Medium

1. In general, the linear relationships between the induction and displacement vectors B and D in a medium and the electromagnetic field vectors H and E can be written in the form

$$\left.\begin{aligned} B_i &= \mu_{ik}H_k + \eta_{ik}E_k, \\ D_i &= \xi_{ik}H_k + \varepsilon_{ik}E_k, \end{aligned}\right\} \; i, k = 1, 2, 3 \tag{1}$$

where the summation convention is used.

Since D and E are by definition true vectors, and B and H are pseudovectors (since the curl of a vector is a pseudovector, and vice versa), it is clear that μ_{ik} and ε_{ik} are tensors, and η_{ik} and ξ_{ik} are pseudotensors. The fact that the components may be complex is of no consequence, since just as a complex vector can be represented as the sum of two real vectors in actual space, a complex tensor can be represented as the sum of two tensors.

Tellegen[1] has shown that the electromagnetic parameters of a nondissipative medium must satisfy the condition

$$\varepsilon_{ik} = \varepsilon^*_{ki}, \quad \mu_{ik} = \mu^*_{ki}, \quad \xi_{ik} = \eta^*_{ki}, \quad (i, k = 1, 2, 3) \tag{2}$$

where the asterisk denotes the complex conjugate. We shall show that conditions (2) remain valid also for a medium with losses, if they are applied to the dissipative and nondissipative parts of the tensors separately.

Let us set

$$\left.\begin{aligned} \varepsilon_{ik} &= \varepsilon'_{ik} - i\varepsilon''_{ik}, \quad \xi_{ik} = \xi'_{ik} - i\xi''_{ik}, \\ \mu_{ik} &= \mu'_{ik} - i\mu''_{ik}, \quad \eta_{ik} = \eta'_{ik} - i\eta''_{ik}, \end{aligned}\right\} \tag{3}$$

and insert Eqs.(1) and (3) into the complex expression for the power per unit volume of the medium, then

$$P + iQ = i\,\frac{\omega}{2}\,(\mathbf{H}^*\mathbf{B} + \mathbf{E}^*\mathbf{D}), \tag{4}$$

where P and Q are real quantities, and correspond to the active and reactive parts of the power.

If we require that the primed tensors determine only the reactive part of the power, and that the double-primed tensors determine the active part, we will have

$$\left.\begin{aligned} H^*_i\mu'_{ik}H_k + H^*_i\eta'_{ik}E_k + E^*_i\xi'_{ik}H_k + E^*_i\varepsilon'_{ik}E_k &= 2\,\frac{Q}{\omega}, \\ H^*_i\mu''_{ik}H_k + H^*_i\eta''_{ik}E_k + E^*_i\xi''_{ik}H_k + E^*_i\varepsilon''_{ik}E_k &= 2\,\frac{P}{\omega}. \end{aligned}\right\} \; i, k = 1, 2, 3$$

Since these relations must be satisfied for all values of E and H, each of the quantities

$$H^*_i\mu'^{(\prime\prime)}_{ik}H_k, \quad E^*_i\varepsilon'^{(\prime\prime)}_{ik}E_k, \quad H^*_i\eta'^{(\prime\prime)}_{ik}E_k + E^*_i\xi'^{(\prime\prime)}_{ik}H_k$$

must be real. But this means that the pseudotensors ξ'_{ik} and η'_{ik} must be Hermitian conjugates, as must ξ''_{ik} and η''_{ik}; also the primed and double-primed parts of μ_{ik} and ε_{ik} must be self-conjugates, i.e., they must satisfy the conditions

$$\{\mu'^{(\prime\prime)}_{ik}\} = \{\mu'^{(\prime\prime)}_{ki}\}^*, \quad \{\varepsilon'^{(\prime\prime)}_{ik}\} = \{\varepsilon'^{(\prime\prime)}_{ki}\}^*, \quad \{\xi'^{(\prime\prime)}_{ik}\} = \{\eta'^{(\prime\prime)}_{ki}\}^*. \tag{5}$$

If a linear medium is gyrotropic about some axis, it must also be symmetric about this axis. In the orthogonal coordinate system in which the z-axis is along the symmetry axis of the medium, the tensor components can be written [r = g = gyrotropic]:

$$\left.\begin{array}{l} \mu_{ik}=\left\{\begin{matrix} \mu & -i\mu_r & 0 \\ i\mu_r & \mu & 0 \\ 0 & 0 & \mu_z \end{matrix}\right\}, \quad \varepsilon_{ik}=\left\{\begin{matrix} \varepsilon & -i\varepsilon_r & 0 \\ i\varepsilon_r & \varepsilon & 0 \\ 0 & 0 & \varepsilon_z \end{matrix}\right\}, \\ \eta_{ik}=\left\{\begin{matrix} \eta & -i\eta_r & 0 \\ i\eta_r & \eta & 0 \\ 0 & 0 & \eta_z \end{matrix}\right\}, \quad \xi_{ik}=\left\{\begin{matrix} \xi & -i\xi_r & 0 \\ i\xi_r & \xi & 0 \\ 0 & 0 & \xi_z \end{matrix}\right\}. \end{array}\right\} \tag{6}$$

It is easily shown that this equation follows from the condition that the tensor and pseudotensor characteristics of the medium are invariant under coordinate rotations about the symmetry axis.

Comparison of (5) and (6) shows that the imaginary parts of

$$\mu,\ \mu_r,\ \mu_z,\ \varepsilon,\ \varepsilon_r,\ \varepsilon_z,\ (\xi+\eta),\ (\xi_r+\eta_r),\ i(\xi-\eta),\ i(\xi_r-\eta_r)$$

characterize the losses and vanish for a nondissipative medium.

2. The solution of Maxwell's equations for a generalized gyrotropic medium defined in terms of Eqs.(6) is not, in principle, more difficult[2] than for what is called in the literature a special case of a gyrotropic medium, in which $\xi_{ik}=\eta_{ik}=0$. If we restrict ourselves to waves propagating longitudinally in a generalized gyrotropic medium, Maxwell's equations for the longitudinal components of the field reduce to the two simultaneous second order equations (see Appendix 1)

$$\left.\begin{array}{l} \nabla^2 E_z + aE_z + bH_z = 0, \\ \nabla^2 H_z + cH_z + dE_z = 0, \end{array}\right\} \tag{7}$$

just as in the case of an ordinary gyrotropic medium, except that the coefficients a, b, c and d are in this case somewhat more complicated expressions in terms of the parameters of the medium.

The absence of mixed second-order derivatives in Eq.(7) is due to the symmetry of the medium about the z-axis. The solution of such equations is well known.

The relation between the longitudinal and transverse components of the field in a generalized gyrotropic medium can be written

$$\left.\begin{array}{l} E_t = (p+qP)\nabla_t E_z + (r+sP)\nabla_t H_z, \\ H_t = (t+uP)\nabla_t E_z + (v+wP)\nabla_t H_z, \end{array}\right\} \tag{8}$$

where $p,\ q, r, s, t, u, v$ and w are constants defined in terms of the parameters of the medium, ∇_t is the projection of the gradient onto the t plane orthogonal to the z-axis, P is an operator whose action is equivalent to vector multiplication on the right by the unit vector k directed along the z-axis, i.e.,

$$P\mathbf{A}_t = [\mathbf{A}_t\mathbf{k}]; \tag{9}$$

here A_t means the projection of the vector A onto the t plane. From this it is easy to find the characteristic equation which serves to determine the propagation constant γ. In the case of a round waveguide, this equation is

$$\frac{inr}{R}(\sigma_1^2-\sigma_2^2) - \sigma_1[qb+(\sigma_1^2-a)s]\frac{J'_n(\sigma_1 R)}{J_n(\sigma_1 R)} + \sigma_2[qb+(\sigma_2^2-a)s]\frac{J'_n(\sigma_2 R)}{J_n(\sigma_2 R)} = 0, \tag{10}$$

where $J_n(x)$ is the Bessel function of n-th order, σ_1^2 and σ_2^2 are the roots of the equation $(\sigma^2)^2-(a+c)\sigma^2-(ac-bd)=0$, R is the radius of the waveguide, and r, q, s, a and b are the constant coefficients of Eqs.(7) and (8).

It should be noted that in the expression for these coefficients, the propagation constant enters both linearly and to second power, so that the value of propagation constant determined by the characteristic equation should depend on the direction of propagation of the wave. Thus a generalized gyrotropic medium, in addition to being gyrotropic, also has the property of being undirectional.

The propagation constants of longitudinal plane waves are easily found. They can be defined by requiring that the constant coefficients p, q, etc., in Eq. (8) become infinite (since only in this case do we have $\mathbf{E}_t, \mathbf{H}_t \neq 0$). when $E_z, H_z = 0$). For the particular case of plane waves in a generalized gyrotropic medium, however, it is simpler to give an independent solution.

Making use of the identity

$$[\nabla[\nabla\mathbf{A}]] = \nabla(\nabla\mathbf{A}) - \nabla^2\mathbf{A} \tag{11}$$

and the fact that for plane waves propagating in the k direction

$$\nabla = -\gamma\mathbf{k}, \tag{12}$$

let us transform Maxwell's equations

$$[\nabla\mathbf{E}] = -i\omega\mathbf{B}, \quad [\nabla\mathbf{H}] = i\omega\mathbf{D}, \quad \nabla\mathbf{B} = \nabla\mathbf{D} = 0 \tag{13}$$

by vector multiplication on the left by the operator ∇. We then have

$$\gamma\mathbf{E}_t = i\omega[\mathbf{B}\mathbf{k}], \quad \gamma\mathbf{H}_t = -i\omega[\mathbf{D}\mathbf{k}], \quad B_z = D_z = 0. \tag{14}$$

We now insert the linear expressions (whose form depends on the direction of propagation relative to the symmetry axis) for B and D in terms of H and E into Eq. (14). This leads to a set of six homogeneous linear equations in six unknowns, H_i and E_i (where i = 1, 2, 3). The propagation constant is found from the condition that the determinant of this set of equations vanishes.

In the case of longitudinal waves (with propagation in the direction of the symmetry axis) in a gyrotropic medium, we have

$$\left.\begin{aligned} B_{x,y} &= \mu H_{x,y} + \eta E_{x,y} \mp i\mu_\mathrm{r} H_{y,x} \mp i\eta_\mathrm{r} E_{y,x}, \\ D_{x,y} &= \xi H_{x,y} + \varepsilon E_{x,y} \mp i\xi_\mathrm{r} H_{y,x} \mp i\varepsilon_\mathrm{r} E_{y,x} \end{aligned}\right\} \tag{15}$$

and

$$\left.\begin{aligned} B_z &= \mu_z H_z + \eta_z E_z, \\ D_z &= \xi_z H_z + \varepsilon_z E_z. \end{aligned}\right\} \tag{16}$$

Inserting (15) into (14), we arrive at the set of equations

$$\left.\begin{aligned} -(\gamma + \omega\eta_\mathrm{r}) E_x + i\omega\eta E_y - \omega\mu_\mathrm{r} H_x + i\omega\mu H_y &= 0, \\ i\omega\eta E_x + (\gamma + \omega\eta_\mathrm{r}) E_y + i\omega\mu H_x + \omega\mu_\mathrm{r} H_y &= 0, \\ \omega\varepsilon_x E_x - i\omega\varepsilon E_y - (\gamma - \omega\xi_\mathrm{r}) H_x - i\omega\xi H_y &= 0, \\ i\omega\varepsilon E_x + \omega\varepsilon_\mathrm{r} E_y + i\omega\xi H_x - (\gamma - \omega\xi_\mathrm{r}) H_y &= 0, \end{aligned}\right\} \tag{17}$$

whose two independent solutions,

$$E_x = \mp iE_y, \quad H_x = \mp iH_y, \quad \frac{E_x}{H_y} = -\frac{E_y}{H_x} = i\frac{\omega(\mu \pm \mu_\mathrm{r})}{\gamma + \omega(\eta_\mathrm{r} \pm \eta)}, \tag{18}$$

correspond to right and left circularly polarized waves.

By inserting (19) in (17), it can readily be shown that the first solution corresponds to

$$\gamma = \frac{\omega}{2}(\xi_\mathrm{r} - \eta_\mathrm{r} + \xi - \eta) \pm i\omega\sqrt{(\varepsilon + \varepsilon_\mathrm{r})(\mu + \mu_\mathrm{r}) - \frac{1}{4}(\eta_\mathrm{r} + \xi_\mathrm{r} + \eta + \xi)^2},$$

and the second to

$$\gamma = \frac{\omega}{2}(\xi_\mathrm{r} - \eta_\mathrm{r} - \xi + \eta) \pm i\omega\sqrt{(\varepsilon - \varepsilon_\mathrm{r})(\mu - \mu_\mathrm{r}) - \frac{1}{4}(\eta_\mathrm{r} + \xi_\mathrm{r} - \eta - \xi)^2}. \tag{19}$$

We note that in the nondissipative case, the expressions under the radical signs in Eqs.(19) are real, and the terms in front of the radical signs are imaginary.

The undirectional character of a generalized gyrotropic medium, substantiated by Eqs.(19), could have been predicted from the fact that ξ_{ik} and η_{ik}, which describe the properties of the medium, are pseudotensors. The reverse wave may be considered as a direct wave with the opposite sense of rotation and in the coordinate system obtained by reflection through the origin. As opposed to true tensors, pseudotensors change sign under this coordinate transformation, and therefore a medium with nonvanishing ξ_{ik} and η_{ik} has different characteristics for waves propagating in opposite directions.

If the symmetry axis of the medium is determined by the direction of propagation, then in a stationary coordinate system the velocity of a right circularly polarized wave in the forward direction is the same as that of a left circularly polarized wave in the reverse direction. In this special case the nondiagonal elements of the tensors and pseudotensors vanish. An example of such media is an optically active substance, which becomes anisotropic when a wave passes through it, due to molecular asymmetry[3]. The unidirectionality is then manifested by the fact that the direction of polarization of a wave in a fixed coordinate system is different for waves in the forward and reverse directions.

In the microwave range, the relation between field vectors and pseudovectors should presumably obtain in a medium which is both ferromagnetic and ferroelectric. The realization of such a medium would make it possible to extend the practical possibilities of designing one-way microwave transmission systems.

Characteristics of the Faraday Effect in Paraffin-Ferrite Mixtures

1. Gyromagnetic and gyroelectric media are currently being used in designing unidirectional transmission systems. The gyromagnetic properties of magnetizable ferrites are of the greatest practical value. The physical explanation of these properties has been given by the theories of Polder[4], Rado[5], and Wangsness[6] based on the classical model of a ferromagnetic substance as developed by L.D.Landau and E.M.Lifshits[7]. There still remain, however, obscure points in the theory of the gyromagnetic properties of real polycrystalline ferromagnetic materials. It is, for instance, of interest to clarify the relation between the gyromagnetic properties of solid (continuous) and powdered (granular) ferrites. The assertion made by Birks[8] that for microwavelengths the magnetic parameters of a paraffin-ferrite mixture at all ferrite-powder concentrations are averages of the component parameters is somewhat doubtful. The experimental data used by Birks is evidently not general enough. This is indicated even by the qualitative changes in the magnetic properties of Fe-Mg-ferrite (Ferramic A) observed by Rado, Wright and Emerson[9]: the resonance frequency of the material was shifted and the entire magnetic spectrum modified when the ferrite was powdered and mixed with paraffin.

Below we present and discuss some results of an investigation of the Faraday effect in paraffin-ferrite mixtures at wavelengths of 10-14 cm. These results show the importance of taking into account the influence of the effective internal anisotropy fields on the gyromagnetic properties of magnetizable ferrites and the dependence of these fields on the mechanical state of the material.

2. The author has earlier described[10] experiments at frequencies from 2200 to 3000 Mc in longitudinal magnetizing fields from 0 to 1800 oersteds on specimens prepared of paraffin mixtures of the following powders: Ni-Zn-ferrite, natural Fe-ferrite (magnetite), and a metallic ferromagnetic, "Alsifer". These experiments give an anomolous rotation of the plane of polarization of waves passing through the samples, in that the rotation is in the direction opposite

to that obtained in solid ferrite discs.

The amount of rotation of the plane of polarization and the ellipticity (the axial ratio of the polarization ellipse) depend not only on the dimensions of the disc and the magnetizing field strength, but also on the frequency of the r-f field and the concentration of the powder.

In mixtures with Ni-Zn-ferrite, the axial ratio increases as a) the concentration of magnetic material is increased, b) the magnetizing field strength is increased (up to a certain limit, after which the axial ratio begins to decrease) and c) the frequency approaches 3000 Mc. The maximum rotation is observed at a definite value of the magnetizing field strength, which depends on the ac field frequency, and the amount of this maximum rotation first increases as the frequency is swept away from 3000 Mc, and then starts to decrease.

In paraffin-magnetite mixtures the amount of rotation and the axial ratio increases monotonically with the frequency.

The rotation observed in mixtures containing Mn-Zn-ferrite is more regular. It first has a positive sign, then passes through zero as the magnetizing field is increased, and finally becomes negative. A small right rotation, followed by passage through zero at low values (200-700 oersteds) of the magnetizing field and subsequent left rotation is also observed for Ni-Zn-ferrite mixtures, but only at frequencies higher than 2600 Mc.

The low losses in paraffin-ferrite mixtures (from 0.5 to 2 db/cm as opposed to 30 db/cm in solid ferrite samples) makes it possible to observe the dependence of the rotation on the thickness of the disc over a wide range (from 15 to 90 mm). This dependence, as may have been expected, is found to be highly nonlinear: as the thickness of the disc was increased, in some cases the rotation not only failed to increase, but, on the contrary, decreased by a factor of two.

For the purpose of comparison with the results obtained for mixtures, the Faraday rotation effect was measured in solid discs of Ni-Zn-ferrite in the same frequency and magnetizing field ranges. This rotation had the usual sign (positive or right-hand about the direction of the magnetizing field). Its dependence on the magnetizing field strength is of the hysteresis type; in fact, the rotation curve is quite a good reproduction of the magnetization curve. After magnetization in an 1800 oersted field (internal field of the order of 5 oersteds) a Ni-Zn-ferrite disc of thickness 10.5 mm is observed to give a remanent rotation of 13° (for a wavelength of 10 cm).

It should be noted that the character of the rotation in solid discs also depends on the frequency, although the dependence is opposite to that observed for mixtures; the ellipticity introduced by the solid disc increases, while the amount of rotation decreases as the frequency is reduced from 3000 to 2200 Mc.

3. Measurements of the Faraday rotation were performed on the set-up described in Ref.11.

In order to characterize the angle of rotation and axial ratio of the wave, we used the complex coefficient of polarization, which is the ratio of the amplitudes of the right and left circularly polarized waves constituting the linearly polarized wave. By using this coefficient, we can apply the method for measuring small travelling-wave ratios in transmission lines to the measurement of small ellipticities.

Having determined the angles φ_1 and φ_2 of the two positions of the analyzer at which the square-law detector reads twice the minimum value, we can calculate not only the rotation angle θ of the major axis of the transmitted wave polarization ellipse

$$\theta = \frac{\varphi_1 + \varphi_2}{2} + 90^\circ, \tag{1}$$

but also the axial ratio ϑ (see Appendix 2)

$$\vartheta^2 = \frac{\sin^2\left(\frac{\varphi_1 - \varphi_2}{2}\right)}{1+\sin^2\left(\frac{\varphi_1 - \varphi_2}{2}\right)}. \tag{2}$$

4. The change of sign of the Faraday rotation in Ni-Zn-ferrite when it is powdered and mixed with paraffin can be explained by the fact that in addition to the decrease in the size and interaction of the individual particles, the effective anisotropy field of the magnetic material increases.

This field is effective in the sense that it causes the same precession of the magnetic domains as does the corresponding magnetic field acting on free magnetic moments. It is clear that in the ac field the domains are impelled to precess about the total internal field (the anisotropy field plus the magnetic field), which defines their equilibrium positions, in the case when the material is not able to "adapt itself" to changes in the magnetic field only through domain wall displacements. The precession of the domains and, therefore, also the magnitude of the effective field capable of causing this precession, increase as domain wall displacement becomes more difficult. This is exactly what happens when the material is powdered and the individual particles approach single-domain size.

The theory of the magnetic properties of powders[12] explains the increase of the coercive force as the particle size is reduced and the packing density changes with the approach to the single-domain state.

The resultant anisotropy field in a weakly magnetized polycrystalline specimen may be weak if the preferred magnetization directions of the individual parts of the specimen are oriented at random. Nevertheless, the influence of "local" anisotropy fields on the gyromagnetic properties of the material is substantial.

Analysis of the expressions obtained by Rado[5] and Van Trier[13], for the components of the permeability tensor of an unsaturated material, shows that the (geometric) mean field acting through the whole volume of the sample determines only the absolute value of the gyromagnetic permeability of the substance. As for the sign of this permeability and the gyromagnetic loss tangent, in an unsaturated substance they are determined by the arithmetic mean of the absolute values of the effective internal fields within the individual domains. If the mean value is greater than the critical value at which the frequency of the intrinsic resonance losses, due to rotation processes, coincides with the ac field frequency, the Faraday rotation produced by the specimen will have a negative sign for any external magnetic field strength.

Let us note that ferrites are not, strictly speaking, ferromagnetic, but are ferrimagnetic, and in some cases it is important to take account of their specific ferrimagnetic properties. The theory of the permeability tensor of a ferrimagnetic substance whose crystal structure can be represented in the form of two coupled antiferromagnetic sublattices has been developed by Wangsness[6]. It was found that if magnetic losses and anisotropy fields are neglected, then, whenever the total angular momentum or magnetic moment of the sublattices does not vanish, the magnetic parameters of a ferrimagnet are described by the same equations as are those of a ferromagnet. The only difference is that instead of the true gyromagnetic ratio, one should use a certain effective ratio

$$\gamma_{ef}=\frac{M_1+M_2}{M_1/\gamma_1+M_2/\gamma_2}, \tag{3}$$

where γ_i and M_i are the gyromagnetic ratio and magnetization of the i-th sublattice, respectively.

Wangsness' result is easily generalized to the case of a dissipative medium[2]. It is then seen that the gyromagnetic losses of a ferrimagnetic can be accounted for in the ordinary way, attributing to it the relaxation frequency

$$\delta_{ef}=\left(\frac{\delta_1}{\gamma_1^2}+\frac{\delta_2}{\gamma_2^2}\right)\gamma_{ef}^2, \tag{4}$$

where δ_i is the relaxation frequency which describes the damping of precessional motion of the magnetization in the i-th sublattice.

It is important to note that the influence of the anisotropy fields on the gyromagnetic properties of a ferrimagnet is very strong. In the expression for the total internal field responsible for the gyromagnetic permeability of the ferrimagnetic substance, the anisotropy field should be multiplied by[2] the coefficient $\frac{|M_1|+|M_2|}{|M_1|-|M_2|}$. The role of the anisotropy fields increases as the absolute values of the sublattice magnetizations $|M_1|$ and $|M_2|$ become more nearly equal. Specifically, in ferrites a small change in the anisotropy field may lead to a noticeable effect.

In powdered Ni-Zn-ferrite the mean effective anisotropy field would seem to be greater, and in the solid ferrite, to be smaller than the critical value. The intrinsic resonance frequency in the former case is of the order of 3000 Mc, and in the latter case 2000 Mc. For mixtures with Mn-Zn-ferrite, it lies near 2100 Mc, and for mixtures with magnetite it is greater than 3000 Mc. This explains not only the various signs of the rotation, but also the particular character of the frequency dependence of the rotation and axial ratio observed for solid ferrites and for paraffin-ferrite mixtures of various compositions.

Appendix 1

Longitudinal Guided Waves in a Generalized Gyrotropic Medium

1. In order to write Maxwell's equations in a generalized gyrotropic medium, let us make use of the operator P, introduced by Suhl and Walker[14], whose action is equivalent to vector multiplication on the right by the unit vector **k** along the z axis

$$PA = [\mathbf{Ak}]. \tag{1}$$

It is easily shown that

$$\left.\begin{aligned} &[\mathbf{AB}]_z = \mathbf{A}_t(P\mathbf{B}_t),\\ &[\mathbf{AB}]_t = (P\mathbf{A}_t)\,B_z - A_z(P\mathbf{B}_t)\\ &(P\mathbf{A}_t)\,\mathbf{B}_t = -\mathbf{A}_t(P\mathbf{B}_t)\end{aligned}\right\} \tag{2}$$

and

$$P^2 = -1, \quad \frac{1}{a-bP} = \frac{a-bP}{a^2+b^2}, \tag{3}$$

where a and b are arbitrary numbers; the index t indicates projection of the vector on the t plane orthogonal to the z-axis.

On the assumption that all the components of the field vary as $\exp(i\omega t - \gamma z)$ and that the z-axis is along the symmetry axis of the medium, Maxwell's equations

$$[\nabla\,\mathbf{E}] = -i\omega\mathbf{B} \quad \text{and} \quad [\nabla\,\mathbf{H}] = i\omega\mathbf{D} \tag{4}$$

can be written in the new notation

$$\left.\begin{aligned} \omega(\varepsilon_r - i\varepsilon P)\,\mathbf{E}_t - (\gamma - \omega\xi_r + i\omega\xi P)\,\mathbf{H}_t &= \overline{\nabla}_t H_z, && \text{(a)}\\ (\gamma + \omega\eta_r - i\omega\eta P)\,\mathbf{E}_t + \omega(\mu_r - i\mu P)\,\mathbf{H}_t &= -\overline{\nabla}_t E_z, && \text{(b)}\\ \overline{\nabla}_t(P\mathbf{H}_t) &= i\omega(\varepsilon_z E_z + \xi_z H_z), && \text{(c)}\\ \nabla_t(P\mathbf{E}_t) &= -i\omega(\eta_z E_z + \mu_z H_z). && \text{(d)}\end{aligned}\right\} \tag{5}$$

Eqs.(5a) and (5b) are projections of Eqs.(4) on the t plane, while (5c) and (5d) are the projections on the z-axis; these are derived with the aid of (2) and (3) and the relations

---

Note: As above the subscript r = *gyromagnetic*. Trans.

$$\left.\begin{aligned} D_z &= \varepsilon_z E_z + \xi_z H_z, \\ B_z &= \eta_z E_z + \mu_z E_z, \\ \mathbf{D}_t &= (\varepsilon - i\varepsilon_\mathrm{r} P)\,\mathbf{E}_t + (\xi - i\xi_\mathrm{r} P)\,\mathbf{H}_t, \\ \mathbf{B}_t &= (\eta - i\eta_\mathrm{r} P)\,\mathbf{E}_t + (\mu - i\mu_\mathrm{r} P)\,\mathbf{H}_t, \end{aligned}\right\} \tag{6}$$

which follow from our definition of a generalized gyrotropic medium.

2. If we apply the operator $\overline{\nabla}_t$ to Eqs.(5a) and (5b), and then apply the operator $P\overline{\nabla}_t$ and invoke (5c), (5d) and (2), we arrive at

$$\left.\begin{aligned} \varepsilon\,\overline{\nabla}_t \mathbf{E}_t + \xi\,\overline{\nabla}_t \mathbf{H}_t &= [(\gamma - \omega\xi_\mathrm{r})\,\varepsilon_z + \omega\varepsilon_\mathrm{r}\eta_z]\,E_z + [(\gamma - \omega\xi_\mathrm{r})\,\xi_z + \omega\varepsilon_\mathrm{r}\mu_z]\,H_z, \\ \eta\,\overline{\nabla}_t \mathbf{E}_t + \mu\,\overline{\nabla}_t \mathbf{H}_t &= [(\gamma + \omega\eta_\mathrm{r})\,\eta_z - \omega\mu_\mathrm{r}\varepsilon_z]\,E_z + [(\gamma + \omega\eta_\mathrm{r})\,\mu_z - \omega\mu_\mathrm{r}\xi_z]\,H_z \end{aligned}\right\} \tag{7}$$

and

$$\left.\begin{aligned} (\gamma - \omega\xi_\mathrm{r})\,\overline{\nabla}_t \mathbf{H}_t - \omega\varepsilon_\mathrm{r}\,\overline{\nabla}_t \mathbf{E}_t &= -\nabla_t^2 H_z + \omega^2(\xi\varepsilon_z - \varepsilon\eta_z)\,E_z + \omega^2(\xi\xi_z - \varepsilon\mu_z)\,H_z, \\ \omega\mu_\mathrm{r}\,\overline{\nabla}_t \mathbf{H}_t + (\gamma + \omega\eta_\mathrm{r})\,\overline{\nabla}_t \mathbf{E}_t &= -\nabla_t^2 E_z - \omega^2(\gamma\mu_z + \mu\xi_z)\,H_z + \omega^2(\eta\eta_z + \mu\varepsilon_z)\,E_z. \end{aligned}\right\} \tag{8}$$

Eliminating $\overline{\nabla}_t \mathbf{E}_t$ and $\overline{\nabla}_t \mathbf{H}_t$ from (7) and (8), we obtain a pair of simultaneous equations of second order for the longitudinal field components, namely,

$$\left.\begin{aligned} \nabla_t^2 E_z + aE_z + bH_z = 0, \\ \nabla_t^2 H_z + cH_z + dE_z = 0, \end{aligned}\right\} \tag{9}$$

where

$$\left.\begin{aligned} a &= A_3B_4 - A_1A_2 - \omega^2(\eta\gamma_z + \mu\varepsilon_z), & c &= B_3A_4 - B_1B_2 - \omega^2(\xi\xi_z - \varepsilon\mu_z), \\ b &= A_3B_1 - A_4A_2 + \omega^2(\eta\mu_z + \mu\xi_z), & d &= B_3A_1 - B_4B_2 + \omega_2(\varepsilon\eta_z - \xi\varepsilon_z) \end{aligned}\right\} \tag{10}$$

and

$$\left.\begin{aligned} \Omega\cdot A_1 &= \eta_z\gamma + \omega(\eta_\mathrm{r}\eta_z - \mu_\mathrm{r}\varepsilon_z), & \Omega\cdot B_1 &= \xi_z\gamma - \omega(\xi_\mathrm{r}\xi_z - \varepsilon_\mathrm{r}\mu_z), \\ \Omega\cdot A_2 &= \xi\gamma + \omega(\eta_\mathrm{r}\xi - \mu_\mathrm{r}\varepsilon), & \Omega\cdot B_2 &= \eta\gamma - \omega(\xi_\mathrm{r}\eta - \varepsilon_\mathrm{r}\mu), \\ \Omega\cdot A_3 &= \mu\gamma + \omega(\eta_\mathrm{r}\mu - \mu_\mathrm{r}\eta), & \Omega\cdot B_3 &= \varepsilon\gamma - \omega(\xi_\mathrm{r}\varepsilon - \varepsilon_\mathrm{r}\xi), \\ \Omega\cdot A_4 &= \mu_z\gamma + \omega(\eta_\mathrm{r}\mu_z - \mu_\mathrm{r}\xi_z), & \Omega\cdot B_4 &= \varepsilon_z\gamma - \omega(\xi_\mathrm{r}\varepsilon_z - \varepsilon_\mathrm{r}\eta_z). \end{aligned}\right\} \tag{11}$$

Here $\Omega = \mu\varepsilon - \xi\eta$.

3. The transverse field components are readily expressed in terms of the longitudinal ones with the aid of Eqs.(5a) and (5b), from which it follows immediately that

$$\left.\begin{aligned} &[\omega^2(\varepsilon_\mathrm{r} - i\varepsilon P)(\mu_\mathrm{r} - i\mu P) + (\gamma + \omega\eta_\mathrm{r} - i\omega\eta P)(\gamma - \omega\xi_\mathrm{r} + i\omega\xi P)]\,\mathbf{E}_t = \\ &\qquad = \omega(\mu_\mathrm{r} - i\mu P)\,\overline{\nabla}_t H_z - (\gamma - \omega\xi_\mathrm{r} + i\omega\xi P)\,\overline{\nabla}_t E_z, \\ &[\omega^2(\varepsilon_\mathrm{r} - i\varepsilon P)(\mu_\mathrm{r} - i\mu P) + (\gamma + \omega\eta_\mathrm{r} - i\omega\eta P)(\gamma - \omega\xi_\mathrm{r} + i\omega\xi P)]\,\mathbf{H}_t = \\ &\qquad = -(\gamma + \omega\eta_\mathrm{r} - i\omega\eta P)\,\overline{\nabla}_t H_z - \omega(\varepsilon_\mathrm{r} - i\varepsilon P)\,\overline{\nabla}_t E_z. \end{aligned}\right\} \tag{12}$$

Using Eqs.(3), some simple operations lead to

$$\left.\begin{aligned} \mathbf{E}_t &= (p + qP)\,\overline{\nabla}_t E_z + (r + sP)\,\overline{\nabla}_t H_z, \\ \mathbf{H}_t &= (t + uP)\,\overline{\nabla}_t E_z + (v + wP)\,\overline{\nabla}_t H_z, \end{aligned}\right\} \tag{13}$$

where

$$\left.\begin{aligned} \Delta\cdot p &= -N(\gamma - \omega\xi_\mathrm{r}) - iM\omega\xi, & \Delta\cdot v &= -N(\gamma + \omega\eta_\mathrm{r}) + iM\omega\eta, \\ \Delta\cdot q &= M(\gamma - \omega\xi_\mathrm{r}) - iN\omega\xi, & \Delta\cdot w &= M(\gamma + \omega\eta_\mathrm{r}) + iN\omega\eta, \\ \Delta\cdot r &= \omega(N\mu_\mathrm{r} - iM\mu), & \Delta\cdot t &= -\omega(N\varepsilon_\mathrm{r} - iM\varepsilon), \\ \Delta\cdot s &= -\omega(iN\mu + M\mu_\mathrm{r}), & \Delta\cdot u &= \omega(iN\varepsilon + M\varepsilon_\mathrm{r}), \\ N &= \omega^2(\varepsilon_\mathrm{r}\mu_\mathrm{r} + \varepsilon\mu - \eta\xi - \eta_\mathrm{r}\xi_\mathrm{r}) + \omega\gamma(\eta_\mathrm{r} - \xi_\mathrm{r}) + \gamma^2, \\ M &= i\omega[\gamma(\xi - \eta) + \omega(\eta\xi_\mathrm{r} - \varepsilon\mu_\mathrm{r} - \mu\varepsilon_\mathrm{r} + \xi\eta_\mathrm{r})], \\ \Delta &= M^2 + N^2. \end{aligned}\right\} \tag{14}$$

In the case of plane waves it follows from $\nabla B = \nabla D = 0$ that $E_z = H_z = 0$ (if the special relation $\eta_z \xi_z = \varepsilon_z \mu_z$ is not fulfilled). But then from (13) and (14) we obtain

$$\Delta = M^2 + N^2 = 0 \quad \text{or} \quad N = \pm iM, \tag{15}$$

since in order for E_t and H_t to be nonzero when $E_z = H_z = 0$, it is necessary that the coefficients p, q, etc., be infinite. Eq.(15) makes it possible to determine the propagation constants of transverse waves in a generalized gyrotropic medium.

In the case of guided waves, the propagation constants are determined by the characteristic equation, which can be obtained by setting the tangential component of E equal to zero at the wall of the waveguide.

Appendix 2

The Angle of Rotation and Axial Ratio of the Polarization Ellipse

If in the complex representation the field is given by the expression

$$Ae^{i\omega t} = (A_1 e^{-i\varphi} + A_2 e^{i\varphi})\, e^{i\omega t} = |A_1|\, e^{i(\omega t - \varphi - \psi_1)} + |A_2|\, e^{i(\omega t + \varphi - \psi_2)}, \tag{1}$$

then on going to the instantaneous values of the field, we obtain

$$\operatorname{Re}(Ae^{i\omega t}) = a = a_0 \cos(\omega t - \psi), \tag{2}$$

where

$$a_0 = \sqrt{|A_1|^2 + |A_2|^2 + 2|A_1||A_2| \cos(2\varphi + \psi_1 - \psi_2)} = |A|. \tag{3}$$

The dependence of the field amplitude a_0 on the coordinate φ is given by the equation for the ellipse. The maximum value of a_0 (the major axis of the ellipse) is $|A_1| + |A_2|$ and occurs when

$$\varphi_{max} = \theta = \frac{\psi_2 - \psi_1}{2} \pm n \cdot 180^\circ \quad (n = 1, 2, 3, \ldots). \tag{4}$$

The minimum value of a_0 (the minor axis of the ellipse) is $|A_2| - |A_1|$ and occurs when

$$\varphi_{min} = \theta \pm 90^\circ. \tag{5}$$

The angle θ defines the angle of rotation of the major axis of the polarization ellipse with respect to the direction $\varphi = 0$.

Let us now introduce the coefficient of polarization, which is the ratio between the complex amplitudes of the right and left rotated waves, namely

$$S = \frac{A_1 e^{-i\varphi}}{A_2 e^{i\varphi}} = \frac{|A_1|}{|A_2|}\, e^{-i2(\varphi - \theta)} = -\frac{|A_1|}{|A_2|}\, e^{-i2(\varphi - \varphi_{min})}. \tag{6}$$

Then

$$|A|^2 = |A_2 e^{i\varphi}|^2 \cdot |1 + S|^2 = |A_2|^2 \{1 + |S|^2 - 2|S| \cos 2(\varphi - \varphi_{min})\} \tag{7}$$

and

$$|A|^2_{min} = |A_2|^2 (1 - |S|)^2. \tag{8}$$

If

$$|A|^2 = n^2 |A|^2_{min}, \tag{9}$$

then

$$n^2 = 1 + \frac{4|S|}{(1 - |S|)^2} \sin^2(\varphi_{1,2} - \varphi_{min}) = 1 + \left(\frac{1}{\vartheta^2} - 1\right) \sin^2(\varphi_{1,2} - \varphi_{min}),$$

or

$$\vartheta^2 = \frac{\sin^2(\varphi_{1,2} - \varphi_{min})}{n^2 - \cos^2(\varphi_{1,2} - \varphi_{min})}, \tag{10}$$

where

$$\vartheta = \frac{1 - |S|}{1 + |S|} = \frac{|A_2| - |A_1|}{|A_2| + |A_1|} \tag{11}$$

is the axial ratio of the polarization ellipse, and $\varphi_{1,2}$ are the angular positions pertaining to Eq.(9). It is obvious that $\varphi_1 - \varphi_{\min} = \varphi_{\min} - \varphi_2$, i.e., that $\varphi_{\min} = (\varphi_1 + \varphi_2)/2$.

When $n^2 = 2$, Eq.(10) becomes

$$\vartheta^2 = \frac{\sin^2\left(\frac{\varphi_1 - \varphi_2}{2}\right)}{1 + \sin^2\left(\frac{\varphi_1 - \varphi_2}{2}\right)}.$$

"V.M.Molotov" Moscow Power Engineering Institute

References

1. B.D.Tellegen, Philips Res. Rep., 3, 81 (1948).
2. V.A.Fabrikov, Dissertation, Moscow Power Inst., 1955.
3. M.Born, Optics.
4. D.Polder, Phil. Mag., 40, 99 (1949).
5. G.T.Rado, Phys.Rev., 89, 529 (1953).
6. R.K.Wangsness, Phys.Rev., 95, 339 (1954).
7. L.D.Landau and E.M.Lifshitz, Sow. Phys., 8, 153 (1935).
8. J.B.Birks, Proc. Phys. Soc., 60, 282 (1948).
9. G.T.Rado, R.W.Wright & W.H.Emerson, Phys. Rev., 80, 273 (1950).
10. V.A.Fabrikov, Doklady AN SSSR, 103, 807 (1955).
11. K.M.Polivanov, Ia.N.Kolli & M.B.Khasina, Izv. AN SSSR, Ser. fiz., 18, 350 (1954). (Trans. in Bulletin Vol. 18, No.3, p. 46.)
12. E.I.Kondorskii, Doklady AN SSSR, 70, 215 (1950); 80, 197 (1951); 82, 365 (1952).
13. A.A.Van Trier, Appl. Sci. Res., Sec. B, 3, 305 (1953).
14. H.Suhl & L.R.Walker, Bell System, Tech. J., 33, No.3 (1954).

APPROXIMATE METHODS OF CALCULATING GYROMAGNETIC MEDIA

- V.A.Fabrikov and Ia.N.Kolli

1. A gyromagnetic medium by definition is one whose permeability tensor can be written in the form [r = gyromagnetic]:

$$\mu_{ik} = \begin{Bmatrix} \mu & -i\mu_r & 0 \\ i\mu_r & \mu & 0 \\ 0 & 0 & \mu_z \end{Bmatrix}. \qquad (1)$$

Such a medium is capable of rotating the direction of polarization of a wave propagating within it along the z-axis (in the coordinate system in which the permeability tensor is of the form given by Eq.(1).

At high frequencies, as has been shown by Polder[1], any magnetic substance magnetized by a constant field becomes gyromagnetic. In practice gyromagnetic media are made of substances that have a high saturation magnetization and are sufficiently transparent to the electromagnetic radiation in the operating frequency range: for instance, ferrites in the microwave range.

A gyromagnetic medium is a special case of a linear electrodynamic medium. Its gyrotropic properties stem from the presence of a single symmetry axis. Any problem related to periodic phenomena in such a medium should be treated by ordinary phenomenological methods, i.e., by means of Maxwell's equations.

The solution of Maxwell's equations for longitudinal propagation of guided waves in gyromagnetic (and, in some cases, in gyroelectric) media was given at almost the same time by several authors: M.A.Gintsburg[2], Suhl and Walker[3], Kales[4], Gamo[5] and Van Trier[6]. A transcendental characteristic equation is found which determines the propagation constant γ for various types of normal waves in a gyrotropic waveguide with given parameters. This propagation constant enters the equations raised to the second power.

For longitudinal waves in a generalized gyrotropic medium (i.e., a linear electrodynamic medium characterized by a single symmetry axis) Maxwell's equations have been solved by one of the present authors[7,8]. An interesting characteristic of the general case is the attribute of unidirectionality which stems from the pseudotensor character of the linear relations between the field vectors **E** and **D** and the pseudovectors **H** and **B**.

It should be noted that in practice the propagation constant of a gyrotropic wave can be found by means of the transcendental characteristic equation only through somewhat complex graphical methods[3] or by an iteration procedure[11]. Even when the propagation constants of various gyrotropic waves are known, however, the problem of satisfying the boundary conditions at the interface between two waveguides, one of which is gyrotropic, is quite complicated and requires taking into account the entire infinite spectrum of the normal waves in both waveguides. The difficulty of matching the solutions for an isotropic and a gyrotropic waveguide at their interface is due to the fact that in the gyrotropic one the field distribution over the cross section is determined not only by the geometry of the section but also by the parameters of the medium.

Furthermore, the practical application of gyrotropic media (both gyromagnetic and gyroelectric media are now realized in practice) the design of unidirectional microwave transmission systems and various types of controlled attenuators, switches, etc., calls for methods of calculation that allow of relating experimentally measurable quantities (such as the angle of rotation and axial ratio of the polarization ellipse of the transmitted wave, the complex reflection coefficient at the output) with the parameters of the medium. The necessity of taking into account the finite thickness of the gyrotropic specimen has been demonstrated for plane waves in a gyrotropic layer (with a matched load at the output) by Polivanov, Kolli and Khasina[9].

In the present work we show the possibility of making engineering calculations in the case of some applications of gyromagnetic media. We consider the problem of a gyromagnetic disc of finite thickness completely filling the cross section of a circular waveguide terminated by an arbitrary load.

2. This problem can be solved in one of two approximations, the plane wave approximation in which the diameter of the waveguide is assumed sufficiently large compared to the wavelength in the gyromagnetic medium, and the first approximation with respect to the gyromagnetic parameter μ_r, when the medium is assumed to be weakly gyromagnetic.

In both cases the field in the gyromagnetic medium can be written as the sum of two right and left circularly polarized waves, with regard to which the medium is characterized by an effective scalar permeability[7-9] or, what is equivalent, by an effective wave impedance for the operating mode (with known propagation constants). This resolution of the field into circularly polarized waves is obviously also feasible for the isotropic parts of the waveguide.

Let us find the reflection and transmission coefficients for each component wave separately, using the usual methods applicable to isotropic media. The former are given by

$$\rho_{1,2} = \frac{A^-_{1,2}}{A^+_{1,2}} = \frac{(Z_{1,2} - 1/Z_{1,2}) + 2n \operatorname{cth} \gamma_{1,2} l - n (Z_{1,2} + 1/Z_{1,2})}{(Z_{1,2} + 1/Z_{1,2}) + 2 \operatorname{cth} \gamma_{1,2} l - n (Z_{1,2} - 1/Z_{1,2})} \cdot \tag{2}$$

and the transmission coefficients by

$$K_{1,2} = \frac{C^+_{1,2}}{A^+_{1,2}} = \frac{1}{\operatorname{ch} \gamma_{1,2} l + \frac{1}{2} (Z_{1,2} + 1/Z_{1,2}) \operatorname{sh} \gamma_{1,2} l - \frac{n}{2} (Z_{1,2} - 1/Z_{1,2}) \operatorname{sh} \gamma_{1,2} l}, \tag{3}$$

where A and C are the wave amplitudes at the input and output of the disc, Z is the normalized effective wave impedance of the disc, and $n = C^-/C^+$ is the load factor at the output (see Appendix 1). The indices (+) and (-) refer to the forward and reflected waves, and the indices 1 and 2 refer to the right and left polarized waves.

If the forward wave is linearly polarized in front of the disc, i.e., if $A^+_1 = A^+_2$, then the total reflection coefficient at the output, which can be experimentally determined with the aid of a measuring line, (in the plane of polarization of the incident wave) is

$$\rho = \frac{1}{2} (\rho_1 + \rho_2). \tag{4}$$

It is convenient to characterize the angle of rotation and the axial ratio of the polarization ellipse at the output by the complex coefficient of polarization S, which is the ratio between the complex amplitudes of the right and left circularly polarized waves at the output. Using Eq.(3), we obtain

$$S = \frac{C_1}{C_2} = \frac{2 \operatorname{ch} \gamma_2 l + (Z_2 + 1/Z_2) \operatorname{sh} \gamma_2 l - n (Z_2 - 1/Z_2) \operatorname{sh} \gamma_2 l}{2 \operatorname{ch} \gamma_1 l + (Z_1 + 1/Z_1) \operatorname{sh} \gamma_1 l + n (Z_1 - 1/Z_1) \operatorname{sh} \gamma_2 l}. \tag{5}$$

When the load is matched at the output, $n = 0$ and

$$S = \frac{2 \operatorname{ch} \gamma_2 l + (Z_2 + 1/Z_2) \operatorname{sh} \gamma_2 l}{2 \operatorname{ch} \gamma_1 l + (Z_1 + 1/Z_1) \operatorname{sh} \gamma_1 l}. \tag{6}$$

In the case of a lossy (dissipative) medium, when $\operatorname{Re} (\gamma_{1,2} l)$ is so large that we may set

$$\operatorname{ch} \gamma_{1,2} l = \operatorname{sh} \gamma_{1,2} l = \frac{1}{2} e^{\gamma_{1,2} l}, \tag{7}$$

the expressions for S and ρ for $n = 0$ become

$$S = \frac{2 + (Z_2 + 1/Z_2)}{2 + (Z_1 + 1/Z_1)} e^{(\gamma_2 - \gamma_1) l},$$

and

$$\rho = \frac{1}{2}\left(\frac{Z_1 - 1}{Z_1 + 1} + \frac{Z_2 - 1}{Z_2 + 1}\right) = \frac{Z_1 Z_2 - 1}{(Z_1 + 1)(Z_2 + 1)}. \quad (8)$$

For a weakly gyromagnetic medium

$$\gamma_{1,2} = \gamma_0 \mp \Delta\gamma, \quad Z_{1,2} = Z_0 \pm \Delta Z, \quad (9)$$

wherein

$$\gamma_0 = \gamma_0(\mu, \varepsilon), \quad Z_0 = Z_0(\mu, \varepsilon), \quad \frac{\Delta\gamma}{\gamma_0} \ll 1, \quad \frac{\Delta Z}{Z_0} \ll 1. \quad (10)$$

Expanding in a Taylor's series according to

$$\left.\begin{aligned} & f(x_0 \pm \Delta x) = f(x_0) \pm \Delta x \left(\frac{\partial f}{\partial x}\right)_{x=x_0} + \cdots \\ \text{and} \quad & \frac{\varphi(x_0 + \Delta x)}{\varphi(x_0 - \Delta x)} = 1 + 2\,\Delta x \left(\frac{\varphi'(x)}{\varphi(x)}\right)_{x=x_0} + \cdots, \end{aligned}\right\} \quad (11)$$

Eqs.(3)-(5) lead to

$$S = 1 + \Delta\gamma l \frac{1 + (r_1 Z_0 + r_2 / Z_0) \operatorname{cth} \gamma_0 l + 1/l \left[\frac{\partial}{\partial\gamma}(r_1 Z + r_2/Z)\right]_{\gamma=\gamma_0}}{\operatorname{cth} \gamma_0 l + (r_1 Z_0 + r_2/Z_0)}, \quad (12)$$

where $r_1 = \frac{1-n}{2}$, $r_2 = \frac{1+n}{2}$, and

$$\rho = \rho_0 = \frac{(Z_0 - 1/Z_0) + 2n \operatorname{cth} \gamma_0 l - n(Z_0 + 1/Z_0)}{(Z_0 + 1/Z_0) + 2 \operatorname{cth} \gamma_0 l - n(Z_0 - 1/Z_0)}. \quad (13)$$

For a matched load, $n = 0$ and

$$S = 1 + \Delta\gamma l \frac{2 + (Z_0 + 1/Z_0) \operatorname{cth} \gamma_0 l + 1/l \left[\frac{\partial}{\partial\gamma}(Z + 1/Z)\right]_{\gamma=\gamma_0}}{2 \operatorname{cth} \gamma_0 l + (Z_0 + 1/Z_0)}. \quad (12a)$$

It follows from Eqs.(12) and (13) that the reflection coefficient and the dependence of the polarization coefficient on the thickness of the weakly gyromagnetic specimen are determined by the usual isotropic parameters μ and ϵ. The gyromagnetic properties of the sample, which are characterized by μ_r, affect the magnitude of the polarization coefficient.

3. The polarization coefficient is just as simply related to the angle of rotation and axial ratio of the polarization ellipse at the output of the sample[8] (both experimentally measurable quantities) as the reflection coefficient is related to the traveling wave ratio and the position of the minimum electric field strength at the input to the specimen.

If S and ρ are measured for two known loads at the output (for instance, with a short circuit, $n = -1$, and with an open circuit, $n = 1$), Eqs.(3)-(5) can be used to calculate $Z_{1,2}$ and $\gamma_{1,2}$. It is more convenient, however, to perform the measurement with three known loads (for instance $n = 0$, $+1$ and -1) and then use Eqs. (3)-(5) to calculate $Z_{1,2}$, $\operatorname{sh}\gamma_{1,2}l$, and $\operatorname{ch}\gamma_{1,2}l$ and to test the results so obtained by the identity

$$\operatorname{ch}^2 \gamma_{1,2} l - \operatorname{sh}^2 \gamma_{1,2} l = 1.$$

In the case of a weakly gyromagnetic medium, two measurements of ρ (with $n = \pm 1$) and one measurement of S (with $n = 0$) are sufficient. One can then use the experimental data and Eqs.(12) and (13) to calculate

$$\left.\begin{aligned} Z_0 &= \sqrt{\frac{1+\rho_x}{1-\rho_x}\frac{1+\rho_k}{1-\rho_k}} = \sqrt{Z_{\text{in}}^x \cdot Z_{\text{in}}^k}, \\ \operatorname{cth} \gamma_0 l &= \sqrt{\frac{1+\rho_x}{1-\rho_x} \cdot \frac{1+\rho_k}{1+\rho_k}} = \sqrt{Z_{\text{in}}^x / Z_{\text{in}}^k} \end{aligned}\right\} \quad (14)$$

and

$$\left.\begin{aligned} \Delta\gamma &= \frac{1}{2}\cdot\frac{2\,\mathrm{cth}\,\gamma_0 l + (Z_0 + 1/Z_0)}{l\,[2 + (Z_0 + 1/Z_0)\,\mathrm{cth}\,\gamma_0 l] + \left\{\frac{\partial}{\partial\gamma}(Z + 1/Z)\right\}_{\gamma=\gamma_0}}\cdot(S_{n=0} - 1), \\ S - 1 &= \left(\frac{1-\rho}{1+\rho}\cos 20 - 1\right) + i\left(\frac{1-\rho}{1+\rho}\sin 20\right), \end{aligned}\right\} \quad (15)$$

where Z^{x}_{in} is the input impedance of the disc with $n = 1$, Z^{k}_{in} is the input impedance with $n = -1$, θ is the angle of rotation, and ρ is the ellipticity or axial ratio of the polarization ellipse at the output.

In order to obtain the final formulas relating the experimentally determined quantities S and ρ to the electromagnetic parameters ϵ, μ, μ_r, we must express the quantities $Z_{1,2}$ and $\gamma_{1,2}$ (and in the case of a weakly gyromagnetic medium, also Z_0, γ_0 and $\Delta\gamma$) in terms of these parameters.

For plane waves we have[8,9]

$$Z_{1,2} = \sqrt{\frac{(\mu \pm \mu_r)}{\varepsilon}}, \quad \gamma_{1,2}^2 = -\,\omega^2\varepsilon\,(\mu \pm \mu_r)\,\varepsilon_0\mu_0, \quad (16)$$

where μ_0 and ϵ_0 are the permeability and dielectric constant for vacuum.

For a weakly gyromagnetic disc which completely fills the cross section of a circular waveguide of radius R whose isotropic part transmits only the fundamental H_{11} mode we have (with the additional condition that $\mu_z = \mu$) (see Appendix 2):

$$\begin{gathered} Z_{1,2} = Z_0\frac{\gamma_{1,2}}{\gamma_0}, \quad \gamma_{1,2} = \gamma_0\left(1 \pm 0{,}42\frac{\mu_r}{\mu}\right), \\ Z_0 = \frac{\mu\gamma_B}{\gamma_0}, \quad \gamma_0^2 = \left(\frac{1{,}84}{R}\right)^2 - \omega_2\varepsilon\mu\varepsilon_0\mu_0, \quad \gamma_B^2 = \left(\frac{1{,}84}{R}\right)^2 - \omega^2\varepsilon_0\mu_0. \end{gathered} \quad (17)$$

In this case Eqs.(12) and (15) become

$$\left.\begin{aligned} S &= 1 + 2\,\Delta\gamma l\,\frac{1 + (r_1Z_0 + r_2/Z_0)\,\mathrm{cth}\,\gamma_0 l + \frac{1}{\gamma_0 l}(r_1Z_0 - r_2/Z_0)}{\mathrm{cth}\,\gamma_0 l + (r_1Z_0 + r_2/Z_0)}, \\ \Delta\gamma &= \frac{1}{2}\cdot\frac{2\,\mathrm{cth}\,\gamma_0 l + (Z_0 + 1/Z_0)}{l\,[2 + (Z_0 + 1/Z_0)\,\mathrm{cth}\,\gamma_0 l] + \frac{1}{\gamma_0}(Z_0 - 1/Z_0)}\,(S_{n=0} - 1). \end{aligned}\right\} \quad (18)$$

The values of the propagation constants obtained in the plane wave approximation can be checked and in some cases made more accurate by means of an iteration method which involves inserting them into the transcendental characteristic equation which determines the propagation constant of the funcamental gyrotropic wave in a waveguide. Such calculations have been performed for the particular case of a Ni-Zn-ferrite disc 10.5 mm thick completely filling the cross section of an 82 mm diameter circular waveguide and magnetized by a longitudinal constant field H = 1400 oersteds, and for a wavelength of 10 cm. The calculations[11] showed that the values of $\gamma_{1,2}$ as deduced from the plane wave equations and from the transcendental characteristic equation for quasi-H_{11} waves differ by 6%.

Eqs.(13) and (18), which pertain to weakly gyromagnetic media in circular waveguides, were used and verified in investigating the Faraday effect in paraffin-ferrite mixtures. Good agreement was obtained between the theoretical and experimental curves for the dependence of the effect on the thickness of a longitudinally magnetized paraffin-ferrite disc in a circular waveguide.[7]

Appendix 1

Reflection and Transmission Coefficients of a Homogeneous Isotropic Disc in a Waveguide

Let us divide the space within the waveguide into three regions, I, II and III: regions I and III are empty sections of the waveguide, and region II is the section filled by the disc.

We specify the field in each of the three regions in the ξ, η, z orthogonal coordinate system by the expressions

$$\left.\begin{aligned} &\text{I. } E_\xi = E_\xi^+ + E_\xi^- = A_1 e^{-i\beta z} + A_2 e^{i\beta z}, \\ &\text{II. } E_\xi = E_\xi^+ + E_\xi^- = B_1 e^{-\gamma z} + B_2 e^{\gamma z}, \\ &\text{III. } E_\xi = E_\xi^+ + E_\xi^- = C_1 e^{-i\beta z} + C_2 e^{i\beta z}, \end{aligned}\right\} \quad H_\eta = \frac{E_\xi^+ - E_\xi^-}{Z}. \tag{1}$$

Let us introduce the notation

$$n = \frac{C_2}{C_1} \quad \text{and} \quad Z = \frac{Z_{II}}{Z_{I,\,III}}. \tag{2}$$

The validity of the integral relations (1) follows from the fact that the respective field components depend on ξ and η in the same way in all three regions.

In order to find the arbitrary constants in the solution to Maxwell's equations given by Eqs. (1), let us use the boundary conditions on the faces of the disc, which follow from the requirement that the tangential components of the field be continuous:

Interface I-II

$$\left.\begin{aligned} A_1 + A_2 &= B_1 + B_2, \\ (A_1 - A_2) Z &= B_1 - B_2, \end{aligned}\right\} \quad \left.\begin{aligned} A_1 &= \frac{1}{2}\left(1 + \frac{1}{Z}\right) B_1 + \frac{1}{2}\left(1 - \frac{1}{Z}\right) B_2, \\ A_2 &= \frac{1}{2}\left(1 - \frac{1}{Z}\right) B_1 + \frac{1}{2}\left(1 + \frac{1}{Z}\right) B_2; \end{aligned}\right\} \tag{3}$$

Interface II-III

$$\left.\begin{aligned} B_1 e^{-\gamma l} + B_2 e^{\gamma l} &= C_1 (1 + n), \\ B_1 e^{-\gamma l} - B_2 e^{\gamma l} &= Z C_1 (1 - n), \end{aligned}\right\} \quad \left.\begin{aligned} B_1 &= \left(\frac{1+Z}{2} + n\frac{1-Z}{2}\right) C_1 e^{\gamma l}, \\ B_2 &= \left(\frac{1-Z}{2} + n\frac{1+Z}{2}\right) C_1 e^{-\gamma l}. \end{aligned}\right\} \tag{4}$$

Inserting (4) into (3), we obtain

$$\left.\begin{aligned} C_1 &= \frac{A_1}{\operatorname{ch}\gamma l + \frac{1}{2}(Z + 1/Z)\operatorname{sh}\gamma l - \frac{n}{2}(Z - 1/Z)\operatorname{sh}\gamma l}, \\ A_2 &= C_1\left[n \operatorname{ch}\gamma l + \frac{1}{2}(Z - 1/Z)\operatorname{sh}\gamma l - \frac{n}{2}(Z + 1/Z)\operatorname{sh}\gamma l\right] = \\ &= A_1 \frac{n \operatorname{ch}\gamma l + \frac{1}{2}(Z - 1/Z)\operatorname{sh}\gamma l - \frac{n}{2}(Z + 1/Z)\operatorname{sh}\gamma l}{\operatorname{ch}\gamma l + \frac{1}{2}(Z + 1/Z)\operatorname{sh}\gamma l - \frac{n}{2}(Z - 1/Z)\operatorname{sh}\gamma l}. \end{aligned}\right\} \tag{5}$$

This immediately determines the transmission and reflection:

$$\left.\begin{aligned} K &= \frac{C_1}{A_1} = \frac{1}{\operatorname{ch}\gamma l + \frac{1}{2}(Z + 1/Z)\operatorname{sh}\gamma l - \frac{n}{2}(Z - 1/Z)\operatorname{sh}\gamma l}, \\ \rho &= \frac{A_2}{A_1} = \frac{(Z - 1/Z) + 2n \operatorname{cth}\gamma l - n(Z + 1/Z)}{(Z + 1/Z) + 2\operatorname{cth}\gamma l - n(Z - 1/Z)}. \end{aligned}\right\} \tag{6}$$

Appendix 2

Method for Determining the Effective Wave Impedance of a Weakly Gyromagnetic Disc for the Fundamental Wave in a Circular Waveguide

The solution of the boundary problem at the face of a gyrotropic disc in a waveguide requires expanding the gyrotropic waves, produced at the inner surface of the disc, into an infinite series of nongyrotropic components, i.e., functions with a single amplitude, that characterize the distribution of the different nongyrotropic modes over the cross section of the waveguide. Equating the expansion coefficients to the amplitudes of the corresponding nongyrotropic waves originating at the outer surface of the disc, we obtain an infinite set of equations for determining the infinite number of unknown amplitudes of the gyrotropic and nongyrotropic waves excited at the interface.

In a waveguide which transmits only one type of wave, we are directly interested only in the amplitude of this mode, since all the other waves are damped at the surface of the disc and have almost no influence on the field distribution in the waveguide outside the disc. In other words, we are interested only in the first coefficients of the series of nongyrotropic components; but to find these coefficients we must know the field distribution in the disc, and this is impossible to calculate without taking into account all higher gyrotropic and nongyrotropic modes.

In the case of a weakly gyromagnetic medium, however, in the first approximation to the small gyromagnetic parameter μ_r, considering all the gyrotropic wave amplitudes in the disc, except that of the quasi-H_{11} wave, to be negligibly small, we can join the H_{11} wave incident on the disc only to the quasi-H_{11} wave. In the expression for the first expansion coefficient, we shall treat all terms due to higher gyrotropic waves as second order quantities.

The disc may be considered isotropic, and the H_{11} wave within it (or, more accurately the right or left circularly polarized component of this wave) can be described in terms of the propagation constant of the quasi-H_{11} wave and an effective wave impedance which is equal to the ratio of the first terms in the expansion of the transverse components of the electric and magnetic fields of the quasi-H_{11} mode. Using the orthogonality and normalization conditions for the nongyrotropic components, and Green's and Stokes' theorems for the transformation of two-dimensional surface integrals into line integrals, we can compute this ratio and thus determine the effective wave impedance.

This method has been used by one of the authors[7] to find expressions for the effective wave impedances of a weakly gyromagnetic disc in a circular waveguide for circularly polarized H_{11} waves; these expressions are Eqs.(17) of the present article.

"V.M.Molotov" Moscow Power Engineering Institute

References

1. D.Polder, Phil. Mag. 40, 99 (1949).
2. M.A.Gintsburg, Doklady AN SSSR, 95, 489 (1954); Dissertation, Moscow Power Eng. Inst. 1953; Izv. AN SSSR, Ser. fiz., 18, 444 (1954). (Trans. of last in Bulletin, Vol. 18, No.4, p.136).
3. H.Suhl & L.Walker, Phys.Rev., 86, 122 (1952); Bell Syst. Tech. Journal, 33, No.3 (1954).
4. M.L.Kales, Trans. IRE, Antennas 4, 104 (1952); J.Appl.Phys., 24, 604 (1953).
5. H.J.Gamo, Phys. Soc. Japan, 8, 176 (1953).
6. A.A.Van Trier, Appl. Sci. Res., Sect.B, 3, 305 (1953).
7. V.A.Fabrikov, Dissertation, Moscow Power Eng. Inst., 1955.
8. V.A.Fabrikov, Present issue of the Bulletin, p. 1204.
9. K.M.Polivanov, Ia.N.Kolli & M.B.Khastina, Iav. AN SSSR, Ser. fiz., 18, 350 (1954). (Trans. in Bulletin Vol.18, No.3, p.46.)
10. V.A.Fabrikov, Doklady AN SSSR, 103, 807 (1955).
11. Ia.N.Kolli, Moscow Power Eng. Inst., 1955.

MAGNETIC SPECTRA OF SOLID SOLUTIONS OF Ni-Zn-FERRITES IN THE RADIOFREQUENCY RANGE AT TEMPERATURES CLOSE TO THE CURIE POINT

- L.A.Fomenko

1. Introduction

The dependence of r-f magnetic spectra of polycrystalline mixed ferrites on the temperature was first partially studied by Lindenhovius[1]; however, since his investigations comprised only measurements of the dispersion curves it was impossible to draw any quantitative conclusions regarding the general nature of the temperature dependence of the magnetic spectra, i.e., (according to Arkad'ev[2]) the curves characterizing the dispersion of the real (elastic) $\mu(f)$* and the absorption of the imaginary (viscous) $\rho'(f)$ components of the complex magnetic permeability $\mu' = \mu - j\rho'$ of the ferromagnetic material.

The results of complete investigations of the magnetic spectra of ferrites, including measurements of both dispersion and absorption curves at different temperatures can be found in earlier contributions of the writer[3] and the reports of Rado, Wright, Emerson and Terris[4]. The general nature of the temperature dependence of the r-f magnetic spectra observed in these investigations agrees with the qualitative data of Lindenhovius as well as those of Smit and Wijn[5] (p.116), although it is substantially different from the analogous dependence for single crystal specimens[6,7]. Quantitatively, the temperature dependence of the magnetic spectra of ferrites observed in the investigations of Refs.3 & 4 has been described by different formulas. In Ref.4 dependence is described by the formula

$$f_0 \approx f'_0 \approx F'_0 \approx gJ_s, \tag{1}$$

where g is the spectroscopic splitting factor, f_0 and f'_0 are the average resonance frequencies of r-f and microwave dispersion for a solid polycrystalline ferrite specimen, respectively, defined as $f_0 \approx f_u$ and $f'_0 = f'_u$, F'_0 is the average resonance frequency of microwave dispersion for the same ferrite specimen but ground into a fine quasi-single domain powder which was mixed with wax, f_u, f'_u and F'_u are, respectively, the frequencies of the absorption maxima and J_s is the saturation magnetization.

In Ref.3 the same dependence was described by the formula

$$f_u \approx f_o \approx C(J_s/(\mu_a - 1)), \tag{2}$$

where μ_a is the initial permeability, C is a certain constant for the ferromagnetic material which is approximately equal to the gyromagnetic ratio for the electron spin $ge/2mc \approx e/mc$.

A theoretical basis of the last expression is furnished by the formulas of Snoek - Eq.(5) - and Döring - Eq.(6) - provided condition (7) (see below) is satisfied.

Calculations according to Eq.(2) using the data from Ref.4 regarding the temperature dependence of the left part of the formula $f_u \approx f_o$ show that in this case very good agreement with experiments is obtained (which cannot be said where expression (1) is concerned). This indicates that the temperature dependences of the r-f magnetic spectra obtained in the investigations of Refs. 3 & 4 are in quantitative agreement.

Measurements of the temperature dependence of the magnetic spectra in the above mentioned investigation were carried out in the temperature region $t < \theta$, where θ is the ferromagnetic Curie point temperature. The purpose of the present investigation was to determine the temperature dependence of the r-f magnetic spectra of ferromagnetic substances (specifically Ni-Zn-ferrite) at temperatures close to the Curie point and to see whether the dependence in this region can be described by expression (2).

---

*f is the frequency of a very weak alternating magnetic field.

2. Investigated Material and Experimental Procedure

1. For the purpose of providing for the possibility of measurement in a wide range of temperatures particular attention was given to selecting a material for which the $\mu_a(t)$ curve above the Curie point would not fall off rapidly, but would have a long "tail". As a result of tests on a large number of different samples we selected a toroidal core of Oxifer 2000-I Ni-Zn-ferrite[8] which was characterized by a lower Curie point as compared with other materials of this type. The dimensions of the sample were the following: outside diameter of the toroid 37.4 mm, inside diameter 23.4 mm, axial thickness 4.38 mm.

2. Saturation in ferrites occurs at very high field strengths. However beginning with 10-60 oersted the induction of ferrite changes very little and this value is commonly taken as the saturation induction for experimental purposes[9]. In our case J_s was approximately determined by extrapolation to $H = 0$ of the quasi-horizontal parts of the magnetization curves $J(H)$ recorded in fields of up to 200 oersted at different temperatures on a ballistic set-up. According to Ref.10, the values obtained for J_s in this manner in the temperature region $t \geqslant \theta$ must be regarded as approximate and probably underestimates.

By way of the initial permeability of the specimen we took its high-frequency permeability measured in very weak alternating fields in the region of constant values of μ with $f \ll f_r$ by means of a high-frequency bridge. According to Refs.5 & 11 the value of this permeability is approximately equal to μ_a measured by the ballistic method or to the permeability measured at audio frequencies.

The temperature of the ferromagnetic Curie point, in conformity with the indications of Refs.12, 13 & 14, was determined by extrapolation of the curves for $J_s(t)$ and $\mu_a(t)$.

3. The measurements were made following the procedure utilized in the investigations of Refs.3 & 15 and comprised two independent groups of experiments: a) investigations of the dependences $\mu(t)$, $\rho'(t)$ and $\tan\delta(t) = \rho'(t)/\mu(t)$ at different frequencies and b) investigation of the temperature dependences of $\mu(f)$ and $\rho'(f)$.

The sample was heated in an oil bath by means of an ultrathermostat. The winding on the ferrite core was connected to a high-frequency bridge by means of a short (~ 15 cm) section of r-f coaxial cable, the influence of which on the results was allowed for by calculation (see Ref.16, p.137). We also used a simplified heating apparatus which made it possible to shorten the conductors linking the sample to the bridge. Measurements of the complex dielectric constant $\epsilon' = \epsilon - j\sigma'$ of the ferrite and of its resistivity ρ were carried out on a high-frequency bridge and with dc current in weak electric fields. All possible measures were taken to enhance the accuracy of magnetic and electric measurements[17] and minimize the influence of chance factors.

3. Auxiliary Measurements and Investigation of the Temperature Dependence of the Permeability and Loss Tangent at Different Frequencies

1. The temperature dependences of the initial permeability and saturation magnetization of the ferrite specimen are shown in Fig.1. The somewhat lower than typical[8] value of J_s at 20° and the absence of a clear maximum in the $\mu_a(t)$ curve are to be explained by the exceptionally low value of the Curie point of the investigated specimen; according to the data of Fig.1, $\theta \approx 70^\circ$.

The results of measurements of ϵ, σ' and ρ of the ferrite specimen are shown in Figs.3 & 4. Calculations show that in the range of frequencies employed the

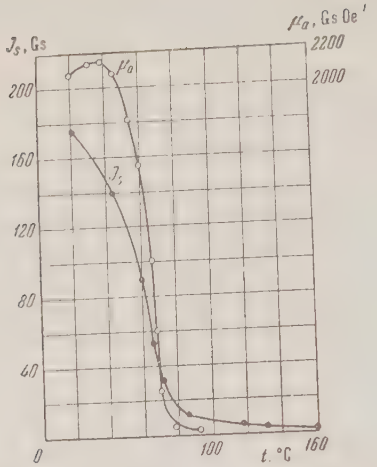

Fig.1. Temperature dependences of J_s and μ_a for the Ni-Zn-ferrite specimen.

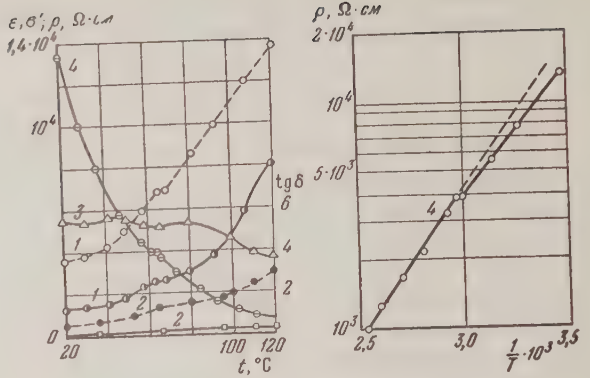

Fig.3. Temperature dependences of ε, σ' and tan δ at different frequencies and of the resistivity ρ of Ni-Zn-ferrites: 1) ε and σ' at 1 Mc, 2) ε and σ' at 10 Mc, 3) tan δ at 1 Mc, 4) ρ measured with dc at a constant voltage of 1 v (the surface of the specimen was thoroughly cleaned immediately prior to the resistivity measurements).

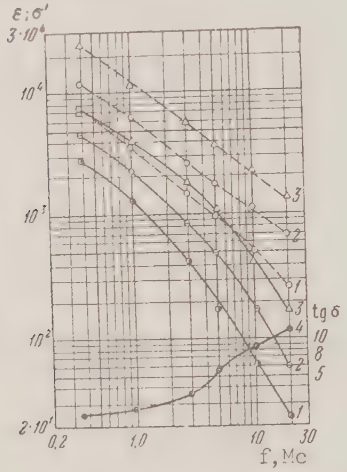

Fig.2. Frequency dependences of the real ε (solid curves) and imaginary σ' (dash curves) components of the complex dielectric constant and the loss tangent (tan δ = σ'/ε) of the Ni-Zn-ferrite at different temperatures: 1) ε and σ' at 20°, 2) ε and σ' at 65.8°, 3) ε and σ' at 117° and 4) tan δ at 20°.

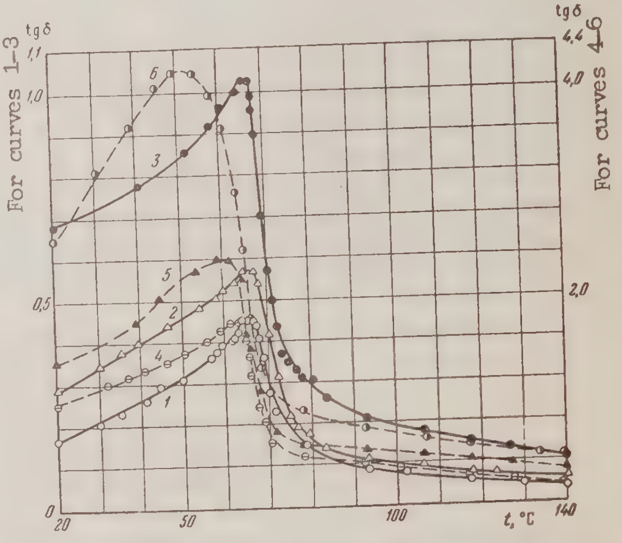

Fig.4. Temperature dependence of the magnetic loss tangent tan δ for Ni-Zn-ferrite at different frequencies: 1) 0.25, 2) 0.38, 3) 1.0, 4) 3.0, 5) 5.0, 6) 10.0 Mc.

influence of volume resonance[18-20] and the skin effect[2,3,18-20] can be neglected. Measurements of ρ(t) (Fig.3) showed that in agreement with Refs.17, 21 & 22, the temperature dependence of the resistivity for this ferrite is similar to that common to semiconductors, i.e., that log ρ varies linearly as 1/T; however, in the vicinity of the Curie point, as was noted in Ref.22, there is a break in the straight line, which substantiates our determination of the Curie temperature θ. The curves for ε(t) and σ'(t) also exhibit anomalies in the vicinity of θ, as was noted in the investigation of Ref.23.

2. The results of our investigations of the temperature dependence of μ, ρ' and tan δ at different frequencies are plotted in Figs.4 & 5.

A characteristic of all the tan δ(t) curves is the presence of a maximum at a temperature which we shall hereinafter designate as $t_{\delta\ max}$. Curves 1, 2 & 3 of Fig.4, which are recorded at frequencies $f \lesssim f_u$, have a maximum at $t = t_{\delta\ max} \approx 60^\circ \lesssim \theta$. In contrast to this, curves 4, 5 & 6, for which $f > f_u$, the temperature $t_{\delta\ max}$ exhibits a frequency dependence and gradually decreases with increasing frequency.

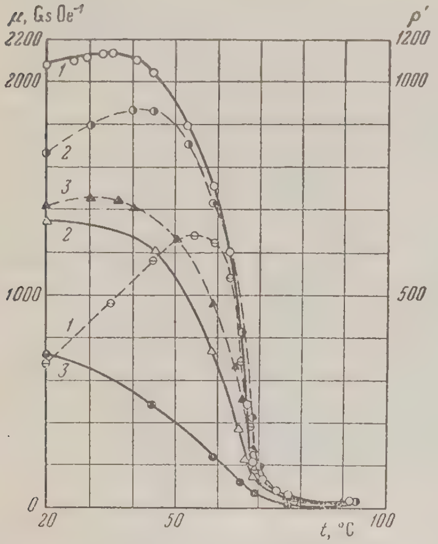

Fig.5. Temperature dependence of μ (solid curves) and ρ' (dash curves) of the Ni-Zn-ferrite at different frequencies: 1) 0.25, 2) 1.0, 3) 3.0 Mc.

The temperatures corresponding to the permeability maxima μ_{max} (Hopkinson's maximum) and ρ'_{max} are also displaced to the side of lower temperatures with increasing frequency. It may also be noted that the temperatures corresponding to ρ'_{max} are invariably higher than the temperatures for μ_{max}.

Inasmuch as, according to Refs. 3 & 15, for frequencies $0.01\ f_u \leqslant f \leqslant f_u$

$$\tan\delta = \rho'/\mu \approx f/f_u \approx (f/C)\left[(\mu_a - 1)/J_s\right], \quad (3)$$

for $f \lesssim f_u$ the variation of tan δ with temperature (shown by curves 1-3 in Fig.4) can also be described at first by a gradual decrease and then by an increase of the frequency f_u.

Hence it might be assumed that at the temperature $t = t_{\delta\ max} \approx 66^\circ \lesssim \theta$ we are dealing with a new state of the ferromagnetic material, a state characterized by minimal values of the frequency f_u and, consequently, of the mean relaxation frequency f_c and, probably, of the resonance frequency f_o (maximum mean relaxation time τ_c) and a maximum value of the high-frequency magnetic viscosity of the material. Let us call this temperature the point of the "thermal maximum of the r-f magnetic viscosity."

We note that, as graphic differentiation of the experimental curves shows, the temperature $t_{\delta\ max}$ corresponds approximately to the temperature at which the derivatives $d\mu_a/dt$ and $(d\rho'/dt)_{\mu=\mu_a}$ are maximal.

4. Investigation of the Temperature Dependence of the Magnetic Spectra and Phenomenological Description of the Magnetic Spectra

The results of our investigation of the temperature dependences of the magnetic spectra are shown in the form of experimental points in Figs. 6, 7 & 8. The temperatures used in the experiments were selected taking into account the probable temperature dependence of f_u deduced from an analysis of curves 1-3 in Fig.4. The curves are indicative of the relaxation nature of the magnetic spectra and show that the rate of decrease of the frequency $f_u \approx f_c$ with increasing temperature in the 20—60° interval slows down as temperatures in the vicinity of the Curie point are approached. We note that the slowing down of the rate of change of the relaxation frequency in the temperature range below the Curie point for polycrystalline specimens also follows from the results of investigation of ferromagnetic resonance[24,25], which may be taken as an indication of the quasi-identical nature of the attenuation processes in ferrites in both frequency ranges. From a comparison of the dash curves 1 & 3 in Fig.6, it will also be seen that as the temperature approaches θ there is also observed a broadening of the relaxation frequency band, leading to an increase of the losses at frequencies $f \ll f_u$. At $t \approx 66^\circ$, the frequency $f_u \approx f_c$ is minimal, after which f_u begins to

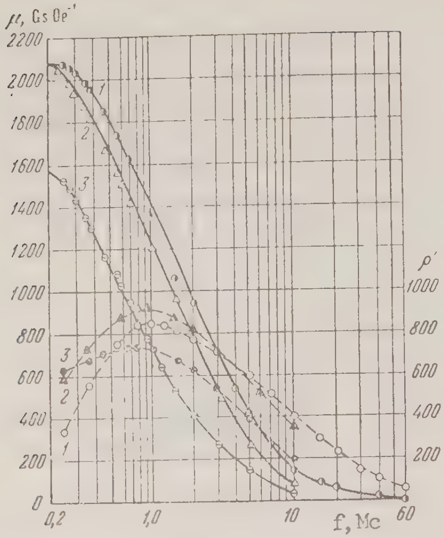

Fig.6. Magnetic spectra (solid curve: μ; dash curves: ρ') of Ni-Zn-ferrite at different temperatures: 1) 20°, 2) 45°, 3) 59°.

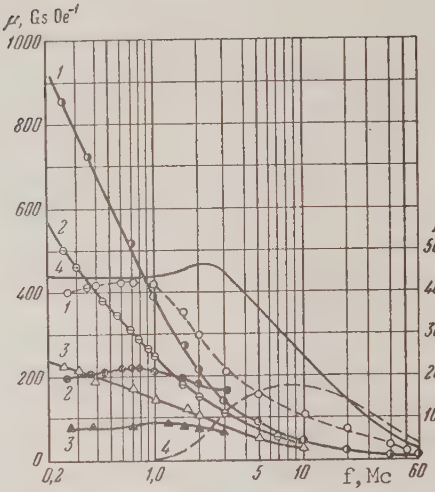

Fig.7. Same as Fig.6 but at 1) 65.8°, 2) 67.5°, 3) 66.8°; 4) magnetic spectra of 0-400 ferrite at 20° according to Ref. 15.

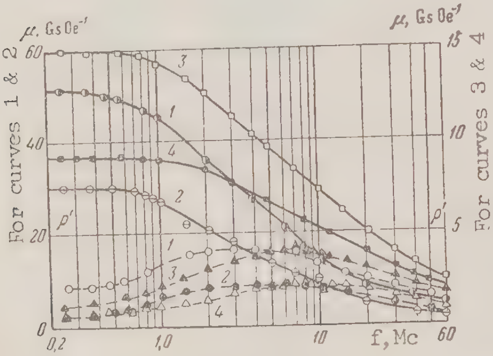

Fig.8. Same as Fig.6 but at 1) 78°, 2) 92.6°, 3) 117°, 4) 139°.

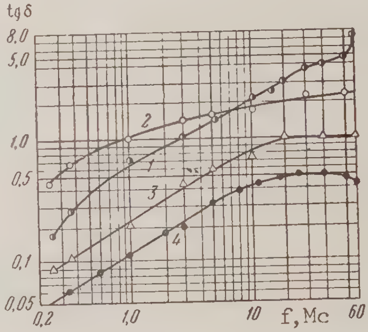

Fig.9. Frequency dependence of tan δ for the Ni-Zn-ferrite at different temperatures: 1) 20°, 2) 65.8°, 3) 92.6°, 4) 139°

increase with temperature at first rapidly and then more slowly. Analogous data cannot be obtained in investigations of ferromagnetic resonance inasmuch as resonance vanishes in the region of the Curie point[26,27].

The nature of the frequency dependence of the loss tangent of the ferrite also changes with the temperature in the r-f range (see Fig.9); in the range of high frequencies the loss tangent of this material is usually greater than unity at room temperature and falls off appreciably at higher temperatures. The magnitude of the ratio ρ'_{max}/μ_a also changes with the temperature which is evidence of broadening of the ferrite relaxation frequency band. The values of f_u obtained from the experimental data are listed in the accompanying table together with the values of f_u computed according to Eq.(2). Comparison of the results indicates that Eq.(2) holds approximately over the entire range of investigated temperatures. This assumption is not invalidated by the inaccuracy in determining J_s at high temperatures since the values of J_s obtained by us are smaller than the actual ones.

The approximate validity of Eq.(2) is also substantiated by comparison of curves 2 & 4 in Fig.7: curve 2 is for the specimen of 0-2000-I ferrite at 67.5°, while curve 4 is for a specimen of 0-400 ferrite at 20°; the values of μ_a for these are approximately equal, while the values of J_s are appreciably different (for 0-400 ferrite, $J_s \approx 210$ gauss).

Values of initial permeability, saturation magnetization and absorption peak frequency for Oxifer 2000-I

t, °C	μ_a, Gs Oe⁻¹	J_s, Gs	f_u exper., Mc	f_u theo., from (2), Mc	t, °C	μ_a, Gs Oe⁻¹	J_s, Gs	f_u exper., Mc	f_u theo., from (2), Mc
20	2075	177	1,0	1,0	68,8	250	40	1,2	1,86
30	2120	165	1,0	0,91	78	51,2	20	3,5	4,6
38	2150	154	1,0	0,84	92,6	30,2	10,5	5,5	4,2
45	2070	134	0,9	0,76	117	14,7	5,8	6,7	4,9
59	1550	95	0,8	0,72	131	10,3	3,8	7,5	4,8
65,8	1010	54	0,6	0,63	139	9,0	3,1	7,5	4,5
67,5	600	45	0,7	0,88	160	6,7	2,5	8,5	5,2

5. Discussion of Results

1. According to Vonsovskii[29] the expression for the average permeability of a polycrystalline material can be written as

$$\mu = \mu_r + \mu_d - 1, \tag{4}$$

where μ_r and μ_d are the permeabilities associated, respectively, with rotation of the magnetization vector and with displacements of the 90 and 180° walls.

If it be assumed, according to Refs.5, 19 & 30-33, that the magnetization of Ni-Zn-ferrite in very weak r-f fields occurs mainly due to rotation processes $(\mu_{a-d} - 1)/(\mu_{a-r} - 1) \ll 1$, dispersion and absorption effects in the specimen can be regarded, according to the theory of Landau-Lifshits[34] and Snoek[30], as gyromagnetic resonance, the frequency of which is given by

$$f_{o-r} = g\frac{e}{4\pi mc} H_i \approx \frac{1}{\pi} \cdot \frac{ge}{2mc} \cdot \frac{k}{J_s} \approx \frac{4}{3} \frac{ge}{2mc} \cdot \frac{J_s}{u_{a-r} - 1} \tag{5}$$

where H_i is the internal effective magnetic anisotropy field defined as $H_i = 2k/J_s = 8J_s/(u_{a-r} - 1)$, k is the effective anisotropy constant and $u_{a-r} - 1 = 4J_s^2/k$ (Refs. 4, 29, 35 & 36).

In the light of this hypothesis the temperature dependence of the frequency f_u* in our case could be explained in the temperature interval from 20 to 66° by the gradual decrease of the magnetic anisotropy, which falls off faster than

---

*The average resonance frequency of a ferromagnetic material, according to experimental data, is usually approximately defined as $f_o \approx f_u$ or $f_o \approx f_r^{\bullet}$, where $f_r^{\bullet}$ is the frequency at which the permeability μ is equal to 0.5 of its value at low frequencies (Refs. 4, 5, 18, 19 & 36).

Where resonance spectra are concerned theoretical grounds for the above are furnished by Eq.(51) of Ref.35 and Eq.(10) of Ref.37. In our case on the basis of an evaluation of the magnitude of C in Eq.(1) and the small resonance "rises" of μ before the permeability falls off, observed by other authors[11,38] and by us in individual specimens of Ni-Zn-ferrite with $\mu_a \approx 2000$ gauss/oersted, it may be assumed that the value of damping in ferrite is approximately equal to its critical value. Hence to an accuracy within a factor of the order of 2 we also assume $f_r^{\bullet} \approx f_o \approx f_u$.

$J_s(t)$ (Ref.12, p.278 and Refs.7, 25, 39 & 42). However, the further growth of f_u cannot be explained by formula (5), since for $t \geqslant \theta$ we have $k = 0$, which is substantiated by the variation of k_1 with temperature for single crystal specimens (Fig.10), the disappearance of ferromagnetic resonance at the Curie point and the low-temperature transformation observed in polycrystalline specimens[24-26, 39]. Nor can the further growth of f_u be connected with anomalies of the g-factor[40-42] inasmuch as measurements on Oxifer 2000-I did not disclose a "compensation" temperature[43] while numerous investigations[44-49] of Ni-Zn-ferrites (carried out to $t \geqslant \theta$) showed that the Landé factor remains virtually constant; according to Miles[48] g may be taken equal to 2.04 at 20° for the investigated specimen. In addition, we note that in the region of the supposed anomaly of the g-factor $H_i = 0$ (Ref.50) and consequently any growth of f_u in this region is improbable. Consequently, the r-f dispersion in the $t > \theta$ region cannot be described with the aid of present concepts, although in all probability it is associated with dispersion of rotation processes.

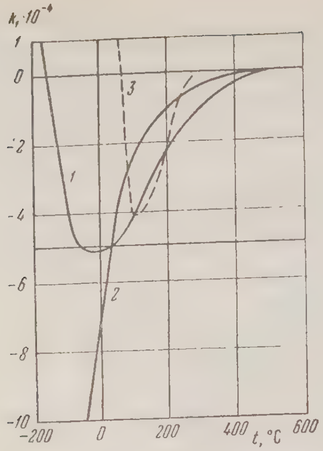

Fig.10. Temperature dependences of the anisotropy constant k_1 (erg/cm^3) of some types of ferrites investigated up to the Curie point: 1) $NiO \cdot Fe_2O_3$, $\theta = 585°$ (Ref.25), 2) $CuO \cdot Fe_2O_3$, $\theta = 430°$ (Ref.39), 3) $(CoO)_{0.7} \cdot (ZnO)_{0.3} \cdot Fe_2O_3$, $\theta = 340°$ (Ref.39).

The assumption regarding the predominance of rotation processes in Ni-Zn-ferrites at 20° is based mainly on the approximate applicability of expression (5) (Refs.5,19,31,33 & 51) and on the "single-dispersion" character of the spectrum (Refs.5,3 & 51). In view of the data and deductions in Refs.3,4,36 & 37, it must be admitted that this interpretation of the experimental results is not sufficiently well founded.

In particular, evaluation of the constant k of the investigated ferrite at 20° according to formula (5), on the assumption that $\mu_a = \mu_{a-r}$ yields an implausibly small value of ~ 60 erg/cm^3 for k, which differs by more than two orders of magnitude from the value of k for the ferrite $(NiO)_{0.55} \cdot (ZnO)_{0.75} \cdot Fe_2O_3$ studied by Miles[48]; the value of μ_a for the polycrystalline specimen used by Miles should be about 200 gauss/oersted and consequently should differ from the value of μ_a for the Oxifer 2000-I ferrite only by a factor of 10, all of which does not agree with the expression $\mu_{a-r} - 1 \approx 4J_s^2/k$. An appreciably greater value of k (~ 5000 erg/cm^3) of the investigated specimen is obtained when k is evaluated from the data on H_i of Ref.48 for a ferrite having a similar composition: $(NiO)_{0.25} \cdot (ZnO)_{0.75} \cdot Fe_2O_3$. However, a value of k of the same order of magnitude (specifically ~ 2500 erg/cm^3) can be obtained by extrapolating the $\mu(f)$ curve in Fig.6 for 20° to the $\mu - 1 = 0$ ordinate if we assume $f_{0-r} \approx 80$ Mc.

In addition we investigated the magnetic spectra of Oxifer 2000-I in the state of residual magnetization at 20°; the results showed that $\mu_{a-R}/\mu_a \approx 0.7$, $(\rho'_R/\rho')_{\mu=\mu_a} \approx 0.5$ and $J_R/J_s \approx 0.5$.* With increasing frequency the $\mu(f)$ curves for both states of the ferrite rapidly approach each other and merge at a frequency $f \approx 3.5$ Mc; in contrast the $\rho'(f)$ curves merge only at $f = 12$ Mc. Taking the approach of the $\mu'(f)$ and $\mu'_R(f)$ curves as evidence of the gradual increase with frequency of the contribution to the magnetization by the rotation processes, one can evaluate the value of μ_{a-r} of the investigated specimen: we obtain $\mu_{a-r} \approx 120$ gauss/oersted and $k \approx 1000$ erg/cm^3, which agrees as regards order of magnitude with the values of k obtained by other methods. An analogous evaluation of μ_{a-r} for Mg-Fe-ferrite in Ref.37 also leads to values of μ_{a-r} agreeing with those derived from independent experiments.

---

*The subscript R indicates the remanence state.

2. Hence let us describe the magnetic spectrum of the investigated ferrite at 20° in terms of the dispersion of the displacement processes $(\mu_{a-d} - 1)/(\mu_{a-r} - 1) \gg 1$, which is due to the inertia of the effective mass of the ferromagnetic domain walls, according to the theories of Landau-Lifshits[34] and Döring.[52]

For the 90° wall[53], we have:

$$f_{o-d} = \frac{ge}{2mc}\sqrt{\frac{\delta}{d}}\,(J_s/\sqrt{\mu_{a-d} - 1}) \qquad (6)$$

where δ/d is the ratio of the effective thickness of the wall layer to the size of the ferromagnetic domain.

This expression is apparently valid for ordinary polycrystalline homogeneous materials[12] not having magnetic texture; some types of high-permeability ferrites belong in this class of materials since a high value of μ_a can be obtained only for solid solutions of ferrites[54].

3. From a comparison of Eqs.(2), (5) & (6) it follows that if, within the accuracy of a constant factor, we take the temperature dependence to be given by

$$\delta/d \approx 1/(\mu_{a-d} - 1), \qquad (7)$$

all three of the above expressions will give equivalent numerical results. Experimental justification of this assumption is furnished by the results obtained by Rado et al[4] and the data in the table in the present article, since it may be assumed that wall displacement processes play a predominant role at all the temperatures used in the investigation of Ref.4.

In the general case, in the temperature region where displacement processes predominate, the temperature dependence of μ_{a-d} of the ferrite will be determined, according to Kondorskii's[12] general theory of reversible displacement of domain walls, by the number and volume of inclusions and by the magnitude and distribution of internal stresses σ_i in the material.

In the heterogeneous case $\mu_{a-d}(t)$ and $f_{o-d}(t)$ can be described taking (2), (6) and (7) into account, in accordance with Kersten's[12] theory of inclusions, by

$$\mu_{a-d} - 1 \approx D(J_s^2/k^{1/2}) \text{ and } f_{o-d} \approx (C/D)(k^{1/2}/J_s). \qquad (8)$$

Then, according to (5), we obtain a temperature dependence $(\mu_{a-d} - 1)/(\mu_{a-r} - 1) \sim \sim k^{1/2}$ and, consequently, assuming k to be decreasing, come to a conclusion regarding the increase in the contribution of rotation processes to magnetization with increasing temperature that is in good agreement with general physical concepts.

In the homogeneous case the dependences $\mu_{a-d}(t)$ and $f_{o-d}(t)$ for the case of displacement of the 90° walls can be described from the standpoint of Kondorskii's (Ref.12) theory of stresses by

$$\mu_{a-d} - 1 \approx 4(J_s^2/\lambda_s\sigma_i) \text{ and } f_{o-d} \approx (C/4)(\lambda_s\sigma_i/J_s). \qquad (9)$$

We then obtain for the temperature dependence

$$(\mu_{a-d} - 1)/(\mu_{a-r} - 1) \sim k/\lambda_s\sigma_i.$$

Assuming that k decreases with the temperature more rapidly than the magnetoelastic energy $\lambda_s\sigma_i$ (which in any case is true for temperatures in the vicinity of the Curie point - Ref.1, p.31 and Refs.21, 39 & 55), we come to the same conclusion.

In particular, in the case of the Mg-Fe-ferrite investigated by Rado et al[4] the dependence $f_{a-d}(t)$ can be qualitatively described* both by the expression (8) and expression (9). It is obvious that the frequency f'_o, as determined by expression (5), must decrease with temperature more rapidly (as it actually does) than $f_{o-d} \sim k^{1/2}/J_s$ or $f_{o-d} \sim \lambda_s\sigma_i/J_s$ determined from expressions (8) or (9). The slower variation with temperature of F'_o as compared with the variation of f'_o is interpreted as being due to the influence of the anisotropy of the shape of the powder particles.

We note that if we use the data on pp.257 & 260 of Vonsovskii's[29] book, the expression for δ/d can be written as

$$\delta/d \approx (A/a_o^5L^2)^{1/4}k^{-1/4}. \tag{10}$$

This expression is not consistent with (7) since the lattice constant a_o and the dimensions of the crystal L are virtually independent of the temperature, while the assumption regarding the temperature dependence of the exchange integral A is implausible. The evaluated values of δ/d at 20° = $2.2\cdot10^{-4}$ for Oxifer 2000-I and $15\cdot10^{-4}$ for the ferrite investigated by Rado[37] - also cast doubt on the validity of this expression.

4. In the case of Oxifer 2000-I evaluation of $\lambda_s\sigma_i$ at 20° by means of formula (9) yields $\sim$60 erg/cm³; inasmuch as $\lambda_s \approx 10^{-6}$ (Ref.60), we obtain a reasonably small value for the mean amplitude of the internal stresses: $\sigma_i \approx 0.6$ kg/mm². With increasing temperature, λ_s decreases, as a rule, more sharply than J_s; σ_i in all probability also decreases with increasing temperature and, consequently, the decrease of the frequency f_u with increasing t in the range from 20 to 66° appears to be entirely logical from the standpoint of formula (9).** Calculations by means of formula (9) of the probable temperature dependence of $(\lambda_s\sigma_i)_t/(\lambda_s\sigma_i)_{20°}$ indicates a linear decrease of $\lambda_s\sigma_i$ with increasing temperature for the 20-66° temperature interval (Fig.11), which is in qualitative agreement with the results for $\lambda_s(t)$ obtained in the investigation of Ref.55 for one Ni-Zn-ferrite. For Oxifer 2000-I at t = 66° ≈ θ, it may be assumed that $\lambda_s \neq 0$ and, consequently, according to Akulov[61], $\lambda_s = a_1 + a_{10}(1 - T/\theta)$, where a_1 is an additive constant and a_{10} is a numerical coefficient.

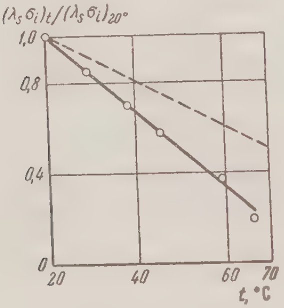

Fig.11. Probable character of the temperature dependence of $(\lambda_s\sigma_i)_t/(\lambda_s\sigma_i)_{20°}$ for Oxifer 2000-I ($\theta \approx 70°$) in the temperature range from 20 to 66°. The dash line is the same dependence for an Ni-Zn-ferrite with μ_a = 278 gauss oersted and $\theta \approx 120°$ (from Ref.55).

Above 66°, f_u increases and the ferrite might be regarded as a magnetically "soft" material with a very small inherent anisotropy and a distribution of internal stresses having the form of uniformly stressed small volumes in which[12] the magnetization can be realized beginning in the very weakest fields by rotation processes, while the value of μ_{a-r} is determined by the anisotropy of the stresses, i.e., by an expression analogous to (9).

---

*For a more accurate description it is necessary to take into account the influence of inclusions and internal stresses; the neglect of these in Ref.4 is not fully justified. In particular, we have the indicative fact that two dispersion regions are observed (Refs.4,5,36 & 56-58) in the magnetic spectra of ferrites characterized by small values of λ_s and are absent in Ni-ferrite which has a high value of λ_s (Refs.5,58 & 59).

**Another possible method of describing the effect would consist of taking into account the joint influence of inclusions and internal stresses.

However, in this case it must be assumed that $\lambda_s \sigma_i$ passes through a maximum at $t \approx 78^o > \theta$ and that noticeable residues of spontaneous striction persist up to 160^o. The only indication in the literature of such a temperature dependence of λ_s is the location of the points for magnetostriction of nickel in the region of θ reported in Ref.12 (p.454).

It is possible also that the mechanism of dispersion at $t > 66^o$, analogously to that of low frequency dispersion[5,7], can be ascribed to electron diffusion, which yields a temperature dependence of the relaxation frequency similar to that observed in our case, particularly since calculations of the activation energy from the data for ρ (Fig.3) and f_u (Fig.8) yield, respectively, $E_r \approx 0.2$ ev and $E_m \approx 0.1$ ev, i.e., rather close values.

6. Conclusions

1. As the results of investigations of the magnetic spectra of a specimen of Ni-Zn-ferrite with μ_a = 2075 gauss/oersted at 20^o and a Curie point $\theta \approx 70^o$ in the radiofrequency range from 0.2 to 60 Mc at temperatures from 20 to 160^o, it was found that as the temperature is increased the dispersion and absorption bands of the magnetic spectrum are displaced at first to the side of the lower and then to the side of higher radio frequencies.

2. We found that there is a temperature $t_{\delta\ max}$ at which the tan $\delta(t)$ curves obtained at all frequencies $f \lesssim f_u$ peak and at which the r-f magnetic viscosity attains its maximum value.

3. The experimental results are characterized at low temperatures by the inertia of the effective mass of the oscillating domain walls and at high temperatures by gyromagnetic resonance observed in the "effective magnetic field".

4. We have suggested a new method for approximate determination of the Curie point of an investigated specimen from the temperature maximum of the r-f loss tangent.

References

1. J.L.Snoek, New Developments in Ferromagnetic Materials (in Russian trans. M.1949).

2. V.K.Arkad'ev, ZhRFKhO (Journal of the Russian Physical and Chemical Society) Physics Section, 45, 302, (1913); Elektromagnitnye protsessy v metallakh (Electromagnetic processes in metals) Part II, M.-L., 1934; in collection of articles "Problemy ferromagnetizma i magnetodinamiki" (Problems of Ferromagnetism and Magnetodynamics) p.7, M.-L., 1946.

3. L.A.Fomenko, VI Nauchno-tekhnich. konfer. (Sixth Scientific-Technical Conference), Pub. VNORiE im.A.S.Popov, L.1951; Nauchnaia sessiia, posviashchennaia prazdnovaniiu "Den' Radio" (Scientific session dedicated to "Radio Day") Sviaz'izdat, M., 1951; Zhur.eksp.i teor.fiz., 25, 107 (1953).

4. G.T.Rado, R.W.Wright, W.H.Emerson & A.Terris, Phys. Rev., 86, 599 (1952); 88, 909 (1952).

5. J.Smit & H.P.J.Wijn, Advances in Electronics and Electron Physics, v. VI, p. 70, N.-Y., 1954.

6. J.K.Galt, B.T.Mattias & J.P.Remeika, Phys. Rev., 79, 391 (1950).

7. J.K.Galt, Bell Syst. Tech. Journ., 33, 1023 (1954).

8. N.N.Shol'ts, Izv. AN SSSR, Ser. fiz., 18, 465 (1954). (Translation in Bulletin, Vol.18, No.4, p.155).

9. In "Vestnik informatsii" (Journal of information) No.17, p.1, Pub. "Sov. Radio", M. 1954.

10. W.Sucksmith, C.A.Clark, D.J.Oliver & J.E.Thompson, Rev.Mod.Phys., 25, 34, (1953).

11. R.Feldtkeller & O.Kolb, ZS. angew. Phys., 4, 448 (1952).

12. S.V.Vonsovskii & Ia.S.Shur, Ferromagnetizm (Ferromagnetism, m. 1948).

13. F.Fraunberger, ZS. f. Naturforsch, 52, 129 (1950).

14. L.Bochirol, C.R., 232, 1474 (1951); N.L.Howard & J.S.Smart, Phys.Rev., 91, 17 (1953).

15. L.A.Fomenko, V.Nauchno-tekhnich. konfr. (Fifth Scientific-Technical Conference), Pub. VNORiE im.A.S.Popov, L.1950; Zhur.eksp.i.teor.fiz., 21, 1201 (1951); 24, 365 (1953); 30, 18 (1956).

16. Spravochnik po radiotekhnike (Radioengineering Handbook) GEI, M.-L., 1950.

17. A.L.Frumkin & S.D.Kholodnyi, Izv. AN SSSR, Ser. fiz., 18, 409 (1954). (Translation in Bulletin, Vol. 18, No.3, p.105).

18. F.G.Brockman, P.H.Dowling & W.G.Steneck, Phys.Rev., 75, 1298 (1949); 77, 85 (1950).

19. D.Polder, Proceedings IEE, II, 97, 246 (1950).

20. K.M.Polivanov, in "Trudy MEI" (Proceedings Moscow Power Engineering Institute) No.14, p.116, M.-L., 1953.

21. Ia.G.Dorfman, Izv.AN SSSR, Ser.fiz., 16, 412 (1952).

22. A.P.Komar & V.V.Kliushin, Izv. AN SSSR, Ser. fiz., 18, 400 (1954). (Translation in Bulletin, Vol.18, No.3, p.96).

23. F.Brockman, P.Dowling & W.Steneck, Phys.Rev., 75, 1440 (1949).

24. T.Okamura, Y.Kojima & Y.Torizuka, Phys.Rev., 85, 693 (1952).

25. D.W.Healy, Phys.Rev., 86, 1009 (1952).

26. L.R.Bickford, Phys.Rev., 76, 137 (1949); 78, 449 (1950).

27. T.Okamura, Y.Torizuka & Y.Kojima, Phys.Rev., 84, 372 (1951).

28. L.I.Rabkin & B.Sh.Epshtein, Zhur.tekh.fiz., 24, 1568 (1954).

29. S.V.Vonsovskii, Sovremennoe uchenie o magnetizme (Modern science of magnetism), M.-L., 1952.

30. J.L.Snoek, Philips Tech. Rev., 8, 353 (1946); Nature, 160, 90 (1947); Phys. the Hague, 14, 207 (1948).

31. J.J.Went & E.W.Gorter, Philips Tech. Rev., 13, 181 (1952).

32. J.Lucas, ZS. angew. Phys., 6, 127 (1954).

33. P.J.Wijn, M.Gevers & C.M. van der Burgt, Rev. Mod. Phys., 25, 91 (1953).

34. L.D.Landau & E.M.Lifshits, Sow. Phys., 8, 157 (1935).

35. C.Kittel, Phys. et rad., 12, 291 (1951).

36. G.T.Rado, Rev. Mod. Phys., 25, 81 (1953).

37. G.T.Rado, R.W.Wright & W.H.Emerson, Phys. Rev., 80, 273 (1950).

38. N.G.Katkov, Dissertation, Moscow Power Engineering Institute, M. 1954; Izv. AN SSSR, Ser. fiz., 18, 4 (1954); V.V.Kuznetskii, Dissertation, Moscow Power Eng. Inst., M. 1955; Abstracts of reports delivered at the Conference on Magnetic Radiospectroscopy, Kazan 1955.

39. T.Okamura,& Y.Kojima, Phys. Rev., 86, 1040 (1952); 85, 690 (1952).

40. J.Kaplan & C.Kittel, Chem. Phys., 21, 760 (1953).

41. J.S.Wieringen, Phys. Rev., 90, 488 (1953).

42. McGuire, Phys. Rev., 91, 206 (1953); 93, 682 (1954).

43. E.W.Gorter & J.A.Schulkes, Phys. Rev., 90, 487 (1953); E.W.Gorter, Philips Res. Rep., 9, 295 (1954).

44. H.G.Beljers, Phys. the Hague, 14, 629 (1949).

45. H.G.Beljers, D.Polder, Nature, 165, 800 (1950).

46. T.Okamura & Y.Torizuka, Nature, 167, 986 (1951).

47. E.I.Kondorskii & N.A.Smol'kov, Doklady AN SSSR, 93, 237 (1953).

48. P.A.Miles, Nature, 174, 177 (1954).

49. T.Okamura, Y.Kojima & Y.Torizuka, Sci. Rep. Res. Insts. Tohoku Univ., A, 3, 725 (1951); T.Okamura, ibid., A, 6, 69 (1954).

50. T.Torizuka, Y.Kojima & T.Fujimura, Phys. Soc. Japan, 9, 298 (1954).

51. D.Park, Phys. Rev., 95, 652 (1954); 97, 60 (1955).

52. W.Döring, ZS.f.Naturforsch, 3a, 373 (1948).
53. R.Becker, Phys. et rad., 12, 332 (1951).
54. N.A.Toropov, L.I.Rabkin, E.Zh.Freidenfel'd & B.Sh.Epshtein, Zhur.tekh. fiz., 23, 1541 (1953).
55. A.I.Suchkov, Dissertation, Moscow State University, M. 1953; Zhur. tekh. fiz., 9, 1570 (1954).
56. A.J.Welch, P.F.Nicks, A.Fairweather & F.F.Roberts, Phys. Rev., 77, 403 (1950).
57. M.Roberts, Phys. et rad., 12, 301 (1951).
58. R.S.Weisz, Phys.Rev., 96, 300 (1954).
59. P.Popper in "Soft Magnetic Materials for Telecommunications" Article 35.- Pergamon Press, London, 1953.
60. G.A.Smolenskii, Doklady AN SSSR, 78, 921 (1951).
61. N.S.Akulov, Ferromagnetizm (Ferromagnetism), M.-L., 1939.

Note: Many of the Physical Review and other English articles are listed as available in Russian translation in "Ferromagnitnyi rezonans" (A collection of articles on "Ferromagnetiz resonance"). Trans. Editor.

INVESTIGATION OF THE RF MAGNETIC SPECTRA OF MIXED FERRITES IN THE STATE OF RESIDUAL MAGNETIZATION

- L.A.Fomenko

1. Introduction

There have been many diverse investigations of the r-f magnetic spectra of polycrystalline ferrites. Among the simple ferrites, the spectra of Ni-ferrites (Refs.1-6) have been investigated in greatest detail, although the spectra of Mg-ferrites [1,3,7-9], Li-ferrites[3] and Fe-ferrites[1,7] have also received attention. Among the double ferrites, the spectra of Ni-Zn-ferrites have been the subject of the greatest number of studies[2,4,5,10-24]. One type of Mg-Fe-ferrite has been studied in great detail[3,25]; there have also been studies of Ni-Fe-ferrites[5], Li-Zn-ferrites[3], Cu-Zn-ferrites[7,18,26] and Ni-Zn-Cu-ferrites[12]. The available data[2] on the spectra of Mn-Zn-ferrites[2,10,11,14,16,27] were apparently obtained (except in the investigation of Ref.27) without allowing for the influence of dimensional effects: the skin effect and volume resonance. In addition there is some very fragmentary information in the literature on the spectra of Cu-Pb-ferrites,[1-7], Mn-Fe-ferrites[10] and Mg-ferrite-aluminates[9].

Investigations[3,8,9,25,34] have shown that in general the magnetic spectra of ferrites have two distinct dispersion regions: a radiofrequency region, characterized by the inertia of the effective mass of the domain walls according to Landau-Lifshits[28] and Döring[29], and a microwave region characterized by gyromagnetic resonance, according to Landau-Lifshits[28] and Snoek[27]. Both dispersion regions have been observed in ferrites having a relatively high value of k and a low value of λ_s and were found to be absent in other types of ferrites[1-7] characterized by a smaller value of k or a larger value of λ_s.* According to the theory of rotation processes[30], Kersten's[31] theory of inclusions and Kondorskii's (Ref.31) theory of stresses, variations in these parameters are apparently responsible for the merging of the two dispersion regions into one region which, therefore, cannot be characterized by gyromagnetic resonance alone.

Our earlier investigations of the magnetic spectra of ferrites were carried out in the state of absolute demagnetization of the material, although Rado, Wright and Emerson[25] have shown that investigation of the spectra in the state of residual magnetization may be a source of additional information regarding the character of the magnetization processes in ferrites. Furthermore the investigations of the spectra were carried out without taking into account[5-7] the possible influence on the dispersion of the sintering temperature t_s, although it may be assumed[12] that the ratio $(\mu_{a-d} - 1)/(\mu_{a-r} - 1)$ is in general a function of a decrease in the number and volume of inclusions and a reduction of internal stresses σ_i - up to a certain maximum value (temperature), after which it should fall off as a result of decomposition of the ferrite leading to an increase in the number and volume of inclusions.

The purpose of the present study was to investigate the magnetic spectra of certain types of polycrystalline ferrites of different composition sintered at different temperatures t_s and investigated in the absolute zero magnetization state and in the state of residual magnetization.

2. Investigated materials and experimental procedure

The composition, dimensions and magnetic characteristics of the specimens are listed in Table 1. The experiments were carried out at 20°. The values of J_s, H_c and B_R were determined by the ballistic method in a 100 oersted field.

---

*In the present article we shall use the terminology and designations of the preceding article.

Table 1

Magnetic characteristics of the investigated toroidal cores

Sample Nos.	Type of ferrite	Composition, mol %	t_s, °C	μ_a, $GsOe^{-1}$	J_s, Gs	H_c, Oe	B_R, Gs	θ, °C	Toroid dim., mm		
									diameter		Axial thickness
									outside	inside	
1	Ni-Zn	Fe_2O_3—49 ZnO—32 NiO—19	—	483	240	1,0	1450	—	33,6	20,8	6,62
2	Ni-Zn-Cu	Fe_2O_3—49 ZnO—26 NiO—21 CuO—4	1140	334	350	0,55	2380	232	33,88	20,7	6,20
3	Ni-Zn-Cu	Fe_2O_3—49 ZnO—26 NiO—19 CuO—6	1125	303	350	0,5	2180	250	33,9	21	6,22
4	Ni-Zn-Cu	Fe_2O_3—49 ZnO—26 NiO—19 CuO—6	1075	348	370	0,55	1170	250	33,8	21	6,27
5	Ni-Zn-Mg	Fe_2O_3—464 ZnO—32 NiO—16 MgO—56	—	350	254	1,2	880	155	33,3	20,6	5,97
6	Ni-Zn-Be	—	—	598	176	0,55	750	180	34,25	21,3	5,87
7	Li-Zn	—	1100	303	190	0,65	1100	220	30,33	20,0^5	6,45
8	Li-Zn	—	1150	420	205	0,43	1080	—	30,03	19,7	6,34
9	Ni-Zn	Fe_2O_3—49 ZnO—26 NiO—25	1125	116	224	4,0	1640	—	30,75	22,2	6,74
10	Ni-Zn-Cu	Fe_2O_3—49 ZnO—26 NiO—19 CuO—6	1175	188	280	2,0	1800	—	30,65	20,3	6,49

* All the specimens were prepared from mixtures of the oxides.

In addition we determined the frequency dependences of ϵ and σ' (Table 2). The experimental procedure was the same as that employed in the investigations of Refs. 12 & 24. The investigation comprised three independent series of experiments the results of which are given below.

Table 2

Values of the real and imaginary components of the dielectric constant of the investigated ferrite specimens at different frequencies

Sample Nos.	Frequencies, Mc									
	0,25		1,0		3,0		10		20	
	ε	σ'	ε	σ'	ε	σ'	ε	σ'	ε	σ'
1	18	2,0	17	2,0	16	1,5	15	1,0	15	0,5
2	23	2,4	15	1,2	16	0,77	15	0,31	15	0,25
3	21	2,1	13	1,4	13	1,1	13	0,6	13	0,5
4	21	1,1	19,7	0,9	18,4	0,72	16	0,6	14	0,5
5	20	1,2	15	0,8	14	0,5	13	0,25	13	0,25
6	22	1,7	21	1,1	18	0,5	15	0,5	13	0,25
7	39	195	39	110	38	38	30	19	23	14
8	42	150	41	80	35	40	32	30	30	20

3. Investigation of Ni-Zn-Be-ferrite in different remanence states

The results of investigation of Ni-Zn-Be-ferrite are shown in Figs.1, 2, 3 & 7. The permeability μ_R is the reversible permeability $\mu_R = (\Delta B/\Delta H)_{\Delta H \to 0}$ (where ΔB and ΔH are the increments in induction and field strength referred to the displaced hysteresis loop) determined at the point of residual induction B_R. Hence in the 0.2-0.8 Mc region the character of the $\mu(H_o)$* curves in Figs.1 & 2

---

*H_o is the field producing the remanence.

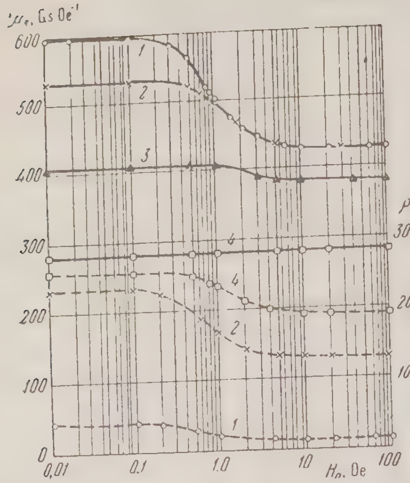

Fig.1. Dependences of the elastic μ_R (solid lines) and viscous ρ'_R (dash lines) permeabilities of specimen No.6 (Ni-Zn-Be-ferrite) on the intensity of the field H_o at different frequencies: 1) 0.2-0.8 Mc, 2) 3 Mc, 3) 5 Mc, 4) 8 Mc.

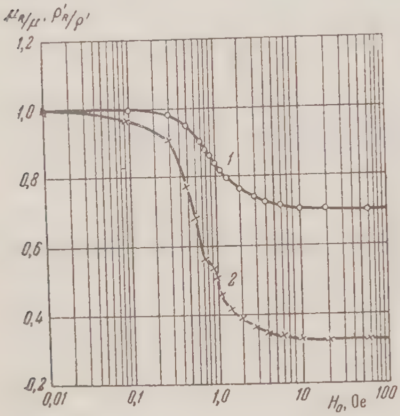

Fig.2. Dependences of the relative elastic and viscous permeabilities of specimen No.6 (Ni-Zn-Be-ferrite) on the field intensity H_o at a frequency of 0.8 Mc: 1) μ_R/μ, 2) ρ'_R/ρ'.

can be explained by the constant decrease in the slope of the displaced hysteresis cycle relative to the $H = 0$ axis. Beginning the H_o 10 oersted the slope of the loop apparently no longer depends on the field intensity H_o. The slope of the displaced loop apparently decreases with increasing frequency and beginning with f   8 Mc remains constant regardless of the value of H_o. We note that the relative permeability ρ'_R/ρ' is appreciably more strongly dependent on the field intensity H_o than the relative permeability μ_R/μ (Fig.2).

The observed dependence $\mu(H_o)$ at low radio frequencies can be qualitatively described by an analytic function if we utilize the curves of Fig.3 and Arkad'ev's[32] formula approximating Hahns' law. In the region of high frequencies Hahns' law is not even quantitatively applicable.

4. Investigation of the magnetic spectra of mixed ferrites of different chemical composition

1. The results of this series of experiments are shown in Figs.4-8. An examination of the curves shows that the magnetic spectra of the ferrites in this group have a resonance character. The values of the frequency f_u are given approximately by expression (2) of Ref.24 (the preceding article), where C = 9-20 Mc/oersted.

The relative heights of the resonance maxima μ_{max}/μ_a for specimens of different composition differ appreciably (see Table 3), the greatest value being attained in the case of specimen No.2 (Ni-Zn-Cu-ferrite). If the specimens are arranged in the following order: No.2,5,1,6 and 7 the values of the ratio μ_{max}/μ_a as well as of ρ'_{max}/μ_a and $\Delta f = f_d - f_a$* will gradually decrease as we go along the series. This decrease must apparently be connected with the corresponding increase from specimen to specimen of the loss tangent $\tan \delta_a$ (Table 3) at the frequency f_a. From a comparison of the data for $\tan \delta_a$ and $\tan \delta_b$ in Table 3 it will be seen that the limiting value of $\tan \delta_a$ at which the spectrum has a relaxation character is $\tan \delta_a = \tan \delta_b \approx 0.15$.

The small values of $\tan \delta$ for specimen No.2 in the frequency region $f < f_u$ (Fig.9) are phenomenologically due to a) the relatively high value of f_u which in turn is due to the large value of J_s and b) the relatively narrow band of resonance frequencies of the material (evinced by the large value of ρ'_{max}/μ_a and μ_{max}/μ_a and the pronounced absorption peak).

2. An examination of curves 3 & 4 in Figs.4 through 8 shows that the resonance character of the spectrum is usually retained in the remanence state.

---

*Here f_a, f_b and f_d are, respectively, the frequency of the beginning of the resonance rise of the curve for $\mu(f)$, the frequency corresponding to μ_{max} and the frequency corresponding to $\mu = \mu_a$ in the region of the falling off of the $\mu(f)$ curve.

Table 3

Magnetic characteristics of the specimens

Sample No.	μ_a, Gs Oe^{-1}	μ_{max}' Gs Oe^{-1}	ρ'_{max} Gs Oe^{-1}	Characteristic frequencies, Mc				$\frac{\mu_{max}}{\mu_a}$	$\frac{\rho'_{max}}{\mu_a}$	tg δ_a	tg δ_b	Remarks
				f_a	f_b	f_d	f_u					
2	334	400	192	2,5	6,0	9,2	12	1,20	0,58	0,015	0,18	Completely demagnetized state
5	350	388	155	1,2	2,8	4,2	8,5	1,11	0,44	0,017	0,15	
1	483	532	221	1,5	3,0	4,4	9,0	1,10	0,46	0,02	0,15	
6	598	625	263	0,65	1,4	2,1	6,5	1,045	0,46	0,03	0,15	
7	303	312	126	1,2	2,4	3,2	8,0	1,027	0,415	0,06	0,17	
2	168	200	76	3,0	7,0	13	17	1,19	0,45	0,012	0,14	Remanence state
5	278	300	117	1,2	3,2	4,7	10	1,07	0,415	0,014	0,14	
1	430	475	192	1,6	3,2	4,5	9,0	1,10	0,45	0,014	0,14	
6	431	453	199	0,8	1,8	3,1	8,0	1,05	0,46	0,021	0,12	
7	202	207	75	1,5	3,0	3,5	11	1,022	0,37	0,047	0,18	

The values of the ratios μ_{a-R}/μ_a and $(\rho'_R/\rho')_{\mu=\mu_a}$ are different from the different specimens; however, in all cases for any given specimen $(\rho'_R/\rho') < (\mu_R/\mu)$ and, consequently, in all cases $\tan\delta_R < \tan\delta$.

As the frequency is increased the magnetic spectra for both states tend to approach each other. The frequencies f_μ and $f_{\rho'}$, i.e., the frequencies corresponding to equal values of $\mu = \mu_R$ and $\rho' = \rho'_R$. are different for different specimens, but in all cases $f_\mu < f_{\rho'}$. It will be seen that in going over to the residual magnetization state the frequencies f_a, f_b, f_d and f_u are displaced to the side of higher frequencies, the magnitude of the shift being approximately given by Eq.(2) of Ref.24.

3. For ferrites for which $J_R/J_s \approx 0.5$, it is known[25,31] that if the complex permeability μ' is due exclusively to rotation processes, then $\mu'_R = \mu'$; on the other hand, if the permeability μ' is due to primarily wall displacements, $\mu'_R \approx \approx 0.5\mu''$. In the case of specimens Nos.2 & 7 the fact that the ratios J_R/J_s, μ_{a-R}/μ_a and $(\rho'_R/\rho')_{\mu=\mu_a}$ are close to 0.5 indicates that wall displacement processes predominate in their technical magnetization. In the case of specimens Nos.1,5 & 6 it may be assumed that rotation processes play a significant if not dominant role. Changes in the relative importance of the contribution from the processes of rotation and displacement occurring incident to changes in the composition of the mixed ferrites can be characterized by changes in the value of J_s, the ratio $k/\lambda_s\sigma_i$ and the number and volume of inclusions.

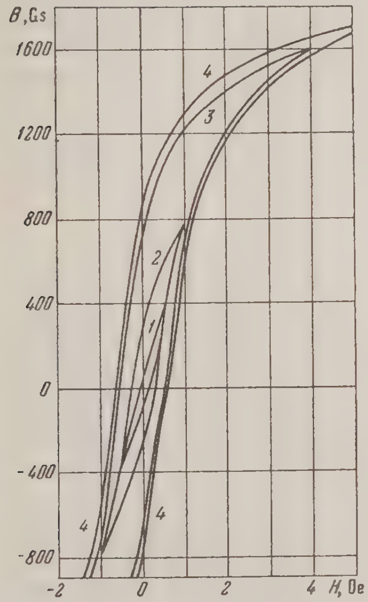

Fig.3. Family of hysteresis loops for specimen No.6 (Ni-Zn-Be-ferrite): 1) $H_o = 0.6$ oersted, $H_c = 0.1$ oersted, $B_R = 64$ gauss, 2) $H_o = 1.0$ oersted, $H_c = 0.28$ oersted, $B_R = 266$ gauss, 3) $H_o = 4.0$ oersted, $H_c = 0.54$ oersted, $B_R = 690$ gauss, 4) $H_o = 10$ oersted, $H_c = 0.55$ oersted, $B_R = 720$ gauss.

Inasmuch as in the case of pure rotation $\mu_a = \mu_{a-R}$, according to formula (5) of Ref.24, we should have f_{o-r} = const. regardless of the state of residual magnetization of the ferrite. In the case of resonance with wall displacements of any type, according to expression (6) of Ref.24, $f_{o-d}/f_{o-R-d} = \sqrt{(\mu_{a-r}-1)/(\mu_a-1)}$;

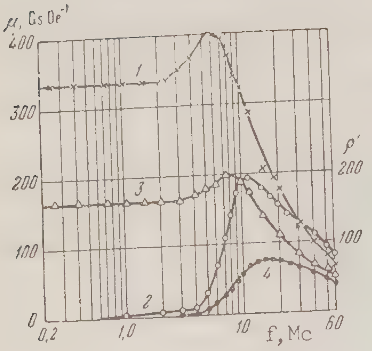

Fig.4.

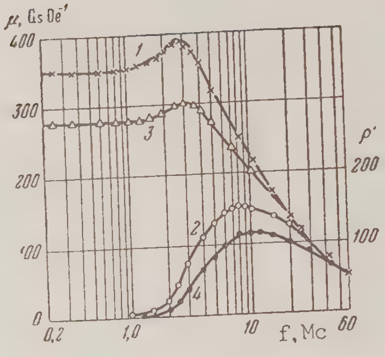

Fig.5.

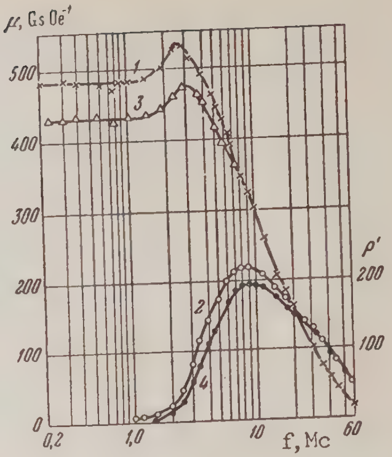

Fig.6

Fig.4. Magnetic spectra for specimen No.2 (Ni-Zn-Cu-ferrite) measured in the demagnetized state of the specimen (curves 1 & 2) and in the state of residual magnetization for H_o = 100 oersted (curves 3 & 4). Curves 1 & 3 are for μ; curves 2 & 4 are for ρ'.

Fig.5. Magnetic spectra of specimen No.5 (Ni-Zn-Mg-ferrite). Curve designations are the same as in Fig.4.

Fig.6. Magnetic spectra of specimen No.1 (Ni-Zn-ferrite). Curve designations are the same as in Fig.4.

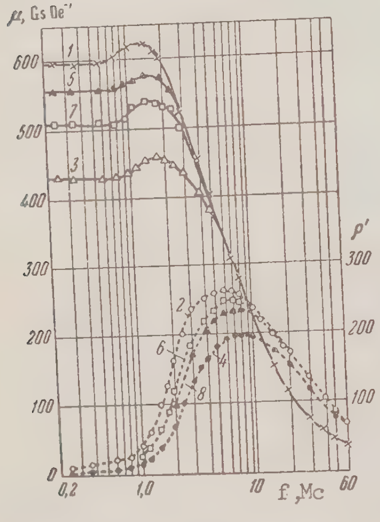

Fig.7.

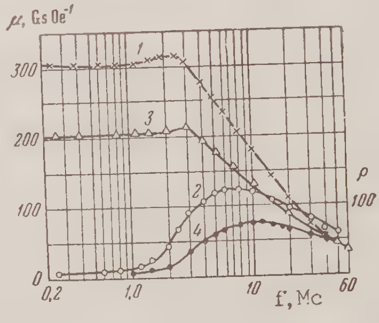

Fig.8.

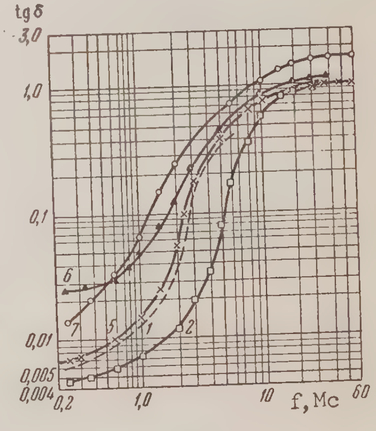

Fig.9.

Fig.7. Magnetic spectra of specimen No.6 (Ni-Zn-Be-ferrite) measured in the demagnetized state (curves 1 & 2) and in the state of residual magnetization: curves 5 & 6 - H_o = 0.6 oersted and μ_{a-R} = 558 gauss/oersted, curves 7 & 8 - H_o = 1.0 oersted and μ_{a-R} = 509 gauss/oersted, curves 3 & 4 - H_o = 10-100 oersted and μ_{a-R} = 431 gauss/oersted. Solid lines - μ; dash lines - ρ'.

Fig.8. Magnetic spectra of specimen No.7 (Li-Zn-ferrite). Curve designations are the same as in Fig.4.

Fig.9. Frequency dependence of the loss tangent for specimens Nos.1,2,5,6 & 7 (for the sake of greater clarity the curve for specimen No.1 is given only in the $f<n$ region and the experimental points are omitted).

in the case of relaxation, on the other hand, according to formula (16) of Ref.25, $f_{c-d}/f_{c-R-d} = \sqrt{(\mu_{a-R} - 1)/(\mu_a - 1)}$. Consequently, the dependence of the frequency $f_u \sim f_o \sim f_c$ on the state of residual magnetization in general is described by the inequality

$$(\mu_{a-R} - 1)/(\mu_a - 1) \leqslant f_u/f_{u-R} \leqslant 1$$

which, rigorously speaking, is valid only in the case when the resonance and relaxation frequencies of the ferromagnet are discrete.

Calculations show that for specimen No.2 $f_u/f_{u-R} = 12/17 = 0.71 = \sqrt{(\mu_{a-R} - 1)/(\mu_a - 1)} = \sqrt{167/333} = 0.71$, which substantiates the predominance of displacement processes in this type of ferrite. For the other specimens we found for the most part that $(\mu_{a-R} - 1)/(\mu_a - 1) < f_u/f_{u-R} < \sqrt{(\mu_{a-R} - 1)/(\mu_a - 1)}$. In particular, for specimen No.7 we obtained $(\mu_{a-R} - 1)/(\mu_a - 1) = 0.67 < f_u/f_{u-R} = 0.71 < \sqrt{(\mu_{a-R} - 1)/(\mu_a - 1)} = 0.8$.

The value of $\sim 13 \cdot 10^{-4}$ obtained for the ratio δ/d for specimen No.2 is of the same order of magnitude as the value deduced by Rado et al[25]. In the case of specimen No.7 δ/d $51 \cdot 10^{-4}$. The value of the ratio η/J_s, where η is the Landau-Lifshits phenomenological constant, for specimen No.7 is $\sim 1.6 \cdot 10^{-2}$, while for specimen No.2 $\eta/J_s < 0.4 \cdot 10^{-2}$, which may be considered satisfactory inasmuch as in the theory of Landau & Lifshits it is assumed that $\eta \ll J_s$.

5. Investigation of the magnetic spectra of mixed ferrites obtained at different sintering temperatures.

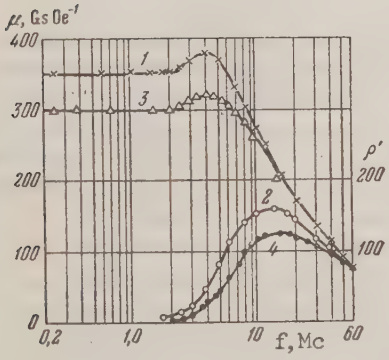

Fig.10. Magnetic spectra of specimen No.4 (Ni-Zn-Cu-ferrite). Curve designations are the same as in Fig.4.

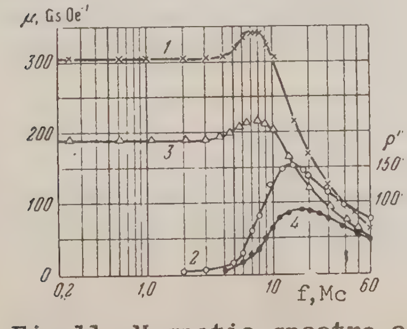

Fig.11. Magnetic spectra of specimen No.3 (Ni-Zn-Cu-ferrite). Curve designations as in Fig.4.

The results of our investigation of specimens of Ni-Zn-Cu-ferrite sintered at four different temperatures are shown in Figs.10, 11, 4 & 12 (the respective sintering temperatures t_s are 1075, 1125, 1140 and 1175°). It follows from the relative shape of the curves for $\mu'_R(f)$ and $\mu'(f)$ that in conformity with the physical considerations set forth above (see "Introduction"), the magnitude of the ratio $(\mu_{a-d} - 1)/(\mu_{a-r} - 1)$ is a function of t_s: as t_s is increased, the ratio first increases to a maximum at $t_{s-opt} \approx 1140^o$ and then begins to fall off. The relatively low value of t_{s-opt} for the Ni-Zn-Cu-ferrite can be explained by the presence in it of CuO which decomposes at relatively low temperatures.

It is interesting to note that the ratio μ_{max}/μ_a attains its greatest value for specimen No.2; as we go to specimens in which the contribution of rotational processes increases, the value of μ_{max}/μ_a decreases (Figs.10, 11 & 12), although the value of $\tan \delta_a$ remains quasi-constant.

When the CuO in Ni-Zn-Cu-ferrite is replaced by NiO the values of the ratio μ_{a-R}/μ_a (see Figs. 11 & 13) and, consequently, of $(\mu_{a-d} - 1)/(\mu_{a-r} - 1)$, too, remain quasi-constant. The ratio $(\mu_a)_9/(\mu_a)_3 = 0.348 \approx [(J_s)_9/(J_s)_3]^2 = 0.41$*; it follows therefore that the change of μ_a is due mainly to the change in J_s. Evaluations of the ratio δ/d give $(\delta/d)_9 \approx 69 \cdot 10^{-4} > (\delta/d)_3 \approx 17 \cdot 10^{-4}$. The damping $(\eta/J_s)_3 < 0.48 \cdot 10^{-2}$, while $(\eta/J_s)_9 < 2.1 \cdot 10^{-2}$ and hence the smaller resonance deviation of μ for

---

*Subscripts 3 & 9 pertain to the specimen Nos. as listed above.

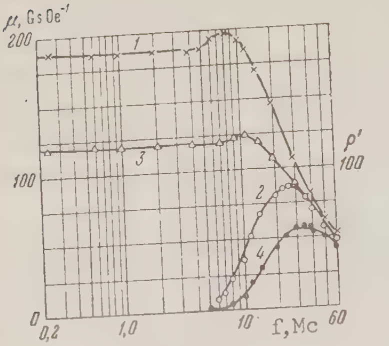

Fig.12. Magnetic spectra of specimen No.10 (Ni-Zn-Cu-ferrite). Curve designation as in Fig.4.

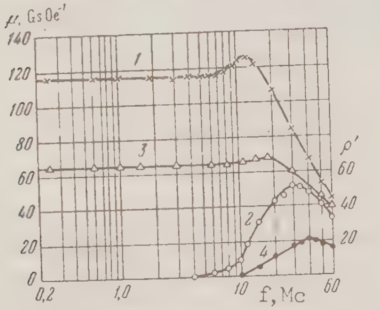

Fig.13. Magnetic spectra of specimen No.9 (Ni-Zn-ferrite). Curve designations as in Fig.4.

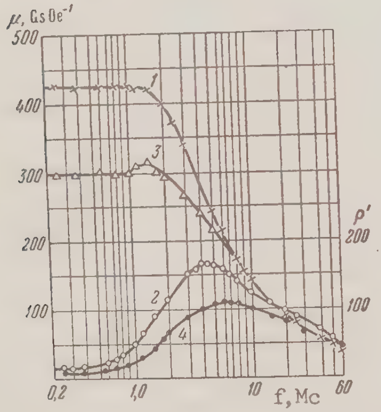

Fig.14. Magnetic spectra of specimen No.8 (Li-Zn-ferrite). Curve designations as in Fig.4.

specimen No.9 is explained by its greater damping. Our conclusions regarding the predominance of displacement processes in specimen No.9 is substantiated by the data of Ref.33 obtained for a ferrite of similar composition; evaluation of μ_{a-r} for specimen No.9 yields $(\mu_{a-r})_9 \approx (4\cdot 224/105) + 1 \approx 10$ gauss/oersted $\ll (\mu_a)_9$.

The curves of Fig.14 serve as further illustration of the influence of t_s on the nature of the magnetic spectra of ferrites.

The ferrite core specimens were kindly put at our disposal by V.I.Evseev.

6. Conclusions

1. The results of our investigation of the magnetic spectra of mixed Li-Zn-, Ni-Zn-Mg-, Ni-Zn-Cu-, Ni-Zn-Be- and Ni-Zn-ferrites with $\mu_a \approx 100$-600 gauss/oersted in the absolutely demagnetized state and in the state of residual magnetization showed that in the main these spectra have a resonance character, which usually persists in the transition to the remanence state and which does not depend on the diameter of the toroid (the core thickness was ~0.6 cm in all cases).

2. The resonance character of the spectra was the more pronounced, the smaller the losses in the ferromagnetic material in the region of the beginning of the resonance rise of permeability and, possibly, the greater the relative contribution of wall displacement processes to the general technical magnetization of the specimen.

3. The difference in the quantitative relationships between the spectra of each specimen in the demagnetized and in the magnetized states indicates that the relative contribution of displacement as against rotation processes in mixed ferrites depends on their composition and the sintering conditions.

4. For some of the investigated types of ferrites we found that magnetization occurs virtually only through domain wall displacement and that the radio-frequency dispersion can be characterized by the inertia of the oscillating effective mass of the walls.

References

1. F.Wagenknecht, Frequenz, 5, 145 (1951).
2. J.J.Went, E.W.Gorter, Philips Tech.Rev., 13, 181 (1952).
3. G.T.Rado, Ref.Mod.Phys., 25, 81 (1953).
4. H.P.Wijn, M.Gevers & C.M. van der Burgt, Rev. Mod. Phys., 25, 91 (1953).
5. H.P.Wijn, in "Soft Magnetic Materials for Telecommunications" Art.7 - Pergamon Press, London, 1953; L'onde Electr., 34,418 (1954); Philips Res.Rep., 10,239 (1955); J.Smit, H.P.Wijn, Advances in Electronics and Electron Physics, v. VI,

p.70. -Academic Press, N.-Y., 1954; E.W.Gorter, Proc. IRE, 43,1941 (1955).

6. F.Brown & C.L.Gravel, Phys.Rev., 97, 55 (1955).

7. F.Flegler, Arch. f. Electrotech., 40,4 (1950).

8. A.J.Welch, P.F.Nicks, A.Fairweather & A.A.Roberts, Phys.Rev., 77,403 (1950).

9. M.Roberts, Phys. et rad., 12, 301 (1951).

10. J.J.Went, H.P.Wijn, Phys.Rev., 82, 269 (1951); Phys. the Hague, 17, 977 (1951).

11. D.Polder, Proc. IEE, II, 97, 246 (1950); H.G.Beljers & J.L.Snoek, Philips Tech. Rev., 11, 313 (1950).

12. L.A.Fomenko, Zhur.eksp.i teor.fiz., 21, 1201 (1951); 24, 365 (1953); 25, 107 (1953); 30, 18 (1956); Fizika metallov i metallovedenie (Physics of metals and metallurgy), 2, 16, 22, 27 (1956).

13. R.Feldtkeller & O.Kolb, ZS. angew. Phys., 4, 448 (1952).

14. M.Kornetzki, ZS.angew.Phys., 3,5 (1951); M.Kornetzki, J.Brachmann, J. Fray & W.Gieseke, ZS.angew.Phys., 4, 371 (1952).

15. J.R.Blewett, M.H.Blewett & M.Plotkin, Rev.Sci.Instr., 24, 800 (1953).

16. R.E.Alley, F.J.Schnettler, J.Appl.Phys., 24, 1524 (1953).

17. N.N.Shol'ts, Izv.AN SSSR, Ser.fiz., 18, 465 (1954). (Translation in Bulletin, Vol.18, No.4, p.155).

18. W.Heister, Arch.f.Electrotechn., 41, 3, 142 (1953).

19. L.I.Rabkin & B.Sh.Epshtein, Zhur.tekh.fiz., 24, 1568 (1954).

20. N.G.Katkov, Dissertation, Moscow Power Eng.Inst., 1955; Izv.AN SSSR, Ser.fiz., 18, 432 (1954). (Translation in Bulletin, Vol.18, No.4, 0.125.)

21. J.Lucas, ZS.angew.Phys., 6, 127 (1954).

22. V.V.Kuznetskii, Dissertation, Moscow Power Eng. Inst., 1955.

23. J.Rozes, L'Onde Elect. 35, 336, 374 (1955).

24. L.A.Fomenko, Preceding article in present issue of the Bulletin.

25. G.T.Rado, R.W.Wright & W.H.Emerson, Phys. Rev., 80, 273 (1950); G.T.Rado, R.W.Wright, W.H.Emerson & A.Terris, Phys.Rev., 88, 909 (1952).

26. Ia.Snoek, New Developments in Ferromagnetic Materials (In Russian trans., M. 1949).

27. F.G.Brockman, P.H.Dowling & W.G.Steneck, Phys. Rev., 77, 85 (1950).

28. L.D.Landau & E.M.Lifshits, Sow.Phys., 8, 157 (1935).

29. W.Döring, ZS.Naturforsch., 373 (1948).

30. S.V.Vonsovskii, Sovremennoe uchenie o magnetizme (Modern Science of Magnetism), M.-L., 1952.

31. S.V.Vonsovskii & Ia.S.Shur, Ferromagnetizm (Ferromagnetism), M.-L., 1948.

32. V.K.Arkad'ev, Elektromagnitnye protsessy v metallakh (Electromagnetic processes in metals), Part II, M.-L., 1936.

33. P.A.Miles, Nature, 174, 177 (1954).

34. H.P.J.Wijn, Physika, 19, 555 (1953).

BULLETIN of the Academy of Sciences of the USSR - Physical Series
Vol.20, No.11 - Transactions of the Conference on Magnetic Radiospectroscopy
(Kazan, 30 May-2 June, 1955)

TABLE OF CONTENTS

	Page Orig.	Trans.
Paramagnetic resonance - E.K.Zavoiskii, S.A.Al'tshuler & B.M.Kozyrev	1199	1091
On the theory of paramagnetic spin-lattice relaxation - S.A.Al'tshuler	1207	1098
Some remarks concerning the processing of experimental data on nuclear paramagnetic absorption - R.A.Zhitnikov	1215	1105
Hyperfine splitting of electron levels in paramagnets - M.M.Zaripov	1220	1110
Electronic paramagnetic resonance in natural beryllium crystals - M.M.Zaripov & Iu.Ia.Shamonin	1224	1114
On the signal shape in nuclear magnetic resonance in the case of medium relaxation times - N.M.Ievskaia	1226	1116
On paramagnetic absorption in parallel fields at superhigh frequencies - A.I.Kurushin	1232	1122
Experimental verification of an expression for resonance paramagnetic rotation - N.N.Neprimerov	1236	1126
Investigation of proton magnetic resonance - N.M.Pomerantsev	1238	1128
On the spin-spin relaxation time in nickel fluosilicate in the absence of a static magnetic field - V.Ia.Kharanen	1245	1134
Towards a phenomenological theory of resonance paramagnetic rotation - L.M.Tsirul'nikova & I.G.Shaposhnikov	1251	1140
On the meaning of spin-spin relaxation time in paramagnetic substances - I.G.Shaposhnikov	1255	1144
Towards a general theory of relaxation phenomena - I.G.Shaposhnikov & A.S.Kuznetsov	1258	1147
On the rotation of the plane of polarization of microwaves in paramagnetic substances - L.Ia.Shekun	1262	1151

Relation between paramagnetic resonance absorption and paramagnetic resonance rotation - L.Ia.Shekun	1265	1154
Ferrite disc in a coaxial line - II. Method of active and reactive loads - Ia.N.Kolli	1267	1156
Frequency characteristics of magnetodielectrics - V.V.Kuznetskii	1274	1163
Investigation of the parameters of ferrites - L.K.Mikhailovskii	1279	1167
Influence of inhomogeneous demagnetizing fields on ferromagnetic resonance - A.I.Pil'shchikov	1284	1172
Ferromagnetic resonance under nonuniform conditions - A.I.Pil'shchikov, Z.D.Trishina & T.A.Zvereva	1299	1186
General properties of linear systems - E.M.Polivanov & V.V.Kuznetskii	1310	1196
Some problems in the theory of gyrotropic media - V.A.Fabrikov	1318	1204
Approximate methods of calculating gyromagnetic media - V.A.Fabrikov & Ia.N.Kolli	1329	1214
Magnetic spectra of solid solutions of Ni-Zn-ferrites in the radiofrequency range at temperatures close to the Curie point - L.A.Fomenko	1336	1220
Investigation of the r-f magnetic spectra of mixed ferrites in the state of residual magnetization - L.A.Fomenko	1348	1232

Translated in 1957 by
Columbia Technical Translations
5 Vermont Ave., White Plains, N.Y.

GAMMA-RADIATION FROM ZN^{65}*

- B.S.Dzhelepov, V.P.Prikhodtseva, A.I.Feoktistov & Iu.V.Khol'nov

Zn^{65} transmutes to Cu^{65} by orbital electron capture and positron decay. The positron decay leads to the ground level of Cu^{65}. Electron capture leads both to the ground level of Cu^{65} and to an excited state at 1122 kev. The transition from the excited to the ground state of Cu^{65} is accompanied by γ-rays of this energy.

No other dependably observed γ-rays of nuclear origin are known. Gamma-rays of 210 and 1370 kev have been reported by some investigators[1,2] but other authors[3,4] do not substantiate these observations.

In addition to the above mentioned γ-line, the spectrum of Zn^{65} contains a weak 511 kev line associated with positron annihilation.

A detailed review of the available data on the radiation from Zn^{65} appears in Ref.3.

The purpose of the present investigation was to determine the ratio of the intensities of the Zn^{65} γ-rays of nuclear and annihilation origin and to check on the possible existence of the 210 and 1370 kev γ-rays by means of the Ritron[5], a γ-spectrometer utilizing recoil electrons, under improved experimental conditions[6].

The experimental γ-spectrum of Zn^{65} with the background subtracted is shown in the accompanying figure. The background in the vicinity of 511 kev amounts to 25%; that in the region of 1122 kev, to 0.1% of the total effect. The section of the spectrum comprising the annihilation line is shown to an enlarged scale in the insert.

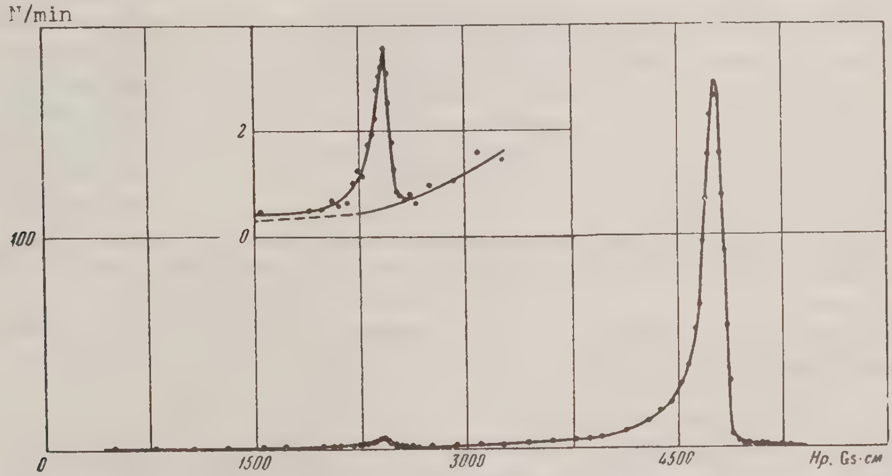

Experimental γ-spectrum of Zn^{65} (background subtracted)

In order to find the ratio of the intensities of the annihilation and nuclear γ-rays from a comparison of the areas under the lines and heights of the peaks, it was necessary to introduce appropriate corrections for the sensitivity of the instrument and the absorption of γ-rays in the source. The former correction is described in Ref.6; the latter amounted to $\sim$20%.

The ratio of the intensities was determined by two methods[6]: from the heights of the peaks and from the areas under the lines. The first method yielded a value of $(6.54\pm0.5)\cdot10^{-2}$; the second yielded $(6.80\pm0.5)\cdot10^{-2}$.

We therefore have a mean value

---

*Preliminary results of the investigation were presented at the Third All-Union Conference on Nuclear Spectroscopy (1953).

$$\frac{\gamma_{511}}{\gamma_{1122}} = (6.70\pm0.5)\cdot10^{-2}.$$

We made a special search for the 210 and 1370 γ-lines but failed to detect them. Even if such γ-rays exist their intensity must be less than $5\cdot10^{-2}$ and $5\cdot10^{-4}$ quanta per decay, respectively. The rather high upper limit in the first case is explained by the relatively low sensitivity of our instrument in this energy region.

In the energy range from 1400 to 3000 kev there are no γ-rays from Zn^{65} having an intensity greater than $5\cdot10^{-4}$ quanta per decay.

From the ratio of the intensity of the annihilation and nuclear γ-rays we obtain $\beta^+/\gamma_{1122} = (3.35\pm0.25)\cdot10^{-2}$, i.e., a value which is in good agreement with that obtained in the investigation of Ref.3 ($3.0\cdot10^{-2}$) from observation of photoelectrons.

The γ-ray conversion coefficient may be written as

$$\alpha_{K+L} = \frac{e}{\gamma} = \frac{e}{\beta^+}\cdot\frac{\beta^+}{\gamma}$$

If for determining the conversion coefficient for the 1122 kev γ-transition we take $e/\beta^+ = 5.5\pm0.5\cdot10^{-3}$ from Ref.3 and β^+/γ from our data, we obtain $\alpha_{K+L} = 1.84\cdot10^{-4}$ and $\alpha_k \approx 0.9\ \alpha_{K+L} \approx (1.66\pm0.3)\cdot10^{-4}$.

The theoretical values of the conversion coefficients obtained by interpolation of the data of Rose for Z = 29 and E = 1122 kev are listed in the following table.

K conversion coefficients for Cu (1122 kev) - Ref.7

Type transition	E1	E2	E3	M1	M
α_K	$(9,3-10,5)\cdot10^{-5}$	$2,03\cdot10^{-4}$	$4,4\cdot10^{-4}$	$1,94\cdot10^{-4}$	$3,74\cdot10^{-4}$

From a comparison of our value with the theoretical values it will be seen that satisfactory agreement is obtained if we assume that the 1122 kev γ-transition is E2, M1 or a mixture of E2 + M1.

This deduction is evidence in favor of the first excited level of Cu^{65} being a collective level.

The writers desire to thank L.S.Lebedev and I.B.Golovanov for their assistance in making the measurements.

"V.G.Khlopin" Radium Institute of the
Academy of Sciences of the USSR

References

1. R.Bouche, Physica, 18, 1171 (1952).
2. K.Mann, D.Rankin & P.Daykin, Phys. Rev., 76, 1719 (1949).
3. A.Bashilov, N.Anton'eva, D.Broder & B.Dzhelepov, Izv. AN SSSR, Ser. fiz., 17, 468 (1953).
4. M.Good, Phys. Rev., 81, 891 (1951).
5. B.Dzhelepov, N.Zhukovskii & Iu.Khol'nov, Izv. AN SSSR, Ser. fiz., 18, 599 (1954). (Translation in Bulletin, Vol.18, No.5, p.285.)
6. B.Dzhelepov, V.Prikhodtseva & A.Feoktistov, Iu.Khol'nov, Present issue of the Bulletin, p. 1245.
7. K.Siegbahn, editor, Beta- and Gamma-Ray Spectroscopy, Amsterdam, 1955.

GAMMA-SPECTRUM OF As^{76}*

- B.S.Dzhelepov, V.P.Prikhodtseva, A.I.Feoktistov & Iu.V.Khol'nov

Apparatus

The complex γ-spectrum of 1.1-day As^{76} was studied by means of the Ritron[1]. This instrument was considerably improved in 1956: the vacuum system of the counters was separated from that of the spectrometer case. The main difficulty in doing this stemmed from the fact that the counter at the first focus of the instrument has very large windows(0.8 x 3.3 cm), which were originally covered with cellophane. In connection with the separation of the vacuum systems, it was necessary to prepare thin ($\sim$1-2 μ) window films capable of withstanding a pressure differential of $\sim$10 cm Hg. We prepared them of collodion film 1-2 μ thick, consisting of some dozens of very thin laminae.

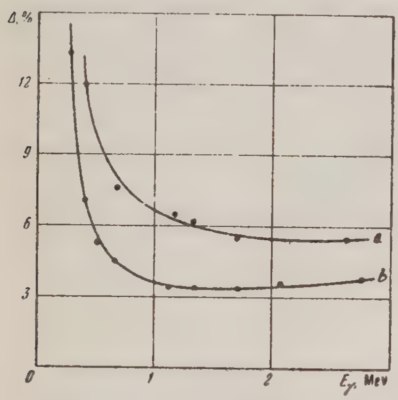

Fig.1. Energy dependence of the relative line half-width before and after modification of the Ritron.

The counters were filled with a 50-50 mixture of Ar and CH_4 at a pressure of 10.4 cm Hg. The instrument chamber is continuously evacuated by a forevacuum pump. All the other parameters of the instrument remained as described in Ref.1. Fig.1 illustrates the improvement in the principal characteristic of the instrument obtained as the result of the modifications. The curves show the dependence of the relative line half-width on the energy under the old conditions (curve a) and under the new ones (curve b).

Mention should also be made of the very appreciable reduction of the background (with the target down), which was formerly produced by the Compton recoil electrons ejected from the gas in the region of the target. This obviously facilitates the study of the weak lines.

The instrument was recalibrated in energy (accuracy $\sim$1%) with reference to the following known γ-lines: 190 kev line of In^{114*}, 279 kev of Hg^{203}, 412 kev of Au^{198}, 511 kev of Cu^{64}, 661 kev of Cs^{137}, 1122 kev of Zn^{65}, 1171 and 1331 kev of Co^{60}, 597 and 1691 kev of Sb^{124} and 1380 and 2760 kev of Na^{24}.

Calibration in intensity is, of course, the most difficult problem where instruments of this type are concerned. Since there is a first counter in the path of the electrons it is difficult to calculate the theoretical spectral sensitivity. Consequently we calibrated the spectrometer by measuring the γ-lines of the following nuclides whose decay schemes are well known: Hg^{203} (279 kev), Au^{198} (412 kev), Cs^{137} (661 kev), and Co^{60} (1171 and 1331 kev).

The absolute activity of the sources was determined by E.A.Khol'nov on the VNIIM[2] (All-Union Scientific Research Institute of Metrology) calorimeter with an accuracy of 3 to 5%.

For obtaining the spectral sensitivity we determined the area under each line (after subtraction of the background, conversion to equal energy intervals and introduction of the appropriate corrections for γ-ray absorption and the efficiency of the counters); the resultant values were divided by the activity of the given source and the points plotted on a graph, the scale of which was adjusted so that at $E_\gamma = 1$ Mev the spectral sensitivity S_γ of the instrument would equal unity (see determination of S_γ in Ref.1). The five points on the left in Fig.2 correspond to the data obtained for the sources listed above. The two points in the high energy region correspond to the two cascade γ-lines of

---

*Preliminary results of the investigation were presented at the Third All-Union Conference on Nuclear Spectroscopy (1953).

Na^{24} (1380 and 2760 kev). The absolute activity of the Na^{24} source was not determined. We made use of the fact that the energy of the first (1380 kev) γ-line of Na^{24} is close to that of the second (1331 kev) line of Co^{60}. If the area under the first Na^{24} line be represented by the point on the extension of the curve into the hard region, the area under the second line, expressed in the same units, will show how the spectral sensitivity curve must be drawn in the high energy region. The described calibration is also an absolute calibration. We can determine the number of quanta of any energy emitted by an investigated source. To do this one must know that in the case of 1022 kev γ-rays emitted by a 1 curie source in the amount of one photon per decay the instrument will record 589 coincidences per minute at the line peak.

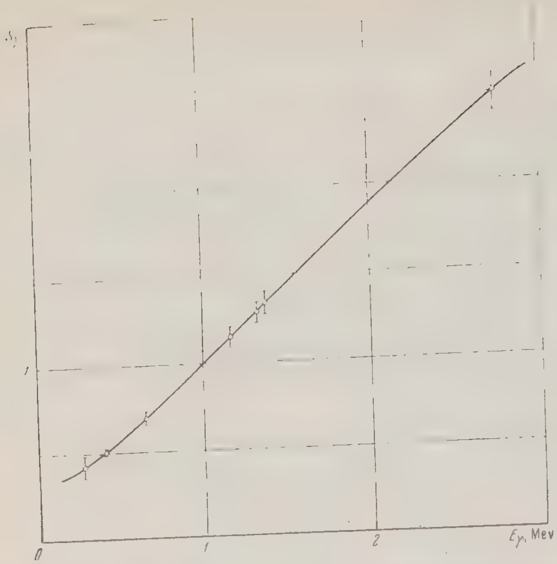

Fig.2. Calibration of spectrometer in intensity. Each division on the vertical scale equals 1/3.

Experimental results

The γ-spectrum of As^{76} was studied under the conditions described above. The experimental spectrum is shown in Fig.3 with the background subtracted. The background under the 562 kev line amounted to 0.7% of the effect; under the 2085 kev line, it amounted to 0.2%. The insert in Fig.3 shows the hardest part of the As^{76} spectrum. To facilitate the search for weak lines, the transmission factor was increased: a 400 μ thick beryllium target was mounted in place of the standard 50 μ thick cellophane target; the slits were widened and the instrument was filled with pure helium to 32 mm Hg pressure. These changes obviously lowered the resolution of the instrument.

The results of an investigation of the 2070 kev line of Sb^{124} under analogous conditions are given by the ✕ points. The hardest γ-lines of Sb^{124} have a very low intensity ($\sim 2\cdot 10^{-3}$ quanta per decay[3]) and do not appear in the spectrum.

It will be seen from the figure that in the case of Sb^{124} the intensity falls off rapidly to zero with increasing energy, whereas for As^{76}, it differs appreciably from zero up to ~2800 kev. The difference between the ordinates of the Sb^{124} and As^{76} spectra can be resolved into components in different ways; in particular, it can be interpreted as being due to the existence of two lines of 2500 and 2750 kev energy and a total intensity of 0.16 (referred to an intensity of 100 for the 562 kev line). A summary of the data on the spectrum of As^{76} is given in the table.

Energy and intensity of the γ-lines of As^{76}

Line number	E, keV	I, %	Line number	E, keV	I, %
1	562	100	8	(1510)	0,10
2	660	14,3	9	(1620)	0,04
3	(730)	0,5	10	1765	0,72
4	(870)	0,5	11	(1850)	0,05
5	1222	12,7	12	2085	1,95
6	(1400)	0,17	13	~2500	0,16
7	1430	0,80	14	~2750	

The spectrum was resolved into components by using "standard" lines, i.e., single lines obtained under the same conditions. In the table the energy values of very weak γ-lines are given in parentheses; we cannot positively assert the existence of these lines. They were obtained as remainders

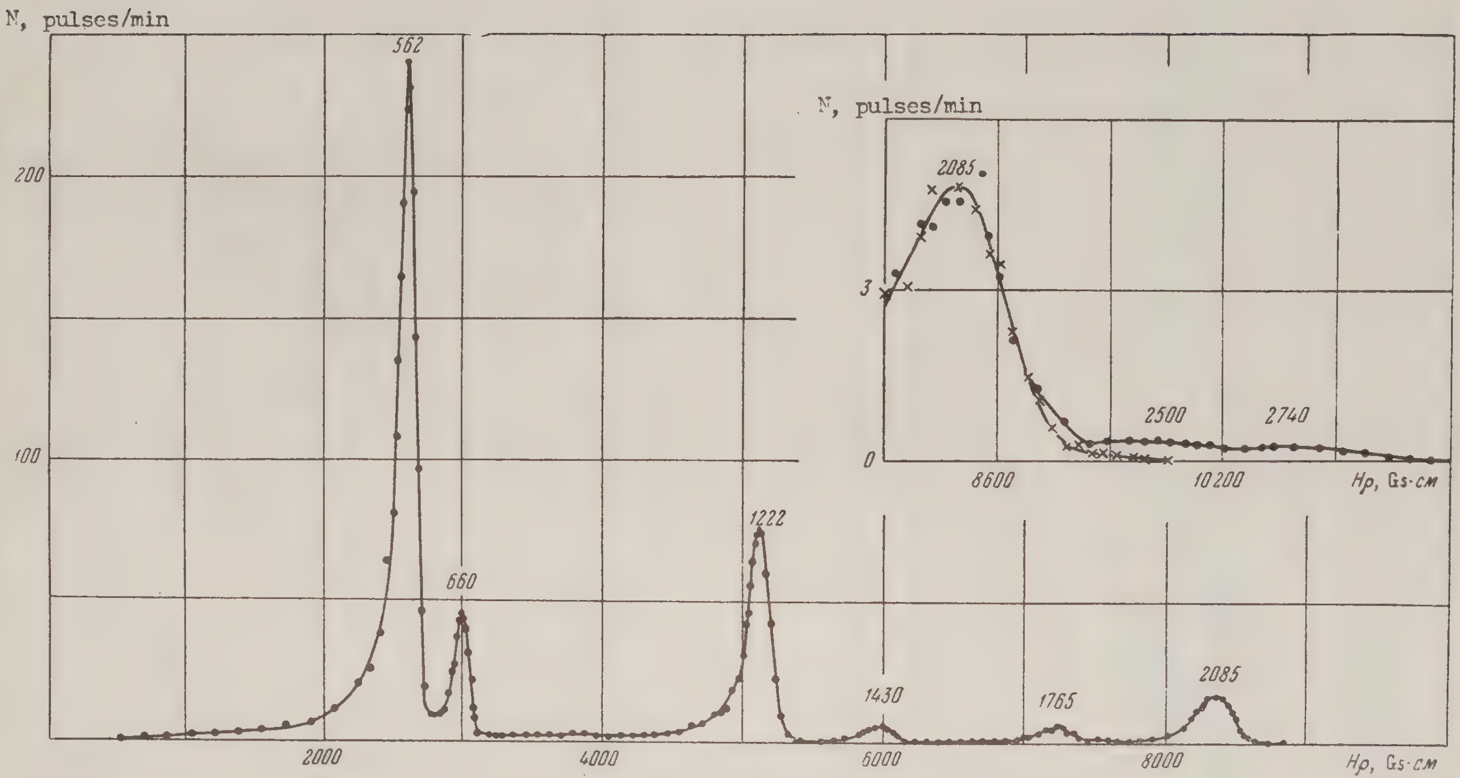

Fig.3. Experimental γ-spectrum of As^{76} (background subtracted). The figures at the peaks indicate the energy in kev.

after subtracting the principal lines. Consequently, the indicated energies and relative intensities are tentative and approximate.

The writers desire to thank E.A.Khol'nov for measuring the activities of the specimens used for calibrating the instrument in intensity and graduate students I.B.Golovanov and L.S.Lebedev for their help in making the measurements.

"V.G.Khlopin" Radio Institute of the
Academy of Sciences of the USSR

References

1. B.Dzhelepov, N.Zhukovskii & Iu.Khol'nov, Izv. AN SSSR, Ser.fiz., 18, 599 (1954). (Translation in Bulletin,Vol. 18, No. 5, p. 285)

2. K.Aglintsev, E.Khol'nova, Doklady AN SSSR, 98, 357 (1954).

3. B.Dzhelepov & I.Iaritsina, Izv. AN SSSR, Ser.fiz., 20, 343 (1956). (Translation in Bulletin, Vol.20, No.3, p.314.)

INVESTIGATION OF COULOMB EXCITATION OF NUCLEI BY NITROGEN IONS

- D.G.Alkhazov, D.S.Andreev, A.P.Grinberg & I.Kh.Lemberg

Introduction

The trend towards ever higher energies of the particles used for Coulomb excitation of nuclei is connected with the fact that the cross section for this process increases sharply with the energy of the bombarding particles. This energy, however, can be increased only up to a certain limit, a limit determined by the condition that the utilized particles should not produce nuclear reactions in the given target. When such reactions occur, interpretation of the experimental results and calculation of the Coulomb excitation cross section becomes difficult: some of the lines in the γ-ray spectrum in this case prove to be due to the nuclear reactions and not to Coulomb excitation; for other γ-lines the quantum yield is only partially related with the process of Coulomb excitation.

In Ref.1 it was shown that if, instead of protons or α-particles, one uses nitrogen ions accelerated to a sufficiently high energy for Coulomb excitation, it is possible to obtain larger cross sections for this process; at the same time there is little danger of inducing nuclear reactions at these nitrogen ion energies. Another advantage of using heavy ions is that the interfering background consisting of the characteristic x-rays of the target atoms is relatively much weaker than when protons are employed[1,2].

In the case of quadrupole excitation the cross section for Coulomb excitation is given by

$$\sigma = \frac{m^2 v_f^2}{Z_2^2 e^2 \hbar^2} B_e(2) f_2(\xi), \tag{1}$$

where

$$\xi = \frac{Z_1 Z_2 e^2}{\hbar}\left(\frac{1}{v_f} - \frac{1}{v_i}\right), \tag{2}$$

m is the reduced mass of the bombarding particle, Z_1 is the number of protons in its nucleus, v_i and v_f are its relative velocities before and after collision, Z_2 is the number of protons in the nucleus of the target atoms, $B_e(2)$ is the reduced probability of an electric quadrupole transition for this nucleus from its ground state to the given excited state and $f_2(\xi)$ is the Coulomb excitation function.

Fig.1 shows the results of calculations of the ratio σ_N/σ_p, where σ_N is the cross section for Coulomb excitation of some state of the nucleus by nitrogen ions (N^{14}) and σ_p is the cross section for Coulomb excitation of the same state by protons (having a different energy - see below). The curves for $\sigma_N/\sigma_p = f(\xi_p)$ were calculated for three targets characterized by appreciably different values of Z_2. In each case the characteristic parameter of the family of curves is $k = \Delta E/E_p$, where ΔE is the excitation energy of the nuclear state in question and E_p is the collision energy in bombardment of the given target with protons having a kinetic energy $E_{1,p}$ in the laboratory system. ($E_p = \frac{m_2}{m_p+m_2} E_{1,p}$, where m_p is the mass of the proton and m_2 is the mass of the nucleus of the target atoms).

In calculating the values of σ_N/σ_p we assumed that $E_N = 7E_p$.

There is a definite energy E_p corresponding to each value of ξ_p at a given k (it can be shown that $E_p = \text{const.}/\xi_p^2$). Some of these values of E_p are listed in Fig.1.

As may be seen from the curves for values of ξ_p in the region from 0 to 1, which comprises virtually all the cases of interest, the ratio σ_N/σ_p is much greater than unity. For example, if we are interested in Coulomb excitation of the first and second excited states of tantalum ($\Delta E_1 = 0.137$ mev and $\Delta E_2 = 0.303$

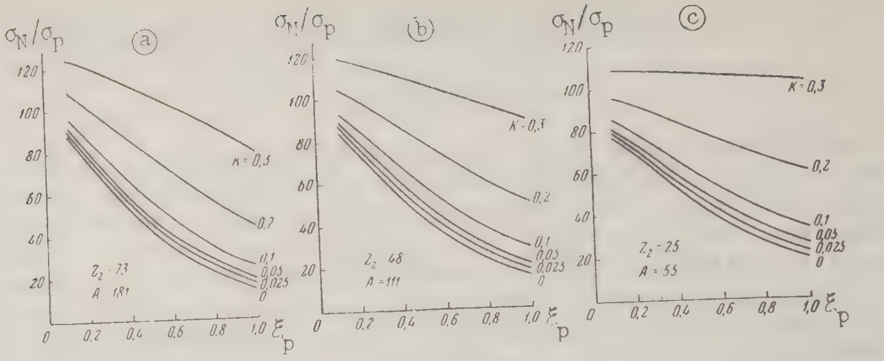

a

E_p, Mev			56	31	20	14	10,2	8	6,2	5	K=0,3
		46	20	11	7,3	5,1	3.7	2,9	2.3	1,8	0,2
	38	9,6	4,3	2,4	1,5	1,1	0,8	0,6	0,48	0,38	0,1
	8,8	2,2	0,98	0,55	0,35	0,24	0,18	0,14	0,11	0,09	0,05
	2,14	0,54	0,24	0,13	0,09	0,06	0.04	0,033	0,026	0.021	0,025
ξ_p	0,1	0,2	0,3	0,4	0,5	0,6	0,7	0,8	0,9	1,0	

b

E_p, Mev		54	24	13,5	8,6	6	4,4	3,4	2,7	2,2	K=0,3
		20	8,8	4,9	3,2	2,2	1.6	1,2	0,98	0,79	0,2
	16,6	4,2	1,8	1	0,66	0,46	0,34	0,26	0,2	0,17	0,1
	3,8	0,96	0,43	0,24	0,15	0,11	0.08	0,06	0,05	0,04	0,05
	0,92	0,23	0,10	0,06	0,04	0,026	0,019	0,014	0,011	0,009	0,025
ξ_p	0,1	0,2	0,3	0.4	0,5	0,6	0,7	0,8	0,9	1,0	

c

E_p, Mev	58	14,5	6,4	3,6	2,3	1,6	12	0,9	0,7	0,6	K=0,3
	21	5,3	2,4	1,3	0,9	0,6	0,4	0,33	0,26	0,21	0,2
	4,5	1,1	0,5	0,28	0,18	0,12	0,09	0,07	0,06	0,04	0,1
	1,03		0,114		0,041		0,021		0,013		0,05
	0,25		0,028		0,010		0,05		0,003		0,025
ξ_p	0,1	0.2	0,3	0,4	0,5	0,6	0,7	0,8	0,9	1,0	

Fig.1. Dependence of the ratio σ_N/σ_p on ξ_p with different values of $k = \Delta E/E_p$. The curves 0 were computed according to the expressions of semiclassical theory[3,4], applicable when k → 0.

mev) and the target is bombarded with 15.6 Mev nitrogen ions (i.e., $E_N = 14.5$ mev and $E_p \approx 2.1$ mev), we have $(\sigma_N/\sigma_p)_1 = 75$ and $(\sigma_N/\sigma_p)_2 = 50$.

When a thick tantalum target is used the ratio of the yield of 0.37 Mev γ-quanta under bombardment by nitrogen ions with $E_N = 14.5$ Mev to the yield of the same quanta under bombardment by protons with $E_p = 2.1$ Mev equals 12 (Ref.1).

Calculations also show that under these same experimental conditions the ratio of the number of K x-ray quanta produced by ionization of tantalum atoms by the incident particles to the number of γ-quanta of 0.137 Mev energy obtained must be 15 times smaller with nitrogen ion bombardment as compared with proton bombardment.

Our experiments have verified the above deductions. We investigated Coulomb excitation of nuclei of 21 elements by nitrogen ions. In choosing the procedure we had in mind two independent problems: 1) determining the energy of the lower excited levels of the investigated nuclei, and 2) calculating the reduced transition probability $B_e(2)$. Knowing $B_e(2)$, one can calculate the intrinsic quadrupole moment of the given nucleus, if it is known that the given excited level is a rotational one.

In the present article we shall describe the results pertaining only to the first of these problems.

Description of the experiment

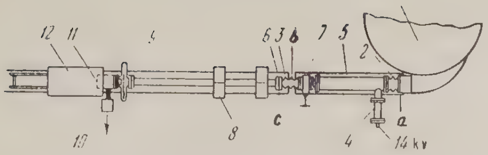

Fig.2. Diagram of apparatus (view from above): 1) cyclotron chamber, 2 & 3) bellows, 4) porcelain bushing insulator for voltage lead to one plate of the deflecting capacitor, 5 & 6) hinged mounting beams, 7) vacuum gate for replacing target, 8) magnetic lenses, 9) glass section for observing screen, 10) input stage of current integrator, 11) target, 12) iron housing with photomultiplier.

The 15.6 Mev triply-charged nitrogen ions were obtained on the cyclotron of Leningrad Physical-Technical Institute of the USSR Academy of Sciences. We used an ion source with a tubular graphite anode and a cathode of thick (3.5 mm dia.) tantalum wire. A "drawing electrode was mounted a short distance from the anode slit; it was screwed to one of the cyclotron dees. The cathode was supplied from a separate dc generator.

The beam used for the work was extracted by means of a conventional deflector; only the small part of the beam passing through an oval aperture 20 mm high and 10 mm wide (the plate with this aperture was mounted in plane a in Fig.2) was utilized. Consequently, the beam of triply-charged ions incident on the target was fairly homogeneous as regards energy. Virtually the only triply-charged particles in the beam were the ions which emerged triply-charged from the ion source and were accelerated in the cyclotron at the principal frequency of the accelerating field. The probability of passing through the entire deflector channel was very small where particles emerging from the ion source in the form of singly-charged ions and then losing two electrons due to collisions with molecules of the residual gas were concerned, inasmuch as for such ions the center of curvature of the last turn of the orbit would be close to the geometric center of the chamber only in exceptional cases.

In the course of testing it was found that in addition to the triply-charged ions there were singly-charged nitrogen ions in the extracted beam. These were ions which emerged as singly-charged particles from the ion source, were accelerated in the cyclotron without changing their charge and finally passed through the deflector. Such ions obviously have the same magnetic rigidity as the triply-charged ones and consequently their energy is one ninth that of the triply-charged ions.

In order to obtain experimental data from which it would be possible to calculate the absolute values of the cross sections for Coulomb excitation it was obviously essential to eliminate these singly-charged ions from the beam. Their energy is so low that in striking the target they would not yield Coulomb excitation γ-rays; however, the total ion current on the target would be the sum of the singly- and triply-charged ion components in unknown proportions.

The triply-charged ions were separated from the singly-charged ones by means of deflection in an electrostatic field. The beam was passed between the parallel horizontal plates of a capacitor to which a voltage of $\sim$14 kv ($E \approx \approx 7$ kv/cm) was applied. The length of the capacitor plates was 25 cm.

After the capacitor, the beam of triply-charged ions passed through a 30 mm diameter opening located in plane b (Fig.2) and then through a system of two magnetic quadripole lenses which focused the beam on the target. The basic parameters of each of the lenses were the following: diameter of aperture - 4 cm, radius of curvature of the cylindrical surface of the pole piece - 2.3 cm, length of lens - 10 cm, weight of lens (with windings) - 50 kg, total number of turns in the four windings $\sim$4000, current at optimal focusing $\sim$1.8 amp.*

---

*The requisite current values in the lens windings for optimal focusing of the beam as a function of the focal plane position were established in a separate series of tests.

The distance of the central plane of the first lens from the exit windows of the cyclotron was ~1.6 meters; the distance between the central planes of the lenses was 50 cm; the distance of the target from the central plane of the second lens was 1.25 meters.

The introduction of the magnetic lenses led to a five-fold increase in the intensity of the nitrogen ion beam incident on the target and made it possible to move the recording unit to a considerable distance from the cyclotron.

The target in the form of a 28 mm diameter disc was placed at the bottom of an insulated metallic cup which served as the beam catcher (Faraday cup). In front of the cup there was a slider with a disc of ZnS. This slider could be moved back and forth in the vacuum by means of a solenoid over a core attached to the slider so as to cover or uncover the Faraday cup.

With the ZnS coated disc over the cup the luminous spot due to the beam could be observed through the glass section of the tube. This arrangement made it possible to check the centering of the beam and the focusing. With optimal currents in the lens windings the spot on the beam was ~5 mm high and ~14 mm wide.

The mounting beams 5 and 6 (Fig.2) were linked by means of a universal joint which made it possible to rotate the latter about point c in any direction and thereby adjust the system so that the ion beam would be incident on the central part of the target.

The amount of electricity in the beam incident on the target was measured by a vacuum tube current integrator which was calibrated before and after each Coulomb excitation measurement (to this end the known current from an outside emf source was passed through the integrator). In order to eliminate possible errors in measuring the ion beam current (errors associated with secondary-electron emission), a ring was mounted in front of the Faraday cup and a potential of 90 v relative to the cup applied to it. The triply-charged nitrogen ion current attained 0.5 microamp (the total current of the extracted beam measured in the plane a in Fig.2 amounted to 10-15 microamp).

The γ-radiation from the bombarded target was investigated by means of a scintillation spectrometer with a NaI(Tl) crystal 29 mm in diameter and 13 mm thick. A block diagram of the spectrometer is shown in Fig.3. The type FEU-S (ФЭУ-С) photomultiplier and the first cathode follower were provided with efficient magnetic shielding in the form of a triple-layer iron cylinder. The photomultiplier was supplied from a dry cell assembly (V ≈ 1.2 kv). The potential applied to the photomultiplier was monitored by means of a potentiometer circuit and maintained constant to within 0.01%. From the cathode follower, the photomultiplier pulses were transmitted over a 50 meter long high-frequency cable to a linear amplifier with negative feedback from which the pulses entered the 50-channel pulse height analyzer. (The analyzer was constructed by L.N.Gal'tserin.) This instrument utilizes the principle of transforming pulse heights into durations (times). The analyzer circuit incorporates a blocking arrangement which disconnects the analyzer input from the amplifier output for 16 msec after each pulse accepted by the analyzer. This is the time interval required for completion of the pulse analysis process terminating in tally on the register of one of the channels. Usually under the conditions of our experiment the number N_o of pulses arriving on the input of the amplifier (Fig.3) during the time of the experiment appreciably exceeded the number N_b of pulses

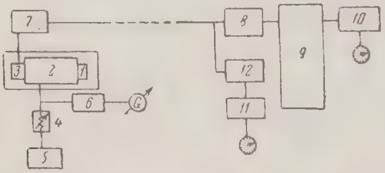

Fig.3. Block diagram of the γ-spectrometer: 1) scintillator, 2)FEU-S photomultiplier, 3) cathode follower, 4) regulating resistor, 5) dry cell assembly, 6) potentiometer circuit for measuring voltage, 7) heavy-duty cathode follower, 8) linear amplifier, 9) 50-channel pulse height analyzer, 10 & 11) scaling circuits with 1:1024 scaling ratio, 12) integral discriminator.

accepted for analysis by the pulse height analyzer 9. In order to be able to calculate the absolute values of σ from the experimental spectrograms it was obviously necessary to know the ratio N_b/N_o. To this end the fast integral discriminator 12 and the scaling circuit 11 were introduced into the set-up for recording the N_o. The total number of operations of the blocking circuit during this same period (i.e., the value of N_b) was recorded by means of the scaling circuit 10.

The analyzer circuit had provision for introducing a regulating bias voltage V_b; with the bias voltage applied the height of a pulse entering the measuring assembly is therefore $V_a - V_b$ where V_a is the amplitude of the initial pulse. The gate in the discriminator 11 was adjusted in each experiment so that it would coincide with the lower level of discrimination of analyzer 9.

The pulse height analyzer was calibrated prior to each experiment by means of a standard pulse generator (calibrator) incorporated in the analyzer unit 9 and an accurate voltmeter. In all measurements the analyzer gate width was 1 volt.

Calibration of the γ-spectrometer as a whole was affected with reference to the γ-lines of Ce^{141} (146 kev), Hg^{203} (279.5 kev), Cs^{137} (661 kev) and Co^{60} (1.17 and 1.33 Mev). The choice of reference source for each experiment was dictated by the requirement that the energy of the calibration γ-line be as close as possible to that of the investigated γ-lines. As an indication of the resolution of the spectrometer we note that the relative half-width of the 661 kev Cs^{137} γ-peak was 9.5%.

In our set-up there were the following absorbing layers between the target and the crystal: Cu - 0.19 mm, Al - 1 mm and MgO - 1 mm. In addition, in some cases the target had a copper support, varying in thickness from 80 μ to 0.5 mm (see following section), which obviously also absorbed the γ-rays.

Experimental Results

The data obtained on the excitation energies of a number of nuclei are listed in the table below. When known we also list the mass number of the nucleus to which the given levels pertain.

Bombarded nuclei and γ-ray energies, kev*

F^{19}_{9}	125 205	Ge^{73}_{32}	72	Ag_{47}	310 409	Ta^{181}_{73}	138 301
Na^{23}_{11}	435	Se^{77}_{34}	238 452	Cd^{113}_{48} Cd^{111}_{48} Cd^{114}_{48}	279 325 543	W_{74}	112
V^{51}_{23}	320	Mo^{95}_{42} Mo^{100}_{42}	210 540	In^{115}_{49}	562	Au^{197}_{79}	286 580
Mn^{55}_{25}	127 590	Rh^{103}_{45}	295 358	J^{127}_{53}	60 205	Pb^{207}_{82}	580

*The gamma energies were determined with an accuracy of 1–3%.

No γ-lines were observed for K, Ni, Cu, Sn and Bi. In the case of all these elements except K we bombarded metallic targets. We used the results of these measurements for introducing the requisite correction for the bremsstrahlung produced by the slowing down of the nitrogen ions in different targets (these corrections were necessary in computing the absolute values of σ).

Below we give the experimental data on Coulomb excitation for each of the investigated elements.

F^{19}. Coulomb excitation of F^{19} has been studied in detail by Sherr, Li & Christy[5] who used α-particles for bombarding their targets. They observed levels with ΔE = 109 and 196 kev. These levels were detected earlier in the $Ne^{21}(d,\alpha)F^{19}$ reaction. In our experiments the target materials was CaF_2 deposited on a 0.35 mm thick copper support from a suspension in benzine. The superficial density of the CaF_2 layer was 2.3 mg/cm^2.

Na^{23}. Coulomb excitation of Na^{23} has been studied by Temmer & Heydenburg[6,7] who also used α-particles. They detected a γ-line of 439 kev energy. It follows from the excitation curve that this γ-line is associated with electric quadrupole excitation of Na^{23}. A level with ΔE = 440 kev was known earlier from data on inelastic scattering of protons and neutrons from sodium. There was no information on this level from β-decay data until recently when this level was detected by Nemilov & Ovchinnikov[8] in studying β^--decay of Ne^{23}.

In our experiments we used a target consisting of a compressed disc of NaCl ~130 mg/cm^2 in thickness on a 0.5 mm thick copper support. It is evident from control experiments with a KCl target that the observed γ-line at 435 kev belongs to sodium rather than to chlorine.

V^{51}. Natural vanadium contains 99.8% V^{51}. Coulomb excitation of vanadium by α-particles has been investigated by Temmer and Heydenburg[6,9] and its excitation by protons by Mark, McClelland & Goodman[10]. These investigators detected a 320 kev γ-line which corresponds to the excited level of V^{51} known from data on β-decay and inelastic proton scattering. In our experiments the target was prepared by depositing vanadic acid from a suspension in benzine on a copper support 0.5 mm thick. The superficial density of the target was ~20 mg/cm^2.

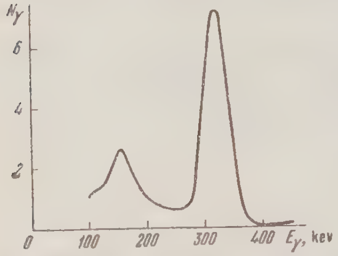

Fig.4. Coulomb excitation γ-spectrum of vanadium.

The γ-spectrum we obtained for vanadium is shown in Fig.4. The background due to cosmic rays and bremsstrahlung has been subtracted (this applies to all the other spectra appearing below). The vertical axis is scaled in N_γ the number of γ-quanta recorded by the scintillation counter in a 10 kev wide energy interval per 1 microcoulomb nitrogen ion current.

Mn^{55}. Coulomb excitation of manganese by α-particles has been studied by Temmer & Heydenburg[9] and by protons by Mark, McClelland & Goodman[10]. The former report a line at 128 kev; the latter at 131 kev. The corresponding level was detected earlier in investigating inelastic scattering of protons[11]. Mark, McClelland & Goodman also observed γ-lines of energies 420, 505, 650 and 975 kev, the densities of which relative to the 131 kev line ranged from 0.2 to 0.01.

The results of our measurements are given in Fig.5. The target was a ~2 mg/cm^2 layer of Mn deposited by vacuum evaporation on a 150 μ thick copper support.

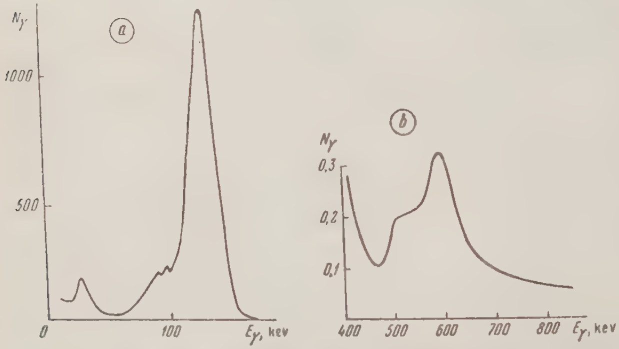

Fig.5. Coulomb excitation γ-spectrum of manganese.

According to our data the energy of the first excited level of Mn^{55} is 127 kev. Bernstein & Lewis[12] on the basis of measurements of energy of the conversion electrons emitted by electrically excited Mn^{55} give a value of 128 kev.

Fig.5,b shows the results obtained when a bias potential was applied in the pulse height analyzer. In this case there is no overloading and blocking of the analyzer by a large number of small pulses (in this particular case the pulses due to γ-quanta with $E_\gamma < 400$ kev) so that the necessary number of counts corresponding to γ-quanta with $E_\gamma > 400$ kev could be obtained in an appreciably shorter interval. As may be seen from Fig.5,b there appears a γ-line at 590 kev, the intensity of which (without correction for the internal conversion coefficient) amounts to 0.02% of the intensity of the 127 kev γ-line.

Our data substantiate the assumption advanced in Ref.10 that the 420, 650 and 975 kev lines are associated with nuclear reactions rather than with Coulomb excitation. Our data do not allow of drawing any definitive deduction regarding the origin of the 505 kev line.

Ge^{73}. Natural germanium consists of a mixture of several isotopes. Coulomb excitation of germanium by α-particles has been repeatedly studied by Tremmer and Heydenburg[6,9,13].

In our experiments the target was a 0.83 mm thick disc cut from a germanium single crystal. Our results are shown in Fig.6. The spectrum was recorded in the energy region up to 210 kev. It will be seen that a 72 kev line was observed. Tremmer and Heydenburg give $E_\gamma = 68$ kev. As was shown in Ref.6, in which targets enriched with the various isotopes were studied, this line should be assigned to Ge^{73}.

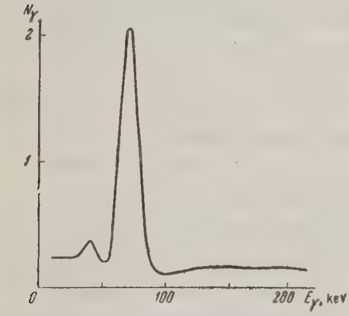

Fig.6. Coulomb excitation γ-spectrum of germanium.

It will be seen that the curve in Fig.6 does not fall to zero in the region of high energies. This indicates that under bombardment with nitrogen ions the Ge target emits more energetic (210 kev) γ-rays.

Se^{77}. Coulomb excitation of selinium by α-particles has been studied by Tremmer and Heydenburg (Ref. 6,9,14). According to their data the γ-ray energies are 244 and 457 kev. The 457 kev level was not previously known from β-decay data. In the investigation of Ref.14 targets enriched with various isotopes were used and it is shown that both the excited levels must be attributed to Se^{77}.

In our experiments the target was a 32 mg/cm^2 layer of selinium applied by vacuum evaporation to a copper support 80 μ thick.

Mo. Natural molybdenum contains four even-even isotopes (Z = 40, A = 94, 96, 98 and 100) and two even-odd isotopes (A = 95 and 97). This makes assignment of the observed γ-lines difficult.

Tremmer and Heydenburg[9] (α-particle excitation) report a 198 kev γ-ray. A line of approximately this energy (201 kev) is known from the data on positron decay of Tc^{95} (Ref.15). In Ref.13, based on work with enriched targets, it is shown that in Coulomb excitation of Mo^{100} there is observed a γ-line at 528 kev, while in excitation of Mo^{98} there appears a line at 786 kev.

In our experiments the target was a molybdenum foil 100 μ thick. We investigated the energy region to 750 kev. From the data cited above it follows that the 210 kev line in our spectrum should be ascribed to first level of Mo^{95} and the 540 kev line to the first level of Mo^{100}.

Rh^{103}. Coulomb excitation of rhodium by α-particle bombardment has been studied by Tremmer & Heydenburg[9,16]; excitation by protons by Stelson & McGowan[17].

According to Ref.16 the level excitation energies are 295 and 357 kev, while according to Ref.17 the respective values are 305 and 365 kev. Corresponding energy levels have been reported by Huus & Lunden[18] who studied orbital electron capture by Pd^{103}.

In our experiments the target was a rhodium disc ~0.35 mm thick. We observed γ-lines at 295 and 358 kev but did not detect the 440 kev line mentioned by Stelson and McGowan. This substantiates the assumption of these investigators that the 440 kev γ-ray is not associated with Coulomb excitation of Rh (they ascribe it to a nuclear reaction with Na^{23}).

Ag. Coulomb excitation of silver by protons and α-particles has been studied by a number of investigators[10,16,17,18]. Two hitherto unknown levels have been found for each of the two isotopes Ag^{107} and Ag^{109}. According to Ref. 16 the energies of these levels are 318 and 413 kev in Ag^{107} and 305 and 400 kev in Ag^{109}.

Inasmuch as these isotopes are present in almost equal amounts in natural silver, in working with this material one may expect to observe peaks at ~312 and ~407 kev. Stelson and McGowan[17] in working with natural silver obtained $E\gamma$ = 325 and 427 kev; the values obtained by Bernstein and Lewis[12] in studying conversion electrons were 320 and 420 kev.

We used a target of silver foil 100 μ thick and observed peaks at 310 and 409 kev.

Cd. Natural cadmium comprises a large number of isotopes. Mark, McClelland & Goodman[10] and Heydenburg and Tremmer[16] studied Coulomb excitation of cadmium by protons and α-particles using targets enriched with various isotopes.

In our experiments the target was a cadmium foil 0.4 mm thick. We detected only three γ-lines. We did not observe the 420 and 500 kev γ-lines reported by Mark, McClelland and Goodman[10].

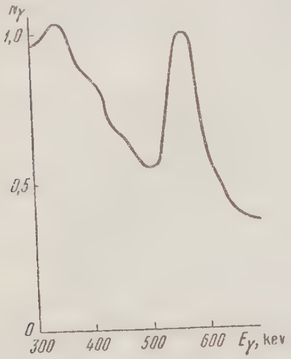

Fig.7. Coulomb excitation γ-spectrum of indium.

This again substantiates the assumption advanced by the last named investigators that these γ-lines are associated with nuclear reactions rather than with Coulomb excitation. From a comparison of our data with those of the above named investigators it follows that the 297 kev line in our spectrum should be attributed to Cd^{113}, the ~325 kev line to Cd^{111} and the 543 kev line to Cd^{114} (it is possible that some fraction of the γ-rays of this energy is due to Cd^{113}).

In^{115}. Coulomb excitation of indium by protons was investigated by Tremmer & Heydenburg[9] and Mark, McClelland and Goodman[10]. In both investigations a level at ~500 kev was observed.

In our experiments the target was an indium foil 80 μ thick mounted on a copper support of the same thickness. Fig.7 shows the Coulomb excitation spectrum under bombardment with nitrogen ions recorded with an appropriate bias voltage in the pulse height analyzer. It will be seen that there is a γ-line at 562 kev, but no line at 500 kev. Consequently, the latter should be ascribed to nuclear reactions. We note that according to the data on β-decay of Cd^{115}, the In^{115} nucleus has an excited level at 595 kev.[20]

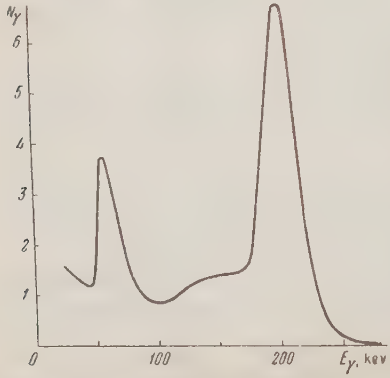

Fig.8. Coulomb excitation γ-spectrum of iodine.

I^{127}. Coulomb excitation of iodine by α-particles has been studied by Tremmer and Heydenburg[9] and excitation by protons by Mark, McClelland and Goodman[10]. Gamma-lines at 57 and 200 kev were observed; these are also known from data on β-decay. Fearing nuclear reactions with potassium, the latter investigators used targets of PbI rather than of KI. Since lead iodide is very volatile even at low temperatures, it was impossible for these investigators to evaluate the cross section for Coulomb excitation of iodine. In our work the target was a disc of KI ~150 mg/cm² thick pressed onto a copper backing 0.5 mm thick. Our results are shown in Fig.8. Control experiments with KCl target showed the absence of Coulomb excitation of potassium.

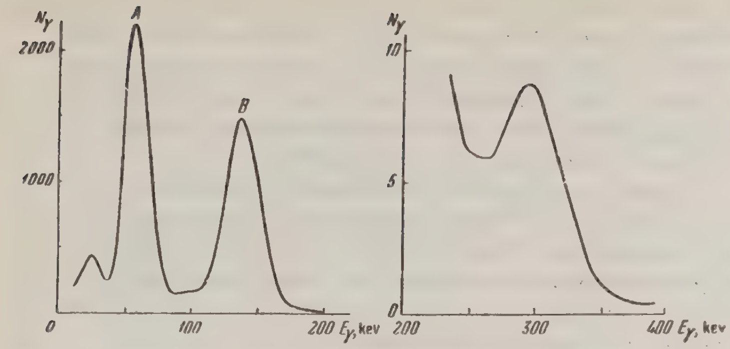

a б

Fig.9. Coulomb excitation γ-spectrum of tantalum.

Ta^{181}. Coulomb excitation of tantalum by protons and α-particles has been studied by a number of investigators[9,16,17,22 & 23].

In our experiments the target was a tantalum foil of 110 μ thick. The results are shown in Fig.9. Peak A corresponds to 57.2 kev K x-rays from tantalum (according to our data E = 57 kev). On the basis of the curves given by Huus & Zupancic[22] one can calculate the ratio $(I_K/I_\gamma)_p$, i.e., the ratio of the number of K-quanta due to ionization of the tantalum atoms by 2.1 mev protons to the number of γ-quanta of energy 137 kev associated with Coulomb excitation of tantalum. This ratio proves to be 12.4. Hence according to the calculations given in the beginning of this article, in our experiments we should obtain

$$(I_K/I_\gamma)_N = \frac{12.4}{15} \approx 0.83.$$

Actually we obtained the very close value of ~0.65 (this value was found after subtracting the part of the K-quanta associated with the process of internal conversion on the K-shell in the 137 kev transition from the total number of K-quanta). The result obtained substantiates the theory upon which the calculations in Ref.1 were based.

Peak B corresponds to excitation of the first level of Ta^{181} with ΔE = 137 kev. This level is known from β-decay data. The spin of the ground state of Ta^{181} is 7/2. If this level is a first rotational level, its spin should be 9/2, while the spin of the second rotational level of Ta^{181} should be 11/2; for this second level, according to the theory of rotational levels,

$$\Delta E = 137 \frac{20}{9} \approx 304 \text{ kev.}$$

Huus and Zupancic did in fact detect γ-rays of 303 kev energy. This level had not been previously detected.

The probability of excitation of the second level of Ta^{181} is appreciably lower than the probability of excitation of its first level. This is connected with the fact that the reduced transition probability to the second level is four times lower than the transition probability to the first level and with the fact that the function $f_2(\xi)$ falls off rapidly with increasing ξ. Moreover the relative probability of Coulomb excitation by nitrogen ions (as compared with excitation by protons) decreases with increasing energy of the excited level. Nevertheless, by introducing the appropriate bias voltage in the pulse height analyzer we could readily observe γ-rays of 301 ± 9 kev (Fig.9,b).

W. Investigations[24] of Coulomb excitation of tungsten with targets enriched with the various isotopes have shown that there exist levels with ΔE = = 101, 112 and 124 kev assignable to W^{182}, W^{184} and W^{186}, respectively, and a level with ΔE = 103 kev belonging to W^{183}.

In our work we bombarded natural tungsten in the form of a disc 25 μ thick mounted on a copper support 80 μ thick. We observed a broad peak at 112 kev. The shape of the peak indicates that it consists of several unresolved lines.

Au^{197}. Coulomb excitation of gold by α-particles has been studied in the investigations of Refs.25 & 18 and by protons in the investigations of Refs. 17, 23 & 26. Gamma-lines at 191, 277 and 550 kev were observed. From a comparison with the data on β-decay it follows that the 191 kev γ-ray is emitted in the cascade transition from the level for which ΔE = 268 kev while the 277 kev γ-ray is emitted in the transition from the level for which ΔE = 277 kev. The 550 kev line apparently is associated with excitation of a hitherto unknown level of Au^{197}.

In our experiments we used a target of 100 μ thick gold foil. The results are shown in Fig.10. The spectrum was obtained with a bias voltage in the pulse height analyzer, so that the part of the spectrum associated with the characteristic x-rays of gold has been eliminated.

Pb. Until recently no one had succeeded in observing Coulomb excitation of lead in view of the fact that the energy of the particles used for bombardment were not sufficiently high to produce excitation. Finally Stelson & McGowan[17] using protons of energies to 5 Mev excited levels with ΔE = = 570 and 810 kev in lead. The first of these, on the basis of β-decay data, is ascribed to Pb^{207}; the second, on the basis of results obtained with enriched targets, is ascribed to Pb^{206}.

In our work we investigated the γ-spectrum of lead in the energy region to 750 kev. The target was a lead foil 45 μ thick on a copper support 80 μ thick. The results for Pb are shown in Fig.11, where a line at 580 kev can be seen.

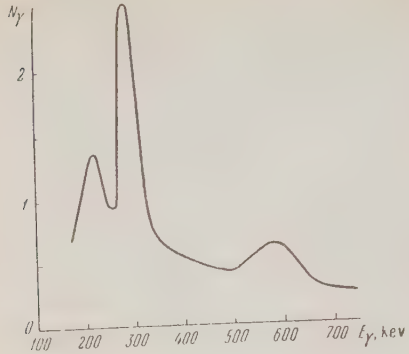

Fig.10. Coulomb excitation γ-spectrum of gold.

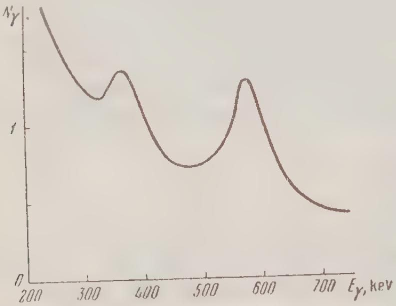

Fig.11. Coulomb excitation γ-spectrum of lead.

As will be evident from an examination of our data the γ-spectra of nuclei with $Z_2 \geqslant 9$ under bombardment with nitrogen ions contain only γ-lines associated with Coulomb excitation; no γ-lines attributable to nuclear reactions were observed.

There are indications that in the case of bombardment of a target by heavy ions nuclear reactions can proceed not only through formation of a composite nucleus into which the incident particle enters as a whole but also through break-up of this particle into α-particles, protons and neutrons, one or more of which penetrate into the target nucleus[27]. In the latter case the threshold for the reactions will be appreciably higher than follows from the height of the Coulomb barrier calculated for the bombarding nucleus as a whole. It is possible that if one uses nitrogen ions of appreciably greater energies than in our case, this "shrapnel effect" will become manifest and then the advantages of working with heavy ions will be lost. However, a separate experimental investigation is necessary to determine the allowable upper bound for the energy of the heavy bombarding particles as a function of the charge number of the target nuclei.

Confusing results have been obtained in investigations of Coulomb excitation of nuclei with bombardment by protons or α-particles because of the presence of small admixtures of light elements in the investigated heavy elements. This is due to the fact that in investigating heavy elements high energy particles were used since there was no danger of nuclear reactions with heavy nuclei; however, reactions with the light impurity nuclei could and did occur. In our work, despite the fact that we took no special measures to purify or refine the target materials there were no spurious effects that could be ascribed to impurities.

Leningrad Physical-Technical Institute of the
Academy of Sciences of the USSR

References

1. A.Grinberg & I.Lemberg, Zhur.eksp.i teor.fiz., 30, 807 (1956).
2. D.Hill, Phys.Rev., 93, 923 (1954).
3. K.Ter-Martirosian, Zhur.eksp.i teor.fiz., 22, 284 (1952).
4. K.Alder & A.Winther, Phys. Rev., 91, 1578 (1953).
5. R.Sherr, C.Li & R.Christy, Phys.Rev., 96, 1258 (1954).
6. G.Temmer & N.Heydenburg, Phys. Rev., 96, 426 (1954).
7. G.Temmer & N.Heydenburg, Phys. Rev., 98, 1198 (1955)(X5).
8. V.Ovchinnikov, Iu.Nemilov, M.Aleksandrova & I.Lomonosov, Present issue of the Bulletin.
9. G.Temmer & N.Heydenburg, Phys. Rev., 93, 351 (1954).
10. H.Mark, C.McClelland & C.Goodman, Phys.Rev., 98, 1245 (1955).
11. H.Hausman, A.Allen, J.Arthur, R.Bender & C.McDole, Phys.Rev., 88, 1296 (1952).
12. E.Bernstein & H.Lewis, Phys.Rev., 99, 617 (CA7) (1955).
13. N.Heydenburg & G.Temmer, Phys.Rev., 99, 617 (CA 10) (1955).
14. G.Temmer & N.Heydenburg, Phys.Rev., 100, 961 (M9) (1955).
15. O.Huber, H.Medicus, P.Preiswerk & K.Steffen, Phys.Rev., 73,1211 (1948).
16. N.Heydenburg & G.Temmer, Phys.Rev., 95, 3, 861 (1954).
17. P.Stelson & F.McGowan, Phys.Rev., 99, 112 (1955).
18. T.Huus & A.Lundén, Phil.Mag., 45, 966 (1954).
19. G.Temmer & N.Heydenburg, Phys.Rev., 98, 1308 (1955).
20. J.Varma & C.Mandeville, Phys.Rev., 97, 977 (1955).
21. L.Rietjens, H.Bold & P.Endt, Physica, 20, 107 (1954).
22. T.Huus & C.Zupancic, Mat.-fys. Meddelelson, 28, 1 (1953).
23. W.Goldburg & R.Williamson, Phys.Rev., 95, 767 (1954).
24. C.McClelland, H.Mark & C.Goodman, Phys.Rev., 93, 904 (1954).
25. N.Heydenburg & G.Temmer, Phys.Rev., 93, 906 (1954).
26. C.Cook, M.Class & J.Eisinger, Phys.Rev., 96, 658 (1954).
27. K.Chackett, J.Fremlin & D.Walker, Phyl.Mag., 45, 173 (1954).

INFLUENCE OF CHARGE DISTRIBUTION IN THE NUCLEUS ON ANGULAR CORRELATION IN β-DECAY

- A.Z.Dolginov & I.N.Toptygin

Introduction

Despite the fact that there has been accumulated a wealth of material on β-spectra, it has not yet been possible to establish uniquely the form of β-interaction. The difficulty stems from the fact that the shape of allowed β-spectra does not depend on the theoretical interaction variant, while forbidden spectra are hard to interpret. The character of β-interaction can be determined by investigating the angular distribution of recoil nuclei (β-ν correlation). The angular distribution in this case is anisotopic for allowed transitions and sensitive to the type of β-interaction. Investigations of electron-neutrino correlation[1,2] has made it possible to establish that β-interaction is a linear combination of the tensor and, in all probability, scalar forms. However, such correlation experiments cannot yield information on the relative sign of the S and the T interactions since the descriptive formulas contain only the squares of the matrix elements. Pseudoscalar interaction gives no contribution at all in allowed transitions.

Angular correlation between the β-particle and the subsequent γ-quantum is absent for allowed transitions. For first forbidden transitions the correlation is sensitive to the variant of the theory and thus makes it possible to determine the character of the β-interaction. However, the necessity of determining several unknown matrix elements from comparison with experiment imposes very exacting requirements as regards experimental accuracy. The theory of β-γ correlation has been examined by a number of authors[3-7]. Morita[7] deduced β-γ angular correlation formulas for a linear combination of the theoretical interaction variants, but failed to utilize the assumption that the wave function of the β-particle inside the nucleus is equal to its value on the nuclear surface. This leads to appreciable errors. For example, for the Tu^{170} nucleus our formulas, deduced not taking this assumption into account, yield an angular correlation value which differs by ~50% from the results cited in Refs.8 & 9.

The relativistic wave function of the β-particle in a point charge field tends to ∞ as $r \rightarrow 0$. Its value at the boundary of the nucleus differs noticeably from the true value which can be determined better by joining the internal solution for an electron in the field of a diffused positive charge with the external solution. In this case the wave function inside the nucleus when $r \rightarrow 0$, tends to 0 rather than to ∞.

One of the present authors obtained explicit expressions for β-ν angular correlation[10] and β-γ correlation[5] for the different interaction variants separately, taking into account the finite length of the electron wave.

Inasmuch as the experimental data can be explained only by a linear combination of the different interaction variants, we have here generalized the results of Refs.5 & 10.

We examine the two extreme cases: the case when the charge is uniformly distributed over the volume of the nucleus and the case when the charge is wholly on the surface. It was found that the β-γ angular correlation for these two cases may differ by ~20%. If one varies the assumed radius of the nucleus, the angular correlation also changes and inaccuracy as regards the radius can mask the influence of charge distribution.

Assumption of invariance of the electron wave function inside the nucleus also leads to errors in computing the β-spectrum shape. This was first pointed out by Sliv[11] who carried out precise calculations for the separate interaction variants, assuming volume or surface distribution of charge in the nucleus. Subsequently this problem has been examined by other investigators[12-14].

1. Expressions for angular correlation in β-decay

We shall calculate the β-ν and β-γ angular correlations by the method outlined in Refs.5 & 10. Outside the region of the nucleus we take the relativistic electron wave function in the Coulomb field of a point charge with a definite value of momentum at infinity (see Ref.15):

$$\psi_{p\nu} = \sum_{j\mu\lambda} i^{j-\lambda+2\nu} C^{j\mu}_{lm-\frac{1}{2}\,\nu} Y^{*}_{lm}(\vartheta_p, \varphi_p)\, \psi_{j\mu\lambda} e^{-i\delta_{j\lambda}}, \tag{1}$$

where

$$\delta_{j\lambda} = \eta_{j\lambda} - \arg\Gamma(\gamma_j + i\alpha ZE/p) - \frac{\pi}{2}(\gamma_j - j + \lambda); \tag{2}$$

$$\exp[2i\eta_{j\lambda}] = \left[(i\alpha Z/p) - 2\lambda\left(j+\frac{1}{2}\right)\right]/(\gamma_j + i\alpha ZE/p), \tag{3}$$

$$\gamma_j = \pm\sqrt{\left(j+\frac{1}{2}\right)^2 - (\alpha Z)^2}; \quad \hbar = c = m = 1;$$

here E is the energy and p is the momentum of the electron, q is the momentum of the neutrino, and $\psi_{j\mu\lambda}$ is the bispinor wave function[16] with a definite value of the total j and orbital $l = j + \lambda$ angular momenta. We denote the radial parts of $\omega_{j\mu\lambda}$; corresponding to the two possible signs of γ_j, through $F^{\pm}_{j\lambda}$ and $G^{\pm}_{j\lambda}$. Inside the nucleus the solution with a negative γ_j does not satisfy the boundary conditions at the origin of the coordinates. Let us denote the radial parts of the internal wave function by $f_{j\lambda}$ and $g_{j\lambda}$. The expressions for $f_{j\lambda}$ and $g_{j\lambda}$ will be different for the cases of surface and volume distribution of nuclear charge. The coefficients joining the external and internal solutions will enter into our expression for the angular correlation. Let us denote them in terms of (Ref.11):

$$A_{j\lambda} = N_{j\lambda}(F^-_{j\lambda}G^+_{j\lambda} - F^+_{j\lambda}G^-_{j\lambda})/(F^-_{j\lambda}g_{j\lambda} - G^-_{j\lambda}f_{j\lambda}), \tag{4}$$

where

$$N_{j\lambda} = \{1 - 2C_{j\lambda}\cos(\delta^+_{j\lambda} - \delta^-_{j\lambda}) + C^2_{j\lambda}\}^{-\frac{1}{2}} \tag{5}$$

and

$$C_{j\lambda} = (f_{j\lambda}G^+_{j\lambda} - g_{j\lambda}F^+_{j\lambda})/(f_{j\lambda}G^-_{j\lambda} - g_{j\lambda}F^-_{j\lambda}). \tag{6}$$

Here $\delta^{\pm}_{j\lambda}$ are the phases (2) corresponding to the two signs of γ_j. The values of $F^{\pm}_{j\lambda}$, $G^{\pm}_{j\lambda}$, $f_{j\lambda}$ and $g_{j\lambda}$ in (4) should be taken at the boundary of the nucleus. The expressions for the angular correlation will comprise not the phases $\delta^{+}_{j\lambda}$ separately, but $\Delta_{j\lambda}$, as defined by the formula

$$\mathrm{tg}\,\Delta_{j\lambda} = (\sin\delta^+_{j\lambda} - C_{j\lambda}\sin\delta^-_{j\lambda})/(\cos\delta^+_{j\lambda} - C_{j\lambda}\cos\delta^-_{j\lambda}). \tag{7}$$

The β-particle-neutrino angular correlation for first forbidden transitions will be given by

$$W(\vartheta) = \sum_{n=0}^{2}\sum_{i\leqslant k}[Re(M_i M_k^*)]c^{(n)}_{ik} P_n(\cos\vartheta), \tag{8}$$

where Re denotes the real part and M_i and M_k are the matrix elements of the β-transition, the explicit form of which is given in Table 1. In (8) we have already utilized the requirement of invariance under time reversal and the phase shift between the matrix elements, chosen so as to satisfy this requirement. The quantities $c^{(n)}_{ik}$ are functions of the energy of the β-particle and the nuclear charge and differ for different interaction variants. Their explicit form is given in Table 2. The coefficients $c^{(n)}_{ik}$ have been calculated for the linear combinations STP and VT. Inasmuch as the experimental data are in conflict with the axial vector variant, it will not be examined here.

For Z = 0 our formulas reduce to those of the Born approximation, while with $Z \gg A^{1/3}E_{Mev}$ (where E_{Mev} is the total electron energy in Mev) they differ greatly from those of the Born approximation. For example, for pure scalar interaction with Z = 0 we have

$$W(\vartheta) = (p^2 + q^2 + 2pq\cos\vartheta)[(1 - p/E)\cos\vartheta],$$

while with $Z \gg A^{1/3}E_{Mev}$, we get

$$W(\vartheta) \approx 1 + (p/3E)\cos\vartheta. \tag{9}$$

For pure vector interaction with $Z \gg A^{1/3}E_{Mev}$, we obtain

$$W(\vartheta) \approx 1 - (p/3E)\cos\vartheta.$$

Analogous results are obtained for all the other forms of interaction in β-decay.

In Ref.10 it was shown that even if the finite length of the electron wave (in the field of a spherical nucleus) is taken into account, the β-ν angular correlation for allowed transitions will not depend on Z.

The expression for β-γ angular correlation for first forbidden transition can be written as

$$W(\vartheta) = \sum_{n=0,2} \sum_{II'} \sum_{ik} [Re(M_{Ii}M_{I'k}^*)] U_{II'}^n c_{ik}^{nII'} B_n P_n(\cos\vartheta), \tag{10}$$

$$U_{II'}^n = U(Ij_1nj_2;\, j_2I') = \sqrt{(2j_2+1)(2I'+1)}\, W(Ij_1nj_2;\, j_2I'), \tag{11}$$

where $W(Ij_1nj_2;\, j_2I')$ is Racah's function. The values of $c_{ik}^{nII'}$ for STP and VT are listed in Table 3; $j_1 \xrightarrow{\beta} j_2 \xrightarrow{\gamma} j_3$ are the moments of the three levels of the nucleus participating in the transition. B_n pertains to the γ-transition and in the case of emission of a quantum of multipolarity 2^L has the form

$$B_n = \left[1 - \frac{n(n+1)}{2L(L+1)}\right] U(Lj_3nj_2;\, j_2L)\, C_{L0n0}^{L0}. \tag{12}$$

In the case of mixed 2^L magnetic radiation and 2^{L+1} electric radiation, we obtain

$$B_n = B_n^{(L)} + |a|^2 B_n^{(L+1)} \pm 2a\sqrt{\frac{2L+3}{L+2}}\, U(L1nL;\, LL+1)\, U(j_2j_3nL+1;\, Lj_2)\, C_{L0n0}^{L0}, \tag{13}$$

where $B_n^{(L)}$ is identical with (12), while $B_n^{(L+1)}$ differs from $B_n^{(L)}$ by the replacement of L by L + 1; $|a|^2$ is the ratio of the intensities of the electric and magnetic radiations, here $a = \pm|a|$, inasmuch as the phase shift between the matrix elements of the electric and magnetic transitions can be either 0 or π.

If we are interested in the correlation between β-particles and conversion electrons, then in (10) together with B_n one must introduce an additional factor which can be found, for example, in Ref.17 (also see Ref.18).

If the observed γ-quantum does not immediately follow the β-decay but is preceded in the general cascade by one or more other quanta, the directions of which are not determined in the experiment, then a factor Q_n must be introduced into Eq.(10); this factor is given by[19]

$$Q_n = \prod_{K=3}^{N-1} U(j_kL_knj_{k-1};\; j_{k-1}j_k), \tag{14}$$

where the $j_{N-1} \to j_N$ transition is accompanied by the emission of the observed γ-rays, L_k are the multiple orders of the γ-quanta emitted in the transitions of the nucleus from the state with j_{k-1} to the state with j_k. If a mixed radiation is emitted in the intermediate transitions, the intensities are added, inasmuch as the interference terms drop out.

To illustrate the importance of correctly taking into account the behavior of the electron wave function inside the nucleus, let us examine the β-γ angular correlation with Z = 71 and A = 170. The interaction of the electron with the Coulomb field is independent of the nuclear matrix elements. Hence to evaluate the effect it is sufficient to examine the angular dependence with one of the matrix elements.

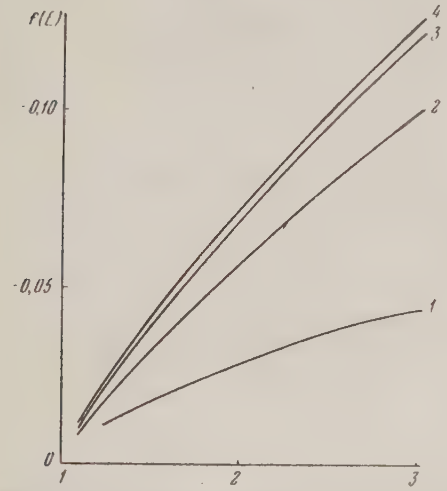

Fig.1. Values of the factor f(E) for the nucleus with Z = 71 and A = 170.

Representing $W(\vartheta)$ in the form const. $[1 + f(E)P_2 (\cos \vartheta)]$ and dropping all terms except those pertaining to the matrix element M_3, we obtain for f(E) the curves shown in Fig.1. Curves 2 & 4 correspond to the cases of uniform distribution of charge over the volume for nuclei having a radius $R = 1.2 \cdot 10^{-13} A^{1/3}$ cm and $R = 1.5 \cdot 10^{-13} A^{1/3}$ cm, respectively, while curve 3 is for the case of surface distribution of charge and $R = 1.2 \cdot 10^{-13} A^{1/3}$ cm. Our curves differ by about 50% from curve 1 which was plotted according to the formulas of Ref.6 for a nuclear radius $R = 1.2 \cdot 10^{-13} A^{1/3}$ cm, formulas deduced on the assumption of invariance of the electron wave function inside the nucleus. For nonspherical nuclei the orbital moment of the electron is not an integral of the motion. However, the length of the β-particle wave is much greater than the dimensions of the nucleus, consequently the contribution from states with values of l greater than those already taken into account in the formulas is negligibly small. The influence of asphericity on the states with l = 0 and l = 1 will differ, which may somewhat change the angular distribution. However, the main part of this change can be allowed for by slightly modifying the effective radius of the nucleus.

If we leave only one term with η = 0 in expression (8) and multiply it by $(2j_2 + 1)q^2\varkappa / (2j_1 + 1)108\,\pi^3$ (the values of $\varkappa$ for volume and surface charge distributions are listed in Table 2), we will obtain expressions for the β-spectrum with STP or VT interactions.

Table 1

Matrix elements
$$M_{Ii} = \int \psi^*_{j_2 m_2} \tau O^I{}_i \psi_{j_1 m_1}\, d\mathbf{r};$$

$$O_1^1 = g_s C_1 r \beta Y_{1M}; \qquad O_2^0 = g_T C_0 r \beta (\vec{\sigma}\, \mathbf{Y}_{00}^1);$$

$$O_3^1 = g_T C_1 r \beta (\vec{\sigma}\, \mathbf{Y}_{1M}^0); \qquad O_4^2 = g_T C_2 r \beta (\vec{\sigma} \mathbf{Y}_{2M}^{-1});$$

$$O_5^1 = i g_T C_1 \beta (\vec{\alpha}\, \mathbf{Y}_{1M}^{-1}); \qquad O_6^1 = g_V C_1 r Y_{1M};$$

$$O_7^1 = i g_V C_1 (\vec{\alpha}\, \mathbf{Y}_{1M}^{-1}); \qquad O_8^0 = i g_p C_0 \beta \gamma_5 Y_{00};$$

$\psi_{j_1 m_1}$ and $\psi_{j_2 m_2}$ are the wave functions of the initial and final states of the nucleus, respectively, τ is an operator acting on the isotopic spin variables, the g's are the β-interaction constants β, γ_5, $\vec{\sigma}$ and $\vec{\alpha}$ are Dirac matrices, $\mathbf{Y}_{lM}^{\lambda}$ is the spherical vector:

$$(\vec{\sigma}\, \mathbf{Y}_{IM}^{\lambda} (\vartheta, \varphi)) = - \sum_{\nu=-1}^{1} C_{I+\lambda M+\nu 1-\nu}^{IM}\, \sigma_{-\nu} Y_{I+\lambda M+\nu} (\vartheta, \varphi); \tag{15}$$

where

$$C_I \equiv [C_{1M j m_1}^{j_2 m_2}]^{-1}; \quad \sigma_0 = \sigma_z, \quad \sigma_{\pm 1} = \pm 2^{-\frac{1}{2}} (\sigma_x \pm i \sigma_y);$$

$C_{1M j_1 m_1}^{j_2 m_2}$ are Clebsh-Gordan coefficients.

Table 2

$$c_{11}^{(0)}(q) = c_{66}^{(0)}(-q) = 3a_1^+q^2 - 2a_2^+q + 2a_4^+ + a_5^+;$$

$$c_{22}^{(0)} = 3(a_1^+q^2 - 2a_2^+q + a_5^+);\quad c_{33}^{(0)} = 3a_1^+q^2 + 4a_2^+q + a_4^+ + 2a_5^+;$$

$$c_{44}^{(0)} = 3(a_1^+q^2 + a_4^+);\quad c_{55}^{(0)} = c_{77}^{(0)} = c_{88}^{(0)} = 27a_1^+;\quad c_{13}^{(0)} = 2\sqrt{2}(a_4^+ - a_5^+);$$

$$\sqrt{2}\,c_{28}^{(0)}(q) = \sqrt{6}\,c_{15}^{(0)}(q) = \sqrt{6}\,c_{67}^{(0)}(-q) = -\sqrt{3}\,c_{35}^{(0)}(-q) = -18\sqrt{2}(a_1^+q - a_2^+);$$

$$c_{37}^{(0)} = -\sqrt{2}\,c_{56}^{(0)} = 6\sqrt{6}(a_1^-q + a_2^-);\quad c_{57}^{(0)} = -54a_1^-;$$

$$c_{36}^{(0)} = 2\sqrt{2}(2a_2^-q + a_4^- + a_5^-);$$

$$3c_{11}^{(1)}(q) = -3c_{66}^{(1)}(-q) = -18a_7q^2 + 12(a_8^+ + a_9^+)q + 2a_{10} - 8a_{11}^+ - 4a_{12};$$

$$c_{22}^{(1)} = -6(a_7q^2 - 2a_8^+q + a_{10});\quad 5c_{44}^{(1)} = 6a_7q^2 + 30a_9^+q + 6a_{12};$$

$$3c_{33}^{(1)} = 18a_7q^2 + 6(a_9^+ + 4a_8^+)q + 4a_{10} + 8a_{11}^+ - 2a_{12};$$

$$3c_{55}^{(1)} = -3c_{77}^{(1)} = -c_{88}^{(1)} = 54a_7;\quad c_{35}^{(1)} = -4\sqrt{6}(3a_7q + a_8^+ + a_9^+);$$

$$3c_{13}^{(1)} = 4\sqrt{2}(3a_9^+q - 6a_8^+q + a_{11}^+ - a_{10} - a_{12});$$

$$c_{15}^{(1)}(q) = -c_{67}^{(1)}(-q) = 4\sqrt{3}(3a_7q + a_8^+ - 2a_9^+);$$

$$c_{36}^{(1)} = 4\sqrt{2}(2a_8^-q + a_9^-q + a_{11}^-);\quad c_{56}^{(1)} = -4\sqrt{3}(a_8^- + 2a_9^-);$$

$$c_{37}^{(1)} = 4\sqrt{6}(a_9^- - a_8^-);\quad c_{28}^{(1)} = 36(a_7q - a_8^+);$$

$$3c_{11}^{(2)} = -6c_{33}^{(2)} = -10c_{44}^{(2)} = -3c_{66}^{(2)} = -12a_3^+q;\quad c_{36}^{(2)} = -4\sqrt{2}a_3^-q.$$

All the other $c_{ik}^{(n)}$ vanish.

Here and below $c_{ik}^{(n)}(-q)$ indicates that in the corresponding expression q is replaced by $-q$.

In the case of uniform charge distribution over the volume the values of $a_i^\pm$ are

$$a_1^\pm = \varphi_0[(\varepsilon-1)\beta_1 \pm (\varepsilon+1)\beta_2];\quad \varphi_0 = 1 - 11(\varkappa R)^2/75;$$

$$a_2^\pm = \varphi_4(\beta_1 \pm \beta_2)\varkappa^2 - (3\alpha Z/10R)[(\varepsilon-1)\beta_1 \pm (\varepsilon+1)\beta_2];$$

$$\varphi_4 = 1 - 7(\varkappa R)^2/75;$$

$$a_3^\pm = \varphi_5(\beta_7 \pm \beta_8)\varkappa^2;\qquad \varphi_5 = 1 - 4(\varkappa R)^2/35;$$

$$a_4^\pm = \varphi_2[(\varepsilon-1)\beta_3 \pm (\varepsilon+1)\beta_4]\varkappa^2;\quad \varphi_2 = 1 - 3(\varkappa R)^2/35;$$

$$a_5^\pm = \varphi_1[(\varepsilon+1)\beta_1 \pm (\varepsilon-1)\beta_2]\varkappa^2 - (3\alpha Z/5R)(\beta_1 \pm \beta_2)\varkappa^2 +$$

$$+ (3\alpha Z/10R)^2[(\varepsilon-1)\beta_1 \pm (\varepsilon+1)\beta_2];\quad \varphi_1 = 1 - 2(\varkappa R)^2/35;$$

$$a_6^\pm = \varphi_3[(\varepsilon+1)\beta_7 \pm (\varepsilon-1)\beta_8]\varkappa^2 - (3\alpha Z/10R)(\beta_7 \pm \beta_8)\varkappa^2;$$

$$a_7 = \varphi_0\beta_5\varkappa;\quad \varphi_3 = 1 - 12(\varkappa R)^2/175;$$

$$a_8^+ = \varphi_4\beta_5\varepsilon\varkappa - (3\alpha Z/10R)\beta_5\varkappa;\quad a_8^- = \varphi_4\beta_5\varkappa;$$

$$a_9^\pm = \varphi_5[(\varepsilon-1)\beta_6 \pm (\varepsilon+1)\beta_9]\varkappa;$$

$$a_{10} = \varphi_1\beta_5\varkappa^3 - (3\alpha Z/5R)\beta_5\varepsilon\varkappa + (3\alpha Z/10R)^2\beta_5\varkappa;$$

$$a_{11}^\pm = \varphi_3(\beta_6 \pm \beta_9)\varkappa^3 - (3\alpha Z/10R)[(\varepsilon-1)\beta_6 \pm (\varepsilon+1)\beta_9]\varkappa;$$

$$a_{12} = \varphi_2\beta_{10}\varkappa^3;$$

$$\varepsilon = E + 3\alpha Z/2R;\qquad \varkappa = (\varepsilon^2 - 1)^{1/2}.$$

In the case of distribution over the surface:

$$a_1^{\pm} = \varphi_0[(\varepsilon-1)\beta_1 \pm (\varepsilon+1)\beta_2]; \quad a_2^{\pm} = \varphi_2(\beta_1 \pm \beta_2)\varkappa^2;$$

$$a_3^{\pm} = \varphi_2(\beta_7 \pm \beta_8)\varkappa^2; \quad a_4^{\pm} = \varphi_1[(\varepsilon-1)\beta_3 \pm (\varepsilon+1)\beta_4]\varkappa^2;$$

$$a_5^{\pm} = \varphi_1[(\varepsilon+1)\beta_1 \pm (\varepsilon-1)\beta_2]\varkappa^2; \quad a_6^{\pm} = \varphi_1[(\varepsilon+1)\beta_7 \pm (\varepsilon-1)\beta_8]\varkappa^2;$$

$$a_7 = \varphi_0\beta_5\varkappa; \quad a_8^{+} = \varphi_2\beta_5\varepsilon\varkappa; \quad a_8^{-} = \varphi_2\beta_5\varkappa;$$

$$a_9^{\pm} = \varphi_2[(\varepsilon-1)\beta_6 \pm (\varepsilon+1)\beta_9]\varkappa; \quad a_{10} = \varphi_1\beta_5\varkappa^3;$$

$$a_{11}^{\pm} = \varphi_1(\beta_6 \pm \beta_9)\varkappa^3;$$

$$a_{12} = \varphi_1\beta_{10}\varkappa^3; \; \varphi_0 = 1-(\varkappa R)^2/5; \; \varphi_1 = 1-3(\varkappa R)^2/25;$$

$$\varphi_2 = 1-4(\varkappa R)^2/25; \quad \varepsilon = E + \alpha Z/R; \; \varkappa = (\varepsilon^2-1)^{1/2}.$$

The values of β_i, entering into $a_i^{\pm}$, are determined in terms of the joining coefficients (4) and (7):

$$\beta_1 = A^2_{\frac{1}{2}\cdot\frac{1}{2}}; \quad \beta_2 = A^2_{\frac{1}{2}-\frac{1}{2}}; \quad \beta_3 = A^2_{\frac{3}{2}\cdot\frac{1}{2}}; \quad \beta_4 = A^2_{\frac{3}{2}-\frac{1}{2}};$$

$$\beta_5 = A_{\frac{1}{2}\cdot\frac{1}{2}}A_{\frac{1}{2}-\frac{1}{2}}\cos\left(\Delta_{\frac{1}{2}\cdot\frac{1}{2}} - \Delta_{\frac{1}{2}-\frac{1}{2}}\right);$$

$$\beta_6 = A_{\frac{1}{2}\cdot\frac{1}{2}}A_{\frac{3}{2}\cdot\frac{1}{2}}\cos\left(\Delta_{\frac{1}{2}\cdot\frac{1}{2}} - \Delta_{\frac{3}{2}\cdot\frac{1}{2}}\right);$$

$$\beta_7 = A_{\frac{1}{2}\cdot\frac{1}{2}}A_{\frac{3}{2}-\frac{1}{2}}\cos\left(\Delta_{\frac{1}{2}\cdot\frac{1}{2}} - \Delta_{\frac{3}{2}-\frac{1}{2}}\right);$$

$$\beta_8 = A_{\frac{1}{2}-\frac{1}{2}}A_{\frac{3}{2}\cdot\frac{1}{2}}\cos\left(\Delta_{\frac{1}{2}-\frac{1}{2}} - \Delta_{\frac{3}{2}\cdot\frac{1}{2}}\right);$$

$$\beta_9 = A_{\frac{1}{2}-\frac{1}{1}}A_{\frac{3}{2}-\frac{1}{2}}\cos\left(\Delta_{\frac{1}{2}-\frac{1}{2}} - \Delta_{\frac{3}{2}-\frac{1}{2}}\right);$$

$$\beta_{10} = A_{\frac{3}{2}\cdot\frac{1}{2}}A_{\frac{3}{2}-\frac{1}{2}}\cos\left(\Delta_{\frac{3}{2}\cdot\frac{1}{2}} - \Delta_{\frac{3}{2}-\frac{1}{2}}\right).$$

For the case when $(\alpha Z)^2 \ll 1$ and $(\alpha Z)^2 \ll p^2$, one can obtain simple expressions for β_i:

$$\beta_1 = p(E-1)/\varkappa(\varepsilon-1); \; \beta_2 = p(E+1)/\varkappa(\varepsilon+1); \; \beta_3 = (p/\varkappa)^3\beta_1;$$

$$\beta_4 = (p/\varkappa)^3\beta_2; \quad \beta_5 = (p/\varkappa)^2; \quad \beta_6 = (p/\varkappa)^2\beta_1\cos\omega; \; \beta_{10} = (p/\varkappa)^4;$$

$$\beta_7 = \beta_8 = (p(\varkappa)^3\cos\omega; \quad \beta_9 = (p/\varkappa)^2\beta_2\cos\omega; \quad \omega = \operatorname{arc\,tg}\frac{\alpha ZE}{p};$$

$$\varphi_k = 1.$$

Table 3

The values of $c_{ih}^{0II'}$ are equal to the values of $c_{ik}^{(0)}$ from Table 2.

$$3c_{11}^{211}(q) = 3c_{66}^{211}(-q) = -\sqrt{5}c_{34}^{212}(-q) = 3\sqrt{10}(2a_3^{+}q - a_4^{+} - 2a_6^{+});$$

$$\sqrt{2}c_{44}^{222} = -3\sqrt{7}a_4^{+}; \quad \sqrt{2}c_{33}^{211} = \sqrt{5}(4a_3^{+}q - a_4^{+} + 4a_6^{+});$$

$$3c_{15}^{211} = 3c_{67}^{211} = \sqrt{15}c_{48}^{202} = \sqrt{10}c_{45}^{212} = 3\sqrt{2}c_{35}^{211} = -18\sqrt{30}a_3^{+};$$

$$c_{24}^{202} = 6\sqrt{2}(a_3^{+}q - a_6^{+}); \quad c_{13}^{211} = 2\sqrt{5}(3a_3^{+}q - a_4^{+} + a_6^{+});$$

$$c_{14}^{212} = 6(a_3^{+}q + a_4^{+} - a_6^{+}); \quad 3c_{36}^{211} = -\sqrt{5}c_{46}^{212} = -6\sqrt{5}(a_3^{-}q + a_4^{-} + a_6^{-});$$

$$3c_{56}^{211} = 3\sqrt{2}c_{37}^{211} = \sqrt{10}c_{47}^{212} = 18\sqrt{30}a_3^{-}.$$

All the other $c_{ik}^{nII'}$ are zero.

2. Comparison with experiment and selection of a nucleus suitable for investigation of β-γ angular correlation

The principal requirement in choosing a suitable nucleus for investigating β-γ angular correlation is the possibility of unambiguous interpretation of the experimental data. Inasmuch as the interaction variant in β-decay is not definitively established, there is little point in carrying out these experiments for the purpose of determining the angular momenta of the nucleus. For purposes of refining β-decay theory it is desirable to use nuclei for which the spins and parities of the levels are known.

If the change in nuclear spins is one unit greater than the order of forbiddenness, only one matrix element makes a contribution to the interaction. In this case the angular correlation no longer depends on the form of the linear combination of the interaction variants and hence is of no particular interest to us. If Δj is one unit smaller than the order of forbiddenness, the pseudoscalar variant makes a contribution to the linear combination of interaction variants. If there is a question of the relative sign of the S and T interactions, one should select transitions for which Δj equals the order of forbiddenness. In this case the applicable expressions contain the smallest number of unknown matrix elements.

When the initial and final states of the nucleus are satisfactorily described by the nuclear shell model one can theoretically determine the ratios of the matrix elements. To determine the sign of the S and T interaction variants it is sufficient to have even a rough (but with the correct sign) evaluation of these ratios.

Let us examine from this standpoint some nuclei which apparently are most suitable for investigation of β-γ angular correlation.

1. The transition of In^{117} from the isomeric state to the excited 0.161 Mev level of Sn^{117} is a first forbidden transition with $\Delta j = 1$.

It may be assumed that the β-decay of In^{117} is associated with a single nucleon transition since the observed characteristics of the levels are in agreement with the prediction of the shell model.[20] The isomeric level of In^{117} corresponds to the $p_{1/2}$ state, while the excited level of Sn^{117} is $d_{3/2}$. The transition to the ground $s_{1/2}$ level is accompanied by magnetic dipole radiation.

2. β-decay of the ground state of Ba^{139} to the excited 0.163 Mev level of La^{139} is also a first forbidden transition[21] with $\Delta j = 1$. Ba^{139} has one neutron outside the closed shell in the $f_{7/2}$ state. In β-decay this neutron is transformed to a proton on the $d_{5/2}$ level. The transition from $d_{5/2}$ to the ground state $g_{7/2}$ is accompanied by magnetic dipole radiation.

3. The Ce^{141} nucleus, like Ba^{139}, has one neutron outside the closed shell. The neutron goes over from the $f_{7/2}$ state to the excited 0.145 Mev level of Pr^{141}. The $g_{7/2} \rightarrow d_{5/2}$ transition to the ground state of Pr^{141} is accompanied by magnetic dipole radiation[22]. In contrast to the case of Ba^{139}, the proton $g_{7/2}$ state in Pr^{141} lies higher than $d_{5/2}$. This does not conflict with the shell model inasmuch as the $g_{7/2}$ and $d_{5/2}$ levels are close and may cross. Ce^{141} decays with $\Delta j = 0$, which, in general, should make it possible to determine the relative contribution of pseudoscalar interaction, but at the same time appreciably complicates interpretation of the experimental data since instead of one unknown ratio g_S/g_T and three ratios of the matrix elements, our expressions will comprise two unknown ratios g_S/g_T and g_P/g_T and five matrix element ratios.

There are a few other nuclei, for example, Hg^{203} (Refs.23-25) and Tl^{208} (Refs.26-28), that apparently satisfy the above requirements.

If the β-γ angular correlation for such nuclei as In^{147}, Ba^{139} or Ce^{141} is investigated with at least the accuracy already achieved in the better correlation measurements it should be feasible to realize a unique interpretation of the experimental data and determine the ratios of the matrix elements by means of the nuclear shell model.

Of the already experimentally investigated cases, the most interesting is that of Tu^{170} inasmuch as for it the momenta of the levels are known and the β-decay is a first forbidden transition with $\Delta j = 1$.

Let us introduce the following notation for the ratios of the matrix elements M_i:

$$x = M_1/M_3; \; (\alpha Z/2R)\, y = M_5/M_3; \; u = M_4/M_3$$

(x is the product of the ratio g_S/g_T by the ratio of the matrix elements). The requirement for invariance under time reversal leads to a selection of the matrix elements phases with which the quantities x, y and u are real. The angular momenta involved in the β-γ transition in Tu^{170}, according to Rose[29,30], are $1^- \rightarrow 2^+ \rightarrow 0^+$. The experimental points[29] for the β-γ angular correlation are plotted in Fig.2. The vertical axis is scaled in values of the quantity $a(E)$ which enters into expression (10), if this is written in the form

$$W(\vartheta) = 1 + a(E)\cos^2\vartheta.$$

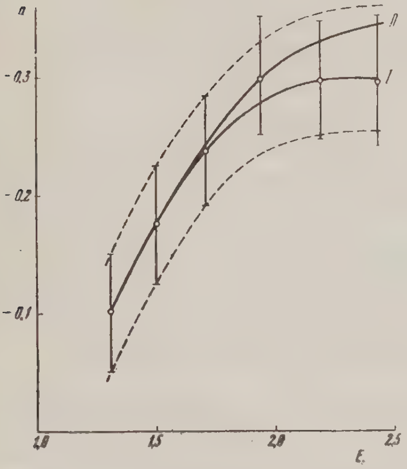

Fig.2. Experimental points for β-γ angular correlation for Tu^{170} according to Ref.29.

Without making any assumptions regarding the matrix elements of the nucleus, we determined the region of values of x and y (with u real), for which the angular correlation curve does not fall outside the experimental uncertainty limits. This region is limited by curve II in Fig.3. If we reduce the uncertainty and consider only the points above curve I in Fig.2, the region of allowable values of x and y is greatly reduced (curve I in Fig.3). In this case $x > 0$ for any value of y and to determine the sign of g_S/g_T it is sufficient to establish only the sign of the ratio of the matrix elements. There is no valid reason for assuming that the β-transition in Tu^{170} is a single nucleon one. If, however, for a rough evaluation we make this assumption and utilize the results of Ref.31 for calculating the ratio of the matrix elements, then in the case of a $p_{1/2} \rightarrow s_{1/2}$ transition (as indicated in Ref.30) comparison with experiment yields $g_S/g_T < 0$; on the other hand, if we assume $P_{3/2} \rightarrow s_{1/2}$, then $g_S/g_T > 0$.

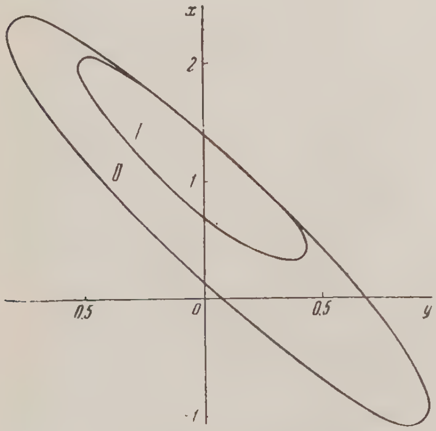

Fig.3. Region of allowable values of the parameters for Tu^{170}. Curve II bounds the region of values of x and y for which the values of the factor $a(E)$ lie within the spread of the experimental points; curve I corresponds to values of x and y for which $a(E)$ lies above curve I in Fig.2.

Leningrad Physical-Technical Institute of the Academy of Sciences of the USSR

References

1. B.Rustad & S.Ruby, Phys.Rev., 89,880 (1953).
2. D.Maxson, J.Allen & W.Jentscke, Phys.Rev., 97, 109 (1955).
3. A.Dolginov, Zhur.eksp.i teor.fiz., 20, 636 (1950).
4. D.Falkoff & G.Uhlenbeck, Phys.Rev., 79, 334 (1950).

5. A.Dolginov, Zhur.eksp.i teor.fiz., 22, 668 (1952).
6. M.Yamada & M.Morida, Progr. Theor. Phys., 8, 431 (1952).
7. M.Morita, Progr. Theor. Phys., 10, 363 (1953).
8. M.Morita & M.Yamada, Progr. Theor. Phys., 11, 219 (1954).
9. Y.Kato & M.Morita, Progr. Theor. Phys., 13, 276 (1955).
10. A.Dolginov, Zhur.eksp.i teor.fiz, 22, 658 (1952).
11. L.Sliv, Zhur.eksp.i teor.fiz., 17, 1049 (1947).
12. M.Rose & D.Holmes, Phys.Rev., 83, 190 (1951).
13. M.Yamada, Progr.Theor.Phys., 10, 241 (1953).
14. I.Malcolm, Phil.Mag., 43, 1011 (1952).
15. V.Berestetskii, A.Dolginov & K.Ter-Martirosian, Zhur.eksp.i teor.fiz., 20, 527 (1950).
16. M.Rose, Phys.Rev., 51, 484 (1937).
17. L.Biedenharn & M.Rose, Rev. Mod. Phys., 25, 729 (1953).
18. A.Dolginov, Iav. AN SSSR, Ser.fiz., 17, 332 (1952).
19. A.Dolginov, Zhur.eksp.i teor.fiz., 23, 493 (1952).
20. C.McGinnis, Phys.Rev., 97, 93 (1955).
21. A.Mitchell & E.Hebb, Phys.Rev., 97, 1031 (1955).
22. J.Jones & F.Jensen, Phys.Rev., 97, 1031 (1955).
23. S.Thulin & K.Nybö, Ark.Phys., 7, 289 (1953).
24. A.Wapstra, D.Macder, G.Nijgh & L.Ornstein, Physica, 20, 169 (1954).
25. N.Marty, C.R., 240, 291 (1955).
26. L.Elliot, R.Graham, J.Walker & J.Wolfson, Phys.Rev., 93, 356 (1954).
27. N.Feather, J.Kyles & R.Pringle, Proc.Phys.Solc, 61, 466 (1948).
28. D.Martin, H.Richardson & Y.Hsu, Proc.Phys.Soc., A 61, 466 (1948).
29. H.Rose, Phil. Mag., 43, 1146 (1952).
30. R.Richmond & H.Rose, Phil.Mag., 43, 367 (1952).
31. M.Rose & R.Osborn, Phys.Rev., 93, 1326 (1954).

NUMERICAL VALUES OF THE K-ELECTRON FUNCTIONS DETERMINING THE PROBABILITY OF ALLOWED AND FORBIDDEN K-CAPTURE

- I.M.Band, L.N.Zyrianova & Tsin Chen-Zhui

For analysis of the experimental data on K-capture it is necessary to know a number of coefficients that depend on the wave functions of the captured electron. Below we give the numerical values of these coefficients calculated taking into account the effect of finite nuclear size and screening on the wave functions of the K-electrons.

1. K-electron wave functions

The wave functions of the s-state used in the present work were found by the method of numerical integration of Dirac's equation for the potential taking into account the presence of orbital electrons and finite size of the nucleus. The atomic potential was taken as the solution of the Thomas-Fermi-Dirac equation for a statistical atom by the method of Metropolis-Reitz[1]. The effect of finite dimensions of the nucleus was taken into account by the method of Sliv[2] for the case of uniform distribution of protons over the volume of the nucleus, the radius of which was taken to be $R = 1.2 \cdot 10^{-13} A^{1/3}$ cm.

The values of the K-electron wave functions at the boundary of the nucleus obtained in this manner are listed in Table 1. We give the values of G_K and F_K - the large and small components of the wave function of the s-state, E_K - the theoretical K-electron binding energy and the parameter $U_o = \sqrt{2R}$.

Table 1

Values of the K-electron wave functions at the nuclear boundary

Z	$U_0 = \sqrt{2R}$	E_K	$G_K R$	$F_K R$
25	0,1540	0,98723	0,0019973	—0,00014624
33	0,16050	0,97671	0,0035224	—0,00023658
41	0,16677	0,96271	0,0057705	—0,00069685
49	0,17378	0,94502	0,0088587	—0,0013835
57	0,17940	0,92335	0,013126	—0,0022225
61	0,18110	0,91091	0,015671	—0,0028470
65	0,18353	0,89733	0,018771	—0,0036441
69	0,18544	0,88256	0,022306	—0,0046106
73	0,18747	0,86651	0,026476	—0,0058081
77	0,18963	0,84911	0,031377	—0,0072850
81	0,19132	0,83025	0,037058	—0,0090834
84	0,19280	0,81509	0,042007	—0,010708
88	0,19457	0,79342	0,049543	—0,013282
92	0,19623	0,76993	0,058385	—0,016432
95	0,19746	0,75103	0,066053	—0,019258
98	0,19865	0,73092	0,074714	—0,022547

2. Values of the function f_K

In the case of allowed transitions the expression for the probability of K-capture comprises the function

$$f_K = \frac{\pi}{2} G_K^2 (E_0 + E_K)^2, \qquad (1)$$

where E_o is the energy of the transition in $m_o c^2$ units and E_K is the binding energy of the K-electron in the same units.

In most studies of K-capture the atomic electric field is assumed to be the pure Coulomb field of the nucleus. Accordingly the relativistic wave functions of a hydrogen-like atom are generally used for the function G_K. The expression for f_K for a pure Coulomb field has the form[3]:

$$f_K^{cou} = 2\pi(\alpha Z)^{2\gamma+1}(2R)^{2\gamma-2}e^{-2\alpha ZR}\frac{\gamma+1}{\Gamma(2\gamma+1)}(E_0+E_K)^2, \tag{2}$$

where

$$\gamma = \sqrt{1-\alpha^2 Z^2}.$$

Slater[4] gave an approximate method for taking into account the screening effect of orbital electrons on the wave functions of bound states. Where K-capture is concerned this method reduces to replacing Z in Eq.(2) by $Z_K = Z - 0.35$. Numerical calculations of the function f_K for a Coulomb field taking into account screening according to Slater have been carried out by a number of investigators[5-7]. The screening corrections for K-electrons, evaluated according to Slater, are not large: about 4% for elements with $Z \approx 20$ and 1-2% for intermediate and heavy elements. For this reason more accurate calculations of the screening correction for K-electrons[8,9] with relativistic wave functions, obtained by Reitz[10] for the statistical Thomas-Fermi-Dirac atom, agreed within 1% with the results of calculations by the method of Slater.

The effect of taking into account the finite size of the nucleus has been evaluated by Rapoport[11] on the basis of the model of a uniformly charged sphere. Rapoport found that for allowed transitions the correction for finite nuclear size is of the order of 3% for elements in the region of Z = 80 and is even smaller for lighter elements. Malcolm & Strachan[12] evaluated the correction for finite size of the nucleus on the basis of surface distribution of the protons; the correction proved to be 14% for Z = 80.

In the present investigation we used the K-electron wave functions listed in Table 1 in calculating f_K. The values of the wave functions were taken at the surface of a nucleus of radius $R = 1.2 \cdot 10^{-13} A^{1/3}$ cm.

The values of f_K calculated according to Eq.(1) for all values of Z from 5 to 98 are listed in Table 2.

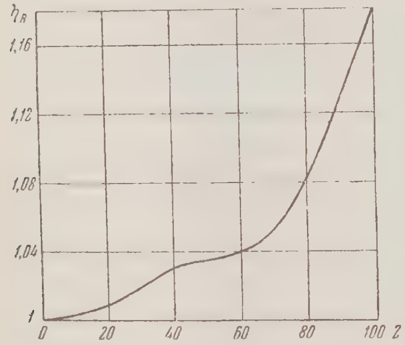

Fig.1. Correction for finite size of the nucleus and screening for allowed K-capture.

To evaluate the effect of taking into account screening and the finite size of the nucleus on the probability of allowed K-capture, we found the ratio of the function f_K as listed in Table 2 to the value of f_K for a pure Coulomb field. The values of this ratio, which is the correction for screening and finite nuclear size for allowed K-capture, is plotted as a function of Z in Fig.1.

This correction is of the order of 15% for heavy elements and equals 1% for Z = 25. Inasmuch as calculations of the K-electron wave functions were not made for $Z < 25$, the values of f_K for $Z < 25$ were found by means of the expression for a pure Coulomb field and corrected for the effect of screening and finite nuclear size on the basis of the extrapolated curve in Fig.1.

The values of f_K are listed in Table 2 for 20 values of the transition energy E_0. Intermediate values of the function can be found by interpolation. The character of the variation of f_K as a function of the transition energy is shown in Fig.2. In regions where the variation is rapid, the values of f_K can be found by means of Eq.(1). To facilitate rapid calculation the values of the function $(\pi/2)G_K^2$ are listed in Table 3. To obtain f_K, the values in Table 3 should be multiplied by $(E_0 + E_K)^2$.

Table 2

Values of the function f_K

z	E_0				
	−0,80	−0,50	0,30	0,00	0,25
5	$1,020\cdot10^{-5}$	$6,389\cdot10^{-5}$	$1,253\cdot10^{-4}$	$2,558\cdot10^{-4}$	$3,997\cdot10^{-4}$
6	$1,823\cdot10^{-5}$	$1,433\cdot10^{-4}$	$2,243\cdot10^{-4}$	$4,579\cdot10^{-4}$	$7,156\cdot10^{-4}$
7	$2,963\cdot10^{-5}$	$1,861\cdot10^{-4}$	$3,651\cdot10^{-4}$	$7,455\cdot10^{-4}$	$1,128\cdot10^{-3}$
8	$4,514\cdot10^{-5}$	$2,838\cdot10^{-4}$	$5,569\cdot10^{-4}$	$1,136\cdot10^{-3}$	$1,778\cdot10^{-3}$
9	$6,515\cdot10^{-5}$	$4,107\cdot10^{-4}$	$8,082\cdot10^{-4}$	$1,647\cdot10^{-3}$	$2,575\cdot10^{-3}$
10	$9,070\cdot10^{-5}$	$5,728\cdot10^{-4}$	$1,125\cdot10^{-3}$	$2,299\cdot10^{-3}$	$3,594\cdot10^{-3}$
11	$1,220\cdot10^{-4}$	$7,726\cdot10^{-4}$	$1,518\cdot10^{-3}$	$3,103\cdot10^{-3}$	$4,852\cdot10^{-3}$
12	$1.599\cdot10^{-4}$	$1,015\cdot10^{-3}$	$1,995\cdot10^{-3}$	$4,081\cdot10^{-3}$	$6,383\cdot10^{-3}$
13	$2,051\cdot10^{-4}$	$1,306\cdot10^{-3}$	$2,570\cdot10^{-3}$	$5,258\cdot10^{-3}$	$8,227\cdot10^{-3}$
14	$2,582\cdot10^{-4}$	$1,650\cdot10^{-3}$	$3,247\cdot10^{-3}$	$6,647\cdot10^{-3}$	0,01040
15	$3,198\cdot10^{-4}$	$2,050\cdot10^{-3}$	$4,037\cdot10^{-3}$	$8,270\cdot10^{-3}$	0,01294
16	$3,910\cdot10^{-4}$	$2,516\cdot10^{-3}$	$4,960\cdot10^{-3}$	0,01016	0,01592
17	$4,717\cdot10^{-4}$	$3,048\cdot10^{-3}$	$6,013\cdot10^{-3}$	0,01233	0,01931
18	$5,633\cdot10^{-4}$	$3,658\cdot10^{-3}$	$7,224\cdot10^{-3}$	0,01482	0,02322
19	$6,663\cdot10^{-4}$	$4,351\cdot10^{-3}$	$8,597\cdot10^{-3}$	0,01765	0,02766
20	$7,803\cdot10^{-4}$	$5,122\cdot10^{-3}$	0,01013	0,02081	0,03263
21	$9,082\cdot10^{-4}$	$5,994\cdot10^{-3}$	0,01187	0,02441	0,03828
22	$1,049\cdot10^{-3}$	$6,966\cdot10^{-3}$	0,01381	0,02842	0,04457
23	$1,205\cdot10^{-3}$	$8,049\cdot10^{-3}$	0,01597	0,03291	0,05164
24	$1,374\cdot10^{-3}$	$9,238\cdot10^{-3}$	0,01836	0,03785	0,05941
25	$1,562\cdot10^{-3}$	0,01058	0,02105	0,04343	0,06821
26	$1,772\cdot10^{-3}$	0,01209	0,02409	0,04977	0,07820
27	$1,991\cdot10^{-3}$	0,01369	0,02731	0,05647	0,08879
28	$2,238\cdot10^{-3}$	0,01552	0,03101	0,06419	0,1010
29	$2,484\cdot10^{-3}$	0,01737	0,03476	0,07204	0,1134
30	$2,773\cdot10^{-3}$	0,01957	0,03922	0,08139	0,1282
31	$3,045\cdot10^{-3}$	0,02170	0,04357	0,09052	0,1426
32	$3,351\cdot10^{-3}$	0,02412	0,04849	0,01009	0,1590
33	$3,673\cdot10^{-3}$	0,02671	0,05383	0,1121	0,1770
34	$4,012\cdot10^{-3}$	0,02951	0,05959	0,1243	0,1962
35	$4,376\cdot10^{-3}$	0,03257	0,06588	0,1376	0,2174
36	$4,759\cdot10^{-3}$	0,03585	0,07266	0,1520	0,2402
37	$5,188\cdot10^{-3}$	0,03957	0,08038	0,1684	0,2664
38	$5,607\cdot10^{-3}$	0,04335	0,08826	0,1853	0,2933
39	$6,102\cdot10^{-3}$	0,04785	0,09768	0,2054	0,3253
40	$6,622\cdot10^{-3}$	0,05266	0,1078	0,2269	0,3598
41	$7,168\cdot10^{-3}$	0,05794	0,1188	0,2508	0,3979
42	$7,715\cdot10^{-3}$	0,06330	0,1302	0,2751	0,4369
43	$8,257\cdot10^{-3}$	0,06892	0,1421	0,3010	0,4783
44	$8,833\cdot10^{-3}$	0,07505	0,1552	0,3293	0,5239
45	$9,388\cdot10^{-3}$	0,08119	0,1683	0,3580	0,5700
46	$9,892\cdot10^{-3}$	0,08724	0,1814	0,3867	0,6166
47	0,01042	0,09377	0,1957	0,4179	0,6669
48	0,01094	0,1005	0.2104	0,4504	0,7192
49	0,01141	0,1072	0,2251	0,4832	0,7727
50	0,01192	0,1145	0,2412	0,5189	0,8325
51	0,01245	0,1226	0,2593	0,5593	0,8955
52	0,01294	0,1307	0,2775	0,5999	0,9627
53	0,01349	0,1399	0,2982	0,6464	1,038
54	0,01406	0,1500	0,3207	0,6973	1,121
55	0,01465	0,1610	0,3456	0,7535	1,213
56	0,01530	0,1736	0,3745	0,8187	1,320
57	0,01602	0,1877	0,4066	0,8918	1,440
58	0,01657	0,2009	0,4370	0,9610	1,555
59	0,01706	0,2146	0,4691	1,035	1,676
60	0,01748	0,2284	0,5017	1,111	1,802
61	0,01782	0,2428	0,5362	1,190	1,939
62	0,01808	0,2590	0,5755	1,284	2,089
63	0,01837	0,2753	0,6149	1,377	2,243
64	0,01841	0,2911	0,6540	1,470	2,399
65	0,01881	0,3094	0,6981	1,574	2,572
66	0,01849	0.3265	0,7425	1,682	2,755

Table 2 continued

Z	E_0				
	−0,80	−0,50	−0,30	0,00	0,25
67	0,01856	0,3473	0,7945	1,807	2,965
68	0,01832	0,3664	0,8439	1,928	3,170
69	0,01801	0,3866	0,8966	2,058	3,389
70	0,01772	0,4096	0,9562	2,204	3,637
71	0,01723	0,4325	1,017	2,356	3,895
72	0,01662	0,4570	1,083	2,521	4,177
73	0,01577	0,4789	1,144	2,677	4,445
74	0,01503	0,5056	1,217	2,862	4,761
75	0,01395	0,5316	1,292	3,054	5,092
76	0,01274	0,5559	1,363	3,241	5,417
77	0,01154	0,5829	1,442	3,449	5,778
78	0,01033	0,6142	1,534	3,688	6,194
79	$9,323\cdot10^{-3}$	0,6448	1,623	3,923	6,601
80	$7,520\cdot10^{-3}$	0,6716	1,711	4,165	7,031
81	$5,893\cdot10^{-3}$	0,7072	1,811	4,439	7,515
82	$4,409\cdot10^{-3}$	0,7288	1,901	4,691	7,964
83	$3,097\cdot10^{-3}$	0,7605	2,007	4,990	8,495
84	$1,826\cdot10^{-3}$	0,7963	2,128	5,329	9,098
85	$8,162\cdot10^{-4}$	0,8320	2,254	5,687	9,742
86	$1,891\cdot10^{-4}$	0,8657	2,376	6,043	10,38
87		0,8953	2,494	6,394	11,02
88		0,9263	2,620	6,773	11,71
89		0,9611	2,761	7,202	12,50
90		0,9934	2,905	7,649	13,32
91		1,023	3,046	8,101	14,17
92		1,052	3,189	8,560	15,03
93		1,085	3,357	9,111	16,05
94		1,112	3,513	9,634	17,04
95		1,136	3,668	10,17	18,07
96		1,171	3,863	10,83	19,31
97		1,189	4,028	11,44	20,50
98		1,201	4,182	12,03	21,67

Z	E_0				
	0,50	0,75	1,00	1,25	1,50
5	$5,576\cdot10^{-4}$	$7,836\cdot10^{-4}$	$1,024\cdot10^{-3}$	$1,295\cdot10^{-3}$	$1,599\cdot10^{-3}$
6	$1,031\cdot10^{-3}$	$1,403\cdot10^{-3}$	$1,833\cdot10^{-3}$	$2,320\cdot10^{-3}$	$2,864\cdot10^{-3}$
7	$1,679\cdot10^{-3}$	$2,285\cdot10^{-3}$	$2,985\cdot10^{-3}$	$3,778\cdot10^{-3}$	$4,664\cdot10^{-3}$
8	$2,561\cdot10^{-3}$	$3,487\cdot10^{-3}$	$4,555\cdot10^{-3}$	$5,765\cdot10^{-3}$	$7,118\cdot10^{-3}$
9	$3,710\cdot10^{-3}$	$5,052\cdot10^{-3}$	$6,598\cdot10^{-3}$	$8,353\cdot10^{-3}$	0,01031
10	$5,179\cdot10^{-3}$	$7,052\cdot10^{-3}$	$9,211\cdot10^{-3}$	0,01166	0,01440
11	$6,993\cdot10^{-3}$	$9,521\cdot10^{-3}$	0,01244	0,01575	0,01945
12	$9,198\cdot10^{-3}$	0,01252	0,01637	0,02072	0,02559
13	0,01186	0,01615	0,02110	0,02671	0,03299
14	0,01499	0,02042	0,02669	0,03378	0,04172
15	0,01866	0,02542	0,03322	0,04207	0,05195
16	0,02295	0,03126	0,04085	0,05173	0,06389
17	0,02785	0,03794	0,04960	0,06281	0,07759
18	0,03349	0,04564	0,05967	0,07557	0,09336
19	0,03991	0,05440	0,07112	0,09009	0,1113
20	0,04707	0,06418	0,08391	0,1063	0,1313
21	0,05524	0,07531	0,09849	0,1248	0,1542
22	0,06436	0,08777	0,1148	0,1454	0,1797
23	0,07457	0,1017	0,1330	0,1686	0,2073
24	0,08584	0,1171	0,1532	0,1941	0,2400

Table 2 continued

z	E_0				
	0,50	0.75	1,00	1,25	1,50
25	0,1052	0,1345	0,1760	0,2230	0,2757
26	0,1130	0,1543	0,2019	0,2559	0,3163
27	0,1284	0,1752	0,2294	0,2908	0,3595
28	0,1460	0,1994	0,2611	0,3310	0,4092
29	0,1641	0,2240	0,2934	0,3721	0,4600
30	0,1855	0,2534	0,3319	0,4209	0,5205
31	0,2065	0,2822	0,3696	0,4689	0,5799
32	0,2303	0,3148	0,4125	0,5233	0,6474
33	0,2563	0,3504	0,4592	0,5827	0,7209
34	0,2844	0,3890	0,5099	0,6471	0,8007
35	0,3152	0,4314	0,5656	0,7179	0,8885
36	0,3487	0,4771	0,6257	0,7944	0,9833
37	0,3868	0,5294	0,6945	0,8820	1,092
38	0,4258	0,5832	0,7653	0,9721	1,203
39	0,4728	0,6478	0,8502	1,080	1,337
40	0,5232	0,7170	0,9411	1,196	1,481
41	0,5789	0,7936	1,042	1,324	1,641
42	0,6359	0,8722	1,146	1,457	1,805
43	0,6967	0,9560	1,256	1,597	1,979
44	0,7635	1,048	1,378	1,752	2,171
45	0,8312	1,141	1,500	1,909	2,367
46	0,8993	1,236	1,625	2,068	2,564
47	0,9739	1,338	1,761	2,241	2,780
48	1,051	1,445	1,903	2,422	3,004
49	1,130	1,554	2,046	2,606	3,233
50	1,215	1,674	2,203	2,808	3,483
51	1,312	1,807	2,381	3,034	3,767
52	1,410	1,943	2,562	3,265	4,054
53	1,523	2,100	2,769	3,530	4,384
54	1,646	2,270	2,995	3,820	4,745
55	1,782	2,460	3,246	4,142	5,147
56	1,940	2,680	3,539	4,517	5,614
57	2,118	2,928	3,868	4,938	6,139
58	2,290	3,166	4,184	5,345	6,641
59	2,470	3,419	4,520	5,775	7,185
60	2,657	3,680	4,868	6,223	7,744
61	2,859	3,962	5,243	6,698	8,343
62	3,088	4,282	5,671	7,255	9,033
63	3,319	4,606	6,103	7,810	9,728
64	3,556	4,938	6,546	8,382	10,44
65	3,814	5,300	7,030	9,003	11,21
66	4,091	5,691	7,553	9,679	12,07
67	4,410	6,136	8,149	10,45	13,03
68	4,718	6,572	8,733	11,20	13,98
69	5,050	7,042	9,363	12,02	15,00
70	5,426	7,572	10,07	12,94	16,15
71	5,819	8,128	10,82	13,90	17,36
72	6,248	8,735	11,64	14,96	18,69
73	6,658	9,317	12,42	15,97	19,97
74	7,142	10,00	13,35	17,17	21,47
75	7,650	10,73	14,32	18,43	23,06
76	8,150	11,44	15,28	19,68	24,64
77	8,706	12,23	16,36	21,08	26,40
78	9,346	13,14	17,59	22,68	28,42
79	9,973	14,03	18,75	24,24	30,39
80	10,64	15,00	20,10	25,95	32,55
81	11,40	16,08	21,57	27,87	34,97
82	12,10	17,09	22,95	28,95	37,24
83	12,93	18,29	24,57	31,79	39,93
84	13,87	19,65	26,42	34,21	43,00
85	14,88	21,10	28,41	36,81	46,28
86	15,89	22,56	30,40	39,41	49,58
87	16,90	23,03	32,41	42,05	52,93

Table 2 continued

Z	E_0				
	0,50	0,75	1,00	1,25	1,50
88	18,00	25,63	34,61	44,93	56,60
89	19,24	27,44	37,09	48,19	60,73
90	20,08	29,37	39,74	51,67	65,17
91	21,91	31,34	42,46	55,26	69,74
92	23,29	33,37	45,24	58,93	74,43
93	24,95	35,80	48,60	63,36	80,07
94	26,55	38,16	51,87	67,68	85,59
95	28,22	40,63	55,80	72,20	91,37
96	30,24	43,60	59,41	77,65	98,33
97	32,19	46,49	63,44	82,99	105,2
98	34,12	49,39	67,47	88,37	112,1

Z	E_0				
	1,75	2,00	2,30	2,70	3,00
5	$1,935\cdot10^{-3}$	$2,303\cdot10^{-3}$	$2,787\cdot10^{-3}$	$3,504\cdot10^{-3}$	$4,095\cdot10^{-3}$
6	$3,465\cdot10^{-3}$	$4,124\cdot10^{-3}$	$4,991\cdot10^{-3}$	$6,274\cdot10^{-3}$	$7,333\cdot10^{-3}$
7	$5,644\cdot10^{-3}$	$6,717\cdot10^{-3}$	$8,124\cdot10^{-3}$	0,01021	0,01194
8	$8,613\cdot10^{-3}$	0,01025	0,01240	0,01559	0,01823
9	0,01248	0,01485	0,01797	0,02260	0,02642
10	0,01742	0,02074	0,02510	0,03156	0,03688
11	0,02353	0,02801	0,03391	0,04260	0,04980
12	0,03096	0,03686	0,04459	0,05608	0,06556
13	0,03992	0,04751	0,05751	0,07232	0,08454
14	0,05050	0,06011	0,07277	0,09145	0,1069
15	0,06288	0,07485	0,09057	0,1139	0,1332
16	0,07733	0,09206	0,1114	0,1401	0,1638
17	0,09391	0,1118	0,1353	0,1702	0,1990
18	0,1130	0,1345	0,1629	0,2048	0,2394
19	0,1347	0,1604	0,1941	0,2442	0,2854
20	0,1590	0,1893	0,2292	0,2882	0,3371
21	0,1866	0,2222	0,2690	0,3383	0,3957
22	0,2176	0,2591	0,3138	0,3947	0,4613
23	0,2523	0,3004	0,3638	0,4576	0,5349
24	0,2906	0,3461	0,4189	0,5270	0,6165
25	0,3339	0,3977	0,4815	0,6059	0,7085
26	0,3831	0,4564	0,5527	0,6955	0,8133
27	0,4355	0,5187	0,6282	0,7906	0,9245
28	0,4958	0,5906	0,7154	0,9002	1,053
29	0,5573	0,6640	0,8040	1,012	1,184
30	0,6307	0,7514	0,9102	1,146	1,340
31	0,7027	0,8374	1,015	1,277	1,494
32	0,7846	0,9349	1,133	1,426	1,668
33	0,8736	1,041	1,262	1,589	1,858
34	0,9706	1,157	1,402	1,764	2,065
35	1,077	1,284	1,557	1,960	2,293
36	1,192	1,421	1,723	2,169	2,539
37	1,324	1,578	1,912	2,410	2,819
38	1,460	1,739	2,109	2,658	3,111
39	1,622	1,934	2,345	2,954	3,457
40	1,797	2,143	2,599	3,274	3,833
41	1,991	2,374	2,881	3,631	4,247
42	2,190	2,613	3,168	3,993	4,676
43	2,402	2,866	3,477	4,384	5,130
44	2,636	3,145	3,817	4,811	5,634
45	2,873	3,429	4,160	5,248	6,143

Table 2 continued

Z	E_0				
	1.75	2.00	2.30	2.70	3.00
46	3,114	3,717	4,511	5,688	6,660
47	3,376	4,030	4,890	6,168	7,224
48	3,650	4,358	5,291	6,675	7,815
49	3,928	4,691	5,694	7,186	8,419
50	4,232	5,055	6,139	7,744	9,075
51	4,578	5,468	6,641	8,381	9,817
52	4,929	5,888	7,151	9,032	10,58
53	5,330	6,369	7,735	9,766	11,45
54	5,770	6,896	8,374	10,50	12,40
55	6,260	7,484	9,094	11,48	13,46
56	6,830	8,166	9,924	12,54	14,70
57	7,471	8,934	10,86	13,72	16,09
58	8,083	9,669	11,76	14,87	17,43
59	8,747	10,46	12,72	16,09	18,87
60	9,430	11,28	13,72	17,36	20,34
61	10,16	12,15	14,79	18,70	21,94
62	11,01	13,18	16,03	20,28	23,79
63	11,86	14,20	17,28	21,87	25,65
64	12,73	15,25	18,56	23,49	27,57
65	13,67	16,38	19,55	25,25	29,64
66	14,72	17,64	21,48	27,20	31,93
67	15,90	19,05	23,21	29,40	34,52
68	17,06	20,45	24,92	31,57	37,07
69	18,31	21,95	26,76	33,91	39,82
70	19,73	23,65	28,84	36,56	42,94
71	21,21	25,45	31,03	39,34	46,23
72	22,84	27,40	33,43	42,40	49,82
73	24,41	29,30	35,75	45,35	53,31
74	26,26	31,52	38,48	48,83	57,40
75	28,21	33,88	41,37	52,51	61,74
76	30,15	36,22	44,23	56,17	66,05
77	32,32	38,83	47,44	60,25	70,87
78	34,80	41,83	51,12	64,94	76,40
79	37,23	44,76	54,71	69,54	81,82
80	39,89	47,97	58,66	74,58	87,78
81	42,88	51,59	63,10	80,26	94,48
82	45,68	54,97	67,27	85,60	100,8
83	49,00	58,99	72,21	91,91	108,2
84	52,77	63,56	77,83	99,10	116,7
85	56,84	68,48	83,89	106,8	125,9
86	60,92	73,43	89,98	114,7	135,1
87	65,07	78,46	96,18	122,6	144,5
88	69,61	83,96	103,0	131,3	154,8
89	74,73	90,18	110,6	141,2	166,5
90	80,23	96,86	118,9	151,7	179,0
91	85,91	103,7	127,4	162,7	192,0
92	91,70	110,8	136,1	173,9	205,3
93	98,74	119,3	146,6	187,4	221,8
94	105,5	127,1	157,0	200,8	237,1
95	102,8	136,5	167,9	214,8	253,7
96	121,4	147,0	180,9	231,6	273,7
97	130,0	157,4	193,8	248,2	293,4
98	138,6	168,0	206,9	265,1	313,5

Table 2 continued

Z	E_0				
	3,30	3,70	4,00	5,00	7,00
5	$4{,}732\cdot10^{-3}$	$5{,}654\cdot10^{-3}$	$6{,}015\cdot10^{-3}$	$9{,}214\cdot10^{-3}$	0,01638
6	$8{,}474\cdot10^{-3}$	0,01012	0,01146	0,01650	0,02934
7	0,01380	0,01649	0,01866	0,02687	0,04778
8	0,02106	0,02517	0,02848	0,04102	0,07292
9	0,03053	0,03648	0,04128	0,05946	0,1057
10	0,04263	0,05091	0,05762	0,08300	0,1476
11	0,05756	0,06878	0,07785	0,1121	0,1994
12	0,07577	0,09054	0,1024	0,1476	0,2624
13	0,09766	0,1167	0,1321	0,1902	0,3383
14	0,1236	0,1477	0,1671	0,2407	0,4281
15	0,1539	0,1839	0,2082	0,2998	0,5332
16	0,1893	0,2262	0,2560	0,3688	0,6559
17	0,2299	0,2748	0,3111	0,4480	0,7968
18	0,2768	0,3307	0,3744	0,5392	0,9593
19	0,3300	0,3943	0,4464	0,6430	1,144
20	0,3895	0,4656	0,5270	0,7594	1,351
21	0,4573	0,5467	0,6188	0,8915	1,586
22	0,5335	0,6375	0,7215	1,040	1,850
23	0,6186	0,7393	0,8369	1,206	2,146
24	0,7126	0,8518	0,9641	1,390	2,473
25	0,8191	0,9790	1,108	1,597	2,843
26	0,9402	1,124	1,272	1,834	3,264
27	1,065	1,278	1,447	2,085	3,712
28	1,217	1,455	1,648	2,375	4,228
29	1,369	1,636	1,853	2,672	4,757
30	1,550	1,852	2,098	3,024	5,386
31	1,728	2,065	2,339	3,373	6,006
32	1,929	2,307	2,612	3,768	6,709
33	2,149	2,570	2,910	4,197	7,477
34	2,389	2,857	3,235	4,666	8,312
35	2,651	3,171	3,592	5,181	9,232
36	2,936	3,512	3,977	5,738	10,23
37	3,263	3,902	4,419	6,376	11,37
38	3,598	4,304	4,876	7,035	12,54
39	4,000	4,787	5,422	7,825	13,95
40	4,435	5,305	6,010	8,674	15,47
41	4,915	5,881	6,662	9,616	17,15
42	5,412	6,473	7,334	10,59	18,89
43	5,939	7,105	8,051	11,63	20,74
44	6,520	7,800	8,840	12,77	22,78
45	7,110	8,512	9,643	13,93	24,86
46	7,709	9,227	10,46	15,11	26,97
47	8,364	10,01	11,35	16,39	29,27
48	9,047	10,83	12,28	17,74	31,68
49	9,743	11,67	13,23	19,11	34,13
50	10,50	12,58	14,26	20,61	36,82
51	11,37	13,62	15,44	22,32	39,88
52	12,25	14,68	16,63	24,06	42,99
53	13,26	15,88	18,01	26,05	46,55
54	14,36	17,21	19,51	28,22	50,46
55	15,60	18,68	21,19	30,66	54,83
56	17,03	20,41	23,14	33,49	59,90
57	18,64	22,34	25,33	36,69	65,62
58	20,21	24,21	27,47	39,76	71,10
59	21,86	26,20	29,72	43,04	77,05
60	23,59	28,29	32,07	46,45	83,19
61	25,43	30,49	34,59	50,12	89,77
62	27,59	33,08	37,53	54,39	97,44
63	29,74	35,67	40,47	58,66	105,1
64	31,97	38,35	43,52	63,09	113,1
65	34,37	41,24	46,80	67,86	121,7
66	37,04	44,45	50,44	73,16	131,2
67	40,05	48,06	54,54	79,13	142,0

Table 2 continued

Z	E_0				
	3,30	3,70	4,00	5,00	7,00
68	43,02	51,63	58,60	85,04	152,6
69	46,22	55,48	62,98	91,42	164,2
70	49,84	59,84	67,94	98,44	177,2
71	53,66	64,44	73,17	106,3	190,9
72	57,84	69,47	78,89	114,6	206,0
73	61,90	74,35	84,44	122,7	220,6
74	66,66	80,08	90,96	132,2	237,8
75	71,71	86,17	97,89	142,3	256,1
76	76,74	92,24	104,8	152,4	274,3
77	82,35	98,99	112,4	163,7	294,7
78	88,78	106,8	121,3	176,6	318,1
79	95,10	114,3	129,9	189,2	340,9
80	102,0	122,7	139,5	203,2	366,3
81	109,9	132,2	150,2	218,9	394,9
82	117,2	141,0	160,4	233,7	421,8
83	125,9	151,5	172,3	251,3	453,6
84	135,8	163,5	186,0	271,2	489,9
85	146,5	176,4	200,7	292,8	529,1
86	157,3	189,4	215,5	314,6	568,7
87	168,3	202,7	230,6	336,8	609,1
88	180,3	217,3	247,2	361,1	653,5
89	193,9	233,7	266,0	388,7	703,8
90	208,5	251,4	286,2	418,4	758,0
91	223,7	269,8	307,1	449,2	814,3
92	239,2	288,6	328,6	480,8	871,8
93	258,1	311,3	354,6	519,1	942,0
94	276,5	333,7	380,1	556,8	1011
95	295,9	357,2	407,0	596,4	1083
96	319,2	385,5	439,4	643,8	1170
97	342,5	413,7	471,5	691,3	1257
98	366,0	442,1	504,0	739,6	1346

Table 3

Values of the function $\frac{\pi}{2}G_K^2$

Z	$\frac{\pi}{2}G_K^2$	Z	$\frac{\pi}{2}G_K^2$	Z	$\frac{\pi}{2}G_K^2$	Z	$\frac{\pi}{2}G_K^2$
5	$2,560\cdot10^{-4}$	29	0,07465	53	0,7393	77	4,784
6	$4,584\cdot10^{-4}$	30	8,455	54	0,8020	78	5,169
7	$7,467\cdot10^{-4}$	31	9,431	55	0,8719	79	5,546
8	$1,140\cdot10^{-3}$	32	0,1054	56	0,9533	80	5,967
9	$1,652\cdot10^{-3}$	33	0,1175	57	1,045	81	6,440
10	$2,307\cdot10^{-3}$	34	0,1306	58	1,134	82	6,888
11	$3,117\cdot10^{-3}$	35	0,1452	59	1,229	83	7,417
12	$4,102\cdot10^{-3}$	36	0,1609	60	1,328	84	8,021
13	$5,291\cdot10^{-3}$	37	0,1789	61	1,434	85	8,675
14	$6,695\cdot10^{-3}$	38	0,1975	62	1,558	86	9,337
15	$8,340\cdot10^{-3}$	39	0,2198	63	1,683	87	10,02
16	0,01026	40	0,2438	64	1,812	88	10,76
17	0,01247	41	0,2705	65	1,951	89	11,61
18	0,01501	42	0,2980	66	2,106	90	12,52
19	0,01791	43	0,3274	67	2,281	91	13,47
20	0,02115	44	0,3598	68	2,454	92	14,45
21	0,02484	45	0,3928	69	2,642	93	15,63
22	0,02898	46	0,4264	70	2,854	94	16,80
23	0,03362	47	0,4631	71	3,079	95	18,03
24	0,03875	48	0,5015	72	3,325	96	19,51
25	0,04456	49	0,5407	73	3,565	97	21,00
26	0,05118	50	0,5836	74	3,847	98	22,52
27	0.05822	51	0,6325	75	4,148		
28	0,06334	52	0,6823	76	4,449		

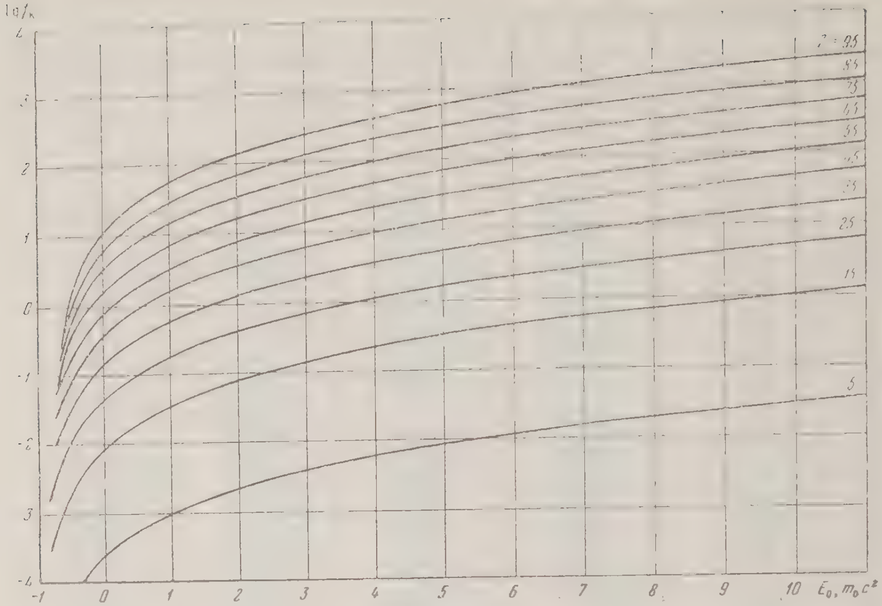

Fig.2. Dependence of the function f_K on the transition energy E_0.

3. Functions necessary for calculating the probability of forbidden K-capture.

The probability of forbidden K-capture, just as the probability of β-decay, can be characterized in terms of the appropriate "forbidden transition" correction factor C (Refs. 13 & 14), if use is made of the following coefficients which are expressed in terms of the K-electron wave function:

$$L_0 = G_K^2, \qquad P_0 = G_K^2,$$
$$M_0 = R^{-2}F_K^2, \qquad Q_0 = -R^{-2}F_K^2,$$
$$N_0 = R^{-1}G_KF_K, \qquad R_0 = R^{-1}G_KF_K.$$

We tabulated the values of these functions on the basis of the data of Table 1. Knowing these functions makes it possible to analyze forbidden transitions by K-capture, which together with analysis of the positron decay branch allows of obtaining significant information in the change of the nuclear states during β-decay.

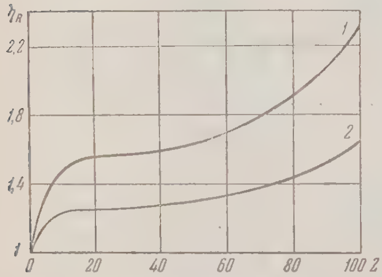

Fig.3. Corrections for finite size of the nucleus and screening: 1) for the function M_0 and 2) for the function N_0.

It will be seen from Fig.3 that in the case of forbidden transitions (the expressions for the probability of which comprise the small components F_k of the wave functions) the corrections for finite nuclear size and screening are much more appreciable than in the case of allowed transitions. In the case of heavy elements the corrections reduce the value of M_0 by a factor of two and the value of N_0 by a factor of one and a half. For Z = 25 the corrections are 55 and 25%, respectively.

The values of the functions L_0, M_0 and N_0 found taking into account finite size of the nucleus and screening are listed in Table 4 (see next page).

Scientific Research Physical Institute of
"A.A.Zhdanov" Leningrad State University

Table 4

Values of the functions L_0, M_0 and N_0 for K-capture

Z	L_0	M_0	N_0	Z	L_0	M_0	N_0
5	$1,630\cdot10^{-4}$	$8,065\cdot10^{-4}$	$-3,626\cdot10^{-4}$	53	0,4706	51,96	—4,946
6	$2,918\cdot10^{-4}$	$1,831\cdot10^{-3}$	$-7,307\cdot10^{-4}$	54	0,5105	56,70	—5,380
7	$4,754\cdot10^{-4}$	$3,640\cdot10^{-3}$	$-1,315\cdot10^{-3}$	55	0,5550	61,01	—5,818
8	$7,256\cdot10^{-4}$	$6,597\cdot10^{-3}$	$-2,188\cdot10^{-3}$	56	0,6068	66,74	—6,363
9	$1,052\cdot10^{-3}$	0,01077	$-3,365\cdot10^{-3}$	57	0,6654	73,66	—7,001
10	$1,468\cdot10^{-3}$	0,01758	$-5,082\cdot10^{-3}$	58	0,7217	81,40	—7,666
11	$1,984\cdot10^{-3}$	0,02636	$-7,231\cdot10^{-3}$	59	0,7823	89,83	—8,387
12	$2,612\cdot10^{-3}$	0,03895	—0,01009	60	0,8455	100,4	—9,213
13	$3,368\cdot10^{-3}$	0,05585	—0,01372	61	0,9132	112,1	—10,12
14	$4,262\cdot10^{-3}$	0,07812	—0,01824	62	0,9920	122,8	—11,04
15	$5,310\cdot10^{-3}$	0,1066	—0,02380	63	1,071	135,1	—12,03
16	$6,533\cdot10^{-3}$	0,1399	—0,03024	64	1,154	148,8	—13,10
17	$7,937\cdot10^{-3}$	0,1856	—0,03838	65	1,242	165,0	—14,32
18	$9,557\cdot10^{-3}$	0,2406	—0,04794	66	1,341	181,2	—15,59
19	0,01140	0,3099	—0,05945	67	1,452	199,8	—17,04
20	0,01346	0,3826	—0,07177	68	1,563	220,2	—18,51
21	0,01581	0,4864	—0,08766	69	1,682	242,9	—20,21
22	0,01845	0,5977	—0,1050	70	1,817	266,8	—22,01
23	0,02140	0,7391	—0,1257	71	1,960	293,8	—23,99
24	0,02467	0,9002	—0,1356	72	2,117	320,9	—26,07
25	0,02837	1,080	—0,1750	73	2,270	353,7	—28,34
26	0,03258	1,345	—0,2093	74	2,449	397,4	—30,84
27	0,03706	1,596	—0,2432	75	2,641	428,4	—33,63
28	0,04223	1,952	—0,2871	76	2,833	466,8	—36,37
29	0,04752	2,310	—0,3313	77	3,045	507,8	—39,32
30	0,05382	2,631	—0,3763	78	3,291	553,7	—42,69
31	0,06003	3,132	—0,4336	79	3,531	605,8	—46,25
32	0,06708	3,615	—0,4923	80	3,799	667,4	—50,36
33	0,07479	4,281	—0,5659	81	4,100	735,4	—54,91
34	0,08323	4,795	—0,6317	82	4,385	799,6	—59,21
35	0,09242	5,579	—0,7182	83	4,722	883,4	—64,58
36	0,1024	6,367	—0,8076	84	5,106	960,1	—70,02
37	0,1139	7,329	—0,9140	85	5,523	1065	—76,70
38	0,1257	8,482	—1,032	86	5,944	1156	—82,89
39	0,1399	9,801	—1,171	87	6,376	1263	—89,77
40	0,1552	11,08	—1,312	88	6,850	1374	—97,02
41	0,1722	12,98	—1,495	89	7,388	1523	—106,1
42	0,1897	14,19	—1,640	90	7,969	1657	—114,8
43	0,2084	16,28	—1,842	91	8,573	1818	—124,8
44	0,2290	18,65	—2,066	92	9,196	1965	—134,4
45	0,2500	21,23	—2,303	93	9,948	2160	—146,8
46	0,2714	24,47	—2,577	94	10,69	2380	—159,5
47	0,2948	28,28	—2,887	95	11,48	2568	—171,7
48	0,3192	32,23	—3,207	96	12,42	2837	—187,7
49	0,3442	36,82	—3,560	97	13,37	3092	—203,3
50	0,3715	40,11	—3,860	98	14,34	3309	—217,8
51	0,4026	43,77	—4,197				
52	0,4343	47,81	—4,558				

$P_0 = L_0;\ Q_0 = -M_0;\ R_0 = N_0;\ L_1 = P_1 = 0.$

References

1. M.Metropolis & J.Reitz, J.Chem.Phys., 19, 555 (1951).
2. L.Sliv, Zhur.eksp.i teor.fiz., 17, 1049 (1947).
3. E.Konopinski, Rev.Mod.Phys., 15, 209 (1943).
4. J.Slater, Phys.Rev., 36, 51 (1930).
5. S.Moszkowski, Phys.Rev., 82, 35 (1951).
6. E.Feenberg & G.Trigg, Rev.Mod.Phys., 22, 399 (1950).
7. Landolt-Börnstein, 1, st. 5.-Berlin (1952).
8. P.Benoist-Gueutal, Ann. de Phys., 8, 593 (1953).
9. P.Zweifel, Phys.Rev., 96, 1572 (1954).
10. J.Reitz, Phys.Rev., 77, 10 (1950).
11. L.Rapoport, Zhur.eksp.i teor.fiz., 25, 282 (1953).
12. I.Malcolm & C.Strachan, Proc.Cambr.Phil.Soc., 47, 610 (1951).
13. E.Konopinski & G.Uhlenbeck, Phys.Rev., 60, 308 (1941).
14. A.Smith, Phys.Rev., 82, 955 (1951).

ON THE ROLE OF THE PSEUDOSCALAR FORM OF INTERACTION IN THE THEORY OF β-DECAY

- L.N. Zyrianova

In recent years there has been marked progress in establishing the invariant forms of interaction in β-decay. It has been found that the predominant role is played by the S and T forms ($\lambda_T/\lambda_S \approx 1.3$) and that V and A interactions are virtually absent. Until now, however, there has been no direct proof of the possible presence of the P form in the general law for β-interaction. A number of deductions regarding the importance of the pseudoscalar form and the magnitude of the coefficient λ_P were arrived at some years ago$^{1-4}$ on the basis of analysis of the shape of the RaE β-spectrum on the assumption that the spin of RaE is 0. However, these deductions were subsequently invalidated when it was shown that the spin of RaE equals 1. It has been suggested^5 that an indirect proof of the existence of P interaction is furnished by the relatively low value of the reduced lifetime ft for first forbidden β-transitions with $\Delta I = 0$ as compared with the values of ft for transitions with $\Delta I = 1$.

In the present investigations we make a number of deductions regarding the role of P interaction in β-decay on the basis of analysis of the shape of forbidden β-spectra.

From the selection rules for β-decay it follows that the P term is most important for first forbidden β-transitions between levels with zero spin and different parity. For the purpose of clarifying the role of P interaction in β-decay we undertook an analysis of the known $0 \rightarrow 0$ (yes) transitions.

At present there have been reported over ten cases of β-decay in which a $0 \rightarrow 0$ (yes) transition is known or is assumed to exist. Only those cases are suitable for theoretical analysis in which the β-spectrum corresponding to the $0 \rightarrow 0$ transition is not masked to any appreciable extent by the spectra of transitions to other levels, while the spins of the nuclear states are established with reasonable certainty. At present these requirements are satisfied only by the β-spectra associated with the transition between the ground levels of Pr^{144} & Nd^{144} and of Tl^{206} & Pb^{206}. Below we shall therefore consider these two β-spectra.

Pr^{144} (17.5 min) is the product of β-decay of Ce^{144}. The Ce^{144}—Pr^{144} β-spectra and their decay scheme has been studied by several investigators$^{6-10}$. The Ce^{144}—Pr^{144}—Nd^{144} decay scheme found by Emmerich and his coworkers^{10} is reproduced in Fig.1. For our purpose we are interested mainly in the hard component of the Pr^{144} β-spectrum with an end point energy 2.98 Mev (97.3±0.8%), associated with the transition between the Pr^{144} (0-) and Nd^{144} (0+) ground levels. The Kurie plot of the Ce^{144}—Pr^{144} β-spectrum is shown in Fig.2. In addition to the hard 2.98 Mev component, the β-spectrum contains two weak components of Pr^{144} - 2.28 Mev (0.8±0.3%) and 0.80 Mev (1.9±0.5%) - and a number of components of the β-spectrum of Ce^{144} that lie in the region below 0.3 Mev. In the interval between 2.3 and 2.8 Mev the Kurie plot of the Pr^{144} β-spectrum is rectilinear. Extrapolation of the hard spectrum into the soft region according to Fermi's formula makes it possible to separate two β-components of end point energies 2.3 and 0.8 Mev, the intensities of which agree within 2% with the intensities obtained from direct and more accurate γ-ray measurements. Thus it is known from the experimental data that in the region of energies above 300 kev there is no deviation exceeding 2-3% of the hard β-spectrum of Pr^{144} from the Fermi shape.

In the decay scheme shown in Fig.1 the 0- assignment for the ground states of Ce^{144} and Nd^{144} was made on the basis of the general rule regarding the levels of even-even nuclei. The odd parity of the ground level of Pr^{144} follows from the ft values for the Ce^{144}—Pr^{144} ($\log ft = 7.5$) and Pr^{144}—Nd^{144} ($\log ft = 6.5$) transition, values that are characteristic of first forbidden transitions in the

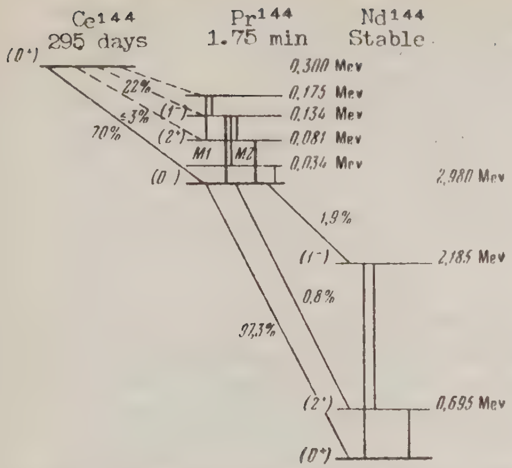

Fig.1. Decay scheme for Pr^{144}.

region removed from nuclei with closed shells. There is no direct experimental evidence from the 0 spin assignment for the ground state of Pr^{144}, but this assignment makes possible a consistent decay scheme and is used by all the above mentioned authors. In our analysis of the 2.98 Mev spectrum of Pr^{144} we assume that this is in fact a 0- → 0+ transition.

The β-spectrum of Tl^{206} has been studied by Alburger & Friedlander[11]. Pb^{206} (Fig.3), in addition to the 0+ ground level, is reported to have a 2+ level at 800 kev. However, careful search with a strong Tl^{206} source failed to disclose γ-rays or conversion electrons, which gives reason to assume that the β-spectrum of Tl^{206} is a simple one. The Kurie plot of the spectrum is shown in Fig.4. The plot is a straight line in the region from 0.6 to 1.5 Mev. The deviation from the Fermi shape in the soft region, as the above authors note, may be due to the thickness of the source. The end point energy (1.51±0.01 Mev) and the half-life (4.2±0.1 min) lead to a value of log ƒt = 5.2. This value is characteristic of first forbidden β-transitions in the region of nuclei having almost filled neutron and proton shells (Tl^{206} has 81 protons and 125 neutrons). This is the basis of the assumption that the parity changes in the $Tl^{206} \rightarrow Pb^{206}$ β-transition. The absence of γ-rays in the β-decay of Tl^{206} indicates that the transition to the excited level of Pb^{206} is forbidden. This is the basis of the 0 spin assignment for the lower state of Tl^{206}.

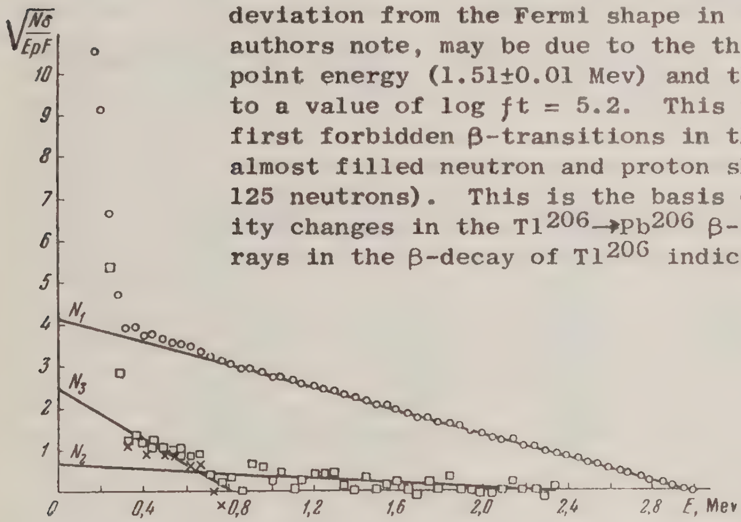

Fig.2. Experimental β-spectrum of Pr^{144} (Kurie plot based on the measurements of Emmerich, Auth & Kurbatov[10].

Thus there is good reason to assume that the β-decay of Tl^{206} involves a 0- → 0+ transition and that the Kurie plot corresponding to this transition is rectilinear in the region above 600 kev.

In the analysis of the shape of the β-spectra of Tl^{206} and Pr^{144}, given below, we have assumed that the experimental accuracy of measuring the shape of the β-spectra is 5%.

Let us see now what the theory of β-decay predicts regarding the shape of the spectra of these transitions.

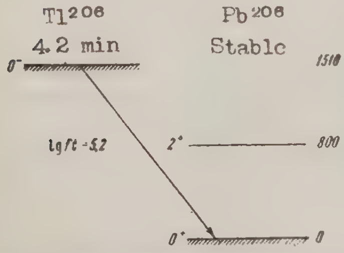

Fig.3. Decay scheme for Tl^{206}.

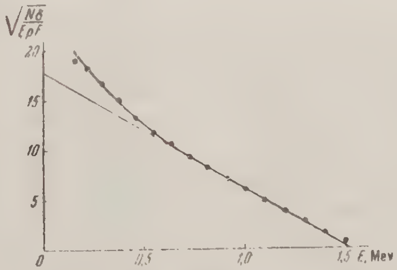

Fig.4. Experimental β-spectrum of Tl^{206} (Kurie plot based on measurements of Alburger & Friedlander[11].

From the selection rules, it is known that in the S and V variants of the theory there are no 0 → 0 transitions with change of parity. If, further, on the basis of deductions from the theory of allowed transitions, we disregard the A form, then there remain only two possibilities for describing 0 → 0 (yes) transitions: the T form and a linear combination of T and P.

Let us first examine the theoretical shape of the spectra of Pr^{144} and Tl^{206} in the case of pure tensor interaction. The correction factor C_T for a 0 → 0 (yes) transition is[12]

$$C_T = \left(\frac{1}{9} K^2 L_0 + M_0 + \frac{2}{3} K N_0\right) \left| \int \sigma \cdot r \right|^2, \tag{1}$$

where K is the energy of the neutrino.

For determining C_T we calculated the coefficients L_0, M_0, N_0, P_0, Q_0 and R_0 taking into account the Coulomb field, screening and the finite dimensions of the nucleus. The finite dimensions of the nucleus were taken into account using the model of a uniformly charged sphere, the radius of which was assumed to be $1.2 \cdot 10^{-13} A^{1/3}$ cm. The values of the coefficients calculated in this manner are listed in Tables 1 & 2. The coefficients are written on the assumption that in calculating the theoretical shape of an allowed spectrum according to Fermi's formula the effects of screening and finite dimensions are duly taken into account. In this case the function $L_0 \equiv 1$.

Table 1

β-particle functions necessary for analysis of the shape of the Pr^{144} spectrum

ε, kev	M_0	N_0	P_0	Q_0	R_0
1	121,106	—11,0038	0,896368	—107,025	—9,79579
100	123,768	—11,1228	0,749844	—89,3754	—8,18961
400	130,470	—11,4184	0,500826	—59,3558	—5,46038
600	134,402	—11,5889	0,409701	—48,3319	—4,46102
800	138,204	—11,7516	0,346453	—40,6702	—3,76764
1000	141,914	—11,9082	0,300645	—35,1189	—3,26600
1200	145,710	—12,0664	0,263767	—30,7082	—2,86503
1500	151,082	—12,2869	0,224289	—25,7596	—2,42721
1800	156,596	—12,5092	0,194719	—22,1115	—2,10259
2000	160,302	—12,6565	0,178914	—20,1485	—1,92900
2200	164,038	—12,8032	0,165459	—18,4644	—1,78103
2400	167,811	—12,9497	0,153862	—17,0051	—1,65351
2600	171,616	—13,0957	0,143745	—15,7245	—1,54224
2800	175,456	—13,2414	0,134886	—14,5972	—1,44480
2950	178,370	—13,3510	0,128896	—13,8263	—1,37877

Table 2

β-particle functions necessary for analysis of the shape of the Tl^{206} spectrum

ε, keV	M_0	N_0	P_0	Q_0	R_0
1	186,149	—13,6418	0,795865	—144,541	—10,274
100	189,395	—13,7593	0,664589	—120,323	—8,94598
200	192,408	—13,8678	0,569281	—102,773	—7,65444
400	197,765	—14,0590	0,441584	—79,1896	—5,92188
600	202,949	—14,2420	0,360175	—64,1844	—4,84951
800	207,841	—14,4124	0,303681	—53,7148	—4,05299
1000	212,642	—14,5780	0,262231	—46,0043	—3,49030
1200	217,427	—14,7412	0,230498	—40,0838	—3,05950
1400	222,192	—14,9017	0,205484	—35,3876	—2,71920
1500	224,582	—14,9817	0,194846	—33,3858	—2,57455

The shape factors C_T calculated by means of Eq. (1) for Pr^{144} and Tl^{206} are shown in Figs. 5 & 6 (solid lines). The dash lines indicate the limits of the values of the experimental coefficient C for the β-spectra of Pr and Tl based on an accuracy of measurement of ±5%. The experimental curves for C have been adjusted to match the theoretical values at 300 kev for Pr^{144} and at 600 kev for Tl^{206}.

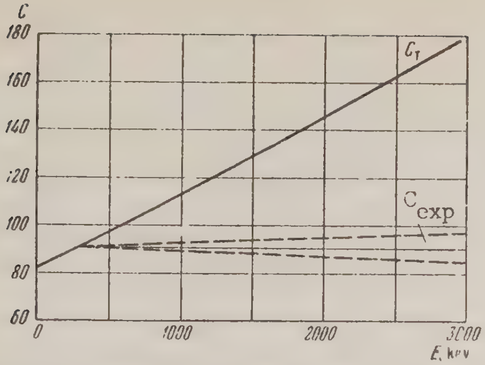

Fig.5. Correction factors C_T and C_{exp} for Pr^{144}. The dash lines indicate the limits for C based on 5% uncertainty in the measurements.

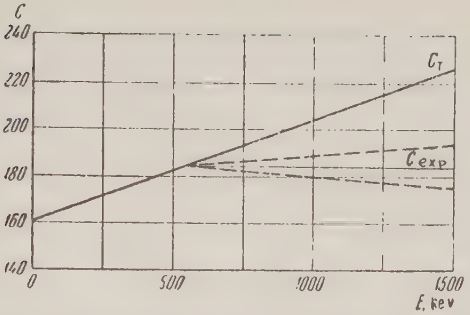

Fig.6. Correction factors C_T and C_{exp} for Tl^{206}. The dash lines indicate the limits for C based on 5% uncertainty in the measurements.

As may be seen from these figures, in the case of Pr^{144} the divergence between the experimental and theoretical factors is appreciably greater than the experimental uncertainty. In the case of Tl^{206} there is also a noticeable, although smaller, divergence between the theoretical and experimental data. It may be concluded therefore that the pure T variant predicts a spectrum shape that is inconsistent with the experimental data. As may be seen from Eq.(1), the theoretical shape of the spectrum associated with a first forbidden $0 \rightarrow 0$ transition on the assumption of pure tensor interaction, in contrast to the case of the shape of most other forbidden β-spectra, depends only on one nuclear matrix element and hence is unique. This fact leads to the inescapable conclusion that the T variant alone cannot explain the observed shape of the Pr^{144} and Tl^{206} spectra.

Thus to explain the observed shape of the β-spectra of Pr^{144} and Tl^{206} we must turn to the pseudoscalar variant of the theory.

Let us now examine the theoretical shape of the spectra associated with the transitions in question on the assumption of T+P interaction. The correction factor in this case must be taken in the form[12]

$$C = \lambda_T^2 \left[C_T + \frac{\lambda_P}{\lambda_T} C_{PT} + \left(\frac{\lambda_P}{\lambda_T}\right)^2 C_P \right], \tag{2}$$

$$C_P = \frac{1}{4M^2}\Big\{(U^2+1)M_0 - 2UQ_0 + \frac{2}{3}K[(U^2-1)N_0 + 4(UM_0 - Q_0)] + \\ + \frac{K^2}{9}[(U^2+1)L_0 - 2UP_0 + 16M_0 + 8(UN_0 - R_0)]\Big\}\left|\int \sigma\cdot r\right|^2, \tag{3}$$

$$C_{PT} = -\frac{1}{M}\Big\{UM_0 - Q_0 + \frac{2}{3}K(2M_0 + UN_0) + \frac{K^2}{9}(UL_0 - P_0 + 4N_0)\Big\}\left|\int \sigma\cdot r\right|^2, \tag{4}$$

where M is the nucleon mass, E is the electron energy, U = E - V - K and V is the potential of the central field.

A distinctive feature here again is the fact that all the correction factors C_T,C_P and C_{PT} contain one and the same nuclear matrix element. Consequently, the shape of the spectrum depends only on the known β-particle functions L, M, N, etc., and the values of the coefficients λ_T and λ_P. Thus investigation of the β-spectrum shape in this case makes it possible through comparison with experiment to determine the magnitude of the ratio λ_P/λ_T characterizing the relative contribution of the P and T interactions.

The calculated factors C_T, C_P and C_{PT} for Pr^{144} are shown in Fig.7; those for Tl^{206} are shown in Fig.8. As may be seen all three factors increase with increasing energy, from which one can determine the unknown sign of $(\lambda_P/\lambda_T) \equiv \varkappa$.

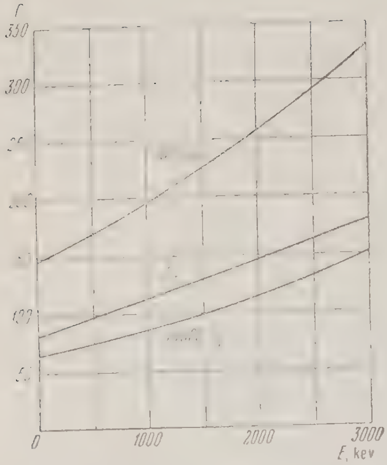

Fig.7. Correction factors with TP interaction for Pr^{144}.

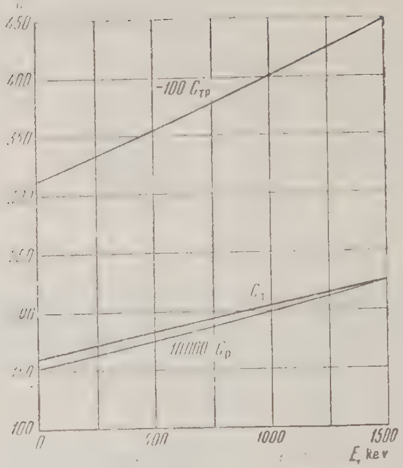

Fig.8. Correction factors with TP interaction for Tl^{206}.

It is obvious that if we take the sum of the factors, disagreement with experiment at any value of $\varkappa$ can only increase since the total factor C will increase rapidly with increasing particle energy. In order to obtain a theoretical factor C as little dependent on the energy as possible, the C_{PT} term should be subtracted from the sum of the other two terms. From this we can immediately determine that the sign of λ_P/λ_T is positive. Inasmuch as here again the theoretical predictions are unique, there can be no doubt regarding this deduction.

Let us now turn to the question of a numerical value of the quantity $\varkappa$. To evaluate this we investigated the energy dependence of the factor C for different values of $\varkappa$.

Fig.9 shows the correction factor C for Pr^{144} plotted as a function of $\varkappa$ at different β-particle energies. The weakest dependence of C on the energy is observed in the region where $\varkappa = 100\text{-}120$. The values of the factor C in this region were compared with experiment. The best agreement with the experimental data on the β-spectrum of Pr^{144} was obtained for $\lambda_P/\lambda_T = 110\text{-}114$. The values of C computed for TP interaction with $\lambda_P/\lambda_T = 112$ are plotted in Fig.10. Fig.11 shows the theoretical shape of the Pr^{144} β-spectrum in Kurie coordinates calculated on the assumption of TP interaction with $\lambda_P/\lambda_T = 112$. It will be seen that the shape of the β-spectrum is not rectilinear; in the hard region (> 1000 kev) the theoretical spectrum is nearly unique, while in the soft region there is a marked increase in the number of electrons.

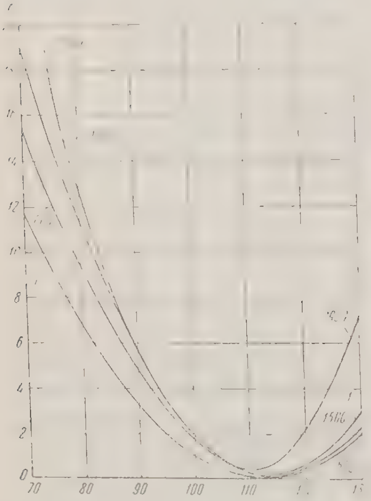

Fig.9. Variation of the factor C for Pr^{144} as a function of $\varkappa \equiv \lambda_P/\lambda_T$. The figures at the curves are β-particle energies in kev.

Although the theoretical factor C for Pr^{144} lies somewhat outside our ±5% accuracy limits for the slope of the experimental factor curves, this is not necessarily in conflict with the experimental results if we bear in mind the actual uncertainty in the experimental shape of the spectrum

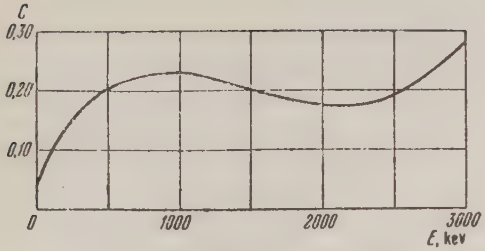

Fig.10. Values of the factor C for Pr^{144} computed on the basis of TP interaction for $\lambda_P/\lambda_T = 112$.

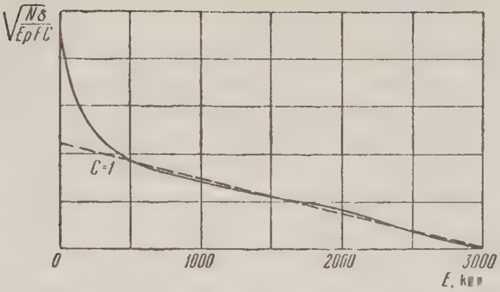

Fig.11. Theoretical shape of the Pr^{144} β-spectrum computed for TP interaction with $\lambda_P/\lambda_T = 112$ (Kurie plot). The dash line represents the allowed spectrum shape.

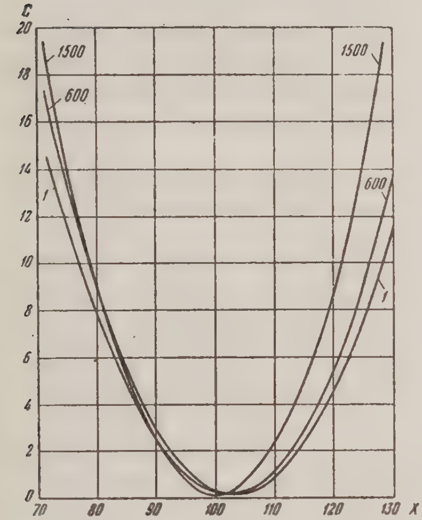

Fig.12. Variation of the factor C for Tl^{206} as a function of $x = \lambda_P/\lambda_T$. The figures at the curves are β-particle energies in kev.

associated with the $0 \rightarrow 0$ transition in Pr^{144} (specifically the uncertainty stemming from the presence of the weak components with end point energies 2280 and 800 kev) as well as the tendency to rectification of the experimental spectrum components. In Fig.11 the dash line represents the straight line spectrum. Taking into account the presence of the weak 2280 and 800 kev components, it may be seen that the deviation of the theoretical spectrum from this straight line does not exceed the experimental error.

Thus it may be concluded from analysis of the shape of the Pr^{144} β-spectrum that the best agreement of the theoretical spectrum with experiment is obtained for the TP combination with $\lambda_P/\lambda_T \approx \approx +112$.

Let us now turn to the β-spectrum of Tl^{206}. The dependence of C on λ_P/λ_T at different energies is shown in Fig.12. The weakest energy dependence is again observed at values of λ_P/λ_T close to 100. The best fit to the experimental curves was obtained for $\lambda_P/\lambda_T = 101$ (Figs.13 & 14). In the case of Tl^{206} there is good agreement with experiment in the energy region above 600 kev for which

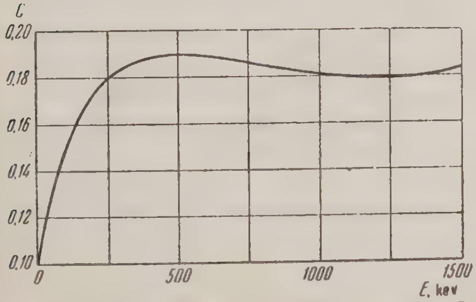

Fig.13. Values of the factor C for Tl^{206} computed on the basis of TP interaction for $\lambda_P/\lambda_T = 101$.

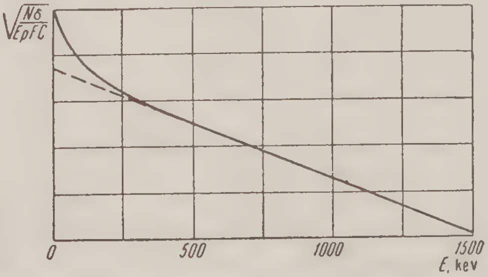

Fig.14. Theoretical shape of the Tl^{206} β-spectrum computed for TP interaction with $\lambda_P/\lambda_T = 101$ (Kurie plot). The dash line represents the allowed spectrum shape.

reliable experimental data are available. It will be seen that again the theoretical spectrum is characterized by an increase in the number of slow electrons (rise above the straight line) at energies under 300 kev.

Thus from independent analyses of two spectra we have obtained values of λ_P/λ_T close to each other (+112 and +101). This close agreement, which in view of the approximations and simplifying assumptions made in the theory must be regarded as good, cannot be considered trivial. For the sake of greater reliability of our conclusions regarding the value of the ratio λ_P/λ_T in β-decay it would be desirable to have even more accurate measurements of the shape of the β-spectra of Pr^{144} and Tl^{206} as well as of the β-spectra associated with other first forbidden $0 \rightarrow 0$ transitions, particularly in the region of low energies.

It will be noted from Figs.10 and 13 that the resultant factor C that provides agreement with experiment is actually small compared with each of its addends. In view of this strong compensation it is obviously important to take into account the influence of the atomic field on the β-particles, i.e., to calculate the functions L, M and N with the greatest degree of accuracy. In order to check what influence the above deductions might have on the method of calculating L, M and N, analyses of the Pr and Tl spectra were repeated with the functions L, M and N calculated without taking into account screening and the finite size of the nucleus and also taking into account nuclear size and assuming a radius equal to $1.5\cdot 10^{-3}\ A^{1/3}$ cm. The results of the calculations showed that our basic conclusions are not affected by the nature of the assumptions made in computing the electron wave functions.

It must be noted that our analyses of the β-spectra were carried out within the framework of the extant theory which comprises a number of approximations that may distort the results. In particular, the expressions for C_P and C_{PT} given above were derived from the nonrelativistic approximation for nucleons. It is known[12] that for the P form this approximation is appreciably more rough than for the S and T forms (in addition, a number of other simplifying assumptions were made in deducing the cited expressions). For this reason it is possible that the theoretical shape of the spectrum for Pr^{144} and Tl^{206} will not be substantiated in detail by experiment. There can, however, be no doubt regarding the general validity of our conclusion regarding the need for taking into account the contribution from P interaction in β-decay in order to explain the shape of the Pr^{144} and Tl^{206} spectra and our deduction that $\lambda_P \gg \lambda_T$.

The smallness (~ 0.2) of the C factor explaining the experimental data on the shape of the β-spectra of Pr^{144} and Tl^{206} is evidence of the presence of "destructive interference" in the case of the given transitions. This deduction, however, is not in agreement with the fact that the ft values for both transitions are comparable to the ft value for the other first forbidden β-transitions with $\Delta I = 0$, wherein, as is known, there is no nullifying compensation. It is possible that the disagreement stems from the fact that the theory for P interaction, as already noted, is appreciably less accurate than that for the other forms of interaction. At the same time it is possible that the assumption regarding the relatively large value of the matrix element $|\int\sigma\cdot r|$ must be made in connection with the small value of C is not a serious contradiction of theory. It has been shown by Ruderman[13] and Herbst[14] that the magnitude of $|\int\sigma\cdot r|$ greatly depends on the assumptions made regarding the character of the nuclear forces; at present it is impossible to evaluate $|\int\sigma\cdot r|$ or the ratio of this matrix element to other matrix elements in first forbidden transitions even as regards the order of magnitude.

I desire to thank B.S.Dzhelepov and L.A.Sliv for valuable discussions.

Scientific Research Physical Institute of
"A.A.Zhdanov" Leningrad State University

References

1. A.Petschek & R.Marshak, Phys.Rev., 85, 698 (1952).
2. T.Ahrens, E.Feenberg & H.Primakoff, Phys.Rev., 87, 663 (1952).
3. G.Alaga, Kgl. Danske Selsk. Vidd., Math.-fys. Medd., 28, 3 (1953).
4. M.Nataf, Compt.Rend., 239 341 (1954).
5. R.King & D.Peaslee, Phys.Rev., 94, 1284 (1954).
6. F.Porter & C.Cook, Phys.Rev., 87, 464 (1952).
7. W.Emmerich, John, J.Kurbatov, Phys.Rev., 82, 968 (1951).
8. H.Keller & J.Cork, Phys.Rev., 84, 1079 (1951).
9. D.Alburger & J.Kraushaar, Phys.Rev., 87, 448 (1952).
10. W.Emmerich, W.Auth & J.Kurbatov, Phys.Rev., 94, 110 (1954).
11. D.Alburger & G.Friedlander, Phys.Rev., 82, 977 (1951).
12. M.Rose & R.Osborn, Phys.Rev., 93, 1314 (1954).
13. M.Ruderman, Phys.Rev., 89, 1227 (1953).
14. R.Herbst, Phys.Rev., 96, 372 (1954).

EXPERIMENTAL EVALUATION OF A NEW TWO-LENS β-SPECTROMETER AND IMPROVEMENT OF ITS ANNULAR FOCUSING

- Ia.I.Gaziev, K.P.Mitrofanov & V.S.Shpinel'

Introduction

Two-lens β-spectrometers are finding increasing application in nuclear spectroscopy. As regards resolution η (1-4%), transmission ω and the value of L ($L = \omega\sigma$, where σ is the area of the source) spectrometers of this type are superior to many others. The high transmission and the design characteristics of two-lens β-spectrometers, which make it convenient to use these instruments in conjunction with scintillation equipment, are very important where coincidence investigations are concerned.

The shape of the magnetic field of a β-spectrometer and, consequently, its focusing properties are determined by the size of the lenses and the distance between them. In general the characteristics of the instrument and its economy of operation (power required) depend largely on these geometric parameters. Spectrometers with a large separation between the lenses producing a U-shaped field generally have the best characteristics, but are expensive to operate. Thus, for example, the spectrometer used by Bent, Bonner & Sippel[1] requires a power of about 30 kw for focusing 4 Mev electrons.

Economy is improved by bringing the lenses closer to the center of the instrument, but at the same time the resolution and transmission are impaired. It should be noted that the electron-optical properties of two-lens spectrometers have not yet been fully studied. Theoretical investigations of such instruments are hampered by the necessity of performing cumbersome numerical calculations for each selected field configuration.

The present report is devoted to an experimental investigation of the focusing properties of the two-lens β-spectrometer produced by the "Fizpribor"* Plant and improvement of its annular focusing by means of an internal correcting coil. The instrument was developed at the request of the Second Scientific Research Physics Institute of Moscow State University by "Fizpribor" engineers I.M.Bekkerman and L.M.Rommer.

1. Characteristics of two-lens β-spectrometers

The trajectories (tracks) of electrons in lens type spectrometers are shown schematically in Fig.1. It is well known that spherical aberration, which depends on the shape of the field used, imposes severe limitations on the resolution and transmission of such instruments.

Theoretical calculations of a longitudinal magnetic field not producing spherical aberration have been made by Glaser[2]. It is, however, impossible to realize such a field within a limited region in practice, since at the boundary of this region the field intensity must be infinite. Some approximation to the theoretical field can be obtained with a magnetic lens placed in a cylindrical iron shield closed at the ends with cylindrical pole pieces[3] or by means of two thin magnetic lenses mounted along a common axis a certain distance from each other[4].

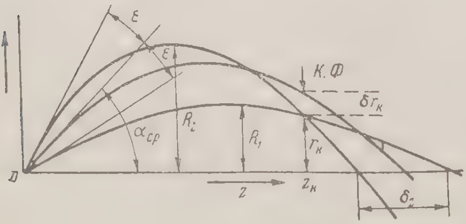

Fig.1. Electron trajectories in the lens spectrometer and the designations used in the report.

Advantageous features of iron-free magnetic lenses are a lower spherical aberration and the absence of hysteresis. Usually thin lenses are used; the magnetic field of these is given by[5]

---

*Initial syllables of "Physical Instrument". Trans.

$$H(z) = \frac{H_o}{1 - z^2/a^2}$$

where H_o is the magnetic field at the center of the lens ($z = 0$) and a is the half-width of the magnetic field distribution.

Obviously the shape of the magnetic field produced by two thin lenses is determined by the ratio a/d where d is the distance between the centers of the lenses. As was shown by Paquen & Grivet[6], the useful range of a/d values is small. Usually $1/6 \leqslant a/d \leqslant 1/3$, since with $a/d > 1/3$ the field no longer has the requisite U-shape, while with $a/d < 1/6$ the focusing properties of the instrument differ little from those in the case when $a/d \approx 1/6$ or $1/5$, but the instrument becomes very long.

However, in two-lens spectrometers even with a magnetic field shape close to the theoretical[2] (Fig.2 a, curve 1) spherical aberration is still appreciable, particularly with $a/d = 1/3$. Hence in these instruments as in other longitudinal type spectrometers it is important to use an exit baffle with a ring slit positioned in the region of the annular image. Two-lens spectrometers with a field such as that shown in Fig.2,a (1) and equipped with a suitable exit ring slit have excellent characteristics: for example, $\omega = 4.5\%$ of 4π and $\eta = 1\%$ for a point source[7].

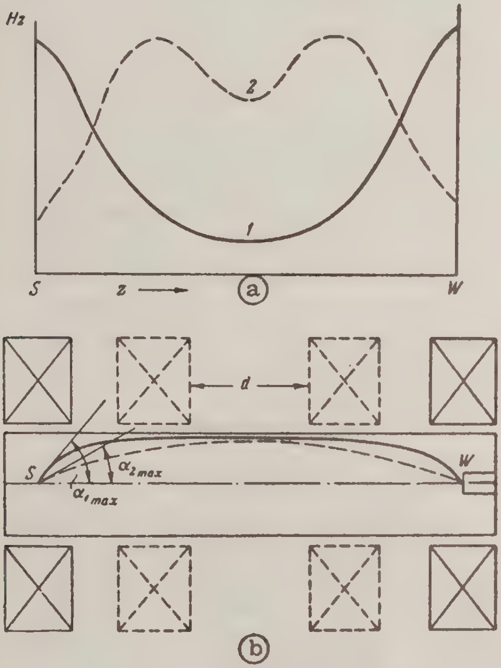

Fig.2. Distribution of magnetic field H(z) along the axis of a two-lens spectrometer (a), for two locations of the lenses (b); S - source, W - counter, α_{max} - maximum angle of emission of focused electrons.

The theory of such instruments is given in Refs. 8 & 9. The basic focusing properties of the spectrometer for trajectories not far distant from the axis of the instrument are defined in Ref.8. It follows from the expression deduced for the ring focus radius r_k and its position z_k on the z axis that as the angle of emission of the electron increases, r_k increases, while z_k decreases.

As a result of this dependence, in the case of a point source, the ring image for angles of emission in the interval from $\alpha_{av} - \epsilon$ to $\alpha_{av} + \epsilon$ has a finite width

$$\delta r_k = 3C_s\alpha\epsilon^2,$$

where C_s is the coefficient of spherical aberration[8]. If the current through the lens windings is changed by $\pm\Delta I/I$ or the electron momentum is changed by $\Delta P/P$, according to Ref.8, the radius of the annular image will be changed by

$$\mp\delta r_c = 2\alpha_{av}C_c\frac{\Delta P}{P},$$

where C_c is the coefficient of chromatic aberration. For a two-lens spectrometer the values of C_s and C_c computed by Glaser[5] for a thin lens must be multiplied by a factor of two.

The resolution $\eta = \Delta P/P$ is determined from the condition $\delta r_c = \delta r_k$. Thus for a point source and a ring exit slit the resolution is given by

$$\eta = \frac{3}{2} \cdot \frac{C_s}{C_c} \cdot \epsilon^2$$

Inasmuch as the transmission $\omega = \epsilon \sin \alpha_{av}$, according to Ref.7, we have

$$\frac{\omega}{\sqrt{\eta}} = \sqrt{\frac{2}{3} \cdot \frac{C_c}{C_s}} \cdot \sin \alpha_{av}$$

It follows from these expressions that both to obtain a good transmission factor and insure an advantageous transmission-resolution ratio it is essential to utilize as large a range of electron emission angles as possible. The value of α_{max} is limited by the radius of the spectrometer chamber and depends on the distance between the detector and source and on the shape of the electron trajectories.

In the case of a two-lens spectrometer the character of the trajectories allows of greater values of α_{max} than in the case of a thin lens spectrometer with an equal chamber radius and the same source to detector distance.

Daniel & Bothe[7] describe a two-lens spectrometer with $\alpha_{av} \approx 50^o$. For this instrument the ratio $\omega/\sqrt{\eta}$, calculated according to the expression given above, is equal to 0.9, while the experimental value of this ratio was 0.5 ($\omega = 4.6\%$ and $\eta = 0.9\%$). This divergence must be attributed to inaccuracy of the theoretical expression for large values of α. The case of large values of α in a U-shaped field with a/d = 1/5 but for somewhat different fields has been analyzed by Snowdon[10]. The economy of operation of a two-lens β-spectrometer can be substantially improved by using a focusing field intermediate between that shown in Fig.2, a, curve 1, and the type of field used in a single lens spectrometer. The configuration of such a field and the corresponding location of the lenses are shown by dash lines in Fig.2. Bringing the lenses in towards the center of the instrument with the positions of the source and detector unchanged leads to reduction of the field region where $\partial H(r,z)/\partial r < 0$, an increase in spherical aberration and a decrease in the value of α_{max} (Fig.2,b). In other words the characteristics of the instrument are impaired. Very little theoretical work has been done on such instruments[10].

Rundle et al[11] used an electron beam procedure to investigate the dependence of spherical aberration on the distance between the two inner planes of the lenses, which in their experiments was varied from 0 to 25 cm. They found that the spherical aberration decreases monotonically with increasing distance between the lenses.

The dependence of spherical aberration on the distance between the lenses was first studied in the investigation of Ref.12, but in this investigation it was erroneously[11] found that the spherical aberration passes through a minimum as the lens coils are moved further apart. Rundle et al established experimentally that the familiar formula of Deutsch[13] is valid for the dependence of the resolution of a two-lens spectrometer on the size of the source. This formula, which was deduced for the case of a thin lens without taking spherical aberration into account, is

$$\eta = 0.2 \frac{mS + W}{R_1(m + 1)},$$

where S is the diameter of the source, m is the magnification of the lens, W is the diameter of the counter window, R_1 is the maximum deviation of the inner ray of the beam from the axis. Usually m = 1 and then

$$\eta = 0.1 \frac{S + W}{R_1}.$$

For the general case the expression for η contains yet another term due to spherical aberration.

To improve the resolution of a two-lens spectrometer Shpinel'[14] used correcting coils mounted coaxially inside each lens; installation of the correcting coils resulted in a certain reduction in the half-width of the apparatus line. However, Shpinel' did not investigate the influence of the magnetic field of the correcting coils on the shape of the electron trajectories in detail.

The possibilities of correcting a spherical aberration of a thin lens by means of an internal coil mounted on the axis of the instrument outside the principle field of the lens has been noted by Persico[15] and Nadeu[16]. It is difficult, however, to utilize the suggested correcting procedure in practice.

An analogous correcting procedure in the case of a thick lens (correcting coil mounted at the center of the instrument) was used by Hubert[17] with a resultant improvement of the spectrometer characteristics. Hubert was able to obtain $\eta = 0.6\%$ for a 2 mm diameter source with $\omega = 1.5\%$. The characteristics of a number of two-lens spectrometers are compared in the accompanying table.

Characteristics of some two-lens spectrometers

Authors	Year	Source dia., mm	Trans., (ω), %	η, %	E_{max}, MeV	Power consumed, kw
Agnew, Andersen (4)	1949	4	1.5*	2.2	2.8	
Rundle, Ellis, Griffith, Tomlinson (11)	1954	1	0.4	0.97	4	6
Daniel, Bothe (7)	1954	0.1	4.6*	1	4	40
		4	2*	1.9	4	40
Bent, Bonner (1)	1955	3	9	2.7	4.2	33
		3	4	2	4.2	33

---

*Efficiency (18)

2. The two-lens β-spectrometer produced by the "Fitzpribor" Plant

A schematic sketch of the "Fitzpribor" β-spectrometer is shown in Fig.3. Each of the spectrometer lenses 1 is assembled of two sections consisting to 360 turns of glass-insulated 2.44 x 6.9 mm section copper strip. The dimensions of the individual lens are: inside diameter 25 cm, outside diameter 59 cm, thickness 10 cm.

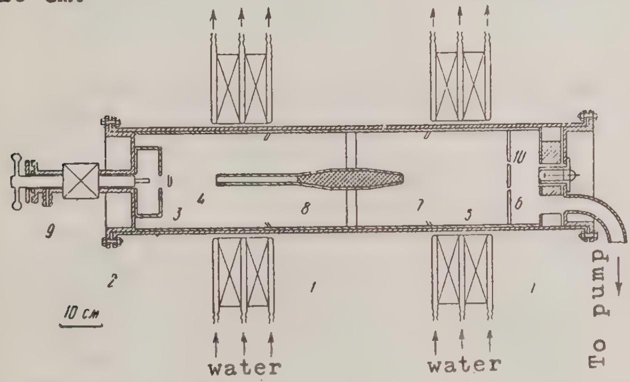

Fig.3. Diagram of "Fizpribor" β-spectrometer: 1) magnetic lenses, 2) vacuum chamber, 3) source, 4) movable entrance slit disc, 5) exit baffle with ring slit, 6) counter, 7) lead slug, 8) aluminum tube, 9) vacuum lock, 10) lead shielding for counter.

The lenses have water cooling which makes it possible to dissipate up to 5.5 kw power. Adjustment of the lenses is provided for in the design of the mounts which have provision for small horizontal, vertical and angular displacements. The lenses can also be displaced simultaneously and symmetrically relative to the central plane of the instrument by means of a worm gear. With the coils in the extreme end positions, their centers are in the planes of the source and counter window, respectively, and in this case the maximum energy of the focused electrons is ~1 Mev. With the coils at their minimal separation electrons of up to 6 Mev energy can be focused. The vacuum chamber 2 is made of copper pipe with an inside diameter of 225 mm and is 1130 mm long. The inside surface of the chamber is lined with aluminum. A lead slug 7 mounted at the center along the axis of the instrument shields the counter from direct γ-rays. The chamber is evacuated by a TsVL-100 diffusion pump to $2 \cdot 10^{-5}$ mm Hg pressure. The vacuum system provides for working with thin films over the counter window when necessary, i.e., allows of simultaneous evacuation of the chamber and β-counter.

The effective angle of the electron beam can be smoothly varied without disturbing the vacuum by moving the entrance slit disc 4. The radioactive source can be installed without disturbing the vacuum by means of the vacuum lock 9. Two pairs of compensating coils are provided to cancel out both components of the earth's magnetic field.

3. Investigation of the electron trajectories and the ring focus

We elected to use a distance of d = 36 cm between the lenses, this being the condition for focusing electrons of up to 3 Mev energy. There are no reliable data on such an interlens distance in the literature[12]. For investigating the trajectories we utilized an electron gun and a fluorescent screen which could be moved along the axis of the spectrometer without disturbing the vacuum. The luminous spot on the screen was observed through a window mounted in the end flange in place of the β-counter. The position of the spot on the screen could be determined to within 1 mm with the aid of a coordinate grid on the screen; the grid was adequately illuminated by scattered light from the beam. The beams with different values of the angle α of electron emission were defined by a small aperture (0.3 mm) in the hemispherical anode. With our geometry the maximum angle α_{max} allowed by the diameter of the chamber was 24°. The electron gun was also utilized for centering the lenses and ajusting the current in the compensating coils cancelling the earth's magnetic field.

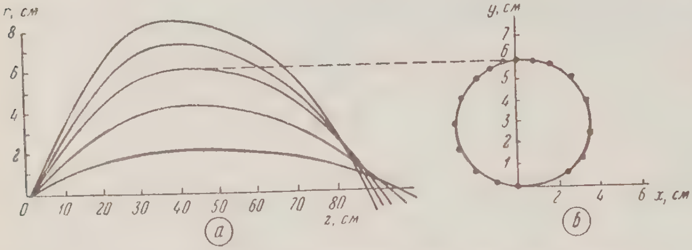

Fig.4. Electron trajectories: a) projections on the meridional plane (tracks), b) projections of trajectories of electrons with $\alpha = 14°$ on a plane perpendicular to the instrument axis. The points were recorded at 5 cm intervals, beginning with z = 10 cm.

The tracks recorded for electrons with different emission angles α are shown in Fig.4,a. Fig.4,b shows the projection of the trajectories of electrons with $\alpha = 14°$ on a plane perpendicular to the axis. On the basis of the recorded trajectories one can determine the dimensions and position of the ring focus as a function of the selected aperture.

We also studied the shape of the trajectories with multiple focusing, when the focused electrons cross the instrument axis several times. Such trajectories, shown schematically in Fig.5, correspond to the case of simultaneous focusing of electrons of three different energies. Normally, multiply focused electrons are prevented from reaching the counter by the centrally positioned lead slug and aluminum tube (dash line in Fig.5 and 7 & 8 in Fig.3).

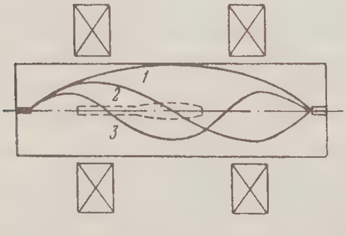

Fig.5. Character of electron tracks with 1) single, 2) double, 3) triple focusing.

The results of measurement of the spherical aberration of the spectrometer are shown in Fig.6; here $I(\alpha)$ is the current through the lens coils corresponding to focusing of electrons with an emission angle α at z = 90 cm and α_0 is the minimum angle of emission under the conditions of our experiment ($4^o30'$). This experimental curve can be described by the following analytic expression:

$$\frac{I(\alpha_o) - I(\alpha)}{I(\alpha_o)} = 2.10^{-2}(\alpha^2 - \alpha_o^2).$$

In these measurements an appreciable part of the heater filament of the electron gun was enclosed in a porcelain tube in order to reduce the dimensions of the luminous spot on the screen and enhance the accuracy. The exposed part of the filament, which served as the electron source, was less than 0.5 mm in length; the apertures in the anode were reduced to 0.1 mm. In order to obtain sufficiently accurate values of α the position of the screen in the region of the linear initial sections of the tracks was changed in steps of 2.5 cm, beginning with z = 5 cm.

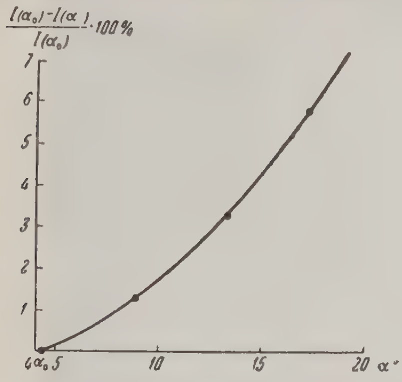

Fig.6. Spherical aberration curve: $I(\alpha)$ - current for focusing at z = 90 cm of electrons emitted at the angle α.

For studying the annular focusing we used a circular section electron beam obtained by means of an anode with a ring slit. The size of the beam was defined by an entrance slit. We positioned the screen in the plane of the ring image and determined the width of the ring δr_k and the change in the radius of the ring with changes in current $\delta r_I/\delta I/I$. For example, for a beam limited by the angles $\alpha_1 = 22^o$ and $\alpha_2 = 15^o$ ($\omega = 2\%$), we obtained

$$\delta r_k = 2.5\text{-}3 \text{ mm and } \delta r_I/\delta I/I = 2\text{-}2.5 \text{ mm}/\%.$$

Consequently, the use of an entrance baffle with a slit corresponding to the ring image should give a resolution $\eta = 1\text{-}1.3\%$.

For smaller values of α_1 and α_2 and the same value of $\omega = 2\%$, the resolution was appreciably worse, as might be expected from theoretical considerations[8]. We note that when the above described beam is used without a ring slit the resolution of the spectrometer, as evaluated from the curve of Fig.6 taking into account the dimensions of the axial image (15 mm diameter), is ~7%.

The data obtained with the electron gun are inadequate for accurate positioning of the ring slit, since they do not include the influence of the source dimensions. Hence we photographed a beam of F-line conversion electrons from ThB (with a lens current appropriate to the line peak energy), using a source 3 mm in diameter, with $\alpha_1 = 20.5^o$ and $\alpha_2 = 16^o$ ($\omega = 1.2\%$).

The procedure for determining the z coordinate of the ring focus was the following: an x-ray film in a special cassette (the location of which was accurately determined) was mounted along the axis of the spectrometer in the region of the ring image. Then with a constant controlled current through the lens coils the film was exposed for 12 hours with a 1-2 millicurie source.

A longitudinal photograph obtained in this manner is reproduced in Fig.7. Here $\bar{a}$ is the beam of conversion electrons forming a ring image in the plane K at a distance of 8 cm from the outer window; the diverging beam $\underline{b}$ along the axis of the instrument is due to slower electrons comprising the continuous β-spectrum. For a more accurate determination of the width and radius of the ring image we made exposures in the plane of the image. The photography was carried out at two values of the current through the lens coils, which made it possible to determine the ratio $\delta r_I/\delta I/I$; this proved to be 2.5 mm/% in agreement with the above cited value obtained with the electron gun.

The width of the annular image was not exactly the same at all points on the circle: δr_k varied between 3.2 and 3.5 mm (r_k = 30 mm). Accordingly an exit

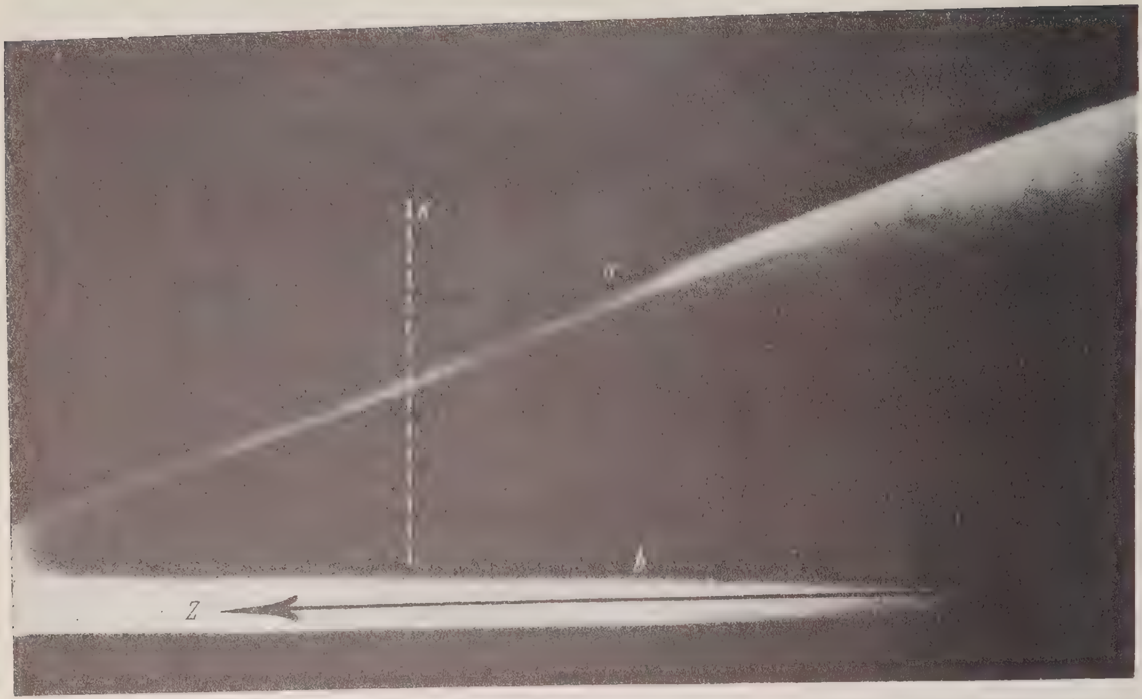

Fig.7. a) Longitudinal photograph of beam of conversion electrons from ThB; b) image due to electrons of the continuous β-spectrum.

ring slit having a slit width of 3.6 mm was installed in the instrument.

With this slit in place we carried out measurements of the conversion lines of ThB and Cs^{137}. Using a source 3 mm in diameter with $\omega = 1.2\%$, we obtained $\eta = 1.6\%$, which is in good agreement with the value of η evaluated from the observed annular focusing characteristics. Measurements carried out with sources having diameters of 2, 4 and 5 mm yielded resolutions values of 1.5, 1.7 and 1.9%, respectively.

The K and L conversion lines of Cs^{137} obtained using a 2 mm diameter source are shown in Fig.8. It follows from the calibration of the spectrometer that at the maximum allowable power dissipated

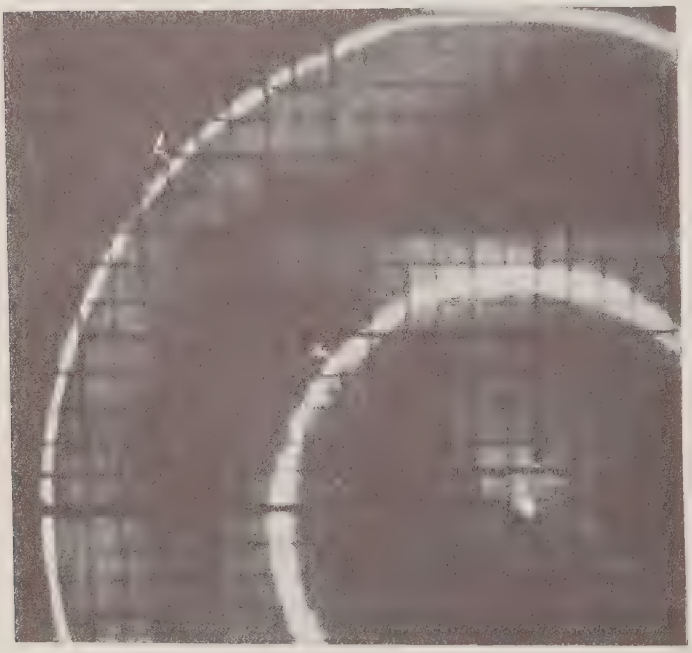

Fig.11. Photographs of ring image: a) with no current in the internal correcting coil, b) with optimal current in this coil. The light spots in the photographs are due to light from the electron-gun filament.

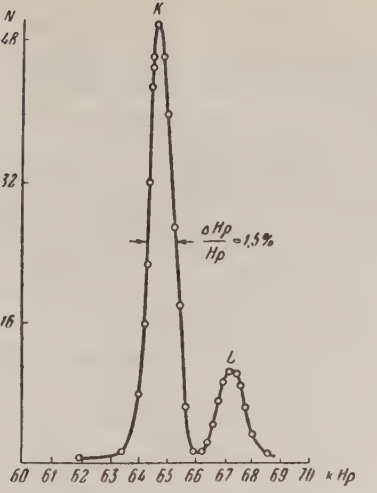

Fig.8. K and L conversion lines of Cs^{137}; $16^\circ < \alpha < 20.5^\circ$.

in the lenses the energy of the focused electrons is 3.4 Mev.

4. Improvement of annular focusing

From the point of view of improving the characteristics of the spectrometer we felt it would be of interest to investigate the effect of internal correcting coils. In one of the experimental arrangements (Fig.9) we used a coil wound of enameled 0.8 mm diameter wire. The outside diameter of the coil was 100 mm; its length (width) was 100 mm. The distance from the source to the center of the coil was 25 cm.

From observation of the fluorescent screen it could be seen that the magnetic field of the internal coil produced additional deflection of the rays, displacing them towards the periphery. The direction of the additional rotation coincides with that produced by the lens when the direction of the current through the respective coil windings is the same and is obviously opposed when the currents through the correcting coil and lens coils are in opposite directions.

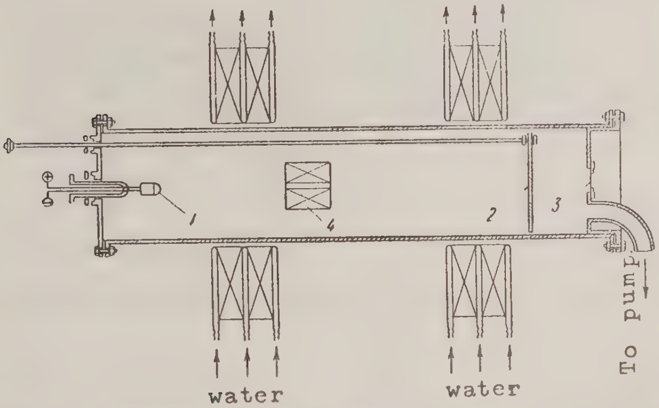

Fig.9. Diagram of experiments aimed at investigating the influence of an internal correcting coil on the focusing: 1) electron gun, 2) movable fluorescent screen, 3) viewing window, 4) internal coil.

The rays are displaced toward the periphery in both cases but in the former the magnitude of the displacement is greater. The internal coil has a greater scattering effect on the trajectories passing close to it as compared to the more distant trajectories. In consequence, the annular focusing is altered (Fig.10). When current is sent through the internal coil, the ring image is displaced towards the source and its radius increases. As the current through the correcting coil is increased the width of the image at first decreases then, after passing through a minimum value, begins to increase. The diameter of the axial image increases continuously with increasing current through the coil. Two illustrative photographs taken through the viewing window are superimposed in Fig.11. The electron beam used in the experiments was defined by the angles $\alpha_1 = 22^\circ$ and $\alpha_2 = 15^\circ$ ($\omega = 2\%$).

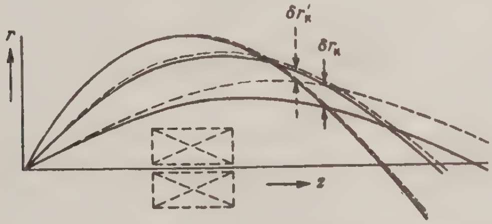

Fig.10. Influence of the internal coil on the electron trajectories and ring image. Solid lines - trajectories with no current in the internal coil; dash lines - trajectories with current in the correcting coil.

In photographing, part of the ring was masked by the light areas due to the light from the electron gun filament; for this reason only the clearer part of the photograph is reproduced in Fig.11. This extraneous illumination did not interfere with visual observation since it was white, while the ring image on the screen was bright green. The smaller ring image, obtained with the internal coil disconnected has a width of 3-3.5 mm. The other large radius image was obtained with an optimum (i.e., minimum image width value) current through the internal coil and its width is only 1.2-1.5 mm. At the same time the diameter of the axial image was increased by a factor of 1.5 and became 2 cm. Inasmuch as our electron gun was not an ideal point source it obviously made some contribution to the width of the ring image. From measurements of the width of the ring image as the solid angle was gradually decreased it was found that the ring image width goes down to 0.5 mm and then remains constant at this value. If we take this residual width, due to the geometry of the gun, into account we find that the internal coil reduces the spherical aberration by a factor of three.

Observations showed that the value of $\delta r_I/\delta I/I$ for $\delta r_I = \pm 2$ mm remains the same (2.5 mm/1%) as before installation of the correcting coil.* It follows therefore that the spectrometer with improved annular focusing (i.e., with the correcting coil) has superior characteristics, namely, $\eta = 0.3$-0.4% for a point source with $\omega = 2\%$.

With the arrangement shown in Fig.9 the power consumed by the internal coil amounts to 10% of the power dissipated in the spectrometer lenses. This figure can be reduced by a factor of 1.5-2 by eliminating some of the internal turns of the coil which are not essential for its operation.

The influence of the correcting coil on the trajectories depends on its position in the instrument. The influence is stronger and, consequently, the power consumed is lower when the coil is moved towards the beginning of the trajectories (to the left in the figures). Hence the coil was installed as close as possible to the source.

Second Scientific Research Physics Institute of
Moscow State University

---

*It was noted that if the radius r_k is reduced by more than 5 mm $\delta r_I/\delta I/I$ decreases appreciably.

References

1. R.Bent, W.Bonner & R.Sippel, Phys.Rev., 98, 1237 (1955).
2. W.Glaser, ZS.f.Phys., 116, 19 (1940).
3. K.Siegbahn, Phil.Mag., 37, 162 (1945).
4. H.Agnew & H.Andersen, Rev.Sci.Instr., 20, 869 (1949).
5. W.Glaser, ZS.f.Phys., 117, 285 (1941).
6. G.Paquen & P.Grivet, C.R., 230, 65 (1950).
7. H.Daniel & W.Bothe, ZS.f.Naturforsch, 9a, H. 5, 402 (1954).
8. G.Paquen & P.Grivet, C.R., 230, 196 (1950).
9. G.Paquen,& P.Grivet, C.R., 230, 1048, 1652 (1950).
10. S.Snowdon, Rev.Sci.Instr., 22, 878 (1951).
11. G.Rundle, T.Ellis, T.Griffith & H.Tomlinson, Pros.Phys.Soc., 67,(B), 52 (1954).
12. E.Quade & D.Halliday, Rev.Sci.Instr., 19, 234 (1948).
13. M.Deutsch, L.Elliot & R.Evans, Rev.Sci.Instr., 15, 178 (1944).
14. V.Shpinel', Zhur.eksp.i teor.fiz., 22, 255 (1952).
15. E.Persico, Rend.Lindcei, 7 (1950).
16. G.Nadeu, Rend.Lindcei, 10, 225 (1951).
17. P.Hubert, Annales de Phys., 8, 662 (1953).
18. E.Persico, in Problemy sovremennoi fiziki (Problems of modern physics), No.7, 151 (1952).

DECAY SCHEME OF Ne^{23}

- V.M.Ovchinnikov, Iu.A.Nemilov, M.L.Aleksandrova & I.I.Lomonosov

We investigated the γ-spectrum of Ne^{23} (40.2 sec) by means of a scintillation γ-spectrometer. We obtained the isotope by the Na^{23} (n,p) Ne^{23} reaction induced by bombardment of metallic sodium enclosed in a nickel capsule with neutrons from a D-Li source at $E_d = 4.5$ Mev. The detecting section of the γ-spectrometer consisted of a CsI-TlI crystal (2 x 3 cm) and an FEU-12 type photomultiplier.

The pulses from the crystal were investigated by means of a 50-channel analyzer or in the case of low intensities by photometry of photographs of the pulse distribution on the screen of an oscillograph with a driven sweep.

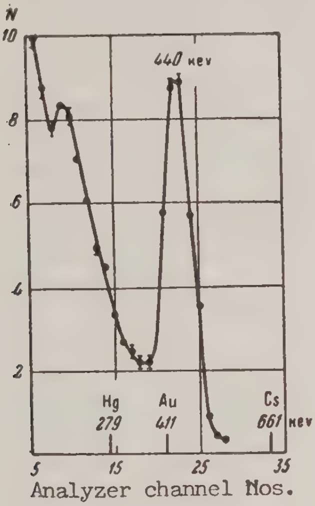

Fig.1. γ-spectrum of Ne^{23}.

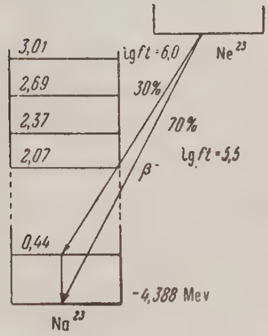

Fig.2. Proposed decay scheme for Ne^{23}.

The relative half-width of the 661 kev Cs^{137} line was about 10%. The spectrometer was calibrated with reference to the known γ-lines of Tu^{170}, Hg^{203}, Au^{198}, Cs^{137}, Zn^{65}, Co^{60} and Na^{24}. The response was linear in the investigated energy interval.

We detected a line of 440±5 kev energy in the γ-radiation from Ne^{23}. The observed pulse distribution is shown in Fig.1. We did not detect the 3 Mev line observed by Pollard & Watson[1] and Peretz-Mendez & Brown[2] by γ-absorption in lead. The upper bound of its intensity, as follows from our measurements, cannot be more than 0.2% relative to the intensity of the 440 kev γ-line.

We also observed a 1.63 Mev γ-line which, after investigation of its decay period, was attributed to F^{20} (10.7 sec), formed by the Na^{23} (n,α) F^{20} reaction. We also investigated β-γ coincidences by means of CsI and stilbene crystals. The CsI crystal was shielded by an aluminum absorber that stopped β-particles of energies up to 5 Mev. To obviate the influence of radiation from F^{20}, the beginning of measurement was delayed for ten periods of the latter after cessation of bombardment. These experiments showed that the β-spectrum associated with the 440 kev γ-line has an end point energy some 400±100 kev lower than the continuous β-spectrum of Ne^{23}. We determined the ratio of the number of transitions to the 440 kev excited state of Na^{23} to the total number of decays as 30±5%.

Thus it may be assumed that Ne^{23} decays according to the scheme shown in Fig.2.

The publications containing Refs.3 & 4 were received after completion of our investigation. Our results differ from the data of Ref.3 in which the 1.63 Mev line is attributed to Ne^{23}, but are in agreement with the conclusions of Ref.4.

References

1. E.Pollard & W.Watson, Phys.Rev., 58, 12 (1940).
2. V.Peretz-Mendez & H.Brown, Phys.Rev., 78, 812 (L) (1950).
3. J.Penning & R.Schmidt, Bull.Amer.Phys.Soc., 30, 5, 8 (1955).
4. H.Gerber, M.Garcia Munoz & D.Maeder, Helv.Phys.Acta, 28, 478 (1955).

MEASUREMENTS OF γ-γ COINCIDENCES IN THE SPECTRA OF Ir^{192} and Sb^{124}

- L.L.Pelekis

The γ-γ coincidences were measured by means of two scintillation γ-spectrometers with single-channel pulse height analyzers connected in a coincidence circuit. The resolving time of the latter was $1 \cdot 10^{-6}$ sec. The number of pulses in each channel and the number of coincidences were recorded simultaneously by separate scaling circuits. The number of chance coincidences was about 5% relative to the total number of coincidences recorded. The detectors were NaI(Tl) and CsI(Tl) crystals with a MgO reflector and FEU-19 photomultiplier tubes.

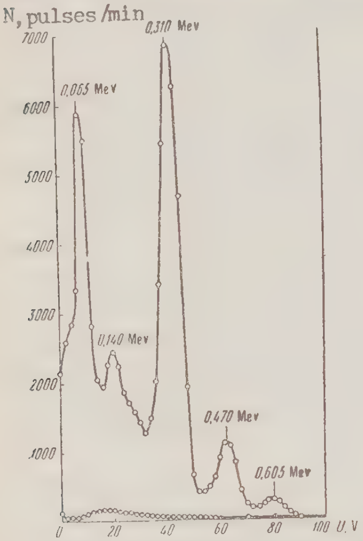

Fig.1. γ-spectrum of Ir^{192} recorded on the scintillation spectrometer. Curve at bottom = background.

Ir^{192}. A detailed review of the experimental data on the radiation from Ir^{192} published up to 1952 can be found in Ref.1. The decay schemes given in later publications[2-7] on this isotope agree in the main with the scheme given in Ref.1.

The most intense region of the γ-spectrum of Ir^{192} obtained in our investigation with an NaI(Tl) crystal is shown in Fig.1. In these experiments the NaI(Tl) crystal in the form of a 29 mm diameter and 13.3 mm thick cylinder was exposed to an uncollimated γ-ray beam. The gate width of the pulse height analyzer was 19 kev. Under these conditions the half-width of the reference Cs^{137} (661 kev) line was 11%.

The relative intensities of the individual γ-line groups were evaluated from the areas under the photopeaks. In allowing for the spectral sensitivity of the instrument we utilized the calculations of Maeder et al[8] and the reference points obtained by means of the monenergetic γ-rays of Cs^{137} and Cr^{51}. The results of our evaluation of the relative intensities of the three principle groups of γ-lines are shown in the accompanying table. For purposes of comparison of relative intensities as evaluated by the other authors are also listed. The agreement may be considered satisfactory if we bear in mind that the overall error in evaluating the relative intensities may attain 10-20%.

Relative intensities of the γ-line groups in the spectrum of Ir^{192}

γ-ray energy, Mev	Data of other authors				Our values
	[1]	[5]	[6]	[9]	
0,310 (0,296; 0,308; 0,316)	100	100	100	100	100
0,470 (0,468; 0,484)	29.6 (without the 0.484 line)	47,6	50,4	35,8	38,5
0,605 (0,589; 0,605; 0,613)	12,6	18,4	19,1	19,7	19,8

The γ-γ coincidence distributions obtained are shown in Figs.2 & 3. The width of the gate in the first "fixed" channel was 60 kev; that in the second 19 kev. The geometry of the experiment is shown in the insert in Fig.2. The NaI(Tl) crystal was mounted at 180° relative to the source. The distance between the source and each of the crystals was 25 mm. The β-particles from the Ir^{192} were absorbed by an aluminum plate 0.8 mm thick. A 5 mm thickness of lead absorber was mounted symmetrically relative to the sides of the source and served to eliminate coincidences due to photons scattered from one crystal to the other. A lead absorber plate having a 5 mm diameter aperture was mounted centrally opposite the source.

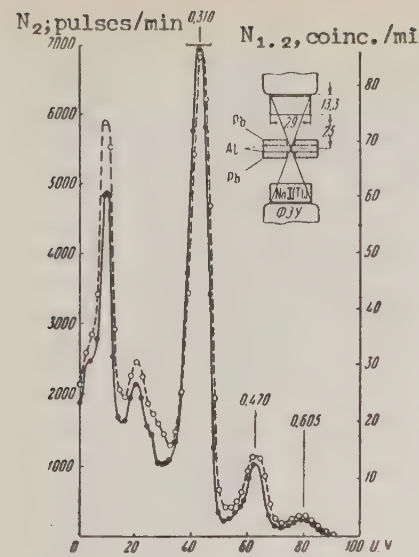

Fig.2. γ-γ coincidence distribution of Ir^{192}. Solid line - γ-spectrum correlating with the 0.310 Mev γ-rays; dash line - γ-spectrum of Ir^{192} obtained simultaneously with the coincidence distribution by means of the analyzing channel; the horizontal segment shows the position of the gate in the "fixed" channel.
ФЭУ = photomultiplier.

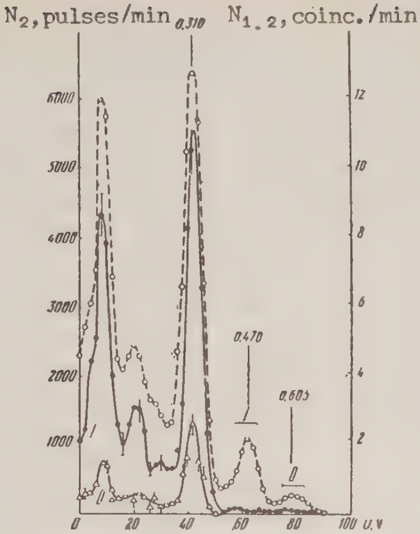

Fig.3. γ-γ coincidence distribution for Ir^{192}. Solid curves I & II - γ-spectra correlating with the 0.470 Mev and 0.605 Mev γ-rays, respectively; dash curve - γ-spectrum of Ir^{192} obtained by means of the analyzing channel.

The experimentally obtained numbers of γ-γ coincidences agreed satisfactorily within the limits of the measurement error with the expected numbers as computed (for our experimental conditions) on the basis of the decay scheme for Ir^{192} given in Ref.1. In the calculations the 0.468 Mev transition was assumed to be the most intense in accord with the results obtained in the investigations of Refs.5 & 6.

It follows from the decay scheme of Ref.1 that the radiation emitted in the decay of Ir^{192} should comprise x-rays from Pt (internal conversion of γ-rays) and Os (K-capture and internal conversion). To investigate the x-ray—γ-ray coincidences the "fixed" channel was set at the photopeak of the x-ray line. In order to reduce the intensity of the K x-rays from the lead, the lead absorber (shield) was covered with a 1 mm thick layer of Cd and a 0.5 mm layer of Cu.

Two coincidence spectra were recorded: the first without an x-ray absorber in front of the crystal of the "fixed" x-ray channel, the second with an absorber consisting of Cd (1 mm) and Cu (0.5 mm).

In the first case, obviously, we observed the total effect due to coincidences between the given γ-line and the x-ray quanta and the coincidences between the two cascade γ-rays, one of which yields the photopeak in the analyzing channel and the second undergoes Compton scattering in the crystal of the "fixed" channel. In the second experiment, the presence of the absorber obviates the coincidences due to the successive emission of the gamma and x-ray quanta. Thus the difference between these two coincidence distributions yields the pure spectrum of coincidences between the γ-rays of the given energy and the x-ray radiation. This difference spectrum is shown in Fig.4.

The x-ray—γ-ray coincidence spectrum shows γ-line photopeaks at 0.207 and 0.485 Mev; these must, presumably, be attributed to Os^{192}.

$\underline{Sb^{124}}$. The experimental conditions used in investigating the distribution of γ-γ coincidences for Sb^{124} were analogous to those described above. The β-particles were absorbed by an aluminum plate 4 mm thick. The scintillators were

CsI(Tl) crystals in the form of cylinders; that in the "fixed" channel was 29 mm in diameter and 13 mm thick, while the crystal in the analyzing channel was 34 mm in diameter and 16 mm thick. The coincidence distributions for Sb^{124} are shown in Fig.5. The γ-spectrum correlating with the $\sim$0.6 Mev γ-rays indicates the presence of cascade transitions involving γ-rays of 0.646, 0.720, 1.69, 2.09, 1.36, 1.1 and 0.98 Mev energy. That the first four enumerated γ-rays occur in cascade with the 0.603 Mev γ-ray has been noted earlier by Langer and his coworkers[10,11]. The last three lines have been detected in the spectrum of Sb^{124} by a number of investigators[12-14] using different types of spectrometers. However, the association of these lines with 0.603 Mev transition has not been established. Our experimental evidence of the possible cascade 2.09--0.603 Mev transition agrees with the results obtained by Langer, Lazar & Moffat[10]. In view of the low intensity of the 2.09 Mev line, however, this deduction must be regarded as tentative. The question can only be resolved on the basis of a thorough quantitative evaluation of all the factors that may influence the experimental number of coincidences in this energy region. For this it is necessary to determine accurately the spectral sensitivity of the instrument and carry out a number of additional experiments.

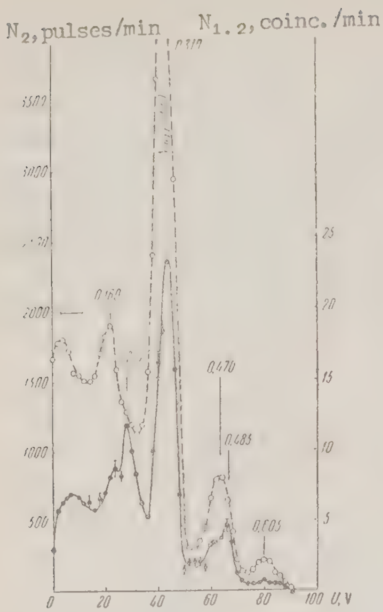

Fig.4. X-ray—γ-ray coincidence distributions for Ir^{192}. Solid line - γ-spectrum correlating with the 65 kev x-rays; dash-line - γ-spectrum of Ir^{192} obtained by means of the analyzing channel; x-rays absorbed by a shield consisting of 1 mm Cd and 0.5 mm Cu.

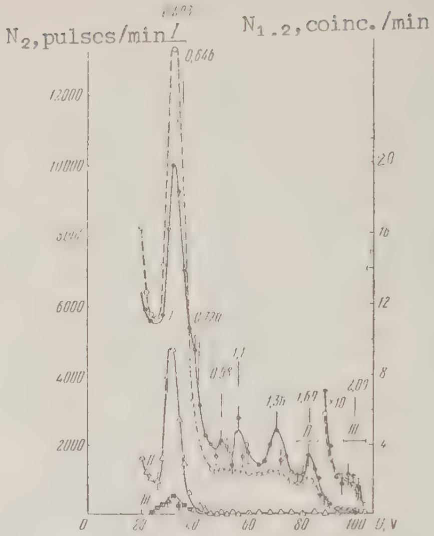

Fig.5. γ-γ coincidence distribution for Sb^{124}. Solid curves I, II and III - γ-spectra correlating with the $\sim$0.6, 1.7 and 2.1 Mev γ-rays, respectively. Gate width of fixed channel 160 kev. Dash line - γ-spectrum of Sb^{124} obtained by means of the analyzer channel.

In conclusion I desire to thank L.Bambe and Z.Pelekis for their participation in the measurements.

Institute of Physics of the
Academy of Sciences of the Latvian SSR

References

1. A.A.Bashilov, N.Anton'eva & B.Dzhelepov, Izv. AN SSSR, Ser.fiz., 16, 264 (1952).
2. K.Roulston & R.Pringle, Phys.Rev., 87, 930 (1952).
3. C.Daniel & M.Wiedenbeck, Phys.Rev., 94, 501 (1954).
4. R.Pringle, N.Turshinetz & N.Taubor, Phys.Rev., 95, 115 (1954).
5. M.Johns & S.Nablo, Phys.Rev., 96, 1599 (1954).
6. M.Glazunov, B.Dzhelepov & Iu.Khol'nov, Izv. AN SSSR, Ser.fiz., 19, 294 (1955). (Translation in Bulletin, Vol.19, No.3, p.267.)
7. H.Taylor & R.Pringle, Phys.Rev., 99, 1345 (1955).
8. D.Maeder, R.Müller & V.Wintersteiger, Helv.Phys.Acta, 27, 3 (1954).
9. N.Jaffe, UCRL - 2537 (1954); Nuc.Sci.Abstr., 9, 12B, 282 (1955).
10. L.Langer, N.Lazar & R.Moffat, Phys.Rev., 91, 338 (1953).
11. L.Langer & J.Starner, Phys.Rev., 93, 253 (1954).
12. N.Lazar, Phys.Rev., 95, 292 (1954).
13. K.Gromov, B.Dzhelepov, N.Zhukovskii, A.Silant'ev & Iu.Khol'nov, Doklady AN SSSR, 86, 225 (1952).
14. A.Zolotavin, E.Grigor'ev & M.Abroian, Izv. AN SSSR, Ser,fiz., 20, 289 (1956). (Translation in Bulletin, Vol.20, No.3, p.271.)

A COMBINED BETA AND GAMMA SPECTROMETER

- M.P.Glazunov & V.I.Spitsyn

Among the different types of magnetic β-spectrometers developed so far, probably the most popular are spectrometers with corrected focusing of the electrons in one or two directions in an inhomogeneous transverse magnetic field. This is explained by the fact that such spectrometers are characterized by a high resolution together with a satisfactory transmission factor. As Dzhelepov & Bashilov[1] showed spectrometers of the "Ketron" type with improved focusing of the electrons through 180° in one direction are hardly inferior as regards resolution to a Siegbahn & Svartholm[2] double focusing spectrometer at equal values of the transmission factor. At the same time, in the case of "Ketron" type spectrometers the calculation of the magnetic field, design of the pole pieces and final fine adjustment of the field configuration are appreciably more simple than in the case of double-focusing spectrometers. By means of a "Ketron" type spectrometer it is possible to analyze with high accuracy both β-spectra and γ-spectra, the latter by observing internal conversion electrons and photoelectrons.

On the other hand, for investigating nuclear decay schemes, it is necessary to know the relative intensities of individual γ-lines. These can be determined with the highest accuracy through γ-spectrum studies based on observation of recoil electrons. For these purposes Dzhelepov, Zhukovskii, Khol'nov and others[3,4] constructed special spectrometers such as the Ritron and Elotron.*

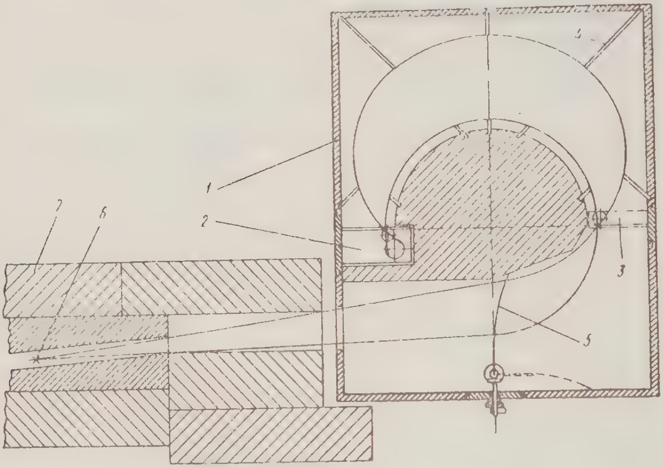

Fig.1. Diagram of combined β-γ-spectrometer: 1) measurement chamber, 2) large counter chamber, 3) small counter chamber, 4) baffle, 5) target, 6) γ-ray source, 7) collimator.

We developed a combined β-γ-spectrometer which reunites a Ketron type β-spectrometer and an Elotron type γ-spectrometer. This instrument is diagramed in Fig.1.

Having only one magnet, one measuring chamber and one system of controls, this instrument can be used to effect measurements which commonly require two different spectrometers.

I. Design of the Combined β-γ-Spectrometer

1. Electromagnet, power supply and controls.

To enhance the focusing we used an inhomogeneous magnetic field falling off in the radial direction. Korsunskii, Kel'man & Petrov[5] were the first to suggest the use of an inhomogeneous magnetic field focusing a wide flat electron beam and construced a β-spectrometer employing such a field. The theory of fields of this type is examined in Ref.1. A complete solution of the problem of focusing plane electron beams in an inhomogeneous magnetic field has been given by Pavinskii (Ref.6).

---

*The Ritron is described in Vol.18, No.5 of the Bulletin; the Elotron, in Vol.20, No.3. Translator.

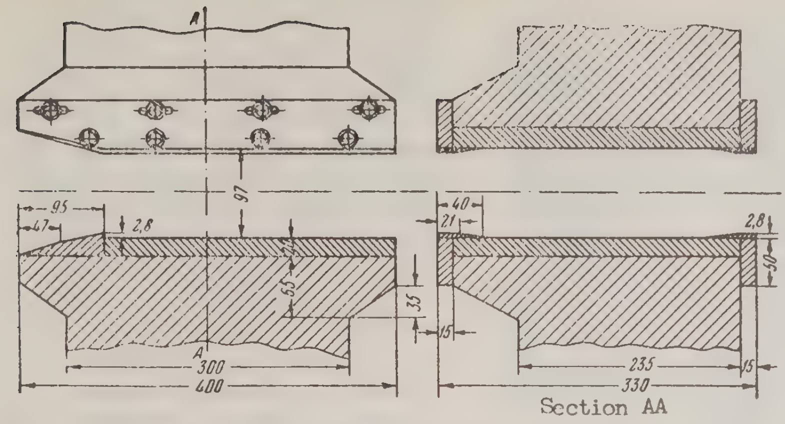

Fig. 2. Design of the magnet pole pieces.

For our spectrometer we used a C-shaped electromagnet with two sectional coils wound of copper strip 6 x 1.5 mm in cross section. The magnet core is assembled of St.20 steel bars. The pole pieces measure 300 x 400 mm and are made of low carbon steel. The cross section of the magnet assembly at its narrowest point is 255 x 300 mm. Saturation magnetization of the iron was not observed with a field of 300 oersted in the gap between the pole pieces.

For convenience in "fitting" the magnetic field to the theoretical distribution the auxiliary pole pieces were made in two parts. The first part was intended for producing a uniform field, the second for obtaining the nonuniform one. Both parts were attached to the face of the magnet by connecting cleats. These cleats increased the width of the pole to 330 mm. Special auxiliary shims were provided to compensate for the fringing effect. The design and dimensions of the pole pieces are shown in Fig.2.

The magnetic field distribution was measured by means of fluxmeter and a ballistic galvanometer connected to a flip coil. This coil had the following parameters: length 6 mm, mean diameter 8 mm, winding wire diameter 0.1 mm, number of turns 1500. It may be noted that with the given length to mean diameter ratio (L/D = 0.72) the accuracy of measurement is virtually independent of the dimensions of the coil[7]. In this case the measured field strength is that at the center of the coil. Our measurements of the absolute intensity of the magnetic field in the gap were of an auxiliary character and were made with a fluxmeter equipped with calibrated coils. The deviations of the magnetic field from the theoretical distribution did not exceed 0.5%. The "topography" of the magnetic field did not change with changes in the overall field intensity within the limits of the measurement error (0.2%).

The magnet was supplied from storage batteries delivering a voltage of 120 v. The current in the magnet circuit was monitored by a compensation circuit incorporating a PPTV-1 potentiometer. The monitoring accuracy is of the order of 1 part in $2 \cdot 10^5$.

2. Spectrometer chamber

The design of the measurement chamber was based on the following parameters: 1) radius of curvature of the principal electron trajectory - 110 mm, 2) horizontal angle of divergence of the electron beam - to 45°, 3) vertical angle of divergence - ±5°, and 4) height of source - to 20 mm. Another prime design consideration was provision for rapid conversion from β-spectrum measurements to γ-spectrum measurements by observation of recoil electrons.

The measurement chamber was constructed in the form of a brass box with a removable cover. The thickness of the walls was 8 mm; that of the cover 10 mm. The cover was provided with a rubber gasket seal.

A lead block 180 mm thick was used to shield the counters from direct γ-radiation from the source. Appropriate openings were provided in the chamber walls from the counters, the source holders and the target. The source and entrance slit of the counter chamber are in the same plane. The distance between the entrance slit and the source ($2\rho_o$) was set after assembly of the chamber. To facilitate this, the instrument design provides for adjusting the position of the slit jaws and source holder.

In studying γ-spectra (recoil electrons) the source holder can be replaced by a small counter chamber or an adjustable slit. The target can be brought into or retracted from the γ-ray beam without disturbing the vacuum. The instrument can be converted from γ-spectrum measurements to detection of photoeffect or conversion electrons within about an hour.

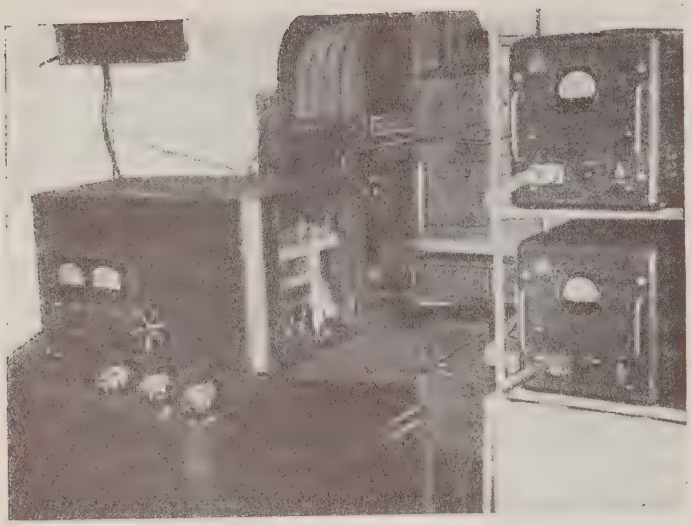

Fig. 3. General view of the combined β-γ-spectrometer. The vacuum system is housed in the separate cabinet visible in the foreground.

In order to reduce the number of scattered electrons the walls and cover of the chamber were lined on the inside with aluminum. All parts of the chamber were kept as far as possible from the electron beam. Appropriate baffles were provided to shield the counters from scattered electrons; two of these define the electron beam within the specified divergence angles. These baffles are adjustable radially.

The entire vacuum system and the system for filling the counters are mounted in a separate cabinet (Fig.3).

3. Counter chambers and counters

The electrons are recorded by means of Geiger-Muller counters located in the large and small counter chambers (see Fig.1). The housing of the large counter chamber is a cylinder with a cover. The inside of the cylinder has recesses for two counters. The housing is attached to the mounting flange by means of a special bracket which has a projection that enters a mating slot in the lateral frame of the measurement chamber. Thus the entrance slit is always accurately positioned relative to the source. The width of the entrance slit can be adjusted without disturbing the vacuum by means of a micrometric screw. The counter chamber is separated from the measurement chamber by a thin (10-15 $\mu g/cm^2$) collodion film. The counters were made of copper, the inner surfaces being carefully polished. The counter closures were made of plexiglass. The presence of two windows in the first counter greatly distorted the shape of the electric field. Hence it was necessary to cover one (the large) window of the counter with a thin 2-3 $\mu g/cm^2$ collodion film overlayed with a thin layer of copper. The counter chamber was filled to a pressure of 9-12 cm Hg with a 10:1 mixture of argon and dehydrated ethyl alcohol.

The γ-spectrum as evinced by recoil electrons can be studied using two counters, both located in the large counter chamber and connected into a coincidence circuit. However, in view of the fact that the counters are close together and thus receive not only direct γ-radiation from the source but also electrons scattered in the neighboring counter, there is in this case observed a large spurious coincidence background; this hampers investigation particularly when low-intensity lines are being studied. In view of this we provided the additional small counter chamber housing one counter and located it so that the counter could be set at the first focus (3 in Fig.1). This small chamber is also separated from the measurement chamber by a collodion film, but communicates with the large counter chamber. The entrance window of the small chamber measures 2 x 20 mm; the exit window measures 8 x 20 mm. In order to reduce the unsupported area of the film over the exit window, this is equipped with a narrow cross brace.

The counters usually have a working range (plateau) of 200 v at a potential of 800-900 v on the filament. V.I.Gavrilov and N.Ia.Titova, members of the staff of the Institute of Physical Chemistry of the USSR Academy of Sciences, participated in the design of the measurement and large counter chambers.

4. Counting-recording system

The counter pulses are recorded directly by a PS-64 type scaler or in the case of operation with two counters through a coincidence circuit. The resolving time of the coincidence circuit is approximately $5 \cdot 10^{-6}$ sec. The circuit can be set for counting double or triple coincidences. One of the circuit channels can be connected for anticoincidence. The coincidence circuit was assembled by V. Salmin, student of MIFI, as a thesis project.

II. Resolution and Transmission of the β-γ-Spectrometer

1. Half-width of conversion and photoelectron lines

Dzhelepov & Bashilov[1] give the following formula for calculating the relative half-width of lines in a β-spectrometer:

$$R = \frac{1}{4} \cdot \frac{(\Delta x) + d + q + 2\sigma}{\rho},$$

where Δx is the width of the linear source image, d is the width of the slit, q is the width of the source, σ is the spectral width and ρ is the radius of the instrument.

The relative half-width as calculated by this formula is approximately 0.6% for a slit and source width of 0.8 mm, source height of 15-20 mm, horizontal divergence angle of 30° and vertical divergence angle of ±3°. A half-width of this order was obtained in recording the spectrum of conversion electrons from Cs^{137} under conditions of operation with one counter.

2. Half-width of recoil electron lines

In general the shape and half-width of the spectral lines depends on the energy of the γ-quanta, the geometry of the instrument, the scattering and slowing down of the recoil electrons in the target and counter windows and the dimensions of the source. Calculations of the line shape for a γ-spectrometer with a homogeneous magnetic field (Ritron type) have been carried out by Khol'nov[8], taking into account some of the factors influencing the line shape. The question of line shape in γ-spectrometers has also been examined by Dzhelepov, Zhukovskii & Khol'nov[3]. It follows from their investigation that the theoretical and experimental half-width differ appreciably. Dzhelepov[9] explains at least part of this divergence by the "inherent" width of the recoil electron lines.

It is extremely difficult to calculate the recoil electron line half-width in a γ-spectrometer with an inhomogeneous field. However, in view of the experimental results obtained with the Ritron and Elotron γ-spectrometers, it was estimated that the half-width of the recoil electron line in our case should be of the order of 2-2.5% for the γ-line of Cs^{137}. This was substantiated by tests.

III. Calibration of the Spectrometer

1. Calibration with reference to conversion or photoelectron γ-lines

We calibrated our instrument with reference to the high-energy sides of conversion peaks. By way of standards we used the K and L conversion electron lines of Cs^{137} (Fig.4); the energy of this γ-transition, as determined by the crystal diffraction method, is 0.6616 Mev.

Inasmuch as up to magnetic field intensities of 2000-3000 oersted there is no evidence of saturation of the iron parts of the magnet, we assumed the field strength to be directly proportional to the current in the magnet windings. The current value corresponding to zero field intensity in coming out of the negative hysteresis loop was found from a plot of the loop. The field strength was checked by a magnetometer. The calibration was further verified with reference to the γ-line of Zn^{65}. The recorded spectrum showed the K and L photoelectron lines at 1033 and 1105 kev, which corresponds to a γ-ray energy of 1120.6 kev. Lead foil was used as the radiator.

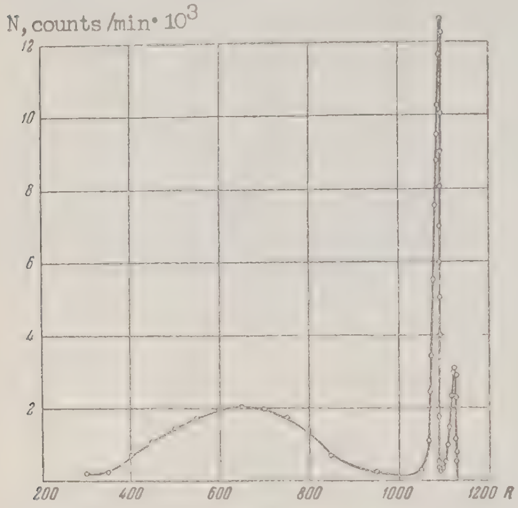

Fig.4. β-spectrum of Cs^{137}. R = divisions on potentiometer scale.

2. Calibration with reference to recoil electrons

In this case the calibration was effected with reference to the peaks of the recoil electron lines. The γ-lines of Co^{60} and Cs^{137} were selected as the standards. The calibration curves based on conversion electrons (1) and recoil electrons (2) are shown in Fig.5. The horizontal scale is graduated in divisions of the potentiometer scale, the vertical scale is laid off in Hρ units.

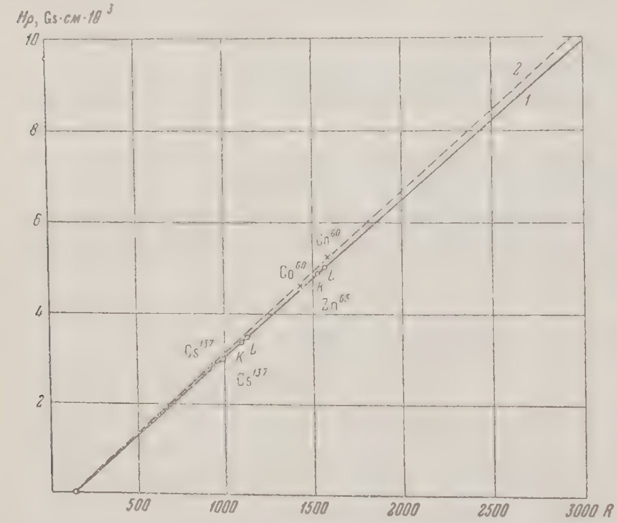

Fig.5. Energy calibration: 1) based on conversion electrons, 2) based on recoil electrons.

VI. Reproducibility of Results and Accuracy of Measurements

It was obviously essential to establish with what degree of accuracy the magnetic field corresponds to the measured current in the magnet windings and the reproducibility of the current-field relationship. To this end we carefully investigated the hysteresis loops with different current variation cycles. It was established that the so-called "minor" hysteresis loop, obtained when the current is varied 0 → I_{max} → → 0, starts at a certain appreciable initial field strength and is not linearly dependent on the current, particularly at the beginning of the loop. The reproducibility of the complete hysteresis loop obtained when the current is varied $0 \rightarrow I_{max} \rightarrow 0 \rightarrow (I_{min} = |I_{max}|) \rightarrow 0$ is better than in the case of the "minor" loop. In addition, the field strength over a large interval including the vicinity of zero field is directly proportional to the current. In view of this we selected the complete hysteresis loop as the "working loop". The constant, reproducible relation between the current and the magnetic field intensity is established after 3-5 current cycles. As repeated measurements of the conversion line of Cs^{137} showed the constant current-field relation is maintained with an accuracy of 1 part in $2 \cdot 10^3$. In other words, the results of measurement of the same spectrum line in different series of experiments differed by 1-1.5 kev at an electron energy of ~600 kev. This characterizes the accuracy of our instrument in this respect.

The writer desires to thank B.S.Dzhelepov, Iu.V.Khol'nov, N.N.Zhukovskii & P.P.Zarubin for help in acquiring the measurement techniques and for their attention and encouragement in the work.

Institute of Physical Chemistry of the
Academy of Sciences of the USSR

References

1. B.Dzhelepov & A.Bashilov, Izv. AN SSSR, Ser.fiz., 14, 3 (1950).
2. K.Siegbahn & N.Svartholm, Nature, 157, 872 (1946).
3. B.Dzhelepov, N.Zhukovskii & Iu.Khol'nov, Izv. AN SSSR, Ser.fiz., 18, 5 (1954).
4. B.Dzhelepov, N.Zhukovskii, A.Karamian & S.Shestopalova, Iav. AN SSST, Ser.fiz., 17, 518 (1953).
5. M.Korsunskii, V.Kel'man & B.Petrov, Zhur.eksp.i teor.fiz., 14, 394 (1944).
6. P.Pavinskii, Izv. AN SSSR, Ser.fiz., 18, 2 (1954).
7. R.Herzog, O.Tischler, Rev.Sci.Instr., 24, 1000 (1953).
8. Iu.Khol'nov, Dissertation, Radium Institute of the USSR Ac. of Sci., 1952.
9. B.Dzhelepov, Doklady AN SSSR, 101, 5 (1955).

A TWO-CRYSTAL SCINTILLATION γ-SPECTROMETER

- E.L.Stoliarova & I.E.Konstantinov

A coincidence γ-spectrometer utilizing Compton electrons has been described by Hofstadter & McIntyre[1]. The schematic of this spectrometer is shown in Fig.1.

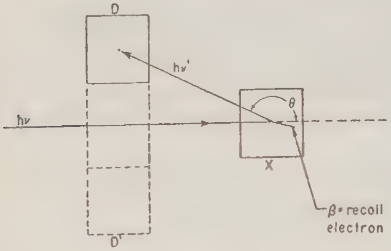

Fig.1. Schematic of coincidence spectrometer utilizing Compton electrons.

The collimated γ-beam ($h\nu$) falls on the crystal X. As a result of Compton encounters there are formed in X recoil electrons and scattered γ-quanta; the γ-quanta scattered at the angle θ are detected by the crystal D. The pulses from both crystals are recorded by photomultipliers and applied to a coincidence circuit; the pulses from crystal X are discriminated, i.e., the recoil electron spectrum is investigated. Thus the crystal X plays the part of an analyzer, the crystal D that of a detector. The energy of the photons is uniquely determined from the energy of the recoil electrons and the scattering angle θ.

It must be noted that for large scattering angles θ the recoil electron energy E_β is virtually independent of θ. Hence with large scattering angles the size of the detecting crystal (solid angle subtended by D) has less effect on the energy resolution than at small scattering angles.

We constructed a two-crystal coincidence γ-spectrometer utilizing photomultipliers of the new type (FEU-S) developed in the laboratory of N.S.Khlebnikov. In these photomultipliers the electron-optical system of the entrance section insures complete collection of the electrons from the photocathode, which is very important for good resolution.

Our spectrometer is based on the same principle as the instrument of Hofstadter and McIntyre[1] which is most suitable for investigation of γ-rays in the 0.2 to 2 Mev interval.

Fig.2 shows a block diagram of the instrument. The two photomultipliers 6 & 7 with their crystals C_1 & C_2 are housed in a light-proof box. The scattering angle θ equals 150°. The lead collimator K measures 15 x 15 x 22 cm and has an opening 6 mm in diameter. The source S can be located either inside the box or outside it. The pulses from the photomultipliers (6 & 7) go to the preamplifiers 5, consisting of one amplification stage and a cathode follower, then to the linear pulse amplifiers 1 and finally to the coincidence circuit 8 which has a resolving time $\tau = 1.5\cdot10^{-7}$ sec.

An output pulse from the coincidence circuit triggers the multivibrator 9 which opens the electronic gate 11 passing the pulses from the analyzer-crystal photomultiplier to the single channel discriminator 10, after which the pulses are recorded by the scaling circuit 3. The 1 microsec delay line was introduced to hold back the analyzed pulse for the time necessary for complete opening of the gate. The block diagram also shows the power supply units for the photomultipliers, amplifiers and discriminator. We used 29 x 12 mm NaI(Tl) crystals.

To investigate the resolution and efficiency of the instrument we recorded the recoil electron spectra produced by the monoenergetic γ-rays from Hg^{203}, Cs^{137} and Co^{60}. The pulse height distributions obtained are shown in Figs.3,4 & 5.

In the case of the 280 kev Hg^{203} line (Fig.3) the relative half-width is 18.6%. The lower peak at 40 kev (half-width 36.8%) is due to the radiation from Tl^{203}, the product of Hg^{203} decay. By appropriate discrimination of the pulses from the detector crystal this peak can be eliminated from the recorded spectrum. The half-width of the Cs^{137} line is 12%; the half-widths of the Co^{60} lines are

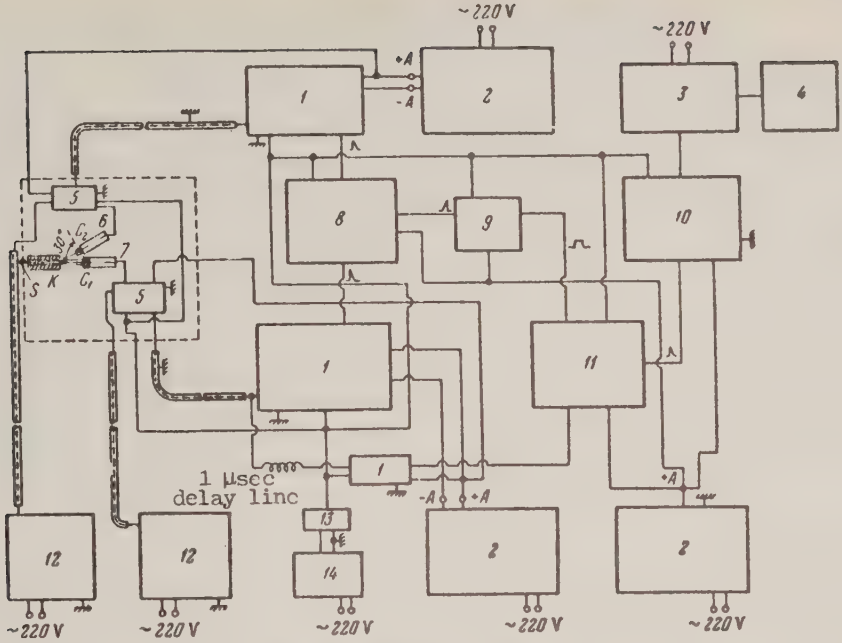

Fig.2. Block diagram of the two-crystal scintillation γ-spectrometer: 1) linear amplifier, 2) anode voltage stabilizer, 3) scaling circuit, 4) mechanical register, 5) preamplifier, 6) photomultiplier II, 7) photomultiplier I, 8) coincidence circuit, 9) multivibrator, 10) single channel discriminator, 11) electronic "key" (gate), 12) high voltage stabilizer, 13) storage battery, 14) selenium rectifier (filament supply).

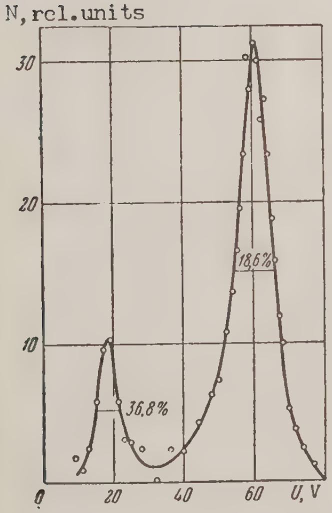

Fig.3. Pulse height distribution obtained for Hg^{203}.

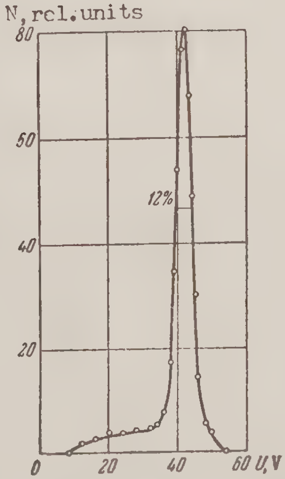

Fig.4. Pulse height distribution obtained for Cs^{137}.

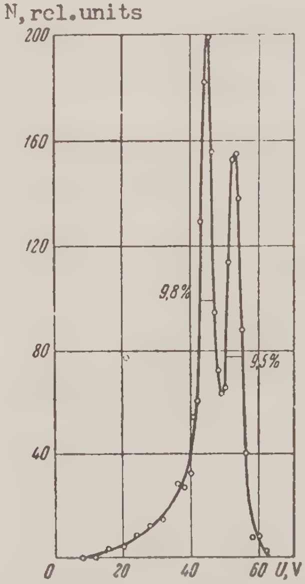

Fig.5. Pulse height distribution obtained for Co^{60}.

9.8 and 9.5%.

The calibration curve for the spectrometer is shown in Fig.6. The spectra of Co^{60}, Cs^{137} and Hg^{203} were obtained with different amplification factors (to take full advantage of the instrument's energy scale). In Fig.6 the values have been recalculated for the same amplification factor. It will be seen that the γ-ray energy vs pulse height plot is linear.

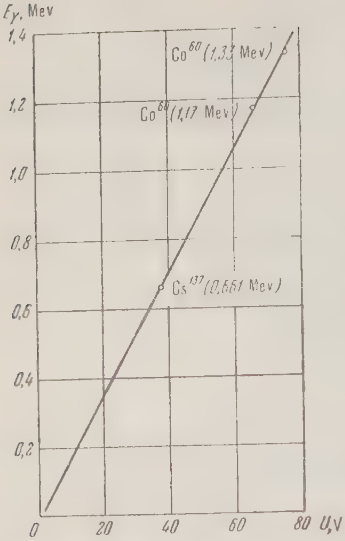

Fig.6. Calibration curve for the two-crystal γ-spectrometer.

The energy resolution of a two-crystal spectrometer is somewhat inferior to that of a single-crystal one at the same energy for the following reasons.

1. The analyzer crystal in a two-crystal spectrometer has to record an energy smaller than that recorded in a single-crystal instrument inasmuch as the scattered photons carry off only half the energy of the initial photon.

2. The finite size of the aperture of the detector crystal also contributes to line broadening.

We carried out an experimental evaluation of the influence of the statistical and aperture factors on the energy resolution for the above-listed isotopes.

The amount of broadening due to the analyzer at the recorded energies was determined on the basis of the $\sigma \approx 1/\sqrt{E_\gamma}$ (σ is the half-width) law, taking into account the energy carried off by the scattered photon.

For determining the contribution to broadening from the crystal and photomultiplier, we utilized the half-width for the Cs^{137} line, equal to 7.7%. This value was obtained on the same apparatus but operated as a single-crystal spectrometer. The results of our calculations are given in the accompanying table.

Isotope	Contribution from multiplier, %	Contrib. from aperature angle of cryst. %	Total broadening, %
Hg^{203}	16,2	2,4	18,6
Cs^{137}	9,2	2,8	12
Co^{60}	6,4 (1,17 Mev)	3,4	9,8
	5,9 (1,33 Mev)	3,6	9,5

The efficiency of our two-crystal spectrometer under our experimental conditions was 0.1% for Co^{60} and 0.125% for Cs^{137}, i.e., approximately two orders of magnitude lower than the efficiency of a single-crystal spectrometer. Nevertheless the two-crystal spectrometer can be successfully used for investigating sufficiently strong sources.

Moscow Engineering-Physical Institute

References

1. K.Hofstadter & I.McIntyre, Phys.Rev., 78, 619 (1950).

USE OF A PULSE IONIZATION CHAMBER FOR INVESTIGATING ALPHA-GAMMA ANGULAR CORRELATION

- Iu.I.Filimonov & G.A.Petrov

At present the most common method of investigating α-γ angular correlation is that of two detectors oriented successively at a series of angles relative to each other. A shortcoming of this method is that it is time-consuming in view of the necessity of successive measurements of coincidences from detectors located at different angles, the counting rates generally being low in view of the poor geometry.

Use of an ionization chamber for recording the direction of ejection of the α-particles makes it possible to increase the transmission factor of the instrument and measure the angular distribution simultaneously in an angular range from $\pi/2$ to π. At the same time a pulse chamber makes it possible to obtain a better α-particle energy distribution than, for example, a scintillation detector.

Below we describe the method we used for recording the direction of ejection of α-particles by means of a pulse ionization chamber with a grid.

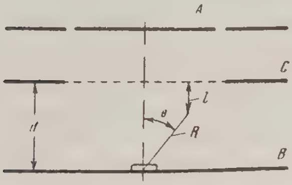

Fig.1. Diagram of grid ionization chamber.

When an appropriately grounded grid C (Fig.1) is installed between the collecting electrode A and the high-voltage electrode B, the collecting electrode A is shielded from the influence of charges formed in the space CB. Consequently, if at the initial instant there appears in the space between electrodes C and B the track of a charged particle at an angle θ to the axis of the chamber, a detectable signal will be induced in the collecting electrode A only after a time t, the time required by the electrons to cover the distance l:

$$l = d - R \cos \theta, \tag{1}$$

where R is the range of the α-particle.

Thus, we have

$$t = \frac{d - R \cos \theta}{w} \tag{2}$$

where w is the drift rate of electrons in the space between the grid and the high-voltage electrode.

This signal delay effect was utilized for determining the angle of ejection of the α-particle from the source in the correlation measurements.

Angular α-γ correlation is observed in cases when the instants of ejection of the α-particle and the photon in cascade with it are separated by an interval of not over 10^9-10^{10} sec^1. Hence for our purposes the time of ejection of the α-particle is given with sufficient accuracy by the instant of emission of the photon.

The angular correlation was investigated by means of the set-up diagramed in Fig.2. The grid and high voltage electrode of the plane chamber were made in the form of discs 20 cm in diameter. The collecting electrode, 10 cm in diameter, was surrounded by a ring-shaped shielding electrode. The high voltage was brought in to the grid and the high-voltage electrode through hollow porcelain insulators which also served to support these electrodes. The distance between the collecting electrode and the grid was 1.5 cm; that between the grid and the high-voltage electrode was 3.3 cm.

The 1 cm diameter α-particle source was deposited on an aluminum plate and mounted on the high-voltage electrode.

The housing containing the NaI(Tl) crystal and the FEU-19-S type photomultiplier was fastened over an opening in the bottom of the chamber; this aperture also served for replacement of the specimens.

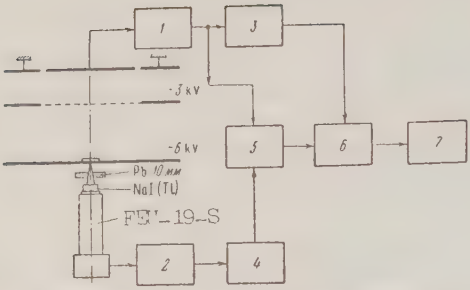

Fig.2. Block diagram of the set-up for measuring α-γ angular correlation: 1) amplifier of pulses due to α-particles, 2) amplifier of pulses due to photons, 3 & 4) discriminators, 5) sawtooth voltage generator, 6) gating circuit, 7) 20-channel pulse height analyzer. FEU-19-S = Photomultiplier.

The solid acceptance angle of the counter was 10^{-2} of 4π. The photomultiplier housing was covered with a 5 cm thick layer of lead. The chamber was operated with chemically pure argon at pressures from 2 to 3 atmospheres. Before filling, the chamber was evacuated to $\sim 10^{-2}$ mm Hg.

An amplifier with a gain factor of up to 10^6 was used for amplifying pulses from the collecting electrode. The differentiation and integration time constants of the amplifier were 4 microsec.

The pulses from the photomultiplier were applied to an amplifier with a factor of up to 10^4 and a pass band extending up to 2 Mc. The output signals from the amplifier were shaped by trigger circuits. Sawtooth pulses were generated in the circuit 5 (Fig.2) upon the arrival of a pulse from the amplifier 2 and cut off with the arrival of a pulse from the ionization chamber.

Thus the pulse height was

$$V = ct \tag{3}$$

where t is given by Eq.(2) and c is a calibration constant.

The gating circuit 6 discriminated the pulses according to the α-particle energies. The pulse height distribution was recorded by means of the 20-channel pulse height analyzer 7, each channel of which corresponded to a certain angle between the direction of ejection of the α-particle and the correlated photon.

The electronic circuits were adjusted by means of a twin pulse generator. The constant c was made equal to 7.7 v/microsec.

The inherent instability of the apparatus was 0.5 v in the range of output pulses from 10 to 50 v.

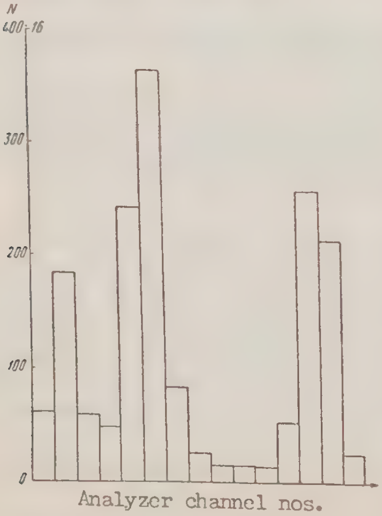

Fig.3. Histogram of angular resolution of the apparatus.

To determine the angular resolution of the set-up we carried out experiments with beams of α-particles directed at angles of 0, 45 and 90° relative to the axis of the chamber. The beams were defined within 5°.

The instant of appearance of an α-particle track was given by the signal from a high-voltage electrode. One of the histograms recorded at a pressure of 2.75 atmospheres in the chamber and a 2.5 kv potential difference between the grid and the high-voltage electrode is shown in Fig.3. The half-width of the peaks of the average is 12%. The resolution is somewhat impaired due to the poor conditions of taking the signal off the high-voltage electrode. This factor was not foreseen in designing the chamber; hence the signal to noise ratio amounted to 10-20.

The operation of the apparatus was checked in investigating the α-γ angular correlation for ThC". As a first step we recorded the angular distribution in the transitions

$$\text{ThC} \xrightarrow[720\ \text{kev}]{\gamma} \text{ThC}' \xrightarrow[8.78\ \text{kev}]{\alpha} \text{ThD}. \qquad (4)$$

In this case the spin of the ground state of ThC' is zero and the angular distribution should be isotropic[1]. Hence in measurements by the above described method the pulse height distribution should also be isotropic. From Equs. (2) & (3) we have:

$$\Delta V = c\Delta t = \frac{cR}{w} \sin\theta\,\Delta\theta.$$

On the other hand,

$$\Delta N = N_o \sin\theta\,\Delta\theta, \qquad (5)$$

where ΔN is the number of counts in one channel of the analyzer and N_o is the total number of counts comprised in the pulse height distribution as defined by Eq. (3). ΔV is the width of the analyzer channel.

From the above we get

$$\Delta N = \frac{N_o w}{cR}\Delta V = k\Delta V, \qquad (6)$$

where k is an experimentally determined constant.

It may be seen from Fig. 4 that the experimental points fall on a straight line.

Next we investigated the angular correlation between the 6.04 Mev α-particles from ThC and the γ-rays associated with the first excited level of ThC'' (40 kev).

The resolution in energy of the ionization chamber was determined for the α-particles from ThC' and found to be 60 kev.

The resolution of the scintillation spectrometer was determined with reference to the characteristic radiation of Te^{127} (32 kev) and was found to be 30%.

Consequently, the two groups of α-particles from ThC having energies of 6.04 Mev and 6.08 Mev were not resolved in our experiments. For this reason and also because of the high value of the internal conversion coefficient for the 40 kev γ-rays from ThC''* ($\alpha = 19.6$)[2], the chance coincidence background amounted to about 50% of the total coincidence count.

The chance coincidence background was measured by introducing a delay in circuit recording the pulses due to α-particles.

The results of the α-γ correlation measurements were processed by the method of least squares. The deduced correlation function (Fig. 5) had the form:

$$w(\theta) = 1 - (0.24 \pm 0.05)\cos^2\theta. \qquad (7)$$

This function agrees within the limits of experimental error with the theoretical function

$$w(\theta) = 1 - 0.22\cos^2\theta, \qquad (8)$$

computed on the assumption that the spins of the respective states are:

$$I_{ThC} = 1,\ I_{ThC''*} = 4 \text{ and } I_{ThC''} = 5.$$

The values of the coefficients in expression (7) obtained in our experiments are in agreement with the corresponding results of Weale[2].

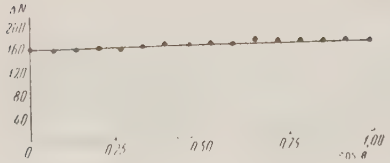

Fig.4. Isotropic angular distribution for ThC'.

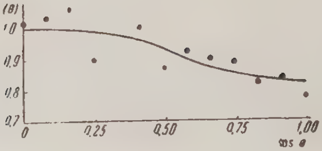

Fig.5. α-γ angular correlation in ThC".

Thus our preliminary investigation shows that an ionization chamber with electron collection can be successfully used for investigation of α-γ angular correlation.

In conclusion we desire to thank Prof. L.I.Rusinov for his interest in the work.

Leningrad Physical-Technical Institute of the
Academy of Sciences of the USSR

References

1. A.Z.Dolginov, Zhur.eksp.i teor.fiz., 23, 493 (1952).
2. E.W.Weale, Proc.Phys.Soc., A68, 35 (1955).

LIFETIMES OF EXCITED STATES OF NUCLEI IN THE RARE-EARTH ELEMENT GROUP

- E.E.Berlovich

Introduction

De-excitation of the lower excited states of nuclei can occur 1) by emission of γ-rays, 2) by transfer of energy to one of the electrons of the atomic shell (internal conversion), or 3) when the excitation energy $E > 2m_0c^2$, by electron-positron pair formation (internal conversion with pair formation). The probabilities of the second and third processes, occurring beyond the boundaries of the nucleus, virtually do not depend on the details of the nuclear structure. In theoretical considerations only the finite dimensions of the nucleus appear to have a noticeable influence on these processes[1]. However, the probabilities of conversion transitions and, particularly, the ratio of the probabilities of the conversion on different shells and subshells prove to be very sensitive to the characteristics (energy, spin and parity) of the nuclear levels involved. Hence experimental determination of conversion coefficients provides an effective means for obtaining information on the characteristics of nuclear levels and the type (multipole order, parity change, etc.) of nuclear transitions.

The probability of radiative transitions is largely determined by the nuclear structure. Different nuclear models (the drop, shell, generalized, etc.) therefore lead to different formulas for the probability. Naturally, experimental investigation of the probability of radiation transitions is an important means of testing the adequacy of different nuclear models. The generalized model suggested by Bohr & Mottelson[2] which has been successfully developed in recent years for rotational states, yields the dependence of radiative transitions on such nuclear characteristics as the deformation parameter, the electromagnetic moments and spin. Hence if the character and multipole order of a transition between rotational states are known from data on the conversion coefficients or on angular correlation of cascade radiation, one can obtain information on the enumerated nuclear parameters from measurements of the probability of the transition. It may be assumed that as the theory is developed further measurements of transition probabilities will make it possible to deduce information on parameters connected with oscillatory motion.

The probabilities of radiative transitions are investigated either by measurement of the lifetime of excited states (directly or indirectly) or by determining the Coulomb excitation cross section which is connected with the probability of transition to the excited level and, consequently, the probability of the inverse radiative transition.

The present investigation is devoted to determination of transition probabilities through lifetime measurements by the method of delayed coincidences.

1. Description of the delayed coincidences method

Measurement of lifetimes of excited states by the method of delayed coincidences amounts essentially to determination of the number of coincidences between pulses, produced by two radiations in cascade, as a function of the delay time introduced into one of the measurement channels. The following cases are possible.

1. When the lifetime of the state appreciably exceeds the resolving time of the coincidence circuit, the shape of the coincidence curve proves to be asymmetric and the sought lifetime is found from the flatter exponential branch of the curve[3].

2. If the lifetime of the investigated state is very short and a clear exponential curve cannot be obtained, the determination can be effected by comparison of the coincidence curve obtained for the investigated state with the curve

for "prompt" coincidences obtained for a known very short-lived state. The comparison can be made either by the method of Bay[4] or by the method of Newton[5].

3. Bell, Graham & Petch[6], using a twin magnetic spectrometer, applied the method of "self-comparison"; they adjusted one branch of the spectrometer for the conversion line corresponding to the investigated level and the other to a nearby section of the β-spectrum, and then interchanged the roles of the spectrometer branches. By this method the magnitude of the displacement of the centroid of the curves was made double that in the method of Bay.

We employed a scintillation coincidence spectrometer (see Ref.7 for description of the apparatus) and measured the coincidence curves for two positions of the β-particle (or conversion electron) absorber: 1) between the source and the first photomultiplier and 2) between the source and the second photomultiplier.

The delayed coincidence method is a direct method of measuring the lifetimes of excited states, in contrast with such other indirect methods as the method of resonance scattering of γ-rays or the method based on determining the radiative width of levels in (n,γ) or (p,γ) reactions.

At the same time this method does require particular care as regards taking into account different instrument effects which can appreciably modify the experimentally determined lifetimes. By way of illustration of the importance of procedure factors in such measurements, we can cite the numerous investigations of the lifetime of the 411 kev level of Hg^{198} occurring in the β-decay of Au^{198}. Table 1 gives the results of measurements reported by different investigators.

Table 1

Half-life of the excited state of Hg^{198}
according to the data of different authors

Authors	Ref.No.	T
Madansky & Wiedenbeck	8	$2\text{-}3 \cdot 10^{-7}$ sec
Meyer, Baldinger & Huber	9	$3.5 \cdot 10^{-8}$ sec
Jastram, Konneker & Kleland	10	$4 \cdot 10^{-8}$ sec
MacIntyre	11	$2.3 \cdot 10^{-8}$ sec
Bell & Petch	12	$< 3 \cdot 10^{-9}$ sec
Bell & Graham	13	$< 2 \cdot 10^{-10}$ sec
Deutsch & Wright	14	$< 4 \cdot 10^{-9}$ sec
Bell, Graham & Petch	6	$< 3 \cdot 10^{-11}$ sec
Moon (resonance scattering)	15	$< 10^{-11}$ sec

As may be seen the values range from $2\text{-}3 \cdot 10^{-7}$ to 10^{-11} sec, i.e., there is a spread extending to four orders of magnitude. Moreover, even the same authors report different values, obtained at different times as their procedure was modified.

The principal reasons for this "shotgun" scatter of the results obtained by different authors, who for the most part are known as experienced investigators, are apparently the following.

1. The presence of accompanying or "satellite" pulses in the photomultipliers. A coincidence between a true pulse in one of the photomultipliers and a satellite pulse in the other will result in a spurious delayed coincidence (the delay in this case will be introduced into the channel of the first photomultiplier). One of the causes for the appearance of such satellite pulses in photomultipliers is optical feedback which can be due to glow of one of the last dynodes at high amplifications or to leakage of light to the photocathode. Optical feedback can be eliminated by proper design of the photomultiplier and housing. It can also be eliminated through proper selection of the dynode material (for example, use of Cu-Be).

Satellite pulses can also arise as the result of ionic feedback in which a positive ion falling on the photocathode or one of the first emitters can initiate a secondary pulse. Ionic feedback can also be eliminated by careful design of the photomultiplier.

2. The presence of secondary pulses due to afterglow of the phosphor. Organic phosphors - stilbene and anthracene - generally have several light emission components with different persistence times and different intensities. If the resolving time of the coincidence circuit corresponds to the shortest lived component, the height of the pulse corresponding to this component will be greatest inasmuch as most of the excited states in the scintillation crystal will emit photons within the selected time. Longer lived excited states in the crystal will yield individual flashes of low intensity (the circuit resolves single photons), the frequency of which will be inversely proportioned to the phosphorescence time of the state. These secondary pulses will result in delayed coincidences if the pulse height analyzer is adjusted to select coincidences with small amplitude pulses in one of the branches.

3. Influence of the pulse front on the shape of the resolution curve. The influence of the energy of the recorded particles on the shape of the resolution curve has been noted by Bell et al[6] and Bay et al[16]; we investigated this effect in detail. The results are described in the following section.

2. Influence of the pulse front on the shape of the coincidence curve.

Fig.1 shows the β-γ coincidence curves for the $Au^{198} \longrightarrow Hg^{198}$ transition obtained for the two different positions of the absorber (β-γ coincidences and γ-β coincidences*). In this case we recorded the entire spectrum of the β-particles, the end point energy of which is 960 kev, and the complete spectrum of the Compton electrons,

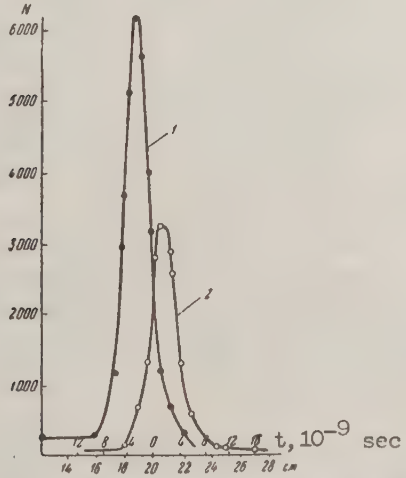

Fig.1. Curves of coincidences between the β-particles of Au^{198} and the γ-rays of the 411 kev transition in Hg^{198}. The entire β-spectrum and the entire Compton distribution were recorded: 1) γ-β coincidences, 2) β-γ coincidences.

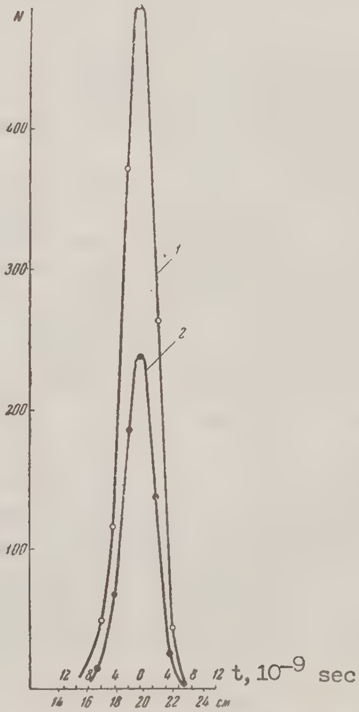

Fig.2. Curves of coincidences between the β-particles of Au^{198} and the γ-rays of the 411 kev transition in Hg^{198}. In this case only equivalent sections of β-spectrum and Compton distribution were recorded: 1) γ-β coincidences, 2) β-γ coincidences.

---

*These curves were obtained by means of the coincidence circuit with a variable delay line described in Ref.7.

the end point energy of which for 411 kev photons is 253 kev. The vertical scale is laid off in the number of coincidences per unit time; the horizontal scales are laid off in terms of the position of the indicator on the variable delay line scale (in cm) and the corresponding delay times. As may be seen the curves are displaced and the lifetime of the level as determined from the magnitude of the displacement is $\sim 2 \cdot 10^{-9}$ sec. The experiment shows, however, that the measured value of the lifetime can change within certain limits if the sensitivity of the channels is altered by adjustment of the threshold triggers in the side channels of the amplifiers. The resultant displacement of the curves is increased if the trigger of the channel registering the β-particles is set to cut off the greater part of the spectrum, passing only the harder part. And, on the contrary, the relative displacement of the curves is reduced if the greater part of the Compton electron distribution is cut off.

We modified our original apparatus by introducing a single-channel pulse height analyzer into each of the side channels. This made it possible to select coincidences in energetically equivalent pulse intervals. The results of measurement of the same $Au^{198} \rightarrow Hg^{198}$ transition with this modified set-up are shown in Fig.2. It will be seen that in this case there is no noticeable relative displacement of the curves obtained with the two positions of the absorber. The upper bound of the lifetime of the level as determined from these curves is $\sim 10^{-10}$ sec. It is obvious, therefore, that the relative displacement of the curves in Fig.1 is spurious and does not correspond to a true physical lifetime of the level. Moreover, the very character of the curve does not correspond to any physically meaningful displacement. Actually, if the displacement were caused by a measurable lifetime of the level, the branch of the curve to the side of the displacement should be flatter (closed to an exponential shape) than the opposite, purely Gaussian branch. The situation in Fig.1 is rather the contrary, which would indicate that the displacement must be attributed to the experimental procedure.

The influence of the particle energy on the position and shape of the coincidence curves may be interpreted in the following manner. Let us assume that the pulses produced by the cascade radiations arrive at the ends of our variable delay line virtually simultaneously (i.e., that the lifetime of the intermediate level is very short). The steepness of the leading edge of the pulse is determined primarily by the energy of the particle, since with a greater energy lost by the particle in the crystal the intensity of scintillation and accordingly the number of photoelectrons will be greater and, consequently, the rise time of the pulse will be shorter. In Fig.3,a the bottom solid straight line represents the delay line, while the upper dash line represents the discrimination level determined, for example, by the blocking potential of the diode. Pulses 1 & 2 are produced by particles of equal energy, hence after being clipped in amplitude by the shaping pentodes (see circuit in Ref.7) and limited in time by the shaping cable they will have the same amplitude and steepness. Obviously, with the pulses superimposed, the potential will reach the value of the level of discrimination at the midpoint of the delay line.

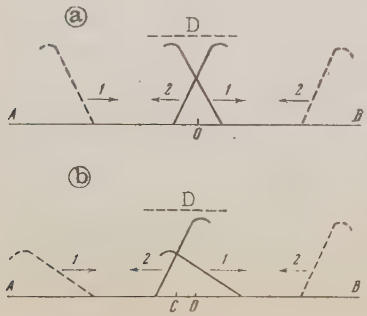

Fig.3. Influence of the steepness of the pulse fronts on the coincidence distribution along the delay line: a) Coincidence between pulses with fronts of equal steepness (A & B are the ends of the delay line, 0 is the midpoint of the line and D is the discrimination level); in this case the coincidence occurs at the midpoint of the delay line. b) Coincidences between pulses with fronts of different steepness; the pulse coming from point A was produced by a low energy particle, that coming from point B was produced by a high energy particle. The coincidence occurs at point C displaced some distance to the left of the midpoint of the line.

The situation is different when the two coinciding pulses are due to particles of different energies. In Fig.3,b the pulse from the left end of the delay line is produced by a low energy particle, while that from the right end of the line is produced by a high energy particle. After the clipping pentodes the pulses have the same height, but after shaping in the short-circuited cable they become equal in width but differ as regards amplitude and steepness. Obviously, in this case upon superposition of the pulses, the potential will reach the level of discrimination not at the midpoint of the delay line but somewhat closer to the end at which the pulse due to the lower energy particle originated.

Hence the entire configuration of the resolution curve will be determined not only by the mean value of the energy of the particles of both kinds but also by the overall shape of the energy spectra of the particles.

In order to exclude the influence of the difference in the energy spectra of the particles on the results of lifetime measurements by the method of delay coincidences it has been the practice to select coincidences of particles within more or less narrow energetically equivalent intervals. This can be accomplished either by means of pulse height analyzers or by means of magnetic spectrometers (Bell et al[6]). Sometimes it is sufficient simply to limit the spectrum with the greater maximum energy. In the case when the spectra of the two types of particles in question do not differ greatly (as for example in the examined case of Au^{198}) or when the time being measured is very great one can dispense entirely with discrimination in amplitude. However, in all such experiments it is important to evaluate the influence of the above mentioned factors on the accuracy of measurement.

In some cases measurement of coincidences with energetically equivalent intervals is difficult in practice since the number of pulses in one of the channels may prove to be small and hence the number of resulting coincidences low. This situation occurs, for example, in measuring the coincidence between conversion electrons, the energy of which is usually low ($\sim$100 kev) and the electrons of a β-spectrum having a large end-point energy (1-2 Mev). Here the energy interval corresponding to the conversion electron energy range will be only the initial, low intensity part of the β-spectrum. In such cases it is necessary to have recourse to the procedure of comparing the delayed coincidences curve with a "prompt" coincidence curve recorded in the same pulse height interval. The pulse height intervals in this case should be selected not on the principle of energy equivalence but on the basis of a maximum coincidence count.

3. Results of level lifetimes measurements

Investigation of the decay of Eu^{152} and Eu^{154}. The decay schemes of the long-lived isotopes Eu^{152} and Eu^{154}, according to the latest data of Slattery, Lu & Wiedenbeck[17] are shown in Fig.4. Both isotopes were present in the investigated mixture in approximately equal amounts. Specifically, we investigated the lifetimes of the first excited levels of Sm^{152} at 122 kev, Gd^{152} at 344 kev and Gd^{154} at 123 kev. We used stilbene crystals in our quick-acting coincidence circuit; in consequence separation of the γ-lines was possible only on the basis of the Compton distribution (the role of the photoeffect in view of the small atomic numbers of carbon and hydrogen was virtually negligible). The 122 and 123 kev transitions were recorded by detecting conversion electrons. In investigating the lifetime of the first level of Sm^{152} we measured the e-γ coincidences. In the experiments the conversion electrons were incident only on the crystal located on the uncovered (no absorber) side of the source. An aluminum absorber, stopping all β-particles, was mounted between the source and the second crystal. With this arrangement there could, in principle, occur coincidences of conversion electrons from the 122, 123 and 240 kev transitions with γ-rays, as well as β-γ and γ-γ coincidences. Let us denote these by

$$e_{122}\text{-}\gamma,\ e_{123}\text{-}\gamma,\ e_{240}\text{-}\gamma,\ \beta\text{-}\gamma \text{ and } \gamma\text{-}\gamma \qquad (1)$$

Now if the aluminum foil to the left of the source absorbs all the conversion electrons from the 122 and 123 kev transitions, there will remain the coincidences

$$e_{240}\text{-}\gamma,\ \beta\text{-}\gamma \text{ and } \gamma\text{-}\gamma. \qquad (2)$$

The difference in the number of coincidences obtained with the two indicated arrangements will be due almost exclusively to the coincidences

$$e_{122}\text{-}\gamma \text{ and } e_{123}\text{-}\gamma. \qquad (3)$$

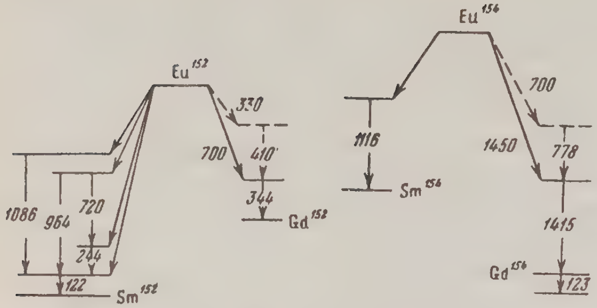

Fig.4. Decay schemes for Eu^{152} and Eu^{154}.

Spectrometric investigations carried out by B.V.Bobykin at the Leningrad Physical-Technical Institute on a spectrometer with double focusing showed the ratio of the intensities of the K peaks associated with the 122 and 123 kev transitions is 2.5, while the ratio of the intensities of the K peaks associated with the 122 and 240 kev transitions is ~15. The efficiency in recording the γ-rays in cascade with the 122 kev transition and having energies of 1084, 964, 720 and 240 kev (particularly the last) should be greater than the efficiency for recording the 1415 kev γ-rays in cascade with the 123 kev transition.

If we bear in mind these considerations and the important fact that the energy intervals selected for both channels corresponded to the region of the conversion electrons and that, consequently, only an insignificant fraction of the Compton electron distribution for the 1415 kev γ-rays was recorded, it will be obvious that the difference (3) will represent almost exclusively the e_{122}-γ transitions of interest to us.

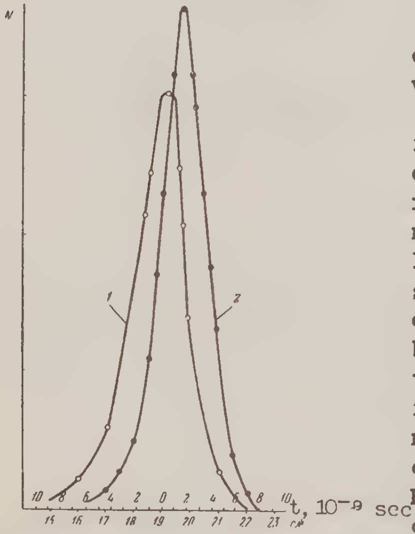

Fig.5. Determination of the lifetime of the 122 kev level of Sm^{152}: 1) e-γ coincidences for the $Eu^{152} \rightarrow Sm^{152}$ transition, 2) "prompt" coincidences for the $Co^{60} \rightarrow Ni^{60}$ transition.

With the selected energy intervals, possible coincidences of conversion electrons with x-rays were also not recorded.

The experimental coincidence curve is shown in Fig.5 together with the curve of the "prompt" coincidences for the $Co^{60} \rightarrow Ni^{60}$ transition, obtained for the same energy intervals. Both curves were normalized to the same area. The lifetimes of both levels of Ni^{60}, according to Bay et al[16], are shorter than 10^{-11} sec. In this case determination of the lifetime of the level from the exponential branch of the curve (as was done, for example, for the level of Ta^{181} with a lifetime of 10^{-8} sec)[7] is not justifiable inasmuch as the lifetime does not exceed the resolving time of the coincidence circuit. In such cases one can apply the method of Bay[4], which amounts to determining the displacement of the centroid of the delayed coincidence curve relative to the "prompt" coincidence curve.

$$\theta = \frac{\int\limits_{-\infty}^{\infty} F(t)\,dt}{I} - \frac{\int\limits_{-\infty}^{\infty} P(t)\,dt}{I}, \qquad (4)$$

where θ is the mean lifetime of the level, t is the delay introduced, F(t) is the delayed coincidences curve, P(t) is the "prompt" coincidences curve and

$$I = \int_{-\infty}^{\infty} F(t)\,dt = \int_{-\infty}^{\infty} P(t)\,dt. \qquad (5)$$

Graphic integration yields the following value for the period

$$T = \log 2 \cdot \theta = 1.31 \cdot 10^{-9} \text{ sec.}$$

The sought lifetime can also be calculated by the method of Newton[5]:

$$\theta = \frac{1}{\lambda} = \frac{\int_A^B [F(t) - P(t)]\,dt}{F(A) - F(B)}, \qquad (6)$$

where A and B are two arbitrary values of t, which should be selected in the region of overlapping of the curves, preferrably where the statistical accuracy is good. The numerator in (6) is the part of the area between the two curves in the delay time interval A to B, and the denominator is the difference between the ordinates at the ends of the selected interval. The functions F(t) and P(t) are assumed to satisfy the condition (5). The half-life determined in this manner proves to be $1.29 \cdot 10^{-9}$ sec. The mean value is therefore $T = 1.3 \cdot 10^{-9}$ sec. This value is somewhat less than that obtained by Sunyar[18]:

$$T = 1.4 \cdot 10^{-9} \text{ sec.}$$

From the experimental value of the half-life one can, of course, determine the radiative period $T\gamma$ by means of the expression

$$T\gamma = T(1 + \alpha), \qquad (7)$$

where α is the total conversion coefficient. Taking $\alpha = 1.27$ (from Sunyar[18]), we get

$$T\gamma = 3 \cdot 10^{-9} \text{ sec.}$$

To measure the lifetime of the 344 kev excited level of Gd^{152} one must cut off on one side (channel) all the β-particles (for recording γ-rays) and on the other side arrange to absorb the conversion electrons associated with the 122, 123 and 240 kev transitions in order to record the β-particles. From the decay scheme shown in Fig.4 it will be seen that there could in this case be observed β-γ coincidences for the β-spectra with end point energies 700 kev and 1450 kev and γ-γ coincidences. In our experiments the energy interval was selected so that the coincidences of the soft β-spectrum would predominate; the γ-γ coincidences accounted for only a few percent of the coincidence count. Coincidence curves were recorded with the above described positions of the β-particle and conversion electron absorbers and with the positions of these absorbers interchanged (same amplitude intervals in both cases). The centroids of both curves virtually coincided, i.e., there was no detectable displacement. Taking into account the accuracy of our measurements, the upper bound of the half-life of the investigated level may be evaluated as

$$T < 10^{-10} \text{ sec.}$$

The β-spectrum with end point energy 700 kev has been measured on twin spectrometers by Shavtvalov[19] and Slattary & Wiedenbeck[17]. Ours, however, is the first evaluation of the lifetime of the 344 kev level.

No coincidences between conversion electrons associated with the 120 kev transition and β-particles were detected in either of the above mentioned investigations[19,17] in which coincidences between the 344 kev conversion electrons and the continuous β-spectrum were measured. In both investigations the coincidences circuit had a resolving time $\tau = 3\text{-}4 \cdot 10^{-7}$ sec (or $2\tau = 6\text{-}8 \cdot 10^{-7}$ sec). Slattary and his co-workers conclude that the lifetime of the second excited level to which the 1450 kev end point energy β-decay leads is greater than 10^{-6} sec. In our experiments, however, we did detect coincidences between 120 kev transition conversion electrons and hard β-particles having an energy over 700 kev. The β-spectrum with end point energy 700 kev was completely absorbed by the aluminum absorber mounted in front of one of the crystals. The other crystal was left uncovered, allowing the passage of all radiation. With this arrangement the following coincidences could be recorded:

$$e_{123}\text{-}\beta_{hard},\ e_{122}\text{-}\gamma,\ e_{123}\text{-}\gamma,\ \gamma_{123}\text{-}\beta_{hard},\ e_{240}\text{-}\gamma,\ \beta_{700}\text{-}\gamma,\ \beta_{hard}\text{-}\gamma,$$
$$\gamma\text{-}\gamma,\ e_{122}\text{-}X \text{ and } e_{123}\text{-}X.$$

Next we increased the thickness of the aluminum absorber sufficiently to insure stopping all β-rays of up to 1450 kev energy. This increase in absorber thickness could have only a minor effect on the intensity of the γ-rays (~ 4% reduction). In this case the possible coincidences are

$$e_{122}\text{-}\gamma,\ e_{123}\text{-}\gamma,\ e_{240}\text{-}\gamma,\ \beta_{700}\text{-}\gamma,\ \beta_{hard}\text{-}\gamma,\ \gamma\text{-}\gamma,\ e_{122}\text{-}X \text{ and } e_{125}\text{-}X.$$

The difference between the number of coincidences with the two arrangements, which amounted to 25-30%, could obviously be attributed to the $e_{123}\text{-}\beta_{hard}$ and $\gamma_{123}\text{-}\beta_{hard}$ coincidences which are associated with the 123 kev level of interest.

The fact that such coincidences were not detected in the investigations of Refs.11 & 17 may be attributed to the low intensity of the hard β-spectrum, for it may have been impossible to distinguish this against the chance coincidence background. In view of the relatively low resolving power of the coincidence circuit and the inefficient experimental geometry, the background in these investigations was probably large. Apparently, coincidences of this type were observed by Sunyar[18]. On the basis of our measurements, we evaluate the half-life of the 123 kev excited level to be $1.1 \cdot 10^{-9}$ sec (average of the values obtained by the methods of Bay and Newton), which is close to the value of $1.2 \cdot 10^{-9}$ sec obtained by Sunyar. Whence, for the radiative period we obtain $T\gamma = 2.7 \cdot 10^{-9}$ sec. The lifetime of the second excited level is apparently $< 10^{-10}$ sec.

Er^{166}. Our results for the 81 kev level of Er^{166} are shown in Fig.6. We recorded the coincidences between the 81 kev conversion electrons and the β-spectrum of Ho^{166} with an end-point energy 1.76 Mev. In view of the fact that there are very few electrons in this β-spectrum in the pulse amplitude interval equivalent to that comprising the conversion electrons, it was impossible to adhere to the principle of equivalent energy intervals for both types of coinciding radiations in these measurements. Hence the pulse height interval for the channel recording the β-rays was selected to obtain a maximum coincidence rate. The lifetime of the level was determined by comparison with the "prompt" coincidence curve obtained for the Co^{60}→Ni^{60} transition in the same pulse height intervals. The average value of the half-life evaluated by the methods of Bay and

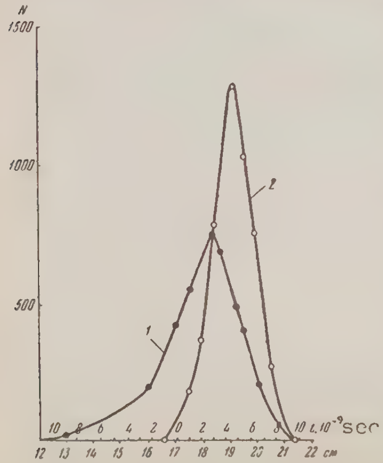

Fig.6. Determination of the lifetime of the 81 kev level of Er^{166}: 1) e-β coincidences for the Ho^{166}→Er^{166} transition, 2) "prompt" coincidences for the Co^{60}→Ni^{60} transition.

Newton was found to be $T = 2\cdot10^{-9}$ sec (Sunyar[18] reports $T = 1.7\cdot10^{-9}$ sec); this yields $T\gamma = 1.8\cdot10^{-9}$ sec.

Hf^{177}. Fig.7 illustrates the case of the 113 kev level of Hf^{177}; this is a case when we used the method of "self-comparison" for determining the very short lifetime. In this case we recorded the e-β coincidence and β-e coincidence curves and determined the magnitude of the displacement of the centroids of the two curves. This led to a value of $T = (4.2 \pm 0.6)\cdot10^{-10}$ sec. Hence, $T\gamma \simeq 1.6\cdot10^{-9}$ sec. In view of the smallness of the measured value it was determined as the average of several series of measurements under different conditions. Sunyar[18] gives $5\cdot10^{-10}$ sec as the upper bound for the half-life of this level.

Pr^{141}. In addition to the above cases, all pertaining to E2 type transitions, we also investigated the case of a magnetic dipole transition: the 146 kev transition in Pr^{141}, which forms in the decay of Ce^{141}. This case is characterized by a simple decay scheme with one excited level. The half-life was easily measured: we found $T = 2\cdot10^{-9}$ sec. De Waard & Gerholm in Ref.20, received after completion of our experiments, report $T = 1.9\cdot10^{-9}$ sec. The value of $T\gamma$, calculated on the basis of our results, is $2.8\cdot10^{-9}$ sec.

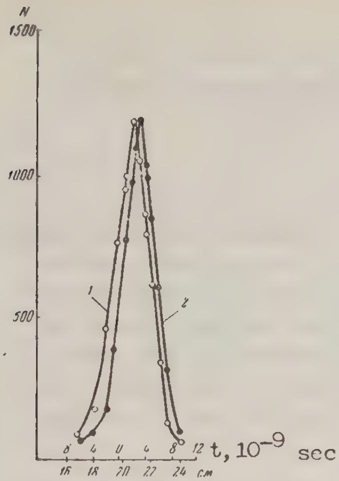

Fig.7. Determination of the lifetime of the 113 kev level of Hf^{177}: 1) e-β coincidences for the $Lu^{177} \rightarrow Hf^{177}$ transition, 2) β-e coincidences for the same transition.

4. Analysis of the results

The region of rare earth nuclei is characterized by large quadrupole moment values. It is well known[2,19] that the probabilities of quadrupole transitions in nuclei of this group are some two orders of magnitude greater than the probabilities given by the formulas of Weisskopf[21] and Moszkowsky[22] for single-particle transitions.

In the case of the generalized model of the nucleus[2,23] the nucleus is regarded as a system which the motions of the individual nucleons are connected with the collective motion of the entire nucleus. Only nuclei with filled proton or neutron shells possess spherical symmetry. Nucleons outside the filled shell, interacting with the nucleons of the core, deform the nucleus. At the same time the character of the motion of these nucleons is also modified due to alteration of the field of the deformed core in which they move.

The higher probability of E2 transitions in such nuclei is directly connected with their greater deformation and, consequently, greater electric quadrupole moment. Strongly deformed nuclei are characterized by the existence of rotational states. The energy of rotational levels of even-even nuclei, according to Bohr and Mottelson[2], is given by the expression

$$E = \frac{\hbar^2}{2J} I(I+1), \tag{8}$$

where $\hbar = h/2\pi$, J is the effective moment of inertia of the nucleus about the axis perpendicular to the symmetry axis and I is the spin of the nucleus in a given state. The spins of neighboring rotational states differ by two units.

The probability of electric quadrupole transitions for rotational states with an energy difference ΔE is

$$\lambda(E2) = \frac{4\pi}{75} \cdot \frac{1}{\hbar} \cdot \left(\frac{\Delta E}{\hbar c}\right)^5 B(E2), \tag{9}$$

where B(E2) is the reduced probability of the transition, which is independent of ΔE. In the case of even-even nuclei for a I + 2 → I transition

$$B(E2) = \frac{15}{32\pi} e^2 Q_0^2 \frac{(I+1)(I+2)}{(2I+3)(2I+5)}. \tag{10}$$

Here Q_0 is the internal quadrupole moment of the nucleus, characterizing the deformation of the nucleus and measured in the coordinate system connected with the nucleus. It is given by

$$Q_0 = \frac{4}{5} Z R_0^2 \frac{\Delta R}{R_0}, \tag{11}$$

where Z is the number of the element, ΔR is the difference between the major and minor semiaxes, and $R_0 = 1.2 \cdot 10^{-13}$ cm is the mean radius of the nucleus. From the experimentally measured mean lifetime (the reciprocal of the transition probability) one can determine by means of Eqs.(9), (10) and (11) the deformation parameter $\Delta R/R_0$ of the nucleus and the internal quadrupole moment Q_0 for the even-even nuclei Sm^{152}, Gd^{154} and Er^{166}. The above equations are not applicable to case of Hf^{177}. For nuclei with odd-A the energies of the rotational states are given by

$$E = \frac{\hbar^2}{2J}[I(I+1) - I_0(I_0+1)], \tag{12}$$

where I_0 is the spin of the ground state. Here, if the projection of the Ω angular momentum on the axis of symmetry of the nucleus is not equal to 1/2, the nuclear spin may assume the values I_0, $I_0 + 1$, $I_0 + 2$.... The reduced probability of an E2 transition in the rotational spectrum with a unit spin change is[2]

$$B(E2) = \frac{15}{16\pi} e^2 Q_0^2 \frac{\Omega^2 (I+1-\Omega)(I+1+\Omega)}{I(I+1)(2I+3)(I+2)}, \tag{13}$$

where the projection of the angular momentum $\Omega = I_0$.

The rotational spectrum of even-even nuclei is evinced both through the value of the energy, which for the first level lies in the region of 100 kev, and by the ratio of the energies of the second (if it exists) and first levels, which ratio, as may be seen from Eq.(8) equals 3.33 (the spin of the ground state of even-even nuclei is zero). In addition, rotational (and in general collective) levels, in contrast to single-particle ones, are excited by the Coulomb field under bombardment with heavy charged particles (protons, α-particles and multiply charged ions).

Table 2

Summary of data on the investigated levels

Nucleus	F_γ, kev	Type trans.	T, obs. sec	$\alpha = \frac{N_e}{N_\gamma}$	T_γ	T_{theo}	$F = \frac{T_{theo}}{T_\gamma}$	$\frac{\Delta R}{R_0}$	$Q_0 \cdot 10^{24}$, cm^2
Pr_{59}^{141}	146	M 1	$2 \cdot 10^{-9}$	0,42	$2,8 \cdot 10^{-9}$	$7,2 \cdot 10^{-12}$	$2,6 \cdot 10^{3}$	—	—
Sm_{62}^{152}	122	E 2	$1,3 \cdot 10^{-9}$	1,27	$3 \cdot 10^{-9}$	$4,3 \cdot 10^{-7}$	140	0,29	5,9
Gd_{64}^{152}	344	E 2	$<10^{-10}$	—	$<10^{-10}$	$2,5 \cdot 10^{-12}$	—	—	—
Gd_{64}^{154}	123	E 2	$1,1 \cdot 10^{-9}$	1,42	$2,7 \cdot 10^{-9}$	$4,1 \cdot 10^{-7}$	150	0,29	6,1
Er_{68}^{166}	81	E 2	$2 \cdot 10^{-9}$	8,1	$1,8 \cdot 10^{-8}$	$3 \cdot 10^{-6}$	160	0,29	6,8
Hf_{72}^{177}	113	E 2	$4,2 \cdot 10^{-10}$	2,7	$1,6 \cdot 10^{-9}$	$5,3 \cdot 10^{-7}$	330	0,31	8,2

The data on the investigated nuclei are summarized in Table 2: the second column gives the energy of the first level, the third - the type of transition as deduced from data on conversion coefficients, the fourth - the observed half-life of the state, the fifth - the accepted value of the conversion coefficient (from Ref.18), the sixth - the radiative period $T\gamma$, the seventh - the half-life as computed by Weisskopf's formula, the eighth - the F factor which is the ratio of the observed probability to the probability computed according to Weisskopf's formula, the ninth - the deformation parameter $\Delta R/R_0$ and the tenth - the internal quadrupole moment Q_0.

In the Gd^{152} nucleus, for which we established an upper bound for the lifetime, the lower levels probably belong to the vibrational spectrum[24]; this follows from the ratio of the energies of the first two excited levels (close to two) and from the energy value (344 kev).

The spin of the ground state of Hf^{177} was measured in 1956 by Speck & Jenkins and proved to be 7/2. Knowing this and the lifetime one can find the quadrupole moment Q_0 and the deformation parameter $\Delta R/R_0$ by means of Eqs.(9), (10) and (11).

Temmer & Heydenberg[26], studying Coulomb excitation, determined the reduced probability of the quadrupole transition from the ground state to the 113 kev level of Hf^{177} from the cross section for quadrupole excitation. They found $B_{if}(E2) = 2.8$. Using the ratio between the reduced probabilities for the direct and reverse transitions,

$$B(i \to f) = B(f \to i)\frac{2I_f + 1}{2I_i + 1}, \tag{14}$$

where I_i and I_f are spins of the ground and excited states, respectively, the Eq.(9) and the measured lifetime of the state, we calculated the same quantity and obtained $B_{if}(E2) = 2.6$, which is in good agreement with the results of Temmer & Heydenberg.

Marmier & Boehm[27], who carried out precision energy measurements of the γ-rays from Hf^{177}, give values of 112.97 and 249.59 kev, respectively, for the first two excited levels.

Utilizing Eq.(12), the ground state spin $I_0 = 7/2$ and the energy of the first level, we obtain $\hbar^2/2J = 12.56$ kev.

Applying the same formula to the second level (249.69 kev), we find that the spin of the second excited state should be 11/2. The crossover transition from the second excited level to the ground state should therefore be E2, and not M1 as indicated by Marmier & Boehm.

Inasmuch as both the first levels of Hf^{177} are excited by the Coulomb field, application of Eq.(12) for the rotational states appears justified and the sequence of spins 7/2, 9/2 and 11/2 for the ground and first and second excited levels seems plausible (Marmier & Boehm assume 1/2, 5/2 and 3/2).

In all investigated cases of E2 type transitions between lower rotational states, the lifetimes of the levels proved to be 140 to 330 times shorter than the estimates arrived at by the single-particle formula of Weisskopf. The values of the deformation parameters for the investigated nuclei proved to be close to 0.3. The internal quadrupole moment goes up from $5.9 \cdot 10^{-24}$ cm^2 in Sm^{152} to $8.2 \cdot 10^{-24}$ cm^2 in Hf^{177}.

The Pr^{141} nucleus has a filled neutron shell (N = 82) and must therefore have a spherically symmetric shape. The 146 kev level is not excited by the Coulomb field[26] and has single-particle attributes. The K/L conversion ratio, according to the data of Jones & Jensen[28], is 6.4, which is closest to Rose's theoretical value[29] of 7.7 for M1 transitions. In view of the fact that L, M and N lines were not resolved in the investigation and that Jones & Jensen actually calculated the ratio K/(L + M + N), it may be assumed that the experimental value of the ratio K/L is even closer to the theoretical value for M1 transitions. The fact that the transition in question is almost pure M1 also follows from the experiments on the angular distribution of the γ-rays from oriented Pr^{141} nuclei performed by Ambler, Hudson & Temmer[30].

It follows from the nuclear shell model and the measured value of the ground state spin ($I_0 = 5/2$) that the transition in question occurs between levels having the configurations $g_{1/2}$ and $d_{5/2}$. In contrast to the above examined cases of E2 transitions between rotational states, in the case of the magnetic dipole transition in Pr^{141}, the lifetime of the level proved to be 380 times greater than the value estimated according to Weisskopf's formula.

Graham & Bell[31] investigated similar "retarded" magnetic dipole transitions. They explain the lowered transition probability by forbiddenness with respect to the orbital quantum number l (theoretically forbidden transitions). In the case of the Pr^{141} nucleus with a filled shell l is a good quantum number and the pertinent selection rules probably apply. It should be noted, however, that among the cases investigated by Graham & Bell there were also transitions in which the orbital quantum number l did not change (for example, $p_{3/2} \rightarrow p_{1/2}$ in Hg^{199} and $p_{1/2} \rightarrow p_{3/2}$ in Fe^{57}). Nevertheless, the observed probability for these transitions, too, proved low. This would indicate that in addition to the l-restriction, there are apparently other factors reducing the probability of magnetic transitions. One such factor is the magnetic moment induced in the nuclear core in single-particle magnetic transitions.

Leningrad Physical-Technical Institute of the
Academy of Sciences of the USSR

References

1. L.Sliv, Zhur.eksp.i teor.fiz., 21, 770 (1951).
2. A.Bohr & B.Mottelson, Klg. Danske Vidensk. Selsk., Mat.fys.Medd., 27, No. 16 (1953).
3. F.Van Name, Phys.Rev., 75, 100 (1949).
4. Z.Bay, Phys.Rev., 77, 419 (1950).
5. T.Newton, Phys.Rev., 78, 490 (1950).
6. R.Bell, R.Graham & H.Petch, Canad. J. Phys., 30, 35 (1952).
7. E.Berlovich, Izv. AN SSSR, Ser. fiz., 19, 343 (1955). (Translation in Bulletin Vol. 19, No.5, p. 305.)
8. L.Madansky & M.Wiedenbeck, Phys.Rev., 72, 185 (1947).
9. K.Meyer, E.Baldinger & P.Huber, Helv. Phys. Acta, 23, 517 (1950).
10. P.Jastram, W.Konneker & M.Kleland, Phys.Rev., 79, 243 (1950).
11. W.MacIntyre, Phys.Rev., 76, 312 (1949).
12. R.Bell & H.Petch, Phys.Rev., 76, 1409 (1949).
13. R.Bell & R.Graham, Phys.Rev., 78, 490 (1949).
14. M.Deutsch & W.Wright, Phys.Rev., 77, 139 (1950).
15. P.Moon, Proc.Royal Phys.Soc., A64, 76 (1949).
16. Z.Bay, V.Henry & F.McLernon, Phys.Rev., 97, 561 (1955).
17. R.Slattery, D.Lu & M.Wiedenbeck, Phys.Rev., 96, 465 (1954).
18. A.Sunyar, Phys.Rev., 98, 653 (1955).
19. L.Shavtvalov, Zhur.eksp.i teor.fiz., 21, 1123 (1951).
20. H.De Waard & I.Gerholm, Physica, XXI, 599 (1955).
21. J.M.Blatt & V.F.Weisskopf, Theoretical Nuclear Physics, 1952 (in Russian translation, M.1954).
22. S.Moszkowsky, Phys.Rev., 89, 1071 (1951).
23. D.Hill & J.Wheeler, Phys.Rev., 89, 1102 (1953).
24. G.Scharff-Goldhaber & J.Weneser, Phys.Rev., 98, 212 (1955).
25. D.Speck & F.Jenkins, Phys.Rev., 101, 1831 (1956).
26. N.Heydenberg & G.Temmer, Phys.Rev., 100, 150 (1955).
27. P.Marmier & F.Boehm, Phys.Rev., 97, 103 (1955).
28. J.Jones & E.Jensen, Phys.Rev., 97, 1031 (1955).
29. K.Siegbahn, editor, Beta and Gamma-Ray Spectroscopy, 1955.
30. E.Ambler, R.Hudson & G.Temmer, Phys.Rev., 97, 1212 (1955).
31. R.Graham & R.Bell, Canad. J. Phys., 31, 377 (1953).

ALPHA-GAMMA DIRECTIONAL CORRELATION IN ThC''(Tl^{208})

- V.A.Korolev, L.A.Kul'chitskii & A.I.Zhernovoi

Introduction

Previous measurements of α-γ directional correlation in ThC-ThC'' in our laboratory[1] did not yield satisfactory results since the individual α-particle groups were not resolved, while the use of gas-filled counters made it impossible to obtain good statistics.

Weale[1] measured the α-γ directional correlation for the transition to the first excited level of ThC''. On the basis of the angular dependence

$$W(\theta) = 1 - (0.022 \pm 0.05)\cos^2\theta,$$

found by Weale in conjunction with other data obtained in investigating the decay of the preceding and succeeding nuclei, the following spin and parity assignments were made for the corresponding levels: 1^+ or 2^+, 4^+ and 5^+.

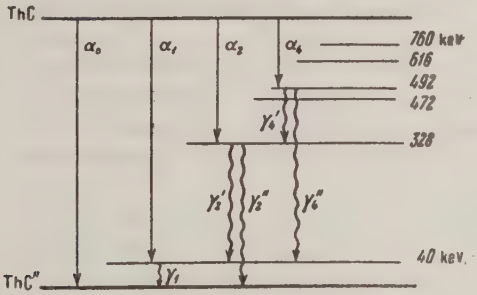

Fig.1. Energy levels of ThC'' (Tl^{208}) (only the more intense transitions are shown).

We investigated the α-γ directional correlation in the transitions to the second and fourth excited levels of ThC'' (Fig.1). The relative intensities of the transitions to these levels are 1.8 and 1.1%. The low intensity of these transitions and the presence in the thorium active deposit spectrum of a large number of additional γ-lines from ThB, ThC' and ThD make for experimental difficulties in measuring the angular correlations in question and require good separation of the α-particle or γ-ray lines.

Experimental procedure

A diagram of the apparatus is shown in Fig.2. The magnetic spectrometer separating the individual α-groups, provided a resolution (relative half-width) of ~0.5% with a transmission factor of nearly $8\cdot10^{-4}$ of the 4π solid angle. The α-particles were recorded by means of a scintillation counter with an anthracene crystal ~50 μ thick and a FEU-19 type photomultiplier; the γ-rays were recorded by means of a scintillation counter with an NaI(Tl) crystal.

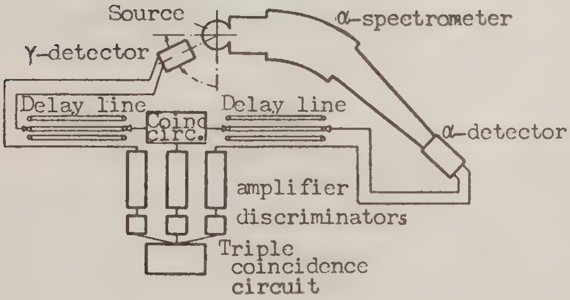

Fig.2. Diagram of apparatus.

The γ-counter crystal and the FEU-19 photomultiplier were shielded from the magnetic field of the spectrometer by means of a triple iron casing. Tests showed no change in the counting rate for γ-rays when the magnetic field was switched on or off.

The thorium active deposit was applied to one side of an aluminum foil measuring 10 x 1 x 0.007 mm. The output pulses from the photomultipliers, after shaping, were applied to a Rossi type fast coincidence circuit employing germanium diodes[3]. The resolving time of the coincidence circuit was ~$2\cdot10^{-8}$ sec. A suitable variable delay line was provided to compensate for the time of flight of the α-particle in the spectrometer and the difference between the times of passage of the pulses through the FEU-19 photomultipliers. The pulses from the first dynodes of the photomultiplier and from the fast coincidence circuit were amplified by an amplifier with a ~3 Mc pass band and a gain factor of 1000 and then, after discrimination, were fed into a triple coincidence circuit with a resolving time of $\sim 10^{-6}$ sec.

This fast-slow coincidence set-up made it convenient to set the appropriate discrimination level in each channel and register (scale) the coincidences as indicated by the level of discrimination in each channel and the pulse load in the individual channels.

Measurements and results

The measurements were affected by comparing a number of true coincidences at different angles with the number of coincidences at 180°. The coincidences were counted over time intervals (from 8 to 25 min) corresponding to a certain number of recorded α-particles and repeated numerous times in the direct and reverse directions in order to obviate corrections for decay and possible fluctuations in the operation of the electronic circuits.

The background of chance coincidences for the α_2 group was approximately equal to the number of true coincidences (at a counting rate of 3 true coincidences per minute); the background for the α_4 group was 1.5 times greater. The background was measured with the magnetic field in the spectrometer adjusted so as to record the α-particles of the principal group.

The total number of true coincidences recorded at each of the angles for the α_2-γ correlation was about 6000 on the average; the corresponding average value for the α_4-γ correlation was about 4000. An appropriate correction was made for the finite size of the solid angles and the eccentricity of the source (above 1%). The results were reduced to a unit solid angle.

Curves of the type

$$W(\theta) = 1 + AP_2(\cos\theta) + BP_4(\cos\theta),$$

where $P_n(\cos\theta)$ is the n^{th} order Legendre polynomial, were drawn through the resultant points by the method of least squares.

The following angular distributions (Figs.3 & 4) were obtained: $W_{exp}(\theta) = 1 - (0.063 \pm 0.017)\ P_2(\cos\theta) + (0.105 \pm 0.021)\ P_4(\cos\theta)$ for the α_2-γ correlation and $W_{exp}(\theta) = 1 - (0.083 \pm 0.016)\ P_2(\cos\theta)$ for the α_4-γ correlation.

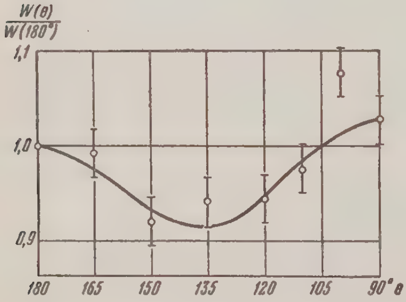

Fig.3. Directional correlation in the α_2-γ transition.

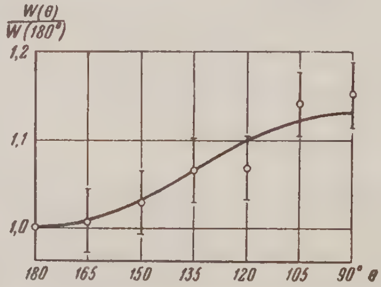

Fig.4. Directional correlation in the α_4-γ transition.

(Curves plotted by the method of least squares.)

Interpretation of the results

The experimental correlation curves were compared with the curves computed according to the theoretical expression of Biedenharn & Rose[4] for different combinations of the spins of the states, multipole orders of the γ-radiation and orbital moments of the α-particle. For the initial nucleus we tried two values of the angular momentum: 1^+ and 2^+. For the α_2-γ transition, we have two spin values for the final state: 4^+ and 5^+ (transition to the first excited level and to the ground state), while for α_4-γ we have only one value: 4^+ (the transition to the ground state is of very low intensity, while the transition to the second excited state is over discriminated).

In testing the combination $2^+ \rightarrow J \rightarrow 4^+$ (for α_4-γ), we found no theoretical function close to the experimental one. Among the $1^+ \rightarrow J \rightarrow 4^+$ combinations, the theoretical function coming closest to the experimental one was $W_{theo}(\theta) = 1 - 0.124\, P_2(\cos\theta)$ corresponding to $1^+ \rightarrow 3^- \rightarrow 4^+$ and E1 γ-radiation. The approximately 30% divergence between the theoretical and experimental functions can be explained by the fact that the correlation is reduced under the influence of the field of the atomic electron shell.

In addition, exact agreement with the experimental results can be obtained with the combination $1^+ \rightarrow 3^+ \rightarrow 4^+$ (here interference of the transitions with momenta 2 and 4 is possible for the α-particle), provided the γ-radiation is taken to be the mixture $M(1) + 0.001\, E(2)$ with a 180° phase difference.

Interpretation of the experimental results in the case of α_2-γ is complicated by the fact that two branches are involved: $1^+ \rightarrow J \begin{smallmatrix} \nearrow 4^+ \\ \searrow 5^+ \end{smallmatrix}$. Calculations for $J = 3^+$ yield almost exact agreement with the theoretical function, if it be assumed that 1) the ratio of the intensity of the electric quadrupole radiation to the intensity of the magnetic dipole radiation for the transition to the first excited level is 8 with a 180° phase difference, and 2) that the ratio of the intensity of the α-radiation with momentum 4 to the intensity of the α-radiation with momentum 2 is from 0.1 to 0.01 with different phases. Here the ratio of the intensities of the transitions calculated from the known coefficients of conversion equals 0.34. Under these assumptions we get

$$W_{theo}(\theta) = 1 - 0.063\, P_2(\cos\theta) + 0.090\, P_4(\cos\theta).$$

For $J = 5^+$, under the assumption that in the $J \rightarrow 4^+$ transition the γ-radiation consists of a mixture of M(1) and E(2) in the ratio $\delta^2 = 10$ with a 180° phase difference and that in the $J \rightarrow 5^+$ transition the radiation is purely quadrupole, the theoretical function is

$$W_{theo}(\theta) = 1 - 0.212\, P_2(\cos\theta) + 0.280\, P_4(\cos\theta).$$

Here the ratio of the intensities of the radiation in the $J \rightarrow 5^+$ transition to the intensity in the $J \rightarrow 4^+$ transition, calculated from the known conversion coefficients, amounts to 0.331. The disagreement with the experimental function, as in the case of α_4-γ may be due to partial removal of correlation. However the spin value 5^+ is doubtful in view of the following considerations. From the experimental correlation function for α_4-γ, the γ_4'' radiation (Fig.1) is identified as dipole. However, with spin values of 5^+ and $3^\pm$ for the second and fourth excited levels, the γ_4' radiation can only be M(2) or E(2). If this were the case, the intensity of the γ_4' radiation would be much lower than the intensity of γ_4'', whereas from an examination of the intensities of the conversion electrons for these lines it follows that the intensity of γ_4' is not less than that of γ_4''.

Conclusions

Our analysis leads us to the following conclusions.

Of the two possible values (1^+ or 2^+) for the spin of the ground state of

ThC(Bi^{212}) one must choose the former: 1^+.

The most probable assignment for the second excited level of ThC"(Tl^{208}) is 3^+. It may also be assumed that the γ-radiation is primarily E(2) with a small admixture of M(1). Regrading the characteristics of the fourth excited level we can only say that its spin is 3, but cannot definitively determine the parity. In this case the γ-radiation can be either M(1) or E(1).

Leningrad Physical-Technical Institute of the
Academy of Sciences of the USSR

References

1. L.Kul'chitskii, Doklady AN SSSR, 73, 1153 (1950).
2. J.Weale, Proc.Phys.Soc., 68, 35 (1955).
3. S.DeBenedetti & H.Riching, R.S.I., 23, 37 (1952).
4. L.Biedenharn & M.Rose, Rev.Mod.Phys., 25, 729 (1953).

USE OF A PULSE IONIZATION CHAMBER AS AN ALPHA-SPECTROMETER

- B.A.Bochagov, A.A.Vorob'ev & A.P.Komar

Design and Operation of the Chamber

The principle of operation of ion chambers with electron collection has long been familiar. Our chamber (Fig.1) consisted of a high voltage electrode 1, a grid 2, and a collecting electrode 3. The α-particle source was mounted on the high voltage electrode. If the range of an α-particle lies within the volume between the voltage electrode and the grid there are formed N = E/W ion pairs, where E is the kinetic energy of the α-particle and W is the mean energy expended on the formation of one ion pair.

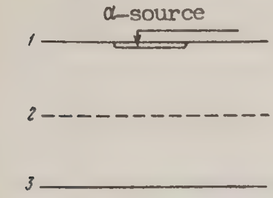

Fig.1. Arrangement of ion chamber.

The potentials on the high voltage electrode and grid should be such that recombination of the ions is precluded and passage of the electrons through the grid is insured.

Under the influence of the electric field the electrons drift towards the collecting electrode and after a certain interval t_1 (~1 microsec) are all collected on the electrode. Meanwhile the positive ions remain virtually stationary inasmuch as their mobility is almost 1000 times less than that of the electrons. The pulse on the collecting electrode is due exclusively to the electrons inasmuch as the collecting electrode is shielded by the grid from the influence of the charge of the positive ions. Hence the amplitude of the pulse on the collecting electrode is given by

$$V_1 = -\frac{Ne}{C_1},$$

where e is the electron charge and C_1 is the capacitance of the collecting electrode relative to the ground.

On the other hand, the amplitude V_2 of the pulse on the high voltage electrode is determined by the positive ions. It can be shown that

$$V_2 = \frac{Ne}{C_2}\left(1 - \frac{X}{d}\cos\varphi\right),$$

where d is the distance between the high voltage electrode and grid, X is the center of gravity of the ions over the track:

$$X = \frac{\int_0^R r\rho(r)\,dr}{\int_0^R \rho(r)\,dr}$$

(ρ(r) is the ion density over the track), φ is the angle between the direction of emission of α-particle and the normal to the electrodes and C_2 is the capacitance of the high voltage electrode relative to the ground.

The pulse on the grid is determined by the joint influence of the charges of the positive ions and electrons. Calculations show that the pulse on the grid at first rises to a certain negative value V_3 and then falls off, changes sign and towards the time t_1 becomes

$$V_4 = \frac{Ne}{C_3} \cdot \frac{X}{d}\cos\varphi.$$

For α-particles V_3 with good accuracy (~1%) is given by the expression

$$V_3 = -\frac{Ne}{C_3}\left(1 - \frac{R}{d}\cos\varphi\right),$$

where R is the α-particle range and C_3 is the capacitance of the grid relative to the ground. Thus the pulse V_1 on the collecting electrode is determined by the kinetic energy E of the α-particle, while the pulses V_2, V_3 and V_4 depend both on E and on cos φ.

Hence simultaneous measurement of V_1 and V_2, V_3 or V_4 can give the energy E of the α-particle and the angle between the direction of ejection of the α-particle and the normal to the surface of the electrodes. This circumstance can be utilized for solving a number of physical problems and, in particular, those of α-spectroscopy.

Utilization of the Apparatus for Measurement of α-Particle Energies

From what has been said above it will be obvious that the pulses from the collecting electrode can be used to measure the energy of α-particles.*

Let us examine the various possible sources of error in determining E and evaluate the resolving power of the apparatus. The resolution is characterized by the half-width of the α-spectrum lines, which is related to δ (the root mean square deviation of V_1) by the formula: half-width = 2.35δ.

A. δ_1 - RMS deviation in the number of ion pairs

This error is connected with the fluctuation in the number of ion pairs formed by an ionizing particle and is therefore intrinsic to all ionization methods. There are as yet no accurate data regarding the magnitude of δ_1. However, it is commonly assumed[4] that

$$\delta_1 = \sqrt{0.3 \cdot N},$$

where N is the number of ion pairs produced. For the case of argon ionized by 5 Mev α-particles, this gives δ_1 = 6.6 kev (which corresponds to half-width of 16 kev).

B. δ_2 - RMS deviation due to tube noise in the preamplifier

Inasmuch as the pulses appearing on the collecting electrode are small (~1 mv), they must be amplified. Hence the noise in the first stages of amplification becomes an important factor.

There are a number of publications[5,6] in foreign literature devoted to the design of preamplifiers with a low noise level. The best results were obtained by Engelkemeir & Magnusson[5], in whose design δ_2 = 10 kev (half-width = = 23.5 kev).

We succeeded in reducing δ_2 to 7.7 kev, which corresponds to a line half-width of 18 kev.

C. δ_3 - RMS deviation due to losses in the source

Alpha-particles emitted in the lower layers of the source lose part of their energy passing through the upper layers, the loss obviously being greater for greater angles of rejection relative to the normal. In order to reduce this error to a minimum one should record only α-particles emitted at angles close to the normal. For the source used in our investigations δ_3 was evaluated to be 2 kev (equivalent half-width - 5 kev).

---

*This method is widely used for measuring the kinetic energy of both α-particles and fission fragments. See, for example, Refs. 1-3.

Adding the above errors according to the square law we obtain

$$\delta = \sqrt{\delta_1^2 + \delta_2^2 + \delta_3^2} = 10.5 \text{ kev}$$

which corresponds to a line half-width of 25 kev.

Acceptance of the Instrument

If no collimation is used the chamber records about 50% of the emitted α-particles. In order to improve the resolution, however, it is necessary to collimate the α-particles. Hitherto this has been accomplished only by means of a mechanical collimator. Such collimators have two serious shortcomings: 1) the entire area of the source is not fully utilized, which reduces the effective transmission and 2) part of the ions forming in the openings of the collimator do not reach the collecting electrode, which impairs the resolution.

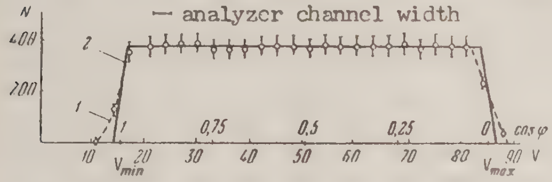

Fig.2. Differential distribution of negative pulses from the grid for 8.8 Mev α-particles from ThC': 1) experimental curve, 2) theoretical curve taking the channel width into account.

Utilizing the possibility of simultaneous measurement of the angle of emission and the energy of the α-particles one can introduce collimation without recourse to a mechanical collimator.

It can be shown that in the case of an isotropic distribution of α-particles of some given energy, the differential distribution in height of the pulses (V_3, for example) will be of the form shown in Fig.2, where the vertical scale is laid off both in amplitudes of V_3 in volts and in values of cos φ; cos φ and V_3 are linearly related. Pulses with the minimal amplitude V_{min} correspond to α-particles emitted perpendicularly to the surface of the electrodes, while the pulses with the maximum amplitude V_{max} correspond to α-particles emitted parallel to the electrode surface. It follows that collimation can be introduced by recording pulses V_1 in coincidence with pulses V_o in the interval $V_{min} < V_3 < V_o \leqq V_{max}$. Obviously, one can vary the degree of collimation by changing the value of V_o.

Instead of V_3 one can also utilize the pulses V_2 or V_4. With this method of collimation the acceptance is reduced by not more than a factor of 3-4 and amounts to 10-15%. It is interesting to compare these data with the data for magnetic spectrometers. The acceptance of the best magnetic spectrometers is only ~0.02%. In most cases, however, the efficiency of spectrometers is determined not simply by the acceptance but by the quantity Φ = IS (the transmission), where I is the transmission factor of the instrument and S is the area of the source.

In magnetic spectrometers S is usually about 0.1 cm^2. In an ionization chamber, in contrast, the area of the source is not limited in principle (for example, we used a source having an area of 75 cm^2).

From this it will be seen that the transmission in an ionization chamber is some 5-6 order of magnitude greater than in a magnetic spectrometer, which makes it possible to investigate the α-spectra of elements with a long period (low intensities), such as U^{238} and Th^{232}. Despite the much higher transmission, the resolution of the chamber is only 3-4 times lower than that of a magnetic spectrometer.

One of the great advantages of ionization chamber is the possibility of using it in conjunction with a multiple-channel pulse height analyzer, which makes it feasible to record all the points of the spectrum simultaneously and

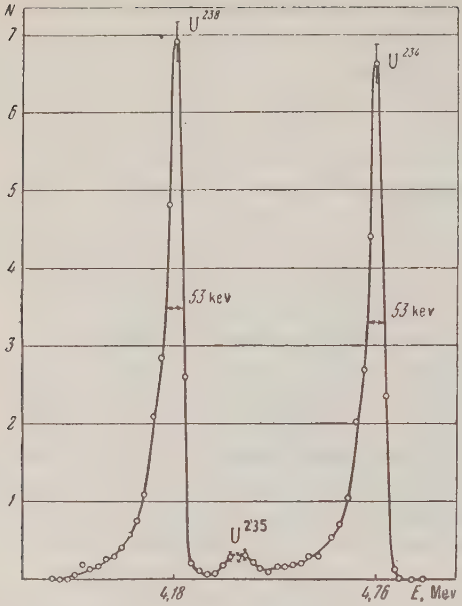

Fig.3. Spectrum of a natural mixture of uranium isotopes obtained without collimation.

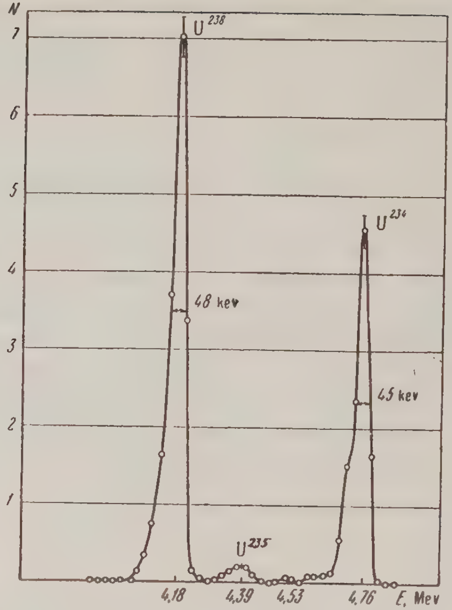

Fig.4. Spectrum of a natural mixture of uranium isotopes recorded with a channel gate of 24 kev.

under identical conditions. This is an important consideration in studying the spectra of α-emitters with a very short period (of the order of minutes, seconds or even milliseconds). Hence a pulse ionization chamber can be used for investigating the spectra of α-emitters having a wide range of lifetimes.

The spectrum of a natural mixture of uranium isotopes recorded without collimation is shown in Fig.3. The total recording time for this spectrum was 8 min.

Fig.4, above, shows how use of the above described collimation procedure improves the shape of the spectrum. The counting rate with collimation was reduced by a factor of only 3. It must be noted that the figure does not show the true relative intensities of the lines inasmuch as the degree of collimation used for U^{234} was greater than for U^{238}. It will be seen from a comparison of Figs.3 and 4 that the use of collimation sharply reduced the low-energy tails and made it possible to bring out the second group of α-particles from U^{235}. The line of U^{234} obtained under the same conditions as the spectrum of Fig.3 but with a narrower channel width is shown in Fig.5.

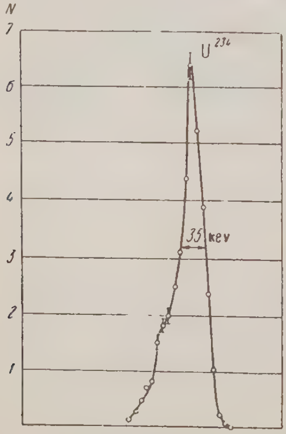

Fig.5. Spectrum of U^{234}; channel width - 8 kev.

As may be seen in Fig.5, the half-width of the line is 35 kev. We attribute this deviation from the expected 25 kev half-width to the instability of the loop oscillograph used for pulse height analysis and to somewhat inadequate shielding of the grid.

There is, however, another factor inherent in the effect that mitigates against resolution of the fine structure. Part of the group of low energy α-particles is accompanied by conversion electrons which produce additional ionization in the chamber. Consequently, the pulses corresponding to such α-particles are stronger than for the other α-particles of this group.

In order to eliminate the conversion electrons we plan to place the chamber in a constant magnetic field. Under the influence of the magnetic field conversion electrons will be returned to the source without producing noticeable ionization in the volume of the chamber. We believe that this arrangement should make it possible to investigate the rotational levels of α-emitters.

Use of the Apparatus for Investigating α-γ Correlation

Inasmuch as the chamber allows of simultaneous measurement of the energy and angle of emission of α-particles, it can obviously be utilized for investigating α-γ correlation. To this end one need only record the differential distribution of one of the pulses V_2, V_3 or V_4 in coincidence with pulses from a suitable scintillation counter arranged to detect photons emitted perpendicularly to the surface of the electrodes. This method for studying α-γ correlation was first used by Valladas et al[7]. They employed a two-electrode chamber; hence their method is applicable when there is only one group of α-particles.

Usually, however, there are several α-particle groups present. One can separate any one of the groups by using coincidences with pulses V_1 corresponding to the group. Fig.2 shows the differential distribution of the pulses V_3 from the grid in coincidence with pulses V_1, corresponding to the energy of 8.8 Mev α-particles from ThC'. It will be seen that the experimental points lie close to the theoretical curve (in the given case the α-particle distribution is isotropic). The error in measuring $\cos \varphi$ is not over 3%.

Let us again make a comparison with magnetic spectrometers. Just as in the case of α-particle measurements, in the case of angular correlation studies the efficiency of an ionization chamber can be 4-5 orders of magnitude greater than that of a magnetic spectrometer. Moreover, the ionization chamber does not require the use of such complicated technical equipment as fast coincidence circuits, provision for field stabilization, etc.

This indicates that not only can an appreciable saving of time be realized by using an ionization chamber instead of a magnetic spectrometer for studying α-γ correlation but also that it should be possible to investigate correlation in elements not susceptible of such studies by means of magnetic spectrometers.

The writers desire to thank S.N.Nikolaev for valuable advice and help in designing and adjusting the electronic equipment.

Leningrad Physical-Technical Institute of the
Academy of Sciences of the USSR

References

1. J.L.Fower & L.Rosen, Phys.Rev., 72, 926 (1947).
2. I.S.Wahl, Phys.Rev., 95, 126 (1954).
3. S.Baranov & K.Shliagin, Sessiia AN SSSR po mirnomu ispol'zovaniiu atomnoi energii (Meeting of the USSR Ac. of Sci. on the Peaceful Uses of Atomic Energy), P.251, 1955.
4. U.Fano, Phys.Rev., 70, 44 (1946).
5. D.Engelkemeir & L.Magnusson, Rev.Sci.Instr., 26, 295 (1955).
6. O.Buneman, T.Granshaw & J.Harvey, Can. J. Res., 27,A, 191 (1949).
7. G.Valladas, I.Teilac, P.Falk-Vairant & P.Benoist, J. de Phys., 16, 125 (1955).

INVESTIGATION OF THE SHORT-LIVED ISOMERS Y^{88*} AND Pb^{206*}

- I.A.Kondurov, L.I.Rusinov & V.B.Cherniaev

At present only a few nuclear isomers with half-lives in the range from 10^{-5} to 10^{-1} sec are known.

Commonly short lifetimes ($<10^{-4}$ sec) are determined by the method of delay coincidences. This method is applicable, however, only to the investigation of isomeric states resulting from β- or α-decay; it is ineffective in the range of times of interest to us because of the strong background from chance coincidences.

Recently a number of investigators have begun to use the pulsed radiation source method for investigating short-lived isomers. In conjunction with pulse height and time analyzers this method holds great promise for the investigation of metastable states with lifetimes in the range of 10^{-5} to 10^{-1} sec.

It must be noted in connection with the recent contribution by Mazets & Rusinov[1] that in the case of isomers with the indicated periods the transitions must either quadrupole with low excitation energies (10-100 kev) or octupole with relatively high energies (>0.5 Mev). Thus, it may be assumed that isomers with an intermediate transition energy must have lifetimes outside the indicated interval. Moreover, in the case of electric quadrupole transitions the presence of collective rotational levels[2] leads to a reduction of the lifetime of the isomers ($<10^{-5}$ sec), while in the case of octupole transitions the lifetime may be appreciably increased due to deformation of the nucleus ($>10^{-1}$ sec). It should also be noted that the observed lifetime for quadrupole transitions with low energies prove to be shorter than the times of interest to us due to the large internal conversion coefficient.

Thus the relatively small number of isomers with lifetimes in the 10^{-5} to 10^{-1} sec interval may be connected with the intrinsic properties of atomic nuclei rather than due to inadequacies of present-day measurement procedures.

In view of this we felt it would be of interest to investigate nuclear isomers with half-lives in the 10^{-5} to 10^{-1} sec range.

Apparatus

The pulsed γ-radiation source used in the investigation was the LFTI (Leningrad Physical-Technical Institute) 100 Mev synchrotron with a repetition frequency of 50 cps and an effective Bremsstrahlung pulse width of 15 microsec. The γ-ray pulses were used to irradiate the target containing the investigated element. The induced γ-activity was detected by an NaI(Tl) crystal coupled to an FEU-19 type photomultiplier. The decay of the induced activity in the investigated target was studied by means of a multiple channel time selector. The γ-spectra of the investigated isomers were investigated by means of a pulse height analyzer.

A block diagram of the set-up is shown in Fig.1. The pulses from the output of the FEU-19 photomultiplier 1, after preamplification (in 2) are fed through a 75 meter cable to the linear amplifier 3 that has a signal rise time of 0.1 microsec and an amplification factor of 40. The bilateral clipping and shaping of the pulses, necessary for the following units of the circuit, is effected in the differential pulse height analyzer 4. Both in the case of recording gamma energy spectra and in determining lifetimes, the investigated part of the distribution is separated out from all the pulses coming from the amplifier 3.

In investigating γ-spectra, the selected pulse height range was subdivided into ten parts corresponding to the ten principal channels of the time selector. With the apparatus operated in this way (selector switch in the block diagram in position 1), the unit 5 converts the pulse heights into times (i.e., pulse durations) which are measured by the time selector assembly 6-10. To this end the

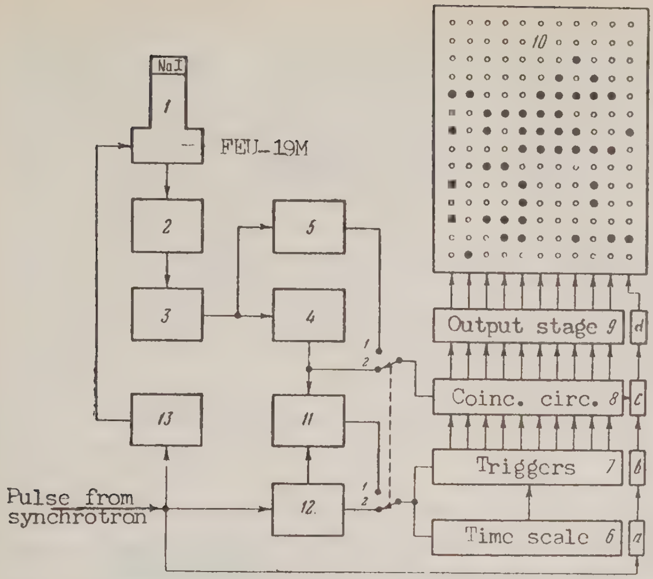

Fig.1. Block diagram of apparatus: 1) NaI(Tl) crystal and FEU-19M photomultiplier, 2) preamplifier, 3) linear amplifier, 4) single channel discriminator, 5) pulse height-time (width) converter, 6) time interval signal generator, 7) square "channel" pulse unit, 8) signal and "channel" pulse coincidence circuit, 9) circuit shaping the recorded pulses, 10) information unit, 11) pulse circuit determining the effective (measurement) part of the period, 12) variable delay generator, 13) modulating circuit for blocking the FEU-19M photomultiplier.

pulse from unit 4, through the blocking circuit 11, actuates the "time" scale 6 and simultaneously the first trigger (a vacuum tube relay with two stable positions) of the network 7 comprising ten triggers, where a succession of equal time intervals is produced. Coincidence in unit 8 of a delayed (in proportion to the magnitude of the measured signal) pulse from unit 5 with one of these time intervals produces a recording pulse in the corresponding channel of the output unit 9.

In measuring half-lives of nuclei the interaction of the circuit components is different. In this case (selector switch in position 2), the channels of the time selector and the "time scale" 6 are gated by a signal from unit 12, delayed any desired time with respect to the γ-radiation pulse from the synchrotron. Now the coincidence circuit 8 receives pulses from unit 4, corresponding to the investigated part of the energy spectrum. The blocking circuit 11 makes it possible to select pulses for amplitude discrimination over a definite time interval. This operating (measuring) time interval can be set for any part of the period of the synchrotron pulses. In order to avoid overloading the amplifier, during this interval the photomultiplier is blocked by a square signal of 150 v from the modulator 13. The last is triggered analogously to the delay generator 12.

The control channel - a,b,c,d - is provided for measuring the background due to long-lived activities; the duration (width) and position of this channel on the time scale can be set as called for by the requirements of the experiments.

The information unit 10 consists of 11 identical binary counter tanks designed about MTKh-90 thyratrons; it has a capacity of 16,383 pulses for each channel. The basic parameters of the set-up are the following. The pulse height analyzer is linear with an accuracy of ±2% to 90 v. The maximum counting rate is 2000 periodic pulses per second. The minimal channel width is 2 v. The gate of the time selector channel can be set in steps of 5, 10, 16, 20, 30 and 150 microsec. The uncertainty in time connected with determination of the effective width of the channel does not exceed 0.1 microsec. Pulse distributions characterizing the interaction of the principal components of the set-up are shown in Fig.2.*

---

*Detailed description of this part of the work will be published later.

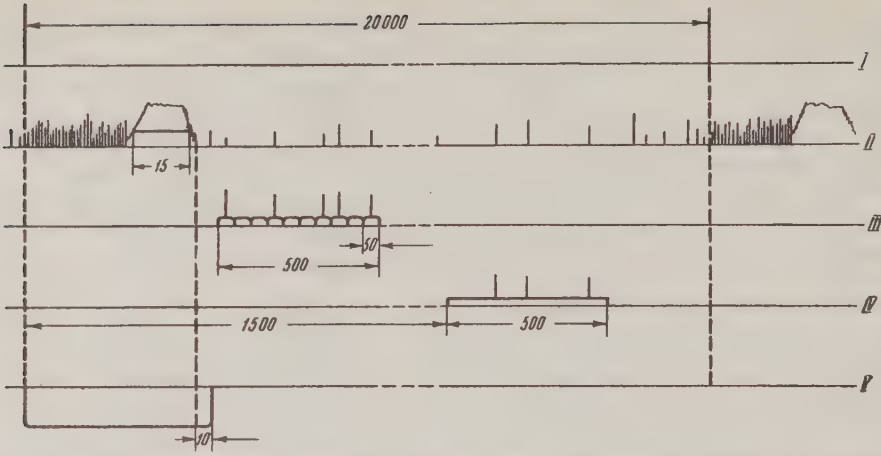

Fig.2. Distribution in time of pulses at different points in the time analyzer circuit in measuring half-lives: I) triggering pulses from synchrotron, II) γ-ray beam and pulses from amplifier without modulation of the FEU-19M photomultiplier, III) pulses on the coincidence circuit input, IV) pulses in the control channel, V) photomultiplier modulation.

Procedure and results

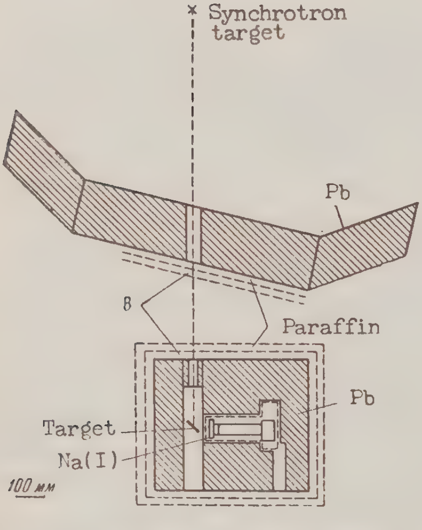

Fig.3. Diagram of experiment.

During the experiments the crystal and photomultiplier were surrounded by a layer of lead 200 mm thick and were located at a distance of 1.5 meters from the accelerator target. There was also a 200 mm thick lead wall between the synchrotron and the crystal-photomultiplier (Fig.3). The γ-ray beam was collimated twice by lead collimators; the first (40 mm diameter, 100 mm thick) was located 1 meter from the photomultiplier; the second (30 mm diameter, 100 mm thick) was situated next to the lead shielding. The first collimator and the lead shielding were covered with a layer of paraffin and boron. The irradiated target was inserted at an angle of 45° into the γ-ray beam from the synchrotron.

The factors affecting the separation in energy of the investigated γ-spectra and impairing the accuracy of determining the half-lives under the conditions of our experiment are the appreciable background from extraneous reactions (slow neutron capture and the reactions γ-γ', γ-n, γ-2n, etc.) and the direct influence of the synchrotron γ-pulses on the detector. The last leads to a dead time of about 30-50 microsec after each γ-pulse. There is reason to assume that this is connected with the reaction of the FEU-19 photomultiplier to the signal from unit 13 (see Fig.1) by which it is modulated for the purpose of avoiding overloading the recording system at the instant of the synchrotron γ-pulse. In addition, the scattered photons of the beam produce phosphorescence in the crystal, which falls off with 2 decay rates: one of the order of 100-200 microsec, the other $>$1000 microsec. The first excitation has a high phosphorescence pulse density which leads to

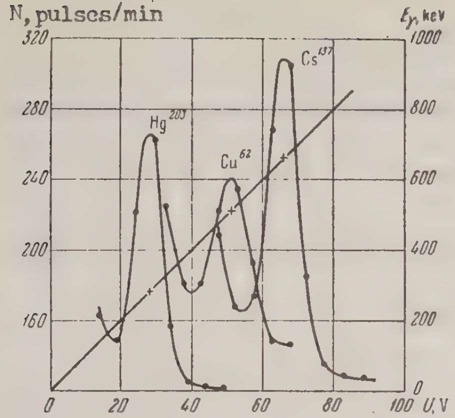

Fig.4. Calibration curves for the scintillation α-spectrometer.

additional measurement errors. The influence of phosphorescence can be weakened either by reducing the thickness of the investigated target, but unfortunately both these measures lead to an increase in the relative intensity of the background. The background from extraneous reactions in our measurements amounted to an appreciable percent of the recorded pulses and fell off with a (half-life) period of about 200 microsec.

For calibrating the scintillation spectrometer we used the 280 kev γ-line of Hg^{203}, the 661 kev γ-line of Cs^{137} and the annihilation radiation from Cu^{62} (Fig.4). It was noted that modulation of the photomultiplier displaces the spectral peaks somewhat to the side of lower energies.

By way of elements for investigation of short-lived isomers we chose yttrium and lead. We carried out a series of experiments in preparing these isomers by means of photonuclear reactions. The lifetimes of the metastable states were measured by means of the time analyzer.

The measurements of the half-life of Pb^{206*} were carried out with a lead target which was irradiated in the synchrotron at a maximum Bremsstrahlung energy of 70 Mev.

In the preliminary experiments the induced activity was measured by means of a GM counter which was surrounded by a lead cylinder with 7 mm thick walls and placed in the γ-beam from the accelerator. The half-life value obtained for the lead was 140±10 microsec.

As noted above in the main experiments the γ-activity was detected by means of an NaI(Tl) crystal coupled to an FEU-19M photomultiplier. In investigating the short-lived isomeric states of lead the target was a plate having a superficial density of 1.5 g/cm^2.

The half-life of Pb^{206*} was measured in the interval of energies from 200 to 900 kev inasmuch as according to the data of Alburger & Pryce[3] the decay of the metastable of Pb^{206*} with an excitation energy 2.2 Mev is accompanied by cascade transitions having energies ranging from 203 to 880 kev. From the measurements by means of the time selector we obtained a value of $T_{1/2}$ = 145±10 microsec (Fig.5) for Pb^{206*} which was most probably produced by the Pb^{207} (γ,n) Pb^{206*} reaction. Our value of the half-life agrees with the data of Alburger & Pryce[3] who studied the 6.4-day K-capture of Bi^{206} by the method of delayed coincidences.

In the yttrium experiments the target was prepared of yttrium nitrate and

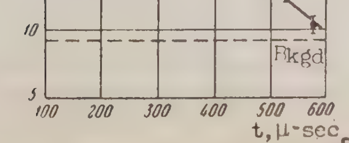

Fig.5. Decay curve for Pb^{206*}.

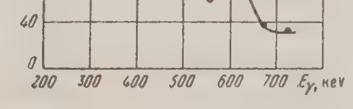

Fig.6. Spectra: I) γ-radiation from Y^{88*} and II) annihilation radiation from Cu^{62}.

had a thickness of 2.1 g/cm^2. The γ-spectrum obtained is shown in Fig.6. The energy of the γ-transition proved to 400±30 kev.

Next we measured the lifetime of the metastable state of Y^{88*} with an excitation energy of 100 kev, obtained as a result of the Y^{89} (γ,n) Y^{88*} reaction. The half-life was found to be 280±15 microsec (Fig.7). Hyde, Florence & Larsh[4] give a value of 370±30 microsec for the half-life of Y^{88*} obtained as the result of K-capture by Zr^{88} (85-day). Our value, however, is in agreement with the period reported by Vegors & Axel[5].

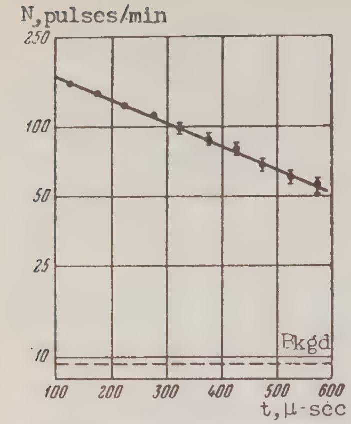

Fig.7. Decay curve for Y^{88*}.

Our results and the data on conversion[3,4] give reason to assume that the transitions from the metastable states of Y^{88*}(E_γ = 400 kev) and Pb^{206*} (E_γ = 500 kev) are E3. The ratios of the lifetimes obtained experimentally (taking into account the internal conversion coefficients) to the lifetimes computed according to the formulas of Moszkowsky[6] are 0.2 for Y^{88*} and 3.2 for Pb^{206*}. The relatively moderate divergence of these ratios from unity is apparently due to the fact that these nuclei have nucleon numbers close to the critical values.

To evaluate the integral cross section for the formation of Y^{88*} we measured the ratio of the yields of the $Y^{89}(\gamma,n)Y^{88*}$ and $Cu^{63}(\gamma,n)Cu^{62}$ (10 min) reactions on the basis of the areas under the photopeaks (400 kev for Y^{88} and 510 kev for Cu^{62}) (Fig.6) taking into account the Compton part of the spectra. The measurements for both elements were performed with the same geometry. As calculations showed, more than 90% of the positrons formed in the decay of Cu^{62} are absorbed in a target 2.7 g/cm^2 thick. This made it possible to utilize annihilation radiation for determining the yield of the $Cu^{63}(\gamma,n)Cu^{62}$ reaction. The ratio of the yields of these reactions taking into account the minor influence of Cu^{64} positrons was found to be

$$N_Y/N_{Cu} = 0.8 \pm 0.1.$$

In order to calculate the integral cross section for the formation of Y^{88*} from the above yield ratio one must know the variation of σ_Y as a function of E, the energy of the Bremsstrahlung gammas. For an approximate evaluation of the cross section it may be assumed that the function $\sigma_Y = \sigma_Y(E)$ does not differ appreciably from the corresponding function for copper. This is substantiated by the relatively close values of the reaction thresholds and energies corresponding to the maximum photonuclear reaction cross sections for the elements in the middle part of the periodic table[7]. On the basis of this assumption evaluation of the cross section for the formation of the metastable state of yttrium by the $Y^{89}(\gamma,n)Y^{88*}$ reaction yields

$$\int \sigma_Y(E)\,dE = 0.5 \text{ Mev barn}.$$

The value of the integral cross section for the formation of Cu^{62} (0.66 Mev barn) is taken from Ref.7.

In addition we carried out experiments on the excitation of the metastable states of S, Ge, Ag and Sn by photonuclear reactions. No induced activities within the 10^{-5}-10^{-1} sec lifetime interval were detected.

The writers desire to thank A.P.Komar for making the synchrotron available for the experiments and N.N.Charnov and his group for preparing and adjusting the synchrotron.

Leningrad Physical-Technical Institute of the
Academy of Sciences of the USSR

References

1. E.Mazets & L.Rusinov, Doklady AN SSSR, 101, 253 (1955).
2. A.Bohr & B.Mottelson, Dan.Mat.Fys.Medd., 27, 16, 3 (1953).
3. D.Alburger & M.Pryce, Phys.Rev., 95, 1482 (1954).
4. Hyde, Florence & Larsh, Phys.Rev., 97, 1255 (1955).
5. S.Vegors & P.Axel, Phys.Rev., 101, 1067 (1956).
6. S.Moszkowsky, Phys.Rev., 89, 474 (1953).
7. R.Montalbetti, L.Katz & J.Goldenberg, Phys.Rev., 91, 659 (1952).

BULLETIN of the Academy of Sciences of the USSR - Physical Series
Vol.20, No.12(a) - Transactions of the Sixth All-Union Conference on
Nuclear Spectroscopy (Moscow, 26-30 January 1956)

TABLE OF CONTENTS

	Page Orig.	Page Trans.
Gamma-radiation from Zn^{65} - B.S.Dzhelepov, V.P.Prikhodtseva, A.I.Feoktistov & Iu.V.Khol'nov	1359	1243
Gamma-spectrum of As^{76} - B.S.Dzhelepov, V.P.Prikhodtseva, A.I.Feoktistov & Iu.V.Khol'nov	1361	1245
Investigation of Coulomb excitation of nuclei by nitrogen ions - D.G.Alkhazov, D.S.Andreev, A.P.Grinberg & I.Kh.Lemberg	1365	1249
Influence of charge distribution in the nucleus on angular correlation in β-decay - A.Z.Dolginov & I.N.Toptygin	1377	1260
Numerical values of the K-electron functions determining the probability of allowed and forbidden K-capture - I.M.Band, L.N.Zyrianova & Tsin Chen-Zhui	1387	1269
On the role of the pseudoscalar form of interaction in the theory of β-decay - L.N.Zyrianova	1399	1280
Experimental evaluation of a new two-lens β-spectrometer and improvement of its annular focusing - Ia.I.Gaziev, K.P.Mitrofanov & V.S.Shpinel'	1407	1288
Decay scheme of Ne^{23} - V.M.Ovchinnikov, Iu.A.Nemilov, M.L.Aleksandrova & I.I.Lomonosov	1417	1297
Measurements of γ-γ coincidences in the spectra of Ir^{192} and Sb^{124} - L.L.Pelekis	1419	1298
A combined beta and gamma spectrometer - M.P.Glazunov & V.I.Spitsyn	1423	1302
A two-crystal scintillation γ-spectrometer - E.L.Stoliarova & I.E.Konstantinov	1430	1308
Use of a pulse ionization chamber for investigating α-γ angular correlation - Iu.I.Filimonov & G.A.Petrov	1434	1311
Lifetimes of excited states of nuclei in the rare-earth element group - E.E.Berlovich	1438	1315

Alpha-gamma directional correlation in ThC"(Tl^{208})
- V.A.Korolev, L.A.Kul'chitskii & A.I.Zhernovoi 1451 1327

Use of a pulse ionization chamber as an α-spectrometer
- B.A.Bochagov, A.A.Vorob'ev & A.P.Komar 1455 1331

Investigation of the short-lived isomers Y^{88*} and Pb^{206*}
- I.A.Kondurov, L.I.Rusinov & V.B.Cherniaev 1461 1336

Translated in 1957 by
Columbia Technical Translations
5 Vermont Avenue, White Plains, N.Y.

Transactions of the Eighth All-Union Conference on Semiconductors (Leningrad, November 15-21, 1955)

The Eighth All-Union Conference on Semiconductors, called by the Commission on Semiconductors of the Presidium of the USSR Academy of Sciences was held from the 14th through the 20th of November 1955 in Leningrad.

Specialists from different scientific research and pedagogical institutions of the Soviet Union as well as a number of scientists from the Peoples' Democracies participated in the work of the Conference. In all, 142 reports were presented at the Conference, most of them being heard at Section meetings.

Some of the Conference reports have already been published in the form of individual articles in the "Zhur. Tekh. Fiz." (Journal of Technical Physics) and in the Doklady of the USSR Academy of Sciences.

The principal papers presented to the Section on "Electric and Thermal Properties of Semiconductors" are published in the present issue of the Bulletin (Izvestiia) of the USSR Academy - Physical Series. The transactions of the Sections on "Theory of Semiconductors", "Chemistry and Metallurgy of Semiconductors" and "Semiconductor Catalysis and Surface Effects in Semiconductors" will be published in Nos. 1 and 2 of Volume 21 of the Bulletin. The most important transactions of the Sections on "Semiconductor Electronic Devices", "Photoelectric Effects in Semiconductors" and "Magnetic Properties in Semiconductors" will be published in the eighth and following numbers of "Radiotekhnika i Elektronika" (Radio Engineering and Electronics) for 1956 and into 1957.

Commission on Semiconductors
of the
Presidium of the USSR Academy of Sciences

THERMAL EQUILIBRIUM OF ELECTRONS ON SURFACE AND VOLUME LEVELS IN A SEMICONDUCTOR

- V.E.Lashkarev

Introduction

In recent years there have appeared a number of reports with descriptions of effects proving the existence of surface electronic states in semiconductors; these proofs have been obtained in investigating such phenomena as the change in the conductivity of semiconductors incident to adsorption[1-3] and under the influence of external (transverse) electric fields[2-6], changes in the work function due to adsorption[1-3], the influence of adsorption on photoconductivity[7-10], the influence of the degree of dispersion of the semiconductor on the sign of the concentration of dark current carriers[11,12] and the effect of an external field on the photo-emf[13-15].

Nevertheless, despite the progress made in this field, there is much that still remains obscure regarding the energy configuration of the surface levels and of the influence of adsorption upon it. We feel that this is primarily due to the fact that the problems connected with the equilibrium of electrons on surface and volume levels have not been discussed as fully as necessary. A contribution by Pikus[16] on the subject is concerned only with the particular case of one surface band.

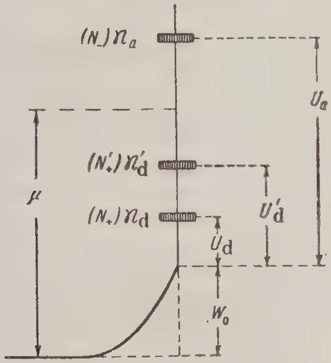

Fig. 1

In the present report we shall attempt to fill in this gap. We shall examine the most general scheme of surface states both band and local. For the sake of simplicity of mathematical operations, however, we impose the restriction that both the surface and the volume levels are so weakly ionized that the degree of their ionization can be found from the Boltzmann distribution.

We shall refer to the scheme of surface levels shown in Fig.1. We assume the semiconductor to be of the p-type; $\mathfrak{N}_a$ is the concentration of acceptor surface levels; $\mathfrak{N}_d$ and $\mathfrak{N}'_d$ are the concentrations of donor levels. The concentrations of electrons on the surface acceptor levels are denoted through N_-, the vacancies on the donor levels are designated through N_+ and N'_+, respectively. The heights of the levels are reckoned from the top of the volume hole band and are expressed in kT units. Fig.1 corresponds to the presence of an antibarrier layer in the volume. The hatched areas represent the regions of space charge. In the depth of the semiconductor the space charge equals zero; W is the potential (in kT units), μ is the distance from the Fermi level to the top of the hole band in the depth of the semiconductor.

The calculations for the concentration $N_\pm$ which we shall carry out below are also valid for the case of surface bands. In the presence of two surface bands U_a should be interpreted as the height of the bottom of the empty band and U_d as the height of the top of the filled band; in this case $\mathfrak{N}_a$ should be replaced by B_- and $\mathfrak{N}_d$ by B_+, where

$$B_\pm = T_\pm \frac{2\pi m^\pm_{ef}\, kT}{h^2}\,. \qquad (1)$$

Here $T_\pm$ is a weight factor ($T \geqslant 2$), and $m^\pm_{ef}$ are the effective masses of free electrons and holes in the surface bands; in this case, N_+ and N_- will prove to be the concentrations of the free holes and electrons at the surface. The local levels $\mathfrak{N}'_d$ will be sticking levels for surface holes. One can, of course, consider only one surface band as a particular case.

With this formulation of the problem, surface conductivity of the metallic type is automatically excluded.

As for the volume energy scheme of a semiconductor, basic calculations will be carried out for the case of weak ionization of the hole band and local levels. The results can readily be generalized to the case of fully ionized acceptor levels in the volume of the semiconductor.

Hereinafter we shall assume that the semiconductor is "thick", i.e., satisfies the familiar criterion

$$\varkappa\alpha \gg 1,$$

where $\varkappa$ is the screening length defined by the equality

$$\frac{1}{\varkappa} = \left(\frac{\varepsilon kT}{8\pi e^2 p n^0}\right)^{1/2},$$

wherein n^0 is the concentration of holes in the depth of the specimen and p is the sticking factor for holes:

$$p = 1 + \frac{\mathfrak{N}_{st}}{Q} e^{U_{st}}. \tag{2}$$

Here

$$Q = T\left(\frac{2\pi m_{ef} kT}{h^2}\right)^{3/2}, \tag{3}$$

m_{ef} is the effective mass of the holes in the volume, $\mathfrak{N}_{st}$ is the concentration of volume sticking levels and U_{st} is the height of these levels.

Obviously, in the case of thick specimens the processes on both surfaces of the semiconductor can be considered independently of each other.

1. Calculation of the concentrations

In addition to the surface concentrations N we shall also have to calculate the volume concentrations integrated over the thickness of the specimen. Let us agree to call these specific concentrations and designate them by the subscript e.

The specific concentration of holes is made up of

a) the specific concentration of $n^0_e = n^0 d$, corresponding to the absence of space charge, and

b) of an additional specific concentration connected with the presence of space charge (distortion of the band):

$$n_e = n^0 \int_0^\infty (e^W - 1)dx = \frac{2n^0}{\varkappa}(e^{\frac{W_0}{2}} - 1) = \beta(e^{\frac{W_0}{2}} - 1), \tag{4}$$

where $\beta = \frac{2n^0}{\varkappa}$.

The specific space charge concentration is

$$\nu_e = n^0 p \int_0^\infty (e^W - e^{-W})\,dx = p\beta(e^{\frac{W_0}{2}} - e^{-\frac{W_0}{2}}). \tag{5}$$

From (4) we obtain the auxiliary formula

$$e^{\frac{W_0}{2}} = \frac{1}{\beta}(n_e + \beta). \tag{6}$$

Invoking Boltzmann's equation, we can immediately write the expressions for

$$N_+ = \alpha_+ e^{W_0}, \tag{7a}$$

$$N'_+ = \alpha'_+ e^{W_0} \tag{7b}$$

and

$$N_- = \alpha_1 e^{-W_0}, \tag{7c}$$

where

$$\alpha_+ = \mathfrak{N}_d e^{U_d - \mu}; \quad \alpha'_+ = \mathfrak{N}'_d e^{U'_d - \mu}; \quad \alpha_- = \mathfrak{N}_a e^{\mu - U_a}.$$

As for μ, it can be found from the relationship

$$e^{\mu} = \frac{Q}{n^0}. \tag{8}$$

For determining e^{W_0}, we must utilize the neutrality relationship.

Let us assume for our case that the semiconductor plate is one plate of a capacitor; let us further assume that the second plate is metallic and is charged negatively with a surface charge density N_M. Then the condition for neutrality of the capacitor as a whole will have the form

$$N_+ + N'_+ - N_- + \nu_e = N_M. \tag{9}$$

Substituting the concentration values from (5) and (7) into Eq.(9), we get

$$(\alpha_+ + \alpha'_+) e^{W_0} - \alpha_- e^{-W_0} + p\beta \left(e^{\frac{W_0}{2}} - e^{-\frac{W_0}{2}}\right) = N_M. \tag{9a}$$

Thus for determining e^{W_0} we have obtained a fourth power algebraic equation, which it may be useful to investigate for certain particular cases.

Let us assume that the capacitor is not charged ($N_M = 0$):

a) there are no surface levels (all the α's are zero); in this case there is no distortion of the bands;

b) there are present on the surface only acceptor levels producing a "strong" antibarrier layer ($W_0 \gg 1$), then it follows from the equality that

$$\alpha_- e^{-W_0} = p\beta e^{\frac{W_0}{2}} \text{ and } e^{W_0} = \left(\frac{\alpha_-}{p\beta}\right)^{2/3},$$

further we have

$$N_- = \mathfrak{N}_a^{1/3} \left(\frac{\varepsilon kT}{4\pi e^2}\right)^{2/3} Q^{1/3} p^{1/3} e^{-1/3 U_a}, \tag{10}$$

and

$$n_e = N_- p^{-1}; \tag{11}$$

if $p = 1$ the variation of n_e with temperature will be determined only by the arrangement of the surface levels;

c) there are so many surface levels and they are so located that

$$N_+ + N'_+ \gg \nu_e \quad \text{and} \quad N_- \gg \nu_e.$$

In this case neutrality is assured primarily by the distribution of electrons on the surface. Let us assume for the sake of simplicity that $N_+ \gg N'_+$. Then the neutrality condition is reduced to the equality $N_+ = N_-$, whence

$$e^{W_0} = \left(\frac{\alpha_-}{\alpha_+}\right)^{1/2}. \tag{12}$$

If $\alpha_- > \alpha_+$, we obtain an antibarrier layer on the boundary of the semiconductor; if $\alpha_- < \alpha_+$ we obtain a barrier layer. Further we have

$$N_+ = N_- = (\mathfrak{N}_a \mathfrak{N}_d)^{1/2} e^{-1/2 (U_a - U_d)} . \tag{13}$$

From (12) and (7b) it follows that

$$N'_+ = \mathfrak{N}'_a \left(\frac{\mathfrak{N}_a}{\mathfrak{N}_d} \right)^{1/2} e^{-1/2 (U_a + U_d - 2U'_d)} . \tag{14}$$

Finally substituting (12) in (4) we also find n_e. Let us write out the final expression only for the case of a strongly pronounced antibarrier layer ($n_e \gg \beta$):

$$n_e = \left(\frac{\varepsilon kT}{8\pi e^2} \right)^{1/2} Q^{1/2} \left(\frac{\mathfrak{N}_a}{\mathfrak{N}_d} \right)^{1/4} e^{-1/4 (U_a + U_d)} . \tag{15}$$

For purposes of comparison let us write the familiar expression for n^0 with $p = 1$:

$$n^0 = Q^{1/2} \mathfrak{N}_0^{1/2} e^{-1/2 U_0} . \tag{16}$$

Here $\mathfrak{N}_0$ is the concentration of the acceptor levels in the volume and U_0 is their height (energy).

If as a result of the presence of a positive surface charge on the boundary there is created a strong barrier layer ($|W_0|/2 \gg 1$), then, as follows from (4)

$$n_e = -\frac{2n^0}{\varkappa} ,$$

i.e., n_e becomes independent of further distortion of the band. This case is not likely to arise in practice and will not be further examined here.

2. "Longitudinal" and "transverse" conductivities of semiconductors

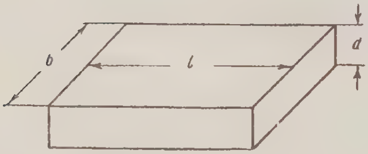

Fig. 2.

Let us take a semiconductor in the form of a thin plate as shown in Fig. 2. Let us assume that $l, b \gg d$. By applying electrodes to the end faces bd, we can readily measure the longitudinal conductivity of the sample. Again applying appropriate electrodes with guard rings to the faces bl, we can measure the transverse conductivity. In both cases we can obtain the mean specific conductivity: the longitudinal $|\sigma_2|$ and the transverse $|\sigma_1|$.

Investigating cuprous oxide samples the writer and Liashenko[17] showed that σ_2 can be a hundred or more times greater than σ_1. Moreover, the activation energy of σ_1 proved to be appreciably smaller (by as much as a factor of two). The reason for these differences will become clear from what follows.

In measuring the longitudinal conductance k_2 of the specimen, this can be regarded as composed of the volume conductance k^V corresponding to a homogeneous semiconductor with a hole concentration n^0, the "superficial" or "quasisurface" conductance k^{VS} connected with the presence of a volume (space) charge and, finally, the surface band conductance k^S (assuming, of course, that the last is present). We note that $k^{VS} > 0$ if the layer is an antibarrier one, and $k^{VS} < 0$ if the layer is a barrier; k^{VS} is localized on the effective screening length (cf. (Ref. 18) $1/\varkappa^*$ where

$$\varkappa^* = \varkappa \operatorname{ch} \left(\frac{W_0}{2} \right) . \tag{17}$$

Incidentally, utilizing (6) for a well pronounced antibarrier layer ($W_0/2 \gg 1$), we have:

$$\varkappa^{*} = \frac{2\pi e^{2} p}{\varepsilon k T} n_{e}, \tag{17a}$$

where n_e determined from the Hall effect[1]. Hence

$$k_{2} = k^{\mathrm{S}} + k^{\mathrm{VS}} + k^{\mathrm{V}}. \tag{18}$$

If the concentrations of free electrons and holes on the surface are N_- and N_+, respectively, and the mobilities are U_-^{S} and U_+^{S}, then

$$k^{\mathrm{S}} = \frac{b}{e} e (U^{\mathrm{S}} N_{-} + U_{+}^{\mathrm{S}} N_{+}). \tag{19}$$

For k^{V} and k^{VS}, we have

$$k^{\mathrm{V}} = \frac{b}{e} e U_{+} n_{e}^{0} \tag{20}$$

and

$$k^{\mathrm{VS}} = \frac{b}{e} e U'_{+} n_{e}. \tag{21}$$

In general U'_+ need not be equal to U_+ in view of the fact that the superficial layer will contain a different concentration of scattering ionized centers. Moreover, if $1/\varkappa^*$ is very small - of the order of the mean free path - there may obtain additional scattering from crystal defects near the surface (defects produced by machining or other mechanical treatment of the crystal) and also at the surface itself. The last effect has been examined in Ref.19.

Obviously measurement of the longitudinal conductance is particularly suitable for investigation of antibarrier layers near the surface of a semiconductor. In the presence of an antibarrier layer the transverse conductance may yield information on the volume properties of the semiconductor. The transverse conductance is given by

$$k_{1} = \frac{hl}{\varkappa'} enn^{0},$$

where α' is the thickness of the sample reduced by the sum of the thicknesses of the antibarrier layers on its surfaces.

Both the absolute values of σ_2 and σ_1 and their temperature dependences may differ appreciably from each other. This fact may be utilized for investigating surface electronic states (see below).

3. Modulation of the conductance by an external (transverse) electric field

On the basis of published reports on the subject we can establish the following facts.

1. A negative charge on the metallic plate of the capacitor increases the conductance of the semiconductor plate if this is made of a hole semiconductor, and decreases it if it is an electron conductor. A positive charge on the metallic plate produces the opposite effects.

2. The effective change in conductance $\gamma = \Delta k/\alpha$ is always smaller than the change calculated on the assumption that the entire charge of the semiconductor is due only to the change in the number of current carriers present in it.

This discrepancy is usually explained by the presence of surface electronic states, the charge of which changes under the influence of the external field but which, being bound, does not change the conductance of the specimen (field screening by the surface levels).

Another explanation, considered by the present writer in Ref.17, amounts to the assumption of a surface relief. In Ref.17, however, it was tacitly implied that the relief is always convex, i.e., consists of a series of projections, as shown schematically in Fig.3a. In this case the electric field would be concentrated on the projections and the change in conductance may not penetrate into

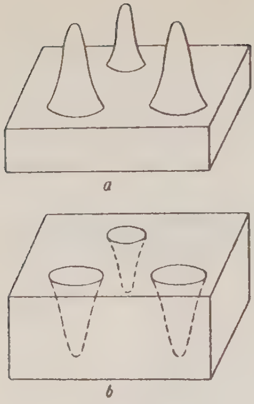

Fig.3

the region of the semiconductor where the current measured in finding the conductance flows. The conditions when the effect of the convex relief should be small were indicated in Ref.17.

Actually the relief may be concave as shown in Fig. 3b. The relief of the concave type (micropores) would not substantially change the concentration of the additional current carriers appearing under the influence of the transverse field. If the micropores are sufficiently numerous, however, they could substantially reduce the mobility of the carriers provided, of course, an appreciable part of the conductivity of the sample is localized at the depth of the micropores. Generally speaking, a concave relief should not introduce the serious complications into investigations of the modulation of conductance by a transverse field that may be expected in the case of a convex relief. Which of the two types of relief obtains in a given case will undoubtedly depend on the treatment to which the semiconductor surface has been subjected. It is doubtful whether one can eliminate a convex relief entirely on the surface of finely dispersed polycrystalline specimens. It can be reduced to a minimum by using single crystals cut to retain all or most of the crystal faces.

In what follows we will neglect the influence of relief and moreover will assume that $p = 1$. Let us examine a number of specific cases.

A. Absence of surface band conductance

The levels $\mathfrak{N}_a$ and $\mathfrak{N}_d$ are local levels. It follows from (20) and (21) that

$$\gamma = \frac{\Delta k}{k} = \frac{\Delta n_e}{n_e^0 + n_e}, \tag{22}$$

where Δn_e is the increment in concentration under the influence of the external field.

The maximum possible value of the depth of modulation of the conductance is obtained when we have $\Delta n_e = N_M$. Then

$$\gamma = \frac{N_M}{n_e^0 + n_e}. \tag{23}$$

The equality $\Delta n_e = N_M$ can be realized in a p-type semiconductor only in the case of ionization of the volume acceptor levels and the absence of surface levels.

Let us call the ratio $\eta = \gamma_M/\gamma$ the modulation attenuation factor and see what happens with η in different cases.

Let us assume that the modulation depth is small, i.e., that $\Delta n_e \ll n_e^0 + n_e$ and $\Delta W_0 \ll 1$. Let us return to Eq.(9a). If hereinafter under W_0 we understand the limiting value of W with no field (i.e., when $N_M = 0$), then the increment in the left-hand side of Eq.(9a) will be equal to N_M. We will have

$$\left[(\alpha_+ + \alpha'_+)\, e^{W_0} + \alpha_- e^{-W_0} + \frac{1}{2}\, p\beta \left(e^{\frac{W_0}{2}} + e^{-\frac{W_0}{2}}\right)\right] \Delta W_0 = N_M. \tag{24}$$

It follows from (4) that

$$\Delta n_e = \frac{1}{2}\, \beta e^{\frac{W_0}{2}}\, \Delta W_0. \tag{25}$$

Expressing $e^{\pm\frac{W_0}{2}}$ in terms of n_e from (6) in Eq.(25) and the third term in (24) and invoking (7), we finally obtain

$$\eta = 2\,\frac{N_+ + N'_+ + N'_-}{n_e + \beta} + p\,\frac{(n_2 + \beta)^2 + \beta^2}{(n_e + \beta)^2}. \tag{26}$$

Let us now examine the particular cases considered in section 2 above.

a) No surface levels present: $N_+ = 0,\ n_e = 0.$

$$\eta = 2p. \tag{27}$$

It appears that $\eta = 2$ even in the case when there are no special sticking levels for the holes. This is connected with the fact, noted earlier by the author, that the acceptor levels themselves are also sticking levels for holes, capable, in the case of weak filling, of localizing additional holes in the amount of 50%.

Let us now turn to the case of a sharply pronounced antibarrier layer $|n_e \gg \beta|$, for this

$$\eta = p + 2\frac{N_+ + N'_+ + N_-}{n_e}. \tag{28}$$

b) Only acceptor levels exist on the surface, i.e., $N_+ = N'_+ = 0$.

It follows from neutrality condition that $N_- = \nu_e \approx p_{n_2}$. Then from (28) we have

$$\eta = 3p. \tag{29}$$

If $p = 1$, then in this case the modulation attenuation factor is small.

c) Both types of levels are present in so high a concentration that both $N_+ + N'_+$ and $N_- \gg \nu$, whence

$$N_+ + N'_+ \approx N_- = N.$$

We then have

$$\eta = p + 4\frac{N}{n_e}, \tag{30}$$

i.e., η, even with $p = 1$, can be very large. If $\frac{4N}{n_e} \gg p$, then

$$\eta = 4\frac{N}{n_e}. \tag{31}$$

As for the temperature dependence of the attenuation factor, it may be noted that with $p = 1$ it is absent in cases "a" and "b". In case "c", on the contrary, a temperature dependence always obtains. Below we will assume $p = 1$.

Using Eqs. (13) and (15) for case "c", we obtain

$$\eta \approx e^{-1/4\,(U_a - 3U_d)}. \tag{32}$$

The distinctive feature of this expression is that not only the magnitude but also the sign of the change of η with temperature depends on the energy "relief" of the surface layers only. The temperature dependence can readily be found provided $n_e \gg n_e^0$. In this case

$$\gamma = \frac{1}{4}\cdot\frac{N_M}{N}. \tag{33}$$

Whence, invoking (13), we have

$$\gamma = \frac{1}{4}\cdot\frac{N_M}{(\mathfrak{N}_a\mathfrak{N}_d)^{1/2}}\,e^{1/2\,(U_a - U_d)}. \tag{34}$$

Inasmuch as U_a is always greater than U_d, γ decreases with increasing temperature. Liashenko's experiments have shown that this is always true. It follows from Eqs. (33) and (34) that in principle it should be possible to determine U_a and U_d separately. The temperature dependence of σ_2 in the case when surface conductivity predominates can also be utilized for determining U_a and U_d. From (15) and (21) it follows that

$$\sigma \approx n_e \approx e^{-{}^1/_4(U_a + U_d)}. \tag{35}$$

B. Presence of a dominating surface band conductivity

The sign of the change in the surface conductivity under the influence of an external field will, obviously, be the same as that of the change in volume conductivity; consequently, the character of the surface conductivity, just as that of the volume conductivity, can be determined from the sign of its modulation by an electric field. We shall limit our examination to pure hole conduction, assuming the level $\mathfrak{N}_d$ to be a band one and the $\mathfrak{N}_d'$ and $\mathfrak{N}_a$ levels to be local.

In our case the "surface" γ and η can be written as

$$\gamma_s = \frac{\Delta N_+}{N_+} \quad \text{and} \quad \eta_s = \frac{N_M}{\Delta N_+}. \tag{36}$$

Utilizing Eqs. (7), (9) and (24) in which we assume $\gamma_e = 0$ we obtain

$$N_M = (N_+ + N_+' + N_-)\,\Delta W; \quad \Delta N_+ = N_+ \Delta W, \quad N_+ + N_+' = N_-$$

From which it follows that

$$\gamma_s = \frac{N_M}{2(N_+ + N_+')} \quad \text{and} \quad \eta_s = 2\,\frac{N_+ + N_+'}{N_+}. \tag{37}$$

Thus great attenuation of the modulation of conductivity (η_s large) can be obtained only in the case when $N_+' \gg N_+$, i.e., due to surface sticking levels. In this case $\gamma_s = N_M/2N_+$.

Let us examine this case in more detail. The final expressions for γ_s and N_+ ($\sim k^s$) have the form

$$\gamma_s = \frac{N_M}{2(\mathfrak{N}_a \mathfrak{N}_d')^{1/2}}\, e^{(U_a - U_d')}, \tag{38a}$$

$$N_+ = B_+ \left(\frac{\mathfrak{N}_a}{\mathfrak{N}_d}\right)^{1/2} e^{-{}^1/_2(U_a + U_d' - 2U_d)}. \tag{38b}$$

It can readily be seen that the sign of the changes of γ_s and k^s with temperature is the same as in the case of quasisurface conductivity.

4. Influence of adsorption

Adsorption of polar molecules on hole semiconductors is accompanied by two effects:

a) a decrease in the surface conductivity and

b) a reduction of the work function ($\Delta\varphi$), indicating that the surface becomes more electropositive incident to adsorption.

The hypothesis of quasisurface conductivity makes it possible not only to obtain the correct sign of $\Delta\varphi$ but also to deduce its magnitude. In Cu_2O, where surface conductivity dominates both in vacuum and in the presence of adsorption, there obtains strong antibarrier distortion of the bands, the magnitude of which can be determined from the equality

$$n_e = \frac{2n_0}{\varkappa}\, e^{\frac{W}{2}}. \tag{39}$$

Then for the change in work function due to adsorption we have

$$\Delta\varphi = 2\,\frac{kT}{e} \ln \frac{n_e'}{n_e''}; \tag{40}$$

where n'_e and n''_e are the values of n_e in vacuum and after adsorption, respectively.

According to Liashenko[17], n'_e / n''_e attains 10, which gives $\Delta\varphi$ = 120 mv, i.e., a value agreeing with that measured by Liashenko.

The assumption of band-type (zonal) surface conductivity does not lead to such a clear relationship. It can be shown that a change in the energy "relief" (field distribution) of the surface levels, leading to a reduction of the concentration of surface holes by a certain factor, can, in this case, be accompanied by different changes of the surface charge, i.e., by different changes in the work function. However, if we assume that adsorption does not produce any changes in position and concentration of the levels in the surface band, then $\Delta\varphi$ will prove to be two times smaller than in the case of quasisurface conductivity. This follows from Eqs.(38) and (39).

The decreases in surface conductivity incident to adsorption may be caused by two factors: a) the decrease in the concentration of the acceptor surface levels or an increase in their energetic height (deactivated acceptor levels) and b) an increase in the concentration of donor levels or, again, an increase in their energetic height (activated donor levels).

Both causes, in addition to reducing the conductivity, will also lead to a decrease in the work function and, hence, will be indistinguishable. It may, however, be possible to identify the operative or predominant cause from the influence of adsorption on the modulation of conductivity by an electric field.

Earlier it was shown that in the presence of strong screening there are present both acceptor and donor levels at the surface. Let us examine this case. Let us rewrite (15) and (34) in the following form:

$$n_e \approx e^{-1/4[U_a - \ln \mathfrak{N}_a]} e^{-1/4[U_d + \ln \mathfrak{N}_d]}, \text{ and } \gamma \approx e^{+1/2[U_a - \ln \mathfrak{N}_a]} e^{-1/2[U_d + \ln \mathfrak{N}_d]}. \tag{41}$$

The expressions in the brackets contain separately the influence on the conductivity (n_e) and γ of the distributions of the acceptor and donor levels. It can readily be seen the change in the distribution of the donor levels yields a change having the same sign where n_e and γ are concerned. On the contrary, a change in the distribution of the acceptor levels yields changes of n_e and γ having opposite signs.

As Liashenko informed us adsorption on cuprous oxide at low vapor pressures of the adsorbed substance always leads to an increase in γ with a simultaneous decrease of n_e. This indicates that in a given case the adsorption acts on the acceptor levels, rather than on the donor ones, i.e., serves to deactivate the acceptor levels.

An analogous situation would obtain in the case of surface band conductivity.

Conclusions

To investigate the distribution (energy "relief") of surface layers and changes in this distribution under the influence of adsorption, it is necessary to study the temperature dependence of the surface conductivity in conjunction with changes in this conductivity under the influence of external fields.

If attenuation of the modulation of conductivity by an electric field is very great, this means that there are present at the surface both acceptor levels and localized donor levels in high concentrations.

Comparison of the activation energy for the surface conductivity and the extent of its change under the influence of an external field should make it possible to determine the energetic heights of the former and latter levels. Comparison of the sign of the change in the surface conductivity as a result of adsorption and its modulation by an electric field should make it possible to determine which levels (donor or acceptor) are affected by the adsorption.

Physical Institute of the
Ukrainian SSR Academy of Sciences

References

1. V.E.Lashkarev & V.I.Liashenko, in "Sbornik, posviashchennyi 70-letiiu Akad. A.F.Ioffe." (Symposium dedicated to the 70th anniversary of Academician A.F.Ioffe), M. 1950.
2. V.I.Liashenko & N.I.Stepko, Izv. AN SSSR, Ser.fiz., 16, 210 (1952).
3. V.I.Liashenko, Trudy (Transactions) Institute of Physics, Ukrainian SSR Ac. of Sci., No.4, 33 (1953).
4. W.Shockley & C.Pearson, Phys.Rev., 74, 232 (1948).
5. K.Zuckler, Z.S.f.Phys., 136, 40 (1953).
6. S.G.Kalashnikov & A.E.Iunovich, Zhur.tekh.fiz., 25, 952 (1955).
7. V.I.Liashenko, Doklady AN SSSR, 87, 33 (1952).
8. E.D.Putseiko, Doklady AN SSSR, 91, 1071 (1953).
9. V.I.Liashenko & O.V.Snitko, Trudy (Transactions), Institute of Physics, Ukrainian SSR, Ac. of Sci.), No.5, 65, (1953).
10. V.I.Liashenko, O.V.Snitko & I.M.Semeniuchenko, Trudy (Transactions), Institute of Physics, Ukrainian SSR Ac. of Sci.) No. 5, 77 (1954).
11. S.G.Kalashnikov & Ia.E.Pokrovskii, Zhur.tekh.fiz., 22, 888 (1952).
12. Ia.E.Pokrovskii, Zhur.tekh.fiz., 24, 1229 (1954).
13. E.K.Putseiko, Doklady AN SSSR, 59, 471 (1948); 67, 1004 (1949); Izv. AN SSSR, Ser.fiz., 16, 34 (1952).
14. V.E.Lashkarev, Doklady AN SSSR, 70, 813 (1950).
15. V.E.Lashkarev, Trudy (Transactions) Institute of Physics, Ukrainian SSR Ac.of Sci.), No.3, 3 (1952).
16. G.E.Pikus, Zhur.eksp.i teor.fiz., 21, 1227 (1951).
17. V.E.Lashkarev & V.I.Liashenko, Doklady AN SSSR, 106, 243 (1956).
18. V.E.Lashkarev, Izv. AN SSSR, Ser.fiz., 16, 203 (1952).
19. J.R.Schrieffer, Phys.Rev., 97, 641 (1955).

THERMOELECTRIC EFFECTS IN SEMICONDUCTORS WITH NONEQUILIBRIUM CURRENT-CARRIER CONCENTRATIONS

- Ia.Tauts

1. Dependence of the thermo-emf on the temperature gradient

Processes involving a change in the concentration of current carriers in a semiconductor play an important part in the operation of p-n junction rectifiers and transistors. Obviously such processes must also occur in connection with thermoelectric effects.

Investigation of the influence of nonequilibrium concentrations on thermoelectric effects is thus a natural extension of the theory of such processes to semiconductors with a temperature gradient. We were impelled to the present investigation of these effects, however, not by the above theoretical considerations but by the need for interpreting the experimental facts described below.

Back in 1952, in connection with some work on germanium, we noted that powdered germanium always gives a positive thermo-emf regardless of whether the pulverized material was of the p- or the n-type; similar observations have been reported by Kalashnikov and Pokrovskii[1]. In attempting to explain this effect we noted that the individual powder particles make contact over small areas so that the temperature differential is concentrated at the grain boundaries. In order to produce similar conditions on the surface of a germanium single crystal, we measured the thermo-emf in the following manner: a cold tungsten needle point was brought into contact with an n-type germanium crystal that was heated to a temperature T". After an appropriate interval a temperature T' was established at the point of contact of the tungsten point. The variation of a T' as a function of T" was determined experimentally. The dependence of the measured thermo-emf U on T' and T" is shown by curve a in Fig.1. This temperature variation differs appreciably from the variation of the thermo-emf obtained for flat electrodes with the same temperature difference $\Delta T = |T'' - T|$ (curve b in Fig.1). The additional thermo-emf, shown by curve c, is due to the transfer of holes from points with a high temperature and, consequently, a higher hole density (i.e., the bulk of the crystal) to the point with a lower temperature and, consequently, a lower concentration of holes, i.e., to the point of contact with the tungsten needle. There is thus formed on the germanium surface under the needle a p-n junction which holds back electrons but passes holes. These holes build up a positive charge on the needle and thus change the sign of the measured thermo-emf. Calculations, given in Ref.2, lead to the following expression for this additional thermo-emf:

$$\Delta U = 2\pi r_0 k T' \mu_p R \left[p_r(T'') - p_r(T') - \Delta T \left(\frac{\partial p_r}{\partial T} \right)_{T'} \right].$$

here r_0 is the radius of the contact which is assumed to be spherical, μ_p is the hole mobility, p_r is the equilibrium hole concentration, $\Delta T = T' - T''$ is temperature difference and R is the contact resistance. This expression is valid when $\Delta T \ll T'$ and $p_r \ll n_0$, where n_0 is the equilibrium electron concentration.

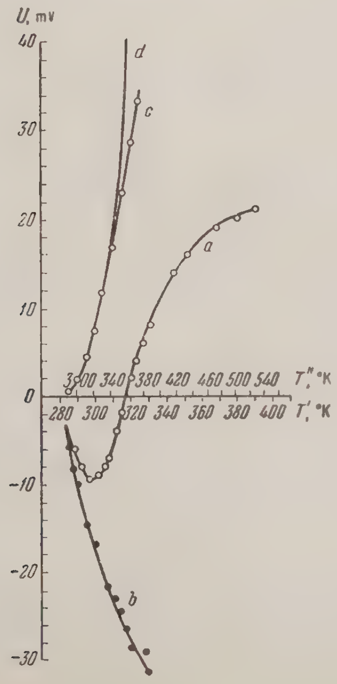

Fig. 1.

As may be seen from Fig.1 the theoretical curve d is in good agreement with the experimental curve c in the interval of not excessively high temperatures.

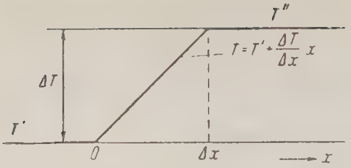

Fig. 2.

This experiment clearly shows that the thermo-emf in a semiconductor can depend on the temperature gradient. In the given experimental arrangement the potential barrier near the point of contact plays an important part. Later we turned our attention to simpler cases in which potential barriers can play no part. It was found that in these cases, too, the thermo-emf can depend on the temperature gradient. For this one must produce conditions such that the temperature drop occurs over distance comparable to or smaller than the diffusion length L_p of the minority carriers.

Such conditions obtain, for example, when the temperature distribution in a semiconductor is such as that shown in Fig.2. Calculations, carried out by the writer^3, show that with $\Delta x \ll L_p$, $p_r \ll n_0$ and $\Delta T \lll T$ the concentration of minority current-carriers in the vicinity of the temperature differential region differs substantially from the equilibrium concentration. In the region $0 < x < \Delta x$, it is constant and equal to

$$p = \frac{p_r(T') + p_r(T'')}{2}; \tag{1}$$

hence the hole concentration is lower than the equilibrium value at the point $x = \Delta x$ and higher than the equilibrium value at the point $x = 0$. As we move away from this interval the carrier concentration approaches the equilibrium value:

$$\begin{aligned} &\text{for}\quad x > \Delta x, \quad \Delta p = p - p_r = -\frac{p_r(T'') - p_r(T')}{2}\, e^{-\frac{x-\Delta x}{L_p}};\\ &\text{for}\quad x < 0, \quad \Delta p = p - p_r = \frac{p_r(T'') - p_r(T')}{2}\, e^{\frac{x}{L_p}}. \end{aligned} \tag{2}$$

This deviation from the equilibrium concentration leads to the appearance of an additional emf, given by the formula

$$\Delta U = \frac{k\Delta T}{2e}\left[\frac{Q_n^x + Q_p^x}{kT} + (b-1)\right]\frac{p_r(T'') - p_r(T')}{bn_0}, \tag{3}$$

where $b = \frac{\mu_n}{\mu_p}$, Q_n^x and Q_p^x are the values of the mean kinetic energy brought in by one carrier.

For a nondegenerate semiconductor

$$Q^x = \frac{\int\limits_0^\infty l(E)\, E^2 e^{-E/kT}\, dE}{\int\limits_0^\infty l(E)\, E e^{-E/kT}\, dE}, \tag{4}$$

where $l(E)$ is the mean free path of a carrier of energy E.

This additional voltage ΔU is usually small compared with the normal thermo-emf. It differs from the latter by the fact that it increases much more rapidly with temperature (at very small temperature differentials ΔT, ΔU_0 is proportional to $(\Delta T)^2$). For example, for germanium with $n_0 = 10^{14}$ cm^{-3} at $\Delta T = 30°$ ($T' = 270$°K and $T'' = 300$°K), ΔU = 0.63 mv, while when ΔT is doubled ($T'' = 330$°K), ΔU = 5.3 mv and when ΔT is tripled ($T'' = 360$°K), ΔU = 21 mv.

For experimental proof of the existence of this additional thermo-emf it is expedient to select conditions under which the normal thermo-emf is compensated. This can be realized by providing a temperature distribution such as that shown in Fig.3. Here the semiconductor has two temperature drop regions. One of them has a length l' appreciably greater than the diffusion length for holes; the length of the second is less than the diffusion length; the ends of the semiconductor are at the same temperature. With this arrangement the first temperature differential does not produce the additional thermo-emf and only the ΔU due to the second temperature difference is evinced and can thus be measured.

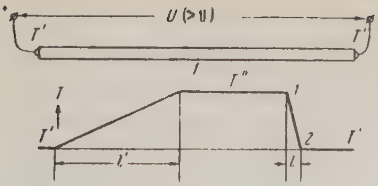

Fig. 3.

Benedix used an analogous procedure in his experiments on determining the dependence of the thermo-emf on the temperature gradient. In contrast to the arrangement in his experiments, in our case the potential is appreciably greater and can readily be measured.

The existence of the predicted effect has recently been proved by Trousil[4]. He cut a thin plate from a germanium single crystal; this plate was cut almost in two; the two parts were connected only by a thin neck (Fig.4). One part was in contact near the neck with a copper block A which was cooled with ice, while the other part was heated by block B to a temperature T''. Thus there was a sharp temperature drop across the neck. The remote ends 3 & 4 of the plate were maintained at the same temperature.

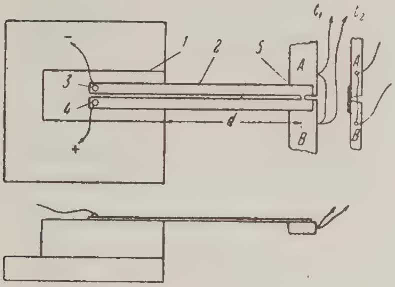

Fig. 4.

The experimental results are shown in Fig.5. The symmetrical arrangement shown was used in order to reduce the normal thermo-emf associated with inhomogeneities of the specimen to a minimum. With a small temperature difference ΔT the additional potential is small and the measuring instrument shows only the normal thermo-emf. However, the additional potential rises rapidly with temperature and soon predominates.

We believe that these experiments prove the existence of the so-called Benedix effect, i.e., the existence of a temperature gradient dependent thermo-emf in semiconductors with current-carriers of both types.

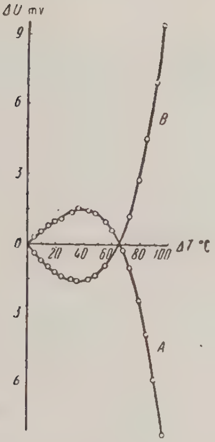

Fig. 5.

2. Thermal photoeffect

A nonequilibrium concentration of holes can also be produced by other means; for example, by illuminating the semiconductor. If at the same time we produce a temperature gradient in the semiconductor, there appears a new effect which we have called the thermal photoeffect. Briefly, if a semiconductor is homogeneous and maintained at a constant uniform temperature, no photo-emf appears when it is exposed to light. However, if the temperature over the length of the semiconductor varies, its properties become different. When such a semiconductor is illuminated there develops a photo-emf just as in the case of illumination of an inhomogeneous semiconductor. We carried out calculations[5] of the thermal photo-emf with the temperature distribution shown in Fig.6. In order to avoid taking into account the influence of the contacts, the temperature differentials were assumed to be inside the semiconductor in the illuminated and nonilluminated regions.

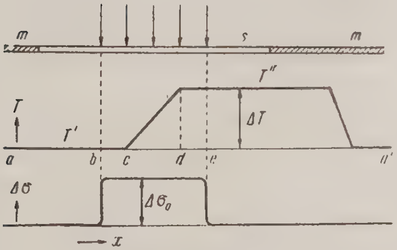

Fig. 6.

According to our calculations with weak illumination in the case of an n-type impurity semiconductor this photo-emf is given by

$$\Delta U = \frac{k\Delta T}{e}\left[\frac{b-1}{b+1} - \frac{1}{b+1}\left(\frac{Q_n^x + Q_p^x}{kT} - 3\right)\right]\frac{\Delta\sigma}{\sigma_0}, \tag{5}$$

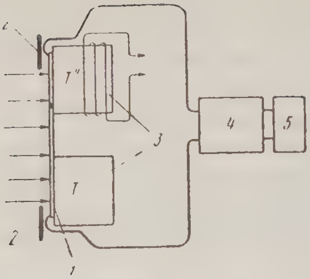

Fig. 7.

where $\sigma_0 = e\mu n_0$ is the dark conductivity of the semiconductor; $\Delta\sigma = e\ (\mu_n + \mu_p)\Delta n$ is the change in the conductivity under the influence of light. Having measured ΔU, we can determine the sum $Q_n^x + Q_p^x$ from this expression. The importance of these qualities lies in the fact that in some cases it is sufficient to know this sum in order to be able to determine the type of scattering of the current-carriers: if, for example, $Q_n^x + Q_p^x = 4\,kT$, the electrons and holes are scattered only by the thermal vibrations of the lattice, whereas if $Q_n^x + Q_p^x = 8kT$, the scattering is solely by ionized impurities.

Exact experimental determination of $Q_n^x + Q_p^x$ is difficult, however, for a number of reasons. The most important of these is inhomogeneity of the specimen which leads to the appearance of a volume photo-emf. So far we have succeeded in making only approximate quantitative measurements by means of the arrangement shown in Fig.7. The semiconductor specimen is attached to the two metal blocks 3 and illuminated by an interrupted beam passing through the aperture 2. Its ends are connected to the vacuum tube voltmeter 4 and amplifier 5. If the semiconductor is homogeneous and the temperature of both ends is the same no photo-emf is observed. Now if the upper block is heated to a higher temperature we obtain a signal due to the thermal photo-emf.

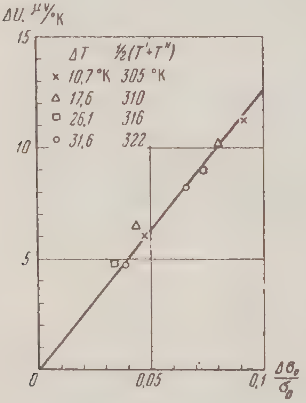

Fig. 8.

Using an analogous set-up we measured the additional thermo-emf produced under the influence of light by means of a dc potentiometer bridge. The results of these measurements are shown in Fig.8, where the relative change in conductivity Δσ is plotted against the thermal photo-emf reduced to a unit temperature difference ΔU/ΔT. It will be seen that the experimental results are in general agreement with our theory. The value of $Q_n^x + Q_p^x$ proved to be 6.4 kT. We feel that it should be possible to develop an accurate procedure for determining the sum $Q_n^x + Q_p^x$, based on the described set-up.

In conclusion, we would like to note that different effects connected with the temperature gradient in semiconductors with mixed conductivity often differ markedly from the effects observed in semiconductors with one type of current carriers. Investigation of these differences should further our understanding of this currently important type of semiconductors.

Institute of Technical Physics of the
Czechoslovakian Academy of Sciences

References

1. S.G.Kalashnikov & A.E.Pokrovskii, Zhur.tekh.fiz., 22, 883 (1952).
2. Ia.Tauts, Czech.Phys.Journal, 3, 120 (1953).
3. Ia.Tauts, Czech.Phys.Journal, 3, 282 (1953).
4. Z.Trousil, Czech.Phys.Journal, 6, 170 (1956).
5. Ia.Tauts, Czech.Phys.Journal, 5, 528 (1955).

ON THE INDUCTION OF A PHOTOELECTROMOTIVE FORCE IN AN ILLUMINATED SEMICONDUCTOR IN AN INHOMOGENEOUS MAGNETIC FIELD

- Ia.Tauts

In 1954 Kikoin[1] reported observing a potential induced under the influence of light in a semiconductor in an inhomogeneous magnetic field. Subsequently, Kikoin and his co-workers showed that the observed effect was due to heating. The light rays heat the specimen which in turn heats the surrounding gas; the gas particles moving under the influence of magnetic forces produce nonuniform heating of the specimen which leads to the appearance of a thermo-emf.

The results of Kikoin's researches led us to ask what potential can be expected in the case of a true internal photomagnetic effect in an inhomogeneous magnetic field when all interfering side effects are eliminated? The inhomogeneous magnetic field acts on both the electrons and holes since they possess magnetic moments; its paramagnetic part is due to electron spin; the diamagnetic part was theoretically discovered by Landau[3] in 1930. Landau gave an expression for the chemical potential of the electrons in a magnetic field. We based our calculations of the photo-emf in an inhomogeneous magnetic field on Landau's theory. For p-type semiconductors with a nondegenerate electron gas under weak illumination the photo-emf is given by

$$U=\frac{kT}{e}\cdot\frac{b}{b+1}\left\{1-\frac{1}{\sigma}\left[\left(\frac{m}{m_n^*}\right)^2+\left(\frac{m}{m_p^*}\right)^2\right]\right\}\frac{\beta^2\left(H_2^2-H_1^2\right)}{k^2T^2}\cdot\frac{\Delta\sigma}{\sigma_n}, \tag{1}$$

where m_n^* and m_p^* are the effective electron and hole masses, H_2 and H_1 are the magnetic fields at the two edges of the illuminated zone, β is the Bohr magneton with respect to the mobility of the electrons and holes, σ_n is the thermal conductivity, $\Delta\sigma$ is the change in thermal conductivity under the influence of incident light, k is Boltzmann's constant and T is the absolute temperature.

Measurement of this potential U is of interest because by means of it one can determine the sum of the magnetic permeabilities of the mobile current-carriers and distinguish them from the permeability of the stationary particles. In the case when the effective mass of the electrons is much smaller than the effective mass of the holes (as, for example, in InSb) it should be possible by means of measurements of U to determine the effective mass of the electrons in a manner analogous to the method of diamagnetic resonance discovered by Dorfman.

With this in mind we undertook a series of experiments with p-type indium antimonide.

In order to exclude the influence of thermoelectric effects we used interrupted lighting. In addition to the effect in question there always arises in the specimen the photomagnetic effect first observed by Kikoin and Noskov[4] in a homogeneous field. However, the two effects have different dependences on the magnetic field. Kikoin's effect is characterized by an odd function of the magnetic field intensity, while the effect in the inhomogeneous field is described by an even function. When the direction of the magnetic field is changed the phase of the signal associated with Kikoin's effect also changes, so that for one field direction both signals are added while for the other direction they are subtracted from each other.

Typical experimental results are shown in the accompanying figure. Curve a and b correspond to two opposite directions of the magnetic field. The trend of the curves in a homogeneous field is the same for both directions of the field within the limit of the experimental error; in an inhomogeneous field, however, the shape of the curve differs. The experimental curves are the sum and difference of the curves Σ and Δ. Curve Σ corresponds to Kikoin's effect in a homogeneous field; curve Δ to the effect in an inhomogeneous field.

Curve Δ, which for weak and moderate fields is described by the square law, corresponds to formula (1). However, after substitution of the appropriate numerical values for InSb, we found that the experimental value of the potential

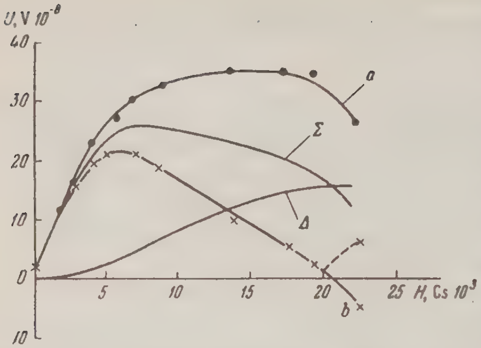

is some 2-3 orders of magnitude greater than predicted by Eq.(1). Theoretical analysis showed that in an inhomogeneous field in addition to the component given by (1) there appears an additional voltage component, which actually predominates under our conditions. This component is due to the influence of the magnetic field on the diffusion current developing along the specimen as the result of diffusion of current carriers from the illuminated to the non-illuminated section. In the case of specimens in an homogeneous field equal voltages are induced at both ends and these cancel each other. If, however, one end of the illuminated section of the specimen is in a field with induction B_1 while the other end is in a field with induction B_2, there develops a voltage U between the ends of a p-type semiconductor:

$$U = -\frac{kT}{e}\,\mu_M^2\,(B_2^2 - B_1^2)\,\frac{\Delta\sigma}{\sigma_n}. \tag{2}$$

After substitution of the measured values we obtained from expression (2) values of from 20,000 to 30,000 cm^2/volt sec for the electron mobility in InSb. This is in good agreement with the mobility determined from measurements of the Hall coefficient and conductivity.

We feel it is safe to assume that both the described effects are electronic effects occurring in an illuminated semiconductor in an inhomogeneous magnetic field.

Institute of Technical Physics of the
Czechoslovakian Academy of Sciences

References

1. I.K.Kikoin, Doklady AN SSSR, 96, 463 (1954).
2. I.K.Kikoin, I.Kh.Ganev & A.V.Karchevskii, Doklady AN SSSR, 99, 51 (1954).
3. L.D.Landau, ZS. f. Phys., 64, 629 (1930).
4. I.K.Kikoin & M.Noskov, ZS. f. Phy., M.5, 586 (1934).

STRUCTURE AND ELECTRICAL PROPERTIES OF INDIUM ANTIMONIDE IN THIN LAYERS

- I.D.Konozenko & S.D.Mikhnovskii

Introduction

In recent years there have been many investigations of intermetallic compounds of the $A^{III}B^{V}$ type. The heightened interest in the elements of these groups of the periodic table is due to their valuable properties which offer great potentialities where engineering and technical applications are concerned. These distinctive properties include a high current-carrier mobility, low melting temperatures and a great diversity as regards the widths of their forbidden energy bands. The nature of a number of anomalous effects observed in this group of compounds also presents considerable theoretical interest.

In studying the properties and possible uses of intermetallic compounds of the $A^{III}B^{V}$ type it may not be without interest to investigate these compounds in the form of thin layers. This was the specific purpose of the present work. Indium antimonide has been fairly extensively studied in the form of massive or bulk specimens[1-7]; however, little is known of its properties in the form of thin layers.

1. Experimental Procedure

The indium antimonide specimens were prepared by vacuum evaporation; the vacuum flask was designed so that after deposition the layer could be studied without removing it from the vacuum.

By way of support we chose molybdenum glass with a polished surface which was carefully cleaned before applying the layer. Contact between the indium antimonide layer and the electrodes was realized by means of a layer of silver applied by sublimation under vacuum.

An important factor in preparing the specimens was selection of the temperature regime for evaporating the indium antimonide. An appropriate amount of crystalline indium antimonide was heated under vacuum in a tantalum boat. In the molten state InSb does not wet the tantalum surface and retains a spherical shape which is important for determining the thickness of the deposited layer. In estimating the thickness of the layer we proceeded on the assumption that we were obtaining a uniform distribution of the condensate over the surface of a sphere having a radius equal to the shortest distance from the molten globule to the support.

The sublimation was carried out at a temperature of 580-640°. The average period required for obtaining a 100 A thick layer was 3 hours.

Tests showed that sublimation of InSb at higher temperatures yields low-resistance specimens; the subnormal resistance is apparently connected with dissociation of the molecules. The samples for electron diffraction and optical studies were prepared by sublimation of indium antimonide on a thin ethyl cellulose film. In all cases the same evaporating conditions were maintained.

2. Structure of the Thin Layers of InSb

Before attempting to investigate the electric properties we felt it would be desirable to clarify the nature of the InSb layer. The structure of the sublimed layers was investigated on an EM-4 electronograph by the transmission method. The electron diffraction pattern obtained for a ~500 A thick layer is shown in Fig.1. For greater accuracy of analysis, both before and after obtaining the sample pattern, we recorded the electron diffraction pattern of a reference standard which was used to calculate the instrument factor.

Analysis of the diffraction patterns indicated that the sublimate is a polycrystalline substance having a zinc blende (sphalerite) type structure with a lattice constant $\underline{a} = 6.46$ A. According to Breckenridge et al[1] the lattice constant of bulk InSb is 6.475 A, while according to the data of Bokii[8] $\underline{a} = 6.461$ A. This would indicate that our condensed material was indium antimonide.

The electron diffraction patterns obtained for such layers have well resolved, clear rings. The electron patterns of thinner specimens (under 100 A thick) show more diffuse rings, indicating a more finely dispersed structure (Fig.2).

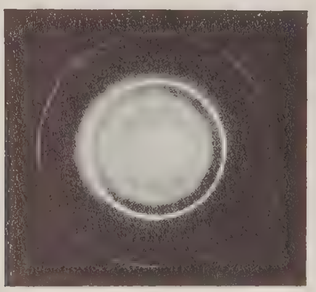

Fig.1

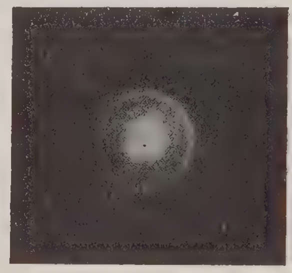

Fig.2.

Electron diffraction patterns of InSb layers.

In observing the sublimed layers of different thickness, including some subjected to heat treatment, through a metallurgical microscope (1000 X), in almost all cases we noted a mirror-like metallic surface. In the case of some specimens, however, there were noticeable light, generally parallel striae.

3. Electric Properties

A. Dependence of the resistivity on the thickness of the layer and the influence of air

The dependence of the resistivity of the layer on its effective thickness was determined in the process of deposition. It was assumed that evaporation of the material was uniform in time, so that for our purposes the measured resistance value could be plotted against the instant of measurement.

The character of the determined dependence is shown in Fig.3 (the maximum layer thickness was $5 \cdot 10^{-6}$ cm).

We note that at the end of evaporation the resistance of the layer did not remain constant. In the case of thicknesses under $5 \cdot 10^{-6}$ cm, the resistance after cessation of sublimation, as a rule increased, while layers of a greater thickness showed a decrease in resistance (Fig.4). We were not able to determine the exact critical thickness at which the break in the resistance curve occurs.

After the passage of 2-3 days the specimens become more stable

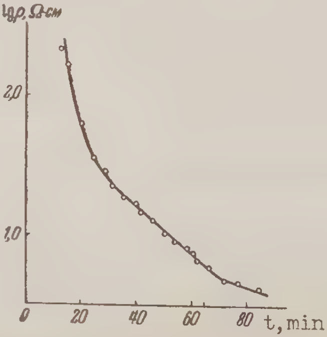

Fig.3. Variation of resistance of InSb layer with thickness (∝ time of deposition).

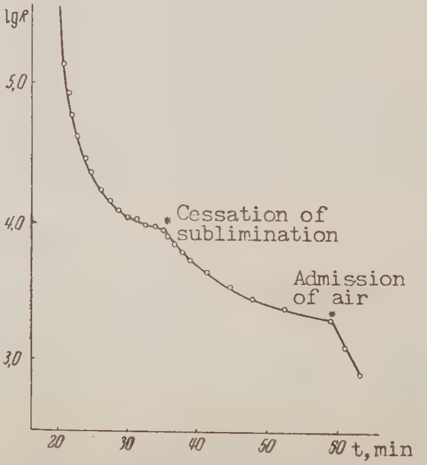

Fig.4. Variation of resistance of InSb layer with time.

as regards resistance characteristics. Fully stabilized, aged in air samples were periodically tested in vacuum and in air. As the air is evacuated the resistance of the layer increases; the vacuum resistance falls of as air is emitted. The change occurs slowly and may continue for up to an hour. The nature of these changes for two samples are shown in Fig.5. (The samples were held an average of 45 min in air and in vacuum.)

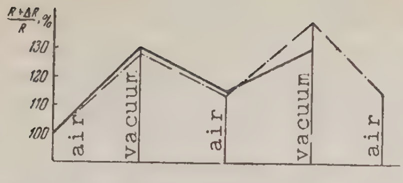

Fig.5. Effect of air on the resistance of two InSb layers.

B. Temperature dependence of the conductivity

The temperature dependence of the conductivity was studied on specimens in which the spontaneous change in resistance had more or less come to an end and hence could not appreciably affect the results. The measurements were carried out in the temperature range from -80 to + 300°. In all cases at a temperature of about 130-150° there occurs an irreversible decrease of the resistance of the layer, averaging two orders of magnitude. The rate of change gradually falls off. In view of this decrease, the values obtained at temperatures below and above 150° are different.

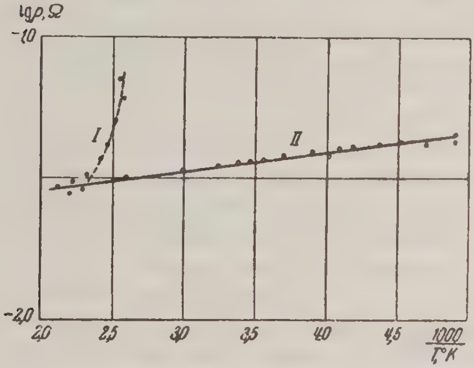

Fig.6. Temperature dependence of the resistivity.

In the case of samples not heated to 150° the temperature coefficient of resistivity attains 3.5% per degree. After heating to 150° the coefficient drops. At temperatures above 150° the coefficient is only 0.2% per degree. The observed temperature dependences of the conductivity for layers subjected to heating are closely described by the expression

$$\sigma = \sigma_0 e^{-\frac{\Delta E}{kT}} .$$

The dependence is plotted in terms of log ρ vs the reciprocal of the temperature in Fig.6. Here curve I pertains to the irreversible decrease in the resistivity, while curve II characterizes the dependence ρ(T) after the layer has been heated to 150°. In this case the value of $\Delta E \approx 0.05$-0.1 ev.

The type of conductivity of the initial material in our layers was determined by means of thermoprobe. Conductivity of all the layers was of the p-type, while the initial raw material was an n-type semiconductor.

Specimens prepared by evaporation on to a support heated to 150° showed a temperature dependence of the conductivity similar to that characteristic of specimens heated to 150° after deposition.

4. Optical Transmission of InSb Layers

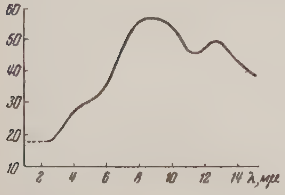

Fig.7. Transmission spectrum of $\sim 10^{-5}$cm thick InSb layers.

We also investigated the optical transmission of the InSb layers in the infrared region (1.5-15 μ). The layers were prepared following the standard procedures described above. The transmission curve for InSb layers about 10^{-5} cm thick is shown in Fig.7. The transmission is given in percent relative to that of the ethyl cellulose base.

A distinctive feature of our spectra is that the transmission falls off with decreasing wavelength only up to a certain point. Below a certain wavelength the transparency of the layers fluctuates about a certain mean value (dash line in Fig.7). The absence of spectral intervals marked by a transmission tending to zero, a feature observed in bulk specimens[5], can partly be explained by the specific structure of the thin layers.

5. Discussion of Results

1. The reason for the irreversible changes in the resistivity of the InSb layers observed in our experiments may be connected with the fact that the initially deposited layer has a finely dispersed structure, possibly interspersed with amorphous formations. Heating to 150° results in further crystallization and the formation of a coarse grained structure. In the process, individual initially separate granules may merge. The fact that no irreversible change in the resistivity is observed when the layer is deposited on a heated support speaks in favor of this hypothesis.

2. In interpreting the reversible changes in the resistivity of the layers connected with the processes of adsorption and desorption of gases one must assume that there are present at the surface Tamm hole levels. In view of the fact that the electric conduction of the layer is in all probability determined by the current-carriers on the intrinsic energy levels of the crystal, the value of the conductivity of the layer must depend on the magnitude of the charge compensating the charge of the Tamm levels. As was noted the conductivity of the layer was of the hole type. Adsorption of gas molecules results in reduction of the surface charge, which leads to an increase in the concentration of holes with a corresponding decrease in the resistance of the layer. The opposite effect is observed incident to desorption of gases from the surface of the layer.

3. The temperature dependence of the conductivity was investigated in the temperature range - 85 to + 300°. It is known[8] that in bulk InSb specimens of sufficiently high purity the influence of the mechanism of intrinsic conduction begins to be manifest only at temperatures above 300°. Thus we investigated the temperature dependence of the conductivity in the region of impurity (extrinsic) conduction.

Inasmuch as in thin layers the fact that the temperature dependence of the conductivity follows the $\sigma = \sigma_0 e^{-\frac{\Delta E}{kT}}$ law may be due to the specific structure of thin layers, it may be assumed that ΔE is not necessarily the value of the impurity activation energy. This pertains particularly to specimens not subjected to heating. The presence of an energy barrier in the thin layers can be explained by the existence of potential barriers between individual groups of atoms or their aggregates produced by discontinuities in the layer.

5. Tannenbaum & Maita[3] report that for their InSb specimens with an intrinsic resistivity of $7 \cdot 10^{-3}$ ohm cm the infrared limit of absorption lies at 7 μ. This location of the absorption limit corresponds to an optical activation energy of 0.18 ev.

From a comparison of the transmission spectrum obtained by us with the spectra for bulk specimens (cf. Ref.5) it may be seen that the character of the infrared transmission spectra of thick specimens is similar to that of thin layers. The absence of a marked absorption limit is connected with the fact that our layers had a thickness of only about 10^{-6} cm. Incidentally, this may be taken as further evidence that our layers consisted of the compound InSb.

Conclusions

From the experimental data described above we can draw the following conclusions regarding the nature and properties of thin layers of InSb.

1. The layers have a polycrystalline structure. The crystal lattice is of the zinc blende type.

2. When the layers are heated to 130-150° further crystallization occurs and

the finely dispersed structure is transformed into a more coarse grained one; initially separate aggregations may coalesce into larger formations. However, even after heating a certain granularity of the layer persists as is evidenced by the large final resistivity of the layers. After heating to 150° the layer becomes relatively stable as regards conductivity characteristics.

3. The InSb layers obtained by us are characterized by a semiconductor type of temperature dependence of the resistivity with p-type conductivity, whereas the initial raw material had n-type conduction. The temperature dependence of the conductivity was investigated in the range of extrinsic conduction in the temperature interval from -80 to +300°.

4. The influence of air on the layer is manifested by a reversible increase in the conductivity, presumably due to adsorption of air molecules.

5. The general character of the infrared transmission spectrum of thin layers of InSb is similar to that of bulk specimens, which substantiates our conclusion that the deposited layers actually did consist of the compound InSb.

Institute of Physics of the
Ukrainian SSR Academy of Sciences

References

1. R.G.Breckenridge et al, Phys.Rev., 96, 571 (1954).
2. H.Burstein, Phys.Rev., 93, 632 (1954).
3. M.Tannenbaum & J.P.Maita, Phys.Rev., 91, 1009 (1954).
4. M.Tannenbaum & Briggs, Phys.Rev., 91, 1561 (1953).
5. H.Hrostovsky & G.H.Wheatley, Phys.Rev., 95, 1683 (1954).
6. M.Tannenbaum & G.L.Pearson, Phys.Rev., 90, 153 (1954).
7. T.C.Harman & R.K.Willardson, Phys.Rev., 95, 699 (1954).
8. B.G.Bokii, Vvedenie v kristallokhimiiu (Introduction to crystal chemistry), M.1954.
9. H.Welker, Physika, 20, 893 (1954).
10. S.A.Vekshinskii, Novyi metod metallograficheskogo issledovaniia (A new method of metallographic investigation), M. 1944.

INVESTIGATION OF THE PELTIER EFFECT AND THERMOELECTROMOTIVE FORCES IN GERMANIUM

- M.Stenbeck & P.I.Baranskii

The basic equations

$$\frac{dP}{dT} - \alpha - \tau = 0 \qquad (1)$$

and

$$\frac{dP}{dT} - \frac{P}{T} - \tau = 0, \qquad (2)$$

relating the Peltier heat P, the Thomson coefficient τ and the differential thermo-emf α do not inevitably follow from the fundamental laws of thermodynamics or the Onsager principle, inasmuch as the latter does not take into account, among other factors, the possible influence of interaction between phonons and electrons. Consequently, the values of P and τ obtained from (1) and (2) on the basis of measurements of α as a function of the temperature may be open to question.

For the purpose of experimental verification of Eqs.(1) and (2), we attempted to carry out a precise investigation of the thermo-emf and the Peltier effect occurring at copper-germanium contacts soldered with pure tin. Tests were made on an n-type single crystal specimen of germanium, measuring 5 x 5 x 10 mm. Inasmuch as the monocrystallicity and the special selection of the section of the ingot from which our sample was cut in the form of a prism did not per se insure the requisite homogeneity of the material, we utilized the conclusions from initial calculations which indicated that the harmful influence of inhomogeneities in the sample can be excluded by using a longitudinal flow of heat, devoid of transverse components, since under these conditions α and P automatically average out in the same way. In order to assure dependable thermal contact, all the thermocouples were soldered at the points where the temperature was to be measured. The Peltier effect was measured by compensation of the difference in heats developed at the ends of the specimen (for both directions of the current). Both the thermo-emf and the Peltier coefficient were measured under the conditions $J \to 0$ and $\Delta T \to 0$. The measurements of the differential thermo-emf α and the Peltier coefficient were made in the interval from -196° to $+100^\circ$, wherein the carrier concentration remains constant ($n_e \approx 3.2 \cdot 10^{16}$ cm^{-3}). The accuracy of determination of the Peltier effect was 1-2%; that for the thermo-emf was 1%. The accuracy in measuring the temperature T_o of the ambient medium was 1% in the range of higher temperatures and somewhat lower in the range of low temperatures. The method of directly measuring the temperature difference in determining the differential thermo-emf made it possible to sharply enhance the accuracy in determining α (for example, in the $0.20 \leqslant \Delta T \leqslant 5.02^\circ$ interval, α deviated from its constant (mean) value by less than 1%).

The following results were obtained. The accompanying figure shows the temperature dependences of the Peltier coefficient P and the product αT (curves I and II, respectively). It may be seen from the curves, the relationship $P = \alpha T$, following directly from Eqs.(1) and (2), is not substantiated by experiment. The difference $\Delta = \alpha T - P$ appreciably exceeds our experimental error. From this alone it may be assumed that the thermoelectric processes involved are thermodynamically reversible. In view of this it is strange that Eq.(2), which is a consequence of the second law of thermodynamics, with $\tau = 1.5$ k/e (as follows from theory) yields fairly good agreement with the experimental results. Actually, the only assumption, consistent with our experimental data, that the difference dP/dT - P/T is constant in the investigated temperature range made it possible to check Eq.(2) in the integral form

$$P = \alpha T + \tau T \log T.$$

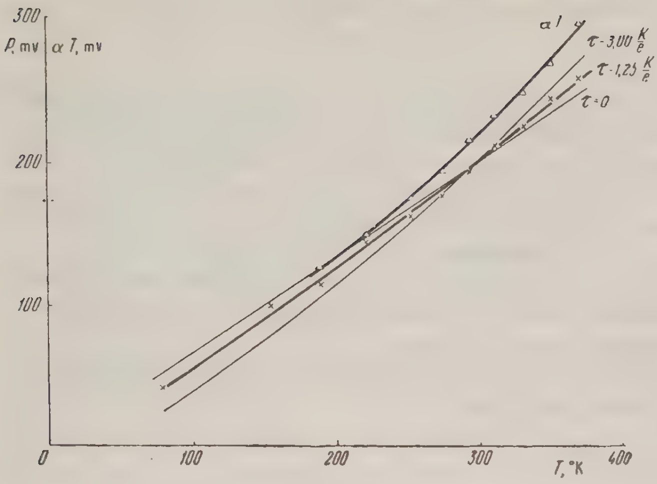

The method of least squares, which we used for finding the values of α and τ, led to a value of τ = 1.25 k/e (to permit of evaluation of the accuracy of measurement we show the calculation curves corresponding to τ = 0, 1.25 k/e and 3 k/e).

Nevertheless it would be erroneous to interpret these results as experimental verification of (2), inasmuch as the Thomson coefficient τ was not measured directly. It can only be asserted that the following equation

$$\frac{dP}{dT} - \frac{P}{T} - \frac{C}{e} = 0, \tag{3}$$

(where C = 1.5 k is the specific heat of a classical carrier gas having a constant concentration) is substantiated by the experimental results.

Equation (3) is obtained by thermodynamic analysis of a reversible process, involving transfer of one mole of the dissolved particles from solution 1 to solution 2, realized at the temperature T by means of semipermeable partitions, heating of the system from T to T + ΔT, reverse transfer of one mole of the particles from solution 2 to solution 1 at the temperature T + ΔT and finally cooling of the system to T. If the conductor is regarded as a solution of current carriers in the lattice (solvent) and the area of contact of the two conductors as the boundary between the nonmixing solutions of two different solvents, analysis of this closed, rigorously reversible thermodynamic process leads to the equation

$$\frac{dQ_{12}}{dT} - \frac{Q_{12}}{T} - (C_1^* - C_2^*) = 0, \tag{4}$$

where Q_{12} is the heat of transfer of one mole of dissolved particles from solution 1 to solution 2 and C* is the difference between the specific heat of the solution containing one mole of the dissolved particle and the specific heat of the pure solvent in the corresponding amount. With Q = AeP (where A is Avogadro's number), $C_1^* = A \cdot 3/2 \cdot k$ (the specific heat of the classical carrier gas in a semiconductor) and $C_2^* = 0$ (specific heat of the Fermi-gas in a metal) Eq.(3) follows directly from (4).

This is the basis of our conclusion that substantiation of Eq.(3) can be regarded as experimental verification of the theoretical concepts regarding the specific heat of the electron gas in a classical semiconductor, but cannot be taken as evidence of constant entropy in thermoelectric processes.

Thus our experiments have shown the basic thermoelectric relationships (1) and (2) are not jointly and rigorously valid; this means that the thermoelectric processes in question also comprise some other irreversible processes.

Physical Institute of the
Ukrainian SSR Academy of Sciences

ELECTRIC PROPERTIES OF SOME COMPOUNDS OF ELEMENTS IN THE THIRD AND FIFTH GROUPS OF THE PERIODIC TABLE (InAs and InSb)

(Abstract - Complete report in Zhur.tekh.fiz., 26, 251 (1956).)

- D.N.Nasledov & A.Iu.Khalilov

The investigation was concerned with the electric properties of indium antimonide and indium arsenide. The temperature dependence of the conductivity of samples with p- and n-type conductivity was determined in the range from 1.3°K. The Hall effect was investigated. It was shown that the Hall coefficient in the region of the transition from intrinsic conductivity changes sign as the magnetic field intensity is increased, which is in agreement with Madelung's theory.

A large change in the resistance in a transverse magnetic field was noted.

An anomalous increase in the carrier mobility with heating of the sample was observed in indium arsenide at high temperatures.

It was shown that it is possible to reduce the impurity concentration in indium antimonide by the method of zonal purification.

DISCUSSION

Z.R.Kopets: Indium arsenide was also investigated at the Semiconductor Institute of the USSR Academy of Sciences. The results obtained by us for samples with high impurity concentrations, concentrations equivalent to those in the specimens used by Nasledov & Khalilov, may yield answers to some of the questions raised by the report we have just hears.

The fact that the plot of log σ vs 1/T does not have a constant slope in the region of high temperatures can perhaps be explained by the peculiar structure of the bands in this semiconductor. We investigated the effective mass of the current carriers on the basis of the variation of the thermo-emf. One and the same evaluation of the effective electron mass ($m_n \leqslant 3.5 \cdot 10^{-2}\ m_o$) is obtained for samples with different impurity concentrations in the entire investigated range of temperatures from 120 to 750°K. This is an exceptionally low value compared to that for other semiconductors of the same type.

The effective mass of holes exceeds m_n by more than an order of magnitude ($m_p \approx 0.55\ m_o$). In view of this great difference in effective masses, the electrons must play the predominant role in determining all the static electric parameters of InSb (for example, σ, α and R) in the intrinsic conduction region. Inasmuch as the level density in the conduction band is very low, the lower levels quickly fill as the temperature is increased and the separation between the electrons in the valence band and the unfilled levels in the conduction band increases. As a result there is a rapid increase in the electron activation energy with increasing temperature. If, for example, the electron concentrations in the conduction band are of the order of 10^{17}, 10^{18} and 10^{19} cm^{-3}, we will have filling of levels at 0.03, 0.13 and 0.60 ev above the bottom of the band. This strong upward shift of the free levels in the conduction band will obviously distort variation of log σ as a function of 1/T. Hence in the region of intrinsic conduction one cannot judge of the width of the forbidden band directly from the slope of this plot.

In specimens with an impurity concentration of the order of 10^{17} cm^{-3} or higher the intrinsic conductivity region begins at temperatures above 600°K. There is obviously a transition region between the intrinsic conductivity region and the region of pure impurity conductivity. In this intermediate region impurity carriers still play a certain part, even though the increase in conductivity is due to the transfer of electrons from the valence band. In this temperature interval we may still encounter (particularly for p-type specimens) fairly long, almost linear sections of the log σ vs 1/T plot, although the slope of these sections may differ markedly from that for specimens with a different concentration of impurities.

P-type specimens with a higher impurity content will have linear sections characterized by a steeper slope as compared with purer specimens, which is in good quantitative agreement with the above described picture in InSb. Here again one cannot directly relate the different slopes with the actual width of the energy gap. This can be obtained by analysis of the algebraic expression relating the electron concentration, the number of ionized impurity atoms and the Hall coefficient. In such analyses it is found that for all specimens the width of the forbidden band at 0°K is about 0.2 ev, a value that is substantiated by measurements of light absorption in InSb.

At room temperature the width of the forbidden energy band is about 0.18 ev.

On the other hand, the existence in InSb of a narrow forbidden band and a low effective carrier mass determines the statistical degeneration of the current carriers in this semiconductor. It can be shown that at temperatures above 250°K all specimens of InSb, regardless of their purity, are degenerate (due to the narrowness of the forbidden band). In fact, specimens having the purity specified by Nasledov & Khalilov must necessarily be degenerate in the entire investigated temperature interval (due to the low effective mass of the current carriers). Analyzing all the electric properties, including, of course, the mobilities, this fact must be borne in mind.

One of the previous speakers suggested that the almost constant value of the mobility in the region of low temperatures can be explained with the operation of the mechanism of scattering by neutral impurity atoms. However, a quantitative evaluation of the mobility produced by the operation of this mechanism shows that to explain the observed (at $T > 100^{\circ}K$) mobilities in n-type InSb specimens with a 10^{18} cm^{-3} carrier concentration, one must assume an implausibly great concentration of neutral impurity atoms.

Our evaluations, carried out for different possible scattering mechanisms, lead to the conclusion that in a wide range of low temperatures the principal scattering mechanism in the case of InSb specimens such as those investigated by us and Nasledov & Khalilov is scattering by vibrations of the lattice and impurity ions. It must be noted that the variation of these mobilities with temperature will be different from that obtaining in the case of classical nondegenerate semiconductors. As the degree of degeneracy (connected with growth in the value of the reduced chemical potential η) increases, the influence of the mechanism of scattering by ions falls off (the electrons participating in the current have a higher kinetic energy and lie on higher energy levels in the band). Hence in the case of strong degeneracy, which obtains in specimens with a high impurity concentration, the dominant role even at low temperature is played by lattice scattering. The lattice mobility μ_L in the case of degeneracy can be expressed in terms of the corresponding classical mobility μ_{L-cl}:

$$\mu_L = \mu_{L-cl} \frac{\sqrt{\pi}\, F_o(\eta)}{2F_{1/2}(\eta)}$$

where F_o and $F_{1/2}$ are the familiar Fermi integrals.

The degeneracy depending on the reduced chemical potential decreases with increasing η. In the region of impurity conductivity η is approximately a linear function of 1/T (the chemical potential, equal to $\eta \cdot kT$, changes very little with temperature) and taking into account the degeneracy will, with decreasing temperature, greatly reduce the slope of log μ as a function of log T as compared with the usual slope for a classical semiconductor. In individual cases this can lead to an almost constant value of the mobility at low temperatures. In the case of minor degeneracy one must take into account both mechanisms.

Experimental data for a p-type specimen with moderate degeneracy was compared quantitatively with the approximate extrapolated formula taking into account both mechanisms. Fair agreement was obtained.

NEW GLASS-LIKE SEMICONDUCTORS

- N.A.Goriunova & B.T.Kolomiets

As we know, many substances can exist in a glass-like or vitreous state.

The most extensive group of glasses of practical importance, consisting of fused mixtures of such oxides as SiO_2, Na_2O, CaO, PbO, etc., has been investigated in great detail. Arsenic sulfide and germanium sulfide base glasses have recently been investigated for purposes of optical technology.[1,2] The possibility of obtaining glasses with a partial replacement of the sulfide by corresponding selenides and tellurides has been discussed by Weyl.[3]

Investigating changes of the electrical properties of the chemical compound $Tl_2Sb_2Se_4$ ($Tl_2Se \cdot Sb_2Se_3$) with changes in the chemical composition brought about by isomorphic replacement of the original component elements by others, we found that when the Sb is completely replaced by As the resultant substance having the composition $Tl_2Se \cdot As_2Se_3$ is amorphous. Through isomorphic replacement of selenium with tellurium in this substance we obtained a whole series of amorphous substances having compositions varying from $Tl_2Se \cdot As_2Se_3$ to $Tl_2Te \cdot As_2Te_3$ (here and below the formulas are indicative rather than exact).

Further researches yielded additional series of amorphous substances in the following systems:

1. As_2Se_3—Sb_2Se_3
2. As_2Se_3—Tl_2Se
3. As_2Se_3—As_2Te_3
4. As_2Se_3—As_2S_3
5. $As_2Se_3Tl_2Se$—$Sb_2Se_3Tl_2Se$
6. As_2S_3—Sb_2S_3

The results of our investigations of some of these systems appear in Ref. 4; descriptions of the results obtained for others will be published shortly.

Synthesis of the substances discussed in the present report was carried out in evacuated quartz flasks (ampoules). The ingredients were weighed to within $2 \cdot 10^{-4}$ g. The purity of the raw materials was the following: Tl - 99.9%; the As (according to spectrum analysis data) contained traces of iron, antimony and silicon; Sb - 99.95%; Te - 99.0%; the sulfur and selenium contained about 0.01% of non-volatile impurities.

The synthesis procedure amounted essentially to holding the molten mixtures for 1-2 hours at the melting point of the most refractory component, followed by heating to 850-950° and cooling for 14 hours at the natural rate of cooling of the furnace.

The amorphous substances of the investigated systems had conchoidal fracture, exhibited no plateaus in their cooling curves, could be pulled into fine filaments or blown to form thin films. From all these indications we concluded that the investigated materials with an amorphous structure were glasses.

This view was substantiated by investigations of their structure. Measurements of small-angle x-ray scattering, kindly carried out at our request by Prof. E.A.Porai-Koshits in the Institute of the Chemistry of Silicates of the USSR Academy of Sciences, and conventional x-ray diffraction photographs showed that the investigated materials are true glasses.

The relative content of the crystalline and amorphous phases in the above listed systems differs. The boundary between these phases may be termed the glass-formation or vitrification boundary. Experiments showed that for all the systems the location of the boundary on the phase diagram is determined not only by the chemical composition but also by the synthesis conditions. We determined the vitrification boundary for a number of the listed systems on the basis of samples cooled at an average rate of 50-70° per hour.

The vitrification boundary for the As_2Se_3—Tl_2Se system, for example, proved to lie at an As_2Se_3 content of 38%. In the As_2Se_3—Sb_2Se_3 system the vitrification boundary lies at an appreciably higher As_2Se_3 content.

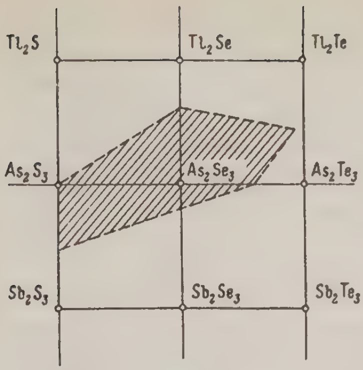

Fig. 1. Vitrification boundary for ternary and quadruple systems.

The location of the vitrification boundary for all the above mentioned systems, with the exception of the complex $Tl_2Se \cdot Sb_2Se_3$—$Tl_2Se \cdot AsSe_3$ system, is shown schematically in Fig. 1. Obviously, the hatched area in the diagram comprises a very large number of different glass-like substances. These substances have different physical and physical-chemical properties which vary continuously with the composition.

We feel that the question of the number of possible glass-like substances is of interest. However, it must be said that Fig. 1 gives only an approximate idea of the possible number since, as noted above, the location of the vitrification boundary depends on the chemical composition and the synthesis conditions.

In our study each system was divided into seven experimental points with corresponding ratios between the binary and ternary components. In view of this alone the vitrification boundary shown in Fig. 1 is obviously an interpolation and hence somewhat inaccurate.

By changing the synthesis conditions, for example, by increasing the rate of cooling - up to a rapid quench - one can appreciably shift the vitrification boundary and enlarge the hatched area in the diagram.

In addition to these two factors, there is yet another important factor determining the number of glass-like substances. Fig. 1 characterizes the group of glass-like substances formed by binary components of stoichiometric composition. Subsidiary experiments showed that the investigated glasses permit of appreciable deviations from stoichiometric proportions. With such deviations the number of glass-like substances is greatly increased and with it the diversity of their properties.

Further investigations established that part of the investigated materials can be obtained either in the glass-like or in the crystalline state depending on the rate of cooling. Such structural reversibility is particularly characteristic of the substances which as regards composition lie at the vitrification boundary. The number of such "reversible" substances is rather large; they may be represented by a rather wide band along the vitrification boundary.

In addition to investigating the vitrification boundaries, we determined certain electric and photoelectric properties of the glasses of the five As_2Se_3-base systems listed above.

These studies showed that a characteristic trait of these and other glasses differing substantially from conventional oxide- and sulfide-base glasses is their high conductivity. Thus, for example, the glass having the composition $Tl_2Se \cdot As_2Te_3$ has a conductivity of the order of 10^{-3} $ohm^{-1}cm^{-1}$, which is at least 10 times higher than the conductivity of the most highly conducting oxide glasses.

Further, it was established that as regards all other attributes except the high electric conductivity these new glasses are typical semiconductors. Thus, the temperature dependence of the conductivity of these substances follows the exponential law and they all exhibit a noticeable photoconductivity. Their conduction may be of either the n-or p-type. They also evince a thermoelectromotive power.

The limiting values of the conductivity and the range of the positions of the spectral sensitivity peaks of the investigated systems are listed in Table 1.

Table 1

Systems	Limiting values of conductivity, $ohm^{-1}cm^{-1}$	Range of observed spectral peak positions, μ
As_2Se_3 — As_2Te_3	10^{-13}—10^{-6}	0,6—1,25
As_2Se_3 — Tl_2Se	10^{-13}—10^{-7}	0,6—1,1
As_2Se_3 — Sb_2Se_3	10^{-13}—10^{-12}	0,6—0,9
$Tl_2Se \cdot As_2Se_3$ — $Tl_2Se \cdot As_2Te_3$	10^{-7}—10^{-3}	1,0—1,2
$Tl_2Se \cdot As_2Se_3$ — $Tl_2Se \cdot Sb_2Se_3$	10^{-8}	0,95—1,15

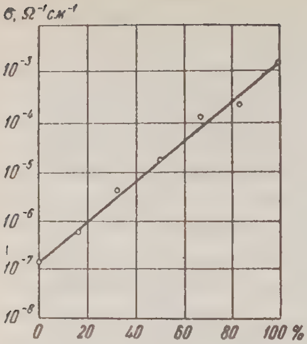

Fig. 2. Variation of the electric conductivity with the Te content for glasses in the $Tl_2Se \cdot As_2Se_3$—$Tl_2Se \cdot As_2Te_3$ system.

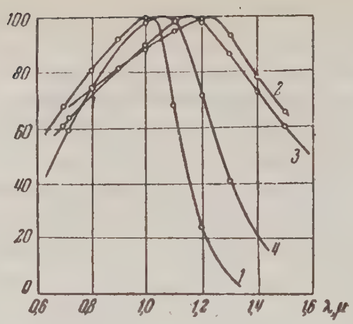

Fig. 3. Spectral distribution of the internal photoeffect in the $Tl_2Se \cdot As_2Se_3$—$Tl_2Se \cdot As_2Te_3$ system: 1) $Tl_2Se \cdot As_2Se_3$, 2) $Tl_2Se \cdot As_2Se_2Te$, 3) $Tl_2Se \cdot As_2SeTe_2$, 4) $Tl_2Se \cdot As_2Te_3$.

The sensitivity values pertain to our specific samples, i.e., to the given synthesis conditions, amounts of impurities present and deviations from stoichiometric proportions due to errors in weighing the raw ingredients.

One may judge of the general variation of electric conductivity and photoconductivity with the composition of the glass-like substances from Figs. 2 & 3, which pertain to one of the systems studied in greatest detail - the $Tl_2Se \cdot As_2Se_3$—$Tl_2Se \cdot As_2Te_3$ system, which is characterized by an appreciable number of glass-like substances.

Let us turn back to Fig. 1. On the basis of our investigation of the electric properties, it may be asserted that an appreciable number of substances lying inside the vitrification boundary are typical semiconductors. A great number of different semiconductor glasses can be obtained both by varying the composition and by departing from stoichiometric proportions. Experiments showed, for example, that as the tellurium is replaced with selenium and sulfur the conductivity of the glasses falls and we pass from the region of semiconductor glasses into the region of dielectric glasses. We have the same transition but in the opposite direction when sulfur is replaced by selenium or tellurium, etc.

As was noted above, many of the substances lying on the vitrification boundary can be obtained either in the glass-like or in the crystalline state. In a number of substances this transition is accompanied by appreciable changes of the electric properties. The change in conductivity incident to the transition from the crystalline to the glass-like state for a number of investigated substances is shown in Table 2.

Table 2

Chemical composition	Conductivity, $ohm^{-1}cm^{-1}$	
	Glass	Crystal
$2As_2Se_3 \cdot 3As_2Te_3$	$2,5 \cdot 10^{-8}$	10^2
$As_2Se_3 \cdot 2Tl_2Se$	$7,5 \cdot 10^{-8}$	$7,2 \cdot 10^{-8}$
$2As_2Se_3 \cdot Sb_2Se_3$	$1,0 \cdot 10^{-10}$	$2,5 \cdot 10^{-6}$
$Tl_2Te \cdot As_2Te_3$	$5,3 \cdot 10^{-3}$	$4,6 \cdot 10^{-1}$
$Tl_2Se \cdot \left(\frac{5}{6} As \frac{1}{6} Sb\right)_2Se_3$	$2,2 \cdot 10^{-7}$	$2,0 \cdot 10^{-8}$

As may be seen from the table the transition may be accompanied by either an increase or a decrease in conductivity, which is presumably indicative of a difference in the character of the interaction of the components during glass formation in the different systems.

One can judge of the nature of the change in photoconductivity incident to transition from the crystalline to the glass-like state from the curves of Fig. 4 which pertain to $2As_2Se_3 \cdot Sb_2Se_3$.

The optical properties of some of the samples of the new glasses were also investigated. The preliminary data on the nature of the absorption in the semiconductor glasses obtained in the Institute of Crystallography* indicate the absence of selective absorption in a relatively wide spectral range.

---

*We take this occasion to thank G.I.Distler for his generosity in making the cited data available.

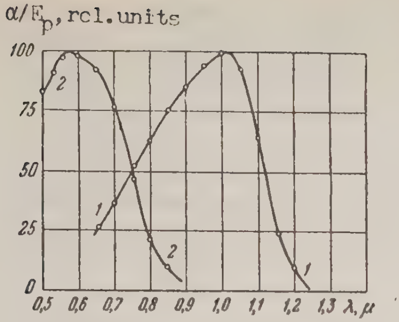

Fig. 4. Change in the spectral sensitivity incident to the transition of $2As_2Se_3 \cdot Sb_2Se_3$ from the crystalline (1) to the amorphous (2) state; α - sensitivity, E_p - incident energy.

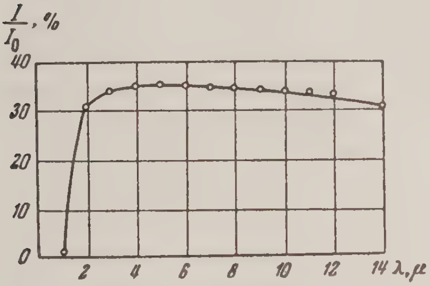

Fig. 5. Light transmission curve for glass having the composition $Tl_2Se \cdot As_2Se_{2.5}Te_{0.5}$.

By way of illustration, the transmission (transparency) curve for glass having the composition $Tl_2Se \cdot As_2Se_{2.5}Te_{0.5}$, measured in the form of a 0.29 mm thick plate, is shown in Fig. 5. The transmission characteristics of glasses of other composition are similar, the main difference being that the absorption limit shifts somewhat with changes in chemical composition.

In accord with their chemical composition the sulfide, selenide and telluride glasses discussed in the present report - in contrast to oxide-base glasses - may be termed chalcogenides.

As regards their physical-chemical properties the new glasses differ appreciably from conventional oxide glasses. Thus, for example, the interval of softening of the chalcogenide glasses lies appreciably lower than the softening interval of oxide glasses: the softening temperature varies between 100 and 230°.

As regards stability of chalcogenide glasses, the preliminary experimental data indicate that the notions developed for oxide glasses[5] may be applicable to these new glasses as well. Thus, for example, glass-like As_2Se_3 could readily be brought into the crystalline state, while $Tl_2Se \cdot As_2Se_3$ could not be crystallized under our conditions. This can be explained if, by analogy with oxide glasses, we accept at optimal value of 0.5 for the number of atoms of the glass-forming cation per atom of selenium.

Possibly the stipulation of the theory of oxide glasses regarding the structural non-equivalence of sites occupied by glass-forming ions and non-glass-forming ions can be applied for interpreting the electric properties of the chalcogenide glasses. For this, however, a great deal more experimental data than is now available would be required.

Two-phase systems - crystal-glass - are undoubtedly of a certain interest. Arsenic selenide forms two-phase systems with a number of substances; in these systems the As_2Se_3 is invariably in the glass-like state, while the other substance (semiconductor) is in the crystalline state. Such two-phase systems are formed, for example, with PbS, PbSe, Cu_2Se, InAs and Sb_2Se_3. One of the interesting characteristics of such systems is the lowered melting temperature of the crystalline phase. It may be assumed that in a given case we are dealing with eutectic interaction.

In view of the simplicity of converting them from the glass-like to the crystalline state, substances lying at the glass-crystal boundary may be of particular interest in connection with studies of conduction in solid and liquid semiconductors.

Back in 1947 A.F.Ioffe wrote that the electric properties of matter are determined by the short-range order in the arrangement of the atoms, in view of which there may be no difference between the electric properties of liquid and solid materials. This notion was experimentally substantiated by A.R.Regel and his co-workers who studied the conductivity of a number of semiconductors in the liquid state.

The existence of glasses with semiconductor properties, which may be regarded as supercooled liquids, may serve as additional confirmation of the ideas advanced by A.F.Ioffe.

T.N.Venbel' and V.S.Aref'eva, students of Leningrad State University, participated in the investigations of the electric and photoelectric properties of the glasses. The authors desire to express their gratitude to D.N.Nasledov for his aid and constant interest in the work.

Leningrad Physico-technical Institute of the
Academy of Sciences of the USSR

References

1. A.Frerichs, J.Opt.Soc.Am., 43, 12, 1153.
2. L.M.Dennis & A.N.Laubengauer, J.Phys.Chem., 30, 1510 (1926).
3. W.A.Weyl, J.Chem.Education, 27, 520 (1950).
4. N.A.Goriunova, B.T.Kolomiets, Zhur. tekh. fiz., 25, No. 13 (1955).
5. Zachariasen, J.Am.Chem.Soc., 54, 3841 (1932).

SEMICONDUCTOR PROPERTIES OF MAGNESIUM-BISMUTH ALLOYS

- A.K.Kikoin & G.D.Fedorov

Compounds of metals of the Groups II and V of the periodic system described by the stoichiometric formula, corresponding to the normal valences of the components, may have a lattice with distinctly heterpolar bonds. This is due to the transfer of valence electrons from the atoms of the Group II element to the atoms of the Group V element with the resultant formation of doubly-charged ions in the first case and triply-charged negative ions in the second. Clearly, as regards their electrical and optical properties such compounds must be closer to insulators than to metals. These suppositions, advanced some time ago by Ioffe[1], Frenkel'[2] and other investigators, have been substantiated experimentally.

Boltaks & Zhuze[3] made a detailed investigation of the compound Mg_3Sb_2 and showed that it is an extrinsic semiconductor. Later Moss[4] again investigated this compound (using specimens in the form of thin films) and came to the conclusion that its properties are close to those of insulators. These results have been further confirmed by the work of Busch, Hullinger & Winkler[5]. It may be assumed that other compounds of this type will have similar properties. We undertook an investigation of the Mg-Bi system which is chemically analogous to the Mg-Sb system. In the diagram of this system, the composition Mg_3Bi_2 corresponds to a sharp maximum of the melting temperature, similar to the corresponding maximum in the diagram of the Mg-Sb system. In order to follow the change in properties as the composition is varied from the pure components, which have metallic properties, to the compound Mg_3Bi_2, we utilized the method of Vekshinskii[6] which allows of investigating the attributes of specimens with continuously varying concentrations of the components.

Preparation of samples

The Mg-Bi films were prepared by vacuum evaporation onto a glass plate measuring 35 x 70 mm. The plate was clamped in a special holder-stand; the tungsten wire heaters containing the bismuth and magnesium pellets were located under the plate. The entire assembly was installed under the vacuum hood. Before the experiment the glass plate was subjected to thorough chemical cleaning. Immediately prior to evaporation the plate was further cleansed by ion bombardment (at the forevacuum pressure) at a potential of about 1000 volts. After the discharge the vacuum was reduced to about 10^{-6} mm Hg and the pellet charge was evaporated.

Bismuth evaporates from the liquid phase, while the magnesium sublimes without melting. Appropriate measures were taken to insure simultaneous and uniform evaporation of both metals. The thickness of the film and its composition at different points on the plate was computed on the basis of the weight of the evaporated metals and the geometry of the set-up[6].

In order to avoid possible changes in the properties of the films under the influence of air, in some cases the films were covered with a protective layer of SiO. This protective coating was applied by vacuum evaporation immediately after deposition of the Mg-Bi film. To provide for this a third heater was installed under the plate and was charged with a mixture of quartz powder and silicon in the requisite proportions: $Si + SiO_2 = 2SiO$. When the mixture is heated to 1000-1100°, the SiO evaporates and forms a thin protective layer over the plate and Mg-Bi film. Films protected in this way are fairly stable as regards atmospheric influences.

As is known the electrical and optical properties of very thin films differ appreciably from the properties of bulk samples of the same substances, but at a certain thickness of the film for each substance these anomalies vanish. Preliminary tests showed that in our case these "film" effects disappear at a thickness of the order of 500-600 Å. Our films always had a thickness of not less than 1000 Å. Hence it may safely be assumed that where our results are concerned such "film" effects were absent or negligible. From the results of other investigators[7], it is known that the properties of films under conditions analogous to those of our experiments do not differ from the properties of the bulk materials.

Optical transmission

Inasmuch as the attributes of compounds close to Mg_3Bi_2 must approach those of a dielectric, there was reason to assume that this would be evidenced in the optical properties of the compound, in particular, as regards its transparency. And, indeed, a Mg-Bi film prepared in the above described manner did contain a narrow strip transparent to visible light at a certain point; the other sections of the film were opaque and had a metallic lustre[8].

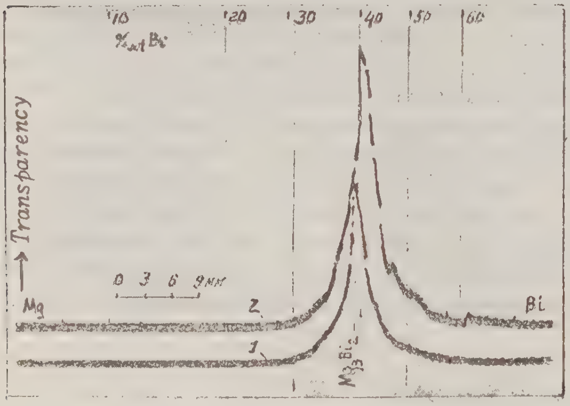

Fig. 1. Transmission curve for Mg-Bi film.

Evaluation of the distribution of components along the plate shows that the transparent strip appears at the point where the composition corresponds to the stoichiometric formula Mg_3Bi_2. Fig.1 shows the transmission curve obtained on a Blokhin recording microphotometer. Curves 1 & 2 were recorded, respectively, 10 minutes after exposure of the film to atmosphere and after 3 hours heating at 230° under vacuum. The films to which these curves pertain did not have a protective coating. However, films with a protective SiO coating yielded very similar curves. It may be noted that the drop in transmission on the side of increasing concentrations of magnesium is somewhat steeper than on the side of excess bismuth.

The absolute magnitude of the transmission coefficient for white light (incandescent bulb) is 20-25%. We also carried out preliminary investigations of the transmission of layers of Mg-As, Ca-Bi and Ca-As (protected with an SiO coating). In all these cases there is observed a transparent strip in the region corresponding to the composition A_3B_2 (where A is the element of Group II and B is the element of Group V).

These results for the transmission of Mg-Bi films have been substantiated by the investigation of Kurov[9].

These experiments proved that Mg-Bi alloys lose their metallic properties as the composition approaches Mg_3Bi_2 (i.e., the A_3B_2 proportions). Hence the electrical properties of this system are of undoubted interest.

Electric conductivity of Mg-Bi alloys

The dependence of the conductivity on the composition of the alloy was investigated in the following manner.

Before evaporation of the test metals a contact layer of a sufficiently hard and well-adhering metal (chromium or magnesium) was applied (also by evaporation) along two edges of the glass plate. The central portion of the glass plate was covered with foil. Next the main foil was removed, the contact strips were partially covered with foil after which the Mg and Bi were evaporated, so that the Mg-Bi film slightly overlapped the contact strips, thus forming a dependable electrical contact. Finally the alloy film was divided into separate isolated strips 1.5 mm (sometimes 1 mm) wide by means of a special cutter on a graduating machine. The concentration steps for the successive strips were evaluated to be about 2$\%_{at}$ Bi.

The plate was then mounted in a special holder with individual steel springs contacting the successive strips. The leads from the springs were brought into a selector switch so that each strip could be connected to the measurement bridge incorporating a high-resistance potentiometer in turn.

To protect the film against the influence of air, the entire assembly was installed under a vacuum hood even when the film was coated with a layer of SiO. Thus the film was exposed only for the 15-20 minutes for installing it in the special holder.

The outlined procedure obviously does not permit of measuring the resistance corresponding to a definite uniform composition. It does, however, yield the general dependence of the resistance on the composition.

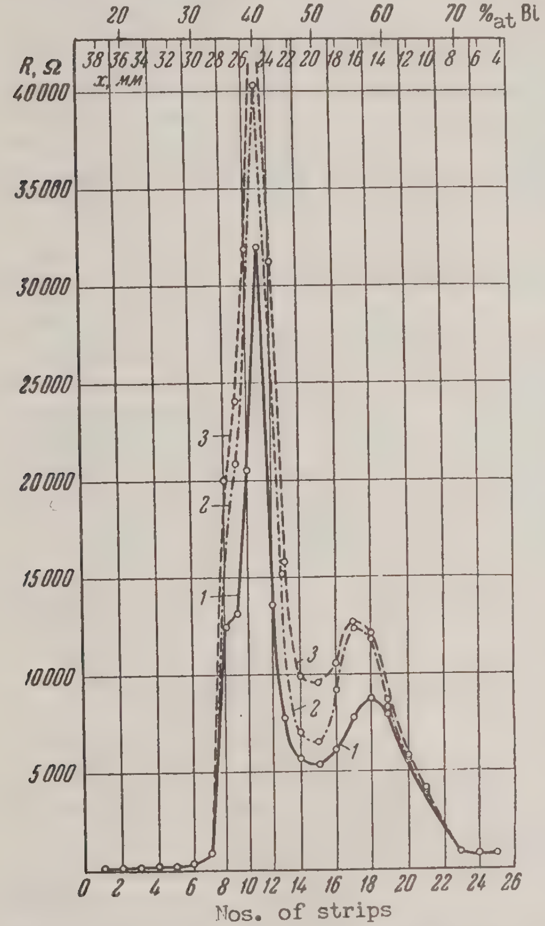

Fig.2. Variation of the resistance with composition for an unprotected Mg-Bi plate: 1) recorded 7 hrs after preparation of the film, 2) recorded 31 hrs after preparation, 3) recorded 10 hrs after preparation.

In all, we investigated several dozen specimens. The qualitative variation of the resistance with composition was the same in all cases. One cannot, of course, expect exact reproducibility of the results, since the cuts separating the strips were positioned arbitrarily and the concentration intervals on different sample plates did not necessarily coincide. Curves giving the variation of resistance with the composition for an unprotected film are shown in Fig.2. As may be seen there is a sharp maximum corresponding to the Mg_3Bi_2 composition. There is another lower peak in the vicinity of the 50$\%_{at}$ concentration. Exposure to air leads to an appreciable increase of resistance in the region of the maximum.

A similar effect of air on the conductivity of Mg-Bi films has been observed by Kurov[9]. However, his explanation of this effect as being due to the formation of MgO and the separation of free bismuth appears doubtful to us. This explanation has also been questioned by Mochan[10]. It should be noted that heating of the film at a temperature of about 250° leads to a greater stability of the electrical properties and to an appreciable lowering of the second peak; this is apparently connected with diffusional ordering processes which go to completion during the heating. The curve of Fig.3 shows the variation of the resistance with the composition for a film protected with a layer of SiO after preliminary heating for 3 hours at 230°. The points on the figure are the results of repeated measurements carried out over a period of 15 days after preparation and heating of the film. Neither prolonged exposure to air nor repeated heating and cooling produced any appreciable change in the properties of the film. This is evidence of the effectiveness of the SiO protective layer.

The resistivity of the strips containing Mg_3Bi_2 (plus a certain amount of material of other composition) was found to be 10^{-1}-10^{-2} ohm cm, i.e, some 4-5

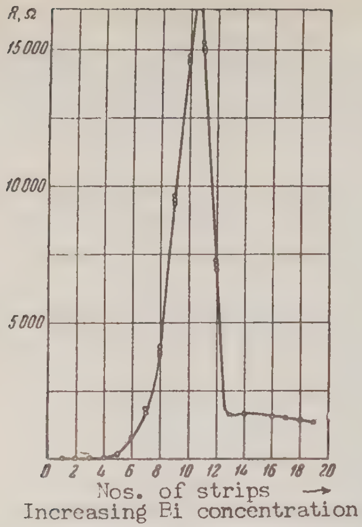

Fig.3. Variation of resistance with composition for a Mg-Bi film protected by a layer of SiO.

orders of magnitude greater than the resistivity of the initial metals. Obviously, the resistivity of pure Mg_3Bi_2 must be appreciably greater, but it could not be determined with our procedure.

We also carried out an experiment with a film prepared not by simultaneous evaporation of Mg and Bi but by successive application of layers of both these metals under the same conditions as those employed in preparing the composite films. The film prepared in this manner does not have a transparent strip and the maximum in the resistance vs composition curve is very weak. After heating for 1 hour at 230° the resistance at the maximum (Mg_3Bi_2) increased by a factor of 3.8; after a second heating for 3 hours at 230° the resistance at the maximum increased to 15 times the initial value. This shows that diffusion leads to ordering with formation of stable Mg_3Bi_2 crystals, rather than to chaotic intermixing of the atoms. No transparent strip was formed in this case, however, probably because the heating temperature was not high enough.

Temperature dependence of the conductivity

In order to ascertain the character of the conductivity it is important to determine its temperature dependence. We investigated the variation of resistance in the interval of temperatures from that of liquid nitrogen to 200°. For the measurements in the higher range of temperatures the plate with the holder was mounted in a container with an appropriate lead-sleeve and the whole assembly was placed in an electric furnace. The specimen was heated by radiation. To accelerate attainment of thermal equilibrium the brass strips, forming the holder, in contact with the glass plate were blackened. For measurements in the temperature range below room temperature the container with the specimen was placed in a Dewar flask with solid carbon dioxide or liquid nitrogen. The temperature of the film in each case was measured by means of a copper-constantan thermocouple mounted in contact with the film. The measurements were made both on SiO protected and on unprotected films. There was no appreciable difference between the results.

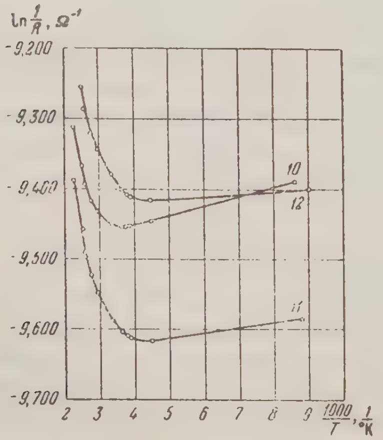

Fig.4. Temperature dependence of the conductivity.

Fig.4 shows the variation of log 1/R with 1/T (R is the resistance and T is the temperature) for one of the investigated films. The curve identified by the number 11 (the number of the strip on the specimen) pertains to the strip containing the Mg_3Bi_2 material, curve 10 pertains to the neighboring strip richer in bismuth, while curve 12 pertains to the neighboring strip richer in magnesium.

As may be seen from the curves the temperature coefficient of the resistance for sections of the film close to Mg_3Bi_2 in composition has a semiconductor character. According to our measurements the range of concentrations of Mg-Bi alloys with semiconductor conductivity appears to be fairly wide. It extends to bismuth concentrations of 80--85$\%_{at}$ on one side and to 60$\%_{at}$ concentrations of magnesium on the other.

Outside this range the sign of the temperature coefficient of resistance of the Mg-Bi alloys is the normal one for metals.

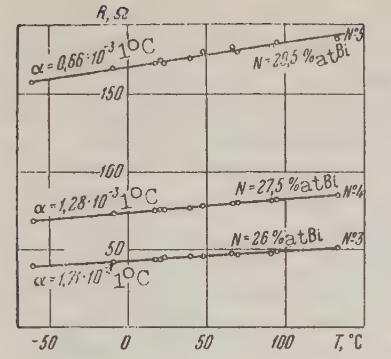

Fig.5. Temperature dependence of the resistance for strips with metallic conduction.

Curves giving the variation of resistance with temperature for three strips with metallic conductivity are shown in Fig.5. The average bismuth concentrations in these strips and the values of the temperature coefficient of resistance are indicated at the respective curves. It will be seen that as semiconductor conductivity is approached, the magnitude of the temperature coefficient decreases. This is the usual regularity for intermetallic compounds (cf. Ref.11).

It will be seen from Fig.4 that for strips in the semiconductor range the temperature coefficient changes sign at about 25°. Below this "inversion" point the temperature coefficient is very small, while at higher temperatures the conductivity increases rapidly with temperature. This type of temperature dependence of the conductivity is observed for many other semiconductors (Refs.12 & 13).

It may be assumed that the left-hand (high-temperature) section of the curves corresponds to intrinsic conductivity, while the right hand section corresponds to extrinsic conductivity. As we know, the width of the forbidden band or the magnitude of the activation energy ΔE can be determined from the slope of the left-hand section of the curves in Fig.4. For our curves ΔE is equal to about 0.06 ev. It should be emphasized, however, that this value pertains to a film strip 1.5 mm wide comprising a range of concentrations of several percent about Mg_3Bi_2. Hence the cited value of ΔE is an average one for the range of concentrations in the given strip. Bearing in mind that any deviation from the stoichiometric proportions reduces the activation energy (see Ref.11) and that our measurements were made at temperatures not exceeding 150°, it may be assumed that the actual activation energy of the compound Mg_3Bi_2 is of the order of 0.1 ev. So low an activation energy may be explained by the fact that bismuth is a less electronegative element than, for example, antimony, for it is known that the activation energy of metallic compounds decreases for less electronegative components (as well as for less electropositive components where the second element is concerned).

In the case of films prepared by separate (non-simultaneous) evaporation of the components, the sign of the temperature coefficient of resistance remains positive throughout. However, after heating at 230°, the temperature coefficient of the resistance of the strip that might be assumed to contain the Mg_3Bi_2 composition does change sign and its resistance, as noted above, increases sharply. This again indicates that the annealing leads to a change in the structure of the film, i.e., to the gradual formation of the compound Mg_3Bi_2 with its characteristic heteropolar bonds.

Thermoelectromotive forces in Mg-Bi alloys

In order to determine the character of the current carriers in the semiconductor Mg-Bi alloys, we investigated the thermo-emf of these alloys with respect to copper. For measuring the thermo-emf the plate with the film was mounted on a special stand which could be displaced by means of a micrometer screw. Two spring-mounted copper probes with sharp points could be brought into contact with the film. The points of the probes were carefully ground and polished in order not to damage the film. The requisite temperature difference between the probes was obtained by means of heaters of nickeline wire wound on the cylindrical parts of the probes. Temperature difference was measured by a differential copper-constantan thermocouple; the junctions of the thermocouple were fastened in recesses in the probes at a distance of 2 mm from the tip. The emf of the differential

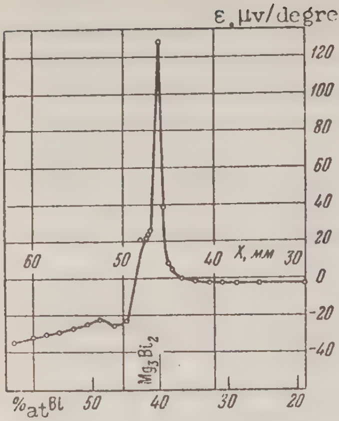

Fig.6. Dependence of the thermo-emf on the composition.

thermocouple was measured with a PT-1 potentiometer. The thermo-emf of the film-copper couple was measured by means of a PPTV-1 potentiometer. As the film was moved along under the probes by means of the micrometer screw, we obtained the thermo-emf for different sections of the film.

Preliminary thermo-emf measurements with films of pure Mg and pure Bi showed that the set-up yielded satisfactory results, for the values obtained were in agreement with the data of other investigators[14]. With film thicknesses exceeding 500 Å for bismuth and 100 Å for magnesium the thermo-emf does not depend on the film thickness and is equal to that characteristic of bulk specimens.

The variation of the thermo-emf with the composition is shown in Fig.6. The horizontal axis is scaled in coordinates of the film, the indicated figures being the corresponding calculated values of the bismuth concentration (percent atomic). The sharp peak in the thermo-emf comes at the same point on the film where the transmission and resistance maxima were observed. The value of the thermo-emf attains about 150 microvolts/degree. The sign of the thermo-emf in the region of the peak is positive. To both sides of the peak the thermo-emf falls off sharply, changes sign and gradually approaches the value characteristic of the respective pure metals. the sign of the thermo-emf remains positive in the entire semiconductor region. This is evidence that the conductivity in the semiconductor Mg-Bi alloys is of the p-type. It is interesting to note that both alloys with an excess of magnesium and alloys with an excess of bismuth are characterized by hole conduction. The hole character of the conduction is also substantiated by our measurements on the current-voltage characteristics of metal-Mg-Bi film junctions.

Conclusions

Our experiments show that Mg-Bi alloys in the vicinity of the stoichiometric Mg_3Bi_2 composition are extrinsic semiconductors. The compound Mg_3Bi_2 itself, as optical measurements show, has attributes characteristic of dielectrics. The current carriers in semiconductor Mg-Bi alloys are holes; hole conduction is observed to persist even with some excess of either of the components. The fact that the temperature coefficient of resistance at low temperatures (below 25^o) has the sign characteristic of metals may be explained if it is assumed that the acceptor impurity levels are located so close to the top of the filled band that even at low temperatures they are already occupied by electrons from this band. Consequently, the concentration of current carriers (holes) remains constant and the temperature dependence of the conductivity is similar to that for metals.

From the methodological standpoint it follows from our experiments that while the method of Vekshinskii does not allow of determining certain important parameters of semiconductors (carrier mobility, etc.), it is highly suitable for preliminary investigation of binary systems.

Department of Physics of the
"S.M.Kirov" Ural Polytechnical Institute

References

1. A.F.Ioffe, Iubileinyi sbornik, posviashchennyi XXX godovshchine Oktiabr'skoi revoliutsii (Symposium dedicated to the 30th anniversary of the October Revolution), 1947.

2. Ia.I.Frenkel', Vvedenie v fiziku metallov (Introduction to the physics of metals), second edition, M.1950.

3. B.I.Boltaks & V.P.Zhuze, Zhur.tekh.fiz., 18, 1459 (1948).

4. T.S.Moss, Proc.Phys.Soc., 63B, 63 (1950).

5. G.Busch, F.Hulliger & U.Winkler, Helv.Phys.Acta, 27, 195 (1954); 27, 249 (1954).

6. S.A.Vekshinskii, Novyi metod metallograficheskogo issledovaniia splavov (A new method of metallographic investigation of alloys), 1944.

7. I.V.Mochan, Zhur.tekh.fiz., 18, 1485 (1948).

8. A.K.Kikoin & G.D.Fedorov, Doklady AN SSSR, 92, 1163 (1953).

9. G.A.Kurov, Doklady AN SSSR, 94, 207 (1954); G.A.Kurov & Z.G.Pinsker, Doklady AN SSSR, 94, 439 (1954).

10. I.V.Mochan, Doklady AN SSSR, 98, 579 (1954).

11. B.I.Boltaks & V.P.Zhuze, Iav. AN SSSR, Ser.fiz., 16, 155 (1952).

12. G.Busch, P.Junod, U.Katz & U.Winkler, Helv.Phys.Acta., 27, 193 (1954).

13. F.Trendelenburg, Z.f.Angew.Chem., 66, 520 (1954).

14. E.Justi, M.Kohler & G.Lautz, Z.f.Naturforsch, 6a, 456 (1951); 6a, 544 (1951).

ELECTRICAL PROPERTIES OF MANGANESE-GERMANIUM ALLOYS

- I.G.Fakidov, N.P.Grazhdankina & V.N.Novogrudskii

Introduction

I. Among the numerous ferromagnetic compounds of the transition metals, those of manganese and chromium with elements of the V-B and VI-B subgroups of the periodic table occupy a special place. Magnetically such compounds as MnS, MnTe, MnSb, MnP, MnN, CrS, CrTe and CrSb have a number of distinctive characteristics which justify putting them in the class of ferrimagnets.

These characteristics, which distinguish the list of compounds from ferromagnetic metals and alloys and assimilate them in a sense to antiferromagnetic materials, are due to the simultaneous existence of ferromagnetism and antiferromagnetism. The crystal lattice of these compounds is divided into two different (as regards type of crystal structure) "magnetic" sublattices with antiparallel magnetization; in each of these sublattices, however, the magnetic moments of all the magnetoactive ions are oriented parallel to each other. The net spontaneous magnetization on the crystal as a whole is not zero in view of the nonequivalence of the magnetic moments of the transition metal ions in the different "magnetic" sublattices. A significant part here is played by the indirect nature of the exchange interaction between the electron spins of the different ions, i.e., the ferromagnetic and antiferromagnetic state in these compounds is determined by a form of interaction between the magnetoactive ions in which a substantial role is played by magnetically neutral ions.

From the point of view of determining the conditions under which ferromagnetism and antiferromagnetism develop it is important to ascertain the influence of the type of crystal lattice and its parameters (as well as any change in the nature of the chemical bonds associated therewith) on the magnetic properties of these alloys. The presence of exchange interaction between the spin magnetic moments leading to antiferromagnetism of these substances cannot but affect their electric properties just as the interaction between the outer electrons (conduction electrons) and inner electrons (i.e., the predominant interaction in ferromagnetism) influences the electric properties of ferromagnetic materials.

It must be admitted that the electric properties of the compounds in question have scarcely been studied despite the fact that complex investigation of the magnetic and electric properties in conjunction with studies of their structure should be of undoubted interest. In the present report we shall give only some of the results of our extensive investigations of the electric, galvanomagnetic, thermo-electric, thermal and magnetic properties of alloys of the transition metals with elements of the fifth and sixth subgroups of the periodic table.

II. Investigation of the electric properties of alloys of manganese with germanium is important for the following two reasons.

1. Alloys of manganese with germanium as one of the representatives of the fourth subgroup and compounds of manganese with elements of the sixth subgroup have the same Ni-As type crystal structure, but differ from each other as regards magnetic properties: the former are ferromagnets, while the latter are ferrimagnets. In view of the similarity of crystal structure the character of the magnetic interaction can be affected only by the difference in spacing between the manganese atoms and the chemical nature of the magneto-neutral atoms whose properties determine the nature of the indirect exchange. These distinctive characteristics in turn cannot but exert a certain influence on the electric properties of the alloys.

2. Analyzing the experimental data on the structure and magnetic properties of alloys of manganese with elements of the fourth and fifth subgroups of the periodic table, Guilland[1] noted that antiferromagnetic interaction occurs in

these compounds when the separation between manganese ions located in the same magnetic sublattice (Mn_I-Mn_I) is smaller than the distance between manganese ions composing two different sublattices (Mn_I-Mn_{II}). At the same time the Mn_I-Mn_{II} distance must not exceed the critical value of 2.81 Å, above which ferromagnetism appears.

According to Castellir[2], the Mn_I-Mn_{II} distance for the Mn_5-Ge_3 alloy is 3.08 Å, which indicates that antiferromagnetic interaction cannot occur in this compound. In connection with this the decrease in the magnetic moment of Mn observed in Mn_5Ge_3 (M = 2.5 μB) is not due to mutual compensation of the moments of the two magnetic sublattices but rather to partial filling of the 3d level of Mn by the outer electrons of Ge, which in turn should lead to the appearance of heteropolar bonds. The presence of even weakly pronounced heteropolar binding in this compound should have a marked effect on the electric properties of the Mn-Ge alloy.

Survey of the literature

Until recently the Mn-Ge system has been studied primarily for the purpose of ascertaining its phase and structural characteristics. Particular attention has been paid to the influence of germanium on the polymorphous transformations of manganese. Zwieckert, Jahn & Schubert[3] investigated the phase diagram of Mn-Ge and established that at germanium concentrations of 23.8, 28.6, 37.5 and 40%$_{at}$ there are formed four intermetallic compounds: $Mn_{3.25}Ge$, Mn_5Ge_2, Mn_5Ge_3 and Mn_3Ge_2 (Fig.1). The weak maxima in the phase diagram observed at 920 and 932° correspond to the chemical compounds Mn_5Ge_2 and Mn_5Ge_3. The compounds $Mn_{3.25}Ge$ and Mn_3Ge_2 form by peritectic transformations: Mn_3Ge_2 forms at 745° from Mn_5Ge_3 and a melt containing 50.5%$_{at}$Ge, while $Mn_{3.25}Ge$ forms at 900° from the γ-solid solution and the liquid phase containing 23.8%$_{at}$Ge. These chemical compounds form a number of eutectics with each other.

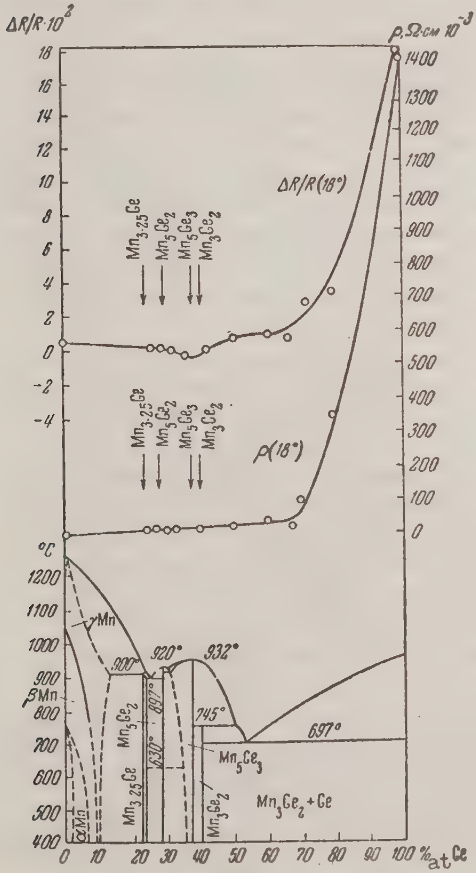

Fig.1. Phase diagram of Mn-Ge alloys and dependence of the resistivity and change in resistivity in a magnetic field on the composition of the alloy.

$Mn_{3.25}Ge$ and Mn_5Ge_2 at 897° and 24.5%$_{at}$Ge form a eutectic which readily decomposes when the alloy is quenched in water. Mn_5Ge_3 and Mn_5Ge_2 also form a eutectic; the eutectic point lies at 915° and 29%$_{at}$Ge. The eutectic mixture of the chemical compound Mn_3Ge_2 with germanium forms at a temperature of 637° and a germanium concentration of 52.5%$_{at}$. So far it is not known whether solid solutions of Mn_5Ge_3 with Mn_5Ge_2 and Mn_3Ge_2 form. It has only been established that Mn_5Ge_2 can form solid solutions with Mn_5Ge_3; however, the homogeneity region is very narrow at room temperatures.

It has been established through x-ray analysis that the compound $Mn_{3.25}Ge$ has a closely packed hexagonal lattice. Specimens subjected to prolonged heat treatment exhibit superstructure.

The compound Mn_5Ge_3 has a crystal structure of the Ni-As type. High temperature annealing, just as in the case of $Mn_{3.25}Ge$, leads to the formation of superstructure. It has been established by microstructural analysis that at a temperature of 630°, Mn_5Ge_2 undergoes a polymorphous transformation as a result of which the relative orientation of the crystals is changed. Specimens quenched from a temperature higher than the indicated transition temperature differ from annealed specimens in that they have a uniform orientation of the crystals relative to each other. The crystal structure of Mn_5Ge_3 was earlier assumed to be of the Ni-As type, but is actually, as Castellir showed[2], a $D8_8$ structure analogous to that of Mn_5Si_3.

Aside from the above described structural features of the Mn-Ge system, little is known regarding its physical properties. Zvieckert, Jahn & Schubert[3] in their study of this system noted that the low temperature modification of Mn_5Ge_2 and the compound Mn_5Ge_3 are strongly ferromagnetic. On the basis of this it was suggested that the phases of composition intermediate between Mn_5Ge_2 and Mn_5Ge_3, i.e., alloys in the 28.6-37.5$\%_{at}$ Ge concentration interval, must also be ferromagnetic. No other ferromagnetic alloys were found in the system.

Some time after the work of Zwieckert, Jahn & Schubert, Castiller[4] investigated the magnetic properties of the compound Mn_5Ge_3; in the course of his investigation he determined the temperature dependence of the magnetization in the 90 to 193°K temperature range, the Curie point ($\theta = 320°K$) and the magnetic moment of the manganese in the compound ($M = 2.57\ \mu B$).

Despite the fact that there are some indications in the literature regarding the existence of another ferromagnetic compound (Mn_5Ge_2) and phases of close composition, we were unable to find any published data on investigations of their magnetic and electric properties.

Preparation of specimens and measurement procedure

The Mn-Ge alloys of different chemical composition were obtained by fusing finely ground and thoroughly mixed manganese and germanium powders in evacuated sealed-off quartz ampoules. For the former component, we used electrolytic manganese having the following chemical composition: 99.8% Mn, 0.07% S, 0.07% C and 0.03% P. In order to drive off all residual gases and oxides, the manganese was remelted under high vacuum. Regarding the purity of the germanium one can judge from the value of the electric resistivity which was 1.43 ohm cm at 18°. Chemical analysis of the germanium used showed the following: Ge $>$ 99.972%, Si $<$ 0.0004%, Al $<$ 0.0004%, Fe $<$ 0.001% and As $<$ 0.001%.

The thermal conditions under which the alloy was prepared proved to have a strong influence on their physical properties. According to the phase diagram (see Fig.1) the melting points of Mn-Ge alloys of different composition (from 25.2 to 80$\%_{at}$Ge) lie in the temperature interval from 930 to 850°. In view of this the thermal regime employed in preparing the alloys was the following: the alloys were heated to 100° above their melting points and held at this temperature for 2 hours; then the temperature was slowly reduced to just below the melting point of the given alloy and held at this point for 3 hours to insure homogenization of the alloy; finally the product was cooled slowly with the furnace.

In all, we prepared and investigated 12 alloys containing 25.2, 27.8, 30, 33.3, 40.8, 50, 60.4, 67.3, 69.2 and 80$\%_{at}$ germanium. All the Mn-Ge alloys proved to be ferromagnetic, but were characterized by different Curie points. The Curie temperature for alloys with a Ge content from 25 to 33.4$\%_{at}$ was nearly the same (+25°). Thus it may be assumed that the ferromagnetism of these alloys is due to the presence of the same single ferromagnetic phase, apparently, Mn_5Ge_2.

The Curie temperature for alloys with a germanium content of 37-40$\%_{at}$ is +50°, which indicates that the ferromagnetic component in this case is the compound Mn_5Ge_3. Alloys with a higher germanium content (above 50$\%_{at}$Ge) have two Curie points: -185° and -12°.

Our initial assumption that in this case we were dealing with two ferromagnetic phases having different Curie points was not substantiated. Examination of microsections* and microhardness determinations showed that all alloys with a germanium content from 40 to $80\%_{at}$ have only two structural components, namely, germanium and the chemical compound Mn_3Ge_2.

Thus the ferromagnetic state of these alloys can be due to the compound Mn_3Ge_2 and obtains only in the limited temperature range from -185° to -12°C. It will be noted that the lower temperature bound for the ferromagnetic state differs appreciably from 0°K. Consequently in the case of Mn-Ge alloys with a germanium content above $50\%_{at}$ one can justifiably speak of a "high-temperature" and a "low-temperature" magnetic transition.

The electric property measurements were carried out on samples in the form of thin plates cut from the different alloys and ground to the desired thickness. The measurements were made by the potentiometric method using direct current. To eliminate errors connected with side effects the resistance measurements were made for two directions of the compensating current, while the Hall emf was determined for two directions of the magnetic field and the current in the specimen. The maximum intensity of the magnetic field attained in the experiments was 22,000 oersted.

Experimental results and discussion

We measured the electric conductivity of the Mn-Ge alloys in the temperature range from 77 to 400°K. We investigated the change in the conductivity and of the temperature coefficient of conductivity as a function of the chemical composition of the alloy. The values of the resistivity for different chemical compositions at a temperature of 18° are shown in Fig.1 and in the accompanying table. Fig.1 also shows the dependence of the change in resistance (ΔR/R) in a magnetic field on the germanium content and the phase diagram for the Mn-Ge system.

Resistivity of some of the Mn-Ge samples at 18°

Composition				ρ, ohm·cm·10^{-4}
$\%_{at}$		$\%_{wt}$		
Mn	Ge	Mn	Ge	
100	0	100	0	3,8
74,8	25,2	69,17	30,83	4,2
72,18	27,82	66,25	33,75	5,4
70,0	30,0	66,8	36,2	6,8
66,74	33,26	60,28	39,72	7,9
59,21	40,79	52,34	47,66	13,7
50,0	50,0	43,1	56,90	237,0
39,75	60,35	33,2	66,8	342,0
32,66	67,34	26,84	73,16	116,0
31,8	69,2	25,19	74,81	1050,0
20,0	80,0	15,9	84,1	3510,0
0	100	0	100	14300,0

It will be seen that the resistivity of Mn-Ge alloys increases with increasing germanium content. This increase becomes more noticeable beginning with $40\%_{at}$Ge, which may be explained by the presence of germanium in the Mn_3Ge_2+Ge eutectic. The sharpest increases in resistivity with increasing germanium content occurs in alloys rich in germanium (over $66.6\%_{at}$); in this case the increase in resistivity is proportional to the increase in the germanium phase. This influence of germanium on the conductivity of the investigated alloys comes through even more clearly when we examine the change in resistance in a magnetic field as a function of the chemical composition of the alloys (see below).

The character of the change in the resistivity with chemical composition in the 20 to $40\%_{at}$Ge range merits particular attention. The absolute value of the resistivity of the alloy in this range is close to the value of ρ for pure manganese ($3.8 \cdot 10^{-4}$ ohm cm). The absence of clear peaks in the ρ vs %$_{at}$Ge curve at the points for component proportions corresponding to $Mn_{3.25}Ge$, Mn_5Ge_2, Mn_5Ge_3 and Mn_3Ge_2 leads us to assume that we are dealing here with materials having a metallic type of conduction. If $Mn_{3.25}Ge$, Mn_5Ge_2, Mn_5Ge_3 and Mn_3Ge_2 were typical chemical compounds with strong ionic-homeopolar bonds, deviations from the exact stoichiometric compositions should be accompanied by a sharp increase in the conductivity, for in this case the change in conductivity would be due to a change in the concentration of current carriers, while the change in carrier mobility would play only a secondary part. Thus we can conclude from the absolute value of the conductivity and its dependence on the composition that these materials are characterized by metallic type conduction.

---

*The etchant used for alloys containing over $30\%_{at}$Ge had the following composition: 15 g $FeCl_3$, 3 g $[Cu(NH_3)_4]Cl_2$, 50 cm³ HCl and 25 cm³ water. The alloys containing less than $30\%_{at}$Ge were etched with a $0.5\%_{at}$ solution of nitric acid in alcohol.

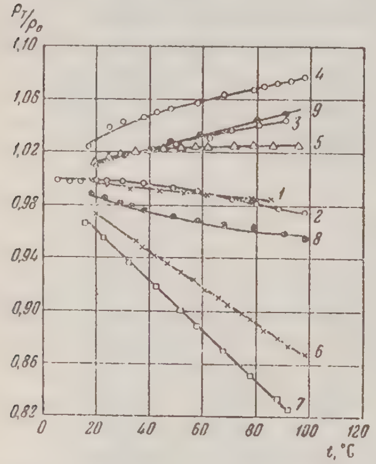

Fig.2. Temperature dependence of the relative resistivity ρ_T/ρ_0 of Mn-Ge alloys of different composition: 1) 25.2%, 2) 27.8, 3) 30, 4) 33.26, 5) 40.79, 6) 50, 7) 60.35, 8) 67.34, 9) 69.2%$_{at}$Ge.

This conclusion is substantiated by the data on the temperature coefficient of resistance, even though at first glance the observed temperature dependence of the resistivity of Mn-Ge alloys of different composition in the temperature range from 273 to 400°K appears to be somewhat complicated. As may be seen from Fig.2 the sign of the temperature coefficient changes four times as the alloy composition is varied.

For the alloy with 25.2%$_{at}$Ge the sign of the coefficient $(1/\rho) \cdot (d\rho/dT)$ is negative. When the germanium content is increased to 30%$_{at}$, the sign changes to positive and in this case the material behaves as a metal (curve 3, Fig.2). Beginning with 50-67.34%$_{at}$Ge, the Mn-Ge alloys in the given temperature interval have a temperature dependence of resistivity characteristic of semiconductors, i.e., a negative temperature coefficient. At a Ge content of 69.2%$_{at}$, the sign of the coefficient again becomes positive. The entire picture becomes clearer as we investigate the temperature dependence of ρ in a wider range of temperatures.

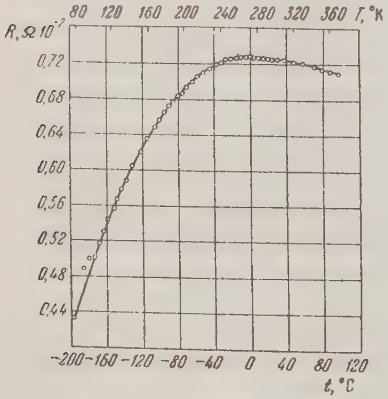

Fig.3. Temperature dependence of the resistivity of Mn-Ge alloy containing 27.82%$_{at}$ Ge.

Our further studies of the temperature dependences of the conductivity in the temperature range from 77 to 400°K showed that as regards electric properties the investigated materials can be classed as semimetals.

Fig.3 shows the temperature dependence of ρ for the Mn-Ge alloy containing 27.82%$_{at}$ Ge. It will be seen that the resistivity increases in the region of low temperatures and then begins to decrease, i.e., that the temperature coefficient changes sign at approximately 0°C. Specimens with a Ge content of 67.34%$_{at}$ also have a negative temperature coefficient only in a limited temperature range. With further increase in temperature, the temperature coefficient decreases and finally changes sign at about 160°. Alloys with germanium contents of 30, 33, 40 and 79%$_{at}$ have positive temperature coefficients of the resistivity. The very low value of the coefficient for the 40.79%$_{at}$Ge alloy suggests that the coefficient may change sign in the 100-150° temperature region. A similar temperature dependence has been observed earlier in PbS and Cr-S[5,6].

From the results it may be concluded that the investigated substances have electrons in the conduction band at low temperatures. The decrease in conductivity with increasing temperatures, just as in metals, is due to changes in the length of the free path and the effective mass of the current carriers, i.e, to changes in the mobility of the conduction electrons. With increasing temperature the current carrier concentration begins to rise with the result that at high temperatures the variation in conductivity is determined (as in semiconductors) not only by the change in the mobility of the conduction electrons but primarily by the change in the number of electrons in the conduction band due to internal thermal ionization. In view of these characteristics of the temperature dependence of the conductivity the investigated substances may be classed as semimetals.

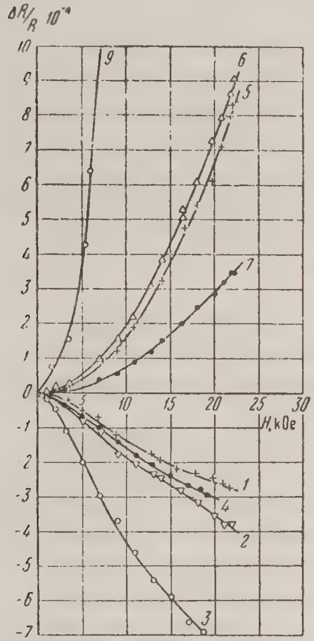

Fig.4. Relative change in electric resistance in a transverse magnetic field observed for Mn-Ge alloys of different composition: 1) 25.2%, 2) 30%, 3) 33.26%, 4) 40.79%, 5) 50%, 6) 60.35%, 7) 67.34%, 8) 69.2%$_{at}$Ge.

We felt it would be of interest to investigate the influence of an applied magnetic field on the relative change in resistance and the magnitude of the Hall coefficient for different Mn-Ge alloys in view of the information such galvanomagnetic measurements can yield on the character of the conduction mechanism and the structural states of the material.

The measurements yielded a very characteristic general regularity (Figs.4 & 1).

Alloys containing from 25.2 to 40.79%$_{at}$ Ge have a negative sign of the change in resistance in a magnetic field, i.e., they exhibit the field dependence of $\Delta R/R$ peculiar to ferromagnets. In specimens containing 50%$_{at}$ and more germanium $\Delta R/R > 0$ and the variation of the change in resistance with magnetic field strength is characterized by the square law (in weak fields), i.e., is analogous to that commonly observed for nonferromagnetic conductors. This is, apparently, due to the fact that in alloys with a high concentration of germanium the galvanomagnetic effects are determined mainly by the pure germanium which is one of the structural components of the alloy and also enters into the second component, namely, the eutectic comprised of pure germanium and the chemical compound Mn_3Ge_2. This assumption is substantiated by the fact that the value of $\Delta R/R$ increases sharply with increasing germanium content; the sign of the effect remains positive regardless of the relative directions of the current in the specimen and the external magnetic field, i.e., $\Delta R/R > 0$ both with $H \perp I$ and with $H \parallel I$.

The signs of $\Delta R_\perp/R$ and $\Delta R_\parallel/R$ are uniformly negative for the Mn-Ge alloys containing 25.2, 27.8, 30, 33.26 and 40.79%$_{at}$Ge; this may be explained by the influence of a paraprocess inasmuch as the Curie point for all these alloys lies in the region of room temperatures. The temperature dependence of $\Delta R_\perp/R$ for the Mn-Ge alloy containing 33.26%$_{at}$ Ge, shown in Fig.5, illustrates the above. As may be seen from the curves the Curie point of this alloy lies at +25°, for all the curves have a sharp minimum at this temperature. In view of this the distinctive features of the dependences of $\Delta R_\perp/R$ and $\Delta R_\parallel/R$ on the magnetic field intensity and temperature can be explained by the influence of paraprocesses. The results of our measurements are in good agreement with the characteristic dependences for even effects in the paraprocess region. According to the theory of Akulov[7], we have

$$\Delta R/R = aH^{2/3} \text{ at the Curie point,} \quad (1)$$
$$\Delta R/R = bH^{2} \text{ above the Curie point,} \quad (2)$$
$$\Delta R/R = cH \text{ below the Curie point.} \quad (3)$$

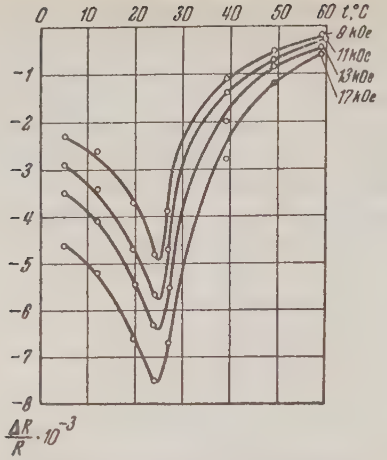

Fig.5. Temperature dependence of $\Delta R_\perp/R$ for the 33.26%$_{at}$ Ge alloy.

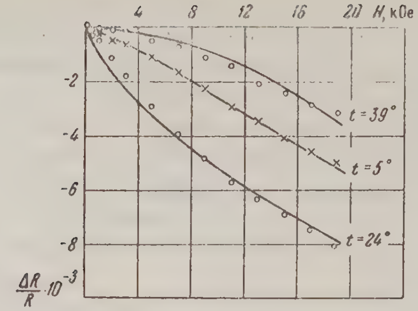

Fig.6. Dependence of $\Delta R_\perp/R$ for the alloy containing 33.26%$_{at}$ Ge on the magnetic field strength at different temperatures. Solid line - theoretical curve; points - experimental data.

By way of illustration, we have juxtaposed our data for the 33.26%$_{at}$ Ge alloy with the dependences given by Eqs.(1), (2) and (3) in Fig.6. As may be seen the theoretical curves lie close to the experimental points (here we have taken $a = 1.13 \cdot 10^{-5}$ and $b = 0.98 \cdot 10^{-11}$).

In order to obtain information on the current carrier concentration and mobility, we measured the Hall effect in a number of specimens. In calculating the carrier concentration we assumed that carriers of only one sign were present inasmuch as all the investigated specimens always had n-type conductivity as evinced both by the sign of the Hall effect and the sign of the thermo-emf.

In addition, utilizing the determined dependences of relative change in resistance in magnetic fields, we evaluated the current carrier mobilities on the basis of the data pertaining to weak magnetic fields according to the familiar formula[6] for conductors with one type of current carrier. The calculated concentration and mobility values vary, depending on the composition of the Mn-Ge alloy: the concentration values range from $1.3 \cdot 10^{17}$ to $1.6 \cdot 10^{19}$ cm^{-3}, while the mobility values range from 400 to 1700 cm^2/volt sec.

Conclusions

In view of the fact that we still do not have sufficient data for a complete quantitative analysis of the electric properties of Mn-Ge alloys, we shall limit ourselves to the following observations.

1. It has been established that as regards the absolute magnitude of the resistivity (from 10^{-4} to 1.4 ohm cm) the investigated materials occupy an intermediate position between metals and semiconductors. From analysis of the observed dependences of ρ and $\Delta R/R$ on the chemical composition of the alloy and the temperature, it may be assumed that metallic type bonds obtain in $Mn_{3.25}Ge$, Mn_5Ge_2, Mn_5Ge_3 and Mn_3Ge_2.

2. It was established from the sign of the thermo-emf and the Hall effect that all the investigated substances are n-type conductors. The current carrier concentration in them varies from 10^{17} to 10^{19} per cm^3. The conduction electron mobilities lie in the range from 400 to 1700 cm^2/volt sec.

3. Determinations of the temperature dependence of the conductivity show that as regards their electric properties Mn-Ge alloys belong in the class of semimetals and, in the temperature range from 77 to 400°K, have a constant number of current carriers, the energy of which lies in the conduction band.

4. It was established that the Mn-Ge system comprises three ferromagnetic phases, corresponding to the compounds Mn_5Ge_2, Mn_5Ge_3 and Mn_3Ge_2. The compound

Mn_3Ge_2 has two ferromagnetic transition points: -185° and -12°C.

The writers desire to thank S.S.Levina for assistance in preparing the microsections and for performing the microhardness measurements.

Institute of Metal Physics of the
Ural Branch of the USSR Academy of Sciences

References

1. Ch.Guilland, C.R., 235, 468-70 (1952), Rev.Modern Phys., 25, 119 (1953).
2. L.Castellir, Z.Metallkunde, 46, 199 (1955).
3. U.Zwieckert, E.Jahn & K.Schubert, Z.Metallkunde, 40, 433 (1949).
4. L.Castellir, Mh.Chem., 82, 1059 (1951); 84, 765 (1953).
5. Iu.Dunaev & Iu.Maslakovets, Zhur.eksp.i teor.fiz., 17, 901 (1947).
6. I.G.Fakidov & N.P.Grazhdankina, Doklady AN SSSR, 63, 27 (1948).
7. N.S.Akulov, Ferromagnetizm (Ferromagnetism), M.1939.
8. F.Seitz, Phys.Rev., 79, 372 (1950).

THERMOMAGNETIC EFFECTS IN SEMICONDUCTORS

(Abstract*)

- Kh.I.Amirkhanov, R.I.Bashirov, A.Z.Daibov & I.M.Tsidil'kovskii

Since 1952 the writers have been engaged in the study of thermomagnetic effects in a number of semiconductors: lead sulfide, selenide and telluride, cuprous oxide and the selenides and tellurides of bismuth, tellurium and germanium. It was shown that the Nernst-Ettingshausen effect allows of calculating the current carrier mobility and identifying the scattering mechanism (scattering by acoustical or optical lattice vibrations or by neutral or ionized impurities dominating at a given temperature. A new thermomagnetic effect, called the longitudinal-transverse effect, has been predicted theoretically and studied experimentally. The case of mixed conductivity was thoroughly analyzed and it was shown that the Nernst-Ettinshausen effect makes it possible to obtain information of the magnitude and temperature dependence of the current carrier mobility in this complicated case as well.

DISCUSSION

P.I.Baranskii: What proofs have you for the assertion that in the investigated p-type germanium scattering from neutral impurities centers obtains at low temperatures? Did you use tagged atoms?

I.M.Tsidil'kovskii: We have no direct proof of the presence in the sample of neutral impurities, scattering of current carriers by which might become predominant at low temperatures. Unfortunately, appropriate tracers were not available. Our assertion of the predominance of scattering by neutral centers in p-type Ge at low temperatures is based on the following facts: when the temperature is reduced below 160°K the hole mobility as determined from the Hall effect virtually does not change, while the Nernst-Ettingshausen field asymptotically approaches zero. Now since at such low temperatures carriers of only one type (holes) participate in the conduction, nullification of the Nernst-Ettinghausen effect can occur only when $n \to 1$ (n is the exponent in the expression for the dependence of the carrier mean free path l on the velocity v: $l \approx v^n$). Both these facts are in good agreement with Erginzoi's familiar formula for scattering by neutral centers. Moreover, the concentration of neutral centers as evaluated by Erginzoi's mobility formula is at least one order of magnitude greater than the concentration of ionized impurities evaluated from the Hall effect. Any assumption of the predominance of scattering by ionied impurities must be rejected first because the Nernst-Ettingshausen effect in this case will have to be negative and second because the resistivity of the samples as calculated by the Conwell-Weisskopf formula proves to be appreciably smaller than the experimentally measured value.

I.V.Mochan: You explain the low temperature negative region of the Nernst-Ettingshausen effect in n-type Ge by impurity ion scattering, but at concentrations of ionized centers of the order of 10^{14} cm^{-3} the electron mobility as computed by the Conwell-Weisskopf formula differs by one or two orders of magnitude from the value of the mobility obtained from the Hall effect. How can one reconcile your explanation with this fact?

I.M.Tsidil'kovskii: We explain the low temperature negative region of the Nernst-Ettingshausen field in n-type Ge not by "pure" scattering by ionized impurity centers but only by the predominance of this type of scattering over other types. We believe that in the investigated specimens at $T \gg 130$°K one cannot disregard carrier scattering by thermal vibrations of the lattice (and possibly by neutral impurity atoms) as compared with scattering by impurity ions. This hypothesis is based on the fact that in the temperature interval $120^{\circ}K < T < 210^{\circ}K$ the electron mobility does not yet obey the $U \sim T^{3/2}$ law, but continues to increase with the temperature although more slowly than according to the $U \sim T^{-3/2}$ law which is valid at higher temperatures. Hence one cannot expect qualitative agreement between experimental data and the theory taking into account only scattering by impurity ions. As for the Nernst-Ettingshausen effect, as follows from calculations made by Iu.N.Obraztsov, it must change sign from positive to negative at a temperature several times greater than the temperature at which the mobility is maximal, i.e., where the $U \sim T^{3/2}$ law is replaced by the $U \sim T^{-3/2}$ law. Thus the Nernst-Ettingshausen effect is a more sensitive indicator of current carrier scattering by ionized impurity atoms than the temperature dependence of the mobility. In view of this we think that the low temperature negative region of the Nernst-Ettingshausen effect can be explained without recourse to new types of scattering.

---

*The principal results of the investigations have been published in Doklady AN SSSR, 98, 557 (1954) and 102, 737 (1955) and in Zhur.tekh.fiz., 25, 742 (1955) and 26, 2195 (1956).

A NEW FORM OF THERMAL ACCEPTORS IN GERMANIUM

- V.A.Zhidkov & V.E.Lashkarev

The electrical properties of germanium subjected to heat treatment at temperatures above 500° with subsequent quenching change due to the appearance of acceptor centers. The equilibrium concentration of these centers as a function of the heat treatment temperature has been studied by a number of investigators (see Ref.1 and the bibliography therein).

In the range of annealing temperatures from 500 to 750° the dependence of the logarithm of the concentration on the reciprocal of the temperature is linear (Fig.1, curve 1), i.e., is described by the law

$$N_a = N_0 e^{-\frac{E}{kT}},$$

where $N_0 = 5.5 \cdot 10^{21}$ cm^{-3} and E = 1.25 ev according to the data of Kalashnikov & Ostroborodova[1]. The acceptor levels are located about 0.05 ev above the filled band[2].

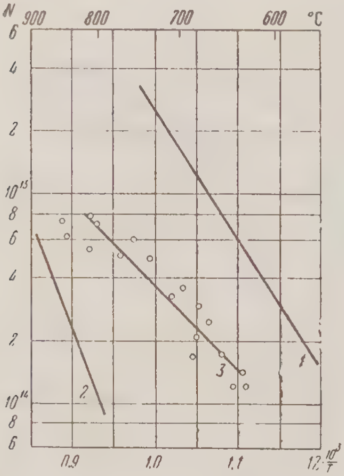

Fig.1. Equilibrium concentration of thermal acceptors as a function of the heat treatment temperature: 1) data of Kalashnikov & Ostroborodova[1], 2) data of Mayburg & Rotondi[3], 3) our data.

Mayburg & Rotondi[3] treated their specimens by passing a current directly through the germanium. The thermal hole concentration was evaluated from the resistance at the temperature of dry ice. The specimens were first held for 40 hours at 636° which led to an appreciable decrease in the concentration of thermal holes.[5] The dependence of log N_a on the reciprocal of the heat treatment temperature was found to be linear in the temperature range from 790 to 880° (Fig.1, curve 2) which corresponds to $N_0 =$ $= 1 \cdot 10^{24}$ cm^{-3} and E = 2.15 ev.

In our experiments the heat treatment of germanium was accomplished by passing a direct current through the 1.5 x 2.5 x 13 mm specimens clamped between tantalum electrodes. Tungsten probes were pressed against the central part of the specimen for measuring the resistivity and Hall effect. The specimen was heated in a vacuum chamber surrounded by the walls of a Dewar which was filled to the requisite level with liquid nitrogen. This provided the necessary conditions for obtaining a high vacuum (to $1 \cdot 10^{-7}$ mm Hg) and minimized the possibility of contamination of the specimen by impurities from the walls of the chamber. The entire assembly was mounted between the poles of an electromagnet producing a 1500 oersted field.

The heat treatment was carried out with continuous evacuation. The temperature of the specimens was determined from the resistivity in the region of intrinsic conductivity on the basis of the data in the literature[4]. The error in determining the temperature on the basis of the data in the literature[4]. The error in determining the temperature in the region of high temperatures did not exceed ±10°. That the influence of heat conduction by the electrodes was negligible where the central part of the specimen was concerned was established by determining the relation between the temperature of the specimen as indicated by the resistivity and the power dissipated at the central part of the specimen. The temperature in the 400 to 900° interval proved to be almost precisely proportional to the dissipated energy to the one-fourth power. Quenching was effected by cutting off the heating current; as a result the specimen was cooled by radiation to a temperature below red heat within a few seconds.

The thermal hole concentration was determined from the Hall effect. The set-up allowed of making these measurements at different temperatures. The measurement temperature was determined by means of a tungsten-molybdenum thermocouple, the junction of which was clamped to the specimen. For exact measurements of the temperature dependence of the thermal hole concentration, the specimen was taken out of the heat treatment assembly and placed in a special thermostatic set-up with provision for accurate temperature measurement. The equilibrium concentration of thermal acceptors was assumed to be established only after repeated heat treatments at the same temperature showed no further change in concentration. Thus in our experiments we measured the dependence of the equilibrium concentration of thermal acceptors on the heat treatment temperature.

In the temperature range from 520 to 740° our results agree with the data of Kalashnikov & Ostroborodova[1] and show good reproducivility both with increasing and decreasing temperature. The value of N_o can vary by more than a factor of two in the same specimen, depending on the initial conditions (for example, if the specimen is touched with bare hands without subsequent cleansing by etching before being mounted in the chamber). The Hall coefficient remains constant from room temperature to about 120°K provided the heat treatment temperature is not close to the temperature of transition from n-type to p-type conductivity for the given specimen. This indicates that the thermal acceptors are situated at a rather low level, in consequence of which they are completely ionized at a relatively low temperature. The carrier concentration measured from the Hall effect is the difference (in p-type germanium) between the thermal acceptor concentration and the concentration of donors initially present in the specimen.

If the specimen is heated above 740° the equilibrium carrier concentration deviates from the linear dependence characterized by curve 1 of Fig.1; the deviation increases with increasing heat treatment temperature. If the initial high temperature heating is followed by annealing at 620-720° the concentration depends on the annealing time (Fig.2).

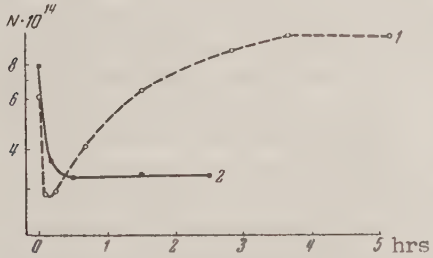

Fig.2. Influence of annealing after high temperature heat treatment: 1) anneal at 680° after 1.5 hours heat treatment at 800°; 2) anneal at 780° after 4 hours heat treatment at 800°.

Sample 1 (Fig.2) which was heated at 800° for less than 2-3 hours shows a sharp drop in concentration during the first ten minutes of annealing followed by a slow increase in concentration; the concentration finally levels off at a value close to the equilibrium concentration observed for the same temperature without preliminary high temperature treatment.

In case of sample 2 heated at a high temperature for over 4 hours the thermal hole concentration monotonically decreases during annealing. The equilibrium thermal hole concentration measured at room temperature varies exponentially with the annealing temperature in the range from 620 to 840°. The straightline plot 3 in Fig.1 corresponds to $N_o = 3.8 \cdot 10^{18}$ cm^{-3} and E = 0.79 ev. The effect is reversible and does not depend on the sequence of annealing temperatures (i.e., on the previous annealing temperature used). If such a specimen is reheated after remounting in the holder it will again have a high concentration of thermal holes which can be reduced only by prolonged annealing.

In order to ascertain the mechanism involved in the described effects we carried out the following experiment. After high temperature heating for 1 hour the direction of current through the specimen was reversed. The incipient decrease in thermal hole concentration was replaced by an increase. Annealing by means of alternating current after high temperature heating always results in a curve analogous to curve 2 in Fig.2.

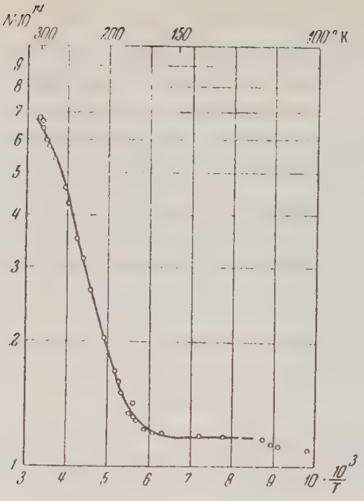

Fig.3. Temperature dependence of the thermal hole concentration.

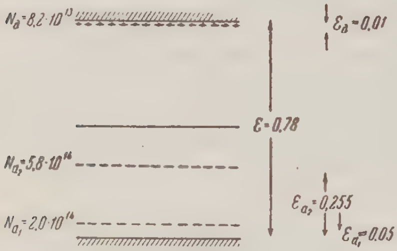

Fig.4. Energy structure of heat treated germanium.

It may be assumed that the principal role in the process of the decrease in hole concentration as a result of heating with direct current is played by electrolytic removal of the impurities responsible for the thermal transformation. Removal of impurities by evaporation plays a far less important part. At high temperatures the impurities are present in the form of ions which migrate to the edge of the specimen under the influence of the field. To obtain a lasting reduction in the equilibrium concentration of thermal acceptors by dc annealing it is not sufficient to remove the impurities from the central region of the sample; the dc annealing must be continued long enough to move the impurity material to the very end of the sample or, if possible, to eliminate it entirely through the electrode. If this is not done the impurity diffuses in the opposite direction when the current is turned off and the sample cools. Specimens purified by high temperature heating by the passage of electric current show a strong temperature dependence of the thermal hole concentration even in the region of room temperatures. Mayburg[5] mentions the difference between hole concentrations at room temperature and the temperature of dry ice. We investigated this phenomenon in detail. The temperature dependence of the thermal hole concentration as determined from the Hall effect for one of the specimens is shown in Fig.3.

To explain this temperature dependence of the concentration we assume that as a result of the given heat treatment there appear new high-lying acceptor levels. The proposed energy diagram is shown in Fig.4. The plateau in the concentration vs temperature curve corresponds to the region where the low-lying acceptor levels are fully ionized while the ionization of the high-lying acceptors has not begun. The hole concentration in this temperature interval determines the difference $N_{a_1} - N_{\partial}$. Analysis of our data carried out by the graphic method of Shockley[6] and utilizing the numerical values of Morin & Maita[4] showed that with an appropriate selection of the values of the density N_{a_2} of the acceptor levels and their energy value $\mathcal{E}_{a_2}$ above the filled band, one can obtain a satisfactory fit of the theoretical curve to the experimental points as shown in Fig.3. The energy is determined primarily by the temperature at which ionization of the high-lying acceptor levels begins. The concentration is given by the difference between the values of the thermal hole concentration before the beginning and after the completion of ionization of these high-lying levels. Thus to describe a curve of this form we need select appropriate numerical values for only two parameters; for the curve shown $\mathcal{E}_{a_2} = 0.255$ ev and $N_{a_2} = 5.8 \cdot 10^{14}$ cm^{-3} (Fig.4). This value of activation energy leads to almost complete ionization of these levels at room temperature (for the specimen in question, ionization in excess of 90%). In case of a lower density of the high-lying acceptor levels, complete ionization occurs earlier.

The accuracy of determining the activation energy depends on the accuracy of the measurements; in our case we evaluated it to be ±0.01 ev. The accuracy in determining the concentration depends greatly on its magnitude, for at low concentrations the influence of the inherent conductivity quickly becomes manifest and hence in processing the data in this region one must make assumptions regarding the mobility. We evaluate the accuracy in determining the concentration for the specimen characterized in Fig.3 as ±10%.

The difference between our data and those of Mayburg is apparently connected with the presence of these high-lying thermal acceptors. Curve 2 (Fig.1) was obtained by Mayburg at the temperature of dry ice, while curve 3 was obtained in our experiments at room temperature. Generally speaking, these straight lines do not give the true dependence of the thermal acceptor concentration on the heat treatment temperature. The values of the concentration of the low-lying thermal acceptors actually lie below curve 2. Our curve 3 approximately corresponds to the sum of the concentrations of the low- and high-lying thermal acceptors in view of the almost complete ionization of the latter at room temperature.

In cases when the sample after heat treatment was taken out of the vacuum apparatus, we used it to determine the lifetime of the extraneous carriers. This was calculated from the diffusion length determined by the familiar light method, observing all the conditions established by Rashba & Tolpygo[7].

Measurements of the lifetime of the extraneous carriers in specimens not subjected to preliminary high temperature treatment showed that the low-lying thermal acceptors are trapping centers with a cross section of $2\cdot10^{-17}$ cm^2, which is in agreement with the data of Kalashnikov & Ostroborodova[8]. In samples heated before annealing for a prolonged time at a fairly elevated temperature the lifetime remains short despite the decrease in the concentration of the thermal acceptors which would indicate that during the annealing there appear centers with a large trapping cross section. We believe that these centers are formed by the thermal acceptors in the high-lying states. We can evaluate the trapping cross section if we assume that the probability of recombination is proportional to the concentration of high-lying thermal acceptors:

$$\frac{1}{\tau} = v_T N_{a_2} S_{a_2}.$$

We computed the capture cross sections on the assumption that v_T, the thermal velocity of holes at room temperature, is 10^7 cm/sec. The calculated data for four specimens are listed in the accompanying table. For the two specimens whose energy structure was obtained from the data on the temperature dependence of the thermal hole concentration we give the calculated values of the capture cross section, while for the two other specimens we give the evaluated lower bound of the cross section based on measurements of the thermal hole concentration at room temperature. The trapping cross section for high-lying thermal acceptors is more than one order of magnitude greater than the cross section for low-lying acceptors.

N_{a_3}, cm^{-3}	τ, 10^{-6}, scc	S_{a_2}, cm^2
$2,2\cdot10^{13}$	13,5	$3,3\cdot10^{-16}$
$5,8\cdot10^{14}$	0,3	$5,5\cdot10^{-16}$
$< 5,4\cdot10^{14}$	0,8	$> 2,3\cdot10^{-16}$
$< 7,2\cdot10^{14}$	0,7	$> 1,9\cdot10^{-16}$

Conclusions

1. High-temperature heating of germanium with direct current results in partial electrolytic purification of the specimen, that is, in removal of the impurities responsible for thermal transformations.

2. Heating in this manner leads to the appearance in the germanium of levels located 0.25±0.01 ev above the top of the filled band.

3. These levels have acceptor characteristics and their concentration is strongly dependent on the temperature.

4. These acceptors are effective recombination centers trapping extraneous carriers.

Institute of Physics of the
Ukrainian SSSR Academy of Sciences
and
"T.V.Shevchenko" Kiev State University

References

1. S.G.Kalashnikov & V.V.Ostroborodova, Zhur.tekh.fiz., 25, 1163 (1955).
2. R.Baum & S.Hung, Phys.Rev., 88, 134 (1952).
3. S.Mayburg & L.Rotondi, Phys.Rev., 91, 1015 (1953).
4. F.Morin & J.Maita, Phys.Rev., 94, 1525 (1954).
5. S.Mayburg, Phys.Rev., 95, 38 (1954).
6. Wm.Shockley, Electrons and holes in semiconductors (in Russian trans., M.1953).
7. E.I.Rashba & K.B.Tolpygo, Ukr.fizich.zhurn. (Ukrainian Physics Journal) 1, 29 (1956).
8. S.G.Kalashnikov & V.V.Ostroborodova, Zhur.tekh.fiz., 25, 1168 (1955).

DIFFUSION OF ANTIMONY AND ZINC FROM THE VAPOR PHASE INTO GERMANIUM

- V.E.Kosenko

One of the methods of introducing different impurities into germanium is by diffusion. By varying the concentration of the diffused element on the surface of the crystal and the temperature and duration of heating one can obtain different distributions of the impurity at different depths in the germanium specimen. This makes it possible to prepare p-n junctions with different impurity concentrations and gradients for the purpose of investigating their properties. Further, by removing successive thin layers (by grinding or etching) from the surface of a germanium crystal with a known impurity distribution in depth, one can study the surface properties of the specific germanium crystal as a function of the concentration of a given impurity.

In the present investigation of the diffusion of antimony and zinc from the vapor phase into germanium our purpose was to determine the following:

1) the diffusion coefficient and activation energy,

2) the maximum concentration C_o and its dependence on the concentration of C_v of the given element in the vapor phase,

3) the termperature dependence of C_o, and

4) the critical concentration C_{v-cr} at which the liquid alloy phase begins to form on the surface of the crystal.

We elected to use the radioactive tracer method. Specifically, we used radioactive antimony Sb^{124} with a period of 60 days and radio-active Zn^{65} with a period of 250 days. The germanium specimens were cut from single crystals in the form of flat discs 0.5-1 mm thick and 6-8 mm in diameter. As the first step in the preparation, the faces of the discs were polished, then the specimens were heated for 30-40 hours under vacuum at 850° and finally a layer not less than 100 μ thick was removed by etching in boiling perhydrol (30% solution of H_2O_2). This etching was carried out for the purpose of removing the superficial layer in which there might persist lattice defects produced by the cutting and grinding.

The radioactive antimony was sublimed under vacuum in a quartz tube. The antimony deposit on fragments of the tube was then used for diffusion. The radioactive zinc was prepared in a similar manner.

A germanium specimen and the quartz tube fragment with the deposit of antimony were placed in a quartz ampoule which was evacuated to 10^{-5} mm Hg, degassed at this vacuum for two hours at 200° and finally sealed. The amount of antimony in the ampoule was determined from its radioactivity (measured with a B-1 counter) by comparing its activity with the activity of an accurately weighed portion of antimony enclosed in a similar ampoule. Subsequently, the different ampoules were heated for 12-24 hours at 750, 800, 975 or 925°. At these temperatures the antimony was completely transformed into the vapor phase. The complete vaporization was checked by condensing the antimony first at one end and then at the other end of the ampoule by rapid local cooling and comparing the activity at the point of condensation with the total activity of the ampoule. The concentration C_v of antimony in the vapor phase in different experiments varied between 10^{15} and 10^{17} cm^{-3}. In withdrawing the ampoules from the furnace appropriate measures were taken to ensure condensation of the antimony vapor on the wall of the ampoule opposite to the location of the specimen which effectively prevented condensation of the antimony on the specimen. For the purpose of determining the antimony concentration at different depths in the crystal successive thin (1-3 μ) and "thick" (5-8 μ) layers were removed by etching in boiling perhydrol. The thickness of the removed layers was determined by weighing the samples in the microbalance. Special tests showed that the etching was uniform over the surface of the specimens. The antimony content in each thin layer was determined from the difference in the activity of the specimens before and after etching. The counting times for the activity and background were selected so that the statistical error in determining the activity of the removed layer would not exceed 6%.

In each case, of course, the activity was compared with that of the standard (the accurately weighed portion of antimony).

It was assumed that some time after the beginning of the diffusion heating the antimony concentration under the surface of the sample would attain a maximum stable value C_0. In this case the diffusion problem is described by the equation

$$C(x, t) = C_0\left[1 - erf\left(\frac{x}{2\sqrt{Dt}}\right)\right], \tag{1}$$

where

$$erf\left(\frac{x}{2\sqrt{Dt}}\right) = \frac{2}{\sqrt{\pi}} \int_0^{x/2\sqrt{Dt}} e^{-y^2}\,dy \tag{2}$$

(x is the diffusion depth).

The temperature dependence of the diffusion coefficient D is given by the formula

$$D = D_0 e^{-E/RT}, \tag{3}$$

where T is the absolute temperature and R is the gas content.

To check the validity of the above assumption we used the method of superposition of a standard curve, which is suitable in all cases where after transformation of the functional dependence of two variables to dimensionless quantities there remain no unknown variables. In the given case the method reduces to the following. The auxiliary function $\eta = 1 - erf\,\xi$ is plotted on logarithmic graph paper; this plot serves as the standard curve. Next the values of log x are plotted against the values of log C on the same type of graph paper. Then if Eq.(1) is applicable, the experimental points can be made to fit the standard curve by appropriate horizontal or vertical displacement of the latter. The point at which the superimposed curve cuts the log C axis will give us the value log C_0, i.e., the limiting maximum concentration C_0. The point of intersection of the curve with the vertical axis will give us the point x_1 for which ξ = 1, i.e.,

$$\xi = \frac{x_1}{2\sqrt{Dt}} = 1,$$

From this we can readily calculate the diffusion coefficient

$$D = \frac{x_1^2}{4t}.$$

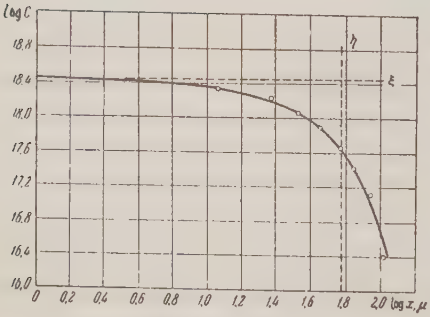

Fig.1. Method of determining the diffusion coefficient and the limiting concentration of antimony in germanium by means of a standard curve.

Fig.1 illustrates the procedure. Here the dash lines identified by η and ξ are the coordinates of the standard curve which is shown as the solid line in the figure. The experimental points are given by the circles. In the illustrated case we found $C_0 = 2.7 \cdot 10^{18}$ cm^{-3} and x_0 = 60 μ; the computed value of the diffusion coefficient was therefore

$$D = 2.0 \cdot 10^{-10}\ \text{cm}^2/\text{sec}.$$

In the case of the given experiment the diffusion temperature was 875°; the heating period 12.5 hours. The concentration of antimony atoms in the vapor was $1.4 \cdot 10^{16}$ cm^{-3}, i.e., approximately 100 times lower than the maximum concentration C_0. The dependence of the diffusion coefficient on the temperature can be found in the usual manner from the slope of the rectilinear plot for log D = = f(1/T). The activation energy for diffusion calculated on the basis of this plot proves to be E = 53 Kcal/mole; then according to Eq.(3), D_o = 1.4 cm^2/sec. The final expression for the coefficient of diffusion of antimony from the vapor phase into a germanium single crystal was obtained as

$$D = 1{,}4e^{-\frac{53000}{RT}}. \qquad (4)$$

The values of the coefficient of diffusion of antimony from the solid phase obtained by other investigators are listed in Table 1. As may be seen from the table our results do not differ appreciably from the values for D_o and E obtained for diffusion of antimony from the solid phase.

Table 1

Diffusion temperature interval	D_o, cm^2/sec	E, cal/mole	Investigators
750 - 925°	1.4	53000	Our data
710 - 905°	0.71	51000	Fuller[1]
	10	57000	Dunlap & Brown[2]

Table 2

Sample No.	Diffusion heating temp., °C	C_v, atom/cm^3	C_o, atom/cm^3	C_o/C_v
20	925	$9{,}6\cdot10^{16}$	$4{,}0\cdot10^{18}$	45
21	925	$1{,}4\cdot10^{16}$	$2{,}5\cdot10^{18}$	200
22	925	$3{,}3\cdot10^{15}$	$2{,}75\cdot10^{18}$	850
18	875	$7{,}4\cdot10^{16}$	$5{,}9\cdot10^{18}$	800
15	875	$3{,}7\cdot10^{16}$	$3{,}2\cdot10^{18}$	100
16	875	$1{,}4\cdot10^{16}$	$2{,}7\cdot10^{18}$	200
26	750	$9{,}2\cdot10^{16}$	$5{,}9\cdot10^{19}$	600
27	750	$2{,}5\cdot10^{16}$	$4{,}7\cdot10^{19}$	2000
28	750	$2{,}4\cdot10^{15}$	$4{,}0\cdot10^{19}$	17000

Worthy of note is the relation between C_o and C_v and the dependence of the ratio C_o/C_v on the temperature and on C_v. These data are listed in Table 2. It will be seen from the table that C_o is little dependent on the concentration of antimony atoms in the vapor. Further, C_o/C_v increases noticeably with decreasing diffusion temperature and may attain a value of several thousand. (We observed a value of up to 17,000.) At certain concentrations, a liquid phase consisting of an antimony-germanium alloy begins to form on the surface of the crystal. Initially forming as a surface film, the liquid phase collects into drops, the size of which increases with C_v. We found that in the investigated temperature range the formation of the liquid antimony-germanium alloy phase begins at a concentration $C_v = 10^{17}$ cm^{-3}. As for the critical values of C_o at which the formation of the liquid phase begins, we may note that, at 750°, for example, C_o attains a value of $4\cdot10^{19}$ cm^{-3}, i.e., there is one atom of Sb per 10^3 Ge atoms. One can hardly imagine so low a concentration of antimony being capable of lowering the melting temperature of germanium to 210°. It must be assumed, therefore, that the experimentally determined limiting concentration of antimony is appreciably less than the concentration of antimony atoms bound directly with the surface layer of the germanium.

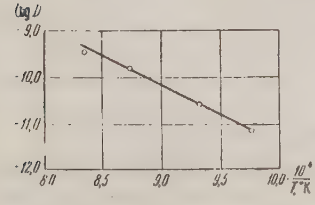

Fig.2. Temperature dependence of the coefficient of diffusion of Sb in Ge.

From the phase diagram for the antimony-germanium system[3] it is evident that the formation of the liquid phase of this alloy at 750° occurs at an antimony concentration of about $60\%_{at}$. Obviously there forms on the surface of the germanium crystal a thin layer of alloy with a very appreciable antimony content. In view of the extreme thinness of this layer, it is difficult to ascertain the exact content of antimony therein or its state at different diffusion temperatures. Further evidence in favor of the existence of such an alloy layer is the fact that the first point in the plot of log C vs log x (Fig.1) systematically appears at some distance from the curve, towards the side of higher antimony concentrations.

It will be seen from Table 2 that the maximum concentration C_o depends both on the concentration in the vapor and on the temperature. To analyze these dependences let us first examine the isothermal dependence $C_o = f(C_v)$.

We plotted the experimental points in logarithmic coordinates. The straight-line plots obtained for the two extreme temperatures - 750 and 925° - are shown in Fig.3. It can be seen that the dependence of C_o on the concentration in the vapor can be described by the formula

$$C_o = AC_v^K, \tag{5}$$

where K is weakly dependent on the temperature. It will be seen from Fig.4 that the temperature dependence of K can be described by

$$K = 8.6\cdot10^{-4}T - 0.78. \tag{6}$$

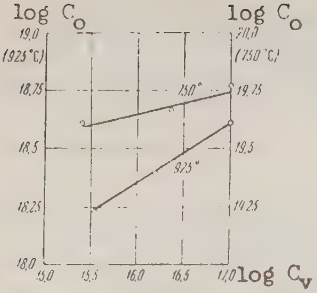

Fig.3. Dependence of the limiting concentration of Sb on its concentration in the vapor.

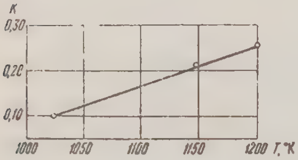

Fig.4. Temperature dependence of K.

In investigating the temperature dependence of the maximum concentration, we plotted the experimental points for log C_o/C_v^K as a function of the reciprocal of the temperature (Fig.5).

The points fell in a straight line. From the slope of this we evaluated the activation energy for the limiting concentration as E_1 = 117 Kcal/mole or 5.1 ev. Thus C_o can be characterized by the formula

$$C_0 = BC_v^K e^{\frac{117000}{RT}}. \tag{7}$$

The value of the coefficient B as determined from Eq.(7) is $1.25\cdot10^{-7}$.

Finally the relation between the maximum concentration and the concentration of Sb in the vapor is described by the empirical formula

$$C_0 = 1{,}25\cdot10^{-7}C_v^K e^{\frac{117000}{RT}}, \tag{8}$$

where $K = 8.6\cdot10^{-4}\,T - 0.78$.

By means of Eq.(8) and the determined values of the diffusion coefficient (4), we can calculate the temperature, diffusion time and antimony vapor concentration necessary to obtain a desired impurity concentration in a germanium crystal.

In passing we note that when the vacuum in the ampoule is not high (10^{-1}-10^{-2} mm Hg) the following effect is observed. If the diffusion heating is made intermittent, the curve characterizing the distribution of Sb in depth is no longer smooth and may even not be monotonic. This effect is possibly connected with a formation of an oxide film during intermittent heating. It was not observed with vacuums of 10^{-5} mm Hg or better.

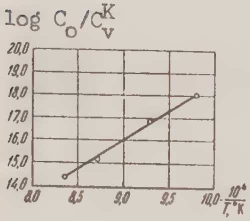

Fig.5. Temperature dependence of the upper bound of the concentration of Sb in Ge.

Diffusion of zinc from the vapor phase into germanium

The procedure used for investigating the diffusion of zinc into germanium was the same as that employed for antimony. As before single crystal specimens of germanium were used. The concentration of zinc in the vapor phase in all the experiments was approximately $1.3\cdot10^{17}$ cm^{-3}. The maximum concentration of zinc and the coefficient of diffusion were determined by the standard curve method described above.

Some of the results obtained in investigating the diffusion of zinc from the vapor phase into germanium are shown in Table 3.

Table 3

Sample No.	Diffusion heating temp., °C	Diffusion heating time, sec	Diffusion coeff., cm^2/sec	Concentr. at. cm^{-3} in vapor C_v	Concentr. at. cm^{-3} maximum C_o	C_o/C_v
42	825	$6,56\cdot10^5$	$1,84\cdot10^{-12}$	$1,29\cdot10^{17}$	$2,4\cdot10^{17}$	1,86
39	840	$3,71\cdot10^5$	$2,84\cdot10^{-12}$	$1,28\cdot10^{17}$	$1,5\cdot10^{17}$	1,17
41	873	$1,8\cdot10^5$	$6,1\cdot10^{-12}$	$1,32\cdot10^{17}$	$4,4\cdot10^{17}$	3,34
37	895	$1,15\cdot10^5$	$9,7\cdot10^{-12}$	$1,31\cdot10^{17}$	$3,7\cdot10^{17}$	2,82
36	918	$4,5\cdot10^4$	$1,72\cdot10^{-11}$	$1,21\cdot10^{17}$	$1,3\cdot10^{17}$	1,07

We determined the activation energy for diffusion of zinc vapor into germanium and found E = 58,700 cal/mole or 2.55 ev. Evaluations similar to those above led to D_o = 0.65 cm^2/sec. Hence the final numerical expression obtained for the coefficient of diffusion of zinc from the vapor phase is

$$D = 0,65e^{-\frac{58700}{RT}}. \tag{9}$$

In Table 4 we compare our data with those obtained by Fuller[1] and Dunlap[4].

Table 4

Diffusion temperature	D, cm^2/sec	E, cal/mole	Investigators
825 - 918°	0.65	58700	Our data
---	--	50000	Fuller[1]
---	--	58000	Dunlap[4]

It will be seen from the values for the upper bound of the concentration of Zn in Ge listed in Table 3 that this maximum concentration is virtually independent of temperature; in fact no noticeable dependence was detected in our experiments. In connection with this it is impossible to determine the activation energy for the maximum concentration; presumably it is low. The values of the ratio of the maximum concentration to the concentration of zinc in the vapor (C_o/C_v) lie in the range from 1 to 3.

The appreciably lower diffusion coefficient for zinc D_{Zn} as compared with D_{Sb} and the relatively weak activity of the zinc isotope used made it impossible to investigate the dependence of C_o on C_v and the temperature in a wider range of vapor concentrations and temperatures. However, the results obtained clearly indicate that the diffusion processes for antimony and zinc differ markedly. This is evidenced by the relatively weak (or nonexistent) temperature dependence of C_o and the consistently small value of C_o/C_v for zinc as compared with the values for antimony; the values of this ratio for antimony are thousands of times greater.

Conclusions

1. We investigated the diffusion of antimony and zinc from the vapor phase into single crystal germanium by the method of radioactive tracers.

The diffusion coefficients were found to be

$$D_{Sb} = 1,4e^{-\frac{53000}{RT}} \quad \text{and} \quad D_{Zn} = 0,65e^{-\frac{58700}{RT}}.$$

The values of the activation energy obtained do not differ appreciably from the values given by other authors who investigated the diffusion of antimony and zinc from the solid phase into germanium.

2. It was found that the maximum concentration C_o of antimony in germanium appreciably exceeds the concentration C_v of antimony in the vapor. The ratio C_o/C_v is greater for lower diffusion temperatures and low vapor concentrations C_v. At 750° and $C_v = 2.4 \cdot 10^{15}$ cm^{-3}, the ratio $C_o/C_v = 17{,}000$. A very thin layer (< 1 μ) of germanium-antimony alloy with a very appreciable Sb content forms on the surface of the germanium crystal.

3. We deduced the following empirical formula for the dependence of the limiting maximum concentration C_o on the concentration of antimony in the vapor and the temperature:

$$C_0 = 1 \cdot 10^{-7} C_V^K e^{\frac{117000}{RT}},$$

where

$$K = 8{,}6 \cdot 10^{-4} T - 0{,}78.$$

This formula can be used to compute the antimony concentration in the vapor, the temperature and the heating time necessary to obtain a desired distribution of antimony in the germanium.

4. No noticeable temperature dependence of the maximum concentration of zinc in the germanium was observed in our experiments; we conclude therefore that in the case of zinc the limiting concentration is virtually temperature independent.

The values of the ratio of the maximum concentration to the concentration of zinc in the vapor in the 825-918° temperature range lie between 1 and 3.

The experimental results show that there is an appreciable difference in the diffusion of antimony and zinc from the vapor phase into germanium; this is evidenced by the weaker temperature dependence of C_o and the weak dependence of C_o/C_v for zinc as compared with these dependences for antimony; in the case of antimony C_o/C_v may reach a value of several thousands.

In conclusion the author desires to thank V.E.Lashkarev for suggesting the subject and for his guidance in the investigation.

Institute of Physics of the
Ukrainian SSR Academy of Sciences

References

1. Fuller, Phys.Rev., 86, 136 (1952).
2. Dunlap & Brown, Phys.Rev., 86, 417 (1952).
3. E.A.Boom, Khimiia redkikh elementov (Chemistry of the rare elements), No.1 (1954).
4. Dunlap, Phys.Rev., 85, 945 (1952).

THERMOMECHANICAL EFFECTS IN THIN SEMICONDUCTOR LAYERS

- I.G.Nekrashevich

The excitation of thermomechanical oscillations in conductors under the influence of alternating current is a familiar effect. The effect is produced by the changes in temperature of the conductor due to periodic changes in the amount of power dissipated therein.

In the simplest case the effect can be observed by passing an alternating current through a metallic wire under tension. At the instants of passage of the crest current the wire will be heated to the greatest extent and, consequently, will elongate; at the instants when the current is zero, the wire will cool and, consequently, contract. As a result, the wire will oscillate with an amplitude that can be appreciably increased by appropriate adjustment of the tension, i.e., by providing the conditions for resonance.

Oscillations can also be excited on a thin flat metallic membrane by bringing the current to it through a suitable point-contact (metallic needle). In this case there will occur periodic heating and cooling of the membrane at and near the point of contact; this heating and cooling will produce changes in the area of the membrane causing it to "bulge" periodically, i.e., to oscillate.

To produce oscillations with the greatest initial amplitude one must provide conditions insuring the greatest possible change in temperature during each half-cycle of the current in the conductor, that is, one must provide a certain optimal relationship between the current frequency and the fluctuations of the heat generated in and removed from the conductor. Obviously, there is no difference in principle as regards these phenomena in metals as aginst semiconductors.

However, it is not practical to use semiconductors in the form of wires for the purpose of studying this effect. It is more convenient to take the semiconductor in the form of a layer sandwiched between two metal plates; the current source is then connected to these plates so that the current passes perpendicularly through the layer.

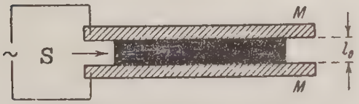

Fig.1.

Let us examine a semiconductor layer S (Fig.1) of thickness l_0 and area S, held between two metal plates M. If an alternating potential V(t) is applied to the plates a certain current i(t) will flow through the semiconductor layer. The power dissipated in the layer will be a function of the time, whose form will depend on the form of the functions V(t) and i(t).

Let us assume for the sake of simplicity that the layer has a constant resistance R and that

$$V(t) = V_0 \sin \omega t,$$

and hence

$$i(t) = I_0 \sin \omega t.$$

The heat evolved in the layer per unit time will obviously be

$$Bi(t)\,v(t) = BI_0V_0 \sin^2 \omega t,$$

where B is conversion factor depending on the units used.

The balance of energy equation for a unit volume of the semiconductor layer will be

$$c\delta \frac{d\theta}{dt} + \frac{b_0}{l_0}\theta = \frac{BI_0V_0}{Sl_0}\sin^2 \omega t, \tag{1}$$

where c is the specific heat and δ is the density of the layer material, b_0 is the heat transfer (removal) coefficient per unit surface of the layer, l_0 is the thickness of the layer at an ambient temperature T_0 and $\theta = T_t - T_0$ where T_t is the temperature of the semiconductor layer at a given instant t.

Let us assume that the variation in thickness of the layer with temperature is described by the linear law

$$l_t = l_0[1+\alpha(T_t - T_0)],$$

where α is the thermal coefficient for linear expansion.

The change in the thickness of the layer incident to a change in its temperature from T_o to T_t will be

$$\lambda = l_t - l_0 = \alpha l_0 \theta.$$

Expressing θ in terms of λ in Eq. (1), we obtain

$$\frac{c\delta}{\alpha l_0}\frac{d\lambda}{dt} + \frac{b_0}{\alpha l_0^2}\lambda = \frac{BI_0V_0}{Sl_0}\sin^2\omega t. \qquad (1')$$

The general solution of this equation is of the form

$$\lambda = \frac{a}{2n} - \frac{4m^2}{2n(n^2+4m^2)}e^{-\frac{t}{\tau_0}} - \frac{an}{2(n^2+4m^2)}\cos 2\omega t - \frac{am}{n^2+4m^2}\sin 2\omega t, \qquad (2)$$

where

$$a = \frac{BI_0V_0}{Sl_0}, \quad n = \frac{b_0}{\alpha l_0^2}, \quad m = \frac{\omega c\delta}{\alpha l_0}, \qquad (3)$$

$$\tau_0 = \frac{l_0 c\delta}{b_0}, \qquad (4)$$

here τ_o is the thermal relaxation time for a unit volume of the layer.

In Eq. (2) the term containing $e^{-\frac{t}{\tau_0}}$ becomes infinitesimal at a sufficiently large value of t and hence can be neglected.

Let us examine Eq. (1) for the two extreme cases:

Case 1: $n \ll 2m$. Bearing in mind (3), we conclude that

$$\tau \ll \tau_0,$$

where τ is the period of the alternating current passing through the layer.

Neglecting the small quantities in (2) and introducing the current density amplitude $j_o = I_o/S$ in the layer, we get

$$\lambda = \frac{Bj_0V_0}{2b_0}l_0\alpha\left(1 - \frac{b_0}{l_0\omega c\delta}\right)\sin 2\omega t.$$

We find that λ has a constant component and a variable one that changes with a frequency 2ω and has an amplitude

$$\Delta\lambda_{1m} = \frac{Bj_0V_0\alpha}{2\omega c\delta}; \qquad (4)$$

we note that this amplitude is inversely proportional to the frequency

Case 2: $n \gg 2m$. In this case $\tau \gg \tau_0$.

After operations analogous to the preceeding, we obtain

$$\lambda = \frac{Bj_0V_0l_0\alpha}{2b_0}(1 - \cos 2\omega t).$$

We see that in this case the constant component of λ is identical with that in Case 1, while the amplitude of the variable component

$$\Delta\lambda_{2m} = \frac{Bj_0V_0}{2b_0}l_0\alpha,$$

in contrast to the preceeding case, is independent of the current frequency* (see footnote on next page).

Obviously, the first case will be approximately realized with good thermal insulation of the layer; the second case will occur when there is rapid heat removal.

In both cases there will be periodic changes in the increment in layer thickness, occurring at a frequency double that of the current passing through the layer.

Let us evaluate the oscillation amplitude that might be expected for a semiconductor layer having a resistivity $\rho = 10^4$ ohm cm, a thickness $l_0 = 0.02$ cm, a thermolinear expansion coefficient $\alpha = 6 \cdot 10^{-5}$, a density $\delta = 5$ g/cm^3 and a specific heat $c = 0.08$ cal/g/°C. In addition let us assume that $\tau \approx 10\,\tau_0$.

Then for an area $S = 10$ cm^2 and a peak voltage $V_0 = 20$ v, the current passing through the layer will be 1 amp; substituting these values in (5), we obtain for the "pulsation" amplitude of the layer $6 \cdot 10^{-7}$ cm. This amplitude lies in the range of values that can be obtained using certain piezoelectro materials.

In different semiconductor devices, we frequently encounter either point contacts at which appreciable current densities develop or extremely thin transition layers to which a considerable potential is applied. In either case the power dissipated per unit volume may be sufficient to produce appreciable local heating of the semi-conductor. Thus, for example, in the case of a metal-point contact with the surface of a semiconductor, having a contact area of 0.005 mm radius, the current density in the contact area is $1.3 \cdot 10^4$ amp/cm^2 when a current of only 10 ma is passing through the device.

Obviously, the heating with such current density will produce not only appreciable changes in the electric properties of the material but also noticeable changes in its volume. This can readily be demonstrated: if we connect an audiofrequency ac generator across such a contact pair, the contact will usually sound (vibrate) with a frequency double the audiofrequency.

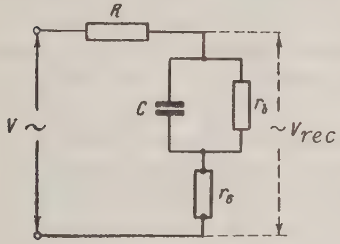

Fig.2.

Let us examine a barrier-layer type semiconductor rectifier from the point of view of this behavior as a pulsating system. The behavior of such a unit in an ac circuit can be analyzed by means of a simple equivalent circuit, such as that shown in Fig.2, in which r_b is the resistance of the barrier layer, r_δ is the resistance of the semiconductor layer and C is the capacitance of the barrier layer.

During passage of current through the rectifier, a certain amount of power is dissipated therein, i.e., transformed into heat. The amount of heat evolved during a complete cycle can be conveniently represented by the sum

$$Q = \int_0^{T/2} iV\,dt + \int_{T/2}^{T} iV\,dt,$$

where the first term is the loss during the forward half-wave and the second term is the loss during the reverse half-wave.

Now let us turn to the equivalent circuit of Fig.2. If during the forward half-wave the voltage drop across the barrier layer is very small, we can assume that $r_b \ll r_\delta$ and, therefore, write the following approximate expressions for the current and power dissipated

$$i_{fo} = \frac{V_{rec}}{r_\delta} \text{ and } Q_{fo} = \int_0^{T/2} iV_{rec}\,dt \approx \int_0^{T/2} i^2 r_\delta\,dt;$$

where V_{rec} is the voltage on the rectifying unit. Consequently, the heating in

---

*(from preceding page) In the present investigation the Lenz-Joule effect in the semiconductor layer is considered to be the principal cause of the observed thermomechanical oscillations. In addition, as has been noted by A.F.Ioffe, a second, simultaneous and independently acting cause of such oscillations can be the Peltier effect at the metal-semiconductor contacts.

this case will occur primarily in the semiconductor layer next to the barrier layer; while in view of the minor thickness of the latter, it can be assumed that the entire semiconductor layer will be heated approximately uniformly by the appreciable forward current passing through the unit.

During the reverse half-cycle, we can with like approximation assume that $r_b \gg r_\delta$ and $i_{re} = V_{rec}/r_b$; the energy liberated in the barrier layer will be

$$Q_{re} = \int_{T/2}^{T} i_{re}^2\, r_b\, dt,$$

and that in the rest of the semiconductor layer will be

$$Q' = \int_{T/2}^{T} i_{re}^2\, r_\delta\, dt,$$

obviously, too, $i_{re}^2 r_b \gg i_{re}^2 r_\delta$.

Thus during the reverse half-cycle the evolution of heat occurs primarily in the barrier layer, the thickness of which is some 2-3 orders of magnitude smaller than that of the entire semiconductor layer in the rectifying unit.

In view of the small thickness and large area of the semiconductor layer, the temperature in it will quickly follow the changes in current since due to the good thermal contact between the layer and the covering metallic plates, the generated heat will be rapidly removed and dissipated into the surrounding medium. The maximum heating of the layer will occur two times during each period of the current; that is, the layer will expand twice during each cycle, which should lead to a detectable acoustic effect if the frequency of fluctuation lies in the audio range. This effect is readily observed experimentally, i.e., the rectifying element can be heard to emit a frequency twice that of the alternating current applied to it. The intensity of the emitted sound will increase with the area of the rectifying unit and the strength of the current flowing through the unit.

If a large external resistance is connected into the rectifying circuit, the intensity of the sound is reduced and in addition the emitted frequency becomes equal to the frequency of the applied alternating voltage. This again substantiates the thermal character of the effect.

Obviously, in case of a large resistance $R \gg (r_b + r_\delta)$ connected in series with the rectifying unit, we will have for the forward current

$$i_{fo} = \frac{V}{r_b + r_\delta + R} \approx \frac{V}{R} \quad \text{and} \quad v = R i_{fo},$$

i.e., most of the voltage drop occurs over the load resistor R and the energy dissipated in the rectifier unit

$$Q_{fo} = \int_{0}^{T/2} i_{fo}^2 (r_b + r_\delta)_{fo}\, dt,$$

will be very small. During the reverse half-cycle, the voltage drop is distributed between the rectifier unit and the load resistor in proportion to $(r_b + r_\delta)$ and R. In this case the energy dissipated in the rectifier unit will be

$$Q_{re} = \int_{T/2}^{T} i_{re}^2 (r_b + r_\delta)_{re}\, dt,$$

and even with a small reverse current can prove to be appreciably greater than Q_{fo}. Consequently, the heating of the semiconductor layer will occur only once during a complete cycle of the alternating current, mainly, during the reverse half-period. In this case the fundamental audible frequency will equal the frequency of the applied voltage.

We found that the mechanical pulsations of a semiconductor layer could readily be observed by means of the device shown schematically in Fig.3. The mechanical oscillations of the pulsating disc are communicated to the ceramic stand T terminating in the graphite rod G with a rounded tip. One lead of the

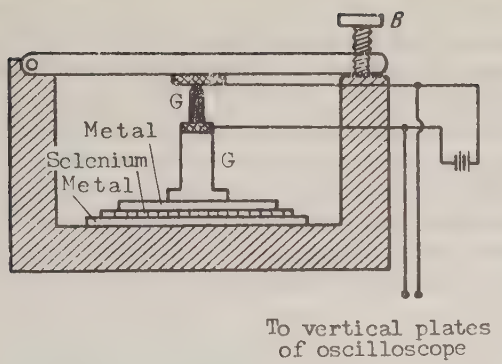

Fig.3.

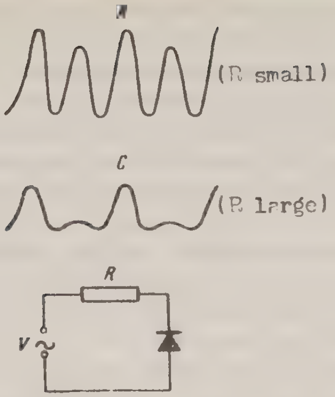

Fig.4.

battery-oscilloscope circuit is connected to the base of the graphite rod, the other to a metal plate which is brought into loose contact with the rounded graphite tip by means of the adjustment screw B. Since the graphite tip-to-metal strip contact resistance varies with the amplitude of vibration of the semiconductor disc, these vibrations can be viewed on the oscilloscope screen. Typical oscillograms are shown in Fig.4, where A is for a small load resistance; R and C is for a large R.

We used an analogous device in which the oscillations of the plate were transmitted to a piezoelectric transducer to investigate the thermomechanical vibrations of a large number of plates with both rectifying and non-rectifying semiconductor layers.

In conjunction with the above described oscilloscope set-up, we used a special vertical deflection measuring device to determine the oscillation amplitude of a number of plates as a function of the frequency with a constant peak voltage and as a function of the peak ac voltage with a constant frequency.

The results of such measurements for one selenium rectifier plate (4 mm in diameter) are shown in Figs. 5 & 6. This plate was then cut in half; the frequency dependence of the oscillation amplitude for one of the half-plates is given in Fig.7.

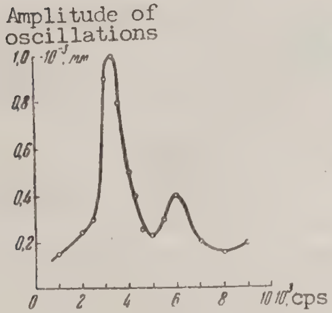

Fig.5.

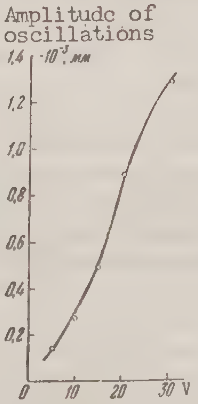

Fig.6.

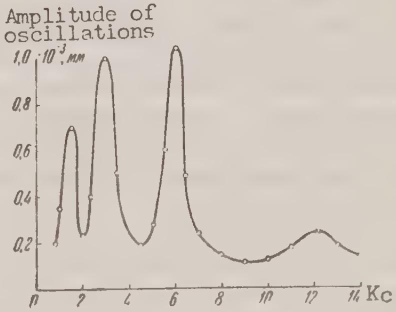

Fig.7.

Oscillations having amplitudes susceptible of detection were observed only at frequencies up to 13-14 kc. At higher frequencies the amplitude fell off below the sensitivity threshold of our set-up.

Immersion of the plates in petrolatum oil resulted in an appreciable (up to

50-60%) reduction of the oscillation amplitude compared with that in air at all the investigated frequencies; the distribution of peaks over the frequency range, however, remained the same.

The experimental peak amplitudes were some 3-4 orders of magnitude greater than the values estimated in the above described approximate calculations. This may be due, first, to the resonance effects and, second, to the fact that the semiconductor layer is never strictly uniform in thickness so that appreciably greater power dissipation may occur at individual spots (local heating effect).

Heating of the pulsating plates to 40-50^{o} produced no noticeable change in either the magnitude or the frequency and voltage dependences of the oscillation amplitudes. In the case of heating to higher temperature (up to 100^{o}) there was observed some reduction of the oscillation amplitudes which was more noticeable at higher frequencies.

Tests of the same plates at supersonic frequencies (above 10^{5} cps) under conditions analogous to those used for piezocrystal acoustic radiators (but with an appropriately reduced potential) failed to yield positive results: no oscillations of detectable amplitude were observed. Nor were we able to detect oscillations of the plates at frequencies under 500 cps.

It does not follow, however, that the semiconductor layer does not pulsate at these higher and lower frequencies. The fact that oscillations were not observed may be attributed to the absence of resonance effects in the investigated plates.

The importance of resonance effects in our experiments is well illustrated by the following observations: a 10 x 10 cm plate began to sound only an appreciable time after the application of the ac voltage; freely suspended plates emit a more intense sound than identical plates cemented to a massive metal plate; the sounding of a semiconductor plate is not fully damped even when the plate is firmly clamped between two metal plates.

The fundamental frequency of a non-rectifying layer, in accord with the considerations set forth above, is always double the frequency of the applied ac voltage.

The frequency of oscillation of a layer with a rectifying junction varied with the amplitude of voltage applied to the electrode plates between which the layer is sandwiched. These changes in frequency were observed visually by means of an oscilloscope. Thus, when the voltage was gradually reduced from 30 to 5 v with the frequency of the voltage source kept constant, the oscillation trace on the screen changed from an almost regular sine curve to a curve with alternating high and low peaks with a fundamental frequency equal to that of the alternating current and then again approached a regular sine curve at an applied voltage of about 5 v.

When a large resistance was connected to the circuit in series with the rectifying plate, the oscillation trace acquired the appearance of the current curve with half-wave rectification, while the fundamental oscillation frequency proved equal to the frequency of the applied voltage. This is also consistent with the results of our theoretical analysis.

We found that with the same dimensions of the rectifying plates and more or less equal parameters (rectification factor, forward and reversed voltage drop at a given current value, etc.) the intensity of the acoustic effect at the same alternating voltage varied greatly for different plates. This was observed not only for freely suspended plates but also in the case of plates cemented to a massive metal or marble support. It must be assumed, therefore, that the pulsations of the semiconductor layer itself were different.

In order to determine the possible reasons for the observed differences in the effect we carried out the following experiment. From among 50 selenium discs we selected the five characterized by the maximum sounding intensity and five others yielding the weakest acoustic effect. We then recorded the voltage-current characteristics for both groups of selected discs in the range of reverse voltages from 0 to 50 v. The spread of the characteristics of plates in each group was approximately the same and no noticeable differences between them were detected. The discs were then tested for breakthrough. Despite the appreciable scattering of the breakthrough voltages for each group it was found that the weak acoustic effect discs were, on the whole, characterized by a higher breakthrough voltage as compared with the strong acoustic effect group. Thus it is logical to assume that the variation in intensity of sounding is connected with fluctuations in the effective thickness of the semiconductor layer. More intense heating occurs in the thinnest microsections of the layer and the more such sections present, the more intense the thermomechanical effect. It must be noted that sounding due to thermomechanical oscillations was observed in all cases of passage of an audio-frequency current through a thin semiconductor layer regardless of whether the conduction was or was not characterized by asymmetry. Such layers, for example, can be thin oxide coatings on metals. In a series of experiments we applied a layer of aquadag over the oxide films on copper, aluminum and tantalum plates; applying an alternating voltage from an audio-generator to the metal plate and the aquadag layer generally produced audible vibrations of the plate with a frequency double that of the applied voltage.

No sound was produced when the oxide coating was replaced by a thin layer of non-conducting varnish (coated with aquadag in the same manner).

The acoustic effect is also readily observed when an audio-frequency current is passed throug the contact of a metal point with the surface of many natural crystals, such as galena, pyrite, zincite, molybdenite, etc.

Mechanical oscillations of the surface of detector crystals are probably an additional source of noise in crystal diodes, particularly in the low frequency range.

Summary

1. The heating of a thin semiconductor layer by an alternating current passing through it under conditions where an appreciable amount of power is dissipated per unit volume results in fluctuations in thickness of the layer. These thickness fluctuations can excite oscillations in mechanical systems coupled to the pulsating layer.

2. The frequency of oscillation of a non-rectifying layer is equal to twice the frequency of the applied alternating voltage. The frequency of a layer containing a rectifying junction is complex and comprises harmonics ranging from the frequency of the applied voltage. The relation between the amplitudes of the different harmonics varies with the magnitude of the applied voltage.

3. The presence of inhomogeneities in the thickness of the semiconductor layer results in an increase in the intensity of the excited oscillations. This effect can be utilized in practice for engineering and quality control in manufacturing semiconductor rectifiers

4. Thermomechanical oscillations also occur in the case of a metal point contact with a semiconductor and may be a source of additional noise in semiconductor diodes.

Department of Experimental Physics of
"V.I.Lenin" Byelorussian State University

TEMPERATURE DEPENDENCE OF THE ELECTRIC CONDUCTIVITY OF ORGANIC SEMICONDUCTORS

- A.T.Vartanian

At present one can recognize a new distinctive group of electronic semiconductor materials: organic semiconductors. Systematic investigation of this class of materials has begun only recently. However, we initiated an investigation of the semiconductor properties of dyes[1,2] back in 1938.

In 1948 we showed[3] that layers of a number of phthalocyanine (a new class of synthetic pigments related to chlorophyll and hemoglobin) prepared by spreading or smearing on are electric semiconductors. On the basis of measurements of the temperature dependence of the electric conductivity, we determined the activation energy E, which for phthalocyanine with no metal proved to be 0.43 ev in vacuum.

Somewhat later Eley[4] found E = 1.2 ev in the same pigment. The large divergence between these two values is undoubtedly due to the different states of the specimens used in the experiments. Eley investigated a fine crystalline powder having a density of only 0.2 g/cm^3. Yet it is known that the conductivity of powders increases with the pressure at constant temperature, while the activation energy decreases.

In their experiments Akamatu & Inokuchi[5] found that the conductivity of violanthrole, pyranthrole and other powders reaches a maximum value at a pressure of 80 kg/cm^2.

Recently Eley and his coworkers[6] again determined the temperature dependence of the conductivity of phthalocyanine powder, in this case under a pressure of 80 kg/cm^2, and obtained a value of E almost identical with ours, namely, 0.41 ev. From this it follows that as regards electric conductivity layers obtained by smearing or spreading are similar to powders under a pressure of 80 kg/cm^2.

In recent years there have appeared several reports devoted to investigations of the semiconductor properties of organic compounds.[6-11] These investigations have been primarily concerned with condensed polynuclear aromatic hydrocarbons: naphthalene, anthracene, coronene, ovalene, pyrathrene, violanthrene and like. In addition to these relatively simple compounds, there have been investigated rather complex substances such as blood albumin, edestin and fibrinogen[6], as well as collagen (ossein), wool, silk and cotton[12]. However, these substances all contain appreciable amounts of water and their conductivity and activation energy strongly depend on the moisture content.

Most of these compounds were investigated in air in the form of compressed powders and only naphthalene and anthracene could be investigated in the form of single crystals[9,10]. The temperature dependence of the conductivity of naphthalene single crystals was also investigated under vacuum and in an atmosphere of oxygen at pressures up to 12 atmospheres. In view of the minute conductivity and the low melting point of naphthalene, the range of measurement temperatures was limited to the interval from 50 to 76°. In this narrow temperature interval the exponential law was fulfilled; under vacuum the activation energy E was found to be 1.85 ev when the direction of the current is perpendicular to the a-b plane. The value of 2E, equal to 3.7 ev and corresponding to W in the formula $\sigma = \sigma_0 e^{-W/2kt}$, agrees with the beginning of optical absorption, which occurs in the wavelength region under 300 mμ. In the presence of oxygen, the naphthalene single crystals are transformed from intrinsic to extrinsic semiconductors; the activation energy falls off to 0.75 ev at an oxygen pressure of over 2 atmospheres.

The conductivity of anthracene single crystals was investigated in air in the temperature range from 85 to 190°. The activation energy equals 0.83 ev. The 1.66 ev value for 2E is appreciably smaller than the value of the energy corresponding to the optical absorption limit (3.2 ev). Possibly the low value of activation energy (0.83 ev) obtained for anthracene by different investigators may, by analogy with naphthalene, be explained by the fact that the measurements were carried out in air and that consequently the investigated specimens were extrinsic semiconductors. Hence investigation of the temperature dependence of the conductivity of anthracene single crystals under vacuum is important for resolving the problem of whether the value of W coincides with the energy corresponding to the optical absorption limit.

Akamatu & Inokuchi[7,8] ascribed the conductivity of condensed polynuclear aromatic compounds to the π-electrons of the conjugate double bonds in the plane carbon network. In general, the electric conductivity grows with increasing number of π-electrons.

In organic dyes there can also be established a conjugate system of valence bonds. For example, in the above mentioned phthalocyanine such a system is formed by the central 16-member ring[13] which determines the optical absorption and the magnetic susceptibility anisotropy[14] of phthalocyanine crystals.

In addition to the phthalocyanines, we investigated the temperature dependence of the conductivity of a number of dyes in the solid state. The results pertaining to methylene blue and crystal violet have been published earlier[15]. In the present article we give the results of our investigations of more than 30 dyes of different types.

A number of difficulties are encountered in investigating the temperature dependence of the conductivity of dyes. Most dyes are fine crystalline powders. Hence for investigating the conductivity we used compact layers prepared by precipitation from an alcohol solution. The individual layers were deposited on the surface of a quartz "finger" to which platinum electrodes at 1 mm intervals were applied beforehand. The quartz "finger" was inserted into a glass jacket connected to a high-vacuum system. The design of the set-up allowed of measuring the conductivity at different temperatures. A number of the dyes we desired to investigate, however, either do not dissolve in water or alcohol or if they do dissolve do not form a continuous layer in settling. In the case of some of these we succeeded in obtaining a satisfactory layer by smearing or spreading on. Another experimental difficulty stems from the low conductivity of the layers of many dyes which limits the possibilities of measurement in the region of low temperatures. The range of measurement on the high temperature side is limited by sublimation (under vacuum) or structural changes of the dye molecules.

Many of the investigated dyes are characterized by photoelectric sensitivity.[2,15 & 16] Hence the measurements were made after prolonged holding under vacuum in the dark.

Our experiments showed that some gases (oxygen, nitric oxide, hydrogen sulfide and others) have an appreciable influence on the conductivity of dye layers. In the present article, however, we shall give only the results obtained under vacuum conditions.

The current was measured either with a mirror galvanometer having a sensitivity of $6.3 \cdot 10^{-10}$ amp or a dc amplifier having a sensitivity of $2.8 \cdot 10^{-14}$ amp per scale division.

The temperature dependences for a number of dyes are shown in the accompanying figure in log σ vs 1/T coordinates. It should be noted that the ordinates are actually logarithms of quantities proportional to the conductivity, namely, logarithms of the dark current; the voltage on the layer in every case was chosen so that the deflection of the galvanometer at the highest temperature of measurement would be about 100 or 200 divisions. This method of measurement is convenient for comparing the slopes of the log σ vs 1/T plots. It will be seen that the temperature dependence of the conductivity is closely characterized by the exponential law for most dyes.

The temperature interval in which the measurements were made differed for different dyes. For some dyes and pigments (for example, methylene blue, crystal violet, Mn and Zn phthalocyanine) it was possible to extend the measurements over a range of up to 100-150°. For most dyes, however, the measurement interval amounted to 50-80°.

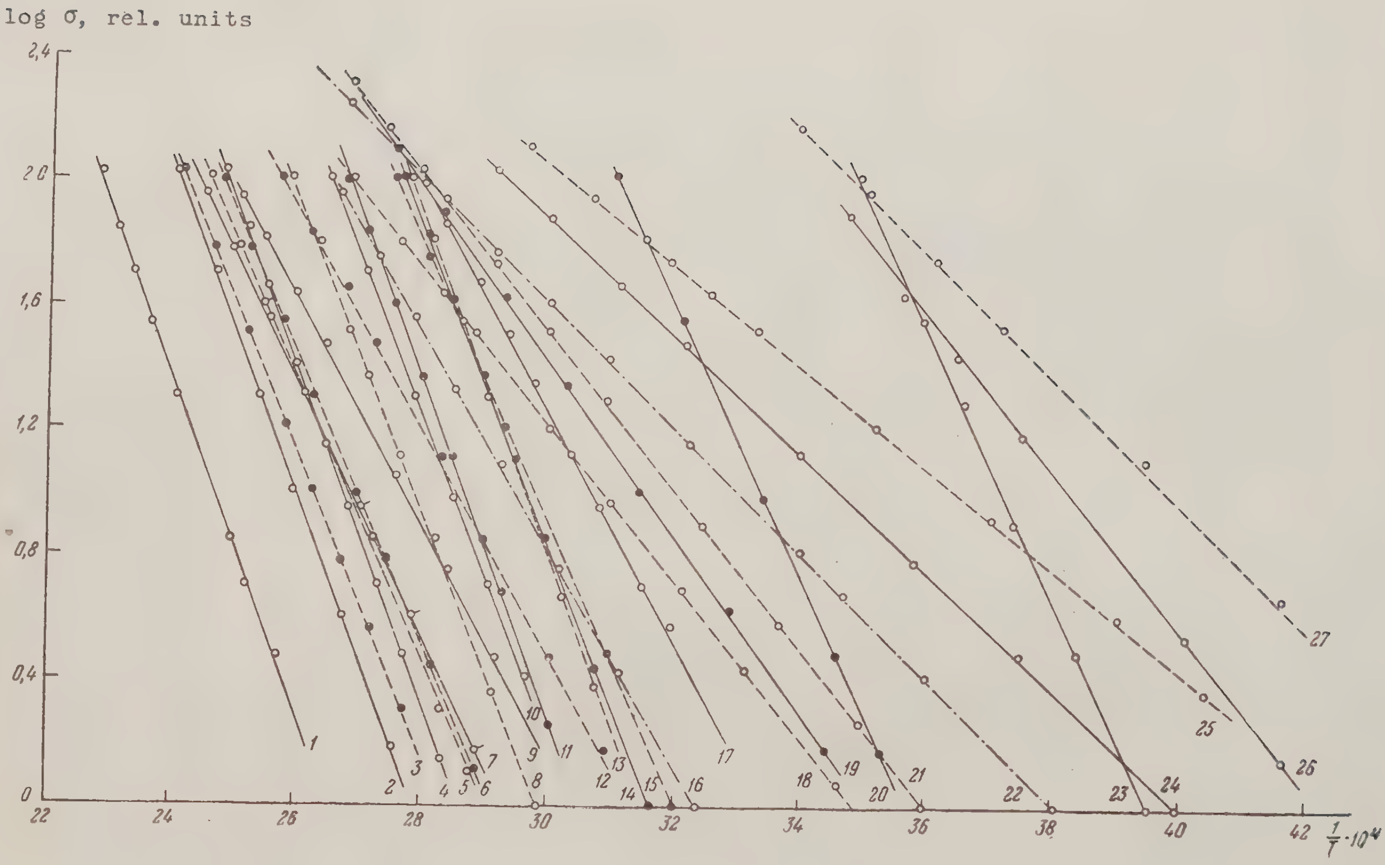

Temperature dependence of the electric conductivity of solid dye layers.

Table 1

No.	Dye	Class	Temp. interval, °C	2E (ev)	λ(mμ), corresp. to 2E	λ(mμ), corresp. to steep rise in absorption curve
1	Erythrosine	Xanthene	116-165	2.15	575	600
2	Phloxin	"	90-143	2.08	594	600
3	Bengal rose	"	88-142	1.9	650	610
4	Eosin	"	80-130	2.13	580	590
5	Rhodamine 6G	"	50-135	1.77	700	620
6	Hematin	Pigment	73-130	1.83	675	---
7	Turquoise blue	Triphenylmethane	73-135	1.6	770	760
8	Rhodamine 5G	Xanthene	60-115	1.9	650	---
9	Magdalen red	Azine	67-136	1.44	857	670
10	Uranine	Xanthene	50-120	2.0	617	550
11	Trypaflavine	Acridine	60-100	2.2	560	550
12	Phenosafranine	Azine	20-116	1.4	880	620
13	Hematoporphyrin	Pigment	73-130	1.83	675	---
14	Chlorophyll a + b	Pigment	40-90	2.0	617	---
15	Auramine	Diphenylmethane	39-90	1.77	700	520
16	Capri blue	Oxazine	36-102	1.38	894	800
17	Safranine	Azine	20-116	1.4	880	660
18	Naphthol green	Nitroso	15-100	0.98	1250	---
19	Thionine	Thiazine	17-100	1.1	1122	720
20	Nocturnal blue	Triphenylmethane	10-49	1.7	725	750
21	Methylene blue	Thiazine	50-100	1.0	1234	750
22	Zn Phthalocyanine	Pigment	-10-100	0.79	1560	~800
23	Nocturnal blue	Triphenylmethane	-20-13	1.7	725	750
24	Crystal violet	"	-30-70	0.74	1670	725
25	Mg Phthalocyanine	Pigment	-30-100	0.78	1580	~800
26	Methylene blue	Thiazine	-50-15	1.0	1234	750
27	Zn Phthalocyanine	Pigment	-33-22	0.79	1560	~800
28*	Phthalocyanine without metal	"	0-100	0.87	1420	~880
29	Cu Phthalocyanine	"	30-100	1.2	1010	~860
30	Phthalocyanine Sulfonated	"	0-100	0.9	1370	---
31	Rhodamine 3B	Xanthene	104-127	4.43	278	---
32	Rhodamine G	"	120-140	4.44	278	---
33	Cyanine	Quinoline	40-100	1.9	650	670
34	Pinacyanol	"	35-85	1.8	686	700

The data and results are summarized in Table 1. The numbers in the first column of the table correspond to the numbers at the curves in the figure. (Nos. 28 through 34 are not plotted in the figure).

It will be seen from the figure that the activation energies of the dyes represented in the figure lie in the range from 0.35 to 1.1 ev. For two dyes - Rhodamine 3B and Rhodamine G - we obtained anomalously large activation energy values, namely, 2.22 ev. This is extremely puzzling, particularly, since for Rhodamine 5G and Rhodamine 6G we obtained 0.95 and 0.89 ev, respectively, i.e., values within the range covering most of the dyes.

---

*The results for dye samples Nos. 28 through 34 are not shown in the accompanying figure.

In investigating the absorption spectra of dye layers obtained by sublimation, we found that Rhodamines 3B and G differ from Rhodamines 5G and 6G as regards spectral characteristics as well. Whereas the absorption spectra of Rhodamine 5G and Rhodamine 6G are virtually the same, regardless of whether the layer was obtained by precipitation from an alcohol solution or by sublimation in vacuum, the absorption spectra of layers of Rhodamine 3B and Rhodamine G prepared by the two methods differ markedly in the ultraviolet[17]. Detailed investigation has shown that Rhodamines 3B and G as well as Rhodamine B undergo changes upon heating as a result of which they are transformed into colorless compounds with strong absorption in the ultraviolet region. The 2.22 ev activation energy is apparently due to this new colorless substance. The conductivity of fuchsin (magneta red) was found to change with the temperature according to the exponential law, but the activation energy was found to decrease with heating, which may be attributed to insufficient purity of the specimen. The 0.85 ev activation energy value for fuchsin given in the table is the most probable one. The activation energy of cyanine is 0.98 ev; this value was obtained after many hours of heating the dye. We were not able to obtain an exponential dependence for Brilliant blue.

It can also be seen from the data given in Table 1 that for some dyes the thermal ionization energy (2E) is rather close to the long-wave absorption limit of the dye in the solid state (it is impossible to determine the absorption limits very accurately since the absorption curves for most of the dyes do not have an abrupt drop (sharp edge) on the long-wave side). Among the dyes having close values are erosin, erythrosine, phloxin and trypaflavine. For a number of other dyes, on the contrary, there is an appreciable divergence between the respective energy (wavelength) values. This divergence is particularly great for crystal violet, methylene blue and phthalocyanines. It is not impossible that the conductivity of the investigated layers of these dyes was not intrinsic but extrinsic.

Further investigations should be directed at preparing and investigating single crystals inasmuch as for these one can expect a clear relationship between the value of 2E and the optical absorption limit. The values of 2E obtained by us lie within the range of values obtained by a number of investigators for many organic compounds. A number of the values from the literature are listed in Table 2.

It will be seen from Table 2 that collagen, wool and silk have almost identical values of 2E (2.7 ev). This can scarcely be a fortuitous coincidence. We believe that these substances as well as some of the others in the list are not electronic semiconductors.

Finally, we note that the photoconductivity of the dyes, observed in the intrinsic long-wave absorption band, also increases exponentially with increasing temperature. The values of 2E determined from the temperature dependence of the photoconductivity, are listed in Table 3 for a number of dyes. It will be seen that for the investigated dyes these values lie between 0.4 and 0.8 ev and as a rule are appreciably lower than the values of 2E determined from the dark conductivity.

Earlier we showed[15,20] that the absorption of a photon by a dye molecule is initially accompanied only be excitation. After excitation the electrons can go over to the triplet levels of the dye molecule, lying below the singlet excitation levels, and to local electron capture levels. The value of 2E determined from the temperature dependence of the photoconductivity characterized the amount of thermal energy necessary for releasing the electrons from these local levels and raising them to the conduction band.

Table 2

No.	Compound	Temp. interval, °C	2E (ev)	Ref. No.	Remarks
1	Naphthalene	50-76	3.7	10	Single crystal in vacuum
	"	50-76	1.5	10	Single crystal in O_2 at 12 atmos.
	"	20-75	1.4	18	Single crystal in air
2	Anthracene	85-190	1.65	9	Single crystal in air
	"	30-70	1.92	11	Sublimated layer
	"	70-204	1.66	6	Powder
	"	20-60	1.50	18	Flakes
3	Coronene	220-280	2.18	6	Powder
4	Ovalene	---	1.13	7	"
5	Diphenylbutadiene	20-140	>4.3	6	"
6	Diphenyloctatetraene	20-230	>4.3	6	"
7	2-Amino-4,6 dimethyl pyrimidine	20-150	>4.3	6	"
8	N-phenylcidnone	50-130	>4.3	6	"
9	Anthanthrene	---	1.67	8	"
10	Anthanthrone	---	1.7	8	"
11	Meso-naphthodianthrene	---	1.2	8	"
12	Meso-naphthodianthrone	---	1.3	8	"
13	Pyranthrene	---	1.07	8	"
14	Pyranthrone	---	1.06	7,8	"
15	Violanthrene	---	0.85	8	"
16	Violanthrone	---	0.78	7,8	"
17	Isoviolanthrene	---	0.82	8	"
18	Isoviolanthrone	30-130	0.75	8	"
	"	50-250	1.54	6	Loose powder
	"	50-250	1.14	6	Compressed powder
19	Blood albumin	70-180	~2.2	6	Dry
	" "	70-180	~1.7	6	Moist
20	Fibrinogen	150-270	~2.8	6	---
21	Edestin	90-204	~2.5	6	---
22	Collagen	---	2.72	12	---
23	Wool	---	2.68	12	Fiber
24	Silk	---	2.68	12	"
25	Cotton	---	1.92	12	"
26	Paraffin	13-40	1.10	18	"
27	Polystyrene	---	0.80	18	"
28	Gelatin	-10-20	1.82	19	Moist

Table 3

No.	Dye	2E from dark conductivity, ev	2E from photoconductivity, ev
1	Capri blue	1.38	0.82
2	Tripaflavine	2.2	0.53
3	Safranine	1.4	0.84
4	Crystal violet	0.74	~ 0.6
5	Phloxin	2.08	0.47*
6	Bengal rose	1.9	0.6*
7	Eritrosine	2.15	0.5*
8	Eosin	2.13	0.6*
9	Pinacyanol	1.80	0.43

---

*2E depends on wavelength of the exciting light; the values in the table are mean values.

References

1. A.T.Vartanian & A.N.Terenin, J.of Phys.USSR, 4, 173 (1941).
2. A.T.Vartanian, Zhur.fiz.khim., 20, 1065 (1946).
3. A.T.Vartanian, Zhur.fiz.khim., 22, 769 (1948).
4. D.D.Eley, Nature, 162, 819 (1948).
5. H.Akamatu & H.Inokuchi, J.Chem.Phys., 18, 810 (1950).
6. D.D.Eley, Q.D.Parfitt, M.J.Perry & D.H.Taysum, Trans.Farad.Soc., 49, 79 (1953).
7. H.Akamatu, H.Inokuchi & T.Handa, Nature, 168, 520 (1951).
8. H.Inokuchi, Bull.Chem.Soc., Japan, 24, 222 (1951).
9. H.Mette & H.Pick, ZS.f.Phys., 134, 566 (1953).
10. H.Pick & W.Wissman, ZS.f.Phys., 138, 436 (1954).
11. D.Northrup & O.Simpson, Proc.Phys.Soc., B, 67, 892 (1954).
12. S.Baxter, Trans.Farad.Soc., 39, 207 (1943).
13. J.M.Robertson, J.Chem.Soc., 1195 (1936).
14. K.Lonsdale, Proc.Roy.Soc.A., London, 159, 149 (1937).
15. A.T.Vartanian, Izv.AN SSSR, Ser.fiz., 16, 169 (1952).
16. A.T.Vartanian, Zhur.fiz.,khim., 24, 1361 (1950).
17. A.T.Vartanian, Zhur.fiz., khim., 30, 1028 (1956).
18. N.V.Ril', Zhur.fiz.khim., 29, 959 (1955).
19. N.V.Ril', Zhur.fiz.khim., 29, 1537 (1955).
20. A.T.Vartanian, Zhur.fiz.khim., 27, 272 (1953).

DEPENDENCE OF THE CARRIER MOBILITY IN GERMANIUM ON THE CONCENTRATION OF ANTIMONY AND PHOSPHORUS

- P. I. Baranskii

Investigation of the mobility of current carriers can not only further our understanding of the physical processes occurring in semiconductors but may also provide the means of improving the engineering qualities of electronic semiconductor devices (i.e., lead to reduction of noise levels, shorter response times, etc.). In contrast to the question of scattering of current carriers by lattice vibrations, which has by now been extensively studied, relatively little attention has been paid by experimentors to the scattering of current carriers by ionized centers.

We investigated the dependence of the current carrier mobility in germanium on the concentration of Sb^{124} and P^{32} at room temperature.

The fact that these impurities are completely ionized in germanium single crystals (this was established experimentally) made it feasible to determine the concentration of scattering centers by the method of tracer atoms. The value of the Hall mobility μ_H was found in the usual manner by means of the formulas:

$$\frac{1}{\rho} = \sigma = \sigma_0 e^{-\frac{E}{kT}},$$

and

$$\mu_H = \frac{8}{3\pi} \cdot \frac{R}{\rho}.$$

The experimental results are shown in Fig.1, where the circles are the experimental points for antimony and crosses are the points for phosphorus.

We believe it is logical to compare these data with the results of the Conwell-Weisskopf impurity scattering theory (scattering of carriers by Coulomb centers[1-5]) in the following manner.

In view of the fact that according to the theory

$$\frac{1}{\mu} = A + B(n),$$

where A is a factor determined by lattice scattering and B characterizes the scattering by the impurities and is a function of their concentration n, one should first calculate B = B(n) and plot the results on tracing paper to a semilogarithmic scale ($1/\mu$ vs log n). The experimental data should then be plotted in the same coordinates and to the same scale. Then the tracing paper should be moved up or down over the latter plot to obtain the best fit of the theoretical curve to the experimental points. The solid curve in Fig.1 represents the theoretical dependence of the carrier mobility on the concentration of ionized impurities and its position on the diagram was chosen by moving the "standard curve" parallel to the vertical axis. The same results are replotted in Fig.2 in the form of log $1/\mu$ vs log n; from this plot one can determine the deviation of the experimental points from the theoretical curve directly in percent. For purposes of comparison we have also plotted in this figure (solid dots) the data of Pearson and his coworkers[6] who investigated the concentration dependence of the current carriers in germanium containing antimony. The relatively low accuracy of their experiments, as evinced by the position of the points in Fig.2, virtually precludes of comparing their results with the deductions from theory.

On the basis of our data it may be considered established that the decrease in mobility of current carriers with increasing concentration of scattering centers (ionized impurity atoms) in the case of admixtures of both antimony and phosphorus is satisfactorily described (within 10-12%) at room temperature by the Conwell-Weisskopf formula.

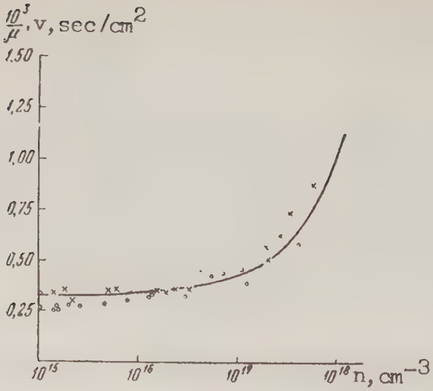

Fig. 1

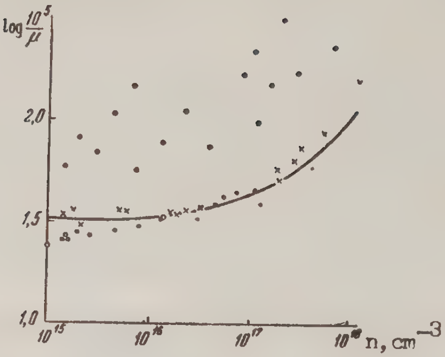

Fig. 2

Dependence of 1/μ on the concentration of Sb and P in Ge.

The writer wishes to thank V.E.Lashkarev for suggesting the subject and providing guidance in the investigation.

Institute of Physics of the
Ukrainian SSR Academy of Sciences

References

1. E.M.Conwell & V.F.Weisskopf, Phys.Rev., 69, 258 (1946).
2. E.M.Conwell & V.F.Weisskopf, Phys.Rev., 77, 388 (1950).
3. E.M.Conwell & E.J.Ryder, Phys.Rev., 87, 190 (1952).
4. P.P.Debye & E.M.Conwell, Phys.Rev., 87, 1131 (1952).
5. E.M.Conwell, Proc. IRE, 40, 1329 (1952).
6. G.L.Pearson, J.D.Struthers & H.Theucrer, Phys.Rev., 77, 809 (1950).

CONCERNING THE THEORY OF THE ELECTRIC STRENGTH OF GERMANIUM AND SILICON

(Condensation of report)

- V.A.Chuenkov

Investigation of the processes occurring in semiconductors placed in a strong electric field is of interest both from the practical and theoretical standpoints. In the presence of a strong electric field (large reverse voltages) there develop in germanium and silicon p-n junctions processes that lead to their electric breakdown. Such processes include heating of the junction, the Zener effect and electron impact ionization.

At present it has been established[1] that when the potential is applied in the form of pulses of 10^{-5} sec or less duration the impairment of the dielectric strength of p-n junctions is due exclusively to impact ionization. At the same time, impact ionization plays an important part in the breakdown of a p-n junction under the influence of dc potentials.

Investigation of impact ionization in a p-n junction, where a highly inhomogeneous electric field obtains, presents a very difficult problem. The first step in the direction of solving this problem, we feel, should be investigation of the processes occurring in a homogeneous semiconductor under the influence of a sufficiently strong uniform electric field applied in the form of a short pulse when thermal effects can be disregarded.

In the present investigation we made an attempt to find the function characterizing the distribution of electrons in a germanium type semiconductor in a strong uniform electric field (the voltage was applied in the form of single pulses of 10^{-5} sec or less duration) taking into account acoustical and optical mode scattering as well as the ionization collisions of the electrons with the lattice atoms. Recombination of electrons plays a substantial role only in a small region in the vicinity of zero energy in phase space[2]. Hence, everywhere except in the immediate vicinity of zero energy the recombination term can be neglected in seeking the distribution function.

On the basis of the deduced distribution function, we formulated the criteria by means of which one can determine the critical field intensity E_{cr} - the potential gradient at which the electric strength is impaired and an electron avalanche occurs - as a function of the temperature and lattice parameters. At room temperature for n-type germanium $E_{cr} = 4.6 \cdot 10^4$ v/cm, while for n-type silicon $E_{cr} = 1.1 \cdot 10^5$ v/cm.

The experimental value of the maximum field intensity E_{max} in a germanium p-n junction at the instant of breakdown (the average value of the field intensity E_{av} in a p-n type junction equals $E_m/2$ for diodes produced by growth from a melt and $E_m/1.5$ for diodes produced by diffusion) is usually 3-4 times greater than the above indicated theoretical value of E_{cr} ($E_m \approx 2 \cdot 10^5$ v/cm). This divergence is due to the fact that the theoretical value of E_{cr} was deduced for a comparatively thick semiconductor layer in a homogeneous electric field, whereas in the case of breakdown of actual p-n junctions we have a rather thin semiconductor layer ($\sim 10^{-3}$ cm) in an inhomogeneous electric field. Consequently, a field E_{cr} of somewhat greater intensity is needed for development of the sufficiently powerful electron avalanche requisite for breaking down the electric strength of the p-n junction. It follows from the above that with increasing width of the junction the value of E_m should approach E_{cr}. Actually Vul & Shotov[3] showed that in the case of a germanium junction having a width of the order of 0.3 mm the value of E_m at the instant of breakthrough equals $7.6 \cdot 10^4$ v/cm ($E_{av} = E_m/2 = 3.8 \cdot 10^4$ v/cm), which is already fairly close to the theoretical value of E_{cr}.

We note that if optical mode scattering is not taken into account, we obtain $E_{cr} = 4 \cdot 10^3$ v/cm for n-type germanium, which is obviously in conflict with experiment. Consequently, the presence of a strong electric field when the mean electron energy ϵ is much greater than kT, scattering from optical vibrations must play a very substantial role. With $E \approx kT$ the dominant role is played by acoustical mode scattering.

Analysis of the distribution function shows that beginning with a certain electron energy ϵ_1 ionizing collisions of the electrons with lattice atoms play a far more important part than scattering by thermal lattice vibrations. With $\epsilon < \epsilon_1$ the dominant role is played by collision with lattice vibrations (lattice scattering). Calculations indicate that the energy ϵ_1 appreciably exceeds the width I of the forbidden band (energy gap). For germanium I = 0.75 ev, while ϵ_1 = 2.2 ev; for silicon I = 1.15 ev, while ϵ_1 = 2.55 ev. This points to one of the reasons why, when a semiconductor is bombarded with electrons, an energy ϵ^*, exceeding the value of I, is expended on electron-hole pair production (experiment gives $\epsilon^* \approx$ 2-3 ev). We propose the following formula for the impact ionization coefficient:

$$\alpha(E) = aEe^{-\frac{b}{E}}, \tag{1}$$

where E is the electric field intensity and

$$a = \frac{3e}{2\varepsilon_1 + I}, \quad b = \frac{2\varepsilon_1 + I}{3el^*} \tag{2}$$

(here e is the electron charge and l^* is the mean free path of an electron having an energy in the interval from ϵ_i to ϵ_1, ϵ_i being the energy of the ionizing and ejected electrons after ionization.

At room temperature for n-type germanium

$$\alpha(E) = 0{,}59Ee^{-\frac{5{,}8\cdot10^5}{E}}, \tag{3}$$

and for n-type silicon

$$\alpha(E) = 0{,}48Ee^{-\frac{8{,}16\cdot10^5}{E}}, \tag{4}$$

where E is in electron volts.

Dependence of the impact ionization coefficient on the intensity of the electric field at room temperature

n-type germanium	E, v/cm	$1{,}67\cdot10^5$	$1{,}75\cdot10^5$	$2\cdot10^5$	$2{,}25\cdot10^5$	$2{,}5\cdot10^5$	$2{,}75\cdot10^5$
	α(E) exper.	$4\cdot10^3$	$5\cdot10^3$	$8\cdot10^3$	$1{,}1\cdot10^4$	$1{,}5\cdot10^4$	$2\cdot10^4$
	α(E) theo.	$3{,}06\cdot10^3$	$3{,}72\cdot10^3$	$6{,}5\cdot10^3$	$1{,}0\cdot10^4$	$1{,}42\cdot10^4$	$2\cdot10^4$
n-type silicon	E, v/cm	$2\cdot10^5$	$3\cdot10^5$	$4\cdot10^5$	$5\cdot10^5$	$6\cdot10^5$	$7\cdot10^5$
	α(E) exper.	$1{,}0\cdot10^3$	$7\cdot10^3$	$3\cdot10^4$	$8\cdot10^4$	$9\cdot10^4$	$1{,}0\cdot10^5$
	α(E) theo.	$1{,}61\cdot10^3$	$9{,}2\cdot10^3$	$2{,}5\cdot10^4$	$4{,}75\cdot10^4$	$7{,}95\cdot10^4$	$1{,}06\cdot10_5$

In the accompanying table we list the theoretical values of α(E) computed according to formulas (3) and (4) together with experimental data from Refs.3,4 & 5. The experimental values of α(E) for germanium were obtained by Vul and Shotov[3]. Their data are more reliable since they were obtained for the breakdown of p-n junctions by voltage pulses when the influence of thermal effects is absent.

We note that formula (1) is valid for both homogeneous and inhomogeneous fields.

The writer takes this occasion to thank B.M.Vul and A.P.Shotov for valuable discussions.

"P.N.Lebedev" Physical Institute of the
Academy of Sciences of the USSR

References

1. A.P.Shotov, Zhur.tekh.fiz., 26, 1634 (1956).

2. E.I.Adirovich, Nekotorye voprosy teorii liuminestsentsii kristallov (Certain problems concerning the theory of the luminescence of crystals), 1951.

3. B.M.Vul & A.P.Shotov, Radiotekhnika i elektronika, 8, 1080 (1956).

4. P.A.Wolff, Phys.Rev., 95, 1415 (1954).

5. S.L.Miller, Phys.Rev., 99, 1234 (1955).

ELECTRON DENSITY DISTRIBUTION IN AND ELECTRIC CONDUCTIVITY OF CADMIUM SULFIDE CRYSTALS

- Iu.N.Shuvalov

The purpose of the present study was to investigate the relation between the electron density distribution in crystals and their electric conductivity.

Several years ago investigators (James[1]) noted the presence of temperature induced changes in the distribution of electron densities in cyrstals as evinced by smearing out of the electron density maxima due to increased intensity of thermal vibrations.

In a series of experiments Brill, Grimm, Hermann & Peters investigated the electron density distribution in crystals of rock salt, diamond, urotropine[2] and magnesium[3], i.e., in substances characterized by ionic (heteropolar), atomic (homeopolar), van der Walls and metallic bonds. Specifically, their study confirmed the existence of exchange electrons in the case of atomic bonds; being located near the line connecting the centers of gravity of the atoms they increase the electron density along this line. Such an increase in electron density in a particular direction appears on the density distribution map as a distinctive "electron bridge" between the atoms. In contrast, rock salt with its ionic bonds has no such "bridges" and in the distribution map for salt the electron density falls off practically to zero along the lines between the sodium and chlorine atoms.

If different samples of the same semiconductor have markedly different conductivity due to the presence of some impurity in greater or smaller amounts, we might expect these different samples to be characterized by different electron density distributions.

We investigated the density distribution by recording rotation x-ray patterns by the method of Weisenberg[4] on a Wooster & Martin x-ray goniometer with subsequent measurements of the intensity of the reflection spots by means of an MF-2 microphotometer. Then the structure amplitudes F with the temperature factor e^{-M} were calculated in relative units on the basis of the determined reflection intensities I:

$$F \cdot e^{-M} = \sqrt{I \cdot \frac{\sin 2\vartheta}{1 + \cos^2 2\vartheta}}\,.$$

The relative electron density at different points in the crystal was computed by Fourier synthesis[5]. We summed the Fourier series primarily by the method of overlays[6] and then plotted electron density distribution diagrams for the investigated crystals.

Our investigation of the relation between the electron density and the electric conductivity was carried out on crystals of cadmium sulfide kindly made available for this purpose by S.M.Ryvkin. These crystals were prepared by S.M.Ryvkin in the Physical-Technical Institute by evaporation of metallic cadmium in an atmosphere of hydrogen and sulfur vapor. Owing to indeterminable variations in the conditions of preparation, the conductivities of different crystals varied over a very wide range.

Crystal CdS has a wurtzite structure; this was first determined by Aminoff[7] and subsequently substantiated by Ulrich & Zachariasen[8]. The crystal structure of CdS consists of an extremely dense hexagonal packing of cadmium atoms, half the tetrahedral vacancies in which are occupied by sulfur atoms.

The investigated crystals had the shape of parallelepipeds strongly elongated along the hexagonal axis c. Their width was of the order of 0.2-0.4 mm with a thickness of 0.03-0.04 mm. When the crystals were rotated about the c axis, the Weisenberg patterns for the zero layer line gave us the zone reflections, from the intensities of which we calculated the projection of the electron density distribution on the (001) plane.

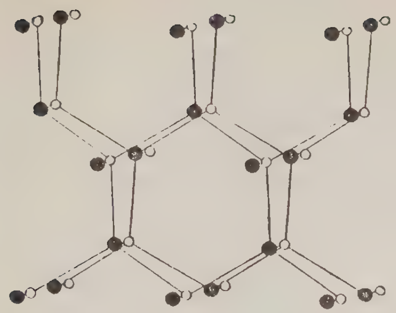

Fig.1. CdS lattice (wurtzite structure). View in direction close to (001).

This projection (Fig.1) is characterized by the fact that it comprises a surposition of cadmium and sulfur atoms in equal numbers. In view of this the Cd and S atoms cannot be distinguished in this projection, but, on the other hand, one can draw a number of deductions regarding the bonds between the atoms, whereas in the case of projections in which the atoms are separated the individual bonds are superposed on the tetrahedral and octahedral vacancies, making analysis difficult.

In measuring the conductivity, the samples were bonded to glass so that the cement layer joined the upper surface of the crystal to the glass; the center of the crystal was covered with a strip of foil 1-2 mm wide. Then the glass and crystal were coated with aluminum by evaporation under vacuum. A potential of up to 100 volts was applied to the ends of the crystal through a galvanometer having a sensitivity of $5 \cdot 10^{-9}$ amp per mm; by this means it was feasible to measure resistances of almost up to 10^{11} ohm.

In all we investigated over 20 samples. Calculations were carried out for 13 samples on the basis of the several best x-ray patterns for each. The resistance values of these crystals varied over a very wide range, namely, from 0.0025 to 110 Megohm cm. As the reference for purposes of comparison we chose one of the higher resistance crystals, hereinafter designated as sample a, the data for which were obtained on the basis of 17 fully satisfactory patterns.

Rotation about the hexad axis (the c axis for a hexagonal crystal) splits all the reflections into six identical sectors of 60° each, so that in practice it is sufficient to analyze the reflection spots in only one of these. In each Weisenberg pattern one can select reflections pertaining to one sector so that they are sufficiently remote from the region of strong absorption; this makes it possible to disregard the factor of absorption. Actually, the primary purpose of the investigation was not to compare experimental data with the theory, although this was done in order to check the general structure of the crystal and from this viewpoint yielded satisfactory results. The primary purpose of the investigation was to compare the experimental data for a number of crystals with each other. For this reason crystals of one particular shape were selected and oriented in the identical manner for x-raying. In addition all the conditions of processing the films and photometering the reflection spots were maintained rigorously constant.

Variations in intensity of the reflections for different specimens proved to be considerable. It was noted that the intensities of some spots as compared with the neighboring ones exhibit a tendency to change in a regular fashion in going from low to high conductivity crystals. These relative changes in the intensity of the reflections were utilized for determining the changes in the electron density distribution. For convenience of comparison these intensity ratios for each sample were divided by corresponding ratios for the repeatedly checked reference crystal a. Thus for each crystal we obtained a set of unified ratios determined by the actual structure of the given crystal in terms of the intensity of its reflections (see accompanying table).

If the samples are arranged in order of increasing conductivity, one can readily follow the changes of each of the ratios from one sample to another (Fig. 2). The table and Fig.2 show that, although there are a number of chance deviations, certain ratios increase more or less regularly with the conductivity (Nos.1,2,6,7 & 10), others decrease (Nos.3,4 & 5), while a third group exhibits no definite tendency (Nos.8,9 & others). The last group of passive ratios comprises the reflections having a low density.

Ratios of reflection spot intensities of the CdS crystals

Crystal specimens	Reflections										Resistivity Megohm·cm
	110:100	110:200	200:210	300:210	300:220	220:310	310:400	400:320	410:320	410:500	
High-resisance	0,86	1,24	1,06	1,37	1,20	1,15	0,92	0,96	0,91	0,72	110
	1,00*	1,00	1,00	1,00	1,00	1,00	1,00	1,00	1,00	1,00	78
	0,85	1,25	1,08	1,26	1,06	1,51	0,97	0,94	1,12	0,89	21
	0,96	1,19	0,91	1,02	0,93	1,11	0,94	1,10	1,11	0,94	17,5
	1,03	1,24	1,01	1,09	1,28	0,90	1,06	0,93	0,98	1,10	13
	1,03	1,28	0,99	0,98	0,92	1,04	0,97	1,07	1,03	0,94	2,15
Average values	0,96	1,20	1,01	1,12	1,07	1,12	0,98	1,00	1,03	0,93	
Low resistance	1,14	1,47	0,99	1,12	0,94	1,20	1,26	1,01	1,09	1,14	0,25
		1,65	1,00	1,07	0,97	1,47	0,90	1,14	1,01	1,47	0,1
	1,13	1,54	0,89	0,91	0,96	1,11	0,98	1,11	0,99	1,10	0,02
	1,27**	1,80	0,75	0,84	0,76	1,15	1,01	0,99	1,05	1,44	0,016
	1,33	2,22	1,00	1,16	0,85	1,69	1,20	1,03	1,63	1,00	0,005
	1,13	2,08	0,87	0,85	0,68	1,39	1,25	0,83	0,97	1,13	0,0025
	1,06	2,13	0,61	0,84	0,80	2,50	0,69	1,10	1,40		
Average values	1,18	1,95	0,82	0,92	0,81	1,57	1,03	1,01	1,21	1,17	

**The data in this line pertains to crystal* a.

***The data in this line pertains to crystal* b.

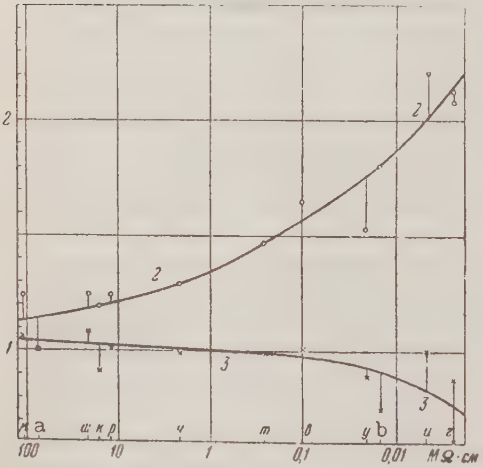

Fig.2. Ratios of reflection intensities for different CdS specimens.

The relationship between the conductivity and the reflection intensity ratios stands out even more clearly when we compare the ratios obtained by averaging over the groups of high and low resistance specimens. By this averaging procedure we eliminate the necessity of complex calculations of the electron density for each crystal individually.

We calculated the structure amplitudes and plotted the electron density distribution projections for two crystals: the high resistance specimen a (Fig.3) and a low resistance specimen designated as b (Fig.4). It will be seen that the maps are very similar. The effect of cutoff of the infinite Fourier series, resulting from the impossibility of utilizing the hard-to-measure reflections of high orders, is manifest in the in the experimental distributions; it is evinced by the appearance of cutoff waves about the maxima (atoms) and minima (octahedral vacancies) of the electron density.

In order to minimize the cutoff effect, in processing the experimental data we used the widely accepted procedure[5] of a fictitious increase in the experimental temperature, which consists essentially of an artificial increase of the

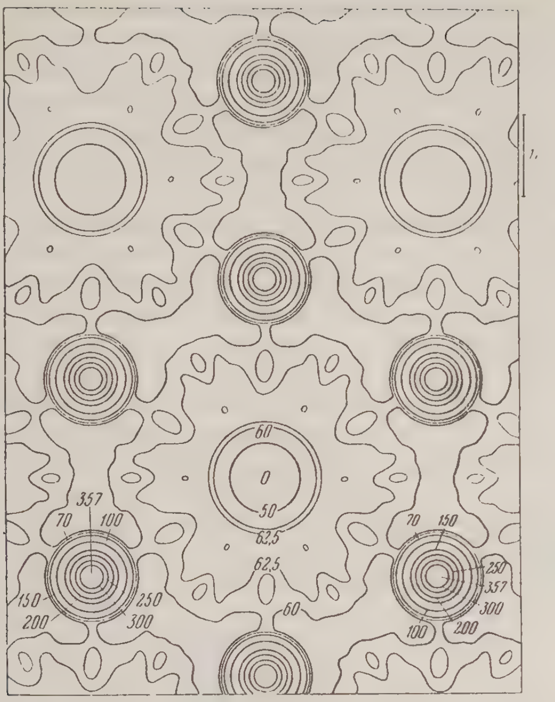

Fig.3. Electron density distribution in a high resistance CdS crystal. (Crystal a). Projection on the (001) plane.

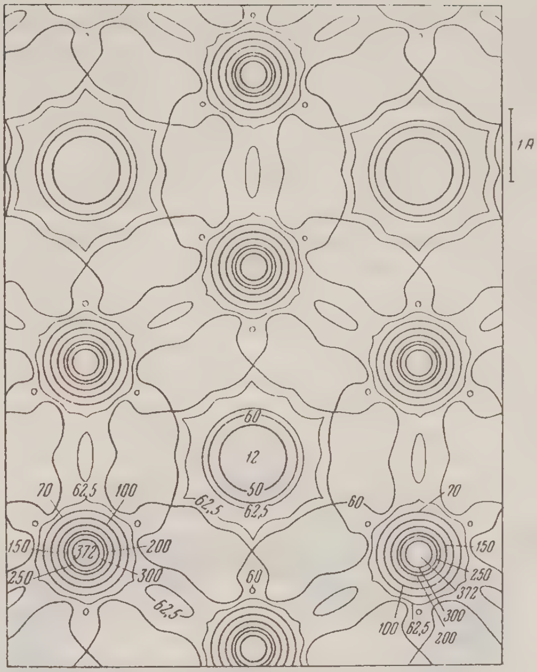

Fig.4. Distribution of electron densities in a low resistance CdS crystal. (Crystal b). Projection on the (001) plane.

exponent M in the temperature factor e^{-M}. This procedure with little detriment to the first important structure amplitudes, greatly reduces the last ones, i.e., the ones that cannot be reliably determined experimentally and thereby legitimizes neglecting them. As a result the cutoff waves, which tend to obfuscate the electron density distribution picture in real crystals, disappear. True, at the same time the principal maxima are lowered and broadened, which corresponds to an increase in the amplitude of the atomic thermal vibrations. The electron density of the smeared out maxima increases the electron background in the space between atoms, but this effect is characterized by spherical symmetry and hence only weakens but does not distort the relative variations in electron density in individual directions. Obviously all this only increases the computational errors, which are superimposed on the already appreciable photometric measurement errors.

Nevertheless by carefully comparing the electron distribution diagrams (Figs.3 & 4) we were able to obtain some indication regarding the regularities characterizing the variations in the electron density in the space between the atomic projections in going from the high resistance crystal a to the low resistance crystal b, even though this distortion effect is close as regards order of magnitude to the overall errors. This effect can be detected by virtue of the fact that in the diagrams, in addition to the principal electron density isolines drawn at intervals of 50 relative units (heavy lines), we also have three isolines within a narrower range (the light lines corresponding to 60, 62.5 and 70 density units) which bring out the fine structure of the electron background.

We plotted the projection of the electron density distribution about an atom at a distance $a\sqrt{3}/6 = 1.19$ Å (half the distance between neighboring atomic projections) on a greatly enlarged scale. In the case of strictly spherical symmetry, the summary electron density at a certain distance from the center of

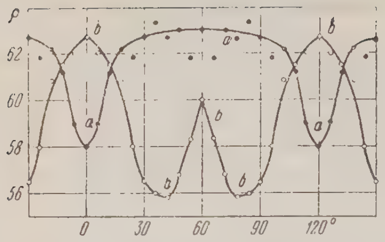

Fig.5. Electron density in different directions around an atom in a high resistance (a) and a low resistance (b) CdS crystal.

the atom should be the same in all directions. It will be seen from Fig.5, however, that the electron shell is obviously distorted, the distortion being different for crystals with different resistivities. Fig.6 shows the redistribution of electron density in the space between the atoms observed in going from the high resistance specimen a (inner belt) to the low resistance crystal b (outer belt).

Among the separations between neighboring projections of atoms, we can distinguish three kinds of distances: short, having a length of $a\sqrt{3}/3 =$ = 2.39 Å, at 0, 120 and 240°; medium, having a length $a = 4.13$ A at 30, 90, 150, 210, 270 and 330°, and long, having a length $2a\sqrt{3}/3 = 4.78$ Å, at 60, 180 and 300°. It will be noted that whereas in the case of the high resistance crystal the electron density about the atom is approximately the same in all directions and falls off slightly only along the short separation line, in the case of the low resistance crystal the electron density increases along the short and long interatomic distances, forming electron bridges between them, while along the medium separation line it decreases, forming what might be termed cols. The long bridges are superimposed on each other, on the medium distance cols and on the octahedral vacancy. Our conclusion regarding the formation of the bridges and cols has been repeatedly verified by detailed investigation of the role played by each reflection individually in the overall background density distribution plot. Careful analysis has shown that the increase in the intensity of certain reflection spots and the decrease in the intensity of others such as is observed in going from low to high conductivity crystals must necessarily lead to an electron density redistribution of the type described.

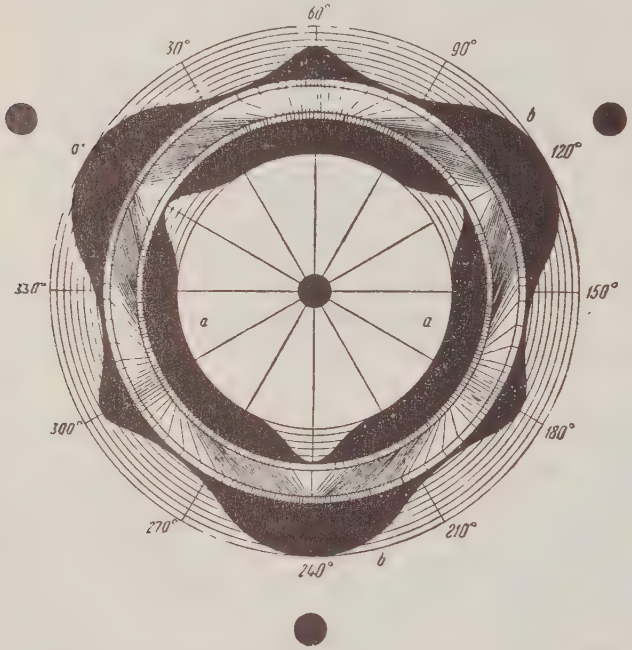

Fig.6. Redistribution of electron density about an atom incident to going from the high resistance crystal a to the low resistance crystal b.

From the structure of the crystals and the character of the projection (Fig.1) one can readily deduce that the medium separations between neighboring atoms do actually lie in the plane of the projection and represent binding between the nearest atoms of the same element. On the other hand, the short and long distances actually represent separations between atoms in different layers. Inasmuch as the layers of cadmium and sulfur atoms alternate, these short and long distances represent separations between different types of atoms. From this viewpoint it is particularly significant that as the conductivity is increased electron bridges with a true length of 2.52 and 4.84 A form between the Cd and S atoms, while the binding between identical atoms is weakened further.

It should be noted that during the experiments the crystals were irradiated with a strong x-ray beam which should have increased their conductivity during the exposure due to photoconductivity[9]. The absolute value of the photoconductivity is the higher, the higher the dark conductivity of the crystal. Consequently, in the case of crystals with an initially higher conductivity, the conductivity during x-raying was further increased, which could enhance the discovered effect and facilitate its detection.

The writer desires to thank A.A.Lebedev for suggesting the subject and his constant interest in the work.

"A.A.Zhdanov" Leningrad State University

References

1. R.W.James, Optical principles of the diffraction of x-rays (in Russian trans. M.1950).
2. R.Brill, H.G.Grimm, C.Hermann & C.Peters, Ann.d.Phys., 34, 393 (1939); Usp. khim, 9, 4, 419 (1940).
3. H.G.Grimm, R.Brill, C.Hermann & C.Peters, D.Naturwiss, 26, 29, 479 (1938); Ann.d.Phys., 41, 37 (1942).
4. M.D.Burger, Rengenovskaia kristallografiia (X-Ray crystallography) M. 1948.
5. A.I.Kitaigorodskii, Rengenostrukturnyi analiz (X-Ray structural analysis), Vol.1, M., 1950.
6. E.V.Stroganov, Dissertation, Leningrad State University, 1953.
7. C.Aminoff, ZS.f.Kristallogr., 58, 203 (1923).
8. F.Ulrich & W.Zachariasen, ZS.f.Kristallogr., 62, 260 (1925).
9. I.Broser, H.Oeser & R.Warminsky, ZS.f.Naturf., 5a, 214 (1950).

AN ATTEMPT TO DETERMINE THE TEMPERATURE RISE OF CURRENT CARRIERS PRODUCED BY AN ELECTRIC FIELD IN GERMANIUM

- M.Stenbeck

The present report is concerned with a possible method of determining the energy relationship between current carriers and the lattice.

When a current of density i flows ghrough a semiconductor, for example, n-type germanium, the mean kinetic energy of the current carriers exceeds $(3/2)kT_o$, where T_o is the temperature of the lattice.

To start, let us purely formally define the electron gas temperature T so that $(3/2)kT$ is equivalent to the mean value of the kinetic energy of the electrons. Then in the presence of a current the electron gas temperature $T > T_o$. Presumably, at not excessively great current density we can write

$$\Delta T = T - T_o = \alpha i^2 \qquad (1)$$

where the coefficient α characterizes the energy relationship between the electrons and the lattice, a relationship which has as yet been little studied either experimentally or theoretically.

Let us examine one of the ways in which α can be investigated experimentally. Under conditions of inhomogeneous current density distribution in a semiconductor (for example, when i at point $A(i_A)$ is greater than i at point $B(i_B)$), the electron gas temperature at these points will differ ($T_A > T_B$), although the lattice temperature T_o may be virtually the same over the entire volume. The thermal inhomogeneity, which is characteristic of an electron gas under such conditions, is a source of a distinctive kind of thermoelectric potential U_T which can be measured by means of needle type probes applied to the specimen at points A and B on condition of no current in the probe circuit. At the same time, true, there is measured an additional voltage between the probes: the voltage due to the resistance drop in the semiconductor. This part of the voltage, however, can readily be excluded since it changes sign when the direction of the current is changed, while the thermal potential in question remains unchanged. We carried out our investigation at room temperature on a highly homogeneous germanium single crystal of the n-type with a carrier concentration $N = 9 \cdot 10^{14}$ cm^{-3}.

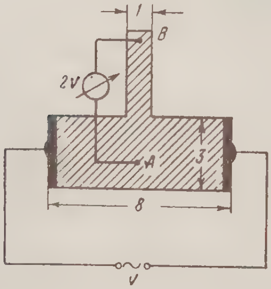

The accompanying figure shows the measurement setup and gives the principal dimensions of the specimen (its thickness was 0.15 mm). The specimen was cemented to a glass plate, ground and etched. The current-carrying electrodes were soldered to the specimen with pure tin at the greatest possible distance from the probes, which minimized the interfering effects. At point B the current density was virtually zero, while at point A it varied from 0 to 12 a_{eff}/cm^2.

We tested tungsten, iron and bronze probes applied with different pressures and having different tip radii. The experimental results showed little dependence on the properties of the probe-semiconductor contacts. Only when the diameter of the shaped tip of the probe exceeded 40 μ did the thermal voltage rise appreciably. In order to exclude the influence of fluctuations in lattice temperature we used alternating current; virtually the same results were obtained over the entire range of frequencies ν from 500 to 20,000 cps. The thermal potential U_T had a frequency of 2ν and was readily measured. The phase of the measured signals of frequency 2ν relative to the applied voltage of frequency ν was checked by means of an oscilloscope; the results were substantially as expected. In the case of the n-type germanium specimens used in our experiments the negatively charged probe was the one located at point A.

All the experimental results satisfy the expression

$$U_T = \beta i^2$$

with $3\cdot10^{-5} \leqslant \beta \leqslant 6\cdot10^{-5}\ v_{eff}/(a_{eff}\ cm^2)^2$.

In view of certain theoretical considerations it would be more correct to operate with an expression of this type not for the current density but for the field intensity. Straightforward conversion yields

$$U_T = \gamma E^2$$

with $1\cdot10^{-5} \leqslant \gamma \leqslant 2\cdot10^{-5}\ v/(v\ cm^{-1})^2$ and $0 \leqslant E \leqslant 30\ v\ cm^{-1}$.

In order to go over from the measured thermal potential to the rise in temperature of the electron gas above the lattice temperature we must have recourse to certain theoretical concepts. Our proposal regarding the interpretation of the cited data is admittedly a rough approximation and is based on the following assumptions: in the region of probe A the electrons have a temperature $T = T_o + {}$ $+ \Delta T$, while the holes in the region of the p-n junction formed by the probe-specimen contact have only the lattice temperature T_o.

Bearing in mind that the mean free path of current carriers in the surface layer is shorter than the mean free path in the volume of the specimen, it may be assumed that the rise in temperature of the current carriers in the surface layer will be appreciably smaller than in the volume. We shall consider in the absence of current a p-n junction in which the electrons have the temperature $T = T_o + \Delta T$ while the temperature of the holes is T_o. The potential distribution in a given volume is virtually determined by the Boltzmann distribution of the density of the majority current carriers in the said region.

In the region where $N^- > N^+$, the potential depends on the concentration of electrons, which is determined by the temperature $T = T_o - \Delta T$; in the region where $N^+ > N^-$ the assumed potential distribution, corresponding to the hole concentration, will depend on the temperature T_o. We assume that the boundary between these regions is situated where the concentrations are equal, i.e., where $N^+ = N^- = N_i$. Although actually the concentration N_i is strongly dependent on T_o, in view of the fact that it is weakly dependent on the temperature of the electron gas, in the first approximation we may regard it as a quasi-constant quantity. On the basis of these assumptions an increment in the electron temperature ΔT leads to an increase of the potential on the p-n junction amounting to

$$\Delta U = \Delta T\, \frac{k}{e} \log \frac{N^-}{N_i} \qquad (2)$$

with a sign in agreement with experimental data. It will be noted that physical factors taking account of the character of the contacts do not enter into this formula, which explains why the investigated effect is independent of the materials and shape of the probe points within a certain range. In addition to the change in contact potential, discussed above, under the conditions of our experiment there developed a difference in thermoelectric potential between points A and B due to diffusion of current carriers through the volume of the germanium; however, this part of the change in potential is insignificant compared to the magnitude of the change in contact potential, provided that $N^- \gg N_i$ and hence we felt justified in neglecting it.

With $N^- = 9\cdot10^{14}\ cm^{-3}$ and $N_i = 2.5\cdot10^{13}\ cm^{-3}$, from (2) we obtain

$$\Delta U/\Delta T = 0.31\ mv/degree.$$

At this value of $\Delta U/\Delta T$, a field of the order of 4-6 v/cm is required for a 1° temperature rise of the electron gas in our specimen, which was at room temperature.

We also carried out a theoretical analysis on the basis of certain simplifying assumptions for the purpose of a) ascertaining the possibility of a theoretical interpretation of the magnitude of the observed effect and b) verifying whether the distribution in velocity of the electrons accelerated in the determined field is Maxwellian.

The calculations were carried out on the basis of the following assumptions:

1. The current carriers were regarded as quasiparticles having an effective mass m and constituting a nondegenerate gas.
2. The electrons were assumed to interact only with phonons.
3. Only elementary interaction events involving single electrons were taken into account.
4. It was assumed that an electron can give off or absorb only the mean energy equal to mvc, where c is the speed of sound, i.e., we excluded from our consideration angular distributions and intensities of electron-phonon interaction that might result in exchange energies in the interval from 0 to 2 mvc.
5. The probability of electron-phonon interaction was assumed to be a function of only the electron velocity (at the given lattice temperature T_o).
6. The above mentioned function was assumed to predetermine attainment of detailed equilibrium in the presence of temperature equilibrium between the electron gas and the lattice.

If the mean free path is assumed to be independent of the electron energy, the calculations lead to the following equation:

$$\frac{T - T_o}{T_o} = \frac{\pi}{4}\left(\frac{W}{c}\right)^2, \tag{3}$$

where W is the drift mobility of the carriers in the electric field. It follows that with the values of the carrier mobility (3600 cm^2/volt sec) and velocity of sound ($4.8 \cdot 10^5$ cm/sec) characteristic for n-type germanium at room temperature a field intensity of 8.6 v/cm is necessary to increase the electron gas temperature 1°C. This deduced value is in good agreement with the results of our experiments.

Under these conditions an electron loses less than 0.1% of its excess energy on the average in each interaction event. And if the carrier concentration $N^- \geqslant 1 \cdot 10^{14}\ \text{cm}^{-3}$, the energy of Coulomb interaction between electrons may exceed by an order of magnitude the energy of interaction of the electrons with phonons, which gives reason to expect the presence of a well established thermal equilibrium of the electron gas similar to the thermal equilibrium of the electron gas in the plasma of a discharge.

The question of why the carrier mobility remains constant up to very strong fields (of the order of 900 v/cm for n-type germanium), when in view of what has been said above one might expect a sharp rise in the electron gas temperature, still remains open. It is entirely possible that the procedures and simplifying assumptions utilized in our analysis become inapplicable in the region of such strong fields.

Institute of Physics of the
Ukrainian SSR Academy of Sciences

FORMATION OF VACANCIES IN A CRYSTAL LATTICE

- N.P.Kalabukhov

Although it has been known for a long time that x-rays produce coloration of alkali halide crystals[1], the coloring process itself has not yet been adequately studied. Tartakovskii[2] suggested that when an alkali halide crystal is irradiated with x- or γ-rays, the incident photons are scattered by the electrons of the negative halide ions; inasmuch as the photon energy is many times greater than the electron-halide atom binding energy, we have Compton scattering, i.e., the photon is scattered and the halide-ion electron is ejected as a recoil electron. The electron goes over to an alkali metal ion, i.e., enters the conduction band. Upon encountering a halide-ion vacancy the electron is trapped at the imperfection and forms a color center (F-center).

These ideas have not been substantiated experimentally. Drukarev[3] takes a different view of the coloration process. He considers that the x-rays themselves can generate halide-ion vacancies. Under the influence of x-rays there occurs not a Compton but a photoeffect, i.e., the photon is not scattered but absorbed; in conformity with the law of conservation of momentum and energy, the ion absorbing the photon undergoes recoil. In the case, when the recoil energy is greater than the binding energy of the ion with the lattice, the ion will be ejected from its site and finally forced to the surface. The ejected electron is captured by an alkali metal ion, i.e., goes over into the conduction band. In moving through the conduction band the electron encounters a halide-ion vacancy and is trapped, forming an F-center.

Drukarev carried out calculations for this process. According to his calculations knowing the minimal frequency of the x-rays producing coloration, one can determine the halide ion-lattice binding energy as well as the concentration of vacancies produced by the x-rays. There has as yet been no experimental confirmation of this mechanism, but the following facts are evidence in favor of the hypothesis that new vacancies are generated as the result of x-ray irradiation. The maximum concentration of F-centers in x-rayed crystals may be of the order of 10^{18} cm^{-3}. If we assume that the vacancies are not generated in the process of irradiation, we must admit that there can be present an equal concentration of vacancies in the original crystal. Further, if we bear in mind that heat treatment increases the intensity of coloration produced by x-raying, we must also admit that the number of vacancies is reduced in annealing which means that annealed crystals should have an appreciably lower density.

However, a careful investigation of the change in density of KCl crystals incident to annealing yielded no positive results, i.e., showed no noticeable change in density. Esterman, Leivo & Stern[4], who, like Drukarev, consider that formation of halide-ion vacancies occurs in the process of irradiation, carried out experiments aimed at determining the change in density of KCl crystals as a result of exposure to x-rays. They utilized a highly original procedure for measuring the density and detected a decrease in density of the order of $1.4 \cdot 10^{-4}$ g/cm^3. These investigators attribute this decrease in density to the formation of new negative and positive ion vacancies in the KCl crystal under the influence of x-rays. The released ions migrate to the surface of the crystal with the result that its volume is increased without change in mass.

In order to verify this hypothesis of the formation of new vacancies in the process of irradiation we carried out experimental measurements of the spectral distribution of the absorption coefficient in KCl crystals in the following sequence:

1) the crystals were irradiated and the spectral distribution of absorption was determined;

2) the crystals were bleached;

3) the crystals were again irradiated under exactly the same conditions as

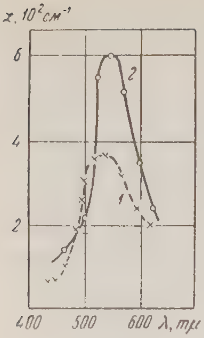

Fig.1

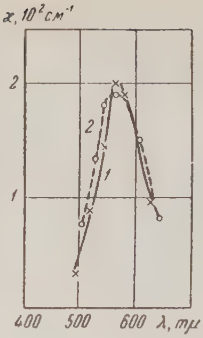

Fig.2

Fig.1. Spectral distribution of absorption in KCl crystals: 1) after first irradiation, 2) after irradiation, bleaching and repeated irradiation.

Fig.2. Spectral distribution of absorption in KCl crystals: 1) after initial irradiation, 2) after irradiation, bleaching, annealing and repeated irradiation.

the first time and the distribution of the spectral coefficient was again measured.

As a result the absorption coefficient of the re-colored crystals increased at the peak by almost 60% compared with the coefficient for the crystals irradiated only once (Fig.1).

If after the first irradiation and bleaching the crystal is annealed for 2 hours at about 150° and then again irradiated in exactly the same way as the first time, the resultant absorption distribution curve is nearly identical with the initial one except that in this case the absorption coefficient is somewhat smaller at the maximum (Fig.2). Comparison of these results shows that new trapping centers are generated in the irradiation process (since the absorption increases after the second irradiation of non-annealed crystals). After heat treatment, however, these trapping centers no longer function as such (the absorption coefficient after the second irradiation of annealed crystals differs little from the coefficient after the initial irradiation).

We also carried out measurements on the electric conductivity of KCl crystals. The experimental treatment was the following:

1) the conductivity of transparent KCl crystals was measured at 110°;
2) the crystals were irradiated with x-rays and then bleached;
3) the conductivity was again measured (the conductivity was measured both immediately after bleaching and after bleaching and annealing).

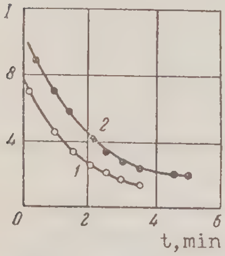

Fig.3. Decrease of current with time in KCl crystals: 1) untreated crystal and irradiated, bleached and then annealed crystal (the curves for these crystals are identical), 2) irradiated and then bleached crystal (measurements made at 110°).

The results are shown in Fig.3. The curves give the falling off of current with time. Curve 1 shows the current decrease in transparent crystals and in crystals annealed after x-raying and bleaching. Curve 2 gives the decrease in current in crystals bleached after irradiation (without annealing). As is evident from the figure non-annealed crystals after irradiation and bleaching exhibit a higher conductivity, while after annealing the conductivity of the crystal becomes identical (experimental accuracy ~5%) with the initial conductivity.

The vacancies are formed in the process of irradiation is further substantiated by the results obtained in measuring the dark current in additively colored KCl crystals. We established[5] that KCl crystals colored in an alkali metal vapor acquire semiconductor characteristics, i.e., develop an electronic conductivity in the dark. It was also established that the reason for the appearance of the dark current is the formation in the KCl crystals of multiple centers (so-called R-centers, consisting of a pair of adjacent F-centers). These centers are responsible for an absorption band peaking at 730 mμ. If new vacancies are formed during irradiation one should logically expect the number of multiple centers in KCl crystals colored in alkali metal vapor to decrease under the influence of irradiation since the newly generated vacancies should provide for a more uniform distribution of the electrons over such sites, i.e., the

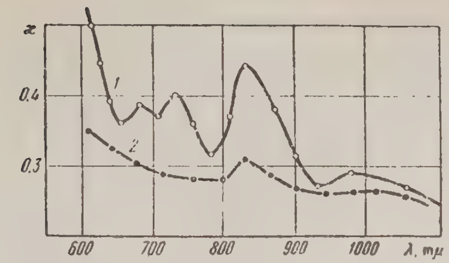

Fig.4. Spectral distribution of absorption in an additively colored KCl crystal: 1) after coloring in potassium vapor, 2) same crystal after x-ray irradiation.

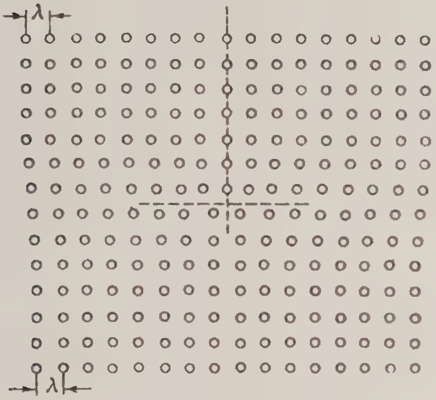

Fig.5. Diagram of edge dislocation.

R-centers should break up with the formation of new F-centers.

The experimental results obtained fully substantiated this. The curve characterizing the spectral distribution of absorption in KCl crystals colored in metal vapor are shown in Fig.4. Curve 1 characterizes the absorption of these crystals after coloring in metal vapor. As will be seen the crystals have an F-band (only the beginning of the rise appears at the left edge of the figure), an R-band (with a peak at 675 mμ), an R'-band (peak at 730 mμ), an M-band (at 825 mμ) and an N-band (peak at 1000 mμ). Curve 2 shows the spectral variation of the absorption coefficient after irradiation. It will be seen that both R and R' bands have completely disappeared, while the M-peak has been greatly lowered.

Investigation of the electric conductivity of these crystals showed that prior to radiation with x-rays these crystals had a noticeable dark conductivity which disappeared after irradiation. This again confirms that the dark current in such crystals is due to the presence of multiple centers.

Thus the described experimental results furnish convincing evidence that new vacant sites are produced in KCl crystals in the process of x-raying. In a number of recent publications Seitz[6], Markham[7] and others advance interesting ideas regarding the formation of vacancies from dislocations.

One can form an idea of such dislocations (so-called line or edge dislocations), if we imagine that a cut is made in some plane of a regular crystal lattice and a row of ions is removed or introduced along this cut. Obviously, in the first case the ions nearest the cut will be closer together, while in the second case they will be forced further apart (Fig.5). The region of a crystal in which such a disturbance in the regularity of the lattice obtains is called an edge dislocation. The horizontal dash line in Fig.5 shows the direction of slip. The ions can readily move along this line under an applied stress. This concept is utilized to explain plastic flow in solids. The plane in which the additional layer of ions is present (or from which it is absent) is called the singular or extra plane.

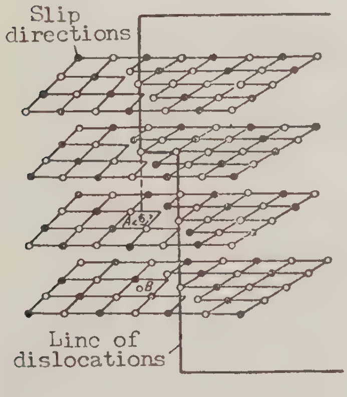

Fig.6. Extra plane in a crystal lattice having a "jog" associated with the appearance of "incipient" vacancies (point A).

Seitz[6] has suggested that the edge of an extra plane may have a break or "jog". Such a jog is illustrated in Fig.6. This figure shows four consecutive crystal planes. The extra plane comprising rows of additional ions extends perpendicularly to these crystal planes. The edge of this plane can have a jog due to the fact that the edge row of ions in the extra plane contains different numbers of ions in the different crystal planes. The edge of the extra plane is called the dislocation line. The direction of slip, as is apparent from the figure, is always perpendicular to this line of dislocations. In the case of a jog in the edge of the extra plane (at the dislocation line), there is formed a potential well near this jog in the crystal lattice (in Fig.6 this point is identified by the letter A), which is equivalent to the presence of a certain effective charge at this point. It can readily be shown that the magnitude of this effective charge α equals ±e/2, where e is the electron charge. Seitz regards this point as an "incipient" vacancy.

That the effective charge of the incipient vacancy equals +e/2 can be demonstrated in the following manner. Let us assume that the jog in the dislocation line is such as shown in Fig.6. Then in the region of point A there will be a certain effective positive charge (incipient negative ion vacancy). A negative ion with charge -e can jump into this region; then the jog will move over a lattice distance and an incipient vacancy will appear at point B (this will already be incipient positive ion vacancy); its sign will be negative. Thus the capture of a negative ion by an incipient vacancy changes the sign of the vacancy. Whence we get $\alpha = e/2$ (inasmuch as $\alpha - e = -\alpha$). The jog in the dislocation line is a remarkable point in the crystal lattice since on the one hand the jog facilitates formation of vacancies through capture of the nearest ion by the incipient vacancy with the resultant inclusion of the ion into the row of ions forming the extra plane (in the process the jog is displaced a lattice distance and the formed vacancy can diffus into the crystal) and, on the other hand, the vacancy can also be absorbed by the dislocation line. This last can occur in the following manner: the vacancy can approach the edge ion at the jog and capture it, thus reducing by one ion the edge row of ions of the extra plane. In this case the jog will also be displaced a distance equal to the lattice distance, but in the direction opposite to that in the foregoing case.

The presence of dislocation lines with jogs facilitates the formation of color centers and extra vacancies during the irradiation of alkali halide crystals with x-rays. The process involved may be pictured as follows: the electron stripped or ejected by an x-ray photon from some halide ion is captured by a metal ion and begins to migrate through the crystal. In its movement through the crystal, the electron may approach a jog in a dislocation line and be trapped by an incipient negative ion vacancy. The electron at this point may be localized and form a j-center[7]. A negative ion vacancy may approach the j-center; then the electron from the j-center will jump to this vacancy (for an electron a vacancy is a deeper potential well than incipient vacancy) and form an F-center with it; this may be regarded as the presence of a neutral alkali metal atom near the jog. In consequence, the binding of the neighboring halide ion with the surrounding ions will be weakened and the probability of its jumping to an incipient vacancy will be enhanced.

As a result of the jump of the negative ion the jog in the dislocation line will move a distance equal to the lattice constant, i.e., the halide ion will move into the extra plane and a new vacancy will appear in the lattice. Thus as a result of x-ray irradiation there form in the crystal an F-center and an extra vacancy, i.e., the action of the x-rays in the case when an edge dislocation with a jog is present in the crystal leads to the appearance of F-centers and additional negative ion vacancies. At the same time this process increases the number of incipient positive ion vacancies inasmuch as the negative ions in the process of being captured by incipient vacancies displace the jog a lattice distance and change the sign of the incipient vacancy. An increase in the number of incipient positive ion vacancies, in turn, leads to an increase in the probability of the generation of positive ion vacancies in the crystal.

Thus irradiation of crystals with x-rays leads to an increase in the number of both negative and positive ion vacancies. These concepts satisfactorily explain the experimental facts cited above. In line with these concepts an increase in the number of halide ion vacancies should lead to an increase in the number of F-centers during the second, repeat irradiation. Furthermore an increase in the number of alkali metal ion vacancies should lead to an increase in the ionic conductivity inasmuch as this conductivity is due to the motion of metal ion vacancies.

Annealing of the crystal leads to an increase in the mobility of the vacancies; this increased mobility furthers the growth of associated vacancies which can gather into chains and finally form planes. This in turn brings about the formation of dislocations in the crystal inasmuch as the presence of such a crystal plane, consisting of vacant sites, essentially amounts to the removal of ions from a certain cross section of the crystal.

Thus the aggregation of vacancies into chains leads to the disappearance of part of the vacant sites and the appearance in their place of dislocation lines. This in turn leads to a reduction of the absorption coefficient in crystals irradiated after annealing as well as to a lowering of their electric conductivity.

Institute of Physics of the Georgian SSR Academy of Sciences
and "I.C.Stalin" Tbilisi State University

References

1. W.C.Roentgen & A.Joffe, Ann.d.Phys., 64, 1 (1921).
2. P.S.Tartakovskii, Vnutrennii fotoeffekt v dielektrikakh (The internal photoeffect in dielectrics), M.-L., 1940.
3. G.F.Drukarev, Doklady AN SSSR, 52, 215 (1946).
4. J.Estermann, W.J.Leivo & O.Stern, Phys.Rev., 75, 627 (1949).
5. N.P.Kalabukhov, Zhur.eksp.i teor.fiz., 26, 242 (1954).
6. F.Seitz, Phys.Rev., 79, 890 (1950); 80, 239 (1950); Rev.Mod.Phys., 23, 328 (1951).
7. J.Markham, Phys.Rev., 88, 500 (1952).

PREPARATION OF PHOSPHORS BY RECRYSTALLIZATION AND ELECTRON MIGRATION

- Z.D'iulai

1. Recrystallization

For the past several years we have been working on the problems of recrystallization in our Institute. The materials investigated have been primarily alkali halide crystals (NaCl and KCl). The finely powdered material (grain size 1-5 μ) is compressed into tablets at pressures from 1000 to 2000 kg/cm^2. In sections of these tablsets prepared by cutting or etching one can distinguish individual crystals. The grain size in the compressed tablets is appreciably greater than that in the original material. Frequently a number of crystals having different initial orientations form a single crystal under pressure. One can often find individual crystals with a perimeter of several tenths of a millimeter. Hundreds and even thousands of the initial tiny crystals occupy new positions in the crystal formed under pressure.

In view of the results obtained with simple salts, we attempted to prepare alkali halide phosphors by means of recrystallization. By way of activator we decided to use TlCl; by way of host material NaCl. We assumed that the activator might be incorporated into the new crystals in the process of recrystallization under pressure. If this happened the compressed tablets should phosphoresce. As is known the NaCl(TlCl) phosphor prepared by R.Hilsch phosphoresces very well under the influence of ultraviolet.

In the experiments, we added a few drops of TlCl solution to the base material, mixed it thoroughly in an agate mortar and thoroughly dried the mixture. After evaporation of the moisture, minute TlCl crystals appeared on the surface of the NaCl crystals. Thus there was obtained a uniform distribution of the activator. After compression we obtained tablets similar in appearance to the ordinary salt tablets, but these phosphoresced under the influence of ultraviolet rays. We feel that this is proof that the Tl ions enter into the NaCl lattice. The powdered mixture before compression did not phosphoresce. And, of course, tablets compressed of pure NaCl did not react to ultraviolet radiation. The emission of tablets with different concentrations of TlCl differed. The phosphorescence intensity of the compressed phosphors nearly equaled the phosphorescence intensity of the crystals grown from a melt by R.Hilsch.

Phosphors obtained by recrystallization are of particular interest because it appears that the activator ions can enter into the host material not only at high temperatures but at room temperature as well. Furthermore, these phosphors exhibit a number of interesting properties. After preparation (extraction from the die) their ability to phosphoresce changes with time: first increases, to a maximum, then slowly falls off. Heat treatment after compression also produces appreciable changes. These changes in the phosphorescence yield are connected with changes in the crystal structure and can be interpreted as indicators characterizing processes occurring inside the crystals. It may be noted that processes of this type are also encountered in nature.

2. Electron migration

In our experiments with recrystallization we encountered an unexpected phenomenon. In some cases the NaCl tablets prepared at the higher experimental temperatures appeared transparent or colored. A number of times we obtained tablets with a distinct brownish yellow color reminiscent of the color of crystals radiated with x-rays. Some slight coloration had been observed in earlier experiments; however, in the given case we could scarcely expect to observe spontaneous coloration.

We determined the absorption spectra of these tablets; the results are

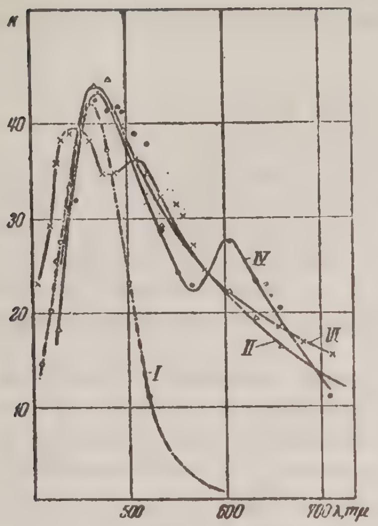

shown in the accompanying figure. Curves II through IV pertain to different tablets, but it will be seen that they all have a pronounced peak at 450-480 mμ. For purposes of comparison we also show the absorption spectrum of a rock salt crystal radiated with x-rays (curve I).

The curves are somewhat diffused due to scattering of light in the tablets; however, the virtual coincidence of the peaks with the absorption peak for an NaCl crystal irradiated with x-rays is unmistakable. It will be noted that some of the tablet curves have an additional peak[1].

Consequently, we can ascribe the peak in the absorption spectra to F-centers. This effect can be explained if we assume that the electrons migrate in the tablet material during the process of compression at the higher tableting temperatures used (650-700°). The higher temperature makes the electron migration more intense so that the developing coloration becomes distinguishable to the naked eye. The compressed tablets are not uniformly colored. It may be noted, however, that similar nonuniform coloration is also observed in the case of so-called additive coloring when crystals are heated in Na vapor or liquid Na.

We feel that in both cases coloring is due to electron migration, but whereas in the case of additive coloring the electrons come from the liquid metallic sodium, in our case they come from the steel of the tablet die. It may be assumed that migration of electrons in dielectrics occurs at any temperature. In fact this effect may play an important role in nature (in geological formations, for example).

Budapest Institute of Experimental Physics of the
Technical College of Construction and Transport

References

1. Tarjan, ZS.f.Phys., 125, 597 (1943).

ELECTRIC PROPERTIES AND APPLICATIONS OF SILICON CARBIDE

- N.P.Bogoroditskii, V.V.Pasynkov, G.F.Kholuianov & D.A.Ias'kov

Introduction

Developments in engineering have created a demand for many special purpose materials; some of the requirements set for such materials can be met by semiconductor carbides. Among the most extensively investigated and already widely used substances in this class is silicon carbide which has long been familiar in industry as an abrasive. However, it is also used for preparing electrical products: Wilite resistor elements for lightning protectors on high voltage transmission lines, Silit heater rods for high temperature furnaces, temperature compensators, etc.

Where lightning protectors are concerned the valuable property of silicon carbide is the nonlinear current-voltage characteristic of agglomerates of carbide grains in the range of high electric field intensities. In the case of heater rods, advantage is taken of the high thermal stability of silicon carbide and its ability to retain its properties at temperatures of the order of 1400°, where chrome-nickel and chrome-aluminum heater elements become useless. In addition, silicon carbide can be used for temperature compensators because the electric conductivity of its different modifications varies over a wide range, while its temperature coefficient of resistance is negative but close in absolute magnitude to the temperature coefficient of copper.

Silicon carbide is a compound of silicon and carbon described by the formula SiC. Its molecular weight is 40.07. The grain density is 3.2 g/cm^3. At present seven different modifications of SiC are known. The stoichiometric carbide consists of 70.045% Si and 29.955% C. Silicon carbide is obtained only artificially by current-heating of a mixture of quartz sand and coal to a temperature of 1800-1900°. Depending on the raw materials used and the conditions of the technological process, there are formed either colorless and light green or black and blue-violet silicon carbide crystals.

The color is determined by the presence of impurities and excess silicon or carbon over and above the stoichiometric proportions. The character of the impurities present determines both the type of conductivity (n or p) and the absolute value of the conductivity, which may vary from 1 to 10^{-13} mho/cm for green SiC (and to 10^{-14} mho/cm for the transparent) and from 0.5 to 10^{-1} mho/cm for the black modification.

The electric conductivity also depends to some extent on the direction of current flow in the crystal and on the presence of oxide films. The temperature coefficient of resistance of black and green silicon carbide crystals is close to 0.2-0.3 percent per degree. The thermal conductivity of black silicon carbide is of the order of 0.02 cal/°C/cm/sec; the specific heat at 20 is about 0.18 cal/g/°C. Silicon carbide is characterized by a relatively small linear expansion coefficient: $(5-7)\cdot 10^{-6}$ per degree.

The silicon carbide druses formed in the electric furnace are ground up to obtain powders of different grain size (commonly within the 40-300 μ range). The grains are irregular fragments with extremely jagged edges.

The researches on silicon carbide carried out over the last decade in the department of dielectrics and semiconductors of the Leningrad Electro-Technical Institute have made it possible to utilize it as the principal component in the design of waveguide absorbing loads in the medium power range, miniature nonlinear resistors for automatic equipment and integral-formed ignitron electrodes of high mechanical strength.

1. Waveguide absorbers

Energy at frequencies above 1000 Mc is generally transmitted by means of waveguides. The energy is carried by the electromagnetic field and the walls of the waveguide act as a guiding channel for the propagating waves. For measurement purposes use is frequently made of devices capable of separating part of the power or sometimes of absorbing all the power put into the waveguide. Such devices (see Fig.8) are called attenuators, terminal loads or absorbers[1-3]. Design of such absorbers involves two problems: choice of the material in which the power is dissipated and matching the absorber (terminal load) and waveguide impedances so as to minimize or exclude reflection.

A waveguide attenuator absorbing all the power in the waveguide at a certain frequency is a "black body" for this frequency. Inasmuch as electromagnetic waves are almost fully reflected from magnetic conductors and fully transmitted through matched plates of low-loss dielectrics, it is necessary to use a semiconductor material for such "black body" purposes. Where high frequency engineering is concerned the attributes of semiconductors are characterized by the ratio $\gamma/\omega\epsilon$, where γ is the conductance, ω is the frequency and ϵ is the dielectric constant of the material. Where $\gamma/\omega\epsilon \gg 1$, we have a material in which conductance currents predominate, i.e., a conductor; in the contrary case, we have a material in which polarization currents predominate, i.e., a dielectric. Semiconductors occupy the intermediate position. The behavior of some of the materials depends on the frequency, that is, the same material at different frequencies may be classed as a conductor, semiconductor or dielectric. It should be noted that the parameters γ and ϵ are themselves functions of the frequency. The dissipation of energy in a material is determined not only by the conduction current and the active component of polarization current but also by the magnetic losses and, consequently, for purposes of absorption it is best to utilize semiconductor-magnetodielectric combinations; when such substances are used minimal reflection can be obtained[4] when the condition $\overline{\epsilon} = \overline{\mu}$ is fulfilled. Waveguide attenuators have been prepared in the Institute for mean powers in the range from a fraction of a watt to several hundred watts and for pulse powers of up to several hundred kilowatts; they provided attenuation of the order of 30-40 db.

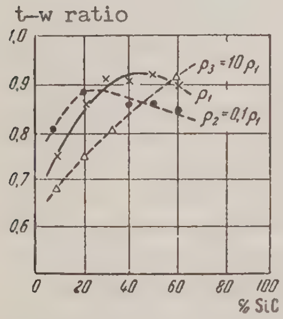

Fig.1. Variation of the traveling wave ratio of the attenuator on the silicon carbide content.

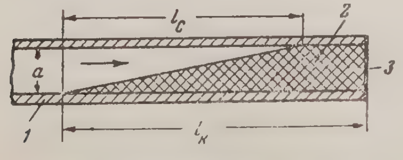

Fig.2. Arrangement of the absorbing load (attenuator) in the waveguide: 1) waveguide walls, 2) absorbing load, 3) back wall.

The basic criterion where the quality of a waveguide attenuator is concerned is the traveling wave ratio (hereinafter t-w ratio) which is defined as the ratio of the amplitude of the minimum to the amplitude of the nearest maximum of the wave in the waveguide. The t-w ratio is a complicated function of the complex dielectric constant and magnetic permeability of the material and of the geometry of the absorber. On the basis of experimental work carried out at the Institute is has been possible to develop materials, which with proper geometric design of the attenuator, yield a t-w ratio $\geqslant 0.95$. Since in operation the temperature of the attenuator may rise 200-300°C above the ambient temperature, it is important to use heat stable components. Hence by way of binder we chose ceramics characterized by good thermal conductivity and high mechanical strength. Among the many different absorbing semiconducting components tried, the best results were obtained with silicon carbide which is not only heat resistant but also has a linear expansion coefficient close to that of the ceramic binding material. Measurements of the t-w ratio of the absorbers as a function of the silicon carbide content (Fig.1) show that the t-w ratio of the attenuator rises at first with increasing SiC content. It may be assumed that in this range of concentrations reflection from the front wall of the attenuator plug is small and that absorption in the material is not complete and there is some reflection from the back wall (Fig.2). At a certain point the optimal concentration of SiC is reached and the t-w ratio attains its maximum value. Further increase in the SiC concentration leads to a decrease of the t-w ratio which must be attributed to increased reflection from the front slanting face of the attenuator plug since at such high concentrations absorption in the material must be adequately high.

The mechanical strength of the plugs proved to be adequate when the SiC content was above 60%. Introduction of a magnetic component - iron carbonyl or powdered alcifer - as replacement for part of the silicon carbide content yields an increase in the t-w ratio in a certain frequency range.

It is impossible to attain a high content of the magnetic component due to the resultant more rapid heating of the plugs particularly at high temperatures if the attenuators dissipate an appreciable power. The height (a in Fig.2) and the width of the absorber plug are determined by the dimensions of the waveguide. The length of the wedge section should be fairly large. The fact that the t-w ratio shows a regular periodic variation with the length of the slanting (wedge) part of the absorbing plug (Fig.3) makes it possible to "tune" (i.e., change the parameters) a prepared plug by shortening the length of the wedge.

This method of adjustment works satisfactorily as long as the length of the slanting part of the plug is 2-3 times greater than the wavelength. The attenuators prepared at the Institute were stable at temperatures from -60 to +70° and air humidities up to 98%. The preparation procedure consists of selecting and weighing the raw material, grinding and mixing it in a ball mill, rough shaping of the plug, low temperature heating, mechanical treatment to form the wedge and finally high temperature sintering. The high temperature treatment is carried out in a reducing atmosphere for 10-12 hours including the heating and cooling periods of the furnace. The final stage of preparation consists of measuring the t-w ratio and mechanical adjustment of the wedge length in order to obtain maximum ratio in accordance with the data of Fig.3.

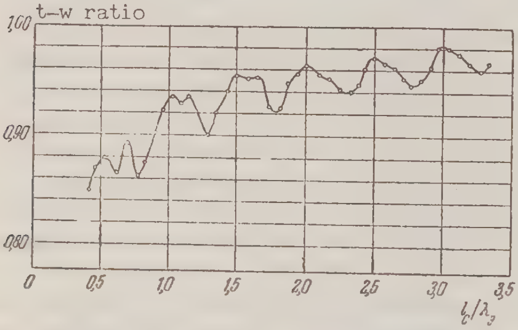

Fig.3. Experimental dependence of the t-w ratio of an attenuator with silicon carbide on the ratio of the length of the wedge section of the plug to the wavelength.

2. Miniature nonlinear resistors

Nonlinear resistors are units whose resistance sharply depends on the applied voltage. Nonlinear resistors may be either symmetric or unsymmetric. Symmetric resistors have identical current-voltage characteristics for both polarities of the applied voltage. In unsymmetric resistors the flow of current at the same voltage is different for the two directions of the field gradient.

In the case of semiconductor nonlinear resistors, we commonly distinguish between resistors with flat (areal) metal to semiconductor contacts and units with metal point contacts of one or both the electrodes. Resistors with point contact electrodes are characterized by a lower value of the self-capacitance which, as a rule, is evinced when the units are operated at frequencies above 5000-10,000 cps.

The principal characteristic of nonlinear resistors - the current-voltage curve - is approximated in most Russian and foreign publications[5-10] by the formula

$$V = A \cdot I_{\alpha}$$

or

$$I = B \cdot V^{\beta}$$

where A, B, α and β are constants. These expressions do not hold exactly in practice; α and β are not really constant and this leads to appreciable difficulties in evaluating the quality of linear resistors. On the basis of the curves shown in Fig.4 (Ref.7), we suggest the following formula for silicon carbide resistors (with a small amount of binder):

$$j = \gamma_o e^{b\sqrt{E}} \cdot E = \gamma E$$

where j is the current density, E is the mean voltage (field) on the resistor, γ_o is the electric conductivity in a very weak field and b is a coefficient characterizing nonlinearity of the resistor. Setting $b = 0$ in the above formula we obtain Ohm's law as a particular case. This is in effect a substantiation of the view that metallic conductors may be regarded as a limiting case of semiconductors. The cited expression can also be derived from the concept of a granular resistance in the form of a large number of parallel networks with contacts that tend to close as the voltage increases.

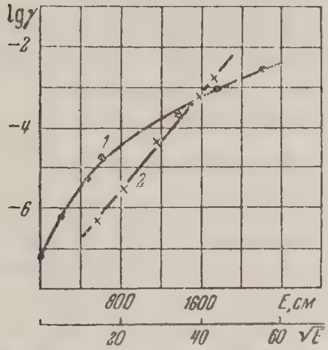

Fig.4. Dependence of the electric conductivity of silicon carbide powder on 1) the electric field intensity E and 2) on $\sqrt{E}$.

It can be shown that the conductivity with a mean grain size d is characterized by

$$\gamma = ce^{\varphi d},$$

where c and φ are constants.

The above equation for j and γ are in good agreement with experimental data. An approximate evaluation of the electric field intensity in the gaps between the jagged teeth of the grains indicates that $E_{av} \approx 10^4$ v/cm, although of course in view of the irregularities of the grains and the presence of sharp edges local field intensities can be much higher. Since the contact-closing effect develops at gaps of 0.1-1 μ, comparable in length with the electron mean free path at normal air pressure, placing a granular resistor of silicon carbide into vacuum or under elevated pressure should not significantly alter its characteristics; this is substantiated by experiment. It may be noted in passing that some investigators have attempted to use the pressure invariance of granular resistors as an argument against the theory of nonlinear resistances based on closing of the intergranular gaps.

In light of the above deductions regarding the mechanism of nonlinearity, the Institute proceeded to develop miniature nonlinear resistors on the basis of silicon carbide. It was found that resistors formed of powdered silicon carbide even if strongly compressed in an insulating housing between metallic electrodes are not shock and vibration stable due to shifting of the grains. In order to obtain more stable nonlinear characteristics it is necessary to bind the silicon carbon grains with at least a small amount of binder. Investigations of the influence of binding materials indicated that their presence reduces the nonlinearity of silicon carbide resistors. It was shown by Teszner[5,10], however, that this is true only when the binding material is an inert medium like clay, porcelain and the like. On the other hand, if one incorporates into the binder particles capable of field emission (at a certain value of the electric field) or secondary emission (under the influence of electrons ejected from the silicon carbide grains) the characteristics of the granular resistors become even more nonlinear.

At low values of the field intensity the resistance of the resistor will be increased, since under these conditions the binder acts as an inert medium, but beginning at a certain value of the field there develops a sharp increase in the current flowing through the resistor. We prepared resistors in the form of compressed discs 1 mm in thickness and 1 cm^2 in area; the electrodes were silver plates. The activating additives were alkaline earth metal oxides, added in the amount of about 5% by weight. The current-voltage characteristics were recorded by means of an oscilloscope at the commercial (50 cps) and audio frequencies.

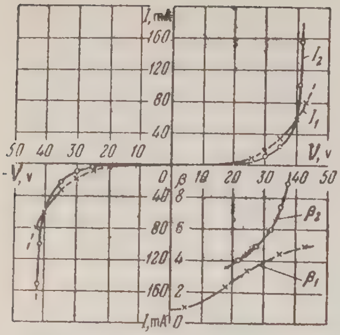

Fig.5. Current-voltage characteristics of nonlinear resistors recorded at 20°: 1) resistor with an inert binder, 2) resistor with activating additive.

The resistance curve for resistors with an activating additive (Fig.5) rises more rapidly and intersects the curve for resistors without additives. The curve for the coefficient of nonlinearity as a function of the field intensity for resistors without additives rises slowly and approaches a limiting value of 5. The nonlinearity coefficient of resistors with activating additives at first rises less steeply but after a certain point its rate of growth is appreciably increased.

Harmonic analysis by approximate methods of current curves plotted as a function of a sine voltage indicates that the current curve for a resistor without additives comprises about 30% third harmonic and about 3% fifth harmonic, while the curve for a resistor with an activating additive comprises in addition to the same third harmonic content about 15% fifth, 8-9% seventh, 5% ninth and 3% eleventh harmonics. Temperature did not appear to have any noticeable influence on the current-voltage characteristic in the limited range of applied voltages; this we checked by immersing the resistors in liquid air. At higher frequencies, a hysteresis loop appears in the current-voltage characteristic of the nonlinear resistors (Fig.6). This is evidence that at elevated frequencies the resistor is no longer a pure resistance, i.e., that a reactive component due to self-capacitance appears. In order to obtain nonlinear resistors with characteristics stable in time it is recommended that they be protected from the influence of humidity by an appropriate housing or coating.

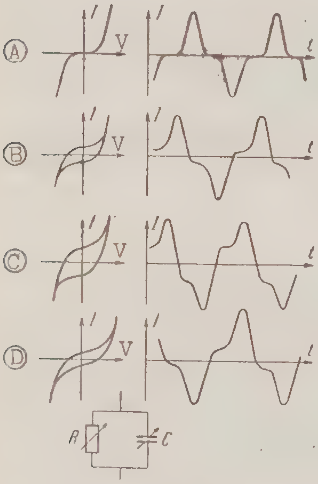

Fig.6. Oscillogram of current flowing through a nonlinear resistor at different frequencies and equivalent resistance circuit:
A) V_m = 15 v, f = 100 cps, I_m = 1 ma; B) V_m = 15 v, f = 10,000 cps, I_m = 1 ma; C) V_m = 15 v, f = 20,000 cps, I_m = 1 ma; D) V_m = 30 v, f = 20,000 cps, I_m = 1 ma.

The technological process of preparing the resistors is not complicated. First, the components are sifted through appropriate screens, proportioned and mixed. Next, an appropriate amount of binder is added; this should insure sufficient strength of the thin disc after compression at 4-5 ton/cm^2 to see it through the sintering. The sintering is carried out in an electric resistance furnace at a temperature of 1200° in an inert or reducing medium, since the formation of oxide films on the grain surfaces under the influence of air increases the resistance of the material and lowers the nonlinearity coefficient. The compressed resistors are slowly heated with the furnace to the above indicated maximal temperature over a period of 3-4 hours; then the furnace is allowed to cool for 5-6 hours. The sintered discs are then cleaned by grinding and the electrodes are applied. These nonlinear semiconductor resistors (NSR), depending on whether they are connected in parallel or in series with the load (Fig.7), can be utilized in pulse circuits, in relay circuits or for frequency multiplication, smoothing and stabilizing voltages, spark suppression, etc. By appropriate changes in the composition of the mixture and variation of the fabrication process, one can obtain nonlinear resistors suitable for different voltage ranges including voltages lower than those indicated in Fig.5. The general appearance of a number of miniature nonlinear resistors is shown in the photograph of Fig.9.

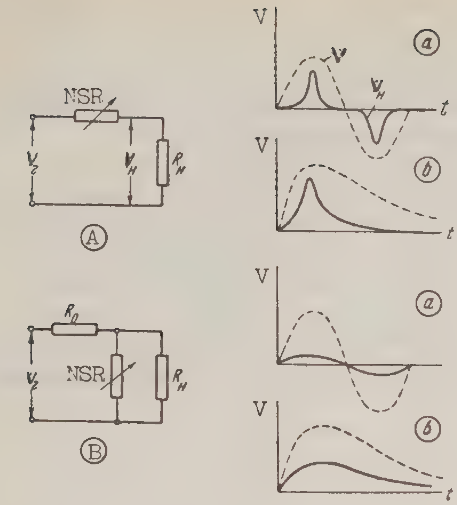

Fig.7. Series (A) and parallel (B) connection of a nonlinear semiconductor resistor (NSR) in a circuit with a load R_H. Applied voltage: a) sinusoidal, b) pulse.

3. Ignitron electrodes

Ignitrons are a form of mercury-vapor rectifiers. They differ from ordinary mercury-vapor rectifiers in that the cathode spot on the mercury surface, which is the source of free electrons, is produced in them periodically by current pulses passing through a semiconductor electrode called the igniter. The results of development work on integral formed, high mechanical strength igniters has been described earlier by one of the present authors[11]; two types of igniter electrodes are shown in Fig.10.

The semiconductor material used for ignitron electrodes must meet the following requirements: it must have a resistivity of 1-10 ohm·cm, must not be wetted by mercury, should not impair the vacuum in the rectifier envelope, should not be affected by temperatures up to 600-700° and must have a mechanical bending strength over 100 kg/cm^2 so that the tip of the igniter will not be broken off by impact of the splashing mercury during transportation and operation.

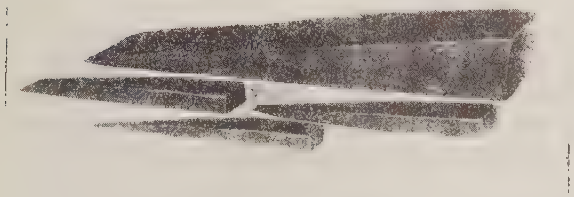

Fig.8. Waveguide absorbing loads (attenuators) for different wavelengths.

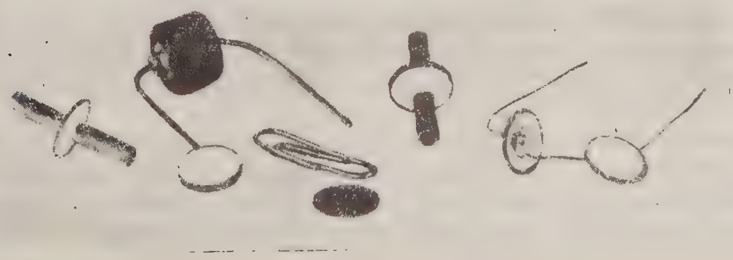

Fig.9. Miniature nonlinear semiconductor resistors.

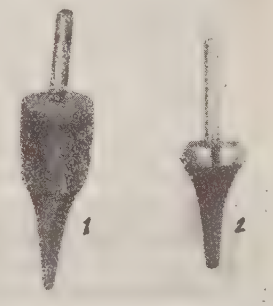

Fig.10. Two types of semiconductor igniter electrodes: 1) with pressed in molybdenum holder, 2) with crown type contacts.

The basic electric parameters of an igniter are the voltage and current at the instant of ignition.

The igniters now in mass production are characterized by an average ignition voltage of up to 100 v and a current value of 4 amp. The igniters are compressed of powdered silicon carbide and crystalline silicon with a bakelite binder. The compressed igniters are covered with a special coating and sintered at a high temperature for 1 min. The ignition parameters of the igniters can be controlled to some extent by changing the roughness of the surface by ion bombardment. This is feasible because the ignition mechanism, as has been shown by a number of investigators[11-14], is due to field emission from the mercury cathode in the microgaps between the bulk of the igniter and the surrounding mercury. Ignition occurs when the electric field intensity in the transition layer (Fig.11) attains a certain magnitude. Obviously, the ignition current density for a semiconductor igniter with a resistivity ρ_s will be given by

$$E = \rho_s \cdot j.$$

The ignition current will be

$$I = j \cdot s,$$

where S is the area of the teeth on the annular layer of the electrode near the surface of the mercury (Fig.11) through which the current from the igniter flows into the mercury. In view of the fact that $\rho_s \gg \rho_{Hg}$, the height of the transition layer Δh will be small.

By changing the roughness of the surface, we can decrease (or increase) the effective area S and, consequently, the magnitude of the ignition current.

The ignition voltage is

$$V = V_b + V_t = IR_b + V_t,$$

where V_b is the voltage drop in the body of the igniter, V_t is the voltage drop over the transition layer and R_b is the resistance of the body of the igniter. By decreasing the magnitude of the ignition current, we reduced the voltage drop in the igniter rod and thereby the effective ignition voltage.

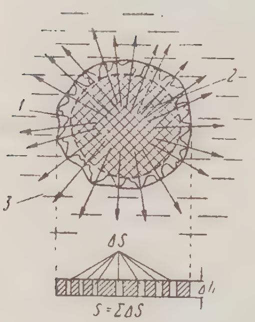

Fig.11. Flow of current from igniter to mercury: 1) toothed transition layer, 2) body of igniter, 3) mercury.

Abroad ignitron electrodes are also being made of boron carbide and beryllium oxide[14].

Conclusions

1. A number of different electric and electronic devices are being made of silicon carbide: lightning protectors, nonlinear resistors for use in automatic control equipment, Silit heaters, temperature compensators, ignitron electrodes and waveguide attenuators.

2. In view of the increasing use of silicon carbide for the manufacture of such electric and electronic devices, measures should be taken to have the plants producing SiC (Zaporozhie and Taskent Plants) put out a certain amount of silicon carbide meeting technical specifications set up with such applications in view (i.e., SiC powders having a certain resistivity and other electric parameters).

3. Silicon carbide has many interesting properties (nonlinearity, good thermal stability, hardness and strength of single crystals, etc.) in view of which it merits further study and research with a view to expanding its applications

in the electrical engineering field.

"V.I.Ul'ianov (Lenin)" Leningrad Electrotechnical Institute

References

1. Tekhnika izmerenii na santimetrovykh volnakh (Measurement techniques at microwave frequencies), edited by G.A.Remez, Vol.1, M., 1949.
2. G.K.Teal, M.D.Rigterink & G.K.Froch, Tr.AIEE, 67, pt.1, 419 (1948).
3. G.K.Teal, El.En.S., 8, 754 (1948).
4. A.Sommerfeld, Optik, 4, 33 (1950).
5. M.S.Teszner, P.Seguin & I.Millet, Ann.Tetecom., 8, 271 (1953).
6. V.I.Pruzhnina-Granovskaia, Elektrichestvo (Electricity), 7, 32 (1945).
7. N.P.Bogoroditskii & E.F.Vorobei, Zhur.tekh.fiz., 24, 811 (1954).
8. F.A.Schwertz & I.I.Mazenko, J.Appl.Phys., 24, 8, 1015 (1953).
9. A.A.Gorev & A.N.Piriazeva, Zhur.tekh.fiz., 21, 1469 (1951).
10. M.S.Teszner, Bull.Soc.Franc.Electr., 4, 40 (1954).
11. V.V.Pasnykov, Zhur.tekh.fiz., 25, No.3 (1955).
12. I.Slepian & L.Ludwig, Tr.AIEE, 52, 693 (1933).
13. E.F.Arnott, J.Appl.Phys., 12, 660 (1941).
14. W.W.Rigrod, J.Appl.Phys., 22, 787 (1951).

BULLETIN of the Academy of Sciences of the USSR - Physical Series
Vol. 20, No. 12(b) - Transactions of the Eighth All-Union Conference on Semiconductors

TABLE OF CONTENTS

Section on Electric and Thermal Properties of Semiconductors

	Page	
	Orig.	Trans.
Thermal equilibrium of electrons on surface and volume levels in a semiconductor - V.E.Lashkarev	1469	1347
Thermoelectric effects in semiconductors with non-equilibrium current-carrier concentrations - Ia.Tauts	1479	1357
On the induction of a photoelectromotive force in an illuminated semiconductor in an inhomogeneous magnetic field - Ia.Tauts	1484	1361
Structure and electrical properties of indium antimonide in thin layers - I.D.Konozenko & S.D.Mikhnovskii	1486	1363
Investigation of the Peltier effect and thermoelectromotive forces in germanium - M.Stenbeck & P.I.Baranskii	1491	1368
Electric properties of some compounds of elements in the third and fifth groups of the periodic table (InAs and InSb) - D.N.Nasledov & A.Iu.Khalilov	1494	1370
New glass-like semiconductors - N.A.Goriunova & B.A.Kolomiets	1496	1372
Semiconductor properties of magnesium-bismuth alloys - A.K.Kikoin & G.D.Fedorov	1501	1377
Electrical properties of manganese-germanium alloys - I.G.Fakidov, N.P.Grazhdankina & V.N.Novogrudskii	1509	1384
Thermomagnetic effects in semiconductors - Kh.I.Amirkhanov, R.I.Bashirov, A.Z.Daibov & I.M.Tsidil'kovskii	1519	1392
A new form of thermal acceptors in germanium - V.A.Zhidkov & V.E.Lashkarev	1521	1394
Diffusion of antimony and zinc from the vapor phase into germanium - V.E.Kosenko	1526	1399
Thermomechanical effects in thin semiconductor layers - I.G.Nekrashevich	1533	1405

Temperature dependence of the electric conductivity of organic semiconductors - A.T.Vartanian 1541 1412

Dependence of the carrier mobility in germanium on the concentration of antimony and phosphorus - P.I.Baranskii 1548 1419

Concerning the theory of the electric strength of germanium and silicon - V.A.Chuenkov 1550 1421

Electron density distribution in and electric conductivity of cadmium sulfide crystals - Iu.N.Shuvalov 1553 1424

An attempt to determine the temperature rise of current carriers produced by an electric field in germanium - M.Stenbeck 1560 1430

Formation of vacancies in a crystal lattice - N.P.Kalabukhov 1563 1433

Preparation of phosphors by recrystallization and electron migration - Z.D'iulai 1569 1438

Electric properties and applications of silicon carbide - N.P.Bogoroditskii, V.V.Pasnykov, G.F.Kholuianov & D.A.Ias'kov 1571 1440

Translated in 1957 by
Columbia Technical Translations
5 Vermont Ave., White Plains, N.Y.

Summary of the contents of Volume 20

of the

Bulletin of the USSR Academy of Sciences - Physical Series

The issues of Volume 20 of the Bulletin comprise the transactions of the following All-Union scientific conferences and departmental meetings:

	Issue Nos.	First page	T of C page
Physics of cosmic rays (con't from Vol.19)	1	1	147
Semiconductors (Meeting of Phys.-Math.Dept.)	1	52	147
X-ray spectroscopy	1	97	147
Piezoelectricity	2	149	257
Nuclear spectroscopy (β- & γ-spectroscopy, decay schemes, lifetimes, instruments)	3	259	343
Luminescence (molecular luminescence and luminescence analysis)	4	345	463
	5	465	553
Applications of x-rays to the investigation of materials (structure of metals)	6	555	657
	7	659	779
Nuclear spectroscopy	8	781	879
Cathode electronics (characteristics of cathode materials, secondary and field emission, work functions)	9	881	973
	10	975	1089
Magnetic radio spectroscopy (para- and ferromagnetic resonance; ferrites)	11	1091	1241
Nuclear spectroscopy	12a	1243	1343
Semiconductors (Section on Electric and Thermal Properties)	12b	1345	1449

The transactions of the Eighth All-Union Conference on Semiconductors will be continued in Vol.21, Nos. 1 & 2.

Tables of contents of the individual issues - free on request.

Single issues - $20
Volume/year - $215

- 1957 -
Columbia Technical Translations
5 Vermont Ave., White Plains, N.Y.